FROM TURBO-MACHINES TO SOLAR CHIMNEYS

by

Theodor W. von Backström

Dissertation presented for the degree of Doctor in Engineering in the Faculty of Engineering at Stellenbosch University

Department of Mechanical and Mechatronic Engineering,
Stellenbosch University,
Private Bag X1, Matieland 7602, South Africa.

Promoter: Prof. T.M. Harms

December 2012

Declaration

By submitting this dissertation electronically, I declare that the entirety of the work contained therein is my own, original work, that I am the sole author thereof (save to the extent explicitly otherwise stated), that reproduction and publication thereof by Stellenbosch University will not infringe any third party rights and that I have not previously in its entirety or in part submitted it for obtaining any qualification.

Date: .....

Abstract

FROM TURBO-MACHINES TO SOLAR CHIMNEYS

T.W. von Backström

Department of Mechanical and Mechatronic Engineering,
Stellenbosch University,
Private Bag X1, Matieland 7602, South Africa.

Dissertation: DEng

December 2012

This dissertation is basically a summary, with some interpretation, of published research by the author. The scope is limited to the fields of turbo-machinery, computational fluid dynamics and solar chimney power plants.

The main contribution in the field of turbo-machinery in general is in the development of a through-flow method that automatically satisfies mass conservation. Concerning fan design, the contributions are the realization of the importance of the exit kinetic energy in the determination of the efficiency of rotor-only axial flow fans, and the quantification of the effect of off-axis inflow into cooling system fans on their performance. In the field of centrifugal fans and compressors an original, unifying model for the prediction of slip factor was developed. To investigate accident scenarios in closed cycle gas turbine nuclear reactors, all possible operational modes of multi-stage axial compressor operation caused by flow and rotation direction were investigated experimentally and computationally. Spanning the fields of turbo-machinery and solar chimneys, the basic theory of solar chimney turbines was developed, showing that high turbine efficiency was possible.

In the field of solar chimneys, an original thermodynamic approach was developed to predict the main relationships that govern solar chimney performance, and to solve the through-flow equations for non-ideal systems with losses. Equations for the accurate determination of all the thermodynamic variables in a solar chimney as dependent on chimney height, wall friction, additional losses, internal drag and area change were derived and solved. Coefficients of wall friction, bracing wheel loss and exit kinetic energy were determined experimentally, and empirical equations were developed to predict the loss coefficient of the collector to turbine transition section and and the turbine inlet flow angle. A simple power law approach allowed the calculation of the optimal turbine pressure drop in solar chimney power plants. A comparison of two sets of equations used to calculate the heat fluxes into, inside and leaving the solar collector, resulted in similar air temperature rises in the collector, and similar produced power. It turned out however that the optimal flow for minimal turbine pressure drop was dependent on the heat transfer models.

Investigation of the performance of various solar chimney turbo-generator layouts using analytical models and optimisation techniques showed that the optimal number of turbines varies with plant size, but the individual turbine size, the number of blades and even the efficiency remains close to constant. It was found that the cost of a turbo-generator system, however, varies significantly with size. A joint paper with several German universities and institutions did a comparative cost analysis of solar chimney power plants.

Uittreksel

VAN TURBOMASJIENE TOT SONSKOORSTENE

T.W. von Backström

Departement Meganiese en Megatroniese Ingenieurswese,
Universiteit van Stellenbosch,
Privaatsak X1, Matieland 7602, Suid Afrika.

Proefskrif: DIng

Desember 2012

Hierdie verhandeling is basies ’n opsomming, met interpretasie, van gepubliseerde navorsing deur die outeur. Die omvang is beperk tot die gebiede van turbomasjinerie, berekeningsvloeidinamika en sonskoorsteenkragstasies.

Die hoof bydrae op die gebied van turbomasjinerie in die algemeen is in die ontwikkeling van ’n deurvloeimetode wat outomaties massabehoud bevredig. Wat waaierontwerp betref is die bydrae die besef van die belangrikheid van die uitlaat kinetiese energie in die bepaling van waaierbenuttingsgraad, en die kwantifisering van die effek van af-as invloei in verkoelingswaaiers op hulle gedrag. Op die gebied van sentrifugaalwaaiers en -kompressors is ’n oorspronklike, samevattende model vir die voorspelling van glipfaktor ontwikkel. Om ongeluk-scenario’s in geslote kringloop gasturbine kenreaktors te ondersoek is al die moontlike werksmodusse veroorsaak deur vloei en rotasie rigting van ’n multistadium aksiaalkompressor eksperimenteel en numeries ondersoek. As brug tussen turbomasjinerie en sonskoorstene is die basiese teorie van sonskoorsteenturbines ontwikkel met die aanduiding dat hoë turbine benuttingsgraad moontlik is.

Op die gebied van sonskoorstene is ’n oorspronklike termodinamies benadering ontwikkel om die hoofverwantskappe te voorspel wat sonskoorsteen gedrag bepaal, en om die deurvloei vergelykings op te los vir nie-ideale stelsels met verliese. Vergelykings vir die akkurate bepaling van al die termodinamiese veranderlikes in ’n sonskoorsteen soos afhanklik van skoorsteenhoogte, wandwrywing, bykomstige verliese, interne sleur en oppervlakte verandering is afgelei en opgelos. Koëffisiënte vir wandwrywing, verstywingswiel-verlies en uitlaat kinetiese energie is eksperimenteel bepaal, en empiriese vergelykings is ontwikkel om die verlieskoëffisiënt van die kollektor-tot-skoorsteen oorgang en die turbine inlaatvloeihoek te bepaal. ’n Eenvoudige magswet benadering het dit mootlik gemaak om die optimum turbine-drukval in sonskoorsteen aanlegte te bepaal. ’n Verglyking van twee stelle vergelykings om warmtevloede in, binne en uit die sonkollektor te bereken het gelei na soortgelyke temperatuurstygings en gelewerde drywing. Die optimale vloei vir maksimum drywing was egter afhanklik van die warmteoordrag modelle.

Ondersoek van die gedrag van verskeie turbo-generator uitlegte, deur gebruik van analitiese modelle en optimeringstegnieke het getoon dat die optimale aantal turbines wissel met aanleg grootte, maar die individuele turbine grootte, die aantal lemme en selfs die benuttingsgraad bly feitlik konstant. Daar is egter gevind dat die koste van ’n turbogenerator stelsel beduidend wissel met grootte. ’n Gesamentlike artikel met verskeie Duitse universiteite en instansies het ’n vergelykende koste analise van son-skoorstene gedoen.

Acknowledgements

The work presented in this dissertation would not have been possible without the guidance, discussions, co-operation, help and hard work of many colleagues, academic and non-academic, and especially of MEng and PhD students. A special word of thanks is due to colleagues Paul Erens and Anton Basson who led the Departement for extended periods, and to Cobus and Ferdi Zietsman who took care of the laboratories.

Former students and later colleagues Thomas Harms and Gerrie Thiart were my comrades in exploring computational fluid mechanics. My PhD supervisor and later colleague, Prof. Detlev Kröger set the scene for much of my research and often challenged me to solve specific problems. I am still learning from him. I also wish to acknowledge the contributions to published papers made by colleagues in other departments: Prieur du Plessis and Marius Sinclair of Applied Mathematics, and Johan Buys of Mathematics.

Thomas Harms, Gerrie Thiart, Wolf Stinnes, Johan van der Spuy, Carl Kirstein, Rene Heise, Ant Gannon, Tom Fluri, Marco Bernardes and Andrew Gill were the major, direct contributors to the papers presented in this submission.

Major funders of my research were Armscor, the National Research Foundation, the Volkswagen Stiftung and the Department of Trade and Industry. I thank the Department of Mechanical and Mechatronic Engineering who supported me financially while completing this submission, and the University of Stellenbosch who allowed me to spend sabbaticals at Cambridge University, The Pennsylvania State University and the Naval Postgraduate School in California.

Lastly I would like to thank Carien Janse van Rensburg who translated the manuscript into LaTeX while learning how to use it, and Danie Els who made this possible.

Dedications

To Mari,

We shall not cease from exploration, and the end of all our exploring will be to arrive where we started and know the place for the first time. *T. S. Eliot*

Contents

List of Figures

Nomenclature

List of symbols

Symbol	Meaning	Units	Ref.	Page
A	constant, chimney flow area	m^2	(2.2)	9
C_T	torque coefficient	–	Fig 2.5	8
c	blade length	m	Fig 2.3	6
c	velocity	m/s	(2.1)	9
c	isentropic compression temperature ratio	–	(3.8)	21
c_p	specific heat at constant pressure	J/kg·K	(3.2)	20
eta	fan efficiency	–	Fig 2.7	11
F_ν	function of ν		(2.6)	10
g	gravitational acceleration	m/s^2	(3.1)	20
H	stagnation enthalpy	J/kg	(3.1)	20
H_D	collector deck height divided by chimney diameter	–	(3.21)	28
K	turbine constant	–	Fig 3.10	34
L	friction and minor loss variable	–	(3.14)	25
M	Mach number of flow in chimney	–	(3.14)	25
m	exponent in pressure potential power law	–	(3.23)	30
$\dot{m}$	mass flow	kg/s	(3.4)	20
n	exponent in loss chimney loss power law	–	(3.23)	30
P	power	W	(3.4)	20
P^*	specific power	–	(3.4)	20
p	pressure	Pa	(2.1)	9
p_p	pressure potential	Pa	(3.6)	21
R	gas constant, turbine degree of reaction	J/kg·K	(3.15)	25
R_R	blade leading-to-trailing edge ratio	–	Fig 2.3	6
r	radius	m	(2.1)	9
s	blade spacing at outer radius	m	Fig 2.3	6
T	temperature	K	(3.2)	20
t	cycle temperature ratio	–	(3.10)	22
U	rotor blade speed	m/s	Fig 3.9	33
U_0	rotor blade tip speed	m/s	(2.4)	10

Symbol	Meaning	Units	Ref.	Page
V	absolute velocity	m/s	Fig 3.9	33
$V_{ch,\max}$	maximum velocity in chimney	m/s	(3.3)	20
X	ratio of turbine pressure drop to pressure potential	–	(3.23)	30
Z	number of blades	–	Fig 2.3	6
z	altitude	m	(3.1)	20
Subscripts				
ave	average over chimney height	–	(3.18)	26
C	Carnot cycle	–	(3.9)	21
i	section of chimney under consideration	–	(3.13)	25
MFP	maximum fluid power	W	Fig 3.7	31
opt	optimum	–	(3.23)	30
ts	total-to-static	–	(2.3)	10
ts-m	total-to-static (measured)	–	Fig 2.7	11
z	axial	–	(2.1)	9
0	stagnation	–	(2.1)	9
1	condition in external atmosphere at chimney exit	–	(3.1)	20
2	condition at collector inlet	–	(3.1)	20
3	condition at turbine inlet	–	(3.1)	20
4	condition inside chimney at exit	–	(3.1)	20
23	from position 2 to 3	–	(3.5)	20
0, 1, 2, 3	Positions relative to turbine IGV and rotor	–	(3.9)	21
θ	circumferential direction	–	(2.1)	9
Greek Symbols				
α	absolute flow angle	°	Fig 3.9	33
β	blade angle, turbine inlet guide vane setting angle	°	(3.21)	28
β	relative flow angle	°	Fig 3.9	33
γ	specific heat ratio	–	(3.14)	25
Δ	step change in value of variable following Δ	–	(2.4)	10
δ	small step change in value of variable following δ	–	(3.14)	25
η	efficiency	–	(2.3)	10
θ	air flow angle into turbine	°	(3.21)	28
ν	hub-to-tip radius ratio	–	(2.3)	10
ρ	density	kg/m^3	(2.1)	9
ϕ	flow coefficient	–	(2.4)	10
$\phi_{\min}$	minimum possible flow coefficient	–	Fig 3.10	34
ψ	load coefficient	–	(2.4)	10
Ω	Angular velocity	s^{-1}	Fig 2.1	5

Abbreviations

CFD	computational fluid dynamics
IGV	inlet guide vane
PBMR	pebble bed modular (nuclear) reactor
PCU	power conversion unit
PIV	particle imaging velocimetry
SCM	streamline curvature method
SCPP	solar chimney power plant
SRE	single relative eddy
STFM	streamline through-flow method
SU	Stellenbosch University
TFC	through-flow code
Ucor	Uranium Enrichment Corporation

Statement by the author

This submission presents research in areas ranging from turbo-machinery to solar chimney power plants. It is based on a selection of papers contributed to by the author (referred to as Backström) from 1987 to 2012. The objective is to present a cohesive body of work, based on cited papers in peer-reviewed journals. Apart from a few exceptions for the sake of continuity, only cited journal papers relevant to the major themes of the present dissertation have been included.

The main research theme in the turbo-machinery area is the development of analytical models based on insights derived from experimental and numerical data. The solar chimney research themes cover systems models and the determination of the characteristics of subcomponents affecting the operation of solar chimney power plants. The common thread is the interest in sometimes unusual turbo-machines and their applications, with the solar chimney as the most prolific application area in terms of publications.

The submission has five parts:

- A preview, describing in short the main original contributions in the fields of turbo-machines and solar chimney power plants.
- A more detailed discussion starting with gas turbines, fan design limitations, the effect of distorted flow on fan operating characteristics and the use of actuator discs in the numerical modelling of turbo-machines. This is followed by a discussion of the thermodynamic approach to the operation of solar chimneys, the effect of compressibility on the flow through very tall chimneys and the accurate calculation of all the thermodynamic properties of the air in the chimney. System and chimney modelling then sets the boundaries for determining the turbine design point. Ways of finding the optimal turbine design point for maximum instantaneous power are presented, followed by the governing characteristics of solar turbines as determined by inlet guide vane and rotor blade layout. This is then expanded to find the optimal layout and number of turbines in multiple turbine systems as determined by wind turbine engineering and cost considerations.
- A numbered list of endnotes (footnotes, listed after the main text, to avoid cluttering it up) that are referred to in the text by superscript numerals. The list consists of a few of Backström's non-peer reviewed papers, of all relevant theses supervised and co-supervised by him, as well as all papers that do not have him as participating author, but are cited in this submission.
- A list of the peer reviewed journal papers that Backström authored and co-authored, but confined to papers referenced to in this submission. These papers are referenced in the text by numbers in square brackets.

- The complete set of papers mentioned in the previous item above, in electronic format on a CD.

Many papers were co-authored, but where Backström's name is first, he formulated the topic of the paper and wrote it, with the co-author contributions in the form of critical discussion, computer programming, bits of data, equation checking and preparation of figures and tables. Where the students' names are first, the papers are based on their PhD or M-theses. The VGB Powertech paper [1] was a joint effort with equal contributions from all authors and their students.

Theo von Backström

Stellenbosch

August 2012

Chapter

1

Preview

A preview is presented of Backström's research on the theory of turbo-machines and solar chimneys. It is based on the most cited peer reviewed journal articles, authored or co-authored by him from 1987 to 2012 while employed at Stellenbosch University (SU). For the sake of continuity, a few other articles and conference papers are included.

During previous employment at the Atomic Energy Corporation and the Uranium Enrichment Corporation (Ucor) Backström had been involved in uranium enrichment technology, enrichment plant fluid mechanics, computational fluid dynamics (CFD), compressor fluid mechanics and compressor design. Appointment at the Department of Mechanical Engineering of SU led to the opportunity to study and teach graduate level subjects that would feature in later research. Initial research areas were gas turbines, compressors and torque converters, followed by CFD, fans, and solar chimneys.

The exposure to the design of process compressors at Ucor led to later involvement in gas turbine compressor design[1] [2, 3]. An annular dump diffuser for a gas turbine was optimised with Lewis [4]. The aerodynamic design of an axial flow compressor for a gas turbine was done by Backström [2] using commercial through-flow codes (TFCs). The streamline through-flow method (STFM) was developed as an alternative through-flow approach to the industry standard streamline curvature method (SCM) [5, 6]. The optimum arrangement of a set of rotor blades to minimise rotor unbalance was done by mathematical optimisation [7, 8].

For centrifugal impellers the slip factor accounts for the flow deviation from the ideal, blade-aligned direction at the rotor exit. The numerical solution of Busemann[2] for inviscid flow through rotors with logarithmic spiral blades was approximated by Stodola[3] by assuming that each rotor blade passage contains one vortex. Backström, however, developed a new model where the complete impeller contains only vortex [9, 10]. This so-called single relative eddy (SRE) model made it possible to unify all commonly used correlations.

All possible operational modes of axial compressor operation caused by flow and rotation direction were investigated experimentally and computationally by Gill[4] [11]. Torque converter performance was investigated analytically [12], computationally and experimentally [13, 14] , followed by a review paper [15].

The SIMPLEN CFD algorithm of Thiart[5,6] was further developed in his PhD[7] , and subsequently by Harms in his PhD[8] [16–20]. Comparisons between CFD predictions using commercial codes and our own experimental studies served to verify the use of the codes and allowed additional insight into the flow fields. Applications were: solar chimneys [21, 22], helicopters [23, 24] and turbo-machinery [3, 23, 25, 26], [27].

Bruneau[9] did the minimisation of the exit kinetic energy of rotor-only axial fan by using a modified power law tangential velocity distribution [28]. Subsequently an accurate optimal fan exit swirl velocity distribution was found by means of quadratic programming [29]. The significance of this work[10] is that a simple theory was found to predict the maximum efficiency of single rotor fans, as used by Van der Spuy[11] [30].

Regarding air cooled condenser units, the question was how off-axis inflow would affect their performance. Thiart[7] mounted an axial fan in the side wall of a wind tunnel and measured the flow field behind the fan [31, 32]. CFD simulations with an axi-symmetrical code he had developed agreed well with experiments [31–33]. His dissertations was the first of many at Stellenbosch University using the actuator disc-in-CFD method.

Stinnes[12] [34] introduced off-axis inflow into a model axial flow fan by mounting the fan with its axis at angles of up to 45° to the axis of the pipe connecting it to the plenum chamber of a fan test facility. His study, followed by collaborative paper with Hotchkiss[13] [23], ultimately led to the major finding that the static-to-static pressure ratio was independent of inflow angle. Heise[14] also used the actuator disc-in-CFD approach to model the performance of a helicopter fuselage with an internal tail rotor, which would also reduce the infra-red signature of the engine exhaust by mixing fan flow with engine exhaust flow [24, 35].

To better understand solar chimney power plants (SCPPs)s, an air standard thermodynamic cycle analysis was done. Such an analysis assumes efficiencies of 100% for the plant components such as the collector, chimney and turbine, so that the limitations imposed by the thermodynamic cycle itself become clear. Backström saw that the chimney power plant cycle resembles that of a gas turbine [36]. Subsequently Gannon[15] derived an algorithm for the solution of the thermodynamic cycle diagram of a SCPP with losses [37]. Calculated results compared favourably with measurements from the small scale pilot plant at Manzanares in Spain[16]. The performance of a large (200 MW peak power) SCPP was also predicted [37] . Gannon was also the first to show that high turbine efficiencies (of up to 90 % total-to-total) were possible [38]. Meanwhile Backström derived the basic equations determining the characteristics of solar chimney turbines [39] by assuming simple loss models.

To understand the fundamentals of flow through tall chimneys Backström derived equations for the accurate determination of all the thermodynamic variables in a solar chimney as dependent on chimney height, wall friction, additional losses, internal drag and area change [40]. A subsequent compressible flow approach, valid for small Mach numbers [41] led to two equations for the vertical pressure and density distributions in terms of Mach number.

Backström presented coefficients of wall friction, bracing wheel loss and exit kinetic energy in a model chimney, for both ideal non-swirling uniform flow and for swirling distorted flow [42]. At the bottom of a solar chimney housing a single vertical axis

turbine, the air passes radially through a transition section containing the turbine inlet guide vanes (IGVs)that support the chimney and guide the flow entering the turbine. Kirstein[17] [21] developed equations to predict the loss coefficient and turbine inlet flow angle.

Many early papers[18,19,20,21] make the assumption that the turbine in a SCPP will produce maximum instantaneous power for given value of solar irradiation when the pressure drop across the turbine is 2/3 of the available pressure drop across the system. Backström however derived a simple power law model [43], showing that this is an over-simplification. Bernardes [44] compared the methods used to calculate the heat fluxes into, inside and leaving the solar collector, and their effects on solar chimney performance using the correlations of Pretorius[22,23]. The two approaches resulted in similar air temperature rises in the collector, and similar produced power. Bernardes [45] also investigated the performance of two iterative schemes of finding the maximum power operating point of SCPPs. It turned out that the optimal flow for minimal turbine pressure drop was dependent on the heat transfer models investigated by Bernardes [44].

The basic solar chimney turbine selection criteria were outlined by Gannon[15]. The use of correctly shaped chimney base supports as inlet guide vanes (IGVs) reduces the wasted kinetic energy at the turbine exit and allows more energy to be extracted from the flow, resulting in a solar chimney turbine design with a total-to-static efficiency of 80 % and a total-to-total efficiency of about 90 % [38].

Backström presented analytical equations in terms of turbine flow and load coefficient and degree of reaction to express the influence of blade loss coefficients on solar chimney turbine efficiency [39]. Fluri [46] compares the performance of various solar chimney turbo-generator layouts using analytical models and optimisation techniques. Fluri [22] analysed the performance of the power conversion unit (PCU) and its interaction with the plant and compared three configurations from an efficiency and energy yield point of view. The optimal number of turbines varies, but their individual size, the number of blades and even the efficiency of the PCU remains close to constant. It was found that the cost of the PCU, however, varies significantly with size. Two joint papers, one with several German universities and institutions, funded by the Volkswagen Stiftung, did comparative cost analyses of SCPPs [1, 47].

The detailed reviews in the next two chapters introduce and discuss the two main topics in more detail. A few main research areas are defined and their development is discussed primarily to facilitate the logical flow of arguments and of research programs. Since parallel research threads proceeded at the same time the discussion does not strictly follow the progress chronologically.

Chapter

2

Turbo-machines and CFD

2.1 Introduction

Judged by the number of citations, the major direct contributions of Backström research have been in the subject areas of turbo-machinery and solar chimney power plants. These two will be discussed in this and the next chapter. The turbo-machinery chapter presents papers relating to air cooled condenser fans and distorted flow through them, and axial and radial flow compressors. The solar chimney section covers not only solar chimney turbine performance, but also the performance of the collector-to-chimney transition section, the chimney itself and the thermodynamic performance of the solar chimney power plant as a whole. The author was also involved in the development and use of computational fluid dynamics (CFD) computer programs, and in optimisation, leading to the present interest in the combination of optimisation and CFD[24,25].

2.2 Gas turbines

As member of the team that designed and built the first South African gas turbine, Backström[1] was responsible for the aerodynamic design of the axial flow compressor. CFD codes to predict the blade row performance of transonic axial flow compressors were investigated [2, 3]. The experimental optimisation of an annular dump diffuser for a gas turbine was done with Lewis [4], and annular dump diffusers served as the ultimate test case for the CFD code developed in the PhD of Harms[8].

2.3 Compressors

Turbo-machinery through flow codes are used to calculate the meridional velocity profiles during the initial layout and design of compressors and turbines. In combination with blade deflection and loss models [5] they then provide a quick, reliable way of calculating multi-stage compressor performance during the design process. The streamline through-flow method (STFM) [6] was developed as an alternative to the industry stan-

dard streamline curvature method (SCM). It was shown to be more accurate and faster than the SCM, mainly because it is formulated in terms of the stream function [6] which inherently satisfies the continuity equation. The approach employed a mathematical transformation wherein the radial co-ordinate in the compressor was interchanged with the stream function value, so that the stream function value becomes a coordinate and the radial position of the streamline is turned into the dependent variable. Comparisons with analytical solutions showed excellent agreement with analytical solutions using actuator disc theory [6].

A second contribution to compressor theory was in the prediction of the slip factor of radial compressors. The slip factor is a correction factor for the torque or power demand of centrifugal impellers, as dependent on flow deviation at the exit of the rotor blades. It can also be seen as the factor by which the ideal circumferential velocity component at the impeller exit should be multiplied to give the actual average circumferential component there. Busemann[2], as reported by Wiesner[26] did remarkable numerical work (long before computers!) to accurately predict the slip factor for inviscid flow through rotors with logarithmic spiral blades. To facilitate the use of Busemann's data, the results of his computations were summarised in sets of graphs[26], or approximated by simplified equations. The standard simplified approach of estimating the slip factor, used by Stodola[3] and others has been to assume that each of the blade passages of the impeller contains a vortex, counter-rotating at the impeller speed (figure 2.1). These vortices then induce a slip velocity at the impeller exit. Although this approach was presented in many textbooks, the use of two partially overlapping control volumes set a poor example to students.

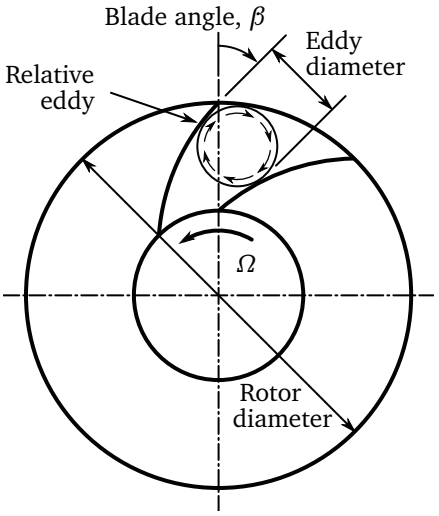

Figure 2.1. Blade passage relative eddy as assumed by Stodola [10]

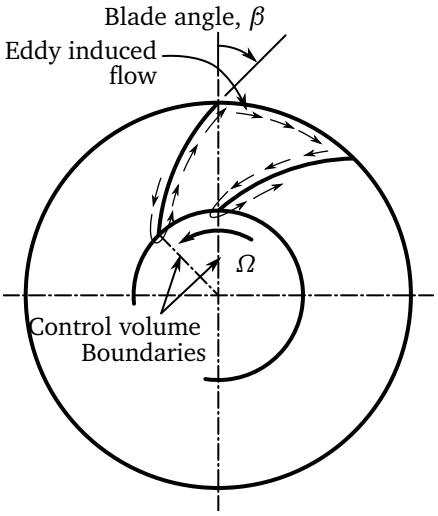

Figure 2.2. Relative flow circulation as assumed with single relative eddy [10]

Careful consideration however led Backström to the realisation that there is in fact only one, complex, vortex centered in each impeller, independent of the number of impeller blade passages. This vortex is multi-lobed (daisy-shaped), with lobes (leaves) extending into each flow passage of the impeller [9] (figure 2.2).

Unlike previous models this so-called single relative eddy (SRE) model exhibited the correct asymptotic behaviour for extremely low or high blade numbers, extreme blade angles and blade row inlet to exit diameter ratios, and made it possible to correlate the various industry-standard methods and unify five different commonly used correlations [9, 10]. Results from this approach turned out to agree with data collected by Wiesner[26] at least as well as his own empirical curve fits. A subsequent paper presented better approximations for the data of Busemann, and a single equation representing the data of Busemann for all blade numbers and blade angles to within about 1% [10] (figure 2.3). (This paper was unfortunately marred by typing errors in the published equations). A final paper presents a slightly less accurate, practical version for use by students [48].

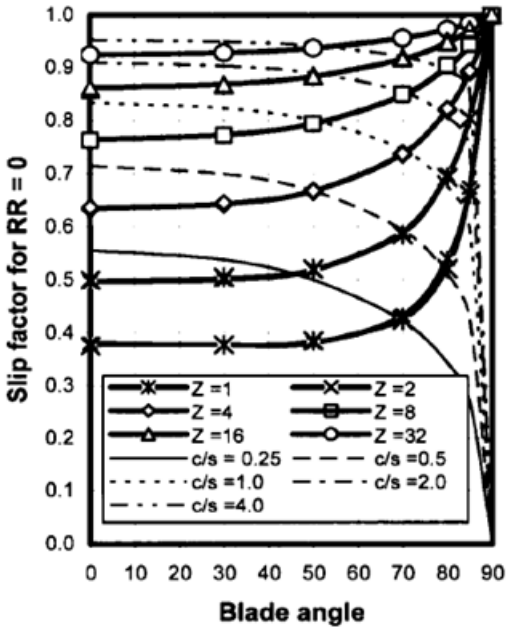

Figure 2.3. Comparison of SRE model with Busemann numerical results [45]

Returning to axial compressors, the initial layout of the pebble bed modular (nuclear) reactor (PBMR) was essentially that of a three-shaft closed cycle nuclear powered gas turbine using helium as the working fluid. The three-shaft layout posed unique accident scenarios for which compressor performance under every conceivable operating condition should be understood. The operating conditions included every possible combination of positive and negative flow, pressure difference and rotation direction affecting a multi-stage compressor. This was investigated experimentally and computationally with PhD student Gill[4],who measured pressure and velocity by means of five-hole pneumatic probes and hot-film probes and simulated the flow through the blade rows with CFD. This was the first detailed description of multi-stage compressor operation in all its possible operational modes. The main finding was that there are in fact six modes of operation [11] (figure 2.4).

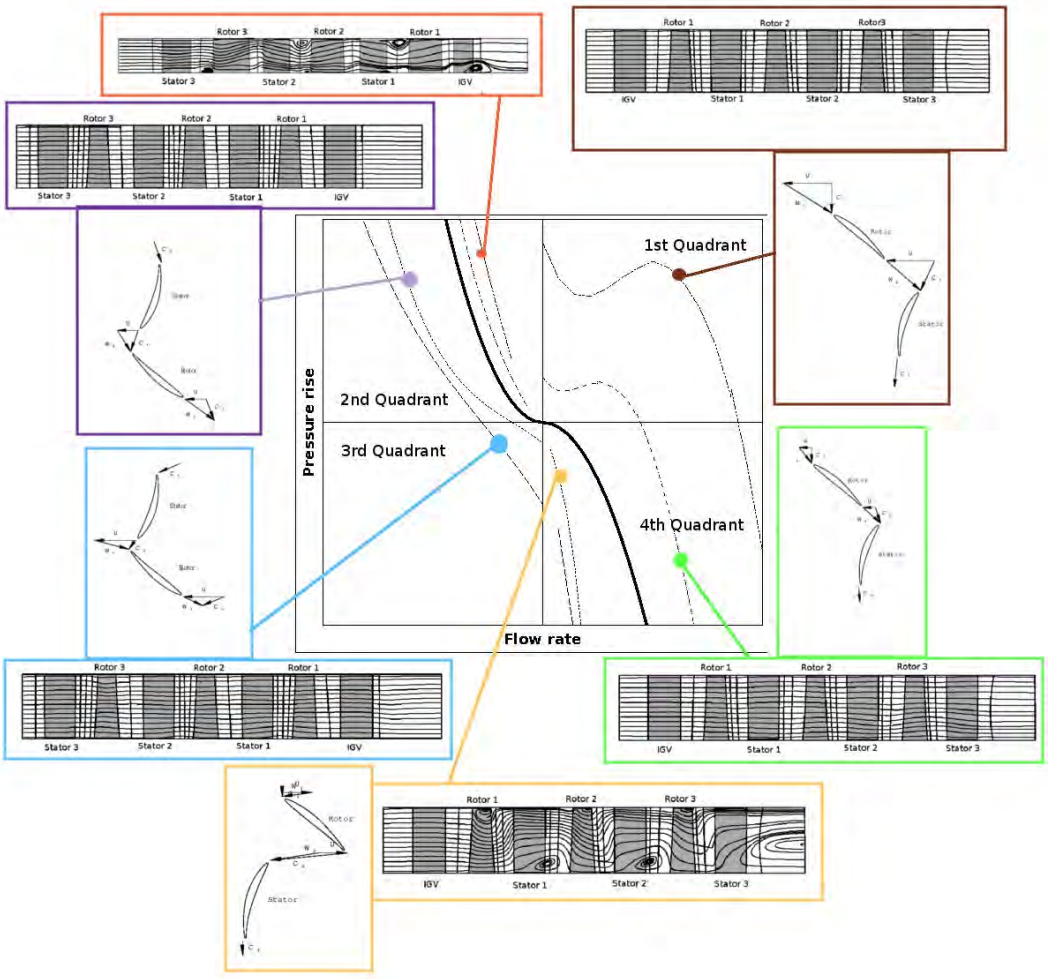

Figure 2.4. Generic four quadrant compressor map[4]

The second and fourth quadrants each house two operating modes and these modes are separated by the zero rotation resistance lines for reversed and normal flow, respectively. Flow structures in the various operating modes were also described. The transition areas between the modes are also presented and cleared up in a diagram.

2.4 Torque converters

The objective of the torque converter work was to develop simple models to simulate the performance of complete torque converters [12], but detailed experimental and computational investigations of the performance of certain parts were also reported, [13, 14]. The culmination of the work was the review paper with Lakshminarayana [15] during a sabbatical at The Pennsylvania State University.

2.5 Computational Fluid Dynamics

Thiart had independently developed the so called SIMPLEN CFD algorithm for determining finite volume interface velocities accurately[5,6]. This approach was further developed in his PhD[7], where he applied it to distorted flow through fans [31, 33]. This was a pioneering application of the actuator disc-in-CFD method for modelling distorted flow through fans. It was the first of many actuator disc-in-CFD studies at SU.

Subsequent development of the SIMPLEN algorithm was done by Harms in his PhD[8] [16–20]. He recommended a proposed treatment of non-orthogonality as a universal method for complex boundary finite volume flow analysis, applicable to any interpolation scheme. Comparison to published experimental data confirmed the feasibility of the method. Subsequent studies involving CFD used commercial codes to gain insight into the structure of flow fields, usually in conjunction with experimental work or experimental data from the literature to verify the code and turbulence model for the particular application. Applications were: flow through transonic axial flow compressor rotors [2, 3] solar chimneys [21], helicopters [23, 24] (figure 2.5), cooling systems and fans [23, 25, 26], wind[27] and ocean current turbines[24].

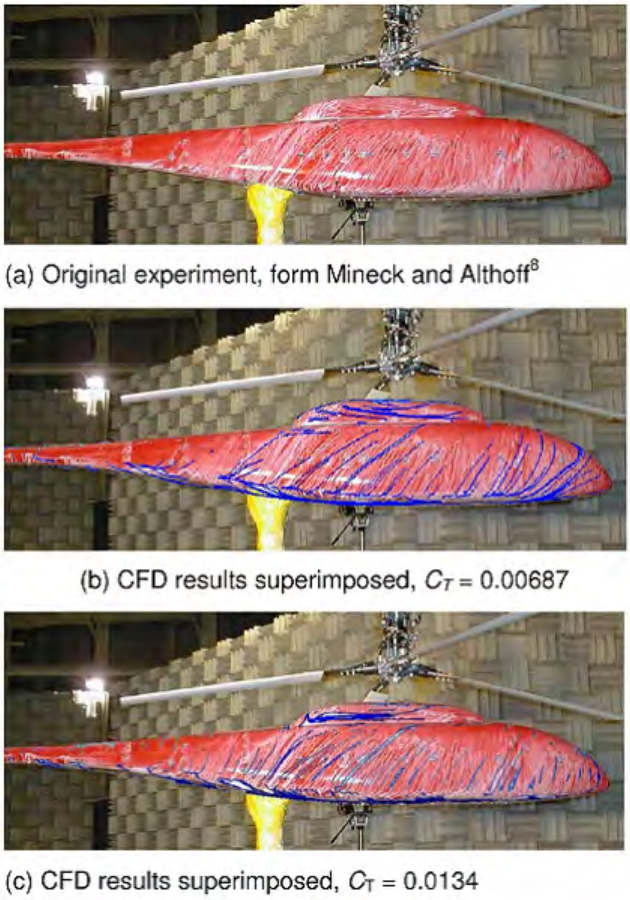

(a) Original experiment, form Mineck and Althoff[8]

(b) CFD results superimposed, $C_T = 0.00687$

(c) CFD results superimposed, $C_T = 0.0134$

Figure 2.5. Comparison of computational (blue) and experimental (white) streak lines on a helicopter fuselage [1]

2.6 Fan performance

In a fan or compressor the objective is to generate a required pressure difference across the machine. This is achieved by changing the angular momentum of the fluid as it passes through successive blade rows. The different circumferential velocity distributions in front of and behind the blade rows imply that the static pressure distributions in front of and behind the blade row are not necessarily similar, so that the axial gradient of the static pressure across a blade row of axial flow turbo machines varies with radial position in the blade disc. This then results in uneven axial acceleration across blade rows, causing the shape of the axial velocity profile to change across the row. The arguments above show that the axial velocity distribution is dependent on the circumferential velocity distribution.

In a rotor-only fan where the flow enters axially, it will leave with some swirl, except in the trivial case when the machine does no work. To minimise kinetic energy leaving the fan, which is equivalent to a loss, the sum of the kinetic energies associated with the axial and circumferential velocity components must be minimised. In the simple radial equilibrium approach, radial velocity components are ignored and the relationship between the radial gradients of the stagnation pressure, p_0 and the axial and circumferential velocity components, c_z and c_θ is given by:

$$\frac{1}{\rho}\frac{dp_0}{dr} = c_z\frac{dc_z}{dr} + \frac{c_\theta}{r}\frac{d(r\,c_\theta)}{dr} \tag{2.1}$$

The first research objective was to find the optimal circumferential velocity distribution at the exit of a rotor-only axial fan, so that the related shapes of the axial and circumferential velocity profiles would result in the minimum kinetic energy flux at the fan exit, while assuming that the total pressure, p_0 is independent of radius. This was done an approximate way in the design of the so-called B-fans in the master's thesis of Bruneau[9] (figure 2.6).

The design procedure was not initially published due to an understanding with a fan company who partially sponsored the work, but the thesis was not restricted and has been cited six times. A paper describing the design procedure has recently been written by Louw[28].

Bruneau[9] assumed circumferential velocity distributions behind the fan of the form:

$$c_\theta = Ar^n \tag{2.2}$$

where A is a constant coefficient and n is an exponent that is equal to -1 for a free vortex design, where the circumferential velocity varies inversely with radius, resulting in a uniform axial velocity.

He found that a value of $n = -0.9$ resulted in the minimum exit kinetic energy. The fan he designed had a relatively large hub-to-tip radius ratio of 0.4 (compared to 0.15 for a typical comparative fan) to prevent back flow at the hub, and the vortex distribution was modified near the hub to minimise the swirl leaving the rotor.

The next step was to abandon the artificial constraint of assuming a power law exit swirl velocity distribution and finding the optimal swirl distribution by means of quadratic programming [29]. The only losses considered in this analysis were those

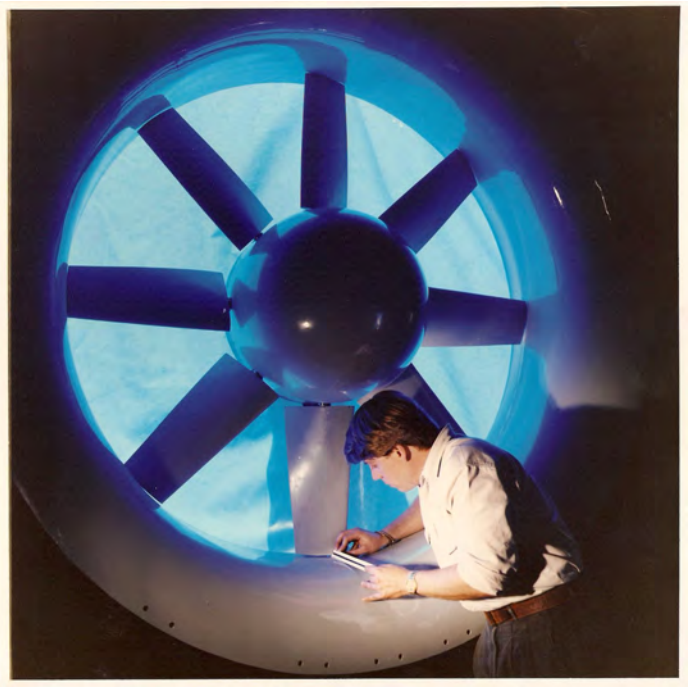

Figure 2.6. B-Fan picture (with Bruneau)

associated with the exit kinetic energy. Now that the "best" solution was found, two questions arose: i) how good was the "best" compared to standard assumptions such as the free-vortex assumption, and ii) how would it perform if applied practically.

The free-vortex assumption of $n = -1.0$ results in a uniform axial velocity profile, as seen from equation (2.2), and Backström[10] showed that the ideal free vortex fan static (or total-to-static) fan efficiency is:

$$\eta_{ts} = 1 - \frac{\phi^2}{\psi} - \frac{1}{2}\frac{\psi \ln \nu}{(\nu^2 - 1)} \tag{2.3}$$

where ν is the hub-to-tip radius ratio of the fan, and ψ and ϕ are the total-to-total load coefficient and the flow coefficient, respectively, given by:

$$\psi = \frac{\Delta p_0}{\rho} \Big/ \frac{{U_0}^2}{2}, \qquad \phi = \frac{c_z}{U_0} \tag{2.4}$$

Here Δp_0 is the total-to-total pressure rise, U_0 is the blade tip speed, and C_z is the axial velocity through the fan.

When the required total-to-static load coefficient, ψ_{ts} is known, the total-to-total load coefficient can be found from:

$$\psi = \frac{1 - \sqrt{1 - 4F_\nu \left(\psi_{ts} + \phi^2\right)}}{2F_\nu} \tag{2.5}$$

Here F_ν is given by:

$$F_\nu = \frac{\ln(\nu)}{2(\nu^2 - 1)} \tag{2.6}$$

According to the analysis[10], optimised swirl distributions could theoretically result in large reductions in exit kinetic energy efflux compared to free vortex designs. Closer inspection however revealed that these large loss reductions were possible only in highly loaded, low hub-tip-ratio fans. In practice however, the maximum fan load coefficient is constrained by two limitations:

- The flow should not be turned beyond the axial relative to the rotor, requiring: $\psi < 2\nu^2$
- Exit swirl velocity at the hub should not exceed the axial velocity, requiring: $\psi < 2\nu\phi$

It is then shown that even at this extreme condition the optimised and free vortex loss coefficients agree to within 1.8 percentage points, with the free vortex prediction being pessimistic. The theory was applied to two commercial fans and it was found that the measured efficiencies were about 0.9 times the values of those predicted with the free vortex theory (figure 2.7). The 10 % margin is understandable since the blade profile and tip clearance losses were ignored in the theory. It was shown that the theory could also be applied to rotor-only turbines. The same theory, without the swirl losses could be applied to fans or turbines with zero exit rotation, which could be achieved in practice by the introduction of inlet guide vanes or exit stators [46]. The significance of this work is that a simple theory was found to predict the maximum efficiency of single rotor fans or turbines. It also confirmed the suspicion that for single rotor fans and turbines the exit kinetic energy losses are by far the dominant ones. This finding is very useful in deciding whether a particular fan design can be improved significantly by changing blade profiles or tip clearances.

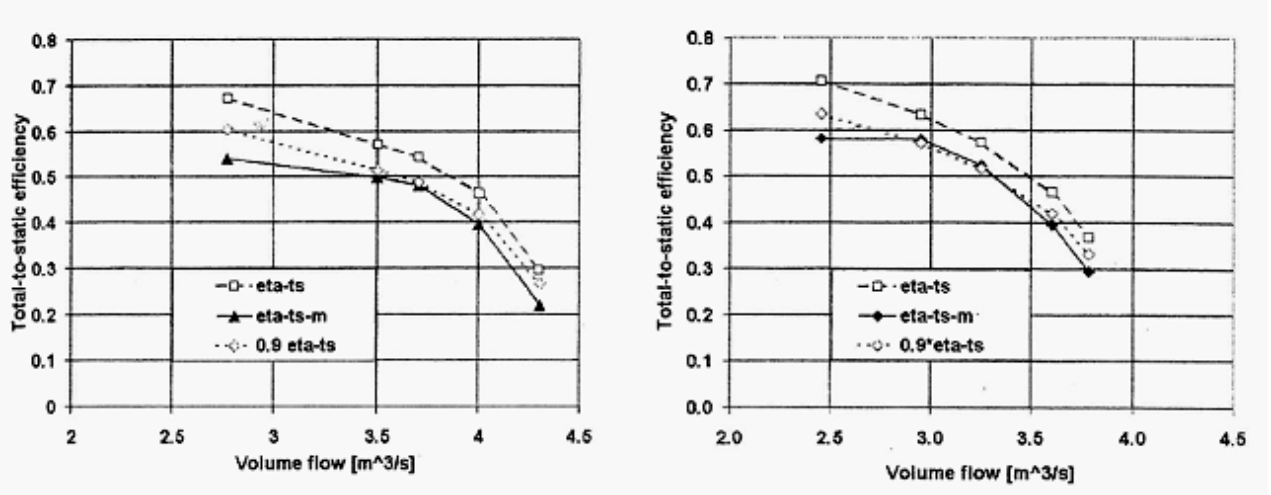

Figure 2.7. Comparison between experimental fan and theoretical fan efficiency characteristics for 7 and 14 bladed fans

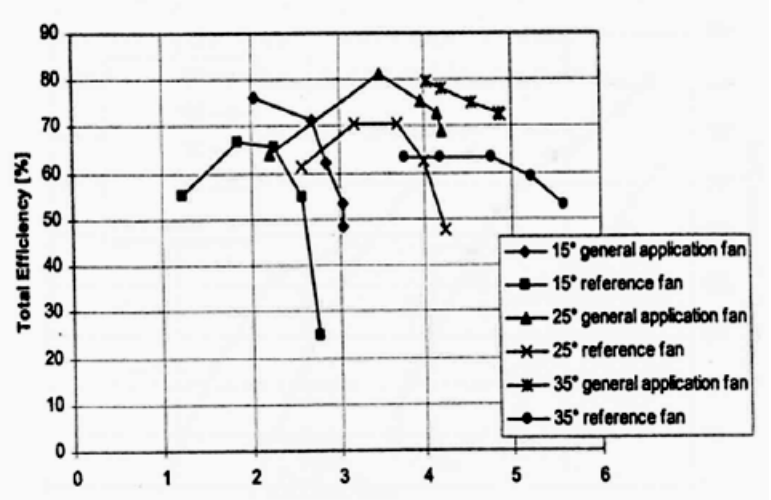

Figure 2.8. Comparison of fan performance [30]

A swirl distribution optimised for minimum exit kinetic energy losses was utilised by Van der Spuy[11] in the design of a series of industrial axial flow fans. They were more efficient (by about 10 %) (figure 2.8) and quieter by 2 dB to 3 dB than the benchmark industrial fans [30]. This supported the proposed design approach as a feasible one.

2.6.1 Fans with cross flow at inlet

In air-cooled power plants, vertical axis axial flow fans are often used to blow air upwards through air cooled condensers arranged in large arrays of for example 6×48 units. Since the air drawn in below the fans enters at the open edges of the array platforms, there is a cross wind, which may be enhanced by atmospheric winds, flowing below the fans closer to the edges. The question was what the effect of cross-flow on the performance of axial flow fans would be.

To simulate the flow into the fans at the edges of large air cooled condensers, Thiart[7] mounted a fan in the side wall of a wind tunnel, with the cross-flow velocity past the fan equal to the velocity through the fan. It was found that "the blade loading is very much non-uniform, and that the stresses in a blade can vary considerably during a revolution. The non-dimensionalized distributions of thrust and torque over the fan blade area, show maxima of more than twice their mean values" [31]. Stinnes[12] introduced off-axis inflow into an axial flow fan by mounting the fan with its axis at an angle to the axis of the pipe connecting it to the plenum chamber of a large fan test facility (figure 2.9).

He effectively investigated the effect of off-axis pipe flow into axial flow fans on their fan static pressure and power consumption.

Some of the important findings reported by Stinnes [34] regarding off-axis inflow were:

- The decrement in fan static pressure is equal to the dynamic pressure based on the cross flow velocity component. This was an original insight of Backström.

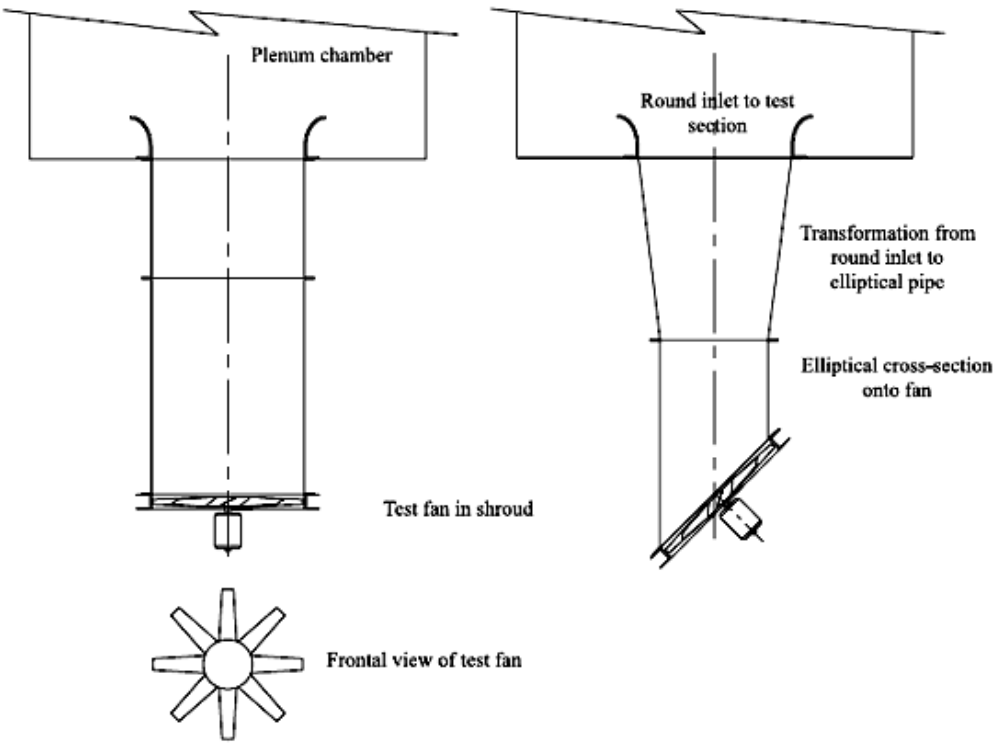

Figure 2.9. Fan cross-flow experimental set-up

- Total-to-total pressure ratio is independent of inflow angle. This finding was based on the assumption that the inlet and exit kinetic energy fluxes in the fan annular passage were equal, which turned out later to be an idealisation. A better formulation would have been to state that the static-to-static pressure ratio was independent of inflow angle.
- Power consumption is independent of inflow angle. This had been suspected, simply because it was known from practical experience that the electrical motors powering the edge fans were not overloaded.
- The cross-flow performance of a row of fans is well predicted by a simple model based on calculating the average cross-flow component at the entrance of each fan.
- To be representative of prototype fans the model fans must have the same ratio of dynamic pressure to fan static pressure (total-to-static pressure rise, a dimensionless number that is usually not given the consideration it deserves.)

2.6.2 Actuator disc modelling in CFD

Thiart [31] wrote a CFD code to model the flow through an axial flow fan situated in the side wall of a wind tunnel. The axial velocity through the fan was equal to the average velocity through the wind tunnel (upstream of the fan). The fan was represented by an

actuator disc. Good agreement was found with measured data. As mentioned, this laid the foundation for many subsequent theses and dissertations using the actuator disc approach.

Hotchkiss[13] modelled the flow around a helicopter using CFD. The main rotor was represented by an actuator disc. For verification of the actuator disc model he simulated the experimental data of Stinnes [34]. The resulting paper [23] graphically illustrated the mechanisms behind the findings of Stinnes [34]. The CFD results confirmed that power consumption is independent of inflow angle. The paper showed that even with large off-axis inflow angles of 45° the relative inflow angle into the rotor blades, and the lift coefficient vary little. Since the variations on the advancing and retreating blades have opposite signs, their effects tend to oppose each other, on average. Hotchkiss [23] however stated that the fan total-to-total pressure rise is not independent of inflow angle, but that the decreased fan static pressure was due to a combination of increased kinetic energy at the fan exit and greater energy dissipation in the fan. It was after this paper that Backström realised that the simple explanation of Stinnes and himself [34] was incorrectly formulated. It should have stated that the fan static-to-static (not total-to-total) pressure rise is independent of inflow angle. Looking at it again this was obvious from the measured data of Stinnes (figure 2.10) and the CFD data of Hotchkiss et al [23]. This insight lead to the realisation that fan modelling in CFD using the so called "pressure jump" (or negative flow resistance) method should employ the fan static-to-static pressure rise characteristic and that fan static pressure could be predicted with great accuracy by using this approach, possibly even under distorted inflow conditions. This is explained by Van der Spuy [26].

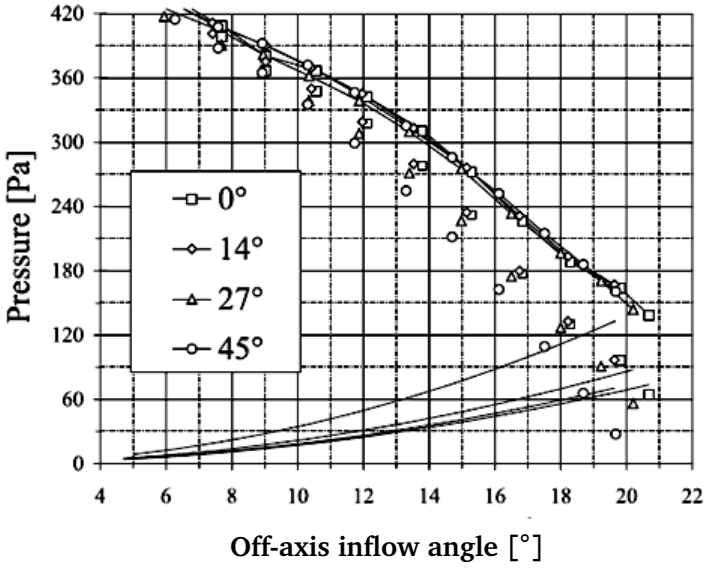

Figure 2.10. B1-fan static-to-static pressure rise (top lines with symbols) as sum of total-to-static pressure rise (symbols only) and cross-flow dynamic pressure (bottom lines only), as dependent on cross-flow angle [34].

Van der Spuy[11] also investigated the performance of axial flow fans operating at the edge of air cooled condenser arrays. He measured the performance of 0.63 m diameter axial flow fans in a three-fan rig. He also simulated the flow through the system with CFD and measured the velocity field upstream of the fans by means of laser particle imaging velocimetry (PIV). He managed to correlate the performance of the edge fans with their hub-tip ratios and solidities. This extends a previous correlation of Salta and Kröger[29] based on the height of the fan from ground level[11]. All of this work has not been published in journals yet, but some of it has been published at conferences[30,31,32].

Chapter

3

Solar chimneys

In 1998 the Department of Mechanical Engineering was approached on behalf of the Provincial Government of the Northern Cape to investigate the performance of solar chimney power plants (SCPPs)s for power generation. A SCPP is one in which air, heated under a glass-decked solar collector, escapes through a power generating turbine at the base of a tall chimney. The solar chimney research project started with a six-month project, led by Prof. D.G. Kröger. Backström was a member of the team, but after the completion of the project reports, Kröger and he each individually pursued their own interests in the field, with frequent informal interaction and some collaboration.

3.1 Fundamentals of SCPPs

The main components of a SCPP are the solar collector, the chimney and the turbo-generator (see figure 3.1). Its operation is as follows:

- Air is heated in the solar collector which is typically a circular green house with a roof sloping upwards towards a tall chimney at its centre, allowing the chimney to fill with hot air.
- Once the chimney is filled with hot air escaping from the green house, the difference in density between air inside and outside the chimney establishes a pressure difference, also called a pressure potential, Δp_p that causes an updraught in the chimney.
- Part of the pressure potential is used to maintain flow through the system, and part to provide a pressure drop, Δp_t across the turbines that drive the electrical generators.

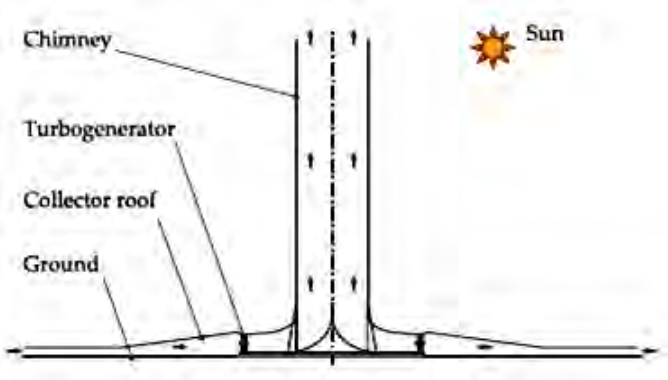

Figure 3.1. Solar chimney power plant

3.2 Introduction to SCPP involvement

Backström concentrated on solar chimney turbine modelling, but system and chimney modelling was required to determine turbine operating conditions for the design of a first model solar chimney turbine. As the chimney and system modelling progressed it was realised that some of the common assumptions in the literature were unsubstantiated, and some were even incorrect. Among the unsubstantiated ones was that the supports at the bottom of the chimney walls could be shaped to form low-loss radial inflow inlet guide vanes resulting in an efficient, vertical axis turbine and still support a tall chimney. Unsubstantiated values were used for pressure drop coefficients associated with various components and for turbine efficiency. Also found among the incorrect assumptions was the application of the (open) wind turbine Betz limit to the (enclosed) solar chimney turbine[33], the assumption that the maximum power is produced when the turbine pressure drop, Δp_t is two thirds of the pressure potential, Δp_p and the implied assumption that the pressure drop associated with flow acceleration due to the density decrease in a constant area tall chimney is negligible.

Some of the questions addressed by Backström and his team of students were: What are the design and operating specifications of the turbines for large solar chimney turbines? What limitations are imposed by the solar chimney thermodynamic cycle? What are the magnitudes of the main stagnation pressure drops in the system? Can the supports at the bottom of the chimney walls be shaped like the radial inflow inlet guide vanes of an efficient, vertical axis turbine and still support a tall chimney? What is the optimum turbine operating condition? What is the optimum turbine layout? What is the optimum number of turbines per plant? How does one determine the optimal instantaneous operating condition of the turbines?

The presentation of the research will follow certain main themes, and some of the minor themes will not necessarily be presented in chronological order, for the sake of readability.

3.3 Early literature

Only a few peer reviewed, generally accessible solar chimney power plant papers had been published up to 1998. Examples are: Haaf et al. (1983)[18], Haaf (1984)[16], Mullett (1987)[19], Yan et al. (1991)[34], Schlaich (1995)[20], Trieb et al. (1997)[35], Pasumarthi and Sherif (1998*a,b*)[33][36]. All of these papers regarded solar chimneys as fluid mechanical systems, not thermodynamic systems, even though Yan et al.[34] called their paper: "Thermo-fluid analysis of solar chimneys". The working fluid was generally regarded as incompressible, with the addition of a buoyancy term. Since the concept of enthalpy was not considered, the notions of thermodynamic cycle analysis and compressible flow were ruled out. Padki and Sherif (1988)[37] did however list the compressible flow energy (stagnation enthalpy) equation, including the potential energy term, as one of the equations used to calculate optimal chimney shapes.

3.4 SCPP thermodynamic and system analysis

In order to understand the solar chimney power generation system, Backström developed an air standard thermodynamic cycle analysis of the SCPP cycle [36]. An air standard cycle analysis assumes efficiencies of 100 % for the system components such as the collector, chimney and turbine, so that the limitations imposed by the thermodynamic cycle itself become clear. This work constituted the first such an analysis and the first Stellenbosch solar chimney paper submitted to a journal [36].

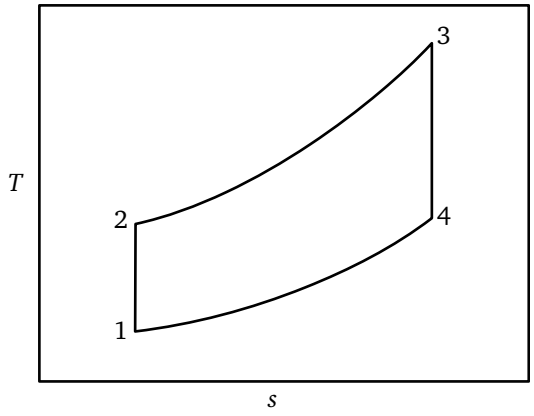

Figure 3.2. Basic temperature-entropy diagram for air standard analysis of solar chimney cycle

It was realised that the thermodynamic cycle representing the operation of a SCPP is similar in some ways to a gas turbine power plant, but it is also different in some ways. The ideal gas turbine thermodynamic cycle (also known as the Brayton cycle) consists of an isentropic compression process, a heat addition process at constant pressure (typically in a combustor), an isentropic expansion process in a turbine and a constant pressure heat removal process (see figure 3.2). If the compressor (and turbine) pressure ratio, the combustor temperature rise and the component efficiencies

are high enough, the pressure in the exhaust stream will be high enough to drive an output power turbine (or the flow through a propulsion nozzle of a jet engine). The cycle approach assumes that the thermodynamic system is closed in the sense that the working fluid leaving the exhaust enters again at the engine intake. This would require a heat exchanger between the exhaust and intake to remove the rejected thermal energy. When air is the working fluid, a so-called open cycle is often used. The exhaust air is released into the atmosphere, to be replaced by fresh atmospheric air at the intake. This eliminates the physical heat exchanger with its associated pressure drop, weight and cost. Thermodynamically however, the cycle can still be considered as closed, with the air experiencing heat extraction at constant pressure between exhaust and intake. In a sense then, the atmosphere is considered to act as an ideal, zero pressure drop heat exchanger that cools the air from the turbine exit to the compressor inlet temperature.

When comparing a SCPP to a gas turbine power plant, it is obvious that the solar power plant has no compressor, and that the turbine provides shaft power to drive the generator only. In gas turbine terminology such a turbine is known as a power generation turbine, to distinguish it from a gas generator turbine that drives the compressor. Since a SCPP has no compressor, there is also no gas generator turbine that drives it. The chimney acts as the gas generator turbine and the slowly descending outer air as the gas generator compressor. Instead of extracting shaft power from the cycle by means of the gas generator turbine and re-introducing it through a compressor, power is extracted and re-introduced as respectively power associated with the potential energy of the air rising inside the chimney and with the air descending in the atmosphere outside.

We have seen that in the gas turbine cycle the atmosphere can be regarded as replacing an ideal heat exchanger. In the case of the solar chimney the inlet temperature of the air entering the virtual compressor is at the ambient temperature at the chimney top. If we now imagine that in our standard model, the air outside the chimney descends in a large diameter, imaginary chimney, it will experience adiabatic, frictionless (isentropic) compression with initial temperature and pressure equal to that at of the atmospheric air at the altitude of the chimney top. In reality the atmospheric temperature lapse rate is not adiabatic, but decreases less slowly with altitude (at typically 6.5 K rather than 9.75 K per 1000 m). In the same way the rising air expanding in the real chimney will experience an adiabatic expansion (if the heat loss through the chimney walls is negligible) and an isentropic expansion if the chimney walls are frictionless as well. During the expansion of an elemental volume of air in the chimney, it does work on the adjacent fluid elements by expanding and pushing itself and the ones above it upwards, resulting in a decrease in its enthalpy and an increase in its potential energy. The approach described above was described in two papers [36, 37].

The first paper describing the thermodynamic approach to SCPPs presents the air standard thermodynamic analysis for the solar chimney cycle [36]. Simple equations were derived for the cycle efficiency, power per unit mass flow and available turbine pressure drop, assuming ideal air as process gas and ideal reversible processes. In the chimney the full energy conservation equation in terms of total enthalpy, with the retention of the potential energy term, is valid. It has to be applied from above the

turbine to the chimney exit.

$$\Delta H = H_3 - H_2 = -g\,\Delta z \tag{3.1}$$

Note that this is in fact an altitude lapse rate equation for total enthalpy, derived directly from the energy equation for adiabatic flow, with no dependence on pressure or density distributions as required in the fluid mechanics approach.

The main conclusions derived from the air standard analysis will be discussed in the next few paragraphs. The first one is that the cycle efficiency is directly proportional to the chimney height:

$$\eta = \frac{g\,\Delta z}{c_p T_2} \tag{3.2}$$

This is the defining equation of solar chimneys, since it shows that in practice the cycle efficiency is determined by the chimney height. (The other three variables in the equation are not adjustable in practice.) It follows that the limiting efficiency of a plant with a 1000 m high chimney and 330 K chimney inlet temperature is about 3 %, excluding the collector and turbine efficiencies. Equation (3.2) was also derived by Mullett[19] and Schlaich[20] with the "simplifying premise that the temperature profiles run parallel inside the chimney and in the open". Schlaich's derivation employs the little known "modified Torricelli equation":

$$V_{ch,\max} = \sqrt{\frac{2g\,\Delta z\,\Delta T}{T_2}} \tag{3.3}$$

Equation (3.3) describes the maximum velocity, $V_{ch,\max}$ at which a gas can escape from a chimney in which the temperature is ΔT higher than the outside temperature, when there is no turbine or other resistance affecting it. It appears that the incompressible flow approaches of Mullett[19] and Schlaich[20], which did not employ the concept of enthalpy, encouraged them to first convert the potential energy to kinetic energy, before converting it into fluid energy (enthalpy). The thermodynamic approach of equation (3.1) however recognises the direct conversion.

The second conclusion from the air standard analysis is that the solar chimney cycle has no optimal pressure ratio for maximum specific power. The specific power is the power of the plant divided by the thermal power of the flow entering it:

$$P^* = \frac{P}{\dot{m}\,c_p\,T_2} \tag{3.4}$$

Backström [36] showed that, in contrast to gas turbines, there is no particular pressure ratio that ensures maximum specific power for each particular temperature ratio, and consequently no optimal chimney height for each collector size. It turns out that the specific power developed by a SCPP is directly proportional to the cycle efficiency (and chimney height) and to the fractional temperature rise in the solar collector:

$$P^* = \frac{\Delta T_{23}}{T_2}\eta \tag{3.5}$$

The specific power is consequently maximized by maximizing the fractional temperature rise across the solar collector (e.g. by increasing the collector size) and maximizing

the chimney height. This was also found by Mullett[19], Schlaich[20] and others, but the thermodynamic approach explains succinctly why it is so: since both the power per unit mass flow produced by the turbine ($\dot{m}\, c_p \Delta T_{23}\, \eta$) and the power absorbed by the air in the collector ($\dot{m}\, c_p\, \Delta T_{23}$), are proportional to the temperature rise in the collector, the temperature rise has no effect on the efficiency of the plant, in agreement with equation (3.2).

The system pressure potential, Δp_p can be interpreted as the pressure difference available to drive the flow through the system including the turbine, for given chimney inlet temperature and ambient conditions. A simplified interpretation of the pressure potential is that it is analogous to the hydraulic head of a hydro-electric power system, where it is the fixed difference in altitude between the water surfaces of the upper and lower reservoir.

The third conclusion from the air standard analysis is that in a solar chimney power plant the pressure potential is not fixed, as the pressure potential depends on the solar irradiation and ambient conditions, and is proportional to the chimney height and the collector temperature rise:

$$\Delta p_p = \rho_3\, g\, \Delta z\, \frac{\Delta T_{23}}{T_2} \tag{3.6}$$

Using the equation of state, equation (3.6) can also be written as:

$$\Delta p_p = \rho_2 g \Delta z \frac{\Delta T_{23}}{T_3} \tag{3.7}$$

Haaf[18] and Schlaich[20] derived this form of the equation by assuming that the density difference between the inside and outside of the chimney is independent of chimney height, and the pressure at the chimney bottom is equal to the atmospheric pressure. In the air standard analysis the assumption is that the temperature-pressure relationships inside and outside the chimney are both isentropic. This assumption will be discussed in detail later.

From the preceding it emerges that the thermodynamic cycle approach duplicates the previously derived characteristics of SCPP cycles in a simple, straight forward way. It will be shown that the thermodynamic approach leads to other insights as well.

Following Cohen[38] the analysis of [36] showed that the air standard efficiency of a gas turbine or a solar chimney cycle is given by:

$$\eta = 1 - 1/c \tag{3.8}$$

were c is the temperature ratio associated, through the isentropic relationship, with the compression ratio of the cycle.

Thus, for gas turbines as well as solar chimneys the efficiency is essentially determined by the cycle pressure ratio, not by the cycle temperature ratio, as one could possibly expect from fundamental Carnot cycle considerations, where the limiting efficiency is determined by the cycle temperature ratio, $t = T_3/T_1$ as:

$$\eta_C = 1 - 1/t \tag{3.9}$$

For an ideal, non-recuperated gas turbine, it can however be shown that the value of $c = \sqrt{t}$ is the one that will maximise the specific power for a given value of the cycle

temperature ratio, $t = T_3/T_1$. The air standard efficiency of such plants will then be given by:

$$\eta = 1 - 1/\sqrt{t} \tag{3.10}$$

The thermodynamic investigation of the solar chimney [36] however shows that as the efficiency is given by equation (3.8) it is independent of the cycle temperature ratio. Consequently equation (3.9) does not determine the ideal efficiency limit. It can be shown however (compare equations (3.8) and (3.9)) that the Carnot efficiency of a solar chimney cycle always exceeds the air standard efficiency, as $t > c$. If the height of the chimney is increased to increase the efficiency, the temperature at the top of the chimney decreases, following the temperature lapse rate in the air standard atmosphere, thereby increasing the cycle temperature ratio, so that the limiting Carnot efficiency also increases. This removes the apparent paradox of the fluid mechanical approach that by increasing the chimney height sufficiently the efficiency of a SCPP can exceed that given by the Carnot limit. Another limiting factor is that if the density lapse rate in a real atmosphere outside a real chimney is less than the adiabatic then there is a maximum chimney height beyond which the chimney draught will stop. This will be achieved when the average density inside the chimney is equal to that outside for the same altitude span.

Novikov[39] has shown from heat transfer considerations that an equation of the form of equation (3.10) generally gives a better practical estimate than the limiting Carnot efficiency of the practically attainable levels of efficiency of realistic power plants. It is interesting that a similar equation applies to gas turbine cycles and that it is associated with maximum specific power. For solar chimney power plants equation (3.10) does not however correspond to the maximum specific power condition, as discussed above.

The presented ideal air standard cycle analysis of the SCPP gives the limiting performance, the theoretical efficiency of the plant and the relationships between the main variables. The apparent paradoxes involving the Carnot efficiency are also cleared up.

The next step in the analysis of SCPPs was to include chimney friction and other system losses such as turbine and exit kinetic energy losses in the analysis. To accurately model the performance of the turbine, a reliable SCPP system model is required. None of the SCPP models available at the time were considered to be suitable for our purposes, and the comprehensive models of Kröger and his collaborators were still being developed in parallel. The Kröger and Blaine[40] paper concentrated on the driving (pressure) potential of the chimney and did not model the collector or turbine. To design a turbine one needs to know the volume flow and available pressure drop, and the associated inlet conditions and physical properties of the fluid at the inlet. The turbine speed of rotation may also be fixed or limited due to generator and electrical grid considerations.

Backström and Gannon [37] derived an algorithm for the solution of the thermodynamic cycle diagram of a SCPP with losses (figure 3.3). This work was part of the PhD study of Gannon[15]. Its main objective was to investigate the feasibility and performance characteristics of the traditional single rotor vertical axis turbine layout in SCPPs. Through a combination of analysis and experimental work carried out on a model turbine system, Gannon was the first to show that a high turbine efficiency (of up to 90 % total-to-total) was possible.

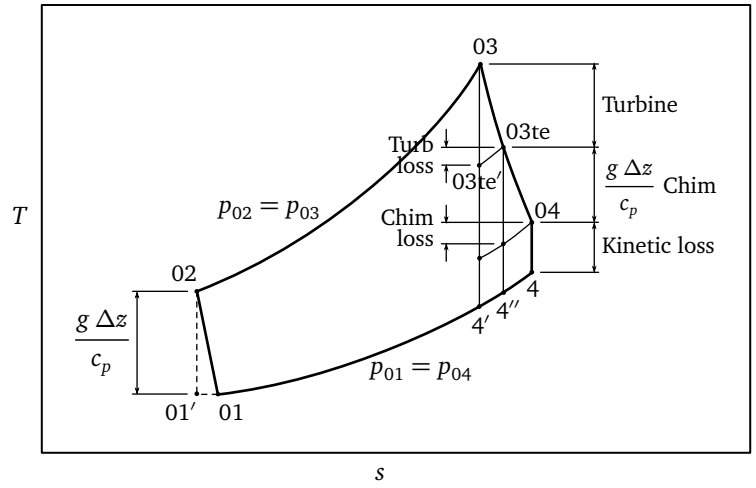

Figure 3.3. Solar chimney temperature-entropy diagram with losses [21]

The solar chimney system pressure drop (or so-called loss) mechanisms considered were those associated with friction and, as in fans, with exit kinetic energy in the chimney and the turbine. The total system pressure drops included those associated with the drag of the collector roof supports and bracing wheels inside the chimney. A simple solar collector model was developed to couple the mass flow through the system to the temperature rise in the solar collector [37]. As discussed, the temperature of the air in the chimney determines its density and the available system pressure drop, Δp_p. The available and actual pressure drops in the system determine the flow. The solar collector model took into account the radiation, conduction and convection heat transfer at the glass deck of the solar collector and at its floor. Calculated results compared favourably with measurements from the small scale pilot plant at Manzanares in Spain[16]. The performance of a large (200 MW peak power) SCPP was predicted. This work won a best paper award at an ASME Solar Energy conference, and the journal article [37] has been highly cited since. The model was good enough to determine turbine operating points.

What also emerged from this work was a solution algorithm to determine the power produced at each flow condition. The solution algorithm has been adopted by Papageorgiou[41] in his analysis of floating solar chimneys. With this relationship available it was easy to iteratively adjust either the turbine pressure drop or the flow through the system until the maximum power condition was found at each environmental condition. Many previous investigators assumed that for maximum power the pressure drop across the turbine should be two thirds of the pressure drop across the system at the flow condition, as in hydropower systems where the pressure potential is constant. Through a simple analysis it was however shown why this was not the case for SCPPs [43]. This will be discussed in detail later. Before that, other work relating to the determination of loss mechanisms in the chimney and at the collector-to-chimney transition will be discussed.

Post doctoral student Bernardes [44] compared the methods used to calculate the heat fluxes into, inside and leaving the solar collector, and their effects on solar chimney

performance. The heat transfer equations for forced and natural convection found in the literature were compared to those that had been developed by Kröger and Burger[42], and used by Pretorius[23]. The correlations used by Pretorius were introduced into the Bernardes code [44] to run comparative simulations. In general the Pretorius correlations produced higher heat transfer coefficients and higher heat fluxes for both the roof and floor surfaces. The two approaches lead to similar air temperature rises in the collector and thus, similar produced power. This then led to greater confidence in output power predictions for large SCPPs, especially since no large scale collectors had been built.

Other authors[43] also eventually followed the thermodynamic approach.

3.5 Chimney flow analysis

When calculating the pressure distribution along a pipe, the so-called "minor loss" elements, such as elbows and contractions and expansions, and obstructions in the pipe as well as wall friction, cause pressure drops defined by coefficients that are referred to the dynamic pressure at the relevant pipe section. In incompressible flow, the dynamic pressure is affected by the change in velocity as affected by the area variation only. If however there is an air density variation, as in a tall chimney, the velocity, and the dynamic and static pressure will change because of that as well, even in a constant area section. To compensate for this, the pressure change associated with the flow acceleration through the chimney is then calculated by applying the momentum equation over the relevant control volume. This requires an iterative solution since both the velocity and the density are unknown at the exit of the control volume.

Backström stated that "typical analyses of flow through solar power plant tall chimneys make the assumption of incompressible flow, thereby introducing inaccuracies of unknown magnitude"[40]. The incompressible flow approximation requires the addition of a so-called "acceleration term" in the calculation of the flow through a tall, chimney and its correct evaluation. This term was omitted in at least four pre-1999 papers found in the literature by Haaf[18], Schlaich[20], Yan[34] and Pasumarthi[33]. The term was inserted by Kröger and Blaine[40] in their incompressible analysis, but the accuracy of the thus modified incompressible approach when applied to tall chimneys, had not been investigated. It also was not evident how this term would be calculated in chimneys with a varying cross section. It was clear that a more fundamental approach could lead to valuable insights.

3.5.1 Compressible flow through solar power plant chimneys

A one-dimensional compressible flow approach for the accurate determination (at least in principle) of all the thermodynamic variables in a solar chimneys as dependent on chimney height, wall friction, additional losses, internal drag and area change was developed [40].

Since the compressible flow approach is designed to satisfy the mass conservation and energy conservation (including potential energy), as well as the momentum equations, the acceleration term due to density change is included implicitly. Compressible

flows are usually associated with Mach numbers exceeding 0.3. Assuming isentropic conditions in air, with a specific heat ratio of 1.4, it can be shown that, at the usually accepted incompressible flow limit of Mach 0.3, the ratio between the static and stagnation temperature is 0.982, and the ratio of static to stagnation density is then 0.956. As pointed out before, the stagnation enthalpy decreases as follows for a fluid rising through a height $\Delta z = z_3 - z_2$:

$$\Delta H = H_3 - H_2 = -g\,\Delta z \tag{3.11}$$

For a 1000 m tall chimney the temperature drop would then be:

$$\begin{aligned} \Delta T &= -g\,\Delta z/C_p \\ &= -9.81 \times 1000/1005 \\ &= -9.76\,\mathrm{K} \end{aligned} \tag{3.12}$$

If the chimney inlet temperature is assumed to be 330 K, the chimney top internal air temperature will be about 320 K, the temperature ratio due to the height increase is 0.970 and the associated adiabatic density ratio is 0.928. This shows that the effect of compressibility on the flow in the chimney of a typical proposed chimney exceeds the traditional limit in spite of the low Mach number of about 0.03 (assuming an updraught of 11 m/s and a sonic velocity of 364 m/s). Backström and Gannon [40] did a similar derivation for a 1500 m chimney where the compressibility effect was even more important.

The fundamental equations of the compressible flow approach follow below. The stagnation temperature at any section at altitude, z_i in the chimney is calculated from that at an up stream section at altitude, z_{i-1}:

$$T_i = T_{i-1} - g\left(z_i - z_{i-1}\right)/c_p \tag{3.13}$$

Next the Mach number variation is written at the left of the vertical momentum equation as dependent on the chimney flow area, A, and the friction and obstruction loss coefficient, L:

$$\frac{dM}{M} = \frac{1 + \frac{\gamma-1}{2}M^2}{1 - M^2}\left(-\frac{dA}{A} - \frac{1}{2}\frac{(\gamma+1)}{(\gamma-1)}\frac{dT}{T} + \frac{\gamma M^2}{2}L\,\delta z\right) \tag{3.14}$$

where $L\,\delta z$ is the sum of the frictional and minor losses occurring in the short altitude increment δz.

Once the Mach number distribution has been found by integration over each interval of chimney height, the pressure at each level can be found from the mass conservation equation below:

$$p = \frac{\dot{m}}{AM\left(1 + \frac{\gamma-1}{2}M^2\right)^{\frac{1}{2}}\left(\frac{\gamma}{RT}\right)^{\frac{1}{2}}} \tag{3.15}$$

Values of other variables follow from standard gas dynamics.

A major result from this study was that the acceleration pressure drop in the chimney was evaluated and its importance was pointed out. The benefits of a diffuser shaped

chimney top were also mentioned, as was the fact that a correctly expanding chimney designed to keep the vertical flow velocity in the chimney constant, would not be subject to the normal diffuser losses associated with flow separation due to rapidly decelerating boundary layers. Abnormally high diffuser efficiency would be possible. It also turned out that the corrected, incompressible approach of Kröger and Blaine[40] is remarkably accurate for chimneys as tall as 1500 m.

3.5.2 Pressure and density in chimneys

In a follow-up technical note, the compressible flow approach to flow through tall chimneys was expanded, and a solution method, valid for small Mach numbers, was presented [41]. This note derives the equations and develops calculation methods for the pressure drop in very tall chimneys. The methods allow for density and flow area change with height, for wall friction and internal bracing drag.

The note develops a method for finding all the thermodynamic properties for compressible frictional flow through tall vertical chimneys. It finds the stagnation temperature distribution directly from the altitude, by applying the energy equation. It then finds the Mach number distribution from the vertical distributions of stagnation temperature, friction factor, bracing drag loss coefficient and flow area. The static pressure at each altitude follows from the continuity equation. It turns out that the generally used adiabatic temperature lapse rate equation in principle applies to the stagnation temperature, and applying it to the static temperature is valid only when the Mach number is equal to zero. The note presents novel equations for the vertical pressure and density distributions in terms of Mach number. The first of these is a generalisation of the adiabatic pressure lapse ratio equation to include flow at small Mach numbers.

$$\frac{p_i}{p_{i-1}} = \left(\frac{T_i}{T_{i-1}}\right)^{\left(\frac{\gamma}{\gamma-1}\right)\left(1+\frac{\gamma+1}{2}\frac{M^2}{1-M^2}\right)} \left(\frac{A_i}{A_{i-1}}\right)^{\left(\frac{\gamma M^2}{1-M^2}\right)} \mathrm{e}^{-\left(1+\gamma\frac{M^2}{1-M^2}\right)\left(\frac{\gamma M^2}{2} L\,\delta z\right)} \tag{3.16}$$

The right hand side of the equation consists of three factors: the first accounts for the potential energy increase with altitude, which reduces the stagnation temperature according to equation (3.13); the second accounts for the chimney area distribution; the third exponential factor accounts for the frictional and other pressure drop mechanisms. The equation vividly illustrates that the adiabatic relationship used by all other researchers (3.17), is actually a zero Mach number approximation, valid only for constant flow area and zero losses:

$$\frac{p_i}{p_{i-1}} = \left(\frac{T_i}{T_{1-1}}\right)^{\frac{\gamma}{\gamma-1}} \tag{3.17}$$

The other important equation derived in the technical note is analogous to the hydrostatic relationship between pressure and density, extended to small Mach numbers. Its integration leads to an equation for the average density in the chimney. For constant area, frictionless flow, assuming constant Mach number terms, the average density in the chimney is:

$$\frac{\rho_{\text{ave}}}{\rho_{i-1}} = \frac{(1-M^2)}{\left(\frac{\gamma}{\gamma-1}-\frac{1}{2}M^2\right)} \frac{1}{\left(1-\frac{T_i}{T_{i-1}}\right)} \left[1-\left(\frac{T_i}{T_{i-1}}\right)^{\left(\frac{\gamma}{\gamma-1}-\frac{M^2}{2}\right)\left(\frac{1}{1-M^2}\right)}\right] \tag{3.18}$$

A very accurate value of the average density is exactly what the commonly used incompressible flow approach to the problem requires to calculate the hydrostatic pressure drop in the chimney.

When $M = 0$, equation (3.18) simplifies to:

$$\frac{\rho_{\text{ave}}}{\rho_{i-1}} = \left(\frac{\gamma - 1}{\gamma}\right) \frac{1}{\left(1 - \frac{T_i}{T_{i-1}}\right)} \left[1 - \left(\frac{T_i}{T_{i-1}}\right)^{\left(\frac{\gamma}{\gamma-1}\right)}\right] \tag{3.19}$$

By inserting equation (3.12) it can be rewritten as:

$$\frac{\rho_{\text{ave}}}{\rho_{i-1}} = \left(\frac{\gamma - 1}{\gamma}\right) \frac{c_p\, T_i}{g\, \Delta z} \left[1 - \left(\frac{T_i}{T_{i-1}}\right)^{\left(\frac{\gamma}{\gamma-1}\right)}\right] \tag{3.20}$$

It was shown in [41] that equation (3.20) can be further simplified to the form of the standard hydrostatic equation: $\Delta p = -\rho_{\text{ave}}\, g\, \Delta z$, thereby demonstrating that equations (3.18) to (3.20) are generalisations of the hydrostatic equation for low and zero Mach numbers respectively.

The compressible flow approach has been used as a benchmark for the computational accuracy of the incompressible approaches and the validity of their assumptions.

3.5.3 Stagnation pressure drop in chimneys

As pointed out in the discussion of the two papers about the pressure distribution in chimneys, the frictional and other pressure losses in the chimney are required to model the flow resistance in the chimney. Backström wrote a paper based on experimental data measured by Diplomarbeit student Bernhard in a 0.63 m diameter model chimney without and with seven internal bracing wheels [42]. The bracing wheels each had a rim protruding into the chimney, and twelve spokes, each spoke consisting of a pair of rectangular section bars. The drag coefficient of the pair of bars was measured in a wind tunnel. The investigation determined coefficients of wall friction, bracing wheel loss and exit kinetic energy in a model chimney, for both ideal non-swirling uniform flow and for swirling distorted flow. A fan at one end of the chimney model either sucked or blew the flow through it. The flow entering the chimney through the fan and its diffuser simulated the flow leaving the turbine at the bottom of the chimney. The swirling distorted flow increased the total pressure drop by about 28 %, representing 4.7 % of the turbine pressure drop. These were the first reported measurements relating to the pressure drops associated with bracing wheel spokes in tall chimneys. The paper concluded that the pressure drop across the bracing wheels investigated exceeded the frictional pressure drop by far, and that designers of tall, thin walled chimneys should take care to minimise the number of bracing wheels, reduce their rim width as much as possible and investigate the feasibility of streamlining their spoke sections. If at all structurally possible, the top bracing wheel should be far enough from the chimney exit to allow the spoke wakes to decay, and the separated flow to re-attach to the chimney wall downstream of the rims before the flow leaves the chimney, to reduce the exit kinetic energy loss.

At the bottom of a chimney with a single vertical axis turbine, the air, heated within the collector, passes through an inlet guide vane (IGV) and then through a transition section to a turbine that powers a generator. The transition section contains the turbine inlet guide vanes that support the whole chimney in this type of layout, and guides the flow entering the turbine. The primary objective of the study of Kirstein [21] was to determine the loss coefficient and exit swirl angle of the flow passing through the collector-to-chimney transition section of a full-scale SCPP as dependent on IGV stagger angle and collector roof height. Very good agreement was found between experimental values measured in a scaled model and commercial computational fluid dynamics (CFD) code predictions of flow angles, velocity components and internal and wall static pressures. The agreement between measured and predicted total pressure loss coefficients was reasonable. The CFD code served to extend the predictions to the Reynolds numbers in a proposed full-scale geometry.

The performance of a model transition section was calculated and measured. Previous estimates for the transition section loss coefficient were greater than 0.16, but they did not consider the Reynolds number scale effect. This research showed that the loss coefficient is 0.056 at full-scale Reynolds numbers for the geometry described by Kirstein [21]. The CFD prediction of turbine inlet flow angles agrees very well and transition section pressure drops agree satisfactorily with the experimental results.

Semi-empirical equations were developed to predict the loss coefficient, C_L and turbine inlet flow angle θ of SCPPs as dependent on inlet guide vane setting angle, β and non-dimensional collector deck height, H_D, where H_D is the deck height divided by the chimney diameter. The equations are:

$$\tan(\theta) \approx 0.238 \frac{\tan(\beta)}{H_D} \tag{3.21}$$

$$C_L \approx 0.0292 + 0.00114 \left(\frac{\sec(\beta)}{H_D} \right)^2 + 0.190 \tan^2(\theta) \tag{3.22}$$

The two empirical equations are useful in the layout and design of SCPPs with a single vertical axis turbine and radial inflow inlet guide vanes, since they are, as far could be determined the only semi-empirical equations predicting the turbine inlet swirl angle and collector-to-chimney transition section loss coefficient (figures 3.4 and 3.5).

The theoretical and experimental work discussed in this section served to put the values to be used in the calculation of stagnation pressure drop coefficients on a firm basis.

3.6 Turbine Analysis

3.6.1 SCPP turbine design point

In order to design a solar chimney turbine for maximum power and run it at maximum instantaneous power, the optimal pressure drop, Δp_t across the turbine as a fraction of the pressure potential, Δp_p must be determined. At least four early papers make the assumption that the turbine in a SCPP will produce maximum instantaneous power for given value of solar irradiation when the pressure drop across the turbine is 2/3

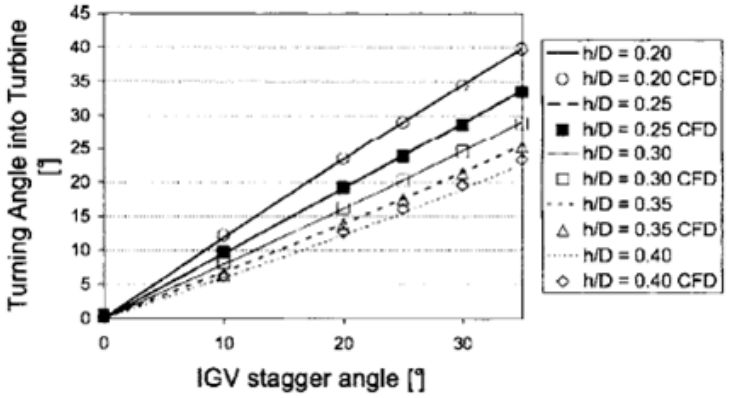

Figure 3.4. Graphical representation of equation (3.21) compared to CFD values

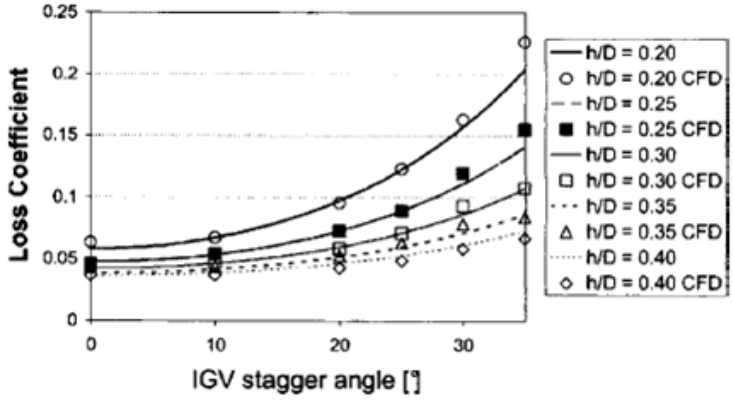

Figure 3.5. Graphical representation of equation (3.22) compared to CFD values

of the available pressure drop across the system (Haaf[18], Lautenschlager[21], Mullett[19], Schlaich[20]). Schlaich[20] apparently used an optimum value of $X = \Delta p_t / \Delta p = 0.82$ as evident from the values of p_t and p_p reported in tables[20]. Hedderwick[44] presented graphs showing values around 0.7. Backström and Gannon [36] used the two thirds assumption only for optimization at constant temperature rise (and thus constant pressure potential) and pressure, since the collector was not considered in that investigation. Gannon [37] employed an optimisation procedure to find the optimum under conditions of constant solar irradiation. Schlaich[20] reported a ratio of turbine to system pressure drop value of about 0.80, while Bernardes[45] reported a value of as high as 0.97. The wide variation in values warranted further investigation. The question was the existence or not of a relevant optimum value of the ratio, X for SCPPs, and how to determine it, since even under conditions of constant solar irradiation the pressure potential of a solar chimney plant is not fixed but is a function of the air temperature rise in the collector, which varies with flow rate.

The two-thirds assumption introduces at least two errors when applied to SCPPs: firstly, the available pressure potential is dependent of the magnitude of the flow, mainly because a higher flow through a collector exposed to a value of given solar irradiation (and collector floor temperature) will result in a lower temperature rise and pressure potential, and secondly, the turbine pressure drop should be referred to the value of pressure potential at that particular flow.

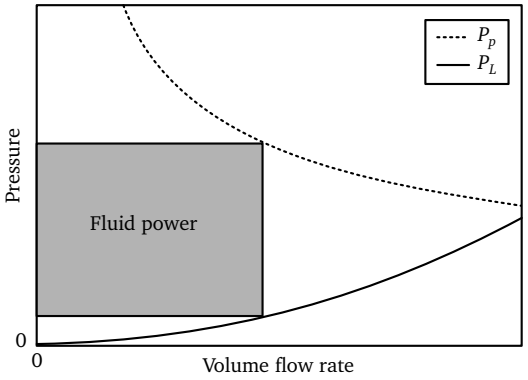

Figure 3.6. Graphical representation of ideal chimney turbine power in relation to power law pressure potential (p_p) and pressure loss curves (p_L)

In an effort to understand the problem better, Backström derived a simple model using power law assumptions [36]. The model assumes that pressure potential is proportional to volume flow to the power m, where m is typically a negative number between 0 and -1 (because the pressure potential decreases as the flow increases) (figure 3.6). It also assumes that the system pressure drop is proportional to the power n, where typically $n = 2$ with losses proportional to velocity squared. The analysis shows that the optimal ratio of turbine to system pressure drop is:

$$X_{\text{opt}} = \frac{n-m}{n+1} \tag{3.23}$$

The ratio X_{opt} is equal to $2/3$ only when $m = 0$, implying a constant pressure potential, independent of flow rate (as in hydro-electric systems). Consideration of a basic solar collector model proposed by Schlaich[20] led to the conclusion that the value of m is equal to the negative of the collector floor-to-exit heat transfer efficiency. This is the ratio of the net rate of heat transferred by the air in the collector exit to the rate of heat lost by the collector floor. A more comprehensive optimization scheme, incorporating the basic collector model of Schlaich[20] into the analysis, shows that the power law approach is sound and conservative. It is shown that the constant pressure potential assumption ($m = 0$) may lead to appreciable under estimation of the performance of a SCPP, when compared to the analyses presented in the paper. More important is that both these analyses predict that maximum fluid power is available at much lower flow rate and much higher turbine pressure drop than predicted by the constant pressure potential assumption. Thus, the constant pressure potential assumption may lead to

overestimating the size of the flow passages in the plant, and designing a turbine with excessive stall margin and excessive runaway speed margin.

Values found in the literature[45] for the optimum value of X vary between 2/3 and 0.97, but it was unclear what factors played a role in the optimum. Bernardes [45] investigated the performance of two iterative schemes of finding the maximum power operating point of SCPPs. The scheme used by Pretorius[23] varied the mass flow, and the one used by Bernardes varied the value of $X = \Delta p_t / \Delta p_s$. Pretorius and Kröger[46] used a parabola fitted through three points near the maximum on the power versus flow graph to find the maximum, while Bernardes increased the value of X step by step until the calculated power no longer increased. The power law theory [43] was further developed [45] to show that the parabolic shape of power versus flow curve near the maximum, as assumed as a first approximation by Pretorius[23] is indeed in general a good assumption. It also showed that near its maximum the shape of the power versus X curve varied from a skew parabola to a saw tooth. Since the steeper side of the saw tooth (see figure 3.7) is on the side of the higher values of X, the method of Bernardes that increases the mass flow in small steps until the power starts to decrease, is also good if the steps are small enough.

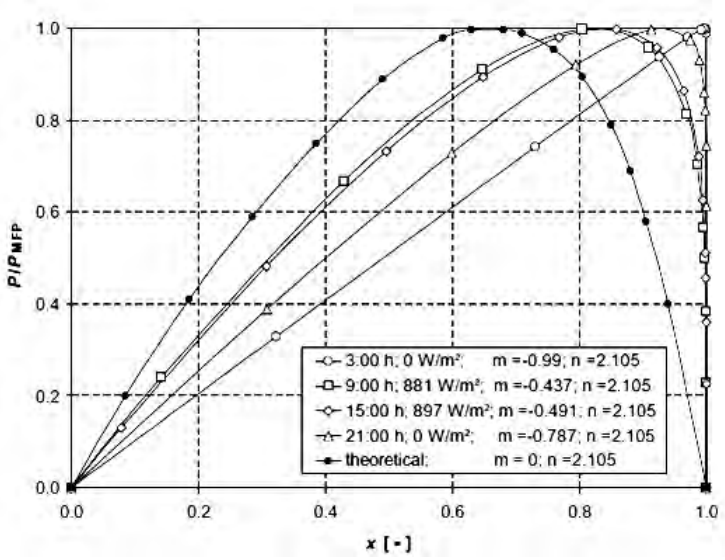

Figure 3.7. Ratio of fluid power to maximum fluid power as dependent on ratio of turbine pressure drop to pressure potential.

The effect on the optimum value of X for the two sets of heat transfer correlations compared by Bernardes [44] was also analysed. It was shown that X varies during the day, and is dependent on the heat transfer coefficients used in modeling the collector performance. The heat transfer coefficients of Bernardes taken from the literature typically resulted in $X = 0.9$, compared to 0.8 when using the heat transfer coefficients of Pretorius[22,23]. While both optimisation schemes can be used to find the optimum during a calculation procedure, the demands of an active control system are different,

and it will be easier, and probably adequate to let the control system adjust the turbine pressure drop to be a fixed fraction of the pressure potential as given by equation (3.6).

3.6.2 Initial turbine design

As the sun moves across the sky during the day and effectively disappears at night, the system pressure potential varies continually. It does not however go to zero during the night due to energy storage in the collector floor. In principle this complicates the design specification of solar chimney turbines. In order to cover mid summer conditions Gannon[15] initially selected three nominal turbine design points based on maximum solar power conditions. He investigated the combination of a vertical axis axial flow turbine and radial inflow inlet guide vanes supporting the chimney. The turbine was a scaled down model of one he designed for conditions in a proposed 200 MW maximum power plant. The required flow deflection in this turbine design representing a full scale turbine was much higher than that of the Manzanares turbine (Haaf[18]), because the specific power was much higher. This required more turbine blades per rotor and per inlet guide vane row, and higher flow deflection in the inlet guide vanes. The Gannon turbine, for example, had 12 rotor blades and 18 IGVs compared to the Manzanares turbine that had 4 rotor blades and no IGVs. The full scale "epic" turbine (as one paper reviewer called it) would, however, be very large, turn very slowly and develop huge torque (figure 3.8).

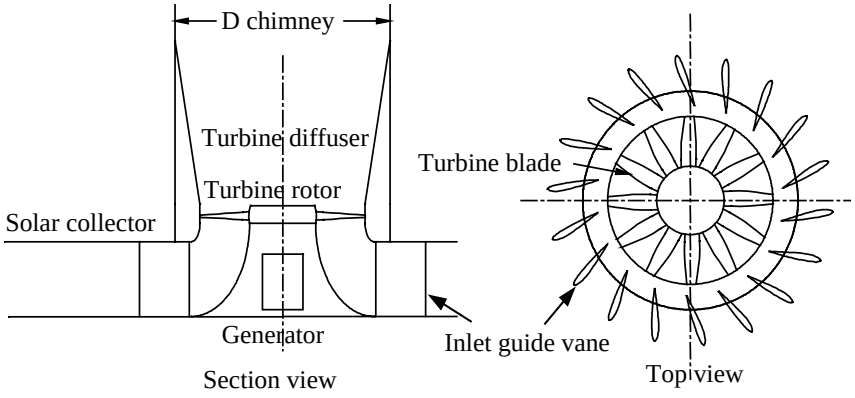

Figure 3.8. Solar chimney single turbine layout [39]

Simulations of the solar chimney operating cycle predict that the pressure drop across the turbine is more than one order of magnitude greater than required by wind turbines. In addition the turbine must be integrated within the base structure of the chimney. The turbine selection criteria were outlined by Gannon[15].

A suitable turbine was designed for a SCPP using a free vortex analysis, the matrix through flow method and a surface vortex panel method[47]. Agreement between the experimental and simulated results showed that the free vortex and matrix through flow methods were effective in predicting the turbine performance. The coupling of the surface vortex method and simplex optimization scheme resulted in efficient low drag blade profiles being developed. The use of the chimney base supports as inlet guide

vanes through radial offset reduced the outflow kinetic energy at the turbine exit and allowed more energy to be extracted from the flow. The blade profiles were optimized for low drag and were designed to give the required flow turning. Results from the experimental program were presented to verify the design method. The design method resulted in a solar chimney turbine design with a total-to-static efficiency of 80 % and a total-to-total efficiency of about 90 %.

3.6.3 Turbine characteristics

Turbine efficiency depends on turbine blade row loss coefficients and turbine diffuser loss coefficients, but for a given set of coefficients the degree of reaction determines the turbine efficiency. Backström [39] presented analytical equations in terms of turbine flow and load coefficient and degree of reaction, to express the influence of each coefficient on turbine efficiency. The velocity triangles are shown in figure 3.9. It finds analytical solutions for optimum degree of reaction, maximum turbine efficiency for required power and maximum efficiency for constrained turbine size (figure 3.10). Points B and C show the unconstrained and constrained maximum efficiency operating points respectively. In this case the chimney diameter is the constraint.

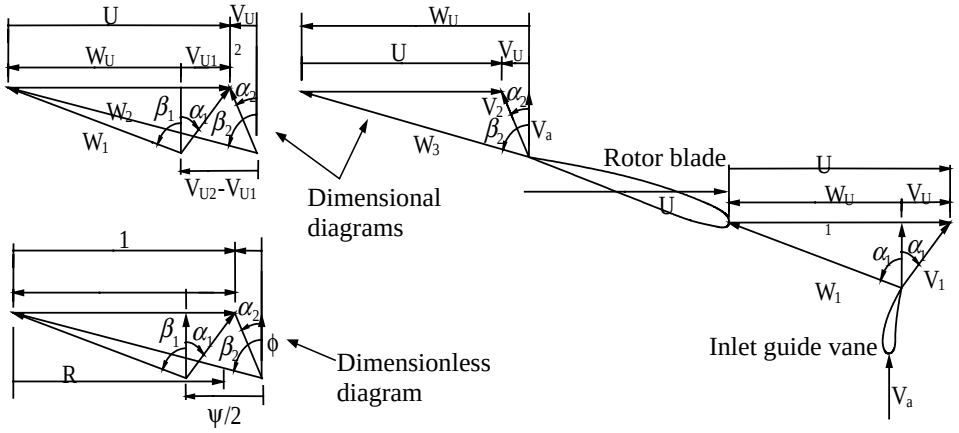

Figure 3.9. Solar chimney turbine velocity diagrams [39]

Characteristics measured on a 720 mm diameter turbine model confirm the validity of the analytical model. The derived equations show the beneficial effect of pre-whirl on turbine performance, and the constraining effects that chimney diameter and design point power may have on maximum attainable turbine efficiency. These considerations are important when making decisions about the initial layout, sizing and design of solar chimney turbines. The models were simple enough to include in SCPP optimisation studies. Application to a proposed large solar chimney plant confirmed that a peak turbine total-to-total efficiency of around 90 % is theoretically attainable (excluding the generator), but not necessarily over the full range of plant operating points.

Various layouts for the turbo generator had been proposed in the literature. Schlaich[20] and Fluri[48] compare the performance of these layouts using analytical models and optimisation techniques. The turbine layouts under consideration are single-rotor and

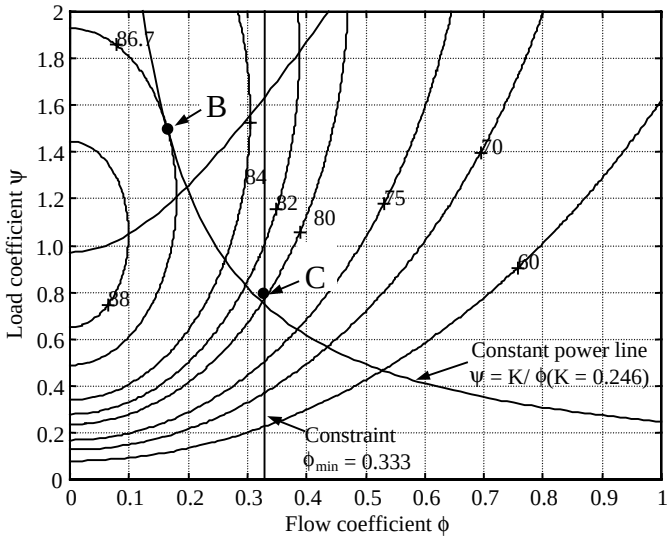

Figure 3.10. Turbine total-to-static efficiency contours on a (ϕ, ψ) map ($R = 1$, $\zeta_s = \zeta_r = 0.05$, $\zeta_e = 0.75$) [39]

counter-rotating turbines, both with or without inlet guide vanes. In contrast to similar investigations found in the literature, various radial sections along the blades are analysed in the turbine model [46]. This approach is more appropriate than using a simple mean line analysis when dealing with turbines with high blade aspect ratio and low hub-to-tip ratio. Furthermore, a limit to the degree of reaction of the turbine has been introduced to avoid diffusion at the hub. It is shown in this paper that these slight changes in modelling approach have a significant impact on the performance prediction. It can be concluded that the single-rotor layout without guide vanes performs very poorly; the efficiencies of the other three layouts are much better and lie in a narrow band. The counter rotating layouts provide the highest peak efficiencies, but at relatively low speeds, which leads to an undesirable higher torque for the same power output. Based on this work the inlet guide vane plus single rotor layout was selected for use in further analyses.

3.6.4 Optimal layout of SCPP turbines

First, a reference plant was chosen as defined by Pretorius[23] and plant performance was simulated with his mathematical model. It was discovered that all the maximum power operating points encountered during a solar year, lie on a single line in a total-to-total pressure ratio versus dimensionless mass flow graph [22]. An equally important discovery was that this line was found to coincide with the ellipse law of Stodola (as reported by Dixon[49]) representing the operating line of a variable speed turbine (figure 3.11).

This finding implies that a variable speed turbine can run optimally throughout the year while handling the seasonal and diurnal variations in flow and pressure drop, with no inlet guide vane or rotor or blade angle adjustment. Conversely it implies that a constant speed turbine would probably need inlet guide vanes and rotor blade adjustment as in Kaplan turbines found in hydro power stations. Stator blade adjustment would

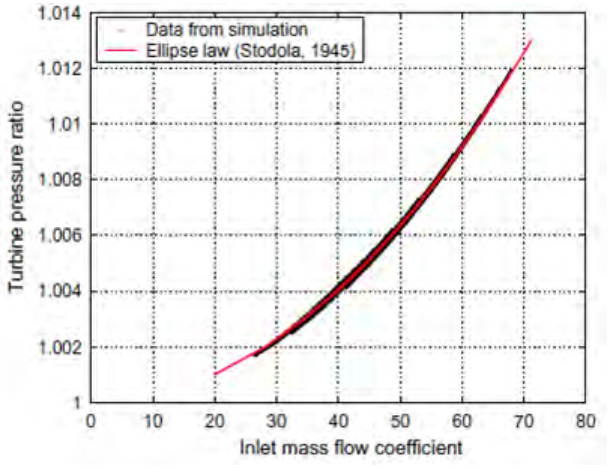

Figure 3.11. Operating line for solar chimney turbine over one year, compared to elliptic law of Stodola.

however be required even in variable speed turbines for turbine shut off and maintenance, otherwise a a very large shut-off valve would be required. Rapid rotor and stator blade adjustment could prevent rotor runaway in case of load rejection, and also allow venting of air during extended periods of zero power generation. In so far unpublished work based on our model turbine, it has been shown that rapid IGV adjustment can prevent initial runaway of the turbine during load rejection, and that IGV control can manage rotor slow down to near zero speed.The optimal design of a turbine for a solar chimney power plant cannot be done without consideration of the generator layout. The turbo generator is a core component of any solar chimney power plant. The rule of thumb is that the mass and cost of the generator increases more or less as the maximum torque it can handle. This favours multiple smaller turbines and generators per chimney rather than fewer larger ones.

The main goals of the paper with Fluri [22] were to analyse the performance of the power conversion unit (PCU) and its interaction with the plant and to compare three configurations from an efficiency and energy yield point of view. The PCU of a large SCPP consists of one or several turbo-generators, power electronics, a grid interface and the flow passage from collector exit to chimney inlet.

Loss models for all components of the power conversion unit were defined, and the impact of the various losses on the overall performance was assessed. Three configurations of the PCU were compared, i.e. the single vertical axis, the multiple vertical axis and the multiple horizontal axis turbine configuration. It was found that the single vertical axis turbine has a slight advantage with regards to efficiency and energy yield because certain loss mechanisms such as stream mixing are not present. But its output torque is large enough to make its feasibility questionable. It is shown that with designing the flow passage in an appropriate manner the aerodynamic losses can be kept low. The thumb-suck assumption made by many other researchers that the total-to-total efficiency of the complete PCU including the generator is about 80 % was confirmed with the presented model. Further, it was shown that the PCU turbine efficiency deteriorates significantly with increasing turbine diffuser area ratio but improves only slightly with

reducing the diffuser area ratio below unity.

The optimal number of turbines varies, but their individual size, the number of blades and even the efficiency of the PCU remains close to constant. It was found that the cost of the PCU, however, varies significantly with size; the specific initial cost of the PCU varies between 437 €/kW and 1644 €/kW.

3.7 Other SCPP chimney and turbine contributions

To round off the description of the SCPP work some incomplete work and work presented at conferences will be discussed. An aspect that was investigated was solar chimney turbine stall with the effect of turbine tip clearance on turbine performance[50]. New data show that the variation of lift coefficient versus angle of attack in solar turbines follows the expected isolated airfoil trends of a linear slope in the unstalled region, with a deviation from this slope depending on *inter alia* Reynolds number. It is also shown that blade sections in turbines may operate at higher lift coefficients than non-rotating similar sections, due to Coriolis force effects on boundary layers suffering from incipient flow separation. An analysis is presented that converts a collection of previously measured load coefficient versus flow coefficient plots to a single lift coefficient versus rotor blade mean span angle of attack plot in the unstalled region, resembling typical isolated airfoil plots. These data confirm the finding presented above that solar chimney turbine theory can be based on isolated airfoil theory. Unfortunately the analysis does not predict the stall angle of attack or lift coefficient exactly, since the performance of the turbine as a whole is more complex, and stall does not occur simultaneously at all spanwise positions along the turbine rotor blades. More experimental work and analysis are required.

The experimental investigation of SCPP turbine tip clearance with Kuhn[51] shows that load coefficient, total-to-total and total-to-static efficiency decrease linearly with increasing rotor tip clearance. The normalized load coefficient decreases by about 6.5 %, the normalized total-to-total efficiency by 2.0 % and the normalized total-to-static efficiency by 4.0 % per percent increase in rotor tip clearance. These results will be useful in future SCPP designs. It is suggested that tip clearance values up to 1 % of the blade height introduce only minor losses. Fluri [46] showed that the minimum cost of electricity for a full size SCPP would be achieved with 32 horizontal axis turbines with a diameter of 30.86 m. Assuming a hub-to-tip ratio of 0.4 and 1 % tip clearance this would result in a tip gap of 93 mm which should be technically feasible.

Future research in this area could focus on the effect of different tip geometries and on the development of a detailed CFD study. Also the effects of rotor eccentricities could be considered more closely.

3.8 SCPP construction and costs

In an effort to improve his understanding of chimney construction and likely chimney shapes Backström contacted the Department of Civil Engineering at Stellenbosch University (SU) in 2003. This eventually resulted in co-operation with the Bergische Universität at Wuppertal in Germany, and in support for the project by the Volkwagen

Stiftung. Three PhDs were funded from this source, and it resulted, amongst other specific papers, to a joint paper [1] describing the state of the art at the time regarding SCPP construction, performance and turbine layout. The main points were that continuous power production, or even load following was possible, as had been shown by Pretorius and Kröger[46], and that tall chimneys with multiple turbines at their bases were feasible.

Another joint paper did a comparative cost analysis of SCPPs. It found that previously published cost analyses were mostly optimistic [47].

In a recent comprehensive solar chimney power technology review paper[52], nineteen of the author's solar chimney power plant papers were cited.

Chapter

4

Summary and conclusion

This dissertation is basically a summary, with some interpretation, of published research by the author. The scope is limited to the fields of turbo-machinery, computational fluid dynamics (CFD) and solar chimney power plants.

In the area of axial flow compressors, the main contributions are in the development of a through-flow method that automatically satisfies mass conservation and the comprehensive description of all the possible flow modes of axial flow compressors. Concerning fan design, the contributions are the realization of the importance of the exit kinetic energy in the determination of the efficiency of rotor-only axial flow fans, and the quantification of the effect of off-axis inflow into cooling system fans on their performance. In the field of centrifugal fans and compressors an original, an original, unifying model for the prediction of slip factor was developed. Spanning the fields of turbo-machinery and solar chimneys, the basic theory of solar chimney turbines was developed, showing that high turbine efficiency was possible.

In the field of solar chimneys, an original thermodynamic approach was developed to predict the main relationships that govern solar chimney performance, and to solve the through-flow equations for non-ideal systems with losses. Equations for the accurate determination of all the thermodynamic variables in a solar chimney as dependent on chimney height, wall friction, additional losses, internal drag and area change were derived and solved. Coefficients of wall friction, bracing wheel loss and exit kinetic energy were determined experimentally, and empirical equations were developed to predict the loss coefficient of the collector to turbine transition section and the turbine inlet flow angle. A simple power law approach allowed the calculation of the optimal turbine pressure drop in solar chimney power plants. A comparison of two sets of equations used to calculate the heat fluxes into, inside and leaving the solar collector, resulted in similar air temperature rises in the collector, and similar produced power. It turned out however that the optimal flow for minimal turbine pressure drop was dependent on the heat transfer models.

The performance of various solar chimney turbo-generator layouts using analytical models and optimisation techniques showed that the optimal number of turbines varies with plant size, but the individual turbine size, the number of blades and even the

efficiency remains close to constant. It was found that the cost of a turbo-generator system, however, varies significantly with size. Two joint papers did comparative cost analysis of solar chimney power plant costs.

The total numbers of Scopus citations of the author's papers referenced in this dissertation are: turbomachinery (45), CFD (35) and solar chimney power plants (201). This shows that the major impact of the author's work has been in the field of solar chimneys, where the split is: solar chimney power plant thermodynamic and system analysis (105); solar chimney flow analysis (63) and solar chimney turbines (33).

Compared to Scopus, Google Advanced Scholar citations are about 40% more than Scopus citations, primarily because Google accesses more Chinese and local publications.

Endnotes

Chapter 1 Preview

[1] Von Backström, T.W.: Expendable turbojet compressor design, test and development. In: *Eighth International Symposium on Air Breathing Engines*, pp. 331–338. Cincinnati, USA, June 1987.

[2] Busemann, A.: Das Förderhöhenverhältniss Radialer Kreiselpumpen mit Logarithisch-Spiraligen Schaufeln. *Zeitschrift fur Angewandte Mathematik und Mechanik*, vol. 8, pp. 371–84, 1928.

[3] Stodola, A.: *Steam and Gas Turbines*, vol. 2, p. 1259. McGraw-Hill, 1945. Reprinted by Peter Smith, New York.

[4] Gill, A.: *Four quadrant axial flow compressor performance*. PhD (Eng), Stellenbosch University, 2012. (Promoters: T.W. von Backström and T.M. Harms)

[5] Thiart, G.D.: Finite difference scheme for the numerical solution of fluid flow and heat transfer problems on nonstaggered grids. *Numerical Heat Transfer, Part B: Fundamentals*, vol. 17, no. 1, pp. 43–62, 1990.

[6] Thiart, G.D.: Improved finite-difference scheme for the solution of convection-diffusion problems with the simplen. *Numerical Heat Transfer, Part B: Fundamentals*, vol. 18, no. 1, pp. 81–95, 1990.

[7] Thiart, G.D.: *A numerical procedure for predicting the effects of distorted inflow conditions on the performance of axial flow fans*. PhD (Eng), Stellenbosch University, 1991. (Promoter: T.W. von Backström)

[8] Harms, T.M.: *A numerical method for the analysis of flow fields with complex boundaries*. PhD (Eng), Stellenbosch University, 1995. (Promoters: T.W. von Backström and J.P. du Plessis)

[9] Bruneau, P.R.P.: *The design of a single rotor axial flow fan for a cooling tower application*. MEng, Stellenbosch University, 1994. (Supervisor: T.W. von Backström).

[10] Von Backström, T.W., Van der Spuy, S.J. and Stinnes, W.H.: The limiting efficiency of rotor-only fans and turbines. In: *Proceedings of SACAM 2000, International Conference on Applied Mechanics*. Durban, South Africa, January 11–13 2000.

[11] Van der Spuy, S.J.: *Design of a low-noise rotor-only axial flow fan series.* MEng (Mech), Stellenbosch University, 1997. (Supervisor: T.W. von Backström).

[12] Stinnes, W.: *Performance of axial fans subjected to forced cross-flow at inlet*. MEng (Mech), Stellenbosch University, 1998. (Supervisor: T.W. von Backström).

[13] Hotchkiss, P.J.: *Development of a rotor model for numerical simulations of helicopter exterior flow-fields*. MEng (Mech), University of Cape Town, 2004. (Supervisors: C.J. Meyer and T.W von Backström).

[14] Heise, R.: *Implementation of a two-stream fan in the CIRSTEL system*. PhD (Eng), Stellenbosch University, 2006. (Promoter: T.W. von Backström).

[15] Gannon, A.J.: *Solar Chimney Turbine Performance*. PhD (Eng), Stellenbosch University, 2002. (Promoter: T.W. von Backström).

[16] Haaf, W.: Solar chimneys: Part II: Preliminary test results from the Manzanares pilot plant. *International Journal of Solar Energy*, vol. 2, no. 2, pp. 141–161, 1984.

[17] Kirstein, C.: *Flow through a solar chimney power plant collector-to-chimney transition section*. MEng (Mech), Stellenbosch University, 2004. (Supervisors: T.W. von Backström and D.G. Kröger).

[18] Haaf, W., Friedrich, K., Mayr, G. and Schlaich, J.: Solar chimneys: Part I: Principle and construction of the pilot plant in Manzanares. *International Journal of Solar Energy*, vol. 2, no. 1, pp. 3–20, 1983.

[19] Mullett, L.B.: The solar chimney—overall efficiency, design and performance. *International Journal of Ambient Energy*, vol. 8, no. 1, pp. 35–40, 1987.

[20] Schlaich, J.: *The Solar Chimney: Electricity from the Sun*. C. Maurer, Geislingen, Germany, 1995.

[21] Lautenschlager, H., Haaf, W. and Schlaich, J.: New results from the solar chimney prototype and conclusions for large power plants. Tech. Rep., Commission of the European Communities (Report) EUR, 1985.

[22] Pretorius, J.P.: *Solar tower power plant performance characteristics*. MEng (Mech), Stellenbosch University, 2004. (Supervisor: D.G. Kröger and T.W. von Backström).

[23] Pretorius, J.P.: *Optimization and Control of a Large-scale Solar Chimney Power Plant*. PhD (Eng), Stellenbosch University, 2007. (Promoter: D.G. Kröger).

Chapter 2 Turbo-machines and CFD

[24] Reinecke, J., Von Backström, T.W. and Venter, G.: Effect of a diffuser on the performance of an ocean current turbine. In: *9th European Wave and Tidal Energy Conference*. University of Southampton, 2011.

[25] Wessels, F.J.L., Venter, G. and Von Backström, T.W.: An efficient scheme for describing airfoils using non-uniform rational B-splines. In: *Proceedings of ASME Turbo Expo 2012*, GT2012-69468. Copenhagen, Denmark, June 11-15 2012.

[26] Wiesner, F.J.: A review of slip factors for centrifugal impellers. *Trans. ASME, Journal of Engineering for Power*, vol. 89, pp. 558–572, 1967.

[27] Pierce, W.T. and Von Backström, T.W.: Laminar separation bubble prediction with CFD. In: *Proceedings of ISES Solar World Congress 2009*, pp. 1057–1064. Sandton Convension Centre, Johannesburg, South Africa, 2009.

[28] Louw, F.G., Bruneau, P.R.P., Von Backström, T.W. and Van der Spuy, S.J.: The design of an axial flow fan for applications in large air-cooled heat exchangers, In: *Proceedings of ASME Turbo Expo 2012*. Copenhagen, Denmark, June 11–15, 2012.

[29] Salta, C.A. and Kröger, D.G.: Effect of inlet flow distortions on fan performance in forced draught air-cooled heat exchangers. *Heat Recovery Systems and CHP*, vol. 15, no. 6, pp. 555–561, 1995.

[30] Van der Spuy, S.J., Von Backström, T.W. and Kröger, D.G.: The use of the actuator disk method to model axial flow fans in CFD. In: *14TH IAHR Cooling Tower and Heat Exchanger Conference*, Paper OP15. Stellenbosch, South Africa, December 1–3 2009

[31] Van der Spuy, S.J., Le Roux, F.N., Von Backström, T.W. and Kröger, D.G.: The simulation of an axial flow fan performance curve at low flow rates. In: *ASME Turbo Expo 2011*. Vancouver, Canada, June 6–10 2011.

[32] Van der Spuy, S.J., Von Backström, T.W. and Kröger, D.G.: Using computational fluid dynamics to simulate multiple axial flow fans in air-cooled steam condensers. In: *ASME 2011 International Mechanical Engineering Congress & Exposition*. Denver, Colorado, USA, November 11–17 2011

Chapter 3 Solar chimneys

[33] Pasumarthi, N. and Sherif, S.A.: Experimental and theoretical performance of a demonstration solar chimney model–Part I: Mathematical model development. *International Journal of Energy Research*, vol. 22, no. 3, pp. 277–288, 1998*a*.

[34] Yan, M.Q., Kridii, G.T., Sherif, S.A., Lee, S.S. and Padki, M.M.: Thermo-fluid analysis of solar chimneys. In: *American Society of Mechanical Engineers, Fluids Engineering Division (Publication) FED*, vol. 132, pp. 125–130. 1991.

[35] Trieb, F., Langniß, O. and Klaiß, H.: Solar electricity generation–a comparative view of technologies, costs and environmental impact. *Solar Energy*, vol. 59, no. 1–2, pp. 89–99, 1997.

[36] Pasumarthi, N. and Sherif, S.A.: Experimental and theoretical performance of a demonstration solar chimney model–Part II: Experimental and theoretical results and economic analysis. *International Journal of Energy Research*, vol. 22, no. 5, pp. 443–461, 1998*b*.

[37] Padki, M.M. and Sherif, S.A.: Fluid dynamics of solar chimneys. In: *Proceedings of the 109th ASME Winter Annual Meeting*, FED-Vol. 70, pp. 43–46. Chicago, Illinois, 1988.

[38] Cohen, H., Rogers, G.F.C. and Saravanamuttoo, H.I.H.: *Gas Turbine Theory*. 4th edn. Addison Wesley Longman Ltd, England, 1996.

[39] Novikov, I.I.: The efficiency of atomic power stations. *Journal Nuclear Energy II*, vol. 7, pp. 125–128, 1958. Translated from Atomnaya Energia, vol. 3, no. 11, p. 409, (1957).

[40] Kröger, D.G. and Blaine, D.: Analysis of the driving potential of a solar chimney power plant. *SAIMechE R&D Journal*, vol. 15, no. 3, pp. 85–94, 1999.

[41] Papageorgiou, C.D.: Floating solar chimney technology. In: Rugesco, R.D. (ed.), *Solar energy*, pp. 187–222. 2010. ISBN 978-953-307-052-0.

[42] Kröger, D. and Burger, M.: Experimental convection heat transfer coefficient on a horizontal surface exposed to the natural environment. In: *ISES EuroSun2004 International Sonnen forum*, vol. 1, pp. 422–430. Freiburg, Germany, 2004.

[43] Nizetic, S., Ninic, N. and Klarin, B.: Analysis and feasibility of implementing solar chimney power plants in the Mediterranean region. *Energy*, vol. 33, no. 11, pp. 1680–1690, 2008.

[44] Hedderwick, R.A.: *Performance Evaluation of a Solar Chimney Power Plant*. MEng (Mech), Stellenbosch University, 2000. (Supervisor: D.G. Kröger).

[45] dos S. Bernardes, M.A., Voß, A. and Weinrebe, G.: Thermal and technical analysis of solar chimneys. *Solar Energy*, vol. 75, no. 6, pp. 511–524, 2003.

[46] Pretorius, J.P. and Kröger, D.G.: Solar chimney power plant performance. *Journal of Solar energy engineering*, vol. 128, no. 3, pp. 302–311, 2006.

[47] Gannon, A.J. and Von Backström, T.W.: Solar chimney turbine Part 1/2: Design. In: *ASME Solar 2002: International Solar Energy Conference (SED2002)*, pp. 335–341. Reno, Nevada, USA, June 15–20, 2002.

[48] Fluri, T.P.: *Turbine Layout for and Optimization of Solar Chimney Power Conversion Units*. PhD (Eng), Stellenbosch University, 2007. (Promoter: T.W. von Backström).

[49] Dixon, S.L.: *Fluid Mechanics and Thermodynamics of Turbomachinery*. 6th edn. Butterworth-Heinemann, 2010.

[50] Von Backström, T.W. and Maliage, S.M.: Stall considerations in solar chimney turbines. In: *ISES Solar World Congress 2009*, pp. 1156–1165. Sandton, South Africa, October 11–14 2009.

[51] Kuhn, M., Von Backström, T.W. and Fluri, T.P.: The influence of tip clearance effects on the performance of solar chimney turbines. In: *Proceedings of the 2nd International Conference on Solar Chimney Power Technology*. 28-30 September 2010.

[52] Zhou, X., Wang, F. and Ochieng, R.M.: A review of solar chimney power technology. *Renewable and Sustainable Energy Reviews*, vol. 14, no. 8, pp. 2315–2338, 2010.

List of References

[1] Von Backström, T.W., Harte, R., Höffer, R., Krätzig, W.B., Kröger, D.G., Niemann, H.-J. and Van Zijl, G.P.A.G.: State and recent advances in research and design of solar updraft power technology. *VGB PowerTech*, vol. 88, no. 7, pp. 64–71, 2008. (Cited on pages xv, 3, 8, and 37.)

[2] Von Backström, T.W.: Transonic compressor optimization by computational fluid dynamics. *Aeronautica Meridiana*, vol. 8, pp. 85–96, 1990. (Cited on pages 1, 4, and 8.)

[3] Von Backström, T.W.: Three-dimensional viscous flow through a highly loaded compressor rotor. *International Journal of Turbo and Jet Engines*, vol. 9, no. 3, pp. 165–182, 1992. (Cited on pages 1, 2, 4, and 8.)

[4] Lewis, K.L. and Von Backström, T.W.: The experimental optimization of an annular dump diffuser. *SAIMechE. R&D Journal*, vol. 7, no. 2, pp. 7–15, 1991. (Cited on pages 1 and 4.)

[5] Roos, T.H. and Von Backström, T.W.: Off-design low-speed NACA-65 loss and deflection correlation with low-Reynolds number correction for compressor through-flow analysis. *Aeronautica Meridiana*, vol. 33, pp. 66–93, 1998. (Cited on pages 1 and 4.)

[6] Gannon, A.J. and Von Backström, T.W.: Comparison of streamline through-flow and streamline-curvature methods. *International Journal of Turbo and Jet Engines*, vol. 17, no. 2, pp. 16–170, 2000. (Cited on pages 1, 4, and 5.)

[7] Sinclair, M., Von Backström, T.W. and Du Buisson, J.J.: Heuristic methods for arranging blades to minimize rotor unbalance. *Engineering Optimization*, vol. 22, no. 1, pp. 19–26, 1993. (Cited on page 1.)

[8] Von Backström, T.W. and Du Buisson, J.J.: Blade arrangement strategies for minimal rotor unbalance. *International Journal of Turbo and Jet-Engines*, vol. 11, no. 2–3, pp. 193–200, 1994. (Cited on page 1.)

[9] Von Backström, T.W.: A unified correlation for slip factor in centrifugal impellers. *Journal of Turbomachinery*, vol. 128, no. 1, pp. 1–10, 2006. (Cited on pages 1, 5, and 6.)

[10] Von Backström, T.W.: A compact equation for the prediction eddy-induced slip in centrifugal impellers. *Proceedings of the Institution of Mechanical Engineers, Part A: Journal of Power and Energy*, vol. 220, no. 8, pp. 911–915, 2006. (Cited on pages 1, 5, and 6.)

[11] Gill, A., Von Backström, T.W. and Harms, T.M.: Fundamentals of four-quadrant axial flow compressor maps. *Proceedings of the Institution of Mechanical Engineers, Part A: Journal of Power and Energy*, vol. 221, no. 7, pp. 1001–1010, 2007. (Cited on pages 1 and 6.)

[12] Strachan, P.J., Reynaud, F.P. and Von Backström, T.W.: The hydrodynamic modelling of torque converters. *SAIMechE. R&D Journal*, vol. 8, no. 1, pp. 21–28, 1992. (Cited on pages 1 and 7.)

[13] Venter, A.A. and Von Backström, T.W.: Panel method prediction of flow through a torque converter turbine. *SAIMechE R&D Journal*, vol. 10, no. 2, pp. 31–40, 1994. (Cited on pages 1 and 7.)

[14] Strachan, P.J. and Von Backström, T.W.: Velocity measurement in a hydrodynamic torque converter. *SAIMechE R&D Journal*, vol. 16, pp. 62–70, 2000. (Cited on pages 1 and 7.)

[15] Von Backström, T.W. and Lakshminarayana, B.: Perspective: Fluid dynamics and performance of automotive torque converters: An assessment. *ASME Journal of Fluids Engineering*, vol. 118, no. 4, pp. 665–676, 1996. (Cited on pages 1 and 7.)

[16] Harms, T.M., Von Backström, T.W. and Du Plessis, J.P.: Reformulation of the "SIMPLEN" algorithm to accommodate non-centralized interfaces. *Numerical Heat Transfer, Part B*, vol. 20, no. 2, pp. 127–144, 1991. (Cited on pages 2 and 8.)

[17] Harms, T.M., Von Backström, T.W. and Du Plessis, J.P.: Derivation of a modified power-law approximation. *Numerical Heat Transfer, Part B*, vol. 22, no. 2, pp. 235–241, 1992. (Not cited.)

[18] Harms, T.M., Von Backström, T.W., Du Plessis, J.P. and Toerien, L.M.: Derivation of a modified hybrid approximation. *AIAA Journal*, vol. 32, no. 7, pp. 1541–1543, 1994. (Not cited.)

[19] Harms, T.M., Von Backström, T.W. and Du Plessis, J.P.: Simplified control volume finite-element method. *Numerical Heat Transfer, Part B*, vol. 30, no. 2, pp. 179 –194, 1996. (Not cited.)

[20] Harms, T.M., Von Backström, T.W. and Du Plessis, J.P.: Comparison of three finite volume interpolation schemes. *SAIMechE R&D Journal*, vol. 13, no. 1, pp. 20–30, 1997. (Cited on pages 2 and 8.)

[21] Kirstein, C.F. and Von Backström, T.W.: Flow through a solar chimney power plant collector-to-chimney transition section. *Journal of Solar Energy Engineering – Transactions of the ASME*, vol. 128, no. 3, pp. 312–317, 2006. (Cited on pages 2, 3, 8, 23, and 28.)

[22] Fluri, T.P. and Von Backström, T.W.: Performance analysis of the power conversion unit of a solar chimney power plant. *Solar Energy*, vol. 82, no. 11, pp. 999–1008, 2008. (Cited on pages 2, 3, 34, and 35.)

[23] Hotchkiss, P.J., Meyer, C.J. and Von Backström, T.W.: Numerical investigation into the effect of cross-flow on the performance of axial flow fans in forced draught air-cooled heat exchangers. *Applied Thermal Engineering*, vol. 26, no. 2–3, pp. 200–208, 2006. (Cited on pages 2, 8, and 14.)

[24] Heise, R., Meyer, C.J. and von Backström, T.W.: CFD simulation of helicopter flow fields using an actuator disk main rotor model. *SAIMechE R&D Journal*, vol. 23, no. 3, pp. 24–32, 2007. (Cited on pages 2 and 8.)

[25] Van der Spuy, S.J., Von Backström, T.W. and Kröger, D.G.: Performance of low noise fans in power plant air cooled steam condensers. *Noise Control Engineering Journal*, vol. 57, no. 4, pp. 341–347, 2009. (Cited on pages 2 and 8.)

[26] Van der Spuy, S.J., Von Backström, T.W. and Kröger, D.G.: An evaluation of simplified methods to model the performance of axial flow fan arrays. *SAIMechE R&D Journal*, vol. 26, pp. 12–20, 2010. (Cited on pages 2, 8, and 14.)

[27] Von Backström, T.W.: Expendable turbojet compressor design, test and development. In: *Eighth International Symposium on Air Breathing Engines*, pp. 331–338. Cincinnati, USA, June 1987. (Cited on page 2.)

[28] Louw, F.G., Bruneau, P.R.P., Von Backström, T.W. and Van der Spuy, S.J.: The design of an axial flow fan for application in large air-cooled heat exchangers. In: *Proceedings of ASME Turbo Expo 2012*, GT2012-69733. Copenhagen, Denmark, June 11-15 2012. (Cited on page 2.)

[29] Von Backström, T.W., Buys, J.D. and Stinnes, W.H.: Minimization of the exit loss of a rotor-only axial fan. *Engineering Optimization*, vol. 26, no. 1, pp. 25–33, 1996. (Cited on pages 2 and 9.)

[30] Van der Spuy, S.J. and Von Backström, T.W.: Performance of a low noise rotor-only axial fan designed for minimum exit kinetic energy. *SAIMechE R&D Journal*, vol. 18, no. 3, pp. 63–69, 2002. (Cited on pages 2 and 12.)

[31] Thiart, G.D. and Von Backström, T.W.: Numerical solution of flow through turbomachinery with the SIMPLEN algorithm. *SAIMechE R&D Journal*, vol. 8, no. 3, pp. 1 –10, 1992. (Cited on pages 2, 8, 12, and 13.)

[32] Thiart, G.D. and Von Backström, T.W.: Numerical simulation of the flow field near an axial flow fan operating under distorted inflow conditions. *Journal of Wind Engineering and Industrial Aerodynamics*, vol. 45, no. 2, pp. 189–214, 1993. (Cited on page 2.)

[33] Thiart, G.D. and Von Backström, T.W.: Extension of the SIMPLEN algorithm differencing scheme to cylindrical polar coordinates. *Numerical Heat Transfer, Part B*, vol. 23, no. 1, pp. 1–19, 1993. (Cited on pages 2 and 8.)

[34] Stinnes, W.H. and Von Backström, T.W.: Effect of cross-flow on the performance of air-cooled heat exchanger fans. *Applied Thermal Engineering*, vol. 22, no. 12, pp. 1403–1415, 2002. (Cited on pages 2, 12, and 14.)

[35] Heise, R. and Von Backström, T.W.: System analysis and optimisation of the CIRSTEL tail boom. *Journal of the American Helicopter Society*, vol. 55, no. 1, pp. 012000/1–012000/6, 2010. (Cited on page 2.)

[36] Von Backström, T.W. and Gannon, A.J.: The solar chimney air standard thermodynamic cycle. *SAIMechE R&D Journal*, vol. 16, no. 1, pp. 16–24, 2000. (Cited on pages 2, 18, 19, 20, 21, 22, 29, and 30.)

[37] Gannon, A.J. and Von Backström, T.W.: Solar chimney cycle analysis with system loss and solar collector performance. *Journal of Solar Energy Engineering – Transactions of the ASME*, vol. 122, no. 3, pp. 133–137, 2000. (Cited on pages 2, 19, 22, 23, and 29.)

[38] Gannon, A.J. and Von Backström, T.W.: Solar chimney turbine performance. *Journal of Solar Energy Engineering – Transactions of the ASME*, vol. 125, no. 1, pp. 101–106, 2003. (Cited on pages 2 and 3.)

[39] Von Backström, T.W. and Gannon, A.J.: Solar chimney turbine characteristics. *Solar Energy*, vol. 76, no. 1-3, pp. 235–241, 2004. (Special Proceedings Issue). (Cited on pages 2, 3, 32, 33, and 34.)

[40] Von Backström, T.W. and Gannon, A.J.: Compressible flow through solar power plant chimneys. *Journal of Solar Energy Engineering – Transactions of the ASME*, vol. 122, no. 3, pp. 138–145, 2000. (Cited on pages 2, 24, and 25.)

[41] Von Backström, T.W.: Calculation of pressure and density in solar power plant chimneys. *Journal of Solar Energy Engineering – Transactions of the ASME*, vol. 125, no. 1, pp. 127–129, 2003. (Technical Brief). (Cited on pages 2, 26, and 27.)

[42] Von Backström, T.W., Bernhardt, A. and Gannon, A.J.: Pressure drop in solar power plant chimneys. *Journal of Solar Energy Engineering – Transactions of the ASME*, vol. 125, no. 2, pp. 165–169, 2003. (Cited on pages 2 and 27.)

[43] Von Backström, T.W. and Fluri, T.P.: Maximum fluid power condition for solar chimney power plants - an analytical approach. *Solar Energy*, vol. 80, pp. 1417–1423, 2006. (Cited on pages 3, 23, and 31.)

[44] Bernardes, M.A.D., Von Backström, T.W. and Kröger, D.G.: Analysis of some available heat transfer coefficients applicable to solar chimney power plant collectors. *Solar Energy*, vol. 83, no. 2, pp. 264–273, 2009. (Cited on pages 3, 23, 24, and 31.)

[45] Bernardes, M.A.D. and Von Backström, T.W.: Evaluation of operational control strategies applicable to solar chimney power plants. *Solar Energy*, vol. 84, no. 2, pp. 277–288, 2010. (Cited on pages 3, 6, and 31.)

[46] Fluri, T.P. and Von Backström, T.W.: Comparison of modelling approaches and layouts for solar chimney turbines. *Solar Energy*, vol. 82, no. 3, pp. 239–246, 2008. (Cited on pages 3, 11, 34, and 36.)

[47] Fluri, T.P., Pretorius, J.P., Van Dyk, C., Von Backström, T.W., Kröger, D.G. and Van Zijl, G.P.A.G.: Cost analysis of solar chimney power plants. *Solar Energy*, vol. 83, no. 2, pp. 246–256, 2009. (Cited on pages 3 and 37.)

[48] Von Backström, T.W.: Relative-eddy induced slip in centrifugal impellers for engineering students. *SAIMechE R&D Journal*, vol. 23, no. 1, pp. 21–27, 2007. (Cited on page 6.)

State and Recent Advances in Research and Design of Solar Chimney Power Plant Technology

Th.W. von Backström, R. Harte, R. Höffer, W.B. Krätzig, D.G. Kröger, H.-J. Niemann and G.P.A.G. van Zijl

Kurzfassung

Forschungs- und Entwicklungsstand beim Entwurf solarer Aufwindkraftwerke

In solaren Aufwindkraftwerken erwärmt die Sonneneinstrahlung in Kollektoren die darin befindliche Luft, die über zentrale Abluftkamine in große Höhen abströmt. Dieser Massenstrom treibt druckgestufte Turbinen am Kaminfuß, deren angekoppelte Generatoren Strom erzeugen. Über keinen anderen Typ von Solarkraftwerken sind so irreführende, oft falsche Aussagen in Umlauf, die zumeist auf betriebliche Fehlinterpretationen des unter der Leitung von J. Schlaich 1982 in Manzanares errichteten 50 kW-Prototyp zurückgehen. Der vorliegende Beitrag skizziert einige der seither erzielten großen Fortschritte in Forschung und Entwicklung dieser für den Einsatz in ariden Gebieten vielversprechenden Stromerzeugungs-Technologie. Er erläutert die flexiblen Steuerungsmöglichkeiten der Leistungsabgabe, gibt einen Überblick über die durch moderne Hochleistungsbetone und Tragwerksforschung beim Bau von Naturzugkühltürmen konzipierten wirtschaftlichen Bauweisen und weist auf den Entwicklungstand besonders leistungsstarker Turbinen für diesen Kraftwerkstyp hin.

Authors

Professor Dr. Theodor W. von Backström
University of Stellenbosch, Stellenbosch/South Africa.

Professor Dr. Reinhard Harte
University of Wuppertal, Wuppertal/Germany.

Professor Dr. Rüdiger Höffer
Ruhr-University Bochum, Bochum/Germany.

Professor Dr. Dr.-Ing. E.h. Wilfried B. Krätzig
Krätzig & Partners, Bochum/Germany.

Professor Dr. Dr.-Ing E.h. Detlev G. Kröger
University of Stellenbosch, Stellenbosch/South Africa.

Professor Dr. Hans-Jürgen Niemann
Niemann & Partners, Bochum/Germany.

Professor Dr. Gideon P.A.G. van Zijl
TU Delft, Delft/The Netherlands and University of Stellenbosch, Stellenbosch/South Africa.

History and General Working Concept

Although fossil-fuelled power plants will be built for many more years, renewable energy sources will play an ever increasing role. One of the available concepts is solar chimney power plants which imitate the daily solar-driven up- and downdraft in the lower atmosphere and convert parts of the energies therein into electric power.

The general working concept is illustrated in Figure 1. A solar chimney power plant (SCPP) consists of the collector area (CA), the turbine(s) with coupled generator(s) as power conversion unit (PCU), and the solar chimney (SC). In the CA, a large glass-covered area, wide-banded solar radiation heats the collector ground and consequently warms up the air inside the CA, which streams towards the centre of the collector. There, in the PCU, the energy in the stream of warm air is partly transformed into electric power. For increased effectiveness, a pressure sink at the PCU outlet is created by the huge solar chimney.

Solar chimney power plants are the most sustainable natural resources for electric power generation. During service, they are completely free of carbon dioxide emissions, since they use solar radiation as fuel. If one incorporates all energies required for plant construction in an energy balance measured by CO_2 emissions, one ends up with around 10 g of CO_2 per kWh of produced electricity, depending on the service-life duration of the plant. Intended designed service lives are 80 to 120 years, admitting renewals of the turbogenerators and parts of the glass-roof.

Such power station concepts, however, will only deliver sufficient efficiency in areas with high solar radiation input of more than 2.0 MWh/a, as valid in all great deserts up to 30° latitude north and south of the equator. The degree of efficiency of a SCPP then depends primarily on the size of the CA (air temperature) and on the height of the SC (pressure difference) [23]: A plant with CA diameter of 7 000 m and with SC height of 1 500 m is estimated to deliver a maximum electric power of 400 MW, on mid-days in summer time.

This solar updraft power generation was first proposed in 1903 by the Spanish engineer *I. Cabanyes* [5]. Another early description can be found in the work [11] of the German author *H. Günther* from 1931. Around 1975, a series of patents were granted to the US engineer *R.E. Lucier* in countries with deserts suitable for SCPPs, like Australia, Israel and the US.

Starting in 1982, a team led by the German civil engineer *J. Schlaich* took the initiative and constructed a prototype SCPP in Manzanares/Spain, with a 200 m high SC and a maximum power output of 50 kW. This plant operated successfully for more than six years. Figure 2 gives an impression of this prototype plant. In 1987, *Pasumarthi* and *Sherif* erected a smaller prototype installation in California and published the first thermo-mechanical plant model [18]. Since those days, projects for SCPPs have been developed in arid zones all over the world, but none of them has been brought to realisation, up to now.

The prototype plant in Figure 2 contained a single PCU with vertical turbine axis. Such solutions have been considered also for bigger plants, but modern designs show a series of single CPUs with horizontal axes around the tower foot perimeter, an arrangement more advantageous for turbine installation, control, and maintenance, and - last but not least - cost of energy output.

The present publication will focus on actual research and development recognition of SCPPs, which have been gained partly by large-scale experiments and mainly by computer simulation. General aspects of these power plants are summarised in [27], including a discussion of their pros and cons. A recent compilation of SCPPs can be found in [22], and the basic source about this power generation from the 1990's is [23]. The principal question of experts as well as laymen, namely if a tower of height more than 1000 m can be built at all, has considerably calmed down since the Burj Dubai Skyscraper in the Arabian Emirates of 818 m of height is under construction.

Thermal Design and Simulation of Air Flux and Energy Output

SCPP Working Principle: Conversion from Solar Energy to Electricity

Direct and diffuse solar irradiation strikes the glass collector roof of the CA, where specific

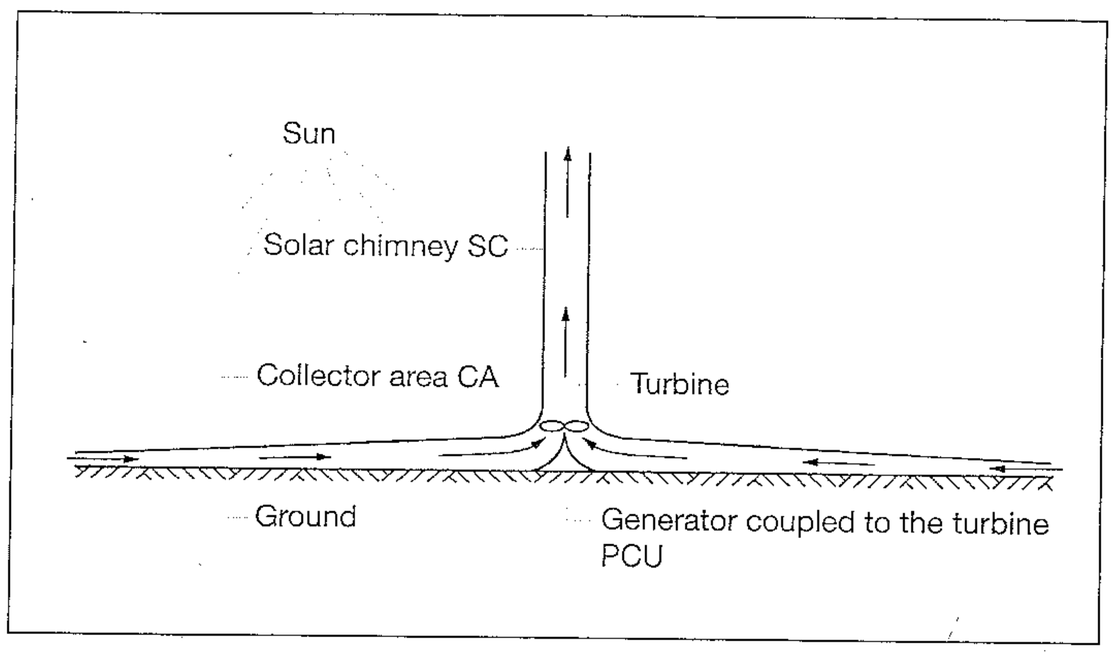

Figure 1. Schematic solar upwind power plant.

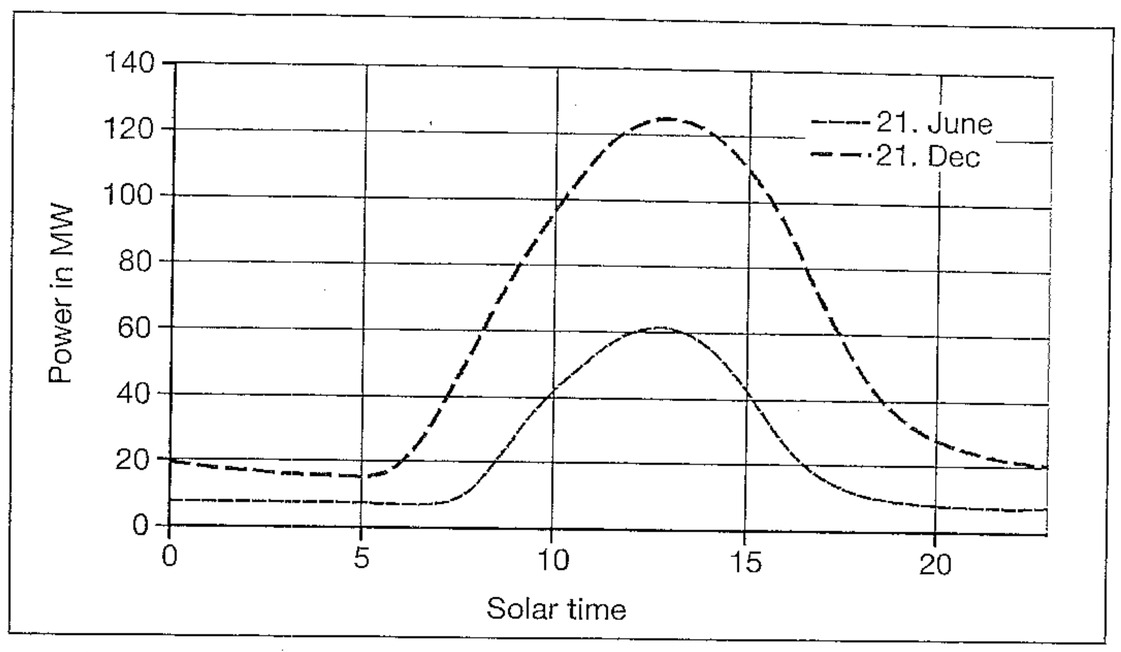

Figure 3. Electrical power output of SCPP for 24 hours during summer and winter.

fractions of the energy are reflected, absorbed and transmitted. The quantities of these fractions depend on the solar incidence angle and optical characteristics of the glass, such as the refractive index, thickness and extinction coefficient. The transmitted solar radiation strikes the ground surface of the CA below the roof, thereby heating it. At the ground surface, a part of the energy is absorbed while another part is reflected back to the roof, where it is again reflected to the ground. The multiple reflection of radiation continues, resulting in a higher fraction of energy absorbed by the ground, known as the transmittance-absorptance product of the ground. Through the mechanism of natural convection, the warm ground surface heats the adjacent air, causing it to rise. The buoyant air rises up into the chimney of the plant, thereby drawing in more air at the collector perimeter and thus initiating forced convection which heats the collector air more rapidly. Through mixed convection, the warm collector air also heats the underside of the collector roof. Some of the energy absorbed by the ground surface is conducted to the cooler earth below, while radiation exchange also takes place between the warm ground surface and the cooler collector roof. In turn, via natural and forced convection, the collector roof transfers energy from its surface to the ambient air adjacent to it. Radiation exchange also takes place between the collector roof and the sky which can be reduced by glass surface coating.

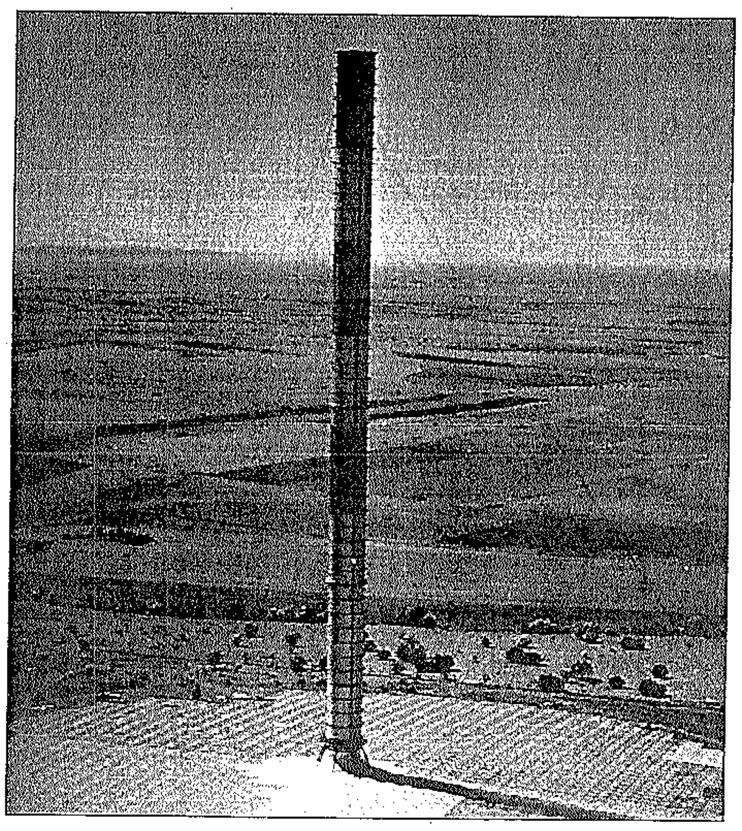

Figure 2. J. Schlaich's prototype SCPP from 1982 at Manzanares/Spain.

As the air flows from the collector perimeter towards the chimney its temperature increases while the velocity of the air stays approximately constant because of the increasing collector height [16, 20]. Due to the decrease in frontal area when entering the chimney, the air velocity increases and again remains approximately constant until it exits the chimney. A temperature drop is experienced across the turbine(s), while within the chimney the temperature decreases with height at a rate approximately equal to the dry adiabatic lapse rate.

The driving force or potential that causes air to flow through the solar chimney power plant is due to the pressure difference between a column of cold air outside and a column of hot air inside the chimney. However, certain pressure losses are experienced as the air flows through the system. As the air moves into the collector from an essentially stagnant condition, it experiences a pressure drop. Under the collector roof, the roof and ground surfaces exert a frictional force while the collector roof supports exert a drag force on the flowing air, thereby causing a further pressure drop. At the turbine inlet, the decreasing flow area causes another pressure drop. A pressure drop is experienced as the turbine(s) extract energy from the flowing air, while in the chimney the internal wall friction and possible supporting bracing structures (spokes) cause a minor pressure drop over the height of the chimney. The air exiting the chimney experiences a pressure differential due to the shape of the chimney outlet and a loss in kinetic energy which results in a dynamic pressure drop.

As the collector air flows across the turbine(s), the kinetic energy of the air turns the turbine blades which in turn drive the generator(s).

Numerical Model and Computer Simulation

Conservation of mass, momentum and energy equations for the collector and chimney air, as well as energy balance for the collector roof and ground form the basis of the numerical model [16, 20]. A draught equation calculates the pressure drop across the turbine by determining the driving potential pressure and subtracting all the pressure losses throughout the system from it. Convective and radiative heat transfer equations calculate all the relevant energy transfers from solar radiation to the energy ultimately absorbed by the collector air. Momentum equations are employed to ascertain the various friction and drag forces imposed on the flowing air.

Relevant conservation equations to determine the thermo-flow field throughout the solar chimney power plant are derived and discretised using finite difference (element) approximations. Ambient meteorological conditions for a reference plant site (near Sishen, South Africa) are used as model input. The equations are solved simultaneously by computer simulation employing standard Visual Basic 6.0 code leading to the results presented in the next sub-chapter. The performance of the solar chimney power plant is ascertained by determining the mass flow rate through the system that will maximise the power output of the plant at a particular time.

This simulation concept is explained in great detail in [20].

Simulation Results: Power Output and Control Possibilities

Figure 3 illustrates the typical daily power output profile during summer and winter for a large-scale solar chimney power plant [19], with main dimensions of a 5000 m collector diameter and a 1000 m high chimney with 210 m inside diameter. No control is involved over the power generated by the plant and therefore it simply produces the maximum power at each moment in time, as determined by the prevailing ambient conditions.

A sensitivity analysis on the influence of various operating and technical plant specifications [21] revealed that the treatment of the top surface of the collector roof to reduce its reflectance or emissivity can potentially mean major enhancements in solar chimney power

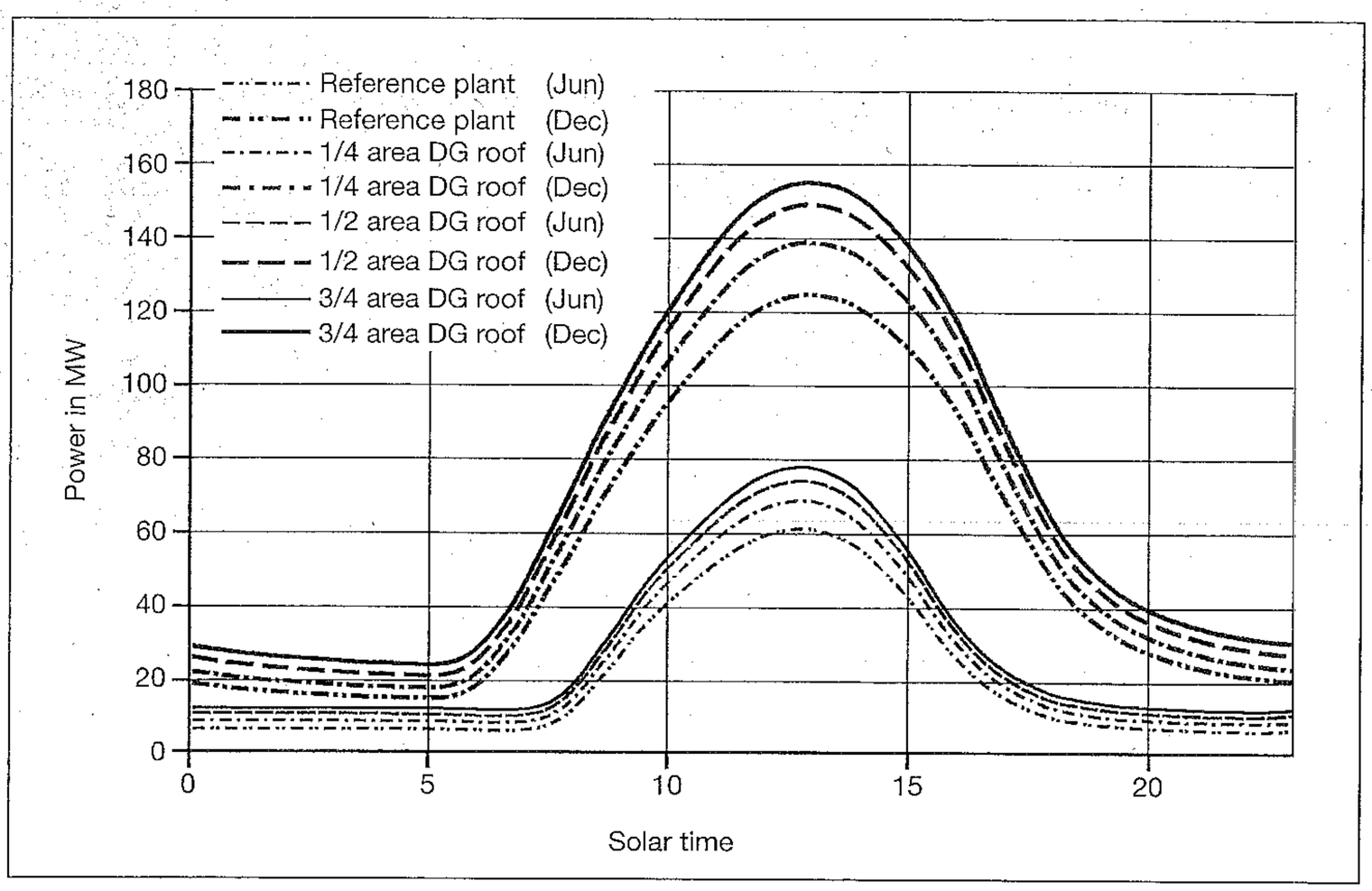

Figure 4. Effect of SCPP performance for a partially double glazed (DG) CA.

plant performance, namely in the order of 13 to 30%.

Methods of enhancing and controlling solar chimney power plant output have been investigated in detail by [20]. This study e.g. shows that double glazing of the collector roof improves plant performance, as illustrated in Figure 4. Here the reference plant refers to the standard plant used in Figure 3. Further simulation results also indicate that by employing a secondary collector roof with airflow-regulating mechanisms, it becomes possible to achieve significant dynamic control over the power output generated by the SCPP, namely to operate the plant either as base or as peak load facility as originally proposed by Kröger (see Figures 5 and 6). Here the power generation again refers to the standard plant in Figure 3. The incorporation of plastic covered water tanks [23] also proved a good mechanism for a static power output control, giving a much more uniform daily output profile compared to a plant without such tanks. It should be emphasized that all basic parameters for these simulations had been measured in large-scale physical experiments.

Special Aspects of Loads on Solar Chimneys

Wind Load and Wind Load Effects

Wind effects together with dead load dominate the feasibility of the tower, and to some extent also of the collector roof. Wind attacks the chimney first statically, considered as constant in time, which is caused by the mean wind speed. Secondly, a broad-banded dynamic loading originates from wind turbulence. Thirdly, vortice-shedding induces on both sides of the chimney a narrow-banded dynamic excitation (*v. Kármán* vortex street). All these loadings are well investigated in theory and in experiments for the lower parts of the atmospheric boundary layer (ABL).

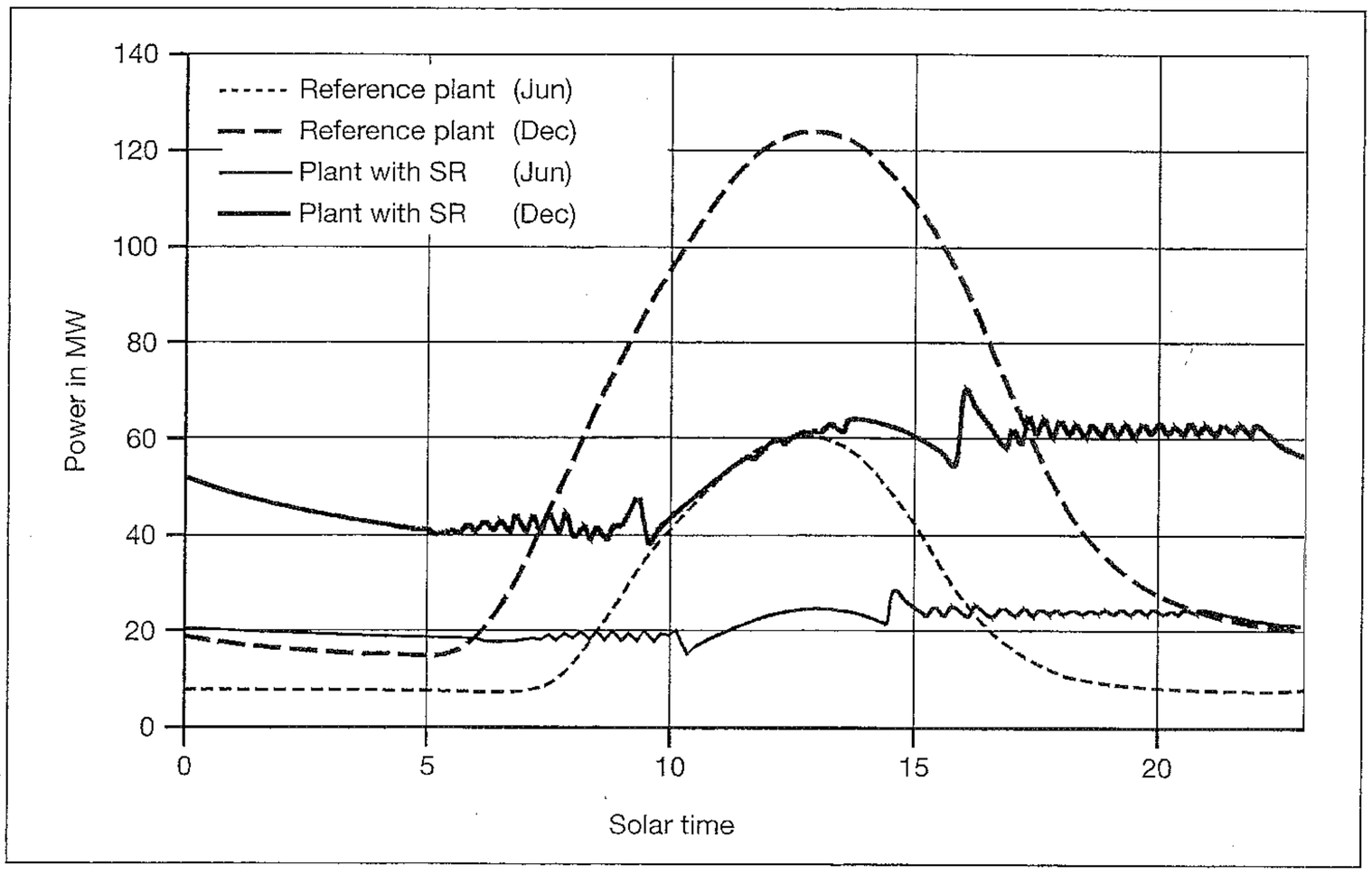

Figure 5. Daily SCPP performance with secondary roof (SR) as base load facility.

Commonly, *Prandtl's* shear layer concept of fluid mechanics provides an adequate basis to describe the natural wind flow and to derive wind loads on structures up to heights of 300 m. This model subdivides the wind flow into mean and fluctuating components. The wind profile specifies the increase of the mean wind speed, so the mean wind load as function of the height z above ground. The standard deviation of the wind speed fluctuations describes the strength of turbulence, i.e. the mentioned broad-band dynamic load, approximately constant throughout the *Prandtl*-layer.

For solar chimneys, this model has to be reconsidered since these structures reach far beyond the atmospheric *Prandtl*-layer into the *Ekman*-layer. Here, *Coriolis*-forces have to be added to the usual friction and pressure gradient forces. The *Coriolis*-forces increase the mean wind speed, diverting the flow from the direction of the isobars according to the *Ekman*-spiral.

A 1500-m-tower e.g. even exceeds the height of the ABL thickness δ, where the ABL ends and the geostrophic wind flow prevails, dominated by pressure gradients and *Coriolis*-forces. Both are in equilibrium with the flow direction tangential to the isobars. At $z \geq \delta$, the shear becomes negligible, meaning that random turbulence and corresponding dynamic load components vanish. Here experimental meteorological data are scarce. However, theoretical considerations provide reliable models as developed by Harris and Deaves [12] for the mean and fluctuating load components. Basic parameters therein are the roughness length z_0 and the thickness δ of the ABL.

The material properties of the fluid, especially its density $\rho = \rho(z)$ and viscosity, vary over tower height. At 1500 m above ground the mass density is 87 % of its value at ground level. The mean velocity pressure q_m diminishes accordingly:

$$\frac{q_m(z)}{q_m(10)} = \left(\frac{V_m(z)}{V_m(10)}\right)^2 \frac{\rho(z)}{\rho_0}, \qquad (1)$$

an effect which may advantageously reduce the total wind load on the tower.

The components of wind turbulence are described by the standard deviation (r.m.s.-values) of the velocity fluctuations: σ_u in the direction of the mean wind, σ_v in horizontal (lateral) direction, and σ_w vertically. Commonly in meteorology the r.m.s.-values are assumed constant in the *Prandtl* layer. Beyond approximately z = 200 m, the r.m.s. fluctuations decrease linearly with the distance to the

ground, and become zero at boundary layer height $z = \delta$. Such properties are included in the loading for description of the dynamic forces by means of the turbulence intensity function I_u.

This intensity I_u is the ratio of the r.m.s.-value of the velocity fluctuations to the mean velocity. It decreases with the height above ground. *Deaves* and *Harris* [12] have based their model on the following parameters: thickness of the ABL δ, roughness length of the terrain z_0, and shear velocity u^*. V. *Kármán's* constant is introduced with $\kappa = 0.4$. The variation of the r.m.s.-value is then given by:

$$\frac{\sigma_u(z)}{\sigma_{u10}} = \frac{(0.539 + 0.09\ln(z/z_0))^{(1-(z/\delta))^{16}}}{(0.539 + 0.09\ln(10/z_0))^{(1-(10/\delta))^{16}}} \frac{1-(z/\delta)}{1-(10/\delta)} \quad (2)$$

The linear term $(1 - z/\delta)$ dominates for $z/\delta > 0.2$, such that the approximation

$$\frac{\sigma_u(z)}{\sigma_{u10}} = (1-1.1(z/\delta)) \quad (3)$$

holds for $z < 1500$ m.

According to our investigations, this theoretical model is an excellent basis of the wind load on solar chimneys. Regarding the broadband excitation by wind turbulence it is questioned whether resonance with the natural frequencies of the structure will become important. Both, beam-like bending modes and ovalling shell modes of vibration, may be excited. The variation of the spectrum of turbulence at high levels is under careful evaluation to provide a basis for future design calculations. Recent investigations indicate that natural frequencies of the tower can be designed sufficiently high to limit the level of resonance to wind turbulence. Turbulence also broadens the bandwidth of vortex excitation. Due to small atmospheric turbulence at high altitudes the excitation of the tower will be approximately mono-frequent with small vibrations. Resonance thus can be avoided by structural means to increase the natural bending frequencies as described in the next chapter.

The pressure distribution of the flow around the solar chimney is sensitive to its Reynolds number and to the surface roughness. The high trans-critical Reynolds numbers in the order of $Re \approx 4 \cdot 10^8$ have been approximately attained in full scale tests performed at hyperbolic cooling towers. The measurements provided static and dynamic wind loading data over the internal and external tower surface, such as

- mean pressure distributions in dependence of surface roughness;
- r.m.s.-pressure distributions and their correlation fields;
- pressure spectra and their coherence fields.

The data of these cooling tower experiences provide a reliable basis for estimation of static and dynamic wind pressures/forces on the solar tower for future model investigations in boundary wind tunnels (Figure 7).

Seismic Sensitivity

Occasionally the sensitivity of solar chimneys due to seismic excitation is questioned, probably due to their extreme height. The sensitivity of structures to earthquakes in general depends on their natural frequencies and the excited ground motions. A classical concept for quantification of the effect of earthquakes to a structure is to measure or to simulate the soil acceleration, and to compute time history responses on single degree of freedom oscillators. The maximal response functions of the oscillators plotted over their eigenfrequencies, so-called response spectra, are design bases also for solar chimneys.

Such design spectra generally exhibit their important contributions between 2 Hz (0.5 s) and 0.2 Hz (5 s), Figure 8. The lower eigenfrequencies of the fundamental oscillation of the beam-like behaviour of the solar chimney of approximately 0.1 Hz or T=10 s classify such towers as very soft cantilevers, optimally isolated against strong earthquake excitations. Some design-relevant internal stresses may arise from higher modes, but a dominant increase of the base bending must not be expected.

In detailed analyses the shell sections between the stiffening rings showed relevant seismic ovallising modes with eigenfrequencies from $0.30 \div 0.35$ Hz leading to local bending. Serious aspects may also be found by systematic examination of the dynamic soil-structure interactions. The loading from the foundations and the subsoil due to both the impact of seismic waves and the reaction forces of the responding structure have to be considered. Subsequent and reflected, re-fractured and superimposed earthquake waves generate non-simultaneous (non-coherent) ground accelerations at the lower parts of the solar chimney. Investigations of such conditions show similarities with long-span bridges and long halls [13, 15]: Multiple asynchronous seismic excitations lead to an even lower overall seismic loading, whereas local effects in the structure and its foundations may then become relevant. This also holds for the vertical component of the seismic ground accelerations which may strongly affect the dimensioning of the substructure.

Solar Chimney Design and Construction

Loading and Response Characteristics

From the point of view of their load-response behaviour, solar chimneys are extremely enlarged, over-dimensioned cooling tower shells, demonstrating all those problems well known to cooling tower designers from more than 40 years of experience with such shell structures, namely:

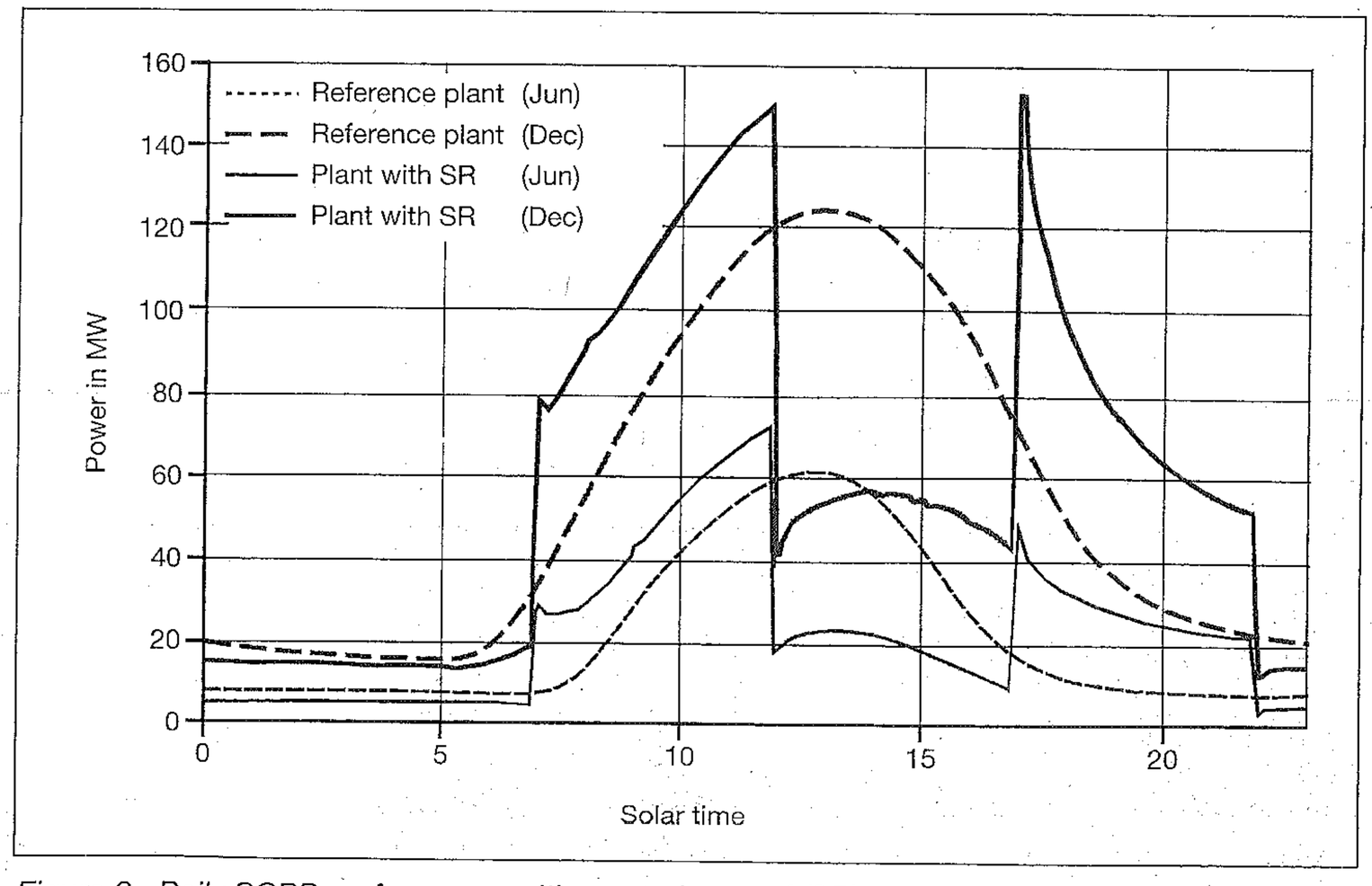

Figure 6. Daily SCPP performance with secondary roof (SR) as peak load facility.

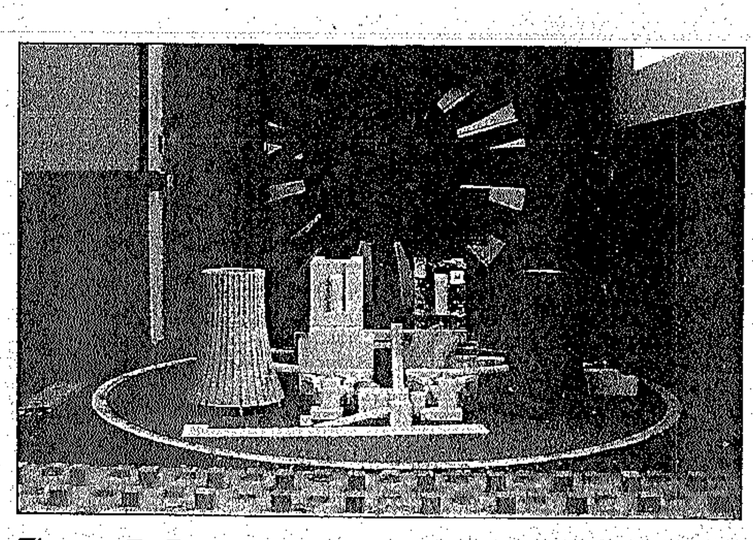

Figure 7. Boundary layer wind tunnel investigation of a thermal power station.

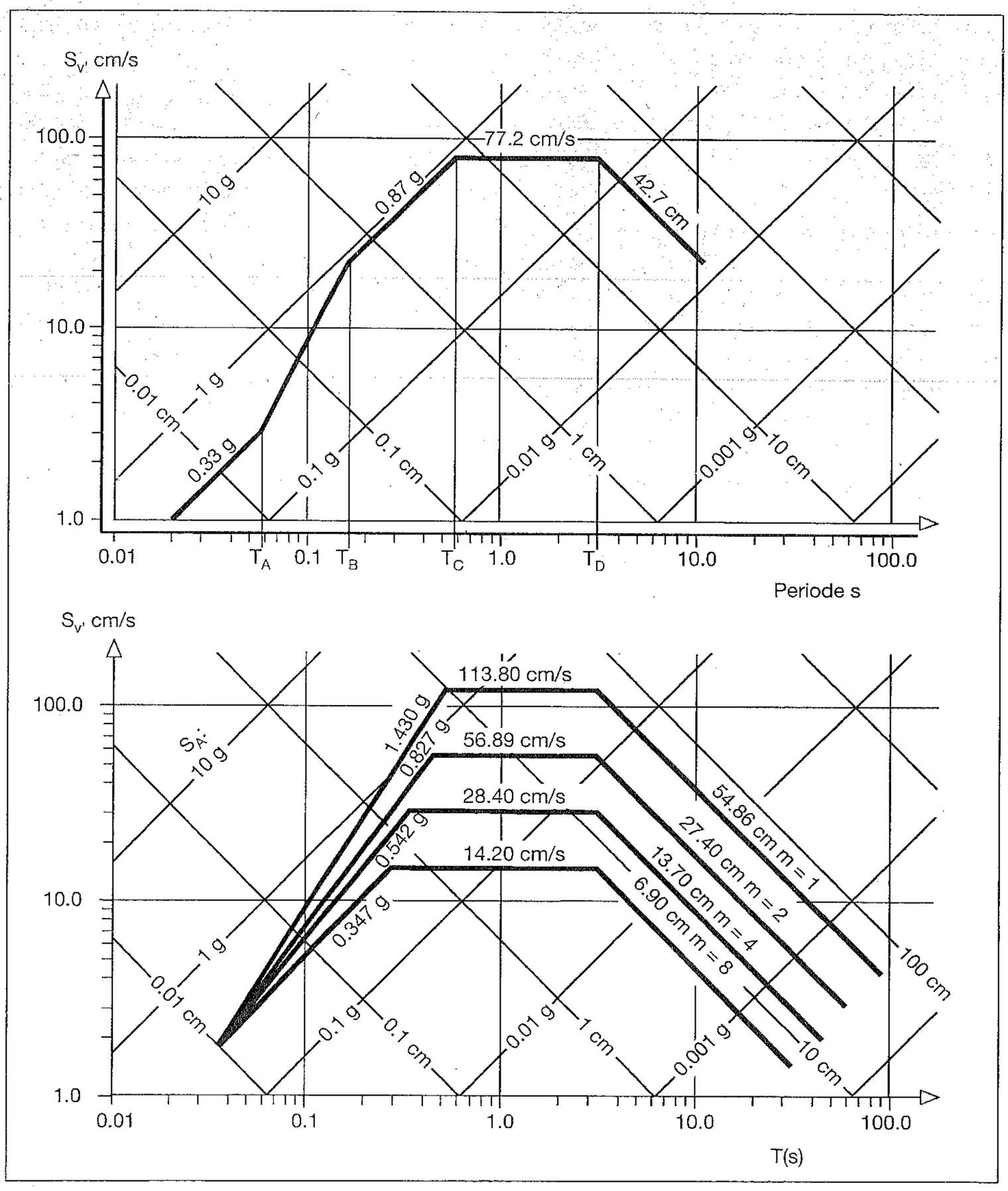

Figure 8. Elastic (top) and inelastic (bottom) design spectra due to Newmark-Hall.

- high compression stresses under deadweight D and wind action W,
- tendency to vertical outside cracking under D, W and service temperature T,
- sensitivity to instabilities like shell buckling under D, W and wind suction S,
- forced wind vibrations including dynamic instabilities,
- strong sensitivity to soil-structure interaction phenomena,
- stress and thermal fatigue of concrete,
- durability problems on the long run of a SCPP's service live duration.

The structural design of a solar chimney is an optimisation process to compromise between several of these conflicting key points. However, the best known basis of any such design is the long-approved technical rule [26].

Figure 9 shows a series of such solar chimneys for SCPPs of different power capacity, pointing out its relationship to natural draft cooling towers. It emphasizes the enormous differences in size, but also the similarities of optimally designed SCs in structural shape, compared to the world largest cooling tower in Niederaussem [3]. Cooling towers are generally constructed without stiffening rings, mainly for reasons of durability, although such auxiliary means have been also applied there [14]. Solar chimneys up to 500 m of height can clearly be executed without any ring stiffeners, certainly with disadvantages to the stability and the maximum stresses. Chimneys of greater height require the application of strong ring stiffeners, with or without internal spokes, for stability, stress safety and for economical reasons.

1000 m Solar Chimney

As a more detailed example, Figure 10 shows a solar chimney of 1000 m of height for a 200 MW plant. The predominant parts of the shell will be constructed by use of high-performance concrete C 70/85, a concrete with compression strength comparable to (low quality) cast iron. In order to control possible cracking on the outer shell face, the concrete may be modified in the sense of a unilateral stress-strain-behaviour, such that its tension strength reduces to that one of a C 30/37. Experiences with such concrete have been gained at the Niederaussem cooling tower [3]. The thickness distribution over the height of the shell can also be seen from Figure 10.

In the upper two thirds the SC shell is formed due to fluid dynamics aspects as a conical frustum in upside-down position. It is stiffened by compression rings with a spacing of 100 m which may be additionally pre-stressed by spoke wheels fabricated of strings from carbon fibre resin. The spokes are directed in such a manner that their mechanical effects are maximum. In the lower third, the solar chimney shell applies the benefits of shape strengthening of shell structures: By use of a hyperboloidal meridional curve the shear stresses there are minimized. This leads to mainly meridional stresses in the narrow residuals of the tower shell between the turbine openings and so simplifies the tower foundation considerably [10].

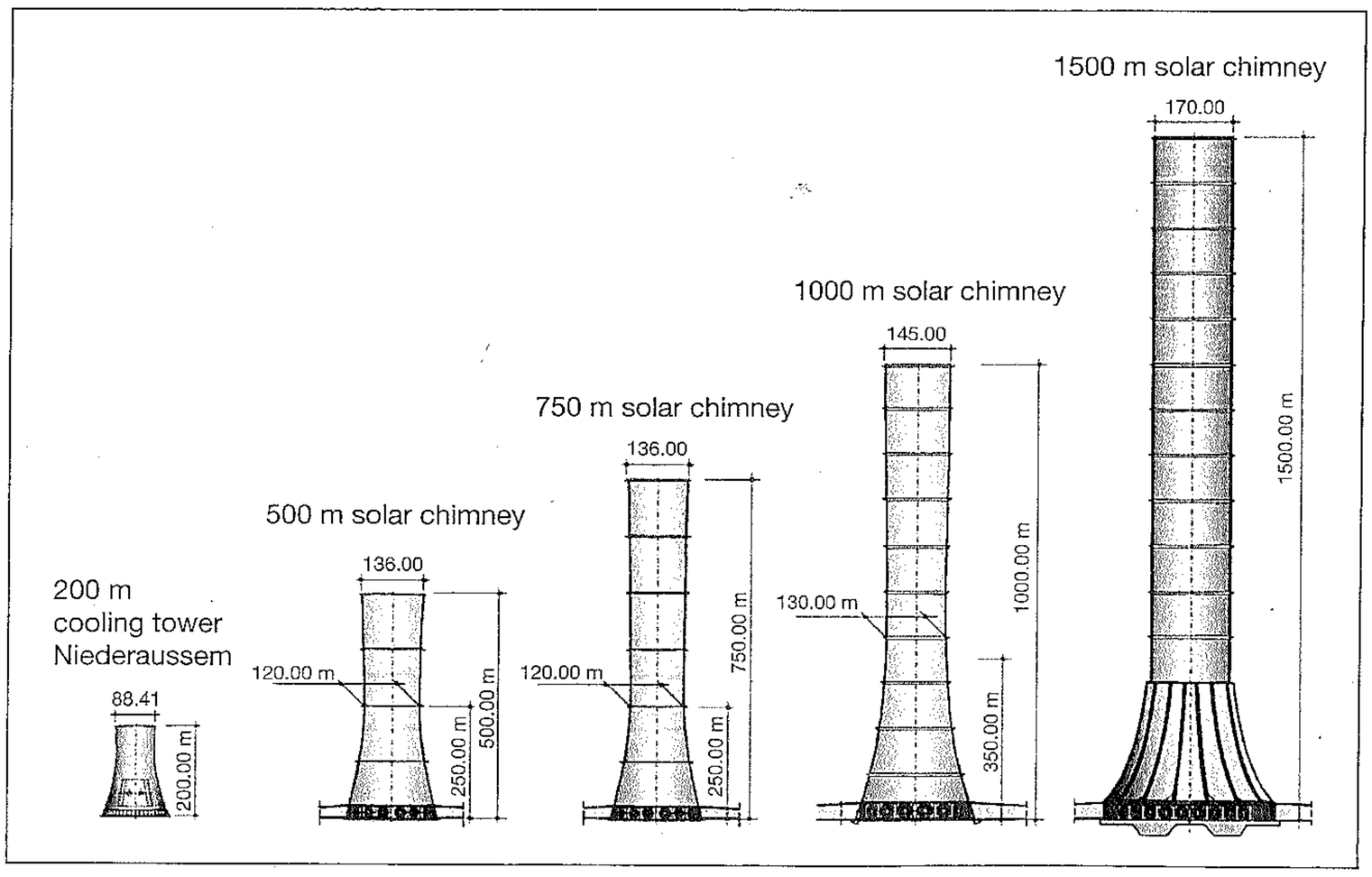

Figure 9. Variants of solar chimneys of different height.

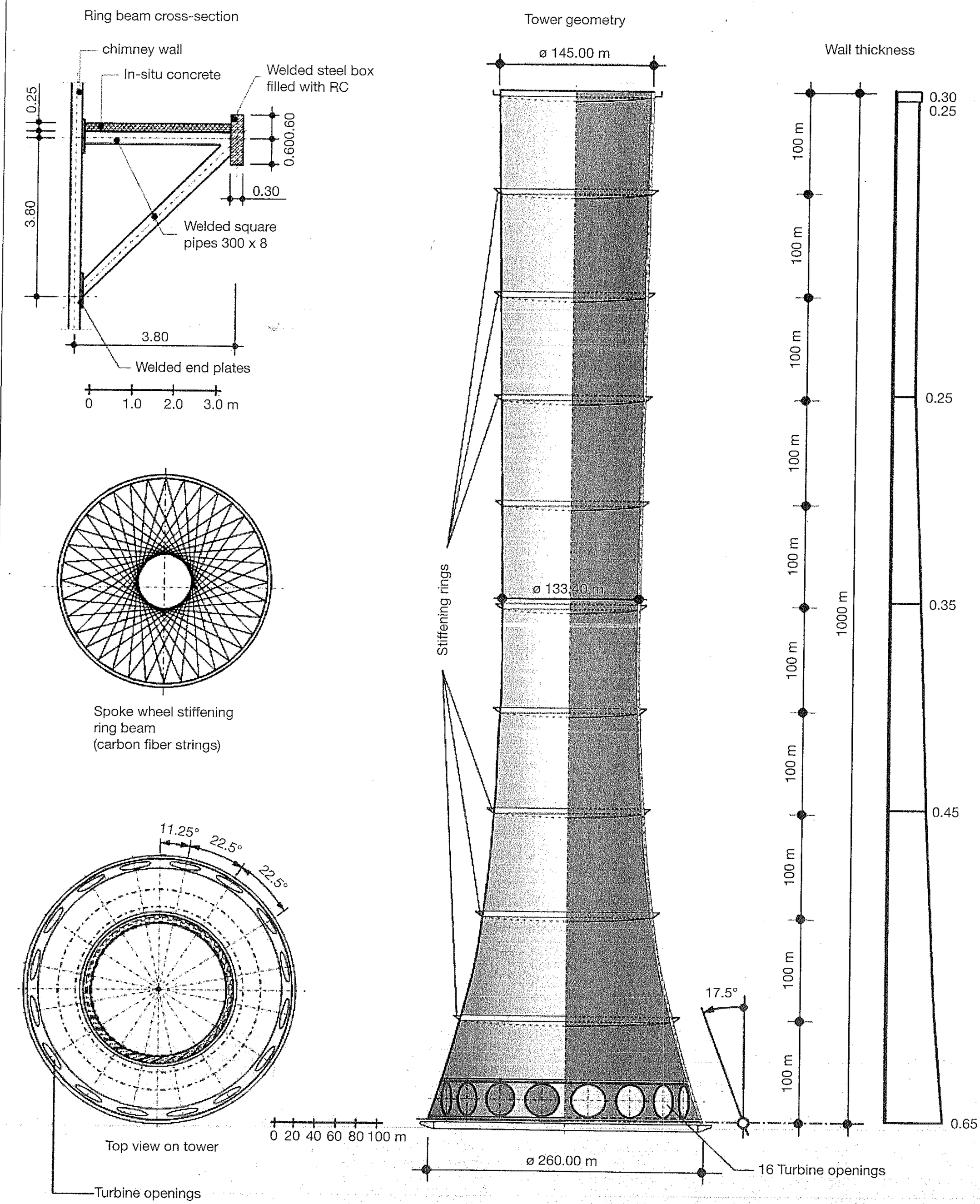

Figure 10. Details of a 1000 m solar chimney.

The turbine openings are stiffened by short cylindrical RC shell pieces, in which the turbo-generators rotate around their horizontal axes. Downstream of the turbine outlets, in the tower interior, membrane structures of Teflon®-coated glass-fibre fabric may provide for an optimised upwards flow of the heated air. These membranes are suspended on and pre-stressed against the chimney shell. Outside the turbines and not detailed in Figure 10, a ring of turbine houses is arranged for separated access for maintenance and repair. The turbine houses are connected to the glass roof of the CA, which is not treated here at all.

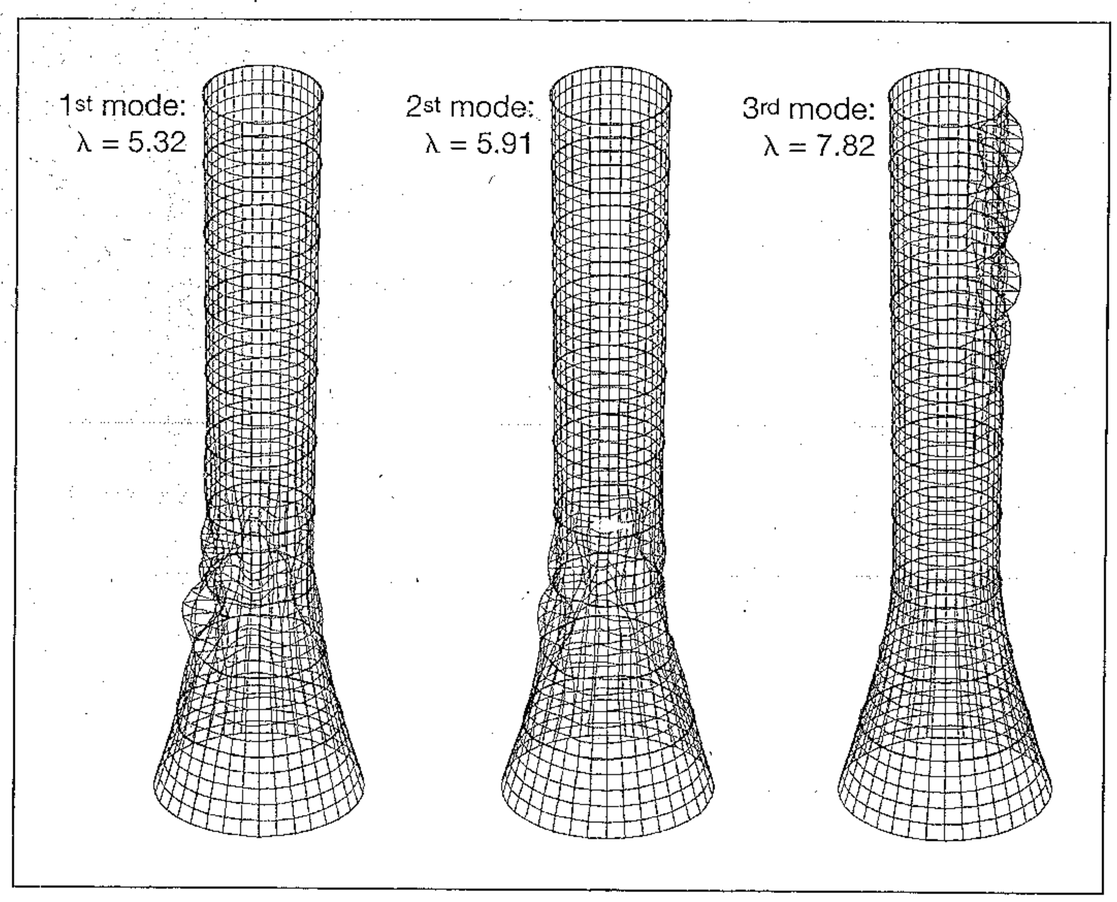

Figure 11. Instability modes and buckling safeties for D+W+S, for SC of Figure 10.

The ring stiffeners in the course of the SC have to serve two mechanical duties. First, they have to force the cross sections from shell-like deformations to beam-like ones, and second, they have to increase the buckling stiffness of the chimney. The latter effect is demonstrated on Figure 11, where weak ring stiffeners lead to an unusual 3rd buckling mode in the upper shell parts. A slight stiffness increase by spokes removes these buckling modes, and increases the buckling safety of the entire structure.

Stability is only one of many aspects in the tower design. Generally speaking, the optimum shaping and ring-stiffening of the SC are those pre-requisites to allow an economical RC construction by use of classical climbing systems, and to guarantee suitable durability for the designed long service life of at least 80 years.

Characteristics of Solar Chimney Turbines

The specifications for solar chimney turbines are in many aspects similar to those ones for large wind turbines [1, 8]. They both convert large amounts of energy in the air flow to electrical energy and feed this into a grid. But there are also various important differences. The following characteristics are typical for solar chimney turbines in contrast to wind turbines.

In solar chimney power plants the turbines are ducted, and their maximum theoretically achievable total-to-total efficiency is therefore 100 %. The *Betz*-limit, which is applicable to wind turbines, is not applicable to ducted ones. Unfortunately, this has been implemented into various codes written for SCPPs, see e.g. [17].

The direction of the oncoming air flow is known and remains constant.

The turbines are protected from harsh weather conditions but have to cope with higher temperatures.

The large volumes of collector and chimney act as a buffer preventing large fluctuations in air flow speed, i.e. dynamic loads on the turbine blades and all the other rotating components are comparably low.

The visual impact of the turbine is small compared to that of the chimney and the collector.

The power output is mainly dependent on solar irradiation, which is much more predictable than wind, improving the power supply quality.

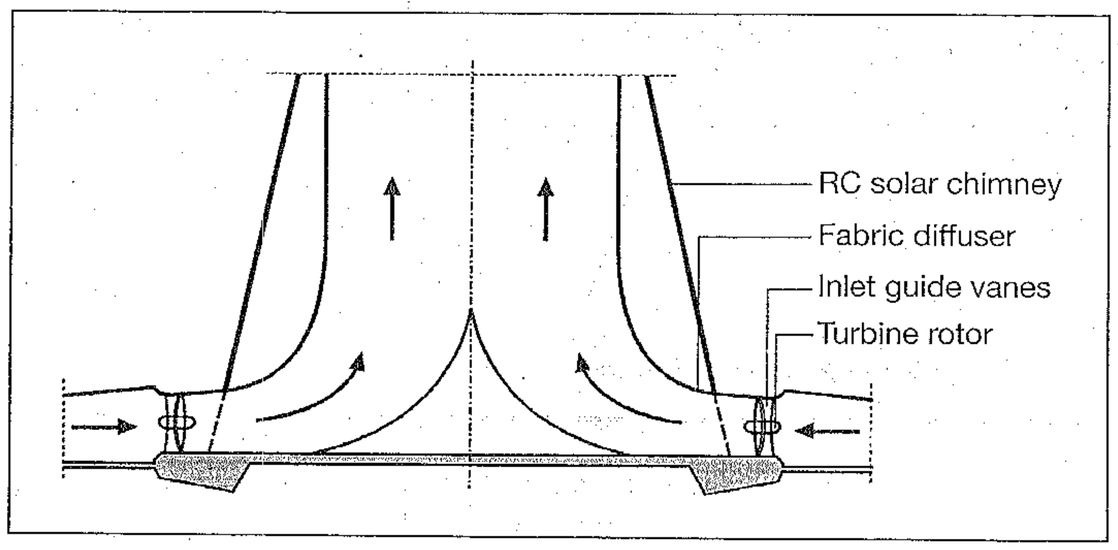

Figure 12. Scheme of a SCPP with multiple horizontal axis turbines.

Furthermore, the turbine pressure drop in SCPPs is about 10 times bigger than in wind turbines [8].

Many of the recent advances in wind turbine technology will potentially be adapted to solar chimney technology, and will have an impact on the design and the cost of solar chimney turbo-generators. As an example, many modern wind turbines use a direct drive variable speed generator [4]. In most of the solar chimney literature it is assumed that a constant speed drive train would be used. A change to a variable speed drive train holds the potential for improved off-design performance.

Various turbine layouts and configurations have been proposed for solar chimney power conversion units (PCU). A single vertical axis turbine without inlet guide vanes was used in

Table 1. Optimum parameters for PCUs of various plant configurations from [6].

Configuration	Ref	Base	Peak	DG
Number of turbines	27	25	29	29
Turbine diameter, m	38.75	41.83	38.52	37.46
Blade length, m	11.62	12.55	11.56	11.24
Turbine speed, rpm	21.00	13.70	21.60	22.80
Maximum tip speed, m/s	42.61	30.01	43.57	44.72
Turbine load coefficient	0.24	0.30	0.26	0.25
Turbine flow coefficient	0.29	0.29	0.28	0.28
Degree of reaction	0.77	0.77	0.77	0.77
Turbine efficiency (tt)	0.89	0.90	0.90	0.89
Stator blades/turbine	32	32	32	32
Rotor blades/turbine	15	16	15	15
Rotor blade mass, ton	1.81	2.17	1.78	1.67
Generator length, m	1.49	1.40	1.53	1.49
Generator diameter, m	5.96	5.61	6.12	5.97
Generator mass, ton	70.93	61.33	75.47	71.39
Torque, MNm	2.31	1.93	2.50	2.33
Power/unit, MW	5.09	2.77	5.66	5.57
Initial capital cost, 10^6 €	96.1	88.8	108.2	102.2
Spec. PCU cost, €/kW	700	1284	660	633
Diffuser area ratio, -	1.30	1.20	1.22	1.29
Efficiency of PCU (tt)	0.78	0.80	0.79	0.79

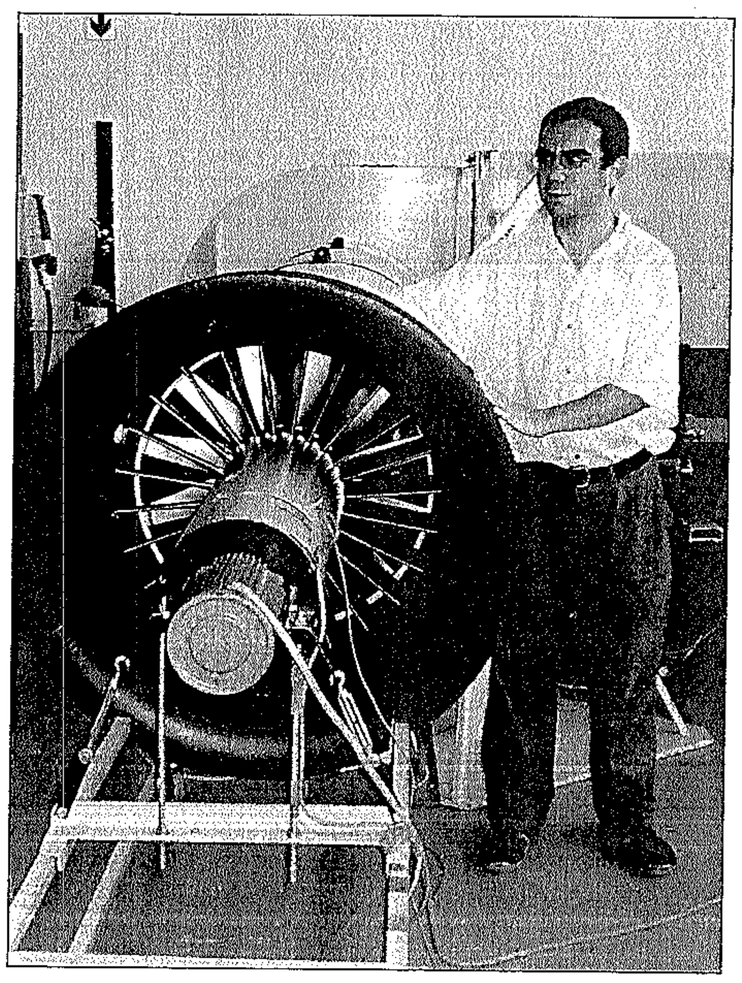

Figure 13. One of several model turbines in the experimental power setup.

the pilot plant in Manzanares [25]. Such single vertical axis turbine layout using the chimney support structure as inlet guide vanes has also been proposed for a large-scale solar chimney [9]. Configurations with multiple vertical axis turbines have been proposed as well [24], and so have turbine layouts consisting of one pair of counter rotating rotors, either with or without inlet guide vanes [6]. It has recently been demonstrated, however, that a configuration with multiple horizontal axis turbines using a single rotor layout with inlet guide vanes (Figure 12) provides the lowest cost of electricity [7]. Table 1 shows optimum parameters for the PCU of various of the plants discussed in [7]. Therein "Ref" refers to the reference plant, "Peak" and "Base" to plants with secondary roofs and airflow-regulating mechanisms allowing for peak or base load operation. DG refers to a plant with the inner half of the collector double glazed, as mentioned already in this manuscript.

In comprehensive solar chimney performance models, as that one described in the paper at hand, it is commonly assumed that the conversion efficiency of the PCU is about 80 %, excluding exit losses [2, 21]. In the research leading to [7] it has been experimentally and theoretically demonstrated, for a wide range of plant geometries, that this is a reasonable global assumption (Figure 13).

Summary and Actuality of SCPPs for Germany

Solar upwind power generation is an interesting modern concept of renewable energy production in desert areas. It copies the daily natural solar uplift and downward air flows in the atmosphere, and gains electric energy out of it. Since it needs no fuel, it operates with the lowest known CO_2 emissions, originated only from the construction material and thus depending on the service life duration of the plant. The present publication has only touched the solar convector, but it should be mentioned that enormous progress has been made recently in raising the efficiency of it by use of specially coated glass sheets. Apart from the Manzanares prototype, SCPPs have not been erected up to now, also because of the enormous investment costs.

Although SCPPs work only with sufficient energy output in arid zones with an adequate solar irradiation, the mechanisms of the Kyoto Protocol, annex 2, to trade CO_2 emission certificates open an interesting gateway also to German energy suppliers. Especially in Central Europe with its limited energy resources, new innovative ideas of energy generation should be evaluated seriously by power technology experts, and should not be disregarded or even condemned in advance.

Acknowledgement: The authors are deeply indebted to the Volkswagen Foundation for considerable financial support. They thank *Mess. Dr. T.P. Fluri, M. Graffmann,* and *Dr. J.P. Pretorius* for their extremely valuable contributions.

References

[1] *Backström, T.W. von, and Gannon, A.J.:* Solar chimney turbine characteristics. ISES Solar Energy J., Spec. Proc. Issue, 76 (2004), 235-241.

[2] *Bernardes, M.:* Technische, ökonomische und ökologische Analyse von Aufwindkraftwerken (Technical, Economical and Ecological Analysis of SCPP). Dr.-Ing. thesis, Universität Stuttgart 2004.

[3] *Busch, D., Harte, R., Krätzig, W.B., and Montag, U.:* New Natural Draft Cooling Tower of 200m of height. J. Engineering Structures 24 (2002), 1509-1521.

[4] *Bywaters, G., John, V., Lynch, J.,Mattila, P., Norton, G., Stowell, J., Salata, M., Labath, O., Chertok, A., and Hablanian, D.:* Northern Power Systems WindPACT drive train alternative design study report. Tech. Rep. NREL/SR-500-35524, National Renewable Energy Laboratory, Colorado. Revised October 2004.

[5] *Cabanyes, I.:* Las chimeneas solares (Solar chimneys). La ernergia eléctrica, 1903. Cited due to Wikipedia.

[6] *Denantes, F, and Bilgen, E.:* Counter-rotating turbines for solar chimney power plants. Renewable Energy 31 (2006), 1873–1891.

[7] *Fluri, T.P.:* Turbine Layout for and Optimization of Solar Chimney Power Conversion Units. Ph.D. thesis, University of Stellenbosch, 2008.

[8] *Gannon, A.J., and Backström, T.W. von.:* Solar chimney turbine performance. ASME J. Solar Energy Engg. 125 (2003), 101-106.

[9] *Gannon, A.J.:* Solar Chimney Turbine Performance. Ph.D. thesis, University of Stellenbosch 2002.

[10] *Graffmann, M., Harte, R., Krätzig, W.B., and Montag, U.:* Sturmbeanspruchte dünne Stahlbetonschalen im Ingenieurbau (Gale-stressed thin RC shells in structural engineering). In: Strack, M., Mark, P., 25 Jahre in Forschung, Lehre und Praxis, Festschrift Prof. Stangenberg, Ruhr-University Bochum 2007.

[11] *Günther, H.:* In hundert Jahren - Die künftige Energieversorgung der Welt (In hundred years - Future energy supply of the world). Kosmos, Franckh'sche Verlagshandlung Stuttgart 1931.

[12] *Harris, R.I., and Deaves, D.M.:* The structure of strong winds. Paper No. 4 of Proc. CIRIA Conf. on "Wind engineering in the eighties". Constr. Indust. Res. and Inf. Assoc., London 1980.

[13] *Hori, M.:* Introduction to computational earthquake engineering. ISBN 1-86094-621-6, Imperial College Press, London, 2006.

[14] *Krätzig, W.B., Harte, R., Lohaus, L., and Wittek, U.:* Naturzugkühltürme (Natural draft cooling towers). Chapter X in Betonkalender, Ernst & Sohn Berlin, 2 (2007), 231-322.

[15] *Meskouris, K., Hinzen, K.-G., Butenweg, C., and Mistler, M.:* Bauwerke und Erdbeben. 2. Auflage, Friedrich Vieweg & Sohn Verlag, Wiesbaden, 2007.

[16] *Pastohr, H.:* Thermodynamische Modellierung eines Aufwindkraftwerkes (Thermodynamic modeling of an updraft power plant). Dr.-Ing.- Thesis, Bauhaus-Universität Weimar, 2004.

[17] *Pastohr, H., Kornadt, O., and Gürlebeck, K.:* Numerical and analytical calculations of the temperature and flow field in the upwind power plant. International J. Energy Research, 28 (2003), 495-510.

[18] *Pasumarthi, N., and Sherif, S.A.:* Experimental and theoretical performance of a demonstration solar chimney model, Part I: mathematical model development. Transactions of the ASME 122 (1998), 138-145.

[19] *Pretorius, J.P., and Kröger, D.G.:* Sensitivity Analysis of the Operating and Technical Specifications of a Solar Chimney Power Plant, ASME Journal of Solar Energy Engineering 129 (2007), 171-178.

[20] *Pretorius, J.P.:* Optimization and Control of a Large-Scale Solar Chimney Power Plant, PhD thesis, University of Stellenbosch, 2007.

[21] *Pretorius, J.P., and Kröger, D.G.:* Solar Chimney Power Plant Performance, ASME J. Solar Energy Engineering 128 (2006) No. 3, 302-311.

[22] *Schlaich, J., Bergermann, R., Schiel, W., and Weinrebe, G.:* Design of Commercial Solar Updraft Tower Systems. ASME J. Solar Energy Engineering 127 (2005), 117-124.

[23] *Schlaich, J.:* The Solar Chimney, Electricity from the Sun. Edition A. Menges, Stuttgart 1995.

[24] *Schlaich, J., Schiel, W., Friedrich, K., Schwarz, G., Wehowsky, P., Meinecke, W. and Kiera, M.:* The solar chimney: Transferability of results from the Manzanares solar chimney plant to larger scale-plants. Tech. Rep., Schlaich Bergermann und Partner CEs, Stuttgart 1995.

[25] *Schwarz, G., and Knauss, H.:* Strömungstechnische Auslegung des Aufwindkraftwerks Manzanares (Aerodynamic design of the SCPP in Manzanares). Tech. Rep., Institut für Aerodynamik, Universität Stuttgart (in German), 1981.

[26] VGB-610 Ue: Structural Design of Cooling Towers. Technical Guideline for the Structural Design, Computation, and Execution of Cooling Towers. VGB Power Tech, Essen 2005.

[27] Wikipedia: Solar_updraft_tower, 2007. □

TRANSONIC COMPRESSOR OPTIMIZATION BY COMPUTATIONAL FLUID DYNAMICS

by T.W. von Backström

Department of Mechanical Engineering

University of Stellenbosch

ABSTRACT

The design of the transonic axial flow compressor of a small gas turbine engine is reviewed. It is shown that the first stage rotor consisting of 23 double circular arc blades probably contributes significantly to the sharp drop in compressor efficiency between 90 and 100% speed. Analysis of this type of blade row with a time marching viscous transonic computational code is shown to be highly realistic and loss predictions are surprisingly accurate. Alternative designs with lower loss levels and larger flow capacity are presented and analysed. This methodology may be useful in the design of turbojet engines.

INTRODUCTION

Three-dimensional time marching codes for the computation of fully viscous transonic flows [1,2] have reached the stage of development where they can be aplied to engineering analysis with confidence. The author has recently successfully modelled the flow through the first stage rotor of the NACA 5-stage transonic compressor [3], using the time marching viscous finite volume computer codes of Dawes [1] and Denton [2],[4] . These investigations and some subsequent computational experiments are relevant to a

locally designed compressor for a low cost expendable turbojet because of its similarities to the NACA 5-stage.

Objectives

The overall objectives of the assessment of the locally designed compressor were to determine the reasons for the steep rise in the equilibrium running line at high speed reported in [5] and [6] and to determine improvement possibilities.

Review

The locally designed four stage transonic compressor develops a pressure ratio of 3.55 at a tip speed of 331 m/s and a first rotor inlet relative tip Mach number of 1.2 [6]. Full speed efficiency and mass flow were about 4 % and 1 % lower than expected [6]. This agreed with the statement of Ball et al that the NACA 5-stage compressor lacked performance but part speed efficiency was excellent [7].

The first stage load coefficient of 0.29 defined as the isentropic enthalpy rise divided by the tip speed squared is high in terms of current practice [6] if the relatively low first rotor tip sodity (chord-to-pitch ratio) of 1.0 is considered. Hearsey [8] claims that an efficient design may be achieved under these conditions by careful optimization, but recommends an extremely high first rotor solidity of 2.6. He also states that the first stage rotor efficiency of the NACA 5-stage rotor might have been raised by several points had the tip solidity been 1.3 rather than 0.98 [8]. This agrees roughly with Wennerstrom's rule of thumb [9] that the tip solidity should equal the rotor relative tip inlet Mach number.

One of the most efficient modern compressors for which data are available is that of the General Electric Energy Efficient Engine (E^3). The agreement between the pitchline solidities of the locally designed compressor and the first

four stages of the E^3 core compressor is surprisingly good, except for the first stage where the E^3 value is 35 % higher (table 1). The similarity between the pitch line meridional Mach numbers is remarkable (table 2), and that between the rotor relative inflow tip Mach numbers is almost as good except for the first stage (table 3). The lower tip Mach number in the locally designed compressor implies that rotor tip solidity has to be increased to only about 1.25 to improve the performance.

The conclusion was that the high losses at high speed were probably caused by too low first stage rotor solidity leading to too high suction surface Mach numbers, and that this could be alleviated by a 25 % increase in first stage rotor solidity or use of a more advanced blade profile such as Multiple Circular Arc (MCA) or both.

Previous computational results [4].

The following conclusions were drawn from the author's previous computational analysis of the flow through the first stage rotor of the NACA 5-stage compressor [4]:

-Shock boundary layer interaction caused suction surface flow separation at radii larger than mid span where the suction surface peak Mach number was 1,38, causing high losses (figure 1).

-Dawes code (BTOB3D) predictions of the losses were good (figure 2).

-In agreement with the measurements, much lower losses were predicted at 90 % speed, and flow separation due to shock boundary layer interaction was absent, with the mid span peak Mach number now only 1,21.

-Denton code (LOSS3D) results agreed with the Dawes code results.

COMPUTATIONAL INVESTIGATION

Using the Dawes code BTOB3D, the effect of the following geometrical variations on the performance of the first stage is investigated computationally in the present study:

- 29 double circular arc (DCA) blades, instead of the 23 in the NACA 5-stage and the locally designed compressor
- 23 multiple circular arc (MCA) blades
- 29 MCA blades

The same hub outlet back pressure was used in all cases.

Effect of Using 29 DCA Blades:

The logical way to investigate the aerodynamic effects of an approximately 25 % increase in solidity as suggested above was to increase the number of blades correspondingly, from 23 to 29. The computational tip clearance of 3,3 % of chord was retained since it had given good agreement with experimental results in the previous work.

The results in table 4 indicate that this option was not very successful in reducing the peak Mach numbers or increasing the maximum mass flow passed at the design outlet static to inlet total pressure ratio. Flow separation due to shock boundary layer interaction still occurred at radial positions larger than 60 % of span (figure 3), although it was less severe than with 23 blades (figure 1).

The mean total pressure loss across the blade row, expressed as fraction of inlet total pressure, was 4,23%. Since the mean ratio of relative inlet dynamic pressure to relative inlet stagnation pressure was 0,419,

this implied a mean conventional loss coefficient of approximately 4,23/0,419 = 0.10 (table 4) compared to 4,5% and 0,11 for the standard case. The comparative spanwise loss distributions in figure 4 also indicate slightly reduced spanwise averaged losses. Because of increased blockage and surface area when using more blades, the losses were in fact increased over most of the blade span. Only in the tip region, where the peak Mach number was slightly reduced were the losses smaller.

It is clear that merely increasing the number of rotor blades by 26%, is not a viable option, especially when the mechanical complications are added.

Effect of Using 23 MCA Blades:

A new version of the data preparation code was written to generate MCA profiles. The underlying geometric assumptions were:

-The profile may be completely described by six arcs, tangential to each other where they meet. These arcs are: leading edge, suction surface supersonic arc, suction surface subsonic arc, trailing edge, pressure surface subsonic arc and pressure surface supersonic arc.

-Leading and trailing edge radii are equal.

-The blade input is completely described by: chord, supersonic chord, camber, supersonic camber, stagger, edge radius (leading edge radius is equal to trailing edge radius), maximum thickness.

The whole idea of using MCA blades instead of DCA is to limit the flow deflection over the front part of the blade suction surface, thereby reducing peak suction Mach numbers and shock boundary layer interaction. The "front

part" (or supersonic arc) of the blade reaches back as far as the blade passage throat, or slightly beyond, to allow an oblique shock. The normal shock position can be found at each blade section by drawing a tangent from the leading edge of one blade to the suction surface of the next. For our design it was decided to make the supersonic camber to total camber ratio equal to 1 minus the supersonic chord to total chord ratio. Total chord and total camber were unchanged from the DCA values as given in [3].

The blade geometry used is summarised in table 5, and the profile shapes may be seen in figures 5 to 7. The shocks at mid span and tip are now oblique, and shock boundary layer interaction, separation, and wake formation in the tip region is limited (figure 5). Suction surface flow separation is confined to the tip region (figure 8).

Loss contours are concentrated in the tip region (figure 12). Figure 9 shows the loss reduction over the full span achieved by using MCA blades. Mass flow has increased by 2,6% at the same back pressure (table 4).

Effect of Using 29 MCA Blades:

Blade profiles were identical to those in the previous section. Increasing the number of blades by 26%, to 29 reduced the peak Mach number at 90% span to 1,33, totally eliminating suction surface flow separation due to shock boundary layer interaction (figure 11).

Loss contours are virtually confined to the tip region (figure 13). A comparison of figures 13 and, 12 shows that increasing the number of MCA blades to 29 reduces losses in the outer third of span only. There is no further increase in mass flow (table 4).

CONCLUSIONS

The high losses at high speed probably originate in the first stage double circular are rotor blades.

Increasing the number of first stage rotor blades without changing the blade profile type will not significantly decrease the losses or increase the choking mass flow, but changing the blade profiles to the MCA type will.

It was recommended that the first stage rotor blades of the locally designed compressors be replaced with the MCA type, without an increase in solidity..

The study showed how computational fluid dynamics could be used to analyse a transonic compressor and critically investigate various improvement possibilities.

Acknowledgements

The computational simulation of the NACA 5-stage compressor was done at the Whittle Laboratory of the University of Cambridge. The author thanks dr N. A. Cumpsty, the acting Director, and drs J. D. Denton and W. N. Dawes for the generous use of their computing facilities and codes.

REFERENCES

1 Dawes, W. N. "Development of a 3D Navier Stokes Solver for Application to all Types of Turbomachinery", ASME paper 88-GT-70, presented at the Gas Turbine and Aeroengine Congress, Amsterdam, The Netherlands, June 6-9, 1988.

2 Denton, J. D. "The Calculation of fully three dimensional flow through any type of turbomachine blade row", Advisory Group for Aerospace Research and Development, Lecture Series No. 140, 1984

3 Kovach, K. and Sandercock, D.M. " Aerodynamic Design and Performance of Five-Stage Transonic Axial-Flow Compressor" J. of Engineering for Power, July 1961.

4 Von Backstrom, T. W. "Dawes and Denton Codes Applied to a Transonic Compressor Rotor" Department of Mechanical Engineering Report No. 1989-1, University of Stellenbosch, July, 1989.

5. Van Eeden, J.A.N. "Development of the APA 350 Gas Turbine" Aerautica Meridiana, Vol.7 No.1, 1988

6 Von Backstrom, T. W. "Expendable turbojet compressor design, test and development" Papers from the Eighth International Symposium on Air Breathing Engines, Cincinnati, Ohio, June 1987.

7 Ball, C. L., Steinke, R. J. and Newman, F.A. "The Design and Development of Transonic Multistage Compressors" Von Karman Institute Lecture Series, 1988-03.

8 Hearsey, R.M. "Practical Compressor Aerodynamic Design", Concepts ETI Principal Lecture Series No. 2, Ch. 1 in "Advanced Topics in Turbomachinery Technology", Edited by Japikse, J.,Norwich, Vermont, 1986.

9 Wennerstrom, A. J. "Design of Critical Compressor Stages", Von Karman Institute Lecture Series, 1988-03.

Table 1

Comparison of Pitch Line Solidities

Rotor	R_1	R_2	R_3	R_4
Local compressor	1,27	1,45	1,38	1,29
GE E^3 core compressor	1,71	1,48	1,39	1,31
Stator	S_1	S_2	S_3	S_4
Local compressor	1,43	1,49	1,32	1,30
GE E^3 core compressor	1,34	1,26	1,28	1,26

Table 2

Comparison of Pitch Line Meridional Mach Number

Position before rotor	R_1	R_2	R_3	R_4	Diffuser (or R_5)
Local compressor	0,61	0,56	0,51	0,49	0,43
GE E^3 compressor	0,60	0,55	0,51	0,48	0,45

Table 3

Comparison of Rotor Rip and Stator Hub Inlet Mach Numbers

Rotor Tip	R_1	R_2	R_3	R_4
Local compressor	1,19	1,10	1,01	0,94
GE E^3 core compressor	1,35	1,08	0,95	0,86
Stator Hub	S_1	S_2	S_3	S_4
Local compressor	0,71	0,67	0,64	0,54
GE E^3 core compressor	0,85	0,79	0,74	0,66

Table 4

Effect of Rotor Blade Number and Blade Shape

Case	Number of Blades	Blade Type	mflo kg/s	Peak Mach No Hub	Peak Mach No Mid	Peak Mach No Tip	Loss %
1	23	DCA	30,4	1,16	1,38	1,50	4.50
2	29	DCA	30,5	1,10	1,30	1,46	4,23
3	23	MCA	31,2	1,16	1,32	1,40	3,70
4	29	MCA	31,2	1,12	1,30	1,33	3,43

Table 5

MCA first stage rotor blade dimensions

Blade Section	1	2	3	4
Radius (mm)	127	152,4	203,4	254
Span (%)	0	20	60	100
Chord (mm)	65,5	66,3	67,8	68,1
Supersonic chord (mm)	31,1	34,8	42,4	49,4
Supersonic chord/chord (%)	47,5	52,5	62,5	72,5
Camber (degrees)	58,4	40,3	19,9	11,7
Supersonic camber (degrees)	30,66	19,14	7,46	3,22
Supersonic camber/camber (%)	52,5	47,5	37,5	27,5
Stagger (degrees)	8,9	22,4	40,2	49,7
Edge radius (mm)	0,38	0,38	0,38	0,38
Maximum thickness (mm)	5,24	4,64	4,07	3,41

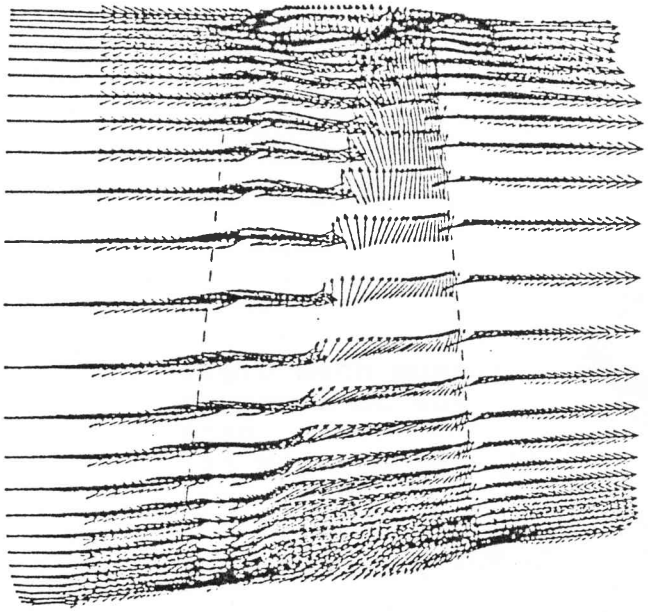

Fig.1 Near suction surface velocity vectors (23 DCA blades)

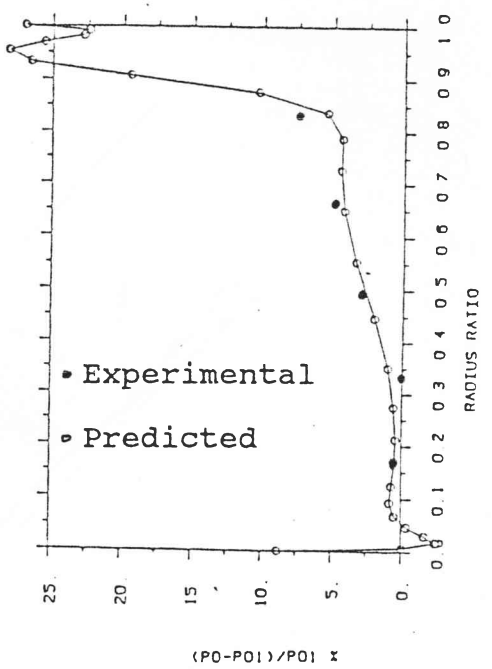

Fig.2 Relative stagnation pressure losses (23 DCA blades)

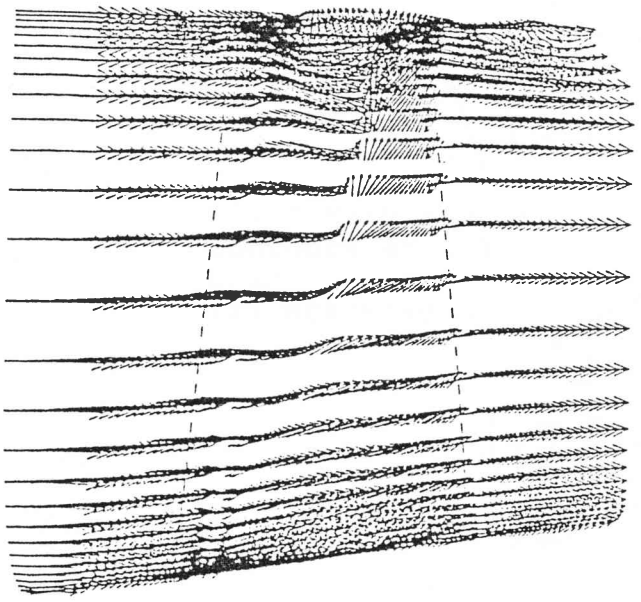

Fig.3 Near suction surface velocity vectors (29 DCA blades)

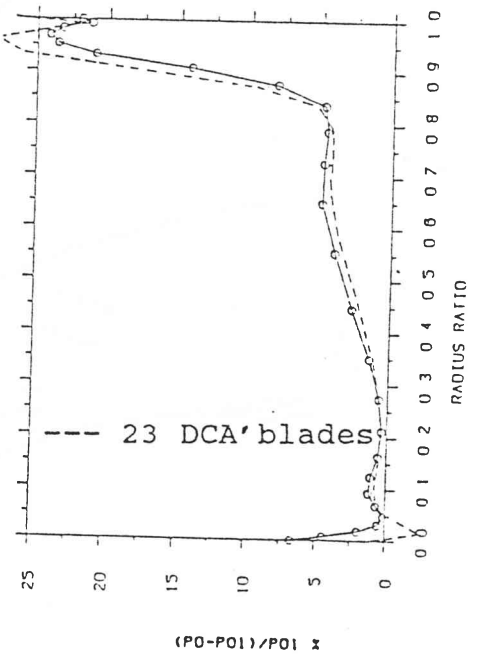

Fig.4 Relative stagnation pressure losses (29 DCA blades)

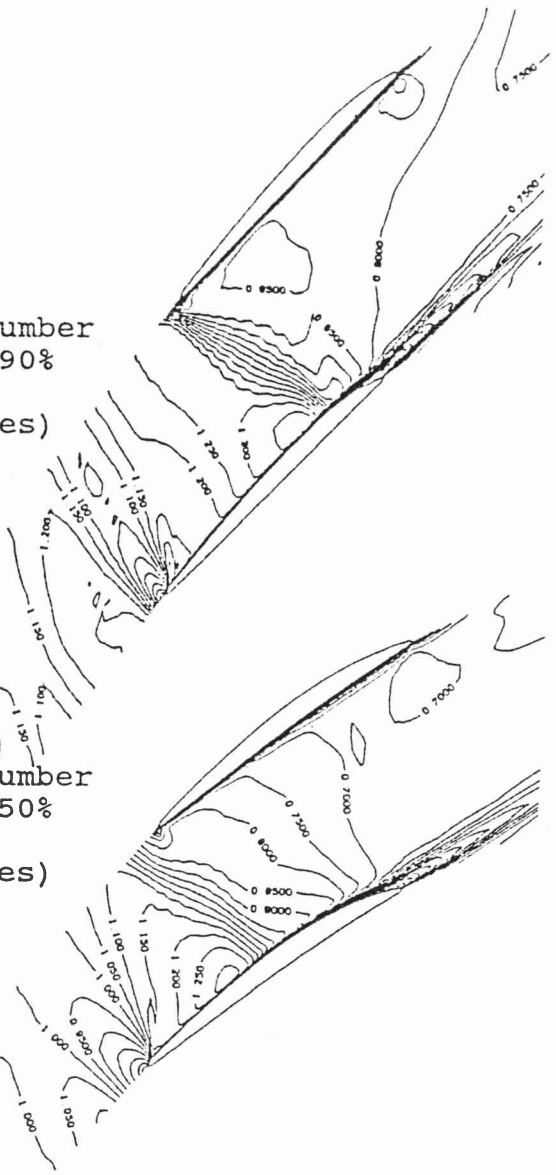

Fig.5 Mach number contours at 90% span
(23 MCA blades)

Fig.6 Mach number contours at 50% span
(23 MCA blades)

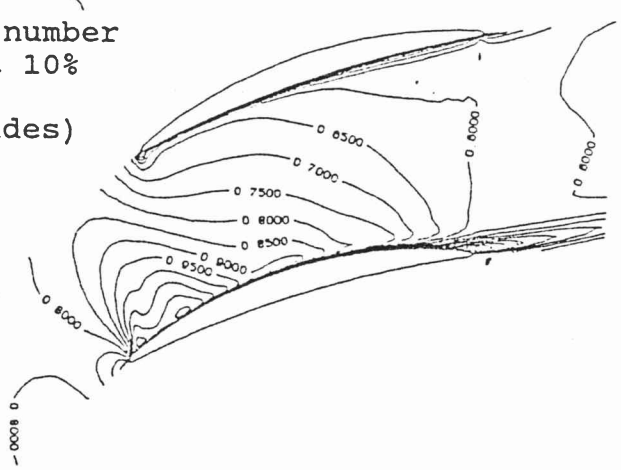

Fig.7 Mach number contours at 10% span
(23 MCA blades)

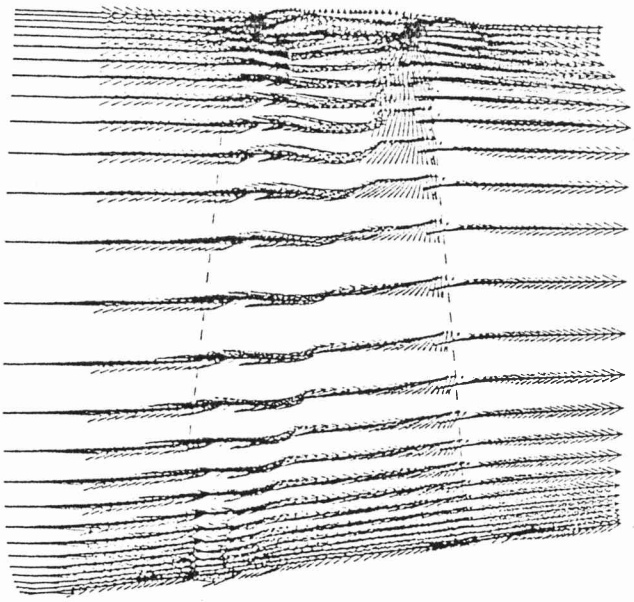

Fig.8 Near suction surface velocity vectors (23 MCA blades)

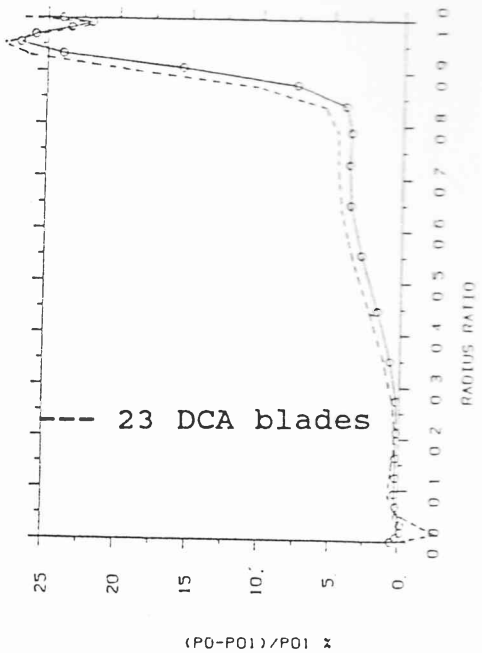

Fig.9 Relative stagnation pressure losses (23 MCA blades)

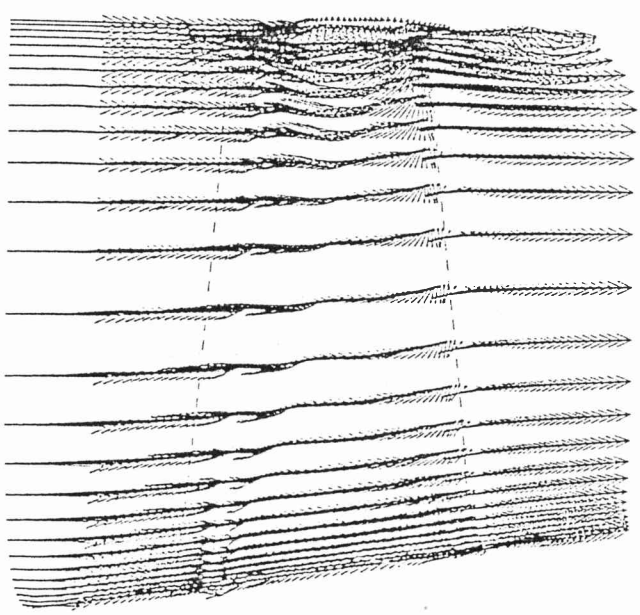

Fig.10 Near suction surface velocity vectors (29 MCA blades)

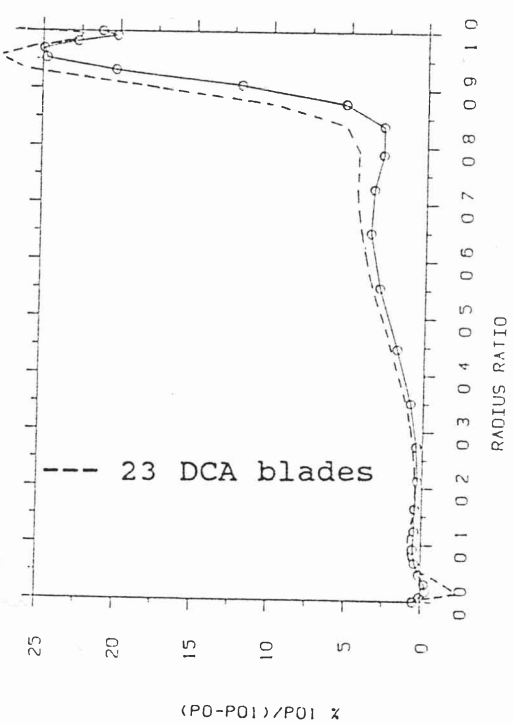

Fig.11 Relative stagnation pressure losses (29 MCA blades)

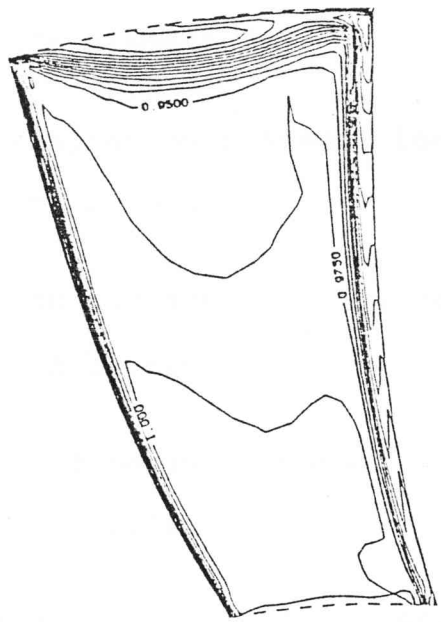

Contours of
Exp (-s/R)
where s is the
entropy and R
the gas constant

Fig.12 Loss contours in the trailing edge plane
(23 MCA blades)

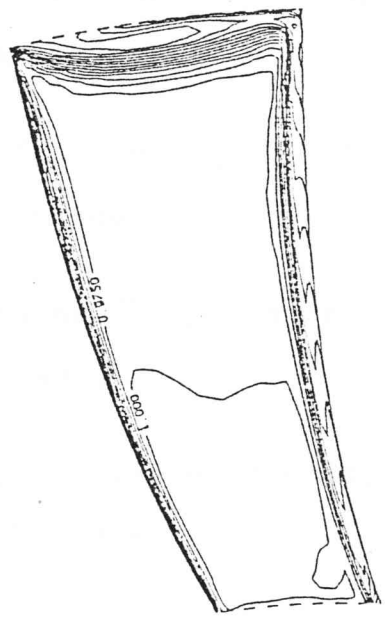

Contours of
exp (-s/R)
where s is the
entropy and R
the gas constant

Fig.13 Loss contours in the trailing edge plane
(29 MCA blades)

Fig. 12 Loss contours in the trailing edge plane (23 MCA blades)

Fig. 13 Loss contours in the trailing edge plane (29 MCA blades)

INTERNATIONAL JOURNAL OF

TURBO & JET-ENGINES

ISSN 0334-0082

CONTENTS VOL. 9, NO. 3, 1992

INTERNATIONAL JOURNAL OF

TURBO & JET-ENGINES

ISSN 0334-0082

CONTENTS VOL. 9, N0. 3, 1992

 International Journal of Turbo and Jet Engines, 9, 165-182 (1992)

Three-Dimensional Viscous Flow Through a Highly Loaded Compressor Rotor

T.W. von Backström
Department of Mechanical Engineering, University of Stellenbosch, 7600 Republic of South Africa.

Abstract

The three-dimensional viscous transonic time marching Denton code LOSS3D, and Dawes code BTOB3D were applied to the first stage rotor of the NACA 5-stage transonic compressor. LOSS3D predicted pressure ratio and loss distributions reasonably well at design point, but did not quite satisfy the convergence criteria. BTOB3D tended to overpredict the total pressure ratio over the outer half of span due to an underprediction of loss in the complicated separated flow region triggered by shock boundary layer interaction on the suction surface, but prediction was good at 90% speed where shock boundary layer interaction was less severe. The use of a computationally convenient excessively large tip clearance is not recommended when shock-boundary layer interaction is expected, especially at off-design conditions. Computing time per solution on a mini-supercomputer was about 9 hours for a mesh of 65000 points.

Introduction

Various versions of the turbomachinery blade row flow computation codes of Denton and Dawes have been verified and compared to experimental results by the authors of the codes (Denton /1,2,3/ and Dawes /4,5,6/ and others (Pierzga and Wood /7/ and Sato et al. /8,9/).

The objective of this study is to make a contribution to this process of verification by applying the current Denton /10/ and Dawes /6/ three-dimensional viscous flow codes to a highly loaded transonic compressor rotor and to compare codes from a user point of view. Some insight would also be gained into the likely flow patterns in highly loaded rotors.

Background

The Compressor

The first stage rotor of the pioneering NACA 5-stage transonic compressor (Kovach and Sandercock /11/) was chosen as subject of this investigation for the following reasons:

i) its simple geometry (cylindrical casing, double circular arc blades, no inlet guide vanes),
ii) the availability of experimental data, including losses,
iii) the high first stage blade loading caused by the combination of high stage pressure ration (1.4), low tip speed (335 m/s) and low tip solidity (1.0),
iv) the highly cambered (11.7°) DCA blade tip sections operating under the above conditions,
v) the author's interest in selecting a code to model the first stage of a small compressor based on the NACA 5-stage design /12/.

Experimental Data

The blade row experimental data of Kovach and Sandercock /11/ consisted fundamentally of spanwise distributions of flow angle, total temperature and total and static pressure, all obtained by means of stationary probes. They checked the accuracy and consistency of their data by considering the following: mass flow balance; comparison of

momentum to temperature rise efficiencies; and comparison of stator outlet to rotor outlet total temperatures. For the first rotor however, the error in the integrated mass flow varied from zero to +5% compared to the inlet bellmouth measurements. It appears from their graphs that at 100% speed (but not at 90%) the total temperature rise after the first rotor is higher than after the first stator. And the scatter in their first rotor loss data appears to be about 5 percentage points; under some flow conditions unrealistic zero losses were recorded, but these cases were avoided in the present study. Although more accurate modern experimental results are available, the choice of the NACA 5-stage was justified in terms of the stated objectives. The loss coefficient is defined as the loss in relative total pressure over the blade row along a stream surface divided by the difference between the relative pressure and the static pressure at inlet on the stream surface. This definition is convenient to apply to both the experimental and computational data, but may, due to rothalphy conservation, result in a negative loss coefficient near the hub where the flow experiences a large change in radius along the stream surface.

Computer Codes

Denton Codes

The original Denton codes /1/ were time marching Euler solvers to which various boundary layer concepts were subsequently applied. Pierzga and Wood /7/ for example reported good agreement between computed and experimental results for a transonic, low aspect ratio fan, using an inviscid Denton code with a simple transpiration type boundary layer.

One of the versions of the Denton codes however, includes viscous effects modelled as a body force, and a basic turbulence model /10/. The model assumes that the grid points next to those at the wall are in the logarithmic law region of the turbulent boundary layer where the velocity, V is given by:

$$V/v^* = 2.5 \ln(\rho v^* y/\mu) + 5.24 \qquad (1)$$

with

$$v^* = (\tau_w/\rho)^{0.5} \qquad (2)$$

where τ_w is the wall shear stress, ρ the density, μ the viscosity and y the distance from the wall. The relationship is approximated by

$$\tau_w/\tfrac{1}{2}\rho v^2 = -0.001767 + 0.03177\,(\ln(Re))^{-1} + 0.25614\,(\ln(Re))^{-2} \qquad (3)$$

with the Reynolds number, $R_e = \rho Vy/\mu$, using the velocity at the grid location one removed from the wall. The shear stress distribution is calculated from

$$\tau = \rho \epsilon_m \left|\frac{\partial V}{\partial n}\right| \qquad (4)$$

and the eddy viscosity from

$$\epsilon_m = (0.41n)^2 \left|\frac{\partial V}{\partial n}\right| \qquad (5)$$

where n is the perpendicular distance from the surface.

Multiplication of the mixing length by an algebraic function reduces it to zero at a fraction FRACB of the passage width and in blade wakes the mixing length (0.41n) is limited to a fraction FRACW of blade pitch. in this study FRACB was 0.25 and FRACW was 0.1.

Denton /10/ warns that the method is strictly speaking valid only for thin attached boundary layers and that it would be of dubious accuracy for complex separated flows.

Dawes Codes

These three-dimensional finite volume codes solve

the Reynolds averaged Navier-Stokes equations on a mesh consisting of six sided cells with centered nodes, by time marching the discretized equations using a two step explicit and single step implicit algorithm, and a single level of multigrid /4,5,13/. The accuracy of the algorithm was demonstrated by Dawes /4/ when he showed that predicted results were consistent with experimental measurements and other calculations for laminar shock-boundary layer interaction. He subsequently indicated that flow prediction agreed very well with experiment for a rotor cascade flow at incidences from -1.7 to +4.5 degrees /5/, but stated that more work was needed on turbulence modelling. The turbulence model is the two-layer mixing length concept of Baldwin and Lomax /14/ that substitutes the absolute value of the vorticity vector for the velocity gradient, and avoids the need to find the edge of the boundary layer. The constants used in the formulation are those proposed by Baldwin and Lomax /14/. Visbal and Knight /15/ found that the outer function in the formulation underpredicts the turbulent length scale in the separated flow region of a two-dimensional compression corner, and that the model fails to predict the observed amplification of the turbulence across a shock boundary layer interaction. They also mentioned that Degani and Schiff /16/ had found that due to ambiguities in the determination of the length scale the Baldwin-Lomax model was unsuitable for regions of cross-flow separation as found in the computation of supersonic flows around cones at incidence.

Comparison of Denton and Dawes Codes

Meshes and Boundary Conditions

A preprocessor code was written to generate the required input for the NACA 5-stage rotor, including the double circular arc blade profile shapes and uniformly expanding meshes.

Mesh selection was based on papers by Dawes /6,13/. He stated that good quantitative accuracy could be achieved in compressor cascade loss prediction when using fine enough meshes (29 x 67 x 7), in the pitchwise, streamwise and spanwise directions), but on coarser meshes (17 x 35 x 7) the calculated loss coefficients were in error by up to 50%. Early truncation of the computation after a three orders of magnitude root mean squared residue reduction however, resulted in only a 5% loss prediction error (Dawes /13/). This indicated that inaccurate solutions were likely to result from too coarse meshes rather than from early truncation.

Consequently a relatively fine computational mesh was chosen for the Dawes code BTOB3D, consisting of 96, 26 and 26 elements in the streamwise, pitchwise and spanwise directions as in Figures 1 and 2. A quarter of the elements were ahead of the leading edge and a quarter behind the trailing edge. At mid span the inflow and outflow boundaries were half an axial chord length from the blade. The mesh spacing ratios were 1.05 in the axial direction and 1.25 in the pitchwise and spanwise directions.

At the design point Reynolds number of 8×10^5 (based on rotor outlet conditions and mean chord) this mesh resulted in typical minimum values of $y^+ = yv^*/\mu$ ranging from 8 in the cells next to the blades to 40 in the cells next to the hub and casing. This implies that the logarithmic skin friction relationship is employed.

For the Denton code LOSS3D the computational mesh was similar to that used for BTOB3D but consisted of 27 cells in the radial and pitchwise directions to allow three levels of multigrid (expanding by a factor of three) to be used.

Standard sea level conditions (288.2K and 101.3 kPa) were assumed at the inlet. Hub and casing outlet static pressure were calculated from the design data of Kovach and Sandercock /11/. The inlet velocity was taken to be uniform and axial with no inlet boundary layer thickness. All walls were assumed to be adiabatic. The hub wall was modelled as rotating but the casing wall was stationary, even in the no tip clearance cases.

Application of the Denton Code LOSS3D

For runs with the fully three-dimensional code LOSS3D /10/ the blade leading and trailing edge cusps were set equal to ten times the edge radius to minimize entropy generation at the leading edge due

to sudden mesh curvature. This was larger than recommended by Denton, but the choice was based on the author's experience with a quasi three-dimensional Denton code.

The convergence criteria were: a maximum change in axial velocity less than 0.005% of the root mean square of all the absolute velocities in the flow field (eavg < 0.005%); mass flow at each streamwise computational surface agreeing to within 0.5% with inlet mass flow (emax < 0.5%); and averaged relative total pressure lost from inlet to outlet constant over several hundred time steps.

The computation did not converge at all unless the back pressure was fixed at both hub and casing. Even then the lowest values of eavg were 0.02%. This was typically achieved in 1500 time steps using a time step multiplier FT of 0.3 times the CFL time step (based on the inlet stagnation speed of sound and the minimum local cell dimension). Run time was 7.5 hours total using two of the four processors of an Alliant FX/4.

The complete convergence (in 1360 time steps) of BASE3D the Euler version of the code on the same mesh and for the same inlet and outlet boundary conditions suggested that the turbulence model caused the lack of convergence of LOSS3D. Modification of the turbulence model was beyond the scope of this study, however. Since Pierzga and Wood /7/ had used eavg = 0.01% as criterion and mentioned that it could be relaxed to 0.02% with little effect, the LOSS3D results were assumed to be converged at eavg = 0.02%. Comparison of results to those obtained with the Dawes code BTOB3D supports this assumption.

LOSS3D Results

The Denton code LOSS3D could not model tip clearance and was used only at the compressor design conditions. With pressures at the hub and casing of 99.7 and 111.9 kPa, the calculated mass flow was 31.1 kg/s, compared to the design and measured values of 30.7 and 31.7 kg/s. LOSS3D underpredicted the relative swirl angle over most of the span (Figure 3). This too high flow deflection explains the too high total temperature ratio (Figure 4). The temptation to explain the low temperature regions at 15 and 85% span in terms of the hub and casing corner vortices is resisted since these regions are absent in the 90% speed data (Figure 9). The overpredicted rotor total temperature ratio leads to an overpredicted rotor total pressure ratio, although the spanwise distribution has more or less the right shape (Figure 5), as has the spanwise loss distribution (Figure 6). The accurate loss prediction at 83% span is indeed remarkable (and probably fortuitous) since this is a complicated region of severe shock boundary layer interaction (Figure 7) and flow separation (Figure 13a). Behind the shock the suction surface flow is almost stationary relative to the blade but further downstream the larger than average circumferential velocity (in the absolute frame) of the separated flow causes a radial velocity component to develop. The Coriolis force acting on the outward moving flow exacerbates the separation. Closer to the casing the blade scraping action forces some flow to move inwards initially. It is clear that no simple (equilibrium) turbulence model can really be expected to be accurate under these conditions.

Losses at the trailing edge plane were concentrated in the suction surface-casing corner due to the absence of a clearance jet (Figure 12a).

Application of Dawes Code BTOB3D

Converged solutions typically took 750 time steps (about 9 hours real time) running on two of the four processors of an Alliant FX/4, using a time step multiplier FT of 0.5 times the CFL time step (based on the inlet stagnation speed of sound and the minimum local cell dimension). Convergence was taken as a three orders of magnitude reduction in the rms axial mass flux residue, associated with a maximum mass flow error of less than 0.5% and a constant value of minimum suction surface pressure over the last 150 time steps.

BTOB3D Results

For comparison with the Denton code LOSS3D, a zero tip clearance case was run. The computed mass flow, using a back pressure of 99.7 kPa was 31.0 kg/s

compared to 31.1 kg/s obtained with LOSS3D.

BTOB3D tended to overpredict the relative swirl angle over the inner two thirds of span (Figure 3), implying too small deflection angles and an underestimation of the total temperature ratio. In fact, the total temperature ratio is well predicted in this region, as well as in the regions close to the annulus walls, except for the scatter in the experimental results (Figure 4). As the comparatively higher LOSS3D total temperature ratio prediction is consistent with the comparatively lower LOSS3D swirl angle prediction and vice versa for BTOB3D. Some doubt is cast over the consistency of the experimental swirl angle and temperature ratio data since both are relatively low.

BTOB3D slightly overestimated the total pressure ratio over the inner third of the span in spite of the generally good prediction of total temperature ratio in this region, but greatly overestimated it over the outer third (Figure 5), due to an underprediction of loss (Figure 6) combined with an overprediction of temperature ratio.

Modelling the rotor in isolation may have been another factor: Dawes /17/ has recently shown that the accuracy of the predicted total pressure and temperature ratios can be substantially improved by the inclusion of the downstream stator in the model /17/.

BTOB3D, like LOSS3D also predicts a region of separated flow, but now the flow near the suction surface has a strong radial component immediately downstream of the shock, possibly due to a lower effective viscosity than in LOSS3D, and the radial inflow due to tip scraping is more confined to the casing (Figure 13b). The underestimation of the losses in the separated flow region and the previously discussed findings of Visbal and Knight /15/ about the inadequacy of the Baldwin-Lomax model in regions of cross flow separation support this hypothesis. Confining the region of application of the Baldwin-Lomax model to 10% of pitch from the blade surfaces, as generally recommended to save computing time is another possible reason for the underprediction of the effective viscosity, but this was not further explored.

For this case without tip clearance the losses in the trailing edge plain were concentrated in the outer 30% of span and especially in the suction surface-casing corner (Figure 12b) as with LOSS3D (Figure 12a).

Comparison between LOSS3D and BTOB3D: Conclusions

Peak Mach numbers at 10, 50 and 90% span predicted by BTOB3D were 1.155, 1.418 and 1.455 corresponding closely to 1.166, 1.411 and 1.473 predicted by LOSS3D, and indicated similar shock losses. Since the largest differences in the radial distributions of total pressure ratio and loss occurred beyond 70% span it is suggested that these are caused by the different assumptions in the turbulence models. The simple law of the wall model in LOSS3D surprisingly enough performs better than the Baldwin-Lomax model in this region.

In spite of being fundamentally about 2.5 to three times faster per time step LOSS3D did not use significantly less computing time than BTOB3D for an acceptable solution. The first reason for this was that the use of a 67% larger time step per BTOB3D iteration reduced computation time by a factor of 0.6 and the second was that BTOB3D succeeded in reducing the rms velocity error by one order of magnitude during the first 100 time steps when running on a coarse grid consisting of only one eighth of the mesh points (every other mesh point in each direction).

Only BTOB3D was selected for further investigation because it did not require significantly more computer time, it did not require specification of the back pressure at the casing as well as at the hub to force convergence, convergence was certain, and it could model tip clearance.

BTOB3D with Tip Clearance

The Dawes code BTOB3D was not programmed for extra computational elements in the small volume between the blade tip surface and the casing; to handle tip clearance the blade thickness had to be reduced smoothly to zero over the few spanwise mesh intervals closest to the tip (Figure 14), from

where the periodic boundary condition was applied up to the casing. The tip clearance was modelled in two ways: firstly as a large clearance (3.3% of span), two mesh cells high, and secondly as a more realistic clearance (1% of span), six mesh cells high. Unfortunately Kovach and Sandercock /11/ did not report the experimental running clearance, but a typical practical value on a primitive compressor would have been 1% of span, as found by the author on a similar compressor /12/.

Large Tip Clearance

The most sensible way of initially introducing tip clearance was to use the existing mesh. The smallest tip clearance that could be introduced in this way and still allow some semblance of a velocity profile in the tip region was by using only two mesh cells between the tip and the casing, resulting in a tip clearance of 3.3% of span (5.3% of chord). This scheme would of course not resolve the flow in the tip clearance correctly but was thought to be worth investigating, since Dawes /13/ had stated that in the computation of the strong interaction between a compressor blade clearance jet and the stalled passage flow good agreement with experiment could be obtained when using a tip clearance of 5% of chord instead of the real 3%. (Dawes used 4 cells in the tip region). He suggested that a larger tip clearance could be acceptable since the rounded blade tip used in the calculation would almost certainly produce a more diffuse leakage jet which would be less effective in entraining and displacing the separated flow.

The results of the case without tip clearance after 1000 time steps were used as initial condition, but the computation still required 750 to 1000 additional time steps to converge. The use of the converged solution of one case as initial condition for another was subsequently dropped.

The introduction of tip clearance affected the spanwise relative swirl angle distribution at the blade trailing edge plane only in the outer 15% of span (Figure 3). Overdeflection is predicted between 85 and 90% span and underdeflection between 95 and 100%. The total temperature distribution at the exit plane is similarly only affected near the casing (Figure 9). The overdeflection of the flow is too small to fully explain the large peak in the predicted total temperature ratio at about 7% from the casing. It is probably caused by the radial movement of separated flow that is entrained and removed from the suction surface casing corner and wake by the tip clearance jet. Figure 13d clearly shows the large radial velocity components at the tip. The cooler region within 7% from the (adiabatic) wall is due to underdeflection there.

The very high predicted total pressure ratio over the outer third of the span (Figure 5) indicates the high work addition here, and cannot be attributed to the low predicted losses in this region (Figure 6). This is believed because with 1% tip clearance the pressure ratio is much lower in spite of equally low losses and between 85 and 95% span the predicted losses are extremely high anyway. The high loss region is no longer concentrated in the suction surface casing corner but spread out along the casing due to the entrainment action of the tip clearance jet (Figure 12d).

Realistic Tip Clearance

The number of cells in the tip region was chosen firstly to agree with the minimum number (six) generally required by BTOB3D for realistic flow modelling. This number derives from five cells being the minimum for fourth order smoothing, and an even number for the multigrid strategy employed /6/. The second consideration was the maximum allowable radial mesh expansion ratio (1.25) and the third the maximum total number of cells in the mesh that could be handled in a reasonable computation time. Consequently, a mesh with the same number of nodes as the preceding one was chosen but the distance between quasi stream surfaces was increased continuously from casing to hub. The flow on the hub was considered to be frictionless, as the previous results had indicated negligible losses in this region, and the large cells at the hub would not model the viscous effect well anyway. Only the design point case was modelled.

With the minimum cell dimension now about four

times smaller than before, the computation needed more time steps and after 1250 time steps eavg was only down to 0.04%, but since the loss distribution had not changed significantly during the previous 500 time steps the solution was accepted as sufficiently converged.

The outcome was less than satisfactory, however, since over the inner half of the annulus the predicted values of relative swirl angle, total temperature ratio, total pressure ratio and loss (Figures 3,4,5 and 6) were completely different from those for zero and 3.3% tip clearance. The predicted mass flow was now 30.5 kg/s.

It was concluded that the spanwise mesh spacing over the inner half span was just too coarse and that attention should be focused on the outer half of span where the spanwise spacing would be smaller than or equal to that of the previous mesh. In this region the relative exit swirl angle and total temperature ratio prediction were very good (Figures 3 and 9), but the total pressure ratio was still overpredicted due to the predicted losses being too low as before (Figures 5 and 6). Losses were now more confined to the suction surface-casing corner, because of the smaller jet blowing across the blade tips (Figures 12c and 13c).

Tip Clearance Summary

Of the three tip clearance models the physically most realistic 1% clearance model was generally the most accurate over the outer half of span, except in loss prediction where the no tip clearance model fared best, probably due to the vagaries of the Baldwin-Lomax model under the applicable conditions. When the full span was considered, the no tip clearance model was in general more accurate than the 3.3% tip clearance model.

A good practical compromise might have been the use of a single cell between the tip and the casing, reducing the tip clearance by a factor of 0.44 to a more realistic 1.4% of span, but this was not considered at the time and the rest of the work was done with the 3.3% tip clearance model.

BTOB3D at Off-Design

Off-design at full speed

Since Kovach and Sandercock /11/ did not label their graphs according to mass flow, but merely by "near maximum weight flow" or "near minimum weight flow", the matching of computed to experimental results at off-design was somewhat arbitrary. We shall consider two off design conditions: hub back pressure 90 kPa and hub back pressure 104 kPa, representing the two mentioned labels.

In the first case the required three order of magnitude reduction in mass flux rms residue was achieved in 750 time steps. The mass flow was 31.3 kg/s, which was closer to the peak efficiency mass flow measured by Kovach and Sandercock /11/. The Mach number contours, however, showed that this was a nearly choked condition, with the shocks well swallowed at 90 and 50% span and the sonic contour almost spanning the full pitch at 10% span. It was therefore concluded that the larger flow of 31.7 kg/s measured by Kovach and Sandercock at the nominal design condition was probably due to blade untwist.

When the back pressure was increased to 104 kPa the predicted mass flow was 29.0 kg/s (5.5% less than design, Figure 15), but good convergence was still achieved in 750 time steps. As a check, a further 250 time steps were done, but once again the change in loss distribution was negligible.

The effect of back pressure on the predicted exit swirl angle was only noticeable near the casing where it showed the correct trend compared to the experimental (Figure 8). No experimental temperature distributions were available. The total pressure distributions also showed the correct trends but the predicted effect was much too large (Figure 10). Agreement between computed and experimental loss coefficients was in general not bad considering the scatter in the experimental data, except for a consistent underprediction over the outer third of span (Figure 11).

Ninety Percent Speed

The computed results at a flow coefficient of 0.63 in Figure 14 were compared to the "near maximum weight flow" (at 90% speed) experimental results at a flow coefficient of 0.65 to give the very good agreement between computed and experimental results in Figures 8 to 11. The lower losses are due to the lower peak Mach numbers (1.21 and 1.38 at 50 and 90% span) and the much smaller areas of separated flow due to shock-boundary layer interaction with the turbulence model apparently coping well under these conditions. It is interesting to note that this good agreement between experimental and predicted results is achieved in spite of the rotor being modelled in isolation.

Conclusions

i) The Dawes code BTOB3D required 20% more computer time for a solution than the Denton code LOSS3D, but convergence was certain.

ii) LOSS3D prediction at design point of spanwise distribution of total pressure ratio and loss agreed reasonably well with experimental data.

iii) BTOB3D tended to overestimate total pressure ratio and underestimate loss over the outer half of span. At 90% speed where shock-boundary layer interaction is less severe, BTOB3D predictions were good overall.

iv) The use of a computationally convenient excessively large tip clearance is not recommended when shock-boundary layer interaction is expected.

Acknowledgements

The work was done while the author was a Visiting Scholar at the Whittle Laboratory, Cambridge, July to December 1988. Thanks are due to Drs. J.D. Denton and W.N. Dawes for the use of their codes and Dr. N.A. Cumpsty, the acting Director for the generous use of the computing facilities of the Laboratory.

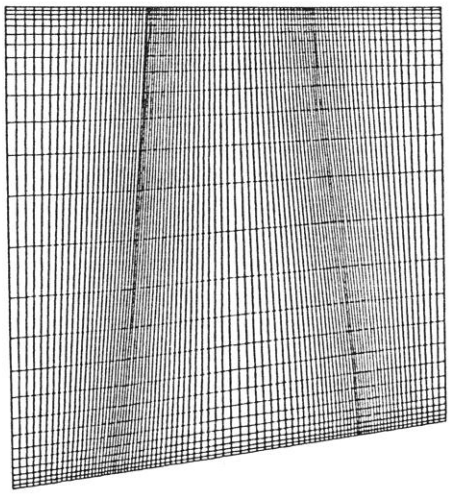

Fig. 1. Mid section view of the computational mesh.

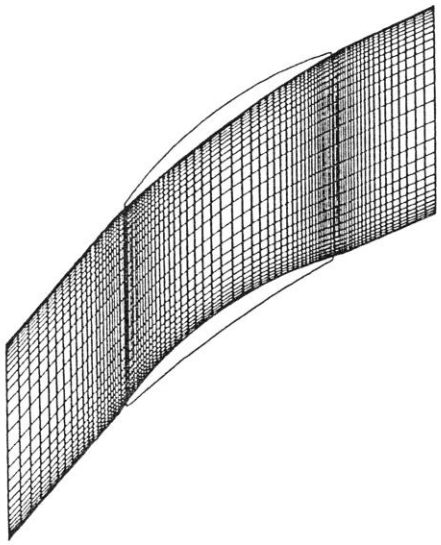

Fig. 2. Meridional view of the computational mesh.

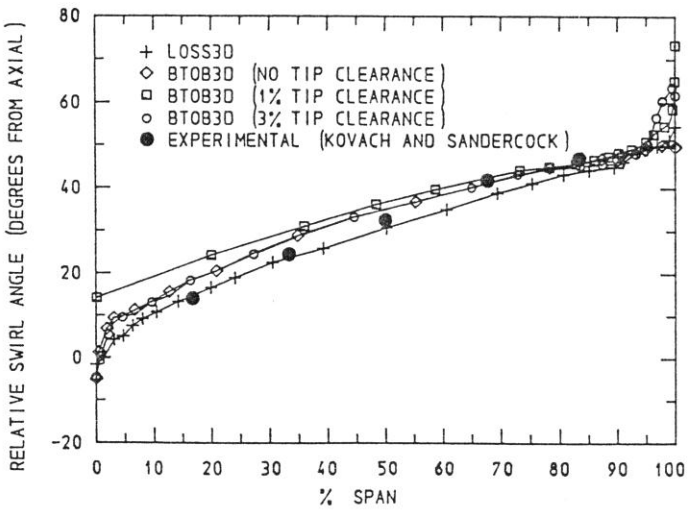

Fig. 3. Relative swirl angles at the blade trailing edge plane.

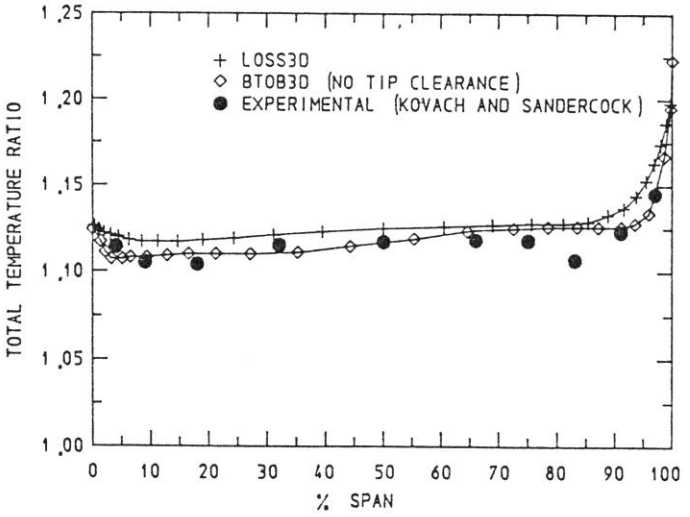

Fig. 4. Total temperature ratios at the exit plane.

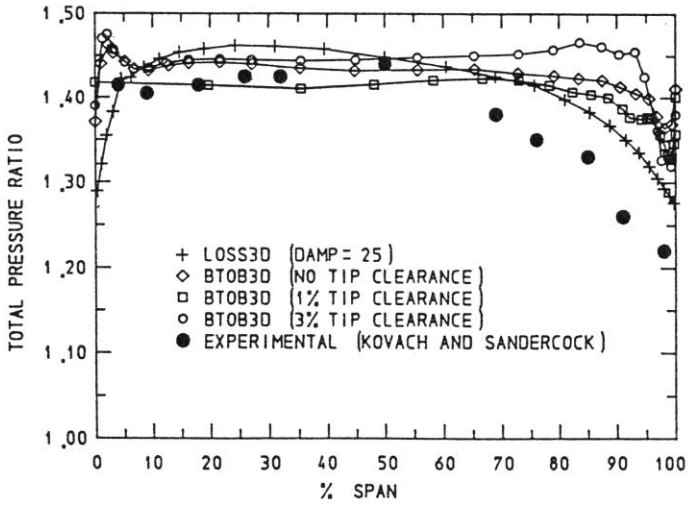

Fig. 5. Total pressure ratios at the exit plane.

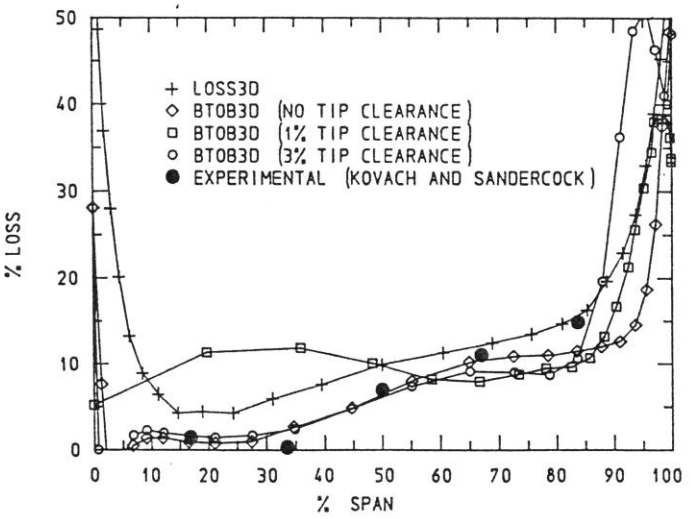

Fig. 6. Loss distribution at the exit plane.

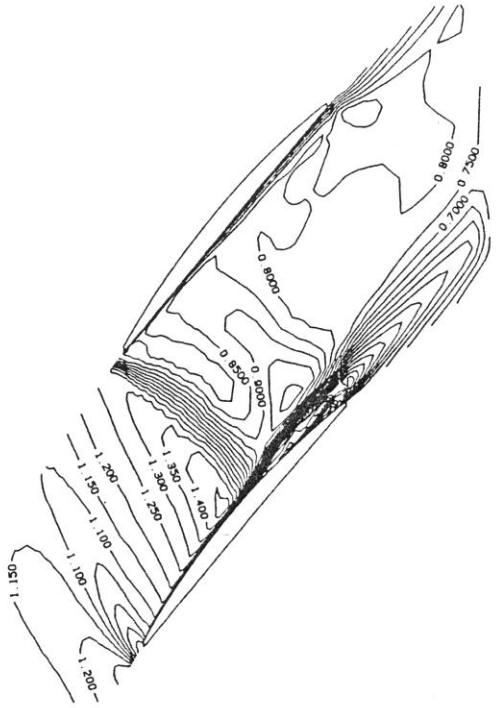

Fig. 7. Mach number contours at 83% span (LOSS3D).

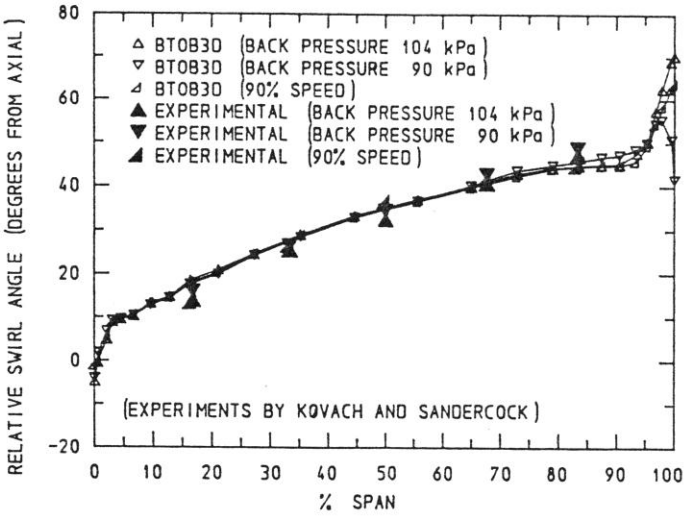

Fig. 8. Back pressure and speed effects on relative swirl angle at the blade trailing edge plane.

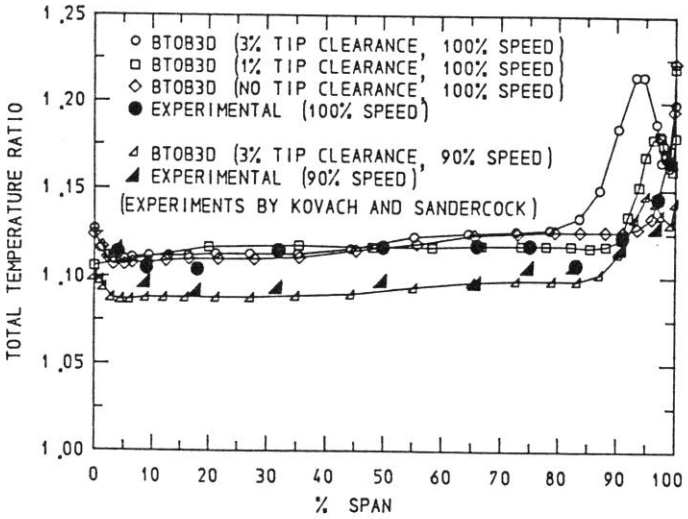

Fig. 9. Tip clearance and speed effects on total temperature ratio at the exit plane.

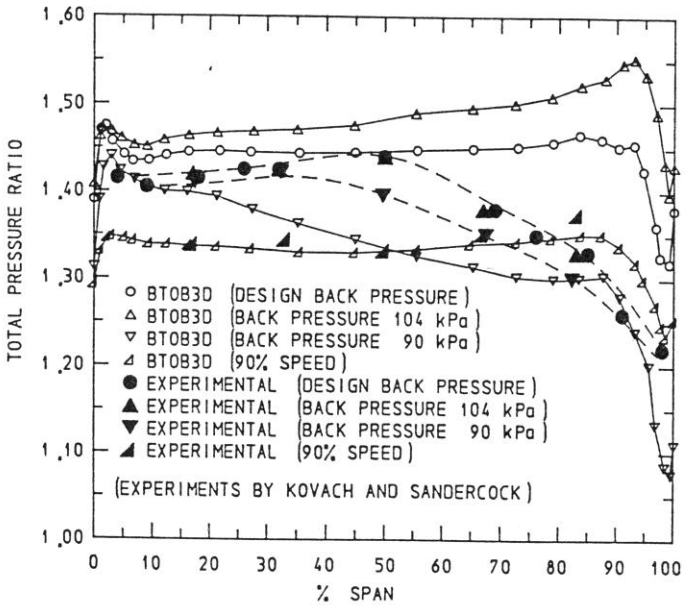

Fig. 10. Back pressure and speed effects on the total pressure ratio.

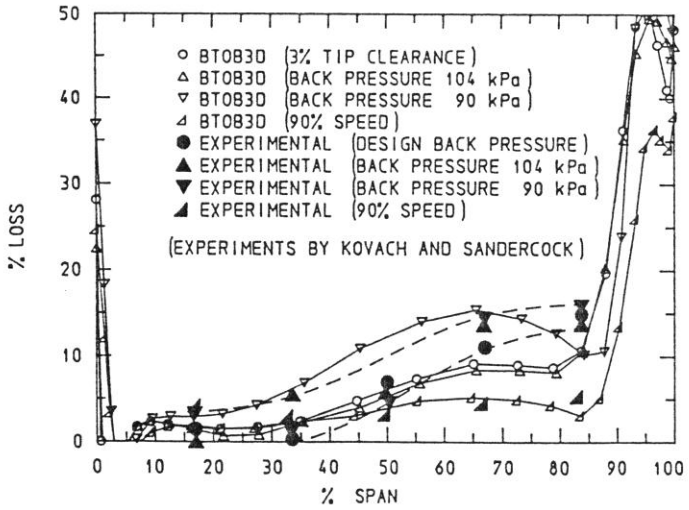

Fig. 11. Back pressure and speed effects on the loss distribution.

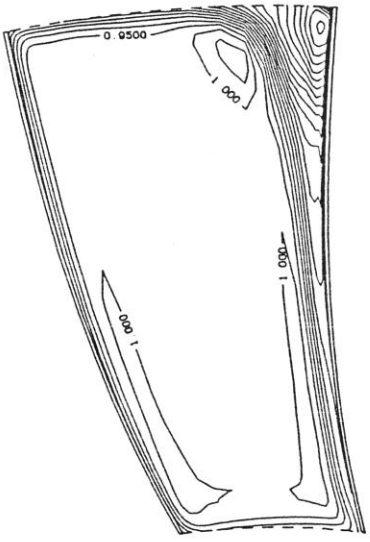

Fig. 12a. Loss distribution in the trailing edge plane (LOSS3D).

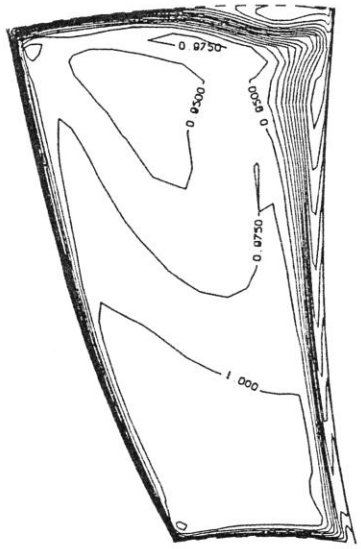

Fig. 12b. Loss distribution in the trailing edge plane (BTOB3D, no tip clearance).

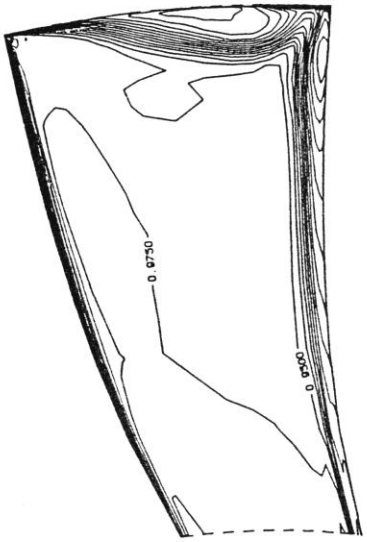

Fig. 12c. Loss distribution in the trailing edge plane (BTOB3D, 1% tip clearance).

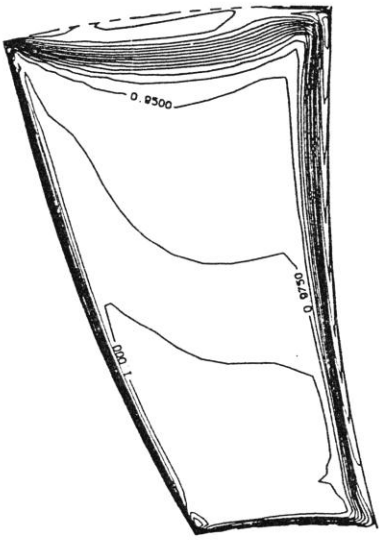

Fig. 12d. Loss distribution in the trailing edge plane (BTOB3D, 3% tip clearance).

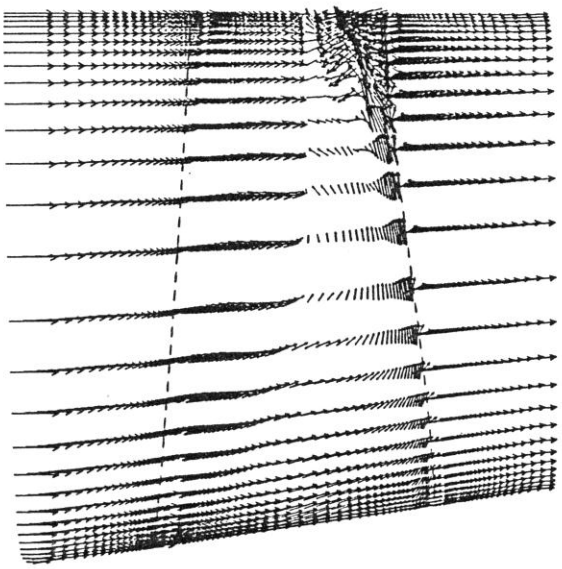

Fig. 13a. Near suction surface velocity vectors (LOSS3D).

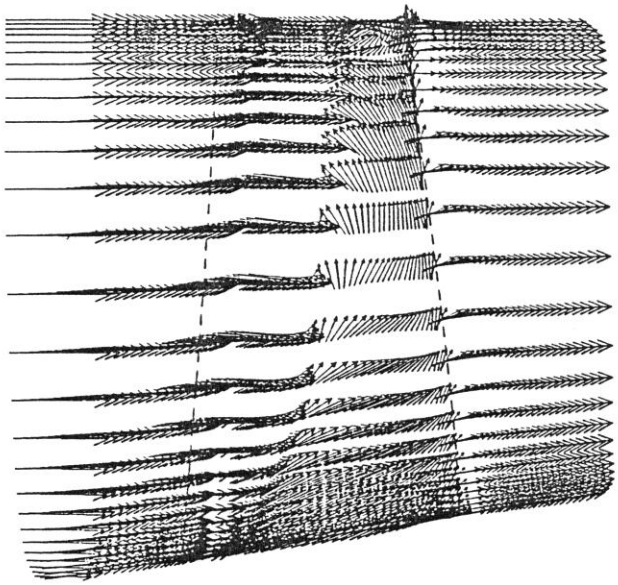

Fig. 13b. Near suction surface velocity vectors (BTOB3D, no tip clearance).

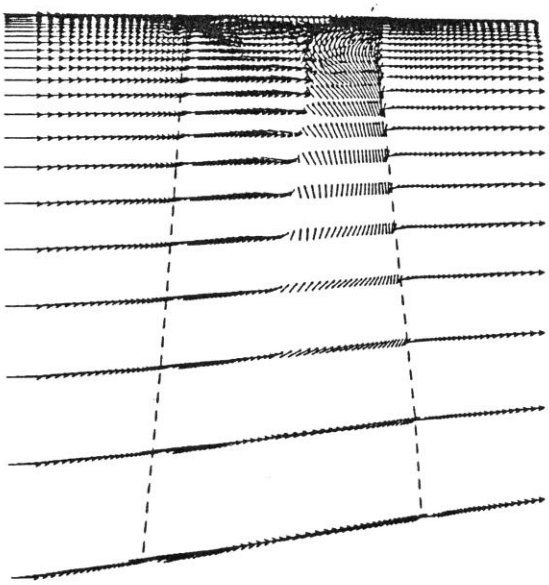

Fig. 13c. Near suction surface velocity vectors (BTOB3D, 1% tip clearance).

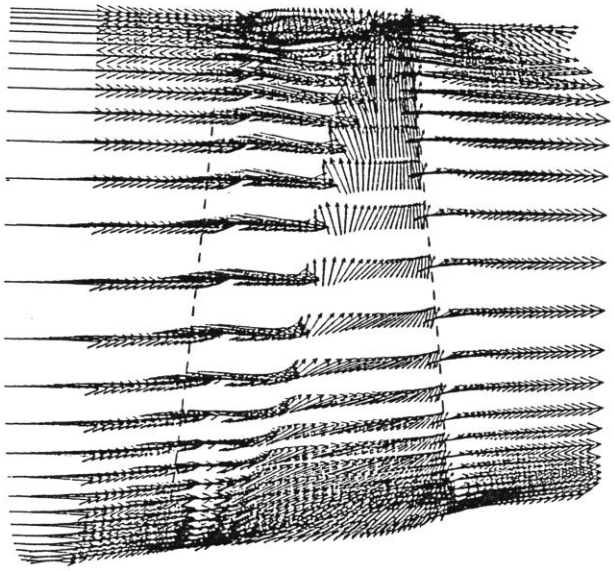

Fig. 13d. Near suction surface velocity vectors (BTOB3D, 3% tip clearance).

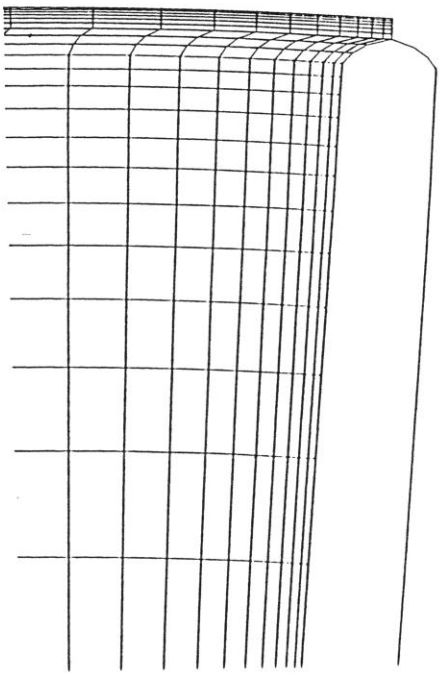

Fig. 14. Small tip clearance mesh detail.

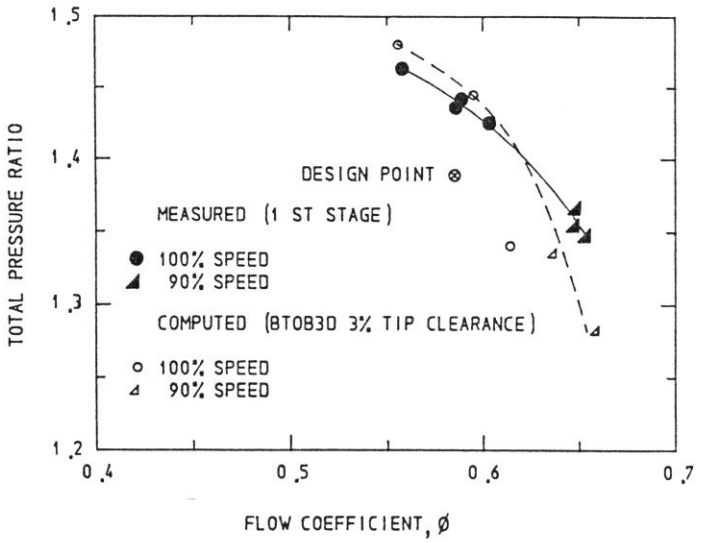

Fig. 15. Calculated rotor characteristics compared to measured stage characteristics.

References

1. DENTON, J.D., "A time marching method for two- and three-dimensional blade to blade flows", Aeronautical Research Council Reports and Memoranda, No. 3775, (1975).
2. DENTON, J.D., "An improved time marching method for turbomachinery flow calculation", ASME Journal of Engineering for Power, Vol. 105, pp. 514-524, (1983).
3. DENTON, J.D., "The calculation of fully three dimensional flow through any type of turbomachine blade row", Advisory Group for Aerospace Research and Development Lecture Series, No. 140, (1984).
4. DAWES, W.H., "Efficient implicit algorithm for the equations of 2-D viscous compressible flow: application to shock-boundary layer interaction", International Journal of Heat and Fluid Flow, Vol. 4, No. 1, pp. 17-26, (1983).
5. DAWES, W.H., "Computation of off-design flows in a transonic compressor rotor", ASME Paper 85-GT-1.
6. DAWES, W.H., "Development of a 3D Navier Stokes solver for application to all types of turbomachinery", ASME Paper 88-GT-70.
7. PIERZGA, M.J. and WOOD, J.R., "Investigation of the three-dimensional flow field within a transonic fan rotor: experiment and analysis", ASME Paper, 84-GT-200.
8. SATO, T., AOKI, S. and NAGAYAMA, T., "Extensive verification of the Denton new scheme from the user's point of view: Part I - Calibration of code control variables", ASME Journal of Turbomachinery, Vol. 108,pp. 162-179, (1986).

9. SATO, T., AOKI, S. and NAGAYAMA, T., "Extensive verification of the Denton new scheme from the user's point of view: Part II - Comparison of calculated and experimental results", ASME Paper 86-GT-58.

10. DENTON, J.D., "Operating instructions for program LOSS3D: Basic 3D program with body force term", Whittle Laboratory Note, Cambridge, (1988).

11. KOVACH, K. and SANDERCOCK, D.M., "Aerodynamic design and performance of five-stage transonic axial-flow compressor", Journal of Engineering for Power, pp. 303-321.

12. VON BACKSTRÖM, T.W., "Expendable turbojet compressor design, test and development", AIAA Eighth International Symposium on Air Breathing Engines, Cincinnati, Ohio, Paper No. 87-7039, pp. 331-338.

13. DAWES, W.H., "Analysis of 3D viscous flows in transonic compressors", Von Karman Institute for Fluid Dynamics Lecture Series 1988-03.

14. BALDWIN, B. and LOMAX, H., "Thin layer approximation and algebraic model for separated flows", AIAA Paper 78-257.

15. VISBAL, M. and KNIGHT, D., "The Baldwin-Lomax turbulence model for two-dimensional shock-wave/boundary layer interactions", AIAA Journal, Vol. 22, No. 7, (1984).

16. DEGANI, D. and SCHIFF, L.B., "Computation of supersonic viscous flows around pointed bodies at large incidences", AIAA Paper 83-0034.

17. DAWES, W.N., "Towards improved throughflow capability: the use of 3D viscous flow solvers in a multistage environment", ASME Paper 90-GT-18.

The experimental optimization of an annular dump diffuser

K. L. Lewis*

T. W. von Backström†

(Received October 1990)

Abstract

Dump diffuser performance is influenced by dump gap, flow split and prediffuser geometry. Maximum static pressure recovery is normally obtained at a flow split different from the ratio of the outer to inner annulus area. To ensure that the optimal flow split occurs at the design value the prediffuser can be canted so as to bias the flow towards one of the annuli. An extensive experimental program was undertaken to define the optimum prediffuser geometry for a predefined diffuser/combustor combination with a fully developed turbulent profile at inlet. Variables included dump gap and prediffuser cant angle, area ratio and length. A 3% improvement in diffuser effectiveness and a 5% reduction in loss was obtained by canting the prediffuser such that the optimal flow split coincided with the design value. A symmetrical distribution around the combustor dome was obtained at this condition. It was found that the prediffuser area ratio could be reduced to below the overall area ratio without significantly affecting the overall performance. Skewing the velocity profile towards the inner and outer walls affected the overall performance of the diffuser configurations but did not change the optimum prediffuser geometry. Decreasing the prediffuser length to below that indicated by the Cp line but retaining the same mean cant angle and area ratio influenced the overall performance detrimentally; skewing the inlet profile tended to exacerbate this further.*

Nomenclature

A cross sectional area [m²]
B blocked area fraction
Cp pressure recovery coefficient
Cp* optimum pressure recovery coefficient
D dump gap [m]
h annulus height [m]
L prediffuser length [m]
m mass flow rate [kg/s]
p static pressure [Pa]
ρ total pressure [Pa]
q dynamic pressure [Pa]
R radius [m]
S flow split
u local axial velocity [m/s]
u′ fluctuating component of axial velocity
U mass derived mean velocity [m/s]
W width of flame tube [m]
y perpendicular distance from wall [m]
α velocity profile energy coefficient
Δ difference
λ loss coefficient
φ fluid density [kg/m³]
ø diffuser wall angle [°]

Subscripts

1 prediffuser inlet
2 prediffuser exit
4 annulus station after settling length
i inner annulus
m maximum
o outer annulus
s dividing streamline

*Bureau for Mechanical Engineering, University of Stellenbosch
†Department of Mechanical Engineering, University of Stellenbosch

Introduction

Gas turbine engines need diffusers to slow down the air between the high pressure compressor and the flame tube. The diffuser designer has to produce in the shortest possible length the highest possible static pressure recovery with a pressure distribution that is uniform around the combustor dome so as to minimise pressure losses and enhance combustion stability. In addition the diffuser system must be dynamically stable such that a perturbation in combustor operation does not cause the diffuser to stall.

The dump diffuser is a system that allows such compromises: it is short and simple (figures 1 and 2), dynamically stable and provides performance levels that can approach those of faired diffusers. Fishenden and Stevens [1] found that most of the pressure recovery obtained in a dump diffuser configuration occurs in the prediffuser, and most of the total pressure loss in the dump region downstream of the prediffuser exit and around the flame tube. They noted that a symmetrical pressure distribution around the flame tube dome not only indicates the flow split at which minimum total pressure loss occurs but it also minimises the possibility of flow reversal through cooling holes located on the dome. In addition the axial location of the flame tube was seen to have a marked effect on the performance and stability of flow in the prediffuser. This was confirmed by Wagner, Tanrikut and Sokolowski [2]. A conclusion of both these studies was therefor that the geometry of the prediffuser, flame tube and surrounding annuli need to be carefully matched to obtain optimum performance. Fishenden and Stevens also showed that the maximum pressure recovery was obtained at flow

splits significantly different to the design flow split based on inner and outer annulus area ratio. To ensure that the optimum flow split occurs at the design value it was suggested that either the design split be changed by adjusting the flow areas around the flame tube, which invokes a constraint on the combustor designer, or the prediffuser be canted so as to bias the flow towards one of the annuli.

A series of tests was conducted on a range of dump diffusers to establish the influence of geometric and flow variables, notably the effect of flow split, dump gap, inlet velocity profile and prediffuser cantangle, area ratio and length. Parameters that were fixed were overall area ratio and flame tube geometry and radial location. The flame tube was simulated by an annular plug with no air passing through it at either the dome head or along the settling length. The objective of the study was to provide a limited data base which could be used to establish diffuser geometries, the geometries being optimized further by either computational or experimental means to account for the additional variables not addressed by this study.

Test facility

The test facility was based on that of Fishenden and Stevens [1]; although the facility is not identical to [1] the overall geometry in non-dimensional terms was made the same because it would be beneficial to use the existing data from [1] for symmetrical annular dump diffusers as a starting point, and to extend from this basis. Secondly, a similar diffuser configuration was required for a prototype engine [3]. The facility is shown in figure 1. It is a "blown" low Mach number system whereby air is supplied to the plenum chamber from a centrifugal fan. Suitable grids are positioned at exit from the fan to ensure a non-pulsating flow and suitable turbulence structure. The air enters the plenum chamber from the fan and exits through the annular duct intake which has a contraction ratio of 5:1. A section of honeycomb straightener and wire mesh is located at entry to the duct to remove any residual swirl or velocity non-uniformity. The annular duct has a height of 48 annulus widths with trip wires positioned at the calculated point of transition. Care was taken to ensure that at exit from the annular duct, flow unsteadiness and asymmetry were less than 3% of the respective mean values.

The air enters the prediffuser which consists of two annular rings that comprise the inner and outer walls of the diffusing passage. These rings can easily be removed and replaced so that the prediffuser geometry can be modified. At exit from the prediffuser the air is dumped into the dump region and is then split between the inner and outer annuli around the flame tube. All the flow exits from these annuli into the atmosphere with no air passing through the simulated flame tube. The system resistance and overall flow split is controlled by the relative positioning of the throttle rings. The axial separation distance between the exit of the prediffuser and the dome head is modified by the movement of the flame tube itself which is mounted on a threaded boss. Figure 2 shows the geometry of the diffuser/simulated combustor combination. Table 1 contains the fixed geometric dimensions of the diffuser configuration.

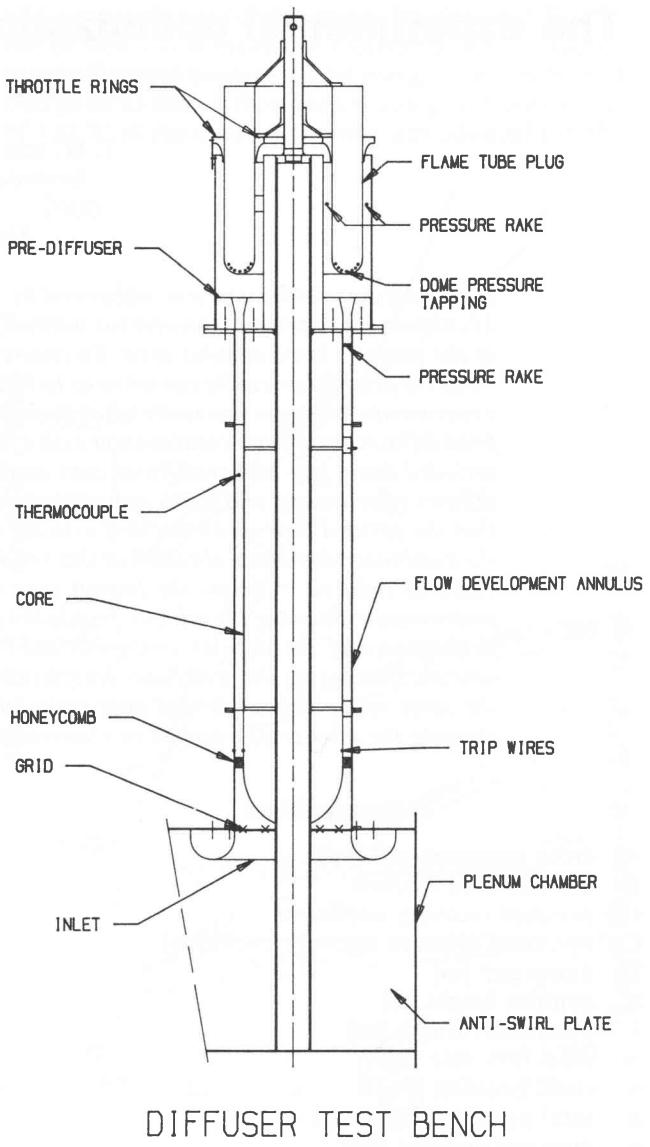

Figure 1 – Schematic of Testbench

Total pressure rakes are positioned at entry to the prediffuser (position 1, figure 2) and downstream of the settling length in the inner and outer annuli (positions 4i and 4o respectively). At each plane three rakes are arranged symmetrically with the rakes being manifolded together to give circumferential averages. Each rake has 6 measuring stations with wall static pressure ports being located in the same axial plane as the rake tube entry plane. These ports are circumferentially offset such that no stagnation flow effects are experienced. Additional wall tappings are located on the flame tube dome. Their positions are donated by the angle θ from the dome head.

Static temperature measurements are performed by a thermocouple positioned upstream of the prediffuser inlet. All pressures are measured by a single Foxboro 823 differential pressure transducer with the 40 pressures from the rakes and wall tappings being sequentially switched to the transducer by a Furness Controls selector box interfaced to a microcomputer. Data acquisition and storage is performed by the microcomputer.

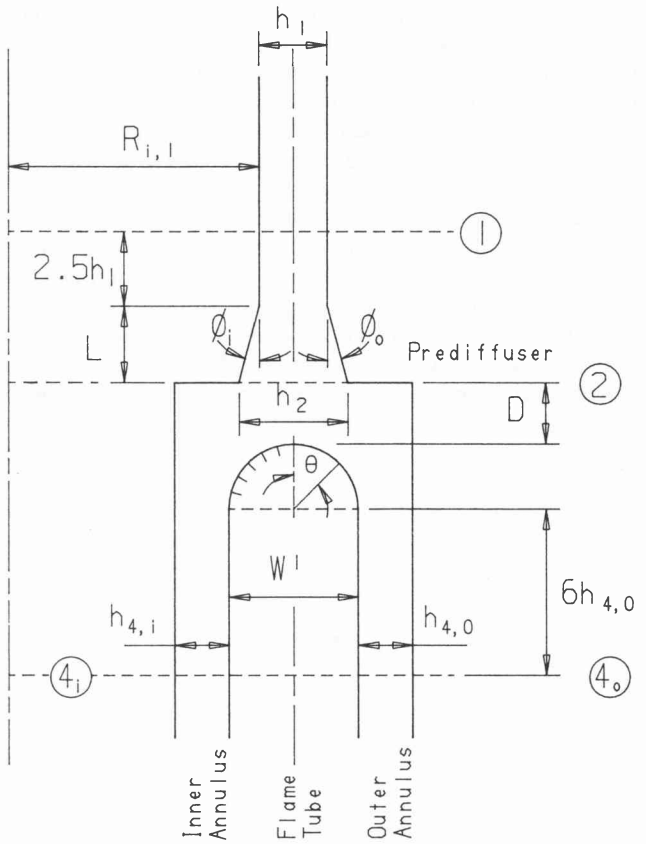

Figure 2 – Measurement Planes and Important Geometrical Parameters

Table 1 Dump Diffuser Geometry

Parameter	Value
h_1	0,028
$R_{1,i}$	0,156
W	0,096
$R_{4,i}$	0,094
$h_{4,i}$	0,028
$h_{4,o}$	0,028
$(A_o + A_i)[SB::4]/A_1$	2,0
$(A_o/A_i)[SB::4]$	2,15

At each measuring plane circumferentially averaged velocity profiles are available by assuming that the static pressure across the respective channels is the same as that measured at the wall. With the inlet temperature known, the performance parameters of the diffuser system as well as the mass flow split can be determined.

Performance parameters

Diffuser performance can be represented by two coefficients: static pressure recovery and total pressure loss. These are defined for the diffuser configuration which includes the prediffuser, the dump region and settling length as

$$C_p = \frac{(m_{4i}\bar{p}_{4i} + m_{4o}\bar{p}_{4o} - m_1\bar{p}_1)}{m_1\alpha_1 \tfrac{1}{2}\rho U_1^2}$$

$$\lambda = \frac{\Delta\bar{P}_{1-4}}{\alpha_1 \tfrac{1}{2}\rho U_1^2}$$

where $\alpha_1 = \frac{1}{A}\int_o^A \left(\frac{u}{U}\right)^3 dA$ and $\bar{p} = \frac{1}{m}\int_o^A pdm$

Pressure recovery coefficient expresses the overall quality of the diffuser performance as it quantifies the conversion of the mass averaged inlet dynamic pressure to static pressure, this being the real function of a diffuser. The parameter allows the direct comparison of any two diffusers excepting for compressibility effects at higher Mach numbers.

The loss coefficient parameter is useful if the overall impact of diffuser performance on engine cycle operation is of interest. It should always be quoted with a pressure recovery as otherwise a diffuser that does not diffuse would appear to be a good system [2]. The two parameters are however not independent of each other as shown below.

$$C_p = 1 - \frac{(m_{4i}\alpha_{4i}\tfrac{1}{2}\rho U_{4i}^2 + m_{4o}\alpha_{4o}\tfrac{1}{2}\rho U_{4o}^2)}{m_1\alpha_1\tfrac{1}{2}\rho U_1^2} - \lambda$$

Prediffuser geometries

Table 2 contains a list of the geometries tested. All configurations were very close to the Cp* line of Sovran and Klomp [6] except for the 4/10,5 combination. (The Cp* line is the locus of points of maximum pressure recovery for a certain non-dimensional diffuser length). The 4/10,5 combination was chosen so as to determine whether a prediffuser that was shorter than that suggested by the Cp* line would give adequate performance of the overall diffuser configuration by close coupling the flame tube dome to the prediffuser exit.

Inlet velocity profiles

Three inlet velocity profiles were used during the experimental test program. The profile that was used for the bulk of the testing was the fully developed turbulent annular profile with a kinetic energy flux velocity profile parameter $\alpha = 1{,}03$. This differs from the measured value of $\alpha = 1{,}06$ mentioned in [1]. By calculating α assuming symmetrical power law or logarithmic law of the wall velocity profiles, it can be shown that the value measured in the present study is acceptable (Appendix 1).

The other two profiles were generated by the fitting of meshes on the inner and outer walls of the annular duct upstream of the prediffuser inlet. The respective profiles are shown in figure 3 together with their α values and corresponding blockage factors, B. The two skewed profiles are seen to have shapes that are similar to those typically found in gas turbines. Turbulence profiles expressed as the root mean square of the fluctuating axial component are shown for all three velocity profiles in figure 4. These measurements were taken at the end of the annulus, with the diffusers removed.

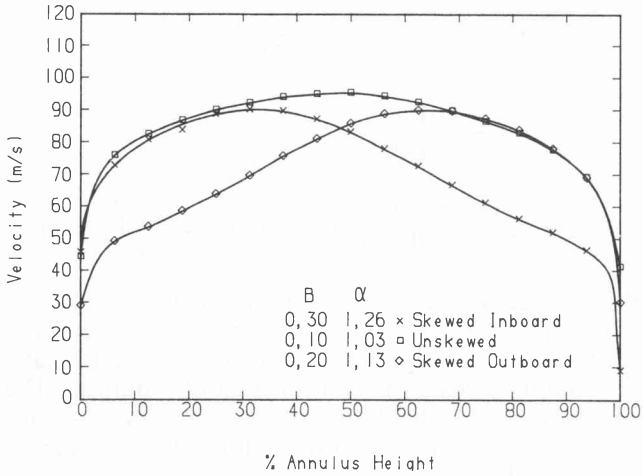

Figure 3 – Inlet Velocity Profiles

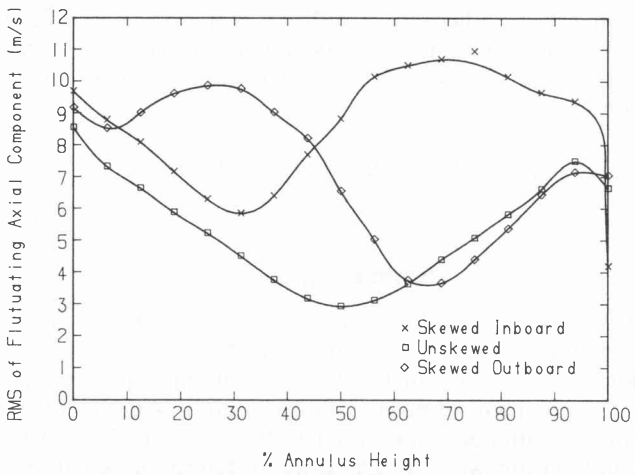

Figure 4 – Inlet Turbulence Profiles

Results and discussion

Verification

All tests were performed within the Reynolds number range 2,0 – 2,4 × 10^5 based on annulus hydraulic diameter, and Mach number range, 0,18-0,22 at inlet to the prediffuser. The objective of the testing was to define the optimum diffuser configuration by changing the prediffuser geometry, flow split and dump gap. The optimum configuration was chosen as that with the highest pressure recovery.

As a starting point an identical configuration to that used in Fishenden and Stevens – prediffuser 3 – was tested at a constant flow split of S = 1,6. This served as a form of calibration of the testbench. A comparison of the published [1] results and those measured in this study is given in figure 5. The degree of agreement is good except at extreme dump gaps. At small dump gaps the influence of effects including the radii of curvature at the prediffuser exit and errors in dump gap measurement become important. No reason could be postulated for the small discrepancy at larger dump daps where the diffuser performance is seen to be very insensitive to dump gap.

Additional tests were performed with the baseline 6/6 prediffuser configuration, by varying the flow split at three dump gaps (figure 6). Similar data were not published in [1] for this particular configuration, but the trends are similar to those obtained for their other prediffuser geometries: pressure recovery peaks at a flow split not necessarily equal to the design value, with the loss coefficient becoming insensitive at the larger dump gaps. Velocity profiles at exit from the prediffuser were also measured and it was found that at the optimum flow split the velocity profile was symmetrical confirming the findings of [1]. The variation of the dome wall static pressures is also in qualitative agreement with [1] with the pressure distribution being approximately symmetrical at the optimum flow split.

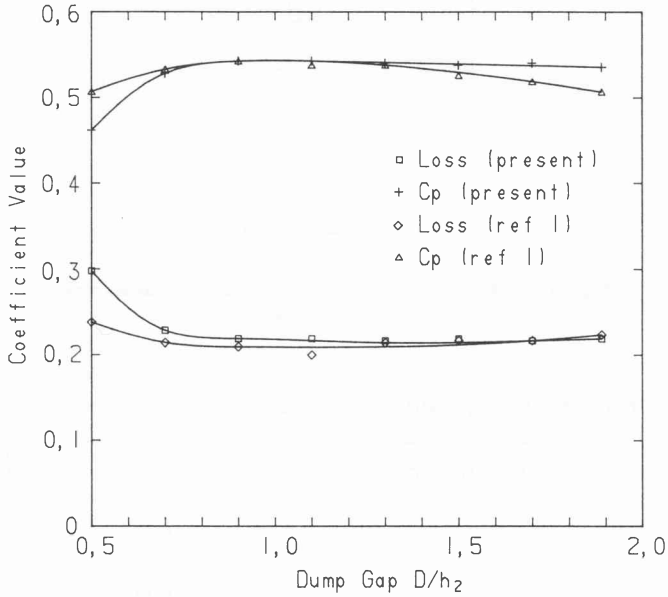

Figure 5 – Comparison of Published [1] and Measured Performance of 6/6 Prediffuser (S = 1,6)

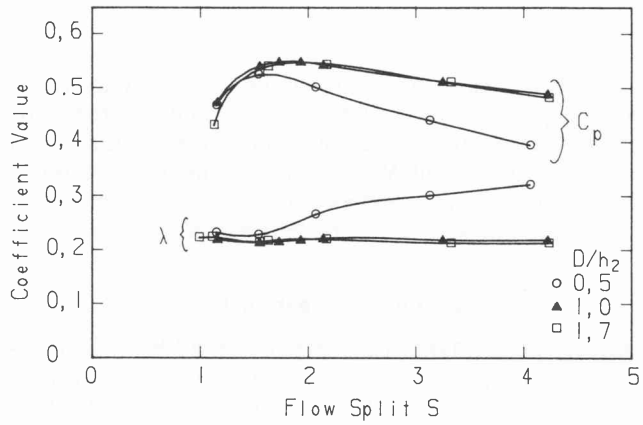

Figure 6 – Performance of Baseline 6/6 Configuration (A_2/A_1 = 1,8)

Table 2 Prediffuser Configurations

ϕ_i	ϕ_o	A_2/A_1	L/h_1	Mean Diffuser Angle	Included Angle
6	6	1,8	3,80	0°	12°
4	7,5	1,8	3,80	1,75°	11,5°
2	9	1,8	3,80	3,5°	11°
0	10,5	1,8	3,80	5,25°	10,5°
4	10,5	1,8	3,80	3,25°	14,5°

Optimum Cant Angle

Similar tests were performed using the other prediffuser combinations listed in table 2. The objective was to find the configuration which had its peak recovery at the design flow split of 2,15. The results obtained are shown in figure 7 where the degree of canting is represented by the mean diffuser angle. This variable is equal to zero for a symmetrical prediffuser. The maximum Cp for all the configurations was obtained at a dump gap of $D/h_2 = 1,0$ although the pressure recoveries were only marginally better than those for the larger dump gaph$D/h_2 = 1,7$. This tends to indicate that the flow in the prediffuser/dump region is only marginally improved in terms of overall performance by the close coupling of the combustor dome to the diffuser exit.

The operation of a dump diffuser at a flow split that differs from the split that results in a symmetrical prediffuser exit profile, can result in deleterious unsteady flows. Reference [1] showed that the stability margin of a prediffuser is very dependent on flow split: if the flow split is such that it results in a nonsymmetrical profile at exit, it means that one of the diffuser walls is closer to separation. This is exacerbated as the flow split is either increased or decreased away from the optimum value which coincides with that of peak recovery. This whole phenomenon is compounded if a highly loaded prediffuser is used. Even conservative diffusers, with diffuser lengths below that indicated by the Cp* line, can stall on either wall at inappropriate choices of flow split and dump gap. In this context a dump gap can also be too small as the close proximity of the dome can amplify the distortion caused by a non-optimal flow split that will propagate up the prediffuser. This explains the high turning losses indicated at $D/h_2 = 0,5$.

An approximately symmetrical pressure distribution about the flame tube dome was always obtained close to the optimum flow split. This is potentially of interest to the diffuser/combustor designer as it gives guidance in the optimization of a configuration by either the numerical computation of the static pressure flow field around the combustor dome or by the physical instrumentation of the combustor dome. This can also be said about the prediffuser exit velocity profile.

Figure 8 summarizes the data of figure 7 by showing the influence of mean diffuser angle on peak pressure recovery for each diffuser configuration for the three dump gaps. It can be seen that the maximum pressure recovery occurs at a mean diffuser angle of 3,5 degrees at a flow split very close to the design value. This indicates that the 9/2 combination is the best configuration. It is seen therefore that by canting the diffuser the optimum flow split can be made to coincide with that of the design ratio and that a small but significant gain in diffuser performance can be obtained by this appropriate matching.

The dome pressure distribution and prediffuser exit velocity profile obtained for the 9/2 combination at peak recovery ($D/h_2 = 1,0$ and $S = 2,15$) are both more or less symmetrical as seen in figure 9. There is less likelihood of experiencing separation or transitory stall in the prediffuser if the flow split is such that a symmetrical velocity profile is obtained at exit from the prediffuser; this fortunately coincides with the value necessary for peak pressure recovery.

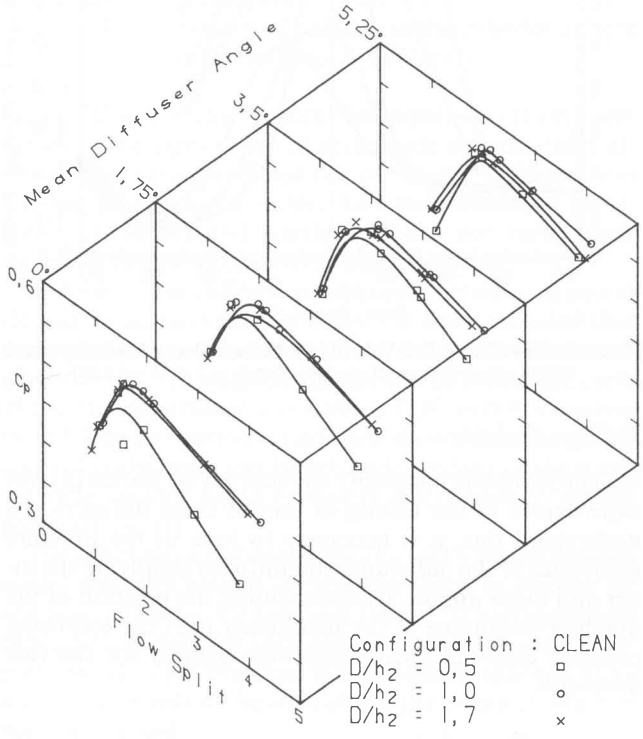

Figure 7 – Influence of Mean Prediffuser Angle on Overall Performance

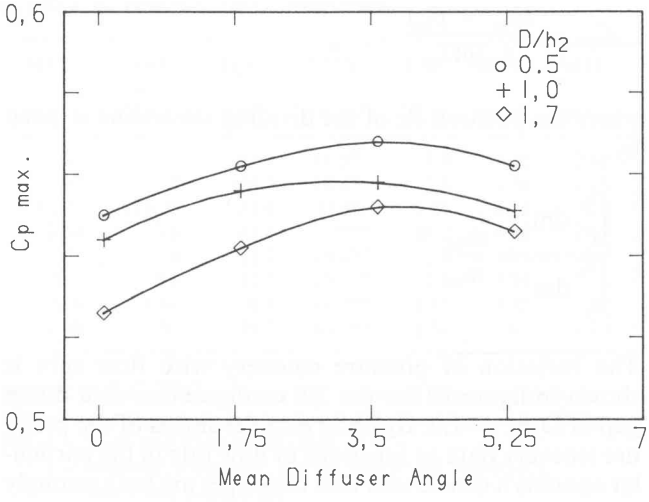

Figure 8 – Influence of Mean Prediffuser Angle on Peak Pressure Recovery

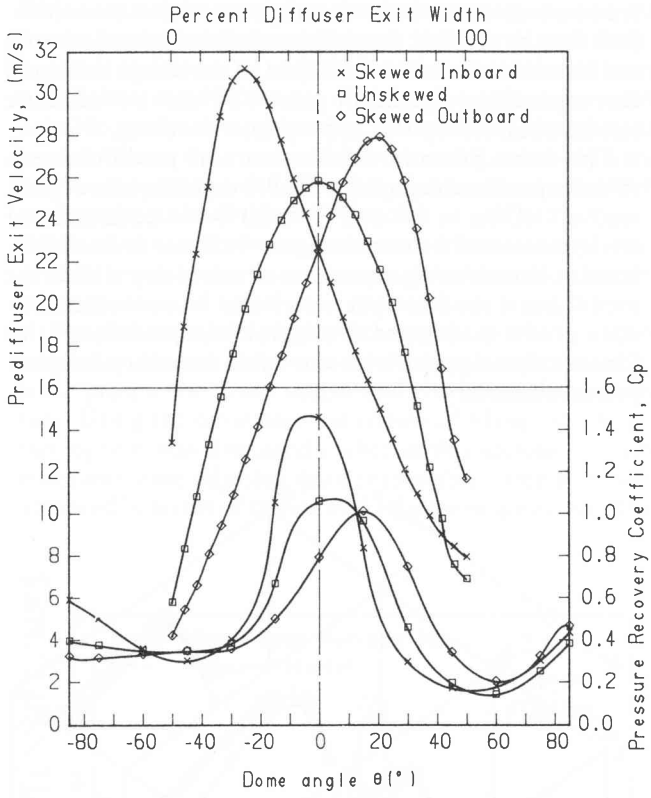

Figure 9 – Prediffuser Exit Velocity Profile and Dome Static Pressure Distribution (9/2 configuration D/h_2) = 1,0; S = 2,15)

Diffuser Stability

No aerodynamic instability as reported by Ehrich [4] was experienced in the testing of any of these diffusers. To understand this, it is necessary to look at the pressure recoveries of the individual streamtubes supplying the inner and outer annuli. By determining the position of the dividing streamline at the prediffuser inlet the following pressure recovery coefficients were defined for the two flowfields

$$C_{pi} = \frac{(\bar{p}_{4i} - \bar{p}_{1i})}{\alpha_{1i}\frac{1}{2}\rho U_{1i}^2}$$

$$C_{po} = \frac{(\bar{p}_{4o} - \bar{p}_{1o})}{\alpha_{1o}\frac{1}{2}\rho U_{1o}^2}$$

where the position R_s of the dividing streamline is given by

$$\frac{\int_{R_s}^{R_o} dm}{\int_{R_i}^{R_s} dm} = \frac{\dot{m}_{4o}}{\dot{m}_{4i}}$$

The variation of pressure recovery with flow split is shown in figure 10 for the 2/9 configuration at a dump gap of D/h_2 = 1,0. By observing the slopes of the pressure recovery data as functions of flow rate in the particular annulus it can be seen that the slopes are both strongly negative for the inner and outer flow fields (except when the flow is extremely low in the outer streamtube). This is the necessary condition as stated by Alford [5] for flow stability with the diffuser characteristic displaying a damping action.

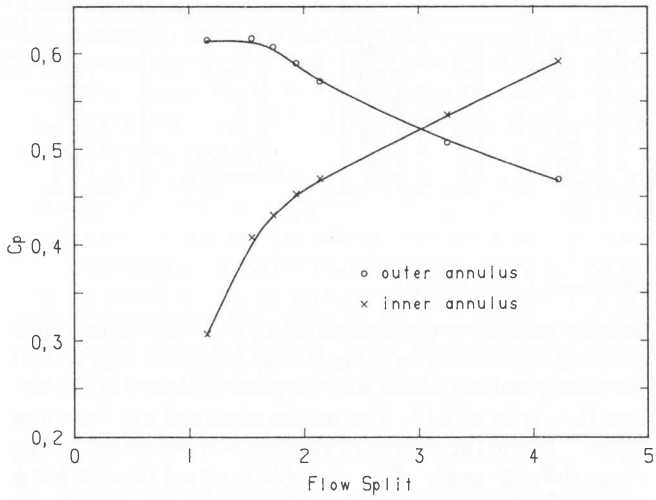

Figure 10 – Pressure Recovery in the Inner and Outer Streamtubes (D/h_2 = 2/9 configuration)

Diffuser Length and Area Ratio

As the most compact diffuser configuration is normally required, the influence of prediffuser area ratio was investigated by fixing the inner and outer wall angles and varying the length. Since most of the published work has been done using the 6/6 combination it was decided to revert back to this and continue with the same wall angles. The effect of two parameters is being evaluated by this approach but it was assumed that the influence of the area change would be qualitatively observed, as pressure recovery is primarily dependent on area ratio. Alternatively it could be reasoned that by increasing the length of a prediffuser the total pressure loss is increased but this would be negligible compared to the losses generated by the dumping action downstream of the prediffuser.

The results in figure 11 show that at the larger dump gaps the response is relatively flat. This behaviour is contrary to what one would assume if the work of Sovran and Klomp [6] is considered where an increase in area ratio resulted in improved pressure recovery. Although it is recognized that most of the pressure recovery in a dump diffuser is achieved in the prediffuser it appears some recovery is obtained in the dump region or settling length. Some form of compensating mechanism is apparent and is probably linked to the overall area ratio that is kept constant at a value of 2,0. Due to the close coupling of the prediffuser and simulated combustor dome at small dump gaps, increased losses are observed especially at the lower area ratios.

It was desired to evaluate the effect of prediffuser length and included angle but with a constant area ratio of 1,8 and a mean diffuser angle of close to the optimum value of 3,5. This was of interest as the most compact prediffuser was required. To this end an additional diffuser combination was tested with an inner/outer wall combination of 4/10,5 at the three previous dump gaps. The results are shown in figure 12. It was thought that with the larger included angle an increased coupling be-

tween the dome and prediffuser would be necessary to obtain peak performance and additional tests were performed at smaller dump gaps. It can be seen that the 2/9 configuration is superior in terms of peak pressure recovery as well as having a flatter response with variation of flow split around the optimum value.

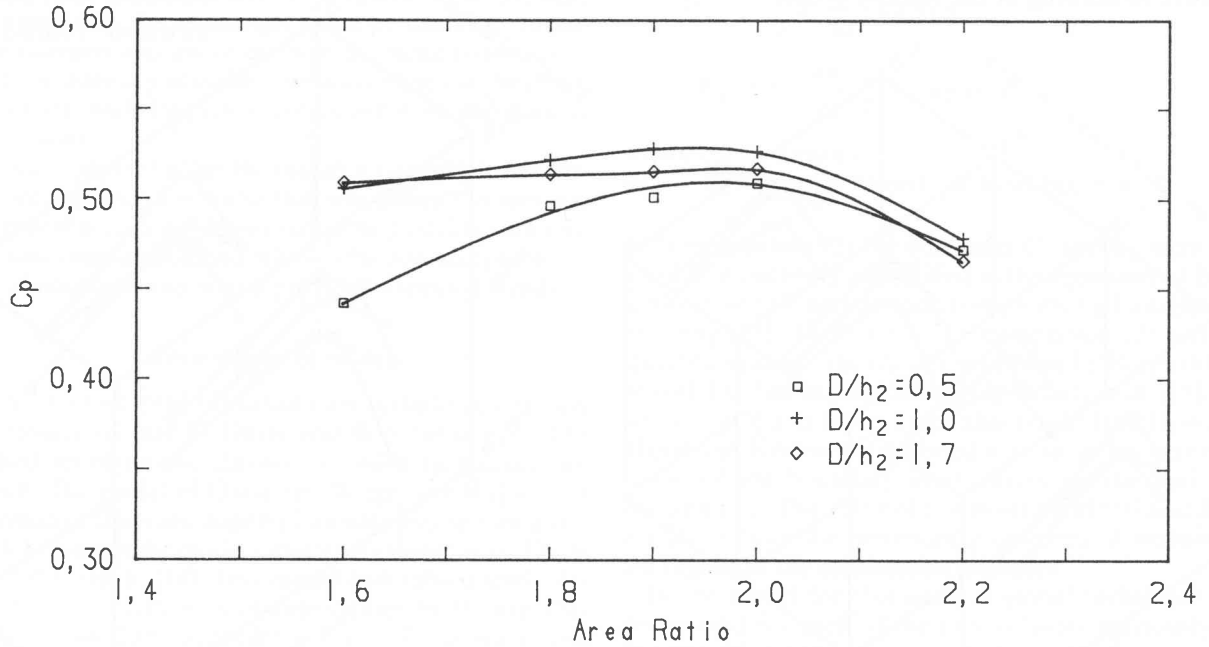

Figure 11 – Influence of Area Ratio on Performance of 6/6 configuration

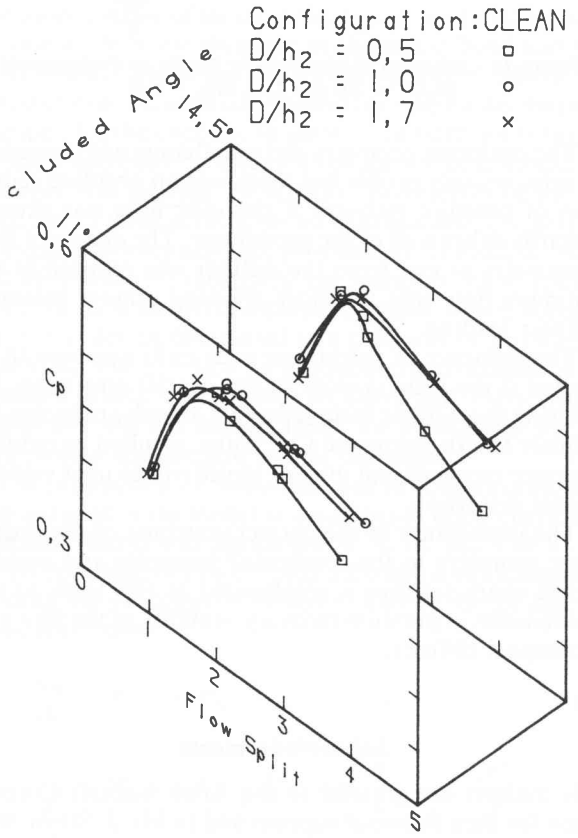

Figure 12 – Influence of Diffuser Included Angle (A_2/A_1 = 1,8; Mean Diffuser Angle = 3,5° and 3,25°)

Optimum Diffuser

Taking into account all the parameters varied and the geometries tested it was concluded that the optimum prediffuser geometry was the 2/9 combination with an area ratio of 1.8 and an optimum flow split equal to that of the design value S = 2,15. If the overall area ratio is considered, the diffuser effectiveness of this optimal geometry and flow split is 75,7%. Comparing this to the 6/6 configuration an increase in effectiveness of 3% is observed. Concomitant with this is a reduction in loss of 5%. This is obviously particular to the inlet velocity profile and to the overall geometry of the diffuser/combustor combination, which was fixed in this study.

Skewing the Inlet Velocity Profile

The question arose as to what effect a skewed, velocity profile would have on the optimum. Two sets of complete tests were repeated with the diffuser geometries of table 2 using the other two profiles generated by the mesh installation. The results are shown in figure 13. It is seen that a distorted inlet velocity profile affects the performance of the diffuser detrimentally with the effect being larger with inboard skewing. This is what one would expect as indicated by the value of the design flow split. The optimum geometry however does not change, with the 2/9 configuration still providing the best performance as shown in figure 14 at a flow split close to the design value. This means that the optimum geometry can be determined using a single inlet velocity profile with the knowledge that this geometry will be close to optimum for any inlet profile. In this manner the dump diffuser performs as an aerodynamic flow conditioner with the appropriate dump gap, redistributing mass flow and momentum. The velocity profiles at exit from the prediffuser at the design flow split of S = 2,15 for the 2/9 configuration are shown in figure 9 with the accompanying combustor dome pressure distribution. This shows the importance of the coup-

ling of the flame tube to the prediffuser and the accompanying flow conditioning. Figure 15 shows that the diffuser with the larger divergence angle is much more sensitive to skewing of the velocity profile.

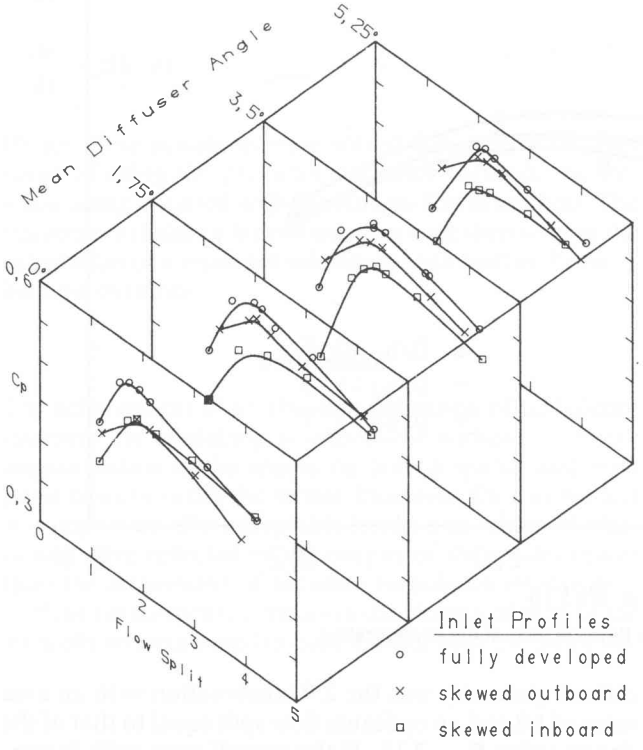

Figure 13 – Influence of Inlet Velocity Profile on Performance (A_2/A_1 = 1,8, D/h_e = 1,0)

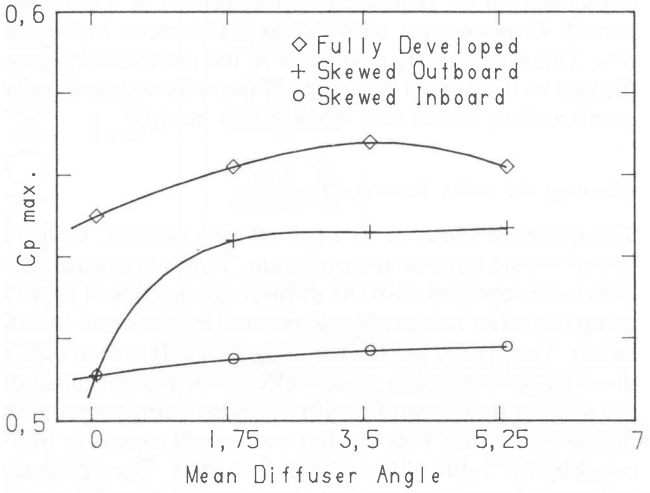

Figure 14 – Influence of Inlet Velocity Profile on Peak Pressure Recovery (A_2/A_1 = 1,8)

Conclusions

A series of prediffuser configurations was tested to establish the influence of flow split, dump gap, inlet velocity profile and prediffuser geometry on the overall performance of an annular dump diffuser. By offsetting the diffuser an improved pressure recovery was obtained at a flow split equal to the design area ratio of the inner to outer annulus. This resulted in a 3% improvement in diffuser effectiveness and a reduction of 5% in pressure loss.

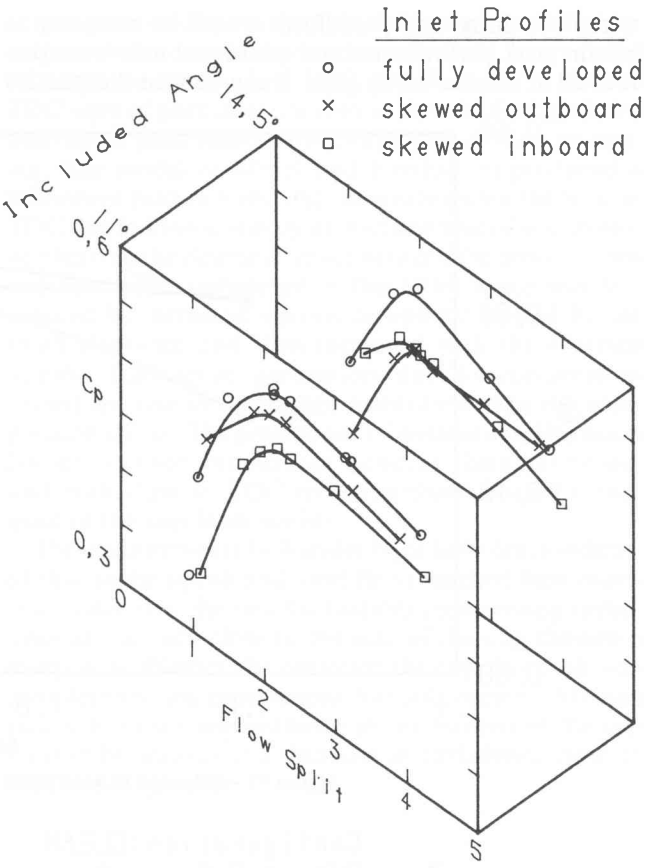

Figure 15 – Influence of Inlet Velocity Profile on Performance (A_2/A_1 = 3,8 and 2,93; D/h_2 = 1,0)

The optimum geometry did not change with variation of inlet velocity profile but there was an absolute reduction of pressure recovery if the inlet flow was skewed towards either wall of the prediffuser. The degree of flow asymmetry at exit from the diffuser was reduced at the optimum flow split therefore allowing a more balanced diffuser loading.

The influence of prediffuser area ratio was seen to be limited if the ratio is close to the overall area ratio. Increasing the diffuser included angle, thereby reducing the diffuser length below the Cp* value, resulted in reduced pressure recovery and greater sensitivity to inlet velocity profile distortion.

The importance of the correct matching of the prediffuser geometry to the combustor geometry and aerodynamic characteristics is emphasized as this leads to improvements in pressure recovery, stability of the flow and a compact diffuser.

Acknowledgements

The authors are grateful to the Atlas Aircraft Corporation for their financial support and to Mr. J. Steyn, who was responsible for the acquisition of the experimental data, and testbench management.

References

1. Fishenden, C. R. and Stevens S. J., "The performance of annular combustor-dump diffusers", Journal of Aircraft, Vol 10, No 1, 1977, pp 60-67.

2. Wagner, W. B., Tanrikut, S. and Sokolowski, D. E., "The performance of annular prediffuser-combustor systems", ASME paper 80-GT-15, 1980.
3. Von Backström, T. W., "Expendable turbojet compressor design, test and development" AIAA Eighth International Symposium on Air Breathing Engines, pp 331-338, Paper No 87-7039, Cincinnati, Ohio, June 1987.
4. Ehrich, F. F., "Aerodynamic stability of branched diffusers", ASME paper 70-GT-27, 1970.
5. Alford, J. S. "Protecting Turbomachinery from Unstable and Oscillatory Flows", ASME paper 66-WA/GT-13, 1966.
6. Sovran, G. and Klomp, E. D. "Experimentally determined optimum geometries for rectilinear diffusers with rectangular, conical or annular cross-section" Fluid Mechanics of Internal Flow, Sovran, G., (Editor), Elsevier, New York, 1967, pp 462-474.

Appendix A

The Kinetic Energy Coefficient

According to Brighton and Jones [1] the maximum velocity in an annulus occurs at the radius R_{max} given by:

$$R_{max} = (1 - (1-k)/(k^{0,343} + 1))\ R_{out}$$

where R_{out} is the other radius and $k = R_{in}/R_{out}$, with R_{in} the inner radius.

For the present geometry $k = 0,8478$ and $R_{max} = 0,9217\ R_{out}$.

The arithmetic mean of the inner and outer radius is:

$$R_m = \frac{170}{184}\ R_{out} = 0,9239\ R_{out}$$

Since the difference between R_m and R_{max} is less than 1,5% of the annular gap we assume that the maximum velocity occurs at R_m. The kinetic energy coefficient may then be calcuated by assuming symmetrical power law or logarithmic law profiles.

Under these assumptions, for the power law where $u \propto y^{\frac{1}{n}}$

$$\alpha_{power} = \left(\frac{n+1}{n}\right)^3 \frac{n}{n+3}$$

According to [2] n varies with Reynolds number Re as in the table at the end of this appendix.

The logarithmic law in terms of the dimensionless velocity u^+ and distance from the wall y^+ is:

$$u^+ = \frac{1}{0,4} \ln y^+ + 5,5$$

By integrating a profile consisting of two logarithmic profiles extending from each wall to the centre of the annular gap, it can be shown that:

$$\alpha = (\ln^3 Y^+ + 3,6 \ln^2 Y^+ + 7,32 \ln Y^+ + 3,528)/(\ln Y^+ + 1,2)^3$$

where

$$Y^+ = \frac{1}{2}(R^+_{out} - R^+_{in}) = \frac{1}{2} Re \sqrt{\Lambda/32}$$

The friction factor Λ is determined from:

$$\sqrt{32/\Lambda} = \frac{2}{0,4}\left[\ln\left(\frac{1}{2} Re \sqrt{\Lambda/32}\right) + 5,5.0,4 - 1\right]$$

The following table for the variation of a α with Reynolds number may then be compiled:

Re	4.10^3	$2,3.10^4$	$1,1.10^5$	$1,1.10^6$	2.10^6	$3,2.10^6$
n	6	6,6	7,0	8,8	10,0	10,0
α_{power}	1,059	1,050	1,045	1,030	1,024	1,024
Λ	0,04249	0,02190	0,01823	0,01170	0,0106	0,01748
$\ln Y^+$	4,289	5,707	7,180	9,261	9,809	10.5
α_{log}	1,087	1,057	1,039	1,026	1,023	1,021

At a typical test Reynolds number of $2,4.10^5$ the two aproaches above would predict the following:

$$\alpha_{power} = 1,040 \quad \text{and} \quad \alpha_{log} = 1,034$$

References to Appendix

1. Brighton, J. A. and Jones, J. B. "Fully Developed Flow in Annuli", Journal of Basic Engineering, Dec. 1964.
2. Schlichting, H. "Boundary Layer Theory", McGraw-Hill, 7th Edition 1979.

Proceedings of the 1st South African Conference on Applied Mechanics (SACAM) '96, 1 - 5 July, 1996 Midrand, South-Africa

[5]

CALCULATION OF THE FLOW THROUGH AN AXIAL COMPRESSOR BY THE STREAMLINE THROUGHFLOW METHOD

T.H. Roos, M.Eng, Engineer Aerotek, CSIR
T.W. von Backström, Professor
A.J. Gannon, BSc (Eng.)
Department of Mechanical Engineering
University of Stellenbosch, Stellenbosch

ABSTRACT

A method based on the transformation of the turbomachinery inviscid throughflow equation is used to model a real compressor. This, the streamline throughflow method (STFM) has previously been shown to be accurate when compared to exact analytical solutions of inviscid flow representative of those found in turbomachines. In the current paper its use in simulating real flows is verified by comparing experimental measurements from a real compressor with results obtained from a simulation of the compressor using the STFM. Howell's correlation is used to take into account deviation and losses due to viscous effects. No allowance was made for the annulus boundary layer. Experimental measurements were made at only one circumferential position. Agreement between experimental and computational results were satisfactory.

NOMENCLATURE

b	blockage factor	T	stagnation temperature
c	velocity, absolute	W	velocity, relative
C	lift, drag coefficient	z	axial co-ordinate
F	body force	Δ	change in value
H	total enthalpy, blade height	Ω	angular velocity
I	rothalpy	ψ	stream function
p	pressure	ρ	density
r	radial co-ordinate, radial position of streamline	ε^*	Howell's nominal deflection angle
s	entropy, blade pitch		

SUBSCRIPTS

a	annulus loss	s	secondary loss
b	blade	z	axial
D	drag	θ	tangential
L	lift	1	upstream
o	total	2	downstream
r	radial		

INTRODUCTION

In the preliminary design of turbomachines a meridional method is often used. While full 3-D simulations are possible for detailed analysis, a need still exists for improved meridional calculation methods for design. These assist the designer in selecting annulus geometry, blade profiles and flow angles. Two common methods used are the streamline curvature method (SCM) [1],[2] and the matrix throughflow method (MTFM) [2].

SCM is streamline based and it has the advantage that flow properties are conserved along streamlines. Computer memory requirements are small. Its disadvantage is that the accuracy of the solution is dependent on the type of curve fit used for the streamlines. MTFM uses a fixed grid and calculates stream function values at each point. The advantages of this scheme are that it uses a standard CFD discretization scheme, but it requires large computer memory and does not make use of conservation of properties along a streamline.

STFM makes use of a co-ordinate transformation to allow streamline position to be the dependent variable. Streamline properties are conserved and use of a CFD type grid can be made for the discretization scheme.

This paper demonstrates the use of STFM in the simulation of a real compressor. Experimental measurements on a laboratory compressor are compared with results from the computer program. Deviation and losses are modelled using Howell's correlation, [7] and [8].

PREVIOUS WORK

Verification of the STFM for various flows representative of those found in turbomachines has been performed [3]. These include flow through a parallel walled annulus, over a sphere and through single and twin actuator discs in a parallel annulus. The results from these test cases showed that the STFM is very good in predicting streamline position for inviscid, incompressible flows. Velocity profiles were well predicted. Errors of less than 1% were obtained when at least 7 streamlines were used.

STFM EQUATIONS

A brief description of the derivation of the STFM equations is given here. A more complete description is given in [3]. A general throughflow equation for inviscid compressible flow through turbomachinery as derived by [4] is:

$$\frac{\partial}{\partial z}\left(\frac{1}{\rho r b}\frac{\partial \psi}{\partial z}\right)+\frac{\partial}{\partial r}\left(\frac{1}{\rho r b}\frac{\partial \psi}{\partial r}\right)=\frac{1}{W_z}\left[\frac{\partial I}{\partial r}-T\frac{\partial s}{\partial r}-\frac{F_{b,r}}{\rho}-\frac{W_\theta}{r}\frac{\partial}{\partial r}(rW_\theta)\right]$$

$$\text{where}\quad \frac{\partial \psi}{\partial r}=\rho r b W_z \qquad (1)$$

$$\text{and}\quad \frac{\partial \psi}{\partial z}=-\rho r b W_r$$

References [5] and [6] derived a throughflow equation based on the following assumptions:

1. The usually small blade radial force term $F_{b,r}$ is ignored.
2. The blade rows are completely represented by actuator discs.

3. Consequently all the flow occurs in blade free space and the blockage factor b is equal to unity (no blockage).
4. As another consequence of point 1, the flow field can be solved in the absolute frame of reference. (Relative velocities replaced by absolute and rothalpy by stagnation enthalpy).
5. Also, gradients with respect to radius in the turbomachinery source term can be replaced with gradients with respect to stream function:

The equation has the following form:

$$\frac{\partial}{\partial z}\left(\frac{1}{\rho r}\frac{\partial \psi}{\partial z}\right)+\frac{\partial}{\partial r}\left(\frac{1}{\rho r}\frac{\partial \psi}{\partial r}\right)=\rho r\left[\frac{\partial H}{\partial \psi}-T\frac{\partial s}{\partial \psi}-\frac{c_\theta}{r}\frac{\partial}{\partial \psi}(rc_\theta)\right] \qquad (2)$$

The above equation is transformed to a form in which the radial streamline position is the dependent variable. The transformation method is given by [9]. The transformed equation for incompressible flow is:

$$\left(\frac{\partial r}{\partial \psi}\right)^2\frac{\partial^2 r}{\partial z^2}+\left(1+\left(\frac{\partial r}{\partial z}\right)^2\right)\frac{\partial^2 r}{\partial \psi^2}=-\frac{1}{r}\left(\frac{\partial r}{\partial \psi}\right)^2+2\frac{\partial r}{\partial z}\frac{\partial r}{\partial \psi}\frac{\partial^2 r}{\partial z\partial \psi}$$

$$+\left(\frac{\partial r}{\partial \psi}\right)^2\frac{\partial r}{\partial z}\frac{1}{\rho}\frac{\partial \rho}{\partial z}-\frac{\partial r}{\partial \psi}\left(1+\left(\frac{\partial r}{\partial \psi}\right)^2\right)\frac{1}{\rho}\frac{\partial \rho}{\partial \psi} \qquad (3)$$

$$-(\rho r)^2\left(\frac{\partial r}{\partial \psi}\right)^3\left[\frac{\partial H}{\partial \psi}-T\frac{\partial s}{\partial \psi}-\frac{c_\theta}{r}\frac{\partial}{\partial \psi}(rc_\theta)\right]$$

For incompressible flow terms containing density gradient are equal to zero. In addition the following substitution may be made:

$$\frac{\partial H}{\partial \psi}-T\frac{\partial s}{\partial \psi}=\frac{1}{\rho}\frac{\partial p_o}{\partial \psi} \qquad (4)$$

DESCRIPTION OF TEST RIG

The test bench consists of a low pressure ratio, namely 1.03, three-stage Rofanco compressor. The design mass flow rate is 2.66 kg/s at standard sea level conditions. The flow is assumed incompressible. The rotor tip design speed is 66 m/s with a hub-tip radius ratio 0.71, a tip solidity of 0.932, aspect ratio of 2 and constant chord. The stator has a hub solidity of 1.3687. The compressor blading was designed for 80% reaction using NACA 65 blade profiles on a circular arc camber line with repeating stages. There are no inlet guide vanes due to the high reaction of the blading. A uniform inlet velocity profile is created using a honeycomb section to remove swirl and a mesh to ensure a uniform turbulence profile and to dissipate wakes from the honeycomb.

Flow angles and dynamic pressure radial profiles were obtained by transversing a 3-hole cobra probe from casing to hub behind each blade row. The readings behind the rotor row are averaged in time and in circumferential direction because of damping in the piping, but the readings behind the stator rows are

averaged in time only as transverses were only made at single circumferential positions relative to the stator trailing edge position [10].

SIMULATION OF COMPRESSOR

The computational grid used to simulate the compressor consists of 11 internal streamlines and 34 axial grid positions. A single radial grid line was placed at the end of each blade row so that the flow angle could be specified using Howell's correlation for deviation of flow from the blades. The remainder of the grid points were equally spaced between the blade rows and the inlet and outlet. It was assumed that the tangential momentum and total pressure between the outlet of one blade row to the inlet of the next remained constant. The total pressure rise across a blade row can be expressed, from the Euler work equation, as follows:

$$\Delta p_{o1,2} = \rho\Omega\left(r_2 c_{\theta 2} - r_2 c_{\theta 2}\right) - \Delta p_{o1,2loss} \qquad (5)$$

where $\Delta p_{o1,2loss}$ is introduced using Howell's loss correlations. The flow rates simulated were near design, near choke and near surge. The simulation was performed on a 386 personal computer and convergence time for the above grid was typically 30 seconds. The convergence criteria was that the absolute change in streamline position was less than 0.001% (0.01mm).

HOWELL'S CORRELATION

Howell's correlations, [7] and [8] were used to obtain values for deviation from the blade rows. Howell defines a nominal deflection ε^* as 80% of the stalling deflection ε_s. The nominal condition is found from Howell's original graphs. An off design correlation is then applied from the graph of Howell's off-design cascade correlation. This deviation is then applied to the outlet angle of the blade at the relevant radius to get the correct outlet flow angle.

There are differing sources of pressure loss across the blade row. Profile loss drag is dependent on the foil profile and can be obtained from Howell's off-design cascade correlation as a function of incidence. A limit should be applied to this value for near surge flows. For incidence values outside the range of Howell's graphs, the corresponding value of deviation and pressure loss for the limiting incidence value from the graph is used to prevent extrapolation. At positive incidence the stalling value is chosen. Howell assumed that two distinct sources combined to produce endwall loss, being frictional drag from the annulus wall and secondary loss, and both correlated by means of drag coefficients. The annulus loss drag coefficient scales on the blade spacing to height ratio.

$$C_{Da} = 0.20\frac{s}{H} \qquad (6)$$

Howell derived the secondary loss by analogy with the trailing vortex loss behind aircraft

$$C_{Ds} = 0.018\left(C_L\right)^2 \qquad (7)$$

COMPARISON OF EXPERIMENTAL AND COMPUTATIONAL RESULTS

At the design flow rate it can be seen from Figure 1 that the agreement between the experimental results and the STFM prediction using Howell's correlation is good after the rotor rows and at the first stator row. For the 2nd and 3rd stator rows the flow angles are underpredicted however. The same trends can

be seen in Figure 2 for tangential velocity profiles at the design flow rate. In both cases this is most likely to be due to the fact that, behind the stators, measurements were taken at only one circumferential position and therefore do not represent a mass average of the blade passage bulk flow and the wake regions. Figure 3 shows that axial velocities are slightly underpredicted in the central region but the shape of the velocity profile can be seen in the prediction. All rotor axial velocity profiles have been increased by 20 m/s for clarity. Part of this underprediction is due to the inviscid analysis. As a result of annulus boundary layer effects the central region is accelerated in practice. Figure 4 shows that the total pressure profiles are well predicted at the design flow rate at the rotor exit, and underpredicted at the stator exit. At each stage the higher line represents the rotor exit and the lower the stator exit.

Figure 5 shows the axial velocity profiles at near choke flow rate. The shape of the profiles are well predicted but the values are underpredicted. The reasons for this underprediction are the same as for that at the design flow rate.

Large variations in the flow angle profiles can be seen at the near surge flow rate. Figure 6 shows the agreement in flow angle prediction for the rotor rows to be good but for the stator rows the flow angles are underpredicted. Figure 7 shows the same trend for the tangential velocity profiles. In Figure 8 the axial velocity profiles at near surge flow rate are shown. The shape of the profiles are well predicted. Figure 9 is a plot of the actual streamlines predicted by the STFM with Howell's correlation distorting the aspect ratio of the compressor for clarity. The shift in position at the near surge flow rate can clearly be seen as compared to the near design flow rate where they are almost parallel to the hub

CONCLUSION

The STFM has been used to simulate a real low speed turbomachine where compressibility effects are small. Using Howell's correlation for deviation and losses good correlation with experimental values were obtained for the rotor exit flows. Incomplete experimental evidence preclude conclusions being drawn concerning stator exit flows. The advantages of the STFM, namely that streamline position is the dependent variable and properties are conserved along streamlines make for efficient computer programs in terms of memory usage and computational effort. The method is currently being adapted to solve compressible flows.

REFERENCES

[1]. Novak, R.A., 'Streamline curvature computing procedures', ASME Journal of Engineering for Power, Vol 89 No 4, Oct 1967, pp 478-490.

[2]. Davis, W.R. and Millar, D.A.J., 'A comparison of the Matrix and Streamline Curvature Methods of Axial Flow Turbomachinery Analysis, From a User's Point of View', ASME Journal Engineering for Power, Oct. 1975, pp. 549-560.

[3]. von Backström, T.W. and Roos, T.H., 'The Streamline Throughflow Method for Axial Turbomachinery Flow Analysis', Papers of the ISABE XI, Tokyo, Japan, September 1993.

[4]. Hirsch, C. And Warzee, G., 'A finite-element method for through flow calculations in turbomachines', Journal of Fluids Engineering, Sept 1976, pp 403-421

[5]. Oates, G.C., 'Aerothermodynamics of Gas Turbine and Rocket Propulsion', Revised and Enlarged, 2nd Edition, AIAA Education series, Washington, 1988.

[6]. Oates, G.C., Knight, C.J. and Carey, G.F., 'A Variational Formulation of the Compressible Throughflow Problem', ASME Journal of Engineering for Power, Jan 1976, pp 1-8

[7]. Howell, A.R., 'Design of Axial Compressors', Proceedings of the Institution of Mechanical Engineers, London, 1945, 153.

[8]. Howell, A.R., 'Fluid Dynamics of Axial Compressors', Proceedings of the Institution of Mechanical Engineers, London, 1945, 153.

[9]. Boadway, J.D., 'Transformation of elliptic partial differential equations for solving two-dimensional boundary value problems in fluid flow', International Journal for Numerical Methods in Engineering.

[10]. Roos, T.H., 'A Prediction Method for Flow in Axial Compressors', M.Eng. Project Report, University of Stellenbosch, January 1995.

FIGURES

All figures show comparison between experimental data and STFM simulation using Howell's correlation.

Key:

+ 1st stage experimental results
o 2nd stage experimental results
x 3rd stage experimental results
—— STFM simulation

For total pressure profiles:

+ rotor experimental results
o stator experimental results

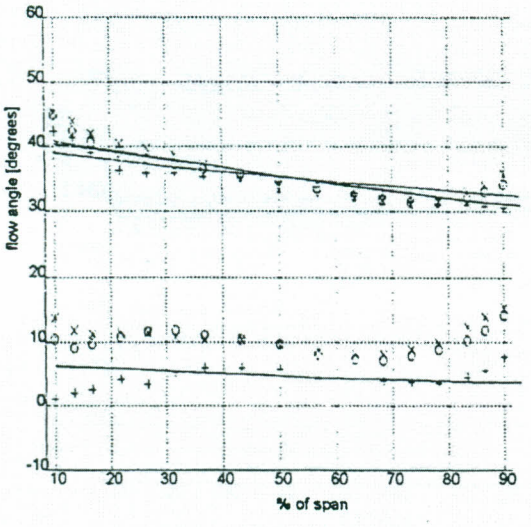

Figure 1 Flow angle profiles at near design flow rate.

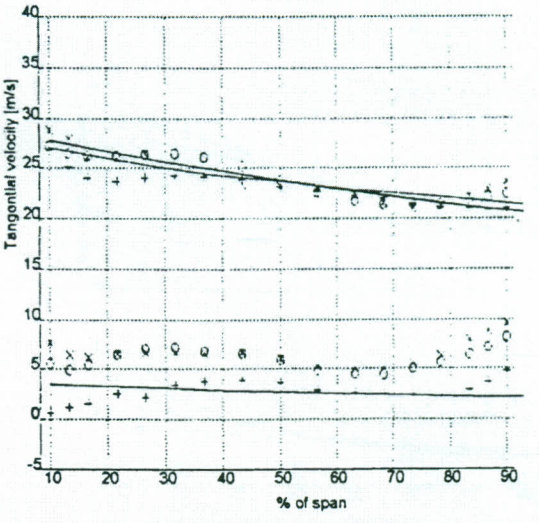

Figure 2 Tangential velocity profiles at near design flow rate.

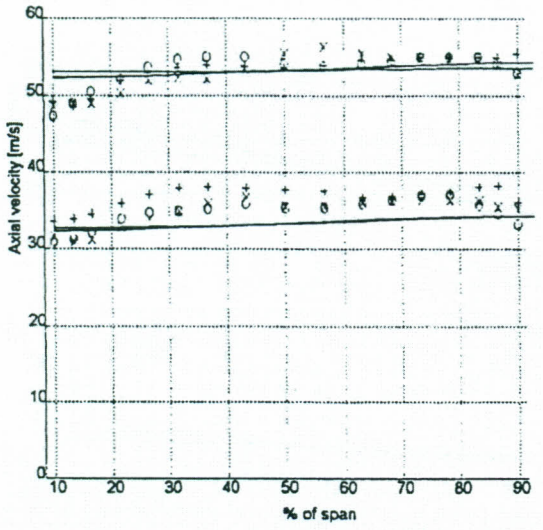

Figure 3 Axial velocity profiles at near design flow rate.

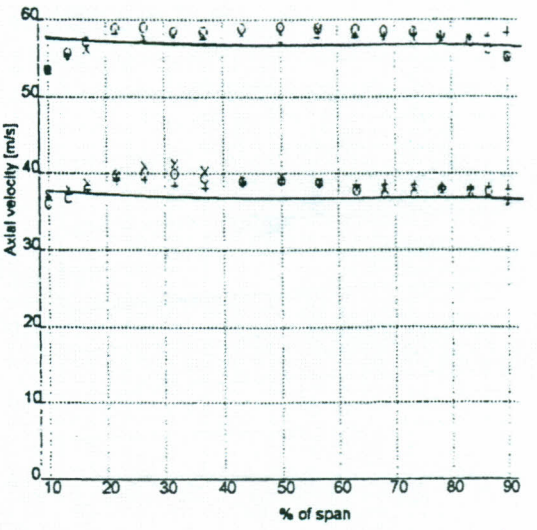

Figure 5 Axial velocity profiles at near choke flow rate.

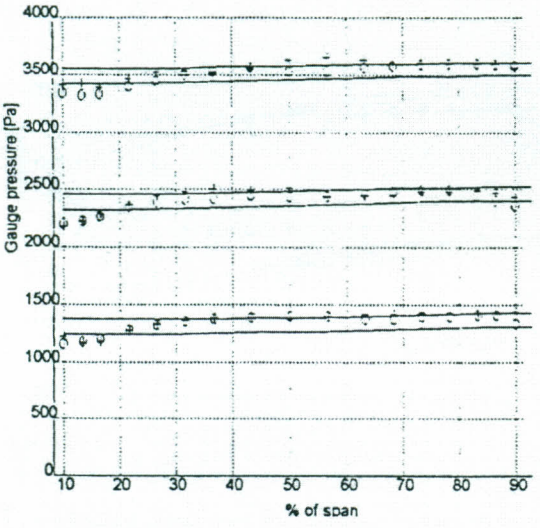

Figure 4 Total pressure profiles at near design flow rate.

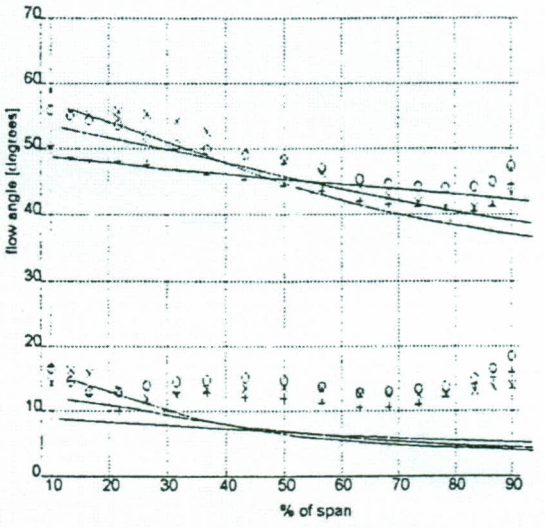

Figure 6 Flow angle profiles at near surge flow rate.

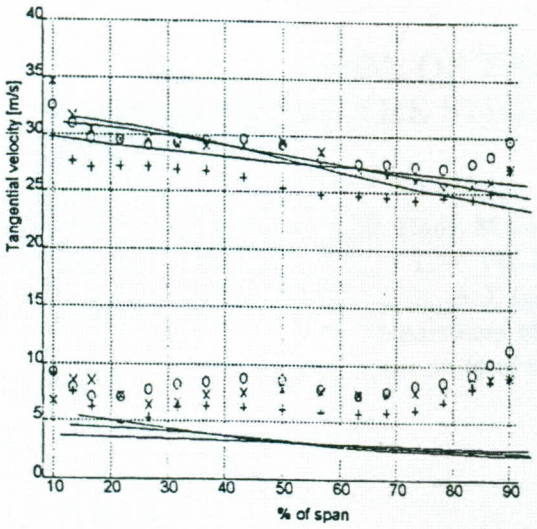

Figure 7 Tangential velocity profile at near surge flow rate.

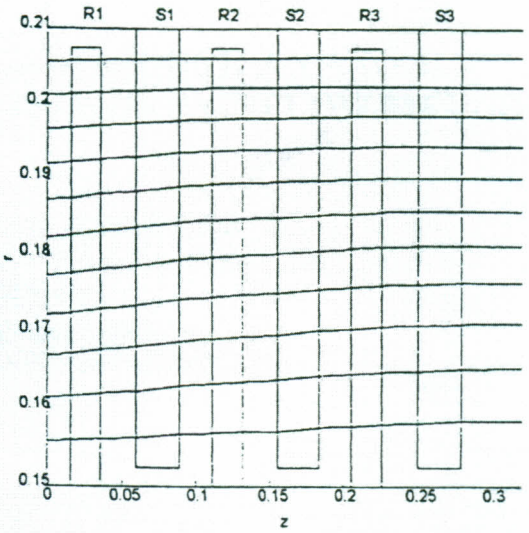

Figure 9 Streamlines at near surge flow rate with rotor and stator positions superimposed.

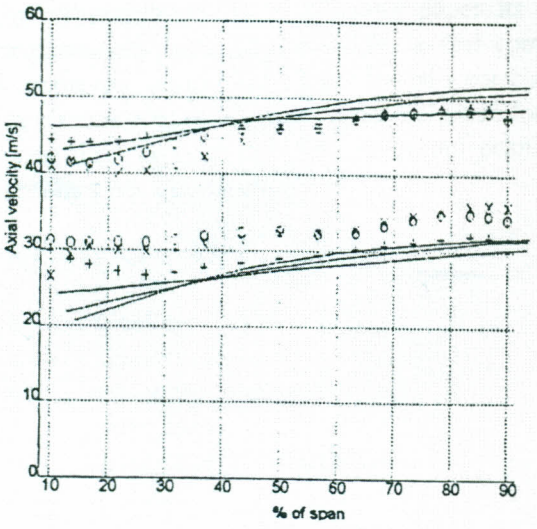

Figure 8 Axial velocity profile at near surge flow rate.

©Freund Publishing House Ltd.London International Journal of Turbo and Jet Engines, 17, 161-170(2000)

Comparison of Streamline Throughflow and Streamline Curvature Methods

Anthony J. Gannon andTheodor W. von Backström
Department of Mechanical Engineering, University of Stellenbosch, South Africa
E-mail: ajgannon@ing.sun.ac.za

Abstract

The axial flow turbomachinery throughflow equation states that radial gradients of rothalpy, entropy and moment of momentum affect the conservation of tangential vorticity. The streamline throughflow method (STFM) transforms this equation, expressed in terms of stream function in a radial-axial co-ordinate system, to an equation for streamline radial position in a stream function-axial co-ordinate system. The paper assesses the accuracy and efficiency of the STFM relative to the streamline curvature method (SCM) by comparing streamline positions and velocity profiles to analytical results. Test cases include flow through a single actuator disc, flow through twin actuator discs using a coarse computational grid, compressible flows through an almost choked nozzle, through single and twin actuator discs, and swirling flow using sloped stations. Results from the STFM and SCM agreed about equally well with analytical solutions for the same number of streamlines. The STFM, however, was much more tolerant of distorted computational grids and used an order of magnitude less computer time to converge. The test cases show that the STFM is suitable for annuli with large variations in hub and tip radius, for highly swirling and compressible flow, and is more robust and converges faster than the SCM. To demonstrate the practical applicability of the STFM a multistage compressor was simulated and STFM results compared with experiment.

Nomenclature

a	=	tangential velocity factor for actuator disc flow; sonic velocity
ADT	=	actuator disc theory
b	=	tangential velocity factor for actuator disc flow;
	=	unblocked fraction
C	=	absolute velocity
c_p	=	specific heat at constant pressure
F	=	force
I	=	rothalpy
h	=	enthalpy
LHS	=	left hand side
M	=	Mach number
MTFM	=	matrix throughflow method
P	=	pressure
r	=	radial co-ordinate, radial position of streamline
R	=	gas constant
RHS	=	right hand side
s	=	entropy
S	=	source term
SCM	=	streamline curvature
STFM	=	streamline throughflow
T	=	absolute temperature
W	=	relative velocity
x, y	=	orthogonal co-ordinate system components
z	=	axial co-ordinate
γ	=	specific heat ratio
ρ	=	density
ψ	=	stream function

Subscripts

b	=	body
in	=	inlet
out	=	outlet
o	=	stagnation property
r	=	radial component
z	=	axial component
θ	=	tangential component

Introduction

During the last decade the main emphasis in turbomachinery flow analysis has been on

computational fluid dynamic (CFD) development. This has led to the ability to simulate the three-dimensional flow in multistage machines. However, due to the possibility of including empirical information from extensive data bases, meridional methods, in which axial symmetry is assumed, and blade rows are represented by actuator discs, are still used as preliminary design tools. (Sanger, 1996, Damle *et al.*, 1997). Development of the associated deviation and loss models also continues as presented by Camp and Horlock (1994) and König *et al* (1996a, 1996b). This leaves scope for further investigation into the improvement of meridional methods.

Requirements of a useful meridional method will now be mentioned. The method should be able to handle large changes in radial co-ordinate and flows with high swirl, high throughflow Mach numbers and high pressure ratios. It must allow sloped quasi-orthogonals to be placed on the leading and trailing edges of the blade rows. The method must be easy to programme and the code should be robust and converge quickly, as throughflow methods are often used to generate entire performance maps consisting of many data points. The method must be accurate, showing good agreement with analytical and experimental results.

This paper will attempt to show that the Streamline Throughflow Method (STFM) has the above properties and could thus be considered as a useful alternative to existing meridional methods. An outline of the STFM development and implementation will be given. The performance of the method in simulating compressible and incompressible flows is investigated by comparing STFM flow fields to flow fields obtained with the well known streamline curvature method (SCM). Both STFM and SCM results will be compared to analytical test cases as absolute reference.

STFM Development

The most popular meridional throughflow method, the SCM as described by inter alia Smith (1966) and Novak (1967), is used in many commercial and in-house codes. The main advantages of the method, as stated by Davis and Millar (1975) are the small computer memory requirements and that it is streamline based: in general properties are determined by the actual flow path or conserved along streamlines as in inviscid flow. The use of streamlines also leads to easy interpretation of computational results without interpolation. The SCM suffers from two inherent disadvantages: firstly, mass conservation must be enforced in a separate loop, since it solves a radial momentum equation, and secondly, the results are dependent on the curve fit used for the streamlines. As a curve is fitted to each streamline independently, there is no guarantee that the chosen curve fit represents the flow accurately between the quasi- orthogonals, and uneven spacing of quasi-orthogonals may even cause computational instability.

Another throughflow method is the Matrix Throughflow Method (MTFM), also investigated by Davis and Millar (1975). It solves the tangential vorticity equation expressed in terms of the stream function as an independent variable on a fixed irregular grid. The method yields values of stream function from which velocities and eventually other variables can be calculated at each grid point. Advantages of the method are the use of standard CFD discretization schemes and solution methods, and its inherent stability, as it is solved as an elliptic Poisson equation of the form:

$$\frac{\partial^2\psi}{\partial z^2}+\frac{\partial^2\psi}{\partial r^2}=\frac{1}{r}\frac{\partial\psi}{\partial r}+S \qquad (1)$$

Consideration of the SCM and the MTFM has led to the question of whether the use of streamlines could be combined with a CFD type approach. Boadway (1976) presented such a method for general irrotational (non turbo-machinery) flows. The transformed tangential vorticity equation, with S = 0, has co-ordinate r exchanged for ψ and dependent variable ψ for r, giving:

$$\left(\frac{\partial r}{\partial \psi}\right)^2\frac{\partial^2 r}{\partial z^2}+\left(1+\left(\frac{\partial r}{\partial z}\right)^2\right)\frac{\partial^2 r}{\partial \psi^2}= -\frac{1}{r}\left(\frac{\partial r}{\partial \psi}\right)^2+2\frac{\partial r}{\partial z}\frac{\partial r}{\partial \psi}\frac{\partial^2 r}{\partial z\partial \psi} \qquad (2)$$

This is called the expanded formulation because the first term on the right hand side (RHS) is not absorbed in the LHS, as in the compact formulation to be discussed later.

Turbomachinery Throughflow Equations

Hirsch and Warzee (1976) derived the general turbomachinery throughflow equation for inviscid compressible flow:

$$\frac{\partial}{\partial z}\left(\frac{1}{\rho rb}\frac{\partial \psi}{\partial z}\right)+\frac{\partial}{\partial r}\left(\frac{1}{\rho rb}\frac{\partial \psi}{\partial r}\right)=$$
$$\frac{1}{W_z}\left[\frac{\partial I}{\partial r}-T\frac{\partial s}{\partial r}-\frac{F_{b,r}}{\rho}-\frac{W_\theta}{r}\frac{\partial}{\partial r}(rC_\theta)\right] \qquad (3)$$

$$\text{where } \frac{\partial \psi}{\partial r}=\rho rbW_z, \text{ and } \frac{\partial \psi}{\partial z}=-\rho rbW_r. \qquad (4)$$

The formulation of the equation given by Davis and Millar (1975) is similar except that on the LHS of the equation only the Laplacian of the streamline radial position is retained, while the terms containing density gradients are included in the RHS source terms.

Equation (3), being formulated in terms of relative velocities and rothalpy, is valid within blade rows and between blade rows. For the sake of simplicity and for the purposes of comparison to analytical solutions certain assumptions will now be made.

Assumptions

1. The radial force term $F_{b,r}$ is negligible.
2. The blade rows are completely represented by actuator discs.
3. Consequently all the flow occurs in blade free space, and the blade blockage factor b is equal to unity (no blockage).
4. As a consequence of point 2 above, the flow field can be solved in the absolute frame of reference. (Relative velocity, W replaced by absolute velocity, C and rothalpy, I by stagnation enthalpy, h_0).
5. Also, gradients with respect to radius in the turbomachinery source term can be replaced with gradients with respect to stream function by using equation (4).

Under these assumptions the turbomachinery equation reduces to the form given by Oates (1988):

$$\frac{\partial}{\partial z}\left(\frac{1}{\rho r}\frac{\partial \psi}{\partial z}\right)+\frac{\partial}{\partial r}\left(\frac{1}{\rho r}\frac{\partial \psi}{\partial r}\right)= \qquad (5)$$
$$\rho r\left[\frac{\partial h_o}{\partial \psi}-T\frac{\partial s}{\partial \psi}-\frac{C_\theta}{r}\frac{\partial}{\partial \psi}(rC_\theta)\right]$$

where

$$\frac{\partial \psi}{\partial r}=\rho rC_z,\ \frac{\partial \psi}{\partial z}=-\rho rC_r \qquad (6)$$

Boadway's (1976) transformation is applied to the LHS, with the equation multiplied by $-\rho r(\partial r/\partial \psi)^3$. The result is the transformed compact formulation of the turbomachinery throughflow equation:

$$\left(1+\left(\frac{\partial r}{\partial z}\right)^2\right)\frac{1}{\rho r}\frac{\partial}{\partial \psi}\left(\rho r\frac{\partial r}{\partial \psi}\right)$$
$$+\left(\frac{\partial r}{\partial z}\right)^2\rho r\frac{\partial}{\partial z}\left(\frac{1}{\rho r}\frac{\partial r}{\partial z}\right)=2\frac{\partial r}{\partial z}\frac{\partial r}{\partial w}\frac{\partial^2 r}{\partial z\partial \psi} \qquad (7)$$
$$-(\rho r)^2\left(\frac{\partial r}{\partial \psi}\right)^3\left[\frac{\partial h_o}{\partial \psi}-T\frac{\partial s}{\partial \psi}-\frac{C_\theta}{r}\frac{\partial (rC_\theta)}{\partial \psi}\right]$$

The STFM solves this equation for r in a field with z and ψ as co-ordinates. Oates *et al.* (1976) solved an equivalent but more complicated equation by means of a finite element method. The question of compatibility of the flow fields on opposite sides of an actuator disc was addressed by them and also by Von Backström and Roos (1993).

The method described is called the streamline throughflow method since it resembles the streamline curvature method in having streamline position as the dependent variable, but is based on the same turbomachinery throughflow equation as the matrix throughflow method.

Discretization and Solution.

The equation is discretized using a non-uniform grid spacing which allows a fine grid to be used in regions of extreme velocity gradients and coarse grids in areas of small gradients. The discretized equation is solved using a Gauss-Seidel method using relaxation factors between 0.9 and 1.8, the finer the grid the smaller the relaxation factor required. The code was written in FORTRAN and run on a Pentium 75 personal computer. The convergence criteria was that the absolute streamlines shift should be less than 1e-5 between iterations (for 1 m maximum streamline radius).

For compressible flows the density of the fluid is influenced by the pressure and temperature. In the isentropic flow between the actuator discs, however, the density can be directly calculated from the velocity, by employing the stagnation speed of sound. The local speed of sound is not used because it is not constant between actuator discs.

$$\rho = \rho_o \left[1 - \frac{\gamma - 1}{2} \left(\frac{C_\theta^2 + C_z^2 + C_r^2}{a_o^2} \right) \right]^{\frac{1}{\gamma - 1}} \qquad (8)$$

$$a_o^2 = \gamma R T_o$$

The method has been extended to handle sloped stations through a scheme described by Harms *et al.*(1996). This allows a local rectangular grid to be used around each point with the neighbouring values being calculated using linear interpolation.

Description of comparative SCM code

The study required a SCM code for comparative purposes. The comparative SCM code was based on the paper of Novak (1967) as implemented in the masters degree thesis of Heyns (1982). It has options to use either cubic spline curve fits or to directly discretize the gradients and curvatures in the method. There was little difference in the convergence times achieved by the two options. The first, more typical SCM type approach was used.

Test Cases

A series of test cases, starting with simple ones, systematically introduces the various requirements and phenomena to be modelled. To eliminate experimental error, test cases with analytical solutions are selected. The exclusion of blade cascade models, boundary layer blockage, mixing, bleed flows etc focuses attention on the essential problem of correctly predicting streamline and velocity profile shape. There is however, no reason why these effects cannot be included in the STFM as shown later by the 10 stage compressor simulation.

Incompressible flow

Test case 1. was the simulation of non-swirling incompressible flow through a parallel walled annulus. The expanded formulation based on the method of Boadway (1976) as reported by Von Backström and Roos (1993) was inaccurate near the inner wall. The new, compact formulation completely eliminated this inaccuracy and placed the streamlines at exactly the same radii as the simple analytical solution.

Test case 2. was non-swirling incompressible flow over a sphere. It introduced radial flow and streamline curvature. This test case is useful as the flow is similar to that of the nose bullet on a turbo-machine hub. The classical inviscid solution was used for comparison of results. The test case used a sphere of radius 0.4 m, with the outer annulus shaped to follow the shape of the analytically calculated stream surface with a maximum radius of 1.0 m. A non-uniform grid spacing was used with a finer grid being used in the region of large radial flows as shown in Figure 1.

For both methods the maximum error of 4 % was on the inner streamline near the front of the circle. For the STFM, convergence time was 2 s and for the SCM 40 s. Increasing the number of internal streamlines of the STFM to 31 increased the convergence time to 8 s and reduced the error on the same streamline to 1.7 %.

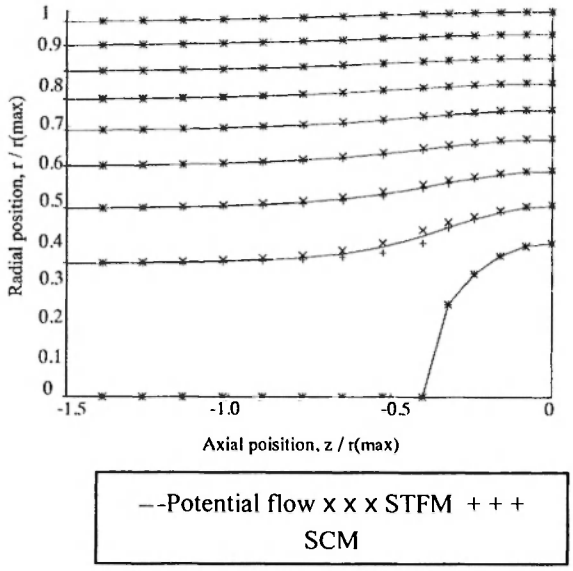

Fig. 1: Streamline positions for flow over a sphere.

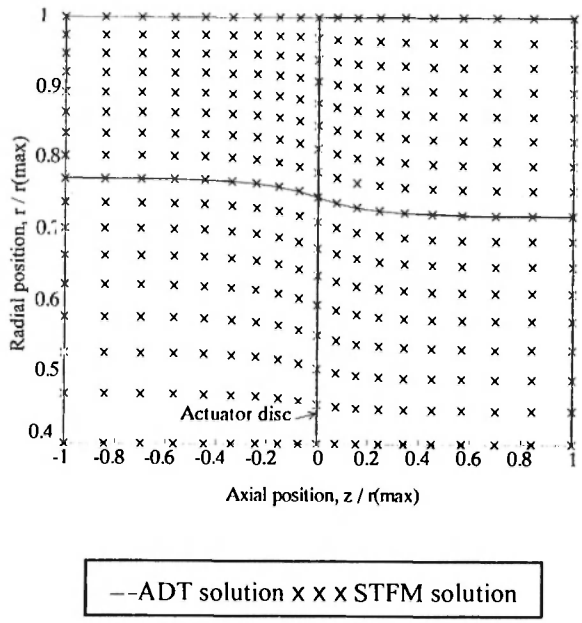

Fig. 2: Incompressible flow through a single actuator disc.

Test case 3. introduced tangential velocities in the simulation of incompressible flow through a single actuator disc in a parallel annulus. The outer diameter was 1 m and the inner 0.4 m with the disc is placed at z = 0. The up and down stream vortex distributions were of the form below, with a = 6.0 s^{-1} and b = 6.0 m^2/s. In all the test cases the tangential velocity at the disc is taken as the average of the upstream and downstream value.

$$C_\theta = ar \pm b / r \qquad (9)$$

The axial velocity at the hub inlet was 10 m/s. Results were compared to the simple actuator disc theory (ADT) as described by Dixon (1978). Figure 2 shows the radial positions of the 7 internal streamlines at each axial station as computed by the STFM, as well as the median internal streamline from the simple ADT solution.

The maximum difference of 0.7 % in median streamline position occurs immediately after the actuator disc. Since simple ADT disregards radial velocities, it is not accurate in the immediate vicinity of the disc, but the general agreement in streamline shape is good. Figure 3 gives an indication of the accuracy of the STFM in predicting velocity profiles in incompressible flows. The test case is similar to

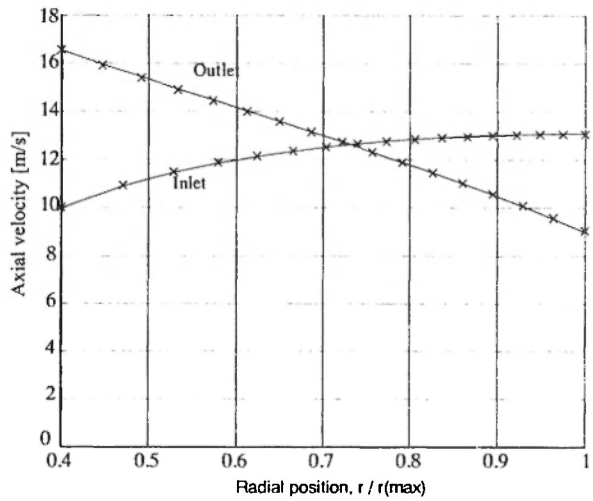

Fig. 3: Inlet and outlet axial velocity profiles of incompressible flow through a single actuator disc.

the previous but there are 15 internal streamlines. The objective in this test case is to predict the far

upstream and downstream velocity profiles where ADT is accurate. The maximum error in inlet velocity far upstream is 0.3 % at the hub and in exit velocity far downstream it is 0.6 % at the casing.

Test case 4. is the same as test case 3 except that a second actuator disc removed the swirl introduced by the first, and the axial velocity at the hub inlet was 5.5 m/s (Dixon, 1978). This test case represents throughflow modelling with one axial station on the blade leading edge and one on the trailing edge. The tangential velocity at the discs is taken as an average of the up and downstream values. There were 7 streamlines and 7 stations in the flow field.

Figure 4 shows only the median streamline as calculated by simple ADT, STFM and SCM. The general impression is that STFM agrees better with the analytical solution. The maximum differences compared to the ADT solution were 0.5 % for STFM between the discs, and 0.6 % for SCM at the discs. STFM took 1 s to converge and SCM took 5 s.

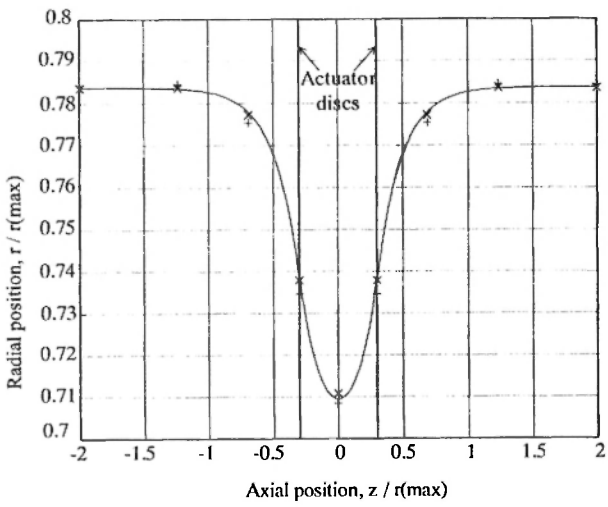

Fig. 4: Median streamline position for twin actuator disc case using coarse axial grid.

Compressible Flow

Test case 5 is compressible non-swirling flow through a nozzle. The nozzle dimensions and fluid properties are given in the following table.

Table 1

Gas constants and nozzle radius at inlet and outlet for compressible flow nozzle.

T_o	300 K	R	287.14 J/kg.K
P_o	600 kPa	c_p	1005 J/kg.K
ρ_o	6.965 kg/m^3	Mass flow	274.5 kg/s
r_{in}	1 m	r_{out}	0.25 m

The nozzle area decreases by a factor of 1/16 starting at z = 3 m. The radius varies according to a cosine function over a length equal to 2.5 upstream diameters. A comparison of selected variables of the STFM and one dimensional solution far downstream is shown in Table 2.

Table 2

Comparison of STFM and 1 dimensional analysis of compressible flow nozzle.

Outlet	STFM	1-D analysis	error
$C_{z\ out}$	306.7202 m/s	306.7152 m/s	0.002 %
ρ_{out}	4.55780 kg/m^3	4.55787 kg/m3	0.002 %
M_{out}	0.96140	0.96138	0.002 %

The STFM results for this test case agree extremely well with the one dimensional solution. Figure 5 shows that the highest velocity in the nozzle is just below sonic The results prove the method to be reliable for non-swirling flow up to just below Mach 1.0, but the present discretisation cannot handle supersonic throughflow velocities. Computation time was 16 s.

Test case 6. is a compressible flow through an inlet guide vane represented by an actuator disc. The flow upstream of the actuator disc has no tangential velocity, while downstream the following distribution was assumed with the tangential Mach number at mid radius being sonic,

$$C_\theta = b / r \qquad (10)$$

Although the throughflow velocity in this test case is always less than Mach 1 there are regions of

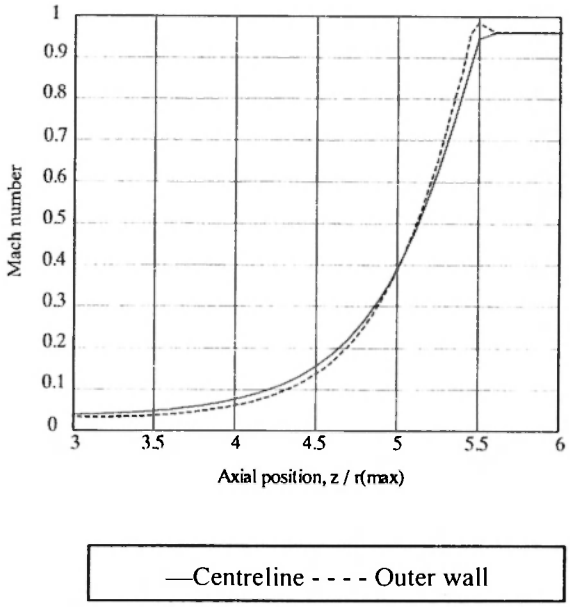

Fig. 5: Compressible flow through a nozzle.

sub, trans and supersonic flow. It is interesting to note that had the flow been incompressible in this test case, no streamline shift would have occurred through the disc, due to the free vortex distribution of the swirl . The shift is entirely due to changes in density, making this a good test case for investigating the effect of compressibility in the method. The problem simulated was the same as that used by Horlock (1978) with the inlet properties and geometry listed in Table 3. There were 15 internal streamlines and 51 axial stations in the STFM model.

Table 3
Constants used for compressible flow through an actuator disc.

T_o	273 K	R	287 J/kg.K
P_o	98 490 Pa	c_p	1004 J/kg.K
$C_{z\,in}$	60 m/s	b	281.5 m^2/s
hub-tip ratio	0.7	Disc co-ordinate	0
Outer radius	1 m	Mean radius tangential Mach number	1.0

Figure 6 shows the variation in axial velocity along the hub and casing (tip) and along the median streamline compared to the analytical solution of Horlock (1978). The STFM predicts a 3.2 % higher velocity at the hub just upstream of the disc when compared to the Horlock (1978) solution that assumes radial velocities to be zero. Using the same grid, the SCM solution was almost identical, predicting a 2.9 % higher velocity. The convergence time using the STFM, however, was 16 seconds, using a relaxation factor of 1.6, while the SCM relaxation factor had to be reduced to 0.002 to obtain convergence to 1×10^{-5}, and consequently took much longer to converge.

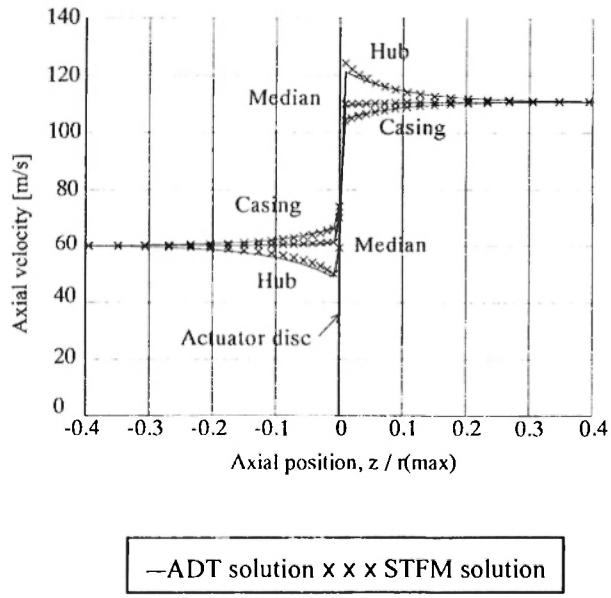

Fig. 6: Axial velocities for compressible flow through a single actuator disc.

Test case 7. simulates compressible flow through a nozzle guide vane and turbine blade row using two actuator discs. This is an extension of test case 6, with the second actuator disc at one third of the blade span downstream. Across the second (turbine) disc the flow is turned back to the axial direction with a stagnation temperature drop of 49 K. Figure 7. shows STFM and SCM solutions, for 15 internal streamlines and 96 axial stations, superimposed on a compressible simple ADT solution given by Hawthorne and Ringrose (1963-4).

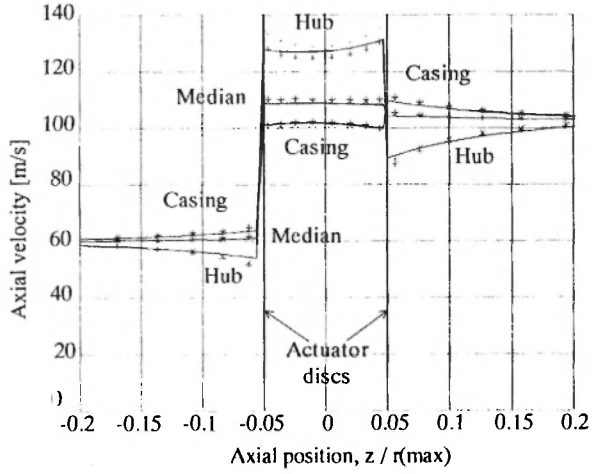

Fig. 7: Axial velocities for compressible flow through twin actuator discs.

Table 4 shows velocity differences compared to ADT theory for STFM and SCM. It is worth noting that the differences between STFM and SCM are typically 2 % but when both methods are compared to ADT the differences are about 4 %. STFM converged to 1.0e-5 in 26 s with a relaxation factor of 1.8, while SCM converged to 7.0e-5 in 10 000 iterations in 3 hours using a relaxation factor of 0.00005.

Table 4
Percentage difference in axial velocity compared to ADT

Position ⇓ Method ⇒	STFM	SCM
Upstream of disc 1	-4.5	-6.5
Downstream of disc 2	4.6	3.0
Upstream of disc 2	4.5	3.5
Downstream of disc 2	-1.5	-3.9

Test case 8 investigates the effects of sloping the axial stations on the performance of the STFM for swirling flow through an expanding annulus as shown in Figure 8. The grid geometry of the reference case consisted of 19 evenly spaced internal axial stations. The geometry and streamline positions of the simulation with sloped stations are superimposed in the figure. There is no discernible difference in streamline position. The sloped station solution required 16 iterations for convergence compared to 14 for the vertical stations.

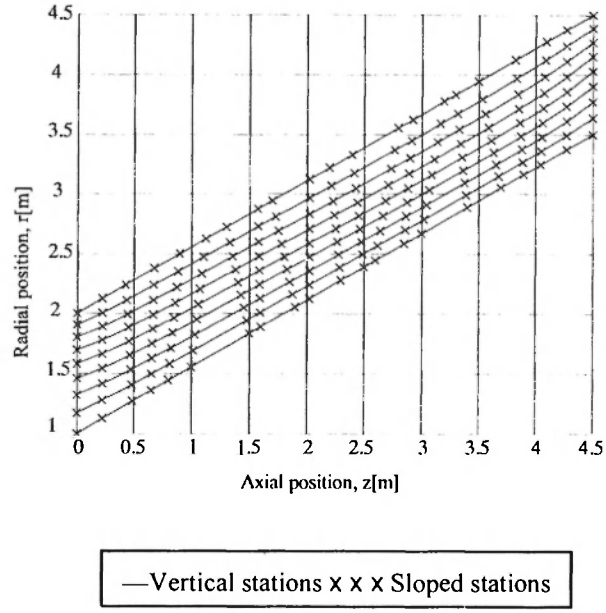

Fig. 8: Swirling flow comparing results from vertical and sloped stations

Compressor Simulation

For a numerical method to be useful it must be able to be applied in practice. For this Howell's (1942, 1945) correlation for loss and deviation were used with the STFM to simulate a repeating 10 stage (21 blade row) process gas axial compressor. Experimental results for air pumped at scaled conditions were available and these were compared to the STFM results. The design pressure ratio for these conditions was 1.3 with a density ratio of 1.21. The inlet casing and hub diameters were 0.246 m and 0.16 m respectively with an operating speed of 4350 rpm. The inlet casing and hub solidities were 1.1636 and 0.7630 respectively.

The grid used for the simulation consisted of three axial stations ahead of the inlet guide vanes and three after the outlet. One axial station was placed at the leading and trailing edge of each blade row while

11 internal streamlines were used. This reasonably coarse grid is similar to that used in many SCM applications. A typical STFM simulation took 45 seconds. The performance map shown in Figure 9 has three curves corresponding to different stagger blade angles as indicated. The experimental results are superimposed over the numerical simulation. There is good agreement between the experimental and numerical results on flow resistance lines through and below the design point but the predicted curves tend to be steeper than the experimental results at higher pressure ratios. The likely cause of these deviations is the simple boundary layer blockage model employed. It is one suggested by Cumpsty (1989, p80) who gives as rule of thumb for design point calculations a blockage increase of 0.5 % per blade row up to a maximum of 4 %.

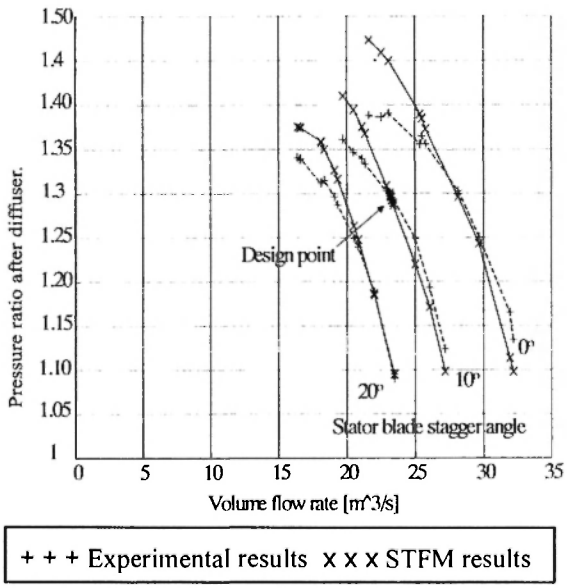

Fig. 9: Comparison of numerical and experimental results for multistage compressor.

Conclusion

Compared to analytical solutions the accuracy of the STFM for the same number of streamlines was similar to the SCM. The STFM, however, used an order of magnitude less computer time to converge to the same criterion because its stream function formulation automatically satisfied mass conservation and did not need a separate mass conservation loop. STFM was also highly tolerant of high aspect ratio grid cells, as it did not require a separate curve fit procedure to calculate streamline gradient and curvature. The more robust STFM would converge with typical over-relaxation factors of up to 1.5 compared to between 0.00005 and 0.2 for the SCM. for the more complex problems the STFM convergence times were orders of magnitude less than for SCM. Similar results were found by Davis and Millar (1975) in their comparison of the matrix throughflow method and the SCM.

The test cases show that the STFM is suitable for annuli with large variations in hub and tip radius, for highly swirling and compressible flow. The ability of the STFM to be practically implemented has also been demonstrated. The discretisation method used at present cannot handle supersonic throughflow.

References

Boadway, J.D., 1976, "Transformation of elliptic partial differential equations for solving two-dimensional boundary value problems in fluid flow," *International Journal for Numerical Methods in Engineering*, Vol. 10, pp. 527-533.

Camp, J.R., and Horlock, J.H., 1994, "An analytical Model of Axial Compressor Off-design Performance," Vol. 116, pp 425-434.

Cumpsty, N.A., 1989, "Compressor Aerodynamics," Longman Scientific and Technical, Harlow.

Damle, S.V., Dang, T.Q. and Reddy, D.R., 1997, "Throughflow Method for Turbomachines Applicable for All Flow Regimes," *Transactions of the ASME Journal of Turbomachinery*, pp. 256-262.

Davis, W.R. and Millar, D.A.J., 1975, "A comparison of the Matrix and Streamline Curvature Methods of Axial Flow Turbomachinery Analysis, From a User's Point of View," *Transactions of the ASME Journal Engineering for Power*, pp. 549-560.

Dixon, S.L., 1978, "*Fluid Mechanics, Thermodynamics of Turbomachinery*," Third Edition, Pergamon Press, pp 174-180.

Harms, T.M., von Backström, T.W. and du Plessis, J.P., 1996, "Simplified Control-Volume Finite-Element Method," *Numerical Heat Transfer*, Part B, 30: pp 179-194.

Hawthorne, W.R. and Ringrose, J., 1963-4, "Actuator Disc Theory of the Compressible Flow in Free-Vortex Turbo-Machinery," *Proc. Inst. Mech. Eng.*, Vol 178, Pt 3I(ii), pp 1-13.

Heyns, P.S., 1982, "*An investigation of a Turbine for a Low-Cost Turbojet Engine*," M.Eng Thesis, University of Pretoria, Pretoria, South Africa.

Hirsch, C. and Warzee, G., Sept. 1976, "A finite element method for through flow calculations in turbomachines," ASME Journal of Fluids Engineering, pp403-421.

Horlock, J.H., 1978, "*Actuator Disk Theory Discontinuities in Thermo-Fluid Dynamics*," McGraw-Hill, U.K., pp 143-148.

Howell, A.R., 1942, 'The Present Basis of Axial Flow Compressor Design: Part 1 - Cascade Theory and Performance', *Aeronautical Research Council Reports and Memoranda No. 2095*.

Howell, A.R., 1945, "Design of Axial Compressors", *Proceedings of the Institution of Mechanical Engineers*, London, Vol 153.

Howell, A.R., 1945, 'Fluid Dynamics of Axial Compressors', *Proceedings of the Institution of Mechanical Engineers*, London, Vol 153.

König, W.M., Hennecke, D.K., and Fottner, L., 1996, "Improved Blade Profile Loss and Deviation Angle Model for Advanced Transonic Compressor Bladings: Part I - A Model for Subsonic Flow. Part II - A Model for Supersonic Flow," ASME Journal of Turbomachinery, Vol 118, pp 73-87.

Novak, R.A., October 1967, "Streamline Curvature Computing Procedures for Fluid-Flow Problems," *Transactions of the ASME, Journal of Engineering for Power*, Vol 89 No 4, pp. 478-490.

Oates, G.C., Knight, C.J. and Carey, G.F., January 1976, "A Variational Formulation of the Compressible Throughflow Problem," *Transactions of the ASME, Journal of Engineering for Power*, pp. 1-8

Oates, G.C., 1988, "*Aerothermodynamics of Gas Turbine and Rocket Propulsion*," Revised and Enlarged, 2nd Edition, AAIA Education Series, New York.

Sanger, N.L., 1996, "Design of a Low Aspect Transonic Compressor Stage Using CFD Techniques," *ASME Journal of Turbomachinery*, Vol. 118, pp. 479-491.

Smith, L.H. JR., 1966, "The Radial-Equilibrium Equation of Turbomachinery," *Transactions of the ASME Journal Engineering for Power*, pp. 1-12.

Von Backström, T. W. and Roos, T.H., September 1993, "The Streamline Throughflow Method for Axial Turbomachinery Flow Analysis," *Presented at ISABE XI*, Tokyo, Japan.

Eng. Opt., 1993, Vol. 22, pp. 19-26
Reprints available directly from the publisher
Photocopying permitted by license only

HEURISTIC METHODS FOR ARRANGING BLADES TO MINIMIZE ROTOR UNBALANCE

M. SINCLAIR*, T. W. VON BACKSTRÖM** and J. J. DU BUISSON**

**Department of Industrial Engineering*
***Department of Mechanical Engineering*
University of Stellenbosch, 7600 Stellenbosch, South Africa

(Received September 7, 1993)

Rotor unbalance in turbomachinery is minimized by allocating rotor blades to specific circumferential positions on the disk or drum according to some fixed allocation scheme. In this paper implementations of various combinatorial optimization heuristics for the rotor unbalance problem are discussed. Their performances in terms of computer time and quality of solution are compared. Real data are used for the comparison. Conclusions are drawn on the method most likely to produce a good solution in practice.

KEY WORDS: rotor balance, combinatorial optimization, heuristics

1 INTRODUCTION

Rotors for turbomachinery consist of essentially a drum with a set of blades fixed to its circumference. These rotors should be well balanced to ensure smooth operation and long life. For the purposes of balancing, a given set of rotor blades may be regarded as a set of balancing weights which must be allocated correctly to a set of rotor blade row positions to effect the minimum rotor unbalance. Since all the unbalance forces exerted by the members of a blade row are confined to a narrow axial region compared to the rotor length, only static unbalance is considered.

The centrifugal force exerted by a blade on a rotor is proportional to the blade mass, the radial position of the blade centre of gravity, and the square of its angular velocity. Any deviation from the mean of either the mass of the blade, or the radial position of the blade centre of gravity when installed will statically unbalance the system. The radial position of the blade centre of gravity is determined by the position of the centre of gravity relative to a reference surface on the blade root and by the radial position of the mating surface in the rotor. As is commonly done in industry, the radial positions of the blade centre of gravity will be assumed to be equal for all blades in all positions. The problem then reduces to balancing a rotor by assigning a set of given balancing weights to a set of circumferentially equally spaced constant radius positions.

The present work was initiated when it was found that the residual unbalance caused by 43 blades weighing approximately 284 g each on a particular rotor disk of 80 Kg could not be reduced below the G2.5 ISO Standard[1] of 5 g mm/kg for turbocompressors.

Traditional methods balance the set of blades by allocating blades of more or less

equal mass to opposite rotor positions, and by alternating light and heavy blades, using a fixed pattern. They rely on the following implicit assumptions:

- blade mass distributions are symmetrical.
- the shape of the distribution is not important.
- unbalance must be measured, not calculated.
- there is only one best allocation pattern for all sets.

The problem of balancing the runners of a hydraulic turbine was first discussed as a combinatorial optimization problem by Mosevich[2]. He used a Monte Carlo approach to reduce the unbalance for Francis turbine blades. Later Laporte and Mercure[3] improved on Mosevich's results by using heuristics designed for the quadratic assignment problem (QAP). This paper presents the results of computational experiments with heuristic solution methods for the QAP formulation of the balancing problem. Real data will be used for the comparison of the performance of these heuristics. The aim is to identify the best approach for the problem from a practical point of view.

The following heuristic methods from the operations research literature were considered in our study: Simulated annealing[4], Genetic Algorithms[5], Tabu Search[6], Great Deluge Algorithms and Record-to-Record Travel[7]. Implementations of these heuristics will be compared to the heuristic in Laporte and Mercure[3], as well as an exchange heuristic developed locally.

The paper will be organized as follows: Section two will present the mathematical formulation of the problem, as well as existing methods for its solution. The heuristic approaches mentioned above will be discussed in section three. Most of them are the subject of extensive reviews in the literature and will be discussed in less detail than the others. Section three will also present the specific computer implementations of these heuristics for the rotor balancing problem. Section four will be devoted to a discussion of the methodology for the computational experimentation. This section will also present the computational results, together with the conclusions drawn from the results. The final section will contain a summary and conclusions.

2 MATHEMATICAL FORMULATION AND PUBLISHED SOLUTION METHODS

The problem of balancing a turbine rotor can be formulated as a discrete combinatorial optimization problem. We use the following notations[3]:

n: the number of blades;

M_i: the mass of blade i;

$\Theta_j = 2\pi(j-1)/n$, $j = 1, \ldots n$: the angles at which blades are positioned;

x_{ij}: a binary variable equal to 1 if and only if blade i is positioned at angle Θ_j;

The resulting formulation is as follows:

(P) Minimize $\Sigma_i \Sigma_j \Sigma_k \Sigma_l \; M_i M_k \cos(\Theta_j - \Theta_l) x_{ij} x_{kl}$

subject to:

$$\sum_i x_{ij} = 1 \qquad j = 1, \ldots n$$

$$\sum_j x_{ij} = 1 \qquad i = 1, \ldots n$$

$$x_{ij} = 0 \quad \text{or} \quad 1 \qquad i, j = 1 \ldots n$$

Problem (P) is a special case of the quadratic assignment problem (QAP) where, if the binary constraints are ignored, the objective function is convex. For the purposes of this paper (P) will be considered to be a QAP.

It is well known that QAP's are NP complete[8] and thus heuristics are the only feasible approaches for solving such problems in practice. The best published algorithm[3] for (P) is a three stage insertion heuristic. In this paper various other heuristics from the literature, as well as a locally developed method, will be compared to this heuristic.

The merits of using real world data for computational comparisons are debated extensively in the literature. Section four will discuss this question among others.

3 THE HEURISTIC METHODS

The heuristic methods mentioned in the introduction were all implemented in the manner described in a separate study[19], except the locally developed one. Therefore this section will discuss in detail only the locally developed method and its implementation.

Since good results were reported for the insertion heuristic for the balancing problem[3], it was felt that another standard heuristic approach to assignment type problems should also be evaluated. We refer to the exchange approach, where an initial solution is manipulated by exchanging items and keeping track of the best solution[14].

The exchange heuristic implemented in the end resulted through the evaluation of various combinations of exchange procedures. The best exchange heuristic was found to be the following three stage procedure (n = number of blades):

1. Pack the blades in order of decreasing mass into the available positions.
2. Start at the first position. Exchange two adjacent blades. If the unbalance decreases, keep the blades in this order. Otherwise, return the blades to the previous order. Continue with the next pair. Repeat the procedure until no improvement is achieved for n consecutive exchanges.
3. Start at the first position. Exchange the blade with the one two positions from it (i.e. skip one position). If the unbalance decreases, keep the blades in this order. Otherwise, return the blades to the previous order. Continue with the next blade. Repeat the procedure until no improvement is achieved for n consecutive exchanges.

4. Start with the blade in the first position. Consider four adjacent blades (numbered 1, 2, 3 and 4). Exchange numbers 1 and 2, as well as numbers 3 and 4. If the unbalance decreases, keep the blades in this order. Otherwise, return the blades to the previous order. Continue with the next group of four positions, with the new number one the same as the previous number 2. Repeat the procedure until no improvement is achieved for n consecutive exchanges.

It was found that this method performed about four orders of magnitude better than the traditional methods. Furthermore, the results obtained were also much more consistent that those for the traditional methods.

4 COMPUTATIONAL EXPERIMENTS

The methodology for the experimental evaluation of optimization algorithms for a specific problem usually follows the following steps:

1. Data for different instances of the problem are collected. For instance, different distance matrices for the TSP are generated. The data may have specific properties, e.g. sparsity, symmetries, etc.
2. The algorithms are applied to the different data sets.
3. Conclusions are drawn from the results.

Whereas it is common to use randomly generated data in step 1, this study will use real world examples. The merits of such an approach have been debated extensively in the literature[5, 15, 16, 17]. The common wisdom seems to be that final claims about the superiority of proposed algorithms can be settled only after sufficient experience with real life situations. It is, however, questionable to make generalizations on the strength of such experimentation, since the real world examples represent only a sample from a certain population. If the sample is large enough, conclusions about the population (in this case all problems with the structure of (P)) are statistically valid, but not necessarily conclusions about another population. Since the aim of this study was to provide insight into the relative performance of the methods under consideration for the rotor balancing problem only, it was decided to go ahead with computational experiments using thirty six real world examples of (P).

The following steps were taken to ensure that side issues did not interfere with the validity of the conclusions of the experiments:

1. During step 2 the same data structures and input/output procedures were used for all heuristics. The construction of the initial solution (where applicable) involved the packing of the blades on the runner in order of decreasing mass. The underlying improvement procedure in all cases but the genetic algorithm made use of the pairwise exchange method commonly used for assignment type problems.
2. The implementation of all heuristics involved various choices of parameters and procedures. An effort was made to choose parameters to ensure that the

different heuristics performed as well as possible in both the performance measures.

3. Programming for all heuristics was done in Turbo Pascal 4.0 by the same programmer.
4. The experiments were run on the same IBM compatible microcomputer with an 80386 processor, under MS DOS 4.0.

Final objective function value and CPU time were chosen as the two performance measures most likely to be of interest in practice. Since some of the algorithms are non-deterministic in the sense that they will not always give the same result for the

Table 1 Computational results: Objective function values in g-cm^2 $\times$ 10^3.

Problem	*QAP*	*S.A.**	*GDA**	*RTR**	*TABU*	*GENETIC**	*EXCHANGE*
1	6.610	6.600	1.928	4.062	0.565	64.442	2.334
2	3.984	8.220	3.105	6.370	1.274	94.117	1.910
3	2.822	5.506	1.210	2.294	1.239	72.527	1.377
4	1.367	7.030	2.517	5.450	1.482	106.946	1.695
5	13.972	5.558	1.546	3.028	0.954	93.457	0.528
6	6.023	3.164	1.069	2.278	1.893	64.561	6.743
7	17.050	5.272	1.710	3.941	1.120	62.981	0.612
8	2.505	12.952	2.280	4.457	2.153	106.731	9.733
9	2.657	6.046	2.622	5.641	0.969	111.781	2.620
10	27.882	6.928	3.081	6.842	1.400	121.918	1.494
11	15.584	14.136	3.717	7.615	2.299	121.314	3.499
12	8.321	7.516	3.161	6.260	0.464	99.263	2.957
13	7.750	5.470	2.644	5.652	1.648	112.972	0.700
14	2.824	5.131	1.599	2.547	0.696	58.937	2.288
15	5.472	6.915	3.045	7.103	0.876	78.897	2.106
16	27.166	16.228	2.720	4.635	3.012	151.749	1.055
17	10.361	7.303	3.201	5.922	1.582	118.318	1.134
18	14.796	6.483	3.209	7.352	3.865	91.440	1.311
19	9.500	4.786	1.841	3.382	1.095	78.280	0.541
20	4.493	6.865	1.451	3.114	2.357	72.259	2.577
21	9.365	7.044	2.533	4.907	2.212	114.516	6.164
22	5.938	6.448	2.764	6.131	1.324	71.242	9.262
23	25.143	11.268	4.354	7.840	2.669	175.246	0.179
24	13.351	6.544	3.178	6.642	0.736	85.251	1.052
25	1.503	7.548	2.930	6.439	1.465	94.770	4.181
26	21.938	9.229	2.708	5.210	3.669	112.154	4.946
27	10.247	4.124	1.646	3.226	1.313	99.995	1.613
28	6.797	11.445	6.576	12.988	3.417	185.931	6.491
29	14.026	12.963	6.054	12.323	2.387	186.075	1.308
30	6.936	6.430	2.606	5.340	1.400	88.306	1.435
31	10.091	19.507	3.415	6.260	4.376	184.643	11.712
32	38.964	15.878	6.442	12.609	3.326	177.583	4.327
33	35.399	8.931	2.401	4.809	1.654	124.313	3.308
34	22.814	9.345	2.355	4.008	1.489	149.786	2.532
35	5.125	10.614	5.210	10.206	0.116	195.046	5.243
36	19.682	13.363	3.954	8.388	0.260	159.655	4.615
MEAN	12.105	8.578	2.966	5.980	1.743	113.539	3.211
STANDARD DEVIATION	9.497	3.741	1.335	2.678	1.034	39.717	2.750

*Average of 100 runs

Table 2 Computational results: Computer run times in CPU seconds.

DEVIATION	*QAP*	*S.A.**	*GDA**	*RTR**	*TABU*	*GENETIC**	*EXCHANGE*
1	22	182	83	13	201	283	4
2	25	181	77	13	200	256	5
3	33	93	105	25	201	271	4
4	28	200	83	13	200	275	5
5	21	195	99	16	199	266	5
6	30	233	101	21	200	234	5
7	22	204	87	14	199	319	5
8	26	162	93	16	200	269	5
9	30	223	89	15	200	225	5
10	23	206	87	13	200	262	5
11	24	168	82	13	200	278	4
12	20	212	82	13	200	255	5
13	30	219	83	13	200	212	5
14	28	203	93	20	201	299	4
15	31	193	75	11	200	251	5
16	24	173	101	18	199	279	5
17	29	220	82	13	201	256	5
18	31	212	84	13	200	291	5
19	22	219	84	14	199	258	5
20	33	206	90	16	200	274	5
21	27	204	92	18	199	294	5
22	26	198	75	12	200	272	5
23	21	203	88	13	200	283	5
24	28	200	80	12	200	248	5
25	23	189	80	12	200	270	4
26	26	194	90	15	200	242	5
27	28	231	90	15	200	265	5
28	24	216	79	14	200	263	4
29	24	193	84	14	200	238	5
30	26	201	84	15	200	295	5
31	33	171	91	14	200	327	5
32	30	185	94	22	200	233	4
33	21	206	101	19	200	259	5
34	30	209	95	17	200	246	5
35	34	206	87	14	200	241	5
36	30	186	83	14	200	288	5
MEAN	26.8	197.1	87.6	15.1	200	266	4.8
STANDARD DEVIATION	3.9	24.2	7.5	3.1	0.5	24.5	0.4

*Average of 100 runs

same problem, these algorithms were each run 100 times for each problem, with the average results reported in Tables 1 and 2.

The results in these two tables indicate that the simple genetic algorithm implemented in the present study is not competitive for the problem (P). The genetic algorithm provides the worst function values, as well as relatively long processing times. In order to make this algorithm more competitive, the main area of further research would be to find a better crossover operator[5].

The first two columns of Table 1 and the first two columns of Table 2 support the following claim in Aarts and Korst[18]: "For a large class of basic problems, including the ... quadratic assignment ... problems, the simulated annealing

algorithm finds solutions with an error comparable to the error of tailored approximation algorithms but at the cost of much larger running times."

As far as quality of solution is concerned, Table 1 shows that tabu search finds the best results in 21 out of the 36 cases.

The only serious challengers to tabu search are the exchange algorithm with 9 best results and GDA with 4 best results. However, the latter two algorithms find their solutions much more quickly (Table 2) than tabu search. For someone for whom quality of solution is of paramount importance, tabu search presents the best option, especially since more long term memory passes could improve the solution even more. Some limited further experimentation confirmed this conjecture.

However, for ease of implementation and speed of execution, together with reasonable quality of solution (certainly better than QAP, the best published algorithm for (P)), the best candidates are obviously the exchange algorithm and GDA. Both give consistently good objective function values. Both also solve the problems quickly, with the exchange algorithm invariably better than GDA in this department. Given the ease of implementation of the exchange algorithm (e.g. no parameters to be fine tuned), the fact that it is a deterministic algorithm and its superior execution speed, it must be the choice for ordinary practical circumstances.

5 SUMMARY AND CONCLUSIONS

Thirty six sets of real data for the rotor balancing problem were used to compare the performance of a collection of recent heuristic algorithms for the problem. These heuristics are: an insertion algorithm, Simulated Annealing, a Genetic algorithm, Tabu Search, the Great Deluge algorithm, the Record-to-Record Travel algorithm and an exchange algorithm.

Details are given of the specific implementations of each of these methods for the problem under discussion. Computational results are presented. The conclusions which can be drawn from these result can be summarized as follows:

1. A simple Genetic algorithm does not perform well on the problem.
2. Simulated Annealing is competitive with existing algorithms for the problem as far as solution quality is concerned, but not as far as solution time is concerned.
3. Tabu Search provides the best solutions, but at the cost of long solution times.
4. On a balance of ease of implementation, solution quality and solution times, the exchange algorithm and the Great Deluge algorithm perform most satisfactorily, with the exchange algorithm superior on balance.

References

1. Schneider, H. (1977) Balancing technology. Translation of *VDI-Taschenbücher T29 Auswuchtechnik*, Carl Schenk Ag.
2. Mosevich, J.(1986) Balancing hydraulic turbine runners–A discrete combinatorial optimization problem. *European J. of Operational Research*, **26**, 202–204.

3. Laporte, G. and Mercure, H. (1988) Balancing hydraulic turbine runners. *European J. of Operational Research*, **35**, 378–381.
4. Collins, N.E., Eglese, R.W. and Golden, B.L. (1988) Simulated annealing–An annotated bibliography. *American J. of Mathematical and Management Sciences*, **8**, 209–307.
5. Liepins, G. E. and Hilliard, M. R. (1989) Genetic algorithms: Foundations and applications. *Annals of Operations Research*, **21**, 31–58.
6. Glover, F. (1990) Tabu search: A tutorial. *Interfaces*, **20**, 74–94.
7. Dueck, G. (1989) New optimization heuristics: The Great Deluge algorithm and the Record-to-Record Travel. *Heidelberg Scientific Center Research Report*, TR89.06.011, IBM Germany.
8. Garey, M. R. and Johnson, D. S. (1979) *Computers and Intractability: A Guide to the Theory of NP-Completeness*. Freeman.
9. Wilhelm, M. R. and Ward, T. L. (1987) Solving quadratic assignment problems by simulated annealing. *IIE Transactions*, **19**, 107–119.
10. Skorin-Kapov, J. (1990) Tabu search applied to the quadratic assignment problem. *ORSA J. on Computing*, **2** 33–45.
11. Goldberg, D. E. (1989) *Genetic Algorithms in Search, Optimization, and Machine Learning*. Addison-Wesley, Reading, Mass.
12. Liepins, G. E., Hilliard, M. R., Richardson, J. and Palmer, M. (1990) Genetic algorithms applications to set covering and traveling salesman problems. In D. E. Brown and C. C. White, eds., *Operations Research and Artificial Intelligence: The Integration of Problem-Solving Strategies*, Kluwer Academic Publishers, Boston, 29–57.
13. Smith, D. (1985) Bin packing with adaptive search. In J. J. Grefenstette, ed., *Proceedings of an International Conference on Genetic Algorithms and Their Applications*, Lawrence Erlbaum Associates, 202–207.
14. Zanakis, S. H., Evans, J. R. and Vazacopoulos, A. A. (1989) Heuristic methods and applications: A categorized survey. *European J. of Operational Research*, **43**, 88–110.
15. Amar, A. D. and Gupta, J. N. D. (1986) Simulated versus real life data in testing the efficiency of scheduling algorithms. *IIE Transactions*, **18**, 16–25.
16. Golden, B. L., Assad, A. A., Wasil, E. A. and Baker, E. (1986) Experimentation in optimization. *European J. of Operational Research*, 27, 1–16.
17. Rardin, R. L. and Lin, B. W. (1982) Test problems for computational experiments–issues and techniques. In J. M. Mulvey, ed., *Evaluating Mathematical Programming Techniques*, Springer-Verlag, Berlin.
18. Aarts, E. and Korst, J. (1989) *Simulated Annealing and Boltzmann Machines*. John Wiley and Sons, Chichester, 93.
19. Sinclair, M. (1993) Comparison of the performance of modern heuristics for combinatorial optimization on real data. *Computers and Operations Research*, **20**, 687–695.

© Freund Publishing House, Ltd., London International Journal of Turbo and Jet Engines, 11, 193-200 (1994)

Blade Arrangement Strategies for Minimal Rotor Unbalance

T.W. von Backström and J.J. du Buisson

Department of Mechanical Engineering, University of Stellenbosch, 7600 South Africa

Abstract

The traditional method of minimizing the unbalance of turbomachinery rotors has been to allocate the rotor blades to circumferential positions on the disk or drum according to a fixed allocation scheme. It is shown that when a microcomputer is used to allocate the blades, the allocation pattern may be flexible; during the allocation procedure the effective unbalance can be recalculated and the strategy adjusted. The advantages of allocating blades two- or three-at-a-time are shown. Finally a very simple system based on position exchange after the initial allocation is evaluated and discussed. The methods developed reduce unbalance by orders of magnitude compared to that obtained by a typical traditional method.

Nomenclature

m_i	blade mass (g)
$\overline{m}$	mean blade mass (g)
Δm	mass difference (g) between heaviest and lightest blade
n	number of blades in blade set and number of blade positions on rotor disk
P	percentage of blades in interval $\overline{m} \pm \sigma$

Greek Symbols

σ	standard deviation of blade mass, $\sigma = \left[\frac{1}{n}\sum_{i=1}^{n}(m_i - \overline{m})^2\right]^{0.5}$

Subscripts

i	blade number

Introduction

Turbomachinery rotors should be well balanced to ensure smooth operation, low vibration levels and long life. A given set of rotor blades may, apart from its primary aerodynamic function, be regarded as a set of balancing weights which must be allocated correctly to a set of rotor blade row positions to effect the minimum static unbalance for the particular blade row.

Since all the unbalance forces exerted by the members of a blade row are confined to a narrow axial region compared to the rotor length, only static unbalance is considered. This study was initiated in response to a real need, where fixed blade allocation schemes were inadequate. The objective of this paper is to discuss and compare six different blade allocation strategies, and select the best one.

Background

The centrifugal force exerted by a blade on a rotor is proportional to the blade mass, the radial position of the blade centre of gravity, and the square of its angular velocity. Any deviation from the mean of either the mass of a blade, or the radial position of the blade centre of gravity when installed will statically unbalance the blade row as installed in the rotor. The radial position of a blade centre of gravity is determined by the position of the centre of gravity relative to a reference surface on the blade root, and secondly, by the radial position of the mating surface in the rotor, which is disregarded in this paper, as commonly done in industry.

 Internaitonal Journal of Turbo and Jet Engines, 11, 193-200 (1994)

Blade Arrangement Strategies for Minimal Rotor Unbalance

T.W. von Backström and J.J. du Buisson

Department of Mechanical Engineering, University of Stellenbosch, 7600 South Africa

Abstract

The traditional method of minimizing the unbalance of turbomachinery rotors has been to allocate the rotor blades to circumferential positions on the disk or drum according to a fixed allocation scheme. It is shown that when a microcomputer is used to allocate the blades, the allocation pattern may be flexible; during the allocation procedure the effective unbalance can be recalculated and the strategy adjusted. The advantages of allocating blades two- or three-at-a-time are shown. Finally a very simple system based on position exchange after the initial allocation is evaluated and discussed. The methods developed reduce unbalance by orders of magnitude compared to that obtained by a typical traditional method.

Nomenclature

m	blade mass (g)
$\overline{m}$	mean blade mass (g)
Δm	mass difference (g) between heaviest and lightest blade
n	number of blades in blade set and number of blade positions on rotor disk
P	percentage of blades in interval $\overline{m} \pm \sigma$

Greek Symbols

σ	standard deviation of blade mass $\sigma = \left[\frac{1}{n}\sum_{i=1}^{n}(m_i - \overline{m})^2\right]^{0.5}$

Subscripts

i	blade number

Introduction

Turbomachinery rotors should be well balanced to ensure smooth operation, low vibration levels and long life. A given set of rotor blades may, apart from its primary aerodynamic function, be regarded as a set of balancing weights which must be allocated correctly to a set of rotor blade row positions to effect the minimum static unbalance for the particular blade row.

Since all the unbalance forces exerted by the members of a blade row are confined to a narrow axial region compared to the rotor length, only static unbalance is considered. This study was initiated in response to a real need, where fixed blade allocation schemes were inadequate. The objective of this paper is to discuss and compare six different blade allocation strategies, and select the best one.

Background

The centrifugal force exerted by a blade on a rotor is proportional to the blade mass, the radial position of the blade centre of gravity, and the square of its angular velocity. Any deviation from the mean of either the mass of a blade, or the radial position of the blade centre of gravity when installed will statically unbalance the blade row as installed in the rotor. The radial position of a blade centre of gravity is determined by the position of the centre of gravity relative to a reference surface on the blade root, and secondly, by the radial position of the mating surface in the rotor, which is disregarded in this paper, as commonly done in industry.

Moment-weighing is sometimes employed where blades are long compared to the rotor diameter, but for the sake of simplicity only blade mass will be considered. The problem then reduces to balancing a rotor by assigning a set of given balancing weights to a set of circumferentially equally spaced constant radius positions.

Review of Previous Work

The present work was initiated when it was found that the residual unbalance caused by 43 blades weighing approximately 284 g each on a particular rotor disk of 80 kg could not be reduced below the G2.5 ISO Standard /1/ of 5 g mm/kg for turbocompressors. For the particular rotor the requirement came to a maximum out of balance mass of 3.3 g at the blade centre of gravity radius. During this work the first four blade allocation schemes of the paper were developed. Du Buisson /2/ later systematically checked the performance of those four schemes plus an additional one, using blade sets no. 6, 18 and 20 in Table 1, plus a normally distributed set with the same mean mass and standard deviation as the averages of the three sets. Mosevich /3/ reduced the calculated unbalance caused by 28 Francis turbine blades by a factor 5 by using a Monte Carlo approach. He limited his randomly selected configurations to about 10,000 in order to limit computer time to five minutes. Laporte and Mercure /5/ improved on Mosevich's results by using heuristics. Sinclair *et al.* /4/ have recently compared heuristic methods for arranging blades to minimize rotor unbalance. Their paper compares a slightly modified version of Method 5 of this paper (but with equal performance) to six of the best known methods from the literature. It finds Method 5 on balance of ease of implementation, solution quality and solution times to be the best method. It does not consider the first four methods presented in the present paper.

Properties of Blade Sets

A blade set is a fixed number of blades to be allocated to an equal number of equally spaced positions in a rotor blade row. The properties of a set of blades may be summarized by the parameters displayed in Table 1 for 39 blade sets considered. Set no. 38 is an artificially generated set with the same mean blade mass and standard deviation σ as the averages of sets 1 to 37. Set 39 has 113 blades, unlike the 43 of the other sets.

Traditional Methods

Traditional methods balance the set by allocating blades of more or less equal mass to opposite rotor positions, and by alternating light and heavy blades, using a fixed pattern. They rely on the following implicit assumptions:

- the deviation of blade mass from the mean is a symmetrical distribution
- the shape of the distribution does not affect the optimum-allocation pattern
- there is only one best allocation pattern for all sets
- human manipulation, using a prescribed procedure, is required
- unbalance can be determined by measurement only and not by calculation.

The traditional method in this paper is based on one currently in use. Blades are paired off in descending mass order. The first and second members of every second pair are then exchanged in order. In a second operation the pairs are rearranged in the order of heaviest, lightest, second heaviest, second lightest, etc. Using the sequence of the second operation, the lightest member of the first pair is then assigned to the first available position to the right of the first blade and the lightest member of the second pair to the first available position to the left of the first blade, etc., in an alternating sequence. For an uneven number of blades in the set, the first blade is the one with a mass closest to the mean blade mass of the set. It is set apart before the pairing operation, to be installed as the first blade.

Blade Arrangement Philosophies

There must be a best blade allocation pattern for any particular blade set, since it is always possible to compare the resultant unbalances of any two known allocation patterns. For a typical set of 43 blades the number of possible combinations is $43!/(2.43) = 7.10^{50}$ if mirror images and distributions differing

Table 1
Statistical properties of blade sets

Set no.	$\bar{m}$ (g)	σ (g)	$\Delta m/\bar{m}$ %	P %
1	263.55	1.33	2.47	62.8
2	264.86	1.99	3.56	65.1
3	260.81	1.53	2.48	67.4
4	266.22	1.94	3.09	67.4
5	293.43	1.75	2.37	67.4
6	263.17	1.27	1.74	69.8
7	293.44	1.48	2.29	72.1
8	294.01	2.39	5.27	79.1
9	286.97	2.32	2.99	72.1
10	286.24	2.40	3.11	65.1
11	287.76	2.72	4.82	65.1
12	294.21	2.22	3.27	69.8
13	293.57	2.27	2.83	62.8
14	259.14	1.26	2.16	65.1
15	262.15	1.64	3.25	72.1
16	288.18	3.48	5.92	83.7
17	285.22	2.84	3.83	69.8
18	266.31	1.97	3.05	67.4
19	296.18	1.61	2.13	67.4
20	261.22	1.70	3.06	76.7
21	299.68	2.33	2.78	55.8
22	295.20	1.56	2.36	69.8
23	288.05	3.82	4.97	69.8
24	281.83	1.86	3.12	69.8
25	292.95	1.89	3.06	72.1
26	286.92	2.33	3.55	65.1
27	298.70	1.83	2.02	62.8
28	286.04	3.97	5.21	72.1
29	289.07	3.73	5.32	58.1
30	287.81	2.28	3.72	67.4
31	287.74	1.80	2.70	69.8
32	290.52	4.57	7.50	81.4
33	292.14	3.80	6.30	69.8
34	287.80	2.59	3.50	67.4
35	287.25	3.07	3.86	69.8
36	286.96	3.56	4.54	62.8
37	285.57	3.49	5.20	58.1
Mean	283.54	2.39	3.61	66.4
38	283.54	2.39	3.88	67.4
39*	49.77	1.32	12.72	68.38

* 113 blades

from each other only in starting position are eliminated. Assuming 3.10^7 seconds per year and 10^{-9} seconds to find one distribution it would require 2.10^{34} years to find all the possibilities. Even for only 20 blades the unrealistic period of 2 years will still be required.

The strategies in this paper allocate blades singly, in pairs or in groups of three, keep track of residual unbalance, and finally reshuffle the blades. If blades or blade subsets are allocated sequentially, and the resulting unbalance calculated after each allocation, the next blade or subgroup can then be allocated optimally to minimize the current unbalance. A practical way of calculating the resultant unbalance of a partially filled blade disk is to assume that the unused positions are filled with blades of average mass. When blades or blade subgroups are allocated in order of decreasing absolute difference from the mean, the above assumption is approached asymptotically. The practical allocation schemes in the next sections do not use mass values as such, but the difference between the mass and the mean mass. Mass values less than the mean will then have a negative deviation from the mean, and average values will have a zero deviation. By setting all mass deviations on the rotor equal to zero before the start of the allocation sequence, average mass values are automatically assigned to unused rotor positions.

Practical Blade Allocation Methods

Method No. 1

This method allocates blades singly in order of decreasing mass difference from the mean, calculates residual unbalance after each allocation, and assigns the next blade to the best available position for minimizing current unbalance. The current unbalance is always calculated as a positive quantity, and the next blade is allocated to the closest to opposite available position if its deviation from the mean is positive, or to an available position as close as possible to the unbalance vector if its deviation is negative. Its main advantages are its simplicity and insensitivity to the number of blades. Its main disadvantage is that the decreasing number of available positions increases the worst possible allocation error to 180° for the critical last blade.

Method No. 2

This method sorts the blades in ascending mass order, pairs off adjacent blades and then arranges the pairs in order of descending pair unbalance. After the members of the first pair of blades have been allocated to opposite positions on the rotor, the next pair is allocated to those two remaining opposing rotor positions that will bring about the largest reduction in residual unbalance. Since the unbalance of a set of two opposing blades is always in the direction of the heaviest blade of the two, the best position for the lightest blade of the pair is the one closest to the direction of the residual unbalance before allocating the pair. This method approximates the traditional method except that the allocation pattern is not fixed, but is continually adjusted during the sequence with the aim of eliminating the remaining unbalance with the next allocation. When the set has an uneven number of blades, the blade differing the least from the mean mass value is allocated last. The deviation from 180° between the members of a pair is taken into consideration by the continual recalculation of residual unbalance. The maximum possible forced allocation error in allocating the last pair is now 90°.

Method No. 3

The set of blades sorted into ascending mass order is divided sequentially into sub-groups of three. The unbalance of each sub-group is then calculated and expressed as a mass value, assuming that the blades are situated 120° apart on a radius equal to the installed radius on the rotor. The unbalance direction for each group is referenced to the heaviest blade of the group. Blade sub-groups are then installed with their members as nearly as possible to 120° apart, in descending unbalance order, and in the position and orientation causing the greatest reduction in unbalance.

When the number of blades in the group is not divisible by 3, the remainder must be either 1 or 2. Having designated the odd blades as those with mass nearest to the mean, they are allocated to positions 1 and $(n + 1)/2$, and the method continues as described above. The distortion of the subgroup spacing from 120° by the positions filled with the odd one or two blades is automatically taken into consideration by the recalculation of the unbalance

after each allocation. The maximum forced error in allocating the last subgroup of three is now reduced to 60°.

Method No. 4

Method No. 4 is the same as Method No. 3 except for an additional systematic reshuffling operation. Adjacent blades are exchanged. If the unbalance is reduced, the new positions are retained and the procedure advanced to the next rotor position. The procedure is continued until no further improvements are possible. The next procedure is similar except that the exchange is between blades one position apart. Finally adjacent pairs are exchanged, and in the group of 4 the first and second, and third and fourth blade are also exchanged. If successful, the new positions are retained and the method advanced by one rotor blade position.

Method No. 5

Method No. 5 is exactly the same as Method No. 4 except that the blades are initially allocated in ascending mass order around the rotor disk. Du Buisson /2/ found that this worked better than random initial allocation.

Results and Discussion

The developed methods are orders of magnitude better and more consistent than the traditional method (Table 2). All the developed methods were 100% successful in reducing residual unbalance mass to below the required 5.33 g for Sets 1 to 37, the traditional method failed in 60% of cases, by factors of up to 7.

The traditional method performed reasonably only for the normally or near-normally distributed Sets 38 and 24 (Figs. 1 and 2), but performed poorly with Set 39 with 113 blades (Fig. 3). So did Method 3 with Set 16 because of the extreme asymmetry (Fig. 4) caused by 2 odd blades, but Method 4 reduced the unbalance to below average for the method. The traditional method performed miserably in this case. Even the gentle asymmetry of Set 35 (Fig. 5) was catastrophic to the traditional method but easily handled by the new methods (Table 2).

The traditional method stresses the rotor disk

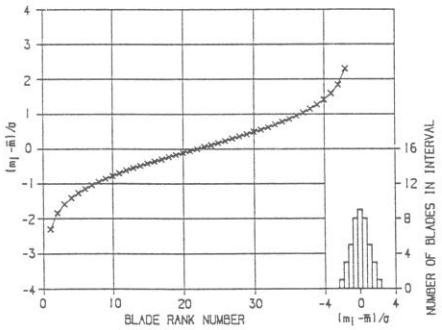

Fig. 1: Normalized blade mass deviation for Set No. 38 (normal distribution).

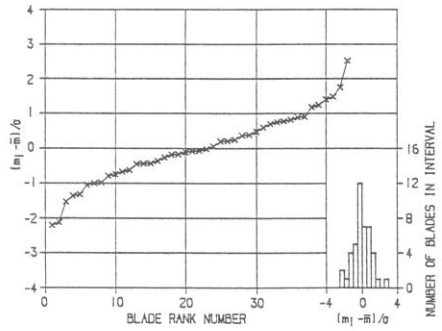

Fig. 2: Normalized blade mass deviation for Set No. 24 (near-normal distribution).

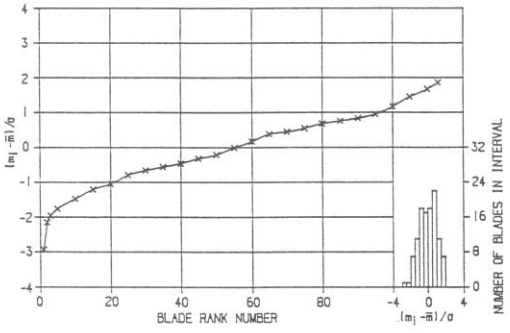

Fig. 3: Normalized blade mass deviation for Set No. 34 (113 blades).

Table 2
Final unbalance mass (as percentage of blade set standard deviation, σ) for various methods

Set no.	Methods					
	Traditional	1	2	3	4	5
1	140.76	82.94	34.94	5.47	1.92	0.14
2	85.39	9.99	14.50	8.00	0.29	0.03
3	738.45	19.37	37.95	11.65	1.05	0.17
4	633.14	4.72	7.86	10.46	0.41	0.19
5	448.92	52.79	1.86	11.51	2.08	0.10
6	664.99	73.35	20.40	3.45	0.70	0.27
7	292.35	5.77	53.89	3.88	0.55	0.09
8	41.46	5.75	74.94	1.04	0.71	0.15
9	357.08	9.26	43.24	4.76	2.32	0.35
10	25.87	25.30	8.97	3.51	0.48	0.16
11	241.58	4.91	24.09	4.38	1.29	0.09
12	282.62	10.10	58.72	3.61	0.48	0.11
13	120.92	18.62	18.13	3.42	0.75	0.24
14	551.91	25.82	36.17	6.87	1.75	0.08
15	51.55	3.39	39.08	4.71	1.20	0.14
16	771.16	8.64	47.07	76.20	0.64	0.31
17	405.11	1.21	29.89	0.48	0.48	0.32
18	253.23	16.78	58.31	3.28	0.91	0.11
19	35.33	18.33	50.97	5.16	3.08	0.08
20	572.10	2.47	68.66	5.26	0.73	0.12
21	572.31	16.45	45.12	9.13	0.57	0.14
22	261.65	39.88	43.39	2.64	1.18	0.16
23	861.14	19.82	105.76	13.04	0.15	0.11
24	6.27	19.92	37.11	2.27	2.27	0.18
25	328.08	2.19	39.69	6.95	1.24	0.14
26	235.00	25.81	24.13	3.12	1.18	0.87
27	473.82	1.60	26.66	9.14	1.66	0.02
28	435.52	3.32	28.11	1.68	1.00	0.29
29	19.48	1.03	8.55	4.06	1.90	0.05
30	92.79	18.81	10.38	1.44	1.03	1.09
31	232.21	27.72	43.99	9.95	0.47	0.14
32	848.76	45.54	14.51	18.67	0.28	0.11
33	293.95	16.47	36.42	4.82	0.98	0.21
34	430.47	4.84	16.15	17.15	0.24	0.30
35	975.48	12.64	17.12	12.93	0.71	0.03
36	69.70	22.79	60.39	3.96	1.15	0.12
37	419.03	6.19	44.17	12.93	0.88	0.12
Mean	349.36	18.24	35.33	8.28	1.03	0.20
Standard deviation	266.94	18.61	21.44	12.00	0.66	0.21
38	5.97	8.54	11.59	3.64	0.60	0.17
39	480.03	9.2	9.79	2.38	0.06	0.04

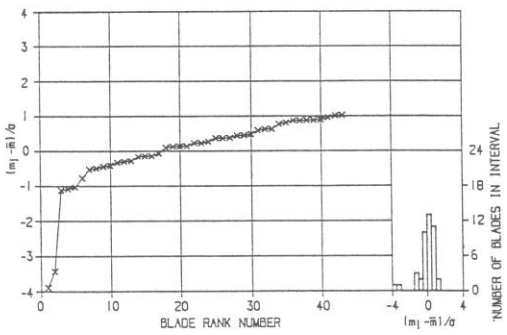

Fig. 4: Normalized blade mass deviation for Set No. 16 (extreme asymmetry).

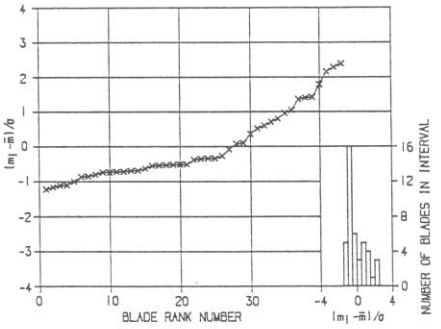

Fig. 5: Normalized blade mass deviation for Set No. 35 (gentle asymmetry).

evenly by alternating heavy and light blades, but Method 5 does not completely destroy the initial ascending mass order sequence and tends to arrange the blades in 6 packets, each with blades of more or less equal weight (Fig. 6). Methods 3 and 4 always flank a heavy blade by at least one light blade. Typically between 0 and 28 blades are exchanged by Method 4. For Sets 1 to 37 Methods 1 to 3 required typically 10 seconds computing time on an Olivetti M24 personal computer with an 8086 processor. Method 4 required 65 seconds and Method 5 required 100 seconds. For Set 39 the corresponding times were 10 seconds and 8 and 25 minutes. Sinclair *et al.* /4/ found that computing time for method 5 could be reduced by a factor of 20 by using an IBM compatible personal computer with an 80386 processor.

Conclusions

1. Flexible blade allocation strategies using a few seconds of micro-computer time can reduce blade disk unbalance by two orders of magnitude compared to fixed allocation schemes.
2. Unbalance can be reduced by a further order of magnitude by using blade exchange strategies after initial allocation.
3. Method 4 is recommended as the best, since it is economical in computing time, avoids blade mass concentrations, is based on a logical approach and results in extremely small rotor unbalance.

References

1. Schneider, H., "Balancing Technology", translation of VDI-Taschenbücher T29 Auswuchtechnik, Carl Schenk Ag. (1977).

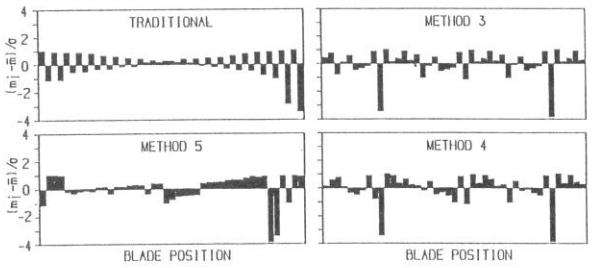

Fig. 6: Comparison of final blade arrangement by various methods for Blade Set No. 16.

2. Du Buisson, J.J., "Optimum arrangement of blades for rotor balancing", B.Eng. Project Report, University of Stellenbosch (1984).
3. Mosevich, J., "Balancing hydraulic turbine runners – a discrete combinatorial optimization problem", *European. Journal of Operational Research,* **26**, 202-204 (1968).
4. Sinclair, M., Von Backström, T.W. and Du Buisson, J.J., "Heuristic methods for arranging blades to minimize rotor unbalance", *Engineering Optimization*, **22**, 19-26 (1993).
5. Laporte, G. and Mercure, H., "Balancing hydraulic turbine runners", *European Journal of Operational Research,* **35**, 378-381 (1988).

A Unified Correlation for Slip Factor in Centrifugal Impellers

Theodor W. von Backström
Department of Mechanical Engineering,
University of Stellenbosch,
Private Bag X1,
Matieland 7602, South Africa

A method that unifies the trusted centrifugal impeller slip factor prediction methods of Busemann, Stodola, Stanitz, Wiesner, Eck, and Csanady in one equation is presented. The simple analytical method derives the slip velocity in terms of a single relative eddy (SRE) centered on the rotor axis instead of the usual multiple (one per blade passage) eddies. It proposes blade solidity (blade length divided by spacing at rotor exit) as the prime variable determining slip. Comparisons with the analytical solution of Busemann and with tried and trusted methods and measured data show that the SRE method is a feasible replacement for the well-known Wiesner prediction method: it is not a mere curve fit, but is based on a fluid dynamic model; it is inherently sensitive to impeller inner-to-outer radius ratio and does not need a separate calculation to find a critical radius ratio; and it contains a constant, F_0, that may be adjusted for specifically constructed families of impellers to improve the accuracy of the prediction. Since many of the other factors that contribute to slip are also dependent on solidity, it is recommended that radial turbomachinery investigators and designers investigate the use of solidity to correlate slip factor. [DOI: 10.1115/1.2101853]

Introduction

The rate at which fans, compressors, and pumps do flow work is less than that calculated with the assumption that the relative flow at the exit of a rotor follows the blade trailing edges. The angular momentum imparted to the flow is reduced by a factor known as the slip factor in radial flow machines.

Despite the recent advances in computational fluid dynamics, engineers and students still need a reliable method for first estimates of the slip factor in centrifugal impellers. Such a method should be direct (no iteration or conditional procedures), have a sound fluid dynamic basis, be widely applicable in terms of basic impeller geometry such as blade number, blade angle, and impeller radius ratio, and be relatively accurate.

Background

The main mechanism usually considered when predicting the slip factor in radial flow machines is the so-called relative eddy. This is an inviscid flow effect. A fluid element entering a radial flow impeller does not rotate around its own axis with an angular velocity equal to that of the rotor, but moves around the machine axis while maintaining a constant orientation relative to the machine casing. Relative to the rotor, however, the fluid element rotates at an angular velocity equal but opposite to the angular velocity of the rotor. The relative vorticity of the flow entering the rotor will set up a recirculating flow pattern relative to the rotor. In centrifugal impellers it affects the primary flow by causing underturning across the rotor exit plane.

Other mechanisms that cause slip are the relaxation of the cross passage pressure gradient near the blade trailing edges and the unequal boundary layer displacement thicknesses on the pressure and suction sides of the blades. The thicker boundary layers associated with lower Reynolds numbers enhances this effect. The existence of a wake region in the passages of radial flow machines may also play a part, as may hub and shroud drag and tip leakage flow. The wake develops in the suction side shroud corner of the flow passage, as the pressure gradients associated with the flow turning from axial to radial, and the Coriolis force turns low momentum fluid in the boundary layers more than the main flow. At lower Reynolds numbers, the thicker boundary layers will result in larger wakes. Concerning Mach number, Stanitz (in the discussion attached to Wiesner [1]) reported that his results showed only a small effect up to tip Mach numbers of 2.0.

Directly, or by implication, textbooks generally treat the relative eddy as the major factor causing slip in radial flow turbomachines, for example, Stodola [2], Eckert and Schnell [3], Ferguson [4], Wislicenus [5], Osborne [6], Eck [7], Dixon [8], Watson and Janota [9], Cumpsty [10], Logan [11], Johnson [12], Wilson and Korakianitis [13], Aungier [14], and Saravanamuttoo et al. [15]. At least, they generally do not attempt to model the other contributing factors. Dean and Young [16] and Japikse and Baines [17] do, however, consider the effect of the wake region in the blade passage, but jet-wake models still require a slip factor correlation in the jet flow region where viscous effects do not dominate.

Stodola [2] presented a simplified and popular approximate derivation followed by many textbooks. He inserted a circular-shaped control volume between the blades, near the outer radius of the rotor. The circle touches the suction side trailing edge of one blade and is tangent to the pressure surface of its neighbor. For a rotor with exit radius r_e and number of blades, Z, the blade spacing is $2\pi r_e/Z$, the eddy diameter is $2e=(2\pi r_e/Z)\cos\beta$, with β the blade exit angle, measured from the radial direction. Stodola assumed the slip velocity caused by the relative eddy to be equal in magnitude to the speed of rotation of the eddy at its rim: $\Delta w = \Omega e = \pi\Omega r_e(\cos\beta)/Z = \pi U_e(\cos\beta)/Z$. A recent example of such an approach is the paper of Paeng and Chung [18]. The present study was started because the assumption that the eddy rim velocity Δw may be applied along the rotor perimeter (the edge of another control volume) as the so-called slip velocity was difficult to justify, especially in a teaching situation.

Busemann [19] proposed a remarkable slip factor prediction method that was sensitive to the blade radius ratio. The blade radius ratio is the radial distance of the blade leading edge from the axis divided by that of the blade trailing edge. He analytically solved the inviscid flow field through a series of two-dimensional impellers with logarithmic spiral blades. He generated maps of slip factor versus the impeller radius ratio, with the blade number as a parameter, for various blade sweep angles for logarithmic spiral blades. Wislicenus [5] and Wiesner [1] reproduced these maps (for example, Fig. 3). The Busemann maps indicated that slip factor depends on RR, but below a critical value of RR it is relatively constant. The popular method of Wiesner [1] was de-

Contributed by the Computational Fluid Dynamics Committee of ASME for publication in the JOURNAL OF TURBOMACHINERY. Manuscript received April 1, 2004; final manuscript received August 10, 2005. Review conducted by M. Casey.

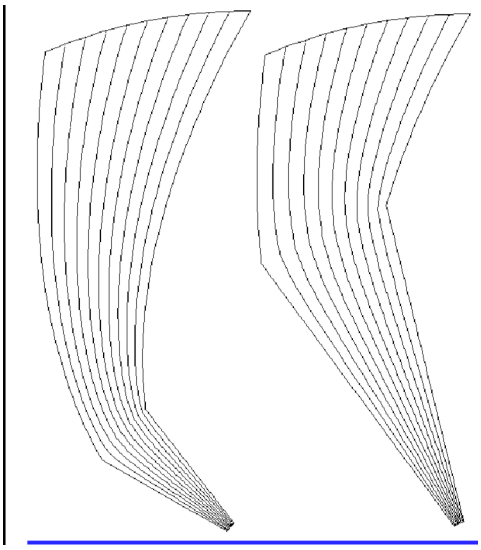

Fig. 1 Control volumes and streamlines for nonrotating low and high radius ratio impellers

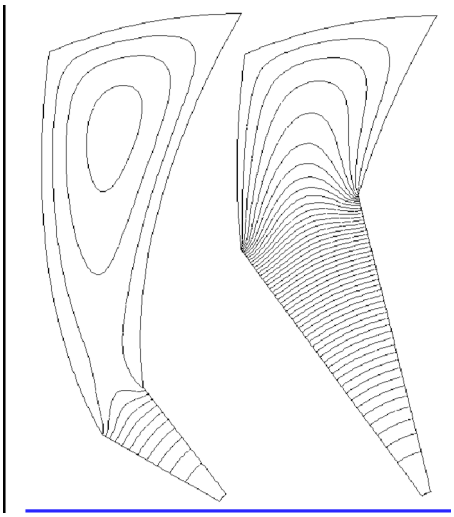

Fig. 2 Control volumes and relative-eddy-induced streamlines for low and high radius ratio impellers

signed to fit the Busemann data in the range where RR has virtually no influence, and includes an empirical correction for the effect of the blade radius ratio on the slip factor, once the critical value is exceeded.

Objectives

The overall objective of this paper is to formulate a simple, approximate but relatively accurate approach to predict eddy-induced slip factor in centrifugal impellers. Specific objectives are as follows:

(1) To propose a suitable control volume for the calculation of a relative-eddy-induced slip factor.
(2) To propose an appropriate relative-eddy-induced flow pattern.
(3) To propose a model for the calculation of the magnitude of the recirculating flow caused by the relative eddy.
(4) To present a new, generally applicable relationship for the slip factor.
(5) To compare the derived relationship to other, commonly used relationships and to experimental data.

The Single Relative-Eddy Method

The approach presented below follows, in principle, from that of Stodola [2], who assumed one relative eddy per blade passage, but it is applied here with the new assumption of a single eddy in the rotor. The detailed assumptions are as follows:

(1) Two-dimensional (2D) flow in a plane perpendicular to the axis.
(2) Logarithmic spiral rotor blades.
(3) The 2D control volume consists of a curved sector bounded by five lines: two logarithmic spirals representing adjacent blades, two radial lines between the blade leading edges and the axis, and by the rotor perimeter between the trailing edges (Fig. 1).
(4) The flow consists of the fixed-rotor flow pattern for flow through the stationary rotor and, superimposed on it, the relative-eddy flow.
(5) The fixed-rotor flow consists of the flow that would occur if the rotor does not rotate, i.e., a radial flow upstream of the rotor and a flow following the blades in the region between them (Fig. 1 is a very rough representation of such a flow).
(6) The throughflow upstream of the rotor blade leading edges has no rotation in the absolute frame, but its radial component is assumed to be proportional to the radius, to ensure a logarithmic spiral flow pattern upstream of the rotor, once the forced vortex relative-eddy-induced flow pattern is added. (This flow pattern is achieved in practice when flow enters the rotor axially.)
(7) The flow induced by the relative eddy causes no throughflow, and, in agreement with Stodola [2] is shown as if the rotor exit area is closed along the rotor perimeter (Fig. 2). Hassenpflug [20] has shown that such flow patterns do indeed resemble the eddy-induced flow component in Busemann's analytical approach reasonably well.
(8) There is only one relative eddy in the whole rotor: it revolves around the axis and protrudes into the blade passages, and when it forms separate cells associated with each blade passage as in Fig. 2, these cells are included in the main cell centered on the rotor axis.
(9) At radial positions inside the rotor leading edges the flow rotates approximately as a solid body relative to the rotor.

With reference to its most distinguishing feature, a suitable name for the method is the single relative-eddy (SRE) method.

Derivation of Equations

The fundamental principles in the derivation are as follows:

(1) Each fluid particle in the rotor has a vorticity equal in magnitude to twice the rotor angular velocity, relative to the rotor.
(2) There is a single average circulation velocity around the edges of the relative eddy.
(3) The integral of the circulation velocity around the control volume divided by the control volume area is equal to the vorticity.
(4) The integration path follows the suction surface from leading to trailing edge, then the rotor exit rim from the blade trailing edge to the next blade pressure side trailing edge, then to its leading edge, and then around its leading edge from the pressure to the suction side.

The eddy-induced velocities along the suction, exit, and pressure surfaces are $f_s \Delta w$, $f_e \Delta w$, and $f_p \Delta w$, where Δw is the average eddy-induced velocity along the control volume boundaries, and the f factors allow for deviations from the average along each section of the boundary. The component of the velocity induced by the relative eddy along the radial lines extending inward from

the blade leading edges is $f_i \Delta w$. The magnitude of the vorticity induced by the relative eddy is $\omega = 2\Omega$, where Ω is the angular velocity of the rotor in radians per second.

Circulation is the integral of the velocity, taken around the edges of the control volume:

$$\Gamma_{cv} = \int_{cv} V\, ds \tag{1}$$

The average vorticity is:

$$\omega = \Gamma_{cv}/A_{cv}. \tag{2}$$

The blade length is:

$$c = (r_e - r_i)/\cos\beta \tag{3}$$

The blade spacing is:

$$s_e = 2\pi r_e/Z \tag{4}$$

The next step is to calculate the circulation by adding the contributions along each section of the control volume boundary. There is no net contribution from the two boundary sections extending inward toward the rotor axis from the blade-leading edges since the velocity components along these two boundaries are equal due to periodicity, but the integration direction is opposite when integrating around the boundary. The circulation is then:

$$\Gamma_{cv} = f_e \Delta w\, 2\pi r_e/Z + (f_p \Delta w + f_s \Delta w)(r_e - r_i)/\cos\beta$$
$$= (f_e \Delta w\, 2\pi r_e/Z)\left(1 + \frac{f_p + f_s}{f_e}\frac{(1 - r_i/r_e)Z}{2\pi\cos\beta}\right) \tag{5}$$

and

$$\Omega = \frac{\omega}{2} = \frac{1}{2}\frac{\Gamma_{cv}}{A_{cv}} = \frac{\Gamma_{cv}}{2\pi r_e^2/Z} \tag{6}$$

$$\therefore \Omega = \frac{(f_e \Delta w\, 2\pi r_e/Z)}{2\pi r_e^2/Z}\left(1 + \frac{(f_p + f_s)}{f_e}\frac{(1 - \mathrm{RR})Z}{2\pi\cos\beta}\right) \tag{7}$$

with $\mathrm{RR} = r_i/r_e$. Then:

$$\frac{\Delta w_s}{U_e} = \frac{f_e \Delta w}{\Omega r_e} = \left(1 + \frac{(f_p + f_s)}{f_e}\frac{(1 - \mathrm{RR})Z}{2\pi\cos\beta}\right) \tag{8}$$

where the average slip velocity along the exit boundary is $\Delta w_s = f_e \Delta w$, and $\Omega r_e = U_e$.

The normal definition of blade row solidity is the blade chord divided by the spacing, but to keep things simple, we shall replace the chord by the blade length (in a plane perpendicular to the rotor axis) and use the spacing at the radius, r_e, of the blade trailing edges (rotor rim). The solidity is then:

$$c/s_e = \frac{(r_e - r_i)/\cos\beta}{(2\pi r_e)/Z} = \frac{(1 - \mathrm{RR})Z}{2\pi\cos\beta} \tag{9}$$

Define the solidity influence coefficient as:

$$F = \frac{f_p + f_s}{f_e} \tag{10}$$

Since it depends on the relative magnitudes $\int V\, ds$ over the blade surfaces, compared to the value over the blade passage exit surface, F can be expected to be a function of the blade angle and of the aspect ratio (or solidity) of the blade passage. The normalized slip velocity is then simply:

$$\frac{\Delta w_s}{U_e} = \frac{1}{1 + F(c/s_e)} \tag{11}$$

Typical values of solidity extracted from the data of Wiesner [1] range from 0.5 to 2.5, with a few values as high as 3.5 and an average of 1.5. We shall see that the average value of F is about 4, implying that for $c/s_e = 1.5$ the normalized slip velocity $(\Delta w_s/U)$ is about 1/7 or 0.14.

Implications of the equation above are as follows:

(1) The eddy-induced slip velocity is dependent on blade solidity.
(2) The eddy-induced slip velocity is independent of the blade number, blade angle, and blade radius ratio individually, but depends on them collectively insofar as they affect solidity.
(3) The factors that determine the influence coefficient F must still be determined, and may include any or all of the above.
(4) When blade solidity is zero (no blades or infinitely short blades), the equation correctly predicts that the slip velocity is equal in magnitude to the rotor rim speed.
(5) Impellers with splitter vanes can be handled by using a control volume that includes two adjacent blade passages, containing two rotor perimeter pitches and a suction and pressure side of each of the main and splitter blades. This will be equivalent to using the mean blade length.
(6) The assumption of logarithmic spiral blades turns out to be unnecessary at this point, but the blade shape may affect the value of F.

Definition of Slip Factor

There are basically two definitions of slip factor. Both are equal to one minus the normalized slip velocity. In the one definition the amount of slip is normalized by dividing the slip velocity by the rotor rim speed and in the other by the ideal (slipless) circumferential fluid velocity component. The second one introduces the complication that the circumferential fluid velocity component is dependent on the flow through the impeller, except in the case of radial blades ($\beta_e = 0$), when the two definitions are equivalent. As the second definition contradicts the assumption made in the derivation that eddy-induced slip is independent of throughflow, we shall follow Wiesner [1] and use the first definition:

$$\sigma_s = 1 - (\Delta w_s/U) = 1 - 1/[1 + F(c/s_e)] \tag{12}$$

Since the magnitude of the other factors affecting slip, like the trailing edge pressure gradient relaxation and boundary layer blockage effect (including the existence of wakes) are also primarily dependent on solidity, solidity should correlate measured slip factors well, at worst with a different coefficient F for each family of impellers.

It is known that in practice slip factors are not independent of flow, but the relative eddy can, in terms of its definition, not be the cause of these variations.

The Dependence of F on Blade Angle

The next step is to determine the dependence of F on Z, β, and RR. As a first approximation the dependence on β alone will be investigated, since Busemann drew separate figures for each blade angle. Busemann [19] (also Wiesner [1] and Wislicenus [5]) presented graphs for each of the following blade angles $\beta_B = 90$ deg, 60 deg, 40 deg, 20 deg, 10 deg, and 5 deg (measured from the circumferential direction), corresponding to our angles $\beta = 0$ deg, 30 deg, 50 deg, 70 deg, 80 deg, and 85 deg (measured from the radial direction). Wiesner's graphs show Busemann's slip factor as a function of radius ratio for blade numbers 1, 2, 4, 8, and 16 with the graph for 30 blades estimated by Wiesner. Figure 3 shows the Busemann graph for $\beta = 30$ deg, with the line for 1 blade removed, to make room for a legend, and Fig. 4 shows the corresponding graph calculated from Eq. (12) with $F = 4.45$. The graphs have roughly the same shape, but the SRE method predicts that the slip factor continues to increase with a decrease in RR, even at low values of RR, say, below RR=0.4. An inspection of the data reported by Wiesner, however, shows that, if we disregard the pump data of Varley (from Wiesner [1]), who presented a set of data for RR=0.338, then 90% of the rest falls within the range $0.4 < \mathrm{RR} < 0.6$.

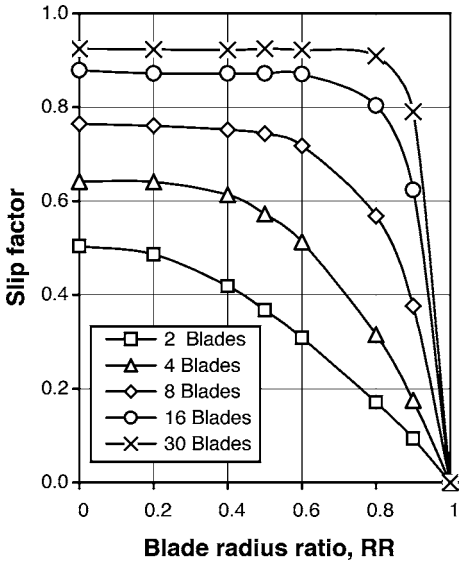

Fig. 3 The Busemann slip factor for β=30 deg versus radius ratio for various blade numbers

Now find, for each of the above blade angles, the value of F that would minimize the sum of the square of the differences between the slip factors calculated with Eq. (12) and the corresponding Busemann values. The nine points selected were those with RR=0.4, 0.5, and 0.6, and blade numbers 8, 16, and 30. Figure 5 shows the resulting relationship between F and $\cos\beta$. The equation $F=F_0(\cos\beta)^{0.5}$, with $F_0=5.0$, presented the trend well enough, except for one point at β=80 deg. It can be shown by differentiating Eq. (12) with respect to F that $\partial\sigma/\partial F=\sigma(1-\sigma)$. At β=80 deg, and for the blade numbers and radius ratios considered, a typical value of slip factor is σ=0.91, so that $\partial\sigma/\partial F$ has a value of 0.08, implying that a 30% error in F would cause only a 2.5% error in slip factor. Conversely, a small error in estimating the Busemann values from Wiesner's graphs would result in a large variation in F.

The SRE slip factor equation then becomes:

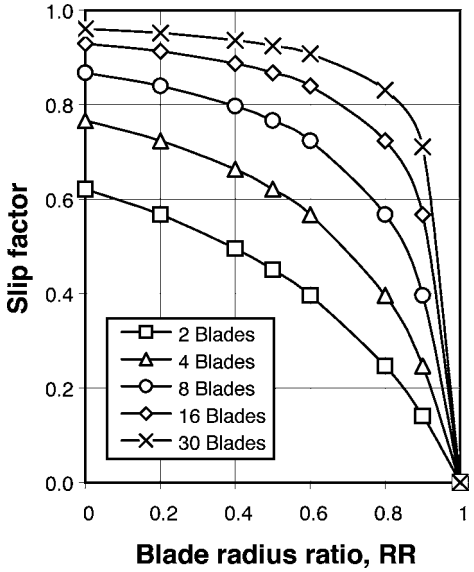

Fig. 4 The SRE slip factor for β=30 deg versus the radius ratio for various blade numbers

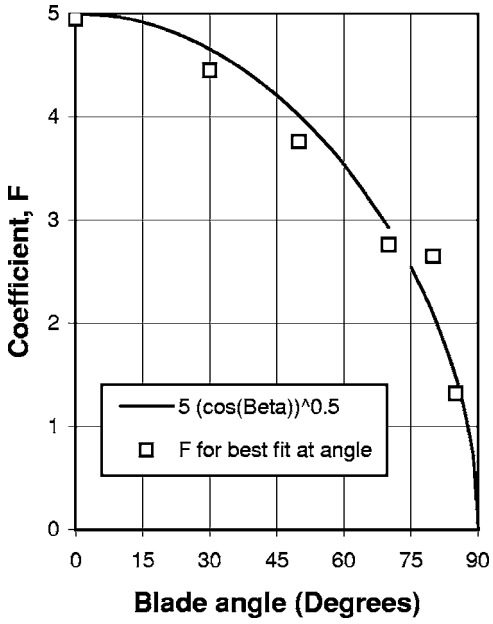

Fig. 5 The relationship between solidity coefficient, *F*, and blade angle, β, in the SRE model

$$\sigma_s = 1 - \frac{1}{1 + 5(c/s_e)(\cos\beta)^{0.5}} \tag{13}$$

Figure 6 is a graphical representation of Eq. (13). It shows the variation of slip factor with solidity, with β as a parameter. Note that for $\beta \leqslant 50$ deg the influence of β is small, and the slip factor is then to a good approximation a function of solidity alone.

The SRE slip factor can also be written in terms of the basic parameters as:

$$\begin{aligned}\sigma_s &= 1 - 1/[1 + 5(\cos\beta)^{0.5}(c/s_e)] \\ &= 1 - 1 \Big/ \left(1 + 5(\cos\beta)^{0.5}\frac{Z(1-\mathrm{RR})}{2\pi\cos\beta}\right) \\ &= 1 - 1 \Big/ \left(1 + 5\frac{(1-\mathrm{RR})Z}{2\pi(\cos\beta)^{0.5}}\right)\end{aligned} \tag{14}$$

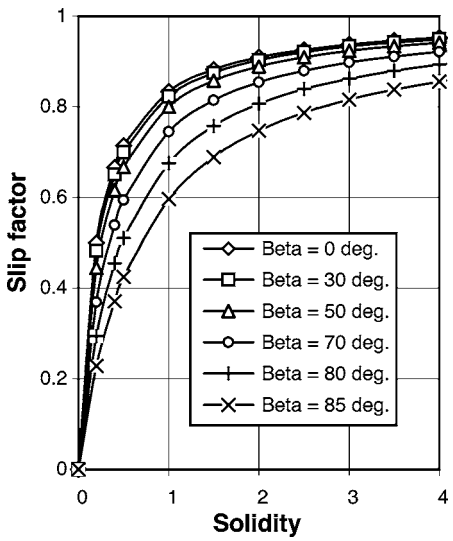

Fig. 6 Variation of the SRE slip factor with solidity, c/s_e, with blade angle, β, as a parameter

Table 1 SRE slip factors compared to Stodola, for RR=0.5 and β=50 deg and 65 deg

Z	4	8	16	32
Exact SRE (50 deg)	0.665	0.799	0.888	0.941
Approximate SRE (50 deg)	0.496	0.748	0.874	0.937
Stodola (50 deg)	0.495	0.748	0.874	0.937
Exact SRE (65 deg)	0.710	0.830	0.907	0.951
Stodola (65 deg)	0.668	0.834	0.917	0.959

Table 2 SRE slip factors compared to predictions by Stanitz, for RR=0.4 and 0.5

Z	4	8	16	32
SRE, β=0 deg, RR=0.5	0.614	0.761	0.864	0.927
SRE, β=0 deg, RR=0.4	0.656	0.793	0.884	0.939
Stanitz	0.706	0.828	0.906	0.951

Comparison to Equation of Stodola

One problem in comparing the SRE equation (14) above with some other slip factor equations, is that they are insensitive to blade radius ratio, RR. For the 66 cases summarized by Wiesner [1] RR varied between 0.338 and 0.6. The average value was 0.47.

Substituting the Stodola derived slip velocity, $\Delta w = \pi U_e(\cos\beta)/Z$, into the slip factor definition normalized with respect to the rotor speed U, leads to:

$$\sigma_s = 1 - \pi(\cos\beta)/Z \tag{15}$$

For average RR, say 0.5 and large Z, say 24, so that in Eq. (14) the second term in the large parentheses $\approx 10 \gg 1$, the first term may be ignored and the SRE method, (Eq. (14)) may be approximated as below:

$$\sigma_s = 1 - 1 \Big/ \left(1 + 5\frac{(0.5)Z}{2\pi(\cos\beta)^{0.5}}\right) \approx 1 - 0.8\pi\sqrt{(\cos\beta)}/Z \tag{16}$$

The major difference between Eq. (16) and Eq. (15) is in the square root, but they are exactly equivalent for β=50.2 deg for any number of blades. Dixon [8] states that the Stodola equation gives the best results in the range of 60 deg to 70 deg. Table 1 compares exact and approximate SRE predictions to Stodola. For 8 or more blades the agreement is within 0.01, but the Stodola equation is inaccurate for small Z, and incorrectly predicts that in the limit of zero blades the slip factor equals minus infinity, whereas the SRE method (in its exact form) correctly predicts it to be equal to zero.

Comparison to Equation of Stanitz

A commonly used expression for the slip factor of radial bladed impellers (β=0 deg) is one proposed by Stanitz [21], based on numerical solution of flow fields in impellers with radius ratio 0.445:

$$\sigma_s = 1 - 0.63\pi/Z \tag{17}$$

Note that this equation does not agree with the Stodola equation (15) for β=0 deg, which gives:

$$\sigma_s = 1 - \pi/Z \tag{18}$$

For β=0 deg and RR=0.5, the approximate SRE equation (16) above reduces to:

$$\sigma_s \approx 1 - 0.8\pi/Z \tag{19}$$

This equation gives values that are about halfway between the Stodola equation (18) for β=0 deg, and the Stanitz equation. For β=0 deg and RR=0.4, however, the approximate equation (14) above reduces to:

$$\sigma_s \approx 1 - \frac{2}{3}\pi/Z = 1 - 0.67\pi. \tag{20}$$

The agreement between Eqs. (17) and (20) is striking. The full SRE is compared to the Stanitz equation in Table 2 and shows that for RR=0.4 agreement is within 0.025 for 8 or more blades. The Stanitz equation, unlike the Stodola equation, consistently predicts higher values of slip factor than the SRE method. It is gratifying to see that the approximation to the SRE equation, in its simplified form exhibits fundamentally the same dependence on the blade number as the Stodola and Stanitz equations, and in its exact form agrees with the two different equations as far as they are reconcilable with each other.

Comparison to Equations of Wiesner and Analytical Values of Busemann

Wiesner [1] proposed an empirical equation, valid for RR less than a limiting value, RR_{lim}, stating, in our angle notation, that:

$$\sigma_s = 1 - \sqrt{\cos\beta}/Z^{0.7} \tag{21}$$

We have seen that the SRE equation may, for small RR, say 0.5, to avoid exceeding RR_{lim}, and large Z, be approximated as:

$$\approx 1 - 0.8\pi\sqrt{(\cos\beta)}/Z \tag{22}$$

The approximate SRE equation resembles the Wiesner equation in its dependence on $\sqrt{\cos\beta}$, but not in its dependence on Z, but Eqs. (21) and (22) predict exactly the same value of slip factor for Z =21.6, for any blade angle. The 0.7 exponent for Z in the Wiesner equation disagrees with the Stodola, Stanitz, and approximate SRE equations. The fundamental Wiesner equation (Eq. (21)), like the Stodola and Stanitz equations, predicts that as Z approaches zero, the slip factor approaches minus infinity, but because of the lower valued exponent (0.7) it does so more slowly. As the fundamental equation also assumes that slip factor is independent of RR, Wiesner proposed an empirical correction factor to force the slip factor to zero as RR approaches unity (and blade length approaches zero). The correction factor is:

$$F_{RR} = 1 - [(RR - RR_{lim})/(1 - RR_{lim})]^3 \tag{23}$$

where $RR_{lim}=\exp[8.16(\cos\beta)/Z]$ is the limiting radius ratio. It must be applied only when the limiting radius ratio is exceeded. Note that Wiesner [1] did not attempt to model the physics by correcting the slip velocity, but applied the correction to the slip factor directly.

Table 3 compares SRE predictions with Busemann and Wiesner for a typical RR value of 0.5, and a wide range of blade angles. The Busemann data is given to two decimals only, having been measured off figures in Wiesner [1]. The asterisk (*) denotes val-

Table 3 SRE slip factors compared to values predicted by Busemann and Wiesner, for RR=0.5

Z	4	8	16	30
Busemann, β=0 deg	0.56	0.76	0.86	0.91
SRE, β=0 deg	0.614	0.761	0.864	0.923
Wiesner, β=0 deg	0.575*	0.763*	0.856	0.908
Busemann, β=50 deg	0.63	0.79	0.88	0.92
SRE, β=50 deg	0.665	0.799	0.888	0.937
Wiesner, β=50 deg	0.676*	0.813	0.885	0.926
Busemann, β=70 deg	0.71	0.83	0.91	0.94
SRE, β=70 deg	0.731	0.845	0.916	0.953
Wiesner, β=70 deg	0.778	0.864	0.916	0.946
Busemann, β=80 deg	0.83	0.92	0.96	0.96
SRE, β=80 deg	0.793	0.884	0.939	0.966
Wiesner, β=80 deg	0.841	0.903	0.940	0.961

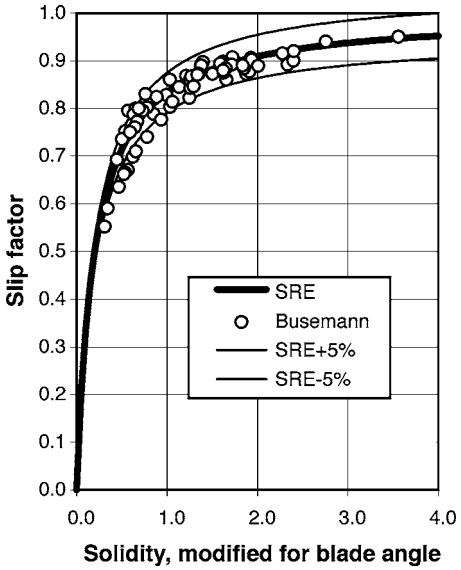

Fig. 7 SRE and Busemann predictions of the slip factor for Wiesner test cases, versus $(c/s_e)\sqrt{\cos\beta}$

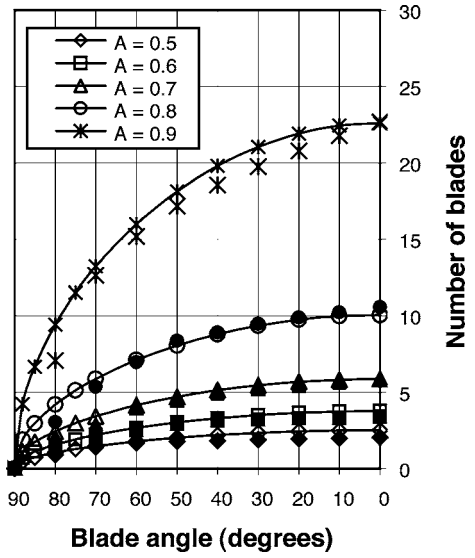

Fig. 9 A comparison of *A*-contours by SRE and Csanady (1960)

ues corrected for exceeding Wiesner's limiting radius ratio. The average value of the SRE value minus the Busemann value is +0.0068 and the standard deviation of the difference is 0.054, compared to +0.0113% and 0.057 for Wiesner. For the 16 points considered, SRE performs slightly better in terms of the average difference and the standard deviation of the difference when compared to Busemann. Although Wiesner typically predicts slip factors to be about 0.005 higher than SRE, the standard deviation based on the difference between them is only 0.002.

Figure 6 is a graphical representation of the SRE slip factor prediction, Eq. (14). It presents the slip factor as a function of solidity, with the blade angle as a parameter. All the lines in the figure can, however, be collapsed onto a single line if the x-axis value is changed to $(c/s_e)\sqrt{\cos\beta}$, the so-called modified solidity. Figures 7 and 8 present comparisons between Eq. (14) and the Busemann and Wiesner slip factors, respectively, for all the applicable test cases in Wiesner [1]. The agreement is good in both cases. Both figures support the notion that a prime factor that determines the slip factor is the modified blade solidity, $(c/s_e)\sqrt{\cos\beta}$.

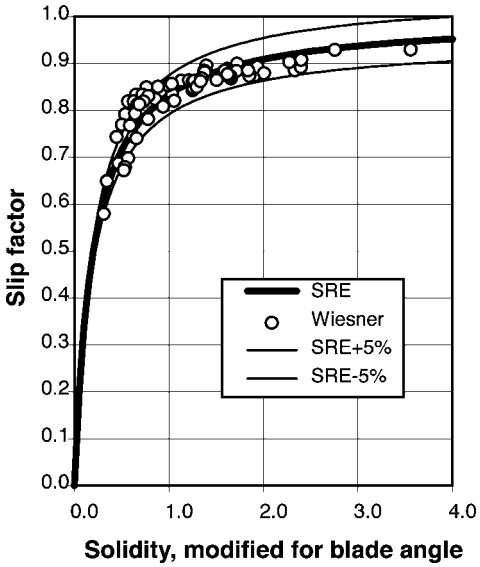

Fig. 8 SRE and Wiesner predictions of the slip factor for Wiesner test cases, versus $(c/s_e)\sqrt{\cos\beta}$

Comparison to Equation of Eck

In the Discussion section attached to Wiesner's paper [1], Love proposed an equation for the slip factor derived by Eck [7], who derived his equation by using pressure gradient arguments. The equation is:

$$\sigma_s = 1 \Big/ \left(1 + \frac{(\pi/2)\cos\beta}{Z(1-\mathrm{RR})}\right) \tag{24}$$

It may be rewritten as:

$$\sigma_s = 1 \Big/ \left(1 + \frac{2\pi}{4}\frac{\cos\beta}{Z(1-\mathrm{RR})}\right) = 1 - 1 \Big/ \left(1 + 4\frac{Z(1-\mathrm{RR})}{2\pi\cos\beta}\right) \tag{25}$$

Equations (14) and (25) are very similar. The only difference is that in the Eck equation the coefficient Z has a constant value of 4 instead of $5(\cos\beta)^{0.5}$. At β=50.2 deg the two equations are identical. The comparisons with Stodola, Stanitz, and Wiesner have, however, confirmed that the $5(\cos\beta)^{0.5}$ coefficient as a good approximation. As the coefficient Z varies between 1.00 at 0 deg and 0.30 at 85 deg, it is unlikely that a constant value would be adequate over a wide range of blade angles.

Neither Eck nor Love pointed out that the fundamental parameter influencing slip factor is solidity.

Comparison With Csanady

Csanady (1960) (reported by Ferguson [4], and Dixon [8]) published curves showing contours of a coefficient A, which is equivalent to the slip factor definition we use. Each curve basically gives the number of blades required to achieve a desired solidity, given the blade angle. The equivalent curves, using SRE, can be drawn by assuming RR=0.5 and rewriting Eq. (14) in the following form:

$$Z = \frac{\sigma_s}{1-\sigma_s}\frac{2\pi\sqrt{\cos\beta}}{5(1-0.5)} \tag{26}$$

Equation (26) opens up the possibility of explicitly calculating the number of blades required to achieve a desired slip factor, for any

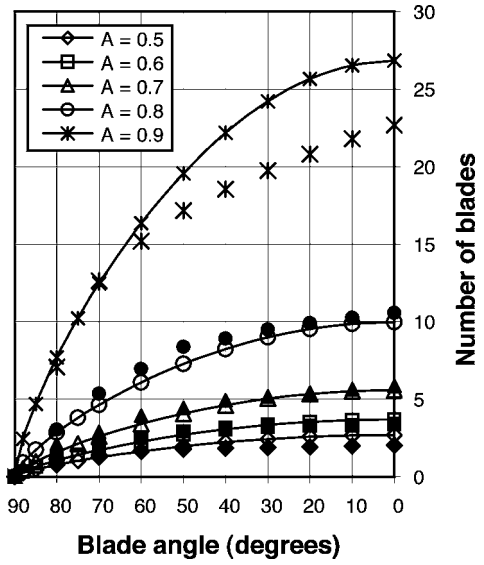

Fig. 10 A comparison of *A* contours by Wiesner and Csanady (1960)

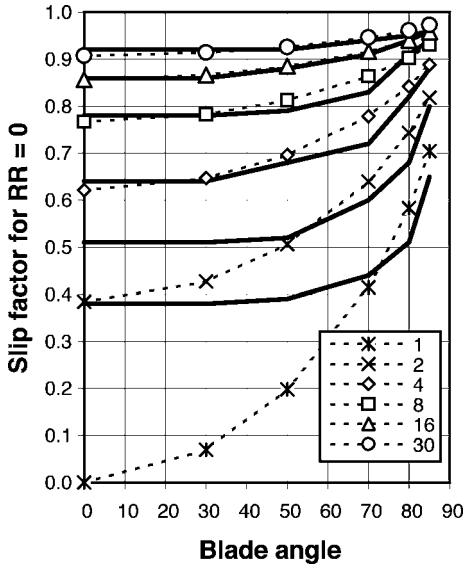

Fig. 12 A comparison of Wiesner and Busemann slip factors for RR=0

blade angle and radius ratio. It is apparent from Fig. 9 that Eq. (26) above (represented by the lines) predicts Csanady's data points surprisingly well. Since these curves were derived from Busemann's data they demonstrate once more how well SRE approximates the Busemann calculations. Figure 10 shows a similar graph using Wiesner's correlation, but the agreement is not nearly as good, except at blade angles exceeding 65 deg, and it cannot model the effect of RR explicitly.

Slip Factor For Low Radius Ratio

The study so far has shown that the SRE method predicts slip factor well for RR≈0.5, but initial comparisons (Figs. 3 and 4) showed that it overpredicted at low values of RR. The simplest way of removing this discrepancy is to assume that if RR$<$0.5, then RR=0.5. This is equivalent to assuming that blade-leading edges extending inward beyond RR=0.5, do not contribute to the control of slip. Figure 11 compares SRE slip factors (for RR=0.5) to those of Busemann (measured from the graphs in Wiesner, for example, Fig. 3) for RR=0. The agreement is generally within three percentage points, but it deteriorates as the blade number decreases. The Wiesner correlation (Fig. 12) is very good for 16 blades (and for 30, where Busemann data did not exist, but were estimated by Wiesner), but it is relatively inaccurate for lower blade numbers or large blade angles.

Figures 13 and 14 present comparisons between Eq. (14) and the Busemann and Wiesner slip factors respectively, as before, but with RR values of less than 0.5 changed to 0.5. The agreement is improved and can be described as excellent in both cases. It is remarkable that the simple SRE correlation manages to represent Busemann's predictions accurately for all Wiesner's data points. SRE agrees better with Busemann than with Wiesner's prediction method.

Although assuming a fixed value of RR=0.5 as the cutoff point may be regarded as simplistic, it works very well. The author has derived a more complicated method, but does not consider it

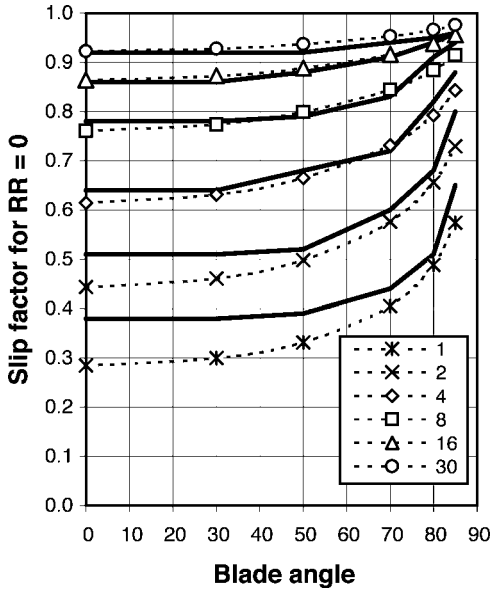

Fig. 11 A comparison of SRE (with RR=0.5) and Busemann slip factors for RR=0

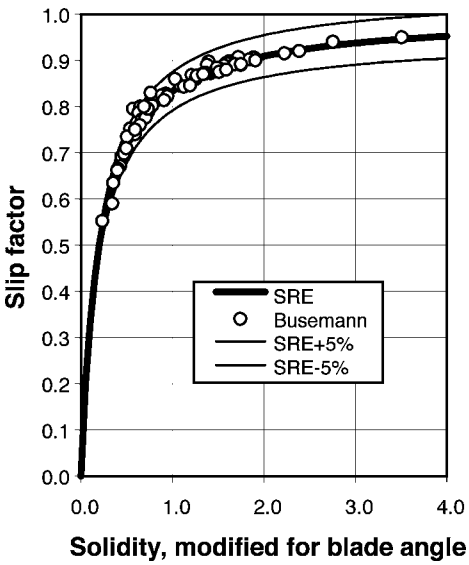

Fig. 13 SRE (with RR≥0.5) and Busemann predictions of the slip factor for Wiesner test cases, versus $(c/s_e)\sqrt{\cos\beta}$

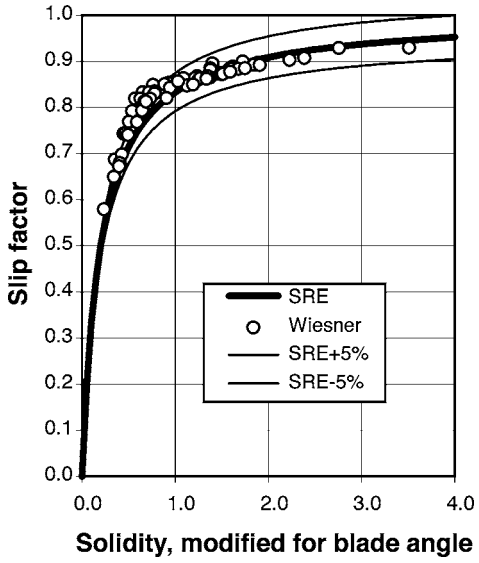

Fig. 14 SRE (with RR≥0.5) and Wiesner predictions of the slip factor for Wiesner test cases, versus $(c/s_e)\sqrt{\cos\beta}$

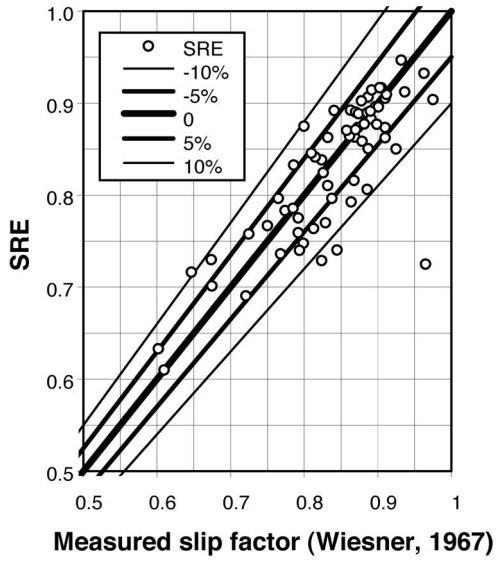

Fig. 16 The slip factor comparison between the SRE prediction and Wiesner test cases

worthwhile since, like the Wiesner method, it would require a conditional procedure involving the calculation of a critical radius ratio.

Comparisons With Measured Data of Wiesner

To qualify as an accepted general method of predicting slip factor the SRE method should show that it represents a considerable body of measured data with sufficient accuracy. Conveniently available experimental results are those reported by Wiesner [1]. Measured slip factors reported by Wiesner were used wherever the blade radius ratio and the so-called "test slip coefficients" were given. In the comparisons that follow we make the standard, tacit assumption that the rotor blade angle at the trailing edge (rotor exit) represents the rotor blade angle, even for nonlogarithmic-spiral blades.

Figure 15 presents a comparison between Eq. (14) (with no limitation on minimum RR values) and the so-called test slip coefficients presented by Wiesner. Here the agreement is not as good as with the Wiesner and Busemann predictions, because of a combination of experimental scatter and nonviscous fluid effects. The figure is, however, experimental confirmation of the notion that a prime factor that determines the slip factor is indeed the modified blade solidity, $(c/s_e)\sqrt{\cos\beta}$.

Figures 16 and 17 show how well the SRE compares to Wiesner in predicting the measured data reported by Wiesner. Wiesner has more points within the ±5% range, but SRE has more within the ±10% range, and is less prone to overpredict. SRE has the potential advantage that each family of impellers may be fitted with its own constant F or F_0, but this needs further investigation.

The question of how much of the scatter is attributable to poor prediction models and how much to the experimental inaccuracies is addressed in the next section.

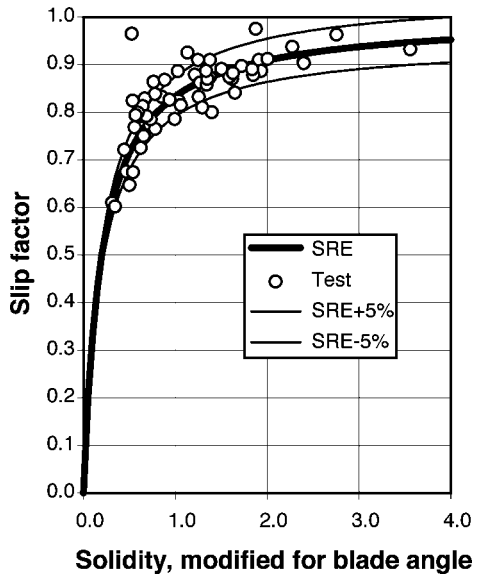

Fig. 15 SRE prediction and Wiesner test cases for slip factors versus $(c/s_e)\sqrt{\cos\beta}$

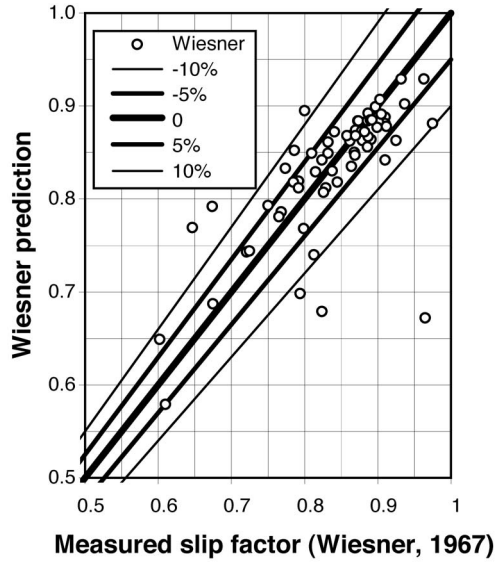

Fig. 17 The slip factor comparison between the Wiesner prediction and Wiesner test cases

Table 4 Estimation of standard deviation of slip factor measurement error, S_σ

Blade exit angle, β_2(deg)	0	30	50	70	80	85
Blade number, Z	20	17	16	7	5	4
Wiesner slip factor, σ	0.877	0.871	0.884	0.850	0.864	0.888
Guessed efficiency, η	0.80	0.80	0.80	0.80	0.80	0.80
Flow coefficient, ϕ	0.300 000	0.300 000	0.200 000	0.150 000	0.100 000	0.050 000
Head coefficient, μ	0.701 742	0.576 735	0.539 194	0.399 930	0.299 746	0.304 936
S_μ	0.007 017	0.005 767	0.005 392	0.003 999	0.002 997	0.003 049
$(S_\mu\ \partial\sigma/\partial\mu)^2$	0.000 077	0.000 052	0.000 045	0.000 025	0.000 014	0.000 015
S_η	0.010 000	0.010 000	0.010 000	0.010 000	0.010 000	0.010 000
$(S_\eta\ \partial\sigma/\partial\eta)^2$	0.000 120	0.000 081	0.000 071	0.000 039	0.000 022	0.000 023
S_ϕ	0.003 000	0.003 000	0.002 000	0.001 500	0.001 000	0.000 500
$(S_\phi\ \partial\sigma/\partial\phi)^2$	0.000 000	0.000 003	0.000 006	0.000 017	0.000 032	0.000 033
S_β	0.017 500	0.017 500	0.017 500	0.017 500	0.017 500	0.017 500
$(S_\beta\ \partial\sigma/\partial\beta)^2$	0.000 028	0.000 049	0.000 072	0.000 503	0.003 360	0.013 203
S_σ	0.014 991	0.013 608	0.013 922	0.024 168	0.058 553	0.115 207

Error Estimate For Experimental Data Reported by Wiesner

Experimental slip factors in Wiesner's paper are calculated as: $\sigma=\mu/\eta+\phi_2\tan\beta_2$, where μ is the pressure or head coefficient, η is the efficiency, ϕ_2 is the impeller discharge flow coefficient, and β_2 is the impeller discharge angle. (The subscripts 2 are omitted from hereon.) If one can estimate the typical standard deviation S_i in determining each of the four independent variables, the variance S_σ^2 and standard deviation of the value of the dependent variable, σ may be derived, by doing a sensitivity analysis. According to Granger [22] the relationship between the standard deviations, S is for the present case:

$$S_\sigma^2=\left(\frac{\partial\sigma}{\partial\mu}S_\mu\right)^2+\left(\frac{\partial\sigma}{\partial\eta}S_\eta\right)^2+\left(\frac{\partial\sigma}{\partial\phi}S_\phi\right)^2+\left(\frac{\partial\sigma}{\partial\beta}S_\beta\right)^2$$

where, for the equation under consideration:

$$\frac{\partial\sigma}{\partial\mu}=\frac{1}{\eta};\ \frac{\partial\sigma}{\partial\eta}=\frac{-\mu}{\eta^2};\ \frac{\partial\sigma}{\partial\phi}=\tan\beta;\ \frac{\partial\sigma}{\partial\beta}=\frac{\phi}{\cos^2\beta}$$

In Table 4 the typical assumption is that the standard deviation of the measurement error is 1%, implying that 95% of the measured values are accurate to within ±2%. The standard deviations are taken as either one percent of the value or one percentage point (for efficiency), and that of the angle measurement error as 1 deg, as summarized below: $S_\mu=0.01\mu$; $S_\eta=0.01$; $S_\phi=0.01\phi$; $S_\beta=0.0175$ rad=1 deg.

The values of the variables were selected as typical ones from Wiesner's data table. Note that the low blade number typically goes with high blade angles to give high slip factors (as in Fig. 9).

For $\beta_2\leqslant 70$ deg and $Z\geqslant 7$, the standard deviation is 0.015 to 0.024, but it is much higher at larger blade angles and lower blade numbers. It implies that in 95% of the cases with $\beta_2<70$ deg and blade numbers $Z\leqslant 7$, the slip factor experimental error should be less than ±0.05, but that for cases with larger blade angles and fewer blades the error may be much larger (±0.12 to ±0.23). Since these conservative guesses for measurement error result in fairly large standard deviations for the slip factor, it may be assumed that a relatively large part of the differences between the predictions and the measured data reported by Wiesner is attributable to inaccuracies in measurement.

Discussion

In the paper we present a simple method for deriving the relative-eddy-induced slip factor in centrifugal impellers. The derivation proposes the concept of a single relative-eddy recirculation zone in the rotor, in contrast to previously used separate recirculation cells. The resulting equation reduces to well-known and trusted equations for the calculation of slip factor when assuming realistic radius ratios and excluding rotors with a few blades, where many trusted methods start to approach an unrealistic limiting value.

The SRE equation is, next to Eck's, the only one to intrinsically predict the zero slip factor for zero blades. It also correctly predicts the zero slip factor for blades of zero length (RR=1), independent of the number of blades, without the need to calculate a limiting radius ratio, and it can handle splitter blades in a logical way. It turned out that the prime variable that determines slip is the blade solidity, c/s_e:

$$c/s_e=\frac{(1-\mathrm{RR})Z}{2\pi\cos\beta}$$

The proposed general equation for relative-eddy-induced slip factor is:

$$\sigma_s=1-\frac{\Delta w_s}{U}=1-\frac{1}{1+F_0(c/s_e)(\cos\beta)^{0.5}}$$

with the constant $F_0=5.0$, but its value may be adjusted for specific families of impellers.

Assuming that radius ratios of less than 0.5 are equal to 0.5 in the previous equations, gives better agreement with Busemann's analytical values, but does not improve agreement with Wiesner's test cases.

Conclusions

Two slip factor correlations are presented: both assume that $\sigma_s=1-[1+F(c/s_e)]^{-1}$ where the solidity influence coefficient is: $F=F_0(\cos\beta)^{0.5}$, with $F_0=5$, but the second one additionally assumes that radius ratios of less than 0.5 should be taken to be 0.5.

Agreement with the methods of Stodola, Stanitz, Wiesner, Eck, and Csanady, with the analytical solutions of Busemann, and with measured data presented by Wiesner, show that the SRE method is a feasible replacement for the Wiesner method: it is not a mere curve fit, but is based on a fluid dynamic model; it is inherently sensitive to an impeller inner-to-outer radius ratio and does not need a separate calculation to find a critical radius ratio; and it contains a constant, F_0, that may be adjusted for specifically constructed families of impellers to improve the accuracy of the prediction.

The three main contributions of this work are as follows: the derivation of a slip factor in terms of a single relative eddy centered on the rotor axis, instead of multiple eddies (one per blade passage); the recognition that blade solidity is the prime variable determining the relative-eddy-induced slip factor; the presentation of a simple, reliable method, that analytically and numerically unifies the tried and trusted methods of Stodola, Stanitz and Wiesner, Eck, Csanady, and Busemann over a wide range of impeller geometries.

Since the effect of many of the other factors that contribute to slip (potential flow and boundary layer effects) are also dependent on solidity, it is recommended that radial turbomachinery investigators and designers investigate the use of solidity to correlate the slip factor.

Acknowledgment

Graduate students René Heise and Louwrens Marais helped with the numerical solutions for finding the streamlines in Figs. 1 and 2.

List of Symbols

A = control volume area, Csanady coefficient
c = blade length
d = rotor diameter
e = eddy radius in Stodola derivation
F = solidity coefficient
f = velocity coefficient
RR = radius ratio
r = rotor radius
s = blade spacing, distance along integration path
U = rotor speed
V = velocity
w = circulation velocity
Z = number of rotor blades

Greek Symbols

β = blade angle
Γ = circulation
η = efficiency
μ = pressure or head coefficient
π = circle circumference to radius ratio
σ = slip factor
ϕ = impeller discharge flow coefficient
ω = vorticity
Ω = rotor angular velocity

Subscripts

cv = control volume
e = exit
i = inner
p = pressure side of blade
s = suction side of blade, slip
β = blade angle
η = efficiency
μ = pressure or head coefficient
φ = impeller discharge flow coefficient
0 = zero blade angle

References

[1] Wiesner, F. J., 1967, "A Review of Slip Factors for Centrifugal Impellers." Trans. ASME: J. Eng. Gas Turbines Power **89**, pp. 558–572.
[2] Stodola, A., 1945, *Steam and Gas Turbines*, McGraw-Hill, 1927, reprinted by Peter Smith, New York.
[3] Eckert, B., and Schnell, E., 1961, *Axial- und Radial-Kompressoren*, Springer-Verlag, Berlin, p. 345.
[4] Ferguson, T. B., 1963, *The Centrifugal Compressor Stage*, Butterworths, London, pp. 85–90.
[5] Wislicenus, G. F., 1965, *Fluid Mechanics of Turbomachinery*," 2nd ed. (in two volumes), Vol. 1, Dover, New York, p. 269.
[6] Osborne, W. C., 1966, *Fans*, Pergamon, Bell and Bain Ltd., Glasgow, p. 129.
[7] Eck, B., 1973, *Fans*, Pergamon, Germany, p. 37.
[8] Dixon, S. L., 1978, *Fluid Mechanics*, Thermodynamics of Turbomachinery, Pergamon, New York, pp. 201–206.
[9] Watson, N., and Janota, M. S., 1986, *Turbocharging the Internal Combustion Engine*, MacMillan Education Ltd., London, p. 89.
[10] Cumpsty, N. A., 1989, "*Compressor Aerodynamics*," Longman Scientific & Technical, England, pp. 245–249.
[11] Logan, E., Jr., 1993, "*Turbomachinery, Basic Theory and Applications*," 2nd ed. revised and expanded, Marcel Dekker, New York, pp. 167, 248.
[12] Johnson, R. W., 1998, "*The Handbook of Fluid Dynamics*," CRC Press, Springer, New York, pp. 41-12–41-14.
[13] Wilson, D. G., and Korakianitis, T., 1998, *The Design of High-Efficiency Turbomachinery and Gas Turbines*, 2nd ed., Prentice–Hall, Englewood Cliffs, NJ, p. 240.
[14] Aungier, R. H., 2000, *Centrifugal Compressors–A Strategy for Aerodynamic Design and Analysis*, ASME Press, New York, p. 55.
[15] Saravanamuttoo, H. I. H., Rogers, G. F. C., and Cohen, H., 2001, *Gas Turbine Theory*, 5th ed., Prentice–Hall, Englewood Cliffs, NJ, pp. 153, 155.
[16] Dean, R. C., and Young, L. R., 1976, "The Fluid Dynamic Design of Advanced Centrifugal Compressors," Creare TN-244, pp. 5–27.
[17] Japikse, D., and Baines, N. C., 1997, *Introduction to Turbomachinery*, Concepts ETI and Oxford University Press, Oxford, pp. 4-6–4-7.
[18] Paeng, K. S., and Chung, M. K., 2001, "A New Slip Factor For Centrifugal Impellers," Proc. Inst. Mech. Eng., Part A, pp. 645–649.
[19] Busemann, A., 1928, "Das Förderhöhenverhältniss Radialer Kreiselpumpen Mit Logarithisch-Spiraligen Schaufeln," Z. Angew. Math. Mech., **8**, pp. 371–384.
[20] Hassenpflug, W. C., 2004, personal communication.
[21] Stanitz, J. D., 1952, "Some Theoretical Aerodynamic Investigations of Impellers in Radial- and Mixed-Flow Centrifugal Compressors," Trans. ASME, **74**, pp. 473–476.
[22] Granger, R. A., 1988, *Experiments in Fluid Mechanics*, Holt, Reinhart and Winston, New York.

A compact equation for the prediction of eddy-induced slip in centrifugal impellers

T W von Backström
Department of Mechanical Engineering, University of Stellenbosch, Private Bag X1, Matieland 7602, South Africa.
email: twvb@sun.ac.za

The manuscript was received on 26 April 2006 and was accepted after revision for publication on 25 August 2006.

DOI: 10.1243/09576509JPE321

Abstract: The single relative eddy (SRE) method for the prediction of relative-eddy-induced slip in centrifugal impellers proposes the existence of only one slip-inducing eddy in a rotating impeller, compared with the commonly assumed multiple eddies, with one eddy per blade passage. In the SRE method, the eddy-induced slip factor depends on the blade solidity, weighted by an auxiliary coefficient F that is a function of blade angle and blade number. The paper presents a series of increasingly accurate new expressions for F. The best fit leads to a compact equation for slip factor, giving very good agreement (within 0.003) with the numerically calculated slip factors of Busemann for impellers with four or more blades and reasonable agreement (within 0.02) for single-bladed impellers for any blade angle from 0° to 90°.

Keywords: centrifugal impellers, slip factor, eddy-induced slip

1 INTRODUCTION

Paeng and Chung [1] presented a relatively simple correlation for relative-eddy-induced slip factor in centrifugal impellers. The derivation is based on finding the radius of a circular relative eddy tangent to adjacent vanes and the rotor rim. The flow in the eddy is assumed to be non-rotating. It rotates backwards relative to the rotor through one revolution for each rotor revolution. Figure 1 shows such an eddy in one of the blade passages. The ratio of the slip velocity along the eddy circumference, Δw_e, to the rotor rim speed, U_e, is then the same as the ratio, α, of the eddy diameter to the rotor diameter. This is a development of an idea proposed by Stodola [2]. The α-ratio is a function of the impeller geometry in terms of the number of blades, Z, the blade angle, β, and the blade shape (Fig. 1). Since logarithmic spiral blades are assumed, it does not matter at which radial position the blade angle is measured. To correct for the inaccurate assumption that the slip velocity along the eddy circumference is equal to that at the rotor rim speed, Paeng and Chung [1] introduced the correction factor, f, into the slip factor equation, giving

$$\sigma = \frac{1 - \Delta w_e}{U_e} = 1 - f\alpha$$

In order to obtain agreement with the analytical data of Visser *et al.* [3], who recalculated the original data of Busemann [4], they developed an empirical expression for $f = f(z, \beta_e)$, using three additional auxiliary functions, containing exponential functions of Z. In the end, they achieved excellent agreement with the analytical data of Visser *et al.* [3].

Reprogramming the method of Paeng and Chung [1] indicated a difference in slip factor of 0.005 for $Z \geqslant 2$ and 0.002 for $Z \geqslant 4$, compared with Busemann values [4] calculated by Hassenpflug (2004, personal communication). Not surprisingly, unrealistic values were obtained for $Z = 1$ when using reference [1], as it is not possible to conceive of a circle tangent to both sides of the single blade and to the rotor rim.

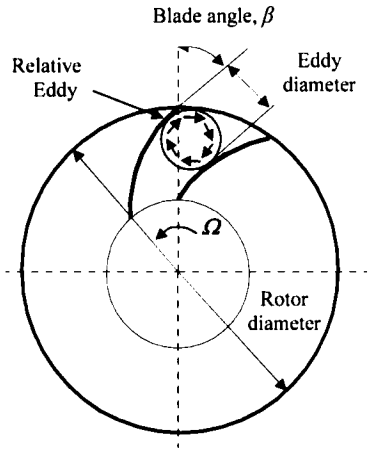

Fig. 1 Centrifugal impeller blade passage with relative eddy as proposed by Paeng and Chung [1]

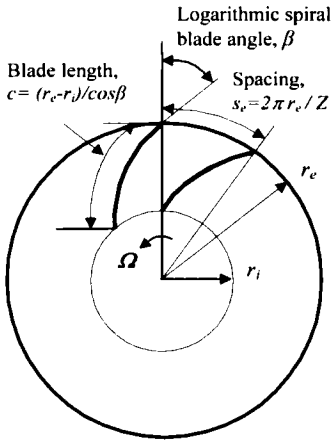

Fig. 3 Centrifugal impeller blade notation for logarithmic spiral blades

2 SINGLE RELATIVE EDDY APPROACH

Another new, approximate method for the derivation of relative-eddy-induced slip in centrifugal impellers has recently been presented [5]. The new assumption is that the eddy-induced slip is determined not by one eddy per blade channel as proposed by Paeng and Chung [1], Stodola [2], and others, but by only one relative eddy in the whole rotor: it revolves around the axis and protrudes into the blade passages, and when it forms separate cells associated with each blade passage, these cells are included in the main cell centred on the rotor axis. Figure 2 shows the eddy-induced flow moving through the control volume. With reference to its most distinguishing feature, it was called the single relative eddy (SRE) method [5].

The complete derivation is given by von Backström [5], but the major assumptions are described briefly below. The two-dimensional flow field in the rotor has vorticity relative to the rotor equal to twice the rotor angular velocity, Ω. The vorticity ω causes an induced circulation velocity Δw along the blade surfaces S and along the rotor rim. The integral $\int \Delta w \, dS$ is known as the circulation, and it is equal to the product of the vorticity (assumed constant over the rotor area) and the rotor area between and inside the blades (Fig. 2). The slip velocity normalized by the rotor rim speed is then derived as

$$\frac{\Delta w_e}{U_e} = \frac{1}{1 + F(c/s_e)}$$

where F is a coefficient that depends on the impeller geometry.

Slip factor is defined as one minus the normalized slip velocity

$$\sigma = 1 - \left(\frac{\Delta w_e}{U}\right) = \frac{1 - 1}{[1 + F(c/s_e)]}$$

F is the sum of the average circulation velocities Δw_s and Δw_p along the blade suction and pressure surfaces, divided by the average circulation velocity along the exit boundary, Δw_e. Because the exact velocity distributions along the blade surfaces and along the rotor outer rim are not known, an expression for the coefficient F must be found to give good agreement with Busemann [4] or with experimental data.

When applied to impellers with notation for logarithmic spiral blades (Fig. 3), to correspond with the analyses of Paeng and Chung [1] and

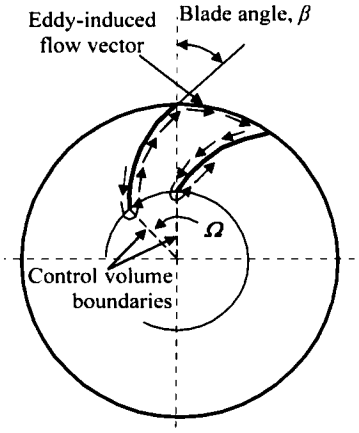

Fig. 2 Centrifugal impeller blade passage with part of singular relative eddy

Busemann [4], the solidity c/s_e is

$$\frac{c}{s_e} = \frac{(r_e - r_i)/\cos\beta}{(2\pi\, r_e)/Z} = \frac{(1 - \mathrm{RR})Z}{2\pi\,\cos\beta}$$

where RR is the ratio of impeller inner radius r_i to outer radius r_e, and β is the blade angle.

3 DEPENDENCE OF F ON BLADE ANGLE

The objective of this paper is to present a series of equations that will represent the Busemann values for slip factor as defined earlier with increasing accuracy. RR is fixed at a typical average value of 0.5 in deriving the SRE approach and also assumed that when using the derived equations for slip factor, the value of radius ratio is taken as RR = 0.5 when RR < 0.5. These assumptions enable one to calculate values of slip factors for all combinations of Z and β and compare them with the corresponding Busemann values for RR = 0.

It has been shown [5] that the equation: $F_1 = F_0 (\cos\beta)^{0.5}$, with $F_0 = 5$, represents the Busemann slip factors measured from graphs of Wiesner [6] well enough. Figure 4 compares the SRE slip factor for F_1 with Busemann slip factors from Hassenpflug (2004, personal communication). The lines of constant solidity are also shown. It is apparent that the equation presents the Busemann data accurately when the solidity exceeds 0.5 and the blade angle is <70°. The agreement can be slightly improved, however, if the exponent in the equation is changed from 0.5 to 0.45 (to give the equation for F_2): the higher angle limit is then increased to 80° (Fig. 5).

When the required value of F for perfect agreement with Busemann is plotted against β for various blade numbers (Fig. 6), it appears that $F_3 = 2 + 3\cos\beta$ should lead to good agreement for four or more blades and blade angles up to 85°. It can be shown that $F = 2$ is the only appropriate value when β equals 90°. The reason is that blades oriented at 90° do not deflect the flow, and the flow inside and outside the rotor blades remains stationary in the absolute frame. The relative velocities over the blade suction and pressure sides are then equal, and they are both equal to the relative velocity along the rotor rim (the slip velocity) and $F = (\Delta w_e + \Delta w_e)/\Delta w_e = 2$. This means that F_3 should lead to good agreement right up to $\beta = 90°$. Inserting F_3 into the SRE then leads to Fig. 7, which shows excellent agreement (within 0.005) with Busemann, for $Z \geqslant 2$ and $c/s_e > 0.5$, and good agreement (within 0.03) for $Z \geqslant 1$ and $c/s_e > 0.25$.

Agreement between SRE and Busemann slip factors can be further improved for low blade numbers if a more accurate approximation for F in Fig. 6 can be found. Such an expression is

$$F_4 = 2 + \left[2.7 + \left(\frac{3}{Z}\right)\cos\beta\right]\cos\beta$$

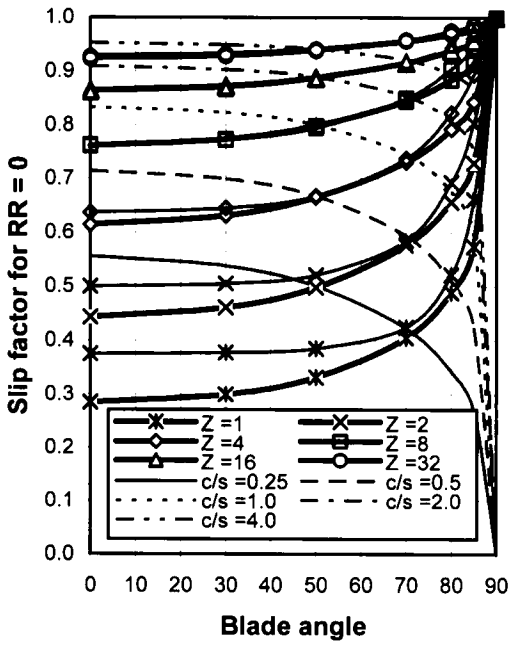

Fig. 4 SRE slip factor for $F_1 = 5\ (\cos\beta)^{0.5}$ compared with Busemann

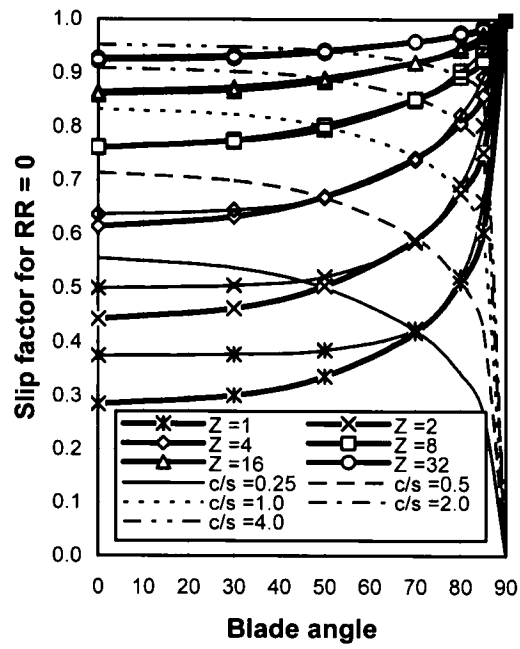

Fig. 5 SRE slip factor for $F_2 = 5\ (\cos\beta)^{0.45}$ compared with Busemann

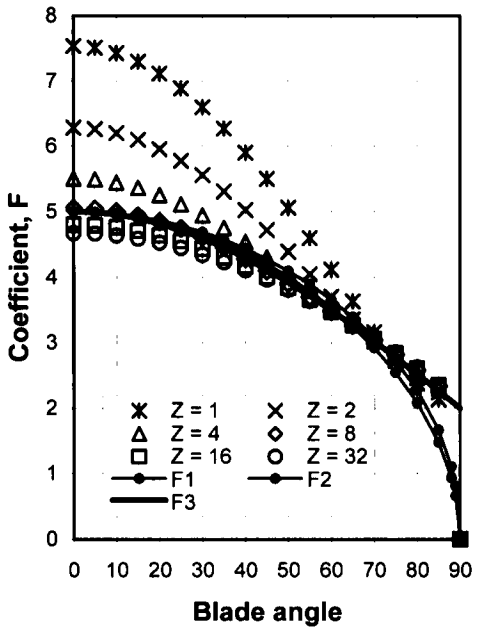

Fig. 6 F_1, F_2, and F_3 compared with required values of F for agreement with Busemann

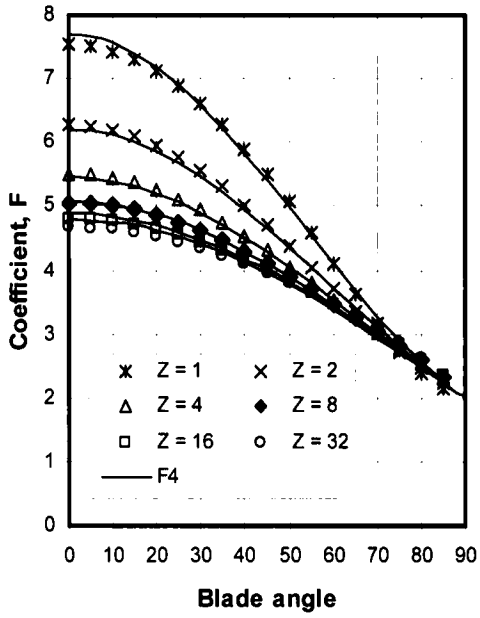

Fig. 8 F_4 compared to required values of F for agreement with Busemann

Figure 8 compares F_4 values with the set of required values from Fig. 6. The agreement between SRE and Busemann slip factors is much better than for F_3, especially for low blade numbers. Figure 9 compares slip factors calculated with F_4 with the Busemann values. Agreement with the Busemann slip factors is within 0.005 for $Z > 2$ and within 0.003 for $Z \geqslant 4$. For $Z = 1$, agreement is within 0.02. When using F_4, there is no lower solidity boundary below which the accuracy deteriorates appreciably. The complete equation for slip factor with F_4 in its fundamental form is

$$\sigma = 1 - \frac{1}{1 + \left[2 + \left(2.7 + \frac{3}{Z}\cos\beta\right)\cos\beta\right]\left(\frac{(1 - \mathrm{RR})Z}{2\pi\cos\beta}\right)}$$

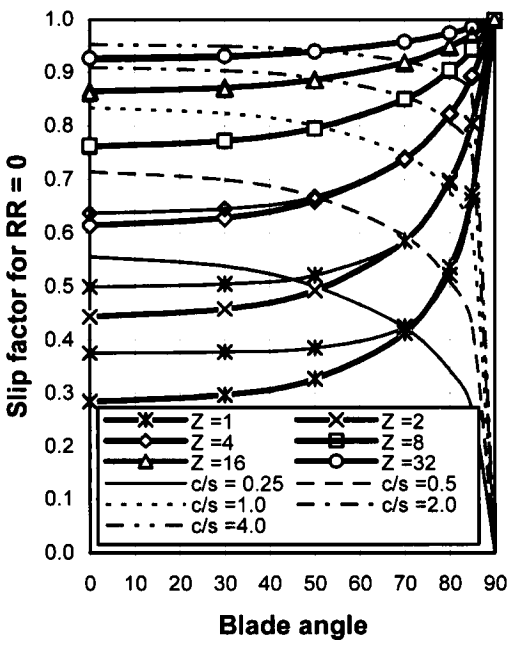

Fig. 7 SRE slip factor for $F_3 = 2 + 3\cos\beta$ compared with Busemann

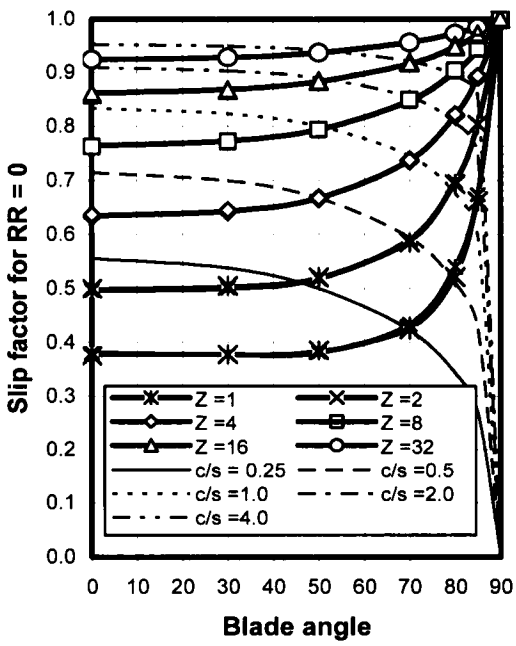

Fig. 9 SRE slip factor for $F_4 = 2 + [2.7 + (3/Z)\cos\beta)]\cos\beta$ compared to Busemann

It should be used with RR taken as 0.5 when RR < 0.5. When RR > 0.5, the SRE method automatically predicts a reduction in the slip factor as RR approaches 1.0, but the SRE predicted values deviate from those of Busemann [4] and the method is not recommended for RR > 0.6. This aspect needs to be investigated further, but meanwhile, the methods of Paeng and Chung [1] or Wiesner [6] may also be considered to model the effect of RR, although they have not yet been proved to agree well over the full range of the Busemann data either.

An advantage of the compact, SRE equation above is that it can be inverted to find explicitly the number of rotor blades for a required slip factor, without iteration

$$Z = \frac{[\sigma/(1-\sigma)(2\pi \cos \beta/1 - \mathrm{RR}) - 3\cos^2 \beta]}{2 + 2.7 \cos \beta}$$

Like the method of Paeng and Chung [1], the SRE approach represents Busemann's slip factor data with an accuracy of appreciably less than a percentage point, for all impellers with two or more blades. The Paeng and Chung [1] method, however, gives completely unrealistic values for $Z = 1$, where the more compact SRE method is accurate to within two percentage points. Agreement between the relatively simple SRE method and Busemann may be further improved by better curve fits for F, but at the price of increased complexity.

4 CONCLUSIONS

New equations for the coefficient F in the singular relative-eddy method for the prediction of relative-eddy-induced slip factor in centrifugal impellers are presented. Very good agreement with the accurate analytical method of Busemann is obtained over a wide range of blade numbers and blade angles from 0 to 90°. It agrees to within 0.003 for four blades or more and to within 0.02 for one blade. The SRE approach with RR taken as 0.5 when RR < 0.5, combined with the relatively simple expression $F_4 = 2 + \{2.7 + (3/Z)\cos \beta\}\cos \beta$, is recommended as a compact method for the calculation of the eddy-induced slip factor of all impellers with RR < 0.6. For high solidity impellers, the use of the very simple expression $F_3 = 2 + 3 \cos \beta$ is recommended.

REFERENCES

1 **Paeng, K. S.** and **Chung, M. K.** A new slip factor for centrifugal impellers. *Proc. Instn Mech. Engrs, Part A: J. Power and Energy*, 2001, **215**, 645–649.

2 **Stodola, A.** Steam and gas turbines with a supplement on the prospects of the thermal prime mover, 1945, pp. 1259–1260 (Imprint, New York) (authorized translation from the sixth German edition by Louis C. Loewenstein, reprinted by Peter Smith).

3 **Visser, F. C., Brouwers, J. J. H.,** and **Badie, R.** Theoretical analysis of inertially irrotational and solenoidal flow in two-dimensional radial-flow pump and turbine impellers with equiangular blades. *J. Fluid Mech.*, 1994, **269**, 107–141.

4 **Busemann, A.** Das Förderhöhenverhältniss Radialer Kreiselpumpen mit Logarithisch-Spiraligen Schaufeln. *Zeitschrift fur Angewandte Mathematik und Mechanik*, 1928, **8**, 371–384.

5 **von Backström, T. W.** A unified correlation for slip factor in centrifugal impellers. *ASME J. Turbomach.*, 2006, **128**, 1–10.

6 **Wiesner, F. J.** A review of slip factors for centrifugal impellers. *Trans. ASME J. Eng. Power*, 1967, **89**, 558–572.

APPENDIX

Notation

c	blade camber line length
dS	incremental distance
f	correction factor
F	coefficient
r	impeller radius
RR	impeller inner-to-outer radius ratio (r_i/r_e)
s	blade spacing
S	distance along edge of flow domain
U	rotor rim speed
Z	number of blades
α	eddy-to-rotor diameter ratio
β	blade angle at rotor periphery (from radial direction)
Δw	eddy-induced circulation velocity
σ	slip factor
ω	vorticity
Ω	rotor angular velocity

Subscripts

e	exit (outer radius)
i	inlet (inner radius)
p	pressure
s	suction
0 to 4	designations of equations for F

Fundamentals of four-quadrant axial flow compressor maps

A Gill, T W von Backström*, and **T M Harms**
Department of Mechanical Engineering, University of Stellenbosch, South Africa

The manuscript was received on 4 August 2006 and was accepted after revision for publication on 5 June 2007.

DOI: 10.1243/09576509JPE354

Abstract: The current paper describes the experimental determination of a complete four-quadrant map for a three stage low-speed axial flow compressor. Non-dimensional pressure rise and torque coefficients and efficiency characteristics were determined. Six possible modes of operation were identified in the four quadrants. The characteristic for a compressor with a rotational speed of zero rpm, in terms of pressure rise coefficient and flow coefficient, is S-shaped and forms the dividing line between two alternate modes of operation which exist in the second and fourth quadrants. First quadrant operation is only possible during positive rotation, and third quadrant operation during negative rotation, as the zero-speed S-curve passes through the origin and so does not pass through these quadrants. Consequently, only one mode of operation is possible in each of these two quadrants. A system of notation for describing the various modes of operation has also been developed. Second quadrant operation for positive compressor rotation, and fourth quadrant operation with negative rotation are highly dissipative conditions of operation. First and third quadrant operation are compressor-like modes. Second quadrant negative rotation and fourth quadrant positive rotation operation are turbine-like modes.

Keywords: axial flow compressor, four-quadrant mapping, reverse flow, reverse rotation

1 INTRODUCTION

Axial flow compressors are widely used in process plants and gas turbine engines. Conditions such as surge and the windmilling of aircraft engines cause the mass flow rate through the compressor to differ significantly in magnitude and direction from design-conditions. Axial flow compressors have also been proposed for use in nuclear powered closed cycle gas turbine power-generation schemes such as the pebble bed modular reactor [**1**]. As the safety of all such applications is an important consideration, it is desirable to determine how the various components which will make up these system would respond to various scenarios corresponding to possible malfunctions of the system, such as flameout for aircraft engines, or pressure vessel or pipe ruptures for process applications or closed cycle power generation. Such conditions may be entirely unlike normal operating conditions, as phenomena such as reverse flow and negative pressure difference along the machine may occur. In addition, the compressor may be driven as a turbine in either the usual or the reverse direction. The aim of present investigations is to determine the possible modes of operation in all four quadrants of the compressor map for an axial flow compressor.

First quadrant operation of axial flow compressors has been extensively explored experimentally, as the usual operating regime of these machines occurs in this region. The most notable off-design phenomena in this quadrant are compressor stall and surge. The former places a limit on the pressure-ratio attainable in an axial flow compressor, and the latter occurs when the limit of stable operation of a compressor operating in a specific system is reached. Day [**2**] and Moore and Greitzer [**3**, **4**] provide the most commonly cited explanations of the mechanisms for these phenomena. A more complete description of these phenomena would be beyond the scope of the current article.

Considerably less work has been done on experimental mapping or numerical prediction of performance in the other three quadrants. Some experimental work on backflow, that is compressor

**Corresponding author: Department of Mechanical Engineering, University of Stellenbosch, Private Bag X1, Matieland 7602, South Africa. email: twvb@sun.ac.za*

operation in part of the second quadrant, has been presented by Gamache [**5**] and subsequently by Gamache and Greitzer [**6**]. A three-stage, non-repeating, high hub-to-tip ratio low-speed compressor was used for these investigations. Two different builds were investigated to determine whether the degree of reaction of the machine had a significant effect on flow in the second quadrant. Non-dimensional pressure rise and torque coefficient reverse flow characteristics were found to be virtually identical for both builds, however. The operational regime of this compressor has a similar design mass flowrate and rotational speed, and has the same number of stages as the compressor used for this investigation, although chord length and blade tip diameter are about 50 per cent larger, and rotor-chord relative Reynolds numbers are higher. Time-dependent velocity and total pressure measurements were taken before and after each blade row and static pressure at the casing at these positions. The results obtained indicated that flow in a compressor operating in this quadrant is dominated by three-dimensional effects, and large radial velocity components.

A fundamental distinction that plays a part in the discussions to follow is the one between a compressor (or fan, or pump) and a turbine. The fundamental difference is that compressors work on the flow, while turbines extract work from the flow. The distinction is made on the basis of whether the torque applied to the rotor by the drive shaft is in the direction of rotation (compressors) or against it (turbines). This implies that the angular momentum increase of the flow is either in the direction of rotation (for compressors) or in the opposite direction (for turbines). It should be stressed that a machine designed as a compressor can, in principle, operate as a turbine and vice versa.

Bammert and Zehner [**7**] obtained a complete four-quadrant non-dimensionalized turbine map for a single axial flow turbine stage, and then proceeded to attempt to map a multi-stage turbine, as described in Bammert and Zehner [**8**]. Although the investigations were performed on a turbine, the studies have significance in the present work, as the laboratory compressor operated as a turbine for some of the modes of operation that were investigated during this study. It is also the most complete investigation of four-quadrant operation of an axial flow turbomachine known to the authors to date.

2 QUADRANTS AND OPERATION MODES

Every turbomachine has a preferred (design) direction of rotation, a preferred flow direction, and a preferred sign (+ or −) associated with the pressure difference across it. The normal operation of a compressor is confined to the positive direction of rotation, and a performance characteristic is represented as a graph of a positive pressure rise versus a positive flowrate. Consequently, when plotted on a graph with both positive and negative flow and pressure coefficient values, such a characteristic occurs in the first quadrant of the graph.

Turbomachines can, however, be forced to operate at various combinations of direction of rotation, flow direction, and pressure rise. This means that at they can, in principle, operate in each of the four quadrants of the general graph. There are $2^3 = 8$ combinations of positive and negative flow, pressure rise, and rotational speed, but there are only four quadrants. It is thus clear that more than one mode of operation will occur in at least some quadrants. To begin to understand which of the above combinations will occur in which quadrant, a non-rotating compressor (rotational speed $N = 0$) is to be first-considered. In the following discussion incompressible flow is assumed, to explain the concepts without adding unnecessary complications.

When the compressor rotational speed $N = 0$, the compressor will do no work and a positive flow, C_x, will result in a negative pressure rise, ΔP, since the exit pressure will be lower than the inlet pressure. The negative pressure rise increases in magnitude as $\Delta P_4 = 1/2 \cdot \rho \cdot K_4 \cdot C_x^2$, where C_x is the average axial velocity at the inlet to the first stage of the compressor. The subscripts denote that the compressor will work in the fourth quadrant, where the flow is positive and the pressure rise is negative. Consequently K_4 is a negative constant. Conversely, a negative flow will result in a positive pressure rise, such that $\Delta P_2 = 1/2 \cdot \rho \cdot K_2 C_x^2$, with K_2 a positive constant. Also note that $\Delta P = 0$ when $C_x = 0$, for any value of K, thereby precluding operation in the first or third quadrant (except at the origin of the coordinate system). It is thus evident that a non-rotating compressor can operate only in the second and fourth quadrants and only along an S-shaped curve (rotated through 90° anti-clockwise, passing through the origin of the coordinate system) as shown in Fig. 1.

The region to the right and above the zero-rotation S-curve can only be accessed under the condition of positive compressor rotation, as only then, the pressure of the fluid can be increased at constant flow, or the flow can be increased against a fixed pressure difference. When the rotor turns in the positive direction ($N > 0$), the compressor may operate in the first, second, or fourth quadrants. Similar arguments relate negative rotation to the area to the left and below the S-curve.

If the compressor rotates in the positive direction, it will add energy to the flow, and the operating point will be to the right and above the zero-rotation S-curve. As the throughflow speed increases, the area of positive pressure rise will increase. This area, situated in the

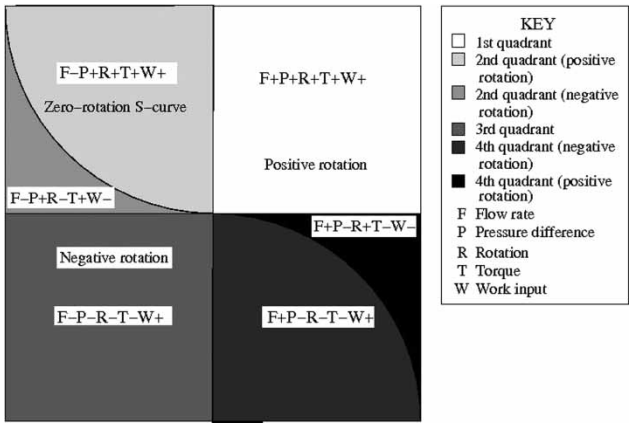

Fig. 1 Generic four quadrant compressor map

first quadrant, is the normal operating map of the compressor, but it includes the region where the compressor is stalled. The compressor cannot, however, operate in the third quadrant when $N > 0$. To operate there, the rotational speed must be negative. Conversely, the compressor cannot operate in the first quadrant when $N < 0$.

The preceding discussion can be summarized as follows.

1. Zero rotational speed in a compressor results in operation in either the second or the fourth quadrant along a line in the form of an S-curve rotated anti-clockwise through 90° and passing through the origin, as shown in Fig. 1.
2. Positive rotational speed in a compressor results in operation in the first, second, or fourth quadrant in a region to the right of and above the zero-speed S-curve.
3. Negative rotational speed in a compressor results in operation in the second, third, or fourth quadrant in a region to the left and below the zero-speed S-curve.

Since the S-curve divides the second and fourth quadrants into two parts each, the four quadrants can accommodate six operational modes. Two of the eight possible combinations are thus eliminated. They are third quadrant operation at positive rotor speed and first quadrant operation at negative rotor speed.

A notation scheme is required to unambiguously denote the mode of operation of the compressor. The scheme developed to designate the various measurement configurations will now be described. The letters F, P, R, and T indicate flow, pressure rise, rotation, and torque respectively, and each may be followed by a plus (+) or a minus (−) sign, indicating whether the particular running condition of the compressor is positive or negative. For example, $F+P+R+T+$ denotes the normal compressor mode of operation where flow, pressure rise, rotation, and torque are positive. A positive torque is defined as one applied in the design direction on the compressor input shaft by the motor, or one applied on the motor by the compressor to the input shaft in the opposite direction.

Power input (symbol W) could also have been used as one of the primary running conditions. However, non-zero torque values occur at zero rotation speed, which is not the case for power. The sign of the power output running condition is defined as the product of the signs of R and T. This convention was chosen to agree with normal compressor practice, even though it disagrees with normal thermodynamic practice where the positive sign is reserved for work output. Table 1 shows designations for all six modes of operation. Although it is redundant, the sign of W is also given in Table 1, as it is useful for determining whether the experimental setup for a given mode must allow for operation as a compressor or turbine. Note that all running condition indicators are positive in the first quadrant.

3 TEST FACILITY

3.1 The compressor test bench

The Rofanco laboratory compressor is a three-stage axial flow compressor supplied by the Royston Fan Co. Ltd. The compressor operates a design speed of

Table 1 Compressor running condition indicators

Quadrant	Running condition	Description
First quadrant	$F+P+R+T+W+$	Normal operation (beyond stall included)
Second quadrant (right of S-curve)	$F-P+R+T+W+$	Compressor pushing against auxiliary fans, but backflow occurs
Second quadrant (left of S-curve)	$F-P+R-T+W-$	Compressor running backwards as turbine under backflow conditions
Third quadrant	$F-P-R-T-W+$	Compressor running backwards as compressor, under backflow conditions
Fourth quadrant (left of S-curve)	$F+P-R-T-W+$	Compressor running backwards, sucking against auxiliary fans under positive flow
Fourth quadrant (right of S-curve)	$F+P-R+T-W-$	Compressor running forwards as turbine

3000 rpm, with a design massflow of 2.7 kg/s, and a nominal total-to-total pressure ratio of 1.022. The entire operating range of the compressor occurs within the incompressible regime, the first stage rotor having a relative blade-tip Mach-number of 0.2 when operating at design point. The relative blade tip Reynolds number at which tests were conducted was 1.25×10^5. The compressor has 43 rotor blades and 41 stator blades per stage. All stages are repeating and identical. It is fitted with NACA-65 blades with the outflow from the stator blade rows is in the axial direction. The compressor has constant hub and casing diameters of 300 and 420 mm. The nominal blade length is 60 mm and the blade chords are 30 mm. The parameters defining the blades are given in Table 2. Spacing between rotor and stator rows in each stage is 22 mm at the mean radius, which is identical to the inter-stage spacing. This is large compared with most commercial compressors (73 per cent of the chord length) to allow the insertion of sensors for research purposes. There are no inlet or exit guide vanes. A section through the compressor is shown in Fig. 2.

The drive system consists of a direct current motor with a thryristor control system. Two air bearings support the motor in such a way that it can pivot freely about its main axis, for the purposes of torque measurement. The motor cooling fan exhausts air through an attached duct fitted with an axially aligned honey comb grid to ensure that the cooling air is swirl-free and does not exert a torque on the motor.

The flow at the compressor exit is exhausted to a venturi meter. Under normal operating conditions the flow is varied by means of an adjustable disc throttle fitted to a threaded spindle at the exit of the diffuser. The throttle is adjustable by rotating it along the spindle, supported by a three-legged spider.

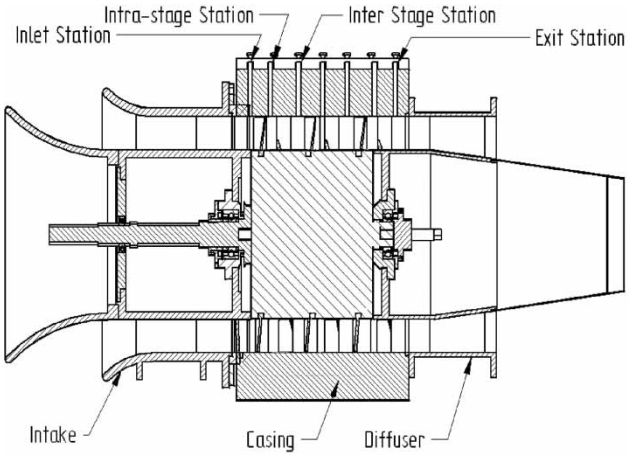

Fig. 2 Cross section of the compressor used in the investigation

3.2 The auxiliary fan

An auxiliary fan can be employed to help or oppose the flow through the compressor, and it can be done when the compressor is running forwards or backwards. The auxiliary fan used for these tests was a 483 mm diameter two-stage, contra-rotating Woods axial flow fan, driven by two 4.1 kW induction motors. The speeds of both stages of the contra-rotating fan were variable by means of a single frequency control system up to 55 Hz, giving maximum fan speeds of 3170 rpm. Figure 3 shows such a layout schematically.

3.3 Instruments and measurement uncertainty

The rotational speed of the axial-flow compressor was measured by means of a 60-tooth wheel and a magnetic transducer, coupled to a frequency counter. Readings were supplemented by a handheld-tachometer, when it was found that the electromag-

Table 2 Rotor and stator blade row descriptions

Blade section radial position (mm)	Blade profile stagger angle (°)	Blade profile camber angle (°)	Blade row solidity	Blade profile maximum thickness-chord ratio	Maximum camber position (fraction of chord)
Rotor					
150.0	38.00	31.04	1.3051	0.10	0.5
165.0	45.00	23.48	1.1864	0.10	0.5
180.0	49.40	17.93	1.0876	0.10	0.5
195.0	53.00	13.85	1.0039	0.10	0.5
210.0	56.10	10.90	0.9322	0.10	0.5
Stator					
150.0	20.38	46.28	1.3687	0.10	0.5
165.0	18.18	43.39	1.2443	0.10	0.5
180.0	16.61	41.05	1.1406	0.10	0.5
195.0	14.90	40.57	1.0529	0.10	0.5
210.0	14.32	40.00	0.9777	0.10	0.5

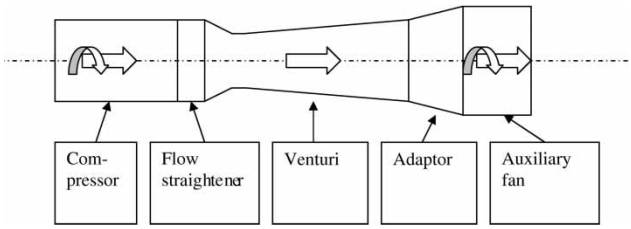

Fig. 3 Schematic diagram of the four quadrant compressor test set-up

netic interference generated by the 3-phase variable speed drive system for the motors of the contra-rotating fans had a detrimental effect on the accuracy of readings from this instrument. The discrepancy between the readings of the two instruments was less than 3 rpm, when no electromagnetic interference was present.

Torque acting on the compressor was measured by means of an HBS 350 load-cell with a nominal load capacity of 20 kg. The combined linearity and hysterisis error for the load-cell was 0.03 per cent of its rated output. The load-cell was connected to a HBM Scout-55 bridge-amplifier. The load-cell is attached to a 320 mm long arm mounted on the side of the compressor motor. The motor housing floats on air-bearings which are concentric to the compressor-shaft, allowing the motor to rotate freely due to the torque generated. The air-bearings also serve to decrease the amount of vibration transmitted to the load-cell. The torque measurement system was calibrated *in situ* for positive and negative torque, using weights.

Static pressure readings were obtained by connecting pressure-transducers to pressure-tappings in the compressor-casing at the compressor inlet, immediately ahead of the first stage, between stages and at the exit, or after the last stage.

A bank of four AutoTran incorporated 705D-215 differential pressure-transducers were used to obtain all the relevant pressure measurements. The transducers each have an input range of 2 kPa, an output range of 10 V, an accuracy of 0.75 per cent FSO. and a temperature-sensitivity of 0.01 °C. All the pressure-transducers had one port connected to their respective pressure-tappings and one open to the atmosphere. The maximum pressure difference recorded during testing was 1.5 kPa, thus the input range of the pressure-transducers was adequate. The pressure-transducers were calibrated by comparison to a Betz water micromanometer. Atmospheric pressure was measured by means of a mercury manometer. All pressures were referenced to the atmospheric pressure. Air temperature was measured at the compressor inlet by means of a T-type thermocouple.

An axial flow turbine-type vaned anemometer which has a tip diameter approximately equal to the throat diameter was fitted in the venturi throat and calibrated for flow in both directions by comparison with a calibrated pitot tube that was traversed across the throat section.

Data was recorded by means of a Hewlett-Packard 34970A 22-channel data logger, which recorded voltages accurate to 10^{-5} V and temperature to 0.1 K. Due to the limitations of this device and the fact that all testing occurred under steady state conditions, sampling frequencies of 1 and 2 samples per second were used.

In order to demonstrate repeatability and precision, the standard deviations were calculated for time-averaged inlet and outlet static pressure readings, volumetric flowrate, and torque for three tests conducted in the first quadrant with a fully open throttle valve at 2400 rpm, with a flow coefficient of approximately 0.567 and a static pressure coefficient of 0.724. The standard deviation values obtained, expressed as percentages of the mean values were 3.1, 1.2, 1.8, and 2.8 per cent, respectively. The large value for inlet pressure can be partially ascribed to the variation of atmospheric conditions between the days on which tests were conducted.

Zero-readings were also recorded before and after testing to ensure that no drift or instrument bias affected results, and to check calibration. All instruments were recalibrated regularly between tests.

3.4 Modifications for negative pressure rise, negative rotation, and backflow

As the compressor inlet was always open to atmospheric pressure, the exit pressure was above atmospheric under normal conditions but below atmospheric under conditions of suction at the compressor exit (fourth quadrant operation), or when running the compressor backwards under power (third quadrant operation).

The direction of motor rotation was reversed by swapping the field winding power-supply wires of the direct current motor between the drive system and the motor. It was also necessary to swap the wires between the drive system speed monitor and the control system, to prevent positive feedback, resulting in motor runaway.

To handle backflow, the venturi meter containing the vaned anemometer and upstream flow straightener were turned around so as to eliminate any errors that reverse flow through the venturi meter might cause. The compressor had honeycomb flow straighteners at either end, therefore the inlet flow direction was always axial, irrespective of flow direction.

In the positive (normal) flow direction the exit flow was also close to axial because each row of stator blades was designed to have an axial exit flow angle. In the negative flow cases, however, the flow direction

could deviate substantially from the axial direction because the compressor had no inlet guide vanes, since it was designed for axial flow into the rotors.

The system also had to be modified to operate in the turbine mode under conditions of positive and negative rotation. In this case, the drive system was replaced by a resistor and a Variac variable resistor, coupled across the field windings of the motor. The purpose of the resistor was to dissipate the power produced by the motor, which was being driven as a dynamo. The amount of electromagnetic braking could be controlled by adjusting the Variac.

4 NON-DIMENSIONALIZATION OF FOUR-QUADRANT DATA

The performance of a turbomachine operating in the incompressible flow regime may be expressed in terms of the non-dimensional flow, pressure, and torque coefficients. Reynolds number insensitivity in the testing range was demonstrated by comparing non-dimensionalised first quadrant characteristics measured at 2100, 2400, 2700, and 3000 rpm. In this paper, the flow coefficient ϕ is expressed as $\phi = C_x/|U|$, where C_x is the average axial velocity at the inlet of the first stage of the compressor, and U is the rotor blade tip speed. It should be noted that the direction of U is disregarded, in order to keep the sign of the flow coefficient and the volumetric flowrate the same during negative rotation, for the purpose of clarity. The static-to-static pressure coefficient ψ is defined as follows: $\psi = (P_2 - P_1)/(1/2\rho U^2)$ where P_2 and P_1 are static pressures at the outlet and inlet, and ρ is the density of the working fluid at the compressor inlet. The torque required to drive the compressor at a certain speed may be non-dimensionalized as the torque coefficient [**6**] $\psi_\tau = T/(1/2\rho r_{\text{tip}} A U^2)$ in which T is the drive shaft torque, and r_{tip} is the inlet tip radius of the first stage rotor row. The torque coefficient may be obtained by dividing the denominator and numerator of the power coefficient $\psi_{\text{p}} = \omega T/(1/2\rho A U^3)$ by the angular velocity of the rotor, and is thus equivalent to the power coefficient for first quadrant operation; the torque coefficient is, however, more suitable for the manipulation necessary to calculate the non-dimensional zero-rotation torque characteristic, as described in the next section.

5 EXPERIMENTAL RESULTS

5.1 Zero rotation speed S-curves

To determine the location of the S-curve, the compressor rotor was locked in a stationary position relative to the casing, and the flow forced through it in a positive and a negative direction. The measured S-curve can be approximated with two parabolic curves of the form $\Delta P = 1/2 \cdot \rho \cdot K \cdot C_x^2$. Because the rotor tip speed U for these characteristics is zero, the non-dimensional flow and pressure coefficient cannot be calculated directly. However, by dividing both sides of the equation by $1/2\rho U^2$ the following relationship is obtained: $\Delta P/(1/2 \cdot \rho U^2) = K \cdot C_x^2/U^2$, which, from the definition of the non-dimensional pressure rise and flow coefficients can be rewritten as $\psi = K \cdot \phi^2$. An average value for K is then determined from experimental data for pressure difference and axial velocity. The parabolic characteristic may then be constructed by calculating values for ψ for a range of values of ϕ using the average value determined for K. The steeper curve in the second quadrant indicates that the stationary compressor offers more resistance to back flow than to forward flow. The resulting static-to-static pressure rise coefficient S-curve is shown as a solid line in Figs 4 and 5.

The torque coefficient S-curve is shown in Figs 6 and 7. Its two parts are also parabolic, since the change in the angular momentum of the flow passing through the rotor is proportional to the mass flow times the circumferential deflection of the flow. The torque coefficient characteristic is determined by means of the same manipulation as the static pressure rise coefficient characteristic.

In the rest of the discussion, reference to the S-curve will indicate the pressure rise coefficient curve, except when otherwise indicated.

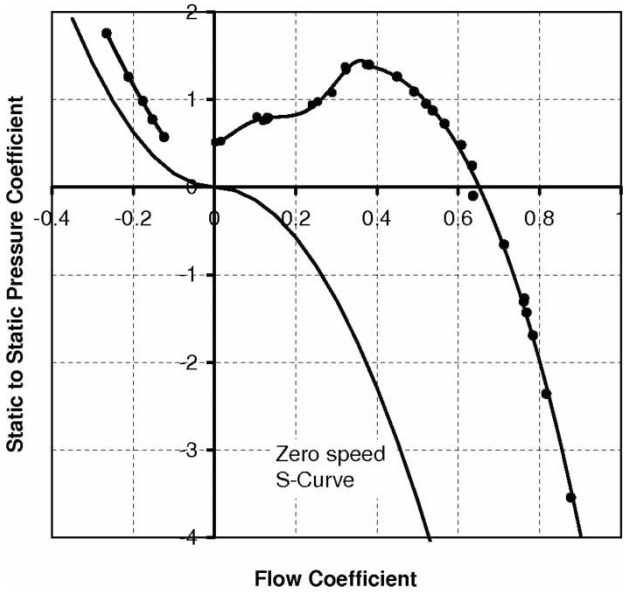

Fig. 4 Static-to-static pressure coefficient characteristic for positive rotation

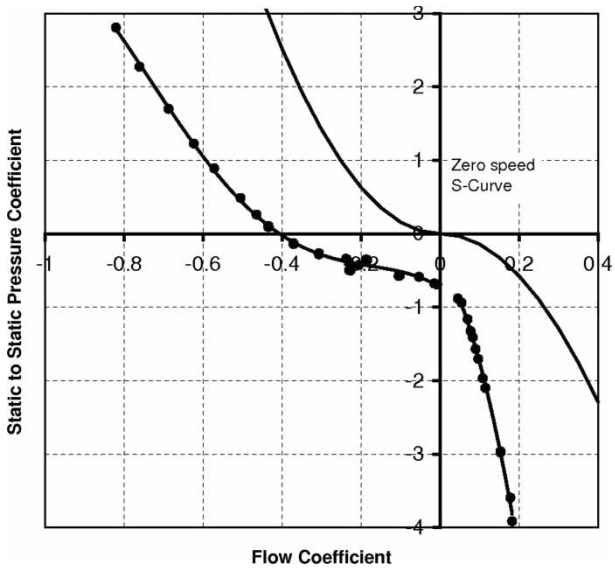

Fig. 5 Static-to-static pressure coefficient characteristic for negative rotation

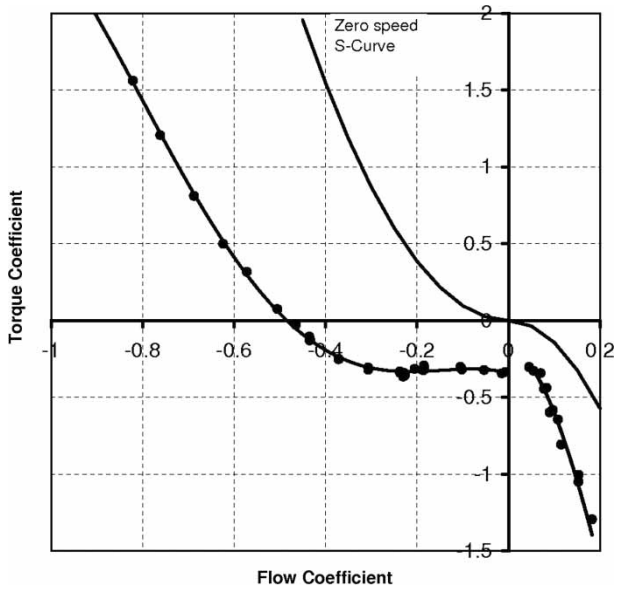

Fig. 7 Torque coefficient characteristic for negative rotation

5.2 First quadrant ($F + P + R + T + W+$)

First quadrant compressor operation may be in the unstalled or stalled condition. The compressor speed of rotation is positive. The conventional operating range of the compressor was accessed by adjustment of the throttling valve. The auxiliary fan was required to access the region far from the y-axis where the system resistance was too high.

All results have been non-dimensionalized in terms of the flow, pressure rise, and torque coefficients. The first quadrant static-to-static pressure rise coefficient characteristic is shown in Fig. 4. The first part of the compressor characteristic is the region between the stall point and the x-axis. The characteristic in this region is of a similar shape to that obtained for other compressors of this class, such as that of Gamache and Greitzer [**3**]. The second part of the first quadrant curve is in the stalled region. In addition to the points obtained by throttling the compressor, some points were obtained by running the auxiliary fans in opposition to the compressor, but with the flow still in the positive direction. These points are also shown in Fig. 4.

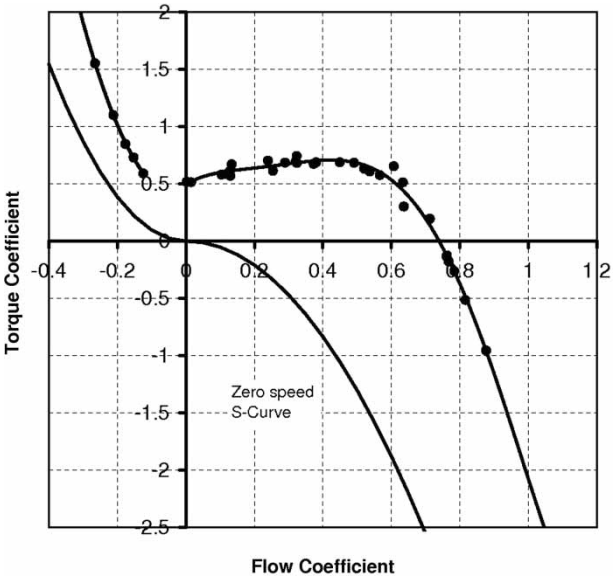

Fig. 6 Torque coefficient characteristic for positive rotation

The first quadrant torque coefficient (Fig. 6) curve resembles the pressure rise characteristic (Fig. 4) in shape. The peak static-to-static efficiency of 80 per cent (Fig. 8) is lower than would be expected for this type of machine. The corresponding total-to-total efficiency for this compressor is similar, as opposed to a value of 90 per cent for compressors used in aircraft engines. However, the efficiency characteristic is of the expected shape for this type of machine. The low operating speed (2400 rpm or less) at which testing was performed may have adversely affected efficiency in two ways. The first effect is related to the low rotor tip chord-based relative Reynolds number, which is approximately 1.56×10^5 at design speed and 1.25×10^5 at 2400 rpm and design flow, and pressure rise coefficients. Low Reynolds numbers are known to have a significant negative effect on axial flow compressor efficiency, as described in Cumpsty [**9**], though the effect is less severe than cascade tests suggest. The second effect is that bearing power loss does not decrease as rapidly as power input when speed is reduced.

There are efficiency points with a negative value. This is possible because the pressure rise and torque

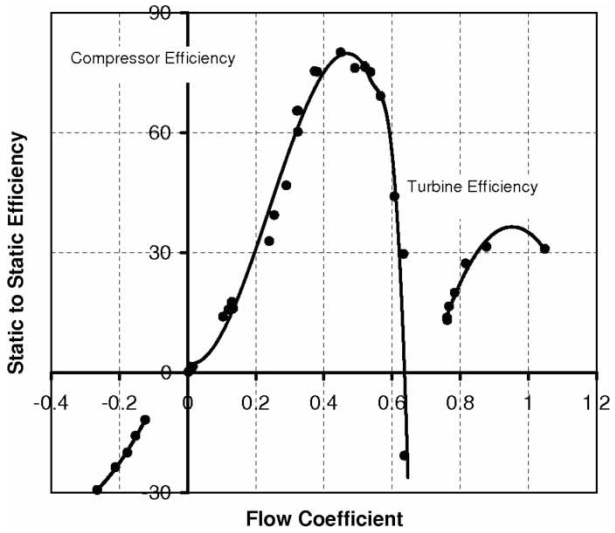

Fig. 8 Static-to-static efficiency characteristic for positive rotation

coefficient characteristics do not cross the x-axis at the same mass flow value, and at flow coefficients between 0.6 and 0.7, the pressure rise coefficient is negative, but the torque is still positive.

5.3 Second quadrant, right of the S-curve ($F - P + R + T + W+$)

Positive rotation operation in the second quadrant, to the right of the S-curve, is achieved by forcing flow backwards through the compressor while it is rotating in the positive direction. The flow direction is negative, the rotation, pressure rise, and torque are positive and the power input is positive, because the motor powers the compressor. Consequently, the efficiency is negative. The pressure rise coefficient characteristic can be seen in Fig. 4, showing a similar trend to that found by Gamache and Greitzer [**6**]. A discontinuity between this characteristic and that of the first quadrant is present near the y-axis, again similar to that observed by Gamache and Greitzer [**6**]. The torque coefficient and efficiency graphs (Figs 6 and 8) show a lot of scatter, due to torsional vibration. This was found to be a dissipative mode of operation. This accounts for the negative efficiency which increases in magnitude as the flow coefficient increases in magnitude. However, a more direct indication of the rate of energy dissipation is the temperature rise coefficient $c_p|\Delta T|/U^2$, in which $|\Delta T|$ is the magnitude of the temperature difference between the compressor outlet and inlet, and c_p is the specific heat of air. At a flow coefficient of -0.158, the temperature rise coefficient was 2.954, compared with a value of 0.577 at design point. The power dissipated increases as the magnitude of the negative flow coefficient increases. This increase is not limited by the compressor, as it is derived from the back-pressure causing the reverse flow, caused by the auxiliary fan in this case. In compressors operating at higher rotational speeds this could constitute a hazard.

5.4 Fourth quadrant, right of the S-curve ($F + P - R + T - W-$)

Fourth quadrant operation occurs when the compressor exit pressure is lower than its inlet pressure, the pressure rise is less than zero and the flow is in the positive direction. This is the normal operating quadrant for a compressor running forwards as a turbine. In this operating mode, the compressor operates as an inefficient turbine, since the flow relative to the blade rows is turned away from the axial direction by blades curved the wrong way.

The pressure rise coefficient characteristic in the fourth quadrant is a continuation of the normal first quadrant characteristic (Fig. 4). The same can be said for the torque characteristics (fourth quadrant, Fig. 6). These agree in principle with the measurements of Bammert and Zehner [**8**].

A turbine efficiency is shaft power divided by fluid power (mechanical energy flux) ($\eta_{\text{turbine}} = \omega T/Q\Delta P$), and is thus, the inverse of a compressor efficiency ($\eta_{\text{compressor}} = Q\Delta P/\omega T$). Flow and rotation are positive, and pressure rise and torque are negative, so both fluid power and shaft power are negative, and efficiency is positive. The efficiency has a peak value of approximately 30 per cent in this operating condition. As the flow coefficient increases beyond the point of peak efficiency, the pressure difference across the compressor and the torque output increase. Rewriting the turbine efficiency definition in terms of the flow coefficient $\phi = C_x/|U| = (Q/A)/\omega r_{\text{tip}}$ yields $\eta_{\text{turbine}} = (r_{\text{tip}}A/\phi)(T/\Delta P)$. Beyond the point of peak efficiency, the turbine efficiency will thus tend towards zero as the flow coefficient increases, but as all quantities are increasing in magnitude, the efficiency will never become negative.

Fourth quadrant turbine operation may occur in axial flow compressors in aircraft engines, when the engine is not operational after flameout, and the compressor is rotating freely (windmilling). As, this phenomenon will most likely occur at low subsonic throughflow velocities and rotational speeds, under incompressible flow conditions, the experimental data obtained should provide a reasonable representation of such scenarios.

5.5 Second quadrant, left of the S-curve ($F - P + R - T + W-$)

In this mode of operation, the compressor runs in reverse as a turbine. The motor was configured as a

generator by coupling it to a resistor. In order to find non-dimensional points over a wide range, the turbine speed also had to be varied between about 1000 and 2400 rpm. Figures 5, 7, and 9 show the data in terms of the non-dimensional flow, pressure rise, and torque coefficients and the static-to-static efficiency.

Turbine characteristics are usually plotted as non-dimensional flow against pressure ratio. The static-to-static pressure rise coefficient characteristic in the second quadrant of Fig. 5 will resemble a typical turbine characteristic when rotated clockwise through ninety degrees. As expected for turbines, the torque output increases with flow as shown in the second quadrants of Fig. 7. In terms of the conventions of the current paper, the product of a negative flow and a positive pressure rise gives a negative fluid power, and the product of a negative rotation and a positive torque yields a negative shaft power. Consequently, the efficiency is positive.

The measured peak turbine efficiency of the compressor running backwards as a turbine is approximately 70 per cent, (Fig. 9), which is more than double that of fourth quadrant turbine operation, and almost equal to peak first quadrant compressor efficiency.

A factor contributing to the high turbine efficiency observed is the comparatively lower susceptibility of turbines to Reynolds number effects, since the pressure decreases in the flow direction. Even the reversed blade profiles relative to the flow direction may help, because the reversed flow now encounters the maximum blade thickness only after having traversed 60 per cent of the profile chord length.

The efficiency is expected to tend towards zero as the flow coefficient becomes increasingly negative, as per the argument for fourth quadrant, positive rotation operation.

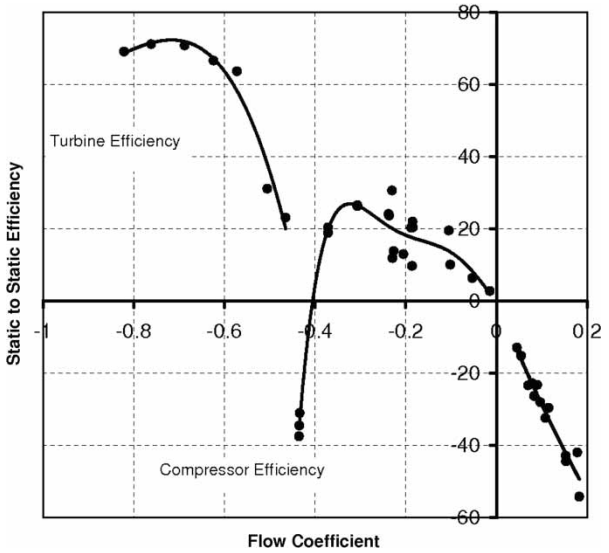

Fig. 9 Static-to-static efficiency characteristic for negative rotation

5.6 Third quadrant ($F-P-R-T-W+$)

In this quadrant, the compressor rotates in reverse and under reverse flow conditions, with the pressure at the normal compressor inlet higher than the pressure at the normal exit. This means that the machine runs backwards as a badly designed compressor with the blade profiles curved and streamlined the wrong way. The characteristics resemble normal compressor characteristics when flow and load coefficients are multiplied by -1, but are closer to the origin of the graph, as is evident when comparing the third quadrant of Fig. 5 to the first quadrant in Fig. 4. No clearly defined stall point is evident. This may be because a large amount of separation occurs on the blades for all operation in this quadrant, due to the direction of curvature of the blades. In other words, the compressor is permanently stalled in this quadrant, irrespective of the flow coefficient. Note that this rotated 'compressor' characteristic joins up smoothly with the 'turbine' characteristic in the second quadrant in Figs 5 and 7.

The torque is generally higher than in the compressor design condition (Fig. 7). There appeared to be more vibration in this mode than in first quadrant operation. This may have been caused by rotating stall in the compressor. The shape of the graphs agree with those measured by Bammert and Zehner [**8**] in an axial flow turbine.

In this quadrant the flow, pressure rise, rotation, and torque are all negative. The efficiency is around 20 per cent (Fig. 9), and it is positive because negative flow and pressure rise result in positive fluid power, and negative rotation and torque result in positive shaft power.

5.7 Fourth quadrant, left of the S-curve ($F+P-R-T-W+$)

Recall that, under negative rotation only the area to the left and below the zero-rotation S-curve is accessible. Here, the compressor is running in reverse but the flow is positive. The compressor tends to induce a negative pressure rise and flow as in the third quadrant, but the opposing auxiliary fans prevail, and the flow is positive.

The static-to-static pressure rise coefficient characteristic resembles the part of the S-curve below the x-axis, but it lies lower than the S-curve, since the speed of rotation is negative (Fig. 5). As in the case of the stationary rotor, the flow is once again highly dissipative with the flow approaching the blades at angles more or less at right angles to the blade chords. Consequently the magnitude of the pressure drop across the compressor increases steeply with flow. So does

the torque (Fig. 7). The compressor efficiency is negative, because the pressure rise is negative, resulting in negative fluid power, but the rotation and torque are both negative, resulting in positive shaft power.

6 SUMMARY AND CONCLUSIONS

The axial flow compressor characteristics for pressure rise, torque, power, and efficiency were measured successfully in all four quadrants using a low speed laboratory compressor.

Ways of accessing all six modes in all four quadrants have been found and the characteristic in each quadrant has been determined and discussed. There are six distinct operating modes in the four-quadrant performance map: two compressor-like modes, two turbine-like modes, and two dissipative modes. Zero-speed S-curves for pressure rise and torque were measured. It was shown that the zero speed S-curve for pressure rise and torque are the dividing lines between positive and negative rotation.

Second quadrant positive rotation operation was a dissipative mode of operation, and the static temperature rise in the working fluid was of the order of 6 times greater than that occurring at design point, which implies that the equivalent of 60 per cent of the fluid power at design point was dissipated as heat. In cooperating at a higher rotational speed this could constitute a hazard.

In the second quadrant, negative rotation turbine mode, the test compressor displayed a static-to-static turbine efficiency of approximately 70 per cent, nearly equal to the first quadrant design point efficiency for this machine. The fourth quadrant turbine efficiency was approximately 30 per cent and thus, less than half the former. Second quadrant turbine efficiencies will be considerably higher than those of the fourth quadrant for virtually all compressors, as the curvature and shape of compressor blades are much more appropriate for the former than the latter.

Fourth quadrant negative rotational operation was dissipative in nature, but the temperature rise in the working fluid for this mode of operation was of the same order of magnitude as that occurring during first quadrant, near-design operation.

Third quadrant operation represents a badly designed compressor with the blades curved in the wrong direction. No stall point could be observed, and considerable vibration occurred during operation, probably indicating that the compressor operated in a stalled state throughout this regime.

ACKNOWLEDGEMENTS

The authors would like to thank L. M. Beviss-Challinor and M. Bailey for contributing some of the data used in the current paper. The work was funded by the National Research Foundation of South Africa.

REFERENCES

1 **Ferreira, T.** Pebble bed company awards contract to MHI. Available from http://www.pbmr.co.za/index.asp?Content=10&MState=DT&Article=50.
2 **Day, I. J.** Stall inception in axial flow compressors. *ASME, J. Turbomach.*, 1993, **115**, 1–9.
3 **Moore, F. K.** and **Greitzer, E. M.** A theory of post-stall transients in axial compression systems: part I – development of equations. *ASME, J. Eng. Gas Turbines Power*, 1986, **108**, 68–76.
4 **Moore, F. K.** and **Greitzer, E. M.** A theory of post-stall transients in axial compression systems: part II – application. *ASME, J. Eng. Gas Turbines Power*, 1986, **108**, 231–239.
5 **Gamache, R.** *Axial compressor reverse-flow performance*. PhD Dissertation, Massachusetts Institute of Technology, Cambridge, MA, 1985.
6 **Gamache, R. N.** and **Greitzer, E. M.** Reverse flow in multistage axial compressors. *Int. J. Turbo Jet Eng.*, 1990, **6**, 461–473.
7 **Bammert, K.** and **Zehner, P.** Measurements of the perfomance of an air turbine stage at positive and negative mass flow and rotational speed (four-quadrant characteritics). *ASME, J. Turbomach.*, 1978, **100**, 22–29.
8 **Bammert, K.** and **Zehner, P.** Measurements of the four-quadrant characteristics on a multi-stage turbine. *ASME, J. Turbomach.*, 1980, **102**, 316–321.
9 **Cumpsty, N. A.** *Compressor aerodynamics*, 1989 (Longman Scientific and Technical, Harlow, UK).

The hydrodynamic modelling of torque converters

by P. J. Strachan,* F. P. Reynaud,** and T. W. von Backström,***

(Received in final form November 1991)

List of Symbols

B factor used in calculation of Y_k
c blade chord length (m)
C_w tangential component of absolute fluid velocity corresponding to β (m/s)
d minimum opening between blades (m)
D NACA diffusion factor
D_h hydraulic diameter (m)
H blade height (m)
i incidence angle (°)
i_s stall incidence angle (°)
k casing friction loss coefficient, or V_1/V_2
k_e tip clearance (m)
k_s height of surface roughness asperities (m)
$\dot{m}$ mass flow rate (kg/s)
r blade radius (m)
p_s static pressure (Pa)
p_t total pressure (Pa)
Re Reynold's number
Re_c casing Reynold's number
s blade inlet pitch (m)
t blade thickness (m)
U blade tip speed (m/s)
V relative fluid velocity (m/s)
V_w tangential component of relative fluid velocity (m/s)
Y_k tip clearance loss coefficient
Y_p primary or profile loss coefficient
Y_s secondary loss coefficient
Z_l blade loading
Z_n number of blades
α absolute inlet flow angle (°)
α_d blade inlet angle (°)
α_m mean flow angle (°)
β absolute outlet flow angle (°)
β_d blade outlet angle (°)
δ shock loss coefficient
ΔC_w $C_{w2} - C_{w1}$ (m/s)
ΔV_w difference between actual and design V_w (m/s)
∈ half blade width, see fig. 9, (m)
ϵ_{Lim} limiting radius ratio
ρ fluid density (kg/m³)
σ slip factor
Λ impeller friction factor

Subscript Notation

1 inlet
2 outlet

* Senior Lecturer,
** M.Eng. Student,
*** Professor, Member
Department of Mechanical Engineering,
University of Stellenbosch

Summary

One method of predicting the performance characteristics of torque converters is by means of a hydrodynamic model in which the geometry of the torque converter and the properties of the fluid are given, and the angular momentum flux over the members is calculated at specific operating points. A number of such models has been developed in the literature, all of which rely on empirical input data for determination of the losses and slip factor. This paper describes a hydrodynamic model in which the empiricism has been removed from the input data and built into the program in the form of empirical equations and loss models. The program can be applied to torque converters having profile and thin blades, and in addition a new shock (incidence) loss model is introduced which is employed in the hydrodynamic model to calculate the shock losses of the different members of a torque converter. Prediction of torque converter performance by means of this model agreed well with published experimental data for a wide range of torque converter geometries.

Introduction

Torque converters are widely used in automotive applications, from passenger cars to heavy commercial and military vehicles. The primary function of the torque converter is to provide torque multiplication. This is a maximum at stall and decreases without step to a value of

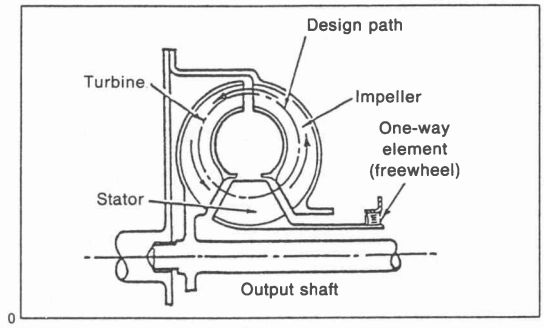

Figure 1 Torque Converter Configuration

unity at the coupling point. The configuration of a typical torque converter is shown in fig. 1 [1]. The torque converter is similar to a fluid coupling, but with the addition of a stator or reactor. In a fluid coupling, power is transmitted from the pump or impeller to the turbine without change in torque, but with the insertion of the stator in the circuit, the angular momentum of the fluid is changed between the turbine exit and impeller entrance, resulting in torque multiplication between impeller and turbine. As

its name implies, the stator is normally stationary but in most modern torque converters it is usually fitted with a one-way clutch.

The characteristic performance curves of torque converters and fluid couplings are shown in fig. 2. The abscissa is speed ratio, the ratio of output (or turbine) speed to input (or impeller) speed. The ordinates are torque ratio i.e. output torque to input torque on the one side and efficiency on the other.

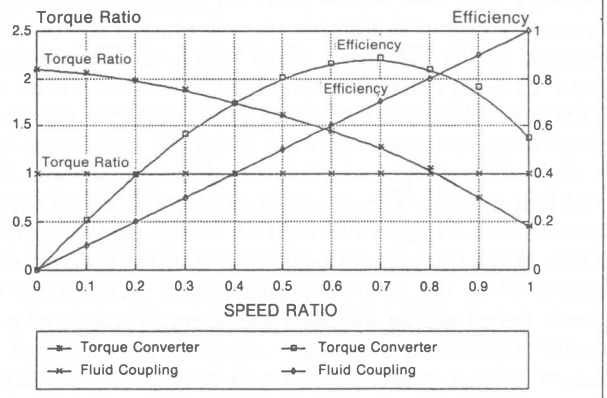

Figure 2 Standard Coupling Characteristics

Between speed ratios of 0.8 and 0.9, the converter torque curve crosses that of the coupling, indicating that the turbine (or output) torque is less than the impeller (or input torque). Simultaneously the converter efficiency drops below that of the coupling. As this is not desirable, it is overcome either by the fitting of a one way clutch, or by the use of a mechanical lock-up device that automatically connects the impeller and turbine above the speed ratio that corresponds to a torque ratio of unity.

This paper describes a comprehensive one dimensional model to simulate accurately the flow processes in a torque converter and predict the performance characteristics.

Torque Converter Hydrodynamic Models

In the torque converter and fluid coupling field one dimensional models are fairly common. Lucas and Rayner [2], Qualman and Egbert [3], Walker [4], Whitfield, Wallace and Patel [5], Wallace, Whitfield and Sivalingam [6], Lamprecht [7] and Adrian [8], have all produced one dimensional models which show more or less agreement with measured results, but all of these require the external specification of total pressure loss coefficients for the members (pump impeller, turbines and stators) and of blade incidence loss coefficients. Lamprecht [7] did however derive equations for the calculation of certain of the loss coefficients, but they were not implemented in the computer program listing of his thesis [7].

With the local availability of the Lamprecht [7] model, it was decided to utilise it as the basis for further development. The Lamprecht [7] model was obtained and completely re-written in the BASIC language to run on a standard IBM compatible personal computer. In the analysis, the input speed, the speed ratio and the geometry of the torque converter are given parameters. There are three main members, the impeller, the stator and the turbine, although each can have more than one stage. The stator in turn can have two phases of operation, namely fixed or freewheel. Further assumptions are;

- steady state conditions throughout
- incompressible fluid
- work done by the fluid is positive and work received by the fluid is negative
- conservation of mass flow, momentum and energy
- the torque applied to the shell is not considered

The process estimates a mass flow inside the torus and this is used to determine firstly, the torque and power transmitted (input power) and absorbed (output power) by the members and, secondly, the power losses due to friction, diffusion, shock and slip.

For conservation of energy, the sum of the input power, output power and power losses, bearing in mind the sign convention, must equate to zero, and the mass flow is then iteratively adjusted until this condition, or close to it, is achieved. The value of mass flow thus derived is then used to determine the input and output torques, torque ratio, and efficiency for different values of speed ratio. In calculating the power losses, values of the stagnation pressure loss coefficients for the impeller, stator and turbine, the shock (or incidence) loss factors and the impeller slip factor are required. At this stage values based on information in the literature were assumed, typically 0,35 for the loss coefficients, and 1,0 for the shock loss and slip factors. Wall friction losses were ignored.

Evaluation of the Initial Model with Externally Specified Loss Coefficients

An extensive series of computer tests was run on the standard Jandasek [9] torque converter geometry. Fig. 3 shows good agreement between calculated and measured torque ratio and efficiency using the loss coefficients and factors above, with maximum differences, as can be seen from Table 1, of about 3%. However, from fig. 4 it can be seen that only qualitative agreement was obtained be-

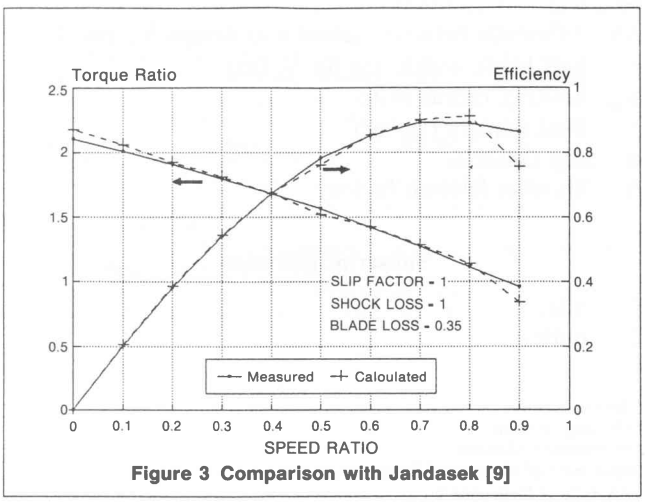

Figure 3 Comparison with Jandasek [9]

(a) Figs. 3 and 4

Torque Ratio			Input Torque ft lbs			Output Torque ft lbs		
Meas	Calc	Diff %	Meas	Calc	Diff %	Meas	Calc	Diff %
2,11	2,18	3,4	348	415	19,3	733	905	23,4
2,01	2,06	2,5	346	406	17,4	696	838	20,3
1,91	1,93	1,0	336	397	17,9	643	766	19,1
1,80	1,81	0,7	325	383	17,9	585	694	18,7
1,68	1,68	0,0	309	367	18,8	520	617	18,7
1,56	1,55	0,7	288	348	21,0	450	541	20,1
1,42	1,42	0,2	264	322	21,9	376	459	22,2
1,27	1,29	1,1	237	290	22,5	302	374	23,8
1,11	1,14	2,4	204	248	21,6	227	283	24,5
0,96	0,99	3,0	167	186	11,1	160	183	14,5
Ave. diff %		1,5	Ave. diff %		19,0	Ave. diff %		20,5
Std. dev.		1,1	Std. dev.		3,1	Std. dev.		2,9

(b) Figs. 10 and 11

Torque Ratio			Input Torque ft lbs			Output Torque ft lbs		
Meas	Calc	Diff %	Meas	Calc	Diff %	Meas	Calc	Diff %
2,11	2,20	4,6	348	341	2,0	733	752	2,5
2,01	2,07	2,8	346	334	3,4	696	691	0,7
1,91	1,93	1,0	336	325	3,4	643	626	2,5
1,80	1,79	0,8	325	313	3,6	585	559	4,4
1,68	1,66	1,7	309	297	3,8	520	492	5,4
1,56	1,52	2,8	288	281	2,4	450	427	5,2
1,42	1,39	1,9	264	264	0,0	376	369	1,9
1,27	1,27	0,4	237	241	2,0	302	306	1,5
1,11	1,11	0,1	204	202	1,1	227	225	1,0
0,96	0,99	2,9	167	167	0,0	160	165	2,9
Ave. diff %		1,9	Ave. diff %		2,2	Ave. diff %		2,8
Std. dev.		1,3	Std. dev.		1,3	Std. dev.		1,6

Table 1 Comparison of measured and calculated results for Jandasek [9] torque converter.

tween the calculated and measured values of input and output torque, although this could be improved by changing the shock loss factor to 0.8.

Jandasek [9] did systematic tests on the influence of torque converter geometry on performance, and in one test the impeller blade outlet angle, was changed from

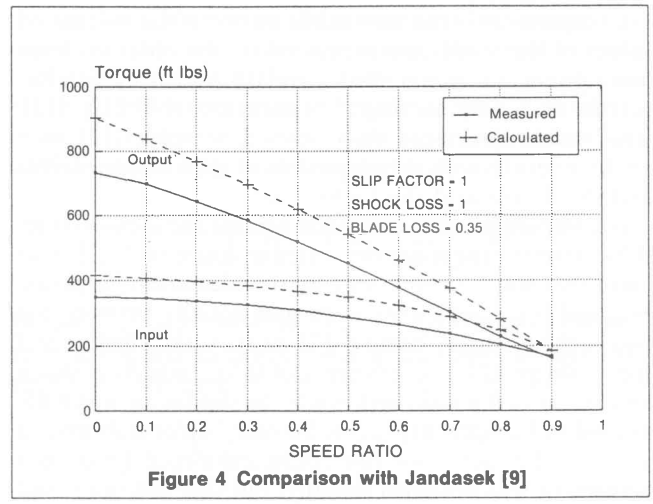

Figure 4 Comparison with Jandasek [9]

$-15°$ to $+55°$, increasing the stall torque ratio from 2.1 to 2.99 and reducing both the peak efficiency and coupling point speed ratio. Particularly good agreement was obtained for torque ratio and efficiency, fig. 5, while fig. 6 shows that there was once again only qualitative agreement for input and output torque for this arrangement, using the original loss coefficients and shock loss and slip factors. Reducing the shock loss factor to 0.8 only had a small effect on the results.

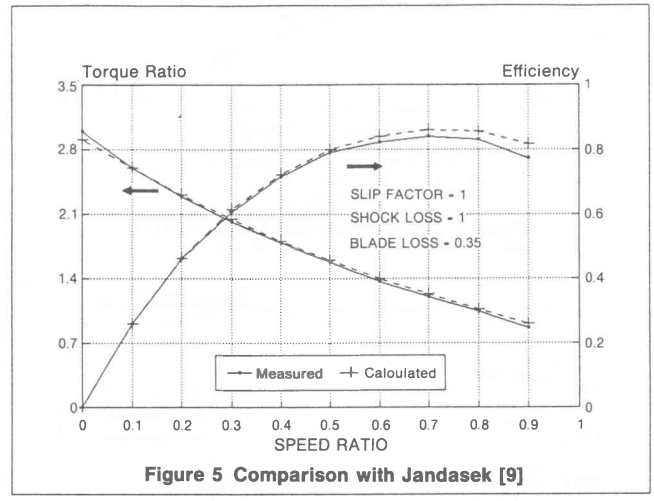

Figure 5 Comparison with Jandasek [9]

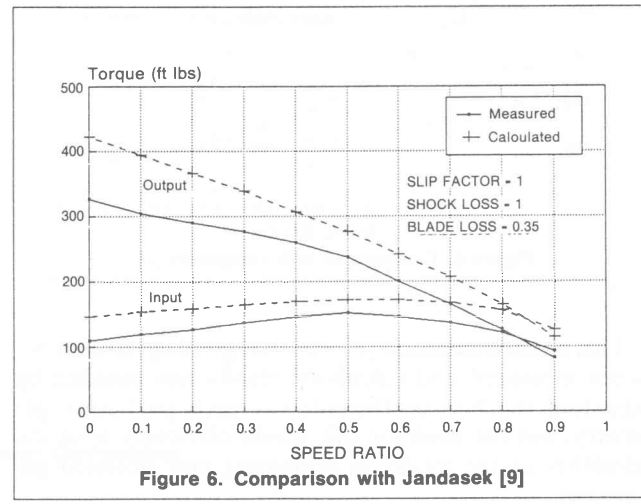

Figure 6. Comparison with Jandasek [9]

Comparisons were also made between the calculated values of the model and measured results obtained from other publications, namely Lucas [10], and Northern Research and Engineering Corporation (NREC) [11]. Reasonable agreement was obtained, Strachan [12], with all these results with varying values of the loss coefficients and shock loss and slip factors.

A comparison was also made against the measured results of the torque converter tested by Lamprecht [7]. This had a two stage turbine, and so for calculation purposes, assigned loss coefficients were split equally between the two turbine stages, being 0.175 each, with impeller and stator assigned loss coefficients of 0.35. Initially a shock loss factor of 0.8 was used, while the slip factor was 0.85, as used by Lamprecht [7]. (the Stanitz [14] formula gives a value of slip factor for this configuration of 0.84) Poor agreement was obtained initially, but this was improved by utilising a shock loss factor of 0.5, figs 7 and 8.

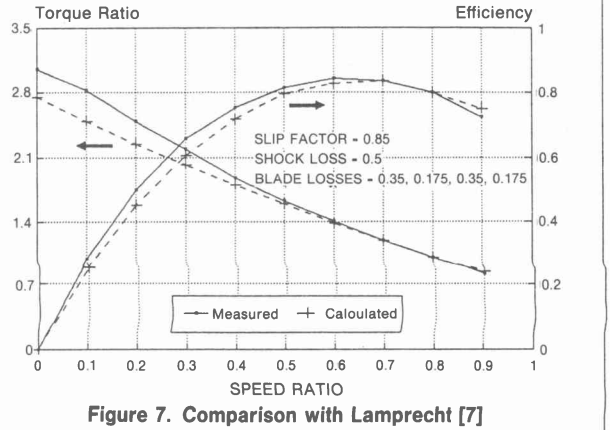

Figure 7. Comparison with Lamprecht [7]

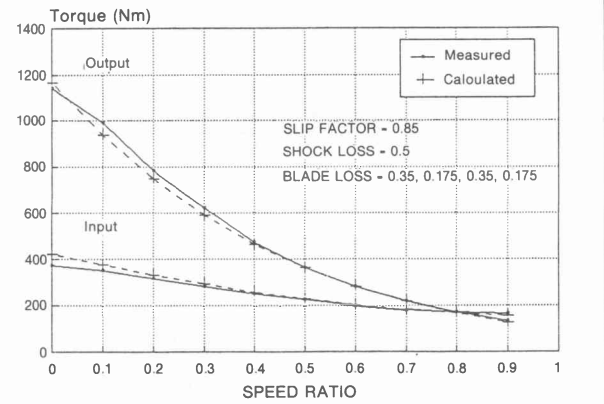

Figure 8. Comparison with Lamprecht [7]

This initial evaluation showed that good agreement between measured and calculated results was possible by adjusting the loss coefficients for each particular geometry, but the need for this would obviously limit the reliability of the model in evaluating new untested geometries.

Model Development

In order to overcome the need to utilise assigned values for the loss coefficient and slip and shock loss factors the model was modified to calculate these values for the impeller, turbine, stator and channels using standard pipe and turbomachinery theory.

Friction, diffusion and profile losses

For pipes, the generally used equation to calculate the friction loss is the Colebrook equation which includes the roughness factor, Giles [13],

$$\frac{1}{\sqrt{\Lambda}} = -2 \times \log\left(\frac{2{,}51}{Re \times \sqrt{\Lambda}}\right) + \left(\frac{k_s}{3{,}7 \times D_h}\right) \qquad (1)$$

where Re = Reynolds number based on the pipe or channel hydraulic diameter.

The above expression is difficult to use due to the presence of the friction loss coefficient on both sides of the equation. However a suitable explicit formula for the friction factor of a turbulent pipe has been published, Haaland [15], as;

$$\frac{1}{\sqrt{\Lambda}} = -1{,}8 \times \log\left[\left(\frac{6{,}9}{Re}\right) + \left(\frac{k_s}{3{,}7 \times D_h}\right)^{1{,}11}\right] \qquad (2)$$

While eq (2) can be applied to the impeller, channel flow was assumed in the casing between the elements, and the casing friction loss coefficient used was the approximation by White [17],

$$k_{(k_s = 0)} = -0{,}495(\log Re_c)^{-2{,}2}$$

The casing friction loss coefficient was modified to take into account the effect of roughness by assuming that the ratio of the casing friction loss k, with and without the roughness factor is equivalent to the ratio of the Colebrook equation, with and without the roughness factor. i.e.

$$\frac{k_{(k_s=0)}}{k_{(k_s)}} = \frac{\Lambda_{(k_s=0)}}{\Lambda_{(k_s)}} = \left(\frac{1}{f(Re, 0)} \Big/ \frac{1}{f(Re, k_s)}\right)^2 \qquad (3)$$

Diffussion losses, due to the high deflection of the working fluid, were accounted for by means of the simplified form of the NACA diffusion factor D given by Cohen, Rogers and Saravanamuttoo [16] as

$$D = 1 - \frac{V_1}{V_2} + \left(\frac{\Delta C_w}{2V_1}\right).\frac{s}{c} \qquad (4)$$

The value of D above can be used in conjunction with fig. 5.8, Cohen et al [16] to determine the losses.

Primary losses or profile losses at the design point for the turbine and stator were determined by a method proposed by Ainley and Mathieson [19] whereby the primary loss coefficient at zero incidence (i = 0) is given by

$$Y_{p(i=0)} = \left[Y_{p(\alpha_d=0)} + \left(\frac{\alpha_d}{\beta}\right)\left(Y_{p(\alpha_d=0)} - Y_{p(\alpha_d=0))}\right]\right]\left(\frac{t}{0{,}2c}\right)^{\left(\frac{-\alpha_d}{\beta}\right)} \quad (5)$$

where $Y_{p(\alpha_d=0)}$ and $Y_{p(\alpha_d=\beta)}$ are the profile loss coefficients from fig. 3.22(a) and (b), Dixon [18], respectively. At any other incidence, the profile loss ratio $Y_p/Y_{p(i=0)}$ is assumed to be defined by a unique function of the ratio, incidence/stalling incidence, i/i_s, from fig. 3.21 in Dixon [18].

Secondary losses arise from complex three dimensional flows – Dixon [18] states that possibly end wall boundary layers are convected inwards along the suction surface of the blades as the main flow passes through the blade row, resulting in a serious maldistribution of the flow, with losses in the stagnation pressure often a significant part of the total loss. Ainley and Mathieson [19] determined an expression for the secondary losses, but Dunham and Came [20] found that this equation was not correct for blades of low aspect ratio and modified the expression to include a better correlation with aspect ratio. The loss coefficient can thus be determined from

$$Y_s = 0{,}1336\left(\frac{c}{H}\right)\left(\frac{\cos^3\beta}{\cos\alpha_d}\right)\frac{(\tan\alpha - \tan\beta)^2}{\cos\alpha_m} \quad (6)$$

Depending upon the blade loading, the number of blades and the size and nature of the clearance gap, the tip clearance loss coefficient Y_k can be found from

$$Y_k = B\left(\frac{c}{H}\right)\left(\frac{k_e}{c}\right)^{0{,}78}.Z_1 \quad (7)$$

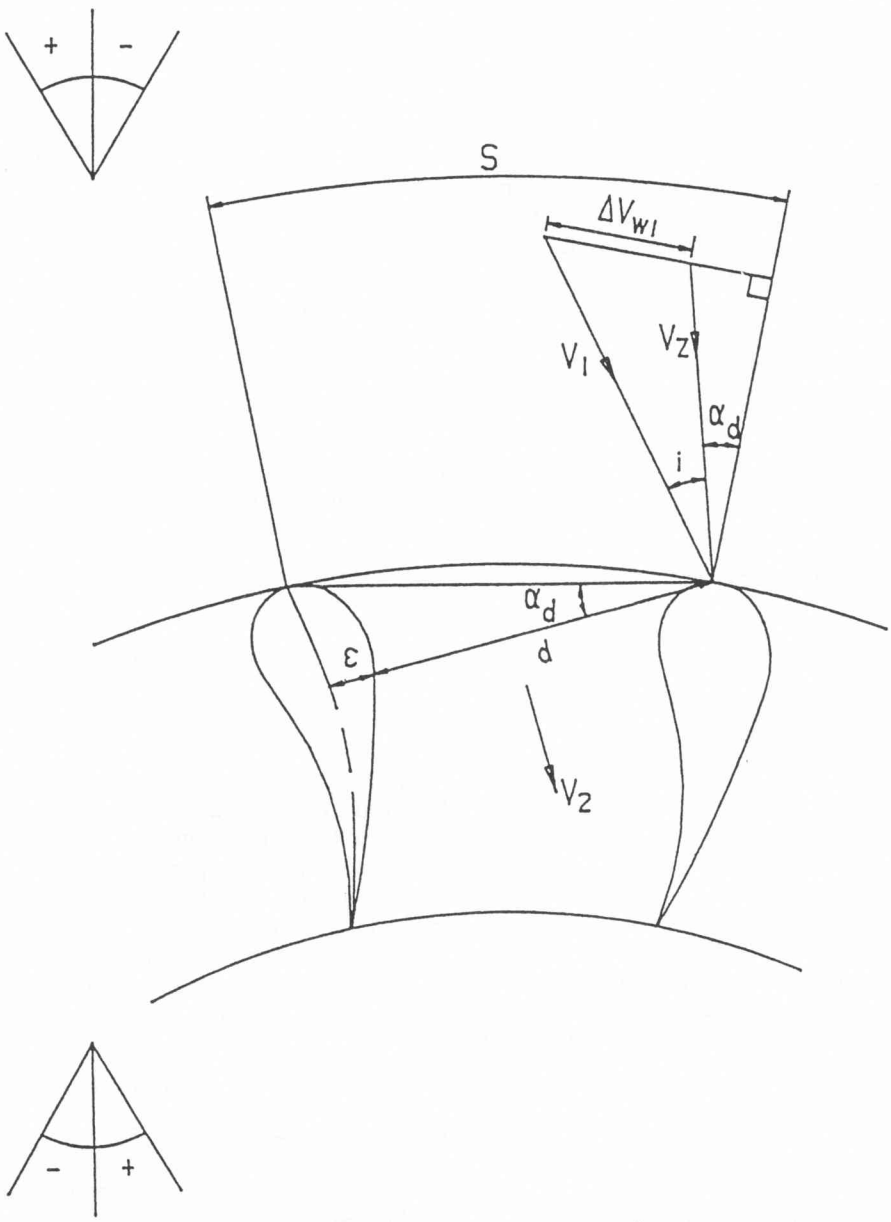

Figure 9. Blade Geometry Configuration

where B = 0,5 for unshrouded tips or 0,25 for shrouded tips and the blade loading is calculated from the secondary loss coefficient, i.e.

$$Z_1 = Y_s\left(\frac{1}{0{,}0334}\right)\left(\frac{h}{c}\right)\left(\frac{\cos\alpha}{\cos\beta}\right) \tag{8}$$

Ainley and Mathieson [19] obtained their data for a mean Reynolds number of 2.10^5 based on the mean chord and exit flow conditions from the turbine stage. Consequently they recommended a correction to be made to the stage efficiency for lower Reynolds numbers. Dunham and Came [20] gave an optional correction which could be applied directly to the sum of the profile, Y_p, secondary, Y_s, and tip clearance, Y_k, losses as follows;

$$(Y_p+Y_s+Y_k)_{Corrected}=(Y_p+Y_s+Y_k)\left(\frac{2.10^5}{Re}\right)^{0.2} \tag{9}$$

Shock (incidence) losses

A shock loss factor, for the impeller, turbine and stator, to take into account the difference between the flow angle and blade inlet angle was calculated, Reynaud [22], using the analogy of Vavra's [21] deduction for supersonic shock losses. However, contrary to Vavra [21] and Lamprecht [7], the calculation takes the blade thickness and curvature into account. Fig. 9 shows the blade geometry.

The shock loss coefficient is defined as the total pressure drop between the inlet and outlet of the control volume, fig. 9, divided by the dynamic pressure at outlet from the control volume. i.e.

$$\delta = \frac{p_{t_1} - p_{t_2}}{\frac{1}{2}.\rho.V_2^2} \tag{10}$$

and substituting for the total pressures

$$\delta = \frac{p_{s_1} - p_{s_2} + \frac{1}{2}.\rho.(V_1^2 - V_2^2)}{\frac{1}{2}.\rho.V_2^2} \tag{11}$$

From consideration of the momentum equation for the component perpendicular to the control volume outflow boundary

$$p_{s_1}.s.\cos\alpha_d - p_{s_2}.d - \tfrac{1}{2}.\epsilon(p_{s_2} + p_{s_1}) = \dot{m}.V_2 - \dot{m}.V_1.\cos i \tag{12}$$

where $d = s.\cos\alpha_d - \epsilon$ and $\dot{m}$ is the mass flow rate per blade channel. It is assumed that the pressure acting on the blade surface forming the boundary of the control volume is equal to the mean of the pressure at the inlet and outlet of the control volume.

From the continuity equation;

$$\dot{m} = \rho.s.V_1.\cos(\alpha_d + i) = \rho.d.V_2 \tag{13}$$

and since $V_2 = k.V_1$ the value of k can be calculated as

$$k = \frac{V_2}{V_1} = \frac{s}{d}.\cos(\alpha_d + i) \tag{14}$$

Substituting for d, $\dot{m}$ and V_2 into eq (12)

$$p_{s_1}.\left(s.\cos\alpha_d - \frac{\epsilon}{2}\right) - p_{s_2}.\left(s.\cos\alpha_d - \epsilon + \frac{\epsilon}{2}\right) = \rho.d.k.V_1^2.\cos i - \rho.d.k^2.V_1^2$$

Rearranging

$$p_{s_1} - p_{s_2} = \frac{d}{s}.\rho.k.V_1^2.\left(\frac{k - \cos i}{\cos\alpha_d - \frac{\epsilon}{2s}}\right) \tag{15}$$

and substituting eq (15) into eq (11)

$$\delta = \frac{\frac{d}{s}.\rho.k.V_1^2\left(\frac{k - \cos i}{\cos\alpha_d - \frac{\epsilon}{2s}}\right) + \frac{1}{2}.\rho.V_1^2.(1 - k^2)}{\frac{1}{2}.\rho.V_1^2.k^2}$$

and rearranging again

$$\delta = \frac{k^2\left(\frac{2d}{s\left(\cos\alpha_d - \frac{\epsilon}{2s}\right)} - 1\right) - 2.k.\cos i.\left(\frac{d}{s\left(\cos\alpha_d - \frac{\epsilon}{2s}\right)}\right) + 1}{k^2} \tag{16}$$

For thin straight blades, this reduces to

$$\delta = \frac{(V_2^2 - 2.V_2.V_1.\cos i + V_1^2)}{V_2^2}$$

Referring to fig 9 and using the definition of k and the Cosine rule it can be shown that

$$\delta = \frac{\Delta V_{w1}^2}{V_2^2} \tag{17}$$

Therefore, equating eqs (10) and (17)

$$p_{t_1} - p_{t_2} = \tfrac{1}{2}.\rho.\Delta V_{w1}^2$$

Thus the equation utilised by Lamprecht [7] is equivalent to the common assumption used by Lucas [2], Whitfield et al [5] and Adrian [8], i.e. that the incidence loss is equal (or at least proportional) to the dynamic pressure associated with the difference between the design and actual relative circumferential velocity component. The incidence loss model, eq (16) above, may thus be regarded as a generalisation of a commonly used model applied to thick, curved blades.

Slip Factor

Even under ideal frictionless conditions, the relative flow leaving a compressor or pump impeller receives less than perfect guidance, and the flow is said to slip. Several methods of determining the slip factor are available in the literature and Lamprecht [7] used the Stanitz [14] method which Dixon [18] states as being suitable for radial vaned impellers ($\beta_d = 0$). For impellers having blade angles in

the range $50° < \beta_d < 70°$, Dixon [18] recommends either the Stodola or Busemann formulas. Wiesner [23] carried out a comprehensive review of published slip factors and found that the Busemann formula gave best agreement with test slip factors determined from measured results. Wiesner [23] further recommended a simple empirical function that correlated very well with the test results, namely;

$$\sigma = 1 - \frac{\sqrt{\cos \beta_d}}{Z_n^{0,7}} \qquad (18)$$

This is only applicable within the following limits

$$\frac{r_1}{r_2} \leq \frac{1}{\exp\left(\frac{8{,}16.\cos \beta_d}{Z_n}\right)} = \epsilon_{Lim}$$

For a radius ratio in excess of the above limit the slip factor is given by;

$$\sigma = \left(1 - \frac{\sqrt{\cos \beta_d}}{Z_n^{0,7}}\right)\left[1 - \left(\frac{\frac{r_1}{r_2} - \epsilon_{Lim}}{1 - \epsilon_{Lim}}\right)^3\right] \qquad (19)$$

Discussion

For the above calculations, the computer model required more detailed data than that given in most publications. However, of the literature already studied, both Lamprecht [7], and Jandasek [9] gave sufficient information to satisfy the input requirements of the model, and figs 10 and 11 show the comparison of measured and calculated results for the Jandasek [9] torque converter using the latest version of the model. When compared to figs. 3 and 4 a significant improvement is apparent. Table 1 lists the numerical values of measured and calculated torque ratio, efficiency, and input and output torque for figs 3 and 4, and figs 10 and 11, and the reductions in the mean and standard deviations of the errors between the two versions of the model are significant. Comparative results for the Lamprecht [7] geometry using the loss models are shown in figs 12 and 13, and compare favourably with figs 7 and 8, for the same torque converter, but where arbitrary values were used for the loss coefficients. Table 2 shows the numerical values for these sets of figures and the efficacy of the loss models to simulate the torque converter over the whole operating range is apparent.

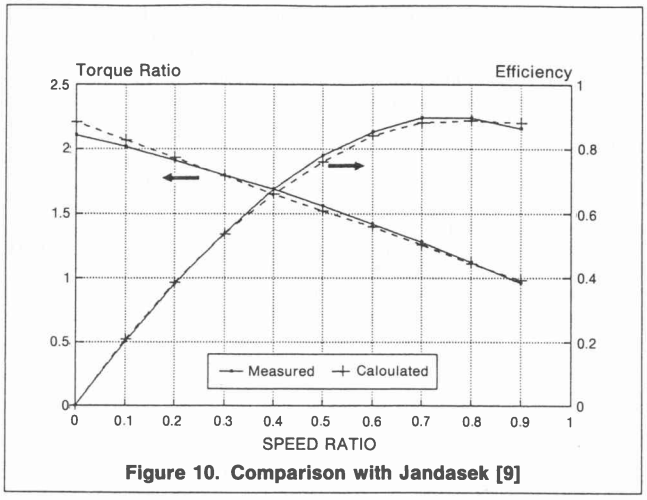

Figure 10. Comparison with Jandasek [9]

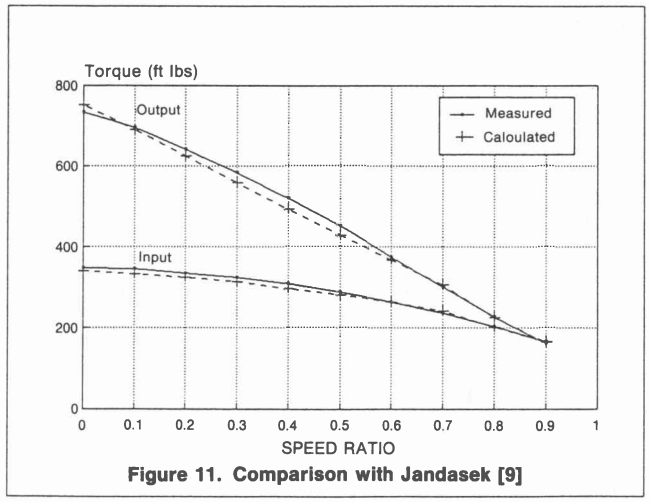

Figure 11. Comparison with Jandasek [9]

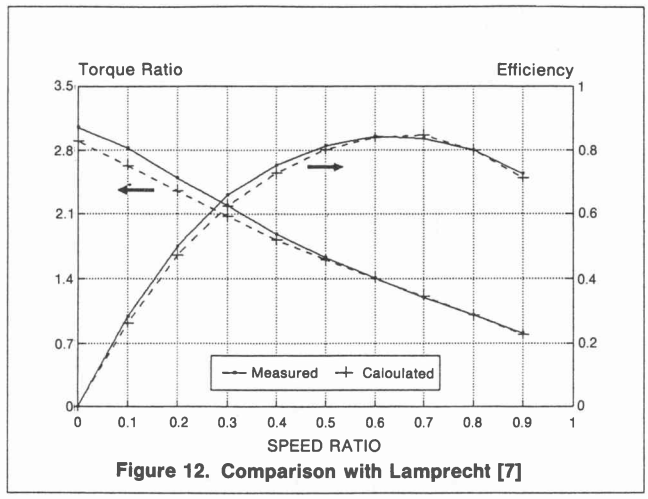

Figure 12. Comparison with Lamprecht [7]

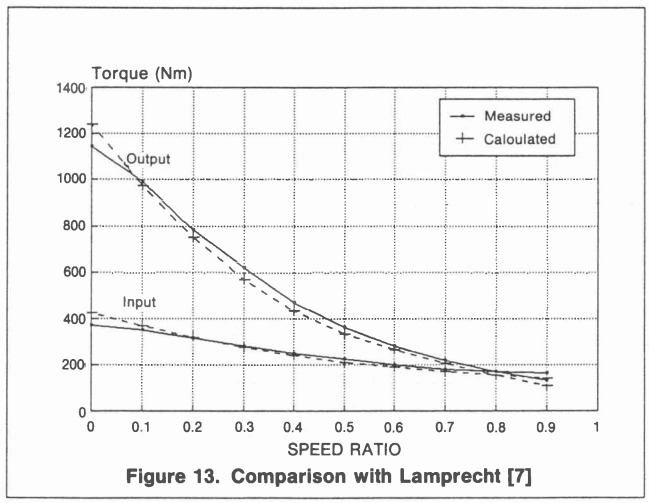

Figure 13. Comparison with Lamprecht [7]

Conclusion

From the foregoing it can be seen that the performance of the torque converter hydrodynamic model has been systematically improved by the introduction of empirical

(a) Figs. 7 and 8

Torque Ratio			Input Torque Nm			Output Torque Nm		
Meas	Calc	Diff %	Meas	Calc	Diff %	Meas	Calc	Diff %
3,05	2,75	9,8	374	424	13,2	1142	1166	2,1
2,82	2,49	11,7	350	376	7,3	990	939	5,2
2,49	2,25	9,7	315	333	5,7	784	748	4,5
2,20	2,02	8,0	283	293	3,5	622	592	4,8
1,88	1,88	4,4	251	257	2,4	473	463	2,1
1,63	1,63	2,3	224	228	1,8	364	362	0,5
1,41	1,41	1,9	200	204	2,0	281	281	0,0
1,20	1,20	0,2	182	184	1,1	218	220	0,9
1,00	1,00	0,0	170	168	1,2	170	168	1,2
0,81	0,83	3,2	164	154	6,0	133	129	3,0
Ave. diff %		11,36	Ave. diff %		4,4	Ave. diff %		2,4
Std. dev.		8,44	Std. dev.		3,6	Std. dev.		1,8

(b) Figs 12 and 13

Torque Ratio			Input Torque Nm			Output Torque Nm		
Meas	Calc	Diff %	Meas	Calc	Diff %	Meas	Calc	Diff %
3,05	2,90	4,9	374	428	14,3	1142	1241	8,7
2,83	2,63	7,1	350	370	5,6	990	972	1,8
2,49	2,35	5,5	315	319	1,3	784	750	4,3
2,20	2,08	5,3	283	275	2,8	622	572	8,0
1,88	1,82	3,4	251	240	4,7	473	436	7,9
1,63	1,60	1,5	224	210	6,2	364	337	7,6
1,41	1,40	0,7	200	190	5,0	281	265	5,6
1,20	1,21	1,1	182	170	6,5	218	206	5,5
1,00	1,00	0,0	170	154	9,3	170	154	9,3
0,81	0,79	1,9	164	143	13,3	133	113	14,9
Ave. diff %		3,1	Ave. diff %		6,9	Ave. diff %		7,4
Std. dev.		2,3	Std. dev.		4,0	Std. dev.		3,3

Table 2 Comparison of measured and calculated results for Lamprecht [7] torque converter.

loss models from the literature and an original incidence loss model which takes blade thickness into account. The relative accuracy and shape of the predicted performance curves in figs 10 to 13 show that the loss models are realistic when applied to two significantly different commercial torque converter geometries and the model can now be confidently used as a preliminary design tool for predicting torque converter performance. Application of the model requires detailed geometry data and as this is not generally available from the literature further comparisons between the model and measured results cannot easily be made.

Further development of the loss models is not considered necessary although one area for future investigation is possibly the effect of fluid temperature on torque converter performance.

References

1. SAE Recommended Practices, Hydraulic Drives Terminology, SAE J641, SAE Handbook 1983
2. Lucas G. G., and Rayner, A. A. "Torque converter design calculations", Automobile Engineer, February 1970
3. Qualman, J. W. and Egbert, E. L., "Fluid couplings", Passenger Car Automatic Transmission, SAE Transmission Workshop Meeting, 2nd Edition, Advanced Engineering, Vol 5, pp 137-150, 1963
4. Walker, F. H., "Multi-turbine torque converter", Design Practices Passenger Car Automatic Transmissions, 2nd Edition, pp 227-240, Society of Automotive Engineers, 1973
5. Whitfield, A., Wallace, F. J., and Patel, A. "Design of three element hydrokinetic torque converters", Int. J. Mech. Sci., Vol 25, No. 7, pp 485-497, 1983
6. Wallace, F. J., Whitfield, A., and Sivalingam, R. "A performance prediction procedure for three element torque converters", Int. J. Mech. Sci., Vol 20, pp 801-814, 1978
7. Lamprecht, J., "Die ontwerp van 'n hidrouliese wringomsetter", Magister tesis in Ingenieurswese, Universiteit van Pretoria, Desember 1983
8. Adrian, F-W., "Strömungsuntersuchungen und analyse in kreisläufen hydrodynamischer wandler.", Doctorarbeit, Ruhr-Universitat Bochum, 1985
9. Jandasek, V. J., "The design of a single stage three-element torque converter", Passenger Car Automatic Transmission, SAE Transmission Workshop Meeting, 2nd Edition, Advanced Engineering Vol 5, p 201, 1963
10. Lucas, G. G., "A technique for calculating the time-to-speed of an automatic transmission vehicle.", Proc. I. Mech. E., Vol. 184, Part 31, 1969
11. Northern Research and Engineering (NREC), "Modification of torque converter analysis procedures", NREC Report No. 1152.1, Northern Research and Engineering Corporation, Cambridge, Mass, USA, March 1969
12. Strachan, P. J., "Torque converter one-dimensional computer program: Comparison of calculated input and output torque with experimental values." BMI Confidential Report 85/15/86/020, March 1987
13 Giles, R. V., "Theory and Problems of Fluid Mechanics and Hydraulics", Schaum's Outline Series, Schaum Publishing Co., New York, 1963
14. Stanitz, J. D., "Some theoretical aerodynamic investigations of impellers in radial and mixed flow centrifugal compressors.", Trans. A.S.M.E., 74, 4, 1952
15. Haaland, S. E., "Simple and explicit formulas for the friction factor in turbulent pipe flow," ASME Journal of Fluids Engineering, Vol. 105, 1983, pp 89-90
16. Cohen, H., Rogers, G. F. C. and Saravanamuttoo, H. I. H., "Gas Turbine Theory", Longman Scientific and Technical, 3rd Edition, 1987
17. White, F. M., "Viscous Fluid Flow", McGraw-Hill, 1974
18. Dixon, S. L., "Fluid Mechanics, Thermodynamics of Turbomachinery", 3rd Edition, Pergamon International Library, 1984
19. Ainley D. G. and Mathieson, G. C. R., "A method of performance estimation for axial flow turbomachines", A.R.C.R. and M. 2974, 1951
20. Dunham, J. and Came, P., "Improvements to the Ainley-Mathieson method of turbine performance prediction", Trans. A.S.M.E., Series A., 92, 1970
21. Vavra, M. H., "Aero-Thermodynamics and Flow in Turbomachines", Kriege, New York, 1974
22. Reynaud, F. P., "BMI one-dimensional torque converter model", BMI Confidential Report 88/28, March 1990
23. Wiesner, F. J., "A review of slip factors for centrifugal impellers.", Journal of Engineering for Power, Trans. of the ASME, Oct. 1967

Panel method prediction of flow through a torque converter turbine

T.W. von Backström[1] and **A.A. Venter**[2]

(First received January 1994; Final version May 1994)

Abstract

The flow around the blades of a torque converter turbine, consisting of an axisymmetrical radial cascade, was investigated. The pressure distribution along the blade surfaces was determined experimentally, using a torque converter model equipped with pressure measuring stations on the blade surfaces of a stationary turbine. A two-dimensional potential flow panel method was developed for the analysis of incompressible flow through axisymmetrical radial cascades. The method was verified by application to a rectilinear cascade and through use of a conformal transformation. It yielded results in excellent correspondence with published data. For the turbine cascade the panel method predicted a blade surface pressure distribution which compared well enough with the experimental results to be considered as a blade profile design tool.

Nomenclature

α	Free spiral vortex parameter
β	Angle between profile surface tangent and global x-axis
Γ	Vortex strength in vortex–sink combination forming free spiral vortex
γ	Function representing local strength of vortex distribution; vortex strength; vortex strength in specific node (when used with index)
θ	Angle in polar coordinate system
Λ	Sink strength in vortex–sink combination forming free spiral vortex
ϕ	Velocity potential
A	Trailing edge tip; quantity defined in Equation (4) (when used with index)
B	Corner on upper profile surface near trailing edge; quantity defined in Equation (4) (when used with index)
C	Free spiral vortex parameter
C_{mom}	Moment coefficient
C_{p}	Coefficient of pressure
C_{ref}	Reference pressure coefficient
j	Index number of node
MAD	Mean absolute deviation measure of fit
N	Number of nodes distributed along profile surface
P	Pressure (static unless otherwise indicated)
r	Radial distance in polar coordinate system; radius
u	Vector component in x-axis direction; velocity component in x-axis direction
V	Flow velocity
v	Vector component in y-axis direction; velocity component in y-axis direction
x	Distance along horizontal axis in cartesian coordinate system
y	Distance along vertical axis in cartesian coordinate system
Z	Number of profiles in cascade

Subscripts

γ	Due to profile surface vortex distribution
dyn	Dynamic pressure $(\frac{1}{2}\rho V^2)$
F	Due to free spiral vortex
j	Index number of node
N	Index number of node N
n	Normal to profile surface
ref	Of reference flow
stag	Stagnation (total) pressure
stat	Static pressure
t	Tangential to profile surface
u	In x-axis direction
v	In y-axis direction
1	Index number of node
2	Index number of node
3	Index number of node

Superscript

*	Indicating local coordinate system of panel

Introduction

To aid in optimizing the operation and improving the efficiency of torque converters, various authors have established theoretical design and analysis tools for hydrodynamic drives. An example is the so-called one-dimensional hydrodynamic model which predicts the performance characteristics of a torque converter by using fluid properties, geometry and the operating conditions as input, to calculate the momentum flux over the members at specific operating points. This study takes a more basic approach by analysing a single element of the torque converter, which is seen as an entity operating under certain inlet conditions. The reasoning is that analysis of the performance of single elements eventually leads to better understanding of the whole torque converter. The ultimate objective is

[1]Department of Mechanical Engineering, University of Stellenbosch, Stellenbosch, 7600 Republic of South Africa (Member)

[2]Department of Mechanical Engineering, University of Stellenbosch

to establish a method whereby blade profile shapes may be optimized.

Specific objectives of this study are

- the experimental evaluation of the pressure distribution around a blade in a torque converter turbine;
- development of a theoretical two-dimensional potential flow analysis technique for calculating this pressure distribution;
- computer implementation of the potential flow analysis technique; and
- verification of this technique through comparison with published data and experimental results.

Background

The subject of this investigation is the second turbine of a commercial torque converter which is illustrated in Figures 1 and 2. The turbine is basically an axisymmetrical radial cascade with 20 identical blades, one of which is shown in Figure 3. This blade profile is defined by series of lines and arcs which are detailed in Table 1.

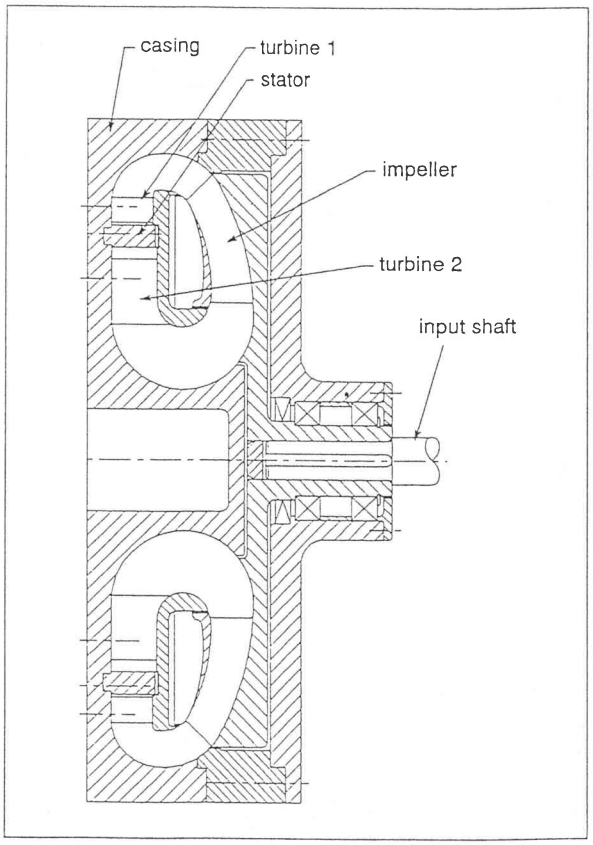

Figure 1 Cross-section of the torque converter model.

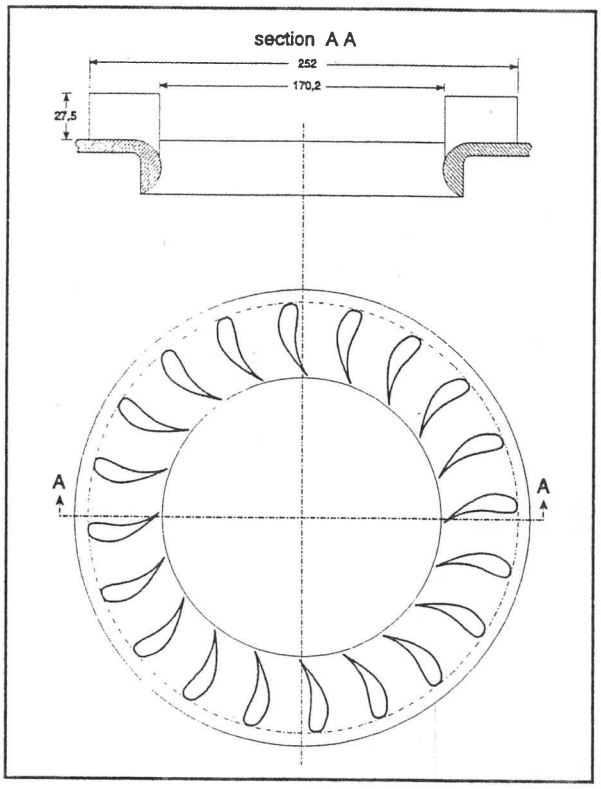

Figure 2 Plan and elevation of turbine.

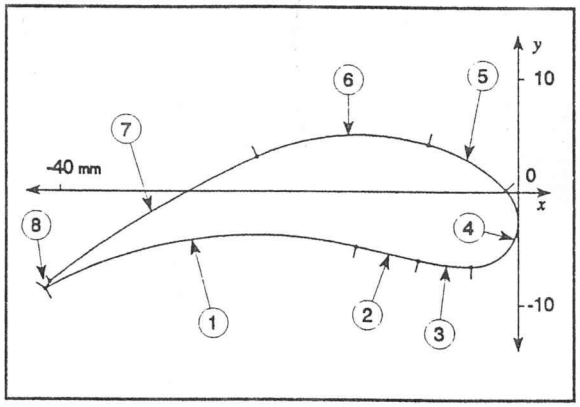

Figure 3 Turbine blade profile.

Experimental work

The torque converter turbine

A full-scale model of the torque converter with water as working fluid was used for the experiments. The model was equipped with two stationary turbines, separated by a stator and thus simulated the torque converter in the stalled mode only. This facilitated pressure measurements on the surfaces of the turbine blades, accomplished by means of holes, drilled in the surfaces of some blades and connected to a manometer, via a system of channels, tubes and valves. In total there were 23 holes on different blades,

Table 1 Detail of curves defining blade profile

Curve No.	Type	Starting point x	Starting point y	Arc centre (mm) x	Arc centre (mm) y	Arc radius (mm)
1	arc	−41.293	−8.677	−22.703	−42.106	38.250
2	line	−13.991	−4.861			
3	arc	− 8.567	−6.065	− 3.869	13.509	20.130
4	arc	− 4.066	−6.620	− 4.020	− 2.600	4.020
5	arc	− 1.076	0.137	−11.427	− 9.423	14.090
6	arc	− 7.677	4.159	−13.673	−17.153	22.140
7	arc	−22.775	3.029	12.981	−75.801	86.560
8	line	−40.913	−8.065			

perpendicular to the blade surfaces and in the middle of the blade span. The blades were accurately NC machined to be identical and the pressure distributions over them are assumed identical. By measuring static pressures at the 23 holes, the pressure distribution over the blade surface was thus obtained. Over the rear 20% of the blade chord the profile was too thin to allow the drilling of holes and no pressures could be measured in this area.

In two-dimensional airfoil theory it is customary to define the pressure distribution along an airfoil surface by means of a dimensionless coefficient of pressure, expressing the pressure with reference to the static and dynamic pressures of the undisturbed stream. Since the 'undisturbed stream' velocity varies inversely with radius in a radial cascade flow, the pressure at a defined location in the model is used as reference. This location is termed the 'reference pressure station' and it was chosen to be at the cascade inlet radius, midway between two adjacent turbine blades. The dimensionless *reference pressure coefficient* is defined as:

$$C_{\text{ref}} = \frac{P_{\text{stat}} - P_{\text{ref stat}}}{P_{\text{ref dyn}}} \qquad (1)$$

A 'Kiel' type probe (shrouded pitot tube) was used to measure the stagnation pressure at the reference pressure station. The dynamic pressure at the reference pressure station was assumed to be the difference between the stagnation pressure and a static pressure measured at the sidewall of the flow circuit, at the same radial position as the reference station, but midway between two other blades. The numerator of equation (1) is the difference between the reference static pressure and the static pressure registered at a blade surface pressure hole. These pressures were measured with a mercury manometer. As will shortly be shown, it is also important to find the flow angle at the reference pressure station. This 'reference flow angle' was measured using a 'wedge' probe in conjunction with two water manometers.

The measurements above were taken with the torque converter impeller running at speeds of 185, 260 and 290 rpm. The reference flow angle, as defined in Figure 4, was found to be 54.3° in all cases. The values for C_{ref} were calculated for each impeller speed, resulting in the distributions shown in Figure 5. The pressure distributions obtained at different speeds are nearly similar, affirming the repeatability of the blade pressure measurements and proving the validity of the reference pressure coefficient derived.

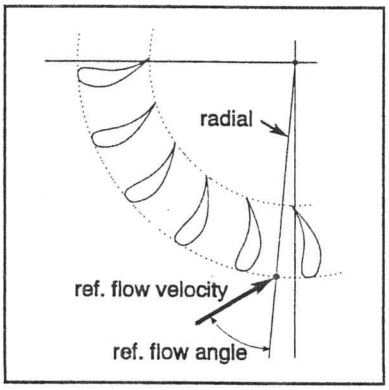

Figure 4 Reference flow.

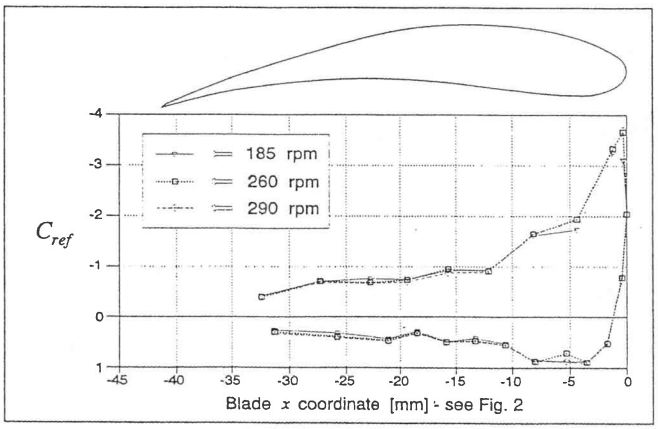

Figure 5 Experimental pressure coefficient distributions.

Potential flow analysis

Assumptions

In this analysis the flow around the torque converter blades is assumed to be incompressible, two-dimensional, inviscid and irrotational. The first assumption (incompressibility) is reasonable. Although the turbine blade aspect ratio is only 0.67, the second assumption (two-dimensionality) is tempting since it greatly simplifies the analysis, and the flow circuit curvature through the turbine is small. However, Reynaud,[1] who experimented on the same torque converter model, measured velocity differences of up to 25% and flow differences of up to 12° across the flow passage upstream of the second turbine blade row. Hence this assumption inevitably sacrifices some accuracy. The inviscid fluid assumption essentially leads to the neglect of the boundary layer on the blade surfaces. Using various techniques of flow visualisation, Reynaud concluded that little or no flow separation occurred in the turbine and, according to Hess & Smith [2] the inviscid flow assumption is thereby justified.

The panel method

According to Lakshminarayana [3] the panel method is the most suitable potential flow analysis method if the interest lies primarily in the pressure distribution. Therefore this method was chosen for the potential flow analysis. The panel method developed here will now be briefly outlined, the full details of the method and related mathematics having been given by Venter.[4]

Nodes and panels

A number of nodes are chosen on each blade surface, starting and ending at the trailing edge tip and proceeding in a clockwise direction. The section of surface between succeding nodes forms the panels and on each panel a local (x^*, y^*) coordinate system is defined with the x*-axis connecting the initial and end nodes of the panel and the y*-axis projecting outwards from the initial node. The blade surface between succeeding nodes is approximated by a cubic polynomial defined in the local coordinate system. In this way nodes and panels are distributed over all blades in the cascade, these distributions all being identical and with the nodes more densely spaced at the leading and trailing edges. A total of N nodes are chosen over the Z blades.

Free spiral vortex

A 'free stream' is commonly defined during the analysis of the flow around single profiles or in rectilinear cascades. The equivalent for the radial cascade is a free spiral vortex which follows from the conformal transformation mapping a Cartesian coordinate system onto a polar system as detailed for example by Wislicenus [5] and Scholz.[6] The free spiral vortex is centred at the cascade centre and consists of the superposition of a vortex (strength Γ) and a sink (strength Λ). With $\alpha = \arctan\left(\frac{\Gamma}{\Lambda}\right)$ and $C = \sqrt{\Gamma^2 + \Lambda^2}$, the flow velocity potential of the free spiral vortex at a point (r, θ) is then (from Anderson [7])

$$\phi_F = -\frac{C}{2\pi}\left(\theta \sin\alpha + \ln r \cos\alpha\right). \tag{2}$$

By differentiation the flow velocities in the x and y directions are

$$\begin{aligned} u_F &= -\tfrac{C}{2\pi r}\cos(\alpha+\theta) \text{ and} \\ v_F &= -\tfrac{C}{2\pi r}\sin(\alpha+\theta). \end{aligned} \tag{3}$$

Distribution of singularities and their induced flow velocities

Distributions of flow singularities are set up over all panels on all blades. Only vortices are used as singularities. The strength of the vortex distribution varies linearly over each panel and its value in the j-th node is denoted by γ_j. It may be shown that the total flow velocities in the x and y directions due to the vortex distributions on all panels on all blades can be expressed as

$$\begin{aligned} u_\gamma &= \textstyle\sum_{j=1}^{N} \gamma_j A_j \text{ and} \\ v_\gamma &= \textstyle\sum_{j=1}^{N} \gamma_j B_j, \end{aligned} \tag{4}$$

where A_j and B_j are quantities that depend only on the geometry of the blades and the cascade and can be calculated explicitly at any field point (x, y). Thus the only unknowns involved in the flow velocities are the vortex strengths γ_j in the nodes.

Control points and equations

At any point in the flow field the flow velocities induced by the free spiral vortex and the vortices distributed on the panels on all the blades, are given by

$$\begin{aligned} u &= u_F + u_\gamma \text{ and} \\ v &= v_F + v_\gamma . \end{aligned} \tag{5}$$

From (3) and (4) and Figure 6 the velocity normal to the blade surface is then

$$\begin{aligned} V_n(x,y) &= -u\sin\beta + v\cos\beta \\ &= \tfrac{C}{2\pi r}\left[\cos(\alpha+\theta)\sin\beta - \sin(\alpha+\theta)\cos\beta\right] \\ &\quad + \textstyle\sum_{j=1}^{N}\gamma_j\left[A_j\sin\beta + B_j\cos\beta\right] \end{aligned} \tag{6}$$

The velocity tangential to this surface is

$$\begin{aligned} V_t(x,y) &= u\cos\beta + v\sin\beta \\ &= \tfrac{C}{2\pi r}\left[-\cos(\alpha+\theta)\cos\beta - \sin(\alpha+\theta)\sin\beta\right] \\ &\quad + \textstyle\sum_{j=1}^{N}\gamma_j\left[A_j\cos\beta + B_j\sin\beta\right] . \end{aligned} \tag{7}$$

The unknown vortex distributions must now be chosen so as to make the blade surfaces streamlines of the flow. It

can be proved that this will be achieved if one of the following equivalent conditions is satisfied: the normal velocity at all points on the boundary must be zero; or the tangential velocity at any point just outside the blade surface must be equal to the vortex strength at the surface; or the tangential velocity just inside the blade surface must be zero (see Anderson [7]). These conditions are termed the streamline boundary conditions.

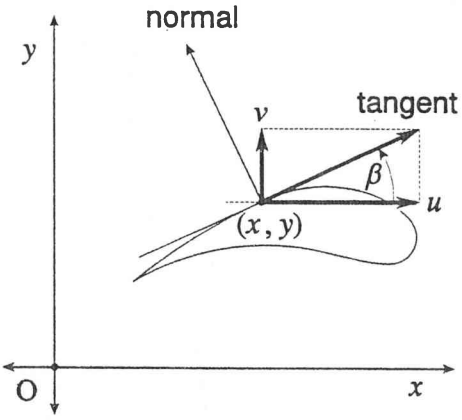

Figure 6 The normal and the tangent to the profile.

Applying the last condition to (7) leads to the linear equation

$$\sum_{j=1}^{N} \gamma_j \left[A_j \cos\beta + B_j \sin\beta\right] = \frac{C}{2\pi r}\left[\cos(\alpha+\theta)\cos\beta + \sin(\alpha+\theta)\sin\beta\right] \quad (8)$$

to be satisfied by the unknown γ_j's. Multiple 'control' points (x, y) are chosen on the blade surface and this equation is applied at infinitesimally small distances away from the control points towards the inside of the blade profile. Thereby enough equations may be generated from which to solve for $\gamma_1, \gamma_2, ..., \gamma_N$. Here the blade surface nodes themselves are chosen as control points. Since the distribution of panels and vortices are identical on the different blades, it is only necessary to set up and solve linear equations on one blade. The blade chosen for this purpose is called the 'control profile'.

As proven by, for example, Moran [8] and Anderson [7] the streamline boundary flow condition is not adequate to allow a unique solution for a blade that is generating lift. Another condition must be applied namely the Kutta condition which specifies the circulation generated by a blade. As shown by Moran [8] this is done by making the vortex strength in the trailing edge tip equal to zero and stipulating that the flow on the upper and lower surfaces of the blade join smoothly at the trailing edge tip and continues along the extension of the bisector of the trailing edge angle, away from the profile (see Figure 7). For a profile with sharp trailing edge the outlet flow angle is hereby fixed to the angle of the trailing edge bisector.

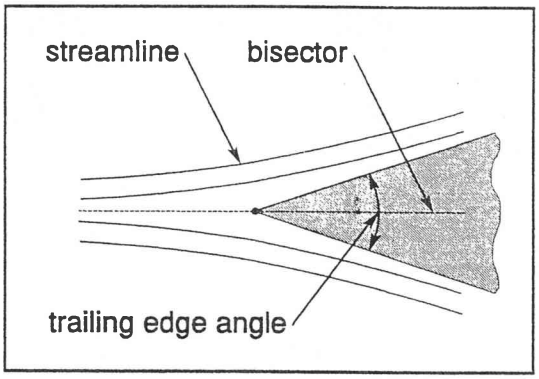

Figure 7 Trailing edge angle bisector.

Computer implementation of the panel method

A set of computer programs were written to apply the panel method to the torque converter turbine. The accuracy of the method and its implementation were verified by comparison to published data.

Application to a rectilinear cascade

The method was first modified by changing the geometry of the cascade and the character of the free stream so that it could be applied to rectilinear cascades. The program was then applied to several cases for which published C_p distributions are available, making comparisons and verifications possible. Figure 8 shows the C_p distribution predicted by the program for the rectilinear Gostelow cascade using cusped blades at a stagger angle of $-37.5°$, a pitch to chord ratio of 0.99 and an inlet angle of $-53.5°$ (Gostelow [9]). This cascade was also used as a test case by several other authors (e.g. Tanaka *et al.* [10] and McFarland [11]). The Kutta condition was applied as for the torque converter turbine blade. To calculate α, the iteration method suggested by McFarland [11] was used. The C_p distribution was calculated using the inlet velocity as reference, as was done in the original paper of Gostelow.[9] The agreement between the analytical C_p distribution given by Gostelow and that calculated here is excellent.

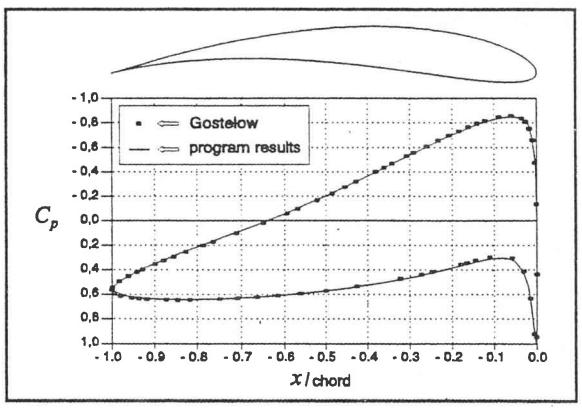

Figure 8 C_p distribution for Gostelow's rectilinear cascade.

Conformal transformation

Having established the accuracy of the analysis for the case of a rectilinear cascade, it is possible to evaluate the accuracy of the analysis for a radial cascade using a conformal transformation which maps a rectilinear cascade onto a radial cascade (Wislicenus [5] or Gostelow [9]). The program for rectilinear cascades was first applied to the Gostelow cascade. By integrating the tangential flow velocity on the profile surface, from the trailing edge in a clockwise direction around a profile in the Gostelow cascade, the flow potential on the profile was calculated in the chosen control points. The Gostelow cascade was transformed to an axisymmetrical radial cascade by means of a conformal transformation and the new locations of the control points were determined. The program for axisymmetrical radial cascades was applied to this cascade and the profile surface potentials calculated in the new control points. The flow potential is invariant under a conformal transformation and consequently the potential values obtained from both programs should correspond. However, since the programs used different conventions regarding their free streams, these potential values differed by a constant scaling factor. To remove this factor the two sets of potential values were normalized by dividing each by its potential value at the leading edge (which was approximately the largest value obtained). These normalized potential values are shown in Figure 9, plotted against the original coordinates of the (unstaggered, untransformed) Gostelow profile. It is clear that the agreement is excellent.

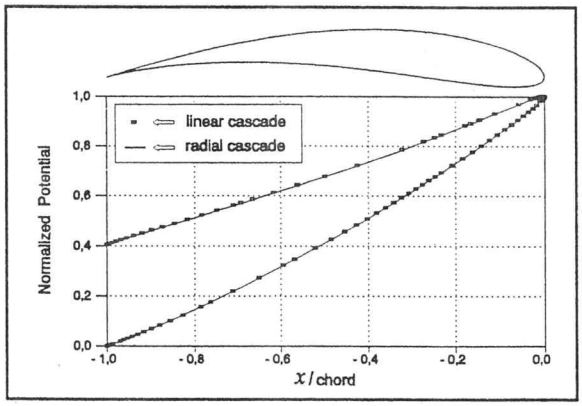

Figure 9 Potential values for linear and radial Gostelow cascades.

It has now been shown that the linear cascade program gives results in accordance with published data. Furthermore, the radial and linear cascade programs agree if applied to conformally related cascades. This leads to the conclusion that the radial cascade program is also substantially correct.

Application to the torque converter turbine

The method was then applied to the radial turbine cascade using the modified blade trailing edges discussed below.

Turbine trailing edge conditions

The trailing edge of the torque converter turbine blade is shown in Figure 10. The shape of this trailing edge creates a problem with the application of the Kutta condition. To simply apply the condition as detailed above would mean the specification of an outlet flow angle which is clearly larger than wat could realistically be expected from the cascade. Also, if the upper trailing edge corner B is not treated in a special way, inviscid flow theory would predict an infinite flow velocity around this corner. Different solutions to this problem, in the form of slight modifications to the blade profile, were investigated.

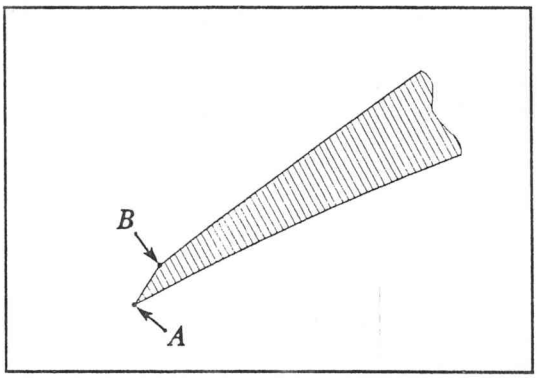

Figure 10 Turbine blade trailing edge.

The blade trailing edge was slightly modified by first smoothing out corner B with an arc and then by extending the two arcs that make up the upper and lower blade surfaces near ;the trailing edge, until they meet. Both trailing edges are illustrated in Figure 11. Although this results in a thin, sharp trailing edge to which the Kutta condition can be applied as explained above, the modifications are arbitrary and the resulting specified circulation may not be realistic. To solve this the outlet flow angle of the cascade must be established by either calculation or measurement. Due to practical considerations regarding the torque converter model, the latter proved impossible and the angle had to be estimated by calculation.

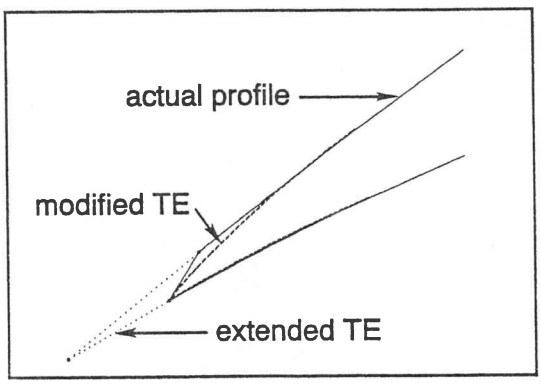

Figure 11 Extended and modified trailing edges.

Dixon [12] describes a geometrical method for the estimation of the outlet flow angle of a linear cascade. This

method may be modified for application to a radial cascade using a logarithmic spiral instead of Dixon's straight line, as illustrated in Figure 12. The logarithmic spiral connects the trailing edge of one profile with the suction surface of the next, intersecting the latter orthogonally. Only one such logarithmic spiral exists. Applied to the torque converter cascade, this method yielded a radial outlet flow angle of 29.59°.

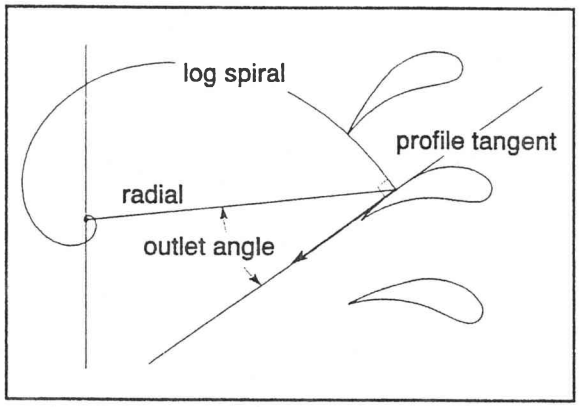

Figure 12 Estimated outlet angle.

The trailing edge was adjusted such that the radial angle of the trailing edge bisector equalled this estimated outlet flow angle. The modification used two arcs, which joined the upper and lower curves of the profile surfaces smoothly and met in a sharp, tip with a bisector at the required angle (see Figure 13). Care was taken to keep the extension as short as possible to avoid inaccuracies. The Kutta condition was then applied to the adjusted blade trailing edge.

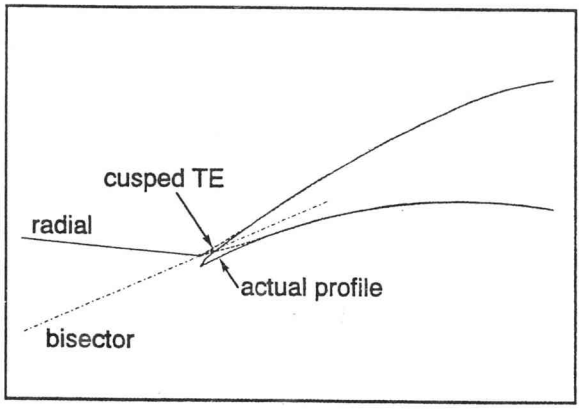

Figure 13 Adjusted trailing edge.

To solve the system of equations the free spiral vortex parameters C and α must be known. It can be proved that C acts only as a constant of proportionality of the flow velocities and that it cancels out of any ratio of one velocity to another. As will shortly be shown the pressure distribution around the blade is expressed by means of such a ratio and consequently any convenient value may be used for C (e.g. $C = 1$). The α parameter has a different influence. If α is known and the γ_j's have been determined, the flow velocity anywhere in the flow field can be calculated using (5). By calculating the angle of the flow at the location of the reference pressure station and changing the value of α until this angle corresponds to the reference flow angle measured experimentally, the α necessary for similarity to the experimental situation can be established. The pressure distribution calculated at this α should then correspond to the experimental pressure distribution.

Calculation of the pressure coefficient

In accordance with the initial assumptions it may be assumed that Bernoulli's equation holds for the flow through the stationary turbine. Then the stagnation pressure will be constant throughout the flow field and (1) may be rewritten as

$$C_{\text{ref}} = 1 - \left(\frac{V_t}{V_{\text{ref}}}\right)^2 . \qquad (9)$$

This gives the pressure coefficient in terms of the blade surface velocity and the velocity at the reference pressure station and allows the calculation of this coefficient by applying (7) at points on the blade surface and using the magnitude of the velocity given by (5). Instead of using (7) for V_t, it may also be equated to the vortex strength solution at the blade surface points (which follows from the streamline boundary condition and is much simpler but does not hold for the trailing edge node).

The calculated distribution of C_{ref} around the profile may now be compared to that obtained experimentally. To quantify this comparison the means of the absolute deviations between experimental C_{ref}'s and their calculated equivalents is used. This parameter is referred to as the *MAD* (mean absolute deviation) measure of fit. The C_{ref} distribution can also be integrated over the radial projection of the profile. By incorporating into this integral multiplication by the distance of every incremental area from the cascade centre, a measure of the moment around the cascade centre (or torque) generated by a single blade, is obtained. This *moment coefficient* is denoted by C_{mom}

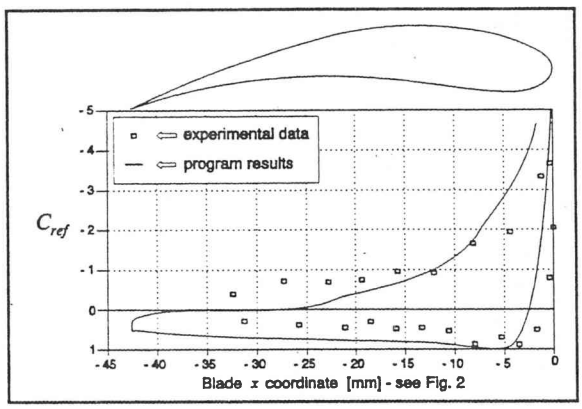

Figure 14 Reference point method results for extended trailing edge (Figure 11).

Table 2 Results for extended (Figure 11) and adjusted (Figure 13) trailing edges

Parameter	Reference point method		Optimal C_{ref} fit method	
	Extended TE	Adjusted TE	Extended TE	Adjusted TE
flow angle at reference station	−54.30°	−54.30°	−35.54°	−36.16°
α	36.02°	28.54°	36.24°	28.80°
MAD measure of fit	0.942	0.950	0.284	0.253
C_{mom} (exp) [mm^2]	−5985	−5985	−5985	−5985
C_{mom} (80%) [mm^2]	−6903	−6695	−8141	−7746
C_{mom} (100%) [mm^2]	−7379	−6935	−8998	−8128
total torque [Nm]	37.69	35.42	45.96	41.52
predicted upstream flow ∠	−68.08°	−67.99°	−50.85°	−51.48°
estimated stator outlet ∠	−55.60°	−55.60°	−55.60°	−55.60°
predicted turbine outlet ∠	33.62°	27.23°	33.90°	27.58°
estimated turbine outlet ∠	30.91°	29.59°	30.91°	29.59°

and may be calculated from the experimental and the panel method predicted C_{ref} distributions, and the results can be compared in further assessment of the accuracy of the analysis. The torque output of the turbine could also be measured experimentally and compared to an output torque calculated from the theoretical moment coefficient.

Since the extended trailing edge in Figure 11 and the adjusted trailing edge in Figure 13 yielded the most realistic results, only these will be discussed. The results for these blades are summarized in Table 2 and in Figures 14 to 17. The meaning of the table entries and the figure captions will shortly become clear.

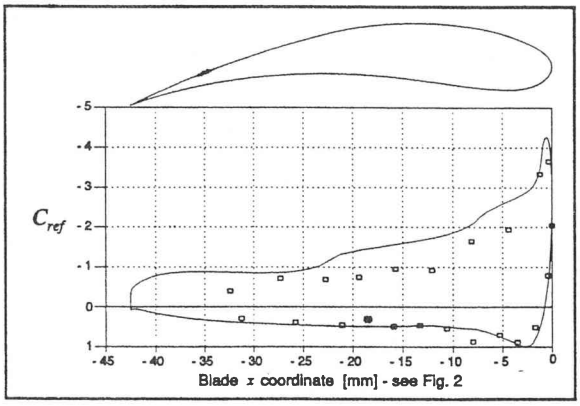

Figure 15 Optimal C_{ref} fit method results for extended trailing edge.

Extended trailing edge blade

Figure 14 shows the **pressure distribution** obtained for the extended trailing edge at the α which makes the calculated flow angle at the reference pressure station equal to the measured reference flow angle. This method for determining α is termed the *reference point method* and according to Table 2 it yields an α of 36.02. The MAD measure of fit is 0.942 and from Figure 14 it is clear that the predicted distribution is not a very good approximation of the experimental distribution over the full profile. It was decided to find the best possible correspondence that the panel method could yield by trying different values of α. This method for determining α is referred to as the optimal C_{ref} fit method and it results in $\alpha = 36.24°$, a minimum MAD of 0.284 and the C_{ref} distribution of Figure 15. The flow angle at the reference point now changes to −35.54°. The improvement in agreement between predicted C_{ref} and experimental C_{ref} distributions due to the optimal C_{ref} fit method, is reflected clearly in the drop in the MAD value. The fit to the experimental data is excellent on the pressure surface and the leading edge of the blade but on the suction surface the predicted C_{ref} values are generally too negative. In part this may be caused by the effect discussed previously whereby the flow deflection specified by the Kutta condition is higher than that of the actual cascade.

Table 2 also shows the **moment coefficient** calculated from the experimental data over the forward 80% of the blade chord (C_{mom}(exp)), that calculated from the panel method results over the forward 80% of the blade chord (C_{mom}(80%)) and that calculated from the panel method results over the entire blade (C_{mom}(100%)). Thus C_{mom}(exp) and C_{mom}(80%) are directly comparable. The reference point method yields a result closer to the experimental value than that of the optimal C_{ref} fit method. However, inspection of Figure 14 indicates that this could be due to a fortuitous cancellation of errors in the predicted pressure distribution rather than a closer approximation of the experimental pressure distribution. The numerically higher C_{mom} value resulting from the optimal C_{ref} fit method is due to the low C_{ref}'s predicted on the

suction surface as discussed earlier. The 'total torque' was calculated using $C_{\text{mom}}(100\%)$ and can be compared to the experimental torque of 30.3 Nm, cited by Reynaud.[1] The discrepancy between the predicted and experimental C_{mom} values discussed above, was the major contributor to this difference.

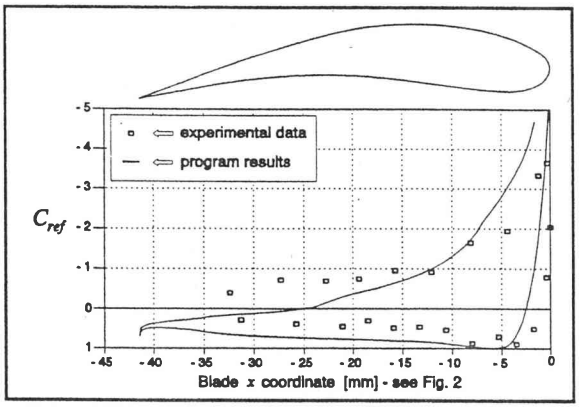

Figure 16 Reference point method results for adjusted trailing edge (Figure 13).

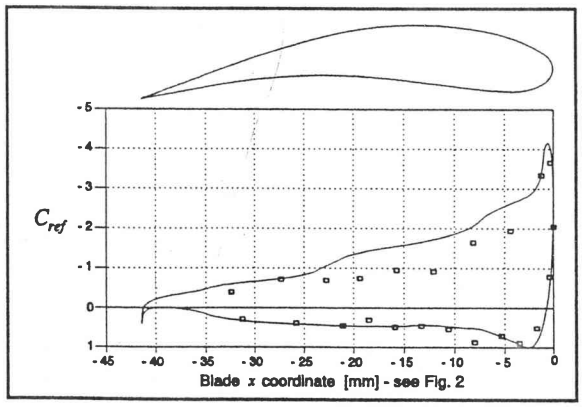

Figure 17 Optimal C_{ref} fit method results for adjusted trailing edge.

Four different flow angles are shown in Table 2. The first angle is defined as follows: if a field point is moved radially outward to infinity and the flow angle at this point calculated by means of the panel method, this flow angle tends to a limit which is indipendent of the coordinates of the field point. This limiting angle is referred to as the 'predicted upstream flow angle'. The program predicts a flow angle that is already within 2° of its limiting value at a radius 15 mm greater than the radius of the cascade leading edge. In the torque converter this upstream flow angle is considered to be the inlet flow angle of the turbine and as such it should be close to the outlet flow angle of the stator cascade, which precedes the turbine in the flow path.

Using the geometrical method of Figure 12 the stator outlet flow angle has been estimated and is referred to in Table 2 as the 'estimated stator outlet angle'. The best correspondence between this angle and the predicted upstream flow angle is obtained using the optimal C_{ref} fit method. The 'predicted turbine outlet angle' in Table 2 is the flow angle calculated by the panel method at a field point on the cascade trailing edge radius, midway between two successive trailing edges. This angle may be compared to the 'estimated turbine outlet angle' again obtained by the geometrical method.

Adjusted trailing edge blade

Figures 16 and 17 indicate that this trailing edge performed somewhat better than the simply extended trailing edge. The C_{ref}'s are significantly less negative over the rear third of the blade suction surface and for the optimal C_{ref} fit method there is a steady pressure recovery with the C_{ref}'s corresponding well to the experimental distribution over this area. For this method then the MAD fit is also the best and this trailing edge also performs better as far as the moment coefficients and the agreement between predictged and estimated flow angles are concerned.

Discussion

It was found that when the turbine blade trailing edge shape was modified to give an outlet flow angle in agreement with that expected from the cascade geometry, the inlet flow angle that would give the best fit to the experimental pressure distribution would agree to within 4° with the upstream stator outlet flow angle. The shape of the predicted pressure distribution then agrees very well with the experimental distribution except in the 10 to 60% chord region on the suction side. Taking into consideration the complex three-dimensional flow in the torque converter, especially at stall as in the current case, the agreement is as good as can be expected.

Conclusions

- A theoretical two-dimensional potential flow technique was developed for the analysis of incompressible flow through a torque converter turbine cascade.
- A set of computer programs implementing this technique was developed.
- The soundness of the technique and computer programs was verified by comparison with published results.
- The technique was applied to the torque converter turbine and yielded results in reasonable agreement with the experimental measurements.
- The agreement between predicted and experimental pressure distributions was good enough to warrant the use of the present method for the analysis of proposed turbine blade profile designs.

References

[1] Reynaud FP. *Hydrodynamic modelling of torque converters.* MEng thesis, University of Stellenbosch, 1991.

[2] Hess JL & Smith AMO. Calculations of potential flow about arbitrary bodies. In: *Progress in aeronautical sciences, Vol. 8.* Pergamon Press, Great Britain, 1967.

[3] Lakshminarayana B. An assessment of computational fluid dynamic techniques in the analysis and design of turbomachinery – The 1990 Freeman Scholar Lecture. *Transactions of the ASME, Journal of Fluids Engineering*, 1991, **113**, 322.

[4] Venter AA. *The flow around torque converter turbine blades.* MEng thesis, University of Stellenbosch, 1993.

[5] Wislicenus GF. *Fluid mechanics of turbomachinery*, 2nd edn. Dover Publications, New York, 1965.

[6] Scholz N. *Aerodynamics of cascades*, Translated and revised by A. Klein. AGARD/NATO, France, 1977.

[7] Anderson JD Jnr. *Fundamentals of aerodynamics.* McGraw-Hill Book Company, USA, 1984.

[8] Moran J. *An introduction to theoretical and computational aerodynamics.* John Wiley & Sons, USA, 1984.

[9] Gostelow JP. *Potential flow through cascades – a comparison between exact and approximate solutions.* ARC CP 807, 1964.

[10] Tanaka S, Murata S & Kurata K. Computation of the potential flow through cascades using the conformal mapping and the singularity method. *JSME International Journal, Series II*, 1991, **34**, 423–430.

[11] McFarland ER. Solution of plane cascade flow using improved surface singularity methods. *Transactions of the ASME*, 1982, **104**, 668–674.

[12] Dixon SL. *Fluid mechanics, thermodynamics of turbomachinery*, 3rd edn. Pergamon Press, Oxford, 1978.

Velocity measurement in a hydrodynamic torque converter

P.J. Strachan[1] and **T.W. von Backström**[2]

(Received September 1999; Final version September 2000)

An experimental torque converter in which flow characteristics could be both observed and measured was manufactured and tested. Flow visualisation was carried out by means of fluorescent tufts, air bubbles and polystyrene particles, and from these visualisations, flow velocities and angles were determined by using video and still photography. Differential pressure probes were used for direct measurement of flow velocity at different stations in the flow path. Agreement between results obtained by these different methods was good. The torque converter performance was also simulated by means of a one-dimensional hydrodynamic model, and acceptable overall agreement was obtained between measured parameters and the model's results.

Introduction

In previous work[1]the description was given of a one-dimensional computer program for analysing torque converter performance, in which much of the empiricism in the input data, found in similar models, had been removed and replaced by empirical equations and loss models built into the program. Due to the model's need for very detailed input data, particularly relating to geometry, its efficacy could only be validated against two sets of published results, namely those by Lamprecht[2] and Jandasek.[3] In both cases the improvement in accuracy over existing models was significant. In order to further validate the model and to evaluate torque converter characteristics, an experimental torque converter was developed in which the flow could be observed and measured.[4] In addition, the dimensions of the experimental torque converter could be accurately measured and used as input to the model.

This paper describes the apparatus and compares the measured results with those determined by the one-dimensional hydrodynamic model.

Description of the apparatus

Torque converter test rig

The test rig (Figure 1) was a universal facility capable of testing a variety of hydrodynamic drives such as torque converters and fluid couplings. It consisted of two sets of identical 5.5 kW, variable speed (0–3 000 rpm) electric motors and 4.45:1 step-down gearboxes, which could be connected to the input and output shafts of either a torque converter or fluid coupling. For reasons given later, the experimental torque converter utilised in the experiment was only operated in stall, and consequently only the input drive system of the test rig was used. The test rig provided controlled, independent and infinitely variable input speed, which was measured by a proximity transducer, excited by a 60-tooth disc attached to the input shaft. Torque measurement was by means of a specifically developed contactless torque transducer.

Experimental torque converter

The experimental torque converter (Figure 2) was a full-size model of a commercial unit for which manufacturing drawings were available. The torque converter had a single stage pump with a two stage turbine and in its commercial form was capable of transmitting 1 500 Nm of torque at 2 600 rpm, an equivalent power of approximately 410 kW. In order to reduce the power requirement for laboratory purposes, water was used as the working fluid and therefore to maintain dynamic similarity a lower rotational speed was required. Assuming kinematic viscosities of 6.0×10^{-6} m^2/s for a typical hydraulic transmission fluid at a temperature of 100°C, and 0.66×10^{-6} m^2/s for water at a temperature of 40°C, the speed ratio for constant Reynolds number should be 10:1. Therefore an input speed of 260 rpm was used on the test rig, resulting in a maximum torque of 68 Nm and a maximum power of about 2 kW.

In order to permit visual observation of the flow conditions, part of the torque converter casing was manufactured from clear perspex. This exposed the two stages of the turbine, the stator and the inlet to the pump. As it would also be necessary to measure flow velocity at various stages in the flow path, it was decided to maintain the output shaft stationary and thus to operate the torque converter in stall. Although this would obviously limit the range of results obtained, it would greatly simplify measurement. In addition, the stall point of a torque converter is probably its most important operating situation and thus it was considered that results obtained at this condition would have the most significance.

As shown in Figures 2 and 3, foot plates for the probe traversing mechanisms were provided at 6 different positions on the torque converter housing, permitting flow measurement by directional pressure probes at 7 different

[1]Department of Mechanical Engineering, University of Stellenbosch, Private Bag X1, Matieland, 7602 South Africa

[2]Department of Mechanical Engineering, University of Stellenbosch, Private Bag X1, Matieland, 7602 South Africa

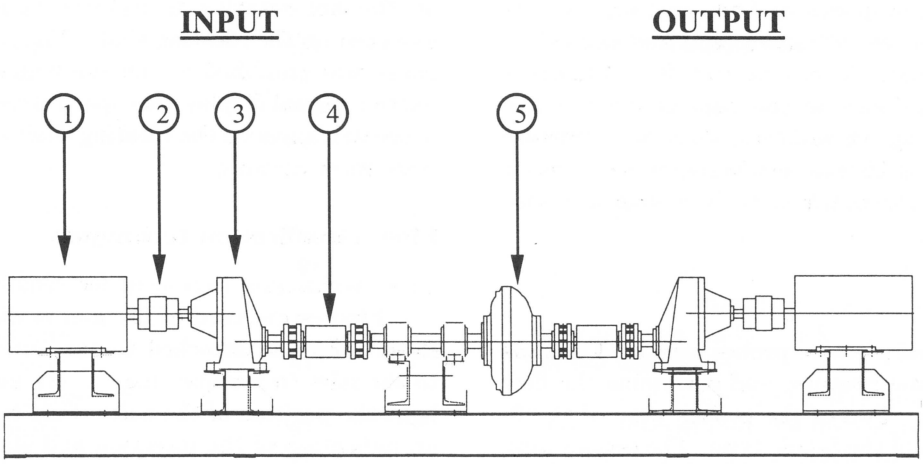

1. Electric motor
2. Flexible coupling
3. Gearbox
4. Torque transducer
5. Torque converter

Figure 1 Experimental test rig setup

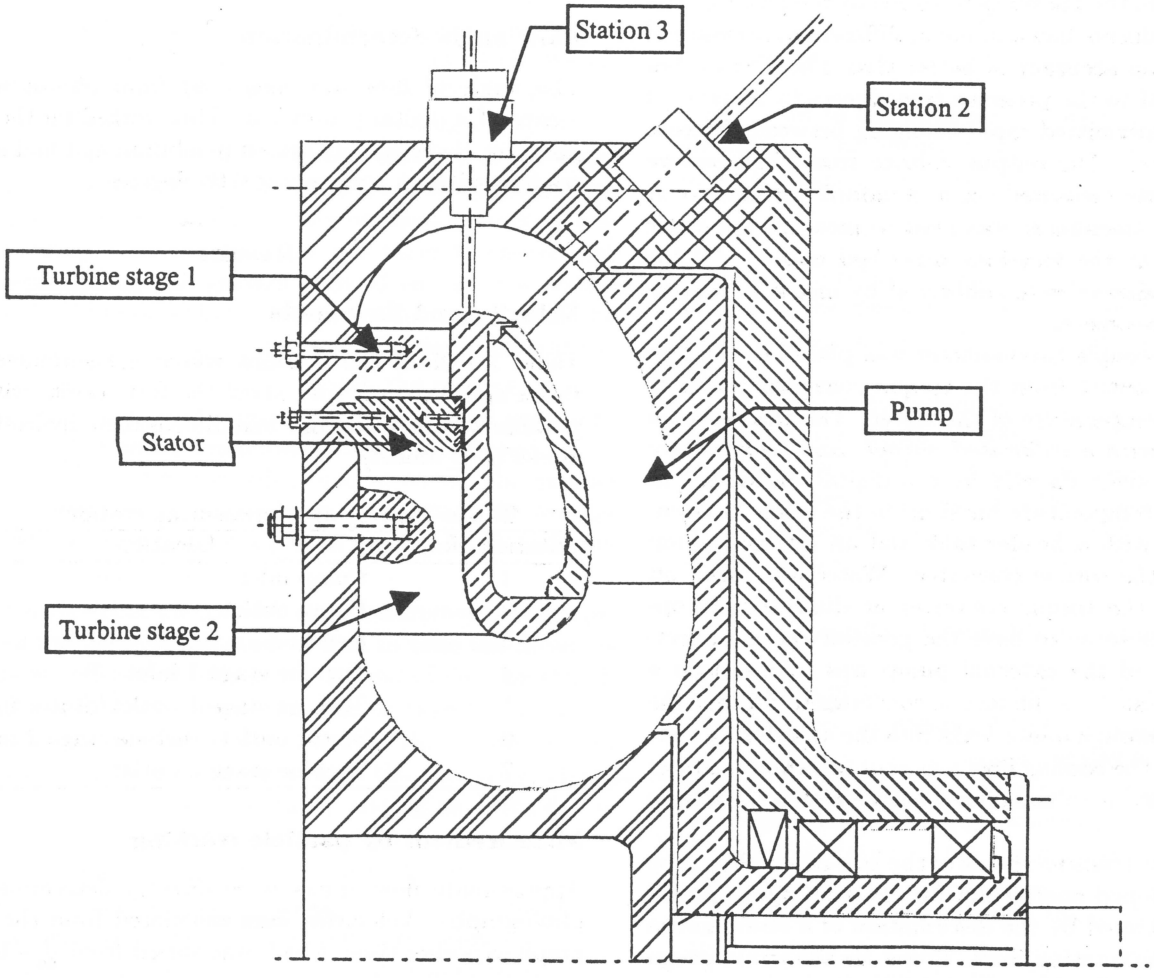

Figure 2 Section through experimental torque converter showing components and measuring stations

locations in the flow path. These were at the entrance to (location 1) and exit from the pump (2), midway in the channel between the pump exit and the entrance to turbine stage 1 (3) and at the entrances (4,6) and exits (5,7) of the two turbine stages. As can be seen from Figures 2 and 3, locations 1 and 7 were at the same position on the torque converter housing. In addition, static wall pressure tapings were provided at 15 locations between the entrance to turbine stage 1 and the exit from turbine stage 2 as also shown in Figure 3.

Instrumentation

Two types of directional pressure probes were used to measure the total and static pressure and determine the flow velocity and direction. Two of the probes were of the 3-hole type and one was of the 5-hole type. The probes were mounted on a traversing mechanism permitting translation and rotation. All the probes were calibrated in a water tunnel in which the flow velocity was measured by means of a flow contraction. The probes and their traversing mechanism were fitted to the side wall of the tunnel and the water velocity was varied between 1 m/s and 9 m/s. The dynamic pressure of the flow was determined from the difference between the total and quasi-static pressures recorded by the probes.

Two electronic differential pressure transducers were used to measure the pressures recorded by the probes. The pressure transducers had a nominal differential pressure of 0.01 bar, and an accuracy of better than 1%. The probes were connected to the pressure transducers by a series of valves, which permitted rapid changing between different probe positions. The output voltage from the pressure transducers was measured on a standard voltmeter. A third pressure transducer was used to measure the static wall pressure at the locations described above. All the pressure transducers were calibrated by means of a standard water manometer.

A thermocouple thermometer was placed in the flow circuit at the outlet from the torque converter pump to measure the temperature of the water. The thermometer was supplied with a calibrated output, and temperature readings were given directly from a digital voltmeter. In order to limit temperature build-up in the water, a circulating system with a header tank and an external pump was fitted to the torque converter. Water was taken off and added to the torque converter at diametrically opposed locations so as to have the greatest cooling effect. A further use of the external pump was to maintain a slight over-pressure on the torque converter to prevent the ingress of air through minor leaks into the unit during testing. However, the cooling flow was shut off when readings were taken to ensure a mass flow balance within the torque converter.

The torque transducer was of the non-contactless type and was developed specifically for the test rig. Applied torque was detected by the deformation of a strain gauge mounted on the rotating shaft. Power for the strain gauge was provided by a remote external power pack and was transmitted inductively between two coils, one mounted on the non-rotating transducer housing and the other mounted on the rotating shaft. The signal from the strain gauge was amplified within the transducer and transmitted to a digital display via capacitative decoupling through concentric rings on the rotating shaft and in the stationary transducer housing.

Flow visualisation techniques

Three techniques were used for visualisation of the flow.

Fluorescent cord of 0.1 mm in diameter was cut into short tufts and attached to the outlet of the pump and to the inlet to turbine stage 1. By means of stroboscopic light the position of the tufts could be determined, giving an indication of the direction and status of the flow. Air bubbles were introduced into the flow stream through the 3-hole probe located in the channel between the pump and turbine stage 1. At certain speeds the path of the bubbles gave a clear indication of the flow direction.

At higher speeds, polystyrene chips of approximately 2 mm diameter, 2 mm in length and having a density 2.8% greater than that of water, were admitted into the unit through the water inlet. A good indication of flow direction was obtained and recorded by means of both video and still photography.

Flow angle determination

The angle of flow was measured from photographs by means of a digital protractor. This worked on the principle of an electronically sensed pendulum and had a digital readout with an accuracy of 0.05 degrees.

Results

Velocity and flow angle

Table 1 defines the stations where measurements were taken and Tables 2 to11 show the test results with comparable values from the one-dimensional hydrodynamic model (1-D Model).

Table 1 Location of measuring stations

Station No.	Location
1	Pump inlet
2	Pump outlet
3	Bend
4	Turbine stage 1 inlet
5	Turbine stage 1 outlet/Stator inlet
6	Stator outlet/Turbine stage 2 inlet
7	Turbine stage 2 outlet

Measurement by particle tracking

Approximate flow angles were directly determined from photographs. Velocities were calculated from the photograph exposure time, which was varied from $\frac{1}{60}$ s to $\frac{1}{250}$ s,

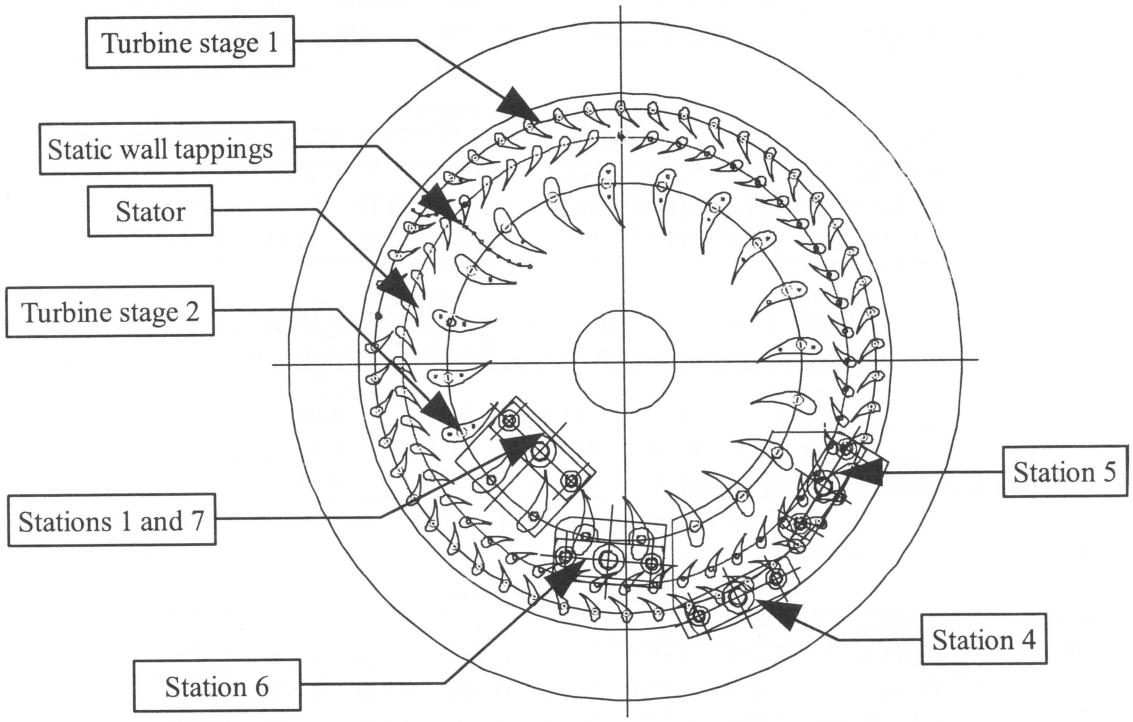

Figure 3 Section through experimental torque converter showing components and measuring stations

Table 2 Absolute flow velocities (m/s)

Station	1	2	3	4	5	6	7
Particle		3	3	2.7		4.4	3.5
Probe	3.65	2.91	2.78	3.30	3.63	4.77	3.54
1-D Model	2.57	3.33		3.39	3.17	4.68	2.45

Table 3 Absolute flow angles (deg)

Station	1	2	3	4	5	6	7
Particle		55	55	−50		−66	42
Probe	53.5	52.9	45.4	−42.1	68.6	−69.6	36.4
1-D Model	58.7	47.9		−63.5	58.5	−67.5	31.7

Table 4 Meridional velocities (m/s)

Station	1	2	3	4	5	6	7
Particle		1.7	1.7	1.7		1.8	2.6
Probe	2.23	1.71	1.9	2.51	1.66	1.82	2.81
1-D Model	2.31	1.62		1.51	1.65	1.80	2.08

Table 5 Flow area (m^2)

Station	1	2	3	4	5	6	7
Particle	0.0171	0.0244	0.0261	0.0261	0.0243	0.0219	0.0192
Probe	0.0192	0.0244	0.0261	0.0261	0.0243	0.0219	0.0192
1-D Model	0.0171	0.0244	0.0261	0.0261	0.0243	0.0219	0.0192

Table 6 Mass flow (kg/s)

Station	1	2	3	4	5	6	7
Particle		41.3	44.2	44.2		39.3	49.7
Probe	42.64	41.56	49.39	65.25	40.18	39.70	53.74
1-D Model	39.34	39.37		39.25	39.81	39.15	39.78

Table 7 Mass flow averaging over all stations (kg/s)

Method	Averaged flow		Standard deviation %	
		*		*
Particle	43.7	41.6	3.52	2.02
Probe	47.49	42.69	8.71	1.85
1-D Model	39.45	39.42	0.25	0.24

(* exc. stations 4 and 7)

Table 8 Radius (m)

Station	1	2	3	4	5	6	7
Particle	0.078	0.170	0.182	0.166	0.148	0.130	0.078
Probe	0.078	0.170	0.182	0.166	0.148	0.130	0.078
1-D Model	0.099	0.170	0.182	0.166	0.148	0.130	0.086

Table 9 Tangential velocities (m/s)

Station	1	2	3	4	5	6	7
Particle		2.5	2.5	2.1		4	−2.3
Probe	−2.9	2.3	2.2	2.2	−3.2	4.2	−2.1
1-D Model	−1.12	2.91		3.03	−2.71	4.33	−1.29

Table 10 Angular momentum/unit mass flow (m^2/s)

Station	1	2	3	4	5	6	7
Particle		0.4	0.5	0.3		0.5	−0.2
Probe	−0.23	0.39	0.40	0.36	−0.47	0.55	−0.16
1-D Model	−0.11	0.49		0.50	−0.40	0.56	−0.11

Table 11 Torque at different members (Nm)

Member	Impeller	Turbine 1	Stator	Turbine 2	Total
Particle				30.6	
Probe	−26.35	35.77	−43.53	30.30	−3.80
1-D Model	−23.88	35.59	−37.98	26.55	0.28

(N.B. Mass flow exc. stations 4 and 7)

and the length of the particle tracks. Since it was difficult to judge how far the particles were from the walls of the flow passages, where large deviations from the mean were expected, these values, summarized in Tables 2 and 3, could only serve as checks of the flow some distance from the wall. Other factors influencing the accuracy of flow velocity measurement by particle tracking are the finite size of the particles and the deviation of their densities from that of water.

Measurement by dynamic pressure probes

Flow angles were determined by turning the probes until the quasi-dynamic pressures on the left and right sides of the probe were equal. The quasi-dynamic pressure was the difference between the probe stagnation pressure and the side hole pressure. Since the model had been designed with all the probe axes in the horizontal plane, flow angles were easily determined by means of the digital protractor. The convention for the flow direction was according to Figure 4 with the observer always on the outside of the flow circuit and looking in. Wakes of upstream blade rows would have had a large influence on the accuracy of the flow measurement by means of probes. The effect of blockage and the shear effects would have had an effect on the velocity magnitude and direction.

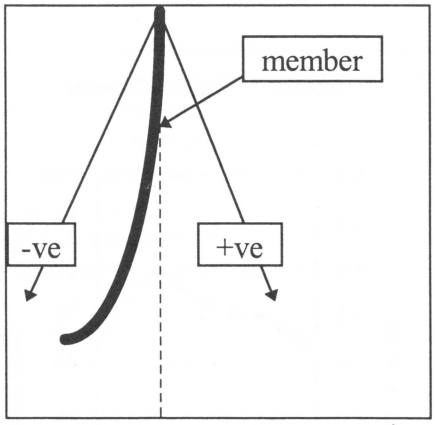

Figure 4 Sign convention for flow angles

Discussion of results

Velocity profiles

The absolute velocity profiles, as shown for the different stations in Figures 5 to 10, were fairly uniform, with a tendency for the higher velocities to occur on the inside of the flow circuit. There were, however, visual indications of flow separation on the inner wall of the section between the exit from turbine stage 2 and the inlet to the pump, although this was not apparent from the probe readings.

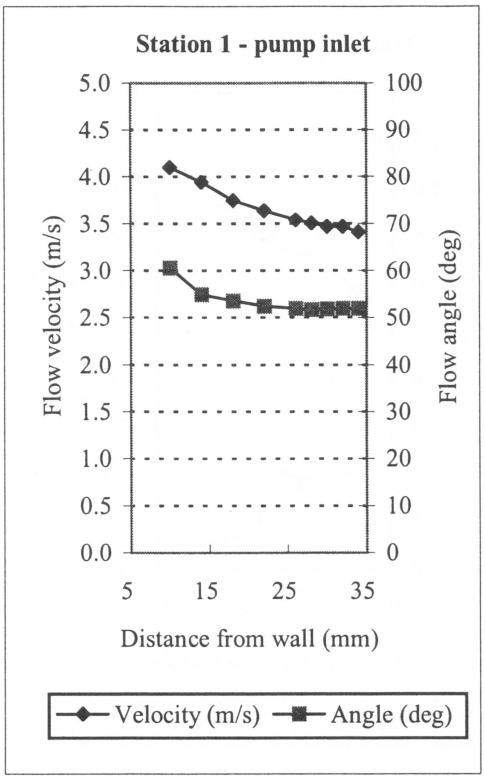

Figure 5 Pump inlet: Velocity and flow angle

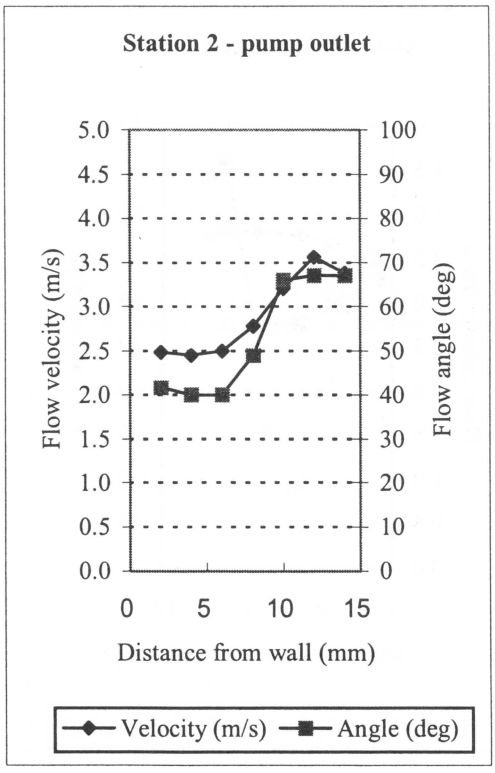

Figure 6 Pump outlet: Velocity and flow angle

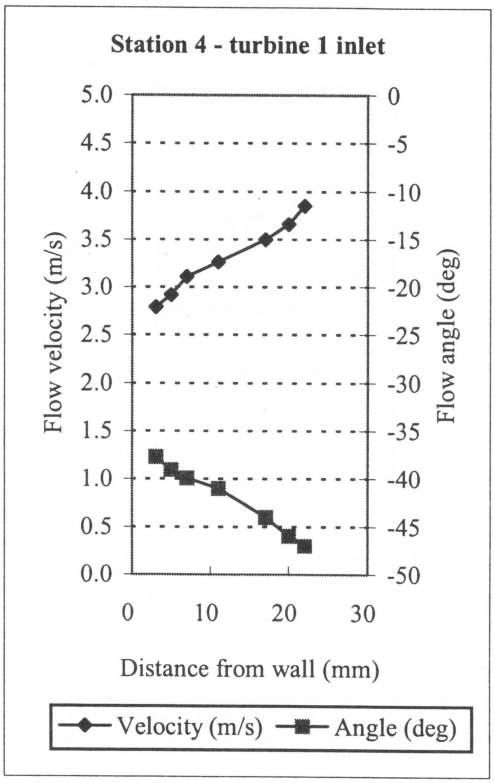

Figure 7 Turbine 1 inlet: Velocity and flow angle

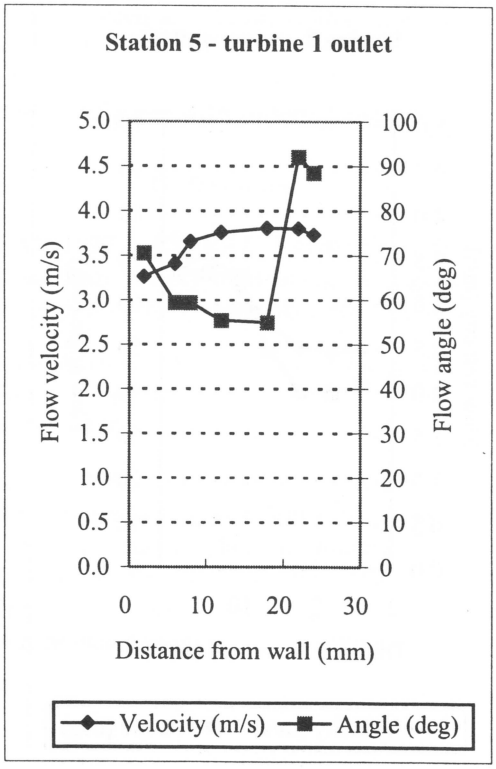

Figure 8 Turbine 1 outlet: Velocity and flow angle

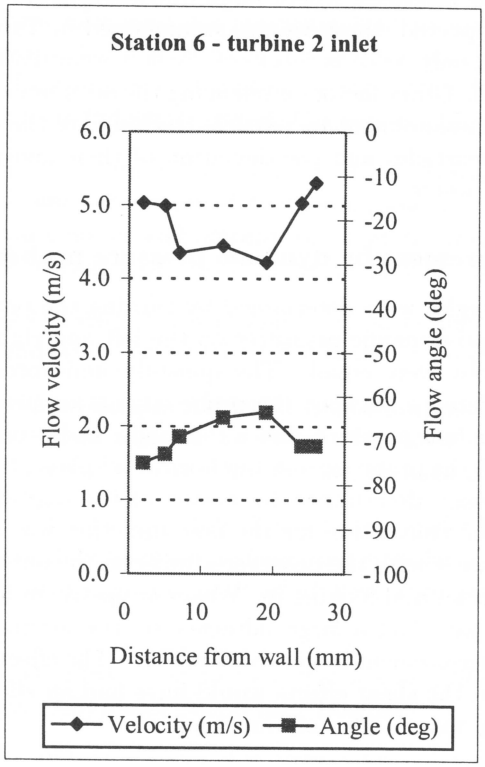

Figure 9 Turbine 2 inlet: Velocity and flow angle

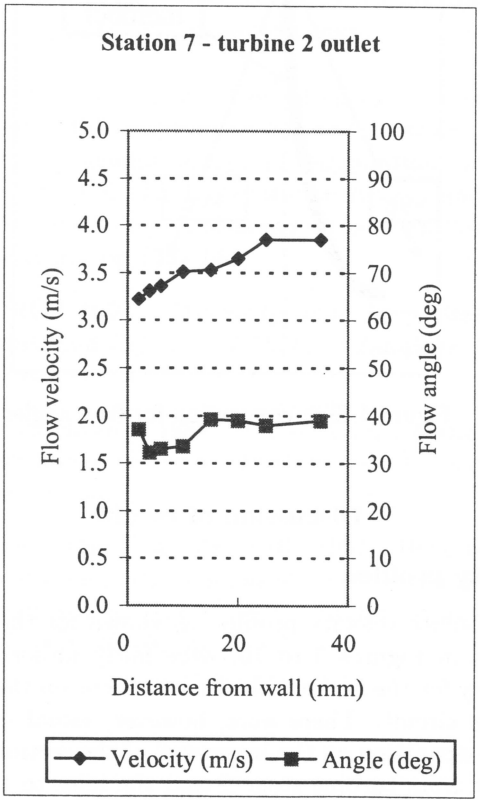

Figure 10 Turbine 2 outlet: Velocity and flow angle

Mean absolute velocities

The mean velocities were calculated as the numerical averages of the values measured by the probes at each station. It is clear from Table 2 that the agreement between the particle tracking results (Particle) and the dynamic pressure probe (Probe) results was good, except at station 4, the turbine stage 1. Despite careful checking no adequate explanation could be found, but the most likely cause was the effect of pitch angle on the probe, coupled with unsteadiness caused by the passing of the pump impeller blade wakes. Agreement between the probe and the one-dimensional model (1-D Model) results was not as good, although the differences were acceptable, apart from stations 1 and 7, the pump inlet and turbine stage 2 outlet, due probably to the difference in radial location for these stations between the Probe and the 1-D Model.

Mean flow angles

The mean flow angles, as given in Table 3, were determined in the same way as the mean velocities. Differences between angles determined by the two methods varied from 4% to 19%, the latter at station 4. Similar to the velocity results, the probe output may have been influenced by upstream wakes. Agreement between the Probe and the 1-D model results was again acceptable, with the exception again of station 4, where the difference was 51%.

Meridional velocities

The agreement between the two methods of measuring the meridional velocity, as shown in Table 4, was good, with the exception again at station 4 where the difference was 32%. Good agreement was also found between the model and the probe results, except at stations 4 and 7, where the differences were 40% and 26%.

Mass flow

The mass flow circulation through the experimental torque converter (Table 6), as calculated from the product of the meridional velocity (Table 4), flow area (Table 5), and density (assumed to be 996 kg/m^3), should have been virtually constant at all measuring stations, as it effectively was for the 1-D hydrodynamic model. The typical standard deviation in mass flow (shown in Table 7) was however only about 2% for the experimental methods, or nearly 9% for the probe, if the doubtful measurements at stations 4 and 7 are included.

Tangential velocities

For practical reasons, the particle and probe results could not always be determined at the same radius as the 1-D model, as can be seen in Table 8. However agreement between the particle and probe methods was reasonable, with differences of between 5% and 14%, but both these results differed markedly from those for the one-dimensional model.

Angular momentum per unit mass flow

The angular momentum per unit massflow was determined from the product of the tangential velocity (Table 9) and the radius (Table 8) at the measuring point. Once again the agreement between the measuring methods was fair, but results from both methods differed from the one-dimensional model.

Torque

The torque exerted on or by each member is the product of the mass flow through the member and the change in angular momentum per unit massflow across the member. From Table 11 it can be seen that differences between the Probe and the 1-D Model varied between 1% for the turbine stage 1 and 13% for the stator.

The pump impeller torque at 260 rpm as measured by the torque transducer was 24.5 Nm, about 2.5% higher than predicted by the one-dimensional model and about 7% lower than that calculated from the measured angular momentum fluxes. Torque at other speeds is shown in Figure 11.

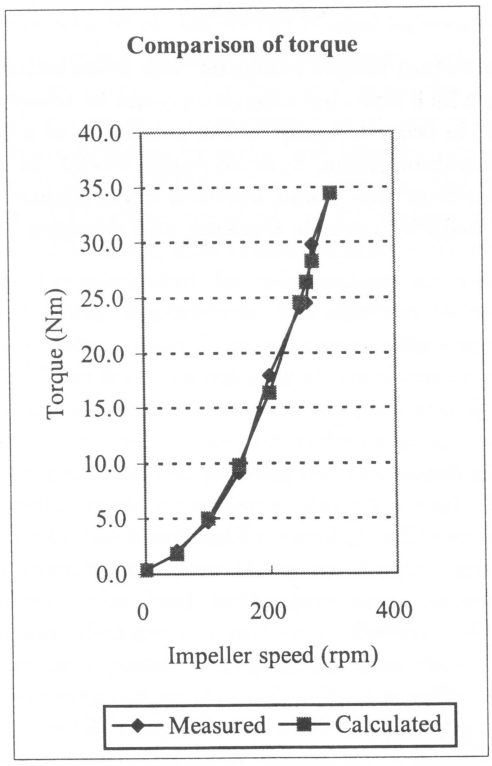

Figure 11Comparison of measured and calculated impeller torques

Von Backstrom and Venter[5] also determined the torque exerted by the second turbine by means of blade surface static pressure measurements. If their results are corrected for the fact that their pressure taps did not cover the rearward 20% of the blades, their measured torque for turbine stage 2 comes to 33.7 Nm at 260 rpm, about 6%

higher than that deduced from the probe readings. It appears that the torque prediction by the 1-D model is low by 5 to 8%. According to the laws of similarity for turbomachinery, the torque should vary with the square of the speed, but the coefficients of the second degree equation are influenced by Coulomb friction, which is independent of speed, laminar friction, which is directly proportional to speed, and Reynolds number effects, which cause a deviation from the quadratic relationship between torque and speed.

Table 12 Comparison of measured and calculated impeller torque

Impeller speed	Torque (Nm)	
(rpm)	Measured	Calculated
0		0.39
50	2.1	1.85
100	4.7	5.00
150	9.1	9.83
200	17.9	16.34
250	24.1	24.55
260	24.5	26.39
270	29.8	28.30
300	34.4	34.44

Conclusion

An experimental torque converter was manufactured and tested, in which flow characteristics could be observed and measured, in order to assist in the validation of a comprehensive one-dimensional hydrodynamic model. In general, good agreement was found between experimental results obtained both by particle tracking and dynamic pressure probes. In some cases, particularly at station 4, the entrance to turbine stage 1, the differences were unacceptably large, but the high level of swirl resulting from the complex geometry increased the difficulty of measurement here. For ease of operation and to facilitate measurement, the experimental torque converter was operated in stall, and at this extreme operating condition, agreement between the experimental results and those produced by the one-dimensional model was within acceptable limits allowing for the large changes in flow angles and velocity experienced by the fluid moving across stationary components.

References

1. Strachan PJ, Reynaud FP & von Backström TW. The hydrodynamic modelling of torque converters. *R&D Journal*, 1992, **8**, pp.21–28.

2. Lamprecht J. Die ontwerp van 'n hidrouliese wringomsetter (The design of an hydraulic torque converter). MIng-tesis, Universiteit van Pretoria, 1983.

3. Jandasek VJ. The design of a single stage three-element torque converter. Passenger Car Automatic Transmission, SAE Transmission Workshop Meeting, 2nd edn. *Advanced Engineering,*1963, **5**, p.201.

4. Reynaud FP. Hydrodynamic modeling of torque converters. MEng thesis, University of Stellenbosch, 1990.

5. Von Backstrom TW & Venter AA. Panel method prediction of flow through a torque converter turbine. *R&D Journal*, 1994, **10**, pp.31–40.

Perspective: Fluid Dynamics and Performance of Automotive Torque Converters: An Assessment

T. W. von Backström
Adjunct Senior Scientist, Aerospace Engineering; Presently, Head of the Department of Mechanical Engineering, University of Stellenbosch, South Africa

B. Lakshminarayana
Evan Pugh Professor of Aerospace Engineering and Director.

Center for Gas Turbine and Power, Pennsylvania State University, University Park, PA 16802

Experimental investigations by various groups over the past decade have uncovered the main features of the flow in hydraulic torque converters. Measurement techniques include laser and hot wire velocimetry, fast response and conventional five-hole probes, and blade and wall static pressure measurement. In both the pump and turbine, the through flow velocity is high near the pressure surface shell corner while the flow in the suction surface core corner is highly turbulent and may be separated and reversed. The position of the stator in a passage curved in the meridional plane leads to secondary flow and low velocities at the core near the pump inlet. Velocity gradients coupled with flow turning and rotor rotation lead to strong secondary flows. By using data from a combination of measurement techniques, torque converter torque, power and efficiency are calculated, and the effect of element efficiency on overall efficiency is demonstrated. It is concluded that design methods should be developed that allow for nonuniform velocity profiles, flow separation, secondary circulation and interaction effects between elements.

Introduction

The automotive torque converter is a complex turbomachine used to transfer power from an engine to a transmission. It has been used in automatic transmissions for numerous applications including passenger cars, trucks, buses, tractors and tanks. It has three important functions. First, it transfers power smoothly and efficiently from an engine to a transmission—the peak efficiency is in the range of 82 to 92 percent. Second, at low vehicle speeds, it has the ability to multiply engine torque for improved vehicle launching—the maximum torque multiplication is in the range of 1.6 to 3.5. Third, it is an effective damper to dampen engine torsional disturbances and shock loads. Maddock (1991), Jandasek (1962), By and Mahoney (1988) are three excellent references on the design and application of the automotive torque converter.

A typical automotive torque converter cross section is shown in Fig. 1, By (1993). It has the following components: 1) a mixed-flow pump connected to the engine crankshaft through the torque converter cover and the engine flexplate, 2) a mixed-flow turbine attached directly to the transmission shaft, 3) either a mixed-flow or an axial-flow stator attached to the transmission housing through a one-way clutch, and 4) a lock-up clutch, which transfers engine power directly to the transmission bypassing the torque converter. To minimize the effects of cavitation and to engage the lock-up clutch, the torque converter is fully filled and is pressurized with a charge pressure supplied by the transmission hydraulic system. Oil is pumped outward from the pump inlet and is discharged axially at the pump exit where it enters the turbine. It then flows inward from the turbine inlet to the turbine exit. The stator provides a reaction torque by directing the flow from the turbine exit back to the pump inlet. This closed-loop motion is repeated continuously. Under a constant input torque condition, maximum through flow velocity and maximum stator reaction torque occur when the turbine is stationary. As the turbine speed increases, the through-flow velocity and the reaction torque are reduced. As the turbine speed further increases, the reaction torque is eventually reduced to zero and the through-flow velocity is reduced to a minimum. This is referred to as the coupling point, where the torque converter ceases to multiply torque and starts to function as a fluid coupling. Beyond this point, the use of a one-way clutch allows the stator to rotate or free wheel in a forward direction.

Key performance parameters of the torque converter are speed ratio, efficiency, pump capacity coefficient, and K factor. Speed ratio, SR, is the ratio of turbine to pump speed. Torque ratio, TR, is the ratio of turbine to pump torque. Efficiency, η, is the ratio of turbine to pump power. It can be shown that efficiency is the product of speed ratio and torque ratio.

Recent interest in reducing automobile fuel consumption and air pollution has stimulated continued research into the fluid dynamics of the hydraulic torque converters. The basic flow field in a torque converter is toroidal and confined by an outer shell and inner core as shown in Figs. 1 and 2. In automotive torque converters, the stator blades are airfoil shaped but the pump and turbine blades are made of plate approximately 1 mm thick. In the torque converters under consideration, the blade inlet and outlet angles are typically 7 and 63 deg for the stator, −32 and 0 deg for the pump and +52 and −60 deg for the turbines. Torque converter flow fields are very complex. They are three-dimensional, viscous, and unsteady. Additional complexities arise due to the differential in rotor speed between the pump and the turbine and the associated wide variation in incidence angles. No other turbomachinery is subjected to such wide operating conditions. The turbine and the pump passages are narrow, long, and dominated by viscous effects, curvature, rotation, separation, secondary flow, and three-dimensional effects. Close coupling of the elements induce potential and viscous interactions at the rotor-rotor and rotor-stator interfaces resulting in large unsteadiness. Its nature and magnitude vary with the spacing between blade rows, the number of blades, the thickness of the trailing edges, the location of areas of flow separation, the characteristics of the blade wake profiles, the existence of secondary flows, and other geometrical and op-

Contributed by the Fluids Engineering Division for publication in the JOURNAL OF FLUIDS ENGINEERING. Manuscript received by the Fluids Engineering Division March 15, 1996; revised manuscript received September 6, 1996. Associate Technical Editor: D. P. Telionis.

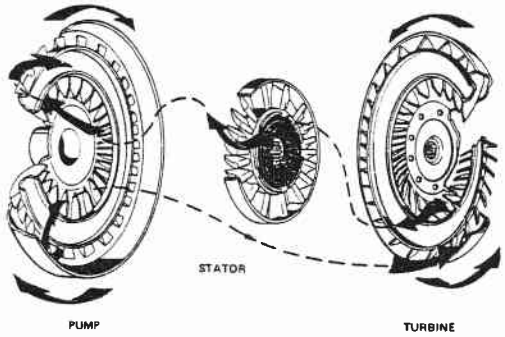

Fig. 1 Configuration and flow path of torque converter

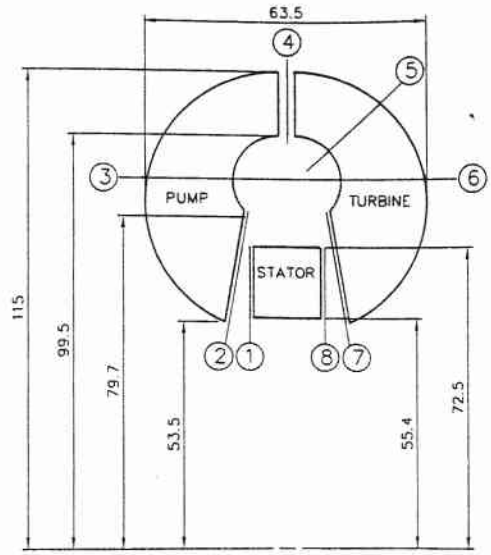

Fig. 2 Schematic of automotive torque converter showing measurement stations (dimensions are in mm)

erating parameters. A fundamental difference between the flow in torque converters and all other types of turbomachinery, except multi-spool gas turbines, is the presence of a least two rotors affecting the time-dependent flow. Further complications are the proximity of the elements to each other and the recirculating nature of the flow. These geometrical and flow characteristics present a challenge for experimentalists and computational fluid dynamicists.

Objectives and Scope

The original research was carried out with the ultimate objective of enabling designers to improve the performance, which can only be achieved if the fluid dynamics phenomena is well understood. Specific objectives present day designers have in mind are reducing the length of the torque converters for automobiles with transverse engines and secondly reducing fuel consumption in urban use. The objective seems to have been to understand the flow field which can be utilized in improving the design and performance. These data are valuable in validating computer codes, which can then be used in the design precess, thereby, reducing the design and development cycle. The objective of the research carried out by these (Bahr et al., 1990; By and Lakshminarayana, 1991; Browarzik, 1994; Marathe et al., 1996; Marathe and Lakshminarayana 1995) groups is to improve the performance and design of automotive torque converters through research and development. This is carried out through acquisition, analysis, correlation, and synthesis of the experimental data on the flow field (including pressure, velocity and turbulence field). An integrated experimental and CFD approach is used by some of these groups to develop codes for design, analysis, simulation, and improvements; thereby reducing the design and development cycle time.

The main objective of this paper is to examine the data available on flow in automotive-type torque converters and provide a coherent and critical assessment of the main characteristics

Nomenclature

$(C_{p_o})_{Abs} = 2((P_o)_{Abs} - p_{hub})/\rho V_{ref}^2$
C_{pb} = blade static pressure coefficient $2(p - p_{ref})/\rho U_{up}^2$
C = chord length
$C_{p_s} = 2(p_s - p_{hub})/\rho V_{ref}^2$
FHP = five-hole probe
L = length
LDV = laser velocimetry
PSU = The Pennsylvania State University
P_s = power
P_o = stagnation pressure normalized by $\rho V_{ref}^2/2$
P_f^* = nondimensional fluid power = $P_f/[(0.5\rho V_{ref}^2)(V_{ref}R_P^2)]$
P_s^* = nondimensional shaft power = $P_s/[(0.5\rho V_{ref}^2)(V_{ref}R_P^2)]$
PS, SS = pressure and suction surface
p, p_s = static pressure normalized by $0.5\rho V_{ref}^2$
p_{ref} = reference pressure on hub
Q = volume flow normalized by $V_{ref}R_P^2$
R = radius
RU = Ruhr-Universitat, Bochum, Germany
r = radial coordinate
SR = speed ratio (turbine/pump)
T = torque
TR = torque ratio (T_T/T_p)
U_{pt} = pump tip blade speed
UVA = University of Virginia
V = absolute velocity normalized by V_{ref}
V_r, V_θ, V_x = absolute radial, tangential and axial velocity
$V_{ref} = U_{pt}(1 - SR)^{0.5}$
V_{sec} = secondary velocity
W, W_θ = relative total and tangential velocity
x = coordinate normal to chosen radial line and to axis
y = coordinate parallel to chosen radial line
Z_n = number of blades
z = axial coordinate
β = blade exit angle measured from tangential direction
Δ = difference operator
η_{TC} = efficiency = $T_P\Omega_P/T_T\Omega_T$
θ = tangential coordinate
σ = slip factor
ρ = fluid density
Ω = angular velocity normalized by $(0.5V_{ref}/R_P)$
ν = kinematic viscosity

Superscripts

- = passaged averaged
= = area averaged

Subscripts

Abs = absolute
f = fluid
h = hydraulic
our = exit
p = pump,
Pt = pump tip radius
ref = reference
S = stator
T = turbine
r, θ, z = components in r, θ, z directions
TC = torque converter
o = stagnation
x, y, z = components in x, y, z, directions

of the flow field and its impact on performance and design. While this paper is a review in the sense of integrating information and insights from various sources, the emphasis is on assembling a clear picture of the typical flow fields in automotive torque converters and their impact on performance and design. Much of the discussion will focus on the mean flow field, as its control will probably remain the main objective of the design and improvement process.

Background

Most of the insights in the present paper were based on the experimental investigations of groups at the Ruhr-Universitat in Bochum (RU), Germany, and at two universities in the USA: The Pennsylvania State University (PSU) and the University of Virginia (UVA). The group at the Ruhr-Universitat investigated the flow and performance of an industrial-type torque converter (Adrian, 1985 and Browarzik, 1994). It consisted of an unshrouded radial outflow (centrifugal) pump of conventional design. The torque converter had a stall torque ratio of 5.7 and a peak efficiency of 87 percent at a speed ratio SR = 0.55.

The discussion of the flow in automotive torque converters is primarily based on pump and turbine measurements at UVA by Brun et al. (1994, 1996a), Brun and Flack (1995a, b), and Gruver, et al. (1996); blade static measurements at General Motors by By and Lakshminarayana (1991, 1995a, b); stator, pump, and turbine exit measurements at PSU by Marathe and Lakshminarayana (1995), and Marathe et al. (1995a, b, 1996). Browarzik (1994), Brun and Flack (1995a, b), and Marathe et al. (1995a, b) have explained in detail how to acquire and analyze time dependent data in torque converters. The main flow visualization methods were the spark tracer method and the wall tracer method (Numazawa et al., 1983; Lee et al., 1994).

The groups at PSU and UVA carried out their research on models of the same automotive-type torque converter with 230 mm outer diameter as shown in Fig. 2. The blade numbers were typically 27, 29, and 19 in the pump, the turbine, and the stator respectively. The gaps between the elements were small and there was meridional flow curvature in all the elements including the nominally axial flow stators, due to the torus curvature. The stall torque ratio was 2.1. The facilities were operated typically at 1100 rpm. PSU used Shell Diala oil with $\nu = 4.8 \times 10^{-6}$ m^2/s, $\rho = 857$ Kg/m^3 at 60°C and UVA used Shell Flex 212 oil with $\nu = 2.2 \times 10^{-6}$ m^2/s. The main flow measurement techniques employed were laser anemometry (LDV) at UVA, hot-film anemometry at RU, and fast response five-hole probe (FHP) and wall static pressure measurements at PSU. The FHP measurements were acquired at station 1 (stator exit), station 4 (pump exit), station 8 (turbine exit or stator inlet) shown in Fig. 2. The LDV data was acquired at station 2 (pump inlet), station 3 (pump mid-chord), station 4 (pump exit), station 5 (turbine $\frac{1}{4}$ chord), station 6 (turbine mid-chord), and station 7 (turbine exit). These data are interpreted together to provide an integrated assessment of the flow field. In many instances, the data were reprocessed to examine critical flow features. Unpublished data from the groups at PSU an UVA are also reviewed. Furthermore, the flow field only at peak efficiency conditions (SR = 0.800) is examined in detail to assess the nature of flow field, even though a brief assessment at stall conditions is also included for completeness.

The computational effort is vigorously pursued by several groups (e.g., By et al., 1995c; Schulz et al., 1996; Kost et al., 1994; Marathe et al., 1996; and Tsujita et al., 1996). The computational effort is not reviewed in this paper due to limitations on the length of the paper and due to the fact that the torque converter flow field has not yet been computed satisfactorily. In addition to reviewing the experimental efforts at RU, PSU, and UVA, an attempt is made to list additional useful references (not quoted in the text) at the end of the paper. These are, however, not discussed as it was decided to concentrate on two torque converter geometries for the sake of brevity. These references also include earlier reviews, design methods, and computational efforts.

Accuracy of Measurements

Gruver et al. (1996) stated that he measured individual velocities to within four percent but that velocities along the suction surface might be contaminated. Bahr et al., 1990 reported agreement of mass flow to within 10 percent between inlet and exit flows of the stator, while Brun and Flack (1995a) reported measurement uncertainties for LDV measurement in a turbine of 0.1 m/s for a velocity of 3.5 m/s (three percent). They stated 95 percent confidence limits as ±0.05 m/s. Marathe and Lakshminarayana (1995) quote the accuracy of pressure measurements to be ±0.01 psi, with maximum cumulative error in velocity and pressure measurements to be about 2–3 percent. In our own correlations of data sets, including both PSU and UVA data, we found the standard deviation of the mean throughflow volume flow to be typically 3 percent of the mean.

Pump Flow Field

Flow at the Stator Exit and at the Pump Inlet. The assessment of the pump inlet field is based on the UVA data (station 2, Fig. 2) presented by Gruver et al. (1996) and the stator exit flow field (station 1, Fig. 2) is based on PSU data (Marathe et al., 1996). Interesting and undesirable flow features occurs as the flow progresses from the stator exit (data taken at 0.36 axial chord downstream of the stator) to the pump inlet (very near the leading edge). The absolute stagnation pressure contours at the exit of the stator, shown in Fig. 3, reveal the presence of a low pressure region near the shell and a distinct wake. The passage mass averaged values of $(C_{p_o})_{Abs}$ shows a nearly uniform distribution from the core to the shell (Fig. 4). The axial velocity contours show lower axial velocities near the core region (Fig. 5). The passage averaged axial velocities shown in Fig. 6 indicate that the axial velocity near the core region is about 70 percent of that near the shell.

The axial velocity at the pump inlet (Fig. 7) shows some dramatic change occurring between the stator trailing edge and the pump inlet. The flow passage changes from axial to radial, with considerable torus curvature effects as the flow progresses from station 1 to 2, shown in Fig. 2. The velocity in the core region has decreased drastically (from a value of 0.335 to −0.013), resulting in reversed flow across the entire pitch within 20 percent of the spanwise distance from the core. The flow deceleration occurs due to the convex curvature near the

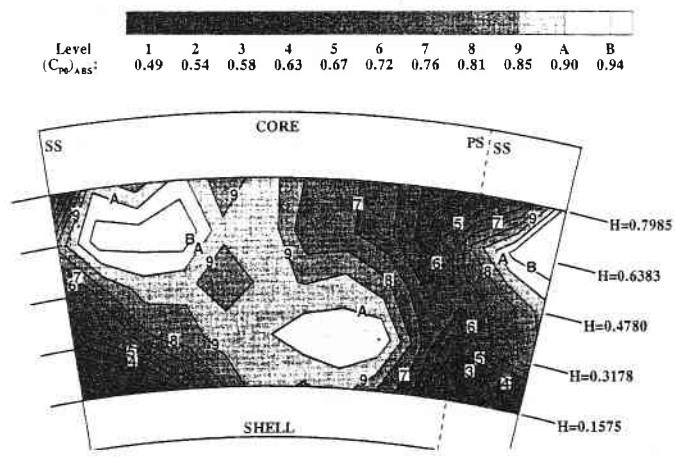

Fig. 3 Contours of absolute stagnation pressure coefficient $(C_{p_o})_{Abs}$ at stator exit at SR = 0.800 (derived from PSU data in Marathe et al., 1996)

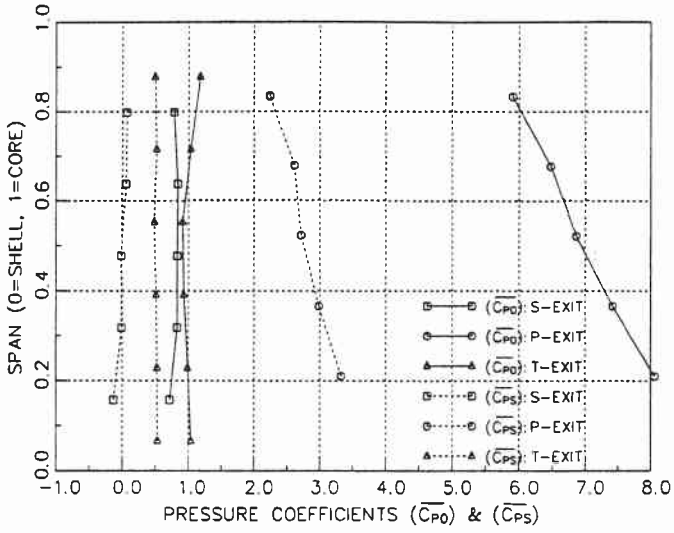

Fig. 4 Spanwise distribution of passage-mass averaged pressure coefficients $(\bar{C}_{p_o})_{Abs}$ and $(\bar{C}_{p_s})$ (PSU data)

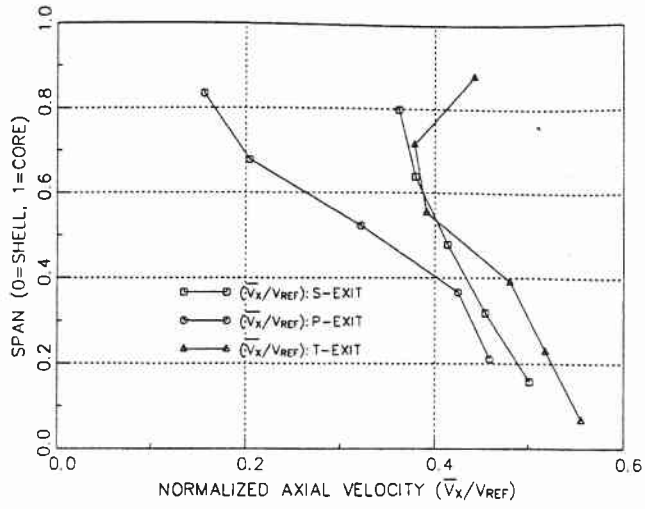

Fig. 6 Spanwise distribution of passage-mass averaged normalized axial velocity (V_x/V_{ref}) (PSU data)

core. It is clear from comparing the passage-averaged distribution of axial velocity (Figs. 6 and 8) that the axial velocity in the mid-span region has accelerated, while that near the core has decelerated substantially, resulting in back flow.

At the pump inlet (SR = 0.800), a strong tangential relative velocity component is directed at the pressure surface of the pump, with low energy flow along the suction surface. The relative tangential and relative total velocity near the core is nearly zero: and the absolute tangential and total velocity is highest in the core region at the pump inlet (Fig. 8). This is caused by pump dragging the separated flow along near the core region. The incidence to the pump blade row in the 20 percent span from the core is very high, resulting in flow separation near the leading edge of the pump. This is evident from the plot of secondary velocity vectors (not shown), where region of flow separation at the suction surface near the inlet is visible as a disturbed flow region. An incipient right-handed circulation pattern occurs near all surfaces, especially near the pressure surface where the flow with the increased angular momentum is flung outwards towards the core. The backflow at the pump inlet near the core is also evident in the pitch-averaged axial velocity profile (Fig. 8). It is caused by a combination of the sudden increase in flow area where the stator core shroud ends, the relatively large mean inlet incidence angle of 15.3 deg, and flow passage curvature.

At SR = 0.065 the contour plot of the axial velocity (not shown) indicates only small local regions of backflow concentrated in the suction and pressure corners in the spanwise range of about 10 percent from the core. The flow is more disturbed near the pressure surface at SR = 0.065 and less disturbed near the suction surface than at SR = 0.800. No backflow was evident in the pitch-averaged flow near the core, but the through flow velocity decreases continuously from mid section to core. The average relative flow angle is −3.1 deg. Since it implies that the flow enters the pump with virtually no relative whirl velocity, the backflow inducing diffusing action in the pump inducer is absent. As the angular momentum of this flow is reduced by impingement on the blade suction side, the radial pressure gradient forces it inwards. This mechanism contributes to setting up the circulatory secondary flow pattern.

It is clear from the discussion above that great care should be taken in designing the flow passage shape. Sudden increases in flow area should be avoided. The curvature of the flow field in the meridional plane is important; a small radius of curvature leads to velocity profile distortion, but a large radius leads to a longer flow path and a longer axial length torque converter. Potential flow methods often used in the design of turbomachinery will not be adequate because of the large stator wakes and secondary flows entering the stator. Leaning the rotor blades may help to suppress flows developing in the rotor inducer. A well-designed flow passage upstream of the pump and an

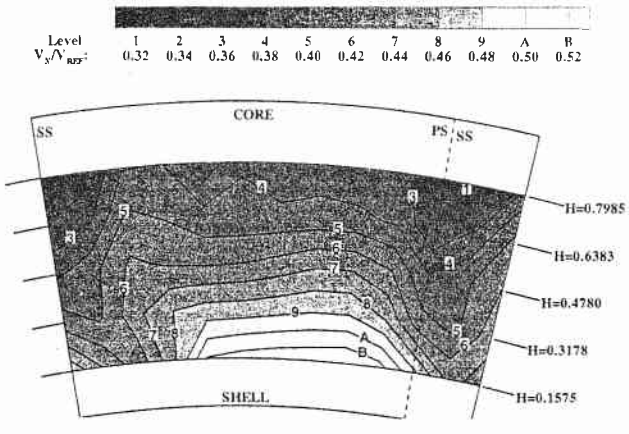

Fig. 5 Normalized axial velocity (V_x/V_{ref}) contours at stator exit at SR = 0.800 (PSU data)

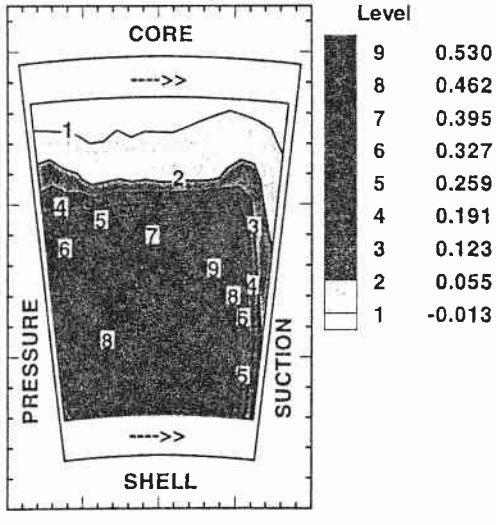

Fig. 7 Pump inlet axial velocity (V_x/V_{ref}) contours from LDV at SR = 0.800 (derived from UVA data in Gruver et al., 1996)

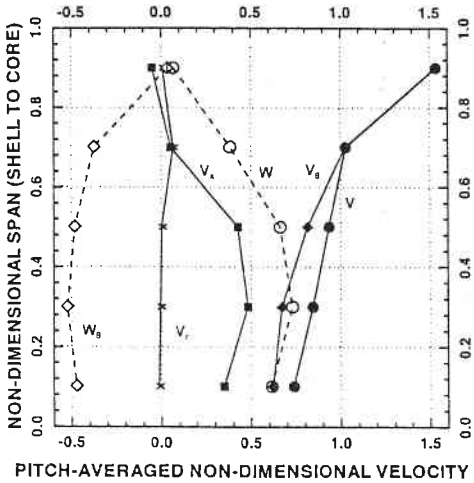

Fig. 8 Pump inlet velocity components from LDV at SR = 0.800 (derived from UVA data in Gruver et al., 1996)

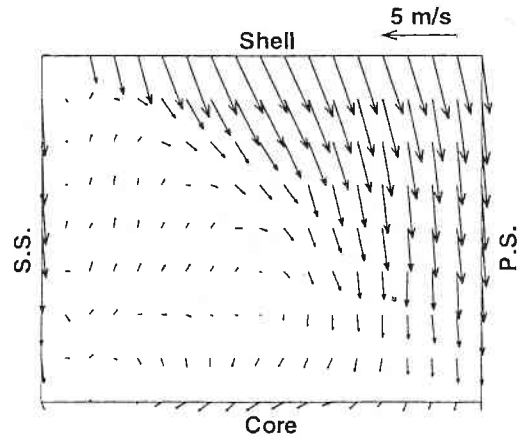

Fig. 10 Secondary velocity vector (V_{sec}) at pump mid-chord from LDV data at SR = 0.800 (derived from UVA data in Gruver et al., 1996)

optimized pump inducer design may result in the elimination of flow separation in the pump inducer.

Flow at the Mid-Chord Plane of the Pump. The pump mid-chord plane is a plane perpendicular to the radial direction at a radial position between the centers of curvature of the core and the shell where the radius is 86.04 mm (station 3, Fig. 2). This plane would correspond approximately with the outlet plane of the pumps in the industrial torque converters of Adrian (1985) and Browarzik (1994). At a speed ratio of 0.065, the through flow velocity is fairly uniform, but at 0.800 there is a velocity gradient from the suction to the pressure surface, with a strong jet near the pressure side occupying nearly half the flow passage (Fig. 9).

At both SR = 0.800 and at SR = 0.065 there is a right-handed circulation centered near the suction surface core corner, as shown in Fig. 10. The secondary flow components are as large as the through-flow components. At a speed ratio of 0.800, the average through-flow secondary flow velocities and vorticity decreases with decreasing pump speed, but at a slower rate than the pump speed.

The through flow velocity contours, show in Fig. 9, clearly reveals major changes between the stations when compared with axial velocities at inlet (Fig. 7). The strong secondary flow that exists in this region (Fig. 10) has transported the high through flow velocity near the shell at inlet toward the pressure surface and the separation zone (up to 20 percent of span near the core, Fig. 7) has been transported toward the suction side spread across the entire core to shell region. This region of separation is not caused by an adverse pressure gradient on the suction surface as evidenced by the blade pressure data presented by By and Lakshminarayana (1995a), but by the secondary flow induced due to shear layers, rotation and curvature effects (Lakshminarayana, 1996, pp. 321–330). The secondary flow pattern shown in Fig. 10 has been captured reasonably well by a Navier-Stokes solver (By et al., 1995c).

Numazawa et al. (1983) found that the streamlines generally show a shell-to-core flow on the pump pressure surface at mid-chord, especially for SR = 0.800, indicating a circulation with the pump rotation, while at the exit there is a core-to-shell flow at a speed ratio of 0.800 and a converged flow towards the center of the surface at SR = 0.0. Lee et al. (1994) found that just before the mid-chord position the shell flow starts flowing up the pressure surface wall, more or less aligning itself with the exit meridional direction. This flow then migrates crosswise and downstream along the core surface toward the suction surface, but does not attach to it. The effect is the now familiar right-handed circulation at mid-chord shown in Fig. 10. In general, the data of Lee et al. (1994) tend to confirm those of Numazawa et al. (1983) and Gruver et al. (1996).

The flow circulation at the mid-chord of an automotive-type torque converter pump is much larger than that at the exit of the industrial type. The reasons are first, the presence of the stator blades immediately upstream of the former. They are conducive to velocity profiles that peak near the shell. Second, in the industrial-type pump the inducer blades lean forward from shell to core, inhibiting shell-to-core flow on the pressure surface.

Flow at the Exit of the Pump. The axial velocity and the secondary flow pattern at the exit of the pump (Station 4) are shown in Figs. 11, and 12, respectively. The secondary flow is

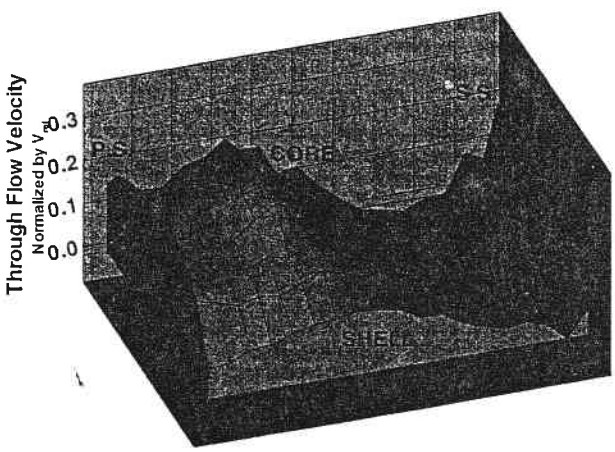

Fig. 9 Axial velocity at pump mid-chord from LDV at SR = 0.800 (derived from UVA data in Gruver et al., 1996)

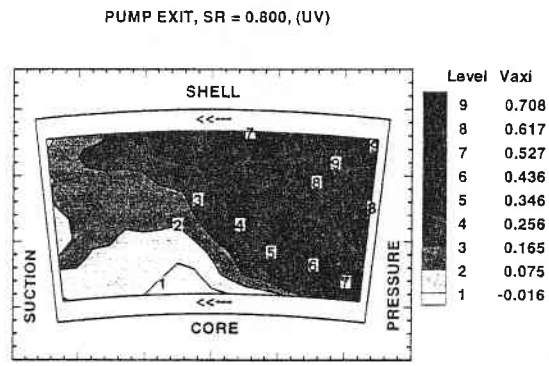

Fig. 11 Pump exit axial velocity contours from LDV at SR = 0.800 (derived from UVA data in Gruver et al., 1996)

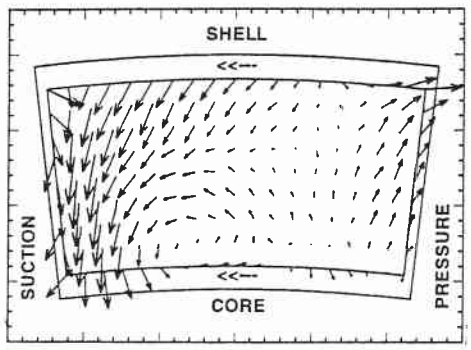

Fig. 12 Pump exit secondary velocity (V_{sec}) vector plot from LDV at SR = 0.800 (derived from UVA data in Gruver et al., 1996)

now left-handed, with a dominant "jet" flow pattern near the suction surface, moving from shell to core. It should be remarked that the magnitude and the direction of the Coriolis force ($2\Omega \times W$) changes as the flow progresses, acting nearly in the blade-to-blade direction near the leading edge and core-to-shell at the pump exit. This indicates that the rotation induced secondary flow dominates the flow field in torque converter pumps. The left-handed circulation transports high energy mean flow from the pressure surface near the mid-chord location to the shell suction surface (Fig. 9). This is evident by comparing Figs. 9 and 11, and the corresponding secondary velocity vector in Figs. 10 and 12. The separated region now has moved to the corner formed by the core and suction surface. The flow at the exit of the pump resembles the "jet-wake" pattern observed in centrifugal compressors (Eckardt, 1980). It is interesting to note that the pitchwise center of the back flow (Fig. 11) is also the center of the vortex.

The passage-averaged mean stagnation pressure (Fig. 4) and the axial velocity (Fig. 6) clearly shows the effect of secondary flow on the spanwise mixing of the flow. The stagnation pressure and the axial velocity are both lower near the core region at the pump exit.

The pitch averaged velocity profiles for SR = 0.065 (not shown) are very similar to those at SR = 0.800. The axial velocity at SR = 0.065 varies more with pitch than with the span except near the core. No backflow region is evident at the core, but the axial velocity is low near the core. The secondary flow pattern (not shown) looks similar to that at SR = 0.800. The core-to-shell velocity gradient is smaller than at the mid-chord plane.

The relative exit flow angle and the slip factor at SR = 0.065 are found to be −7.0 deg and 0.897, for the LDV data. Wiesner (1967) gave the following equation for the slip factor of centrifugal impellers:

$$\sigma = 1 - (\cos \beta_{out})^{0.5}/Z_n^{0.7}$$

With β_{out} = 0.0 deg and Z_n = 27 the calculated slip factor is 0.900 which agrees well with the data. The Wiesner slip factor relationship was empirically derived for radial turbomachines but Strachan et al. (1992) have found that it predicted the pump torque and the overall performance of Jandasek's (1963) torque converter well for various pump exit blade angles.

In ordinary industrial pumps, nonuniform exit profiles and flow separation are to be avoided because these two phenomena generally inhibit pressure recovery in the diffuser or volute of the pump. These effects do not seem to be as serious in torque converters that are primarily momentum transfer devices and have no diffusers.

Blade Static Pressure Distributions for the Pump. By et al. (1995a) measured the blade static pressures near the mid-span, core and shell regions at speed ratios of 0.0, 0.6, 0.800. The data at SR = 0.800 is shown in Fig. 13. Their general observations are as follows. For the 0.0 speed ratio condition the static pressure distribution near the leading edge at the shell and mid-span is reversed, indicating negative incidence. The pump static pressure field changes drastically from shell to core, and the centrifugal and Coriolis force has dominant effects as analyzed in Lakshminarayana (1996, p. 277). A reversal of pressure distributions at the core over the last 25 percent indicates poor flow conditions at the suction surface core corner near the exit. The pressure distributions are better (this means that the pressure surface pressures are everywhere higher than the suction pressure and both vary fairly smoothly) for a speed ratio of 0.6, and slightly worse at 0.800 than at 0.6. At mid section a three-dimensional potential code can reasonably predict the static pressure distribution. A Navier Stokes code can be used to effectively predict the pump flow field (By et al. 1995c).

Discussion of Flow Fields in Pumps. As discussed before, the main features of the flow are the high through flow velocities near the pressure surface-shell corner and the large secondary circulation. Since the main flow in automotive-type mixed-flow pumps has a velocity gradient with the higher velocity near the shell, the blade curvature turns the near-core flow more than the near-shell flow thereby contributing to the right-handed secondary flow circulation. And since in the automotive-type mixed-flow pump, at a speed ratio of 0.800, the main flow has a gradient with a slightly higher velocity near the suction than near the pressure side, the curvature in the meridional plane deflects the flow on the pressure surface towards the core more than the flow near the suction side, also contributing to a secondary right-handed flow circulation. The effects mentioned so far act whether the pump rotates or not, but only when there is a velocity gradient at the inlet. This is one of the reasons why By (1993) found such large differences between the computed flow fields with uniform and non-uniform inlet velocity profiles. As the pump inlet flow has a profile with a higher velocity near the shell than near the core, the passage curvature in the meridional plane will keep the high momentum flow near the shell. As this flow moves outward beyond the quarter chord point it is forced in the direction of the pressure surface by the Coriolis force, while the low momentum fluid is turned more in the direction of rotation. Once the main flow has accumulated near the pressure surface, it will be kept there by the Coriolis force. These effects explain why the high velocity flow accumulates near the pressure surface-shell corner, and why there is typically a secondary flow circulation at the mid-chord plane in the same direction as the pump rotation. The accumulation of boundary-layer flow near the inside of the flow passage also explains the existence of the wake region near the core and why the flow there is highly turbulent.

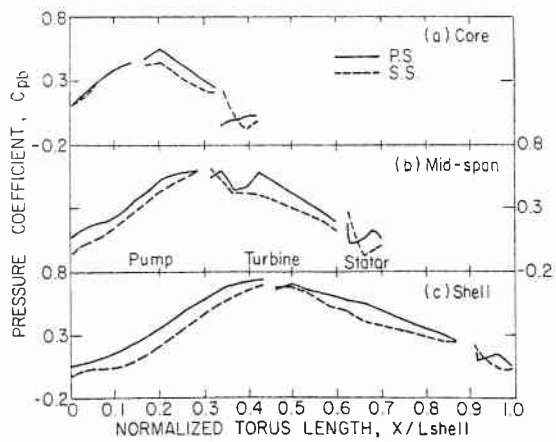

Fig. 13 Blade static pressure distribution at SR = 0.800 (adapted from By, 1993)

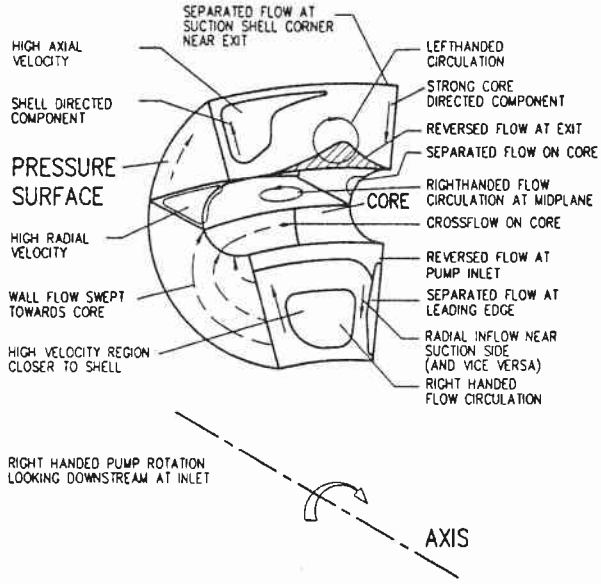

Fig. 14 Main flow features in a torque converter pump at SR = 0.800

A schematic of the flow features, based on the present knowledge of the torque converter flow field is shown in Fig. 14. The assessment of the data in an automotive mixed flow pump reveals the following:

1. The inlet velocity profile typically shows a small region of low velocity at the shell and separated flow at the core, depending on how much the pump shell to core span is larger than that of the stator. Strong secondary flows move this separation region to suction surface (shell-to-core) near mid-chord region and back to core region at the exit. A wake region exits near the core and the suction surface at the exit of pump. This indicates considerable spanwise and blade-to-blade mixing as the flow proceeds from the inlet to the exit.
2. The flow is smooth along the initial part of the pressure surface. At the mid-chord section, the high through flow velocity occurs near the pressure surface shell corner, with evidence of a wake in the suction surface core corner.
3. In a pump that rotates clockwise when looking downstream at the pump inlet, there is a strong right handed flow circulation at mid-chord, and in the opposite direction at the exit.
4. The inlet axial velocity profile is affected by whether the stator is positioned where there is curvature in the meridional plane or not.
5. At the pump exit, most of the flow is concentrated near the shell and pressure surface with little flow near the core, in both the radial and the mixed flow type of pump.
6. The agreement between the CFD predictions and measurements were reasonable, even with the present k-ϵ turbulence models.

Turbine Flow Field

The LDV measurement at inlet (station 4, Fig. 2), quarter chord (station 5), mid-chord location (station 6), (Brun and Flack, 1995a) and the five-hole probe measurements at the exit (station 8) of the turbine (Marathe and Lakshminarayana, 1995) are interpreted in this section to assess the flow features in the turbine.

Flow at the Inlet of an Automotive Torque Converter Turbine. The axial velocity profile shown at pump exit (Fig. 11) at SR = 0.800 (Brun et al., 1996a), undergoes substantial changes as it approaches the turbine inlet. The flow becomes more uniform in the blade-to-blade direction, with highest axial velocity occurring near the shell, and flow separation in the core region (about 10 percent of blade height) measured across the entire passage. The pump blade wake can be clearly seen at this location. It is the secondary velocities that undergo major change. The magnitudes of secondary velocities are substantially reduced at this location.

The main difference between the pump exit and the turbine inlet axial velocity profiles at SR = 0.800 is that at the turbine inlet, the velocities decrease more sharply near the core and shell compared to that at the pump exit. At SR = 0.800 the through flow component is only about a quarter of the absolute tangential component. A fractional adjustment in tangential velocity profile will then result in a noticeable adjustment in through flow profile. The turbine inlet blade angle changes from 55 deg at the core through 52 deg at mid span to 49 deg at the shell. Closer to the shell, however, the flow impinges with increasing angle on what is normally the suction side of the turbine blades. In these regions the turbine blades do work on the fluid, thereby increasing its energy. But the geometry of the flow and the blade passage is such that the flow relative to the turbine is turned farther away from the axial direction, and the relative total velocity increases. The through flow leaving the pump and entering the turbine near the shell is then accelerated and the flow is retarded near the core. This results in the flow lifting off the core, causing a velocity deficit at the core at the quarter and mid-chord sections.

At SR = 0.065, the outer half of the velocity profiles is almost uniform, but the inner half decreases towards the core. Relative flow angles are almost uniform, but the decrease in the pump exit through flow velocity results in an increased relative yaw angle into the turbine near the core. Consequently, the fluid does relatively more work near the core. The fluid energy is then reduced more near the core than elsewhere in the vicinity of the turbine inlet. Near the core, the turbine blades have to turn the flow through a greater angle towards the axial direction. Since this is a diffusing action, the already relatively energy deficient total relative flow near the core experiences a further reduction in velocity. The inlet pitch angle shows that the flow does not lift off the core at the inlet. However, since the inlet incidence angle is large (27 deg) and the turbine blades are thin plates (about 1 mm), the flow separates at the leading edge of the suction surface. Both the centrifugal and the meridional pressure gradient force the low momentum flow inwards toward the axis, causing separation at the core and preventing flow re-attachment to the core before mid-chord. The turbine inlet is a critical area and design methods incorporating all the major flow features are required to match the blade angle to the flow over a wide operating range.

Flow at the Quarter- and Mid-Chord Planes of a Turbine. At SR = 0.800 no flow separation is evident at the quarter chord plane, but there is a low velocity region at the suction surface-core corner. Minimum and maximum non-dimensional through flow velocities here are 0.08 and 0.59, and the circumferential component is 0.34. At mid-chord (Fig. 15), the velocity field shows no separation. Maximum velocity is 0.56 near the core and 0.12 near the pressure surface. A complex secondary flow pattern, which undergoes dramatic changes is observed as the flow progresses from turbine inlet to mid-chord (Fig. 16). The secondary flow pattern is from shell to core near suction surface quarter-chord as the flow approaches mid-chord. But, no vortex pattern is observed at these locations.

At the quarter-chord plane the flow is separated for SR = 0.065 over about 30 percent of the area. At the mid-chord plane the picture is similar except that the reversed flow now covers only about 15 percent of the flow area. A complex secondary flow pattern exists, consisting of two triangular flow regions. In the one, bounded by the core and suction surfaces, the sec-

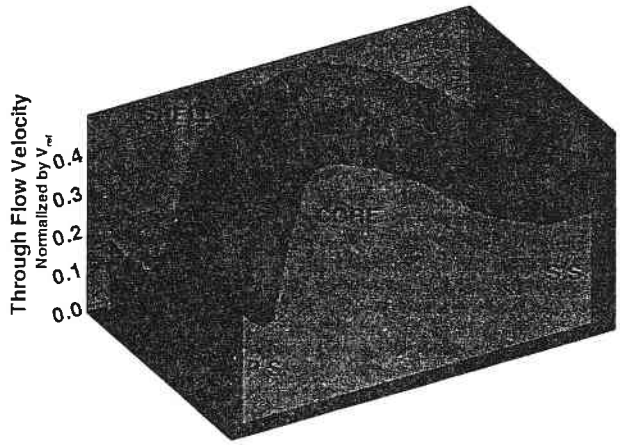

Fig. 15 Axial velocity contours at turbine mid-chord from LDV at SR = 0.800 (derived from UVA data in Brun and Flack, 1995a)

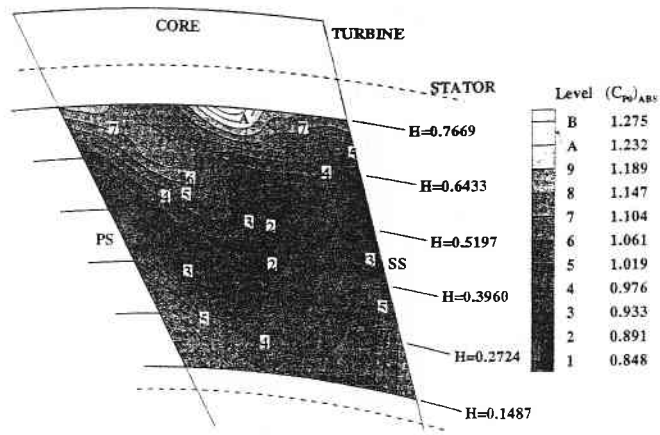

Fig. 17 Coefficient of absolute stagnation pressure $(C_{p_o})_{Abs}$ at turbine exit at SR = 0.800 (derived from PSU data in Marathe et al., 1995a)

ondary flow is directed to the suction surface-core corner feeding the reversed flow.

Lee et al. (1994) did flow visualization in automotive type torque converter turbines by means of a wall tracer method as a described earlier. At a speed ratio of 0.800 in the circular section torus torque converter, there is a flow separation on the suction surface near the turbine inlet. Where the flow reattaches, it more or less follows the blade passage in the meridional plane up to the quarter chord plane where it starts to deviate towards the core, eventually resulting in lift-off from the suction side and reversed flow at the three quarter point. On the pressure surface, there is an immediate flow deviation towards the core, which is strongest at about the quarter chord plane and then decreases again toward the exit.

Flow at the Exit of a Turbine. The stagnation pressure coefficient at the exit, plotted in Fig. 17, shows largest stagnation pressure drop (work done) near the shell and mid-span regions, and lowest work extracted and losses near the core region. The wake decays rapidly due to larger flow path as well as downstream potential effect due to stator blades. The flowfield is uniform for about 80 percent of span from the shell. The high absolute stagnation pressures and low relative stagnation pressures observed near the core is attributed to possible flow separation near the core inside the turbine passage caused by convex curvature of the torus. This is confirmed by the axial velocity distribution shown in Fig. 18, derived from a fast response five-hole probe. The low velocity region near the core region observed from the quarter-chord to the trailing edge region can be attributed to the curvature effects on the convex side. The flow decelerates (even in the absence of flow turning by the blades) in this region and accelerates near the shell region. Hence, the observed velocity profile increasing from the core to the shell is a attributed to curvature effects. The blade pressure distribution due to By and Lakshminarayana (1995b), shown in Fig. 13, does not indicate the presence of an adverse pressure gradient in this region. The low velocity regions observed near the core at quarter chord can be attributed to both adverse pressure gradient (Fig. 13) and curvature effect, while similar features near mid-chord and exit are attributed mainly to the curvature effect.

The passage and mass averaged distribution of absolute stagnation pressure coefficient, shown in Fig. 4, indicate that the stagnation pressure drop is highest near the shell and lowest near the core. This is consistent with axial velocity distribution. The radial distribution of the passage averaged axial velocity distribution (Fig. 6) shows a substantial reduction in axial velocity from shell to core, except at the last measuring point near the core.

The secondary flow pattern, derived from a fast response five-hole probe, plotted in Fig. 19, shows that substantial secondary flow occurs near the core region. A vortex pattern, with left-handed circulation, exists in the core region. The outward (towards the shell) secondary flow in the core region near the suction surface tends to move the low velocity and low pressure regions slightly outward as shown in Figs. 17 and 18.

General Discussion of Turbine Flow Field. A schematic of all the turbine flow features discussed in this section is shown in Fig. 20. By and Lakshminarayana (1995b) measured the wall static pressure distributions on the turbine blade along the mid-span and on the shell and core surfaces near the passage corners. They came to the following conclusions: Simple assumptions

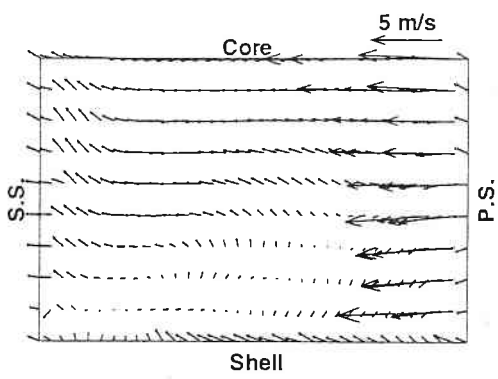

Fig. 16 Secondary velocity vectors (V_{sec}) at SR = 0.800 at turbine mid-chord from LDV data (derived from UVA data in Brun and Flack, 1995a)

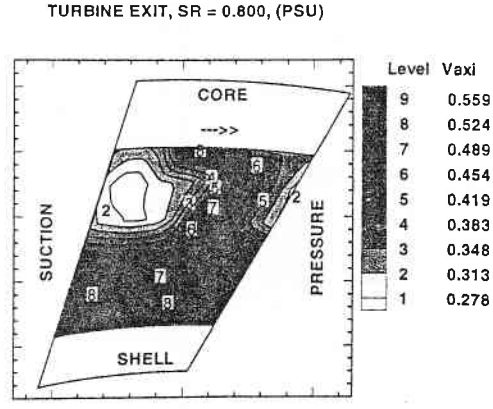

Fig. 18 Turbine exit axial velocity contours at SR = 0.800 (derived from PSU data in Marathe and Lakshminarayana, 1995a)

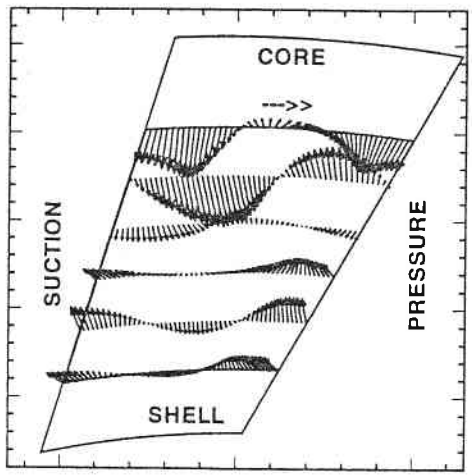

Fig. 19 Turbine exit secondary velocity ($\underline{V}_{sec}$) vector plot at SR = 0.800 (derived from PSU data from Marathe and Lakshminarayana, 1995a)

like one-dimensional flow and simple radial equilibrium were not valid in the turbine. The pressure distribution was better at SR = 0.600 than at 0.800. A three-dimensional potential code could not accurately predict the static pressure distribution even at mid span under all speed ratio conditions, since the flow was not irrotational.

The blade pressure distribution at the mid-span, core, and shell regions, shown in Fig. 13, indicates that the flow in the initial part of the turbine (leading edge to about 10–15 percent chord) develops under an adverse pressure gradient. The blade static pressure actually increases, thus behaving like a pump. The pressure drop is continuous and well behaved beyond this location. Thus, it is clear that there is a mismatch between the pump exit flow and the turbine inlet flow. This is perhaps an area for improvement.

In an automotive-type torque converter with a mixed flow pump and turbine, the turbine operates under a much larger range of conditions than the pump, because under normal working conditions its speed changes much more than that of the pump. At low turbine speeds, the pressure gradient due to flow curvature in the meridional plane obviously has a much larger effect than that due to rotation, while in the pump, as at high speed ratios in the turbine, both effects play their parts.

At low speed ratios the mismatch between the direction of the flow in the turbine relative frame and the turbine inlet blade angle causes separation at the suction surface as reported by Brun and Flack (1995a), Lee et al. (1994), and By and Lakshminarayana (1995b). Because of its momentum, the main flow tends to accumulate in the pressure surface-shell corner, but the blade leaning angle is such that it tends to force the flow inwards, towards the torque converter axis, resulting in some shift in the main flow from the shell to the core, near the pressure surface. Because, at mid-chord the flow passage is deflected in two planes, with roughly the same radius of curvature, both curvatures affect the flow distribution. The turning in the meridional plane forces the main flow towards the shell, and the blade boundary layers towards the core, while the turning perpendicular to the meridional plane forces the main flow towards the pressure surface, and the core and shell boundary layers toward the suction surface (Fig. 20). These two effects result in the main flow migrating toward the pressure surface-shell corner, a process that is assisted by the forward lean of the blades at the mid-chord plane. The low momentum boundary layers are forced to the suction surface-core corner by the pressure gradients as reported by Brun and Flack (1995a). In the design of the torque converter under discussion there is little curvature in the turbine blades beyond mid-chord. Consequently, only the meridional curvature influences the flow beyond mid-chord at low speed ratios. The main flow is then found near the shell at the turbine exit, with the low momentum boundary layer fluid near the core. The disappearance of the blade-to-blade pressure gradient beyond the turbine exit causes a flow adjustment, resulting in a flow from pressure to suction surface at the exit.

Brun and Flack (1995a) found that the flow in the turbine at SR = 0.800 was not fundamentally different from that at SR = 0.065. Flow conditions at SR = 0.800 are generally better, however, because firstly the flow does not separate from the suction surface at the inlet, and secondly, there is a centrifugal pressure gradient component acting in the opposite direction to the meridional gradient near the exit, thereby reducing the nonuniformity of the exit profile and the concentration of low momentum fluid near the core.

Stator Flow Field

The only function of a stator in a torque converter is to impart additional angular momentum to the flow, beyond that imparted by the pump. The high torque ratio at the stall condition, when the turbine is stationary, requires a large flow deflection of about 120 deg, while the unity torque ratio requirement at a high speed ratio demands zero flow deflection. In the torque converter under consideration the stator blade inlet design angle is 7 deg, the outlet angle is 63 deg and the incidence angle varies between about plus and minus 50 deg. The dilemma of the designer is to design a blade row capable of a very high flow deflection, but with a low loss coefficient at a high negative incidence angle (Marathe et al., 1996).

To further complicate matters, it has been found that at off design conditions the stator flow field is highly three-dimensional (Bahr et al., 1990; By and Lakshminarayana, 1991; and Marathe et al., 1995a, 1996). The main flow approaching the stator from the turbine has a higher through flow velocity near the shell than near the casing, and the circumferential component near the core increases faster with speed ratio than that near the shell. Consequently, Bahr et al. (1990) found that the effect of the varying incidence angle with operating point was severe and that the one-dimensional theory was inaccurate: velocity profiles and torque distribution over the blade length were not uniform. The flow averaged turbulence intensity was high near the walls (approximately 20 percent compared to 10 percent near the mid-span).

Marathe et al. (1995a) measured the stator inlet flow field (turbine exit flow) with a five-hole probe coupled to five fast response transducers in an automotive type torque converter

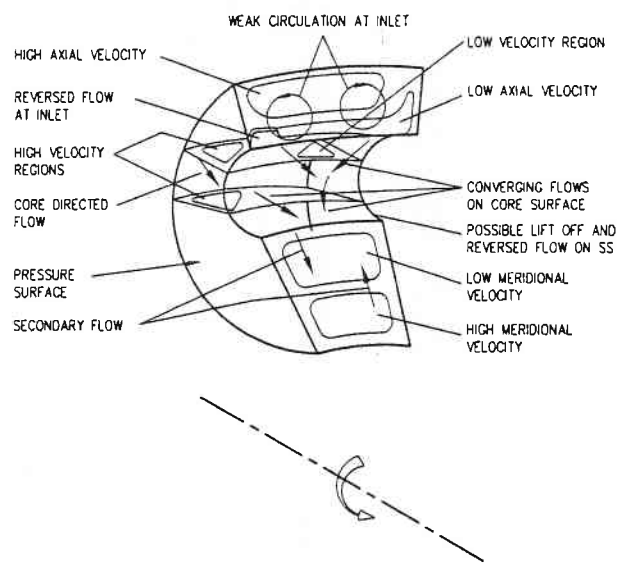

Fig. 20 Main flow features in a torque converter turbine at SR = 0.800

using oil as working fluid. The pressure signals were divided into five parts: the temporal average, the rotor-rotor interaction aperiodic component, the blade periodic component, the blade periodic component and the unresolved component. They found that pressure and velocity fluctuations were moderate but flow angle fluctuations were high. The turbine blade wakes were thin, and near the shell the wake decay was rapid. The secondary flow pattern in the turbine frame of reference showed overturning in the separation region near the core, underturning in the rest of the passage and a radial inflow in the entire passage (Fig. 19).

By and Lakshminarayana (1991) investigated the static pressure distribution over the axial flow stator blades of an automotive torque converter, measuring at the midspan and on the shell and core surfaces near the passage corners. They found that a panel method could predict the pressure distributions well only at mid-span. The blade pressure distribution (Fig. 13) indicates very large positive incidence (+57 deg) at SR = 0 and large negative incidence (−47 deg) at SR = 0.800. Most of the static pressure drop at SR = 0.800 occurs from the leading edge to 50 percent chord, while the static pressure drop at SR = 0 occurs aft of the mid-chord.

Marathe et al. (1995b) also measured the time dependent stator blade surface pressures at five points in the stator mid-chord plane. The location of transducers were at the leading edge and near the leading and trailing edges on the suction and pressure surfaces. The unsteady blade static pressures were found to be high near the leading edge and insignificant near the trailing edge. The source of unsteadiness is found to be the upstream wake as well as the upstream static pressure variation (potential effect).

The stator exit flow is presented in an earlier section (Figs. 3–6). At SR = 0.800 the pitch-averaged axial velocity profile at stator exit indicates large gradients from core-to-shell. The axial velocity is lower near the core. The deviation angle of 1.2 deg derived from FHP measurements at SR = 0.800 indicates that there is almost no flow deflection in the stator: the stator inflow angle is 54.6 deg and the outflow angle is 61.8 deg. The flow deflection at SR = 0.065 is found to be large. A deviation angle of 5.8 deg and turning angle of 95 deg is reported.

Discussion of Stator Flow Fields. One of the major features of the flow in the stator under consideration is large areas of separation found at SR = 0.800 when the flow deflection is small, and the absence of separation at SR = 0.065 when the flow deflection is large. A schematic of the flow field in the stator is shown in Fig. 21. The obvious solution to the flow separation at small defection (negative incidence) is to design the stator blades with almost flat pressure surfaces.

At SR = 0.800 there is separation on the pressure surface extending over the full span at mid-chord. It is caused by the combination of a large negative incidence angle and the concave shape of the stator blade profile. The separation over the full chord near the core is caused by the high incidence angle due to turbine rotation and flow overturning at the turbine exit near the core. The secondary flow at the exit consists of two weak circulation cells near the two blade walls. They induce core-to-shell flow near the walls, indicating a core pressure higher than the shell pressure, which is borne out by the static pressure distribution, although the gradient is very small. The low momentum boundary layer flow transported from core to shell along the suction surface eventually causes flow separation in the suction-shell corner near the exit.

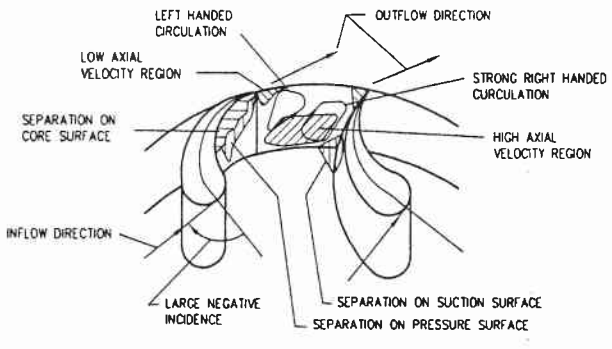

Fig. 21 Main flow features in a torque converter stator at SR = 0.800

At SR = 0.065 the high velocity exit flow is near the pressure shell corner, with a low velocity core near the suction shell corner, more or less coincident with a left handed vortex. The static pressure decreases from shell to core with a gradient that can be explained by a simple streamline curvature model that takes into consideration both the effect of the circumferential and the meridional velocity.

One of the major differences between the industrial and automotive types of torque converter lies in the stator exit meridional through flow velocity profile. In the industrial type, the higher velocity is near the core (Adrian, 1985), while in the automotive type it is near the shell as shown in Fig. 3 (Bahr et al., 1990; Marathe et al., 1996). This trend must be due to the presence of the stator blades near the torque converter axis of the automotive type. It is caused by the passage vortices associated with the curvature of the flow in the meridional plane between the turbine exit and the pump inlet. Consequently the pumps in the automobile type torque converters are exposed to less favorable meridional inlet velocity profiles than ordinary pumps and certain industrial torque converter pumps; the critical part of the flow passage, the core region where boundary layer flow accumulates, now starts with a low through flow velocity at inlet.

A schematic showing of all features discussed in this and earlier sections is shown in Fig. 21. This is based on an assessment of LDV data (UVA) and five-hole probe data (PSU).

Torque Converter Flow Field and Performance—An Integrated Assessment

The global features of the torque converter flow can be ascertained by examining Fig. 4, 6, 13, 14, 20, and 21. The stator inlet and exit stagnation pressure distribution is uniform from core to shell, with maximum losses occurring in the outer and inner third of the blade height. The stagnation pressure distribution at the exit of both turbine and pump is non-uniform, with lower values near the core. Low axial velocity near the core, and in some instances separated flow, in both of these components contribute to low pressure rise in the pump and low pressure drop in the turbine. This is also confirmed by passage average axial velocity distribution shown in Fig. 6.

The blade static pressure distribution (Fig. 13) shows that the stator provides a smooth entry to the pump (except in the core region as indicated earlier) at both SR = 0.800 and 0.065. The pump exit and the turbine inlet have not been matched well, with the initial part of the turbine behaving like a pump at SR = 0.800. The stator inlet and turbine exit matches well only at SR = 0.6, with large positive and negative angles at SR = 0.800 and 0. A two-stage stator with two separate clutches may be a solution here.

The area-mass averaged stagnation and static pressure distribution derived from five-hole probe data (Marathe, 1996) indicate that the stagnation pressure loss between the turbine exit and stator exit is lowest at SR = 0.6, and very high at both SR = 0.800 and 0.065.

The torque converter efficiency is the turbine power divided by the pump power. The efficiency is then essentially equal to the speed ratio multiplied by the torque ratio. The "lost" energy is dissipated in the working fluid, increasing its temperature. Zero efficiency at zero speed ratio in torque converters is unavoidable, as the output power is proportional to the turbine

speed. Torque converter element and overall efficiencies were calculated from the experimental data.

Using area-mass averaged values of angular momentum at the inlet and exit of each of the components, a torque ratio (T_T/T_P) of 1.079 at SR = 0.800 was calculated yielding a torque converter efficiency of η_{TC} = 0.863. This is a fairly realistic internal efficiency for this torque converter, since from Bahr et al. (1990), η_{TC} = 0.820 at SR = 0.800 measured directly by a torque meter. The main reason for the resulting high values was that the cross-sectional areas over which the measurements were taken did not extend right to the walls where the lowest values of momentum and stagnation pressure occurred. The data (Fig. 13) based on blade static pressure (By, 1993) yields η_{TC} = 0.828 and TR = 1.034.

If at SR = 0.065 the LDV pump exit and turbine inlet data are used in conjunction with the FHP stator exit and turbine exit data results in TR = 2.52, with η_{TC} = 0.163. The corresponding data from blade static measurements are TR = 2.09 and η_{TC} = 0.136 which includes drag torque on the pump. The direct measurement yields η_{TC} = 0.13, and TR = 2.0. Thus, it is clear that the flow measurements should provide detailed information on flow field as well as losses in each component.

Conclusions

Detailed conclusions for each component is given in the text and will not be repeated here. The following additional conclusions are drawn based on an integrated assessment of the flow field.

1. The stator inlet and exit stagnation pressure distribution are uniform from core to shell, with maximum losses occurring in the outer and inner third of the blade height.
2. The stagnation pressure distribution at the exit of both turbine and pump is nonuniform, with lower values near the core. Low axial velocity near the core, and in some instances separated flow, in both of these components contribute to low pressure rise in the pump and low pressure drop in the turbine. This is also confirmed by passage-averaged axial velocity distribution.
3. The blade static pressure distribution shows that the stator provides a smooth entry to the pump (except in the core region as indicated earlier) at both SR = 0.8 and 0.065.
4. The pump exit and the turbine inlet flow field have not been matched well, with the initial part of turbine behaving like a pump at SR = 0.8.
5. The stator inlet and turbine exit match well only at SR = 0.6, with large positive and negative incidence angles at SR = 0.8 and 0.
6. The stagnation pressure loss between the turbine exit and stator exit is lowest at SR = 0.6, and very high at both SR = 0.8 and 0.065.
7. The efficiencies and torque ratios derived from flow measurement agrees with those measured directly. The flow measurement provides detailed information as well as losses in each component.
8. The turbine efficiency is higher at design condition.

The flow in torque converters is extremely complex. Design methods accounting for all of the complexity must still be developed. They should at least be able to account for regions of flow separation and secondary flow circulation. Even though torque converters with peak efficiencies of 90 percent have been developed, the next generation would require design methods that allow for blade lean angles, the optimization of the shape of the flow passage and interaction effects between pump, turbine and stator. The development effort should concentrate on pump and stator and proper matching of components. CFD should be used to analyze existing and additional detailed measurements and to investigate the reasons why certain designs perform better than others.

Acknowledgments

This work was sponsored by the Powertrain Division of General Motors Corporation. The authors wish to express their appreciation to D. Maddock and R. By for technical discussions, R. Flack and K. Brun of the University of Virginia for making their data available, and B. Marathe and Y. Dong (PSU) for their assistance in the preparation of the paper. The first author's stay at PSU was funded by the University of Stellenbosch and the Foundation for Research Development of South Africa, and the Howden Group of South Africa.

References (Quoted)

Adrian, F. W., 1985, "Experimental and Analytical investigation of Flows in Hydrodyanmic Torque Converters," Ph.D. thesis (in German), The Ruhr University, Bochum, Germany.

Bahr, H. M. et al., 1990, "Laser Velocimeter Measurements in the Stator of a Torque Converter," SAE paper 901769

Browarzik, V., 1994, "Experimental Investigation of Rotor/Rotor Interaction in a Hydrodynamic Torque Converter Using Hot-Film Anemometry," ASME paper 94-GT-246.

Brun, K., Flack, R. D., and Gruver, J. K., 1996a, "Laser Velocimetry Measurements in the Pump of an Automotive Torque Converter: Part II Unsteady Measurement." *Journal Turbomachinery,* Vol. 118, No. 3, p. 570.

Brun, K., Flack, R. D., and Ainley, S. B., 1994, "Secondary Flow Measurement in a Mixed Flow Pump Using Laser Velocimetry," *Seventh International Symposium on Applications of Laser Techniques to Fluid Mechanics,* Lisbon, Portugal.

Brun, K., and Flack, R. D., 1995a, "Laser Velocimeter Measurements in the Turbine of an Automotive Torque Converter," Part I—Average Measurements, ASME paper 95-GT-292.

Brun, K., and Flack, R. D., 1995b, "Laser Velocimeter Measurements in the Turbine of an Automotive Torque Converter," Part II—Unsteady Measurements, ASME paper 95-GT-293.

By, R., 1993, "An Investigation of Three-Dimensional Flow Fields in the Automobile Torque Converter," Ph.D. thesis, Dept. of Aerospace Engineering, Pennsylvania State University.

By, R. and Lakshminarayana, B., 1991 "Static Pressure Measurement in a Torque Converter Stator," *Journal of Passenger Cars,* Vol. 100, pp. 1756–1764.

By, R., and Lakshminarayana, B., 1995a, "Measurement and Analysis of Static Pressure Field in a Torque Converter Pump," ASME JOURNAL OF FLUIDS ENGINEERING, Vol. 117, pp. 109–115.

By, R., and Lakshminarayana, B., 1995b, "Measurement and Analysis of Static Pressure Field in a Torque Converter Turbine," ASME JOURNAL OF FLUIDS ENGINEERING, Vol. 117, No. 2, pp. 473–478.

By, R., Kunz, R., and Lakshminarayana, B., 1995c, "Navier-Stokes Analysis of the Pump Flow Field of an Automotive Torque Converter," ASME JOURNAL OF FLUIDS ENGINEERING, Vol. 117, No. 1, pp. 116–122.

By, R. R., and Mahoney, J. E., 1988, "Technology Needs for the Automotive Torque Converter," Part I: Internal Flow, Blade Design and Performance, SAE paper 880482.

Eckardt, D., 1980, "Flow Field Analysis of Radial and Back Swept Centrifugal Impellers," *Performance Prediction of Compressors & Pumps, ASME.*

Fister, W., and Adrian, F.-W., 1983, "Experimental Researches of Flow in Hydrodyanmic Torque Converters," presented at the 7th Conference on Fluid Machinery, Hungary, Vol. 1.

Gruver, J. K., Flack, R. D., and Brun, K., 1996, "Laser Velocimeter Measurements in the Pump of a Torque Converter, Part I: Average Measurements," *Journal Turbomachinery,* Vol. 118, No. 3, p. 562.

Jandasek, V. J., 1963, "The Design of a Single Stage Three-Element Torque Converter. Passenger Car Automatic Transmissions," SAE Transmission Workshop Meeting, Second edition, *Advanced Engineering,* Vol. 5, p. 201.

Kost, A., Mitra, N. K., and Fiebig, M., 1994, "Computation of Unsteady 3D Flow and Torque Transmission in Hydrodynamic Couplings," ASME paper 94-GT-70.

Lakshminarayana, B., 1996, *Fluid Dynamics & Heat Transfer of Turbomachinery,* Wiley, New York, NY.

Lee, J.-S. et al., 1994, "Surface Flows Inside Automotive Torque Converters," *Proc. 5th Int. Symposium on Transport Phenomena and Dynamics of Rotating Machinery,* Vol. B, p. 887 (ISRO MAC), Maui, Hawaii.

Maddock, D. G., 1991, "Application and Design of Automotive Torque Converters," GM Powertrain Division, Class notes for an Automatic Transmission Course.

Marathe, B. V., 1996, "Experimental Investigation of Steady and Unsteady Flow Field in Automotive Torque Converters," Ph.D. thesis, Dept. of Aerospace Engineering, PSU, (in preparation).

Marathe, B. V., and Lakshminarayana, B., 1995, "Experimental Investigation of Steady and Unsteady Flow Field Downstream of an Automotive Torque Converter Turbine and Stator," *International Journal of Rotating Machinery,* Vol. 2, pp. 67–84.

Marathe, B. V., Lakshminarayana, B., and Dong, Y., 1996, "Experimental and Numerical Investigation of Stator Exit Flow Field of an Automotive Torque Converter," ASME paper 94-GT-32, to be published *ASME Journal of Turbomachinery*, Oct. 1996.

Marathe, B. V., Lakshminarayana, B., and Maddock, D. G., 1995a, "Investigation of Steady and Unsteady Flow Field Downstream of an Automotive Torque Converter Turbine and Inside the Stator, Part I—Flow at the Exit of the Turbine," ASME paper 95-GT-231.

Marathe, B. V., Lakshminarayana, B., and Maddock, D. G., 1995b, "Investigation of Steady and Unsteady Flow Field Downstream of an Automotive Torque Converter Turbine and Inside the Stator, Part II—Unsteady Pressure on the Stator Blade Surface," ASME paper 95-GT-232.

Numazawa, A. et al., 1983, "An Experimental Analysis of Fluid Flow in a Torque Converter," SAE paper, 830571.

Schulz, H., Greim, R., and Volgmann, W., 1996, "Calculation of Three-dimensional Viscous Flow in Hydrodynamic Torque Converters," ASME *Journal Turbomachinery*, Vol. 118, No. 3, p. 578.

Strachan, P. J., Reynaud, F. P., and von Backstrom, T. W., 1992, "The Hydrodynamic Modeling of Torque Converters," South African Inst. *Mech. E R&D Journal*, Vol. 8, No. 1.

Tsujita, H., Mizuki, S., and Ejiri, E., 1996, "Analysis of Flow Within Pump Impeller of Torque Converter," ASME paper 96-GT-444, presented at ASME IGTI meeting in Birmingham, England, June 1996.

Wiesner, F. J., 1967, "A Review of Slip Factors for Centrifugal Impellers," ASME *Journal of Engineering for Power*, Vol. 89, p. 558.

Additional References (Not Quoted)

Abe, K., and Kondoh, T., 1991, "Three-Dimensional Simulation of the Flow in a Torque Converter," SAE paper 910800.

Bai, L., Kost, A., Fiebig, M., and Mitra, N. K., 1994, "Numerical Investigation of Unsteady Incompressible 3D Turbulent Flow and Torque Transmission in Fluid Couplings," ASME paper 94-GT-69.

Ejiri, E., 1990, "A New Approach to Developing a More Efficient Torque Converter Stator," SAE paper 901765.

Folchert, U., Menne, A., and Waller, H., 1994, "Experimental Identification of the Dynamic Characteristic of Hydrodynamic Torque Converters and Couplings," ASME paper 94-GT-360.

Fujitani, K. R. R. Himeno, and Takagi, M., 1988, "Computational Study on Flow Through a Torque Converter," SAE paper 881746.

Hoshino, A. et al., 1990, "A Consideration on Performance improvement of Hydraulic Torque Converters," *Industrial Applications of Fluid Mechanics*, ASME FED Vol. 100, pp. 65–70.

Ishihara, T., 1955, "A Study of Hydraulic Torque Converters," Ph.D. thesis, University of Tokyo, AHO Report of the Institute of Industrial Science, Vol. 5, No. 7.

Ma, W., Luo, B. J., and Wu, S., 1991, "The Research on Quasi-Three-Dimensional Flow Design of Hydrodynamic Torque Converter Blades," SAE paper 912701.

Mercure, R. A., 1979, "Review of the Automotive torque Converter," SAE paper 790046.

Minato, K. et al., 1989, "A Performance Prediction of Hydrohynamic Torque Converter," SAE paper 900555.

Nagornaya, N. K., 1961, "Impact Losses and Coefficients in Hydraulic Torque Converter Blade Systems," *Russian Engineering Journal*, Vol. 6, pp. 21–24.

Sakamoto, H., Suyama, K., and Saka, T., 1992, "Study on Torque Converter Circuit Profile," SAE paper, 920765.

Wada, A. et al., 1995, "A PTV Analysis of Torque Converter Internal Flow," ASME paper, ASME FED Vol. 218.

Ziebart, E., 1953, "Investigations on a Foettinger Hydraulic Torque Converter," *Z-VDI*, Vol. 95, No, 30, pp. 1027–1036.

Numerical Heat Transfer, Part B, vol. 20, pp. 127–144, 1991

REFORMULATION OF THE SIMPLEN DISCRETIZATION SCHEME TO ACCOMMODATE NONCENTRALIZED INTERFACES

T. M. Harms and T. W. von Backström
Department of Mechanical Engineering, University of Stellenbosch, Stellenbosch 7600, South Africa

J. P. du Plessis
Department of Applied Mathematics, University of Stellenbosch, Stellenbosch 7600, South Africa

The SIMPLEN discretization scheme based on a nonstaggered orthogonal grid is derived from an extension of the original power-law scheme. A revised interface interpolation equation, which no longer requires the interfaces to be located centrally between nodes, is presented. The expression for the orthogonal interface convection–diffusion flux is reformulated and the associated pressure correction factor is provided. The adopted formulation allows boundary control volumes to be treated essentially as internal control volumes and leads to an update of the power-law approximation to improve its accuracy. The extended method is applied to two test cases of laminar incompressible flow.

INTRODUCTION

Thiart [1, 2] has recently proposed a new finite-difference scheme suitable for nonstaggered grids. The method is called SIMPLEN (SIMPLE-nonstaggered) indicating that it is based on the work of Patankar [3] and on earlier contributions by Harlow and Welch [4], Caretto et al. [5], Spalding [6], and Patankar and Spalding [7]. The scheme can be considered a direct extension of the power-law scheme of Patankar [3], since it is also based on the power-law approximation of the analytical solution to a (quasi) one-dimensional convection–diffusion equation. The latter equation is used to obtain the value of the transported variable at the control volume interface. The contribution of the SIMPLEN approach arises from the inclusion of a constant source term S in the convection–diffusion equation.

$$\rho u \frac{\partial \phi}{\partial \xi} - \Gamma \frac{\partial^2 \phi}{\partial \xi^2} = S \tag{1}$$

This extra term is used to account for the otherwise neglected pressure gradient and multidimensional cross-flux terms of the Navier-Stokes equations.

As a result, Eq. (1) not only provides a more accurate interpolation scheme than the one-dimensional homogeneous form, but also, by the inclusion of a pressure gradient in the term S, yields a semi-explicit equation for interface velocity in terms of the local

We gratefully acknowledge the financial assistance from the Council for Scientific and Industrial Research and the Bureau for Mechanical Engineering.

NOMENCLATURE

a	fraction describing the interface location	u	velocity normal to the interface
A, B, C, D	exponential functions and their approximations	U, V	orthogonal velocity components at a node
d	pressure correction coefficient function	Γ	diffusion coefficient
h	height above the cavity floor	ξ	local coordinate
H	square cavity sidewall length	ρ	fluid density
J	flux normal to an interface	ϕ	any transported variable
L	distance between nodes	ω	angular velocity
M, N, O, R, Z	algebraic constants		
n	number of nodes	**Subscripts**	
P	local grid Péclet number; pressure at a node	$0, L$	associated with a node and its neighbor in terms of local coordinates
r_1, r_2	inner and outer cylinder radii	aL	associated with an interface in terms of local coordinates
Re	Reynolds number		
S	local constant volumetric source term	P, E, e	associated with a node and its eastern neighbor or interface

pressure gradient. It is therefore no longer necessary to discretize and solve the momentum equations on a staggered grid to provide such an equation.

An expression for the velocity–pressure coupling at the colocated control volume interface is the starting point for other nonstaggered grid-based schemes (e.g., those of Rhie and Chow [8] or Schneider and Raw [9]). However, in using a source term approach, the present method is more related to the work of Prakash [10] and can be considered a further realization of the potential of the locally analytical differencing scheme (LOADS) proposed by Wong and Raithby [11].

Since solution of Eq. (1) results in exponential terms, the analysis of the present algorithm can become tedious. However, Thiart [1, 2] has shown that grouping these exponentials into a number of repeatedly used weighting functions (which, in turn, are expressed through the power-law approximation of Patankar [3]) results in a compact theoretical package; this lends itself to easier programming. Thiart [1, 2] has also reported that his scheme for nonstaggered grids produces good results and that these are independent of relaxation factors, as opposed to the original method of Rhie and Chow [8]. Therefore, further development of the SIMPLEN method is considered worthwhile.

The original scheme has been presented [1, 2] for the special case where the control volume interface lies centrally between node points. Here we derive a formulation that gives greater freedom with regard to the positioning of nodes relative to interfaces.

DERIVATION OF AN INTERPOLATION SCHEME FOR THE CASE OF NONCENTRALIZED INTERFACES

In Fig. 1 an interface is positioned noncentrally between two adjacent nodes. The adjacent control volume zones of constant properties are designated by the local one-dimensional coordinates of the nodes (i.e., 0 and L). The interface is located at a fraction

a of the distance between the nodes from the left node. Initially $0 < a < 1$; the extreme cases of $a = 0$ and $a = 1$ are dealt with later.

The starting point is the quasi-one-dimensional convection–diffusion Eq. (1) given above. With ρu and Γ constant in the interval $0 < \xi < L$, and with boundary values ϕ_0 and ϕ_L, it has the solution

$$\phi = \phi_0 + \frac{S}{\rho u}\left(\xi - L\,\frac{\exp(\rho u\xi/\Gamma) - 1}{\exp(\rho uL/\Gamma) - 1}\right) + (\phi_L - \phi_0)\,\frac{\exp(\rho u\xi/\Gamma) - 1}{\exp(\rho uL/\Gamma) - 1} \tag{2}$$

Using the refinement proposed by Thiart [2], we now apply this equation to each of two regions of constant source S_0 and S_L shown in Fig. 1. With the boundary values

$$\begin{aligned} \phi &= \phi_0 \quad \text{at } \xi = 0 \\ \phi &= \phi_{aL} \quad \text{at } \xi = aL \\ \phi &= \phi_L \quad \text{at } \xi = L \end{aligned} \tag{3}$$

it then follows that the solutions, respectively, become

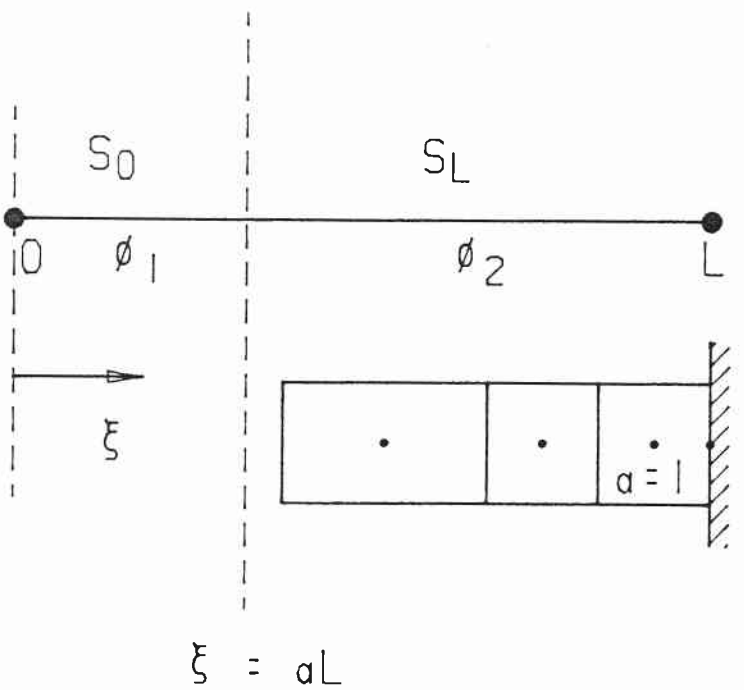

Fig. 1 Noncentralized control volume interface.

$$\phi_1 = \phi_0 + \frac{S_0}{\rho u}\left(\xi - aL\,\frac{\exp(\rho u\xi/\Gamma) - 1}{\exp(aP) - 1}\right) + (\phi_{aL} - \phi_0)\,\frac{\exp(\rho u\xi/\Gamma) - 1}{\exp(aP) - 1} \tag{4}$$

and

$$\phi_2 = \phi_{aL} + \frac{S_L}{\rho u}\left[\xi - aL - L(1-a)\,\frac{\exp[\rho u(\xi - aL)/\Gamma] - 1}{\exp[(1-a)P] - 1}\right] + (\phi_L - \phi_{aL})\,\frac{\exp[\rho u(\xi - aL)/\Gamma] - 1}{\exp[(1-a)P] - 1} \tag{5}$$

with P, the local Péclet number, given by $\rho uL/\Gamma$.

For continuity of the derivative at the interface, we solve for ϕ_{aL} by equating the derivatives at $\xi = aL$. These are given by

$$\left(\frac{\partial\phi_1}{\partial\xi}\right)_{aL} = \frac{S_0}{\rho u} - \frac{S_0}{\rho u}\,\frac{aP\exp(aP)}{\exp(aP) - 1} + (\phi_{aL} - \phi_0)\,\frac{P/L\exp(aP)}{\exp(aP) - 1} \tag{6}$$

and

$$\left(\frac{\partial\phi_2}{\partial\xi}\right)_{aL} = \frac{S_L}{\rho u} - \frac{S_L}{\rho u}\,\frac{(1-a)P}{\exp[(1-a)P] - 1} + (\phi_L - \phi_{aL})\,\frac{P/L}{\exp[(1-a)P] - 1} \tag{7}$$

so that after algebraic manipulation we obtain

$$\phi_{aL} = \frac{\exp(P) - \exp(aP)}{\exp(P) - 1}\,\phi_0 + \frac{\exp(aP) - 1}{\exp(P) - 1}\,\phi_L + \frac{L^2[\exp(-aP) - 1 + aP][\exp(P) - \exp(aP)]}{\Gamma P^2[\exp(P) - 1]}\,S_0 + \frac{L^2\{\exp[(1-a)P] - 1 - (1-a)P\}[\exp(aP) - 1]}{\Gamma P^2[\exp(P) - 1]}\,S_L \tag{8}$$

which is the required interpolation equation.

The computationally more efficient power-law approximation of Patankar [3], given by

$$A(P) = \frac{P}{\exp(P) - 1} \simeq \max[0,\ 1 - 0.1|P|]^5 + \max[0,\ -P] \tag{9}$$

is now introduced to express Eq. (8) in a more compact form. It was found that this is possible through an analogy to Thiart's [2] formulation by introducing weighting functions of two variables. Equation (8) is therefore rewritten as

$$\phi_{aL} = C(1 - a, -P)\,\phi_0 + C(a, P)\phi_L + \frac{L^2}{\Gamma} B(a, -P)D(a, -P)S_0$$

$$+ \frac{L^2}{\Gamma} B(1 - a, P)\,D(1 - a, P)S_L \tag{10}$$

For the sake of clarity, a discussion of the weighting functions B, C, and D is delayed until after the computation of an interface flux.

In terms of a control volume formulation, the generalized convection–diffusion flux at an interface is formulated according to Patankar [3] as

$$J = \rho u \phi_{aL} - \Gamma \left(\frac{\partial \phi}{\partial \xi}\right)_{aL} \tag{11}$$

An expression for ϕ_{aL} is provided by Eqs. (8) or (10). An expression for the differential in the above equation can be obtained by substituting Eq. (8) in either of Eqs. (6) or (7), resulting in

$$\left(\frac{\partial \phi}{\partial \xi}\right)_{aL} = \frac{P/L \exp(aP)}{\exp(P) - 1}(\phi_L - \phi_0)$$

$$- \frac{L[\exp(-aP) - 1 + aP][\exp(P) - \exp(aP)]}{\Gamma P\{\exp[(1 - a)P] - 1\}[\exp(P) - 1]} S_0$$

$$- \frac{L\{\exp[(1 - a)P] - 1 - (1 - a)P\}[\exp(aP) - 1]}{\Gamma P[\exp(-aP) - 1][\exp(P) - 1]} S_L \tag{12}$$

Substituting Eqs. (8) and (12) in the expression for the flux given by Eq. (11) results in

$$J = \rho u \phi_0 + \frac{\Gamma P}{L[\exp(P) - 1]}(\phi_0 - \phi_L)$$

$$- \frac{L[\exp(-aP) - 1 + aP][\exp(P) - \exp(aP)]}{P\{\exp[-(1 - a)P] - 1\}[\exp(P) - 1]} S_0$$

$$- \frac{L\{\exp[(1 - a)P] - 1 - (1 - a)P\}}{P[\exp(P) - 1]} S_L \tag{13}$$

Some algebraic manipulation and the same weighting functions introduced in Eq. (10) are used to efficiently express the interface fluxes as

$$J = \rho u \phi_0 + \frac{\Gamma}{L} A(P)(\phi_0 - \phi_L) + LB(a, -P)C(a, -P)S_0$$

$$- LB(1 - a, P)C(1 - a, P)S_L \tag{14}$$

When similar expressions are formulated for other control volume faces and all are integrated over their respective surfaces, the first term in Eq. (14) will vanish as a result of the application of mass conservation. The second term will produce coefficients identical to those of the power-law scheme [3]. The remaining terms will, as the only

consequence of the inclusion of an additional term S in Eq. (1), make a contribution on the source term side of a conservation balance.

With regard to the momentum equations, the additional source terms contribute to the accuracy of the SIMPLEN method [1, 2] and are therefore included in the calculations presented in this article. They provide a velocity–pressure coupling within a control volume despite the use of a nonstaggered grid. Their inclusion in this regard is, however, not essential as it is necessary and sufficient for the momentum equations to yield the correct velocities, given the correct pressure field. The velocity–pressure coupling can be demonstrated through the example of the U-velocity equation. Applying Eq. (14) to an eastern interface, the source terms S_P and S_E would contain the local pressure gradient, assumed to be constant between nodes and discretized as

$$S_P,\ S_E = -\frac{P_E - P_P}{L_e} + \left[-\rho V \frac{\partial U}{\partial y} + \Gamma \frac{\partial^2 U}{\partial y^2}\right]_{P,E} \tag{15}$$

with the terms in parentheses discretized in the y direction at nodes P and E [2]. It can be shown that, for nonzero interface Péclet numbers, the behavior of the weighting functions B and C ensures the presence of the nodal pressure in a discretized momentum equation, thus addressing another issue originally associated with the introduction of a staggered grid [3].

WEIGHTING FUNCTIONS *B, C,* AND *D*

The function $B\ (a,\ P)$ (both convection and diffusion) is identical to the function $B(P)$ employed by Thiart [1, 2] and $W(P)$ by Schreüder [12], that is,

$$B(a,\ P) = \frac{1 - \{aP/[\exp\ (aP) - 1]\}}{P} \tag{16}$$

and thus expressed in terms of Eq. (9) as

$$\begin{aligned} B(a,\ P) &= \frac{1 - A(aP)}{P} \qquad |aP| \geq Z \\ &\simeq \frac{a(1 - aP/6)}{2} \qquad |aP| < Z \end{aligned} \tag{17}$$

For the present, the constant Z is given the value of the Péclet number at which both approximations produce an equal error and is equal to 1.82756. The graph of $B(a,\ P)$ is shown in Fig. 2 for different values of the fraction a. It is an upwind weighting function, which allows both convection and diffusion to be significant for a large local grid Péclet number range (i.e., approaching its asymptotic values of a and 0 relatively slowly).

It is now useful to consider the function D (diffusion), given by

$$\begin{aligned} D(a,\ P) &= \frac{[\exp\ (aP) - 1]\{\exp\ [(1 - a)P] - 1\}}{P[\exp\ (P) - 1]} \\ &= \frac{[\exp\ (-a|P|) - 1]\{\exp\ [-\ (1 - a)|P|] - 1\}}{-|P|[\exp\ (-|P|) - 1]} \end{aligned} \tag{18}$$

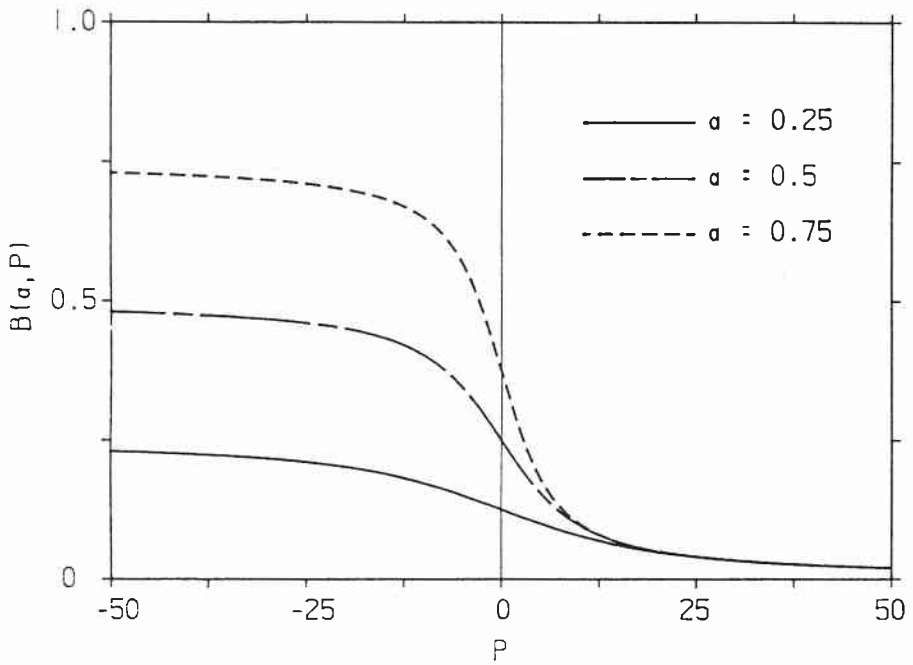

Fig. 2 Function $B(a, P)$.

which is an even function. This is used to express D in terms of A (adjacent) in order to avoid division by zero and otherwise reduced accuracy through the division of small numbers as A approaches its zero asymptote when $aP \to \infty$. The function is therefore approximated by

$$D(a, P) \simeq \frac{a(1 - a)A(-|P|)}{A(-a|P|)A[-(1 - a)|P|]} \tag{19}$$

The graphic representation of D is given in Fig. 3 for various values of a. Its shape has a diffusive character, that is, the influence of a factor of D will significantly diminish for large positive or negative Péclet numbers.

The function C (convection) is given by

$$C(a, P) = \frac{\exp(aP) - 1}{\exp(P) - 1} \tag{20}$$

and the expression for D may be used to obtain

$$C(a, P) = \frac{D(a, P)P}{\exp[(1 - a)P] - 1} \simeq \frac{aA(-|P|)A[(1 - a)P]}{A(-a|P|)A[-(1 - a)|P|]} \tag{21}$$

C is plotted for various values of a in Fig. 4. It is a convection-dominated function with distinct upwind behavior, that is, assuming the values 0 and 1 except for a narrow Péclet number domain near the origin. It represents the solution of the homogenous convection–diffusion type equation used by Patankar [3] and other authors, for example, Blackwell [13].

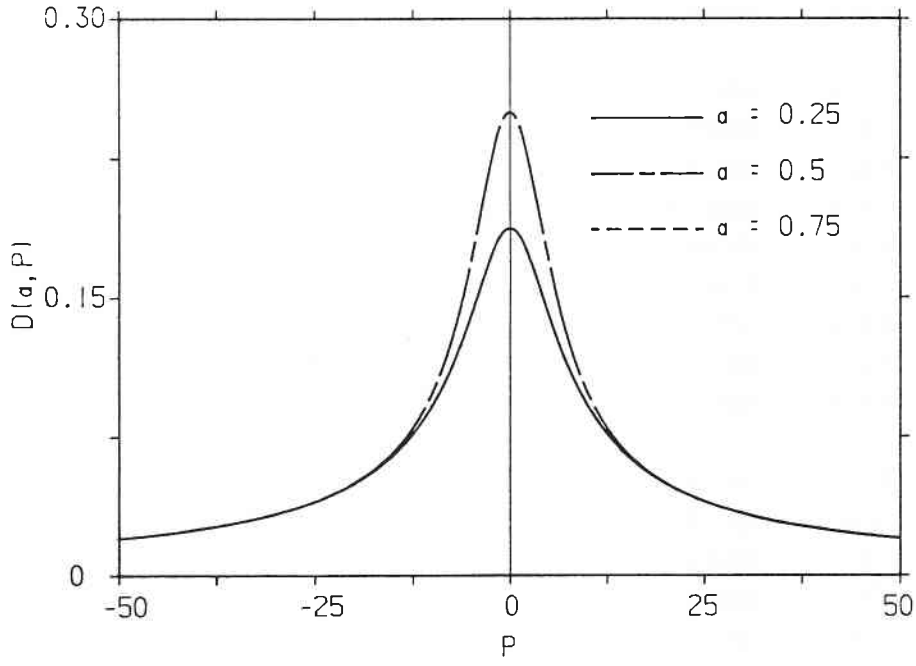

Fig. 3 Function $D(a, P)$.

The approximated and analytical function values are too close for graphic comparison except for noticeable deviations near the origin, which are addressed below. Like Thiart [1, 2], preference was given to relying exclusively on the power-law approximation. In the future, new, more computationally efficient approximations might be developed for each exponential grouping. The functions A, B, C, and D are treated as fundamental, and preference is given to expressing other exponential groupings in terms of these to enhance understanding of the scheme and to avoid the proliferation of functions.

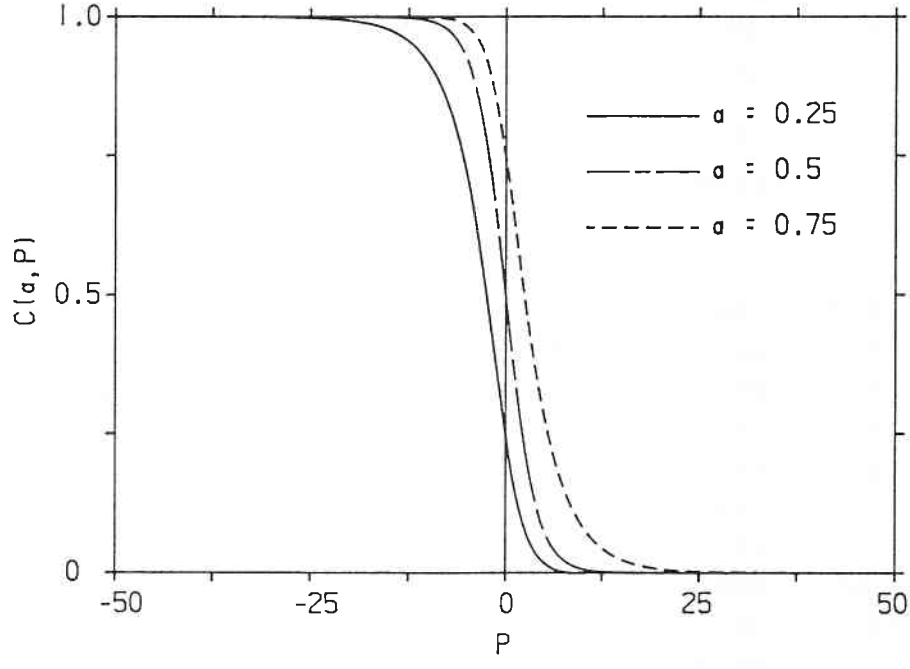

Fig. 4 Function $C(a, P)$.

The significant effect of increasing or decreasing a (i.e., changing the distance between a node and the interface) can be seen clearly in all cases.

With regard to the interpolation Eq. (10), the basic upwinding of the nodal values is borne out by their coefficients in terms of C. The product function $B \cdot D$ is shown in Fig. 5. Its effect is to upwind and to delay the decay of the influence of the local source at high Péclet numbers and, therefore, to dampen out the pure upwinding of the original power-law scheme under such conditions. Keeping in mind that the source terms S_0 and S_L contain multidimensional terms, as shown in Eq. (15), the SIMPLEN interpolation scheme of Thiart [1, 2] does address some of the shortcomings of the original power-law scheme. While the influence of the source terms in Eq. (10) does eventually become negligible at large Péclet numbers, this does not apply when interface fluxes are computed.

With reference to Eq. (14), the behavior of A is well established [3]. The product function $B \cdot C$ is shown in Fig. 6. Since B and C are both upwinding, the product enhances that effect, while at the same time, through the characteristics of B, reducing the influence of the upwind term. Since these terms eventually appear on the source side of a conservation balance, their effect is to introduce upwinding into the source term integration, compatible with the upwinding of fluxes at the control volume interfaces. This weighting of the source term is a characteristic feature of SIMPLEN [1, 2].

Disregarding effects of source term discretization, it is further noted that the diffusion term is expressed through Eq. (12) rather than through direct central differencing. This is a consequence of the locally analytical approach. No substantial decrease in accuracy is therefore expected for values of a other than 0.5.

MODIFICATION OF THE POWER-LAW APPROXIMATION

The error of the original power-law approximation [3] is shown in Fig. 7. It is an even function with a maximum of 0.014668 at a Péclet number of 2.06610. In conjunction with the above derived equations, we found that this error would significantly affect the error values at low Péclet numbers calculated in one of the test cases dealt with below. As a result, we used the following modified power-law approximation:

$$A(P) = \max\left[0,\ 1 - 0.1|P| - \frac{P^2(R - |P|)}{MP^2 + N|P| + O}\right]^5 + \max[0,\ -P] \tag{22}$$

Using the constants given below, which include a new constant for B, the maximum error was reduced to 0.000031. While the original power-law scheme adopted the values of asymptotes of the approximated exponential function at Péclet numbers ± 10, the modified power-law adopts the values of the asymptotes at Péclet numbers ± 16.9738.

The minimum number of terms required to approximate $A(P)$, using a Maclaurin series to equal or better the accuracy of Eqs. (9) and (22), are 6 and 10 at a Péclet number of 2, and 9 and 15 at a Péclet number of 6. Therefore, despite the extra computational effort, Eq. (22) appears more efficient than a series expansion. As an additional feature, the computation of the first term in Eq. (22) might be made subject to the condition $|P| < 16.9738$. For the current work, Eq. (22) was employed with the constants given as follows:

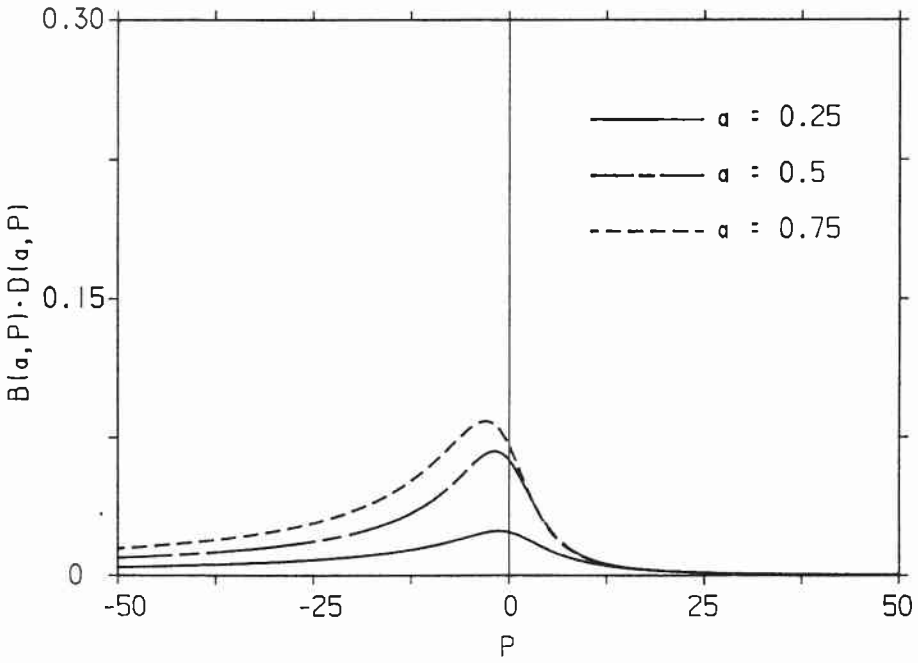

Fig. 5 Product function $B(a, P) \cdot D(a, P)$.

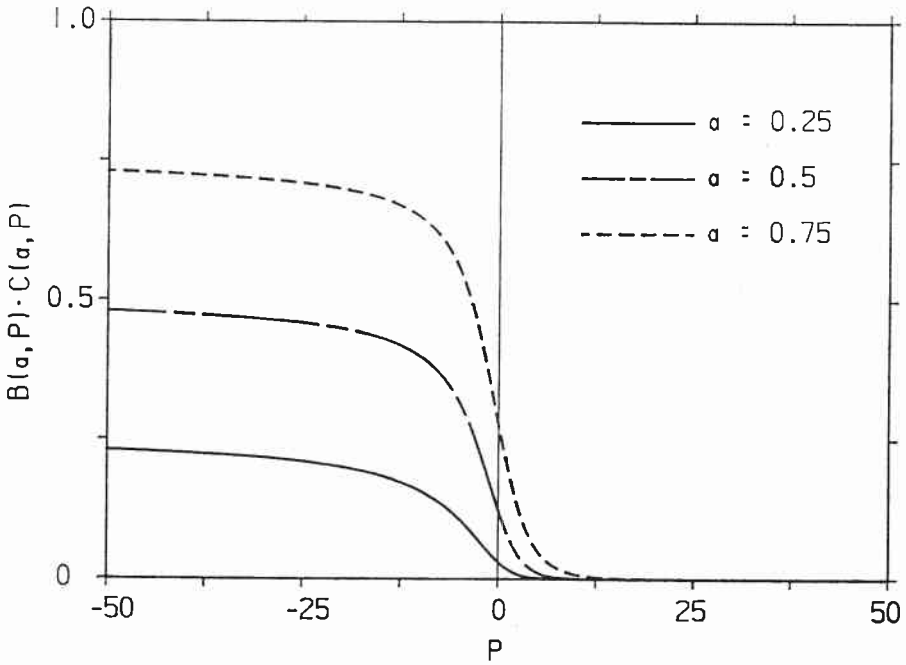

Fig. 6 Product function $B(a, P) \cdot C(a, P)$.

$$M = 13.9029 \qquad N = -9.09632 \qquad O = 1317.72$$
$$R = 4.46233 \qquad Z = 0.324689$$

COMPUTATION OF INTERFACE VELOCITIES AND PRESSURE CORRECTION FACTORS

Although other methods have become available [14], we prefer minimal departure from the proven SIMPLE algorithm [3]. Therefore, using mass continuity to establish a pressure correction equation, a pressure variation dependent interface velocity correction is required. This can be obtained through the explicit use of Eq. (10) to compute interface velocities, employing interface velocities from a previous iteration on the right-hand side. Including the source terms S_0 and S_L, which must at least contain the local pressure gradient, now becomes essential to employ a nonstaggered grid. Therefore, using an idea from CHAM [15] and differentiating Eq. (10) with regard to the discretized pressure gradient results in

$$\frac{\partial u}{\partial(\Delta P)} \simeq \frac{u'}{(P_0' - P_L')/L} = \frac{L^2[a \exp(P) - a - \exp(aP) + 1]}{\Gamma P[\exp(P) - 1]} \tag{23}$$

where nonexplicit dependence on local pressure gradient variations have been ignored. This is analogous to the original SIMPLE approach [3], noting that such dependence vanishes upon convergence. The term on the righthand side of Eq. (23) is equal to the sum of the coefficients of the two source terms S_0 and S_L of Eq. (10), since the local pressure gradient is common to both. This might be the reason why numerically matching the single pressure gradient by the arithmetic average of the two cross fluxes contained in S_0 and S_L, so that $S_0 = S_L$, was found to be slightly beneficial in terms of the accuracy of a pressure field generated when Eq. (10) is used to compute interface

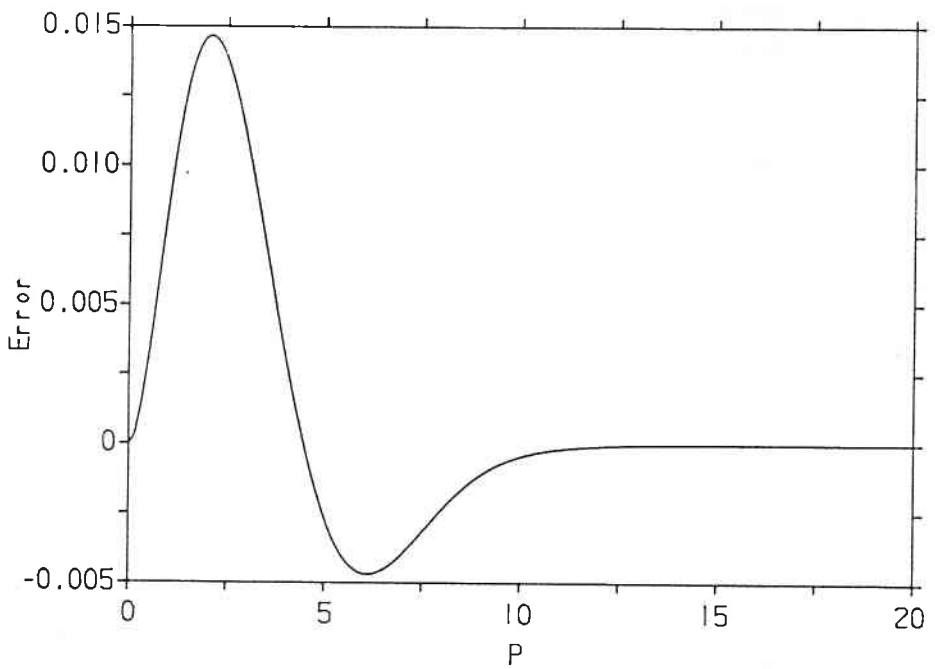

Fig. 7 Error function of the power-law approximation.

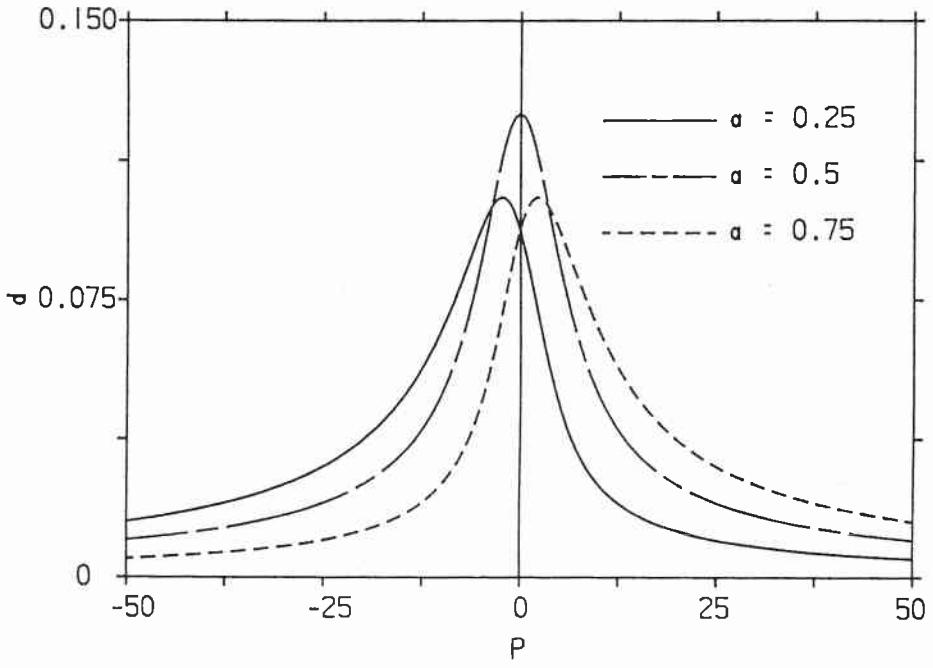

Fig. 8 Pressure correction coefficient function $d(L/\Gamma = 1.0)$.

velocities. However, this does not apply to the formulation of momentum fluxes, as shown by Thiart [2]. The previously introduced weighting functions may be used to obtain

$$u' = d(P_0' - P_L') \tag{24}$$

$$d = \frac{L}{\Gamma}[B(a, -P) + B(1 - a, P)]D(a, P) \tag{25}$$

In Fig. 8 graphs of d for various values of fraction a, with the fraction L/Γ equal to unity, are shown. The influence of the local pressure gradient on the interface velocities rapidly diminishes at large negative or positive Péclet numbers. Some upwinding becomes apparent when the interface does not lie centrally between nodes.

Finally, following the original SIMPLE approach [3] as closely as the nonstaggered grid allows, the resultant algorithm can be described as follows:

1. Start with a guessed flow field solution.
2a. Compute velocities with the aid of Eq. (14).
2b. Compute interface velocities from Eq. (10).
3. Compute pressure corrections using Eq. (25).
4. Add (relaxed) pressure corrections to pressures.
5a. Update the interface velocities with Eq. (24).
5b. Update velocity (cross fluxes) sources.
6. Solve for other properties (ϕ) required.
7. Return to step 2 until convergence.

The algorithm differs from that proposed by Thiart [1]. Interface velocities are directly updated through Eq. (24), thereby fully exploiting the available pressure correc-

tion information. This eliminates the need to compute nodal velocity corrections and the use of Eq. (10) to update interface velocities. No significant deterioration in accuracy or convergence rate was noticed when the two algorithms were compared using the two test cases described below.

BOUNDARY CONDITIONS

In Fig. 1, an irregular grid at a boundary described by Patankar [3] as type B is shown. This grid has become possible as a result of the formulation presented, which allows arbitrary interface locations between nodes. The general transport equations are solved at a node half the regular grid spacing from the boundary. This distance can be further reduced by introducing smaller boundary control volumes if required. As a first approximation, von Neumann boundary conditions are easily implemented by using the given gradient to extrapolate a nodal value to the adjacent boundary point. This approach then simulates a Dirichlet condition, which in turn allows the boundary control volume to be treated like any other control volume, given a suitable description of the geometry. Therefore, with reference to Fig. 1, the case of $0 \leq a \leq 1$ is now introduced. In Table 1, the limits of the weighting functions as a tends to 0 and 1 are given.

At the boundary shown in Fig. 1, the value of a is equal to 1. With regard to the general flux expression given by Eq. (11), the value ϕ_{aL} is therefore equal to ϕ_L. The diffusion differential should be expressed through Eq. (6). But the scheme makes use of a flux given by Eq. (14) based on the general interpolation Eq. (10). It can, however, be shown that, due to the limits given in Table 1, Eq. (14) collapses to the described terms when the fraction a equals 1. Similarly, Eq. (25) ensures that the coefficient of the boundary point becomes zero in a discretized pressure correction equation.

The same considerations, of course, apply to the opposite boundary, where the fraction a equals 0. Therefore, it follows that a boundary control volume can be conveniently treated like any other internal control volume by means of the extended formulations of the present scheme. Finally, note that the corner (node) points of a rectangular domain play no role in the calculations. This is significant, for instance, for the analysis of the flow field in the lid driven cavity.

CASE STUDIES

The configuration of the concentric rotating cylinder problem is shown in Fig. 9. This case was chosen because it has an analytical solution (e.g., Schlichting [16]), and a two-dimensional problem, particularly prone to false diffusion, can be generated by

Table 1 Function Limits as the Fraction a Tends to 0 and 1

Function	$a \rightarrow 0$	$a \rightarrow 1$
$A(a, P)$	1	$A(P)$
$B(a, P)$	0	$B(1, P)$
$C(a, P)$	0	1
$D(a, P)$	0	0

using an orthogonal grid at approximately 45° to the flow. A 9 × 9 node example of the regular grid used is shown in Fig. 9, which implies values of a equal to 0, 0.5, and 1. Analytical velocities were implemented as Dirichlet boundary conditions and the analytical pressure difference was used as a von Neumann condition. Following Prakash [10], we can nondimensionalize the problem and formulate a Reynolds number, which is given by $\rho(\omega r_2)\,(r_2 - r_1)/\Gamma$. All tests were allowed 300 iterations, at which point in most cases the criteria of normalized summation of absolute residuals suggested by Peric et al. [17] for momentum and mass were less than 10^{-6}. Relaxation factors for velocities and pressures were 0.5 and 0.2 respectively.

In Table 2, average absolute percentage errors of the computed U-velocity components are compared with results given by Thiart [2] and Prakash [10] for various Reynolds numbers and grid densities. Compared to the control volume finite-element method proposed by Prakash [10], the current scheme produces quite accurate results, even though Prakash [10] used a grid in line with the main flow direction and, on average, 24 interpolation points on a typical control volume surface. The present approach uses four such points on a grid not aligned with the flow. The results are therefore considered an indication that the SIMPLEN interpolation scheme, incorporating multidimensional terms, does reduce false diffusion errors.

Both Thiart [2] and Prakash [10] used a grid type A [3] (i.e., with half control volumes at the boundaries). For the same number of nodes, such a grid is finer than a grid type B and, therefore, an additional set of results is included in Table 2 based on a grid type B with the same control volume size as employed by Thiart [2]. Very minor differences in the results are noted. These are attributed to different boundary treatment, source term discretization approaches, and the modified power-law scheme used. The

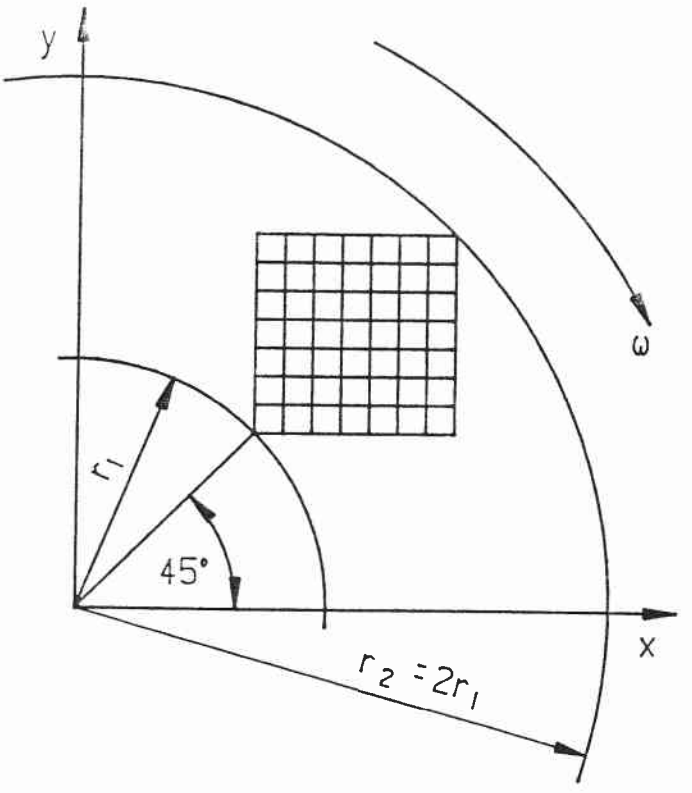

Fig. 9 Configuration of concentric rotating cylinders.

Table 2 Average Absolute Percentage Error in the Computed U-Velocity Components for the Concentric Rotating Cylinders Problem

Grid Size	Source	Percentage Error at Four Re Numbers			
		1	10	100	1000
9 × 9	Computed	0.01631	0.01759	0.05165	0.17193
	[2]	0.01100	0.01581	0.04616	0.12374
	[10]	0.06224	0.06124	0.07604	0.15350
	[18]	0.07461	—	2.1289	3.3202
	*	0.01395	0.11874	0.08395	0.17053
10 × 10	Computed	0.01227	0.01328	0.03462	0.11884
13 × 13	Computed	0.00628	0.00698	0.01320	0.06100
	[2]	0.00516	0.00622	0.01805	0.06473
	[10]	0.02612	0.02590	0.02954	0.06617
14 × 14	Computed	0.00524	0.00588	0.01000	0.04842
17 × 17	Computed	0.00331	0.00379	0.00466	0.02747
	[2]	0.00229	0.00253	0.00802	0.02598
	[10]	0.01435	0.01425	0.01548	0.03533
18 × 18	Computed	0.00290	0.00335	0.00370	0.02319
21 × 21	Computed	0.00222	0.00244	0.00206	0.01541
	[2]	0.00187	0.00203	0.00628	0.02003
	[10]	0.00909	0.00905	0.00915	0.02134
22 × 22	Computed	0.00250	0.00231	0.00179	0.01350

*Results computed with original power law.

results therefore suggest that the modifications introduced in this article do not significantly affect the accuracy of the original SIMPLEN discretization scheme [1, 2]. To further highlight the accuracy of the SIMPLEN scheme, additional results for the 9 × 9 grid provided by Prakash [18] are included in Table 2, which are based on the upwind scheme described by Patankar [3].

Also included in Table 2 and identified by an asterisk is one set of results for a 9 × 9 node grid, computed with the original power law given by Eq. (9) and used in Eqs. (17), (19), and (21) to approximate the functions A, B, C, and D. The results show that due to the extensive use of the power law, the use of the modified power-law approximation is essential with regard to this test case. However, for most practical applications, the original power-law approximation should be sufficiently accurate.

The steady incompressible flow in a lid driven square cavity was chosen as another test case because it complements the previous case inasmuch as it is not a throughflow problem. An irregular grid shown for a 9 × 9 node case (Fig. 10) was used. A finer grid near the lid proved necessary to avoid excessive relaxation otherwise required to deal with the instabilities ascribed to large cross-flux (momentum source) gradients.

The shorter sidewall length of a boundary control volume is calculated from $H/(n - 3)/2$. As a result, the values of a occurring in the 21 × 21 test grid were 0, 0.333333, 0.5, 0.666667, and 1. The Reynolds number in terms of lid speed and sidewall length was 400. Relaxation factors for velocities and pressures were 0.5 and 0.2, respectively. Apart from a lid velocity of unity, all other boundary nodal velocities were set to zero. A zero normal pressure gradient was implemented at the boundaries. Itera-

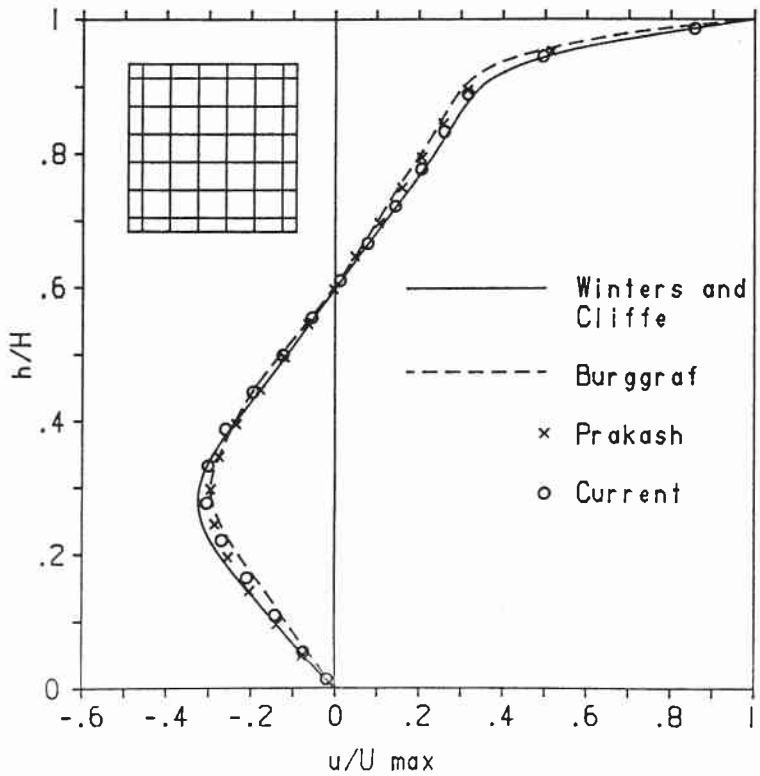

Fig. 10 Results for lid driven flow in a cavity.

tions were halted when the normalized summation of absolute residuals of momentum and mass were less than 10^{-6}. This occurred after 408 iterations.

Normalized computed U-velocity components on the vertical centerline are presented in Fig. 10 together with the result of Prakash [10] using the equal-order control volume finite-element method on a 21 × 21 grid. The results of Burggraf [19], using a streamfunction–vorticity method on a 42 × 42 grid, and the results of Winters and Cliffe [20], using a finite-element method on a 66 × 66 node grid, are also included.

Hobson and Lakshminarayana [14] have confirmed the results of Winters and Cliffe [20]. The results of the current method are closest to the results of the latter. The largest discrepancy occurs at the maximum negative velocity, which is attributed to local grid coarseness. The results presented compare favorably with those of the other authors.

CONCLUSION

The results of the test cases generally confirm the good accuracy of the SIMPLEN discretization scheme although this is obtained at the expense of extra computational effort. However, as pointed out above, not all the source terms are essential for the use of colocated grids. Which source terms to include, for instance, in conjunction with grid refinement supported by a multigrid technique to optimize computational efficiency, must be the subject of future research.

The reformulation, with the geometric description chosen, does achieve the declared objective, to decouple the positions of the nodes from those of the control volume interfaces. This results in greater flexibility for grid generation. Scalar variables inte-

grated as constant over a control volume are more representative when the node lies near the center of a control volume [3]. Node and interface positions can be optimized independently when multigrid or adaptive grid schemes are considered. In the vicinity of complex boundaries or grid lines with high curvature, it follows from the work of Peric [21] that flexibility regarding the location of interfaces is important when nonorthogonal grids are used.

REFERENCES

1. G. D. Thiart, Finite Difference Scheme for the Numerical Solution of Fluid Flow and Heat Transfer Problems on Nonstaggered Grids, *Numer. Heat Transfer, Part B,* vol. 17, pp. 43–63, 1990.
2. G. D. Thiart, Improved Finite-Difference Scheme for the Solution of Convection–Diffusion Problems with the SIMPLEN Algorithm, *Numer. Heat Transfer, Part B,* vol. 18, pp. 81–95, 1990.
3. S. V. Patankar, *Numerical Heat Transfer and Fluid Flow,* Hemisphere, Washington, D.C., 1980.
4. F. H. Harlow and J. E. Welch, Numerical Calculation of Time-Dependent Viscous Incompressible Flow of Fluid with Free Surface, *Phys. Fluids,* vol. 8, no. 12, pp. 2182–2189, 1965.
5. L. S. Caretto, A. D. Gosman, S. V. Patankar, and D. B. Spalding, Two Calculation Procedures for Steady, Three-Dimensional Flows with Recirculation, *Proc. 3rd Int. Conf. Numerical Methods in Fluid Dynamics,* pp. 60–68, 1972.
6. D. B. Spalding, A Novel Finite Difference Formulation for Differential Expressions Involving Both First and Second Derivatives, *Int. J. Numer. Meth. Eng.,* vol. 4, pp. 551–559, 1972.
7. S. V. Patankar and D. B. Spalding, A Calculation Procedure for Heat, Mass, and Momentum Transfer in Three-Dimensional Parabolic Flows, *Int. J. Heat Mass Transfer,* vol. 15, pp. 1789–1806, 1972.
8. C. M. Rhie and W. L. Chow, Numerical Study of the Turbulent Flow Past an Airfoil with Trailing Edge Separation, *AIAA J.,* vol. 21, pp. 1525–1532, 1983.
9. G. E. Schneider and M. J. Raw, A New Control-Volume-Based Finite Element Procedure for the Numerical Solution of the Fluid Flow and Scalar Transport Equations, Final Report, Dept. of Mechanical Engineering, University of Waterloo, Waterloo, Ontario, Canada, 1985.
10. C. Prakash, Improved Control Volume Finite-Element Method for Heat and Mass Transfer, and for Fluid Flow Using Equal-Order Velocity–Pressure Interpolation, *Numer. Heat Transfer,* vol. 9, pp. 253–276, 1986.
11. H. H. Wong and G. D. Raithby, Improved Finite-Difference Methods Based on a Critical Evaluation of the Approximation Errors, *Numer. Heat Transfer,* vol. 2, pp. 139–163, 1979.
12. W. A. Schreüder, Numerical Prediction of Air Flow About an Air-Cooled Heat Exchanger, Ph.D. thesis, University of Stellenbosch, Stellenbosch, South Africa, 1986.
13. B. F. Blackwell, Numerical Prediction of One-Dimensional Ablation Using a Finite Control Volume Procedure with Exponential Differencing, *Numer. Heat Transfer,* vol. 14, pp. 17–34, 1988.
14. G. Hobson and B. Lakshminarayana, Fully Elliptic Incompressible Flow Calculations on Regular Grid by a New Pressure Substitution Method, AIAA 90-0239, 28th Aerospace Sciences Meeting, Reno, Nevada, 8–11 January, 1990.
15. CHAM, The Mathematical Basis of PHOENICS, in *PHOENICS Instruction Courses—Course Notes,* CHAM, London, U.K., TR/300, chap. 5, 1989.
16. H. Schlichting, *Boundary Layer Theory,* 7th ed., McGraw-Hill, New York, 1979.

17. M. Peric, R. Kessler, and G. Scheuerer, Comparison of Finite-Volume Numerical Methods with Staggered and Colocated Grids, *Comput. Fluids,* vol. 16, pp. 389–403, 1988.
18. C. Prakash, Examination of the Upwind (Donor-Cell) Formulation in Control Volume Finite-Element Methods for Fluid Flow and Heat Transfer, *Numer. Heat Transfer,* vol. 11, pp. 401–416, 1987.
19. O. R. Burggraf, Analytical and Numerical Studies of the Structure of Steady Separated Flows, *J. Fluid Mech.*, vol. 24, part 1, pp. 113–151, 1966.
20. K. H. Winters and K. A. Cliffe, A Finite Element Study of Driven Cavity Flow in a Square Cavity, AERE-R9444, Harwell, U.K., 1979.
21. M. Peric, A Finite Volume Method for the Prediction of Three-Dimensional Fluid Flow in Complex Ducts, Ph.D. thesis, University of London, U.K., 1985.

Received 20 July 1990
Accepted 3 January 1991

Derivation of a Modified Hybrid Approximation

T. M. Harms, T. W. von Backström,
J. P. du Plessis, L. M. Toerien

Reprinted from

AIAA Journal

Volume 32, Number 7, Pages 1541-1543

AIAA

A publication of the
American Institute of Aeronautics and Astronautics, Inc.
370 L'Enfant Promenade, SW
Washington, DC 20024-2518

Derivation of a Modified Hybrid Approximation

T. M. Harms, T. W. von Backström,
J. P. du Plessis, L. M. Toerien

Reprinted from

AIAA Journal

Volume 32, Number 7, Pages 1541-1543

AIAA

A publication of the
American Institute of Aeronautics and Astronautics, Inc.
370 L'Enfant Promenade, SW
Washington, DC 20024-2518

Derivation of a Modified Hybrid Approximation

Thomas M. Harms,* Theodor W. von Backström,†
J. Prieur du Plessis,‡ and Louwrens M. Toerien§
University of Stellenbosch, Stellenbosch 7600, South Africa

I. Introduction

CONTROL volume interface interpolation schemes can be classified as to whether they are local grid- or streamline orientated and whether they are algebraically or physically based. The hybrid scheme described by Spalding[1] is an example of a grid-line-orientated physically based scheme. The exponential coefficient function resulting from the analytic solution of a one-dimensional homogeneous convection-diffusion equation, i.e.,

$$A(Pe) = Pe/(e^{Pe} - 1) \tag{1}$$

with Pe the Péclet number, is approximated through its asymptotes, resulting in

$$A(Pe) \equiv \max(-Pe, 1.0 - Pe/2.0, 0.0) \tag{2}$$

Both Eqs. (1) and (2) result in upwinding at high Péclet numbers, which is inadequate in terms of accuracy in multidimensional situations due to the inherent artificial diffusion as pointed out by Pulliam.[2] Algebraic grid-aligned interpolation addresses this problem through higher order interpolation schemes, e.g., central differencing used by Peric′,[3] quadratic upwinding described by Leonard and Mokhtari,[4] or other variations employed by Shyy et al.[5] With regard to physically based interpolation schemes the remedy has been the employment of the solution of a nonhomogeneous convection-diffusion equation, i.e.,

$$\frac{\partial}{\partial \xi}\left(\rho u \phi - \Gamma \frac{\partial \phi}{\partial \xi}\right) = S \tag{3}$$

in both flow-aligned and grid-aligned schemes. Examples can be found in the work of Raithby[6] and in particular control volume finite element schemes such as described by Baliga and Patankar,[7] Prakash,[8] and Schneider and Raw.[9] Furthermore, the function S not only provides the opportunity to account for multidimensional effects but also provides a velocity-pressure coupling allowing the use of nonstaggered grids. This was previously shown by Prakash[8] for flow-aligned interpolation and Thiart[10] for grid-aligned interpolation. It is the physically based analog to the methods of Baliga and Patankar[7] or Rhie and Chow,[11] which are based on central difference velocity interpolation.

Harms et al.[12] previously showed on the basis of orthogonal grids that in the context of Eq. (3) streamline-orientated interpolation with parabolic interface flux integration represents an unnecessary complication with regard to accuracy. Although physical interpolation is realistically attractive, it is at best second order when based on integration that assumes constant properties over surfaces and volumes. It is, on the other hand, computationally expensive and associated with instability as reported by Huang et al.[13] In this Note we wish to address the issue of computational expense by examining two alternatives to obtain and deal with coefficient and other exponential weighting functions arising out of the application of Eq. (3).

II. Derivation

Schneider and Raw[9] proposed to obtain an interface value in the following manner: ρu and Γ are assumed constant in the space ξ (0 to L) between two nodes and known from a previous iteration. The first derivative on the left of Eq. (3) is then discretized as an upwind difference, the second derivative as a central difference, and the source term S (at first $S_0 = S_L = S$) in any appropriate manner (e.g., a pressure gradient in the interpolation direction would follow from the adjacent nodal pressure difference and cross fluxes and other source terms from arithmetic averages of terms discretized at the two adjacent nodes[12]). For a noncentralized interface ($a = \xi/L$) and positive or negative interface velocity, the result is

$$\rho u \frac{\partial \phi}{\partial \xi} = \frac{\Gamma}{L}\left[\max(0, Pe)\frac{\phi_{aL} - \phi_0}{aL} - \max(-Pe, 0)\frac{\phi_L - \phi_{aL}}{(1-a)L}\right] \tag{4}$$

$$\Gamma \frac{\partial^2 u}{\partial \xi^2} = \Gamma \frac{a\phi_L - \phi_{aL} + (1-a)\phi_0}{a(1-a)(L^2/2)} \tag{5}$$

for $0 < a < 1$ and $Pe = \rho u_{aL} L/\Gamma$. Substituting Eqs. (4) and (5) into Eq. (3) results in

$$\phi_{aL} = \phi_0 + \frac{a}{k}[\max(-Pe, 0) + 2](\phi_L - \phi_0) + \frac{L^2}{k\Gamma} a(1-a) S \tag{6}$$

Received Sept. 27, 1993; revision received Dec. 20, 1993; accepted for publication Feb. 22, 1994.

*Graduate Student, Department of Mechanical Engineering.
†Professor, Department of Mechanical Engineering.
‡Associate Professor, Department of Applied Mathematics.
§Graduate Student, Department of Applied Mathematics.

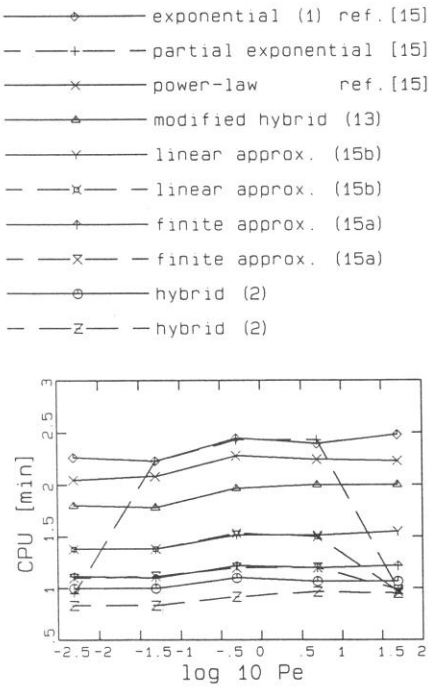

Fig. 1 Results of time trials.

where k is given by

$$k = (1-a)\max(0, Pe) + a\max(-Pe, 0) + 2 \tag{7}$$

As was shown previously,[12] and similar to the approach described by Karki et al.,[14] we can apply Eq. (7) to two regions of constant source to generate a flux spline at the control volume interface. The result is

$$\phi_{aL} = \phi_0 + C(a, Pe)(\phi_L - \phi_0) + \frac{L^2}{\Gamma} BD(a, -Pe) S_0 + \frac{L^2}{\Gamma} BD(1-a, Pe) S_L \tag{8}$$

with the weighting functions being

$$C(a, Pe) = a[a\max(-Pe, 0) + 2] \times [(1-a)\max(-Pe, 0) + 2]/H \tag{9}$$

$$BD(a, -Pe) = a^2(1-a)[(1-a)\max(0, Pe) + 2]/H \tag{10}$$

$$H = (1-a)[(1-a)\max(0, Pe) + 2][a\max(0, Pe) + 2] + a[(1-a)\max(-Pe, 0) + 2][a\max(-Pe, 0) + 2] \tag{11}$$

The interface convection-diffusion flux can now be assembled from previous equations[12] and expressed as

$$J_{aL} = \rho u_{aL}\phi_0 + \frac{\Gamma}{L} A(Pe)(\phi_0 - \phi_L) + L\,BC(a, -Pe) S_0 - L\,BC(1-a, Pe) S_L \tag{12}$$

where

$$A(Pe) = \{2[\max(0, Pe) + 4][\max(-Pe, 0) + 4] - Pe[\max(-Pe, 0) + 4]^2\}/\{[\max(0, Pe) + 4]^2 + [\max(-Pe, 0) + 4]^2\} \tag{13}$$

and

$$BC(a, -Pe) = a^2\{(1-a)\max(-Pe, 0) + 2 + (1-a)[(1-a)\max(Pe, 0) + 2]Pe\}/H \tag{14}$$

Analogous to previous work[12] it is now a trivial matter to extract functions B and D from Eqs. (9–11) and (14). For the sake of brevity, however, attention is rather focused on Eq. (13), noting[12] that it can be used to express the other weighting functions. Equation (13) has been optimized by letting $a = 0.5$ irrespective of the actual interface location, which follows from the homogeneous form of Eq. (3). The result is a modified hybrid approximation. It approaches the asymptotes from below, which could easily be removed by introducing additional absolute value operators.

III. Alternative Approximations

At this point two further approximations of the function $A(Pe)$ (FUNCTION APECL) are introduced as follows in terms of their Fortran 77 equivalent:

```
APECL = ANEW(INT{AMIN1[Z1, ABS (PE) ]/Z3} + 1)
  + AMAX1 (-PE, 0.0)
```

(15a)

```
I = INT{AMIN1 [Z1, ABS (PE) ] / Z3} + 1
APECL = ANEW (I) + BNEW (I) *[ABS (P)
  -REAL (I - 1) *Z3] + AMAX = 1 (-PE, 0.0)
```

(15b)

The finite approximation (15a) is based on an array (ANEW) with $Z2 + 1.0$ elements, in which values determined by a Fortran equivalent[15] of Eq. (1) have been deposited over the range $0 \le Pe \le Z1$ in equal increments of $Z3$, with $Z3 = Z1/Z2$. Whereas $Z1$ determines the maximum accuracy at the asymptotic jump, $Z2$ is determined accordingly to obtain the same accuracy near the origin, where $A(Pe)$ ($Pe > 0$) has a local maximum first derivative. Similarly the constant increment in the linear approximation (15b) is based on the maximum second derivative of $A(Pe)$ occurring at the origin, with BNEW being the incremental slope. In Table 1 the approximate maximum errors based on the Fortran equivalent of Eq. (1)[15] are indicated for the various approximations.

IV. Test Calculations

Time trials were executed on the University of Stellenbosch VAX 6000/410 machine using its VMS 5.5-2 operating system and the Fortran 77 version 5.8. One million calculations of the function product A·B·C·D expressed in terms of $A(Pe)$ (Ref. 12), with $a = 0.5$, were executed at five Péclet numbers in each case (0.005, 0.05, 0.5, 5, and 50). At least three runs each were executed for every data point to minimize the influence of system performance variations. The results are shown in Fig. 1, where we have also included calculations based on previous work[15] for comparison. The dashed lines indicated alternative formulations that employ Fortran IF-statements to eliminate redundant calculations at high Péclet numbers.[15] It can be seen that in terms of accuracy

Table 1 Maximum error of the approximations

Equation	Z1	Z2	Maximum error	Péclet number
(2)	2.0	——	0.313	2.0
(13)	——	——	0.236	12.9
(15a)	10.0	11,013	0.00045	10.0
(15a)	12.61	150,000	0.000042	12.61
(15b)	10.0	2×68	0.00045	10.0

the finite approximations based on Eqs. (15a) and (15b) performed best. In terms of speed it was found that no significant change resulted from employing a 150,000 element array as indicated in Table 1. In the context of the times shown in Fig. 1, the overhead to generate such an array was less than 3 s.

V. Conclusion

The derivation of the exponential-free modified hybrid approximation was motivated by the need to deal as efficiently as possible with the weighting functions arising in the physically based interpolation scheme considered. The alternative approximations, however, clearly appear to represent the most efficient option examined and, in general, can be very effective whenever a parametric dependence on a few variables arises in lengthy calculations. Their accuracies are fully adjustable at the cost of memory allocated rather than computational speed.

References

[1]Spalding, D. B., "A Novel Finite Difference Formulation for Differential Expressions Involving both First and Second Derivatives," *International Journal for Numerical Methods in Engineering*, Vol. 4, No. 4, 1972, pp. 551–559.

[2]Pulliam, T.H., "Artificial Dissipation Models for the Euler Equations," *AIAA Journal*, Vol. 24, No. 12, 1986, pp. 1931–1940.

[3]Peric′, M., "Analysis of Pressure-Velocity Coupling on Nonorthogonal Grids," *Numerical Heat Transfer*, Pt. B, Vol. 17, No. 1, 1990, pp. 63–82.

[4]Leonard, B. P., and Mokhtari, S., "Beyond First-Order Upwinding: The ULTRA-SHARP Alternative for Non-Oscillatory Steady-State Simulation of Convection," *International Journal for Numerical Methods in Engineering*, Vol. 30, No. 4, 1990, pp. 729–766.

[5]Shyy, W., Thakur, S., and Wright, J., "Second-Order Upwind and Central Difference Schemes for Recirculating Flow Computation," *AIAA Journal*, Vol. 30, No. 4, 1992, pp. 923–932.

[6]Raithby, G. D., "Skew Upstream Differencing Schemes for Problems Involving Fluid Flow," *Computer Methods in Applied Mechanics and Engineering*, Vol. 9, 1976, pp. 153–164.

[7]Baliga, B. R., and Patankar, S.V., "A Control Volume Finite-Element Method for Two-Dimensional Fluid Flow and Heat Transfer," *Numerical Heat Transfer*, Vol. 6, No. 3, 1983, pp. 245–261.

[8]Prakash, C., "An Improved Control Volume Finite-Element Method for Heat and Mass Transfer, and for Fluid Flow Using Equal-Order Velocity Pressure Interpolation," *Numerical Heat Transfer*, Vol. 9, No. 3, 1986, pp. 253–276.

[9]Schneider, G. E., and Raw, M. J., "Control Volume Finite-Element Method for Heat Transfer and Fluid Flow Using Colocated Variables - 1. Computational Procedure," *Numerical Heat Transfer*, Vol. 11, No. 4, 1987, pp. 363–390.

[10]Thiart, G. D., "Improved Finite-Difference Scheme for the Solution of Convection-Diffusion Problems with the SIMPLEN Algorithm," *Numerical Heat Transfer*, Pt. B, Vol. 18, No. 1, 1990, pp. 81–95.

[11]Rhie, C. M., and Chow, W. L., "Numerical Study of Turbulent Flow Past an Airfoil with Trailing Edge Separation," *AIAA Journal*, Vol. 21, No. 11, 1983, pp. 1525–1532.

[12]Harms, T. M., von Backström, T. W., and Du Plessis, J. P., "Reformulation of the SIMPLEN Discretization Scheme to Accommodate Noncentralized Interfaces," *Numerical Heat Transfer*, Pt. B, Vol. 20, No. 2, 1991, pp. 127–144.

[13]Huang, P. G., Launder, B. E., and Leschziner, M. A., "Discretization of Nonlinear Convection Processes: A Broad-Range Comparison of Four Schemes," *Computer Methods in Applied Mechanics and Engineering*, Vol. 48, No. 1, 1985, pp. 1–24.

[14]Karki, K. C., Patankar, S. V., and Mongia, H. C., "Three-Dimensional Fluid Flow Calculations Using a Flux-Spline Method," *AIAA Journal*, Vol. 28, No. 4, 1990, pp. 631–634.

[15]Harms, T. M., Du Plessis, J. P., and von Backström, T. W., "Derivation of a Modified Power-Law Approximation," *Numerical Heat Transfer*, Pt. B, Vol. 22, No. 2, 1992, pp. 235–241.

Derivation of a Modified Hybrid Approximation

T. M. Harms, T. W. von Backström,
J. P. du Plessis, L. M. Toerien

Reprinted from

AIAA Journal

Volume 32, Number 7, Pages 1541-1543

AIAA

A publication of the
American Institute of Aeronautics and Astronautics, Inc.
370 L'Enfant Promenade, SW
Washington, DC 20024-2518

Derivation of a Modified Hybrid Approximation

Thomas M. Harms,* Theodor W. von Backström,†
J. Prieur du Plessis,‡ and Louwrens M. Toerien§
University of Stellenbosch, Stellenbosch 7600, South Africa

I. Introduction

CONTROL volume interface interpolation schemes can be classified as to whether they are local grid- or streamline orientated and whether they are algebraically or physically based. The hybrid scheme described by Spalding[1] is an example of a grid-line-orientated physically based scheme. The exponential coefficient function resulting from the analytic solution of a one-dimensional homogeneous convection-diffusion equation, i.e.,

$$A(Pe) = Pe/(e^{Pe} - 1) \tag{1}$$

with Pe the Péclet number, is approximated through its asymptotes, resulting in

$$A(Pe) \cong \max(-Pe,\ 1.0 - Pe/2.0,\ 0.0) \tag{2}$$

Both Eqs. (1) and (2) result in upwinding at high Péclet numbers, which is inadequate in terms of accuracy in multidimensional situations due to the inherent artificial diffusion as pointed out by Pulliam.[2] Algebraic grid-aligned interpolation addresses this problem through higher order interpolation schemes, e.g., central differencing used by Peric′,[3] quadratic upwinding described by Leonard and Mokhtari,[4] or other variations employed by Shyy et al.[5] With regard to physically based interpolation schemes the remedy has been the employment of the solution of a nonhomogeneous convection-diffusion equation, i.e.,

$$\frac{\partial}{\partial \xi}\left(\rho u\phi - \Gamma\frac{\partial \phi}{\partial \xi}\right) = S \tag{3}$$

in both flow-aligned and grid-aligned schemes. Examples can be found in the work of Raithby[6] and in particular control volume finite element schemes such as described by Baliga and Patankar,[7] Prakash,[8] and Schneider and Raw.[9] Furthermore, the function S not only provides the opportunity to account for multidimensional effects but also provides a velocity-pressure coupling allowing the use of nonstaggered grids. This was previously shown by Prakash[8] for flow-aligned interpolation and Thiart[10] for grid-aligned interpolation. It is the physically based analog to the methods of Baliga and Patankar[7] or Rhie and Chow,[11] which are based on central difference velocity interpolation.

Harms et al.[12] previously showed on the basis of orthogonal grids that in the context of Eq. (3) streamline-orientated interpolation with parabolic interface flux integration represents an unnecessary complication with regard to accuracy. Although physical interpolation is realistically attractive, it is at best second order when based on integration that assumes constant properties over surfaces and volumes. It is, on the other hand, computationally expensive and associated with instability as reported by Huang et al.[13] In this Note we wish to address the issue of computational expense by examining two alternatives to obtain and deal with coefficient and other exponential weighting functions arising out of the application of Eq. (3).

II. Derivation

Schneider and Raw[9] proposed to obtain an interface value in the following manner: ρu and Γ are assumed constant in the space ξ (0 to L) between two nodes and known from a previous iteration. The first derivative on the left of Eq. (3) is then discretized as an upwind difference, the second derivative as a central difference, and the source term S (at first $S_0 = S_L = S$) in any appropriate manner (e.g., a pressure gradient in the interpolation direction would follow from the adjacent nodal pressure difference and cross fluxes and other source terms from arithmetic averages of terms discretized at the two adjacent nodes[12]). For a noncentralized interface ($a = \xi/L$) and positive or negative interface velocity, the result is

$$\rho u\frac{\partial \phi}{\partial \xi} = \frac{\Gamma}{L}\left[\max(0, Pe)\frac{\phi_{aL} - \phi_0}{aL} - \max(-Pe, 0)\frac{\phi_L - \phi_{aL}}{(1-a)L}\right] \tag{4}$$

$$\Gamma\frac{\partial^2 u}{\partial \xi^2} = \Gamma\frac{a\phi_L - \phi_{aL} + (1-a)\phi_0}{a(1-a)(L^2/2)} \tag{5}$$

for $0 < a < 1$ and $Pe = \rho u_{aL}L/\Gamma$. Substituting Eqs. (4) and (5) into Eq. (3) results in

$$\phi_{aL} = \phi_0 + \frac{a}{k}[\max(-Pe, 0) + 2](\phi_L - \phi_0) + \frac{L^2}{k\Gamma}a(1-a)S \tag{6}$$

Received Sept. 27, 1993; revision received Dec. 20, 1993; accepted for publication Feb. 22, 1994.

*Graduate Student, Department of Mechanical Engineering.
†Professor, Department of Mechanical Engineering.
‡Associate Professor, Department of Applied Mathematics.
§Graduate Student, Department of Applied Mathematics.

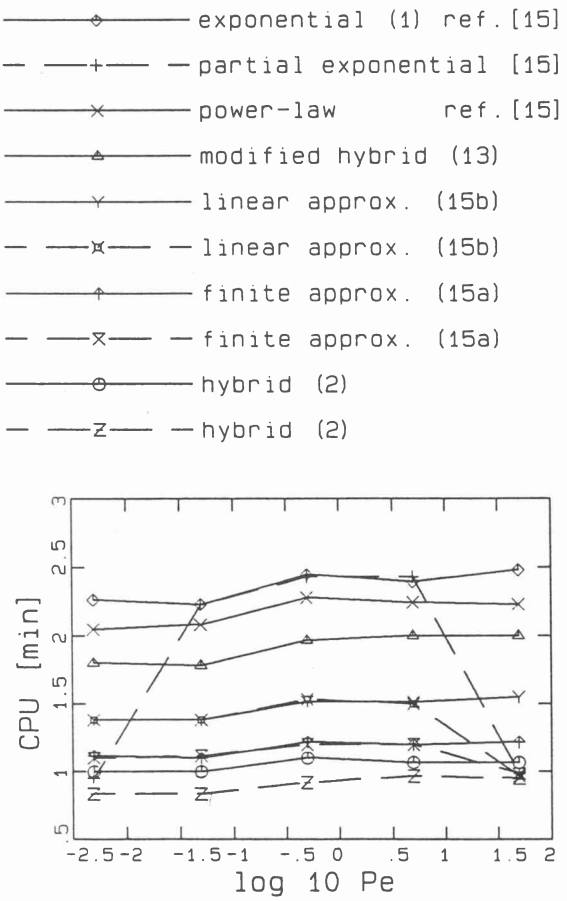

Fig. 1 Results of time trials.

where k is given by

$$k = (1-a)\max(0, Pe) + a\max(-Pe, 0) + 2 \tag{7}$$

As was shown previously,[12] and similar to the approach described by Karki et al.,[14] we can apply Eq. (7) to two regions of constant source to generate a flux spline at the control volume interface. The result is

$$\phi_{aL} = \phi_0 + C(a, Pe)(\phi_L - \phi_0) + \frac{L^2}{\Gamma} BD(a, -Pe) S_0 + \frac{L^2}{\Gamma} BD(1-a, Pe) S_L \tag{8}$$

with the weighting functions being

$$C(a, Pe) = a[a\max(-Pe, 0) + 2] \times [(1-a)\max(-Pe, 0) + 2]/H \tag{9}$$

$$BD(a, -Pe) = a^2(1-a)[(1-a)\max(0, Pe) + 2]/H \tag{10}$$

$$H = (1-a)[(1-a)\max(0, Pe) + 2][a\max(0, Pe) + 2] + a[(1-a)\max(-Pe, 0) + 2][a\max(-Pe, 0) + 2] \tag{11}$$

The interface convection-diffusion flux can now be assembled from previous equations[12] and expressed as

$$J_{aL} = \rho u_{aL}\phi_0 + \frac{\Gamma}{L} A(Pe)(\phi_0 - \phi_L) + L\,BC(a, -Pe) S_0 - L\,BC(1-a, Pe) S_L \tag{12}$$

where

$$A(Pe) = \{2[\max(0, Pe) + 4][\max(-Pe, 0) + 4] - Pe[\max(-Pe, 0) + 4]^2\}/\{[\max(0, Pe) + 4]^2 + [\max(-Pe, 0) + 4]^2\} \tag{13}$$

and

$$BC(a, -Pe) = a^2\{(1-a)\max(-Pe, 0) + 2 + (1-a)[(1-a)\max(Pe, 0) + 2]Pe\}/H \tag{14}$$

Analogous to previous work[12] it is now a trivial matter to extract functions B and D from Eqs. (9–11) and (14). For the sake of brevity, however, attention is rather focused on Eq. (13), noting[12] that it can be used to express the other weighting functions. Equation (13) has been optimized by letting $a = 0.5$ irrespective of the actual interface location, which follows from the homogeneous form of Eq. (3). The result is a modified hybrid approximation. It approaches the asymptotes from below, which could easily be removed by introducing additional absolute value operators.

III. Alternative Approximations

At this point two further approximations of the function $A(Pe)$ (FUNCTION APECL) are introduced as follows in terms of their Fortran 77 equivalent:

```
APECL = ANEW(INT{AMIN1[Z1, ABS(PE)]/Z3} + 1)
  + AMAX1(-PE, 0.0)
```

(15a)

```
I = INT{AMIN1[Z1, ABS(PE)]/Z3} + 1
APECL = ANEW(I) + BNEW(I)*[ABS(P)
  -REAL(I - 1)*Z3] + AMAX = 1(-PE, 0.0)
```

(15b)

The finite approximation (15a) is based on an array (ANEW) with $Z2 + 1.0$ elements, in which values determined by a Fortran equivalent[15] of Eq. (1) have been deposited over the range $0 \le Pe \le Z1$ in equal increments of $Z3$, with $Z3 = Z1/Z2$. Whereas $Z1$ determines the maximum accuracy at the asymptotic jump, $Z2$ is determined accordingly to obtain the same accuracy near the origin, where $A(Pe)$ ($Pe > 0$) has a local maximum first derivative. Similarly the constant increment in the linear approximation (15b) is based on the maximum second derivative of $A(Pe)$ occurring at the origin, with BNEW being the incremental slope. In Table 1 the approximate maximum errors based on the Fortran equivalent of Eq. (1)[15] are indicated for the various approximations.

IV. Test Calculations

Time trials were executed on the University of Stellenbosch VAX 6000/410 machine using its VMS 5.5-2 operating system and the Fortran 77 version 5.8. One million calculations of the function product A·B·C·D expressed in terms of $A(Pe)$ (Ref. 12), with $a = 0.5$, were executed at five Péclet numbers in each case (0.005, 0.05, 0.5, 5, and 50). At least three runs each were executed for every data point to minimize the influence of system performance variations. The results are shown in Fig. 1, where we have also included calculations based on previous work[15] for comparison. The dashed lines indicated alternative formulations that employ Fortran IF-statements to eliminate redundant calculations at high Péclet numbers.[15] It can be seen that in terms of accuracy

Table 1 Maximum error of the approximations

Equation	Z1	Z2	Maximum error	Péclet number
(2)	2.0	——	0.313	2.0
(13)	——	——	0.236	12.9
(15a)	10.0	11,013	0.00045	10.0
(15a)	12.61	150,000	0.000042	12.61
(15b)	10.0	2×68	0.00045	10.0

the finite approximations based on Eqs. (15a) and (15b) performed best. In terms of speed it was found that no significant change resulted from employing a 150,000 element array as indicated in Table 1. In the context of the times shown in Fig. 1, the overhead to generate such an array was less than 3 s.

V. Conclusion

The derivation of the exponential-free modified hybrid approximation was motivated by the need to deal as efficiently as possible with the weighting functions arising in the physically based interpolation scheme considered. The alternative approximations, however, clearly appear to represent the most efficient option examined and, in general, can be very effective whenever a parametric dependence on a few variables arises in lengthy calculations. Their accuracies are fully adjustable at the cost of memory allocated rather than computational speed.

References

[1]Spalding, D. B., "A Novel Finite Difference Formulation for Differential Expressions Involving both First and Second Derivatives," *International Journal for Numerical Methods in Engineering*, Vol. 4, No. 4, 1972, pp. 551–559.

[2]Pulliam, T.H., "Artificial Dissipation Models for the Euler Equations," *AIAA Journal*, Vol. 24, No. 12, 1986, pp. 1931–1940.

[3]Peric′, M., "Analysis of Pressure-Velocity Coupling on Nonorthogonal Grids," *Numerical Heat Transfer*, Pt. B, Vol. 17, No. 1, 1990, pp. 63–82.

[4]Leonard, B. P., and Mokhtari, S., "Beyond First-Order Upwinding: The ULTRA-SHARP Alternative for Non-Oscillatory Steady-State Simulation of Convection," *International Journal for Numerical Methods in Engineering*, Vol. 30, No. 4, 1990, pp. 729–766.

[5]Shyy, W., Thakur, S., and Wright, J., "Second-Order Upwind and Central Difference Schemes for Recirculating Flow Computation," *AIAA Journal*, Vol. 30, No. 4, 1992, pp. 923–932.

[6]Raithby, G. D., "Skew Upstream Differencing Schemes for Problems Involving Fluid Flow," *Computer Methods in Applied Mechanics and Engineering*, Vol. 9, 1976, pp. 153–164.

[7]Baliga, B. R., and Patankar, S.V., "A Control Volume Finite-Element Method for Two-Dimensional Fluid Flow and Heat Transfer," *Numerical Heat Transfer*, Vol. 6, No. 3, 1983, pp. 245–261.

[8]Prakash, C., "An Improved Control Volume Finite-Element Method for Heat and Mass Transfer, and for Fluid Flow Using Equal-Order Velocity Pressure Interpolation," *Numerical Heat Transfer*, Vol. 9, No. 3, 1986, pp. 253–276.

[9]Schneider, G. E., and Raw, M. J., "Control Volume Finite-Element Method for Heat Transfer and Fluid Flow Using Colocated Variables - 1. Computational Procedure," *Numerical Heat Transfer*, Vol. 11, No. 4, 1987, pp. 363–390.

[10]Thiart, G. D., "Improved Finite-Difference Scheme for the Solution of Convection-Diffusion Problems with the SIMPLEN Algorithm," *Numerical Heat Transfer*, Pt. B, Vol. 18, No. 1, 1990, pp. 81–95.

[11]Rhie, C. M., and Chow, W. L., "Numerical Study of Turbulent Flow Past an Airfoil with Trailing Edge Separation," *AIAA Journal*, Vol. 21, No. 11, 1983, pp. 1525–1532.

[12]Harms, T. M., von Backström, T. W., and Du Plessis, J. P., "Reformulation of the SIMPLEN Discretization Scheme to Accommodate Noncentralized Interfaces," *Numerical Heat Transfer*, Pt. B, Vol. 20, No. 2, 1991, pp. 127–144.

[13]Huang, P. G., Launder, B. E., and Leschziner, M. A., "Discretization of Nonlinear Convection Processes: A Broad-Range Comparison of Four Schemes," *Computer Methods in Applied Mechanics and Engineering*, Vol. 48, No. 1, 1985, pp. 1–24.

[14]Karki, K. C., Patankar, S. V., and Mongia, H. C., "Three-Dimensional Fluid Flow Calculations Using a Flux-Spline Method," *AIAA Journal*, Vol. 28, No. 4, 1990, pp. 631–634.

[15]Harms, T. M., Du Plessis, J. P., and von Backström, T. W., "Derivation of a Modified Power-Law Approximation," *Numerical Heat Transfer*, Pt. B, Vol. 22, No. 2, 1992, pp. 235–241.

SIMPLIFIED CONTROL-VOLUME FINITE-ELEMENT METHOD

Thomas M. Harms and Theodor W. von Backström
Department of Mechanical Engineering, University of Stellenbosch, Stellenbosch 7600, South Africa

J. Prieur du Plessis
Department of Applied Mathematics, University of Stellenbosch, Stellenbosch 7600, South Africa

Localized vector algebra treatment of nonorthogonality is applied to two-dimensional quadrilateral control volumes using Cartesian base vectors as a primitive variable formulation of the Navier-Stokes equations for steady incompressible laminar flow. With optional grid-aligned, locally analytic interpolation, a simplified control-volume finite-element scheme is presented. Discretization of source terms, determination of interface convection-diffusion fluxes, pressure correction factors, and geometric quantities are described briefly. Results of three test cases provide useful initial insights into the performance of the method. The conclusion is reached that a simple finite-volume-based approach to nonorthogonality has been achieved.

INTRODUCTION

A locally analytic solution of a nonhomogeneous convection-diffusion equation can be employed to obtain a transported property flux at a control-volume interface. This was previously done by Schneider and Raw [1] and Prakash [2] in their control-volume finite-element methods, i.e., methods suitable for arbitrary, nonorthogonal grids. In both cases their choices served to obtain a control-volume interface velocity–pressure coupling, which allowed the use of nonstaggered grids. The interpolation was carried out along the dominant local stream line (flow aligned) to minimize false diffusion errors.

While there is a steady trickle of control-volume finite-element applications in the literature based on the work of Baliga and Patankar [3], e.g., Hookey et al. [4], Elkaïm et al. [5], Swaminathan and Voller [6], and Chui and Raithby [7], their use is not widespread. This is attributed to the sometimes geometric awkwardness of the flow-aligned interpolation and/or the associated assembly of subdivided control volumes. This might also apply to the tetrahedral grid structure employed successfully by Dawes [8].

Received 31 March 1995; accepted 8 March 1996
Address correspondence to Thomas Harms, Department of Mechanical Engineering, University of Stellenbosch, Stellenbosch 7600, South Africa.

Numerical Heat Transfer, Part B, 30:179–194, 1996

1040–7790/96 $12.00 + .00

SIMPLIFIED CONTROL-VOLUME FINITE-ELEMENT METHOD

Thomas M. Harms and Theodor W. von Backström
Department of Mechanical Engineering, University of Stellenbosch, Stellenbosch 7600, South Africa

J. Prieur du Plessis
Department of Applied Mathematics, University of Stellenbosch, Stellenbosch 7600, South Africa

Localized vector algebra treatment of nonorthogonality is applied to two-dimensional quadrilateral control volumes using Cartesian base vectors in a primitive variable formulation of the Navier-Stokes equations for steady incompressible laminar flow. With optional grid-aligned, locally analytic interpolation, a simplified control-volume finite-element scheme is presented. Discretization of source terms, determination of interface convection-diffusion fluxes, pressure correction factors, and geometric quantities are described briefly. Results of three test cases provide useful initial insights into the performance of the method. The conclusion is reached that a simple finite-volume-based approach to nonorthogonality has been achieved.

INTRODUCTION

A locally analytic solution of a nonhomogeneous convection-diffusion equation can be employed to obtain a transported property flux at a control-volume interface. This was previously done by Schneider and Raw [1] and Prakash [2] in their control-volume finite-element methods, i.e., methods suitable for arbitrary, nonorthogonal grids. In both cases their choices served to obtain a control-volume interface velocity–pressure coupling, which allowed the use of nonstaggered grids. The interpolation was carried out along the dominant local stream line (flow aligned) to minimize false diffusion errors.

While there is a steady trickle of control-volume finite-element applications in the literature based on the work of Baliga and Patankar [3], e.g., Hookey et al. [4], Elkaim et al. [5], Swaminathan and Voller [6], and Chui and Raithby [7], their use is not widespread. This is attributed to the sometimes geometric awkwardness of the flow-aligned interpolation and/or the associated assembly of subdivided control volumes. This might also apply to the tetrahedral grid structure employed successfully by Dawes [8].

Received 31 March 1995; accepted 8 March 1996.
Address correspondence to Thomas Harms, Department of Mechanical Engineering, University of Stellenbosch, Stellenbosch 7600, South Africa.

Numerical Heat Transfer, Part B, 30:179–194, 1996

1040–7790/96 $12.00 + .00

NOMENCLATURE

a	fraction describing the interface location in the ξ direction
A	component of normal surface vector
A	surface vector normal to interface
A, B, C, D	exponential functions and their approximations
C	component of corner displacement vector
C	displacement vector from a node to a corner
E	eastern nodal neighbor
F	component of interface vector
F	interface-corners displacement vector
FC	local η component of the interface vector
FL	local ξ component of the interface vector
FX	local x component of the interface vector
FY	local y component of the interface vector
H	cavity side wall length
J	flux vector component
J	interface convection-diffusion flux vector
L	distance between nodes
M	component of neighbor displacement vector
M	displacement vector from a node to its neighbor
n, N	node or node number
P	pressure at a node
Pe	local grid Péclet number
r_1, r_2	inner and outer cylinder radii
Re	Reynolds number
S	local constant volumetric source
u, v	orthogonal interface velocity ξ–η components
U, V	Cartesian velocity components at a node
Γ	diffusion coefficient
η	local coordinate
μ	dynamic viscosity
ξ	local coordinate
ρ	fluid density
ϕ	any transported variable
ω	angular velocity

Subscripts

aL	associated with an interface in terms of local coordinates
C	associated with interface convection in the η direction
D	associated with interface diffusion in the η direction
e	associated with an eastern interface
O, L, M, N	associated with a node and its neighbor in local coordinates
U	associated with a nodal Cartesian velocity component
V	associated with a nodal Cartesian velocity component
(x)	component in the x direction
(y)	component in the y direction
(η)	component in the η direction
(ξ)	component in the ξ direction
(ϕ)	a function of any transported variable

The present article reports on the first results of an investigation of the feasibility of a simpler control-volume finite-element method than those mentioned above, one suitable for arbitrary geometries. An important feature of the new approach should be that the perceived attractive physicality of a higher-order interpolation scheme [2] based on the solution of nonhomogeneous convection-diffusion equation should be retained as an option.

In the current work the mathematical basis is the primitive-variable formulations of mass and Navier-Stokes momentum conservation equations describing two-dimensional, incompressible, constant-viscosity, steady flows with Cartesian velocity components as unknowns.

$$\frac{\partial U}{\partial x} + \frac{\partial V}{\partial y} = 0 \tag{1}$$

$$\frac{\partial}{\partial x}\left(\rho UU + \mu\frac{\partial U}{\partial x}\right) + \frac{\partial}{\partial y}\left(\rho VU + \mu\frac{\partial U}{\partial y}\right) = -\frac{\partial P}{\partial x} \tag{2}$$

$$\frac{\partial}{\partial x}\left(\rho UV + \mu\frac{\partial V}{\partial x}\right) + \frac{\partial}{\partial y}\left(\rho VV + \mu\frac{\partial V}{\partial y}\right) = -\frac{\partial P}{\partial y} \tag{3}$$

PHYSICAL GRID-BASED DISCRETIZATION

A possible two-dimensional, nonorthogonal, physical grid configuration is shown in Figure 1*a*. It may serve as an example of the degree of nonorthogonality to be accommodated. Following Peric' [9], the use of four-sided quadrilateral control volumes is adopted. One side of the quadrilateral can always be contracted until an almost triangular shape results, should geometric complexity demand this. Another route to obtain triangles is demonstrated in Figure 1*b*, where the solid lines represent four-sided control volumes whose nodes are located at the intersections of the hatched interpolation lines. Here, two interfaces have been folded inward until the angle between them becomes 180°.

The node is located at the arithmetic average of the corner coordinates of the control volume. The fundamental geometric information about a control volume is therefore the corner coordinates. Grid generation is fairly arbitrary, and algebraic methods can be used.

Since the point of departure is the geometrically versatile control-volume finite-element methods, the global transformation of nonorthogonal physical grids to orthogonal computational grids is rejected as a geometrically restrictive complication. The latter method, however, continues to be applied successfully to mildly irregular shapes such as cascades by, e.g., Kunz and Lakshminarayana [10]. More complicated regions require an inconvenient patchwork of mathematical continuous regions as discussed by Thompson et al. [11]. Furthermore, the global transformation approach gives rise to undesirable curvature terms in the conservation equations.

Interpolation is carried out along straight lines between nodes and not along a curve, as curvature terms would arise. With regard to control-volume finite-element methods, this is a simplification. Only one interface interpolation point results; i.e., integration of fluxes along the control-volume interfaces assumes a linear profile, provided the interpolation point lies near the center of the interfaces. On this basis the authors previously [12] reported that, in the orthogonal case, no accuracy advantages seem to arise out of the generation of multiple interpolation points, which allows the assumption of a parabolic interface flux distribution. Wong and Raithby [13] came to a similar conclusion using higher-order surface integration based on interpolated flux gradients along the interface. It is suggested that the latter option can be introduced into the current scheme should

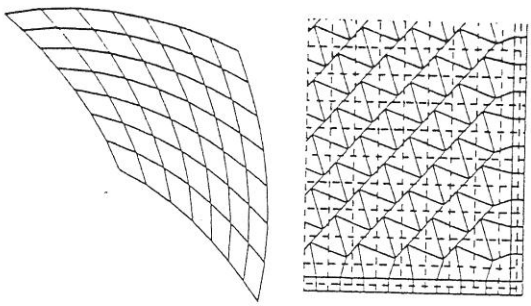

(a) (b)

Figure 1. Typical and atypical nonorthogonal grid examples: (*a*) typical; (*b*) atypical.

the need arise. Alternatively, the desirable simplicity of a single centralized interface interpolation point places a restriction on grid generation, which can be overcome, however, on the basis of local grid refinement. This has been provided for in the current work, as it is clearly generally desirable, by the employment of a nonstructured grid notation. In addition, instead of using, for example, geographic identification of interface fluxes, sequential numeric identification (i.e., 1 to 4) has been used. This facilitates programming and enhances the geometric flexibility of the scheme. Only one interface flux expression is programmed. By adjusting the parameter of the integration loop, (e.g., to 3 or 6), triangular, polygonal or three-dimensional control-volume shapes might be accommodated.

PRINCIPAL FEATURES

Source Term Discretization

The advantages of Cartesian velocity vectors were discussed by, e.g., Peric' [9] and Burns and Wilkes [14]. A consequence is that all of the primary source terms on the right-hand side of Patankar's [15] general conservation Eq. (4) remain Cartesian.

$$\nabla \cdot \mathbf{J}_{(\phi)} = S_{(\phi)} \tag{4}$$

Thus, in Figure 2*a*, a method, inspired by Peric' [9], to discretize first- and second-order Cartesian source term and interface cross flux derivatives is indicated. The four nodal neighbors surrounding a control volume are joined by lines. Employing linear interpolation along such lines yields three discrete property values in any direction required. The necessary geometric factors are derived from vector algebra. A few examples are provided below.

While this approach may not be the most accurate, stable, or computationally efficient (some interpolation is required), it is conceptually simple and thus useful as a starting point for further developments. Such developments should recognize that the problem of discretizing (source term) derivatives in terms of a nodal

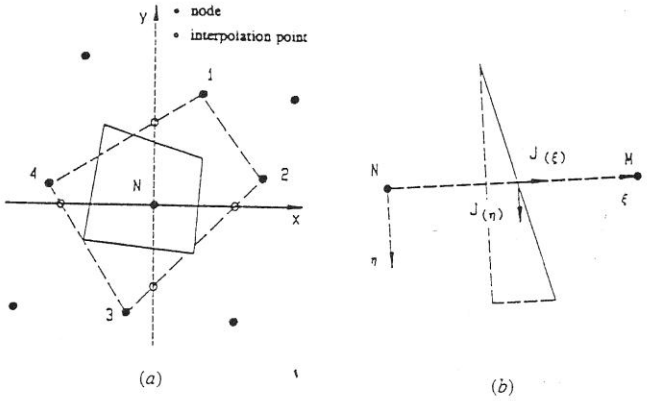

Figure 2. Discretization schematics: (*a*) Cartesian source terms; (*b*) orthogonal flux components.

property value, and property values at neighboring nodes is universal. The current scheme is fully modular inasmuch as whatever emerges as an optimum from any method (e.g., finite-difference, finite-volume, or finite-element) can easily be imported. Examples would be the use of shape functions or purely algebraic local transformations with Jacobian factors, e.g., as described by Thompson et al. [11].

Locally Grid-Aligned Interface Convection-Diffusion Flux Vector Components

The interpolation currently employed is based on the LOAD scheme investigated by Wong and Raithby [13]. It consists of making use of a locally analytic solution of Eq. (4), which is obtained by treating the source function on the right-hand side as piecewise constant [12], for example. Since this interpolation accounts for the local pressure gradient in the source terms (S), it establishes a velocity–pressure coupling at the control-volume interface, which is required for the use of nonstaggered grids. This was previously examined on orthogonal grids by Thiart [16], who applied the term SIMPLEN to an algorithm associated with this interpolation scheme. Assuming ρu and Γ constant in the interval between two adjacent nodes, a basic interpolation equation results which is suitable for noncentralized interfaces and is based on the work of Prakash [17] and the authors [12] and is given by Eq. (5):

$$\phi_{aL} = \phi_0 + C(a, \mathrm{Pe})(\phi_L - \phi_0) + \frac{L^2}{\Gamma} B \cdot D(a, -\mathrm{Pe}) S_0 + \frac{L^2}{\Gamma} B \cdot D(1 - a, \mathrm{Pe}) S_L \tag{5}$$

The exponential weighting functions (A, B, C, and D) have been described previously [12]. These might be efficiently determined by Spalding [18] type hybrid approximations or index equations to look up precalculated function values in

FORTRAN array tables [19]. In the current work, however, efficiency was not our primary concern, and the functions are approximated as described previously [12].

The required interface flux vector is split into components as indicated in Figure 2*b*. The associated local coordinate system is orthogonal. With regard to Eq. (5), the ξ component retains a form analogous to its orthogonal counterpart [12]. It will also be the predominant flux vector component, following the natural tendency of aligning grids for most parts with the predominant flow direction. This is a variation to previous CVFE schemes [1, 2] and follows from the grid-aligned interpolation used. The latter aspect also facilitates the employment of any other interpolation approach preferred, e.g., central differencing as used by Peric' [20]. Furthermore, this component direction simply maximizes the interface velocity–pressure coupling for a given interpolation approach.

Since Cartesian base vectors are used, U_{aL} and V_{aL} can be obtained directly from Eq. (5). The secondary sources (e.g., S_0), arising out of the higher-order interpolation, are discretized as described for the primary sources above, and the general comments made there apply here as well. Furthermore, the locally grid-aligned interface velocities u_{aL} and v_{aL} are easily obtained from a scalar projection of their Cartesian interface counterparts. This is discussed further below. Thus the convection components of the interface flux follow from Eq. (5).

Similarly, the η diffusion gradient follows from a differentiation of Eq. (5) in the η direction, again assuming ρu and Γ constant. For example, in terms of the exponential or power-law schemes described by Patankar [15] [$S_0, S_L = 0$ in Eq. (5)], the interface η gradient would follow from a mixture, depending on the interface Péclet number, between central difference and upwind interpolation, of the η gradient at the nodes adjacent to the interface. Alternatively, typically, the interpolation source $S_{D,N}$, for example, of the U component, is currently treated as

$$S_{D,N} \simeq \left[-\rho v \frac{\partial^2 U}{\partial \eta^2} + \frac{\partial}{\partial \eta}\left(-\frac{\partial P}{\partial x} \right) \right]_N \tag{6}$$

where the third-order derivative has been ignored. The resultant interface flux vector therefore becomes

$$\begin{aligned} J_M = & \left[\rho u_M \phi_N + \frac{\Gamma_M}{L_M} A(\mathrm{Pe}_M)(\phi_N - \phi_M) \right. \\ & \left. + L_M B \cdot C(a_M, -\mathrm{Pe}_M) S_{M,N} - L_M B \cdot C(1 - a_M, \mathrm{Pe}_M) S_{N,M} \right] \xi \\ & + \left[J_{(\eta),N} + C(a_M, \mathrm{Pe}_M)(J_{(\eta),M} - J_{(\eta),N}) \right. \\ & + \frac{L_M^2}{\Gamma} B \cdot D(a_M, -\mathrm{Pe}_M)(\rho v S_{C,N} - \Gamma S_{D,N}) \\ & \left. + \frac{L_M^2}{\Gamma} B \cdot D(1 - a_M, \mathrm{Pe}_M)(\rho v S_{C,M} - \Gamma S_{D,M}) \right] \eta \end{aligned} \tag{7}$$

Upon integration of this interface flux, which follows from Figure 2*b*, all source term contributions and/or η flux contributions are treated explicitly. As a result, the (e.g., Patankar's power-law [15] or Spalding's [19] hybrid) coefficients, primary source terms (e.g., pressure gradient), secondary source terms, and exponential weighting functions remain conceptually identical to the orthogonal case described previously [12]. The variation would arise merely from geometric considerations. Thus the pressure gradient $-\partial P/\partial x$ would now require some additional interpolation as indicated in Figure 2*a*, for example. The essential nonorthogonality manifests itself, however, through the tertiary source as the summation of the integrated η component in Eq. (7) over all four control-volume faces. If mere power-law interpolation were to be used, no secondary sources would arise and the tertiary source would be simplified.

Geometric quantities, i.e., the interpolation ratio a or the interface components indicated in Figure 2*b*, are precalculated from control-volume corner coordinates with the help of vector algebra as indicated by Peric' [9]. Coordinates are therefore no longer employed in the main calculations. In the following, two examples are provided to show how this is accomplished. Some more details are provided by Harms [21].

Calculation of the Interpolation Ratio *a*

In Figure 3*a*, an interface vector F, defined by its associated corner coordinates, and an analog surface vector A, pointing outside the control volume, are indicated. The interpolation ratio a is then given by the ratio of the scalar projections of the corner vector C, and the neighbor vector M onto A, that is,

$$a_M = \frac{\mathrm{C} \cdot \mathrm{A}/|\mathrm{A}|}{\mathrm{M} \cdot \mathrm{A}/|\mathrm{A}|} \tag{8}$$

with the Cartesian vector components defined through coordinate differences.

Calculation of the η Component of the Interface

The situation is indicated in Figure 3*b*. Similar to the previous case, the η component (FC_M) follows from a projection of the interface vector F onto the normal M_N to the neighbor vector M, that is,

$$\mathrm{FC}_M = \frac{\mathrm{F} \cdot \mathrm{M}_N}{|\mathrm{M}|} \tag{9}$$

Pressure Correction

In the classical SIMPLE approach [15], pressure is obtained from the law of mass conservation. The necessary velocity–pressure coupling follows from expressing the interface mass flux in terms of a momentum equation. In the latter the

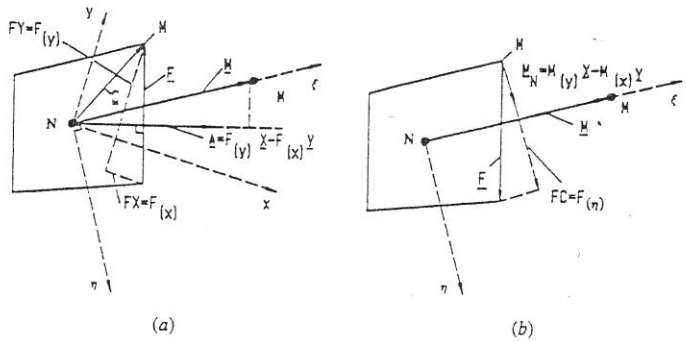

Figure 3. Computation of geometric quantities: (*a*) the interface interpolation ratio; (*b*) the interface η component.

pressure gradient is then discretized on the basis of the nodal pressures adjacent to the interface. Using the same viewpoint previously chosen by the authors [12], a pressure correction factor then simply follows by differentiating the interface velocity component u_{aL} with regard to the interface pressure difference.

$$u_M = \frac{M_{(x)}}{\sqrt{M_{(x)}^2 + M_{(y)}^2}}\left[U_N + C(a_M, \mathrm{Pe}_M)(U_M - U_N) + \frac{L_{M^2}}{\Gamma} B \cdot D(a_M, -\mathrm{Pe}_M) S_{U,N} + \frac{L_{M^2}}{\Gamma} B \cdot D(1 - a_M, \mathrm{Pe}_M) S_{U,M}\right]$$
$$+ \frac{M_{(y)}}{\sqrt{M_{(x)}^2 + M_{(y)}^2}}\left[V_N + C(a_M, \mathrm{Pe}_M)(V_M - V_N) + \frac{L_{M^2}}{\Gamma} B \cdot D(a_M, -\mathrm{Pe}_M) S_{V,N} + \frac{L_{M^2}}{\Gamma} B \cdot D(1 - a_M, \mathrm{Pe}_M) S_{V,M}\right] \tag{10}$$

The v_{aL} velocity corrections are ignored, which Peric' [20] found to be stable for interface nonorthogonality up to 45°. Basson [22] pointed to the use of an intermediate pressure-correction loop, updating v_{aL} explicitly, should stability demand it. Alternatively, the approach of Baliga and Patankar [23] might also be useful here.

Boundary Conditions

Similar to the orthogonal case discussed previously [12], boundary conditions are implemented explicitly; i.e., a boundary interface is initially treated in the same way as an internal interface. Neumann boundary conditions then require some extrapolation between iterations.

TEST CASES

Flow between Concentric Rotating Cylinders

The configuration of the popular concentric, rotating cylinder problem is shown in Figure 4. Analytical velocities were implemented as Dirichlet and the analytical pressure differences as Neumann explicit boundary conditions. The problem is nondimensionalized in terms of a Reynolds number of 1,000, determined by $\rho(\omega r_2)(r_2 - r_1)/\Gamma$ [12].

The nonorthogonal grid shown in Figure 1*a* has been obtained by symmetrically relocating control-volume corners of an orthogonal grid along curves of constant radius. The parameter used to control non-orthogonality is the enlargement fraction (given here a value of 1.5) of the rotation angle measured from the constant radial diagonal. Since this is a one-dimensional test problem, the analytical nodal values are initially not changed as a result of this symmetric distortion. However, the total volume of the computational domain is increased. The Reynolds number and the normalization factor for the problem remain constant, however.

Having generated a nonorthogonal grid, nonorthogonality was measured by applying the cosine rule to all control-volume corners and internodal interpolation lines crossing control-volume interfaces. Thus, in each grid generated for this problem, the corner angles ranged from 43.6° to 143.3° and the acute interface angles from 40.2° to 50.2°, approximately. For the orthogonal case, initially three grids of 9 × 9, 21 × 21, and 41 × 41 nodes were used. The distorted total computational volume grew from the orthogonal volume by a factor of 2.35. Thus, for the nonorthogonal computational domain, calculations were also based on grids of 13 × 13, 32 × 32, and 63 × 63 nodes to maintain the average control-volume size of the orthogonal counterpart.

Starting with a constant radial outward flow field (approximately 50% of maximum analytical tangential velocity), the total number of iterations allowed for the nonorthogonal cases varied between 400 on the smallest to 5,000 on the largest grid, using a TDM routine. In all cases the normalized summation of absolute residuals for momentum and mass were less than 10^{-5} when iterations were halted. Momentum-related quantities were normalized by $\rho(\omega r_2)(\omega r_2)(r_2 - r_1)$.

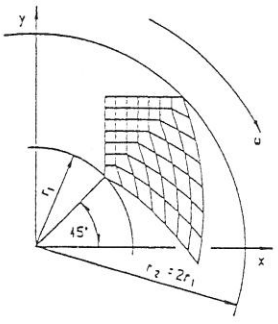

Figure 4. Configuration of the concentric, rotating cylinders problem.

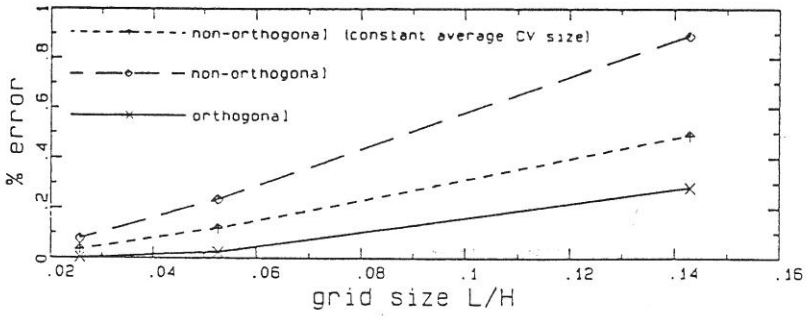

Figure 5. Average absolute percentage error of U velocity components.

Relaxation factors for velocities and pressures were 0.5, 0.5, and 0.2, respectively. Higher-order and nonorthogonal interface momentum flux contributions to the source terms in the discretized momentum equations were also relaxed by a factor of 0.04 for the finest nonorthogonal grid only.

The reason for the additional relaxation required might be found in Eq. (5). Figuratively speaking, an interpolation function, which aims to emulate the curvature in the property field almost exactly, will become indistinguishable from linear or central difference interpolation, when the grid is sufficiently refined. It is rather suggested that some artificial diffusion might be needed [8]. However, in the current work preference was given to avoiding the issue of artificial diffusion altogether.

In Figure 5 the absolute average percentage error of computed U velocity components is shown. While the calculations were not optimized in terms of efficiency, it is suggested that the accuracy obtained, based on the simple nonorthogonal treatment proposed, is satisfactory.

Lid-Driven Flow in a Square Cavity

The steady incompressible lid-driven flow in a square cavity complements the previous case inasmuch as it is not a throughflow problem, but relies on the presence of viscosity to establish a recirculating flow pattern. Huang et al. [24] did report failure to obtain convergence when applying the LOAD scheme [13] to the cavity problem. Prakash [2] showed that for a Reynolds number of 400, given in terms of lid speed and side wall length H, convergence could be obtained for his implementation of LOADS, with the help of near-boundary grid refinement, which the present authors confirmed [12]. The reason for this difficulty is the resolution required for the severe pressure trough and peak shown in Figure 6, which are in both corners necessary to balance the mass flow generated by the shear stress imposed on the fluid by the moving lid.

In Figure 1*b* a typical corner section of the nonorthogonal grid is shown. The initial orthogonal side wall length of the orthogonal boundary control volume is given by $H/(n-3)/2$, where n is the total number of nodes in one direction. The nonorthogonal grid is obtained by marching through the domain and relocating

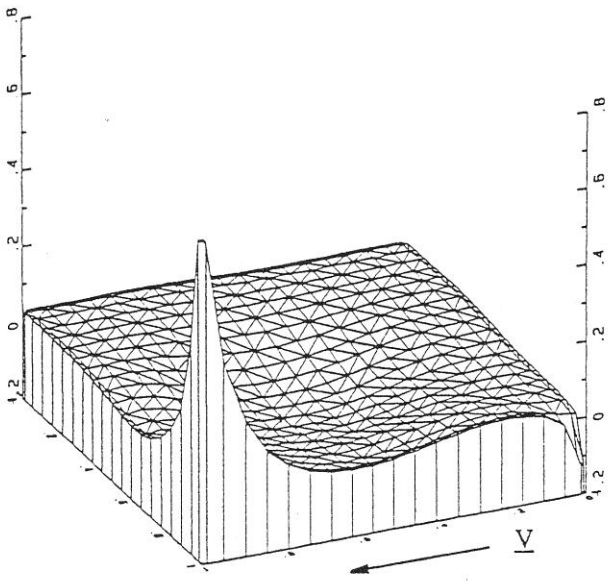

Figure 6. Typical static pressure field of the cavity problem.

control-volume corners in alternate directions. The degree of nonorthogonality is controlled by specifying the relocation distances as a fraction of the average control-volume side wall length. The result of this distortion is that almost all internal nodes remain at their original orthogonal locations, since the arithmetic average of the control-volume corner coordinates is not affected. One node moves slightly near each corner as a result of this procedure. This grid allows a direct comparison between the orthogonal and nonorthogonal cases. In particular, the nonorthogonality arises at the interfaces, while nonorthogonal source term calculations generally do not occur.

For the 21 × 21 case, the angle between the interface and the interpolation line ranged from 90° to 43.4°, while corner angles ranged from 176.7° to 52.5°. For the 41 × 41 nodes grid the angles ranged, respectively, from 90° to 44.9° and 179.9° to 53.1°. For the 81 × 81 nodes case the angles ranged, respectively, from 90° to 44.9° and 179.8° to 53.1°. The grid parameters in these cases were 0.30, 0.27, and 0.26, respectively.

Velocities and pressures were underrelaxed by 0.1. A total of 1,000 to 5,000 outer iterations were allowed for the three cases, which resulted in the normalized summation of absolute residuals to be less than 10^{-5}. An initial constant-magnitude, approximately circular velocity field was imposed.

In Figure 7 an accuracy comparison between orthogonal and nonorthogonal grid-based results is provided in terms of the vertical centerline U component. Finite-element calculations on a 57 × 57 nodes grid with additional corner grid

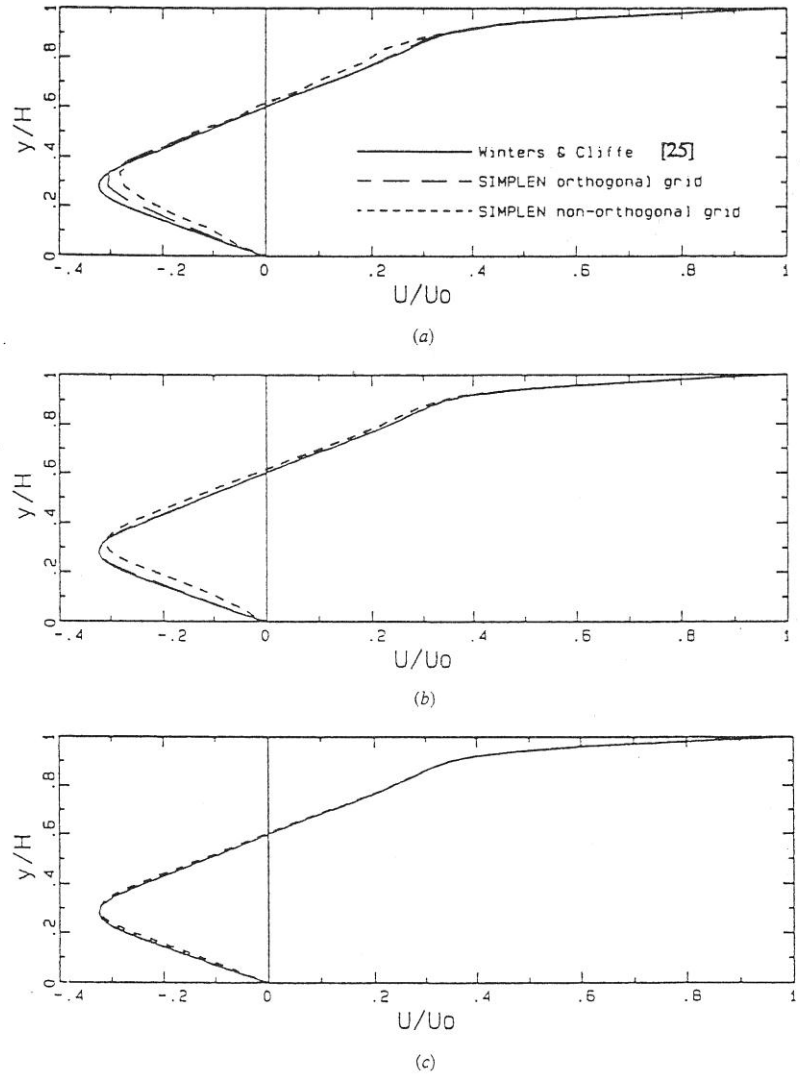

Figure 7. Vertical centerline U velocity components: (a) 21 × 21 nodes; (b) 41 × 41 nodes; (c) 81 × 81 nodes.

refinement by Winters and Cliffe [25] are provided for comparison. Note that the orthogonal grid-based results shown are approximately equivalent to the full control-volume finite-element results obtained by Prakash [2]. Thus, while the accuracy has deteriorated as a result of the simplified nonorthogonal treatment, it approaches full recovery with increasing grid refinement.

COMPARISON OF THREE FINITE-VOLUME INTERPOLATION SCHEMES

T.M. Harms* T.W. von Backström† J.P. du Plessis‡

(Received July 1996; Final version January 1997)

Some fundamental aspects of the finite-volume numerical flow analysis approach, which are generally assumed to be understood but at times still incorrectly interpreted in the literature, are reiterated. In this context an accuracy comparison between linear, upwind quadratic and locally analytic interface interpolation has been carried out. The formulations adopted were chosen with stability and arbitrary non-orthogonal physical grids in mind. Artificial diffusion damping through flux blending has been provided for. A finite-volume quality norm is proposed as a qualitative measure to evaluate different discretization approaches. Three laminar flow problems are employed as test cases, namely, the concentric shear flow, wall driven flow in a square cavity, and the mixing of two scalar streams. The results indicate that in the light of growing computer power, simple linear second order interpolation in conjunction with the ability to introduce controlled artificial diffusion damping is adequately accurate and likely to dominate finite volume thinking in the current decade.

Nomenclature

a	fraction describing the interface location $\xi = aL$
A, B, C, D	exponential functions and their approximations
g	global term characteristic for the flow problem
H	typical domain dimension
$\underline{\mathbf{J}}$	interface convection-diffusion flux vector
J	flux component
L	distance between nodes
m	local property gradient
M	neighbour number
n	number of nodes in one direction
N	node number
Pe	local grid Péclet number $\rho u L/\mu$
p	pressure at a node
Q	finite volume quality norm
r_1, r_2	inner and outer cylinder radii
Re	Reynolds number
S	local constant volumetric source
$\underline{\mathbf{u}}$	local convection velocity
u	normal interface velocity
U, V	orthogonal velocity components at a node
Γ	diffusion coefficient
Ω	control volume size
η	local interface coordinate
λ	flux blending factor
μ	dynamic fluid viscosity
ξ	local interface coordinate
ρ	fluid density
σ	control volume surface
ϕ	any transported variable
ω	absolute value of angular velocity

*Senior Lecturer, MSAIMechE

†Professor, Department of Mechanical Engineering, University of Stellenbosch, Private Bag X1, Matieland, 7602 South Africa

‡Professor, Department of Applied Mathematics, University of Stellenbosch, Private Bag X1, Matieland, 7602 South Africa

1 INTRODUCTION

The segregated SIMPLE numerical finite-volume flow analysis procedure, in conjunction with the pressure correction approach, continues to be extensively applied to every flow problem imaginable. In this context the definition of a fluid by Daugherty and Franzini[1] as 'anything which deforms easily under stress' is useful because it encompasses modelling applications to plastic deformation 'flows' for example. The phenomenal success of the method can partly be attributed to the clarity of the writing of its early contributors, e.g. Patankar and Spalding,[2] Patankar,[3] and Gosman *et al.*[4]

During the past ten years the field of computational fluid dynamics has experienced an explosion-like surge of publications, some extensively mathematical and thus often rendering it difficult to appreciate the new insight into the relationship between the numerics and physics offered. The current paper presents an attempt to reiterate, in the context of a comparison between three

interpolation schemes, some fundamental aspects of the SIMPLE approach, which in the experience of the authors and their students are still often misunderstood.

2 Physical Model

For the purposes of this paper two-dimensional, incompressible, steady, constant viscosity laminar flow is considered, which is well described by the Navier-Stokes momentum equations and the continuity equation. In the general form described by Patankar[3]

$$\nabla \cdot \underline{\mathbf{J}} = S_\phi \tag{1}$$

$$\underline{\mathbf{J}} = \mu \underline{u} \phi - \Gamma_\phi \nabla \phi, \tag{2}$$

$\underline{\mathbf{u}}$ is the velocity vector as a measure of convection, Γ_ϕ the diffusion coefficient and S_ϕ the volumetric source of any conserved scalar property ϕ. In the case of the momentum equations, ϕ becomes the Cartesian velocity component U (or V) as a measure of momentum per unit mass, and S_ϕ the respective negative Cartesian pressure gradient sources. Since the Cartesian velocity components are transformation invariant in space,[5] they can be regarded as scalar quantities, which is significant for the analysis in non-orthogonal geometries. The continuity equation will emerge from equations (1) and (2) by setting ϕ equal to unity and S_ϕ (and Γ_ϕ) equal to zero.

3 Finite Volume Methodology

A conservation law becomes useful through the fact that the property under consideration is conserved, but its distribution or concentration in space (and time) is not. An equation can therefore be formulated from the balance of the integrated convection-diffusion transport, $\underline{\mathbf{J}}$, of the property through the boundary of a control volume and the balancing integrated change of state, S_ϕ, inside this volume. This classical (computational) thermodynamic approach is directly implemented in the physical finite-volume method. The typical cell-centred nodal arrangement (as opposed to corner or interface nodal positions) shown in Figure 1 reflects the unique association between the control volume, the conservation equation and the location of the property value sought. To save space, a local $\xi - \eta$ interface coordinate system is also indicated in Figure 1. This is further referred to below.

The partial derivatives contained in equations (1) and (2) can either be approximated through finite differences or determined exactly from a shape function, which approximates the local property field based on, for example, the nine nodal values shown in Figure 1. In the current work, finite differences have been employed, except where otherwise indicated in the following sections.

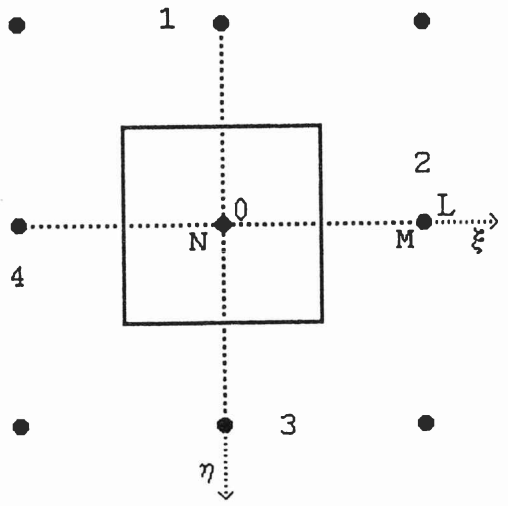

Figure 1 Typical cell-centred control volume and nodes

Specific to the cell-centred formulation is the requirement to determine the interface convection-diffusion flux, which Schneider and Raw[6] referred to as the first closure problem of the method. Spalding,[7] for example, implicitly showed that a stabilizing feature of fluid flows is the fact that, due to the effects of convection, the downstream events in the flow become less influential than upstream events when the local Péclet number exceeds approximately 2. Linear, quadratic or locally analytic interpolation is therefore practical, provided numerical measures are taken to simulate this stability efficiently. Khosla and Rubin[8] showed that, analogous to Spalding's[7] idea, this can be substantially and conveniently achieved by transferring mainly downstream influences in the interface fluxes, $\underline{\mathbf{J}}$, from the left hand divergence side of the discrete integrated form of equation (1), from which coefficients in the matrix equations to be solved are assembled, to the right hand source term side. This idea, previously used for example by Denton[9] and later by Peric',[10] remained surprisingly neglected during the 1980s.

In the current work the central difference or linear interpolation formulation adopted is given by

$$\phi_{aL} = \phi_N + m\xi \tag{3}$$

where m is the discrete gradient defined by the two nodes adjacent to the interface. Substituting this expression in equation (2), and employing a maximum function to heed the stability considerations previously mentioned, results in

$$\begin{aligned} J_{aL} = {} & \rho u \phi + \tfrac{\Gamma}{L} \max(0, 1 - Pe)(\phi_N - \phi_M) \\ & + \lambda \tfrac{\Gamma}{L} [(1 - a) Pe - \max(0, Pe - 1)](\phi_N - \phi_M) \end{aligned} \tag{4}$$

The flux blending factor λ described by Peric[11] identifies those terms, which, upon integration, are to be transferred to the source term side of equation (1), where they then might be referred to as secondary sources. This factor is normally of unit value, but can be reduced to enhance stability by effectively weakening the downstream influences. When this is necessary, it is an indication that the numerical and/or physical model represent the physics inadequately. This is especially the case in high Reynolds number or turbulent flows. Pulliam[12] showed how the reduction of λ is equivalent to generating false or artificial diffusion damping, with of course an associated reduction in accuracy.

Employing the quadratic upstream interpolation for convection kinematics (QUICK) referred to by Leonard and Drummond,[13] the coefficients of an interpolation parabola can be determined from the two nodal values adjacent to the interface and the upstream nodal property gradient in the interpolation direction. Such a formulation is suitable for flow analysis based on arbitrary non-orthogonal physical grids, since three collinear nodes are not required. The two resultant equations (see Appendix 1) can be combined to yield

$$\begin{aligned}\phi_{aL} &= \phi_N + a\left[a\left|Pe\right| - 2\max\left(-Pe, 0\right)\right]/Pe \\ &\left(\phi_M - \phi_N\right) + a\left(1-a\right)L[\max\left(0, Pe\right)m_N \\ &+ \max\left(-Pe, 0\right)m_M]/Pe\end{aligned} \tag{5}$$

and

$$\begin{aligned}J_{aL} &= \rho u\phi_N + \tfrac{\Gamma}{L}2(a + \max\left(-Pe, 0\right) \\ &[-\left(1-2a\right)/Pe + a])\left(\phi_N - \phi_N\right) \\ &+\lambda(-\left|Pe\right|a^2\tfrac{\Gamma}{L}\left(\phi_N - \phi_N\right) \\ &+\Gamma\left[a\left(1-a\right) - \left(1-2a\right)/Pe\right] \\ &[\max\left(0, Pe\right)m_N + \max\left(-Pe, 0\right)m_M])\end{aligned} \tag{6}$$

For the exceptional case of $Pe = 0$, equations (3) and (4) replace equations (5) and (6).

Finally, equation (1) can be solved to yield the locally analytic interpolation function (LOADS) of Wong and Raithby,[14] if multi-dimensional terms on the left hand side are transferred to the right and the resultant source terms on the right hand side are treated as piecewise constant. This idea was previously tested by Prakash,[15] Huang *et al.*[16] and the present authors[17] who adopted the following form:

$$\begin{aligned}\phi_{aL} &= \phi_N + C\left(a, Pe\right)\left(\phi_M - \phi_N\right) \\ &+\tfrac{L^2}{\Gamma}B\cdot D\left(a, -Pe\right)S_N + \tfrac{L^2}{\Gamma}B\cdot D\left(1-a, Pe\right)S_M\end{aligned} \tag{7}$$

$$\begin{aligned}J_{aL} &= \rho u\phi_N + \tfrac{\Gamma}{L}A\left(Pe\right)\left(\phi_N - \phi_M\right) \\ &+\lambda\left[LB\cdot C\left(a, -Pe\right)S_N - LB\cdot C\left(1-a, Pe\right)S_M\right]\end{aligned} \tag{8}$$

Typically, for the U-component, the source S_N would consist of

$$S_N = \left(-\rho v\frac{\partial U}{\partial \eta} + \mu\frac{\partial^2 U}{\partial \eta^2} - \frac{\partial p}{\partial x}\right)_N \tag{9}$$

The exponential weighting functions A, B, C, and D (see Appendix 2) were here approximated as previously described by the authors,[17] although more efficient expressions are now indicated.[18]

Since secondary source terms arise in all three schemes as the result of the deferred correction approach, it is suggested that these schemes are computationally competitive among themselves. This assumes that the various interpolation expressions are optimized with regard to computational expense and comparative associated accuracy. The formulations presented have however been chosen such that the coefficients of the discretized conservation equations approximate those resulting from the locally analytic solution of the homogeneous one-dimensional form of equation (1), i.e. the exponential coefficients described by Patankar,[3] with the view to maximizing stability. All three schemes are of second or higher order accuracy, depending on discretization options and flow conditions.

4 SINGLE GRID

When equations for the velocity components U and V based on equation (1) are differentiated with respect to x and y in turn and the result summed, the following Poisson equation for pressure results

$$-\nabla\cdot\nabla p = \frac{\partial}{\partial x}\left[\nabla\cdot\underline{\mathbf{J}}\right] + \frac{\partial}{\partial y}\left[\nabla\cdot\underline{\mathbf{J}}\right]. \tag{10}$$

This situation is indicated in Figure 2. For an equal order discretization of the Laplacian, it is necessary to obtain a local solution of the momentum equations in the space between nodes. In other words, deriving equation (10) through the classical route[3] of enforcing mass conservation over the control volume interfaces, a function is needed which expresses the interface velocity in terms of the interface pressure gradient. The first of three

routes to obtain this is the solution of the momentum equations on staggered grids, as described by Patankar.[3] Lee and Chiu[19] recently summarized the disadvantages of this initially mathematically attractive route, which must now be rejected as unergonomic, because it complicates the mental task of the analyst. Difficulties generally arise in three-dimensional non-orthogonal physical geometries, especially where the grid structure is complicated.

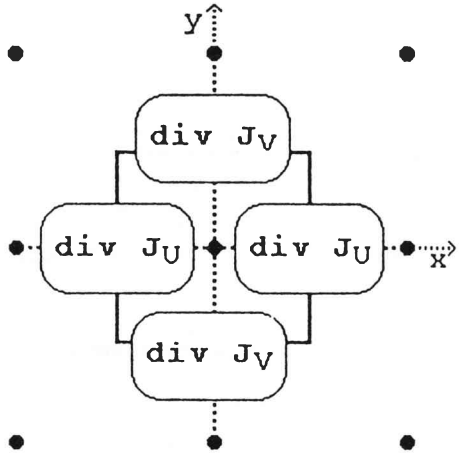

Figure 2 Divergence of momentum flux divergence

An alternative route therefore to obtain a velocity-pressure coupling at the control volume interface is provided by equation (7). Since provision is made for the local pressure gradient in the source term, equation (7) can simply be differentiated with regard to the local pressure gradient to obtain an expression of velocity correction to compile a pressure correction equation.[3,17]

A third method was proposed by Rhie and Chow,[20] who simulated a staggered grid by linearly interpolating the interface velocities in terms of the neighbouring discretized momentum equations, except for the pressure gradient contained therein. In this respect the approach is identical to the unequal order method described by Patankar and Baliga,[21] who solved for pressure at alternate grid points only. In the method of Rhie and Chow[20] the pressures at four nodes, which define the pressure gradients at the two adjacent control volumes in the direction of the interpolation, are assumed to lie on a parabola, i.e. a linear pressure gradient field is implied. This reduction of the degree of freedom, i.e. from an at least cubic to a quadratic pressure profile, provides the pressure field smoothing necessary to avoid checker board pressure fields.[3] It is however also the reason why, when grids are too coarse, the computed interface velocities can produce a checkerboard pattern with regard to the nodal velocities.

5 Quality Norm

Equation (1) suggests a way to quantify the performance or quality of a finite-volume analysis. If the divergence over a control volume is large, or, alternatively the source term is large, an indication is provided that local changes in the flow field are severe. It is then useful to plot contours of absolute integrated source terms to obtain an immediate visual indication of difficult flow regions, where for example grid refinement might be called for.

Such difficulties would not only arise due to say severe physical property gradients, but also due to the numerics. It was discussed above that for numerical stability the upwinding divergence remains on the left of equation (1). As a result, if the net effect of the secondary terms transferred to the right becomes relatively significant, this will also be indicated on the contour plots. The same would apply to non-orthogonal interface flux contributions, which are treated explicitly.

Summing the absolute integrated source terms over the entire flow domain may serve as an attempt to quantify the quality of the solution by a single norm. The conververgence of such a number will indicate to what degree a grid independent solution has been approached by comparison of the value obtained on successive smaller grids. The number should also add useful information for the comparison of different discretization options. Furthermore, the information is *a priori* in the sense that it does not depend on a known solution. If the value is normalized by a characteristic global (g) flux of the problem concerned, the resultant number, Q, may give a comparative indication for different flow problems of the relative significance of 'source term activity' therein:

$$Q = \frac{\sum \left| \int_\sigma \nabla \cdot \underline{\mathbf{J}} \, d\sigma \right|}{(\sigma \, |\underline{u}| \, \phi L)_g} \tag{11}$$

$$= \frac{\sum \left| \int \int_\Omega S \, d\Omega \right|}{(\rho \, |\underline{u}| \, \phi L)_g} \tag{12}$$

6 Implementation

Instead of the classical[3] geographic indentification of fluxes over different control volume faces, nodal neighbours (and the associated interfaces) are numbered sequentially and only one interface flux calculation is programmed as part of a loop. This calculation is based on a local coordinate system, which has been indicated in Figure 1 for interface number 2. This approach provides maximum freedom with regard to the shape of the control volume in more complex geometries.

In the current work boundary conditions are treated explicitly, i.e. Neumann boundary conditions are converted to Dirichlet conditions through extrapolation. As a result boundary interface fluxes are treated exactly as

internal fluxes, since equations (4), (6), and (8) will recover the boundary values automatically, when whole boundary control volumes are employed, i.e. a Patankar[3] type B grid. Steady flow under-relaxation as described by Patankar[3] has been applied and the tri-diagonal, line-by-line algebraic equation solver has been employed.

7 Test cases

7.1 Concentric shear flow

The configuration of the concentric shear flow problem is shown in Figure 3. This frequently used test case previously employed by the authors[17] has an analytic solution given by e.g. Schlichting.[22] It may represent the first configuration towards modelling a mixing vessel for example. A regular square grid implies values of the interpolation ratio a of 0.5 and 1, i.e. the interface lies halfway between nodes or at the location of a global boundary node. Analytical velocities were implemented as Dirichlet boundary conditions and the analytical pressure difference was used as a Neumann condition. Following Prakash[23] the problem can be non-dimensionalized in terms of a Reynolds number given by $\rho(\omega r_2)(r_2 - r_1)/\Gamma$. Laminar flow tests were run at Reynolds number 1 000 using 9×9, 21×21 and 41×41 nodes. The three interface interpolation schemes, described by equations (4), (6), and (8), were employed. Relaxation factors for velocities and pressure were 0.5 and 0.2, respectively, and the net secondary (higher order) source contribution in the momentum equations was relaxed by 0.04 on the finest grid. The latter value is arbitrary and not optimized. Some additional relaxation seems necessary when the velocity/grid size ratio becomes large, i.e. the iteration 'time step' required some reduction. The interface velocity-pressure coupling of Rhie and Chow[20] was used in all cases. For central difference interpolation on the 9×9 grid some artificial viscosity proved necessary to obtain convergence. This was applied by setting λ equal to 0.9. Starting with a constant radial outward flow field (approximately 50% of maximum analytical tangential velocity), the total number of outer iterations allowed varied between 195 on the smallest to 4 182 on the largest grids. In all cases the normalized summation of absolute residuals suggested by Peric' *et al.*[24] for momentum and mass were less than 10^{-6} when iterations were halted. The normalization is based on the above Reynolds number e.g. momentum related quantities were normalized by $\rho(\omega r_2)(\omega r_2)(r_2 - r_1)$. In terms of computational costs such convergence is not normally required. It was however applied to enhance the reliability of the comparison.

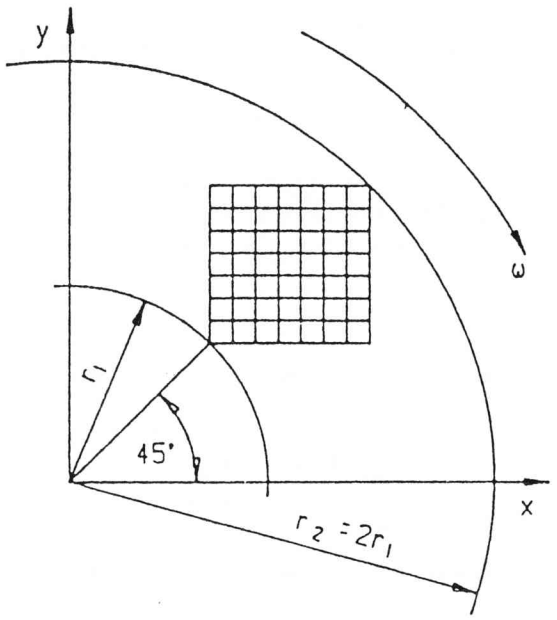

Figure 3 Concentric shear flow schematic

In Figure 4 the average absolute percentage errors of the computed U-velocity components for the three grid sizes and interpolation methods are shown.

In terms of accuracy on the coarsest grid the higher order schemes perform well. The physically based LOADS is slightly better than the numerically based QUICK scheme. On the other hand, as the grid is refined, the second order central difference scheme rapidly approaches the accuracy of the other two schemes. From equations (4), (6), (8), and (9) it follows that the central difference scheme is the simplest to employ. In the context of very large problems, as occur in climatology or oceanography for example, and also hardware limitations, e.g. array sizes, the use of more accurate schemes might on the other hand still be worth while for some analyses.

In Table 1 the final values of the U-momentum quality norm obtained, i.e. as defined by equation,[12] are presented. The values are essentially the same, which is to be expected. All three schemes use similar upwinding coefficients, which follow from equations (4), (6), and (8), and the total integrated source should be independent of grid size. Since this is a relatively regular flow field, these figures may serve as a comparison with data obtained in subsequent test cases.

For this well-behaved tlow, contours of absolute integrated source terms do not highlight any significant features. However in Figure 5 absolute U-velocity component source term contours for the LOADS scheme, in this case locally normalized, can be compared to the contours of the locally normalized percentage error plot.

The maximum error is then found in the vicinity of the fixed inner shaft, where the velocities used for normalization tend to zero. Some correlation between the two figures can be detected.

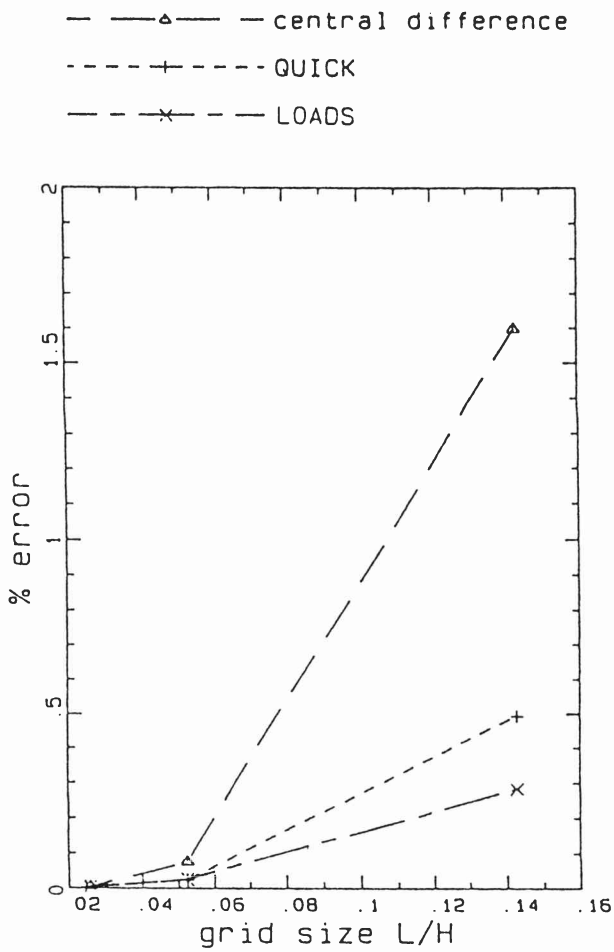

Figure 4 Average absolute percentage error of computed U-velocity components

Table 1 U-velocity component quality norms

Grid	Central difference	QUICK	LOADS
9×9	0.0773 (damped)	0.0818	0.0743
21×21	0.0806	0.0743	0.0757
41×41	0.0863	0.0775	0.0760

7.2 Wall driven flow in a square cavity

The steady incompressible lid driven flow in a square cavity complements the previous case in as much it is not a through-flow problem, but relies on the presence of viscosity to establish a recirculating flow pattern, to be captured using a non-flow aligned square grid. The essential features of such a resulting flow pattern can for example be observed in a fume extraction hood over a conveyor belt.

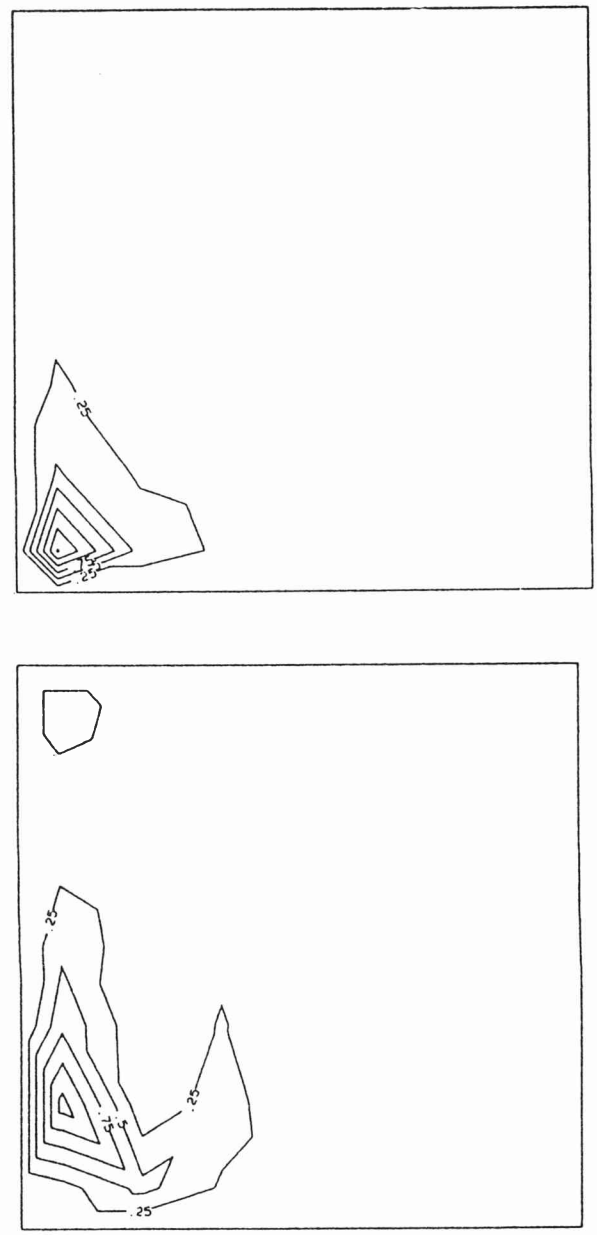

Figure 5 Contours for the absolute locally normalized U-velocity components – 9×9 nodes
a) integrated source terms; b) percentage error

Huang *et al.*[16] did report failure to obtain convergence when applying the LOADS scheme of Wong and Raithby[14] to the cavity problem. Prakash[23] showed that convergence could be obtained for his implementation of LOADS, with the help of near boundary grid refinement. This was confirmed by the current authors[17] for the LOADS scheme. As a result the cavity problem might

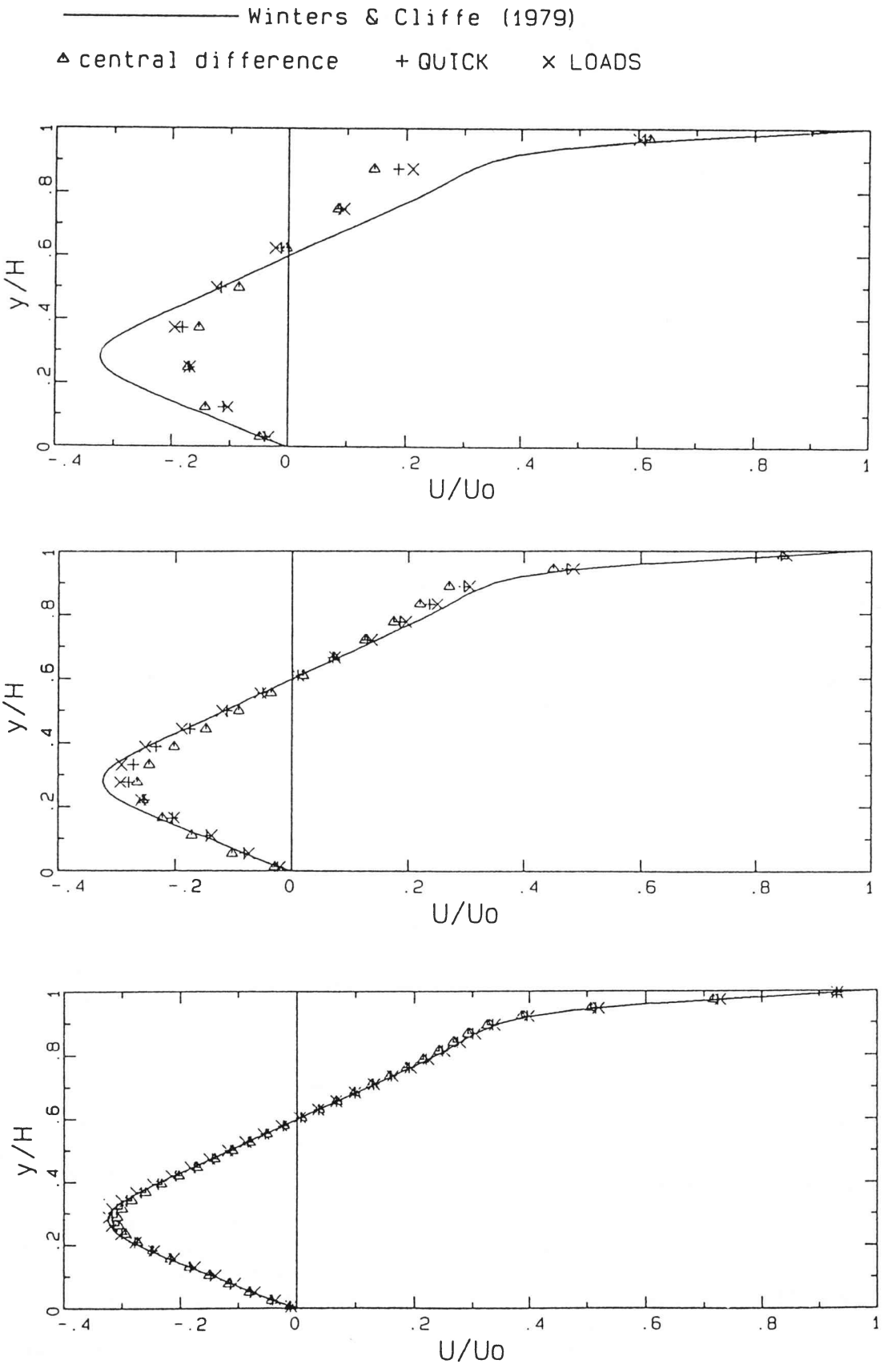

Figure 6 Horizontal (U-) velocity components on the vertical centre line
(a) 9 × 9 nodes; (b) 21 × 21 nodes; (c) 41 × 41 nodes

also provide a test of the quality norm approach proposed.

Thus the shorter side length of half size boundary control volumes of an otherwise regular grid is calculated from $H/(n-3)/2$. The values of the interface interpolation ratio a occurring are therefore 0.33, 0.5, 0.67 and 1.0. The Reynolds number in terms of lid speed and side wall length H tested was 400 and 11×11, 21×21 and 41×41 node grids were employed. Relaxation factors were the same as for the previous case. Apart from the moving top side velocity of unity, all other boundary nodal velocities were set to zero. Using a unity side wall length results in a normalizing factor of unity. Iterations were halted when normalized summation of absolute residuals of momentum and mass were less than $3 \cdot 10^{-6}$. This was achieved after allowing between 500 and 6 000 iterations respectively for the grids used. Again the interface velocity-pressure coupling of Rhie and Chow[20] was used.

In Figure 6 the computed U-component on the vertical centreline obtained for the various schemes are compared to the results obtained by Winters and Cliffe.[24] Their grid consisted of 57×57 finite element nodes with additional local grid refinement in the lid side corners. On the coarsest grid the resolution of the flow field must be considered inadequate. The accuracy improves substantially with grid refinement, the central difference scheme proving once again adequate. The same weak hierarchy of accuracy among the three schemes as indicated in the previous test case can be detected.

Table 2 U-velocity component quality norms

Grid	Central difference	QUICK	LOADS
11×11	0.0972	0.0982	0.12
21×21	0.16	0.15	0.17
41×41	0.22	0.18	0.17

In Table 2 U-momentum quality norms obtained according to equation (12) are presented. Although the data is too limited to make conclusive statements, the following tentative observations can be added to the experience gained in the previous test case. With regard to the first two schemes a grid independent solution has not yet been obtained. All numbers based on LOADS tend towards a lower value than the those based on the other schemes. All the numbers appear to converge to a significantly larger value than those obtained in the previous test case, which might be attributed to the effect of normalization. The accuracy results of both test cases seem to suggest that a lower norm value can be associated with a better quality resolution of the flow field. The particular difficulty of the problem can be identified from a typical absolute integrated U-component source term contours of the central difference case shown in Figure 7 (contours for the other interpolation schemes being similar). The finest grid used appears necessary to resolve the severity of the flow field in the top two corners, where relatively large pressure gradients are required to change the direction of the flow.

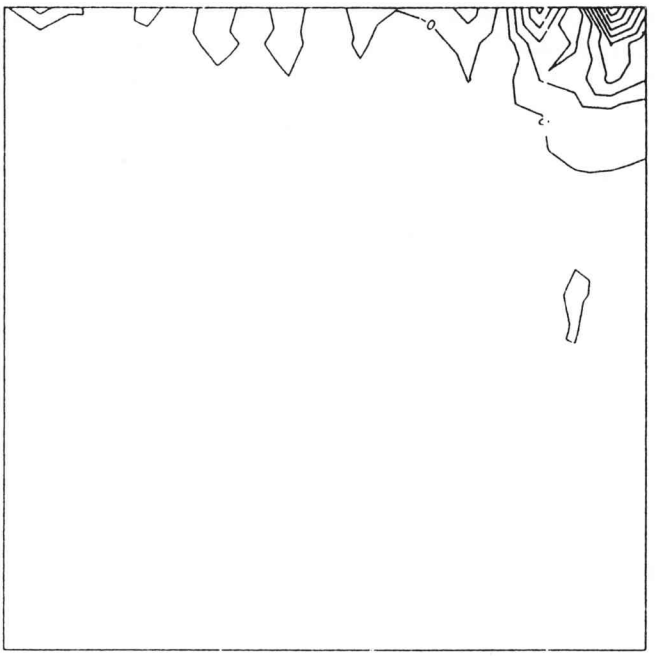

Figure 7 Contours of the absolute U-velocity component integrated source terms for central difference discretization – 41×41 nodes

7.3 SCALAR DIFFUSION TEST

Another frequently used test case to examine interpolation schemes is the transport of a scalar step discontinuity resulting from the joining of two uniforms flows transporting the same scalar at different magnitudes and at various directions relative to the grid. Specifying a 'sharp' inlet profile not only allows an examination of false diffusion 'smearing', but alsc the capacity of the method to deal with steep property gradients in the flow. Furthermore this test tends to give a clear indication of the extent of the inherent dispersion associated with higher order schemes.

The typical configuration is shown in Figure 8. The flow direction is described by the elevation (relative velocity components) of the line, at which the discontinuity occurs. In the current case only a 45° fixed (not computed) flow field is employed. The scalar step profile is imposed by the boundary conditions indicated in Figure 8. In order to examine the three schemes in the context of the general formulations adopted in equations (4), (6), and (8), the diffusion coefficient, e.g. in equation (1)

was set at 10^{-10} and the primary source term was set to zero. The general formulations are not suited for zero diffusion. The value of 10^{-10} was arrived at by noticing no further graphical changes in the scalar profiles examined for a coefficient smaller than 10^{-6}. The regular grid sizes examined were 11×11, 21×21 and 41×41. The initial scalar field value was set to 0.5. In all cases no relaxation was employed and less than a hundred iterations were required to reduce the normalized (by a factor one) scalar residual to below 10^{-6}. However, a non-optimized value of 0.9 was assigned to the value of λ for the central difference interpolation to introduce some artificial diffusion. Without this remedy convergence was either extremely slow or produced 'sawtooth' results on the finest grid.

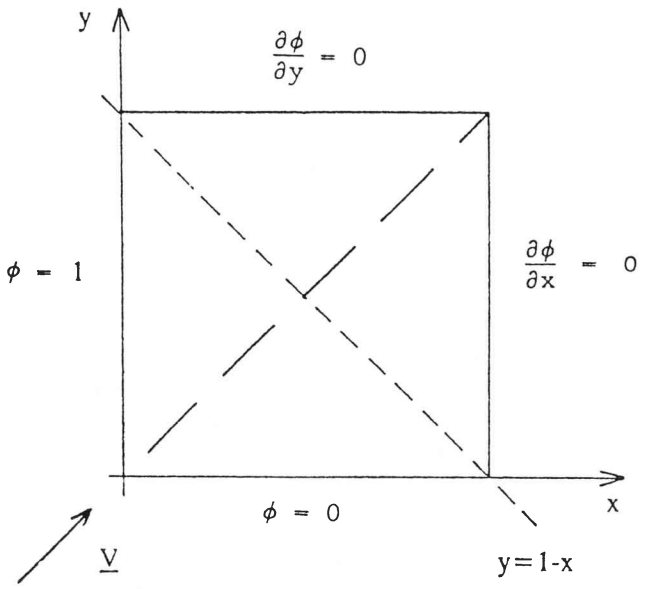

Figure 8 Scalar transport diffusion schematic

In Figure 9 a comparison between the three interpolation schemes is presented in the form of scalar profiles along the line $y = 1 - x$. In the context of yielding a vertical step face, the QUICK scheme seems to perform best. On the coarsest grid, all three schemes produce almost equal order unboundedness. With increasing grid refinement, the dispersive overshoots in the damped central difference based results rapidly disappear while they increase for the other two schemes. In terms of accuracy the central difference scheme performs therefore best, although, through the introduction of artificial diffusion damping, unboundedness was introduced.

In Table 3 the computed quality norms associated with the results presented in Figure 9 are provided. The norm will diminish, as the step is approximated more accurately and the regions of 'flatness', where the first order divergence vanishes, expand and the overshoots disappear. The rapid improvement in the damped central difference based results is clearly distinguishable.

Table 3 Secondary sources based quality norms

Grid	Central difference (damped)	QUICK	LOADS
11×11	0.254	0.315	0.245
21×21	0.223	0.262	0.237
41×41	0.180	0.269	0.219

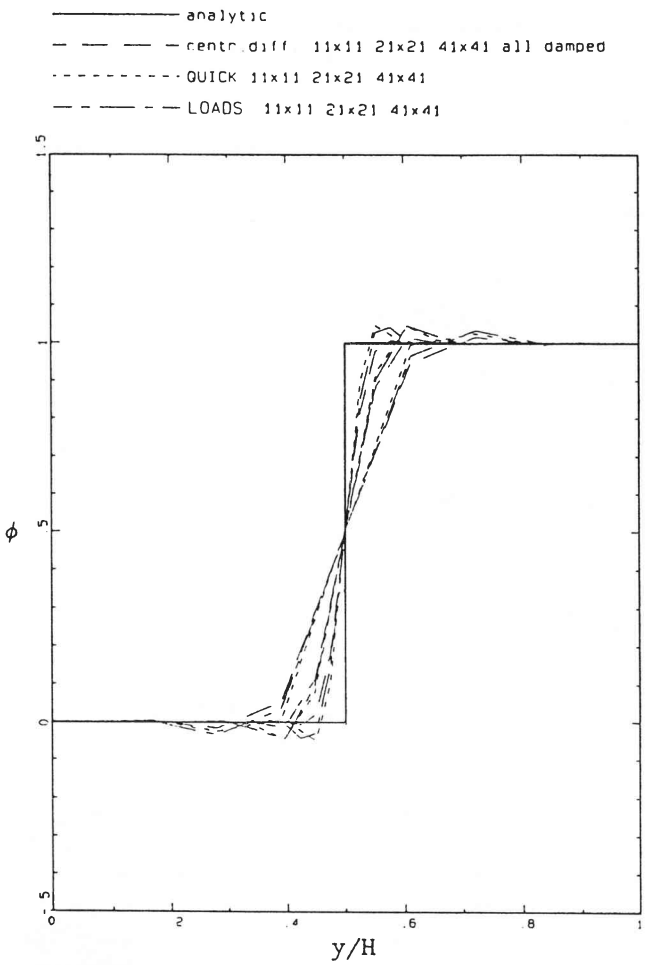

Figure 9 Comparison of scalar profiles along the line $y = 1 - x$

In Figure 10 contours of the source term distribution are provided for the 41×41 nodes central difference case, the other cases being similar. The severity of the boundary condition imposed on the scalar field at the inlet flow corner is quite recognizable in all cases.

8 Conclusion

Due to its simplicity, inherent boundedness and the transparent manner described by Peric',[11] in which ar-

tificial damping or downwind decoupling can be introduced, it is likely that central difference interpolation will be widely employed.

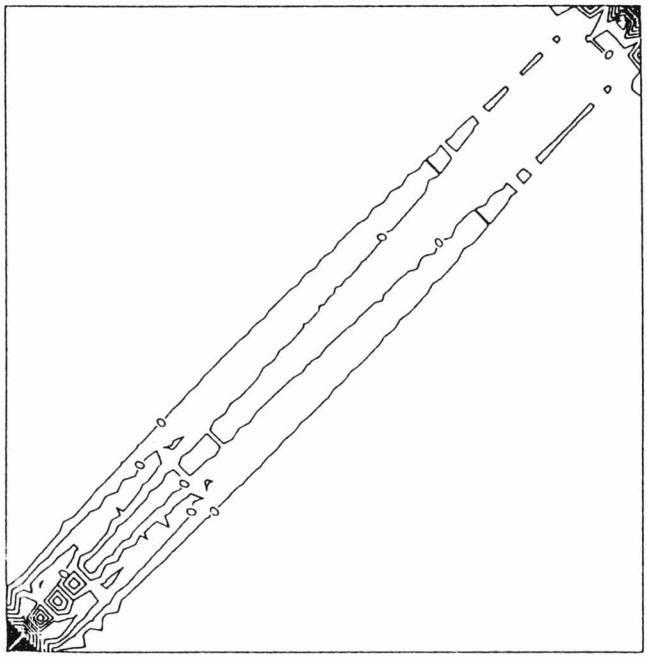

Figure 10 Contours of the absolute integrated secondary scalar source terms for central difference discretization – 41 × 41 nodes

The alternatives are more accurate, but also more complicated and less transparent. In the light of rapidly rising computer power, the latter disadvantage is gaining in significance. The results of the test cases do not indicate that grid convergence is substantially enhanced by non-linear interpolation. However, physical circumstances, where the use of non-linear interpolation is essential, may occur.

The analysis of source term distribution is apt in finite volume methodology. The quality norm proposed is a heuristic quantitative tool. Its formulation is presented as a first attempt to generate a simple but useful index. It is hoped to report on alternatives and their implications in the future.

References

1. Daugherty RL & Franzini JB. *Fluid mechanics with engineering applications.* 7th edn. McGraw-Hill, New York, 1977.

2. Patankar SV & Spalding DB. A calculation procedure for heat, mass and momentum transfer in three-dimensional parabolic flows. *Int. Journal Heat Mass Transfer*, 1972, **15**, pp.1787–1806.

3. Patankar SV. *Numerical heat transfer and fluid flow.* lst edn. Hemisphere, Washington, 1980.

4. Gosman AD, Launder BE & Reece GJ. *Computer-aided engineering: heat transfer and fluid flow.* Horwood, Chichester, West Sussex, 1985.

5. Aris R. *Vectors, tensors, and the basic equations of fluid mechanics.* Prentice-Hall, Inc., Englewood Cliffs, N.J., 1962.

6. Schneider GE & Raw MJ. A new control-volume-based finite element procedure for the numerical solution of the fluid flow and scalar transport equations. Final report, Department of Mechanical Engineering, University of Waterloo, Waterloo, Ontario, N2L 3G1, 1985.

7. Spalding DB. A novel finite difference formulation for differential expressions involving both first and second derivatives. *International Journal for Numerical Methods in Engineering*, 1972, **4**, pp.551–559.

8. Khosla PK & Rubin SG. A diagonally dominant second-order accurate implicit scheme. *Computers and Fluids*, 1974, **2**, pp.207–209.

9. Denton JD. The calculation of fully three dimensional flow through any type of turbomachinery blade row. Lecture series No. 140, Advisory Group for Aerospace Research and Development, 1984.

10. Peric' M. Analysis of pressure-velocity coupling on nonorthogonal grids. *Numerical Heat Transfer*, 1990, Part B, **17**, pp.63–82.

11. Peric' M. A finite volume method for the prediction of three-dimensional fluid flow in complex ducts. PhD thesis, Mechanical Engineering Department, Imperial College, University of London, 1985.

12. Pulliam TH. Artificial dissipation models for the Euier equation. *AIAA Journal*, 1986, **24**, pp.1931–1940.

13. Leonard BP & Drummond JE. Why you should not use 'hybrid', 'power-law' or related exponential schemes for convective modelling – there are much better alternatives. *International Journal for Numerical Methods in Fluids*, 1995, **20**, pp.421–442.

14. Wong HH & Raithby GD. Improved finite-difference methods based on a critical evaluation of the approximation errors. *Numerical Heat Transfer*, 1979, **2**, pp.139–163.

15. Prakash C. Application of the locally analytic differencing scheme to some test problems for the convection-diffusion equation. *Numerical Heat Transfer*, 1984, **7**, pp.165–182.

16. Huang PG, Launder BE & Leschziner MA. Discretization of nonlinear convection processes: A broad-range comparison of four schemes. *Computer Methods in Applied Mechanics and Engineering*, 1985, **48**, pp.1–24.

17. Harms TM, Von Backström TW & Du Plessis JP. Reformulation of the SIMPLEN discretization scheme to accommodate noncentralized interfaces. *Numerical Heat Transfer*, 1991, Part B, **20**, pp.127–144.

18. Harms TM, Von Backström TW & Du Plessis JP. Derivation of a modified hybrid approximation. *AIAA Journal*, 1994, **32**, pp.1541–1543.

19. Lee D & Chiu JJ. Covariant velocity-based calculation procedure with nonstaggered grids for computation of pulsatile flows. *Numerical Heat Transfer*, 1992, Part B, **21**, pp.269–286.

20. Rhie CM & Chow WL. Numerical study of turbulent flow past an airfoil with trailing edge separation. *AIAA Journal*, 1983, **21**, pp.1525–1532.

21. Baliga BR & Patankar SV. A control volume finite-element method for two-dimensional fluid flow and heat transfer. *Numerical Heat Transfer*, 1983, **6**, p.245–261.

22. Schlichting H. *Boundary-layer theory.* 7th edn. McGraw-Hill, New York, 1979.

23. Prakash C. An improved control volume finite-element method for heat and mass transfer, and for fluid flow using equal-order velocity-pressure interpolation. *Numerical Heat Transfer*, 1986, **9**, pp.253–276.

24. Peric' M, Kessler R & Scheuerer G. Comparison of finite-volume numerical methods with staggered and collocated grids. *Computers and Fluids*, 1988, **16**, pp.389–403.

25. Winters KH & Cliffe KA. A finite element study of driven cavity flow in a square cavity. *AERE*-R9444, Harwell, 1979.

Appendix 1

Quadratic upwind interpolation

With reference to Figure 1 consider the interpolation equation

$$\phi = c_1\xi^2 + c_2\xi + c_3$$

Employing the boundary values $\phi_N\,(\xi = 0)$ and $\phi_M\,(\xi = L)$ and either their nodal derivatives m_N or m_M in the ξ-direction, depending whether the interface velocity u is positive or negative, results in

$$\phi_{aL} = \phi_N + a^2\,(\phi_M - \phi_N) + a\,(1-a)\,Lm_N$$

$$\phi_{aL} = \phi_N + a\,(2-a)\,(\phi_M - \phi_N) - a\,(1-a)\,LmM$$

These equations can be combined resulting in equation (5).

Appendix 2

Exponential weighting functions

$$A\,(Pe) = \frac{Pe}{\exp(Pe)-1}$$

$$B\,(a, Pe) = \frac{1-(aPe/[\exp(aPe)-1])}{Pe}$$

$$C\,(a, Pe) = \frac{\exp(aPe)-1}{\exp(Pe)-1}$$

$$D\,(a, Pe) = \frac{[\exp(aPe)-1](\exp[(1-a)Pe]-1)}{Pe[\exp(Pe)-1]}$$

A removable singularity appears in these equations when $Pe = 0$. This is accomodated through the numerical approximation employed.[17]

Flow Through a Solar Chimney Power Plant Collector-to-Chimney Transition Section

Carl F. Kirstein

Theodor W. von Backström
e-mail: twvb@sun.ac.za

Department of Mechanical Engineering,
University of Stellenbosch,
Private Bag X1,
Matieland, 7602,
South Africa

A solar chimney power plant consists of a large greenhouse-type collector surrounding a tall chimney. The air, heated within the collector, passes through an inlet guide vane (IGV)cascade and then through a transition section to a turbine that powers a generator. The transition section contains the turbine inlet guide vanes that support the whole chimney and guides the flow entering the turbine. The primary objective of the study was to determine the loss coefficient and mean exit swirl angle of the flow passing through the collector-to-chimney transition section of a full-scale solar chimney power plant as dependent on IGV stagger angle and collector roof height. Very good agreement was found between experimental values measured in a scaled model and commercial CFD code predictions of flow angles, velocity components, and internal and wall static pressures. The agreement between measured and predicted total pressure loss coefficient was reasonable when considering how small it is. The CFD code served to extend the predictions to a proposed full-scale geometry. Semi-empirical equations were developed to predict the loss coefficient and turbine mean inlet flow angles of solar chimney power plants as dependent on collector deck height and inlet guide vane setting angle. The two empirical equations may be useful in solar chimney plant optimization studies.
[DOI: 10.1115/1.2210502]

Keywords: solar energy, solar chimney, solar tower, radial-to-axial flow, transition duct, loss coefficient

Introduction

A solar chimney power plant Schlaich [1] consists of a large greenhouse surrounding a tall chimney. Hot air escaping through the chimney first passes through a collector-to-chimney transition section and then through a turbine that powers a generator (Fig. 1). The effects investigated experimentally and computationally in this paper are those associated with the collector-to-chimney transition section. The collector-to-chimney transition section is the region between the leading edges of the inlet guide vanes (IGVs), supporting the chimney, and the turbine, where the flow turns from a horizontal direction to a vertical direction. The transition section loss coefficient is defined as the total pressure loss through the transition section normalized by the average dynamic pressure at the chimney exit. Note that the turbine diameter may be smaller than the chimney diameter, D (Fig. 1).

The main objective of this study is to determine the pressure drop and exit swirl angle of the flow passing through the collector-to-chimney transition section of a full-scale solar chimney power plant. New experimental data that assist verification of the computational models will be presented.

Literature Review

Haaf et al. [2] described the experimental performance of a small (50 kW) solar tower chimney power plant. Mullett [3], Pasumarthi and Sherif [4], Gannon and von Backström [5], and Kröger and Buys [6] have published theoretical performance estimates for the full-scale plant, and Gannon and von Backström [7] and von Backström et al. [8] have presented the only available measured loss coefficients on a model turbine and chimney scale models. Haaf et al. [2] and Pasumarthi and Sherif [4] did not state the transition section loss coefficient. Kröger and Buys [6] estimated the collector-to-chimney-transition loss coefficient of a full-scale plant to be 0.25. This estimate agrees with the loss coefficient of a pipe bell mouth entrance when the radius of curvature of the bell mouth profile is about 5% of the pipe diameter [9]. Von Backström et al. [8] used experimental data from Gannon [10] and estimated the collector-to-chimney transition loss coefficient to be 0.161 at model scale. They concluded that this area required more research to clear up the large difference between expected and measured results.

The most applicable general loss coefficient data found was that of Fried and Idelchik [11]. According to them the loss coefficient of a bell mouth, with diameter D and nozzle radius of curvature r, facing a wall a distance h away, varies between 0.04 and 0.08 for $0.36 < h/D < 0.44$ when $r/D \approx 0.2$, for nonswirling flow at Re $> 10^4$ (Fig. 2).

The collector-to-chimney transition section layout may be regarded as that of an inverted Kaplan turbine. Schilling et al. [12] modeled a Kaplan turbine numerically, using air as the fluid in the experimental model instead of water. The numerical prediction of the velocity distribution through the transition section was inaccurate and the agreement with measured pressure coefficients disappointing. Schilling et al. [12] conclude that numerical simulation using a standard k-ε turbulence model for complex 3D boundary layer flow along curved rotating walls where the cross flow due to swirl reaches the same magnitude as the main flow is not adequate to predict losses accurately.

Gannon and von Backström [7] presented velocity profiles just below the turbine, indicating that the swirl velocity component is remarkably uniform and does not resemble a free vortex as might be expected. They did not, however, present a general relationship between IGV angle and the turbine inlet swirl angle.

Contributed by the Solar Energy Division of ASME for publication in the JOURNAL OF SOLAR ENERGY ENGINEERING. Manuscript received June 1, 2005; final manuscript received January 27, 2006. Review conducted by Robert Pitz-Paal. Paper presented at the 2005 International Solar Energy Conference (ISEC2005), August 6–12, 2005, Orlando, Florida, USA.

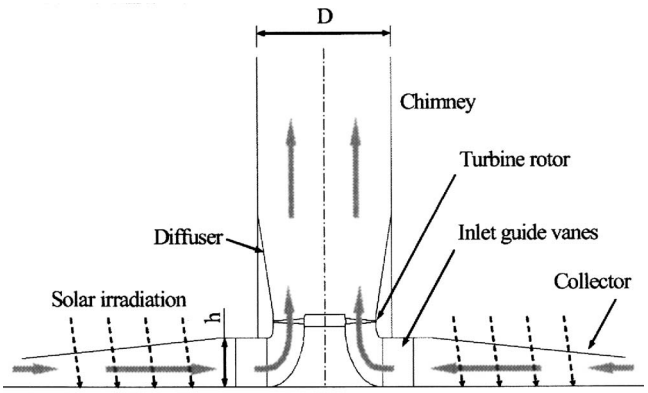

Fig. 1 Solar chimney schematic

Experimental Setup

To make a useful prediction for the full-scale solar chimney power plant, the simulation software has to be verified. Verification was achieved by comparing computational fluid dynamics (CFD) with experimental fluid dynamics (EFD). The EFD results consisted of wall static pressures on the outer wall of the transition section of the experimental rig (Figs. 3 and 4) and of five-hole pneumatic pressure probe (5HPPP) traverses done in an orthogonal array within this transition section (Fig. 5).

The static pressure ports were 0.5 mm diameter holes drilled in the outer wall, coupled by tubing through a computer controlled switch box to a single Autotran™ 750D-250 pressure transducer sampling at 30 Hz for 2 s per reading with 30 s intervals for stabilization.

The 5HPPP has a 1.4 mm diameter with 0.2 mm holes on 45 deg flat planes. The 5HPPP was connected to five Autotran™ 750D-250 pressure transducers sampling at a frequency of 30 kHz for 2 s per reading. The standard deviation of the measurement error (SDME) of the transducers is 1.75 Pa over their entire range of 2000 Pa, including the zero setting, since the transducers reset their zero offsets automatically every 30 s.

The experimental rig is a 1:77 scale chimney model designed and built by Gannon [10] (Fig. 3). Note that the chimney diameter beyond the diffuser (not shown in Fig. 3) is 900 mm. There are four configurations made up of two inlet guide vane (IGV) angles, β (22.5 and 31.5 deg) and two collector roof heights (Table 1 and Figs. 3 and 4).

The project used the outer wall static pressure readings as one of the benchmarks for validating the CFD software. The wall static pressures were measured through 0.5 mm holes, spaced 20 mm apart for the first six points and 10 mm for the rest, along the rows indicated in Fig. 4 Rows 4 and 5 coincide due to IGV periodicity. The start and end of such a row is also indicated in Fig. 4 as start and end of the developed length. The start of the developed length was 480 mm from the chimney axis. The numbers in the figure indicate four lines, spaced at 5 deg intervals, along which the static pressure holes were spaced. Lines 1 and 5 coincide due to periodicity relative to the 18 IGVs and the results shown later are from row 5. Row 5 is 1.2 deg clockwise from the IGV trailing edge.

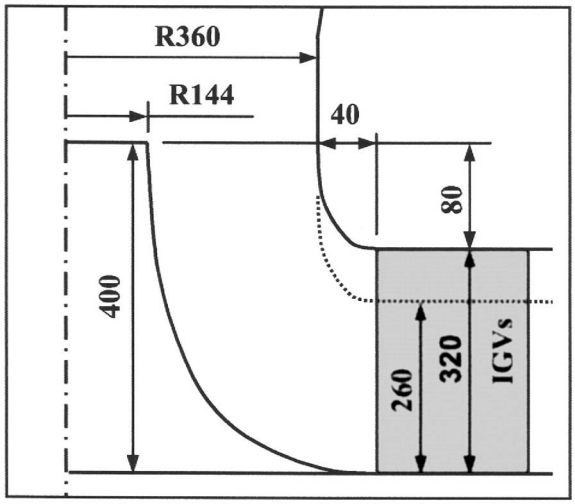

Fig. 3 Geometry of model collector-to-chimney transition section

The velocity traverses were done along the inclined solid lines in Fig. 5. These lines lay in seven meridional planes, spaced at 3.33 deg intervals and numbered as row 1 to 7. Row 7 coincides with row 1 due to periodicity. Row 5 coincides with row 1 of the wall static pressure tappings.

Due to interference from the IGVs and low velocities, it was not possible to measure below the limit line (Fig. 5) with the 5HPPP.

The calibration maps of the five-hole probe were generated by fixing the probe at a known orientation in a small wind tunnel. Using calibration maps to calculate the velocity components in the wind tunnel gave errors of less than 1% of the velocity magnitude.

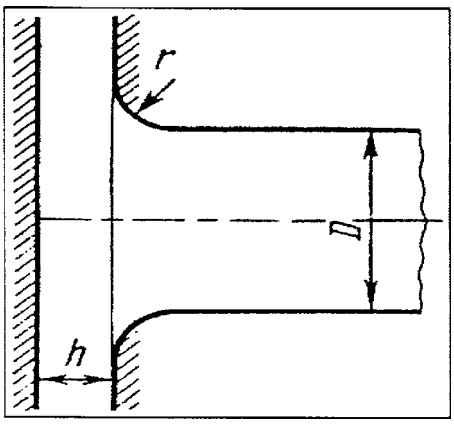

Fig. 2 Bell mouth facing a wall (Fried and Idelchik[11])

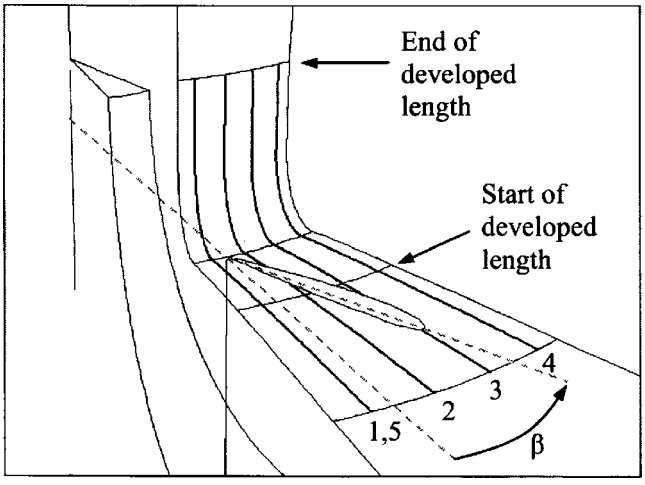

Fig. 4 10 deg sector showing row location and number for static pressure readings on the outer wall

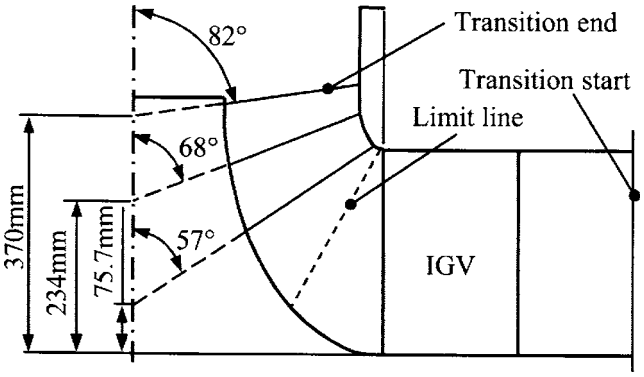

Fig. 5 Schematic of five-hole probe traversing orthogonal array

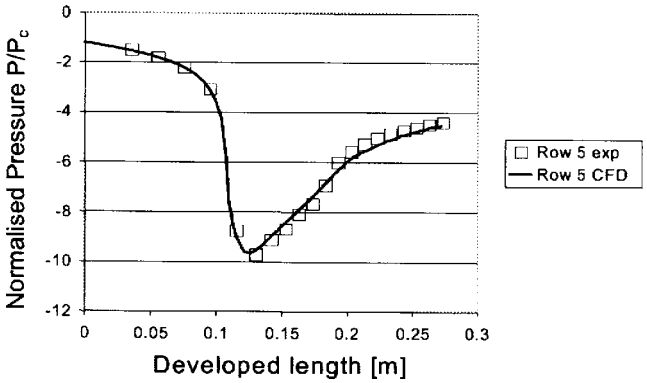

Fig. 6 Outer wall static pressures, configuration D

Also, it was determined experimentally that the SDME of the pressure and angle measurements can be described by the following two equations (n is the number of samples).

$$S_{\text{pressure}} = \frac{3.381}{\sqrt{n}} \quad S_{\text{angle}} = \frac{150}{\sqrt{n}V_{\text{tot}}^2}$$

Most of the measurements were done by taking at least six samples at a measuring point, giving a SDME of 1.38 Pa for the pressure readings. The average velocity measured in the experimental rig was 15 m/s (dynamic pressure=135 Pa), giving a typical velocity error of 1%. Since the boundary layers were 3 to 6 mm thick the probe spatial resolution of 0.9 mm (the distance between the centers of side holes) was deemed to be adequate.

The angular SDME of angles was 0.24 deg for six readings. Realistically the angles could not be measured more accurately than 1 deg due to setting errors in the 5HPPP bracket.

CFD

The measured values were compared with CFD results from CFX 5.5.1. CFD is unfortunately still unreliable still unreliable for predicting flow transition [13], and CFX 5.5.1 does not have the ability to calculate transitional flow. An unstructured mesh was used, assuming fully turbulent flow throughout the flow domain. The SST (shear stress transport) turbulence model was selected. It behaved well for the flow conditions encountered in the transition section. Kirstein [14], however, using an integral method of Thwaites [15], determined that the boundary layers start off laminar at the perimeter of the experimental rig and become fully turbulent within the transition section. This means that both the EFD and CFD boundary layers at the exit of the transitions section will be turbulent, and their thicknesses largely determine the loss coefficient.

The concerns above had little bearing on the half of the paper concerned with the determination of the flow angle at the transition section exit, since the thin boundary layers had only a small effect on the average flow angle.

Table 1 Experimental rig configuration settings

Configuration	IGV stagger angle, β [deg]	Collector roof height [h/D]
A	22.5	0.356
B	31.5	0.356
C	22.5	0.289
D	31.5	0.289

Comparison Between CFD and EFD

Representative comparative figures are shown and discussed.

The outer wall results clearly show that the CFD software performs well in spite of its inability to simulate transitional flow effects (Fig. 6). The pressure is normalized with the dynamic pressure based on the average exit velocity for the nominal 900 mm diameter chimney.

The following three figures show the measured velocity components. These are true axial, radial, and tangential components, relative to the chimney axis. Traverses along the three lines, shown in Fig. 5, show good agreement, even in the boundary layers, between the EFD and CFD results for the velocities (Figs. 7–9), normalized with the average through-flow velocity in the 900 mm chimney. The existence of an inlet guide vane wake is indicated by the slight changes in the slopes of the EFD and CFD profiles at about 16% from the inner wall in Figs. 7 and 10. In Figs. 8, 11, 9, and 12, they have moved to 40% and 48% from the inner wall, respectively.

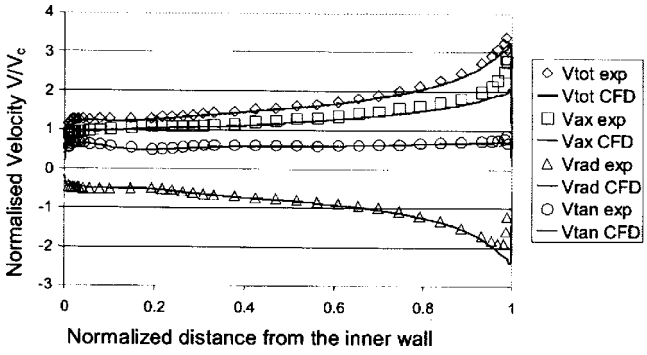

Fig. 7 Velocities: row 7, configuration C, bottom

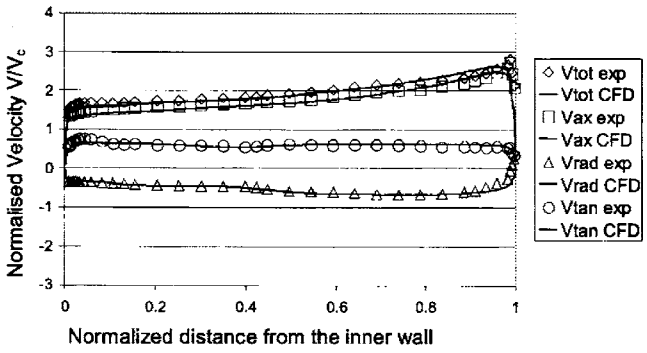

Fig. 8 Velocities: row 7, configuration C, middle

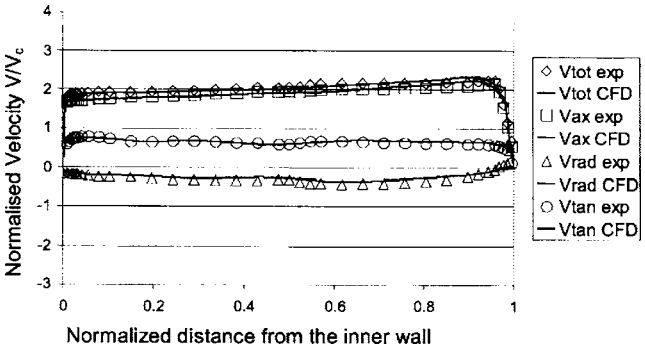

Fig. 9 Velocities: row 7, configuration C, top

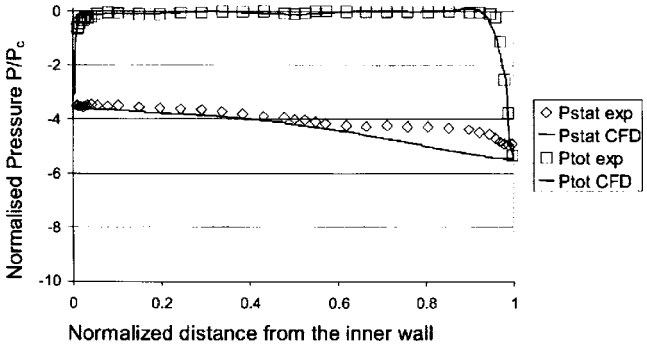

Fig. 12 Pressures: row 7, configuration C, top

To verify the quality of the measured results, a continuity check was made. Since traverses were done in each of the seven meridional planes, the volume flow across an area defined by a traversing line and a $\frac{1}{18}$ sector could be found by numerical integration. The average of the calculated flow rates derived from the five-hole probe results for any configuration differed by less than 0.7% from the readings of a windmill anemometer upstream of the IGVs. The greatest deviation in comparison to the anemometer is 4.5%. Gannon [10] tested this anemometer and determined that its maximum error is 2%. This was confirmed by subsequent recalibrations.

Figures 10–12 show the normalized measured pressures relative to the atmospheric pressure outside the outer edge of the experimental collector. There is a small drop in total pressure in the main flow due to dissipation. There is good agreement between the EFD and CFD results for the total and static pressure, even in the wakes. There is only a discrepancy for the static pressures near the outer wall for the middle and top results. The discrepancy in these areas may be due to the formation of Taylor-Görtler vortices, which occur more readily under transitional conditions Hall [16]. The existence of these vortices implies a different distribution of eddy viscosity compared to that assumed by most turbulence models. This will be discussed more fully in a follow-up paper. As mentioned above, CFX 5.5.1 cannot simulate such transitional flow effects. This is only a problem for the small-scale transition section; in the full-scale plant the flow will be turbulent before it gets to the transition section.

Most of the total pressure losses occurred in the weak wakes of the IGVs and the very thin transition section wall boundary layers. Total pressure values were found by volume flow weighted averaging over the appropriate area. The loss coefficients of configuration A are 0.098 and 0.138, which are low compared to previous experimental values of greater than 0.16. When normalized with the dynamic pressure in the turbine section, these loss coefficients are as low as 0.03, which is extremely difficult to measure accurately, but is in reasonable agreement with the work of Fried and Idelchik [11].

In spite of the excellent agreement between the EFD and CFD total pressure values in Fig. 12, the experimental losses, typically represented by the total pressure deficit in the wakes and wall boundary layers, were too small to be consistently determined with a high degree of accuracy. The maximum zero offset error of the self-resetting pressure transducers is 1.75 Pa, less than 0.1% of the transducer range. If this value is added to the EFD total pressure loss of configuration A given in Table 2, for example, it

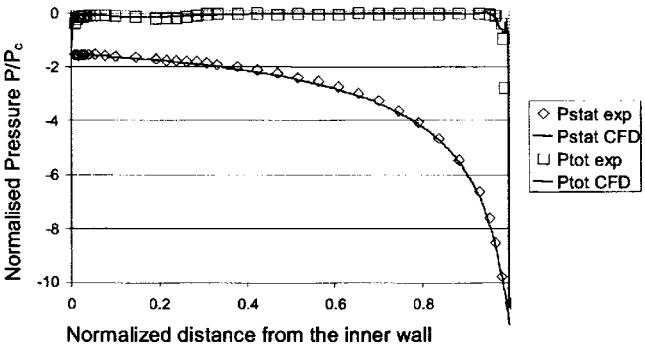

Fig. 10 Pressures: row 7, configuration C, bottom

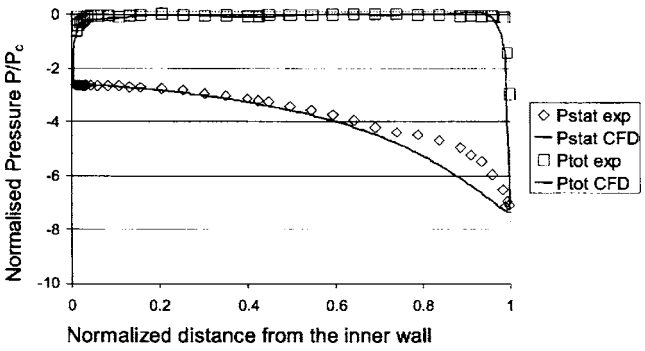

Fig. 11 Pressures: row 7, configuration C, middle

Table 2 Transition section total pressure loss

	CFD		EFD		
Configuration	P_{tot} (Pa)	C_L	P_{tot} (Pa)	C_L	C_L error (%)
A	−3.89	0.098	−5.42	0.138	−29
B	−4.62	0.117	−3.69	0.096	22
C	−6.00	0.151	−5.63	0.144	4.9
D	−7.56	0.191	−7.14	0.195	−1.2

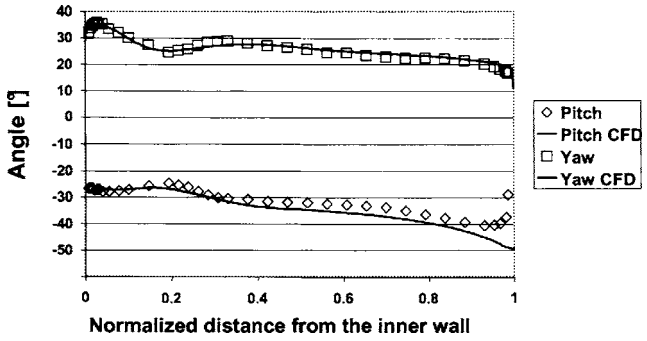

Fig. 13 Angles: row 7, configuration C, bottom

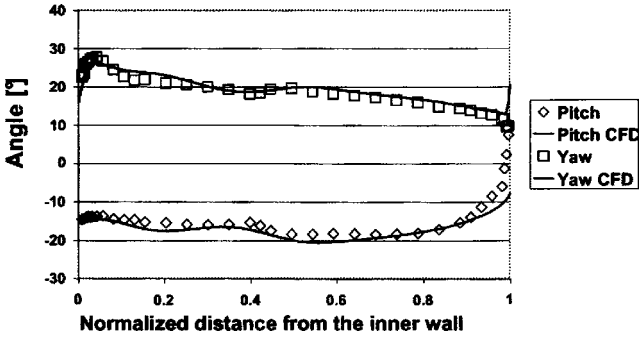

Fig. 14 Angles: row 7, configuration C, middle

changes the error from −29% to +3.7%. Note that the average error is close to zero.

Figures 13–15 compare the flow angle measurements and computations. The angles are described by the following equations:

$$\text{Pitch} = \tan^{-1}\left(\frac{V_{rad}}{V_{\text{axial}}}\right) \quad \text{Yaw} = \tan^{-1}\left(\frac{V_{\tan}}{V_{\text{axial}}}\right)$$

The curve shapes are predicted very well. The angle predictions are within 5 deg of most of the measured values and within 2 deg on average. The yaw angles are more accurately calculated than the pitch angles, with an average error of about 1 deg for most of the cases. EFD and CFD wake prediction agree well. For the design of a turbine, the yaw angles (turning angles) play a direct role in the turbine energy conversion and are more critical than the pitch angles; therefore, the results are satisfactory.

Based on Figs. 6–15 one may conclude that the CFD software simulates the performance of the transition section well enough for the predictions to be extended to a full-scale geometry.

Full-Scale Prediction

The full-scale results were generated by using the same geometry as the experimental rig, and rescaling it. The IGV was swivelled around its trailing edge to adjust the angle and the collector height was adjusted by adjusting the length of the vertical section leading to the turbine. The CFD simulation used the inlet conditions described in Von Backström et al. [17]. The conditions are stagnation temperature of 323.15 K, stagnation pressure of 90 kPa, and mass flow 250,000 kg/s. The model IGV geometry is described by Gannon [10]. It consists of 18 modified NACA four digit profiles with the following description: chord=226 mm; maximum thickness=11.7%; maximum camber=2.64%; position of maximum camber=29.85%; position of maximum thickness =28.58%; and nose radius=5.47/6 of standard value.

The average turning angles just below the turbine disc and the loss coefficient are represented in Tables 3 and 4.

It was found that these results can be closely approximated by empirical formulas. In the case of the flow angle at the transition section exit, the turning angle θ can be described as:

$$\tan(\theta) = 0.238\frac{\tan(\beta)}{H}$$

where β is the IGV stagger angle and H is the collector-height-to-chimney-diameter ratio, h/D. This equation is compared to the full-scale CFD values in Fig. 16. The average error is 1.6%.

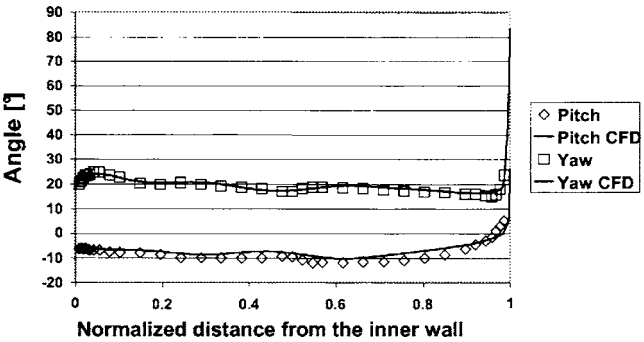

Fig. 15 Angles: row 7, configuration C, top

Table 3 Full-scale plant transition section average turning angle (deg)

Deck height	IGV stagger angle (deg)					
	0	10	20	25	30	35
0.20*D*	0.44	12.18	23.47	28.98	34.39	39.76
0.25*D*	0.44	9.74	19.13	23.85	28.63	33.46
0.30*D*	0.37	8.10	16.08	20.23	24.47	28.81
0.35*D*	0.30	6.31	13.84	17.50	21.30	25.26
0.40*D*	0.30	6.31	12.67	16.07	19.59	23.32

Table 4 Full-scale plant transition section loss coefficient

Deck height	IGV stagger angle (deg)					
	0	10	20	25	30	35
0.20*D*	0.0630	0.0668	0.0953	0.1228	0.1625	0.2257
0.25*D*	0.0434	0.0534	0.0722	0.0885	0.1189	0.1539
0.30*D*	0.0454	0.0467	0.0578	0.0702	0.0923	0.1067
0.35*D*	0.0427	0.0437	0.0524	0.0626	0.0778	0.0835
0.40*D*	0.0363	0.0368	0.0424	0.0483	0.0579	0.0661

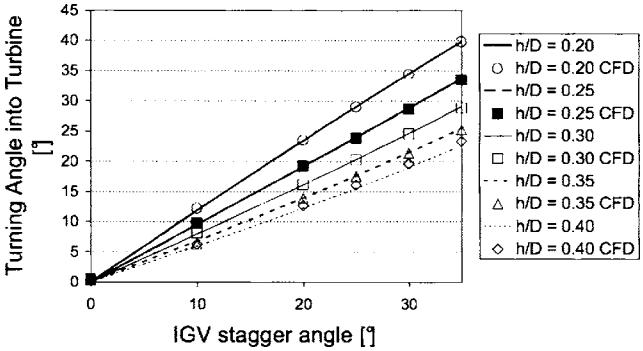

Fig. 16 Full-scale plant transition section exit average turning angle

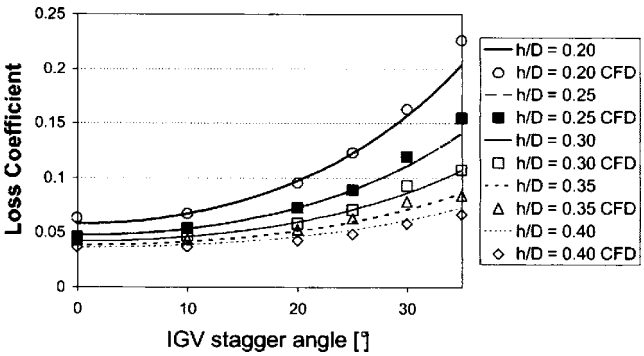

Fig. 17 Full-scale plant transition section loss coefficient

Table 5 Full-scale geometry performance for the four configurations

Configuration	Total pressure loss C_L	Average exit turning angle θ (deg)
A	0.0558	15.5
B	0.0771	22.9
C	0.0676	18.9
D	0.1060	26.7

It is reasonable to assume that the IGVs will contribute to the loss with a component proportional to the square of the velocity through the cascade. Therefore, the three primary loss mechanisms can be summarized as:

- Wall friction of the nonrotational flow component in the transition section
- IGV profile loss, which is proportional to the square of the total velocity through the cascade (proportional to $(\sec \beta)/H$).
- Wall friction of the rotational flow component into the chimney, which is proportional to $\tan \theta$

Curve fitting then yields a loss coefficient based on chimney conditions:

$$C_L \approx 0.0292 + 0.00114\left(\frac{\sec \beta}{H}\right)^2 + 0.190 \tan^2 \theta$$

This equation is compared to the full-scale CFD values seen in Fig. 17. The average error is 4.7%.

The performance of the full-scale geometry for the four configurations may be found by interpolating the full-scale CFD data. These results are summarized in Table 5. The loss coefficient for configuration A in the model was determined to be 0.098. According to CFD analyses for the full-scale geometry, the loss coefficient for configuration A is 0.056. The reduction in loss coefficient by a factor of 1.8 is close to the reduction in friction coefficient found on a Moody chart when the Reynolds number is increased from 10^5 to 10^8. This may explain the difference in loss coefficient between the model and the CFD predictions for the full-scale chimney.

Summary and Conclusions

The performance of a model transition section was computed and measured. Previous estimates for the transition section's loss coefficient were greater than 0.16, but they did not consider the Reynolds number scale effect. This research shows that the loss coefficient is 0.056 at full-scale Reynolds numbers for the geometry described by Gannon [10]. The CFD prediction of turbine inlet flow angles agrees very well with the experimental results. Transition section pressure loss agrees satisfactorily.

Semi-empirical equations were developed to predict the loss coefficient and turbine inlet flow angles of solar chimney power plants as dependent on collector deck height and inlet guide vane setting angle. The two empirical equations may be useful in solar chimney plant optimization studies.

Acknowledgment

The work was financially supported by the National Research Foundation of South Africa, partially through Professor D. G. Kröger, who also brought the work of Fried and Idelchik [11] to our attention.

References

[1] Schlaich, J., 1995, *The Solar Chimney, Electricity From the Sun*, Axel Menges, Stuttgart, Germany, pp. 6–52.
[2] Haaf, W., Friedrich, K., Mayr, G., and Schlaich, J., 1983, "Solar Chimneys Part 1: Principle and Construction of the Pilot Plant in Manzanares," Int. J. Sol. Energy, **2**, pp. 3–20.
[3] Mullett, L. B., 1987, "The Solar Chimney-Overall Efficiency, Design and Performance," Int. J. Ambient Energ., **8**(1), pp. 35–40.
[4] Pasumarthi, N., and Sherif, S. A., 1988, "Experimental and Theoretical Performance of a Demonstration Solar Chimney Model—Part I: Mathematical Model Development," Int. J. Energy Res., **22**, pp. 277–288.
[5] Gannon, A. J., and Von Backström, T. W., 2000, "Solar Chimney Analysis with System Loss and Solar Collector Performance," ASME J. Sol. Energy Eng., **122**, pp. 133–137.
[6] Kröger, D. G., and Buys, J. D., 2002, "Solar Chimney Power Plant Performance Characteristics," S. Afr.Inst. Mech. Eng. R&D J., **15**, pp. 31–36.
[7] Gannon, A. J., and Von Backström, T. W., 2003, "Solar Chimney Turbine Performance," ASME J. Sol. Energy Eng., **125**(1), pp. 101–106.
[8] Von Backström, T. W., Bernhardt, A., and Gannon, A. J., 2003, "Pressure Drop in Solar Power Plant Chimneys," ASME J. Sol. Energy Eng., **125**(2), pp. 165–169.
[9] White, F. M., 2003, *Fluid Mechanics*, 5th ed., McGraw-Hill Higher Education, New York, p. 390.
[10] Gannon, A. J., 2002, "Solar Chimney Turbine Performance," Ph.D. thesis, Department of Mechanical Engineering, University of Stellenbosch, South Africa.
[11] Fried, E., and Idelchik, I. E., 1989, *Flow Resistance: A Design Guide for Engineers*, Hemisphere, New York, p. 53.
[12] Schilling, R., Knapp, W., Bader, R., Fritz, J., and Mochkaai, Y., 1998, "Experimental and Theoretical Loss Analysis in a Kaplan Turbine," Int. J. Hydropow. Dams, **5**(6), pp. 63–67.
[13] Oberkampf, W. L., and Blottner, F. G., 1998, "Issues in Computational Fluid Dynamics Code Verification and Validation," AIAA J., **36**(5), pp. 687–695.
[14] Kirstein, C. F., 2004, "Flow Through a Solar Chimney Transition Duct," Master's thesis, Department of Mechanical Engineering, University of Stellenbosch, South Africa.
[15] White, F. M., 1991, *Viscous Fluid Flow*, 2nd ed., McGraw-Hill International Editions, New York.
[16] Hall, P., 1982, "Taylor-Görtler Vortices in Fully Developed or Boundary-Layer Flows: Linear Theory," J. Fluid Mech., **124**, pp. 475–494.
[17] Von Backström, T. W., Kirstein, C. F., and Pillay, L. A., 2003, "The Influence of Some Secondary Effects on Solar Chimney Power Plant Performance," International Solar Energy Society, *Solar World Congress, ISES 2003*, Göteborg, Sweden, June 16–19.

Available online at www.sciencedirect.com
ScienceDirect
Solar Energy 82 (2008) 999–1008
SOLAR ENERGY
www.elsevier.com/locate/solener

Performance analysis of the power conversion unit of a solar chimney power plant

T.P. Fluri *, T.W. Von Backström

Department of Mechanical and Mechatronic Engineering, University of Stellenbosch, Private Bag X1, Matieland 7602, South Africa

Received 18 September 2006; received in revised form 14 April 2008; accepted 8 May 2008
Available online 5 June 2008

Communicated by: Associate Editor S.A. Sherif

Abstract

The power conversion unit (PCU) of a large solar chimney power plant consists of one or several turbogenerators, power electronics, a grid interface and the flow passage from collector exit to chimney inlet. The main goals of this paper are to analyze the performance of the PCU and its interaction with the plant as well as to compare three configurations from an efficiency and energy yield point of view.

First, a reference plant is defined and the plant performance data taken from simulations with a model found in the literature are analyzed, and the matching of the turbine(s) to the characteristic of the plant is discussed. It was found that a well designed turbine can be run at high efficiency over the entire operating range, as the plant performance data can be fitted using the ellipse law of Stodola.

Loss models for all components of the power conversion unit are then defined, and the impact of the various losses on the overall performance is assessed. Three configurations of the PCU are compared, i.e. the single vertical axis, the multiple vertical axis and the multiple horizontal axis turbine configuration. It is found that the single vertical axis turbine has a slight advantage with regards to efficiency and energy yield because certain loss mechanisms are not present. But its output torque is tremendous, making its feasibility questionable. It is shown that with designing the flow passage in an appropriate manner the aerodynamic losses can be kept low. The assumption made by many other researchers that the total-to-total efficiency of the PCU is 80 % has been confirmed with the present model. Further, it has been shown that the PCU efficiency deteriorates significantly with increasing diffuser area ratio but improves only slightly with reducing the diffuser area ratio below unity.

Keywords: Solar chimney power plant; Power conversion unit; Turbine; Ellipse law

1. Introduction

The main features of a solar chimney power plant are a solar collector and a tall chimney (Fig. 1a). The collector consists of a circular transparent roof and the ground under the collector floor surface. Solar radiation heats the ground, which in turn heats the air under the collector roof like in a greenhouse. The hot air rises and escapes through the chimney. The resulting airflow is used to generate electricity via one or several turbogenerators. A pilot plant was built and tested in the 1980s in Manzanares, Spain. No full scale solar chimney power plant has been built to date.

Besides the layout shown in Fig. 1.a, where a single vertical axis turbine is used, configurations with multiple vertical axis turbines (Fig. 1b) or multiple horizontal axis turbines (Fig. 1c) have also been proposed (e.g. by Schlaich (1995)).

Many mathematical models to predict the performance of solar chimney power plants have been proposed since the early 1980s. Haaf et al. (1983) present a simple model, which they used for the design of the pilot plant in

* Corresponding author. Tel.: +27 218084281.
E-mail address: thomas.fluri@alumni.ethz.ch (T.P. Fluri).

0038-092X/$ - see front matter © 2008 Elsevier Ltd. All rights reserved.
doi:10.1016/j.solener.2008.05.001

Nomenclature

A	area, m^2
C	velocity, m/s
C_p	pressure recovery coefficient
d	diameter, m
h	height, m
K	pressure loss coefficient
k	constant
p	pressure, Pa
r	radius, m
R_d	diffuser area ratio
T_q	torque, Nm
V	volume flow rate, m^3/s

Greek symbols

α	angle
η	efficiency
ζ	loss coefficient
ω	rotational speed, rad/s

Subscripts

amb	ambient
BM	bellmouth
c	component, chimney
col	collector
d	diffuser
ex	exit
h	hydraulic
hv	horizontal vertical transition
id	ideal
in	inlet
m	mixing
t	total condition
tt	total-to-total
ts	total-to-static

Abbreviations

CFD	computational fluid dynamics
DDPM	direct drive permanent magnet generator
PCU	power conversion unit
SCPCU	solar chimney power conversion unit

Manzanares. Pasumarthi and Sherif (1998a) show a more detailed model, which they verify against their own experimental results and results of the Manzanares pilot plant (Pasumarthi and Sherif, 1998b). Gannon and Von Backström (2000) adapted the standard gas turbine cycle to define a standard solar chimney cycle. Recent comprehensive models have been developed by Bernardes et al. (2003) and Pretorius and Kröger (2006b).

The above models usually use one of the PCU configurations without giving reasons for the choice. The only publications, which give a comparison of PCU configurations are a German diploma thesis (Kolb and Helmrich, 1996), in which the single vertical axis and the multiple horizontal axis configuration for a 200 MW plant are compared using CFD, and an article by Denantes and Bilgen (2006), who compare the torque of the various configurations in their study on counter rotating turbines.

The main objectives of the present study are (1) to determine the plant power production spectrum over a year, (2) to determine the required characteristics of the turbine(s) for them to be matching to the plant, (3) to assess the impact on losses of the various components of the PCU, (4) to compare the three PCU configurations mentioned earlier, the single vertical axis, the multiple vertical axis and the multiple horizontal axis turbine configuration, from an efficiency and energy yield per year point of view and (5) to determine typical efficiencies of the PCU.

In the first section, a reference plant is defined and the plant performance data taken from simulations with the model of Pretorius and Kröger (2006b) are analyzed. Loss models for all components of the power conversion unit are then introduced.

2. Plant performance data

The plant performance data used in this work have been generated with a simulation program described by Pretorius and Kröger (2006b). The program solves the relevant conservation of mass, momentum and energy equations for the collector and the chimney of a solar chimney power plant simultaneously using finite difference methods. Main features of the chosen reference plant are the collector diameter of 7.0 km, the chimney height of 1.5 km, the chimney diameter of 160 m, single collector glazing and no heat storage device. Ambient wind effects were not included, but chimney shadow effects were included in the simulation. The plant is assumed to be located near Sishen in the Northern Cape Province of South Africa (27.67° S, 23.0° E). The same meteorological data for one year have been used as by Pretorius and Kröger (2006b).

A widely used approach in wind turbine engineering to get a yield estimate for a specific location is to combine its wind speed distribution—how many hours per year does the wind blow at a certain wind speed—with the power curve of a potential wind turbine—how much power is produced at a certain wind speed (Gasch et al., 2002). Similarly we can extract the number of hours per year for each mass flow from the solar chimney performance data and multiply it with the average power produced at this mass flow

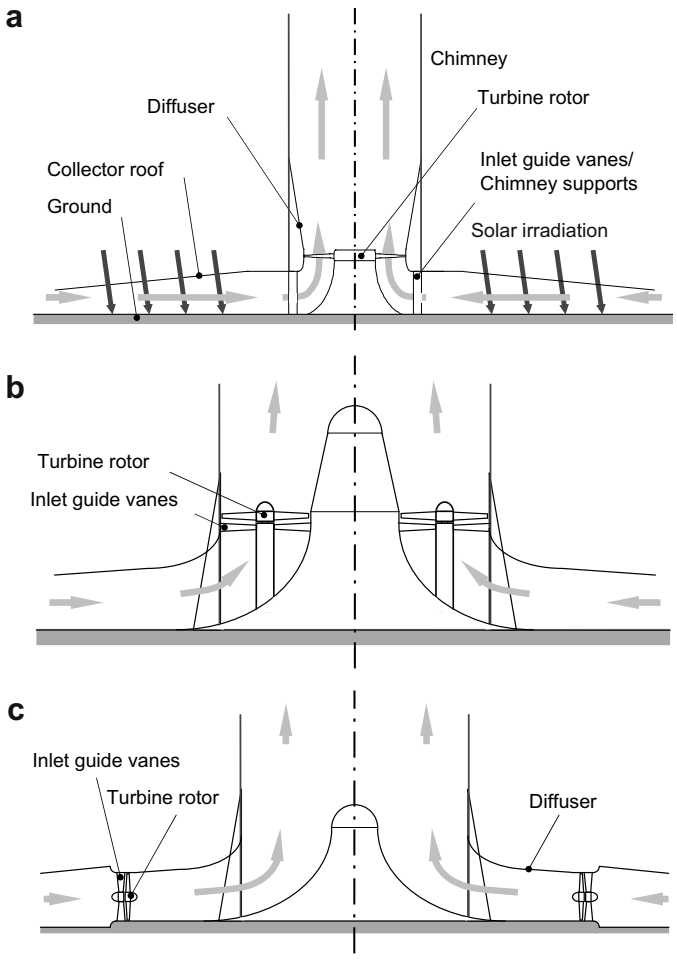

Fig. 1. Schematic of a solar chimney power plant.

to get a yield estimate and a power production spectrum (Fig. 2). To produce Fig. 2, the power was calculated from

$$P = \eta \Delta p_{tt} V \tag{1}$$

where Δp_{tt} is the total pressure drop over the PCU, V is the average volume flow in the turbine section (Pretorius and Kröger, 2006b) and η is the conversion efficiency from fluid power to electrical power. η has been assumed to be constant at 80%. Δp_{tt} and V have been extracted from the simulation results as summarized in Table 1. Most of the yearly yield is produced at a high mass flow rate (around 3×10^5 kg/s), but a significant portion is produced at a much lower mass flow rate (around 2×10^5 kg/s). In the reference data set the temperature at the turbine inlet ranges from 14.6 °C (7 am, 17th of June, $T_{amb} = 10.6$ °C) to 62.9 °C (2 pm, 15th of January, $T_{amb} = 30.5$ °C).

In Fig. 3 the turbine pressure ratio, p_{t1}/p_{t2} extracted from the simulation results is plotted against the inlet mass flow coefficient or "swallowing capacity", $\dot{m}\sqrt{T_{t1}}/p_{t1}$, for every hour of the year. Note that this relationship between pressure ratio and mass flow coefficient was obtained as a result of finding the flow rate that produces the maximum instantaneous power at each time step assuming a constant efficiency of the PCU of 80%. It turns out that the resulting curve can be fitted well using the ellipse law introduced by Stodola (1945), which according to Dixon (1998) reads

$$\dot{m}\frac{\sqrt{T_{t1}}}{p_{t1}} = k\left[1 - \left(\frac{p_{t2}}{p_{t1}}\right)^2\right]^{1/2} \tag{2}$$

where T_{t1} is the total temperature at the turbine inlet, p_{t1} and p_{t2} are the total pressures at inlet and outlet and k is

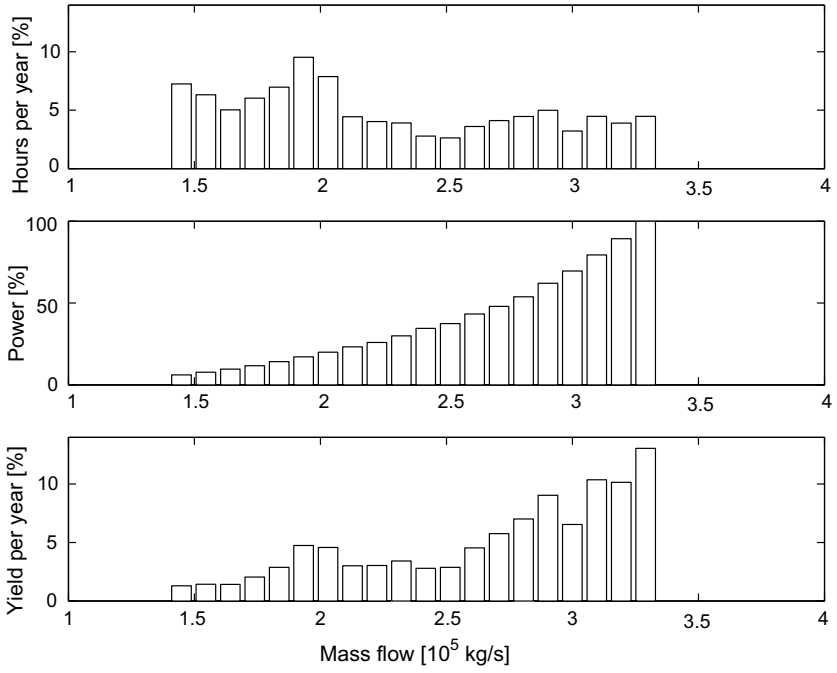

Fig. 2. Power production spectrum.

Table 1
Operating conditions extracted from plant simulation

Mass flow class	1	2	3	4	5	6	7	8	9	10
Hours per year	637	555	442	529	612	837	692	390	353	343
$p_{t1} - p_{t2}$, Pa	164	192	222	252	288	326	360	398	426	469
ρ, kg/m^3	1.08	1.07	1.06	1.05	1.04	1.03	1.02	1.02	1.03	1.02
T, °C	17	20	23	24	27	31	33	34	33	35
V, m^3/s	1.3	1.4	1.6	1.7	1.8	1.9	2.0	2.1	2.2	2.3
P, MW	18	22	28	33	41	49	57	67	74	86
	11	12	13	14	15	16	17	18	19	20
Hours per year	244	231	316	361	392	438	283	393	342	393
$p_{t1} - p_{t2}$, Pa	514	542	596	637	687	753	810	881	950	1020
ρ, kg/m^3	1.01	1.02	1.01	1.01	1.00	0.99	0.98	0.96	0.95	0.94
T, °C	36	34	37	38	39	45	47	52	56	60
V, m^3/s	2.4	2.5	2.6	2.7	2.8	3.0	3.1	3.2	3.4	3.5
P, MW	99	107	124	138	154	178	200	228	256	287

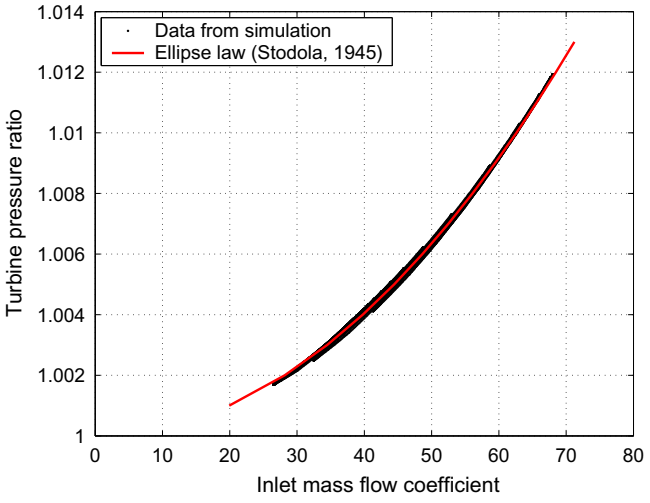

Fig. 3. Turbine pressure ratio vs. mass flow coefficient from simulations compared to a curve following the ellipse law of Stodola (1945).

a constant. The ellipse law has been used for many years to model the off-design behavior of multistage steam turbines. Dixon (1998) gives a derivation of that law employing the assumption that the blade speed is changed in direct proportion to the axial velocity. Adjusting the blade speed in such a manner ensures that the velocity triangles remain similar and so does the turbine efficiency. Hence, the fact that the operating points extracted from the simulations can be fitted well using the ellipse law indicates that a well designed turbine can be run at high efficiency over the entire operating range, especially if a variable speed drive train is used, i.e. the blade speed may be adjusted.

3. System loss modelling

The losses occurring in the PCU can be divided into three groups, namely aerodynamic, mechanical and electrical losses. The aerodynamic losses will be treated in detail and an analytical model is introduced for each loss component; the mechanical and electrical losses are summarized as drive train losses.

The loss models presented here have been implemented in Matlab. The optimization algorithm used is the function "fmincon", which is the Sequential Quadratic Programming implementation for constrained optimization in Matlab. A sample calculation is presented in Appendix A.

3.1. Intake losses

For the multiple horizontal shaft configuration Kolb and Helmrich (1996) propose a rather bulky intake geometry with converging sections and a transition from rectangular to circular and analyze it with CFD. Müller (2002) presents a similar investigation on the same geometry.

Here a circular bellmouth type intake is proposed, because consulting Idelchik (1986) it is found that with a bellmouth, which is much shorter than the geometry proposed by Kolb and Helmrich, lower inlet losses can be expected. Furthermore, a bellmouth provides a more uniform velocity profile leading to a smaller dynamic load on the rotor blades, while the cost of this alternative solution is not expected to be higher. Idelchik's data for a wall-mounted bellmouth can be approximated by

$$\zeta_{BM} = 0.5e^{-14.114(r/d_h)} \tag{3}$$

where r is the bellmouth radius and d_h is the hydraulic diameter of the duct (see Fig. 4). For this investigation

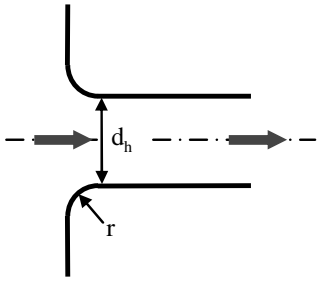

Fig. 4. Schematic of a wall-mounted bellmouth.

r/d_h is assumed to be 0.12, which gives an inlet loss coefficient of 0.09.

For the multiple vertical shaft configuration the same intake loss model is used, and, even though the geometry would look different, it is assumed to be good enough for a first approximation. For the single vertical shaft configuration no special intake is necessary, and the intake losses are accounted for in the horizontal-to-vertical transition loss model, which will be presented in a later section.

3.2. Turbine losses

Gannon and Von Backström (2002) proposed a single rotor layout for a large-scale solar chimney, in which they made use of the chimney support structure as inlet guide vanes. They present an analytical model for this layout, which is adapted from gas turbine literature, and they show that the inlet guide vanes improve the performance (Von Backström and Gannon, 2004). More recently, Denantes and Bilgen (2006) introduced an alternative layout consisting of one pair of counter rotating rotors, either with or without inlet guide vanes. They modified the analytical model of Von Backström and Gannon (2004) to accommodate layouts with counter rotating rotors and compare their performance to the one of the single rotor layout with inlet guide vanes. They find that the single rotor layout has a higher efficiency at the design point but a lower efficiency at off-design conditions.

Fluri and Von Backström (2008) present a comparison of various turbine layouts based on the work of Denantes and Bilgen (2006). However, they modified the evaluation of the turbine efficiency (radial averaging is implemented, and secondary losses are taken into account), they introduced a limit to the turbine reaction to avoid diffusion at the hub, and they assume a free-vortex turbine design.

The mathematical model for an axial turbine with inlet guide vanes presented by Fluri and Von Backström (2008) is used for all configurations in this investigation. Some assumptions used in that model are summarized here:

- In case of multiple turbines, the mass flow is equally shared by the various turbines.
- Constant axial velocity through turbine.
- Zero swirl at turbine inlet.
- Free vortex design.
- The Soderberg loss model, which is an analytical model commonly used in turbine design, is used to assess the aerodynamic losses in the turbine blade rows.

For the actual equations refer to Fluri and Von Backström (2008). Even though for a single vertical axis turbine the inverted Kaplan concept discussed, e.g. by Gannon (2002) would be used, the model for an axial through flow turbine is assumed to be adequate. In the present study the multiple vertical axis turbine configuration contains 6 and the multiple horizontal axis turbine configuration 32 turbines.

3.3. Diffusion losses

There are two areas in the solar chimney power conversion unit (SCPCU) where significant diffusion losses can occur; the first is after the turbine rotor(s) where the hub ends, the second is in the actual diffuser. Japikse and Baines (1994) give an overview on how to model a diffuser. Their nomenclature is adapted here; in this section the subscript "in" refers to the diffuser inlet and the subscript "ex" to the diffuser exit. The coefficient of static pressure recovery is defined as

$$C_p = \frac{p_{ex} - p_{in}}{p_{t,in} - p_{in}} \tag{4}$$

and the total pressure loss coefficient as

$$K = \frac{p_{t,in} - p_{t,ex}}{p_{t,in} - p_{in}} \tag{5}$$

They assume that the square of the mean velocity across any cross section is equal to the mean square of the velocity distribution and derive the ideal pressure recovery of a diffuser, $C_{p,id}$, as a function of the diffuser area ratio, R_d

$$C_{p,id} = 1 - R_d^{-2} \tag{6}$$

The diffuser effectiveness is defined as

$$\eta_d = C_p / C_{p,id} \tag{7}$$

As the exit diameter of the chimney is kept constant in this investigation, the only way of having a diffuser in the system is to make the upstream area smaller. Doing so will result in higher velocities and potentially increase the losses of the upstream components, e.g. the turbine(s). According to Japikse and Baines (1994) common diffuser effectiveness lies between 0.7 and 0.9. A conservative value of 70% is assumed here.

For the multiple horizontal axis turbine configuration it is assumed that for a small diffuser area ratio, $R_d < 1.3$, the area change is located before the horizontal-to-vertical transition section. For a higher diffuser area ratio the area change before the horizontal-to-vertical transition section is set to 1.3 and the remaining area change is assumed to take place in the chimney.

3.4. Mixing losses

With any multiple turbine configuration, losses will be generated where the outflow of the various turbines merge. Idelchik (1986) gives loss coefficients for merging of streams in a converging Y (Fig. 5). Obviously the geometry in the SCPCU looks quite different (Fig. 6), but due to the lack of more applicable data a loss coefficient is derived from this; for a Y with $\alpha = 15°$ and equal volume flow through the two inlet branches Idelchik gives a loss coefficient of 0.10. This value is employed in the present study.

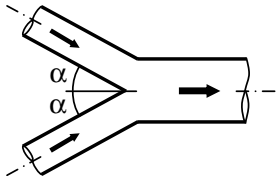

Fig. 5. Schematic of a converging *Y*-junction (adapted from Idelchick (1986), Diagram 7–30).

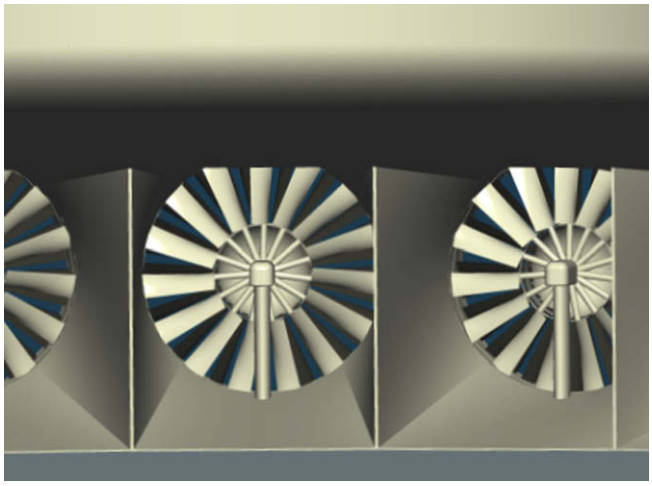

Fig. 6. CAD model of merging ducts at the exit of multiple turbines.

3.5. Horizontal-to-vertical flow transition losses

For the single vertical shaft configuration Kirstein and Von Backström (2006) present data for a horizontal-to-vertical flow transition section designed by Gannon (2002). They investigate various swirl angles. From CFD and for flow with no swirl they give loss coefficients between 0.036 and 0.063 for different inlet heights or, as they call it, different deck heights for a full scale plant. They measured loss coefficients of around 0.03 on a small scale model.

The horizontal-to-vertical flow transition section could also be modelled as a wall-mounted bellmouth with a facing baffle. Idelchik (1986) gives data for such a component and non-swirling flow for values of h/d_h between 0.1 and 0.8 and r/d_h between 0.2 and 0.5. Taking the geometry from Gannon, which gives an approximate value of $h/d_h = (0.36, 0.44)$ and $r/d_h = 0.056$ and linear inter-/extrapolation from the data of Idelchik loss coefficients of 0.098 and 0.080 are obtained for the two inlet heights.

In Idelchik's case there is no centerpiece in the transition section, however, which would prevent local diffusion and lower the losses (Fig. 7). Müller (2002), who works with a geometry for multiple turbines, finds that such a centerpiece can reduce the losses by 43%. Applying a correction factor of this order to the coefficients derived from Idelchik's data brings them reasonably close to the ones of Kirstein and Von Backström (2006).

Pretorius (2006) compares the annual power output from simulations using a loss coefficient for the horizontal-to-vertical flow transition section of 0.25 and 0.14. He finds that the higher loss coefficient reduces the annual power output by only 0.4%. Pretorius and Kröger (2006a) do the same comparison for a different plant configuration and find a reduction of the annual power output of 0.55%. Pretorius (2006) also mentions that his values are mere estimates.

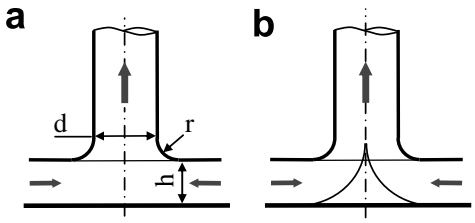

Fig. 7. Schematic drawing of horizontal-to-vertical transition section (a) without and (b) with a centerpiece to redirect the flow.

The above analysis of the work of Müller (2002), Idelchik (1986) and Kirstein and Von Backström (2006) indicates that a realistic value for the loss coefficient of the horizontal-to-vertical flow transition section is in the order of 0.05. For the present investigation this value is assumed for all configurations.

3.6. Other aerodynamic losses

The friction losses in the straight runs are insignificant in relation to the losses due to flow obstructions and components in the PCU and are neglected (Von Backström et al., 2003). The same applies to losses induced by the various struts, which can be shaped in a streamlined manner to keep the losses low. Windage losses are also neglected.

3.7. Drive train losses

In the present report the drive train includes all components necessary to convert the mechanical power delivered by the turbine rotor to electrical power ready for grid feeding, i.e. gearbox, electrical generator, power electronics and grid interface systems. For the multiple horizontal axis turbine configuration drive trains similar to the ones of large wind turbines can be used.

As part of the US Department of Energy's Wind Energy Program two reports on drive train design studies have been released: Poore and Lettenmaier (2003) present technical descriptions and economical analysis of several preliminary variable speed 1.5-MW wind turbine drive train designs. Effects of scaling to 3-MW or 750-kW plants are also discussed using scaling laws. Bywaters et al. (2004) present a similar study but instead of using scaling laws they make a detailed design for each configuration. While the first recommend a configuration with a single stage gearbox and a single permanent magnet generator for further investigation the latter give preference to a direct drive permanent magnet generator (DDPM); although the primary evaluation metrics, which are first cost and cost of

electricity, are similar for both configurations in their study, they see a higher potential for further cost reduction for the DDPM taking into consideration industry and market trends, e.g. the steady decline of cost of magnets and power electronics. Following this line of reasoning the DDPM has been chosen for the present study.

Bywaters et al. (2004) give efficiencies of between 90.1% and 92.4% for loads above 25% for a DDPM of 1.5-MW wind turbines. The efficiency only drops off at very low loads (80.8% efficiency at 6% load). For the same kind of drive train Poore and Lettenmaier (2003) give an almost constant efficiency of about 93% only dropping off at extremely low speeds. Following the more recent publication of Bywaters et al. (2004) a constant drive train efficiency of 91% is assumed for all configurations in this investigation.

4. Impact of various loss components

Using the above loss models the impact of each component on the overall performance of the plant can be assessed. In this section it is assumed that the plant described in Section 2 is operating at peak power, that a multiple horizontal axis turbine configuration is used and that there is no change in flow area from the turbine exit to the chimney inlet. Other configurations will be assessed in later sections.

In order to make all the losses comparable the pressure drops over the various components are translated into an efficiency. For the inlet, the mixing and the horizontal-to-vertical transition loss this is done with the following equation: $\eta_c = (\Delta p_{PCU} - \Delta p_c)/\Delta p_{PCU}$, where Δp_{PCU} is the pressure drop available across the whole PCU and Δp_c is the pressure drop over a specific component. For the exit losses the same equation is used but Δp_c is the exit dynamic head. The evaluation of the drive train and the turbine efficiency is described in Section 3.

The results are presented in Fig. 8. The inlet, the mixing and the horizontal-to-vertical transition section have a very small impact on the overall losses, while the exit losses are very important. The overall efficiency disregarding the exit losses is 80.1%; hence, very close to the 80% chosen by Pretorius and Kröger (2006b) and others before them.

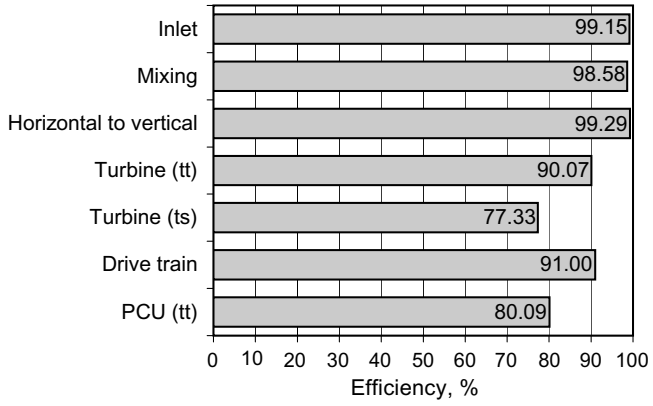

Fig. 8. Plot of efficiencies of the various components of the PCU for peak power conditions.

5. Performance of various configurations

From the results presented in the previous section it can be predicted that the differences in performance of the various configurations will be small; velocities are similar for all of them since the areas are similar, and only loss components with a low impact on the overall performance vary, e.g. mixing losses are obviously non-existent in a single turbine configuration.

This reflects well in Fig. 9 where the power output of different configurations at various operating conditions is shown; at all operating conditions the power is slightly lower for the multiple turbine configurations. As a consequence, the single turbine configuration generates the highest yearly energy yield (738.5 GWh). Both multiple turbine configurations generate 721.1 GWh, which is 97.6% of the above value.

As predicted in Section 2, the optimal turbine parameters and the PCU efficiency remain close to constant over the entire operating range. For the multiple horizontal axis turbine configuration, for example, the optimal parameters are as follows:

- Flow coefficient $\Phi = 0.321$ (± 0.005).
- Load coefficient $\Psi = 0.322$ (± 0.007).
- Degree of reaction $R_{n,a} = 0.771$.
- PCU total-to-total efficiency $\eta_{PCU} = 80.0\%$ (± 0.2).

For a definition of the turbine parameters Φ, Ψ and $R_{n,a}$ refer to Fluri and Von Backström (2008). η_{PCU} is defined as

$$\eta_{PCU} = T_q \omega \eta_{DT} / (\Delta p_{PCU} V) \quad (8)$$

where T_q is the torque on the turbine shaft, ω the rotational speed, η_{DT} the efficiency of the drive train, Δp_{PCU} the pres-

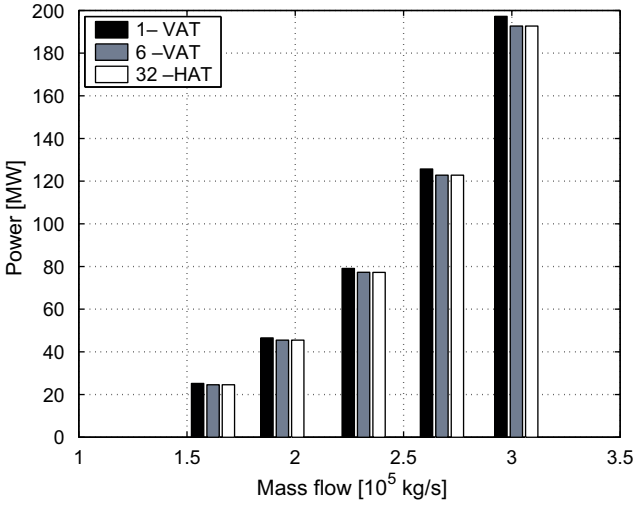

Fig. 9. Power output of different configurations at various operating conditions.

sure drop over the PCU and V the volume flow at the inlet of the PCU.

An important drawback of the configurations with few turbines is the high torque at each turbine; the single vertical turbine operates with a peak torque of 474.3 MNm, each of the six multiple vertical axis turbines at 31.3 MNm and each of the 32 multiple horizontal axis turbines at 2.63 MNm. Thanks to their higher rotational speeds also the overall torque of the multiple turbine configurations is lower for a similar power (187.7 MNm for the vertical and 84.0 MNm for the horizontal axis configuration), which reduces the cost, especially for the generators.

5.1. Nozzle or diffuser

In the above investigation it has been assumed that the turbine area is equal to the chimney area, i.e. the diffuser area ratio equals one. In this section the question is addressed whether it is favourable to have a nozzle or a diffuser downstream of the turbines.

Assuming that the chimney diameter is given, there remain two ways to change the diffuser area ratio and get a nozzle or a diffuser after the turbines: one can either change the number of turbines or their individual size. No matter which of these two options is chosen, or whether one opts for a combination of the two, the turbine efficiency deteriorates with increasing diffuser area ratio (Fig. 10).

Increasing the diffuser area ratio to 2.0, for example, reduces the total-to-total efficiency of the PCU by 15.3% and the efficiencies of the various components are as follows:

- Inlet: 96.59%.
- Mixing: 96.64%.
- Horizontal-to-vertical: 98.32%.
- Turbine (tt): 89.79%.
- Turbine (ts): 74.73%.
- PCU (tt): 64.79%.

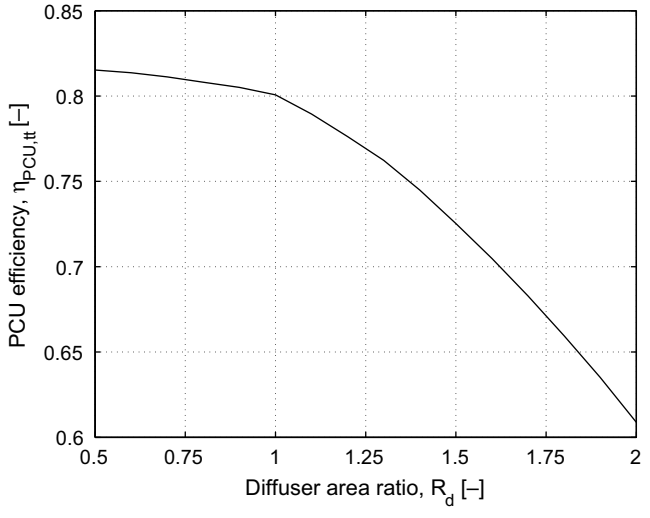

Fig. 10. PCU total-to-total efficiency vs. diffuser area ratio for multiple horizontal turbine configuration.

Fig. 10 also shows that reducing the diffuser area ratio below unity to get a nozzle after the turbine(s) increases the efficiency only slightly; e.g. doubling the total turbine area gives an efficiency benefit of 1.5 percentage points.

6. Conclusions

The plant power production spectrum has been determined over one year, and it was found that a well designed turbine can be run at high efficiency over the entire operating range, especially if a variable speed drive train is used.

A performance model for the SCPCU has been developed; loss models have been defined for all components of the PCU. A comparison of three configurations from an efficiency and energy yield point of view was made, and the impact of the various losses on the overall performance has been assessed.

The results show that, with designing the flow passages in an appropriate manner, the aerodynamic losses over the various components of the PCU can be kept low. The assumption made by many other researchers that the total-to-total efficiency of the PCU is 80% has been confirmed. The single vertical axis turbine has a slight advantage with regards to efficiency and energy yield because certain loss mechanisms are not present. But its peak output torque is tremendous, making its drive train costly and its feasibility questionable.

Further, it has been shown that the PCU efficiency deteriorates significantly with increasing diffuser area ratio but improves only slightly with reducing the diffuser area ratio below unity.

Acknowledgements

The authors would like to express their gratitude to the VolkswagenStiftung, Germany, and the National Research Foundation of South Africa for financial support and to Dr. J.P. Pretorius for providing the plant simulation results.

Appendix A. Sample calculation

The input data for the PCU performance model calculation can be found in Table 2. (Fig. 11) shows a schematic drawing of the solar chimney power conversion unit indicating the various stations in the flow passage; the station (0) refers to the collector exit, (1) to the turbine inlet (after the bellmouth), (2) to the turbine exit, (3) to the exit of the diffuser/nozzle directly after the turbine, (4) to the exit of the mixing section, (5) to the exit of the horizontal-to-vertical transition section and (6) to the exit of the diffuser section in the chimney.

Table 2
Input to the PCU performance model sample calculation

Chimney diameter, d_c, m	160
Number of turbines, Z_t	32
Diffuser area ratio, R_d	1.0
Stator blade aspect ratio, $R_{asp,s}$	4.0
Rotor blade aspect ratio, $R_{asp,r}$	3.0
Hub-to-tip radius ratio, R_{HT}	0.4
Inlet total pressure, p_{t0}, Pa	89,953
Inlet total temperature, T_{t0}, K	336
Exit total pressure, $p_{t,ex5}$, Pa	88,891
Mass flow rate, $\dot{m}$, ton/s	333.9
Specific gas constant, R, J/kg	287
Specific heat at constant pressure, C_p, J/(kg K)	1008
Ratio of specific heats, γ	1.4
Diffuser effectiveness, η_d	0.7
Drive train efficiency, η_{DT}	0.91
Horizontal-to-vertical transition loss coefficient, ζ_{hv}	0.05
Mixing loss coefficient, ζ_m	0.10
Bellmouth loss coefficient, ζ_{BM}	0.09

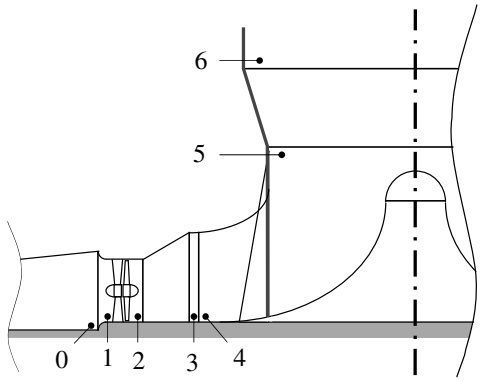

Fig. 11. Schematic drawing of the solar chimney power conversion unit indicating the various stations in the flow passage.

A.1. Pressure losses in the PCU flow passage

In this section it is shown, how the pressure drops over the various components of the PCU flow passage, excluding the turbine, are evaluated to get the boundary conditions for the turbine model.

The density of the air is assumed to be constant. It is assessed at the inlet of the PCU as $\rho = p_{t0}/(RT_{t0}) = 0.922\ \text{kg/m}^3$. The chimney area, $A_c = \pi D_c^2/4 = 20,106\ \text{m}^2$, and the flow velocity at the PCU exit, $C_6 = \dot{m}/(\rho A_c) = 18.0$ m/s, are evaluated. The static pressure at the PCU exit is then $p_6 = p_{t6} - 0.5\rho C_6^2$. Note that the swirl is assumed to be negligible. The flow velocity at the exit of the horizontal-to-vertical transition section is then $C_5 = C_6 R_{dc} = 18.0$ m/s. R_{dc} is the chimney diffuser area ratio A_6/A_5, which is 1.0 in the present case, as the overall diffuser area ratio R_d is also 1.0. The flow velocity is assumed to remain constant over the horizontal-to-vertical transition section and the mixing section: $C_5 = C_4 = C_3$. With $R_{dc} = 1.0$ the ideal pressure recovery of the diffuser in the chimney is

$$C_{p,id} = 1 - R_{dc}^{-2} = 0 \tag{A1}$$

From the rearranged Eq. (7) the coefficient of static pressure recovery becomes

$$C_p = \eta_d C_{p,id} = 0 \tag{A2}$$

Rearranging Eq. (4) the static pressure at the inlet of the chimney diffuser is

$$p_5 = p_6 - 0.5 C_p \rho C_5^2 = 88,892\ \text{Pa} \tag{A3}$$

Adding the dynamic head the total pressure is evaluated as $p_{t5} = p_5 + 0.5\rho C_5^2 = 89,041$ Pa. To evaluate the total pressure at the inlet of the horizontal-to-vertical transition section the definition of the loss coefficient is rearranged, giving

$$p_{t4} = p_{t5} + \zeta_{hv} 0.5 \rho C_5^2 = 89,048\ \text{Pa} \tag{A4}$$

Similarly the total pressure at the inlet of the mixing section is found as

$$p_{t3} = p_{t4} + \zeta_m 0.5 \rho C_4^2 = 89,063\ \text{Pa} \tag{A5}$$

Subtracting the dynamic head the static pressure is evaluated $p_3 = p_{t3} - 0.5\rho C_3^2 = 88,914$ Pa. The turbine exit diffuser area ratio $R_d = A_2/A_3$ is also 1.0 in the present case. The velocity at the turbine exit is $C_2 = C_3 R_d = 18.0$ m/s. If the turbine exit diffuser area ratio R_d is bigger than 1, the ideal pressure recovery coefficient and the coefficient of static pressure recovery are evaluated as in Eqs. (A1) and (A2) and the static pressure at the turbine exit is then

$$p_2 = p_3 - 0.5 C_p \rho C_2^2 = 88,914\ \text{Pa} \tag{A6}$$

If it is smaller than or equal to 1, the total pressure is assumed to remain constant, $p_{t2} = p_{t3}$, and to get the static pressure, p_2, the dynamic head is subtracted.

Assuming that the flow velocity is equal at the inlet and at the exit of the turbine ($C_1 = C_2$) and taking into account the loss over the bellmouth the total pressure at the turbine inlet is

$$p_{t1} = p_{t0} - \zeta_{BM} 0.5 \rho C_1^2 = 89,944\ \text{Pa} \tag{A7}$$

As an example for the evaluation of the component efficiencies the calculation of the efficiency of the bellmouth is given here

$$\eta_{BM} = (\Delta p_{PCU} - \Delta p_{BM})/\Delta p_{PCU} = 0.9915 \tag{A8}$$

Δp_{PCU} is the total-to-total pressure drop over the entire PCU

$$\Delta p_{PCU} = p_{t0} - p_{t6} = 1062\ \text{Pa} \tag{A9}$$

Δp_{BM} is the pressure drop over the bellmouth

$$\Delta p_{BM} = p_{t0} - p_{t1} = 9\ \text{Pa} \tag{A10}$$

References

Bernardes, M.A.d.S., Voss, A., Weinrebe, G., 2003. Thermal and technical analyses of solar chimneys. Solar Energy 75, 511–524.

Bywaters, G., John, V., Lynch, J., Mattila, P., Norton, G., Stowell, J., Salata, M., Labath, O., Chertok, A., Hablanian, D., 2004. Northern Power Systems WindPACT drive train alternative design study report.

Tech. Rep. NREL/SR-500-35524. National Renewable Energy Laboratory, Colorado, revised October, 2004.

Denantes, F., Bilgen, E., 2006. Counter-rotating turbines for solar chimney power plants. Renewable Energy 31, 1873–1891.

Dixon, S., 1998. Fluid Mechanics and Thermodynamics of Turbomachinery. Butterworth–Heinemann.

Fluri, T.P., Von Backström, T.W., 2008. Comparison of modelling approaches and layouts for solar chimney turbines. Solar Energy 82, 239–246.

Gannon, A.J., 2002. Solar chimney turbine performance. Ph.D. thesis, University of Stellenbosch.

Gannon, A.J., Von Backström, T.W., 2000. Solar chimney cycle analysis with system loss and solar collector performance. Journal of Solar Energy Engineering 122, 133–137.

Gannon, A.J., Von Backström, T.W., 2002. Solar chimney turbine part 1 of 2: design. In: International Solar Energy Conference, pp. 335–341.

Gasch, R., Twele, J., Schubert, M., 2002. Wind Power Plants – Fundamentals, Design, Construction and Operation. Solarpraxis AG.

Haaf, W., Friedrich, K., Mayr, G., Schlaich, J., 1983. Solar chimneys; Part I: Principle and construction of the pilot plant in Manzanares. International Journal of Solar Energy 2, 3–20.

Idelchik, I.E., 1986. Handbook of Hydraulic Resistance. Hemisphere Publishing Corporation.

Japikse, D., Baines, N.C., 1994. Introduction to Turbomachinery. Concepts ETI, Inc., Norwich.

Kirstein, C.F., Von Backström, T.W., 2006. Flow through a solar chimney power plant collector-to-chimney transition section. Journal of Solar Energy Engineering 128 (3), 312–317.

Kolb, S., Helmrich, T., 1996. Strömungstechnische Auslegung eines Aufwindkraftwerks mit 200 MW Leistung (Aerodynamic design of a 200 MW solar chimney power plant). Diploma thesis, Institut für Strömungsmechanik und hydraulische Strömungsmaschinen, Universität Stuttgart (in German).

Müller, M., 2002. Dreidimensionale Simulation der Strömungskontur eines Aufwindkraftwerks (Three dimensional simulation of the flow in a solar chimney power plant). Student research project, Institut für Strömungsmechanik und hydraulische Strömungsmaschinen, Universität Stuttgart (in German).

Pasumarthi, N., Sherif, S.A., 1998a. Experimental and theoretical performance of a demonstration solar chimney model – Part I: Mathematical model development. International Journal of Energy Research 22, 277–288.

Pasumarthi, N., Sherif, S.A., 1998b. Experimental and theoretical performance of a demonstration solar chimney model – Part II: Experimental and theoretical results and economic analysis. International Journal of Energy Research 22, 443–461.

Poore, R., Lettenmaier, T., 2003. WindPACT Advanced wind turbine drive train designs study. Tech. Rep. NREL/SR-500-33196. National Renewable Energy Laboratory, Colorado.

Pretorius, J.P., 2006. Optimization and control of a large-scale solar chimney power plant. Ph.D. thesis, University of Stellenbosch.

Pretorius, J.P., Kröger, D.G., 2006a. Critical evaluation of solar chimney power plant performance. Solar Energy 80, 535–544.

Pretorius, J.P., Kröger, D.G., 2006b. Solar chimney power plant performance. Journal of Solar Energy Engineering 128 (3), 302–311.

Schlaich, J., 1995. The Solar Chimney – Electricity from the Sun. Axel Menges.

Stodola, A., 1945. Steam and Gas Turbines. P. Smith.

Von Backström, T.W., Gannon, A.J., 2004. Solar chimney turbine characteristics. Solar Energy 76, 235–241.

Von Backström, T.W., Bernhardt, A., Gannon, A.J., 2003. Pressure drop in solar power plant chimneys. Journal of Solar Energy Engineering, Transactions of the ASME 125 (2), 165–169.

Available online at www.sciencedirect.com
SCIENCE DIRECT®
Applied Thermal Engineering 26 (2006) 200–208
APPLIED THERMAL ENGINEERING
www.elsevier.com/locate/apthermeng

Numerical investigation into the effect of cross-flow on the performance of axial flow fans in forced draught air-cooled heat exchangers

P.J. Hotchkiss [a], C.J. Meyer [a,*], T.W. von Backström [b]

[a] Department of Mechanical Engineering, University of Cape Town, Private Bag, Rondebosch 7701, South Africa
[b] Department of Mechanical Engineering, Private Bag X1, Matieland 7602, South Africa

Received 3 November 2004; accepted 20 May 2005
Available online 2 August 2005

Abstract

Air-cooled heat exchangers (ACHEs) which utilise large arrays of axial fans, commonly suffer from inlet flow losses related to off-axis flow into the fans. This investigation aims to extend current knowledge on the effect of off-axis inflow on the performance of axial fans in this type of installation. An actuator disk fan-model was developed for the Computational Fluid Dynamics (CFD) code, FLUENT™, and validated against experimental data for off-axis inflow angles up to 45°. Agreement between numerical and experimental pressure rise was good, although fan power consumption and fan static efficiency were under and over-predicted respectively. Experimentally observed trends were confirmed numerically: fan static pressure rise and efficiency were adversely affected, while fan power consumption was not significantly affected by the presence of cross-flow into the fan. The investigation revealed that while the torque characteristics over the outer portion of the fan blades are fundamental in determining the global fan power requirements, the net effect of cross-flow in this region is very small. Local variations of blade torque at diametrically opposed orientations more or less cancel each other out, explaining the independence of fan power consumption to cross-flow conditions. The adverse effect of off-axis inflow on fan static pressure rise was attributed to two factors: increased kinetic energy per unit volume at the fan exit, and greater dissipation through the fan itself. Off-axis inflow was found to affect fan-blade loading characteristics, with implications for blade fatigue.

Keywords: Actuator disk; Axial flow fan; Distorted flow; Off-axis inflow; Cross-flow; Fan performance

1. Introduction

Air-cooled heat exchangers (ACHEs) are used extensively in the petro-chemical, process and power industries. These installations typically utilise large numbers of vertically aligned axial flow fans, drawing in air from below, and forcing it upwards through heat exchanger bundles mounted above the fans. It is common for multiple fan-banks to be used adjacently, each bank consisting of any number of axially aligned fan pairs. An example of this type of installation, using two fan-banks, is shown in Fig. 1.

It may be noted that in ACHEs where many banks of fans are used, flow will not ordinarily cross symmetry-planes between identical fans, such as planes 1 and 2 represented in Fig. 1. Consequently, fans along the periphery of the array may have only one "open" side, while the inner fans must operate with none at all, necessarily drawing in air across the inlets of fans closer to the perimeter, shown again in Fig. 1. The resulting

* Corresponding author. Tel.: +27 21 650 3668; fax: +27 21 650 3240.
E-mail address: cmeyer@ebe.uct.ac.za (C.J. Meyer).

1359-4311/$ - see front matter © 2005 Elsevier Ltd. All rights reserved.
doi:10.1016/j.applthermaleng.2005.05.012

Nomenclature

A	fan exit area, m^2	α	kinetic energy correction coefficient
C_l	lift coefficient	γ	effective angle of attack, deg
$\dot{m}$	mass flow rate, kg/s	η	efficiency
$\bar{n}$	unit normal vector	ρ	density, kg/m^3
P_R	fan power consumption, W	ω	fan rotational speed, rad/s
Q	fan torque, N m		
R	fan outer radius, m	*Subscripts*	
r	radial location, m	ave	average
T	fan thrust, N	axl	axial (fan axis)
U	velocity magnitude, m/s	e	fan exit
$\overline{U}$	velocity vector, m/s	s	static
V	volume flow rate, m^3/s	Fs	fan static
v_c	cross-flow velocity component, m/s	Ft	fan total
Δp	pressure rise, N/m^2	i	fan inlet

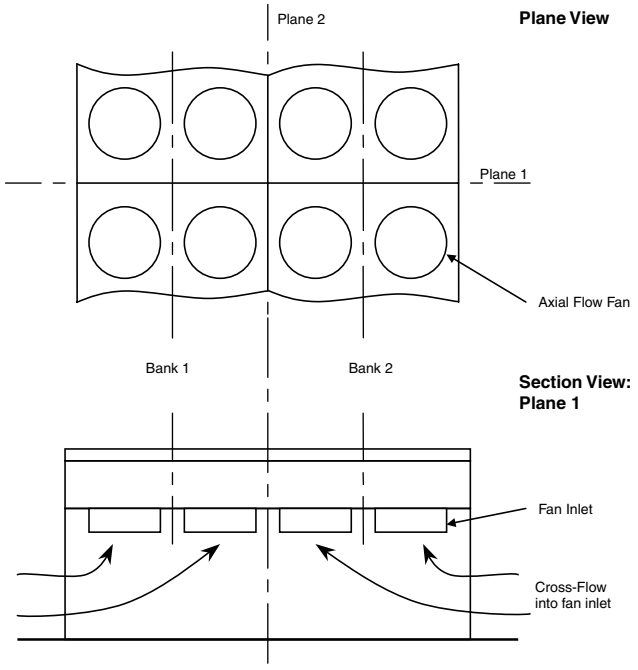

Fig. 1. Diagram representing part of an array of ACHEs consisting of two identical banks, and showing the induced cross-flow at the fan inlets.

maldistribution of flow at the fan inlets has been shown to have an adverse effect on fan performance, and ultimately the effectiveness of the cooling installation [1–6].

Monroe [1] described this type of fan inlet loss, advocating the use of a bell-shaped inlet section, and restriction of the cross-flow velocity component at the fan inlet to less than half the average velocity through the fan throat. The work of Speirs [2] indicated that installations comprising multiple fans are more sensitive than single fan units to reduction of the distance between ground level and fan inlet. A reduction in ground clearance would decrease the flow inlet area around the perimeter of the installation, increasing the cross-flow component at the fan inlets.

In general, such inlet flow losses in ACHEs have been attributed to two sources. The first, flow separation in the region of the fan inlet lip, is described by Russell and Peachey [3], Salta and Kröger [4] and Duvenhage et al. [5]. Fans on the perimeter of the array typically experience higher cross-flow velocities, with flow being drawn towards the interior by the inner fans, and are more likely to experience this type of flow-separation inlet loss.

Off-axis inflow, the second type of fan inlet condition associated with losses in ACHE arrays, was investigated by Stinnes and von Backström [6]. This condition is typically associated with fans in the interior of a large ACHE fan-cluster, for which the inlet flow velocities are not as large as those near the edges. Losses are primarily due to acute off-axis flow into the fan, rather than flow separation. Stinnes and von Backström [6] used a series of inlet duct sections to control the degree of cross-flow into an axial flow fan, illustrated in Fig. 2. This configuration allowed them to isolate the effects of off-axis inflow on the performance of axial flow fans, with results reported for inflow angles of up to 45°. Stinnes and von Backström [6] concluded that the fan power consumption is not adversely affected by cross-flow conditions, while the reduction in fan static pressure characteristics may be represented by the dynamic pressure based on the cross-flow velocity component.

The primary aim of the current investigation is to advance understanding of inflow losses related to the off-axis inflow conditions investigated by Stinnes and von Backström [6]. This is accomplished through the use of numerical techniques to generate detailed flow data in

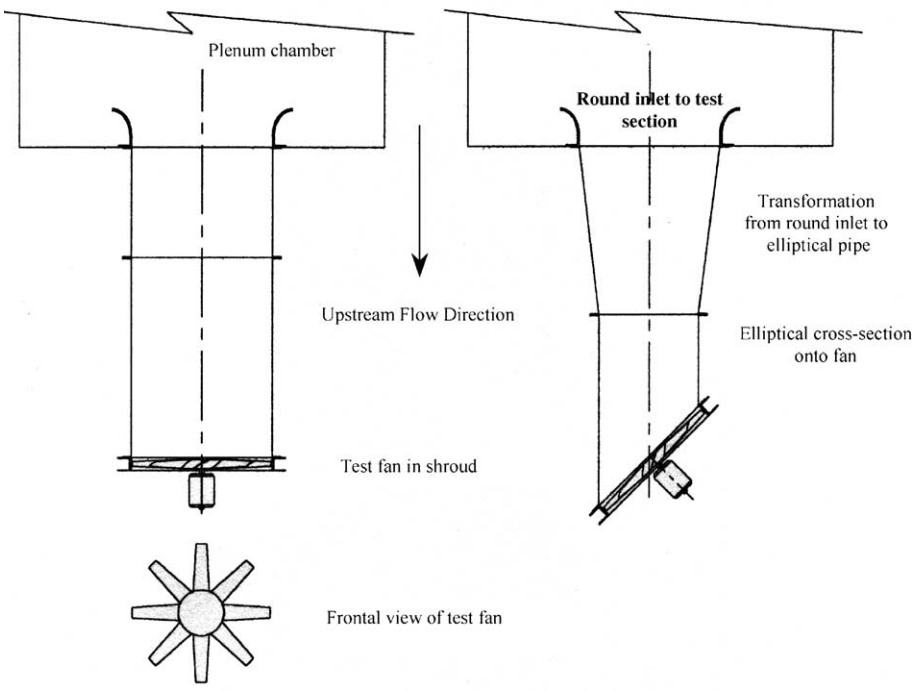

Fig. 2. Plane view showing the experimental model of Stinnes and von Backström [6].

the region of an axial flow fan subjected to off-axis inflow conditions. A numerical fan-model is developed from the methodology described by Meyer and Kröger [7] and its applicability extended to off-axis inflows through validation against the experimental data reported by Stinnes and von Backström [6]. The degree of flow maldistribution at the fan exit is investigated, and reasons are presented for the independence of fan power consumption to off-axis inflow. Finally, the effect of off-axis inflow on fan-blade loading is presented for inflow angles up to 45°. This information has significant implications for fan-blade fatigue in large ACHE arrays.

2. Computational models

The methodology described by Meyer and Kröger [7] is used to develop a numerical fan-model capable of dealing with off-axis inflow conditions. The model calculates the time-averaged aerodynamic forces exerted on the air by the fan blades within the blade-swept region, and permits the user to specify blade properties such as cross-sectional profile and orientation at a particular radial location. The calculated forces are included as source terms within the Reynolds-averaged Navier–Stokes equations for an incompressible fluid, which are solved by the commercial CFD solver, FLUENT™. The effects of turbulence are incorporated through the use of Launder and Spalding's [8] k–ϵ turbulence model.

3. Model geometry

The geometry of the computational model is constructed to represent the physical model of Stinnes and von Backström [6], illustrated in Fig. 2. Inlet ducts are used to create 0°, 14°, 27° and 45° off-axis flow into the fan, with each successive case representing a doubling of the cross-flow component.

The axial fan used in this investigation is the eight-bladed B2-fan tested by Stinnes and von Backström [6], and designed and tested by Bruneau [9]. This may be described as a medium chord fan, with both the blade chord and twist increasing from the blade tip to a maximum at the root. The blades are moulded glass-fibre with a smooth surface finish. Fan properties are given in Table 1.

4. Fan-model validation

The numerical fan-model is validated against experimental data reported by Stinnes and von Backström [6]

Table 1
Axial fan characteristics (B2-fan [9])

Fan casing diameter (mm)	Number of blades	Rotational speed (rpm)	Hub-to-tip diameter ratio	Blade profile	Root pitch angle (°)
1542	8	750	0.40	NASA-LS	28–32

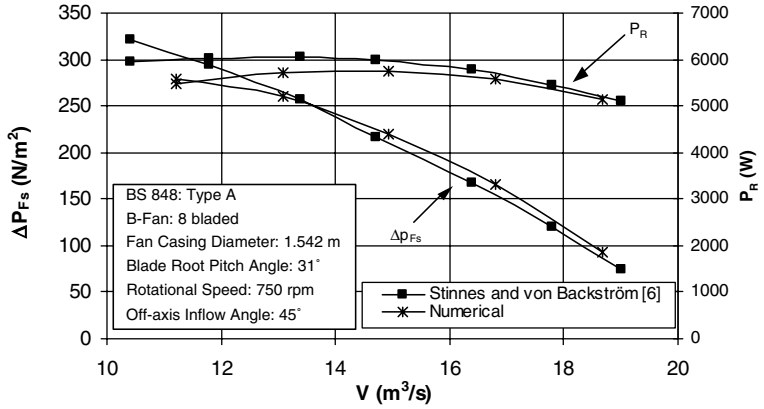

Fig. 3. Fan static pressure rise and power consumption vs. volume flow rate for a blade-root pitch angle of 31° and inlet angle of 45°.

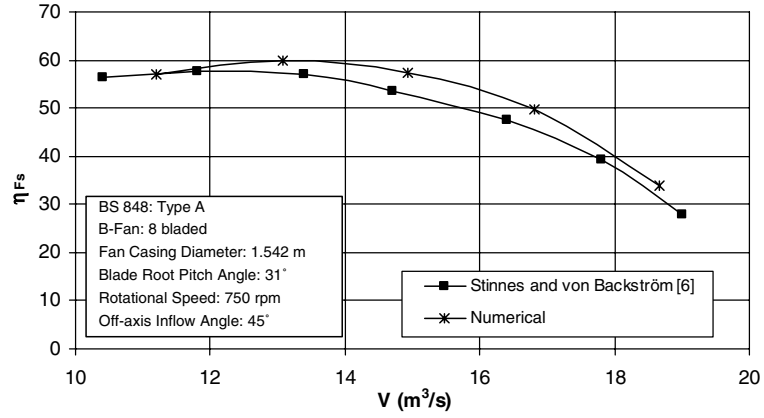

Fig. 4. Fan static efficiency vs. volume flow rate for a blade-root pitch angle of 31° and inlet angle of 45°.

for the B-fan designed by Bruneau [9]. These authors measured fan performance characteristics for off-axis inflow angles of 0°, 14°, 27° and 45° and according to specifications set in BS 848 [10] of the British Standards Organisation, for a type A (free inlet, free outlet) installation. This process is repeated numerically. Blade root pitch angles of 29°, 30°, 31° and 32° are used, this being defined as the included angle between blade chord and plane of rotation. The fan performance characteristics include fan static pressure rise, Δp_{Fs}, fan power consumption, P_{R}, and the fan static efficiency, η_{Fs}, plotted as a function of the volumetric flow rate, V (Figs. 3 and 4).

Agreement between experimental and numerical results is good. Fan static pressure rise is closely predicted by the numerical solution, while fan power consumption and fan static efficiency are under and over-predicted respectively. This error may be attributed to losses not accounted for in the numerical model. These include physical rotational instabilities, leading to increased mechanical losses, and tip effects due to the clearance between the fan-blade tips and the fan casing. Trends are nevertheless consistently predicted by the numerical model for inflow angles up to 45°.

5. Results and discussion

In determining the operating parameters of ACHEs, information regarding the fan performance characteristics is critical. Numerical results for fan power consumption and fan static pressure rise, for inflow angles up to 45°, are shown in Fig. 5, confirming the findings of Stinnes and von Backström [6]. These indicate that fan power consumption is independent of off-axis inflow angle, while static pressure rise and efficiency are adversely affected (note that $\eta_{\mathrm{Fs}} = \Delta p_{\mathrm{Fs}} \times V/P_{\mathrm{R}}$). The investigation aims to further understanding of these observations, as well as providing insight on particular blade loading characteristics resulting from off-axis inflow.

5.1. Fan power consumption independent of inflow angle

Diametrically opposing blade orientations of 0/180°, 45/225°, 90/270° and 135/315° were chosen as reference positions, with the cross-flow upstream component aligned with the azimuth 0° position (Fig. 6). In Fig. 7, the normalised deviation of torque along the length of opposing fan blades is plotted, being

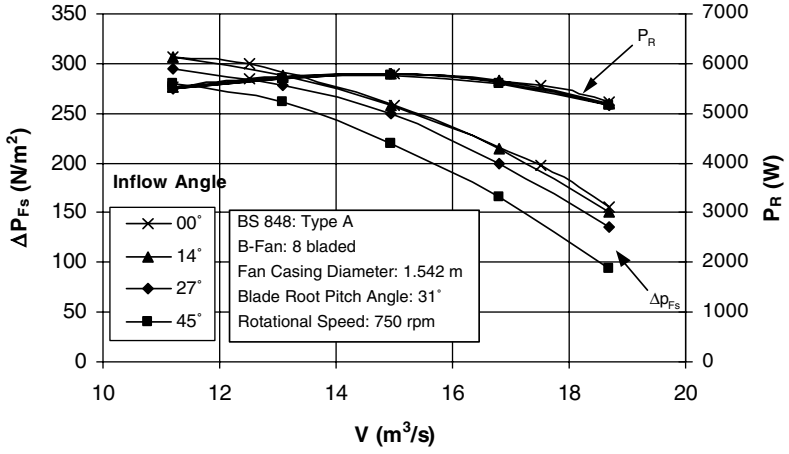

Fig. 5. Fan static pressure rise and power consumption vs. volume flow rate for a blade-root pitch angle of 31° and inlet angles of 0°, 14°, 27° and 45°.

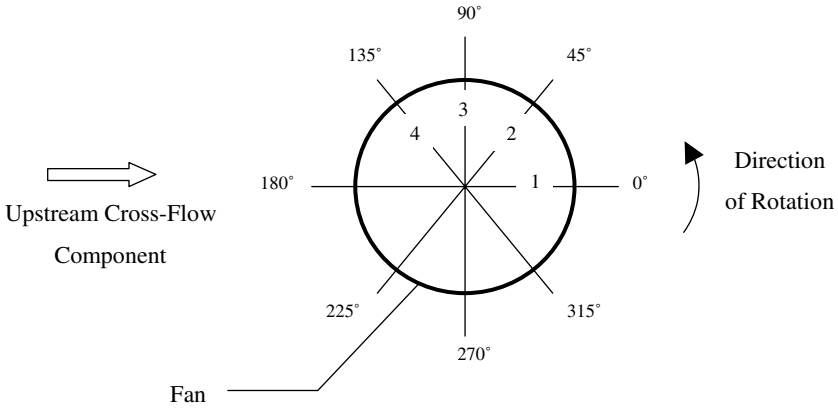

Fig. 6. Fan azimuth reference positions relative to the upstream cross-flow component.

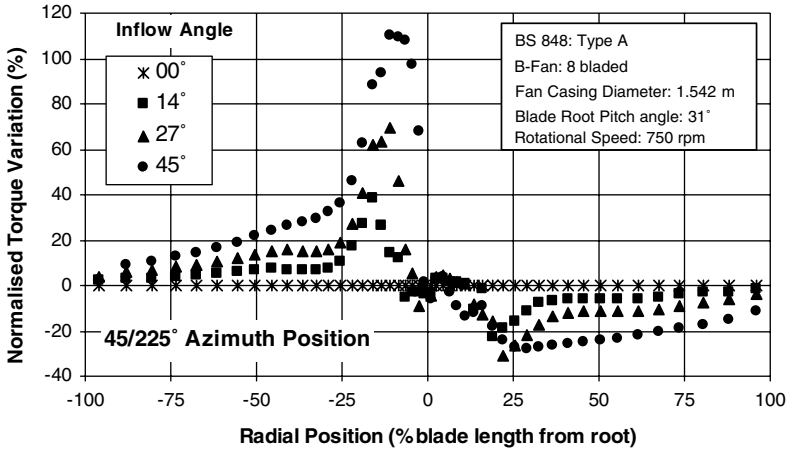

Fig. 7. Normalised fan-blade torque deviation (azimuth reference: 45/225°; off-axis inflow angle: 0°, 14°, 27°, 45°).

calculated as a percentage deviation relative to the 0° reference case. It is evident that, over the outer 75% of the blades span, increased torque values along the blade are matched by proportional decreases along the blade at a position advanced by 180°. This characteristic may be attributed to proportional deviations of angle-of-attack as the fan blades move relative to the cross-flow component.

Over the outer portion of the blades, the angle-of-attack is small, and the relationship with blade torque is linear. Small gains and losses in torque between opposing blade positions therefore more or less cancel each other out. Fig. 8 illustrates the effect of a velocity cross-flow component on the blade effective angle-of-attack and lift coefficient.

Fig. 7 indicates that the largest percentage changes in torque occur near the hub, but it is clear from Fig. 9 that the magnitude of the percentage point change in torque is relatively constant across the span. Torque magnitude at the blade tip is typically shown to be three times the average value, with approximately 70% of the total fan-torque due to loading on the outer half of the blade.

5.2. Fan static pressure rise adversely affected by increasing inflow angle

Fan static pressure characteristics are extremely important for cooling performance in ACHEs. Static pressure is required to overcome flow resistance within the heat exchanger bundle, and kinetic energy at the fan exit is commonly assumed to be dissipated within the plenum chamber. With fan power consumption independent of inflow angle, it was found that the adverse effect of off-axis inflow on fan static pressure rise may be attributed to a combination of increased kinetic energy per unit volume at the fan exit, and greater dissipation through the fan.

The kinetic energy correction coefficient, α, is defined by the expression

$$\int_A \frac{1}{2}U^2\rho(\overline{U}\cdot\bar{n})\mathrm{d}A = \alpha\left(\frac{1}{2}U_{\mathrm{ave}}^2\right)\dot{m} \tag{1}$$

and may be rearranged for the current case as

$$\alpha = \frac{\frac{1}{A}\int_A U^2(u_{\mathrm{axl}})\mathrm{d}A}{(u_{\mathrm{axl}})_{\mathrm{ave}}^3} \tag{2}$$

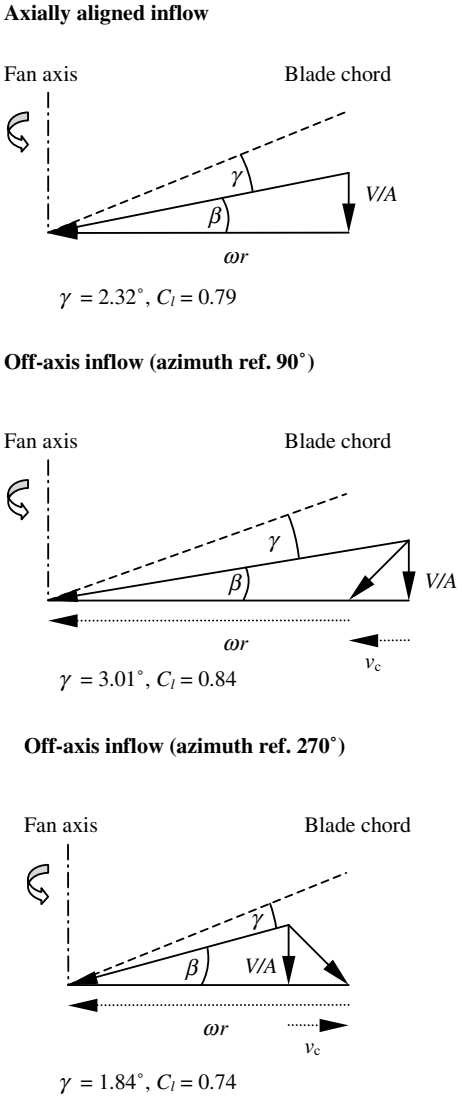

Fig. 8. Velocity triangles showing the small changes in angle-of-attack as a result of a velocity cross-flow component (γ and C_l values are reported here for a position at 67% of the blade span, and off-axis inflow angle of 27°).

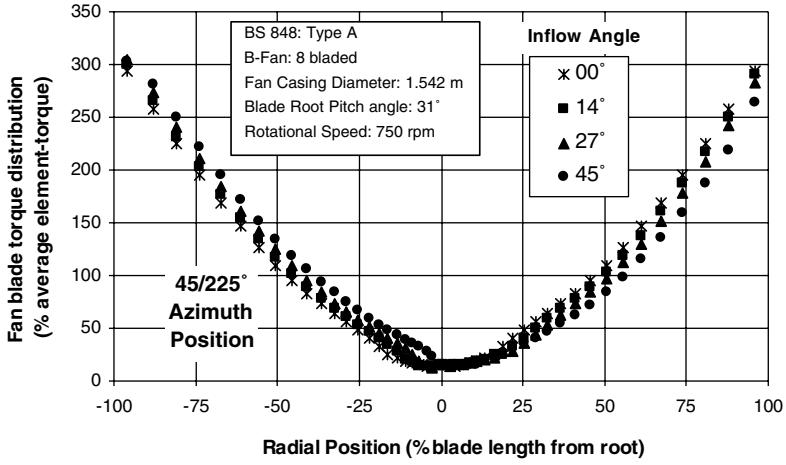

Fig. 9. Fan-blade torque distribution (azimuth reference: 45/225°; off-axis inflow angle: 0°, 14°, 27°, 45°).

where A is the area of the fan exit plane, U is the three-dimensional velocity magnitude at some location in the fan exit plane, u_{axl} is the axial velocity component at this location, and $(u_{axl})_{ave}$ is the average axial velocity at the exit plane.

Fan total-to-total pressure rise is calculated to determine the amount of energy lost due to viscous dissipation, and is defined by the expression

$$\Delta p_{Ft} = \left[p_s + \alpha\frac{1}{2}\rho(u_{axl})^2_{ave}\right]_e - \left[p_s + \alpha\frac{1}{2}\rho(u_{axl})^2_{ave}\right]_i \quad (3)$$

where α is assumed to be unity at the numerically defined fan inlet.

Figs. 10 and 11 present characteristics for ΔP_{Ft} and α respectively, for inflow angles up to 45°. The results suggest that the fan total-to-total pressure rise is not independent of off-axis inflow angle, as previously assumed by Stinnes and von Backström [6]. Careful reading of their paper however reveals that they were referring to the nominal exit total pressure. It is found by adding the dynamic pressure (assumed to be equal to inlet dynamic pressure) to the exit static pressure. A better formulation would have been to state that the static-to-static pressure rise is not affected by inflow angle.

Results confirm the validity of using the prediction model of Stinnes and von Backström [6] as an initial estimate for the effect of off-axis inflow on fan static performance. However, the data suggests that the reduction of fan static pressure rise with increasing inflow angle may in fact be attributed to two factors: increased dynamic pressure at the fan exit, accounting for between 50% and 60% of the fan static pressure rise reduction, and increased dissipation per unit volume through the fan. Fig. 10 shows an increase in the kinetic energy coefficients corresponding to greater off-axis inflow angles, indicating the rise in dynamic pressure at the fan exit. Fig. 11 shows fan total-to-total pressure rise decreasing with inflow angle, with this energy loss per unit volume attributed to increased dissipation through the fan. It should be noted that the kinetic energy coefficient values shown in Fig. 10, for axial inflow, correspond closely with those reported by Meyer and Kröger [11] in an investigation into the effect of fan performance on ACHE plenum chamber aerodynamic behavior.

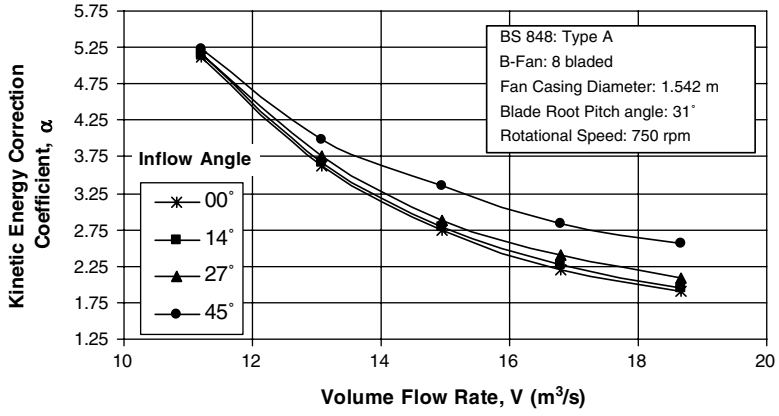

Fig. 10. Kinetic energy correction coefficient at the fan exit, α, for a blade-root pitch angle of 31° and inlet angles of up to 45°.

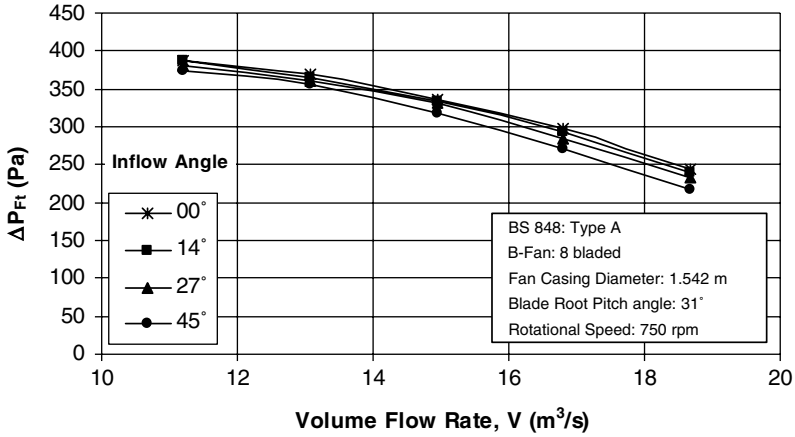

Fig. 11. Fan total-to-total pressure rise, for a blade-root pitch angle of 31° and inlet angles of up to 45°.

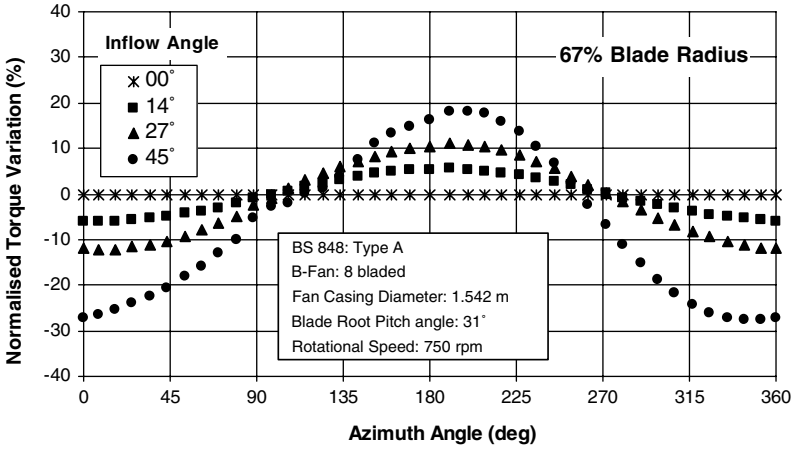

Fig. 12. Normalised azimuthal torque variation at 2/3 blade radius.

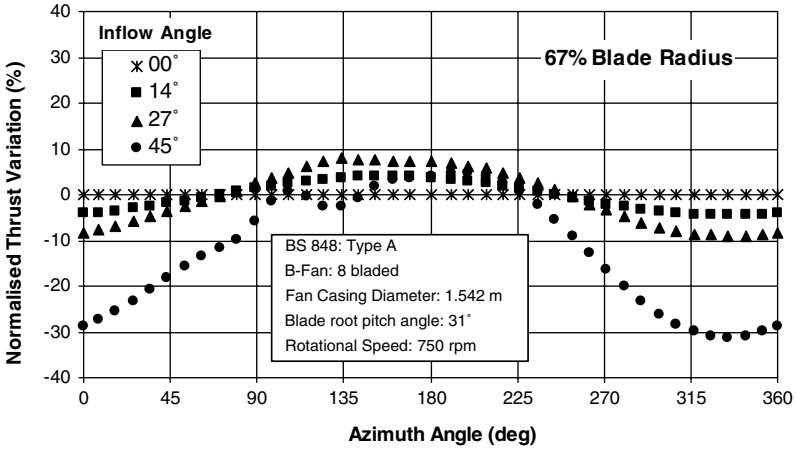

Fig. 13. Normalised azimuthal thrust variation at 2/3 blade radius.

A summation of the change in dynamic pressure content at the fan exit (based on the kinetic energy coefficient), and the additional energy lost to dissipation (from the changes in total-to-total pressure characteristics), yielded a combined pressure loss of similar magnitude to the measured reduction in fan static pressure rise. For example, with 45° off-axis inflow at $V = 15$ m^3/s, dynamic pressure at the fan exit increased relative to the 0° reference case by 23.1 Pa, while the total-to-total pressure difference was 19.2 Pa. Adding these values yields a total of 42.3 Pa, compared to the reduction of fan static pressure rise at this operating condition, of 40.1 Pa. Similarly, using the same configuration with $V = 18.7$ m^3/s, dynamic pressure increased by 40.8 Pa and total-to-total pressure difference was 27.1 Pa. The total of 67.9 Pa is compared to the reduction of fan static pressure rise at this operating condition, of 62.2 Pa.

The discrepancies, which range between 4% and 10%, may be attributed to the non-linearity of the situation; in cross-flow conditions the operating environment of the fan is altered slightly, affecting the fan performance characteristics.

5.3. Blade loading characteristics

The effect of cross-flow on blade loading has significant implications for the design of fan blades to withstand fatigue. The normalised variations of blade torque and thrust, expressed as a percentage difference from the 0° reference case, are shown in Figs. 12 and 13 respectively with respect to azimuth position. Off-axis inflow is shown to cause cyclic load variations, increasing with inflow angle, with large additional fluctuations visible for the 45° case in the region of the 90° azimuth position. This may be attributed to deviation of the blade angle of attack beyond the linear region of the lift and drag curves, for highly angled inflow.

6. Conclusions

This investigation has promoted a more thorough understanding of axial fan performance when subjected to inflow conditions such as may be found in large ACHE fan arrays. In addition, the numerical modeling

methodology was shown to be applicable to the simulation of an axial flow fan in off-axis inflow conditions.

Numerical results confirm the findings of Stinnes and von Backström [6]: fan power consumption was shown to remain independent of inflow angle, while fan static pressure rise and static efficiency were both adversely affected. The global fan power requirements were found to be dependent primarily on the torque characteristics over the outer portion of the fan blades. In this region, local increases or decreases of torque along blades in diametrically opposed orientations were found to more or less cancel each other out. Consequently, the net global effect of cross-flow on measured blade torque was very small, resulting in the observed independence of fan power consumption characteristics to inflow angle. The investigation has further demonstrated that the fan total-to-total pressure rise is not independent of off-axis inflow angle as previously assumed, and the decrease in fan static pressure rise with increasing inflow angle is in fact due to two factors: increased kinetic energy per unit volume at the fan exit, and greater dissipation through the fan itself.

The effect of cross-flow on fan-blade loading has been presented for inflow angles up to 45°. An azimuthal variation of both thrust and torque is evident, with magnitude increasing with inflow angle. Of particular significance are the additional load fluctuations present in conditions of highly off-axis inflow, evident for the 45° case. The amplitude of the variation in torque and thrust is about 40% of the axially aligned inflow mean values.

References

[1] R.C. Monroe, Improving cooling tower fan system efficiencies, Combustion Magazine 50 (11) (1979) 20–26.
[2] R.R.M. Speirs, Inlet tests on a full-size air-cooled heat exchanger, NEL/HTFS 12, H.T.F.S. Paper RS 361, National Engineering Laboratories, 1981, pp. 86–104.
[3] C.M.B. Russell, J. Peachey, Air inflow effects on fan performance in air cooled heat exchangers, International conference on fan design and applications, Guilford, England, 1982.
[4] C.A. Salta, D.G. Kröger, Effect of inlet flow distortions on fan performance in forced draught air-cooled heat exchangers, Heat Recovery Systems and CHP 15 (6) (1995).
[5] K. Duvenhage, J.A. Vermeulen, C.J. Meyer, D.G. Kröger, Flow distortions at the fan inlet of forced-draught air-cooled heat exchangers, Applied Thermal Engineering 16 (8/9) (1996) 741–752.
[6] W.H. Stinnes, T.W. von Backström, Effect of cross-flow on the performance of air-cooled heat exchanger fans, Applied Thermal Engineering 22 (2002) 1403–1415.
[7] C.J. Meyer, D.G. Kröger, Numerical simulation of the flow field in the vicinity of an axial flow fan, International Journal for Numerical Methods in Fluids 36 (2001) 947–969.
[8] F.M. White, Viscous Fluid Flow, McGraw-Hill Book Company Inc., 1991.
[9] P.R.P. Bruneau, The design of a single rotor axial flow fan for cooling tower application, Thesis for the degree of Master of Engineering (Mechanical), University of Stellenbosch, South Africa, 1994.
[10] British Standards Institution. Part 1: Methods of testing performance, Fans for general purposes, BS 848, 1980.
[11] C.J. Meyer, D.G. Kröger, Numerical investigation of the effect of fan performance on forced draught air-cooled heat exchanger plenum chamber aerodynamic behaviour, Applied Thermal Engineering 24 (2004) 359–371.

CFD Simulation of Helicopter Flow Fields Using an Actuator Disk Main Rotor Model

R. Heise[a], C.J. Meyer[b], T.W. von Backström[c]

Received 27 October 2006, in revised form 29 September 2007 and accepted 8 October June 2007

This paper presents the findings of simulating a helicopter fuselage in the presence of a rotor, using computational fluid dynamics. The objective is to simulate steady state rotorcraft fuselage aerodynamics. An actuator disc model is used to simulate the main rotor for the current simulations. The analysis presented here was conducted on the ROBIN fuselage, as substantial experimental data is available on this configuration. Initially a trial series was conducted on a fuselage-only configuration. The actuator disc model used for the simulations is unique in that it calculates the section angle of attack by referencing to upstream and downstream values of the rotor disk, unlike standard models which reference to the flow inside the disc. Thus more accurate answers can be obtained, even for skewed inflows. Acceptable agreement with the experimental data was obtained here, with the asymmetric pressure distribution being captured, though noticeable differences were detected. The rotor hub was also considered in the simulations, using actuator disk theory as well.

Nomenclature

Roman

A_1, B_1	Cyclic pitch angles [degrees]
C_p	Pressure coefficient, $C_p = \frac{p}{\rho V_t^2} \times 100$
C_T	Thrust coefficient, $C_T = \frac{T}{\rho \pi R^2 V_t^2}$
R	Rotor radius, also forms parameter for ROBIN fuselage [m]
U	Free stream velocity [m/s]
V_t	Rotor tip velocity [m/s]

Greek

α_σ	Rotor shaft angle [degrees]
θ_o	Rotor collective pitch angle [degrees]
μ	Advance ratio, $\mu = \frac{U}{V_t}$
ϕ	Polar angular coordinate used for the definition of the ROBIN fuselage [degrees]
ρ	Air density [kg/m3]
σ	Rotor solidity
Ψ	Rotor azimuth angle [degrees]
Ω	Rotor speed, 2000 [rad/s]

Presented at the 31st European Rotorcraft Forum, Florence, Italy, 13-15 September 2005.

[a] Dept. of Mechanical and Mechatronic Engineering, University of Stellenbosch, South Africa
E-mail: rheise@csir.co.za

[b] Dept. of Mechanical Engineering, Univerisity of Cape Town, South Africa

[c] MSAIMechE, Dept. of Mechanical and Mechatronic Engineering, University of Stellenbosch, South Africa.

1. Introduction

Much development has been done on actuator disks for applications in helicopters, either for rotor performance analysis or fuselage aerodynamics, with various degrees of success having been achieved (Chaffin and Berry[1], Lee and Kwon[2]).

Recently computing resources became available that allow for detailed and transient analyses of helicopter aerodynamics, including moving meshes to model individual rotor blades. For helicopter fuselage aerodynamic evaluations an actuator disc model is sufficient if a non-transient solution is sought that requires the modelling of the passage of the blades and associated tip vortices. The current study investigates the agreement of numerical solutions with experimental data, to form a basis for further aerodynamic studies, such as intake performance.

1.1 Actuator disk

A new approach to the modelling of the actuator disk is used. Air approaching an airfoil experiences an up-wash ahead of the airfoil, and thus the section angle of attack must be measured upstream of the airfoil section. Thus for an actuator disk the section angle of attack must be picked up a small distance upstream of the actuator disk, as first suggested by Thiart and von Backström[3] and refined by Meyer and Kröger[4]. The section angle of attack is calculated by the average flow vectors from a finite distance ahead of the actuator disk and behind it. This concept has been shown to give exceptional results when compared to the experimental data of skew inflows to industrial fans (Hotchkiss et al.[5]). These results gave confidence to use the same code to model helicopter rotors.

The actuator disk forms a volume in the flow domain that is normally occupied by the rotor into which the momentum sources are introduced, with an identically meshed volume upstream and downstream of the rotor volume. The upstream volume is placed about one blade chord length directly above the actuator disk, with a sufficiently fine mesh in between to capture the spin-up of the incoming flow. The error of the blade section angle of attack formed by placing the upstream disk not strictly upstream with the skewed inflow is assumed to be small; at least at slow advance ratios, flow vectors do not change significantly for a given small region that affects a given blade section. This could however be a problem at high advance ratios. The actuator disk for the current application does not include any coning or tilt of the tip path plane, but blade pitching was modelled using the standard Fourier harmonic series of

$$\theta = \theta_o - A_1 \cos\psi - B_1 \sin\psi \qquad (1)$$

Balancing of the rotor was done on an iterative basis, with the assumption that the response to the pitching coefficients is linear.

2. Fuselage Only Simulations

In preparation the ROBIN fuselage was evaluated without the rotor to define mesh sizing and compare turbulence models. Experimental data based on the work by Freeman and Mineck[6] is available of a ROBIN fuselage only configuration in a wind tunnel. For this test case the fuselage was modelled at an angle of attack of –10° with zero yaw. Due to the symmetry only one half of the flow domain was simulated. The experimental data is however not exactly symmetrical. The experimental data is in the form of pressure measurements taken at several stations on the fuselage surface, which are compared to the computational fluid dynamics (CFD) data.

The commercial CFD code Fluent (version 6.1) was used for the simulations, with the grid being created in Gambit. For the fuselage only simulations the mesh included up to 630 000 cells. The near wall mesh was constructed to give y^+ values of below $y^+ = 4$ for the expected flows around the fuselage. A y^+ value of 4 or less was selected in order that the laminar sublayer would be resolved for better results from the turbulence models. A guess for the height of the first element can readily be determined from basic boundary layer theory along with the thickness of the boundary layer itself. It was further aimed to keep at least 10 elements in the estimated boundary layer for sufficient resolution of the entire boundary layer. The mesh near the wall consisted of prismatic elements, and for this specific application of the 2 m ROBIN fuselage the first element had a height of 0.05 mm. After reducing the surface mesh length to 15 mm (0.75% of fuselage length) grid independence was obtained. This is of the same order as the mesh used by Chaffin and Berry[1] for similar studies. Full use was made of the unstructured mesh to allow the elements to grow to the selected volume mesh size. Four finite volume mesh sizes were used and tested for grid convergence; namely 35, 30, 25 and 20 mm. For all sizes good agreement to the experimental data was obtained, with the change from 25 to 20 mm not yielding any significant improvements. The coarser 35 mm mesh is still useful as sufficiently accurate answers are still obtained and fewer computing resources are required.

Consecutive tests were done on all the grid sizes to select a turbulence model. Turbulence Models that were evaluated were the k-ε, k-ω, shear stress transport (SST), Spalart-Allmaras and detached eddy simulation (DES) models. Surface pressures were compared along four cross-sectional stations as indicated in figure 1 to figure 4. The data presented here is for the 25 mm volume and 15 mm surface mesh. The pressures are non-dimensionalised with the wind tunnel free stream conditions, which for this case is 21.2 m/s at standard atmospheric conditions. The solutions typically converged after 800 iterations.

The data on the cross sectional stations is presented as a function of ϕ, the polar angular coordinate used for the definition of the ROBIN fuselage. The use of ϕ instead of the commonly used z-coordinate allows for a better presentation and comparison of the data on the upper and lower surfaces of the fuselage.

Good agreement with the experimental data is obtained for all the models over most of the cross sections. At the first station at $x = 0.350$R (figure 1) the k-ω model gives an unrealistically high pressure on the upper surface ($\phi = 90°$) along with a too low pressure below the fuselage. At the station just behind the cowling (figure 2) most turbulence models give good answers, with the SST and k-ω models lying closest to the experimental data. The Spalart-Allmaras and DES models give almost identical results, which results from the near wall treatment of the DES model with the Spalart-Allmaras model and the fact that no significant flow separation occurs to modify the global flow pattern. All models however under-predict the pressure on top of the fuselage ($\phi = 90°$), which could be as a result of the over-prediction of the wake of the cowling. The difference between experimental and numerical data at the bottom of the fuselage is as a result of the wake of the model support strut, which is not modelled in the CFD simulations. The last two stations at $x = 1.135$R and $x = 1.540$R (figure 3 and figure 4) show a separation point on the side of the fuselage at around the $\phi = 60°$ radial, which can be seen by the sharp reversal of the pressure plot. None of the evaluated turbulence models captured the separation point exactly, with the SST model coming closest. The k-ω model however predicts the pressure distribution on the bottom half the best. The discrepancy between the numerical and experimental data at the last two cross sections is assumed to be, in part, due to an insufficiently fine surface mesh that will capture the separation point correctly.

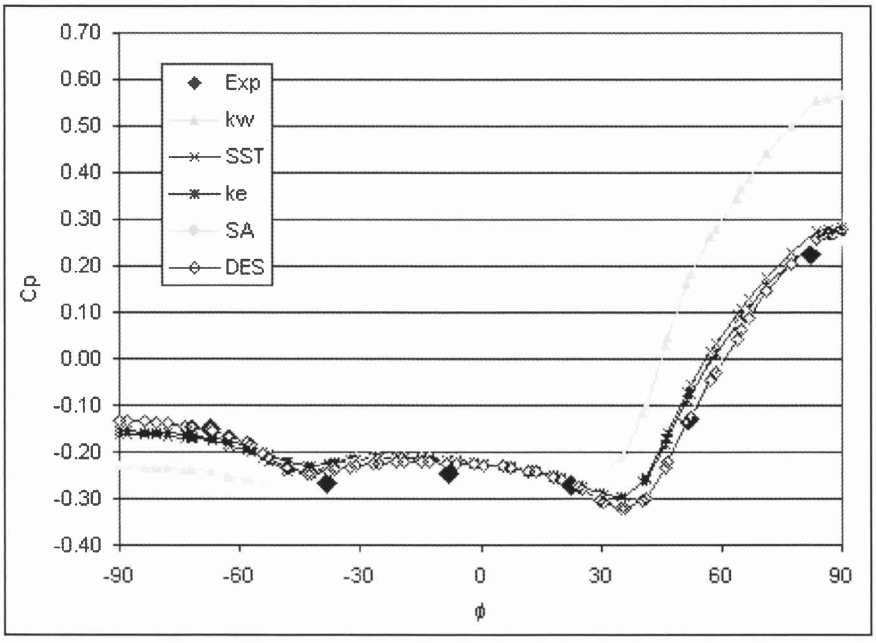

Figure 1: Pressure distribution, fuselage only, x = 0.350R

For the range of turbulence models tested, on average, the SST model performs the best over the range of compared experimental data. It is thus the model selected to be used for the full rotor and fuselage simulations. These CFD simulations were conducted using Fluent version 6.1. Subsequent test runs with the later release, version 6.2, yielded better answers than the older results, the 35 mm mesh giving more accurate results than the 20 mm mesh on the 6.1 solver. This follows as a result of the improved numerics in the solver for better spatial accuracy, especially for tetrahedral meshes such as used for the current application[7]. For consistency, only the results of the 6.1 solver are shown.

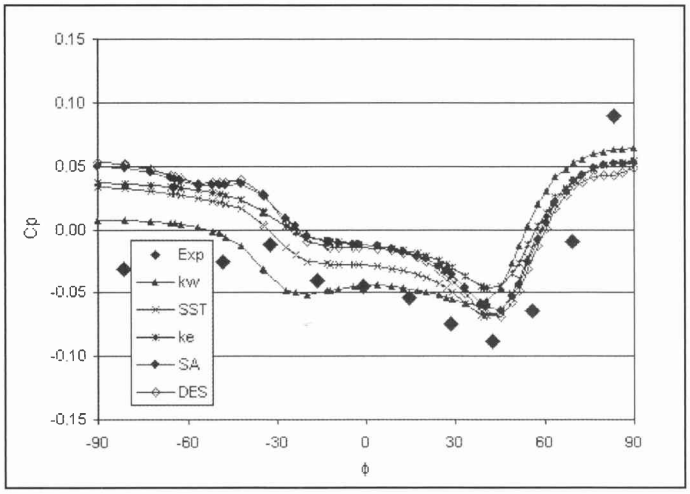

Figure 2: Pressure distribution, fuselage only, x = 1.170R

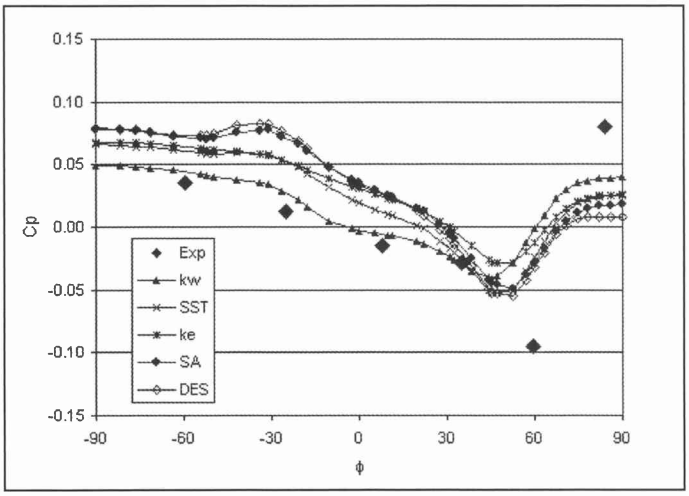

Figure 3: Pressure distribution, fuselage only, x = 1.350R

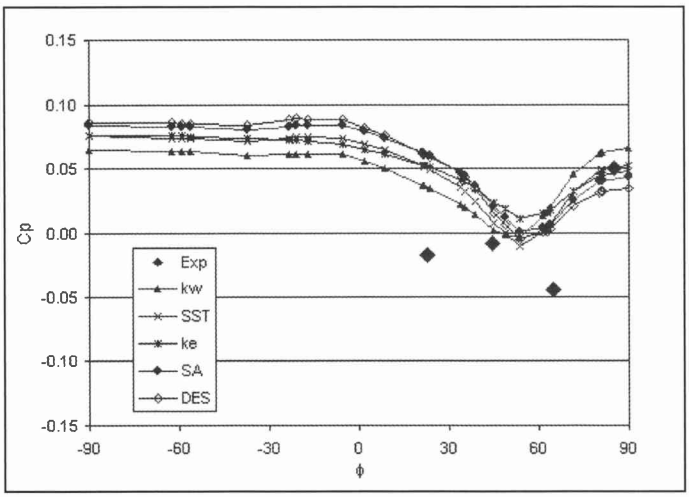

Figure 4: Pressure distribution, fuselage only, x = 1.540R

3. Rotor and Fuselage Simulations

For the initial validation process presented here of using the actuator disk as a helicopter rotor, the simulation was done for one advance ratio and thrust coefficient only. A case from Mineck and Althoff Gorton[8] was selected with an advance ratio of $\mu = 0.05$ and a thrust coefficient of CT = 0.00636. A low advance ratio case was chosen as in such a case the rotor wake impinges on most of the fuselage and the inflow into the rotor is sufficiently skew to test the capabilities of the actuator disk as a helicopter rotor.

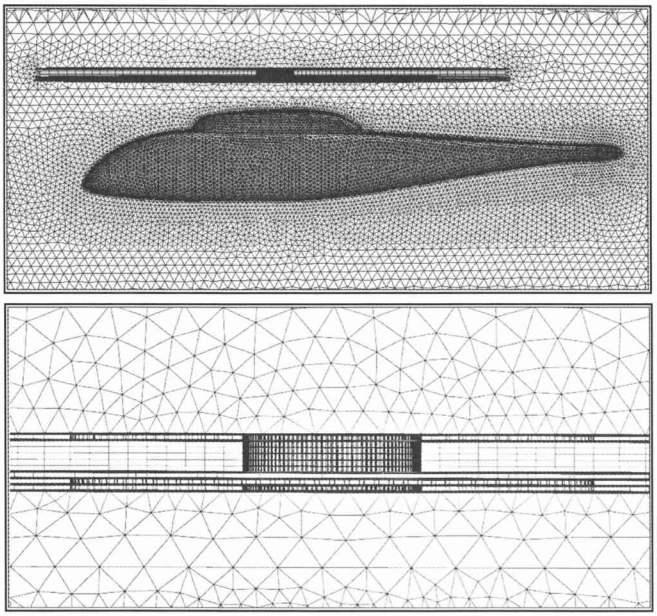

Figure 5: Mesh configuration for ROBIN and detail of rotor and hub mesh

The rotor and fuselage combination was modelled as arranged in the 4,27 m × 6,71 m wind tunnel. The mesh was based on the results of the previous fuselage only trials, this time however the entire flow domain was included to capture the three-dimensional flow effects from the rotor. The mesh now included 1.2 million cells. Added to the actuator disk model that simulates the rotor blades, was a second actuator disk (volume) that modelled the rotor hub, as shown in figure 5. Here the section lift and drag properties for the hub were defined as those of a cylinder. It is thought that the presence of the rotor hub can have a noticeable effect on the aerodynamics of the fuselage, especially in the region of the cowling.

Two sets of experimental data are available for the selected test case, namely from Freeman and Mineck[6] and Mineck and Althoff Gorton[8]. The CFD model was defined to mimic the Mineck tests. The difference of the Mineck data is that a smaller rotor of 0.86 times the defined rotor radius for the ROBIN geometry is used with a solidity of $\sigma = 0.098$ compared to the solidity of $\sigma = 0.0871$ of the Freeman data. However both data sets are used for comparison as they show the same trends of the pressure distribution.

4. Qualitative Analysis

When qualitatively comparing the CFD data to the oil flow experiments done by Mineck and Althoff Gorton[8] one notices that the streak lines for the selected thrust coefficient of $C_T = 0.00636$ do not follow the experimental streak lines closely. The angle of the numerical streak lines is too shallow, almost suggesting that the thrust coefficient used is too low. Based on this assumption a run was conducted for twice the specified thrust coefficient, and for this case the streak lines compare better with the experiments.

Figure 6 graphically compares the two cases to the experimental results on the advancing side of the fuselage; the dark streak lines are from the numerical simulations. On the nose and centre sections the streak lines are better predicted by the high thrust case. The streak lines on the cowling are also better captured with the high thrust case, as well as the wake of the hub at the trailing edge of the cowling and the convection of this wake down the starboard side that is evident from the experiments.

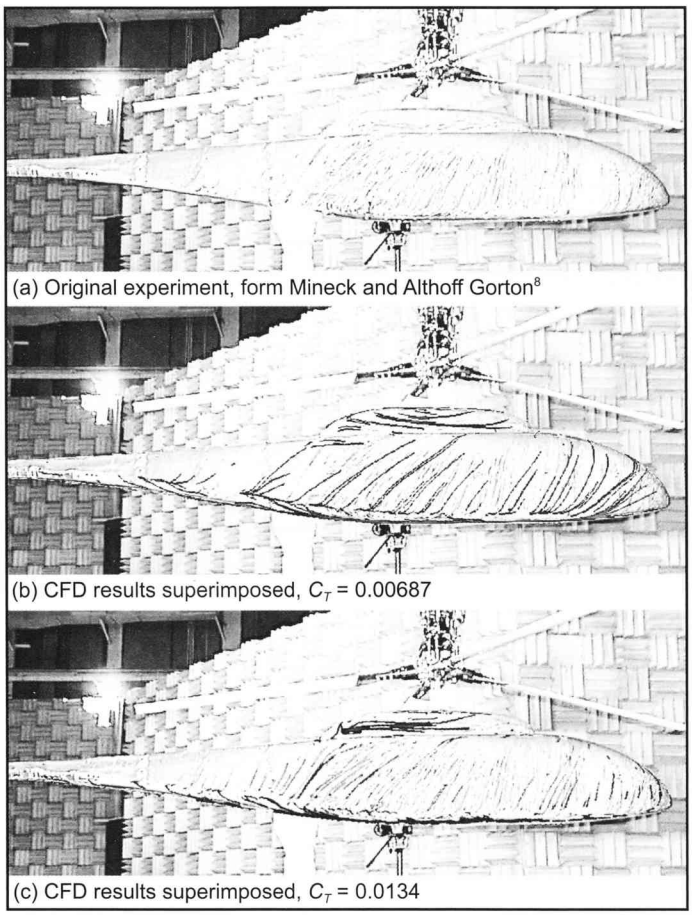

Figure 6: Streak lines, experimental versus numerical on advancing side

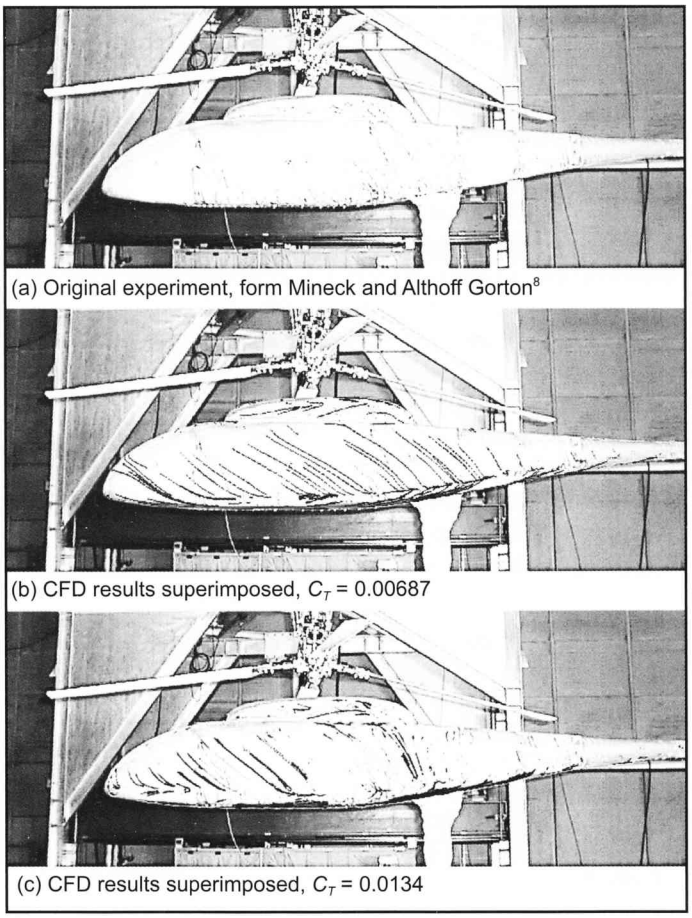

Figure 7: Streak lines, experimental versus numerical on retreating side

None of this is seen in the standard case, the streak lines again only conforming rearwards of the cowling.

5. Quantitative Analysis

The rotor was iteratively balanced to have a zero moment around the hub. Table 1 shows the collective and pitch angles obtained for the two cases, along with the experimental values from Mineck and Althoff Gorton[8]. The difference between the experimental and numeric values for the CT = 0.00636 conditions can mainly be attributed to a lack of coning of the rotor actuator disk.

Case	θ_o	A_1	B_1	α_s
Mineck and Althoff Gorton[8], C_T = 0.00636	11.9°	-1.3°	1.3°	0.0°
CFD, C_T = 0.00687	8.35°	-2.11°	1.25°	0.0°
CFD, C_T = 0.0134	14.72°	-1.73°	2.70°	0.0°

Table 1: Trimmed pitch conditions

Mineck and Althoff Gorton[8] supplies time-averaged data for 12 points measuring transient pressures on the upper surface of the centre line. First comparing the pressures on the centre line shows that the standard CT = 0.00636 case predicts the pressure on the top of the fuselage well; for most of the fuselage length the predictions lie close to the experimental values, except for the nose section and behind the cowling (figure 8).

The pressure distribution for the double thrust case is too high by a factor of two. There are however two sections in which that data predicts the trends well. The first is the nose section; although the pressure is predicted too high, the data predicts the higher pressure ahead of the cowling leading edge, which is not shown in the standard case. This higher pressure corresponds to the leading edge impact point of the rotor wake, which is correctly predicted by the double thrust case, as is also evident from the streak lines.

On the retreating side shown in figure 7 above, the nose forward of the rotor wake the streak lines predicted by the double

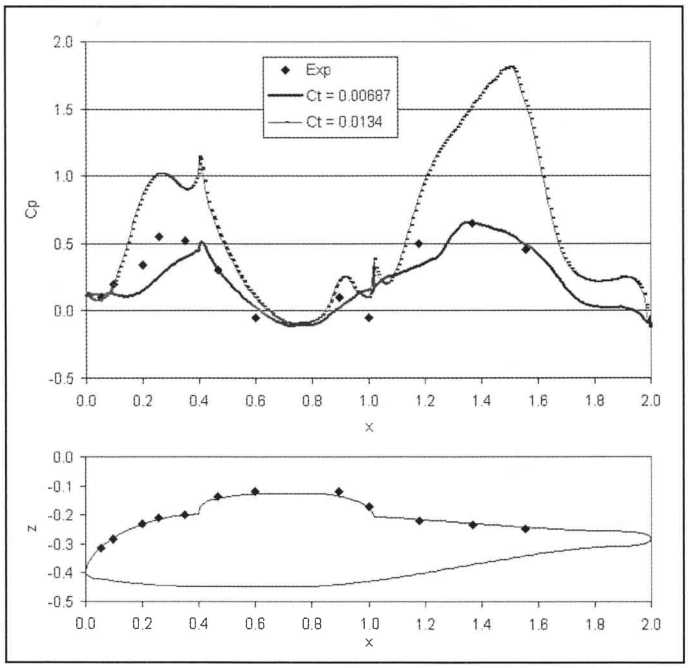

Figure 8: Pressure distribution on centre line, upper fuselage

thrust case are again much better predicted, similar also in the mid-fuselage section. The influence of the hub-wake, which is evident in the experiments, is also only presented in the high thrust case. Only towards the rear of the fuselage behind the cowling do the original results again compare well with the experiments. On the cowling the streak lines are not well presented.

The second area that the double thrust case predicts the trend well is at the trailing edge of the cowling. Though not exactly captured, the low-pressure region is as a result of the rotor hub. For the standard case no evidence of the hub wake is seen.

Comparing the pressure distributions at the four cross-sectional stations shows that, in general, the better the pressure on top of the fuselage is predicted (essentially the stagnation point) the better the pressure distribution around the fuselage is predicted. Data from Mineck and Althoff Gorton[8] is represented by "Exp 1" in the figures while data from Freeman and Mineck[6] is represented by "Exp 2".

For the station at $x = 0.350$R (figure 9) none of the two cases predicts the pressure distribution around the fuselage correctly, though the double thrust case again captures the trend better by displaying the low-pressure at the $\phi = -40°$ position on the advancing side. This is as a result of the rotor wake passing that position, which does not occur in the standard thrust case. The pressure contour on the upper half ($0° < \phi < 90°$ on advancing, $-90° < \phi < 0°$ on retreating side) on both sides is however sufficiently well predicted by the standard case. On the plot for the retreating side the predictions of Chaffin and Berry[9] (C&B on the legend) are plotted as well. Their predictions show a pressure trough at the $\phi = 40°$ position in figure 9 (b) which is not evident in the experiments. Therefore is attributed to a lack of prediction of the separation point on the lower corner of the fuselage in their simulations. Thus the current simulations are a small improvement of what has been achieved until now.

At the section $x = 1.170$R (figure 10) the double thrust case predicts the stagnation pressure well, and following on this the general pressure distribution is well presented. The low-pressure spike, (which is especially well presented by the Freeman and Mineck[6] data, $\phi = 40°$ on the advancing side) is a result of the hub-wake influencing that point. The shallower angle that the hub-wake forms for the standard case means that the wake does not have such a strong influence, as seen by the CFD data. The low-pressure trough on the upper surface ($\phi = -40°$) on the retreating side is, however, not captured by any of the two cases. None of the troughs on the retreating side are captured by the Chaffin and Berry[9] results. Noteworthy here is also the difference in the two experimental data sets.

For the last two sections at $x = 1.350$R and $x = 01.540$R (figure 11 and figure 12) both cases give reasonable answers, although the standard case on average gives more accurate results, especially, as already discussed, the pressure on the upper surface of the fuselage. Whereas the double thrust case over predicts the pressures, but clearly follows the trends.

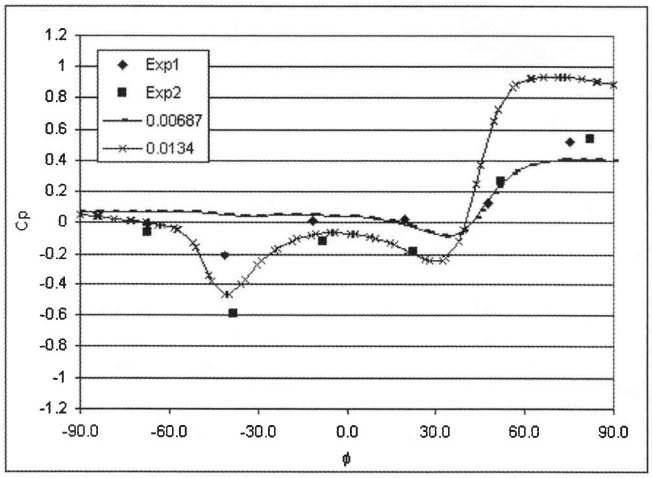

(a) Advancing

(b) Retreating

Figure 9: Pressure distribution around the fuselage at station x = 0.350R

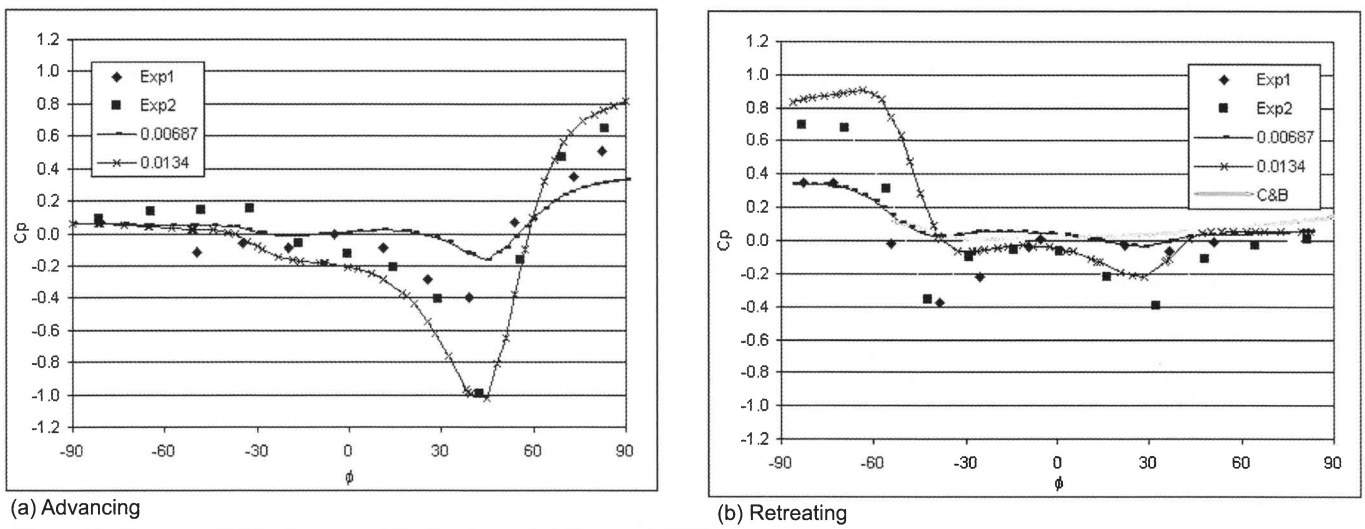

(a) Advancing

(b) Retreating

Figure 10: Pressure distribution around the fuselage at station x = 1.170R

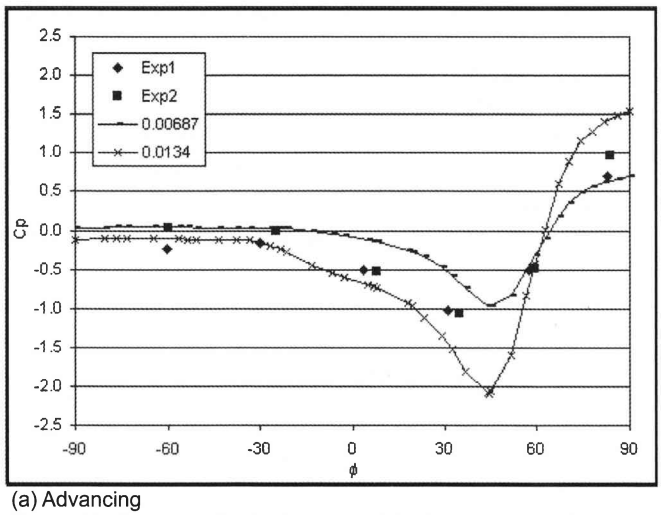

(a) Advancing

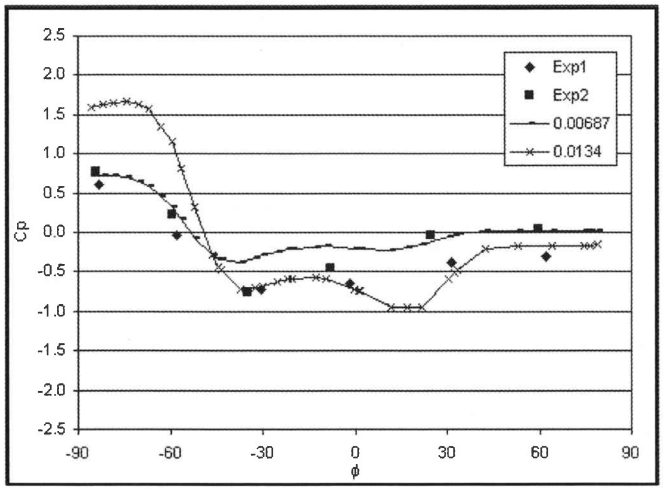

(b) Retreating

Figure 11: Pressure distribution around the fuselage at station x = 1.350R

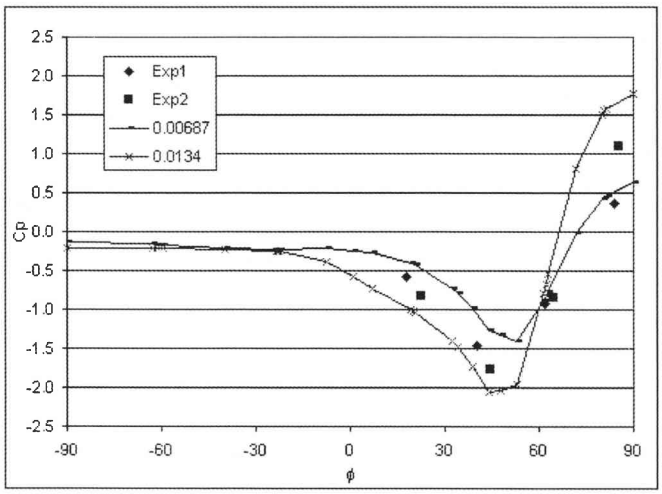

(a) Advancing

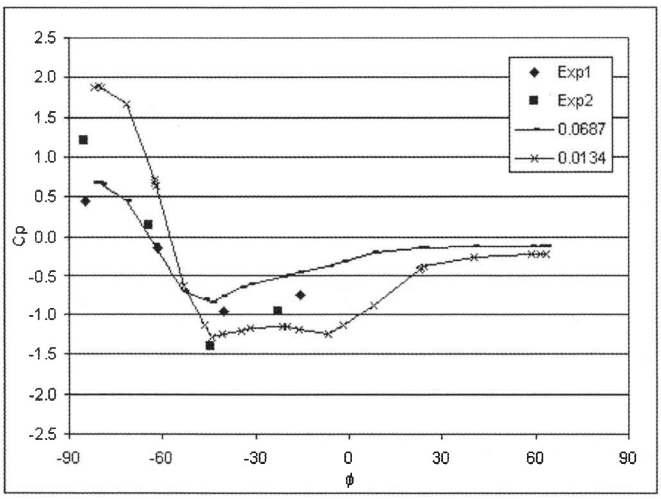

(b) Retreating

Figure 12: Pressure distribution around the fuselage at station x = 1.540

6. Effect of the Rotor Hub

The pressure measurements are of insufficient resolution to trace the effects of the rotor hub sufficiently; the only evidence being on the top surface just behind the cowling. The inclusion of the hub in the simulations could thus not be quantified explicitly. Qualitatively, the streamlines from the hub are compared in figure 13; figure (a) shows the streamlines through the hub with the hub actuator model included and figure (b) hub actuator model switched off. Clearly visible is a helix, which the streamlines form downstream of the hub on the advancing side of the fuselage. This flow pattern is not present in the case, where the hub is not modelled; the flow field is thus noticeably changed in the lee of the hub, which has important effects on the local aerodynamics of the fuselage. The hub wake also influences the trimming of the rotor. Also, due to the backwards "paddling" of the hub on the retreating side the airflow is further modified on that side.

7. Conclusion

Ruffin et al.[10] already indicated that the load distribution of the rotor disk has an important effect on the pressure distribution of the fuselage. In the current application the pressure distribution of the disk was not prescribed as applied by Ruffin et al.; rather the load distribution resulted from the trimming of the rotor disk with the pitching coefficients. Thus the pressure predictions are improved.

From the foregone analysis it would appear that a significant contribution to the differences of the numerical data is the angle the rotor wake makes relative to the fuselage. Using the average induced velocity from the CFD results in a basic momentum analysis confirms that the actuator disk does produce the specified thrust. Further comparing the load distribution of the rotor for the two cases shows that the rotor with the high thrust setting has a higher loading at the leading and trailing rim of the rotor;

the standard thrust case even has a significant portion of the rotor leading edge experiencing an up-wash through the rotor. This will have a significant effect on the structure downwash; a higher loading at the leading edge forces more air downwards at the leading edge.

Further reasons identified for the difference of the numerical to the experimental downwash distribution is the lack of coning and the tilt of the tip path plane. Both these factors influence the load distribution on the rotor and hence the rotor-wake.

Also, the method of determining the blade section angle of attack can introduce some error at the leading edge of the disk. In the trial done by Hotchkiss et al.[5] with this method a shrouded fan was modelled. Unlike that fan the current rotor is not shrouded and this allows the flow pattern to change noticeably between the upstream reference disk and the actuator disk itself, especially at the leading edge of the rotor.

(a) Rotor hub included

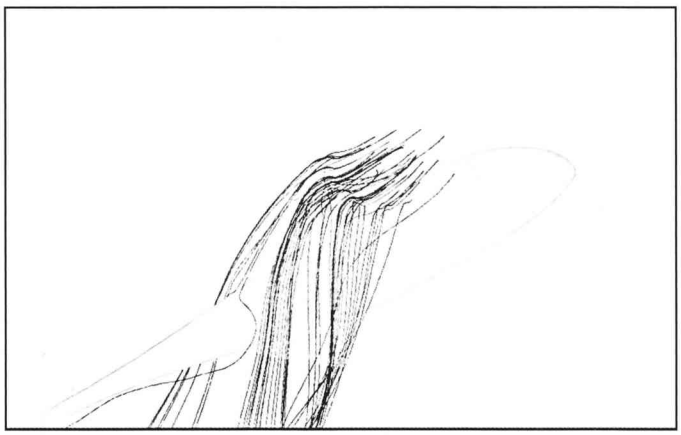

(b) Rotor hub excluded

Figure 13: Streamlines showing the effect of the rotor hub on the flow patterns

As already stated the aim is to develop a method by which rotorcraft intake aerodynamics can be evaluated, and the hub with its control rods can have significant effects on the local aerodynamics around the intakes. All the simulations here were done on a PC desktop machine. The computational effort is low and thus the method forms a useful evaluation tool. Useable results have been obtained from these simulations, with the actuator disk showing promising results that can be improved with fine-tuning on the basis of the points discussed above. In general the wake angle and downwash have to be predicted correctly for the pressure distribution around the fuselage to be correct. Shown here is that the pressure distribution on the upper fuselage surface is correctly predicted apart from the leading edge and the trends of the pressure distribution around the fuselage are captured if the wake angle is closer to the experimental.

References

1. *Chaffin MS and Berry JD*, Helicopter fuselage aerodynamics under a rotor by Navier-Stokes simulation, *Journal of the American Helicopter Society*, July 1997, 42(3), 235-242.
2. *Lee J-K and Kwon OJ*, Predicting aerodynamic rotor-fuselage interactions by using unstructured meshes, *Transactions Japan Society Aero Space Science*, 2002, 44(146), 208-216.
3. *Thiart GD and Von Backström TW*, Numerical simulation of the flow field near an axial flow fan operating under distorted inflow conditions, *Journal of Wind Engineering and Industrial Aerodynamics*, 1993, 45(2), 189 – 214.
4. *Meyer CJ and Kröger DG*, Numerical simulation of the flow field in the vicinity of an axial flow fan, *International Journal of Numerical Methods in Fluids*, 2002, 36, 947 - 969.
5. *Hotchkiss PJ, Meyer C and Von Backström TW*, Numerical investigation into the effect of cross-flow on the performance of axial flow fans in forced draught air-cooled heat exchangers, *Applied Thermal Engineering* 2006, 26, 200 – 208.
6. *Freeman CE and Mineck RE*, Fuselage surface pressure measurements of a helicopter wind-tunnel model with a 3.15 meter diameter single rotor NASA TM 80051, 1979.
7. *Diana, N*, Fluent 6.2 picks up speed, *Fluent News*, 2005, XIV (1), 34-35.
8. *Mineck RE and Althoff Gorton S*, Steady and periodic pressure measurements on a generic helicopter fuselage model in the presence of a rotor, *NASA TM 210286*, 2000.
9. *Chaffin MS and Berry JD*, Navier-stokes simulation of a rotor using a distributed pressure disk method, *51st Annual Forum Proceedings, American Helicopter Society*, May 1995, 112 – 136.
10. *Ruffin SM, O'Brien D, Smith MJ, Hariharan N, Lee J-D and Sankar L*, Comparison of rotor-airframe interaction utilizing overset and unstructured grid techniques, *42nd AIAA Aerospace Sciences Meeting and Exhibit*, Reno, NV, January 2004.

Errata

R Heise, CJ Meyer and TW von Backström, CFD simulation of helicopter flow fields using an actuator disk main rotor model, R & D Journal of the SAIMechE, 2007, 23(3), 26-32, available at http://www.saimeche.org.za

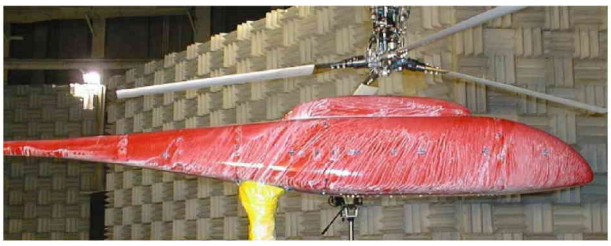

(a) Original experiment, form Mineck and Althoff[8]

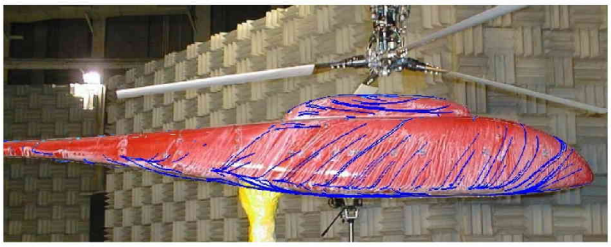

(b) CFD results superimposed, C_T = 0.00687

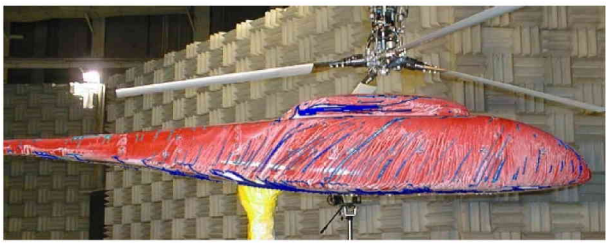

(c) CFD results superimposed, C_T = 0.0134

Figure 6: Streak lines, experimental versus numerical on advancing side

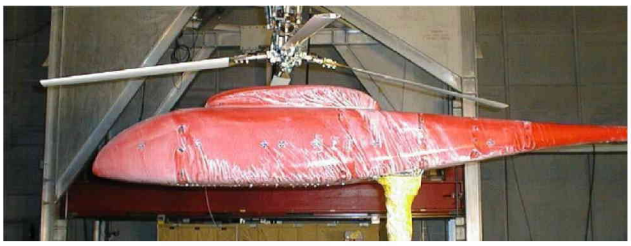

(a) Original experiment, form Mineck and Althoff[8]

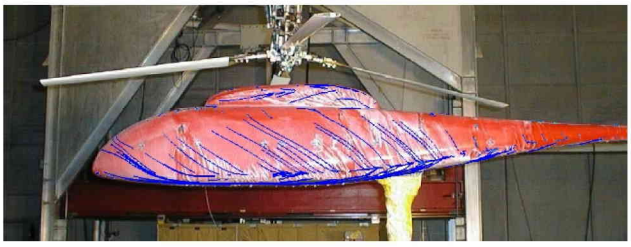

(b) CFD results superimposed, C_T = 0.00687

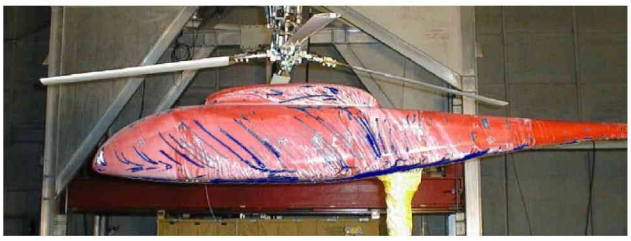

(c) CFD results superimposed, C_T = 0.0134

Figure 7: Streak lines, experimental versus numerical on retreating side

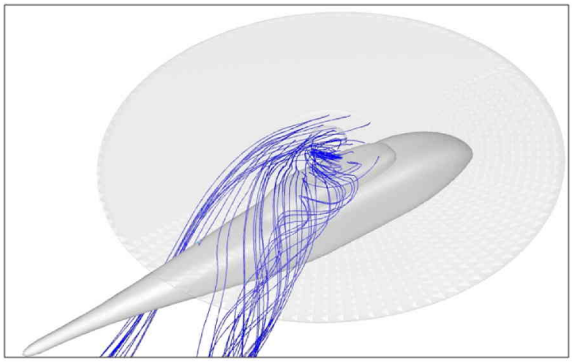

(a) Rotor hub included

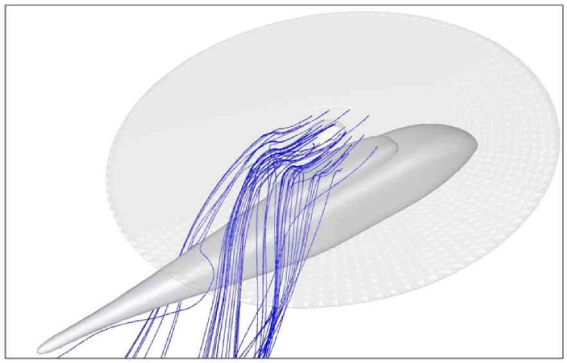

(b) Rotor hub excluded

Figure 13: Streamlines showing the effect of the rotor hub on the flow patterns

Performance of low noise fans in power plant air cooled steam condensers

Sybrand J. van der Spuy[a)], Theodor W. von Backström[b)] and Detlev G. Kröger[c)]

(Received: 09 January 2008; Revised: 13 May 2008; Accepted: 18 May 2008)

Axial fans are often installed in locations where the orientation and surrounding infrastructure can have a detrimental effect on the fan performance indicated by the manufacturer. This paper addresses various aspects of phenomena related to the installation of axial fans, one of these being the use of low-noise fans, and how these can be considered in the CFD performance evaluation of modern air-cooled power plant condensers. © *2009 Institute of Noise Control Engineering.*

Primary subject classification: 11.4.1; Secondary subject classification: 53.1

1 INTRODUCTION

In air-cooled power plant steam condensers, cooling is achieved by blowing air across the finned tube bundles arranged in the form of an A-frame above large-diameter axial flow fans (see Fig. 1). The fans are installed with the plane of rotation horizontally and are driven by electric motors through a gearbox. The fan and A-frame units are arranged in series to form a fan row, with a number of fan rows serving a single turbine unit in parallel. The result is that a power station will have a large array of fan units depending on the number of turbine units. The world's largest direct air-cooled power plant has an array of 288 axial fans, 9.1 m in diameter, located 45 m above ground level[1].

The performance characteristics of these fans have to be such that a prescribed air flow rate is guaranteed for specified flow resistances caused by the heat exchanger bundles and other obstructions, and by non-ideal flow patterns, while at the same time not exceeding prescribed noise levels. The required flow rate, coupled to the pressure losses, is regarded as the primary performance requirements of an installation, since it is directly linked to the effectiveness of the power generation process. The prescribed noise level is seen as a secondary requirement that is based on regulatory restrictions, often linked to the location of the installation. If a fan does not meet the primary performance requirement, it often exhibits increased noise levels due to increased unsteadiness in the flow[2]. Neise[2] referred to tests done with a 90° duct bend at various axial distances upstream of an axial flow fan. He reported that at short distances, the low frequency random noise components were increased by as much as 14 dB, while at the blade passing frequency an increase in the order of 7 dB was observed.

Recirculation of hot plume air and poor performance of the fans located near the edges of the array have been observed in large air-cooled steam condensers. In extreme cases, backflow of air through the fan occurred during windy periods[3,4]. The orientation of the fans means that their axes of rotation are vertical. The fans therefore have flow entering from a direction that is perpendicular to its axis of rotation. This causes fan inlet losses due to the separation of flow at the lip of the fan inlet as well as the off-axis inflow of air into the fan. Fans that are located near the edge or periphery of the array of air cooled condensers are severely affected by flow separation, while off-axis inflow occurs widespread through all fans installed in the array[5].

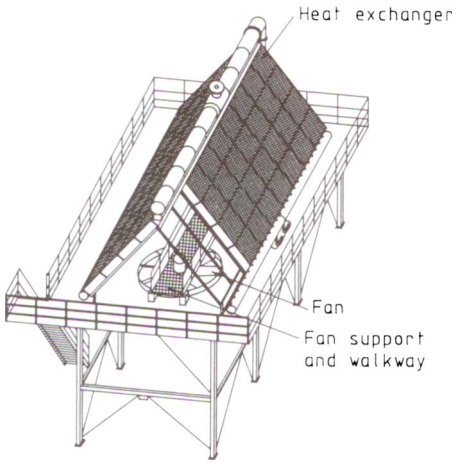

Fig. 1—Typical A-frame air-cooled condenser (Kröger[1]).

[a)] University of Stellenbosch, Department of Mechanical Engineering, Private Bag X1, Matieland, 7602, SOUTH AFRICA; email: sjvdspuy@sun.ac.za
[b)] University of Stellenbosch, Department of Mechanical Engineering, Private Bag X1, Matieland, 7602, SOUTH AFRICA; email: twvb@sun.ac.za
[c)] University of Stellenbosch, Department of Mechanical Engineering, Private Bag X1, Matieland, 7602, SOUTH AFRICA; email: dgk@sun.ac.za

Stinnes et al.[6] derived a relatively simple, though highly effective, model to describe the decrease in performance due to off-axis inflow, based on a series of experiments during which fans were tested with inlet ducts at specific angles to the fan plane of rotation. A number of authors have modelled and investigated the inlet loss effect on fan performance using computational fluid dynamics (CFD)[3–5,7,8]. The circumferential variation in inlet conditions directly upstream of the fan rotation plane causes a significant cyclic variation in the loading of the fan blades and consequently acts as a source of fan blade fatigue and fan noise[2,9]. The use of CFD would potentially enable the plant designer or more specifically the fan designer, to make the necessary adjustments to the plant and fan design to minimize inlet losses. Unfortunately the use of CFD to model these conditions also has its limitations.

Due to the occurrence of backflow through some sections of the fan, conventional, simplified CFD fan models that only take into account the forward flow operation of a fan are not representative. Under these conditions the use of a full 3-dimensional CFD model of the fan or a novel "actuator disk model"[10] is recommended. These models are both however computationally intensive and therefore a simpler approach, referred to as the "pressure jump model", can be applied when flow distortions are less prominent. A number of fan installation and fan configuration effects have been investigated using this combination of methods. These will be discussed in more detail in this document.

2 THE ACTUATOR DISK MODEL

2.1 General Description

The actuator disk model and its application in CFD have been well researched and described in much detail by Meyer et al.[10] The actuator disk model simulates the effect of the individual fan blades on the flow field using blade element theory (see Fig. 2).

The lift and drag forces, δ_L and δ_D, [N] acting on a fan blade element of radial length δr [m] are calculated using the following equations:

$$\delta_L = \frac{1}{2}\rho|W_\infty|^2 C_L \times c \times \delta r \qquad (1)$$

$$\delta_D = \frac{1}{2}\rho|W_\infty|^2 C_D \times c \times \delta r \qquad (2)$$

where ρ is the air density [kg/m^3], W_∞ is the average relative velocity over the blade element [m/s], C_L and C_D are the coefficients of lift and drag (obtained from standard airfoil data based on an angle of attack α) and c is the average chord length of the blade element [m].

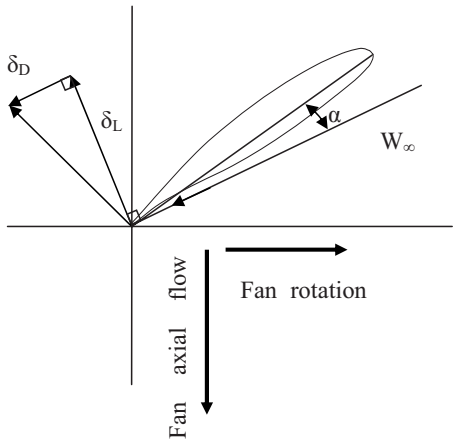

Fig. 2—Fan blade element.

Once the forces acting on the air stream are known, these are transformed into source terms that are inserted into the equation for linear momentum as follows:

$$s - \nabla p + \nabla \cdot \tau_{ij} = \rho \frac{dV}{dt} \qquad (3)$$

where s is the per volume force vector of source terms [N/m^3], ∇p is the gradient of static air pressure [N/m^3], τ_{ij} is the shear stress tensor [N/m^2] and V is the absolute velocity vector of the flow field [m/s].

2.2 Fan Model Validation

The fan considered in this analysis was a 9.145 m diameter, 8-bladed, cooling fan with a hub-to-tip ratio of 0.15, operating at 125 RPM (referred to as the A-fan). Details of the fan blade chord distribution, angle distribution and profile lift and drag coefficients are presented by Bredell[11]. Bredell calculated the lift and drag coefficients for the blade profile over a range of −180° to +180° using CFD. This enabled the actuator disk model to solve the momentum source terms for flow coming from any direction (including backflow) through the rotor disk. The actuator disk model used in this analysis was validated by comparing results from the supplier fan curve to results obtained using the actuator disk model (see Fig. 3), where Υ_{pt} refers to a setting angle at the blade tip based on the line tangent to the bottom of the blade profile. The results obtained from the actuator disk model were calculated according to the guidelines of the test standard used by the supplier, namely BS 848 part 1 (1980), type A[12]. The results show excellent correlation between the supplier and simulated data in the operating range of the fan (between 500 m^3/s and 700 m^3/s) for the fan static pressure.

All CFD simulations were performed using FLUENT™ version 6.2.16. To model the test condi-

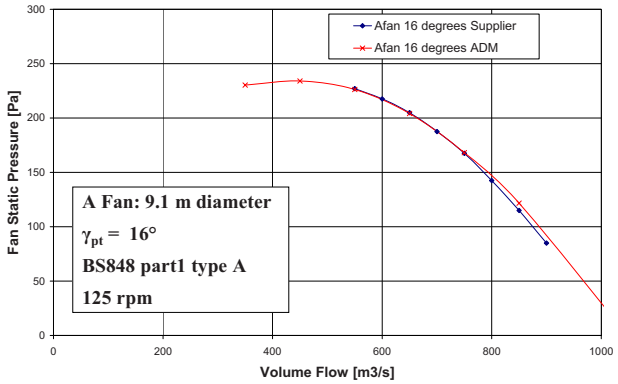

Fig. 3—Actuator disk model validation (fan static pressure).

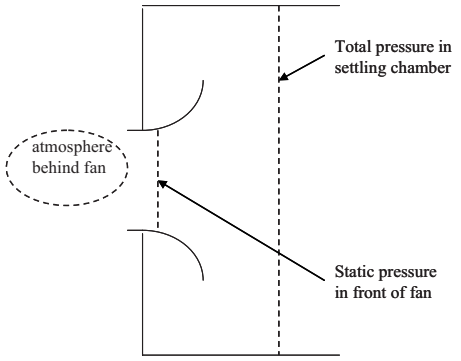

Fig. 4—Derivation of static-to-static pressure jump.

tions dictated by the British Standards, the inlet boundary was specified to be a mass flow inlet, while the outlet boundary was specified to be a total pressure boundary (pressure value set to atmospheric). To allow for dissipation of the fan exhaust dynamic component, the exhaust atmosphere was modelled to have a diameter of 4 × fan diameter and a length of 8 × fan diameter. The CFD model contained 550000 cell volumes. The validated CFD model used the realizable k-ε model[13] to simulate turbulence and the QUICK[14] interpolation scheme to calculate variables at the cell faces. The simulation was allowed to run for 3000 iterations or a residual value of 10^{-4}. Although the simulations were stable, convergence at flow rates less than 500 m^3/s were not good.

3 THE PRESSURE JUMP METHOD

3.1 General Description

The motivation behind considering the use of a pressure jump method lies in its potential ability to model an array of axial fans accurately using a reduced number of cell volumes in CFD. The pressure jump method detailed in this document is in essence the same technique as that used by van Staden[4] to model the performance of axial fans. The difference between the method detailed in this document (referred to as the "pressure jump method") and the one used by van Staden is however the way in which the effect of the fan is implemented into the CFD code. The pressure jump method assumes a static-to-static pressure jump that occurs at the location of the fan rotation plane. This static-to-static pressure value is added to the static pressure term of the linear momentum equation in the flow field directly upstream of the fan rotation plane, shown in Eqn. (3).

Hotchkiss et al.[5] and Stinnes et al.[6] found that under cross-flow conditions (that lead to off-axis inflow) the "fan static pressure" is reduced in magnitude by the dynamic pressure associated with the cross-flow component immediately upstream of the fan ("fan static pressure", as referred to by typical fan supplier data and simulated by the actuator disk model is actually fan total-to-static pressure). The cross flow component affects the static pressure in front of the fan and not the actual value of static-to-static pressure increase. This is shown by Hotchkiss et al.[5] to be attributed to the fact that the cross flow effect on flow angles and velocities over the fan blades effectively cancels out when considering a fan rotor with blades running with and against the direction of cross flow. Based on these results the pressure jump method should yield accurate results when analysing fans subjected to cross flow only. The same can however not be said for flow separation that occurs over a localised area in front of the fan rotation plane. It is therefore expected that, although the pressure jump method would identify possible problematic intakes at the side of an axial fan array, the results would not be accurate and a more accurate analysis would be required.

The fan supplier data was compiled for a type-A fan installation (see Fig. 4). The fan pressure data is derived from an average static pressure value that is measured in a plane, relative to atmosphere, in a settling chamber, 1.25 fan diameters upstream from the fan, where the axial velocity is specified to be less than 2 m/s. The static pressure measured in this location is assumed to equal the total pressure in this location. The total pressure loss between the measurement plane and the fan rotation plane is considered negligibly small because of the smooth bell mouth inlet (as specified by BS 848[12]).

To calculate the static pressure directly upstream of the fan rotation plane, as required for the pressure jump method, the dynamic pressure in the fan rotation plane is added to the "fan static pressure" curve. During the validation of the pressure jump method, it was found that the initial assumption of zero total pressure losses between the measurement plane and fan rotation plane

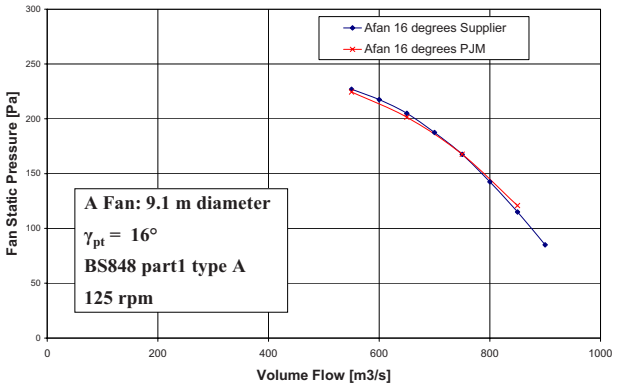

Fig. 5—Pressure jump method validation (fan static pressure).

was not sufficiently accurate and a loss coefficient was subsequently added. A value of 0.07 was used for the loss coefficient, which was based on flow data for rounded inlets, published by Idelchik[15]. The "fan static pressure" curve was therefore translated into a pressure jump value as follows:

$$\Delta p_{fan} = a + bV + cV^2 + dV^3 + \frac{1}{2}\rho V^2 + K_{loss}\frac{1}{2}\rho V^2 \quad (4)$$

where the values for a, b, c and d were derived from a curve-fit as described earlier, V is the average velocity perpendicular to the fan rotation plane [m/s] and K_{loss} is the described loss coefficient.

3.2 Fan Model Validation

The same geometric model that was used to validate the actuator disk method was used to validate the pressure jump method. Instead of using the described momentum sources, the standard FLUENT™ interface for specifying a pressure jump was used. The cell face region where the pressure jump would occur coincided with the fan rotation plane. The same boundary conditions, turbulence model and overall numerical differencing scheme were used as for the actuator disk method. The simulation was once again allowed to run for 3000 iterations or a residual value of 10^{-4}. The simulations were found to be stable and convergence generally occurred after 500 iterations. The resulting comparison of simulated and supplier data showed excellent correlation (see Fig. 5).

4 SIMULATION OF INSTALLED AXIAL FANS

4.1 Computational Model

To simulate the performance of axial fans under installed conditions, a 3-fan section of an array of air-cooled condensers was modelled (see Fig. 6).

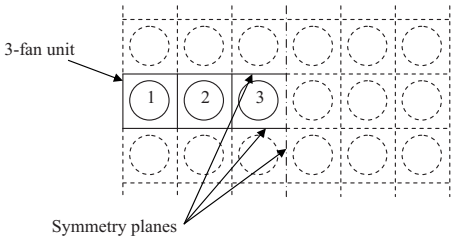

Fig. 6—A 3-fan section of an air-cooled condenser array, viewed from above.

Each of the fan units was modelled to consist of a bell mouth inlet, axial fan, rectangular plenum chamber and heat exchanger. The model had a total pressure boundary 200 m upstream from the fan array and a static pressure boundary 2 m downstream of the fan array (see Fig. 7). The analysis focussed on the inlet effects only, therefore the exit conditions of the system were simplified accordingly.

The heat exchanger was modelled as a porous region with resistance properties given by the equations from Bredell[11]:

$$\Delta p_{HE} = -\left(4.132315 \times 10^{-4} Q^2 + 5.629484 \times 10^{-2} Q\right) \quad (5)$$

where Q is the volume flow rate through the heat exchanger [m^3/s]. The above equation for system resistance coupled to the A-fan characteristics as shown in Fig. 3 corresponds to a reference flow condition of 650 m^3/s.

4.2 Model Validation

The CFD model for a 14 m platform height contained 570000 cell volumes. The validated CFD model once again made use of the realizable k-ε model and the QUICK interpolation scheme. The CFD model for the 3-fan unit was validated by comparing the results from the model, using both the actuator disk model and pressure jump method to simulate the A-fan, with the empirical relation derived by Salta et al.[16] The results showed the volumetric effectiveness of a multiple fan installation as a function of dimensionless platform height as follows:

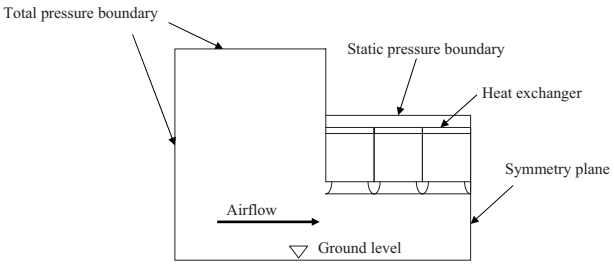

Fig. 7—Side view of computational domain for 3-fan unit.

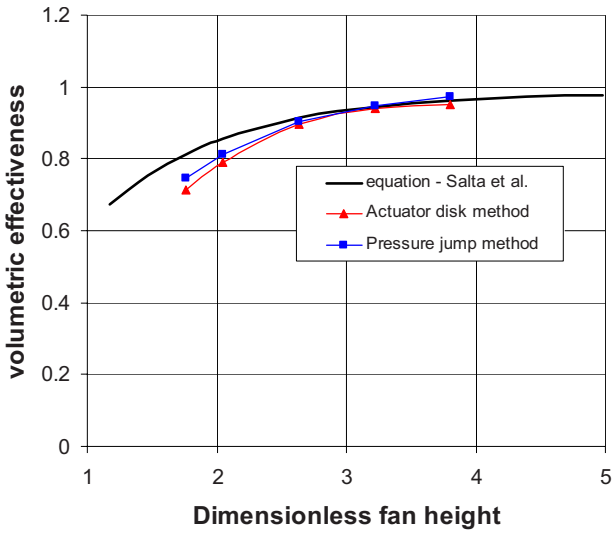

Fig. 8—Comparison of system volumetric effectiveness.

$$(Q/Q_{ref})_{system} = 0.985 - e^{-X} \quad (6)$$

where X is the dimensionless platform height:

$$X = \frac{(1 + 45/n) \times H}{6.35 \times D_F} \quad (7)$$

In the above equation, H is the platform height [m], n is the total number of fans per row (in other words 6 for the modelled 3-fan unit) and D_F is the fan shroud diameter [m]. The reference flow when determining the volumetric effectiveness (Q/Q_{ref}) of the installation was 650 m^3/s. A comparison of the results to the empirical correlation is shown in Fig. 8. The results show good correlation with the equation of Salta, at a dimensionless platform height between 2.5 and 4. The Salta fans had different ratios of dynamic pressure based on throughflow to pressure rise, compared to the A-fan. This leads to a different sensitivity to cross-flow and possibly to distortion and explains the difference in results at lower platform heights. Fig. 9 shows a vector plot with static pressure distribution to illustrate the extent of flow separation experienced by the edge fan of a multiple fan installation.

5 RESULTS

5.1 Fan Model Investigation

The 3-fan unit was first modelled by applying the actuator disk model in all three fans and subsequently compared to results obtained by applying the pressure jump method in all three fans. It was finally compared to a simulation using the actuator disk model on the "edge" fan only, combined with using the pressure jump method on the two inner fans. The actuator disk model is applied to the "edge" fan because of its ability

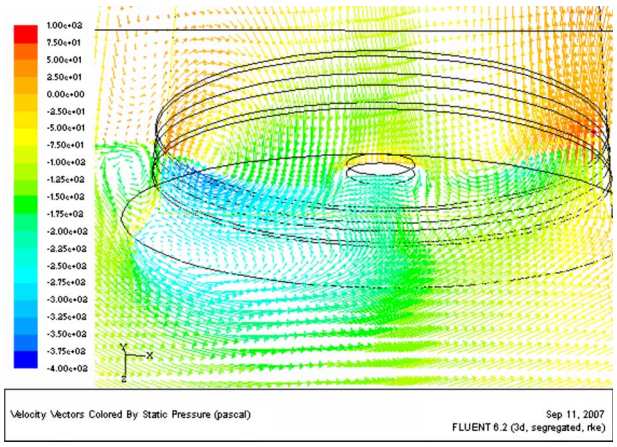

Fig. 9—Vector plot at fan inlet illustrating recirculation zone.

to simulate fan operation when backflow occurs through the fan. The results compare volumetric effectiveness at a height of 14 m and are shown in Fig. 10.

5.2 Platform Height Investigation

The 3-fan unit, using the above combination of fan models, was modelled with various platform heights, ranging from 14 m to 26 m as shown in Fig. 11.

5.3 Fan Geometry Investigation

The combined 3-fan unit was modelled with the standard 9.145 m cooling fan described in this document. This fan is referred to as the "A-fan" by Bredell et al.[9] and has a hub-to-tip ratio of 0.15. The alternative fan was also a 9.145 m fan but with a hub-to-tip ratio of 0.4 and is referred to as the "B-fan" by Bredell. Under standard test conditions, Bredell points out that the B-fan exhibits a much steeper fan static pressure to volume flow rate curve than the A-fan. This is typically found when referring to the performance curves of "low-noise" fans and is the result of a relatively larger value for fan solidity (see Fig. 12). The investigation effectively compares the volumetric effectiveness of a standard industrial

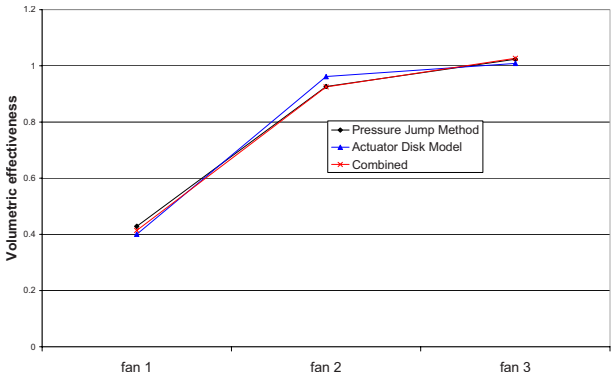

Fig. 10—Comparison of fan modelling methods.

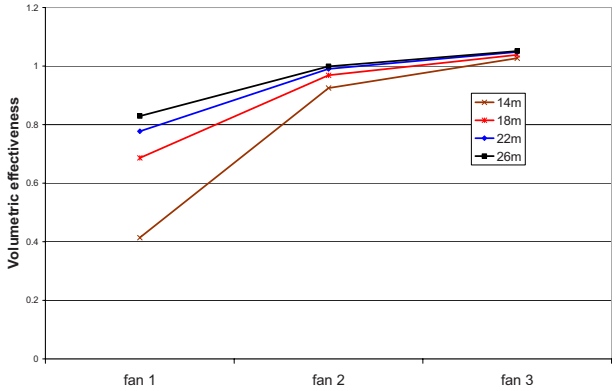

Fig. 11—Results from platform height investigation.

cooling fan (A-fan) to a "low-noise" industrial cooling fan. The results for the 3-fan unit, comparing the volumetric effectiveness of the A-fan to that of the B-fan at a 14 m platform height is shown in Fig. 13.

5.4 System Configuration Investigation

To illustrate the possible application of the fan model, an investigation to show the effect of a building located a distance of 10 m upstream of the fan array on

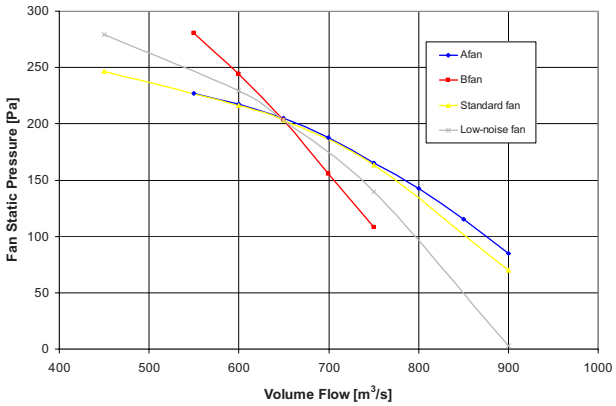

Fig. 12—Typical fan static pressure graphs for industrial fans.

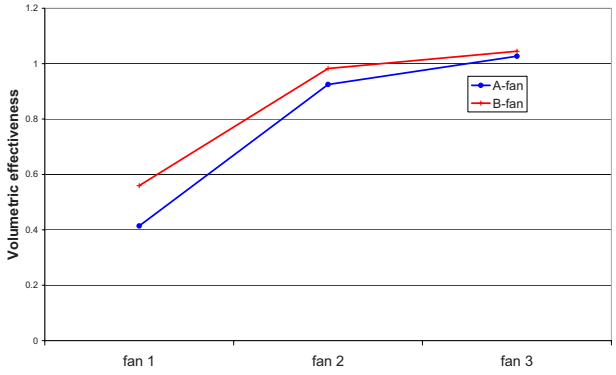

Fig. 13—Comparison of A-fan and B-fan performance at 14 m *height.*

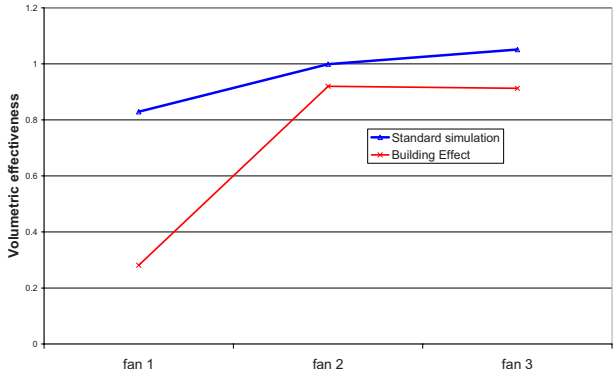

Fig. 14—The effect of buildings on the performance of a fan array at 26 m *height.*

the volumetric effectiveness of the fan array was conducted. The specific distance (10 m) was chosen purely as an example, although as a rule of thumb, any value in the order of or less than the specified platform height should have a detrimental effect on the volumetric effectiveness of the fans. It should be noted that the investigation only considered the effect on the inlet side of the fan array and no allowance was made for interaction between the exhaust and inlet sides. The results for a platform height of 26 m are shown in Fig. 14.

6 DISCUSSION

This document describes various methods of simulating the performance of axial fans under installed conditions. The extent to which an air-cooled condenser plant can be modelled in CFD on a single processor is limited by the size of the geometry being modelled. Distorted inlet conditions generate flow separation at the edge of the fan inlet and off-axis inflow into the fans. The separation that occurs is localised on the edge-side of the inlet of the fans installed on the periphery of a fan array, while the off-axis inflow occurs on all fans installed in the fan array. The flow separation causes an off-balance inlet flow distribution that can be so severe that the edge fans experience back flow through the fan. The actuator disk model is therefore considered to be a good compromise when keeping the size of a CFD model to a minimum while still being able to model the effect that flow from various directions would have on the performance of a fan. Off-axis inflow is distributed across the whole face of a fan. Stinnes et al.[5] has shown that for angles less that 45° the effects of off-axis inflow cancel out on opposing sides of the fan face. Off-axis inflow causes a pressure loss in front of the fan but does not alter the fan performance curve. The pressure jump method is therefore ideal in its application on fans operating in the first quadrant (positive pressure rise and positive volume flow) only. This limits its use to fans on the

inside of the fan array where flow separation is very small to negligible.

It has been found that it is essential to validate the fan models against results obtained under standard BS848 test conditions to ensure that relevant turbulence and discretization schemes are used. The actuator disk model was found to be very stable when using a first order discretization scheme for the continuity and momentum equations but considerable effort (a more detailed mesh and a larger outlet domain) was required to improve this stability when using a second order discretization scheme. It was also found essential to validate the pressure jump method so that a loss coefficient could be specified that accounts for total pressure losses between the measuring plane and the fan rotation plane.

Considering application of these methods to the modelling of power plant air-cooled steam condensers, the following should be taken into account:

1. Non-uniform inlet flow, caused by flow separation, is a potential noise mechanism in a fan installation and any method that would dampen its severity would therefore reduce the noise generated by the fan. Besides flow fluctuations, the non-uniform inlet also causes local regions of high relative velocities and a consequential large increase in fan noise[2].
2. The volumetric effectiveness of a fan array decreases dramatically with platform height, primarily due to the lower static pressure region below the "edge" fans due to increased flow separation in the fan inlet.
3. Fans having steeper fan static performance curves, as typically exhibited by low-noise fans, are less sensitive to flow distortions and exhibit a higher volumetric effectiveness.
4. The volumetric effectiveness of a fan array decreases with the proximity of buildings since it increases the cross flow velocity through the system and causes more severe flow separation at the edge fans.

Using the above CFD simulations, the user would be able to quantify possible increases in plant operating efficiency and compare it to the additional cost required for its manufacture. The biggest potential of the above CFD simulations lie in their ability to model a fan array accurately using a reduced number of cell volumes (conservatively estimated, simplified CFD methods use in the order of 10 times less cell volumes). This document however only investigated and validated the practical application of these methods and further development of the methods, specifically considering grid dependency, is required.

7 REFERENCES

1. D. G. Kröger, *Air-cooled Heat Exchangers and Cooling Towers*, PennWell Corporation, Tulsa, OK, (2004).
2. W. Neise, "Installation effects on fan noise", IMechE, C401/005, 83–91, (1990).
3. H. B. Goldschagg, F. Vogt, C. G. du Toit, G. D. Thiart and D. G. Kröger, "Air-cooled steam condenser performance in the presence of crosswinds", *Proceedings: Cooling Tower Technology Conference, Electrical Power Research Institute*, Palo Alto, California, (1997).
4. M. P. van Staden, *An Integrated Approach to Transient Simulation of Large Air-cooled Condensers using Computation Fluid Dynamics*, D. Eng. Thesis, Department of Mechanical Engineering, Rand Afrikaans University, South Africa, (2000).
5. P. J. Hotchkiss, C. J. Meyer and T. W. von Backström, "Numerical Investigation into the effect of cross-flow on the performance of axial flow fans in forced draught air-cooled heat exchangers", *Appl. Therm. Eng.*, **26**, 200–208, (2006).
6. W. H. Stinnes and T. W. von Backström, "Effect of cross-flow on the performance of air-cooled heat exchanger fans", *Appl. Therm. Eng.*, **22**, 1403–1415, (2002).
7. G. D. Thiart and T. W. von Backström, "Numerical Simulation of the flow field near an axial fan operating under distorted inflow conditions", *J. Wind. Eng. Ind. Aerodyn.*, **45**, 189–214, (1993).
8. J. R. Bredell, D. G. Kröger and G. D. Thiart, "Numerical Investigation of fan performance in a forced draft air-cooled steam condenser", *Appl. Therm. Eng.*, **26**, 846–852, (2006).
9. J. R. Bredell, D. G. Kröger and G. D. Thiart, "Numerical Investigation into Aerodynamic Blade Loading in Large Axial Flow Fans Operating Under Distorted Inflow Conditions", *R&D Journal*, **22**, 11–17, (2006).
10. C. J. Meyer and D. G. Kröger, "Numerical simulation of the flow field in the vicinity of an axial flow fan", *Int. J. Numer. Methods Fluids*, **36**, 947–969, (2001).
11. J. R. Bredell, *Numerical investigation of fan performance in a forced draft air-cooled steam condenser*, M.Sc. Eng. Thesis, Department of Mechanical Engineering, University of Stellenbosch, South Africa, (2005).
12. *Fans for General Purposes, Part 1: Methods for Testing Performance*, British Standards 848 1980, British Standards Institution, London, United Kingdom, (1980).
13. T.-H. Shih, W. W. Liou, A. Shabbir, Z. Yang and J. Zhu, "A new k-ε eddy-viscosity model for high Reynolds number turbulent flows—model development and validation", *Comput. Fluids*, **24**(3), 227–238, (1995).
14. B. P. Leonard, "A stable and accurate convective modelling procedure based on quadratic upstream interpolation", *Comput. Methods Appl. Mech. Eng.*, **19**, 59–98, (1978).
15. I. E. Idelchik, *Handbook of Hydraulic Resistance*, 3rd Edition., Begell House, (1994).
16. C. A. Salta and D. G. Kröger, "Effect of inlet flow distortions on fan performance in forced draft air-cooled heat exchangers", *Heat Recovery Syst. CHP*, **15**, 555–561, (1995).

AQ: #1

AUTHOR QUERIES — 001904NCE

#1 Au: Please provide coden/issn for Ref. 9

An Evaluation of Simplified Methods to Model the Performance of Axial Flow Fan Arrays

Sybrand J. van der Spuy[a], Theodor W. von Backström[a] and Detlev G. Kröger[a]

Received 15 October 2009, in revised form 7 June 2010 and accepted 7 June 2010

This paper investigates two simplified methods to model axial flow fans in a multiple fan operating environment using computational fluid dynamics (CFD). The application of the two methods are explained and illustrated, after which they are applied to a multiple fan CFD model. The CFD results are compared to experimental results to illustrate the applicability of the methods. It is concluded that the simplified presentation of an axial flow fan is particularly helpful in predicting the system volumetric effectiveness of multiple fan installations subjected to adverse inlet flow conditions, particularly during windy periods.

Additional Keywords: Air-cooled, array, pressure jump, steam condenser

Nomenclature

c	chord length [m]
C	dimensionless force coefficient
D	diameter [m]
f	volumetric force term [N/m^3]
H	fan unit platform height [m]
K	dimensionless coefficient
n	number of fans per row
n	number of fan blades
p	pressure [N/m^2]
r	radius [m]
t	time [s]
u	absolute velocity term in momentum equation [m/s]
V	volume flow rate [m^3/s]
v	absolute velocity [m/s]
w	relative velocity [m/s]
x	distance in Cartesian coordinates [m]

Greek Symbols

α	angle of attack [°]
β	flow angle, relative to plane of rotation [°]
δ	force [N/m]
Δ	delta
θ	circumferential angle [°]
ρ	density [kg/m^3]
τ	shear stress tensor [N/m^2]

Subscripts

ave	average over fan plane of rotation
D	drag
F	fan
fan ss	fan static-to-static
fan ss'	fan static-to-static with inlet loss
HE	heat exchanger
inlet	inlet plane just in front of fan
loss	loss coefficient
L	lift
ref	reference
∞	infinity
i,j	tensor subscripts
x,y,z	Cartesian coordinates

a Department of Mechanical and Mechatronic Engineering
University of Stellenbosch, Private Bag X1,
Matieland, 7602, South Africa.
E-mail: sjvdspuy@sun.ac.za

1. Introduction

In power plant steam condensers, the cooling medium, air, is blown across finned tube bundles using a large diameter axial flow fan (see figure 1).

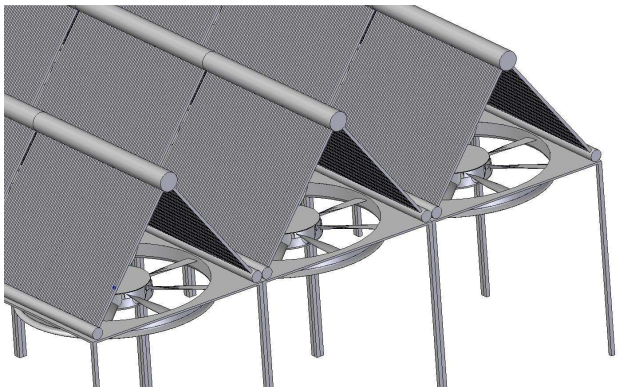

Figure 1: Sketch of an A-frame air-cooled condenser

Direct dry-cooled power stations, favoured in arid regions because of their relatively low level of water consumption, are equipped with large horizontal arrays of steam condensers and axial flow fans. The world's largest direct air-cooled power plant currently in operation has an array of 288 axial flow fans, 9.1 m in diameter, located 45 m above ground level[1]. Operating axial flow fans in an array format causes additional, and often unaccounted, flow losses, due to non-ideal flow patterns[2]. Poor performance of the fans located near the edges of the array has been observed in large power plants, particularly during windy periods[3, 4].

The horizontal orientation of the fan array means that flow enters the volume underneath the array from a direction that is perpendicular to the "designed" flow direction of the fans. Inlet flow separation occurs at fans that are located near the edge or periphery of the array, while off-axis inflow occurs widespread through all fans installed in the array[5, 6].

Various methods have been used to model axial flow fan arrays in computational fluid dynamics (CFD)[3-9]. The most accurate would be an explicit method which models the fan blade geometry in full detail. Since the distorted inlet conditions as described above are asymmetrical, a full 360° CFD simulation of the fan would be required. Assuming that a minimum mesh spacing of 200 units around the perimeter of the blade profile, a mesh spacing of 100 units along the blade length and twenty units

R & D Journal of the South African Institution of Mechanical Engineering 2010, 26, 12-20
http://www.saimeche.org.za (open access)

perpendicular to the blade surface are required to resolve the flow around a single fan blade, a fan with eight blades would require about 3.5×10^6 cell volumes just to resolve the flow around the individual fan blades. The use of simplified, implicit models of axial flow fans that simulate the effect that the fan would have on the flow field should therefore be considered when modelling multiple axial flow fans as part of a larger plant installation. The actuator disk and pressure jump methods described in this document are two such simplifications[9].

This document investigates and compares the actuator disk and pressure jump methods. Both methods were validated by comparing single fan performance predictions with actual test data. After validating single fan performance, the methods were implemented in CFD simulations of multiple fan installations. These simulations were compared with the empirical prediction model derived by Salta and Kröger[10].

Two fan designs are considered in this document. The first is an 8-bladed industry-standard cooling fan, referred to as the "A-fan", and has a hub-to-tip ratio of 0.15. The second fan is also 8-bladed, but with a hub-to-tip ratio of 0.4 and is referred to as the "B-fan". Fan diameters referred to in this document would be either test size (1.542 m) or installed size (9.145 m).

2. The Actuator Disk Model (ADM)

2.1 Description

The actuator disk axial flow fan model, as used for these simulations, is based on the model described by Meyer and Kröger[11]. This particular actuator disk model simulates the effect of the individual fan blade elements on the flow field by using the lift and drag characteristics of the blade profile (see figure 2).

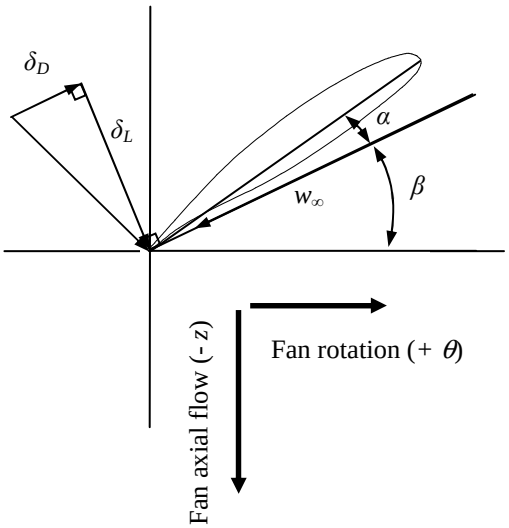

Figure 2: Side view of fan blade element[9]

Each fan blade is subdivided into radial elements (corresponding to the mesh spacing of the CFD model). The lift and drag forces per radial element length of blade acting on the flow are calculated using the following equations:

$$\delta_L = \frac{1}{2}\rho|w_\infty|^2 C_L c \tag{1}$$

$$\delta_D = \frac{1}{2}\rho|w_\infty|^2 C_D c \tag{2}$$

The lift and drag coefficients are the same as those often given in literature for standard two-dimensional airfoil data based on an angle of attack α. Using the methods detailed by Bredell[12] the coefficients were determined from two-dimensional CFD simulations of the specific blade section, with the results shown in figures 3 and 4. It should be noted that w_∞ is the average relative velocity, composed of components in the axial and circumferential directions over the blade element only (the actuator disk model in its current form ignores radial flow).

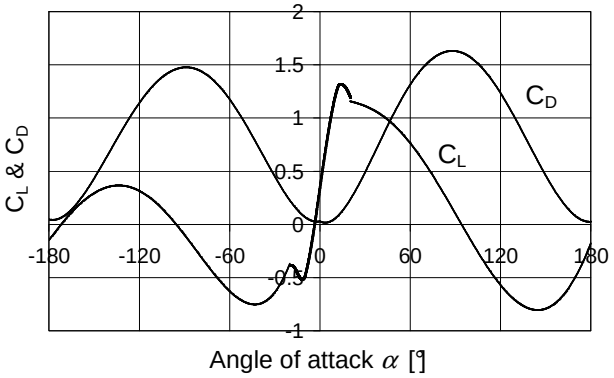

Figure 3: Correlation of C_L and C_D vs. angle of attack (α) for A-fan blade profile

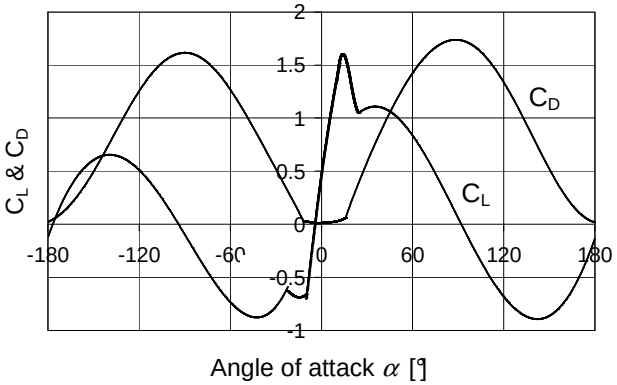

Figure 4: Correlation of C_L and C_D vs. angle of attack (α) for B-fan blade profile

Once the forces acting on the air stream are known, these are transformed into volumetric source terms that are inserted into the equation for linear momentum:

$$f_i - \frac{\partial p}{\partial x_i} + \frac{\partial}{\partial x_i}(\tau_{ij}) = \frac{\partial}{\partial t}(\rho u_i) + \frac{\partial}{\partial x}(\rho u_i u_j) \tag{3}$$

where

$$f_x = -\frac{n}{2\pi r\Delta z}\left(\delta_L \sin\beta + \delta_D \cos\beta\right)\sin\theta \quad (4)$$

$$f_y = \frac{n}{2\pi r\Delta z}\left(\delta_L \sin\beta + \delta_D \cos\beta\right)\cos\theta \quad (5)$$

$$f_z = -\frac{n}{2\pi r\Delta z}\left(\delta_L \cos\beta + \delta_D \sin\beta\right) \quad (6)$$

The actuator disk model is incorporated into the CFD model using a user-defined subroutine where the source terms are calculated using equations 1 to 6, based on velocities extracted from the CFD-simulation (note that the angle θ is defined in the *xy*-plane according to the right-hand rule). The forces exerted on the flow field are calculated for each cell located in the actuator disk, based on the flow conditions at corresponding cells upstream and downstream of the disk.

2.2 Validation of the actuator disk model

The CFD-results obtained using the actuator disk model were compared with fan test results compiled by Stinnes and Von Backström[13] using a type-A fan test installation, as defined by the British Standards 848[14] (see figure 5).

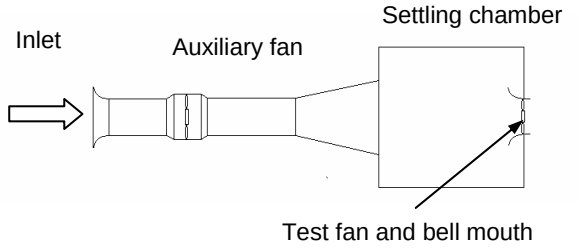

Figure 5: BS848 fan test facility, type-A

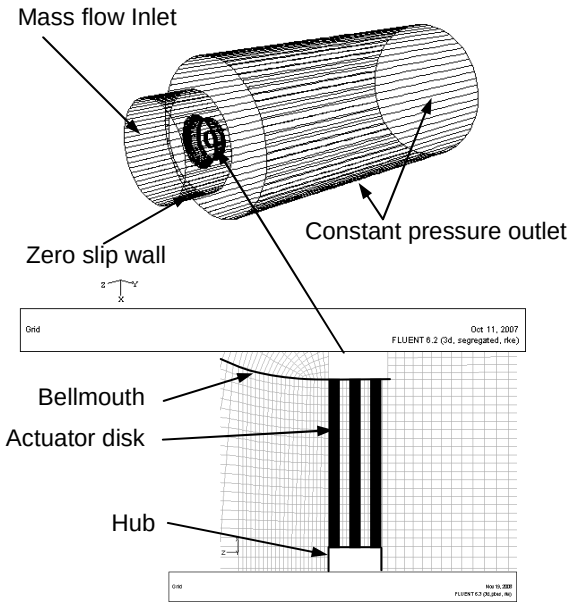

Figure 6: CFD geometry and mesh

To investigate and validate the actuator disk model, a three-dimensional CFD analysis of the fan, inside the test facility, was conducted for its full first quadrant operating range (zero flow point to zero pressure point). The geometry for the simulation was compiled in Gambit version 2.2.30. A typical lay-out of the geometry and the mesh detail surrounding the actuator disk is shown in figure 6.

The total number of cell volumes in this mesh shown in figure 6 was 650 000. The mesh was generated using only hexahedral elements to facilitate the structured approach required by the actuator disk method. The actuator disk method requires the cell volumes in the centre disk to match the radial and circumferential location of the reference cell volumes in the up and downstream disks. The mesh density upstream of the rotor was higher than downstream of the rotor to account for flow variation due to the presence of the solid rotor hub.

An investigation was conducted to evaluate the effect of the refinement of wall cell volume height on the inside surface of the bell mouth from a y^+ value of 300 to 30 and it was found that this had a negligible effect on the results (at the design point it had an effect of less than 0.25 % on the value of fan static pressure). To evaluate the effect of the overall mesh size on the CFD results, adaptive mesh refinement performed on each of the discussed fan models, showed that when increasing the number of cell volumes from 650 000 to 1 000 000 the fan static pressure value at the design point changed by less than 0.5 %

The simulations modelled the BS 848 fan test facility, using FLUENT™ version 6.2.16. Although Meyer and Kröger[11] used the standard k-ε turbulence model in their actuator disk model (ADM), it was decided to use the realizable k-ε turbulence model because of its ability to solve axisymmetric jet flows more accurately, as reported by Shih *et al.*[15]. The realizable k-ε turbulence model and QUICK interpolation scheme were subsequently used for all CFD-simulations.

The results from the analyses, compared with the measured test data for the B-fan, are shown in figure 7 (bear in mind that the realizable k-ε turbulence model was used in all simulations). The graph also includes the results for the pressure jump method (PJM) which are discussed in subsequent sections of this document.

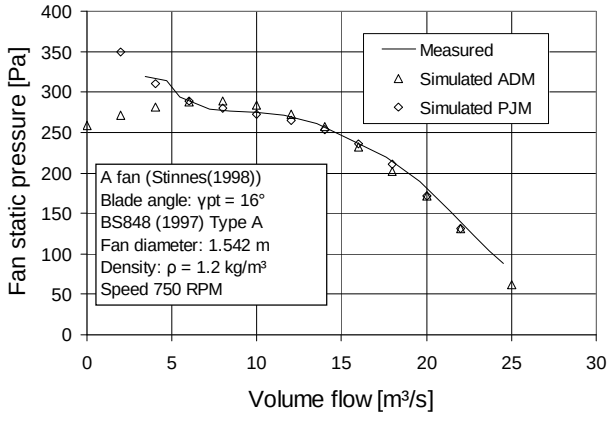

Figure 7: Fan static pressure curve, B-fan

This analysis shows that the actuator disk does not represent the operation of the fan correctly at flow rates below 8 m^3/s (possible reasons for this are discussed at the end of this paper). The validation was repeated for the test-size A-fan. The test results were once again compiled by Stinnes and Von Backström[13]. The results from the analysis are shown in figure 8.

Similar to the B-fan, the results obtained for the A-fan correlate well within the normal operating range of the fan. A larger number of cell volumes were required to model the A-fan to accommodate the effect of flow recirculation close to the hub due to its much smaller hub-to-tip ratio[16].

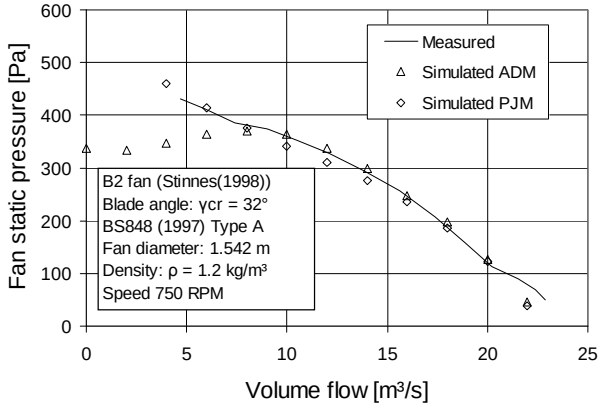

Figure 8: Fan static pressure curve, A-fan

3. The Pressure Jump Method (PJM)

3.1 Description

The pressure jump method utilises a static-to-static pressure increase that occurs at the location of the fan rotation plane. The static-to-static pressure jump is derived from the standard "fan static pressure" curve, as obtained from the fan supplier or standard fan performance test data[9]. It is important to note that the "fan static pressure" values specified by the supplier are actually fan total-to-static pressure values and therefore require conversion to fan static-to-static pressure values.

Although implemented on a per-cell basis, the value of the pressure jump is based on the average velocity through the fan annular area and neglects the local condition of the flow fan as well as the local properties of the fan (compared to the actuator disk model where the value of the source terms vary according to the flow field and fan blade properties). The validity of using the pressure jump method is discussed in further detail in section 4.

3.2 Calculation

As mentioned in section 2, fan supplier data, as used for air-cooled power plant steam condensers, are often compiled using a BS 848 type-A fan test installation. The fan pressure data is calculated from an average static pressure value that is measured in a plane, relative to atmosphere, in a settling chamber, 1.25 fan diameters upstream from the fan. The test standards specify that the static pressure measured at this location may be assumed to equal the total pressure in this location, because of the relatively small axial velocity value[14].

To translate from the total-to-static to the static-to-static curve, the total pressure measured in the settling chamber needs to be converted into a static pressure value directly upstream of the fan rotor mid plane (fan rotation plane) (see figure 9)[9].

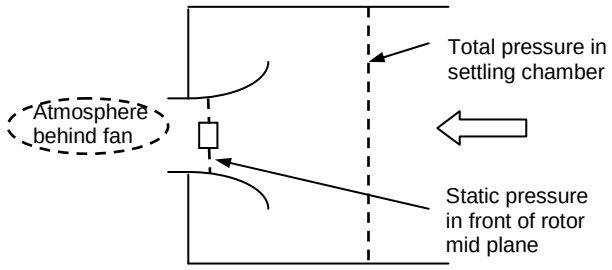

Figure 9: Conversion of pressure value

A 4th order polynomial equation for the "fan static pressure" curve was obtained by fitting a curve to the test data of the 1.542 m test fans shown in figures 7 and 8. To convert this curve to a static-to-static pressure curve, the dynamic pressure, based on the average annular air speed in the axial direction, in the fan rotation plane, is added as follows[9]:

$$\Delta p_{fan\,ss} = a + bV + cV^2 + dV^3 + eV^4 + \frac{1}{2}\rho v_{ave}^{\ 2} \qquad (7)$$

To provide for bell mouth inlet losses in front of the fan, a loss factor, as defined by Idelchik[17], was added to the equation as follows:

$$\Delta p_{fan\,ss}' = \Delta p_{fan\,ss} + K_{loss}\frac{1}{2}\rho v_{inlet}^{\ 2} \qquad (8)$$

Idelchik[17] specifies a value of 0.07 for the loss factor. It should be noted that the velocity related to the loss factor in equation 8 is the axial velocity based on the area of the fan duct only and does not consider the area of the hub.

3.3 Validation

The same geometric CFD model, boundary conditions, turbulence model and differencing scheme that was used to simulate the actuator disk model was used to validate the pressure jump method. The cell face region where the pressure jump would occur represents the rotor mid plane (see figure 10). The effect of the fan is implemented as a pressure gradient in the momentum equation (equation 3), applied to the upstream and downstream cells shown in figure 10. The pressure jump is added to the simulation model by programming a static pressure versus axial velocity curve into FLUENT™'s standard "fan" internal boundary condition.

A typical CFD simulation using the pressure jump method ran about 10 % faster than the same simulation with an actuator disk model.

The correlation achieved between the measured and modelled data within the normal fan operating range was excellent for both fans (see figures 7 and 8).

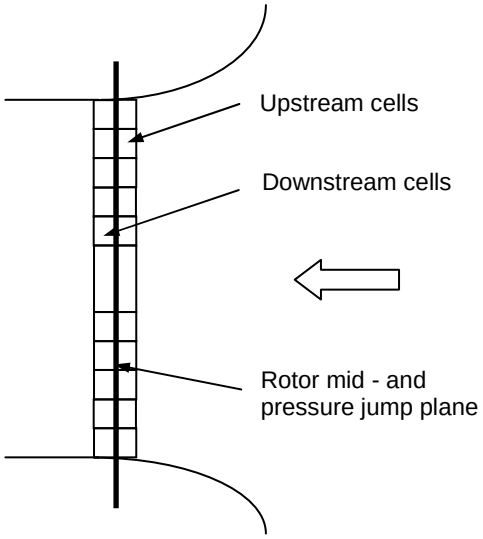

Figure 10: Application of pressure jump method

4. Application of the ADM and PJM

To investigate the performance of axial flow fan arrays with varying degrees of distorted inlet flow, the effective platform height of the installation, as modelled in the CFD simulations, was varied. By doing this, the cross flow velocity and consequent inlet flow distortion in front of the fan could be adjusted.

Hotchkiss *et al.*[5] and Stinnes and Von Backström[13] found that under off-axis inflow conditions (note that for off-axis inflow the cross flow velocity is the same everywhere) the "fan static pressure" is reduced in magnitude by the dynamic pressure associated with the cross-flow velocity component immediately upstream of the fan. The cross flow velocity component affects only the static pressure in front of the fan and not the actual value of static-to-static pressure increase. This is attributed to the fact that the effect of the cross flow velocity on the relative flow angles and velocities over the fan blades effectively cancels out when considering fan blades running 180 ° apart, with and against the direction of cross flow[5].

Since the static-to-static pressure increase is independent of inflow angle, the pressure jump method should yield accurate results when analysing fans subjected to off-axis inflow. When considering flow separation that occurs in front of the fan rotation plane, the fan would follow its static-to-static operating curve as long as the area of separation is such that similar inlet flow conditions prevail over an angular section of the fan annular space. The fact that the pressure jump method is based on average values does however mean that the flow conditions downstream of the fan would not be correct.

In principle it can be expected that, if any deviation or distortion of inlet flow occurs uniformly over an angular annular section of the fan rotation plane, the fan will follow its static-static operating curve obtained under standard test conditions.

4.1 Single fan computational model

To simulate the performance of an axial flow fan under installed conditions, a single fan row section of an air-cooled condenser was modelled in CFD (see figure 11).

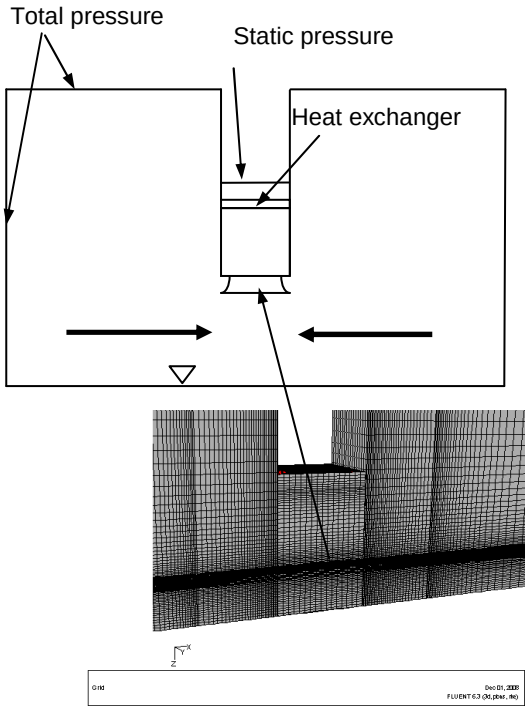

Figure 11: Side view of computational domain and grid for single fan row

The fan unit was modelled to consist of a bell mouth inlet, axial flow fan, plenum chamber and heat exchanger. The model had a total pressure inlet boundary 200 m upstream, on either side of the fan row and a static pressure outlet boundary 2 m downstream of the heat exchanger (see figure 11). The analysis focussed on the inlet effects only.

No provision was made in the model for possible recirculation of the exhaust flow. The model with the smallest platform height made use of 450 000 cell volumes. To investigate the effect of mesh size, this value was extended to 700 000 volumes using adaptive mesh refinement. This had an effect of less than 0.1 % on the simulated value for air mass flow rate through the fan.

The single fan simulations were based on an installed fan diameter of 9.145 m. Both the A-fan and B-fan mentioned in section 1 were considered in these simulations. The installed-size operating curves for these two fans were obtained by scaling test data obtained for 1.542 m diameter fans. A comparison between the above two fan curves shows the B-fan having a much steeper "fan static pressure" curve than the A-fan (see figure 12).

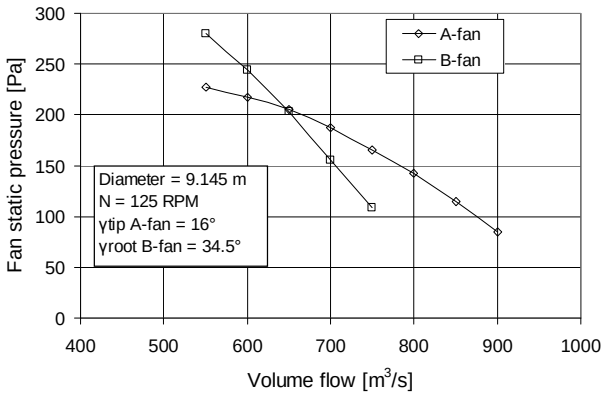

Figure 12: Comparison of fan curves

The heat exchanger shown in figure 11 was modelled as a porous region with resistance properties given by the equations from Bredell[12]:

$$\Delta p_{HE} = -\left(4.132315\times10^{-4}V^2 + 5.629484\times10^{-2}V\right) \quad (9)$$

The above equation for system resistance, coupled to the fan characteristics of both the A-fan and B-fan, using either the actuator disk or pressure jump methods, corresponds to within 2 % of a reference flow condition of 650 m^3/s. The CFD model made use of the realizable k-ε model and the QUICK interpolation scheme.

4.2 Multi-fan computational model

To simulate the performance of multiple axial flow fans, a 2-fan section of an array of air-cooled condensers was modelled to represent a 4-fan row of fans inside a large array of air-cooled condensers (see figures 13 and 14). The model with the lowest platform height consisted of 500 000 cell volumes. Increasing the number of cell volumes to 900 000 using adaptive mesh refinement had a 2.5 % and 0.5 % effect on the simulated value for air mass flow rate through the outer and inner fan respectively.

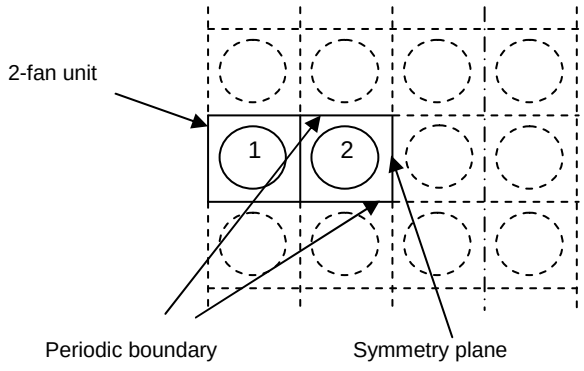

Figure 13: 2-fan section of an air-cooled condenser array, viewed from above

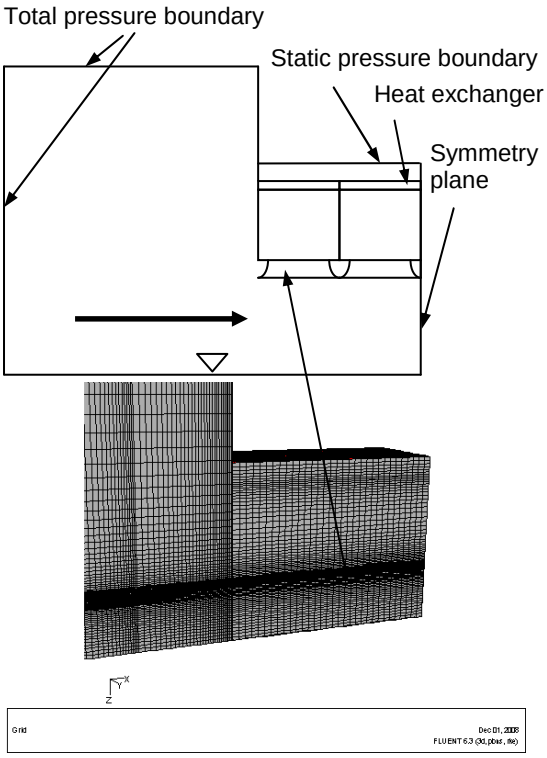

Figure 14: Side view of computational domain and mesh for 2-fan unit

4.3 Installed fan experiments

Salta and Kröger[10] describe a set of experiments where the effect of platform height on the performance of both a single row and a multiple axial flow fan installation were investigated. These experiments were based on similar, earlier work done by Russel and Peachey[18]. Figure 15 shows a picture of the experimental set-up for three fans (the number of fans in the system could be adjusted).

The CFD results were compared with an empirical correlation derived by Salta and Kröger[10], to express the volumetric effectiveness of the installation as a function of dimensionless platform height as follows (Salta and Kröger[10]):

$$\left(V/V_{ref}\right)_{system} = 0.985 - exp^{(-X)} \quad (10)$$

where X is the dimensionless platform height:

$$X = \frac{4.882\times H}{D_F} \quad (11)$$

for a single fan row and

$$X = \frac{\left(1+45/n\right)\times H}{6.35\times D_F} \quad (12)$$

for a multiple fan row. In the above equations n is the total number of fans per row, H is the platform height and D_F is the fan diameter.

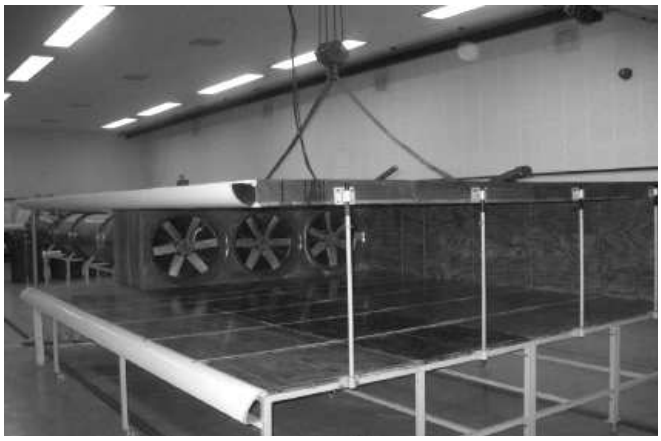

Figure 15: Experimental test set-up

5. Results

5.1 Single fan row correlation

The numerical results obtained for volumetric effectiveness vs. platform height for both the A and B-fan single fan row unit were compared with the experimental correlation of Salta and Kröger[10]. The results of the comparison are shown in figure 16.

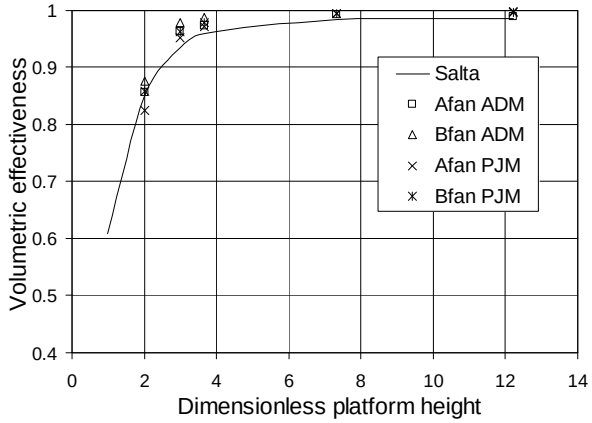

Figure 16: Single fan results comparison

Figure 16 shows that the numerical results for both methods correlate well with the experimental values of Salta and Kröger at all the platform heights that were simulated (within 5 %). The biggest difference in results exist at moderate platform heights where the actuator disk method applied to the B-fan calculates a volumetric effectiveness that is 4.4 % higher than the value predicted by Salta and Kröger.[10]

5.2 Multiple fan correlation

The numerical results for both the A and B-fan, 2-fan unit were again compared with the experimental correlation of Salta and Kröger[10]. The results of the comparison are shown in figure 17.

The numerical results for both methods again correlate well with the experimental values of Salta and Kröger[10] at moderate to high platform heights (within 2 %). At very low platform heights however, the numerical results under predict the experimental values by a maximum of 10 % (A-fan, actuator disk model) and a minimum of 5 % (B-fan, pressure jump method). This can be attributed to the limited range of application of the simplified fan models (as discussed in section 6).

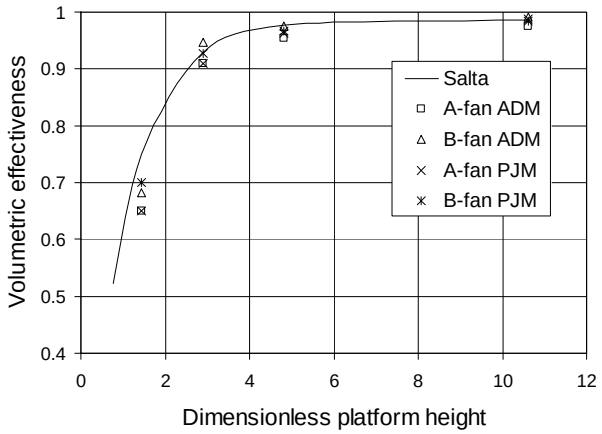

Figure 17: Multiple fan results comparison

5.3 Edge fan separation

Viewing CFD-results of the multiple fan simulation on a plane through the centre of the modelled geometry, the occurrence of separation on the inlet side of the edge fan is clear. A vector plot of the predicted separation in front of the edge fan (simulating the A-fan), predicted using the actuator disk model, is shown in figure 18.

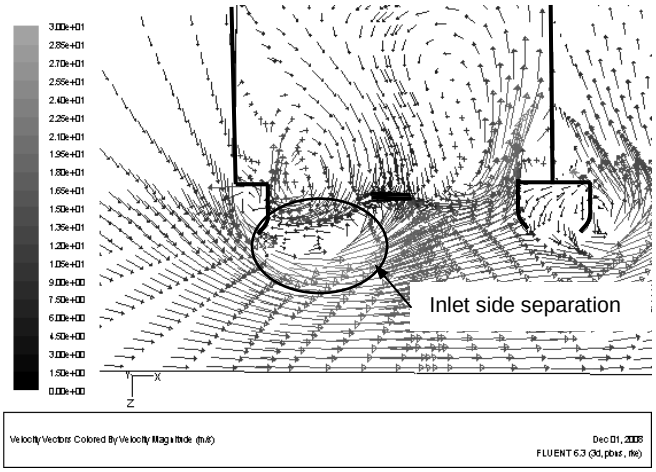

Figure 18: Edge fan separation at low platform height (actuator disk)

Another vector plot of the predicted edge fan separation using the pressure jump method is shown in figure 19.

When comparing the extent of separation occurring at the inlet of the edge fan for figures 18 and 19, it is shown that the pressure jump method predicts a larger volume of separation in front of the fan. Secondly, the nature of the flow patterns downstream of the fan displayed by the results using the actuator disk model is more intricate with distinctive recirculation zones visible after the fan. The results for the pressure jump method do not display the same recirculation zones downstream of the fan.

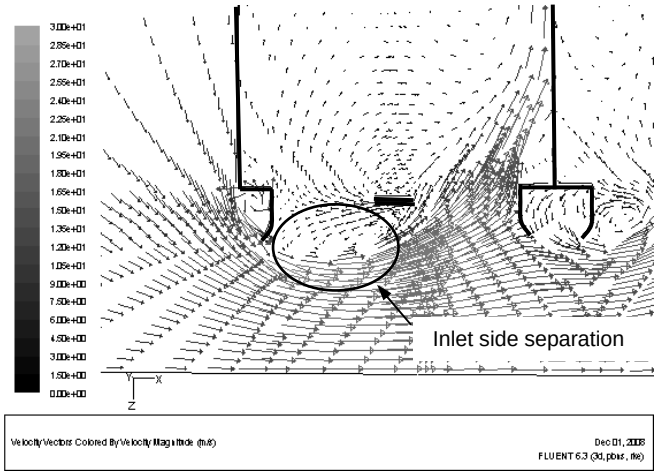

Figure 19: Edge fan separation at low platform height (pressure jump)

6. Conclusion

6.1 Test fan simulation

Two simplified methods to simulate the performance of axial flow fans were investigated. It is shown that both these methods can simulate fan operation accurately when replicating the fan performance curve within its normal operating range. The number of cell volumes required to represent the operation of the axial flow fan is considerably less than when modelling the fan in full detail.

Due to fact that the actuator disk model considers the local blade and flow field properties when calculating the momentum source terms, it gives a more accurate representation of the flow field. However, the actuator disk model does not represent the fan performance curve correctly at low flow rates due to it assuming axial flow over the fan blade at all times and therefore ignoring the presence of radial flow over the blades at low flow rates. The pressure jump method is purely a reflection of the fan performance curve and therefore represents the operation of the test fan (based on the extent to which the simulation predicts the performance curve) correctly at all flow rates.

The above conclusions are applicable to both the actuator disk model and pressure jump method for both fan configurations that were simulated.

6.2 Installed fan simulations

The results from the simulations of the installed fans (both single fan row and multiple fans) correlate within 5 % with the empirical curve of Salta and Kröger[10] at medium to high platform heights and show the detrimental effect of inlet flow distortion on fan volumetric effectiveness. At low platform heights there is however a bigger difference in values (as high as 10 %) between the simulated results and the results of Salta and Kröger[10] as well as between the simulated results for the different fan geometries.

6.2.1 Simplified fan model

Both the simplified methods display the occurrence of flow separation in front of the edge fans and both these methods could be applied to evaluate the effectiveness of fan inlets under distorted inlet conditions.

The pressure jump method displays an improvement over the actuator disk model in its ability to represent the fan performance curve at low flow rates. As mentioned in section 4, if the flow condition is uniform over an angular annular section (as found in a fan test facility), the pressure jump method would work well, since, by nature of its relationship to the fan performance curve, the pressure jump method assumes inlet properties to correspond to the uniform inlet properties found in a fan test facility.

The pressure jump method neglects any form of fan exit swirl velocity distribution. As shown in figure 5, a BS 848 type A test set-up allows the fan exit swirl energy to be dissipated into the free atmosphere behind the fan. This corresponds to the forced draught condition, detailed in section 1 and modelled in section 4, where the downstream heat exchangers remove the swirl generated by the fan. If the detail of the flow patterns downstream of the fan would form part of the investigation, the use of a swirl distribution with the pressure jump method or the use of the actuator disk model should be considered.

6.2.2 Fan geometry

A comparison of volumetric effectiveness for the A-fan and B-fan (both using the pressure jump method) is included in figures 16 and 17. At very low platform heights the volumetric effectiveness of the B-fan is 2.5 % to 5 % higher than that of the A-fan and 5 % lower than the empirical curve of Salta and Kröger. As shown in figure 12, the A-fan and B-fan have distinctly different fan static pressure curves, which in turn can be attributed to the difference in design described in Section 1. Stinnes and Von Backström concluded that the slope of the fan static pressure curve at the operating point determines a fan's ability to handle cross flow[13].

This indicates that the volumetric effectiveness of a fan under distorted inlet conditions is dependant on fan geometry and that the empirical correlation of Salta and Kröger[10] should be extended to make provision for the characteristics of the fan itself, something not mentioned by previous investigators[16].

Finally the simulations confirm previous results by Bredell[12] and van der Spuy *et al.*[9] that suggest that axial flow fans with larger hub-to-tip ratio's (and consequently steeper pressure curves) would be less susceptible to distorted inlet conditions, regardless of whether cross flow or separation occurs in front of the fan.

7. Recommendation for Further Work

Based on the results of this investigation, the authors recommend that a full explicit CFD simulation of an axial flow fan be performed and the results compared with results obtained using the pressure jump method and actuator disk model. It is also recommended that a more detailed study be conducted to determine the range of application of the pressure jump method and actuator disk method.

References

1. *Kröger DG*, Air-cooled Heat Exchangers and Cooling Towers, PennWell Corporation, Tulsa, 2004.
2. *Monroe RC*, Improving cooling tower fan system efficiencies, *Combustion Magazine*, 1979, 50 (11), 20-26.

3. *Goldschagg HB, Vogt F, du Toit CG, Thiart GD and Kröger DG,* Air-cooled steam condenser performance in the presence of crosswinds, EPRI TR-1084832113, *Proceedings: Cooling Tower Technology Conference*, St. Petersburg, Florida, 1997, 1.61 – 1.77.
4 *Van Staden MP,* An Integrated Approach to Transient Simulation of Large Air-cooled Condensers using Computation Fluid Dynamics, PhD Thesis, Department of Mechanical Engineering, Rand Afrikaans University, South Africa, 2000.
5. *Hotchkiss PJ, Meyer CJ and Von Backström TW,* Numerical investigation into the effect of cross-flow on the performance of axial flow fans in forced draught air-cooled heat exchangers, *Applied Thermal Engineering*, 2006, 26, 200-208.
6. *Meyer CJ,* Numerical Investigation of the effect of inlet flow distortions on forced draught air-cooled heat exchanger performance, *Applied Thermal Engineering*, 2005, 25, 1634-1649.
7. *Thiart GD, and Von Backström TW,* Numerical simulation of the flow field near an axial fan operating under distorted inflow conditions, *Journal of Wind Engineering and Industrial Aerodynamics*, 1993, 45, 189-214.
8. *Coetzee RV,* Numerical Simulation of an Air-cooled Heat Exchanger, MEng thesis, School of Mechanical and Materials Engineering, Potchefstroom University for Christian Higher Education, South Africa, 2000.
9 *Van der Spuy SJ, Von Backström TW and Kröger DG,* Performance of low noise fans in power plant air cooled steam condensers, *Noise Control Engineering Journal*, 2009, 57 (4), 1-7.
10. *Salta CA and Kröger DG,* Effect of inlet flow distortions on fan performance in forced draft air-cooled heat exchangers, *Heat Recovery Systems and CHP,* 1995, 15, 555-561.
11. *Meyer CJ and Kröger DG,* Numerical simulation of the flow field in the vicinity of an axial flow fan, *International Journal for Numerical Methods in Fluids*, 2001, 36, 947-969.
12. *Bredell JR,* Numerical investigation of fan performance in a forced draft air-cooled steam condenser, MScEng thesis, Department of Mechanical and Mechatronic Engineering, University of Stellenbosch, South Africa, 2005.
13. *Stinnes WH and Von Backström TW,* Effect of cross-flow on the performance of air-cooled heat exchanger fans, *Applied Thermal Engineering*, 2002, 22, 1403-1415.
14. *British Standards Institution,* Part 1: Methods for Testing Performance, Fans for General Purposes, BS 848. 1980.
15. *Shih TH, William WL, Shabbir A, Yang Z and Shu J,* A new k-ε eddy viscosity model for high Reynolds number turbulent Flows, *Computers Fluids*, 1995, 24 (3), 227-238.
16. *Bredell JR, Kröger DG and Thiart GD,* Numerical investigation of fan performance in a forced draft air-cooled steam condenser, *Applied Thermal Engineering*, 2006, 26, 846-852.
17. *Idelchik IE,* Handbook of Hydraulic Resistance, 3rd Edition, Begell House, 1994.
18. *Russell CMB and Peachey J,* Air inflow effects on fan performance in air-cooled heat exchangers, *International Conference on Fan Design and Applications***,** Guilford, England, September, 1982.

EXPENDABLE TURBOJET COMPRESSOR DESIGN, TEST AND DEVELOPMENT

by

von Backström, T.W.

8th International Symposium on Air Breathing Engines
Cincinnati, pp. 331 - 338
June 1987

EXPENDABLE TURBOJET COMPRESSOR DESIGN, TEST AND DEVELOPMENT

by

von Backström, T.W.

8th International Symposium on Air Breathing Engines
Cincinnati, pp. 331 - 338
June 1987

ISABE 87-7039

EXPENDABLE TURBOJET COMPRESSOR DESIGN, TEST AND DEVELOPMENT

T.W. von Backström*

The University of Stellenbosch Laboratory for Aircraft Propulsion
Stellenbosch, South Africa

Abstract

Two prototype compressors for a small, expendable, low cost turbojet were designed, built and tested. The designs were of the axial transonic type, with double circular arc rotor blades machined from solid 17-4 PH stainless steel, electron-beam welded integral rotor, externally inserted stator blades clamped by cables, and an unsplit aluminium compressor casing. The first prototype exhibited adequate surge margin for starting and running up to idle, and for slam acceleration from idle to full speed. Peak and full speed efficiencies were 80 and 71%. The second prototype had reduced first stage rotor blade camber, and tip clearance of all rotor blades reduced to 0.35 mm instead of 0.5 mm. Peak and full speed efficiencies increased to 0.84 and 0.75. In up to 75% design speed tests on a twice full scale model compressor peak efficiencies of up to 0.87 were measured. Tests are continuing.

Introduction

A compressor for a small, low cost, expendable turbojet engine (figure 1) had to be developed, using limited available resources. These resources were: experience in the design of subsonic axial compressors; availability of axial flow compressor analysis and design computer programs; aluminium casting technology, and stainless steel NC-machining technology.

The basic requirements for the engine were: thrust 3.3 kN, maximum diameter 320 mm, mass 63 kg, life 20 hr.

An axial flow compressor layout was chosen because of the previous experience, the availability of the computer programs, and the smaller diameter of the axial flow type.

Thermodynamic cycle analyses, geometric and rotordynamic considerations, and local state of the art in compressor design resulted in the following basic specification: pressure ratio 3.6 and full speed efficiency 82%, at 27 800 rpm and a sea level standard mass flow of 5.62 kg/s; allowable compressor mass 31.5 kg.

Assuming ideal gas properties and equal enthalpy rise per stage as a first approximation, required first and last stage pressure ratios were 1.44 and 1.32 for a four stage compressor and 1.62 and 1.46 for a three stage compressor.

Background

A comprehensive collection of transonic and supersonic compressor papers and summaries [1,2,3] of the work done at the National Advisory Committee for Aeronautics (NACA) in the fifties was published in 1961. Relevant compressor parameters are summarized in table 1.

When tests of rotors only (numbers 3 and 4 in table 1) are discarded as suggested by Bullock, [2], the rest of the results are quite similar, with pressure ratios of about 1,4 per stage, and tip speed and stage load coefficient equal to 330 m/s and 0.3 respectively. Stage load coefficient is defined as isentropic enthalpy rise divided by tip speed squared.

A survey of literature between 1961 and 1981 yielded the results in table 2.

The most marked difference between the results in the two tables is the post-1961 increase in tip speed to 430 m/s and the increase in stage pressure ratio to 1.7 or more. However, the stage load coefficient was still 0.3 or less except in the case of the Curtiss-Wright supersonic compressor, of which the design details were classified [12].

Assuming a 0.3 stage load coefficient and a 3.6 pressure ratio, the tip speed would be either 380 m/s for a three stage, or 330 m/s for a four stage compressor.

*Professor, Department of Mechanical Engineering, University of Stellenbosch

Table 1 Summary of NACA transonic compressor parameters (pre-1961)

No.	Description	Reference	Pressure Ratio	Tip Speed (m/s)	Isentropic Efficiency	Stage Load Coefficient
1.	Transonic no. 1 (Stage)	1	1.42	305	0.90	0.33
2.	Small Frontal Area (Stage)	1	1.42	335	0.84	0.27
3.	50% Reaction (Rotor)	1	2.17	427	0.89	0.39
4.	80% Speed (Rotor)	1	1.65	350	0.94	0.36
5.	Five Stage (Compressor)	4	5.0	335	0.81	0.30

Design

The compressor design philosophy was to limit stresses and Mach numbers to conservative values in order to minimize the risk of failure and inefficiency. Low blade relative Mach numbers of 1.2 or less allow the use of less sophisticated rotor blade profile shapes such as the double circular arc type 13. With a fixed speed of 27 800 rpm, largely dictated by the turbine, a lower tip speed would result in a smaller compressor diameter and lower weight per stage. Because of these considerations the four-stage design was preferred, in spite of the weight and cost of an extra stage.

The gas turbine layout was largely influenced by the design of the NASA small, low cost expendable turbojet engine [14], characterized by an integral four stage compressor, with unshrouded stator blades, a rear bearing aft of the turbine and the absence of an inner casing between the shaft and the combustor can (figure 1).

The compressor aerodynamic design was based on that of the NACA 5 stage [4], for which detailed design and experimental data were available. This compressor had a pressure ratio of 3.8 over the first four stages, an 81% efficiency at design tip speed of 335 m/s and was tested as part of a gas turbine engine. It, however, suffered from rotor blade overcambering, high first and second stage rotor tip losses and excessive annulus area. These problems could, it was believed, all be eliminated or reduced by decreasing the stage pressure ratio, recontouring the annulus and redesigning the blades. Other features were the absence of inlet guide vanes, high degree of reaction, axial outflow from the stator blades, and a highly loaded second stage. Tests on the NACA 5 stage with distortions that were varied in both magnitude and circumferential extent revealed that the effects were small, with pressure ratio and efficiency remaining essentially unchanged and mass flow falling off by 3 percent [1].

As a point of departure, the fifth stage of the NACA 5 stage transonic compressor design [4] was eliminated, the compressor was scaled down by a factor of 0.45, the tip diameter was slightly reduced and the hub recontoured to adapt the flow area to the mass flow. The compressor performance was analysed by means of a streamline curvature computer program. Blade cambers and staggers were slightly adjusted to improve stall margin.

Blade row solidity was similar to that of the NACA 5 stage, but chords were adjusted to reduce potential resonance problems. Natural frequencies of all blades were calculated, and a finite element program was used to calculate rotor stresses.

Compressor diameter was 226 mm and bladed length 218 mm. Blade heights varied from 46 to 21 mm, and chords from 31 to 17 mm, with maximum thickness between 2.8 and 1.3 mm, and minimum leading edge thicknesses equal to 0.3 mm.

The design had relatively low rotor blade root solidities (1.75 to 1.45) and wide passages between the blades of a particular rotor row, (10 to 12 mm) thereby allowing NC machining of rotor blisks from solid. The throat area between adjacent blades was critical not only as far as choking was concerned but also to allow the maximum possible cutter diameter. An interesting feature of the cutting process was that cutter access to the bottom of the rotor blade passage could only be gained by rotating the rotor while cutting the blade surface.

Design Features

The final compressor design had the following features:

1. Four axial transonic stages with axial outflow from the stators.

2. Double circular arc blades except for the last two stator rows where NACA 65 blades on circular arc camber were used.

3. Rotor blisks were machined from solid 17-4 PH stainless steel, but casting was foreseen in production.

4. Blisks were joined by electron beam welding. Hub was unshrouded.

5. Inlet casing was cast in aluminium.

6. Constant diameter compressor casing was centrifugally cast, and of the non-split type.

7. Stator blades were inserted from the outside through slots milled in the casing. The blades of each row were retained by being pressed into their slots by tightening two cables around the casing. This construction, when combined with

Table 2 Summary of transonic axial compressor parameters (1961 - 1982)

No.	Description	Reference	Pressure Ratio	Tip Speed (m/s)	Isentropic Efficiency	Stage Load Coefficient
6	USAAVLABS	5	1.86	430	0.87	0.30
7	NASA	6	1.68	421	0.85	0.26
8	NASA	7	1.87	480	0.83	0.26
9	NASA (2 stage)	8	1.66	430	0.87	0.25
10	BBC (4 stage)	9	3.60	430	0.82	0.17
11	Microturbo (3 stage)	10	3.65	420	?	0.24
12	High-flow	11	2.06	457	0.88	0.32
13	Curtiss Wright Supersonic	12	2.62	425	0.75	0.51

smaller clearances between rotor hub and stator blades than between rotor blade tips and casing, had the following advantages:

1. Stator blade tips would rub before rotor blade tips.

2. Stator blades could be easily inspected and replaced without dismantling the engine.

3. Rubbing speeds were lower at stator blade tips.

4. Stator blades were virtually mounted as a spring and damper system with the retaining cables acting as the spring, and the blade shanks and sealing paste as the damper.

Test Facilities and Instrumentation

Testing was done in a small engine test cell. Overall parameters measured were: inlet mass flow, speed, and compressor outlet total pressure and temperatures. Outlet total pressure was measured by means of two calibrated rakes [16] consisting of flattened 3 mm tubing with five 1 mm equally spaced holes drilled in their leading edges. The probes were angled in such a way that they always intercepted at least one last stage stator blade wake. Outlet total temperature was measured with two shielded thermocouples with their measuring holes at two thirds of the annulus height. Inlet and outlet total and static pressure and flow angle traverses were done by means of stepper-motor-driven conrad probes. Wall static pressures between blade rows, and second stage bleed flow were also measured.

In addition a twice full scale model of the first prototype compressor was built and tested in a larger compressor test facility, but could initially only be run up to 75% speed due to vibration problems caused by a two-strut inlet.

First Prototype

A first prototype compressor and gas turbine engine was built and tested as a unit. The rotor blades of the first stage were purposely overcambered to improve low speed stall, although a stall line analysis as proposed by Koch [15] indicated that the computer program prediction was pessimistic. It was however thought worth while to sacrifice about 1.5% in compressor efficiency to ensure the starting of the first prototype engine.

First Prototype Test Results

The initially planned gas turbine starting sequence was to accelerate the rotor up to, and maintain its speed at, 7 000 rpm by means of four jets impinging on the turbine blades before and during ignition.

However, blockage of the four jets caused compressor stall the moment the main burners in the combustion chamber ignited. The sequence was changed to shut off the impinging air before ignition, and the engine accelerated well from 7 000 to the idling speed of 19 000 rpm.

These initial performance tests indicated satisfactory performance in terms of pressure ratio and efficiency at speeds up to 87%. Later tests revealed a drop in efficiency and divergence from the computed values when approaching full speed. Isentropic efficiencies measured at 81, 91 and 100% speed were 82, 81 and 74%.

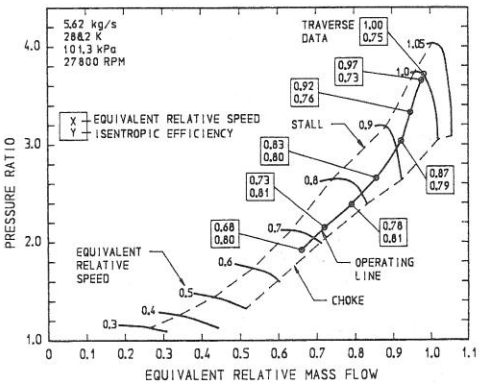

Fig. 2 First prototype test 1-2-64. Operating line, speed and efficiency

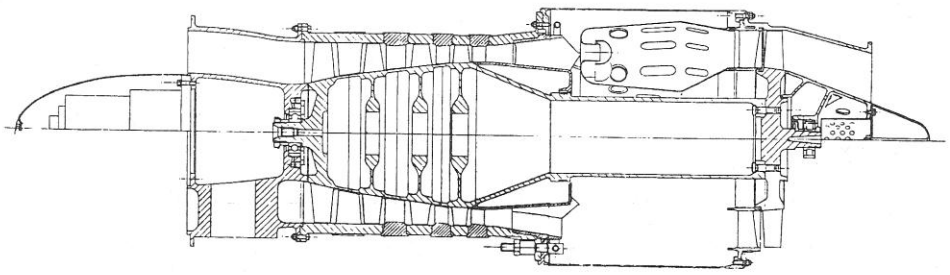

Fig. 1 General Layout of the Small Turbojet

Performance Tests 1-2-64:

These tests were done with the originally designed highly tapered engine rear end, but without the bolt-on nozzle.

The equilibrium operating line climbs away steeply at speeds and mass flows above 85% of design, rapidly approaching the surge line at 100% speed and 95% mass flow (figure 2).

The variation of compressor efficiency with speed, mass flow and pressure ratio is shown in figures 3, 4 and 5 by the upward-pointing triangular symbols. (The other lines and symbols are for comparative purposes and may be disregarded for the moment.) Compressor efficiencies taken from the graph at 81 and 91% and extrapolated to 100% speed are now 80, 77.5 and 71%; respectively lower by 2, 3.5 and 3% than measured previously.

The reason for this discrepancy could not be found when comparing earlier and later calibration constants, but higher outlet temperatures measured during the later tests can be explained by longer settling down times before taking readings (typically 30 seconds). To be on the safe side the later more pessimistic results were assumed to be correct.

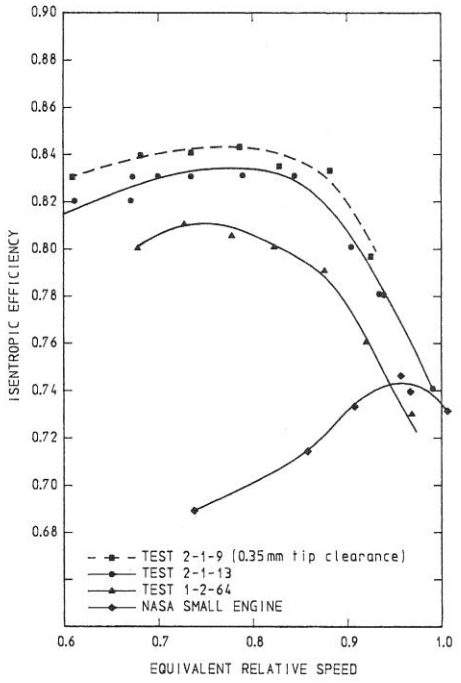

Fig. 3 Variation of compressor efficiency with speed along the operating line.

Performance Tests 1-2-67

After the second prototype tests, discussed later, further tests were done to try and determine the reason for the upward trend of the running line above 90% speed during the first prototype tests. The engine was fitted with a later designed less sharply tapered exhaust housing, with a correctly sized exhaust nozzle. The nozzle guide vane and turbine flow areas were about 1 percent larger because of more accurate allowances for shrinking in the casting process.

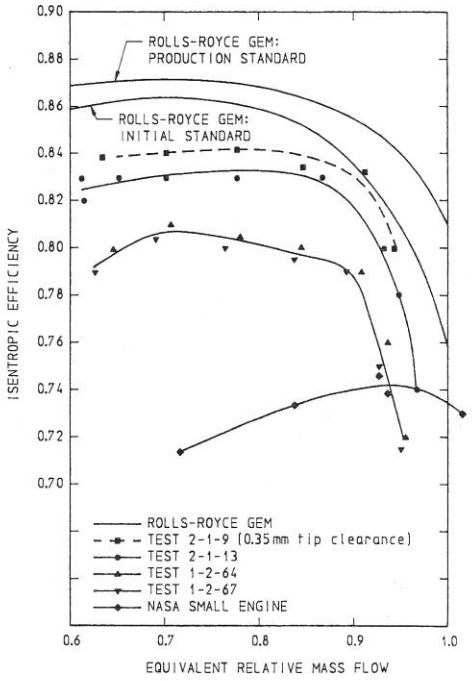

Fig. 4 Variation of compressor efficiency with mass flow along the operating line

The equilibrium operating line is shown in figure 6 and the efficiency against mass flow in figure 4. Unfortunately speed readings were unreliable during this test. Above 85% mass flow (and pressure ratio 2.6) the operating line is practically identical with the earlier test 1-2-64, indicating that at this condition the turbine stage, and not the nozzle, controls the flow. The compressor efficiency curve is also very similar to, but about 0.5% lower than for test 1-2-64.

Full Speed Traverse Test 1-2-64

The overall result of the first full speed traverse test agreed remarkably well with the corresponding fixed probe data: mass flow calculated from the outlet velocity profile was only 1.3% less than the inlet bellmouth measurement.

Pressure ratio, at 3.74, and efficiency, at 75%, were slightly higher, the latter because of very short settling down times (a few seconds) before taking readings: engine speed was reduced to 95% while probes were traversing.

Total pressure and velocity profiles were reasonably uniform for a point so close to the stall line. Total temperature rise was high in the rotor tip region, because of overcambering to increase low speed stall margin. Efficiency was low because of high losses (especially in the first two stages). As pointed out by Kovach and Sandercock regarding the NACA 5 stage transonic compressor: "At design speed the tip regions of the first and second rotors exhibit all the flow conditions that tend toward the incurrence of high losses, including (a) incidence angles below minimum loss values, (b) high inlet relative Mach numbers, and (c) for the second rotor especially, high diffusion factor." [4]

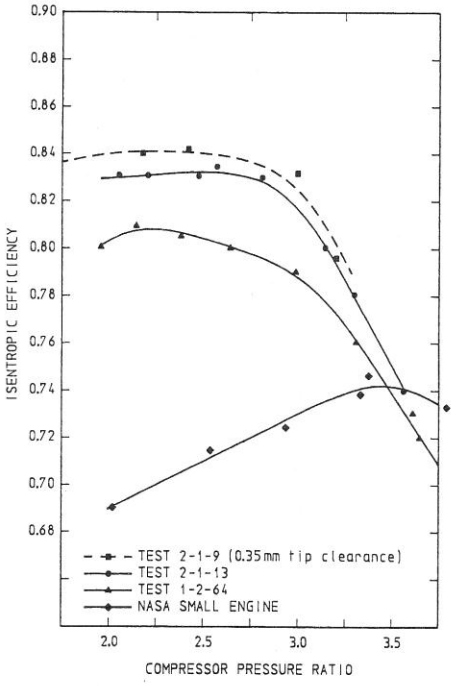

Fig. 5 Variation of compressor efficiency with pressure ratio along the operating line

Wall Static Pressure Rise - Test 1-2-64

Agreement between computed and measured results was fair: measured static pressure rise was 7% higher than predicted. (Measured compressor total pressure ratio at 3.61 was only 2.0% higher than predicted for these test conditions.)

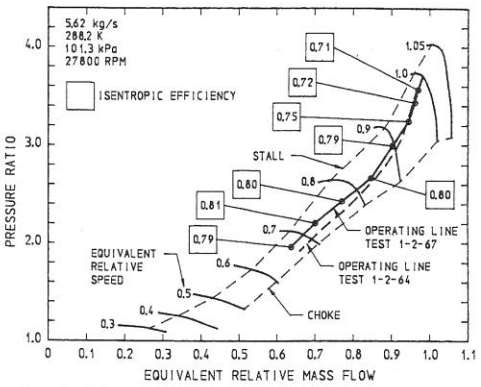

Fig. 6 First prototype test 1-2-67. Operating line, speed and efficiency

First Prototype Full Speed Tests - Summary and Conclusions

The main conclusions were:

1. Maximum mass flow reached at 100.3% equivalent relative speed was 95.9% of the design value.

2. At this reduced mass flow the average pressure ratio of the traverse and fixed probe tests was 3.72 compared to the expected 3.78.

3. Specified pressure ratio of 3.60 was exceeded by 3.3% at the low mass flow of 95.9% of design.

4. Target efficiency of 82% was not reached. Peak efficiency was 81% at 73% speed. Full speed efficiency was 71%, but 78% could be maintained up to 89% speed.

5. An unexpected drop of 3% in efficiency compared to the very first tests gives some idea of the repeatability of efficiency values.

6. Negative incidence stall predicted by the off design computer program is not a problem.

7. Predicted stall line is not optimistic, according to slam acceleration tests from 65 to 100% speed (figure 7).

Second Prototype

A second prototype compressor was designed and built. It was different from the first prototype in the following respects:

1. First stage rotor blade camber was reduced by 4° (at the tip from 14.4° to 10.7°), and blade thickness was reduced exponentially and not linearly towards the tip.

2. Second stage rotor blade tip solidity was increased from 1.18 to 1.31.

3. First and second stage stator blade stagger angles were increased by 1°.

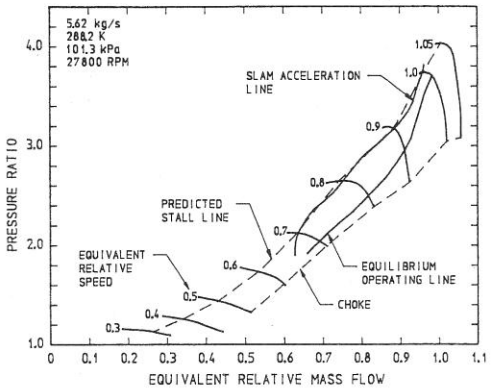

Fig. 7 First prototype test 1-2-64. acceleration line.

Reduced Tip Clearance Tests 2-1-9

This compressor was originally designed with 0.35 mm blade tip clearances to increase stall margin and efficiency, as indicated by Koch [15]. At a later stage some computer runs were done with different tip clearances indicating a negligible increase in stall margin and efficiency in reducing tip clearance from 0.5 to 0.35 mm and a relatively large decrease between 0.5 and 0.65.

The compressor was at first tested with the 0.35 mm rotor and stator blade tip clearances, but the rotor tip clearances were later increased to 0.5 mm by grinding away rotor blade tips as a precautionary measure after engine vibration measurements indicated a possible blade rub.

Due to blade resonance problems the compressor could not be run at speeds exceeding 93%, but up to that speed the running line agreed perfectly with that for test 2-1-13 (figure 8). In both these cases the equilibrium running line started climbing away at a higher mass flow than during the first prototype tests (figure 2). The peak isentropic efficiency was now 84% (86% polytropic) at 80% speed and 82% at 90% (figures 3, 4 and 5). Unfortunately the sharp drop in efficiency above 90% speed was still evident, with 80% efficiency achieved at 92% speed (94% mass flow).

Normal Rotor Tip Clearance Tests 2-1-13

Rotor tip clearance was 0.5 mm and stator tip clearance 0.35 mm. Efficiency still dropped rapidly above 85% speed (90% mass flow). Peak efficiency was 83% at 80% speed, with 80% achieved at 91% and 74% at 100% speed (figures 3, 4 and 5). About 1 percentage point in efficiency was sacrificed by increasing the rotor tip clearance by 0.15 mm. The trends of the two second prototype curves agreed extremely well but was not clear whether the small tip clearance design would retain its advantage up to 100% speed.

Second Prototype Full Speed Traverse Test 2-1-13

Mass flow balance was not as good as previously; mass flow from the outlet traverse test was 5% larger than from the inlet bellmouth. Pressure ratio was 3.58 and efficiency 74% compared to 3.54 and 74% from the fixed probe measurements. In this case the engine was run continuously at full speed for at least 3.5 minutes.

Outlet total pressure and velocity profiles were fairly uniform with a slight deficit at the hub, typical of a point close to the stall line. Although the work distribution across the annulus was much more uniform than for the first prototype design, the efficiency close to the casing was still low.

Wall Static Pressure Rise - Test 2-1-13

Agreement between computed and measured outlet static to total compressor pressure ratio was excellent; the measured value was only 1.4% low. The measured total pressure ratio at 3.65 was only 0.3% lower than the predicted value of 3.66.

Second Prototype Full Speed Tests - Summary and Conclusions

The main conclusions were:

1. Maximum mass flow reached at 99.8% equivalent relative speed was 96.6% of design.

2. At this reduced mass flow the average pressure ratio of the traverse and fixed probe tests was 3.56 compared to the predicted 3.59 at 100%.

3. Target efficiency of 82% was reached, although only at speeds below 87%. Peak efficiency was 83% at 80% speed with 80% achieved at 91% speed, and 74% at 100%.

4. According to the slam acceleration tests the predicted stall line is pessimistic (figure 9).

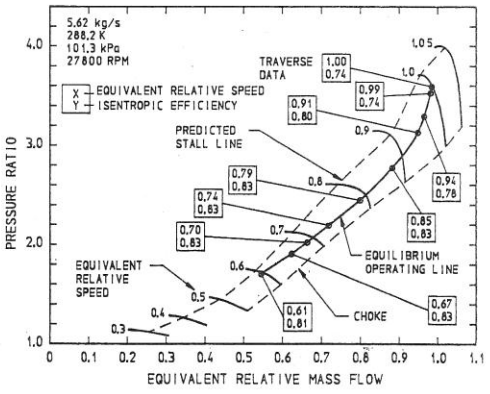

Fig. 8 Second prototype tests 2-1-13. Operating line, speed and efficiency.

5. Compressor efficiency could be improved by 1% by reducing rotor blade tip clearance from 0.50 to 0.35 mm.

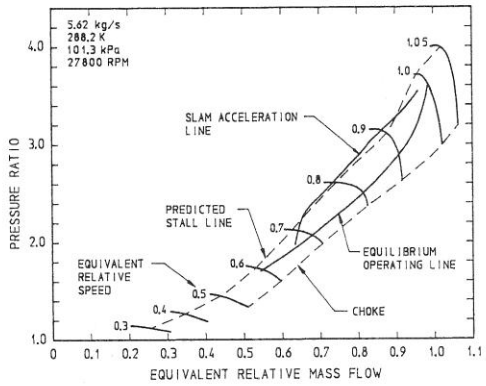

Fig. 9 Second prototype test 2-1-13. Slam acceleration line.

Comparison with Efficiencies of Other Similar Compressors

Available Data

The following comparative data could be found:

1. Rolls-Royce Gem engine [17]. This is a four-stage transonic compressor with axial outflow from the stators, a design pressure ratio of 3.2 and slightly smaller mass flow than the present design. Being a gas turbine engine for a helicopter with three shafts (and four turbine stages) it has a very flat equilibrium running line, and the compressor would be able to generate a pressure ratio of 3.6 at 100% speed with a steeper running line.

2. NASA Small, Low-Cost, Expendable Turbojet Engine [14]. This engine was slightly smaller, being designed for a thrust of 2.54 N.

Comparison of Performance

It is clear from figures 3, 4 and 5 that as far as efficiencies are concerned the order is always:

1. Rolls-Royce (production standard, then initial standard)

2. Second prototype (small tip clearance)

3. First prototype

4. NASA Small Engine

Complete data were not available in every case.

The shapes of all the curves except that of the NASA machine are quite similar. Low efficiency at low or high speed could be caused by stage mismatching. Low efficiency at high speed could also be caused by high Mach number losses. It has been suggested that radiation from the can to the compressor outlet thermocouples may be responsible for excessive values of measured compressor temperature rise especially at high temperatures. A related unresolved problem in the present experimental work was the difference between the two compressor exit thermocouple readings, increasing rapidly from 1° C at idling to 8° at full speed. (The higher of the two readings was used in the calculations of efficiency.)

In the case of the NASA engine where the efficiency drop only becomes evident at high speeds and mass flows, it should be remembered that the leading edge of the can is fitted with a flow splitter which should be a very effective radiation shield.

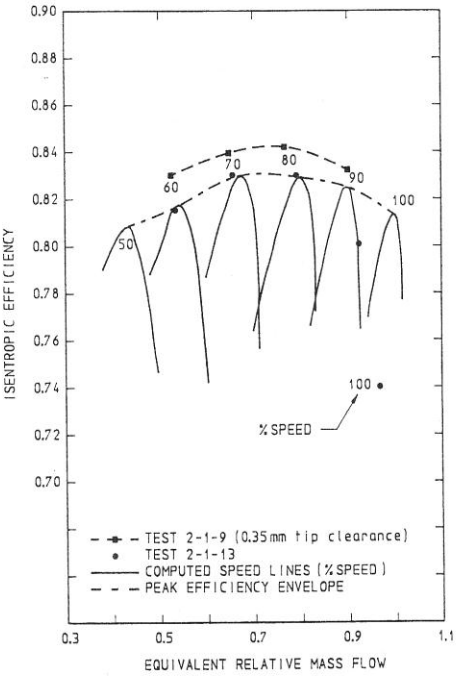

Fig. 10 Comparison between measured and computed compressor efficiencies

A more likely partial cause of the low efficiency at high speed is off-design equivalent mass flow. Figure 10 indicates that at 100% speed, mass flow must be within the range of +1 and -3% of design to achieve high efficiency. This effect is vividly illustrated at 90% speed

by the difference in efficiency between the two measured results. The discrepancy between measured and predicted results at full speed is however just too large to be fully explained by this effect. In the case of the Rolls-Royce engine the flat running line may be the cause of the low efficiency at high speed.

It is significant however, that Rolls-Royce could substantially improve their initial design by changing numbers and settings of stator blades and paying attention to details. This could still be done on the present design.

Generally speaking the prototype compressors (especially the second one) compare quite favourably with available data, but high speed efficiency must be improved without sacrificing surge margin. This is not easy since the blade camber requirements oppose each other exactly as far as these two aspects are concerned.

Summary and Conclusions

1. Both first and second prototype compressor designs were tested successfully as part of a turbojet engine.

2. Reducing first stage rotor blade tip camber from 14,4 to 10,7° together with a few other minor changes resulted in a 3% increase in efficiency.

3. Second prototype peak and full speed efficiencies were 83 and 74%. Efficiency at 91% speed was 80%.

4. Efficiencies could be increased by a further 1% by reducing rotor blade tip clearance from 0.5 to 0.35 mm.

5. Surge margin for both prototypes was adequate for runup from 25 to 65% speed and slam acceleration from 65 to 100% speed.

6. The low efficiencies at high speed have contributed to the compressor not being able to reach design mass flow, due to choking.

7. The compressors should be tested at a series of mass flows (including the design value) by using a nozzle guide vane or turbine (or both) with larger flow area, and an adjustable exhaust nozzle, in order to find peak efficiency at full speed.

8. Although there is room for improvement, the ability to design, manufacture, and test transonic compressors for expendable turbojet engines has been demonstrated.

References

1. Lieblein, S.; Johnsen, I.A.: "Resume of Transonic-Compressor Research at NACA Lewis Laboratory". J. of Eng. for Power, Jul. 1961

2. Bullock, R.O.: "Critical High Lights in the Development of the Transonic Compressor". J. of Eng for Power, Jul. 1961

3. Savage, M.; Boxer, E.; G.W., Jr.; Hartmann, M.J.: "Shock Losses in Transonic Compressor Blade Rows". J. of Eng. for Power, Jul. 1961

4. Kovach, K.; Sandercock, D.M.: "Aerodynamic Design and Performance of Five-Stage Transonic Axial-Flow Compressor". J. of Eng. for Power, Jul. 1961

5. Davis, J.V.; Dellert, E.J.: "Advancement of Small Gas Turbine Component Technology: Advanced Small Axial Compressor Volume II - Test and Redesign". "USAAVLUBS Technical Report 69-10B", Feb. 1978

6. Janetzke, D.C.; Ball, C.L.; Hager, R.D.: "Performance of 1380-Foot-Per-Second Tip-Speed Axial-Flow Compressor Rotor with Blade Tip Solidity of 1.1". NASA TM X-2449, Mrt. 1972

7. Holman, F.F.; Kidwell, J.R.; Ware, T.C.: "Small Axial Compressor Technology Program." (Vol. 1) NASA. CR-134827, Jun. 1976

8. Urasek, D.C.; "Performance of Two-stage Fan having low-aspect-ratio, First-stage Rotor Blading". NASA Technical Paper 1493, Aug. 1979

9. Hirsch, Ch.: "Propulsion and Energetics Panel Working Group 12 on Through Flow Calculations in Axial Turbomachines". AGARD-AR-175, Okt. 1981

10. Anonymous: "Microturbo TRI 60-2 Propulsion Systems." NT 929/79/48.

11. Wennerstrom, A.J.; Derose, R.D.; Law, C.H.: "Investigation of a 1500 ft/sec, Transonic High Through-Flow, Singe-Stage Axial-Flow Compressor with Low Hub/Tip Ratio". Technical Report AFAPL-TR-76-92, Okt. 1976

12. Muller, C.H.; Cox, L.R.: "Single-Stage Axial Compressor Component Development for Small Gas Turbines, Volume III. Supersonic Compressor Stage Development", USSAVLABS-TR-68-90C, Jun. 1969

13. Wall, R.A.: "Axial Flow Compressor Performance Prediction. Modern Prediction Methods for Turbomachine Performance", AGARD Lecture Series, No. 83, Jun. 1976

14. Dengler, P.; Macioce, L.E.: "Small, Low Cost, Expendable Turbojet Engine. I-Design, Fabrication and Preliminary Testing", NASA TM X-3392, May 1976

15. Koch, C.C.: "Stalling Pressure Rise Capability of Axial Flow Compressor Stages", J. Eng. for Power. Vol 103, Oct. 1981

16. Glass, S.J.: "Commisioning of Probe Calibration Wind Tunnel". B. Eng. thesis, University of Stellenbosch, Nov. 1986

17. McKenzie, A.B.; Bayne, B.T.: "Performance Development of the Gem Turboshaft Engine". J. of Eng. for Power, Jan. 1976

Proceedings of ASME Turbo Expo 2012
GT2012
June 11-15, 2012, Copenhagen, Denmark

GT2012-69733

THE DESIGN OF AN AXIAL FLOW FAN FOR APPLICATION IN LARGE AIR-COOLED HEAT EXCHANGERS

Francois G. Louw
Ph.D Eng student
Department of Mechanical
and Mechatronic Engineering
University of Stellenbosch
Stellenbosch
Private bag X1 7602
South Africa
e-mail: francoisl@sun.ac.za

Phillippe R.P. Bruneau
Technical Leader - Fluid Dynamics
Operations Support
SASOL-Sastech
PDP Kruger St.
Secunda 2302
South Africa
e-mail: pbrun@mweb.co.za

Theodor W. von Backström
Researcher
Department of Mechanical
and Mechatronic Engineering
University of Stellenbosch
Stellenbosch
Private bag X1 7602
South Africa
e-mail: twvb@sun.ac.za

Sybrand J. van der Spuy
Senior lecturer
Department of Mechanical
and Mechatronic Engineering
University of Stellenbosch
Stellenbosch
Private bag X1 7602
South Africa
e-mail: sjvdspuy@sun.ac.za

ABSTRACT

The heat transfer characteristics of industrial air-cooled heat exchangers (ACHEs) are dependent on the ability of the fan system to deliver sufficient cooling air. However, under normal operating conditions, variable flow direction and strength often subject peripheral fans to distorted inlet conditions with an attendant reduction in overall volumetric flow rate and cooling capacity. In this paper, a design methodology for single-rotor axial flow fans, appropriate for use in large industrial ACHE's is presented. The primary motivation for this work was to address the issues of robust off-design performance, in particular, distorted inlet flow tolerance. Using this methodology, two 8-bladed prototype fans (B1 and B2) were designed, built and tested in accordance with BS 848 (Type A) standards. The two B-fans have a hub-tip ratio of $x_h = 0.4$ and employ the Clark Y and NASA LS airfoil profiles respectively. Measured performance characteristics were compared to commercial fan designs (V-, DL- and L-fan) used in existing ACHEs. Results indicate that the B-fans have a higher design point operating efficiency. The B-fans also show a steeper fan static pressure rise characteristic compared to the commercial fans, except for the DL-fan, implying a greater tolerance to pressure fluctuations caused by distorted inflows

NOMENCLATURE

Symbols:

A	Area $[m^2]$
a	Swirl coefficient
C_D	Drag coefficient
C_L	Lift coefficient
c	Absolute velocity $[m/s]$
ch	Chord $[m]$
$\dot{m}$	Mass flow rate $[kg/s]$
N	Rotational speed $[rpm]$
n	Swirl exponent
n_b	Number of blades
P	Shaft power $[W]$
R	Dimensionless radius
Re_c	Reynolds number (chord based)
r	Radius$[m]$
$\tan\gamma$	Drag/Lift ratio
u	Tangential velocity of fan blade $[m/s]$
W	Work $[J/kg]$
w	Relative velocity$[m/s]$
x_h	hub-tip ratio
α	Absolute angle
α_{att}	Angle of attack $[^\circ]$
β	Relative angle $[^\circ]$
ε	Swirl factor
μ	Dynamic viscosity $[kg/m.s]$
ξ	Stagger angle $[^\circ]$
ρ	Density $[kg/m^3]$
σ	Solidity
ϕ	Flow factor
Ω	Rotational speed $[rad/s]$

Subscripts:

a	Air
c	Casing
d	Dynamic
h	Hub
m	Mean
max	Maximum
o	Total
rs	Radial station
s	Static
t	Tip
x	Axial direction
θ	Tangential (swirl) direction

1 Introduction

Large air-cooled heat exchangers (ACHEs) find application in many industrial cooling processes. Cooling is achieved by means of large axial flow fans that induce a forced draft of ambient air across arrays of heat exchanger bundles. These fans are typically rotor-only fans, without any stator blade rows or diffusers to recover kinetic energy, adding an extra challenge to the design.

Axial flow fan design procedures depend largely on the work done by Dixon [1], Wallis [2] and McKenzie [3] and usually with the design assumption of two-dimensional flow (axial and tangential). More recent studies by Corsini & Rispoli [4], Corsini *et al.* [5], Vad *et al.* [6] and Lee *et al.* [7] on the effect of tip clearance, blade sweep and fan noise show more sophisticated measures to be included in design procedures in order to obtain better fan performance at lower noise levels. More investigations on the radial flow path in axial flow fans conducted by [8] and [9] propose a model in order to incorporate radial flow in the initial design procedure of axial flow fans.

This article presents a basic design methodology and validation of a rotor-only, large axial flow fan for typical industrial cooling applications such as ACHEs, where the priority was to obtain a high fan efficiency for an existing power plant ACHE. The work presented builds on a study conducted by Venter [10] who investigated the effect of various flow obstacles in a $1/6$th scale version A-frame heat exchanger plenum chamber on axial fan performance, through experimental testing. During tests conducted, Venter [10] did extensive flow measurement on the scaled axial flow fan (referred to as the V-fan) of which a similar full scaled version was installed in an air-cooled steam condenser (ACSC) at a large power plant. The investigation in [10] highlighted two problems associated with the fan:

- The occurrence of reverse flow close to the fan hub, reducing the performance of the fan.
- The fact that fans (especially peripheral fans) are subjected to distorted air inflow leading to blade stall in certain regions of the fan, especially near the hub.

The mentioned aspects suggested that the fan design be reviewed in an attempt to improve the overall fan efficiency, while maintaining the design constraints listed in Tab. 1. Furthermore the absence of stator blade rows and diffusers was also maintained. Given these constraints the following were considered in the fan design:

- Effects of hub-tip ratio (x_h) variation and the inclusion of a nose cone.
- Selection of vortex distribution at the fan outlet.

Table 1. AXIAL FAN DESIGN CONSTRAINTS

Constraint	Value
n_b	8
d_c	1.542 m
Δp_{Fs}	210 N/m^2
V	16 m^3/s
P_{max}	6000 W
N (Ω)	750 rpm (78.5 rad/s)

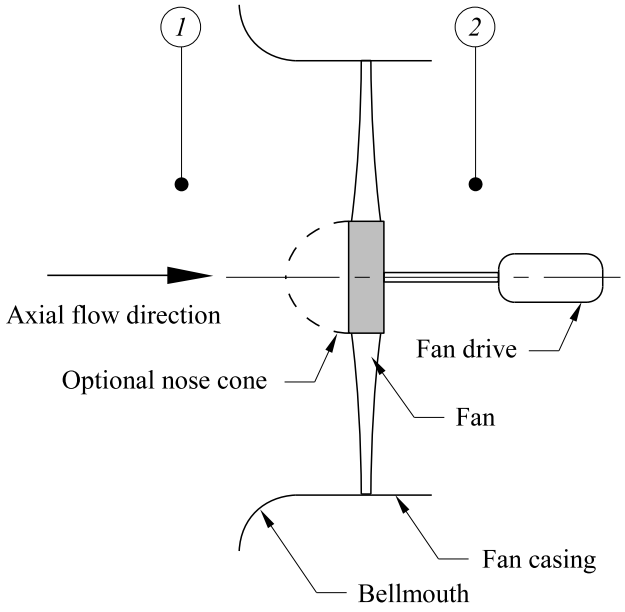

Figure 1. ROTOR-ONLY AXIAL FAN ARRANGEMENT

- Effect of different blade profiles.

The design of two rotor-only axial fans (referred to as the B1- and B2-fan), for operation at the specified operating point is presented. The two fans are designed with the same hub-tip ratio and vortex distribution, but differ in blade profile sections. The first fan employs the Clark-Y aerofoil profile, whereas the second fan is constructed using a NASA LS(GAW1) aerofoil profile. After fan design and construction, testing was done according to the BS 848 fan testing standard in a type A wind tunnel for a spectrum of blade angles and operating points. The performance characteristics of both fans were consequently compared to the performance characteristics of the V-fan. Furthermore performance characteristics of the B-fans were also compared to the DL- [11] and L-fan, also used in ACHEs, for comprehensiveness.

2 Design procedure overview

2.1 General

In a typical ACHE configuration, the use of inlet guide vanes and flow straightening blades is not justified and rotor-only axial

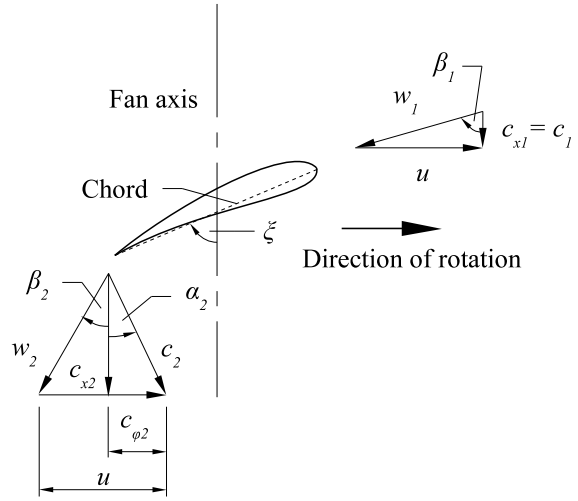

Figure 2. CROSS-SECTION OF A FAN BLADE SHOWING THE VELOCITY VECTORS AND ANGLES FOR A ROTOR-ONLY ARRANGEMENT

fans are used as shown in Fig. 1, depicting the station numbering that will be used in the remainder of the text. Furthermore the velocity triangles at a certain radius for a rotor-only fan are shown in Fig. 2, depicting the symbols that will be used for velocity vectors and angles.

The design process for axial flow fans is an iterative procedure summarized as follows:

1. Specification of the design objectives in terms of pressure rise and volumetric flow rate, which will generally be constrained by the specific application in terms of fan diameter and rotation speed.
2. Establish the general fan configuration (i.e. the number of blades, blade rows and hub-tip ratio).
3. Design blading that will give the desired pressure rise at the specified volumetric flow rate according to specific criteria such as maximum efficiency.
4. Construction and testing of the designed fan for validation purposes.

In the case of the B-fans, focus was placed on procedures 2, 3 and 4, since the pressure rise and volumetric flow rate was constrained by the original application. The B-fan design methodology is confined to vortex distribution, hub-tip ratio and fan blade profiles. The following assumptions are made in the design methodology:

- The flow is incompressible and therefore the density remains constant through the fan.
- The hub and fan casing form concentric cylinders.
- Flow upstream of the fan approaches uniformly and in the axial direction only.
- The blade geometry is made up of two-dimensional blade

sections, stacked in the radial direction, and the flow along the span of the blade is two-dimensional with no radial component.

According to Wallis [2] a central theme among many fan design procedures is the assumption of a *free-vortex* distribution along the fan blades. This is done since it simplifies the design by having a radially constant axial velocity, $c_x(r)$, total pressure rise, $\Delta p_o(r)$, and work distribution, $W(r)$. Wallis [2] and Bass [12] indicate that a free-vortex distribution, generally gives the highest fan efficiencies. However the effect of different swirl velocity distributions, $c_\theta(r)$, on fan efficiency are investigated and presented. Before the details of the design methodology are shown, an overview of the radial equilibrium equations is given and the implications of different vortex distributions are discussed.

2.2 Radial equilibrium

The simplest approach to the study of axial flow turbomachines is to assume that the flow prevailing at the mean radius is representative of the flow conditions along the entire blade span. This approximation is reasonable for large hub-tip ratios in excess of $x_h = 0.8$. However in the case of lower hub-tip ratios, the difference in flow conditions along the blade span needs to be taken into account in design procedures.

Radial flow within a fan is caused by an imbalance between centrifugal forces and radial pressure forces within the fluid. For example, if a fluid element, moving along a certain flow path through a fan is considered, the radial force resulting from the tangential velocity component, must be maintained by a radial pressure force in the opposite direction. The balance of these forces acting on the fluid element is termed "radial equilibrium".

A Simple Radial Equilibrium Equation (SREE), derived in Dixon [1], was used in the fan design procedure, providing a relationship between total pressure, axial and tangential velocity in order for radial equilibrium to be maintained. This equation is given as

$$\frac{1}{\rho}\frac{d\,p_o(r)}{d\,r} = \frac{c_\theta(r)}{r}\frac{d}{d\,r}(r\,c_\theta(r)) + c_x(r)\frac{d\,c_x(r)}{d\,r} \tag{1}$$

where $c_\theta(r)$ is the tangential velocity, $c_x(r)$ the axial velocity and r the radius along the fan annulus. The total pressure distribution, $p_o(r)$, is given by

$$p_o(r) = p_s(r) + \frac{1}{2}\rho\left(c_x(r)^2 + c_\theta(r)^2\right) \tag{2}$$

In the design of axial flow fans, a power law distribution for the outlet swirl velocity has often been used and given as follows:

$$c_{\theta_2}(r) = ar^n \tag{3}$$

where a, the swirl coefficient and n, the swirl exponent are constants. An expression for the outlet axial velocity can be obtained by substituting the power law swirl velocity distribution (Eqn. (3)) into the SREE (Eqn. (1)) and integrating between the limits r and r_h giving:

$$c_{x_2}(r) = \sqrt{2a\Omega(r^{n+1} - r_h^{n+1}) - R(r)a^2(n+1) + c_{x_2}^2(r_h)} \tag{4}$$

where

$$R(r) = ln\left(\frac{r}{r_h}\right)^2 \qquad \text{for} \qquad n = 0 \tag{5}$$

$$R(r) = \frac{r^{2n} - r_h^{2n}}{n} \qquad \text{for} \qquad n \neq 0 \tag{6}$$

2.3 Vortex distribution

As mentioned in section 2.1, a number of standard swirl distributions have been used in turbomachine design, among which the most common are the *free vortex* and *controlled-vortex* swirl distributions.

A *free vortex* swirl velocity distribution is evident when $n = -1$ in Eqn. (3). Recalling that this distribution would give no radial variation in work done as well as the axial velocity, the work calculated at the midspan radius is valid for the entire fan. However, a potential problem in the form of excessive blade twist would occur, that could possibly lead to manufacturing difficulties and excessive bending stresses. This design would also have a large axial blade length near the fan hub. Moreover, in the case of a rotor-only fan, a *free vortex* swirl distribution may lead to excessive swirl velocity at the fan hub which will lead to an increase in flow losses.

Fans designed using *controlled vortex* swirl distributions are less common. Implementation of *controlled vortex* fans is usually done in an attempt to exploit the disadvantages associated with *free vortex* designed fans. A number of *controlled vortex* cases are discussed. A constant outflow angle velocity distribution ($n = 1$) renders similar results to that of a *free vortex* distribution and therefore has the same potential problem. Super

vortex designs ($n = 2$) do not seem to have any advantage, requiring more severe blade twist than *free vortex* and cannot be sustained for $x_h <\approx 0.6$ as shown in the work of Bruneau [13]. Constant swirl distributions ($n = 0$) relieves the excessive blade twist problem. However it results in a large variation in axial velocity and cannot be sustained by fans where $x_h <\approx 0.2$. For rotor-only fans, all *controlled vortex* designs imply a radial variation in axial velocity as well as specific work. Moreover the radial gradient in axial velocity leads to streamline shift as the fluid passes through the turbomachine and the flow conditions at the mean radius is no longer representative of the flow conditions. Integration across the span of the turbomachine blades is therefore required in order to compute the work done and flow rate. Proper design using *controlled vortex* criteria is therefore more complex than the *free vortex* variety.

3 Fan design

Some discussion on the V-, DL- and L-fan design is necessary, before the design methodology of the B-fans is given. Plan views of the V-, DL- and L- and B-fan is depicted in Fig. 3, Fig. 4 and Fig. 5 showing 8-bladed rotor-only fans. The V- and L-fan has a hub-tip ratio of $x_h = 0.15$, whereas the hub-tip ratio of the DL-fan is $x_h = 0.31$. BS 848 type A fan test data of all fans are compared in section 4 of the text.

The standard configuration of the V-, DL- and L-fan does not include a hub shroud or nose cone. The blades of the V-fan and L-fan have little twist implying an arbitrary vortex design. The large blade chords of the DL-fan imply a lower noise fan, but a lower static efficiency compared to fans with smaller blade chords is typical for these fans. The results presented in this text provide a comparison between the V-, DL-, L- and B-fans that would be similar to large scaled versions of these fans.

The fan design methodology is based on a two-step procedure:

1. Investigation into the effect of various hub-tip ratios and vortex flow distributions on fan efficiency.
2. Design of the fan blade geometry.

This two-step procedure was implemented by means of three computer programs conveniently named, FANVTX, FANOPT and FANBLD. These programs were developed at the Mechanical and Mechatronic Engineering Department, University of Stellenbosch, coded using the programming language FORTRAN. The programs employ the design theory discussed in the subsections hereafter. FANVTX and FANOPT were used to investigate the effects of different hub-tip ratio and vortex distributions on fan efficiency for a given design point. Based on the results obtained from these two programs a hub-tip ratio and swirl distribution was chosen for the new design of the B1- and B2-fan and consequently FANBLD was implemented to determine the specific blade details. Details of the programs used are shown, followed by a design discussion.

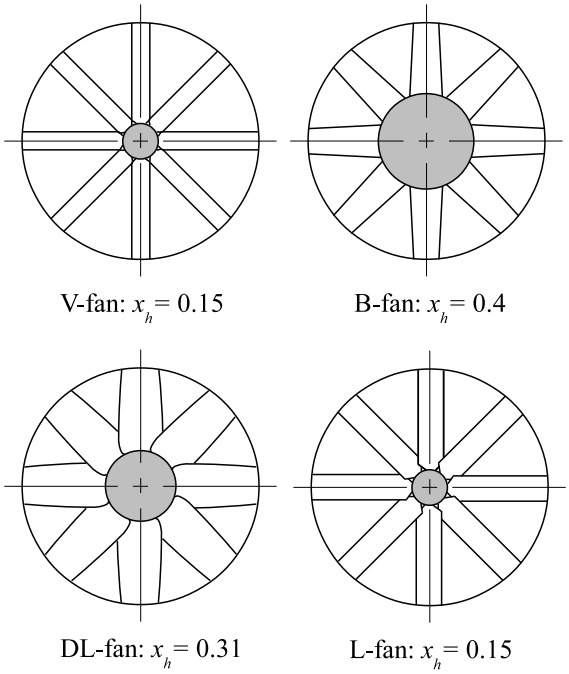

Figure 3. COMPARISON BETWEEN V-, B-, DL- AND L-FAN GEOMETRY

3.1 FANVTX

The program FANVTX firstly divides the entire fan annulus into equally spaced increments (radial stations) along the radius of the fan annulus and then executes some preliminary calculations. Hereafter the velocity triangle vectors, pressure distributions and efficiencies are calculated based on the fan design point for the parameters of fan hub-tip ratio and swirl exponent. The program consequently calculates the swirl and axial velocities by means of an iterative procedure, using Eqn. 3 and Eqn. 4 respectively for a specified air mass flow and static pressure rise across the fan. The appropriate values for the exit axial and swirl velocities are obtained when the air mass flow rate and fan static pressure have converged to a difference between consecutive iterations that are smaller than 0.001.

Once the exit axial and swirl velocity distributions have been determined, the specific work distribution is calculated by means of the Euler work equation which simplifies to the following equation for rotor-only fans:

$$W(r) = \Omega r c_{\theta_2}(r) \tag{7}$$

The total theoretical fan power required is obtained by inte-

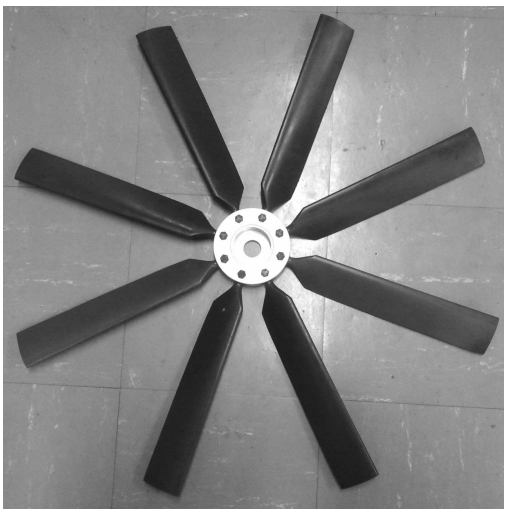

V-fan: $x_h = 0.15$

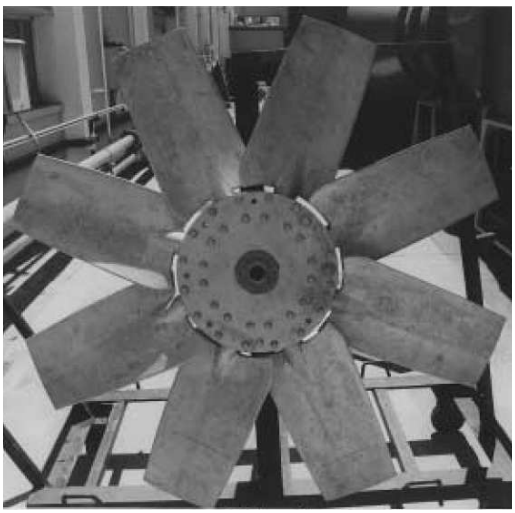

DL-fan: $x_h = 0.31$

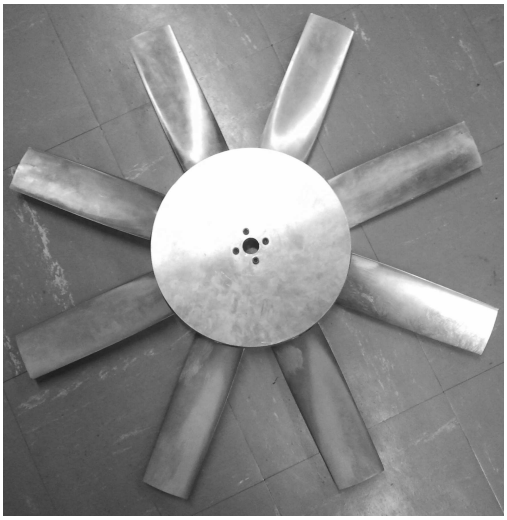

B2-fan: $x_h = 0.4$

Figure 4. PHOTOS OF THE V- and B2-FAN

L-fan: $x_h = 0.15$

Figure 5. PHOTOS OF THE DL- and L-FAN

grating the specific work distribution across the fan annulus as follows:

$$P_{fan} = 2\pi\rho \int_{r_h}^{r_t} c_{x_2}(r) W(r).rdr \approx \sum_{rs=1}^{n_{rs}} W_{rs}\dot{m}_{rs} \tag{8}$$

The pressure distributions at the fan exit are consequently calculated from the velocity components as follow:

$$p_{o_2}(r) = p_{o_1} + \rho\Omega r c_{\theta_2}(r) \tag{9}$$

$$p_{d_2}(r) = \frac{1}{2}\rho\left(c_{\theta_2}(r)^2 + c_{x_2}(r)^2\right) \tag{10}$$

$$p_{s_2} = p_{o_2}(r) - p_{d_2}(r) \tag{11}$$

The mass averaged pressure are consequently obtained by integrating the pressure distribution across the fan annulus:

$$\overline{p}_{o_2} = \frac{2\pi\rho}{\dot{m}_{a,fan}} \int_{r_h}^{r_t} c_{x_2}(r) p_{o_2} . rdr \approx \sum_{rs=1}^{n_{rs}} \frac{p_{o_2,rs}\dot{m}_{rs}}{\dot{m}_{a,fan}} \tag{12}$$

$$\overline{p}_{s_2} = \frac{2\pi\rho}{\dot{m}_{a,fan}} \int_{r_h}^{r_t} c_{x_2}(r) p_{s_2} . rdr \approx \sum_{rs=1}^{n_{rs}} \frac{p_{s_2,rs}\dot{m}_{rs}}{\dot{m}_{a,fan}} \tag{13}$$

From here the theoretical total to total and total to static pressure across the fan can be calculated, since no mechanical energy losses in the annulus and blade drag are taken into account at this stage:

$$\Delta p_{oo,th} = \overline{p}_{o_2} - p_{o_1} \tag{14}$$

$$\Delta p_{os} = \overline{p}_{s_2} - p_{o_1} \tag{15}$$

and the two corresponding non-dimensional pressure coefficients:

$$K_T = \frac{\Delta p_{oo,th}}{\frac{1}{2}\rho c_{x_1}^2} \tag{16}$$

$$K_S = \frac{\Delta p_{os}}{\frac{1}{2}\rho c_{x_1}^2} \tag{17}$$

The theoretical total to static fan efficiency is calculated by:

$$\eta_{os} = \frac{\Delta p_{os}}{\Delta p_{oo,th}} \tag{18}$$

3.2 FANOPT

The program FANOPT is used to obtain a suitable hub-tip ratio and uses an adapted method, presented by Van Niekerk [14] for a rotor-only fan configuration. In this approach the fan is assumed to be of *free vortex* design. The method includes allowances for mechanical flow losses due to the fan blades and annulus walls. The designed fan solidity is lower than unity and therefore, according to Wallis [2], free aerofoil lift and drag data could be used.

The fan total to total and total to static efficiencies can be calculated according to the equations derived in [14] and [13] are given as follow:

$$(1-\eta_{oo}) = \frac{2(\tan\gamma)_{avg}(1-x_b^3)}{3\phi_t(1-x_b^3)} + \frac{2(\tan\gamma)_{avg}(\phi_t - \varepsilon_h x_h)}{1+x_h} + (1-\eta_a)\frac{\phi_t}{2\varepsilon_h x_h} \tag{19}$$

$$(1-\eta_{os}) = (1-\eta_{oo}) + \frac{\phi_t}{2\varepsilon_h x_h}\left[1 - 2(\varepsilon_h x_h)^2 \frac{\ln(x_h)}{1-x_h^2}\right] \tag{20}$$

where $(tan\,\gamma)$ is the average lift/drag ratio, ϕ_t the tip flow factor, ε_h the hub swirl factor and η_a the annulus efficiency. For the B-fan design it was assumed that:

$$tan\,\gamma = 0.0167, \quad \eta_a = 0.8 \tag{21}$$

The flow and swirl factors are defined as follow:

$$\phi(r) = \frac{c_{x_2}(r)}{\Omega r} \tag{22}$$

$$\varepsilon = \frac{c_{\theta_2}(r)}{c_{x_2}(r)} \tag{23}$$

The user specifies the hub-tip ratio, fan static pressure rise and estimated values for the blade lift/drag ratio and annulus efficiency. It should be noted that the values given in Eqn. (21) are assumed since the specific details of the blades and fan annulus are unknown at this stage in the design. However according to Van Niekerk [14] these values are conservative. From here the fan total to total and total to static efficiencies are calculated by means of Eqn. (19) and Eqn. (20). Finally an estimated actual fan total to total and total and static pressure increase can be calculated as follow:

$$\Delta p_{oo} = \Delta p_{oo,th}\eta_{oo} \tag{24}$$

$$\Delta p_{os} = \Delta p_{oo,th}\eta_{os} \tag{25}$$

3.3 FANBLD

The program FANBLD determines the fan blading geometry in order to achieve the flow field as calculated by FANVTX. The program uses the data from FANVTX which includes the number of radial stations and all velocity distributions and angles for the fan inlet and outlet across the fan annulus. The only other inputs are lift coefficients for the hub and tip (obtained from aerofoil lift and drag characteristics) as well as the number of fan blades. The blade profile are then formed by means of scaling, rotating and radial stacking of two-dimensional aerofoil profiles around the centroid of the foil. Once the blading profiles are established the fan static pressure and efficiency are estimated for design point conditions.

The calculation starts by obtaining the mean relative flow angles and velocities;

$$c_{x_m} = \frac{1}{2}(c_{x_1} + c_{x_2}) \tag{26}$$

$$\tan\beta_m = \tan\left(\frac{\beta_1 + \beta_2}{2}\right) \tag{27}$$

$$w_m = \frac{c_{x_m}}{\tan\beta_m} \tag{28}$$

and the blade loading factor:

$$C_L\sigma = 2\left(\frac{c_{\theta_m}}{c_{x_m}}\right)\cos\beta_m \tag{29}$$

From the specified hub and tip lift coefficients and the corresponding loading factors above, the blade chords at the hub and tip are determined from the definition of solidity defined in Wallis [2]:

$$ch = \frac{2\pi r(C_L\sigma)}{n_b C_L} \tag{30}$$

After the blade hub and tip chords have been established, the chords at all other radial stations are obtained by means of linear interpolation. (Although linear interpolation was used in the current design, any interpolation scheme could easily be applied, since the blade angles at the radial stations are adjusted accordingly to give the desired flow field.) Subsequently the solidity, lift coefficient and Reynolds number distributions are determined by means of the following:

$$\sigma = \frac{n_b ch}{2\pi r} \tag{31}$$

$$C_L = \frac{C_L\sigma}{\sigma} \tag{32}$$

$$Re_c = \frac{\rho w_m ch}{\mu} \tag{33}$$

The two-dimensional blade section angles of attack are obtained from the specific aerofoil characteristic curves of lift coefficient as a function of angle of attack. Hereafter the stagger angle distribution in the radial direction of the fan can be calculated by

$$\xi = \beta_1 - \alpha_{att} \tag{34}$$

which is the final part in determining the blade geometry.

The fan blading efficiency can now be determined. Subsequently the total to total and total to static efficiencies are respectively determined as follow:

$$\eta_{oo} = \frac{(\overline{p}_{o2} - p_{o1})_{act}}{(\overline{p}_{o2} - p_{o1})_{act} + \Delta p_{o\ loss}} \tag{35}$$

$$\eta_{os} = \frac{(\overline{p}_{s2} - p_{o1})_{act}}{(\overline{p}_{o2} - p_{o1})_{act} + \Delta p_{o\ loss}} \tag{36}$$

where $\Delta p_{o\,loss}$ is the total pressure decrease due to profile drag and secondary flow losses. The total pressure decrease is determined as prescribed in Wallis [2]:

$$\Delta p_{o\ loss} = \frac{1}{2}\rho K_r c_{x_m}^2 \tag{37}$$

where rotor loss coefficient, K_r, is defined as

$$K_r = K_T \left(\frac{C_D \phi}{C_L cos^2 \beta_m} \right)_{mid} \tag{38}$$

In Eqn. (38) the subscript *mid* indicates that all terms in the brackets be evaluated at midspan radius. Furthermore K_T is defined in Eqn. (16) and the drag coefficient can be calculated through the summation of the profile and secondary drag coefficients. Therefore:

$$C_D = C_{D\ prof} + C_{D\ sec} \tag{39}$$

where $C_{D\ prof}$ can be obtained from the aerofoil profile lift and drag ratio characteristics and $C_{D\ sec}$ is defined by Wallis [2] as

$$C_{D\ sec} = 0.018 C_L^2 \tag{40}$$

As mentioned the program then calculates the fan blade profile by means of a radial aerofoil stacking procedure. Dimensionless tabulated aerofoil coordinate data (specific to each type of aerofoil) are incorporated into the program. These coordinates are then scaled and rotated according to the chord length and angle of attack of each radial station as calculated by FANBLD, presenting the final blade geometry.

3.4 Design discussion

The total to static fan efficiency was calculated by means of FANVTX for a number of swirl exponents and hub-tip ratios at the design condition specified in Tab. 1. The results were subsequently plotted in Fig. 6. It can be seen that the best total to static efficiencies are obtained for a swirl distribution close to *free vortex* (i.e. $n = -1$). It is also seen that a smaller hub-tip ratio gives a higher fan static efficiency. However, the smaller the hub-tip ratio, the more the swirl velocity distribution is confined

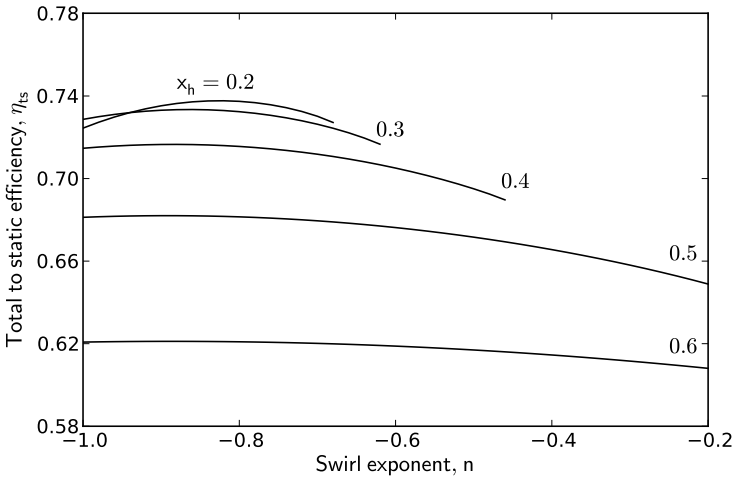

Figure 6. TOTAL TO STATIC EFFICIENCY AS FUNCTION OF SWIRL EXPONENT FOR A SPECTRUM OF HUB-TIP RATIOS AS OBTAINED BY 'FANVTX'

to a smaller range of permissible swirl exponents. For example, if the case of a hub-tip ratio $x_h = 0.2$ is considered, it can be seen that this fan design is confined to $-1 < n < -0.68$. A further increase in swirl exponent would cause the axial velocity to become negative at the fan hub in order to satisfy continuity. A greater range of the swirl exponent can be exploited with an increase in hub-tip ratio, but at the expense of a decrease in static efficiency. The reason for this is that a higher through flow rate causes an increase in dynamic pressure, which has a strong influence on total to static efficiency.

Also noteworthy is the small difference in static efficiency for $0.2 < x_h < 0.4$, which is in the order of 1.5%. This suggests that a small sacrifice made in terms of static efficiency, would allow the use of a higher hub-tip ratio with a reduction in blade twist as well as reduced manufacturing and blade stress problems.

For a given hub-tip ratio, the choice of swirl exponent causes a relatively small difference in fan static efficiency for $-1 < n < -0.8$ and shows maximum static efficiencies for most hub-tip ratios (except $x_h = 0.2$) in the region close to $n = -0.9$ and not $n = -1$, the *free vortex* case. It is however conceded that a small difference in the physically manufactured blade is likely for these respective swirl exponents. For the given design objectives, the *free vortex* design is taken as appropriate, for this part of the design procedure.

A family of curves is presented in Fig. 7 as obtained by FANOPT, showing the fan static efficiency for different values of hub-tip ratios as a function of total to static pressure coefficient, K_S. The swirl factors at the hub and tip of the fan are constrained to $0.3 < \varepsilon < 1.1$ as prescribed in Wallis [2], corresponding to absolute flow angles of $17^\circ < \alpha_2 < 50^\circ$. Wallis [2] mentions that

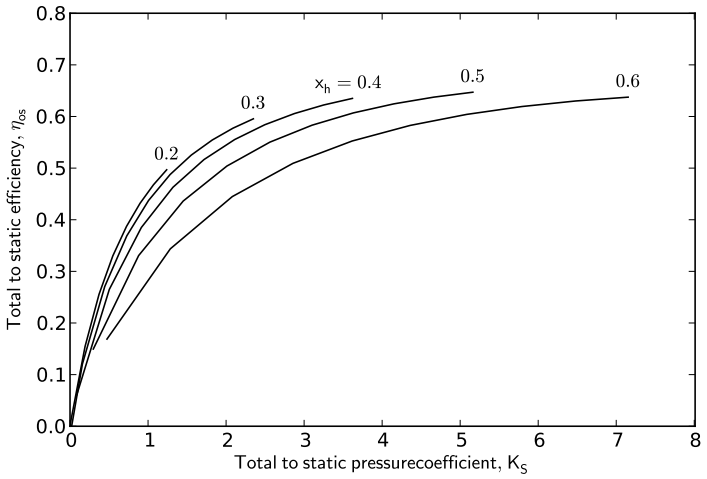

Figure 7. TOTAL TO STATIC EFFICIENCY AS A FUNCTION OF TOTAL TO STATIC PRESSURE COEFFICIENT FOR A SPECTRUM OF HUB-TIP RATIOS AS OBTAINED BY 'FANOPT'

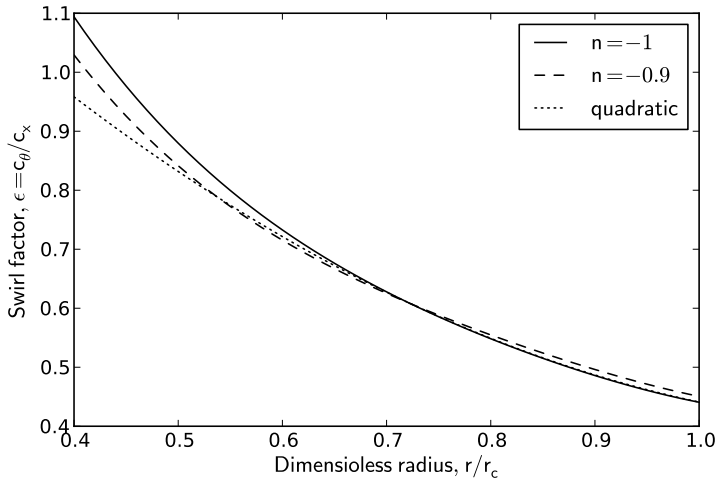

Figure 8. SWIRL DISTRIBUTION PRESENTED IN TERMS OF DIMENSIONLESS RADIUS FOR VARIOUS SWIRL EXPONENTS, n, AND A QUADRATIC CURVE FIT

absolute flow angles larger than 48° lead to high exit flow losses.

It is evident from Fig. 7 that lower hub-tip ratios would give superior fan performance for low total to static pressure difference requirements. However, as the total to static pressure difference requirement increases, the low hub-tip designs cannot attain the higher pressure rises without exceeding the swirl factor constraint. It can be seen that the best alternative for the given design point specifications is obtained for a hub-tip ratio of $x_h = 0.4$, providing an estimated total to static efficiency of $\eta_{ts} = 62.7\%$. Subsequent to the discussed findings a *free vortex* distribution and hub-tip ratio of $x_h = 0.4$ was used for the design of the B1- and B2-fan.

Finalizing the design procedure, the tip flow factor, ϕ_t, and hub swirl factor, ε_{2h}, are given some consideration. The tip flow factor for the *free vortex* design and $x_h = 0.4$ is $\phi_t = 0.168$. According to Wallis' [2] recommendation a tip flow factor of $\phi_t < 0.2$ is acceptable for a rotor-only type axial fan. Wallis [2] also recommends an exit hub swirl factor of $\varepsilon_{2h} < 1.1$ for axial fans without inlet guide vanes, but including exit flow straighteners.

A plot of the swirl factor distribution as a function of dimensionless radius is shown in Fig. 8, showing the swirl distribution for $n = -1, -0.9$ and a specific quadratic curve fit. It can be seen that the swirl factor presented in the figure for the *free vortex* case reaches a maximum at the hub of $\varepsilon_{2h\ (n=-1)} = 0.991$, with an exit outflow angle of $\alpha_{2h\ (n=-1)} = 44.8°$, which is acceptable in terms of Wallis' [2] criterion. It is also visible that the maximum swirl factor increases as the swirl exponent increases. In order to reduce the hub exit swirl factor, a quadratic curve fit, essentially having a *free vortex* distribution from the midspan radius to the tip, is done. The quadratic vortex distribution resulted in a maximum swirl factor and flow angle of $\varepsilon_{2h\ (quad)} = 0.95$ and $\alpha_{2h\ (quad)} = 43.5°$.

Other than reducing blade stress and manufacturing complications of twisted blades, reducing the swirl factor at the hub region is also beneficial in terms of tolerance to distorted inlet flows in that the root section blade loading is reduced. Blade stall generally occurs at the root section of fans installed in large ACHEs. Furthermore, the amount of work imparted to the fluid by the fan increases radially to a maximum at the tip and therefore the critical part of the blade geometry is the midrange to tip region. Consequently the quadratic vortex distribution was chosen for further design.

As mentioned earlier in the text, two blade profiles are selected for the B1- and B2-fan design respectively, being the Clark-Y and the NASA LS(GAW1) aerofoil profile. The Clark-Y profile has been used extensively in aircraft propellers where pressure rise and flow turning requirements are low. The NASA LS(GAW1) profile is chosen based on good lift/drag characteristics, promising a reasonable fan efficiency as well as a good off-design performance and tolerance to distorted inflow.

3.5 Blade geometry and manufacture

The radially stacked blade geometry of the designed B2-fan blade is shown in Fig. 9. Furthermore the comparison between the B-fan, V-fan, DL-fan and L-fan hub size is shown in Fig. 3.

Fan blades consist of a glass fibre shell encasing a plastic foam core into which aluminium threaded stub shafts are secured for the blade to be connected to the fan hub. Blades are connected to the hub and fixed at the correct angle by means of two lock nuts. The blades were designed such that the root section

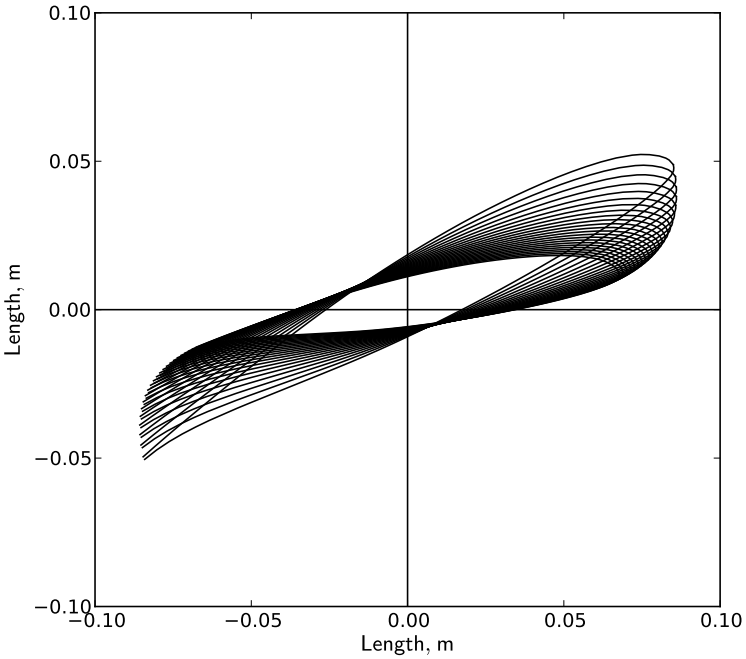

Figure 9. BLADE PROFILE PRESENTED IN THE FORM OF RADIALLY STACKED AEROFOIL PROFILES FOR THE B2-FAN

was perpendicular to the stub shaft in order to test for a range of different blade angles. As a consequence the space between the blade root and hub resulted in a large amount of leakage flow, decreasing fan performance. Consequently, wooden root seals were shaped and fitted in order to alleviate the problem.

4 Fan testing and results

Fan testing was conducted according to fan testing standard BS 848 in a type A wind tunnel. Tests were performed for a range of volumetric flow rates at the design speed of $N = 750\,rpm$, fluid density of $\rho = 1.2\ kg/m^3$ and atmospheric pressure. The B-fan performance characteristics were evaluated and compared to the V-fan, DL-fan and L-fan performance characteristics by measuring the pressure, efficiency and power consumption of the individual fans. The B-fans were also performance tested for a range of blade stagger angles (measured at the blade hub). Fan characteristics are shown for the design point angles only, for brevity. The B-fan performance characteristics for a range of blade angles can be found in the work of Bruneau [13] and Stinnes [15].

Different fan tests were conducted for the B-fans in order to investigate the effect of a fitted nose cone compared to a flat plate hub and the effect of root seals compared to no root seals. The B-fan performance characteristics are subsequently compared to that of the V-fan, DL-fan and L-fan.

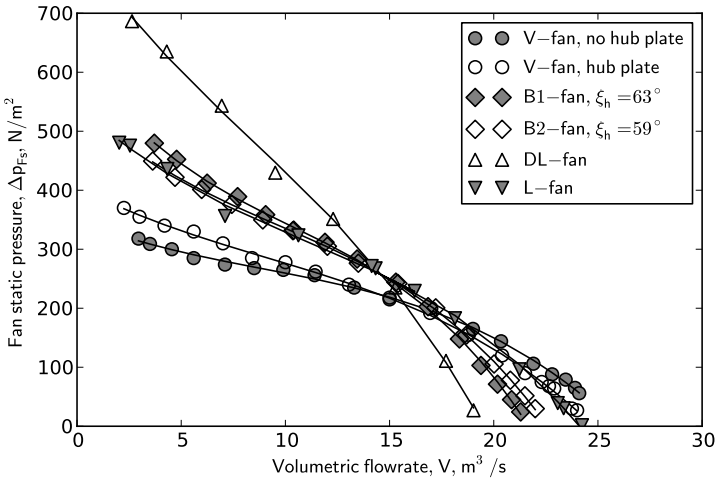

Figure 10. FAN STATIC PRESSURE PRESENTED IN TERMS OF VOLUMETRIC FLOW RATE FOR THE V-, DL-, L-, B1- AND B2-FANS

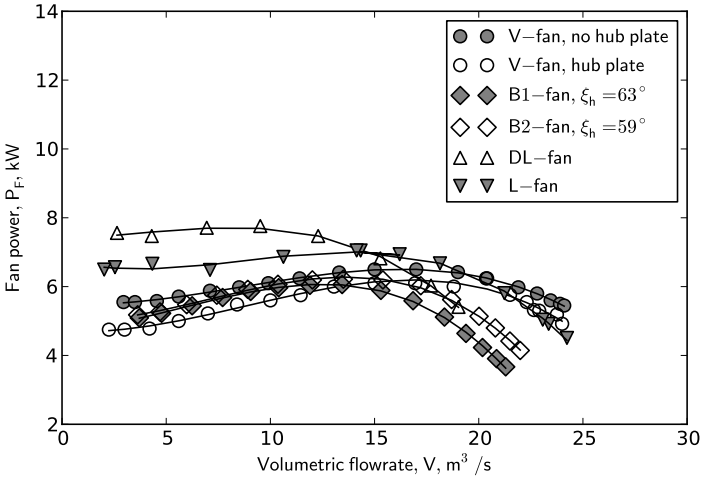

Figure 11. FAN POWER PRESENTED IN TERMS OF VOLUMETRIC FLOW RATE FOR THE V-, DL-, L-, B1- AND B2-FANS

4.1 V-fan performance characteristics

The fan static pressure, power and efficiency characteristics of the V-fan are presented in Fig. 10, Fig. 11 and Fig. 12 respectively. Experiments conducted by Venter [10] showed that the V-fan performance can be increased by simply fixing a flat plate to the fan, effectively increasing the hub-tip ratio from $x_h = 0.15$ to $x_h = 0.289$. This is evident through the steeper gradient fan static pressure curve, lower pressure consumption and higher fan efficiency of the V-fan with the attached hub plate, shown in Fig. 10, Fig. 11 and Fig. 12.

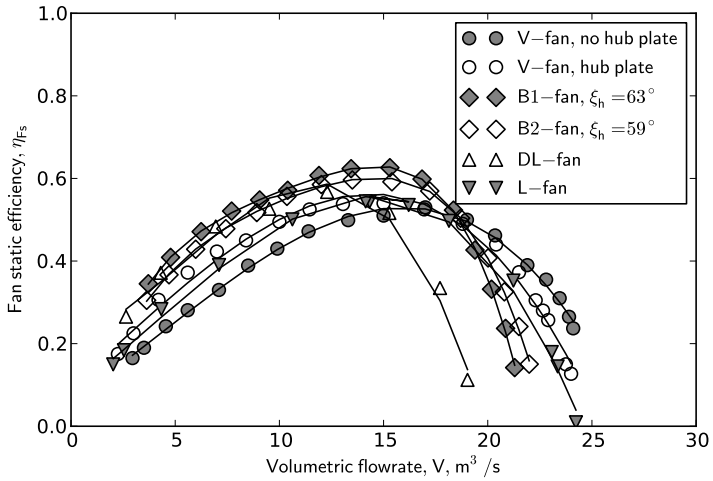

Figure 12. FAN STATIC EFFICIENCY IN TERMS OF VOLUMETRIC FLOW RATE FOR THE V-, DL-, L-, B1- AND B2-FANS

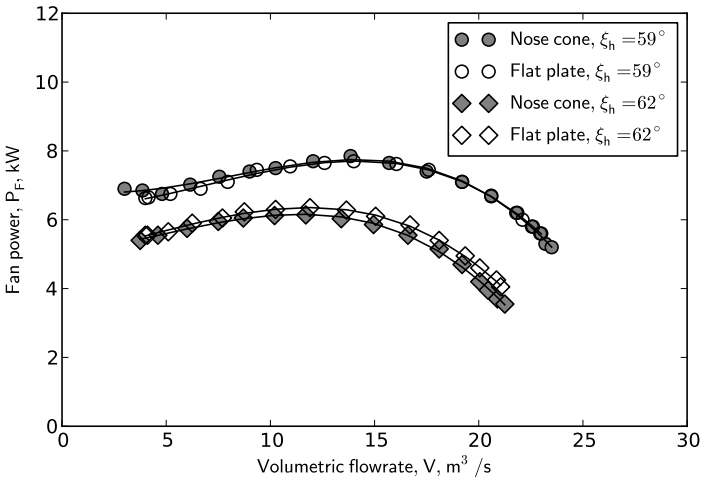

Figure 14. FAN POWER PRESENTED IN TERMS OF VOLUMETRIC FLOW RATE OF THE B1-FAN, SHOWING THE EFFECT OF A FITTED NOSE CONE

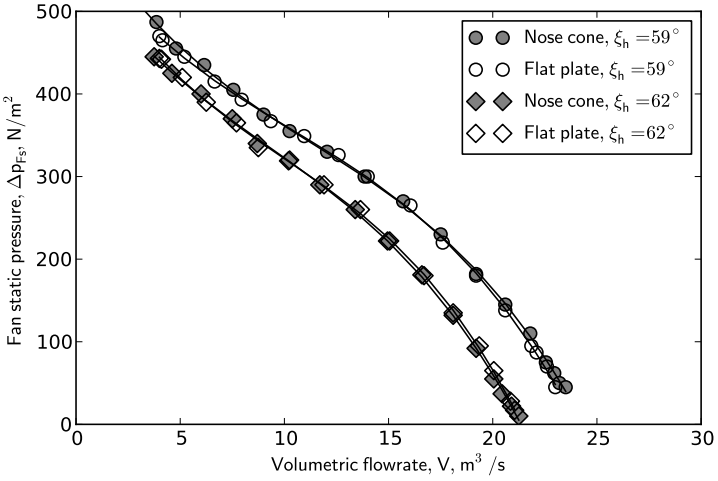

Figure 13. FAN STATIC PRESSURE PRESENTED IN TERMS OF VOLUMETRIC FLOW RATE OF THE B1-FAN, SHOWING THE EFFECT OF A FITTED NOSE CONE

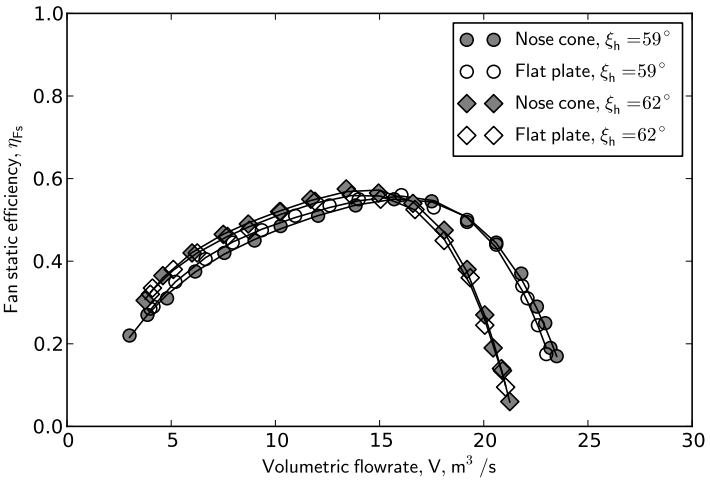

Figure 15. FAN STATIC EFFICIENCY PRESENTED IN TERMS OF VOLUMETRIC FLOW RATE OF THE B1-FAN, SHOWING THE EFFECT OF A FITTED NOSE CONE

4.2 B-fan performance characteristics

The B1-fan was fitted with a semi-spherical nose cone as depicted in Fig. 1 and tested for hub stagger angles of $\xi_h = 59^\circ$ and $\xi_h = 62^\circ$. As shown in the fan characteristics of Fig. 13, Fig. 14 and Fig. 15 it can be seen that the fitted nose cone has no significant influence on fan performance.

The inclusion of root seals (sealing a minimum clearance between the blade root and hub of ≈ 13 *mm*) together with a nose cone were also investigated. Tests conducted on the B2-fan with a hub stagger angle of $\xi_h = 59^\circ$ are shown in Fig. 16, Fig. 17 and Fig. 18. The test results show a significant increase in fan performance due to the inclusion of root seals. For the design condition of $V = 16\ m^3/s$ the inclusion of root seals on the fan results in a static pressure difference of $\Delta p_{Fs} = 227\ N/m^2$ compared to $\Delta p_{Fs} = 191\ N/m^2$ for the case where no seals were present, with power consumptions of 6.151 *kW* and 5.576 *kW* respectively. However the nett effect on the fan static efficiency is a substantial improvement across the entire operating envelope. At the design point the sealed root case gives a static efficiency of $\eta_{Fs} = 0.587$, whereas the open root case gives $\eta_{Fs} = 0.544$. Peak efficiencies occur at approximately $V = 13\ m^3/s$, giving

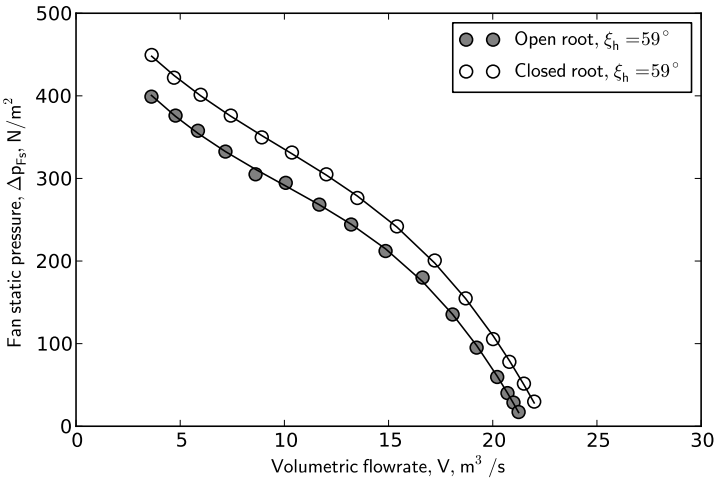

Figure 16. FAN STATIC PRESSURE PRESENTED IN TERMS OF VOLUMETRIC FLOW RATE OF THE B2-FAN, SHOWING THE EFFECT OF ROOT SEALS

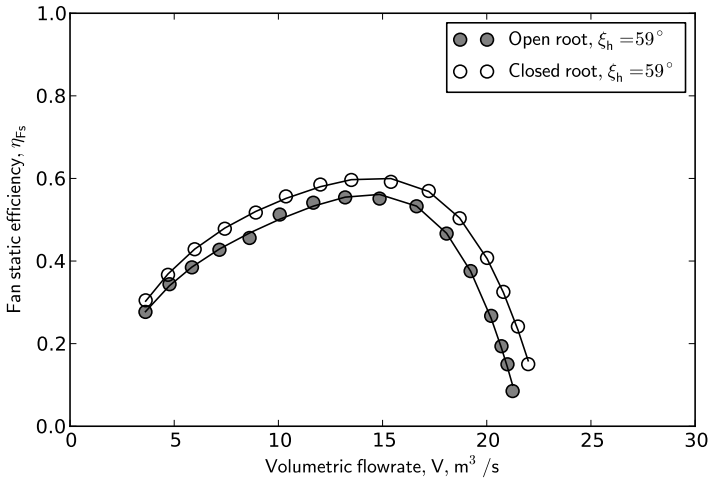

Figure 18. FAN STATIC EFFICIENCY PRESENTED IN TERMS OF VOLUMETRIC FLOW RATE OF THE B2-FAN, SHOWING THE EFFECT OF ROOT SEALS

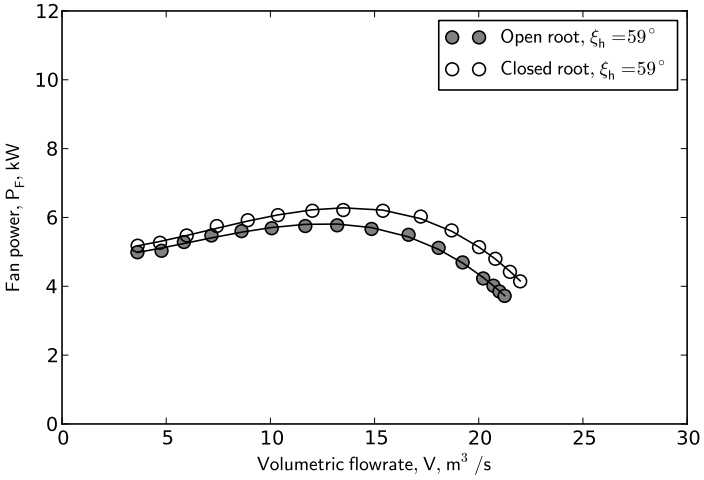

Figure 17. FAN POWER PRESENTED IN TERMS OF VOLUMETRIC FLOW RATE OF THE B2-FAN, SHOWING THE EFFECT OF ROOT SEALS

$\eta_{Fs} = 0.598$ and $\eta_{Fs} = 0.555$ for the respective cases of open and sealed roots.

4.3 Fan performance comparison

A comparison of the B-fan characteristics can be seen in Fig. 10, Fig. 11 and Fig. 12. The reference power characteristic for the V-fan reveals a peak power just beyond 6 kW. In order to compare the B1- and B2-fan to the V-fan, the stagger angles resulting in similar maximum power consumption was selected as B-fan datums. For comparative purposes, the B-fans contain both root seals and a nose cone. The B1-fan datum hub stagger angle is 63° while that of the B2-fan is 59°. Fan performance data of the DL-fan and L-fan is also shown in order to compare the B-fan with other fans used for similar cooling applications in industrial processes.

The most notable feature of the pressure characteristic comparison is the relatively steep pressure gradient of the B1- and B2-fan, $\Delta p_{Fs}/V$, compared to that of the V-fan. This implies that the B-fans are less sensitive to pressure load fluctuations. Thus for a given pressure load change, generally occurring during distorted air inflow, the change in volumetric flow rate would be less for the B-fans compared to the V-fan. The DL-fan has an even larger pressure gradient compared to that of the B-fans and also shows similar power consumption at the design point. The power consumption of the DL-fan at lower flow rates is however higher compared to the B-fans. The DL-fan also shows a low design point efficiency.

Peak power consumptions for the B1- and B2-fan occur at lower volumetric flow rates than that of the V-fan, being $P_F = 6.144\ kW$ at $V = 12.75\ m^3/s$ and $P_F = 6.295\ kW$ at $V = 13.75\ m^3/s$ respectively. The V-fan peak power consumption of $P_F = 6.205\ kW$ occurs at the design point flow rate of $V = 16\ m^3/s$. Furthermore the peak power consumption of the DL-fan and L-fan is $P_F = 7.76\ kW$ at $V = 9.5\ m^3/s$ and $P_F = 7.05\ kW$ at $V = 14.14\ m^3/s$

The performance curves in Fig. 12 show that the B-fan static efficiency is superior to that of the V-fan up to a volumetric flow rate of $V = 18.5 m^3/s$. The B1-fan design point static efficiency is $\eta_{Fs} = 0.618$ while that of the B2-fan is $\eta_{Fs} = 0.592$. The peak static efficiency of the B1- and B2-fan occur at $V = 14.5\ m^3/s$ being $\eta_{Fs} = 0.630$ and $\eta_{Fs} = 0.601$ respectively. The V-fan has

a peak efficiency of $\eta_{Fs} = 0.534$ at $V = 14.89\ m^3/s$ and a design point efficiency of $\eta_{Fs} = 0.531$. Furthermore static efficiency of the B-fans is generally higher compared to the DL-fan and is superior up to a volumetric flow rate of $V = 19m^3/s$ compared to the L-fan. The peak static efficiencies of the DL-fan and L-fan are $\eta_{Fs} = 56.73$ at $V = 12.29\ m^3/s$ and $\eta_{Fs} = 54.45$ at $V = 14.14\ m^3/s$.

5 Conclusion

A design methodology for rotor-only, axial flow fans has been developed and used to design two experimental fans conveniently named the B1- and B2-fan. It was found that for the given design point conditions of fan static pressure difference, $\Delta p_{Fs} = 210\ N/m^2$ and volumetric flow rate, $V = 16\ m^3/s$, the *free vortex* swirl distribution with the parabolic modification was appropriate. Other swirl distributions were also considered, however it was found that significant deviation from the *free vortex* case is only feasible for hub-tip ratios of $x_h > \approx 0.5$. The reason being that for the specified low volumetric flow rate and the corresponding low axial velocity, deviations from the free-vortex case would lead to the axial velocity at the fan tip to approach 0.

The hub-tip ratio has a substantial effect on fan performance, since static efficiencies are higher for lower hub-tip ratios and low static pressure rise. However low hub-tip ratio design are unable to attain higher static pressure differences without excessive hub swirl and the associated losses. The best hub-tip ratio for the specified design constraints were determined to be $x_h = 0.4$.

The V-fan, DL-fan, L-fan and B-fans were performance tested according to BS-848 testing standards in a type-A fan test tunnel. At the design point flow rate and power consumption of $P_F = 6.0\ kW$, the B1- and B2-fan indicate higher fan static efficiencies compared to that of the V-fan. The static efficiencies were respectively obtained as $\eta_{Fs} = 0.618$, $\eta_{Fs} = 0.592$ and $\eta_{Fs} = 0.531$. The fan static pressure rise is also higher for the B-fans at design point, respectively being $\Delta p_{Fs} = 224.7\ N/m^2$, $\Delta p_{Fs} = 227.2\ N/m^2$ and $\Delta p_{Fs} = 211.1\ N/m^2$ for the B1-, B2- and V-fan. Furthermore additional comparisons were done between the B-fans, the DL-fan and the L-fan. The static efficiencies of DL- and L-fan at the design point was found to be $\eta_{Fs} = 0.404$ and $\eta_{Fs} = 0.537$ respectively. The fan static pressure increase of the DL- and L-fan at the design point was found to be $\Delta p_{Fs} = 198.2\ N/m^2$ and $\Delta p_{Fs} = 233.6\ N/m^2$ respectively.

Furthermore the inclusion of a nose cone compared to a flat plate hub had very little to no significant effect on fan performance. The sealing of the B-fan root section of the blades showed a marked performance increase compared to the case where no root seals were present, being in the order of $\Delta p_{Fs} = 35\ N/m^2$ and $\eta_{Fs} = 0.04$. The power consumption for the case of the sealed roots was however higher at $P_F = 6.15\ kW$ opposed to $P_F = 5.58\ kW$ for the unsealed case.

The predicted total to static pressure and efficiency of the B-fans determined by Van Niekerk's [14] method, being $\Delta p_{Fs} = 211\ N/m^2$ and $\eta_{Fs} = 0.627$, compare favourably with that of the tested results at the design point. The fan static pressure and efficiency of the B1-fan being $\Delta p_{Fs} = 224.7\ N/m^2$ and $\eta_{Fs} = 0.619$, and for the B2-fan being $\Delta p_{Fs} = 227.2\ N/m^2$ and $\eta_{F}s = 0.592$ respectively.

REFERENCES

[1] Dixon, S., 1978. *Fluid mechanics-thermodynamics of turbomachinery*, third ed. William Clowes (Beccles) Ltd, Great Brittain.

[2] Wallis, R., 1983. *Axial flow fans and ducts*. John Wiley and Sons Inc.

[3] McKenzie, A., 1997. *Axial flow fans and compressors*. Ashgate publishing company, Burlington, Vermont, U.S.A.

[4] Corsini, A., and Rispoli, F., 2004. "Using sweep to extend the stall-free operational range in axial fan rotors". *Proceedings of the Institution of Mechanical Engineers, Part A: Journal of Power and Energy*, **218**(3), Jan., pp. 129–139.

[5] Corsini, A., Rispoli, F., and Sheard, A. G., 2007. "Development of improved blade tip endplate concepts for low-noise operation in industrial fans". *Proceedings of the Institution of Mechanical Engineers, Part A: Journal of Power and Energy*, **221**(5), Jan., pp. 669–681.

[6] Vad, J., Kwedikha, A. R. A., Horváth, C., Balczó, M., Lohász, M. M., and Régert, T., 2007. "Aerodynamic effects of forward blade skew in axial flow rotors of controlled vortex design". *Proceedings of the Institution of Mechanical Engineers, Part A: Journal of Power and Energy*, **221**(7), Jan., pp. 1011–1023.

[7] Lee, G. H., Baek, J. H., and Myung, H. J., 2003. "Structure of Tip Leakage Flow in a Forward-Swept Axial-Flow Fan". *Flow, Turbulence and Combustion (formerly Applied Scientific Research)*, **70**(1-4), pp. 241–265.

[8] Vad, J., and Bencze, 1998. "Three-dimensional flow in axial flow fans of non-free vortex design". *International journal of heat and fluid flow*, **19**, pp. 601–607.

[9] Vad, J., 2010. "Radial fluid migration and endwall blockage in axial flow rotors". *Proceedings of the Institution of Mechanical Engineers, Part A: Journal of Power and Energy*, **224**(3), Jan., pp. 399–417.

[10] Venter, S., 1990. "The effectiveness of axial flow fans in A-frame plenums". PhD thesis, Department of mechanical engineering, University of Stellenbosch, Stellenbosch, R.S.A.

[11] Meyer, C., 2003. "Numerical investigation of the effect of fan performance on forced draught air-cooled heat exchanger plenum chamber aerodynamic behaviour". PhD thesis, Department of Mechanical and Mechatronic Engineering, University of Stellenbosch, R.S.A.

[12] Bass, R., 1987. *Factors influencing the aerodynamic design*

of low pressure axial flow fans. Industrial fans - Aerodynamic design, Institution of Mechanical Engineers, April.

[13] Bruneau, P., 1994. "The design of a single rotor axial flow fan for cooling tower application". Master's thesis, Department of mechanical engineering, University of Stellenbosch, Stellenbosch, R.S.A.

[14] Van Niekerk, C., 1958. "Ducted fan design theory". *Journal of applied mechanics*.

[15] Stinnes, W., 1998. "The performance of axial fans subjected to forced cross-flow at inlet". Master's thesis, Department of Mechanical Engineering, University of Stellenbosch, Stellenbosch, R.S.A.

Eng. Opt., 1996, Vol. 26, pp. 25–55
Reprints available directly from the publisher
Photocopying permitted by license only

MINIMIZATION OF THE EXIT LOSS OF A ROTOR-ONLY AXIAL FAN

T. W. VON BACKSTRÖM**, J. D. BUYS* and W. H. STINNES**

**Department of Mechanical Engineering
*Department of Mathematics
University of Stellenbosch, 7600 Stellenbosch, South Africa

(Received 9 March 1995)

The main loss source in rotor-only axial fans is that associated with the kinetic energy flux at the fan exit. Both the axial and the tangential velocity components contribute to this loss. In this paper the loss is minimized by sequential quadratic programming under the constraints of constant volume flow and work input. It is shown that, when observing certain simple traditional fan design rules, the exit kinetic energy flux can be reduced by only 1.2 percentage points compared to free vortex fans.

KEY WORDS: Axial fan, kinetic energy, fan efficiency, sequential quadratic programming, fan design rules

NOMENCLATURE

a	outer-to-inner radius ratio [-]
A	dimensionless work rate [-]
B	dimensionless flow rate [-]
C	velocity [m/s]
f	general function of t [-]
F	dimensionless dynamic loss rate [-]
g	general constraint function [-]
h	dimensionless discrete interval length [-]
l	chord length [m]
L	dynamic loss rate [W]
$\dot{m}$	mass flow rate [kg/s]
n	number of discrete points for computation [-]
P	total pressure [Pa]
r	radius [m]
s	blade spacing [m]
t	dimensionless radius [-]
u	dimensionless swirl velocity [-]
U_0	blade tip speed [m/s]
v	dimensionless axial velocity [-]
W_0	fan power consumption [W]
α	flow angle (absolute) [°]; kinetic energy coefficient [-]
β	flow angle (relative to rotor) [°]

Δ change in property, as in ΔP_0
v inner-to-outer radius ratio [-]
ρ density [kg/m^3]
ϕ flow coefficient [-]]
ψ total pressure rise coefficient [-]
Ω rotational velocity [rad/s]

Subscripts

a axial
w whirl, swirl
i inner
i, j indices
o outer
1 inlet
2 outlet

1 INTRODUCTION

The main sources of loss determining the ultimate efficiency of single rotor axial fans are drive line losses, blading losses due to blade drag, tip leakage losses and annulus losses. The greatest, however, is the loss associated with the kinetic energy flux at the fan exit. The objective of this study was to determine the theoretical lower limit of this loss as determined by the radial distribution of circumferential velocity at the fan exit, that is, by the exit vortex distribution. The distribution of axial velocity at the exit is, of course, affected by that of the circumferential velocity via radial equilibrium, and both components contribute to the exit dynamic pressure.

When the inlet velocity has no swirl, the only exit vortex distribution resulting in a work input rate that is constant with radius is the free vortex distribution, where the circumferential component of the exit velocity is inversely proportional to radius. This implies that when any other minimum is sought, the constraint of constant work input rate per unit radius cannot be applied.

2 ASSUMPTIONS

The mathematical model was formulated subject to the following assumptions:

1. Inlet conditions are restricted to uniform total pressure across the inlet cross-section.
2. The Euler turbo-machinery equation for incompressible flow is applicable.
3. Simple radial equilibrium. This implies that the flow has no radial component at the planes of analysis up- and downstream of the rotor, although there may be a streamline shift through the rotor disc.
4. In the expression of radial equilibrium the flow is assumed to be incompressible, inviscid and loss free.

3 TURBOMACHINERY EQUATIONS

In order to facilitate sensible comparison between different radial variations of axial and swirl velocities, total mass flow has to be fixed at a specified value:

$$\dot{m} = 2\pi\rho \int_{r_i}^{r_o} rC_a\, dr$$

Similarly, the fan power consumption has to be specified.

$$W_o = 2\pi\rho\Omega \int_{r_i}^{r_o} r^2 C_a C_w\, dr$$

The radial variations of the axial and swirl velocities are related by the differential equation describing the radial equilibrium of flow to which a swirl component has been imparted[1]:

$$\Omega\left[\frac{d}{dr}(rC_w)\right] = \frac{C_w}{r}\left[\frac{d}{dr}(rC_w)\right] + C_a\frac{dC_a}{dr}$$

For the free vortex solution, where rC_w is constant, the radial gradient of rC_w is zero, the rate of work done on the fluid is constant with radius and the axial velocity C_a is uniform. Because of these simple relationships and also because of its application in practice, the free vortex distribution is chosen as the reference case.

4 TRADITIONAL AXIAL FAN DESIGN LIMITATIONS

Before deciding on a domain of analysis it is appropriate to discuss some traditionally accepted physical design limitations expressed as commonly used rules of thumb. The first is the hub swirl limitation that states that design values of hub exit flow angles α_i in excess of about 50° (from the axial) will result in backflow at the hub. Wallis[2] states that the design ratio of tangential to axial exit velocity at the hub may not exceed $\tan\alpha_{2i} = 1.1 (= \tan 48°)$.

This has the following implications for the free vortex reference case where $r_i C_{wi} = r_0 C_{wo}$ and $C_{ai} = C_{ao} = C_a$

$$\tan\alpha_{2i} = \frac{C_{wi}}{C_a} = \frac{C_{wi}}{C_{wo}}\frac{C_{wo}}{U_o}\frac{U_o}{C_a} = \frac{1}{\nu}\frac{\psi}{2}\frac{1}{\phi} = 1.1$$

where $\nu = r_i/r_o$ is the inner-to-outer radius ratio, $\phi = C_{ao}/U_o$ is the flow coefficient and

$$\psi = 2\Delta P_o/(\rho U_0^2) = 2C_{wo}/U_o$$

is the total pressure rise coefficient. This implies that $\psi < 2.2\,\nu\phi$ to prevent backflow at the hub or, in general, that highly loaded fans with low throughflow velocities must have high hub tip ratios.

A second limitation to fan design concerns the maximum pressure rise coefficient ψ. When a higher stagnation pressure rise across the fan is desired, the number of

blades may be increased until the blades no longer work as isolated airfoils but in a blade cascade, as in compressors. Howell[3] has published curves of the maximum flow deflection in cascades as function of the flow outlet angle. According to Dixon[4] the relationship between the inlet and outlet design flow angles may be approximated by

$$\tan\alpha_1 - \tan\alpha_2 = 1.55/(1 + 1.5s/l)$$

where s is the blade spacing and l the chord length. In compressors, s/l at the hub is usually not less than 0.4 in order to reduce losses. In that case, for rotors:

$$\tan\beta_1 - \tan\beta_2 = 1.55/(1 + 1.5 \times 0.4) = 0.97 \approx 1.0$$

But

$$\tan\beta_1 - \tan\beta_2 = \frac{C_{wi}}{U_i} = \frac{C_{wi}}{C_{wo}}\frac{C_{wo}}{U_o}\frac{U_o}{C_a} = \frac{1}{v}\frac{\psi}{2}\frac{1}{\phi}$$

Thus

$$\psi = 2.0\, v\phi$$

Only the second limitation (the cascade limitation above) applies since it is more stringent than the first (the hub backflow limitation). Only applying the second limitation implies that the absolute flow angle α_i at the hub is limited to 45°.

A third limitation is that the rotor should not turn the flow beyond the axial direction in the co-ordinate system rotating with the rotor. If this limitation is exceeded there will be a static pressure drop across that section of the rotor instead of an increase. For rotor-only fans this limitation implies that $C_{wi} < U_i$:

$$\text{If } \frac{C_{wi}}{U_i} < 1 \text{ then } \frac{C_{wi}}{U_i} = \frac{C_{wi}}{U_o}\frac{U_o}{U_i} = \frac{C_{wi}}{C_{wo}}\frac{C_{wo}}{U_o}\frac{r_o}{r_i} = \frac{1}{v^2}\frac{\psi}{2} < 1.0$$

This implies that $\psi < 2v^2$ to limit the rotor hub relative exit flow angle to 0°. This equation puts an absolute maximum limit of 2 on ψ, since v cannot exceed unity.

5 MINIMIZATION FORMULATION

The functional to be minimized is the expression for the kinetic energy flux of the flow at the fan outlet:

$$L = \pi\rho \int_{r_i}^{r_o} rC_a(C_a^2 + C_w^2)\, dr$$

For easier mathematical manipulation the following non-dimensionalising substitutions are made:

$$t = r/r_i$$

$$a = r_o/r_i$$

$$u(t) = C_w(r_i t)/(r_i\Omega)$$

$$v(t) = C_a(r_i t)/(r_i \Omega)$$

The minimization problem then reads:

$$\text{Find} \quad u(t),\ v(t), \quad t \in [1, a]$$

in order to minimize

$$\int_1^a v(v^2 + u^2)\, t dt = F = L/(\pi \rho r_i^5 \Omega^3) \quad \text{(dimensionless kinetic energy flux)}$$

subject to:

$$\left.\begin{aligned} & t\frac{du}{dt} + u = \frac{u^2}{t} + u\frac{du}{dt} + v\frac{dv}{dt}, \ t \in [1, a] && \text{(radial equilibrium)} \\ & \int_1^a t^2\, uv dt = A = W_o/(2\pi \rho r_i^5 \Omega^3) && \text{(dimensionless work rate)} \\ & \int_1^a tv dt = B = \dot{m}/(2\pi \rho r_i^3 \Omega) && \text{(dimensionless flow rate)} \end{aligned}\right]$$

6 SOLUTION OF THE MINIMIZATION PROBLEM

Since analytical solutions to the differential equation are not readily available, a numerical minimization solution process has to be constructed. The radial domain is discretized into n equal intervals of length h, yielding $n + 1$ discrete points along the radial direction of the annulus:

$$h = (a - 1)/n, \quad t_i = 1 + ih, \quad i = 0, 1, 2, \ldots, n$$

The respective integrals were evaluated using the trapezoidal rule:

$$\int_1^a f(t)\, dt \approx \frac{h}{2} f(t_o) + h \sum_{i=1}^{n-1} f(t_i) + \frac{h}{2} f(t_n)$$

while higher order approximation was used for the derivatives in the differential equation:

$$\begin{aligned} i = 0: f'(t_i) &\approx [-25f(t_0) + 48f(t_1) - 36f(t_2) + 16f(t_3) - 3f(t_4)]/(12h) \\ i = 1: f'(t_i) &\approx [-3f(t_0) - 10f(t_1) + 18f(t_2) - 6f(t_3) + f(t_4)]/(12h) \\ 1 < i < n - 1: f'(t_i) &\approx [f(t_{i-2}) - 8f(t_{i-1}) + 8f(t_{i+1}) - f(t_{i+2})]/(12h) \\ i = n - 1: f'(t_i) &\approx [-f(t_{n-4}) + 6f(t_{n-3}) - 18f(t_{n-2}) + 10f(t_{n-1}) + 3f(t_n)]/(12h) \\ i = n: f'(t_i) &\approx [3f(t_{n-4}) - 16f(t_{n-3}) + 36f(t_{n-2}) - 48f(t_{n-1}) + 25f(t_n)]/(12h) \end{aligned}$$

Writing $u_i = u(t_i)$ and $v_i = v(t_i)$, the minimization problem of the previous section may then be approximated by the following:

Find

$$u_i, v_i, \quad i = 0, 1, \ldots, n$$

in order to minimize

$$F(u_0, \ldots, u_n, v_0, \ldots, v_n)$$

subject to the constraints

$$g_j(u_0, \ldots, u_n, v_0, \ldots, v_n) = 0, \quad j = 0, 1, \ldots, n+2$$

where $F(u_0, \ldots, v_n)$ represents the trapezoidal approximation of the kinetic energy flux, $g_j(u_0, \ldots, v_n)$, $j = 0, 1, \ldots, n$ represent the discretization of the radial equilibrium equation at t_j, and $g_{n+1}(u_0, \ldots, v_n)$ and $g_{n+2}(u_0, \ldots, v_n)$ represent trapezoidal approximations to the work and flow rate equations respectively.

The above minimization problem (with $2n+2$ variables and $n+3$ non-linear constraints) can be solved for given values of a, A and B using a numerical technique for general mathematical programming problems. In this study the sequential quadratic programming (SQP) method of Powell and Han[5] was employed. Between $n = 10$ and $n = 40$ points were used, but $n = 20$ proved sufficient and economical for this analysis.

7 DOMAIN OF ANALYSIS

Taking the physical limitations on fan performance into consideration, the logical domain of analysis was along the constraint $\psi = 2v^2$ and $\psi = 2v\phi$. These two relationships imply that $\phi = v$. The values of a, A and B required in the minimization procedure were calculated from v, ψ and ϕ by the equations given below:

$$a = 1/v$$

$$A = \psi\phi(1 - v^2)/(4v^5)$$

$$B = \phi(1 - v^2)/(2v^3)$$

8 RESULTS

A first glance at the results in Table 1 would indicate uncommonly low values of theoretical fan efficiencies: all below 50%, since all the losses are higher than 50%. It can, however, be shown by an approach similar to that in Section 4 that the fraction of the input power required merely to generate a uniform outlet velocity profile is

$$L_a = \phi^2/\psi$$

Under the constraints previously discussed, where $\psi = 2v^2$ and $\phi = v$, if follows that $\psi = 2\phi^2$ and $L_a = 0,5$ for all the cases in Table 1. By a similar approach it can be shown that the fraction of the power associated with the free vortex whirl component is

Table 1 Comparison of exit kinetic energy flux as fraction of input power for free vortex and optimized designs

		Exit KE fraction		*Percentage point reduction*
$v = \phi$	ψ	*Free vortex*	*Optimized*	
0.1	0.02	0.523	0.521	0.2
0.2	0.08	0.567	0.559	0.8
0.3	0.18	0.619	0.606	1.3
0.4	0.32	0.674	0.658	1.6
0.5	0.50	0.731	0.713	1.8
0.6	0.72	0.787	0.771	1.6
0.7	0.98	0.843	0.830	1.3
0.8	1.28	0.897	0.900	0.7
0.9	1.62	0.949	0.947	0.2

$$L_w = \frac{\psi}{2(1 - v^2)} \ln \frac{1}{v}$$

By using the above two equations it can be shown that single rotor free vortex fans can have theoretical efficiencies higher than 50%; for example, take $v = 0.4$; $\phi = 0.2$ and $\psi = 0.16$. This combination of parameters does not exceed the limitations $\psi < 2v\phi$ or $\psi < 2v^2$. In this case $L_a = 0.25$ and $L_w = 0.087$, and the theoretical efficiency is $(1 - 0.25 - 0.087) = 0.663$.

Another look at the results in Table 1 shows that the percentage point reduction in exit kinetic energy flux between the optimized and free vortex fans is small: typically 0 to 2 percentage points. This, however, is about the same as the improvement achievable by optimizing other parameters such as profile losses and tip clearance. The greatest improvement of 1.8 percentage points is possible when $v = \phi = \psi = 0.5$.

The general trend exhibited for combinations of v, ϕ and ψ not on the constraint line was that the percentage point improvement was rather insensitive to ϕ and it increased with increasing ψ and with decreasing v. This implies that large percentage point improvements are only possible when exceeding the traditional design limitations.

Readers familiar with the kinetic energy coefficient, α = (kinetic energy flux)/(kinetic energy flux for uniform axial flow) may note that α can be calculated from the data in Table 1 by dividing the kinetic energy fraction by 0.5, resulting in an improvement in α from 1.462 for the free vortex case to 1.426 for the optimized case, when $v = \phi = \psi = 0.5$. For the higher efficiency fan mentioned earlier $\alpha = (0.25 + 0.087)/0.25 = 1.348$.

Figure 1 shows how the exit swirl and axial velocity components are affected when $v = \phi = \psi = 0.5$. The velocity values are normalized by the respective free vortex values at the inner radius. The free vortex swirl velocity then decreases from a value of 1.0 at the inner radius to 0.5 at the outer radius while the free vortex axial velocity component remains constant at 1.0 irrespective of radius. The effect of the

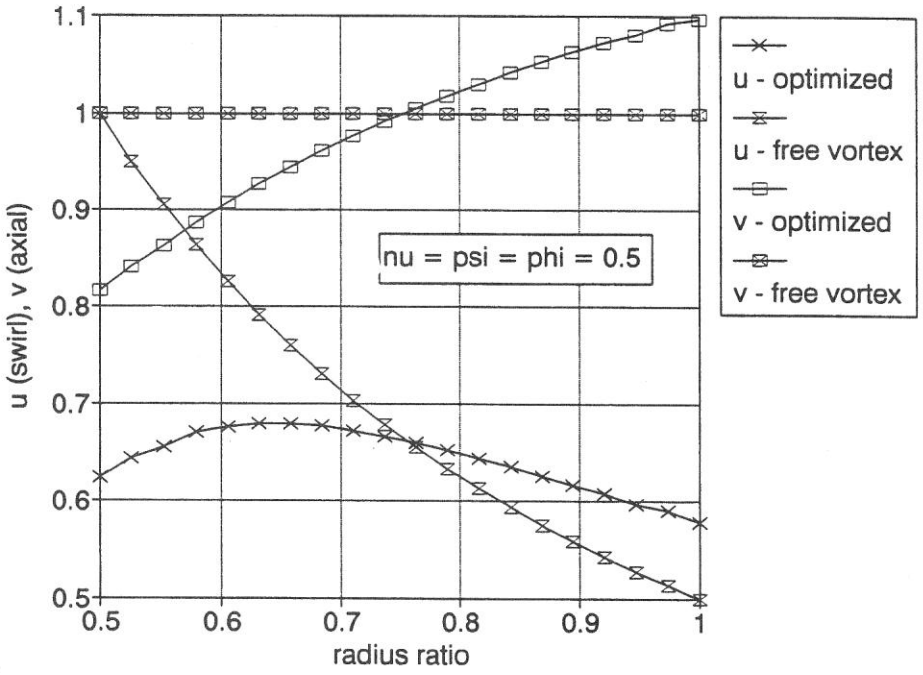

Figure 1 Comparison of free vortex and optimized velocity profiles for $\nu = \phi = \psi = 0.5$.

optimization is to bring about a lower swirl velocity at the inner and a higher velocity at the outer radius, with an inverse effect on the axial velocity. The result is that the flow angle at the inner radius is reduced from 45° to arctan(0.625/0.815) = 37.5°.

The effect of the optimization on the absolute and relative exit flow angles and on the required blade camber is shown in Figure 2. For the sake of simplification it is assumed here that the blade camber equals the flow deflection. The reduction in inner radius absolute flow angle from 45° for the free vortex to 37,5° for the optimized design is evident, as well as a small increase from 27° to 28,5° at the outer radius. The relative exit flow angle (which is a rough indication of the blade trailing edge angle) is increased from 0° to 25° at the inner radius and decreased from 57° to 52° at the outer radius. This means the trailing edge twist is reduced by more than half from 57° − 0° = 57° to 52° − 25° = 27°. The flow deflection and camber are reduced from 45° to 20° at the hub, and increase from 7° to 12° at the tip.

9 CONCLUSIONS

The blades of the optimized fans have much smaller camber at the hub and much less twist, possibly resulting in lower manufacturing costs. The smaller flow deflection at the hub will also reduce flow deflection losses.

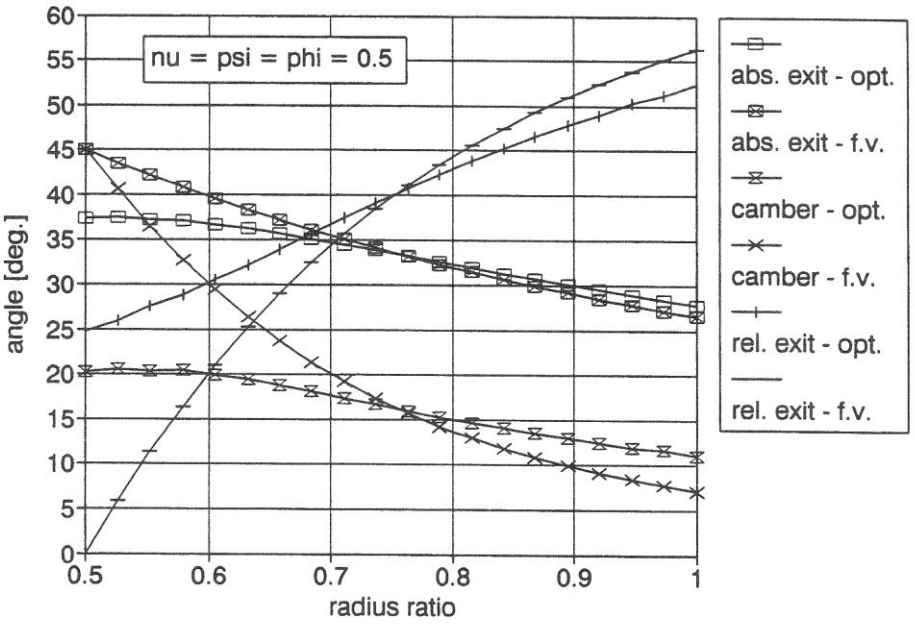

Figure 2 Comparison of free vortex and optimized absolute and relative flow angles and deflaction (camber) profiles for $\nu = \phi = \psi = 0.5$.

For maximally loaded fans the theoretical maximum amount by which the efficiency of a free vortex single rotor fan may be improved by minimizing the exit dynamic losses is 1.8 percentage points. In this case the minimization was done for the same values of inner to outer radius ratio, flow coefficient and pressure rise coefficient as those that would, for the free vortex case, result in turning the relative flow at the hub right up to the axial direction and the absolute flow at the hub up to 45°. The optimized solutions drifted away from these two constraints, indicating further possibilities for optimization, depending on which of hub-to-tip radius ratio, flow coefficient and pressure rise coefficient are allowed to change, according to the application of the fan.

References

1. Cohen, H., Rogers, G. F. C. and Saravanamuttoo, H. I. H. (1987) *Gas Turbine Theory*, 3rd edn, p. 157, Singapore, Longman Scientific & Technical.
2. Wallis, R. A. (1983) *Axial Flow Fans and Ducts*. p. 183, London, John Wiley & Sons, Inc.
3. Howell, A. R. (1945) *Fluid Dynamics of Axial Compressors*. London, Proc. Instn. Mech. Eng.
4. Dixon, S. L. (1978) *Fluid Mechanics, Thermodynamics of Turbomachinery*. 3rd edn, p. 75, London.
5. Powell, M. J. D. (1978) *A fast algorithm for non-linearly constrained optimization calculations*. In GA Watson (Ed.), Numerical Analysis Dundee, 1977, Lecture Notes in Mathematics 630. Springer Verlag, Berlin, pp. 144–157.

Eng. Opt., 1996, Vol. 26, pp. 25–33
Reprints available directly from the publisher
Photocopying permitted by license only

MINIMIZATION OF THE EXIT LOSS OF A ROTOR-ONLY AXIAL FAN

T. W. VON BACKSTRÖM**, J. D. BUYS* and W. H. STINNES**

**Department of Mechanical Engineering*
**Department of Mathematics*
University of Stellenbosch, 7600 Stellenbosch, South Africa

(Received 9 March 1995)

The main loss source in rotor-only axial fans is that associated with the kinetic energy flux at the fan exit. Both the axial and the tangential velocity components contribute to this loss. In this paper the loss is minimized by sequential quadratic programming under the constraints of constant volume flow and work input. It is shown that, when observing certain simple traditional fan design rules, the exit kinetic energy flux can be reduced by only 1.8 percentage points compared to free vortex fans.

KEY WORDS: Axial fan, kinetic energy, fan efficiency, sequential quadratic programming, fan design rules

NOMENCLATURE

- a outer-to-inner radius ratio [-]
- A dimensionless work rate [-]
- B dimensionless flow rate [-]
- C velocity [m/s]
- f general function of t [-]
- F dimensionless dynamic loss rate [-]
- g general constraint function [-]
- h dimensionless discrete interval length [-]
- l chord length [m]
- L dynamic loss rate [W]
- m mass flow rate [kg/s]
- n number of discrete points for computation [-]
- P total pressure [Pa]
- r radius [m]
- s blade spacing [m]
- t dimensionless radius [-]
- u dimensionless swirl velocity [-]
- U_0 blade tip speed [m/s]
- v dimensionless axial velocity [-]
- W_0 fan power consumption [W]
- α flow angle (absolute) [°]/kinetic energy coefficient [-]
- β flow angle (relative to rotor) [°]

Performance of rotor-only axial fans designed for minimum exit kinetic energy

S.J. van der Spuy[1] T.W. von Backström[1]

(First received April 2002; Final version July 2002)

The major loss source in rotor-only axial fans is the kinetic energy associated with the axial and circumferential components of the exit flow. This paper investigated the aerodynamic and acoustic performance of two fans designed to produce minimum exit kinetic energy. The first was a general application fan and the second a low-noise fan with large-chord forward-swept blades. The fans were tested for fan noise and performance in accordance with BS 848. The low-noise fan was the quieter and more efficient of the two fans, whilst both fans were quieter and more efficient than an existing typical general application fan, of unknown design. The results underlined the importance of following a well-defined design methodology when designing rotor-only axial flow fans.

Nomenclature

a	outer-to-inner radius ratio
A	dimensionless work rate
B	dimensionless flow rate
c	chord length, m
C	absolute velocity, m/s
C_w	absolute swirl velocity, m/s
C_a	absolute axial velocity, m/s
L	kinetic energy flux, W
i	incidence angle, °
m	deviation angle coefficient
M_R	radial Mach number
s	blade pitch, m
r	fan radius, m
u	dimensionless swirl velocity $= C_w/(r_i\Omega)$
U	blade speed, m/s
v	dimensionless axial velocity $= C_a/(r_i\Omega)$

Greek

α	angle of attack, °
β	relative flow angle, °
γ	pitch angle (from circumferential), °
δ	deviation angle, °
Δ	change in value
ϕ	flow coefficient, C_a/U_o
η	geometric blade sweep angle, °
η	efficiency
λ	aerodynamic blade sweep angle, °
ν	hub-tip ratio
ρ	density, kg/m^3
θ	camber angle, °
θ_s	blade axis sweep angle, °
σ	solidity = c/s
ψ	load coefficient, $\Delta p/\left(\frac{1}{2}\rho U_o{}^2\right)$
ξ	stagger angle (from axial), °
Ω	rotational speed, rad/s

Subscripts

a	axial
i	inner radius
m	mean value
o	outer radius
s	"swept" blade variables
w	whirl
1	blade leading edge
2	blade trailing edge
$infinite$	axial distance far up- or downstream from rotor

1. Department of Mechanical Engineering, University of Stellenbosch, Private Bag X1, Matieland, 7602 South Africa

Introduction

In rotor-only axial fans designed according to simple traditional rules, the kinetic energy associated with the axial and circumferential components of the exit flow can be almost as large as the useful fan work.[1] The stagnation pressure losses associated with the blade profile, wall friction at the casing and hub, or tip clearance are much smaller than those associated with the exit kinetic energy. The latter have a major effect on the fan efficiency because the exit dynamic pressure in axial fans is large compared to the fan pressure rise, and rotor-only fans never have stator blade rows and rarely have diffusers to increase exit static pressure.

The theory required for the minimisation of exit kinetic energy for a rotor-only axial fan is described by Von Backström *et al.*[1] The main objective of the work presented here was to motivate the use of a well-defined design methodology when designing axial fans, by reporting on the measured aerodynamic and acoustic performance of two rotor-only fans designed for minimal kinetic energy in the flow leaving the rotor. The one fan is a member of a typical general application series of fans (Fig. 1), while the other is a one-off design aimed at low noise generation (Fig. 2). The term "fan series" refers to a scenario where one blade design is used for a number of different fan outer diameter sizes by cutting (also referred to as cropping) the blade to the desired length. The term "general application" refers

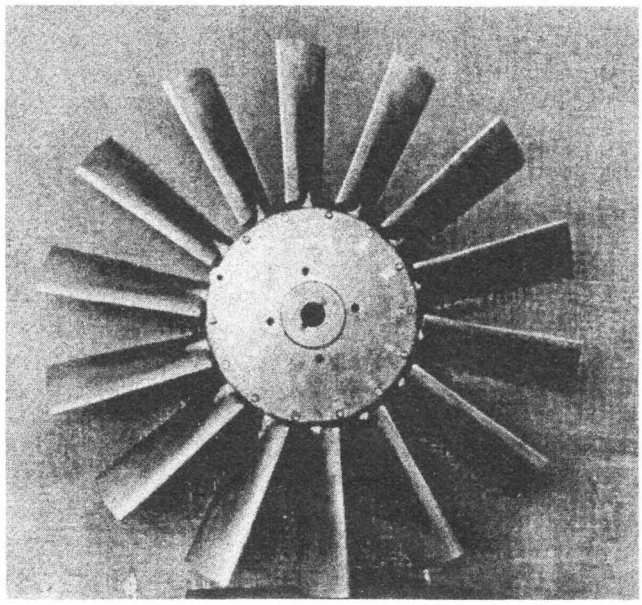

Fig. 1. Photograph of 14-bladed, 630 mm diameter, general application fan

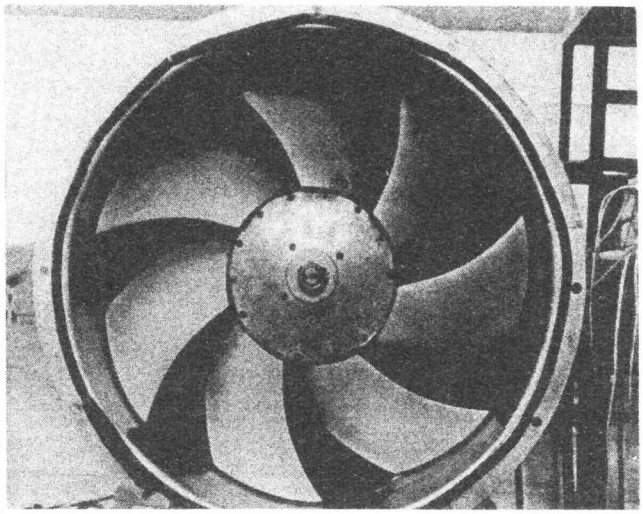

Fig. 2. Photograph of 7-bladed, 630 mm diameter, low-noise fan

to fans typically used in the air-conditioning and building ventilation industry. The performance of the general application and low-noise fan is compared with that of an industry-related "reference fan" with the same "fan series" range as that of the general application fan (the design specifications of the reference fan are not known).

According to Wright,[2], Wright & Simmons,[3] and Van der Spek,[4] the following variables affect axial fan noise most strongly: blade tip speed, blade aspect ratio and blade forward sweep angle. Mesquita *et al.*[5] proposed an axial flow design method where the blade airfoil profile at hub and shroud is optimised for minimum drag and the profile distribution is based on a free vortex outlet velocity profile. Bruneau[6] used elementary airfoil theory, combined with a generic power law equation for the exit velocity profile, to design axial fan blades, whilst Beiler & Carolus[7] used the same theory, combined with corrections for sweep angles, to design forward-swept axial fan blades. References to the effect of minimisation of the exit kinetic energy on fan aerodynamic or acoustic performance were not found in the literature, despite a wide search.

Van der Spuy[8] designed two fan types to investigate how the minimisation of fan exit kinetic energy affects fan total-to-static efficiency and fan noise. The first was a general application fan series, ranging from 315 mm to 1 000 mm diameter (Fig. 1), and the second a 630 mm diameter low-noise fan with large-chord forward-swept blades (Fig. 2).

Optimisation procedure

Von Backstrom *et al.*[1] determined optimum exit velocity profiles for rotor-only fans by minimising the functional representing exit kinetic energy, for given flow and load coefficients:

$$L = \pi \times \rho \times \int_{r_i}^{r_o} rC_a \left({C_a}^2 + {C_w}^2\right) dr \tag{1}$$

The constraints according to which the functional was minimised are:

Radial equilibrium:

$$\Omega \times \left[\frac{d\left(C_w r\right)}{dr}\right] = \frac{C_w}{r} \times \left[\frac{d\left(C_w r\right)}{dr}\right] + C_a \times \frac{dC_a}{dr} \tag{2}$$

Prescribed dimensionless work rate:

$$A = \frac{1}{\Omega^2 \times {r_i}^5} \int_{r_i}^{r_o} r^2 C_a C_w dr \tag{3}$$

Prescribed dimensionless flow rate:

$$B = \frac{1}{\Omega^2 \times {r_i}^3} \int_{r_i}^{r_o} r\ C_a dr \tag{4}$$

The minimisation problem was discretised for solution as a numerical problem for values of A and B and tip-to-hub diameter ratio, a, and solved by sequential quadratic programming.[1] The values for A and B were based on given load and flow coefficients. This approach resulted in exit velocity profiles requiring blades with less twist than the more traditional free vortex velocity distribution. Fig. 3 compares typical exit axial and swirl velocity components for a free vortex and an optimised radial swirl velocity distribution.

Design approach

The book by Wallis[9] on the design of axial flow fans was used for the design procedure. Articles by Wright & Simmons[3] and Smith & Hsuan[10] were used to adapt the design procedure for the forward swept fan blade of the low-noise fan. The design procedures used for both the general application and low noise fans are described by Van der Spuy.[8]

The designs were constrained by industry-related specifications for a general application fan series. This determined the casing diameters, hub diameters and hub-tip ratios, ν, as well as the number of blades. The 150 mm

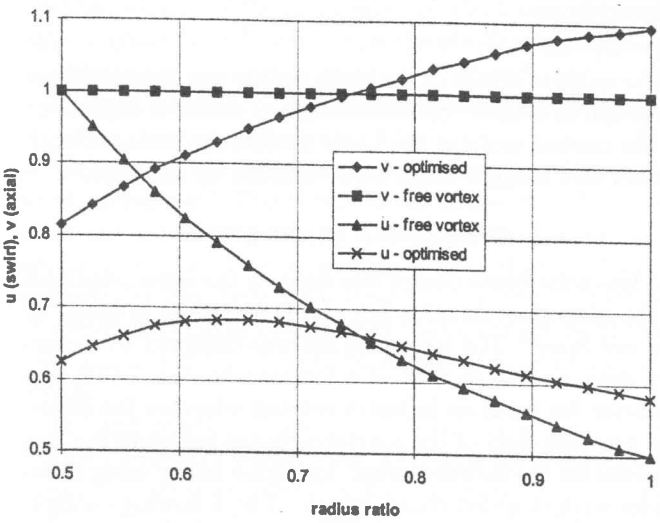

Fig. 3. Example of optimised and free vortex velocity profiles for $v = \phi = \psi = 0.5$ (Von Backström *et al.*[1])

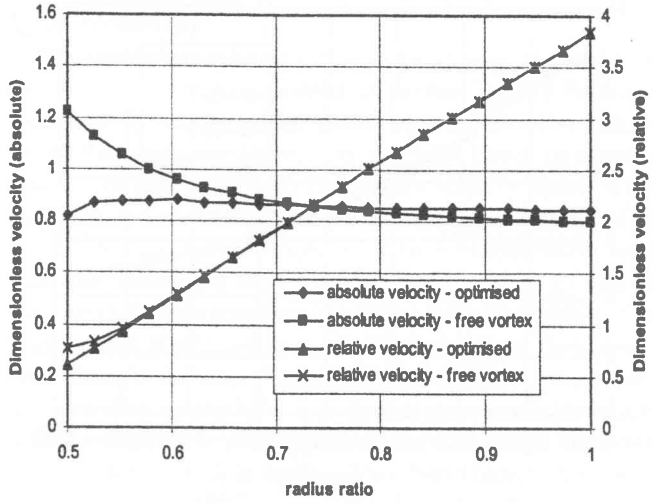

Fig. 4. Absolute and relative velocities for optimised and free vortex velocity profiles ($v = 0.25; \phi = 0.19; \psi = 0.12$)

diameter hubs could carry either five or ten blades and the 250 mm diameter hubs either seven (half solidity) or fourteen (full solidity). A complete series of general application fans was designed, ranging from 315 mm to 1 000 mm diameter in eight steps for standard duct sizes. The smaller diameter fans required cropping of the standard blade. Only one size low-noise fan, 630 mm in diameter, was built, since the forward swept blade was not suitable for cropping.

Flow and work rate values in equations (3) and (4) were chosen based on flow and load coefficients that are competitive with an existing fan series. They were applied to the range of different fan sizes for a few selected hub diameters with full or half sets of blades.

General application fan design

The velocity profiles obtained from the procedure for minimising the exit kinetic energy served as basis for calculating the relative inlet and exit flow angles. The axial inlet velocity profile used in the design was uniform with zero whirl. From the relative inlet and exit flow angles the flow deflection and mean flow angle in the rotor were calculated and used as approximate indications of blade camber and blade twist to compare the different configurations. From these we chose a representative combination as design specification for the whole series: $\nu = 0.25, \phi = 0.19, \psi = 0.12$. This combination refers to a 1 000 mm diameter fan with a 250 mm hub and half solidity (seven blades) and represented the best average radial distribution of blade camber and stagger. Basing the design on the largest specified fan diameter and longest possible blade also eliminated the need for extrapolation of the blade shape.

The exit kinetic energy for the optimised velocity distribution of the general application fan was calculated as 37.7 % of the fan effective power, compared to a value of 38.6 % for a free vortex velocity distribution, based on the same constraints and design parameters, i.e. a reduction of 2.3% of the exit kinetic energy. The effect of the optimised velocity profile is illustrated more clearly in Fig. 4, where the absolute and relative profiles of dimensionless velocity for the free vortex and optimised distributions, for $\nu = 0.25, \phi = 0.19, \psi = 0.12$, are shown. The velocity values are normalised by dividing with the circumferential velocity of the fan blade at the hub. The optimised absolute velocity values vary less between rotor hub and tip than those of the free vortex velocity values (0.05 compared to 0.4). The absolute velocity profile for the optimised distribution shows an almost constant trend between rotor hub and tip, as opposed to the decreasing trend of the free vortex distribution. The dimensionless value for optimised absolute velocity at the hub is considerably less than the value for free vortex absolute velocity at the hub (0.81 compared to 1.21). The small flow coefficient value, $\phi = 0.19$, means that the relative velocity distributions are dominated by the circumferential velocity of the fan (as shown by the near linear trend). The large difference in absolute velocity distribution at the hub is also evident in the higher relative free vortex velocity values, when compared to the optimised profile.

To allow for streamline curvature, "actuator disk theory" was applied to the calculated velocity distribution to determine the velocity profiles at the leading and trailing edge of the fan blade[11] (Figs. 5 and 6). Because of its high lift-drag ratio the fan blade design was based on the F-series profile of Wallis.[9,12]

Chord lengths and lift coefficients

Using the velocity distribution obtained, the blade loading factor, $C_L\sigma$, was calculated:

$$C_L\sigma = 2 \times \left(\frac{C_{w2}}{C_{am}}\right) \times \cos\beta_m \qquad (5)$$

The chord lengths at the hub and tip were calculated

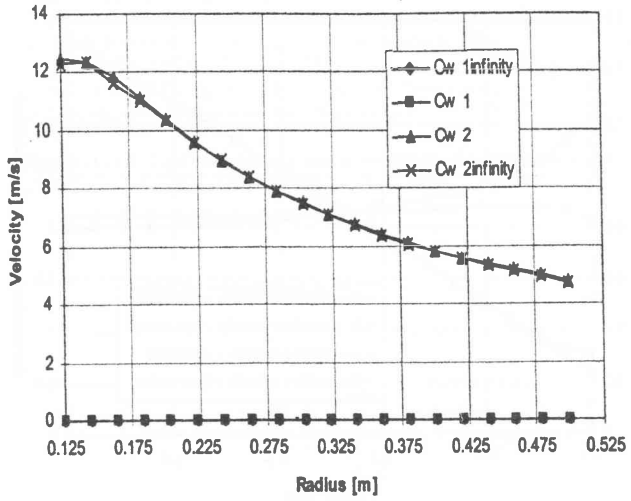

Fig. 5. Swirl velocity profiles for general application fan design

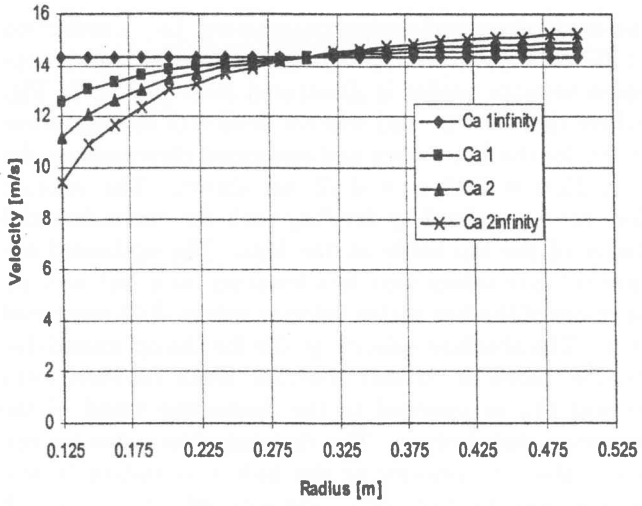

Fig. 6. Axial velocity profiles for general application fan design

by choosing appropriate values for C_L at the hub and tip and inserting them into equation (5). Linear interpolation between hub and tip gave the intermediate chord lengths and allowed calculation of the lift coefficient distribution along the blade length. The hub and tip chord lengths of the uncropped general application fan blade were 87 and 71 mm.

Blade camber and stagger

The values for camber angle were obtained using:

$$\theta = \beta_1 - \beta_2 + \delta - i \tag{6}$$

The values for incidence angle were taken from a graph in Wallis,[9] whilst the values for δ were calculated using an equation from Carter:[13]

$$\delta = \left(m \times (\beta_1 - \beta_2) \times \sqrt{\frac{s}{c}}\right) / \left(1 - m \times \sqrt{\frac{s}{c}}\right) \tag{7}$$

The value for m was calculated as a function of stagger angle, using a curve fit of Bruneau.[6] The stagger angle followed from:

$$\xi = \beta_1 - \alpha \tag{8}$$

The angle of attack of the blade profile was obtained from the graph in Wallis.[9] Since the angle of attack is dependent on the camber angle of the blade profile, the values of both camber and stagger angle were obtained by iteration.

Low-noise fan blade design

The low-noise blade design was done on the same principles as the general application fan and is described in detail by Van der Spuy.[8] The low-noise fan was designed to a pressure duty similar to that of a fourteen-bladed, 1 000 mm diameter fan from an industry-related reference fan series. The pressure duty of the fourteen-bladed reference fan was achieved for the forward swept, low-noise fan by using seven blades with doubled chord length. The following configuration was used in the design process: $\nu = 0.25$, $\phi = 0.2$, $\psi = 0.21$.

The exit velocity profiles were calculated in the same way as for the general application fan. F-series airfoils were also used for the low-noise fan.

Low noise fan blade sweep

The low-noise fan design allowed blade forward sweep. Wright & Simmons[3] provided a set of sweep-angle curves for various wave number modes from which a single suitable curve was selected.

$$\eta = 37.9261 + 79.1634 \times M_R - 0.3152/M_R - 23.0131 \times M_R^3 \tag{9}$$

where η represents the blade sweep angle viewed perpendicularly from the upstream side of the axial flow fan, in the plane perpendicular to the fan shaft and M_R is the radial Mach number based on fan rotational speed. M_R gives an indication of the degree of misalignment between the disturbance and the direction of motion of the blade, i.e. a higher misalignment requires a higher sweep angle.[3] Referring to Smith & Hsuan[10] and Beiler & Carolus[7] the aerodynamic sweep angle, λ was defined. It represents the sweep when viewed perpendicular to the plane connecting the blade sectional chord lines. The complimentary blade stagger angle, $\gamma = 90 - \xi$ was used here:

$$\tan \lambda = \tan \eta \times \cos \gamma \tag{10}$$

All the blade variables were transformed by the angle λ at the different radii.

The preliminary stagger angle was assumed to be equal to β_m, in order to calculate the value for geometric sweep at different radial locations. Once the aerodynamic sweep was calculated, the "swept" values for the flow angles were calculated:

$$\beta_s = \tan^{-1}(\tan \beta \times \cos \lambda) \tag{11}$$

These were used to calculate the blade loading factor and the values for solidity ratio, σ, at the fan hub and tip were calculated by selecting lift coefficient values at the hub and tip. Once the values for solidity ratio at the blade hub and tip were calculated, the values for "swept" blade spacing and chord at the hub and tip were calculated:[10]

$$s_s = s/\sqrt{1+(\tan\eta)^2} \quad (12)$$

$$c_s = \sigma \times s_s \quad (13)$$

Interpolating linearly between the "swept" chord values at the hub and tip gave the "swept" chord and solidity distribution over the blade length.

The values for the solidity distribution were used to calculate the lift coefficient distribution along the blade length. The "swept" camber angle distribution was then calculated:

$$\theta_s = \beta_{s1} - \beta_{s2} + \delta - i \quad (14)$$

where δ and i were determined as before.

The "swept" stagger angle distribution followed:

$$\xi_s = \beta_{s1} - \alpha \quad (15)$$

Finally, the "unswept" values for stagger and camber angle at the different radii were calculated:

$$\xi = \tan^{-1}(\tan\xi_s/\cos\lambda) \quad (16)$$

$$\theta = \tan^{-1}(\tan\theta_s/\cos\lambda) \quad (17)$$

Fan test equipment

A selection of fan sizes was tested on a BS 848, type D, fan test facility at various blade setting angles. The Standards[14,15] were adjusted to provide a test facility on which noise and performance tests could be executed simultaneously, by removing the downstream flow straightener.[8] The 630 mm diameter general application fan was set at a blade angle for the same pressure characteristic as the 630 mm diameter low-noise fan to enable a comparison between the two fans, using the fan scaling laws. The low-noise fan was tested at a constant blade setting angle.

Results

The values of total efficiency, static pressure and sound power level were determined as prescribed by the Standards.[14,15] The curves for the design specification general application fan surround the design point well (Fig. 7) for the blade setting angles originally specified to give an even distribution of the blade operating range on either side of the design point.

General application fan

The twist in the long blades of the large diameter fans caused negative blade tip incidence angles at large blade stagger settings (blade chords nearly in plane of rotation). This was counteracted by the open flow passages and large lift coefficients owing to a relatively larger effective angle of attack near the fan hub contributing more to the functioning of the blade at larger stagger settings (when compared to the reference fan). The blade twist also led to a relatively high angle of attack at the hub for large blade setting angles, implying that stall could occur readily for the large blade setting angles once the system resistance started increasing (Fig. 8).

The general application fan showed higher efficiency values (7% to 10% increase) than that of the reference fan series (the design specifications of the reference fan series were not known), which can be attributed to the optimisation of the design as described (Fig. 9).

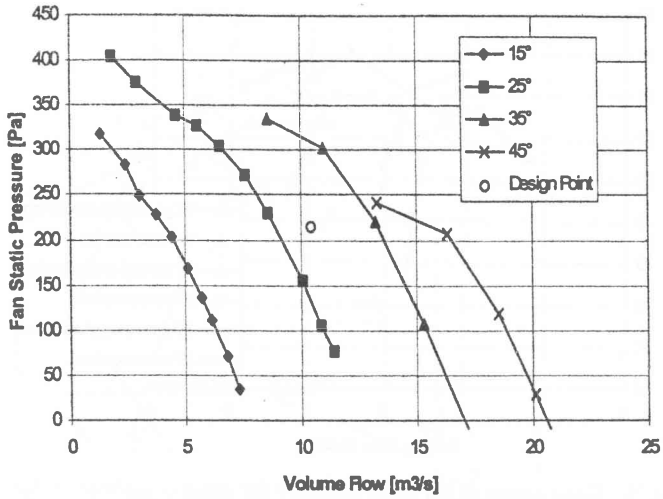

Fig. 7. Test data for 1000/250/7/720 fan, scaled to 1440 r.p.m. and compared with design point

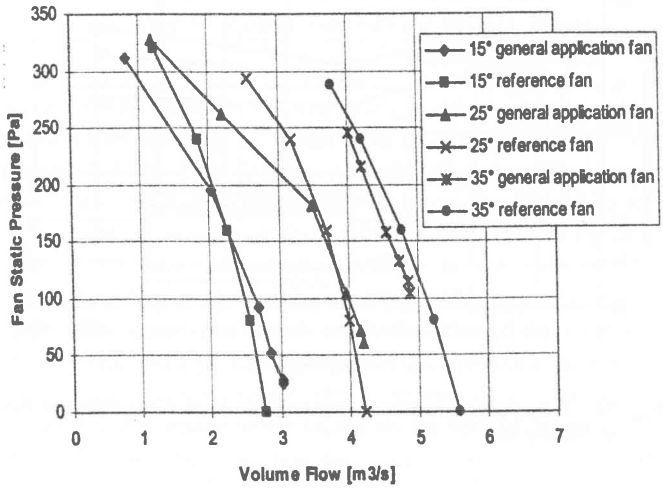

Fig. 8. Comparison of fan static pressure for general application fan and reference fan for 630/150/10/1440 configuration

Low-noise fan

The small number of blades, combined with the large chords used for the low-noise fan, prevented the closing of the air passage surrounding the hub. The forward sweep meant that the proper tip clearance with no interference with the casing was possible at only one blade stagger setting.

As mentioned before, the low comparative noise level of both the low noise and the general application fan could partially be ascribed to the use of the optimised velocity profiles in the design procedures, because fan noise can be related to a loss of energy in a fan (Fig. 10).

Although the low-noise fan was tested at 1 200 r.p.m., its aerodynamic performance was geometrically scaled to 1 440 r.p.m. to enable a direct comparison with the general application fan (Figs. 11 and 12). The figures also

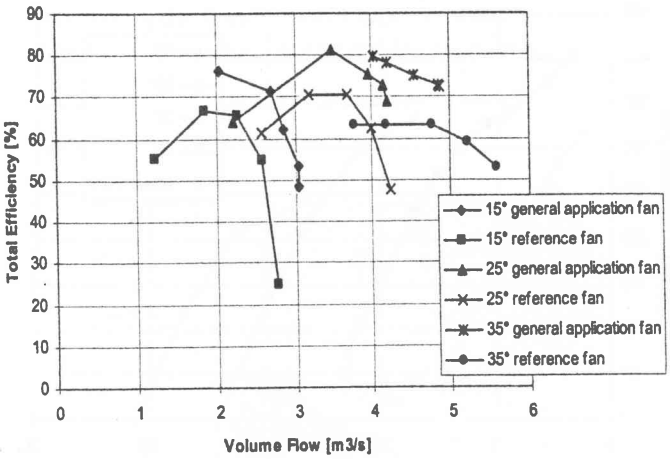

Fig. 9. Comparison of fan total efficiency for general application fan and reference fan for 630/150/10/1440 configuration

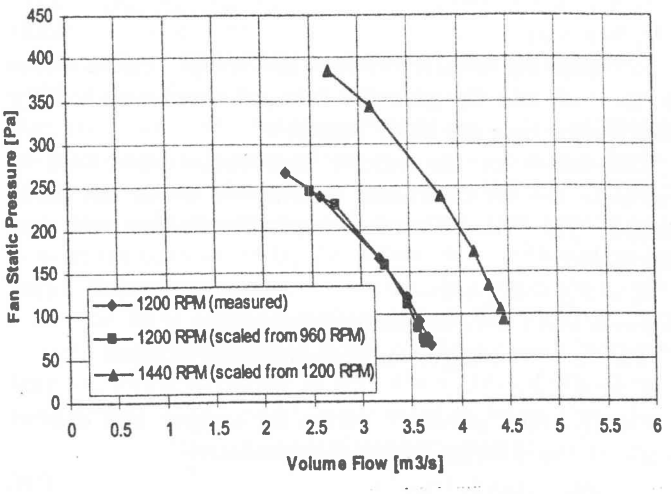

Fig. 11. Static pressure measured and scaled for low-noise fan at 1200 r.p.m. and 1440 r.p.m.

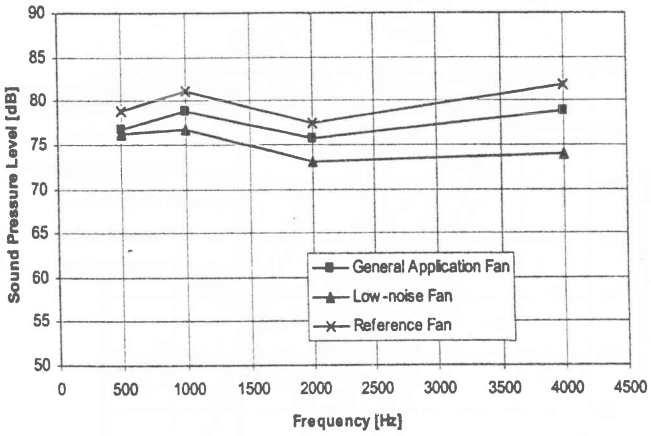

Fig. 10. Comparison of sound pressure levels of three different fans at 960 r.p.m.

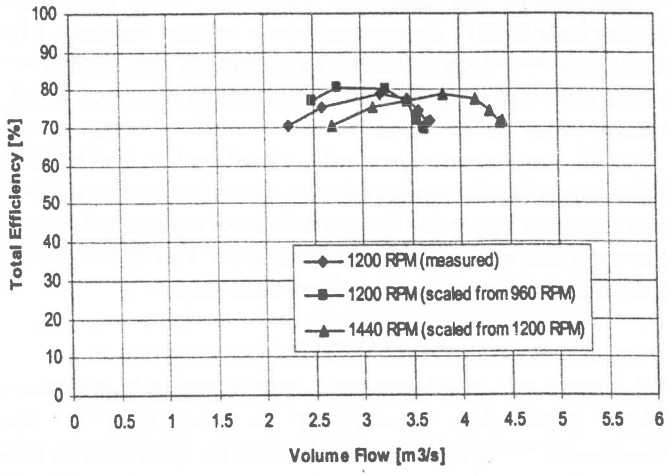

Fig. 12. Total efficiency measured and scaled for low-noise fan at 1200 r.p.m. and 1440 r.p.m.

show measured results at 1 200 r.p.m. compared to values scaled from 960 r.p.m., to verify the reliability of the scaling. Based on a direct comparison of results at 1 440 r.p.m., the low noise fan has a larger static pressure rise than the other two fans tested, although the 70% to 80% efficiency values of the general application fan and the low-noise fan are within the same size-range (Figs. 9 and 12). The higher pressure rise of the low-noise fan can be attributed to its higher solidity (equivalent to 14 short chord blades, not 10).

Conclusions

The low-noise fan had a high fan total efficiency, high static pressure rise, and a low noise level (Table I). The designed general application fan was as efficient and marginally noisier (looking at frequencies between 500 Hz and 4 000 Hz in Fig. 10) than the low-noise fan, due to the smaller chord length and unswept blade plan form (Table I). The designed general application fan was however considerably quieter and more efficient than the reference fan (Table I). This improvement could be attributed to the use of the minimised exit kinetic energy velocity profile, since the blade tip speed, blade chord length, number of blades, and unswept blade plan form for both the reference and general application fans were similar.

The designed general application fan was a good compromise, since it was as cheap to manufacture as the reference fan, but its efficiency was comparable to that of the low-noise fan, and its noise values were roughly half-way between those of the reference fan and the low-noise fan. The main contributor to axial rotor-only fan noise is blade tip speed. If electric motor speed control capability is available, the low-noise fan speed may be reduced to a level that gives the same pressure rise values as for the general application fan, at considerably lower noise emission levels. The manufacturing of a low-noise fan, combined with electric motor speed control would however be costly. Based on the above results, when comparing axial fans running at

the same rotational speed, design methodology is the main contributor towards improving fan efficiency and noise levels.

TABLE I
SUMMARY OF RESULTS

	Maximum total efficiency [%]	Maximum static pressure [Pa]	Sound pressure level @ 400 Hz [dB]
Reference fan	70	295	82
General application fan	80	325	79
Low-noise fan	78	380	74

REFERENCES

[1] Von Backström TW, Buys JD & Stinnes WH. Minimisation of the Exit Loss of a Rotor-only Axial Fan. *Engineering Optimization*, 1996, **26**, pp.28–29.

[2] Wright SE. The Acoustic Spectrum of Axial Flow Machines. *Journal of Sound and Vibration*, Part 2, 1976, **45**, p.193.

[3] Wright T & Simmons WE. Blade Sweep for Low-Speed Axial Fans. *ASME Paper GT-53*, 1989, pp.1–6.

[4] Van der Spek HF. Advanced Low Noise Cooling Fans. 9th *Cooling Tower and Spraying Pond Symposium IAHR*, Von Karman Institute for Fluid Dynamics, Brussels, 1994, pp.3–4.

[5] Mesquita ALA, Serra CMV, Cruz DOdA & Filho NM. A Simplified Method for Axial Flow Turbomachinery Design. *Journal of the Brazilian Society of Mechanical Sciences*, **XXI**, 1999, pp.61–70.

[6] Bruneau PRP. The Design of a Single Rotor Axial Flow Fan for a Cooling Tower Application. MEng thesis, University of Stellenbosch, 1994.

[7] Beiler MG & Carolus TH. Computation and Measurement of the Flow in Axial Flow fans with Skewed Blades. *ASME Journal of Turbo machinery*, 1999, **121**, pp.59–66.

[8] Van der Spuy SJ. The Design of a Low-noise Rotor-only Axial Flow Fan Series. MEng thesis, University of Stellenbosch, 1997.

[9] Wallis RA. *Axial Flow Fans and Ducts*. John Wiley & Sons, Inc. 1983, pp.147–170, 197–200.

[10] Smith LH & Yeh H. Sweep and Dihedral Effects in Axial Flow Turbomachinery. *Transactions of the ASME, Journal of Basic Engineering*, 1963, **85**, pp.401–405.

[11] Dixon SL. *Fluid Mechanics–Thermodynamics of Turbomachinery*. 3rd edn, William Clowes Ltd., Great Britain, 1978.

[12] Wallis RA. The Development of Blade Sections for Axial Flow Fans. *Instn. Engrs. Aus., Mechanical and Chemical Engineering Transactions*, 1972, p.116.

[13] Carter ADS. The Low Speed Performance of Related Aerosols in Cascades. *Gt. Britain Aer. Research Council ARC CP 29*,1950.

[14] British Standards Institution. Fans for General Purpose, Part 1, Methods of Testing Performance. *BS 848*, 1980.

[15] British Standards Institution. Fans for General Purpose, Part 2, Methods of Noise Testing. *BS 848*, 1985.

Numerical Solution of Flow through Turbomachinery with the SIMPLEN Algorithm

G. D. Thiart[1] and T. W. von Backström[2]

(First received December 1991, Final Form December 1991)

Summary

The SIMPLEN algorithm for the numerical solution of convection-diffusion problems on nonstaggered grids is applied to two turbomachinery throughflow problems. Incompressible flow only is considered, and the k-ε model is used to simulate turbulence effects. The first problem is that of flow through a propeller. Both a uniform and a shear approach flow are considered. The thrust and torque exerted by the propeller on the fluid are modelled as prescribed body forces. Good agreement between the numerical results and the corresponding results available in the literature is obtained. The second problem is that of the flow through an axial flow fan. Both an axisymmetric and a distorted inflow is considered. Blade element theory is used to model the thrust and torque exerted by the fan blades on the air. Reasonable correspondence with experimental results is obtained.

Nomenclature

C_1, C_2, C_μ – constants in the k-ε model
C_p – pressure coefficient
D – diameter
G_k – turbulence kinetic energy production term
k – turbulence kinetic energy
m – exponent
N – rotational speeds
$p, p_0, \Delta p$ – static pressure, static pressure at outlet, static pressure difference
P – power
q – volume flow rate
Q – torque
$r, \delta r$ – radial direction, radial distance between grid points
S – source term
T – thrust
u – axial velocity component
U – free stream velocity for propeller flow
v – radial velocity component
V – volume
w – azimuthal velocity component
$z, \delta z$ – axial direction, axial distance between grid points
Δ – actuator disc thickness
ε – turbulence kinetic energy decay rate
μ, μ_t – dynamic viscosity, turbulent dynamic viscosity
ϕ – general dependent variable
ρ – density
$\sigma_k, \sigma_\varepsilon$ – Schmidt numbers in the k-ε model
θ – azimuthal direction
w – angular velocity of fluid particles

1 Senior Lecturer
2 Professor
Department of Mechanical Engineering
University of Stellenbosch
7600 Stellenbosch

Introduction

In recent years, methods based on the SIMPLE (*S*emi-*I*mplicit *M*ethod for *P*ressure-*L*inked *E*quations) algorithm of Patankar and Spalding [1] have been used successfully to solve a wide range of flow problems. In the original SIMPLE algorithm separate grids, staggered in space, are used for the calculation of scalar properties such as pressure, and each of the velocity components. Thus four grids are used for a three-dimensional flow problem, which complicates the implementation of boundary conditions. If all variables are located at the same grid points, on the other hand, a checkerboard pressure field may result. This has been described by, amongst others, Patankar [2], Rhie and Chow [3] and Perić [4].

Several methods that have been proposed to overcome the checkerboard problem on nonstaggered grids, are described by Patankar [5] in a recent review paper. Thiart [6] subsequently presented a new finite difference scheme that also eliminates the need for staggered grids. The scheme was incorporated in an algorithm called SIMPLEN: the "N" attached to SIMPLE being an indication that a nonstaggered grid is used.

The finite difference scheme on which SIMPLEN was originally based, has subsequently been refined by Thiart [7]. It was shown that the new scheme is capable of producing numerical solutions of comparable or superior accuracy to that of other numerical methods. The differencing scheme was originally developed specifically for a Cartesian coordinate system; Thiart and Von Backström [8] recently extended the scheme to cylindrical polar coordinates, which is particularly useful for turbomachinery applications.

It was also shown by Thiart [6] that the SIMPLEN methodology is able to simulate accurately the one-dimensional flow through a thrust-producing actuator disc. In this paper, the actuator disc simulation is extended to two typical turbomachinery throughflow problems: a propeller operating with uniform inflow and with a sheared inflow, and an axial flow fan operating with axisymmetric inflow and with circumferentially distorted inflow.

Governing Equations

The governing equations for the flow problems that are considered in this paper, are the well-known Navier-Stokes equations for incompressible flow (see for example Schlichting [9]), augmented by the k-ε turbulence model. These equations are those for the conservation of mass, i.e.

$$\frac{1}{r}\frac{\partial}{\partial r}(\rho r v) + \frac{1}{r}\frac{\partial}{\partial \theta}(\rho r \omega) + \frac{\partial}{\partial z}(\rho u) = 0 \tag{1}$$

and for the conservation of axial momentum, radial momentum, moment of momentum, turbulent kinetic energy (k) and the decay rate of turbulent kinetic energy (ε), which can be written in the general form

$$\frac{\partial}{\partial r}(\partial r^{2m}\phi) + \frac{1}{r}\frac{\partial}{\partial r}(\partial r^{2m+1} v\phi) + \frac{1}{r}\frac{\partial}{\partial \theta}(\rho r^{2m+1}\omega\phi) + \frac{\partial}{\partial z}(\rho r^{2m} u\phi) = S^{\phi} + \frac{1}{r}\frac{\partial}{\partial r}\left(r^{2m+1}\mu\frac{\partial \phi}{\partial r}\right) + \frac{1}{r}\frac{\partial}{\partial \theta}\left(r^{2m}\frac{\mu}{r}\frac{\partial \phi}{\partial \theta}\right) + \frac{\partial}{\partial z}\left(r^{2m}\mu\frac{\partial \phi}{\partial z}\right) \tag{2}$$

where ϕ denotes a general variable representing either the axial velocity u, the radial velocity v, the angular velocity ω, k or ε, and where m is equal to one for $\phi \equiv \omega$ and zero otherwise. Eq. (2) can be regarded as a transport equation for the general variable ϕ, with transient and convective terms on the left hand side being balanced by a source term and diffusion terms on the right hand side. The source terms are as follows:

$$S^{u} = \frac{\partial T}{\partial V} - \frac{\partial p}{\partial z} + \frac{\partial \mu}{\partial r}\frac{\partial v}{\partial z} + \frac{\partial \mu}{\partial \theta}\frac{\partial \omega}{\partial z} + \frac{\partial \mu}{\partial z}\frac{\partial u}{\partial z} \tag{3}$$

$$S^{\omega} = \rho r\omega^2 - \frac{\partial p}{\partial r} + \frac{\partial \mu}{\partial r}\frac{\partial v}{\partial r} + \frac{\partial \mu}{\partial \theta}\frac{\partial \omega}{\partial r} + \frac{\partial \mu}{\partial z}\frac{\partial u}{\partial r} - \frac{\mu}{r}\left(\frac{v}{r} + 2\frac{\partial \omega}{\partial \theta}\right) \tag{4}$$

$$S^{\omega} = \frac{\partial Q}{\partial V} - \frac{\partial p}{\partial \theta} + \frac{\partial \mu}{\partial r}\frac{\partial v}{\partial \theta} + \frac{\partial \mu}{\partial \theta}\frac{\partial \omega}{\partial \theta} + \frac{\partial \mu}{\partial z}\frac{\partial u}{\partial \theta} + \frac{2}{r}\frac{\partial}{\partial \theta}(\mu v) \tag{5}$$

$$S^{k} = G_k - \rho\varepsilon \tag{6}$$

$$S^{\varepsilon} = \frac{\varepsilon}{k}(C_1 G_k - \rho C_2 \varepsilon) + 0.2 C_2 \rho k \frac{\omega}{r}\frac{\partial}{\partial r}(r^2\omega) \tag{7}$$

The dynamic viscosity μ in Eqs. (2)-(7) is replaced by the eddy viscosity for turbulent flow problems:

$$\mu_t = \rho C_\mu \frac{k^2}{\varepsilon} \tag{8}$$

The k and ε-equations are standard except for the last term on the right hand side of Eq. (7), which is the modification of Launder et al. [10] to account for the destabilizing effect of swirl on turbulence. The empirical constants that appear in Eqs. (6)-(8) are assigned the following values:

$C_\mu = 0{,}09$; $\sigma_k = 1{,}0$; $\sigma_\varepsilon = 1{,}3$; $C_1 = 1{,}44$; $C_2 = 1{,}92$

T and Q represent respectively the external thrust and torque on the fluid, while G_k is the turbulence kinetic energy production term, given by (Gupta and Lilley [11]):

$$G_k = \mu_t\left[2\left\{\left(\frac{\partial u}{\partial z}\right)^2 + \left(\frac{\partial v}{\partial r}\right)^2 + \left(\frac{\partial \omega}{\partial \theta} + \frac{v}{r}\right)^2\right\}\right] + \left(\frac{\partial u}{\partial r} + \frac{\partial v}{\partial z}\right)^2 + \left(\frac{1}{r}\frac{\partial v}{\partial \theta} + r\frac{\partial \omega}{\partial r}\right)^2 + \left(\frac{1}{r}\frac{\partial u}{\partial \theta} + r\frac{\partial \omega}{\partial z}\right)^2 \tag{9}$$

Solution Procedure

The computational domain is subdivided into a number of non-overlapping control volumes, one control volume per grid point. The governing equations are discretized by integration over these control volumes; these discretised equations are solved using the SIMPLEN algorithm. The numerical procedure was incorporated in a computer code called FLOWAX, written in single precision FORTRAN 77. Boundary conditions for k and ε at solid walls are determined by means of wall functions in the manner described by Burns and Wilkes [12]. Details about the discretization, the code itself and the verification of the code are given by Thiart [13]. All computations reported in this paper were performed on a CONVEX 120 computer.

Flow through a Propeller

The three-dimensional turbulent flow through a propeller was simulated by Pelletier [14] (see also Pelletier and Schetz [15]), using a finite element method with a relatively simple turbulence model (compared to the k-ε model): the eddy viscosity is assumed to vary only in the axial direction, the variation being described by a first order ordinary differential equation. The propeller and flow characteristics used for the simulation correspond to those of the wind-tunnel experiments of Kotb [16]. The propeller was modeled as an actuator disk of constant thickness Δ and diameter D. The radial distributions of thrust and swirl force per unit volume, i.e. $(\partial Q/\partial V)/r$, per unit volume was assumed to be trapezoidal, increasing linearly from zero at $r/D = 0{,}125$ to a maximum at $r/D = 0{,}35$ and decreasing linearly again from $r/D = 0{,}425$ to zero at $r/D = 0{,}5$.

Two cases were considered by Pelletier and Kotb: one for uniform flow into the propeller, and one for a shear flow. These two cases were solved with FLOWAX using the same computational domain and, as far as possible, the same boundary conditions as for the calculations of Pelletier.

(a) Uniform Flow

The propeller and flow characteristics are as follows:

Propeller diameter: $D = 0{,}492$ m

Propeller thickness: $\Delta = 0{,}0407\ D = 0{,}020$ m

Air density: $\rho = 1{,}177$ kg/m^3

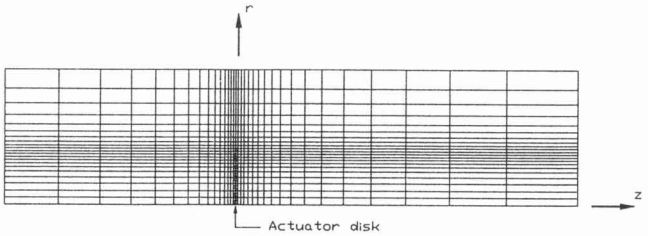

Figure 1 – Computational grid for propeller flow

Relative air velocity: $U = 8{,}52$ m/s
Total thrust: $T = 3{,}80$ N
Total torque: $Q = 0{,}348$ Nm

The computational grid is depicted in Fig. 1. In the axial direction, the computational domain extends two diameters upstream of the propeller face and three diameters downstream of the rear face of the propeller. The rear face is located at $z = 0$, thus locating the inlet plane at $z = -2{,}0407D$ and the outlet plane at $z = 3D$. Radially, the computational domain extends from the propeller axis to $r = 1{,}2D$. The computational grid has 34 stations in the axial direction and 22 stations in the radial direction, giving a total of 748 grid points. The grid has been designed so that expansion ratios (that is, the ratio of successive δz's or δr's) never exceed 1,3. Other constraints were that one radial grid line had to coincide with each of the following axial stations within the computational domain: $z = -0{,}0407D$ (propeller face), $z = 0$ (rear face for propeller), and $z = 0{,}025D$ (location where velocity components and static pressure were measured by Kotb). Similarly, in the radial direction, one grid line had to coincide with each of the radial stations $r = 0{,}425D$ (location for which axial distributions of velocity components and static pressure are given by Pelletier) and $r = 0{,}5D$ (outer radius of propeller).

Boundary conditions for the numerical solution (other than those of the zero-gradient type) were as follows:

$z = -2{,}0407D$: $u = U$, $v = 0$, $\omega = 0$, $k = 0{,}0035U^2$,
$\varepsilon = 2000\rho C_\mu k^2$;
$z = 3D$: $p = p_0 = 0$; $r = 1{,}2D$: $u = U$

The free-stream value of k is one commonly used with the k-ε model, while the free-stream value of ε was chosen so that the free-stream value of eddy viscosity corresponds to that used by Pelletier. Some results are presented in Fig. 2.

The axial distribution of the axial velocity component at $r = 0{,}425D$ (Fig. 2a) appears to have a lower peak value compared to that of Pelletier, and the decay of axial velocity component also seems to be much slower. This is not the case, however; at $r = 0{,}425D$ the thrust and torque distributions and therefore the velocity components change rapidly with radius so that small differences in radial profiles appear as large differences in axial distributions.

The axial velocity profile at $z = 0{,}025D$ is compared with those of Pelletier and Kotb in Fig. 2b (values shown at a negative radius in Figs. 2b, 2d and 2f correspond to the measurements of Kotb on a vertical plane, and values at a positive radius to measurements on a horizontal plane). The numerical procedure does of course yield identical results for the vertical and horizontal planes. The predicted axial velocity profile is almost identical for the two numerical solutions, and shows good correspondence with the measured velocity profile.

The corresponding axial distributions of the azimuthal velocity component are shown in Fig. 2b. Here also a lower peak value and a slower decay with axial distance is observed. In this case, however, there is a real difference, as borne out by the azimuthal velocity profiles, Fig. 2d. The current calculations seems to yield better correspondence with the experimental results. Note also in Fig. 2c the absence of "wiggles" upstream of the propeller compared to the substantial oscillations produced by the finite-element calculations.

Finally, axial distributions and profiles of the pressure coefficient $C_p = (p\text{-}p_0)/0{,}5\rho U^2$ are shown in Fig. 2e-f. Evident in Fig. 2e is the pressure jump associated with thrust provided by the propeller. The axial distributions are almost identical, with the current calculations showing a slightly higher peak value on the upstream face and a slightly lower peak value at the downstream face of the propeller. Correspondence with the experimental results is again reasonable at $z = 0{,}025D$.

(b) Shear Flow

The propeller dimensions and air density are the same as for the uniform flow case, the other characteristics being as follows:

Relative air velocity: $U = U(\theta) = 8{,}52 - 0{,}67\cos\theta$ m/s
Total thrust: $T = 4{,}00$ N
Total torque: $Q = 0{,}332$ Nm

The computational grid is the same in the axial and radial coordinate directions, but now has twelve equispaced azimuthal planes instead of only one. The boundary conditions used here are similar to those for the uniform flow case:

$z = -2{,}0407D$: $u = U(\theta)$, $v = 0$, $\omega = 0$,
$k = 0{,}0035U^2$, $\varepsilon = 2000\rho C_\mu k^2$;
$z = 3D$: $p = p_0 = 0$; $r = 1{,}2D$: $u = U(\theta)$

Note that the inlet boundary condition on k (and therefore also on ε) is based on the average inlet velocity. Some results are presented in Figs. 3-4.

Axial distributions of the axial velocity component at $r/D = 0{,}425$ are shown in Fig. 3a at four azimuthal sections through the computational domain. Pelletier's results differ from these in the same way as for the uniform flow case and are therefore not reproduced here. The nonsymmetrical behaviour of the 0° and 180° axial velocity curves reported by Pelletier is clearly evident in Fig. 3a.

Corresponding axial distributions of the aximuthal velocity component are presented in Fig. 3b. Once again no "wiggles" can be observed upstream of the propeller, and the near-perfect axial symmetry reported by Pelletier is also evident.

Radial profiles of axial and azimuthal velocity components are compared with those of Pelletier and Kotb in

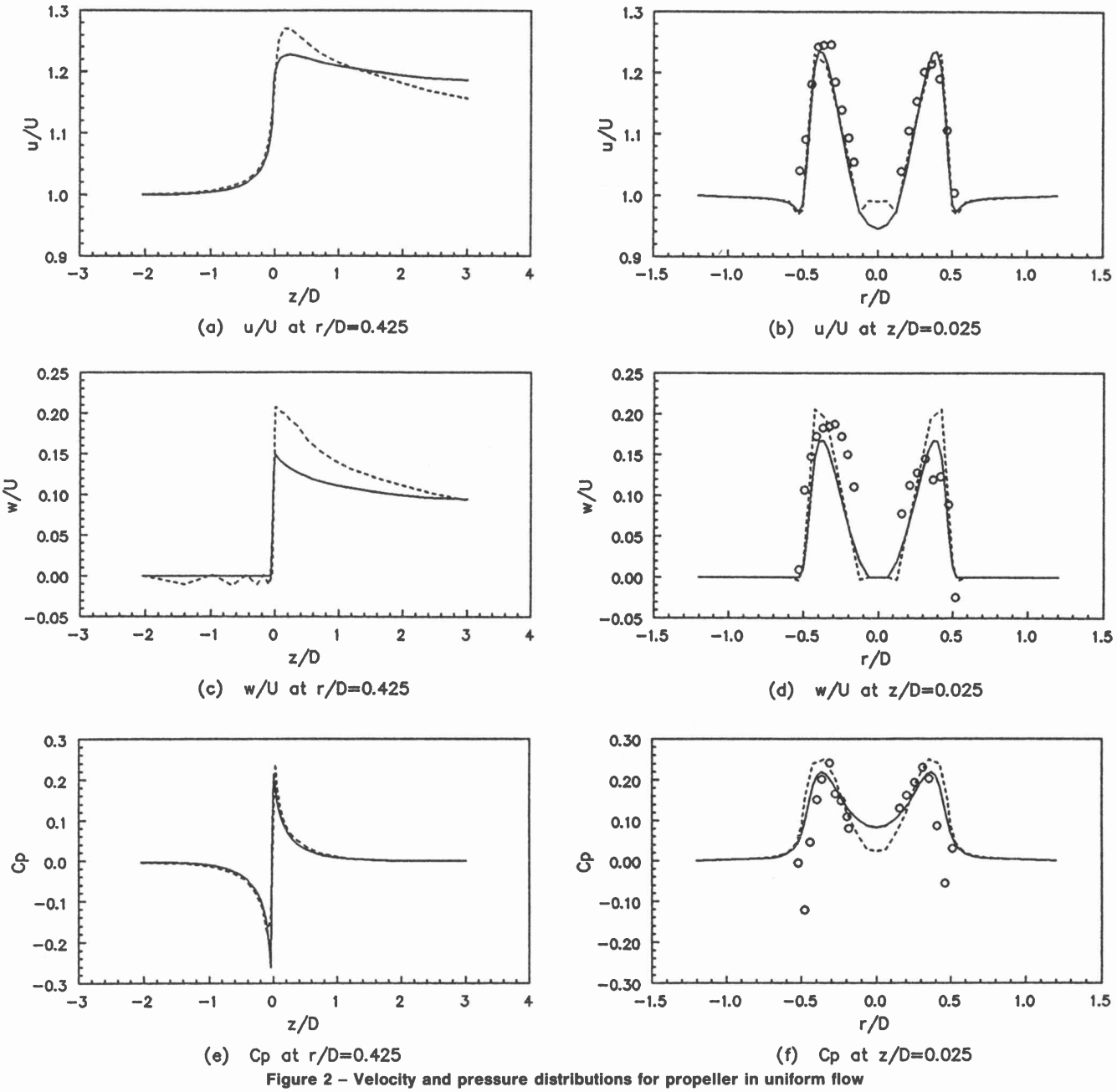

Figure 2 – Velocity and pressure distributions for propeller in uniform flow
[————SIMPLEN, - - - - FEM (Pelletier), o Experiment (Kotb)]

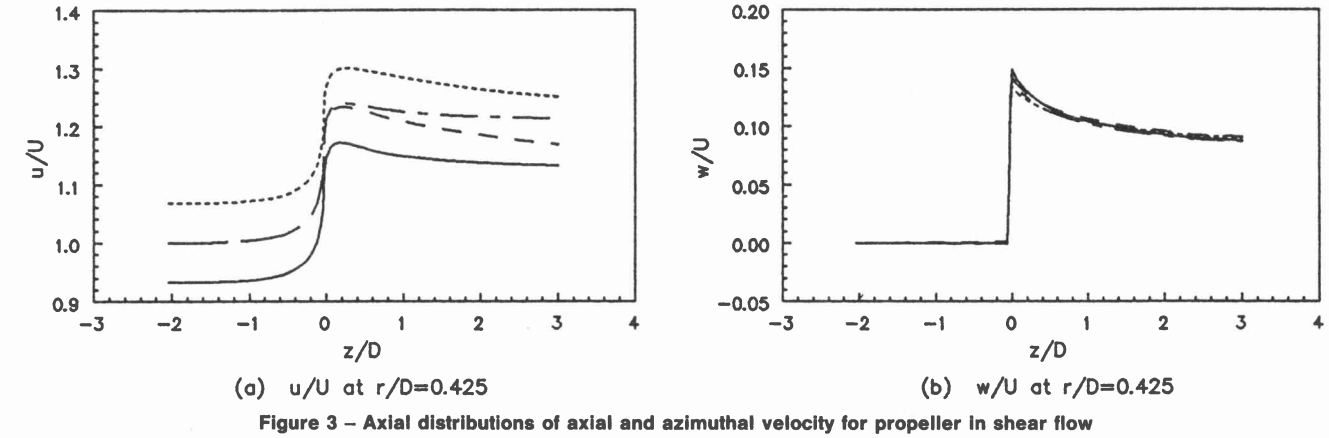

Figure 3 – Axial distributions of axial and azimuthal velocity for propeller in shear flow
[———— 0°, — — — 90°, ---- 180°, —— 270°]

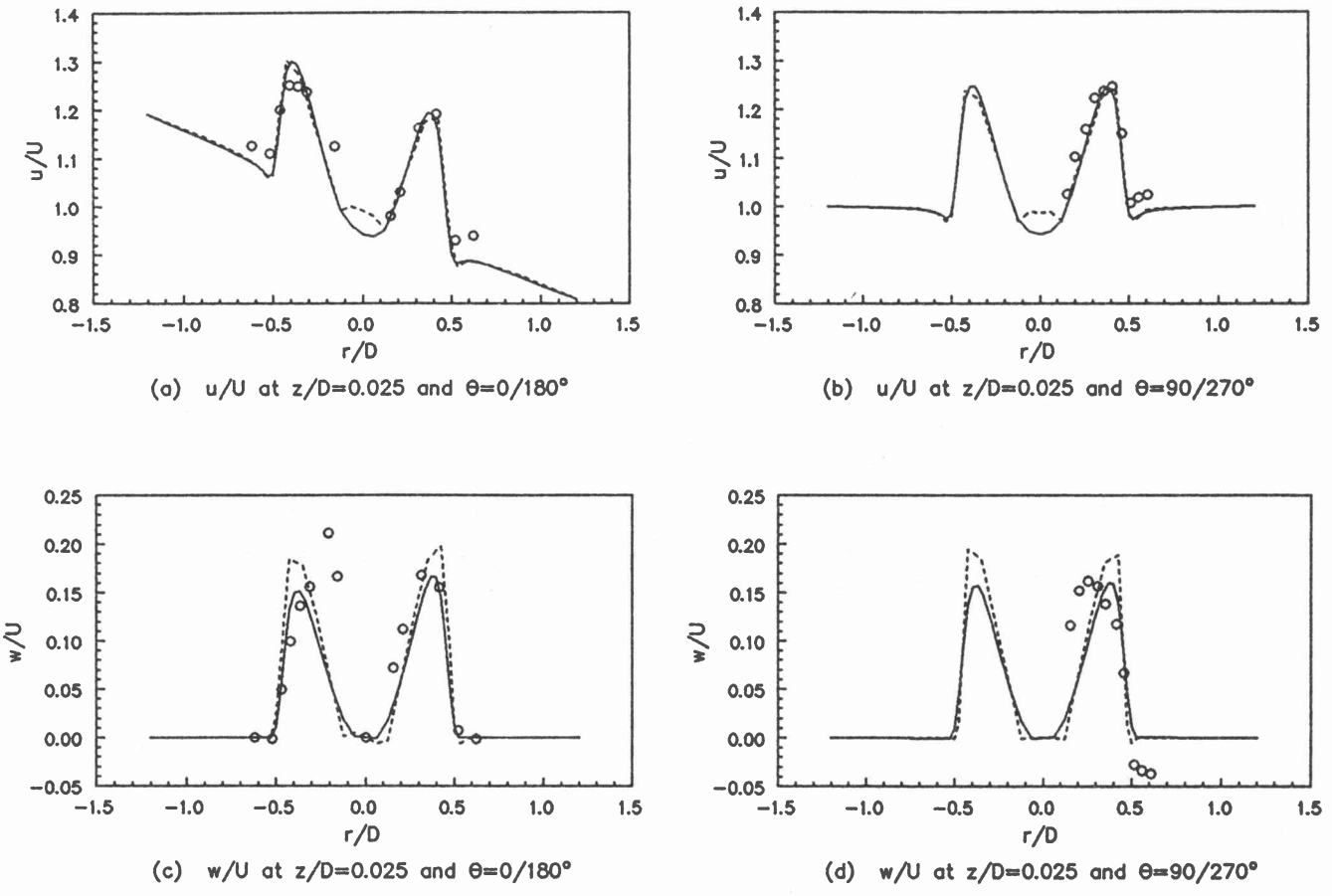

Figure 4 – Radial profiles of axial and azimuthal velocity for propeller in shear flow [————SIMPLEN, - - - - FEM (Pelletier), o Experiment (Kotb)]

Fig. 4. Values shown at negative radii in these figures correspond to results at $\theta = 180°$ and $\theta = 270°$, and values at positive radii to results at $\theta = 0°$ and $\theta = 90°$. The same comments as for the uniform flow case apply generally.

Flow through an Axial Flow Fan

Thiart [13] recently carried out wind tunnel experiments with an axial flow fan operating under distorted inflow conditions; the corresponding numerical simulations will now be described. The idealized computational domain corresponding to the experimental configuration is shown in Fig. 5. In the experiment the test fan was mounted in a round duct, the intake of which was located in a hole in the floor of the subsonic windtunnel of the Departement of Mechanical Engineering at the University of Stellenbosch. The windtunnel was used to simulate crosswind conditions. Measurements of cross-flow velocity, volumetric flow rate, fan static pressure, fan speed and shaft power were taken for two cases: one with no crossflow and one with crossflow of approximately 10 m/s, which is of the same magnitude as the average axial velocity through the duct. Detailed measurements of velocity and static pressure were also taken with a five-hole probe at a location approximately one and a half duct diameters downstream from the inlet.

Several idealizations are incorporated in the computational domain. The wind tunnel test section is modelled as two parallel plates; the spacing between the plates is equal to the height of the test section. No account is taken of the sidewalls of the test section. The duct section extends from the test section to the five-hole probe measuring position. The fan rotor hub and fan motor is modelled as a round cylinder, the length and diameter of which correspond to the combined length of the fan hub and motor and the hub diameter respectively (the motor is actually slightly smaller in diameter than the hub). The small gap between the hub and the motor is not modelled; neither are the cooling fins on the motor surface. The fan blades

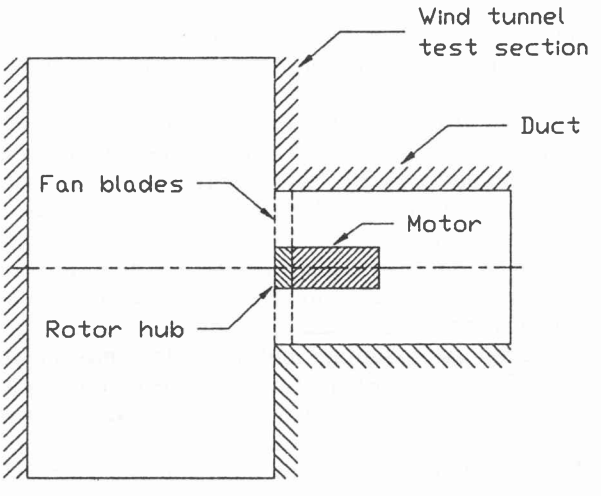

Figure 5 – Computational domain for fan flow

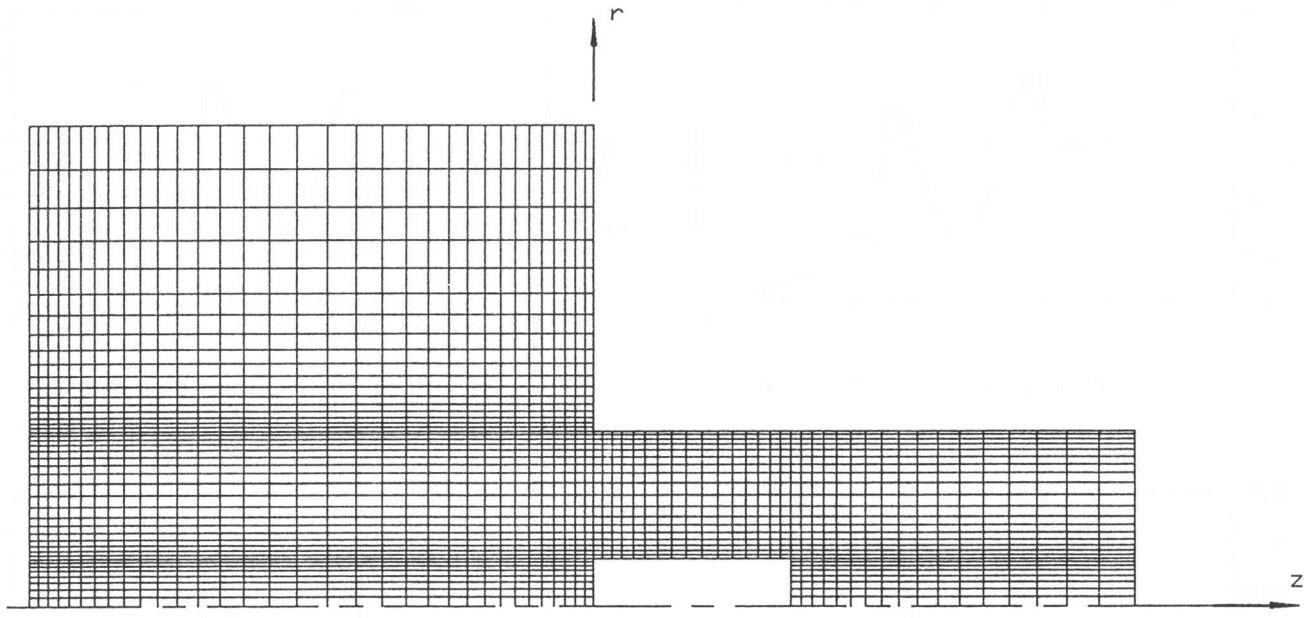

Figure 6 – Computational grid for fan flow

are not modelled directly as rotating solid surfaces, but indirectly: the influence of the fan blades are modelled as body forces by means of the blade element theory commonly employed for aircraft and ship propeller calculations. Full details are given by Thiart [13].

The computational grid for axisymmetric inflow is shown in Fig. 6. There are 67 axial stations and 45 radial stations, for a total of 2301 grid points. Expansions ratios of 1,08 in the axial direction and 1,15 in the radial direction are used throughout. The computational grid for distorted inflow is the same as for axisymmetric inflow, but now has sixteen equispaced azimuthal planes instead of only one. The total number of grid points in this case is 36,036.

The boundary conditions for the fan performance predictions are as follows: at the solid surfaces, the no-slip conditions ($u=v=\omega=0$ except at the rotor hub, were $\omega=\Omega$) and wall functions for k and ε are used; at the duct outlet plane zero-gradient boundary conditions are used for all variables except static pressure, for which the radial equilibrium boundary condition $\partial p/\partial r = \rho r\omega^2$ is used; at the inlet and outlet planes between the parallel surfaces zero-gradient boundary conditions are used for k and ε, while the velocity components are fixed to provide the correct flow rate through the fan.

The velocity profiles to be used as boundary conditions between the parallel surfaces (representing the wind tunnel top and bottom walls) posed a problem: these boundaries are not sufficiently far removed from the fan for uniform flow velocity profiles to be used. To overcome this problem, the inlet velocity profiles (u and v only – ω is equal to zero) were determined from a potential flow solution on part of the computational domain, excluding the duct section and assuming uniform inflow into the duct section. For the distorted inflow case, the required cross-flow velocity is simply added to the potential flow solution.

The potential flow solution was also used to provide initial conditions for the fan performance predictions; static pressure conditions are readily obtained from Bernoulli's equation. In the duct section the initial values for v and ω are taken as zero, while the axial velocity component u is taken as uniform everywhere between the inlet and outlet planes of the duct.

(a) Axisymmetric Inflow

The main experimental data for the case without cross-flow are as follows:

Air density: $\rho = 1{,}172$ kg/m³
Volume flow rate through fan: $q = 2{,}627$ m³/s
Increase in static pressure through fan: $\Delta p = 79$ N/m²
Fan speed: $N = 1409$ r.p.m.
Shaft power: $P = 981$ W

Several solutions were obtained for the axisymmetric inflow case in order to establish reasonable values for some of the constants in the blade element model. For the chosen set of constants, the predicted values of fan static pressure and fan power differed by -5% and ~0% respectively compared to the experimental results. A similar calculation was done for uniform inflow boundary conditions – in this case the predictions differed from the experimental results by -8% and +4% respectively. The introduction of the inflow boundary conditions calculated from the potential flow solution is therefore considered worthwhile.

The general features of the flow field are depicted in Fig. 7, which shows the streamlines in an azimuthal plane. The reverse flow at the outer part of the fan blades, which was also observed during the experiment, is clearly evident in the figure. Another zone of recirculatory flow is predicted downstream of the fan motor, extending beyond the outflow boundary. The reverse flow at the outflow boundary was not observed during the experiment; possible reasons for the discrepancy are inadequacies of the turbulence model and the influence of a right angle

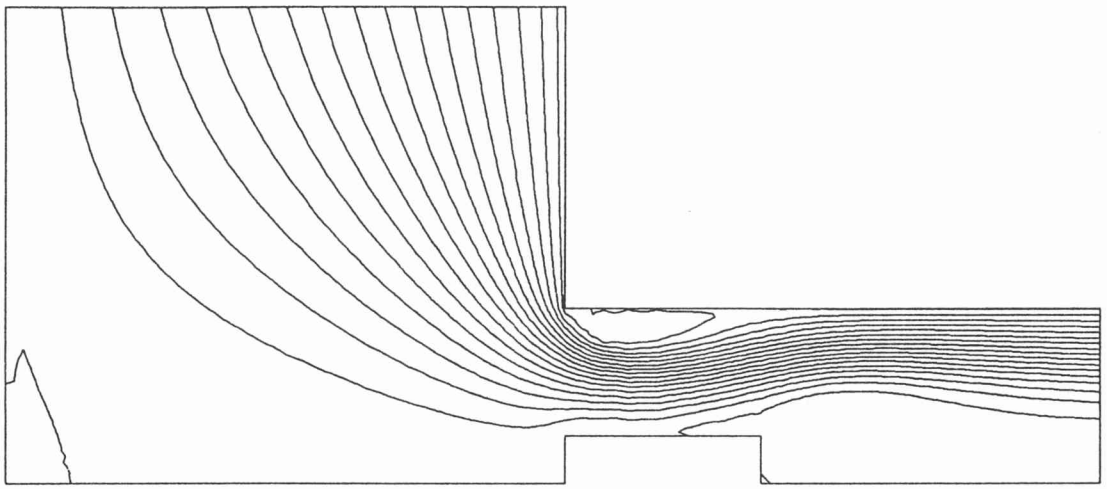

Figure 7 – Streamlines for fan with axisymmetric inflow

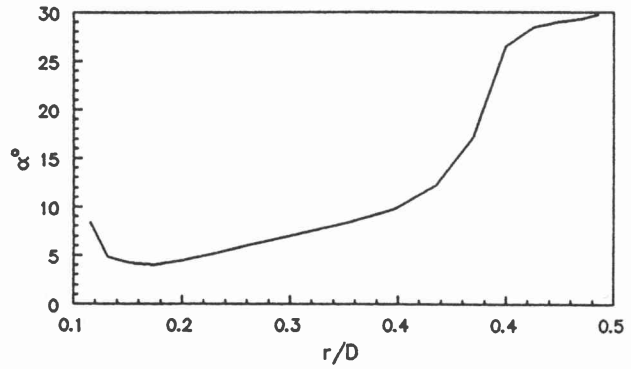

(a) Angles of attack

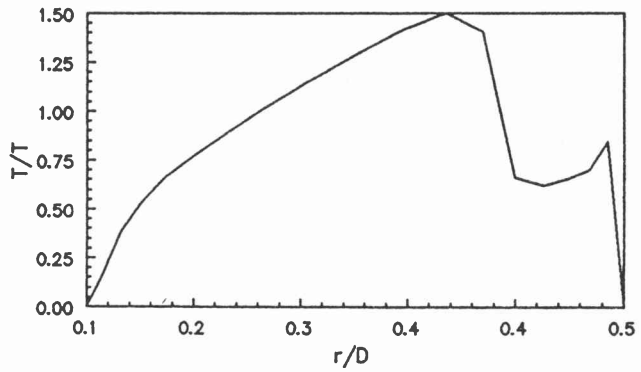

(b) Thrust

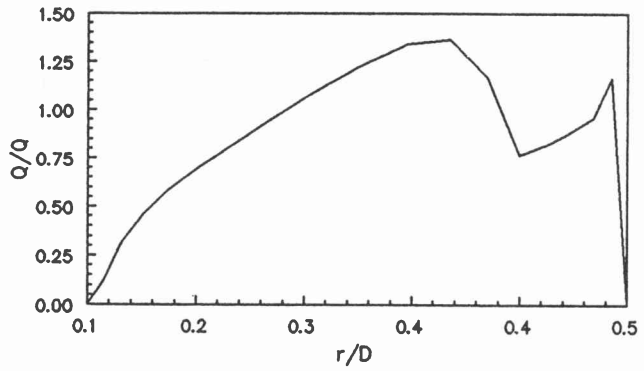

(c) Torque

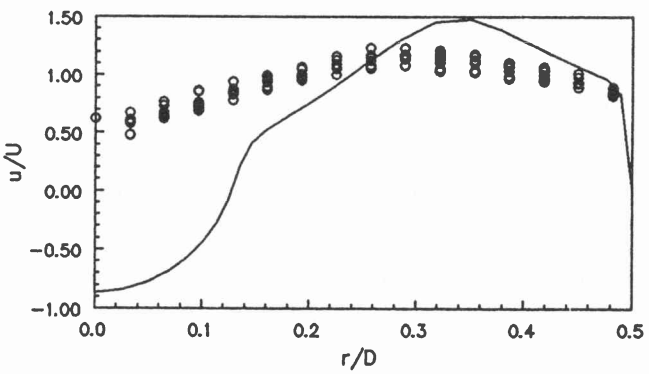

(d) Axial velocity

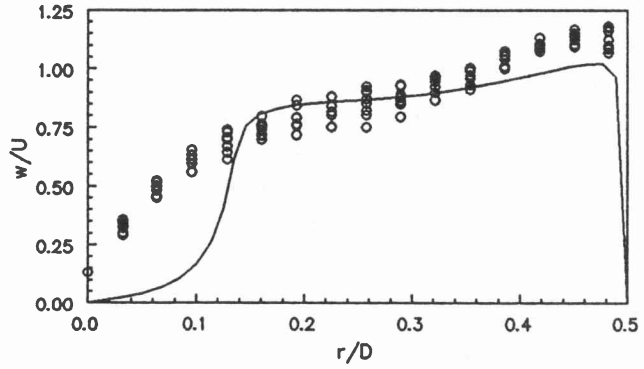

(e) Azimuthal velocity

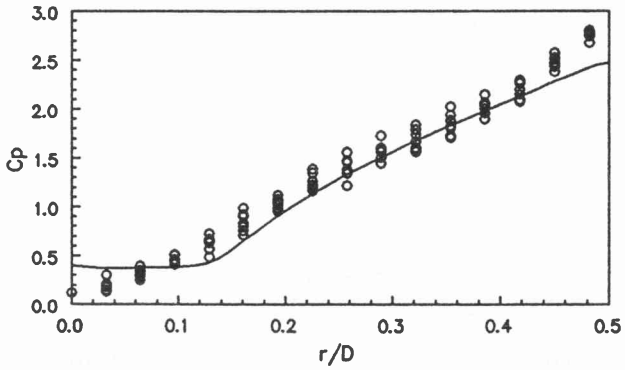

(f) Pressure coefficient

Figure 8 – Angle of attack, thrust, torque, velocity and pressure distributions for fan with axisymmetric inflow [———— SIMPLEN, o Experiment (Thiart)]

bend and turning vanes just downstream of the outflow plane which are not accounted for in the numerical predictions.

The effect of the reverse flow at the outer part of the fan blades is depicted in Fig. 8a-c. Fig. 8a shows the local angles of flow onto the fan blades: separated flow (beyond the blade stall angle, which was taken as 15°) prevails over the outer quarter of the blade span and attached flow over the inner three-quarters. The corresponding thrust and torque distributions, non-dimensionalized by means of the mean thrust and torque respectively, are shown in Fig. 8b-c. There is a sharp drop in thrust, and a corresponding but smaller drop in torque (and hence power requirement) at the outer quarter of the blade span.

Predicted profiles of velocity and static pressure at the outflow boundary are compared with experimental results in Fig. 8d-f (measurements were taken at eight equispaced azimuthal sections). As can be expected from the foregoing discussion, the predicted axial velocity profile (Fig. 8d) does not compare well with the measured one: the reverse flow region at the centreline has to be compensated for by a higher maximum value of axial velocity in the outer region. Also, the predicted radial velocities at the outflow boundary are close to zero, in accordance with the zero-gradient boundary condition on the axial velocity component, whereas the experimental results indicate a significant inward radial flow. Another calculation with a computational domain two duct diameters longer than the original one was also performed: the results were almost identical, indicating that the discrepancies cannot be ascribed to the zero-gradient outflow boundary conditions.

The results for the azimuthal velocity and the static pressure (Figs. 8e-f) are better; both these variables are fairly well predicted over the region excluding the reverse flow zone. The good prediction of w is to be expected to some extent, because the amount of swirl is essentially proportional to the power input by the fan, and the constants in the blade element model have been chosen so as to give the correct power. Also, the static pressure at the outflow boundary is related to w through the radial equilibrium boundary condition, so that if w is predicted correctly, the static pressure must also be predicted correctly. It is nevertheless encouraging that the shapes of the predicted profiles are also essentially correct.

(b) Circumferentially Distorted Inflow

The main experimental data for the case with 10 m/s crossflow are as follows:

Air density: $\rho = 1{,}176$ kg/m^3
Volume flow rate through fan: $q = 2{,}590$ m^3/s
Increase in static pressure through fan: $\Delta p = 102$ N/m^2
Fan speed: $N = 1369$ r.p.m.
Shaft power: $P = 1165$ W

In this case, both the fan static pressure and power were underpredicted by -11,5% with respect to the experimental values. Two recirculation zones are predicted at the blade tips and roots, as can be seen in Fig. 9, which shows

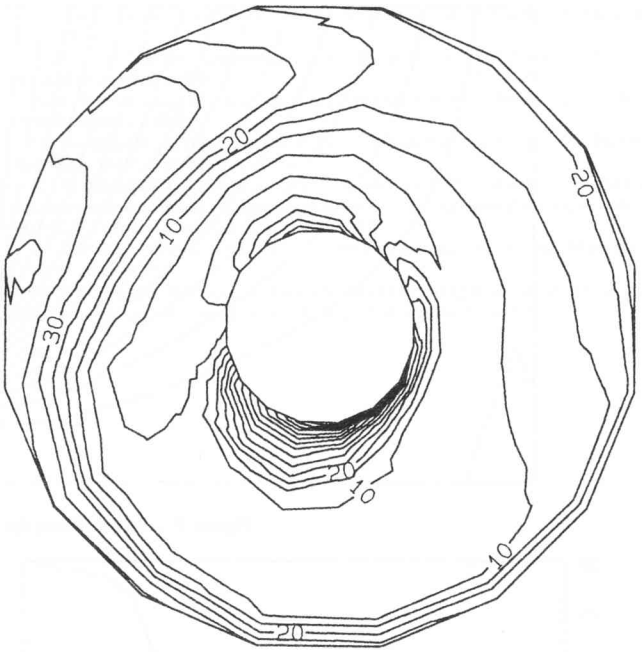

Figure 9 – Angles of attack for fan with circumferentially distorted inflow

the local angles of attack (the crossflow is from left to right; the fan rotation is clockwise). These angles of attack are defined locally as the angle between the relative velocity vector and the blade chord, so that an angle of attack larger than the blade chord angle (which is the angle between the plane of rotation and the blade chord) indicates that the axial velocity is negative and hence that reverse flow exists at that position. The blade tip chord angle is approximately 30°, therefore there must be reverse flow between $\theta = 135°$ and $\theta = 180°$ near the duct surface (θ is measured counterclockwise relative to the crossflow direction). Similarly, because the blade root

Figure 10 – Thrust distribution for fan with circumferentially distorted inflow

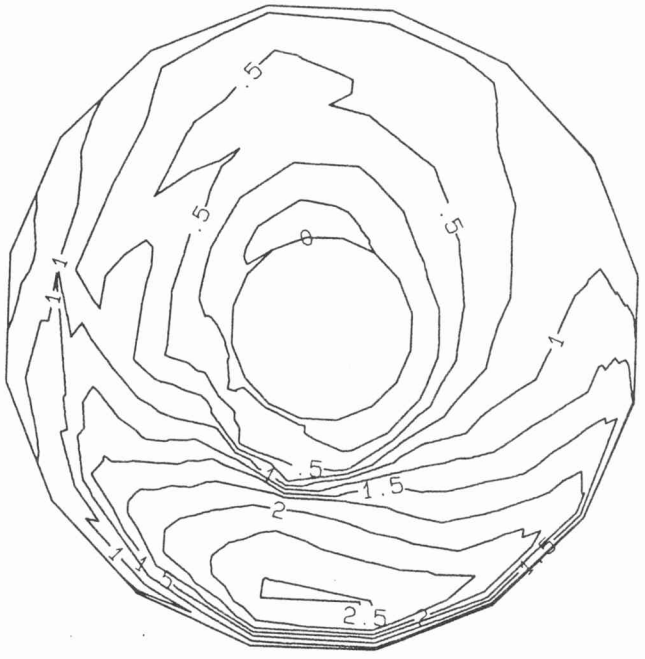

Figure 11 – Torque distribution for fan with circumferentially distorted inflow

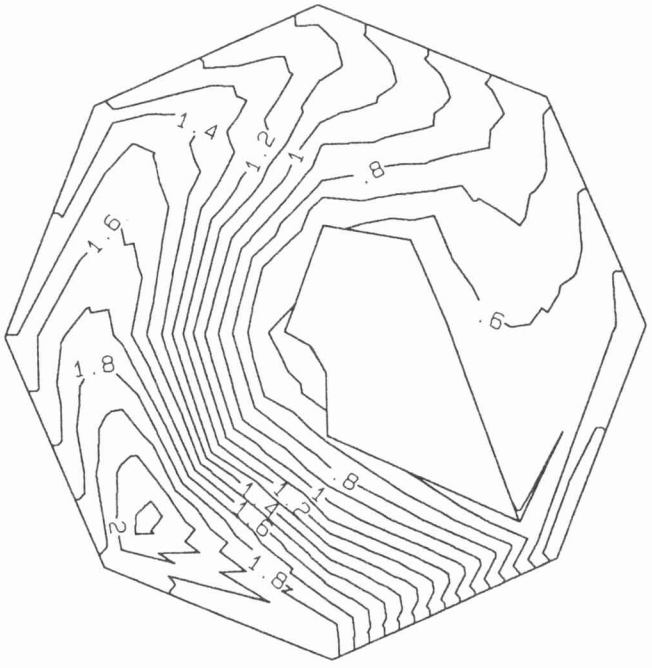

Figure 13 – Measured u/U contours for fan with circumferentially distorted inflow

chord angle is approximately 55°, there must be reverse flow between $\theta = 225°$ and $\theta = 315°$ at the hub surface.

It is evident from Fig. 9 that the flow onto the fan blades is highly distorted, both radially and azimuthally, and that separated flow prevails over a large fraction of the fan blade area. This means that the blade loading is very much non-uniform, and that the stresses in a blade can vary considerably during a revolution. The non-dimensionalized distributions of thrust and torque over the fan blade area are depicted in Figs. 10-11: both distributions show maxima of more than twice their mean values.

The numerically predicted and experimentally determined axial velocity distributions at the duct outlet are compared in Figs. 12-13. The predicted value and position of the maximum axial velocity at the duct outlet compare very well with the experimental values: approximately 2.2 times the mean axial velocity at $\theta = 225°$ and $r/D = 0{,}4$. Comparisons for the azimuthal velocity component and static pressure at the duct outlet (not shown here due to space restrictions) are similar to those for the axisymmetric inflow case.

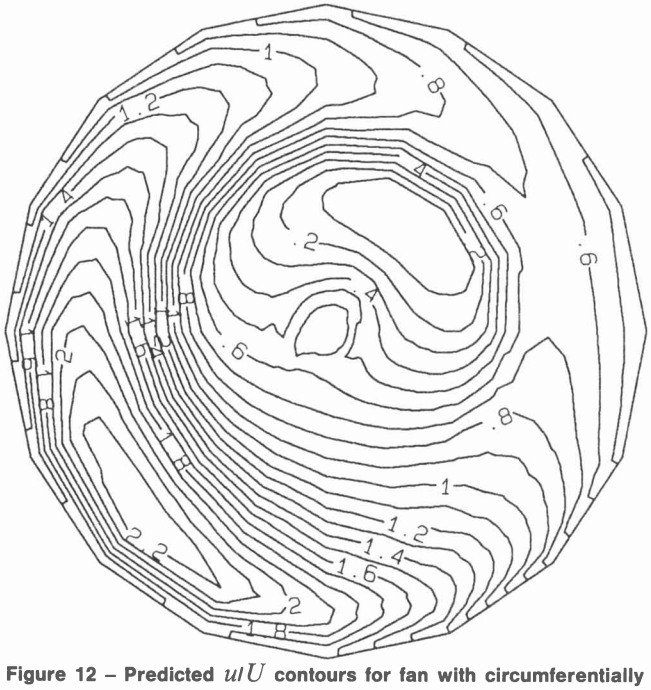

Figure 12 – Predicted u/U contours for fan with circumferentially distorted inflow

Concluding Remarks

The application of the SIMPLEN algorithm to problems involving distorted flow through turbomachinery has been presented in this paper. It is evident from the two case studies that it is possible to simulate practical turbomachinery flow problems with the SIMPLEN methodology incorporating the modified k-ε turbulence model.

The general performance of the numerical procedure is good, considering the complexity of some of the problems, but there is one major deficiency: that of excessive computing time requirements for especially the three-dimensional simulations. Investigations are currently under way to speed up the computer code by means of multigrid schemes, in order to make the methodology more useful as an engineering tool. Further work that is envisaged include the generalization of the numerical procedure to a general curvilinear coordinate system, and the calculation of the flow through multistage turbomachinery.

References

1. Patankar, S. V., and Spalding, D. B. – "A Calculation Procedure for Heat, Mass and Momentum Transfer in Three-Dimensional Parabolic Flows", *Int. J. Heat Mass Transfer*, Vol. 15, pp. 1787-1806, 1972.

2. Patankar, S. V. – "Numerical Heat Transfer and Fluid Flow", Hemisphere, Washington D.C., 1980.

3. Rhie, C. M., and Chow, W. L. – "A Numerical Study of the Turbulent Flow Past an Isolated Airfoil with Trailing Edge Separation", *AIAA J.*, vol. 21, pp. 1525-32, 1983.

4. Perić, M. – "A Finite Volume Method for the Prediction of Three-Dimensional Fluid Flow in Complex Ducts", Ph.D. thesis, University of London, 1985.

5. Patankar, S. V. – "Recent Developments in Computational Heat Transfer", *ASME J. Heat Transfer,* Vol. 110, pp. 1037-45, 1988.

6. Thiart, G. D. – "Finite Difference Scheme for the Numerical Solution of Fluid Flow and Heat Transfer Problems on Nonstaggered Grids", *Num. Heat Transfer,* Vol. 17(B), pp. 43-63, 1990.

7. Thiart, G. D. – "Improved Finite Difference Scheme for the Solution of Convection-Diffusion Problems with the SIMPLEN Algorithm", *Num. Heat Transfer,* Vol. 18(B), pp. 81-95, 1990.

8. Thiart, G. D., and Von Backström, T. W. – "Extension of the SIMPLEN Algorithm Differencing Scheme to Cylindrical Polar Coordinates", to be published in *Num. Heat Transfer,* 1992.

9. Schlichting, H. – "Boundary Layer Theory", 6th ed., McGraw-Hill, New York, 1968.

10. Launder, B. E., Pridden, C. H., and Sharma, B. I. – "The Calculation of Turbulent Boundary Layers on Spinning and Curved Surfaces", *ASME J. Fluids Engrng*, vol. 99, pp. 231-9, 1977.

11. Gupta, A. K., and Lilley, G. D. – "Flowfield Modeling and Diagnostics", Abacus, Tunbridge Wells, Kent, 1985.

12. Burns, A. D., and Wilkes, N. S. – "A Finite Difference Method for the Computation of Fluid Flows in Complex Three-Dimensional Geometries", *AERE Report No. 12342,* Harwell Laboratory, 1987.

13. Thiart, G. D. – "A Numerical Procedure for Predicting the Effects of Distorted Inflow Conditions on the Performance of Axial Flow Fans", Ph.D. thesis, University of Stellenbosch, 1990.

14. Pelletier, D. H. – "Finite Element Solutions of the Navier-Stokes Equations for 3-D Turbulent Shear Flows", Ph.D. thesis, Virginia Polytechnic Institute and State University, 1984.

15. Pelletier D. H., and Schetz, J. A. – "Finite Element Navier-Stokes Calculation of Three-Dimensional Turbulent Flow Near a Propeller", *AIAA J.*, Vol. 24, pp. 1409-16, 1986.

16. Kotb, M. A. – "Experimental Investigation of 3-D Turbulent Free Shear Flows Past Propellers and Windmills", Ph.D. thesis, Virginia Polytechnic Institute and State University, 1984.

Journal of Wind Engineering and Industrial Aerodynamics, 45 (1993) 189–214
Elsevier

Numerical simulation of the flow field near an axial flow fan operating under distorted inflow conditions

G.D. Thiart and T.W. von Backström

Department of Mechanical Engineering, University of Stellenbosch, Stellenbosch, 7600 South Africa

(Received June 14, 1991; revised version received August 26, 1992)

Summary

The results of numerical solutions of the Navier–Stokes equations, augmented by the k–ε model of turbulence, for an axial flow fan operating under distorted inflow conditions are presented. The fan is of the low solidity/low hub-to-tip ratio type: this type of fan has attained some importance with the advent of large directly air-cooled power stations in certain arid regions of the world. The numerical model is the SIMPLEN algorithm, which has been published by one of the authors previously. In the numerical predictions, blade element theory is used to model the thrust and torque exerted by the fan blades on the air. Experiments have shown that flow across the intake of a fan has a detrimental effect on its performance in that an increased amount of power is necessary to deliver the same flow rate as with no crossflow. The numerical results generally confirm the results of the experiment, although the increase in power is underestimated: an increase of only approximately half of the measured increase is predicted.

Nomenclature

c	maximum camber of fan blade
C	fan blade chord
C_1, C_2, C_μ	constants in the k–ε turbulence model
C_D	sectional fan blade drag coefficient
C_f	friction factor for a flat plate
C_L	sectional fan blade lift coefficient
C_p	pressure coefficient
C_Q	sectional fan blade torque coefficient
C_T	sectional fan blade thrust coefficient
D	drag force

Correspondence to: G.D. Thiart, Department of Mechanical Engineering, University of Stellenbosch, Stellenbosch, 7600 South Africa.

G_k	turbulence kinetic energy production term
H	distance between parallel surfaces
k	turbulence kinetic energy
L	lift force
N	rotational speed, number of blades
$p, \Delta p$	static pressure, static pressure difference
P	power
q	volume flow rate
Q	torque
r	radius, radial direction
R	radial coordinate
Re	Reynolds number
$\mathbb{R}$	radial force
t	time, maximum thickness of fan blade
T	thrust
u	axial velocity component
U	mean axial velocity in duct
v	radial velocity component
V	volume
V_R	relative velocity
w	azimuthal velocity component
z	axial direction
Z	axial coordinate
α	angle of attack
α_0	zero-lift angle of attack
$\alpha_1, \alpha_2, \alpha_3$	specific angles of attack on fan blade lift and drag curves
β	relative velocity angle
γ	fan blade angle
Δ	fan rotor thickness
ε	turbulence kinetic energy decay rate
η	efficiency
θ	azimuthal direction
Θ	azimuthal coordinate
μ, μ_t	dynamic viscosity, turbulent dynamic viscosity
ρ	density
σ	solidity of fan rotor
$\sigma_k, \sigma_\varepsilon$	Schmidt numbers in turbulence model equations
ω	angular velocity of fluid particles
Ω	angular velocity of rotating body

Subscripts and superscripts

cr	crossflow
i	index
max	maximum
sf	fan static

$\sim$ dimensionless
$-$ average

1. Introduction

Axial flow fans are used in many industrial installations requiring forced draught air cooling. There are several factors that can cause the inflow to the fans to be non-uniform, as shown in Fig. 1: the proximity of buildings, the cross-draughts caused by other fans, and cross-winds.

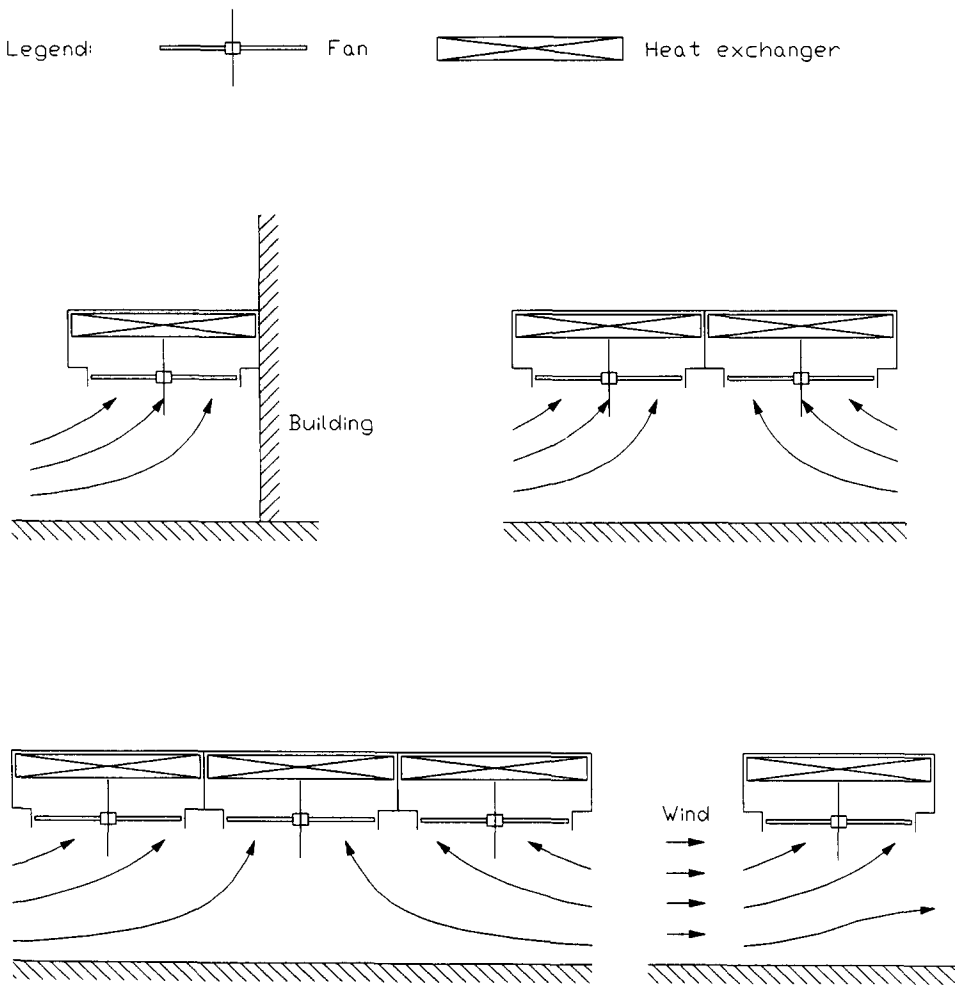

Fig. 1. Factors causing distorted inflow conditions.

Usually a combination of these effects is encountered. One, maybe extreme, example is that of the South African Electricity Supply Commission's (ESCOM) Matimba power station. Air is forced through the condenser tube bundles by 288 (six rows of 48) eight-bladed axial flow fans, each of which has a diameter of 9.145 m and is driven at 125 r.p.m. by an electric motor rated at 275 kW. Every one of these fans experiences distorted inflow conditions to some extent, either due to the proximity of the turbine house, ground surface or adjacent fans, or due to prevailing winds in the area which can reach strengths of more than 8 m/s ($\approx$30 km/h).

In this paper, results are presented of the simulation of the flow field near such a fan operating with cross-winds over its inlet. The numerical results are also compared with the experimental results of Thiart [1].

2. Calculation methods

Thiart [1] has shown that the flowfield of a Matimba-type fan, i.e., one of low solidity and low hub-to-tip ratio, can be characterized as incompressible, turbulent, isothermal, and three-dimensional. In addition, the flowfield is also unsteady, which effectively means that the time-dependent, three-dimensional, incompressible form of the Navier–Stokes equations, augmented by a suitable turbulence model, has to be solved. Unfortunately, there appears to be no solution method that has been developed for the problem under consideration. Methodologies that have been developed for similar problems can be classified broadly as follows:

(a) *Methods based on airfoil theory for non-uniform motion.* In these methods, fan blades are considered as wings of infinite aspect ratio (i.e., airfoils), each experiencing a time-dependent approach flow [2–8]. Although a high degree of sophistication has been reached with the theory of airfoils in non-uniform motion, it is not adequate for the fan problem. The inflow distortion must be prescibed, whereas for the fan in cross-flow the characteristics of the combined fan/duct system determines the characteristics of the distortion. Also, neither the effect of three-dimensional shape of the fan blades nor of the number of blades can be dealt with by the theory.

(b) *Methods for axial flow turbomachinery.* These methods attempt to model the overall behaviour of a high hub-to-tip ratio rotor (or several stator/rotor stages), usually a cascade of closely spaced airfoils in an annular channel [9–14]. These methods are less restrictive than those for airfoils in non-uniform motion, but are still inadequate for the fan problem. The major objection remains that a detailed description of the inflow distortion is required in all cases.

(c) *Methods for marine propellers and helicopter rotors.* These methods attempt to model the overall behaviour of a low hub-to-tip ratio rotor, usually an unshrouded propeller/helicopter rotor of low solidity. A marine propeller is almost always subject to inflow distortions, because it is located in the

wake of the ship it is propelling, and also because a ship's propeller shafts are usually inclined with respect to the direction of travel for practical reasons. The rotor of a helicopter in forward flight is likewise inclined with respect to the direction of travel and, therefore, also experiences non-uniform inflow conditions. Calculation methods for the determination of periodic blade loading in a non-uniform inflow are summarised by Schwanecke and Laudan [15]. These calculation procedures all involve the use of either the velocity potential or acceleration potential, and require the existence of a predominant flow direction throughout the flow field. Such a predominant flow direction does not exist for the fan problem, however. The influence of recirculation zones caused by the ducting system can also not be accounted for by potential flow methods.

The only viable approach for the fan problem appears to be the solution of the Navier–Stokes equations. Several studies reporting numerical solutions of these equations for propeller flows have appeared in recent years [16–19]. Also important in this context is the work of Pericleous and Patel [20], who simulated the flowfield in a stirred chemical reactor. They modeled the impeller with blade element theory, thus coupling the thrust and torque distributions to the flowfield. The flowfield and thrust/torque distributions are calculated iteratively: the direction and magnitude of the fluid velocity within the impeller region of the flowfield are used to calculate the lift and drag coefficients of the blade elements and hence lift and drag forces; these are then used as body forces in the Navier–Stokes equations to recalculate the flowfield. This method is considered to have the greatest potential for adequately representing the interaction between the fan and the duct system, while retaining some simplicity in that the detailed flowfield between and on the blade surfaces do not have to be resolved.

3. Governing equations and solution method

The Navier–Stokes equations for three-dimensional, laminar, isothermal, incompressible flow can be written as follows in cylindrical polar coordinates [1]:

Conservation of mass:

$$\frac{1}{r}\frac{\partial}{\partial r}\rho r v + \frac{1}{r}\frac{\partial}{\partial \theta}\rho r \omega + \frac{\partial}{\partial z}\rho u = 0. \tag{1}$$

Conservation of axial momentum:

$$\frac{\partial}{\partial t}\rho u + \frac{1}{r}\frac{\partial}{\partial r}\rho r v u + \frac{1}{r}\frac{\partial}{\partial \theta}\rho r \omega u + \frac{\partial}{\partial z}\rho u u$$
$$= \frac{\partial T}{\partial V} - \frac{\partial p}{\partial z} + \frac{1}{r}\frac{\partial}{\partial r}\left(r\mu\frac{\partial u}{\partial r}\right) + \frac{1}{r}\frac{\partial}{\partial \theta}\left(\frac{\mu}{r}\frac{\partial u}{\partial \theta}\right) + \frac{\partial}{\partial z}\left(\mu\frac{\partial u}{\partial z}\right) + \frac{\partial \mu}{\partial r}\frac{\partial v}{\partial z} + \frac{\partial \mu}{\partial \theta}\frac{\partial \omega}{\partial z} + \frac{\partial \mu}{\partial z}\frac{\partial u}{\partial z}. \tag{2}$$

Conservation of radial momentum:

$$\frac{\partial}{\partial t}\rho v+\frac{1}{r}\frac{\partial}{\partial r}\rho rvv+\frac{1}{r}\frac{\partial}{\partial \theta}\rho r\omega v+\frac{\partial}{\partial z}\rho uv-\rho r\omega^2$$

$$=\frac{\partial \mathbb{R}}{\partial V}-\frac{\partial p}{\partial r}+\frac{1}{r}\frac{\partial}{\partial r}\left(r\mu\frac{\partial v}{\partial r}\right)+\frac{1}{r}\frac{\partial}{\partial \theta}\left(\frac{\mu}{r}\frac{\partial v}{\partial \theta}\right)+\frac{\partial}{\partial z}\left(\mu\frac{\partial v}{\partial z}\right)+\frac{\partial \mu}{\partial r}\frac{\partial v}{\partial r}+\frac{\partial \mu}{\partial \theta}\frac{\partial \omega}{\partial r}+\frac{\partial \mu}{\partial z}\frac{\partial u}{\partial r}$$

$$-\frac{\mu}{r}\left(\frac{v}{r}+2\frac{\partial \omega}{\partial \theta}\right). \tag{3}$$

Conservation of moment of momentum:

$$\frac{\partial}{\partial t}\rho r^2\omega+\frac{1}{r}\frac{\partial}{\partial r}\rho r^3v\omega+\frac{1}{r}\frac{\partial}{\partial \theta}\rho r^3\omega\omega+\frac{\partial}{\partial z}\rho r^2u\omega$$

$$=\frac{\partial Q}{\partial V}-\frac{\partial p}{\partial \theta}+\frac{1}{r}\frac{\partial}{\partial r}\left(r^3\mu\frac{\partial \omega}{\partial r}\right)+\frac{1}{r}\frac{\partial}{\partial \theta}\left(r^2\frac{\mu}{r}\frac{\partial \omega}{\partial \theta}\right)+\frac{\partial}{\partial z}\left(r^2\mu\frac{\partial \omega}{\partial z}\right)+\frac{\partial \mu}{\partial r}\frac{\partial v}{\partial \theta}+\frac{\partial \mu}{\partial \theta}\frac{\partial \omega}{\partial \theta}$$

$$+\frac{\partial \mu}{\partial z}\frac{\partial u}{\partial \theta}+\frac{2}{r}\frac{\partial}{\partial \theta}\mu v. \tag{4}$$

These equations have to be augmented by a suitable turbulence model to facilitate the calculation of turbulent flows. The most popular (and well-tested) turbulence model being used for general flow situations is the k–ε model. Transport equations for the turbulence kinetic energy k and the decay rate of k (that is, ε) are solved for the purpose of calculating the so-called eddy viscosity μ_t, defined as:

$$\mu_t=\rho C_\mu\frac{k^2}{\varepsilon}. \tag{5}$$

Here C_μ is an empirical constant, taken as 0.09. The eddy viscosity is used to represent the Reynolds stresses in the time-averaged Navier–Stokes equations in that the laminar viscosity μ is replaced by $\mu+\mu_t$. The k and ε-equations used for the fan flowfield simulation are as follows:

Turbulence kinetic energy:

$$\frac{\partial}{\partial t}\rho k+\frac{1}{r}\frac{\partial}{\partial r}\rho rvk+\frac{1}{r}\frac{\partial}{\partial \theta}\rho r\omega k+\frac{\partial}{\partial z}\rho uk$$

$$=\frac{1}{r}\frac{\partial}{\partial r}\left(\frac{\mu+\mu_t}{\sigma_k}r\frac{\partial k}{\partial r}\right)+\frac{1}{r}\frac{\partial}{\partial \theta}\left(\frac{\mu+\mu_t}{r\sigma_k}\frac{\partial k}{\partial \theta}\right)+\frac{\partial}{\partial z}\left(\frac{\mu+\mu_t}{\sigma_k}\frac{\partial k}{\partial z}\right)+G_k-\rho\varepsilon. \tag{6}$$

Turbulence kinetic energy decay rate:

$$\frac{\partial}{\partial t}\rho\varepsilon+\frac{1}{r}\frac{\partial}{\partial r}\rho rv\varepsilon+\frac{1}{r}\frac{\partial}{\partial\theta}\rho r\omega\varepsilon+\frac{\partial}{\partial z}\rho u\varepsilon$$

$$=\frac{1}{r}\frac{\partial}{\partial r}\left(\frac{\mu+\mu_t}{\sigma_\varepsilon}r\frac{\partial\varepsilon}{\partial r}\right)+\frac{1}{r}\frac{\partial}{\partial\theta}\left(\frac{\mu+\mu_t}{r\sigma_\varepsilon}\frac{\partial\varepsilon}{\partial\theta}\right)+\frac{\partial}{\partial z}\left(\frac{\mu+\mu_t}{\sigma_\varepsilon}\frac{\partial\varepsilon}{\partial z}\right)+\frac{\varepsilon}{k}(C_1G_k-\rho C_2\varepsilon)$$

$$+0.2C_2\rho k\frac{\omega}{r}\frac{\partial}{\partial r}r^2\omega. \tag{7}$$

These are the standard forms of the k and ε-equations except for the last term on the right hand side of Eq. (7), which is the modification of Ref. [21] to account for the destabilizing effect of swirl on turbulence. The empirical constants that appear in Eqs. (6) and (7) are assigned the following values: $\sigma_k=1.0$, $\sigma_\varepsilon=1.3$, $C_1=1.44$ and $C_2=1.92$. G_k is the turbulence kinetic energy production term, given by [22]:

$$G_k=\mu_t\left\{2\left[\left(\frac{\partial u}{\partial z}\right)^2+\left(\frac{\partial v}{\partial r}\right)^2+\left(\frac{\partial\omega}{\partial\theta}+\frac{v}{r}\right)^2\right]+\left(\frac{\partial u}{\partial r}+\frac{\partial v}{\partial z}\right)^2+\left(\frac{1}{r}\frac{\partial v}{\partial\theta}+r\frac{\partial\omega}{\partial r}\right)^2\right.$$

$$\left.+\left(\frac{1}{r}\frac{\partial u}{\partial\theta}+r\frac{\partial\omega}{\partial z}\right)^2\right\}. \tag{8}$$

The governing equations are solved numerically, using the SIMPLEN (semi-implicit method for pressure-linked equations on nonstaggered grids) algorithm of Thiart [23,24]. Details of the discretization scheme are given in Refs. [1,25]. The numerical procedure was incorporated in a computer code called FLOWAX, written in single precision FORTRAN 77. All computations reported in this paper were performed on the CONVEX 120 computer of the Bureau for Mechanical Engineering at the University of Stellenbosch.

4. Computational domain and grid

The idealised computational domain corresponding to the experimental configuration of Thiart [1] is shown in Fig. 2. In the experimental setup the test fan was mounted in a round duct, the intake of which was located in a hole in the floor of the subsonic windtunnel of the Department of Mechanical Engineering at the University of Stellenbosch. The windtunnel was used to simulate cross-wind conditions. Measurements of cross-flow velocity, volumetric flow rate, fan static pressure fan speed and shaft power were taken for two cases: one with no crossflow (case 00) and one with crossflow (case 10) of magnitude approximately equal to the average axial velocity through the duct. Detailed measurements of velocity and static pressure were also taken with a five-hole probe at a location approximately one and a half duct diameters downstream from the inlet. The results are summarised in Table 1 along with the relevant

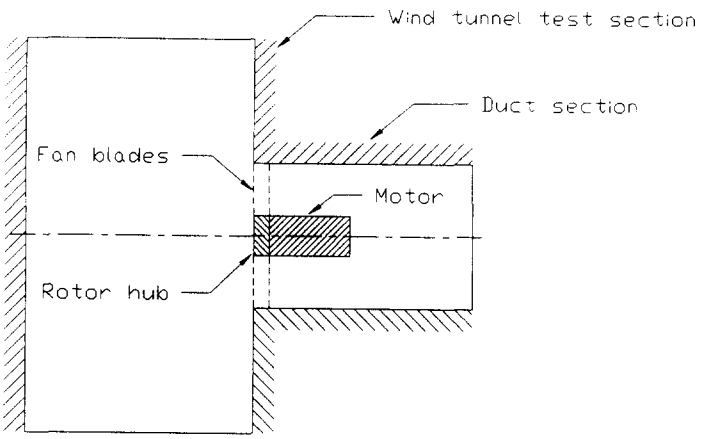

Fig. 2. Computational domain.

Table 1

Summary of input and comparative data for numerical predictions

Case	00	10
ρ (kg/m^3)	1.172	1.176
μ (kg m/s $\times 10^5$)	1.836	1.832
V_{cr} (m/s)	0.00	9.93
q (m^3/s)	2.63	2.59
Δp_{sf} (N/m^2)	79	102
N (rpm)	1409	1369
P (W)	981	1165

fluid property data (the fan static pressure is defined here as the mean static pressure at the measuring station downstream of the fan minus the static pressure at the roof of the test section).

Several idealisations are incorporated in the computational domain:

(a) *Wind tunnel.* The wind tunnel test section is modeled as two parallel plates of diameter equal to 1702 mm, which is the length of the test section measured between two static pressure wall tappings located at either end of the section. The spacing between the plates is equal to the height of the test section, 992 mm. No account is taken of the sidewalls of the test section, which are 1435 mm apart.

(b) *Duct.* The duct section (diameter equal to 622 mm, as for the experiment) extends from the test section to the five-hole probe measuring position. The length of the duct section is therefore modeled as 955 mm.

(c) *Fan.* The main features of the fan used in the experiment are as follows: diameter = 620 mm, number of blades = 7, average blade chord = 86 mm

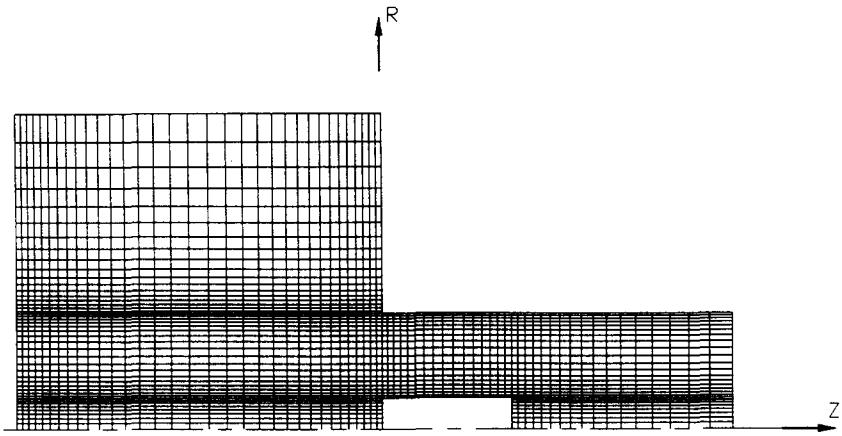

Fig. 3. Computational grid.

(83 mm at the hub, 76 mm at the blade tips), hub diameter = 168 mm, hub length = 69 mm, and design speed = 1400 rpm.

The fan rotor hub and fan motor is modeled as a round cylinder of length 350 mm and diameter 168 mm. The length corresponds to the combined length of the fan hub and motor, while the diameter corresponds to the hub diameter – the motor is actually slightly smaller in diameter than the hub. The small gap between the hub and the motor are not modeled; neither are the cooling fins on the motor surface. The fan blades are not modeled directly as rotating solid surfaces, but indirectly through the forces which they impart on the air; details are given in the next Section.

The computational grid for axisymmetric inflow is shown in Fig. 3. There are 67 axial stations and 45 radial stations, for a total of 2301 grid points. Expansions ratios of 1.08 in the axial direction and 1.15 in the radial direction are used throughout. The computational grid for distorted inflow is the same as for axisymmetric inflow, but now has sixteen equispaced azimuthal planes instead of only one. The total number of grid points in this case is 36036.

5. Blade element model

The influence of the fan blades are modeled as body forces by means of the blade element theory commonly employed for aircraft and ship propeller calculations (see, for example, Ref. [26]). In the present context, the theory is applied as follows:

(a) *Lift and drag forces.* Each blade element between two radii r and δr experiences a lift force δL and a drag force δD (there are assumed to be no radial and drag forces are, respectively, normal and parallel to the vector of

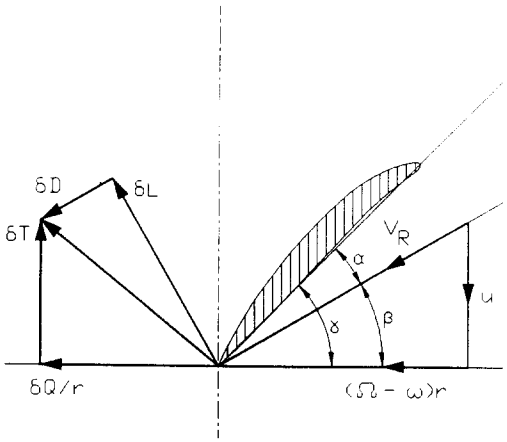

Fig. 4. Forces on a blade element.

relative velocity V_R of the fluid against the element, Fig. 4. The magnitudes of the lift and drag forces are given by, respectively,

$$\delta L = \tfrac{1}{2}\rho V_R^2 C_L C \delta r, \tag{9}$$

$$\delta D = \tfrac{1}{2}\rho V_R^2 C_D C \delta r, \tag{10}$$

where C_L and C_D are the lift and drag coefficients, and C is the chord of the blade element.

(b) *Relative air velocity.* The relative velocity vector is composed of an axial component u which is the average value of the axial velocity components at the leading and trailing edge positions, and an azimuthal component $r(\Omega-\omega)$, which is the azimuthal velocity component of the fluid relative to the blade element, also averaged between the leading and trailing edge positions.

(c) *Thrust and torque.* The thrust δT and torque δQ exerted by the blade element on the fluid (and vice versa) are obtained by decomposing the drag and lift forces into axial and azimuthal components:

$$\delta T = \delta L \cos\beta - \delta D \sin\beta, \tag{11}$$

$$\delta Q = (\delta L \sin\beta + \delta D \cos\beta) r. \tag{12}$$

β is the angle between the relative velocity vector and the plane of rotation of the blade element, as shown in Fig. 4.

The actual body forces, which appear in the Navier–Stokes equations as forces per unit volume, are obtained by taking into account the number of blades

N and the axial "thickness" Δ of the fan rotor:

$$\frac{\partial T}{\partial V}=\frac{N\delta T}{2\pi r\,\delta r\,\Delta}=\frac{\sigma\,\delta T}{C\delta r\,\Delta}, \tag{13}$$

$$\frac{\partial Q}{\partial V}=\frac{N\delta Q}{2\pi r\,\delta r\,\Delta}=\frac{\sigma\,\delta Q}{C\delta r\,\Delta}. \tag{14}$$

Here $\sigma=NC/2\pi r$ denotes the solidity of the rotor. Substitution of Eqs. (9)–(12) into Eqs. (13) (14) yields the final expressions for the body forces, which can also be written in terms of the thrust and torque coefficients C_T and C_Q:

$$\frac{\partial T}{\partial V}=\tfrac{1}{2}\rho V_{\mathrm{R}}^2\frac{\sigma}{\Delta}(C_{\mathrm{L}}\cos\beta-C_{\mathrm{D}}\sin\beta)=\tfrac{1}{2}\rho V_{\mathrm{R}}^2\frac{\sigma}{\Delta}C_{\mathrm{T}}, \tag{15}$$

$$\frac{\partial Q}{\partial V}=\tfrac{1}{2}\rho V_{\mathrm{R}}^2\frac{\sigma}{\Delta}r(C_{\mathrm{L}}\sin\beta+C_{\mathrm{D}}\cos\beta)=\tfrac{1}{2}\rho V_{\mathrm{R}}^2\frac{\sigma}{\Delta}rC_{\mathrm{Q}}. \tag{16}$$

Assuming that the direction and magnitude of V_R is known, it remains to specify the lift and drag coefficients to complete the model. These coefficients are, in general, dependent on the geometry of the blade elements, the local angle of attack $\alpha=\gamma-\beta$ (γ is the angle between the chord of a blade element and the plane of rotation, Fig. 4), and the blade Reynolds number $\mathrm{Re}=\rho V_{\mathrm{R}}C/\mu$.

There are three possibilities for determining C_{L} and C_{D}: experimentally (e.g., wind tunnel testing), theoretically (e.g., thin airfoil theory and boundary layer theory), or using empirical correlations available in the literature. The geometrical features of the fan blades under consideration could unfortunately not be determined with the necessary degree of accuracy required for experimental testing or theoretical calculations. The four parameters necessary for use with most empirical correlations, that is, blade angle γ, chord C, camber ratio c/C, and thickness ratio t/C, could, however, be determinined sufficiently accurately for practical purposes and can be expressed as the following functions of radius [1] (with r in mm):

$$\gamma=132.926-1.80485r+15.6543\times10^{-3}r^2-71.9291\times10^{-6}r^3+166.709\times10^{-9}r^4$$
$$-154.835\times10^{-12}r^5\quad\text{degrees}, \tag{17}$$

$$C=-269.491+9.10529r-86.4337\times10^{-3}r^2+393.699\times10^{-6}r^3-878.461$$
$$\times10^{-9}r^4+773.060\times10^{-12}r^5\quad\text{mm}, \tag{18}$$

$$c/C=6.341-0.003544r\quad\%, \tag{19}$$

$$t/C=8.325-0.006863r\quad\%. \tag{20}$$

It was, therefore, decided to use empirical correlations, in particular those of Hoerner [27], and Hoerner and Borst [28]. Details are as follows:

(a) *Lift below stall.* For small angles of attack the lift coefficient is given by

$$C_{\mathrm{L}}=2\pi\eta(\alpha-\alpha_0), \tag{21}$$

where η is the so-called blade efficiency expressing the deviation of the lift-curve slope from the ideal value of 2π, and α_0 is the zero-lift angle; η is taken as 0.9 and α_0 is calculated from Ref. [28] (Ch. II; Eq. (18)):

$$\alpha_0 = -115c/C \quad \text{degrees}, \tag{22}$$

which is representative for airfoils with circular-arc camber lines.

(b) *Maximum lift.* The maximum value of the lift coefficient, $C_{L_{max}}$, which is attained just before stall, depends on many factors; here it is assumed that it is only influenced by the camber and thickness ratios, and that it can be determined by linear interpolation amongst the following four values taken from Fig. 13, Ch. IV of Ref. [28]:

$$C_{L_{max}} = \begin{cases} 1.234 & \text{for } t/C=0.06;\ c/C=0.045, \\ 1.297 & \text{for } t/C=0.06;\ c/C=0.065, \\ 1.586 & \text{for } t/C=0.09;\ c/C=0.045, \\ 1.657 & \text{for } t/C=0.09;\ c/C=0.065. \end{cases} \tag{23}$$

(c) *Drag below stall.* The drag coefficient for small angles of attack is given by ([27], Ch. VI, Eqs. (6), (13), and (15)):

$$C_D = 2C_f\left\{1+2\frac{t}{C}+\frac{C_L^2}{16}+30\left[\left(\frac{t}{C}+\frac{C_L}{5}\right)^4+\left(\frac{t}{C}-\frac{C_L}{5}\right)^4\right]\right\}. \tag{24}$$

Here, C_f is the skin friction coefficient for one side of a flat plate with length equal to the blade element chord, and which can be approximated, for turbulent flow, by the equation ([27], Ch. II, Eq. (26)):

$$C_f = (3.46\log \mathrm{Re} - 5.6)^{-2}. \tag{25}$$

The second and third terms within the brackets in Eq. (24) are corrections for thickness and circulation, respectively; the last two terms represent the pressure drag of the blade element (the last term is meaningless if $t/C < C_L/5$; a minimum value of zero should be used then).

(d) *Lift and drag beyond stall.* Beyond stall, particularly for angles of attack larger than about 20°, the blade element behaves like a flat plate in separated flow: it experiences a force per unit area of magnitude $0.5\rho V_R^2 C_{D_{max}} \sin\alpha$ in a direction normal to its surface. Here, $C_{D_{max}}$ is the drag coefficient of the plate when it is perpendicular to the flow direction; in the present context the lift and drag coefficients are therefore given by, respectively,

$$C_L = C_{D_{max}} \sin\alpha\cos\alpha, \tag{26}$$

$$C_D = C_{D_{max}} \sin^2\alpha. \tag{27}$$

The value of $C_{D_{max}}$ for a flat plate with sharp edges is 1.98; it is less for plates with rounded edges and is also influenced by factors such as camber and aspect ratio. These correlations have been used in the following manner to obtain the lift and drag characteristics:

(a) *Lift.* Equation (21) is used between α_0 and an angle of attack α_1 corresponding to $C_L = 0.6\,C_{L_{max}}$. A third degree polynomial is used to represent C_L between α_1 and α_2, where $C_L = C_{L_{max}}$. Equation (26) is used for $\alpha > \alpha_3$, and another third degree polynomial between α_2 and α_3. Much the same procedure is used for angles of attack less than α_0: Eq. (26) for $\alpha < -\alpha_3$, a third degree polynomial between $-\alpha_2$ and $-\alpha_3$, and so on. There are two minor differences (which are necessary because α_0 is not equal to zero): Eq. (21) is used between α_0 and $\alpha_0 - \alpha_1$ and the maximum negative value of C_L is taken as $-C_{L_{max}} - 2\pi\eta\alpha_0$.

(b) *Drag.* Equation (24) is used between α_0 and α_1, a third degree polynomial between α_1 and α_3, and Eq. (27) for $\alpha > \alpha_3$. The procedure for angles of attack less than α_0 is similar.

The actual values of α_2, α_3 and $C_{D_{max}}$ are taken as 15°, 30° and 1.4, respectively. These values were found to yield the best results for the prediction of the fan performance for the case of axisymmetric inflow. The resulting variations with angle of attack of the lift, drag, thrust and torque coefficients of the fan blade under consideration are depicted in Fig. 5, for the midspan position.

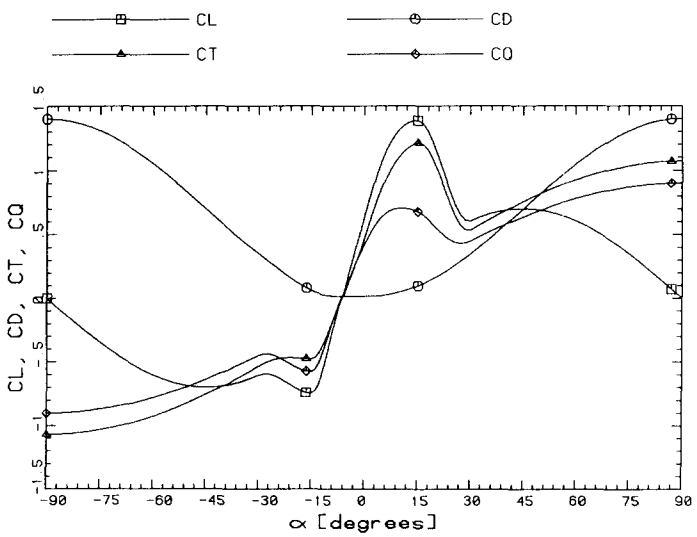

Fig. 5. Lift, drag, thrust, and torque characteristics at midspan.

6. Boundary and initial conditions

The boundary conditions for the fan performance predictions are as follows: at the solid surfaces, the no-slip conditions ($u=v=w=0$ except at the rotor hub, where $w=\Omega$) and wall functions for k and ε (in the manner described by Burns and Wilkes [29]) are used; at the duct outlet plane zero-gradient boundary conditions are used for all variables except static pressure, for which the radial equilibrium boundary condition $\partial p/\partial r=\rho w^2$ is used; at the inlet and outlet planes between the parallel surfaces zero-gradient boundary conditions are used for k and ε, while the velocity components are fixed to provide the correct flow rate through the fan.

The velocity profiles to be used as boundary conditions between the parallel surfaces (representing the wind tunnel top and bottom walls) posed a problem: these boundaries are not sufficiently far removed from the fan for uniform flow velocity profiles to be used. The following procedure was used to overcome this problem:

(a) *Axisymmetric inflow.* The inlet velocity profiles (u and v only – w is equal to zero) are determined from a potential flow solution on part of the computational domain, excluding the duct section and assuming uniform inflow into the duct section. Details are given by Thiart [1]; the velocity profiles (non-dimensionalized by means of the mean radial velocity) are shown in Fig. 6. It is clear that the flow direction at the inlet boundary differs significantly from that of a uniform flow, which would have been purely in the inward radial direction.

(b) *Distorted inflow.* Uniform flow equal to the required crossflow velocity, that is, $v=V_{cr}\cos\theta$, $w=V_{cr}\sin\theta/r$, added to the potential flow solution for

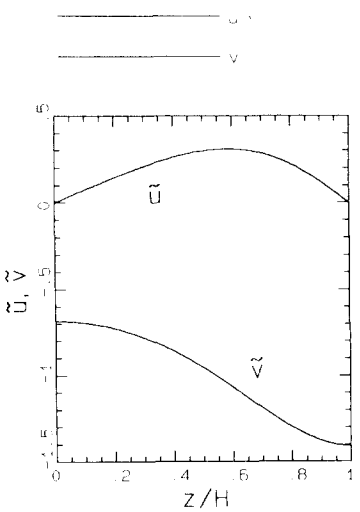

Fig. 6. Velocity profiles at the inlet boundary.

the axisymmetric inflow case, is used to provide the required velocity boundary conditions.

The potential flow solutions are also used as initial conditions for the fan performance predictions; static pressure conditions are readily obtained from Bernoulli's equation. In the duct section the initial values for v and w are taken as zero, while the axial velocity component u is taken as uniform everywhere between the inlet and outlet planes of the duct.

7. Prediction of fan performance

7.1. Axisymmetric inflow

The axisymmetric inflow problem was solved with a time step of 0.0005 s, which is approximately the minimum Courant–Frederichs–Lewis time step for the flowfield and computational grid under consideration. A pressure correction relaxation factor of 0.4 was used, and 5 point Jacobi substitutions were performed per time step. A relaxation factor of 0.001 was used for the body forces during the first 1000 time steps, and 0.01 thereafter.

Convergence to the steady-state solution was achieved in approximately 90000 time steps (18 h CPU time), at which stage the fan static pressure and fan power had stabilized at -5% and $\approx 0\%$, respectively, compared to the experimental results. A similar calculation was done for uniform inflow boundary conditions: in this case the predictions differed from the experimental results by -8% for the fan static pressure, and by $+4\%$ for the fan power. The introduction of the inflow boundary conditions calculated from the potential flow solution is, therefore, considered worthwhile. The calculation was also repeated for other values of α_2, α_3, and $C_{D_{max}}$. It was found that the results were not very sensitive to α_2, and α_3, but quite sensitive to $C_{D_{max}}$. Fan power was underpredicted and fan static pressure overpredicted for $1.5 \leqslant C_{D_{max}} \leqslant 2.0$, and vice versa for $C_{D_{max}} \leqslant 1.4$.

The general features of the flow field are depicted in Figs. 7 through 9. The reverse flow at the outer part of the fan blades, which was also observed during the experiment, is clearly evident in Fig. 7, which shows the streamlines in an azimuthal plane. Another zone of recirculatory flow is predicted downstream of the fan motor, extending beyond the outflow boundary. The reverse flow at the outflow boundary was not observed during the experiment. Possible reasons for the discrepancy are: inadequacies of the turbulence model, and the influence of a right angle bend and turning vanes just downstream of the outflow plane which are not accounted for in the numerical predictions. Static pressure contours are shown in Fig. 8, and contours of the azimuthal velocity component (w) in Fig. 9; the rapid increases in the values of both these variables at the fan rotor are clearly evident.

The effect of the reverse flow at the outer part of the fan blades is depicted in Figs. 10 and 11. Figure 10 shows the local angles of flow onto the fan blades: separated flow (beyond stall) prevails over the outer quarter of the blade span

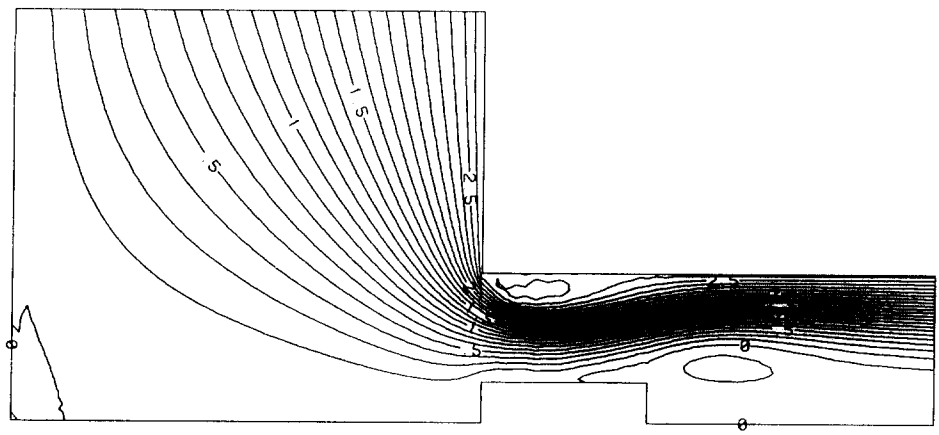

Fig. 7. Streamlines — case 00.

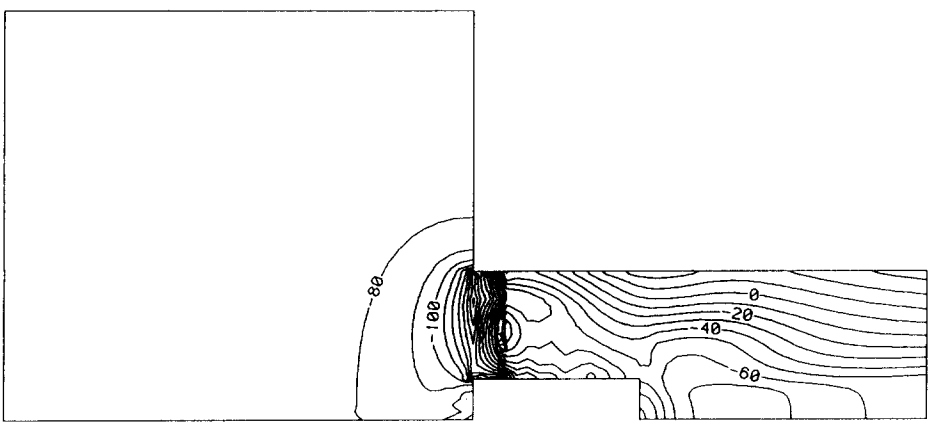

Fig. 8. Contours of static pressure (N/m^2) — case 00.

and attached flow over the inner three-quarters. The corresponding thrust and torque distributions, non-dimensionalized by means of the mean thrust and torque, respectively, are shown in Fig. 11. There is a sharp drop in thrust, and a corresponding but smaller drop in torque (and, hence, power requirement) at the outer quarter of the blade span.

Predicted profiles of velocity and static pressure at the outflow boundary are compared with the experimental results in Figs. 12 through 14 (measurements were taken at eight equispaced azimuthal sections). As can be expected from the foregoing discussion, the predicted axial velocity profile (Fig. 12) does not compare well with the measured one: the reverse flow region at the centreline has to be compensated for by a higher maximum value of axial velocity in the outer region. Also, the predicted radial velocities at the outflow boundary are close to zero, in accordance with the zero-gradient boundary condition on the

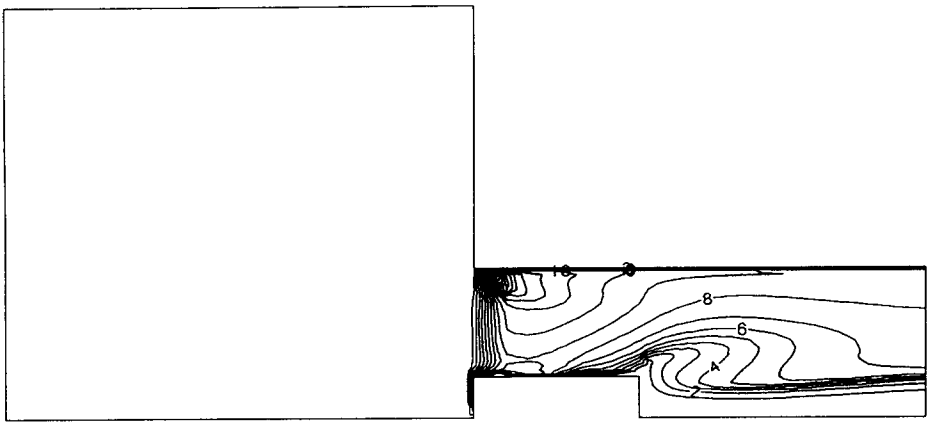

Fig. 9. Contours of angular velocity (m/s) – case 00.

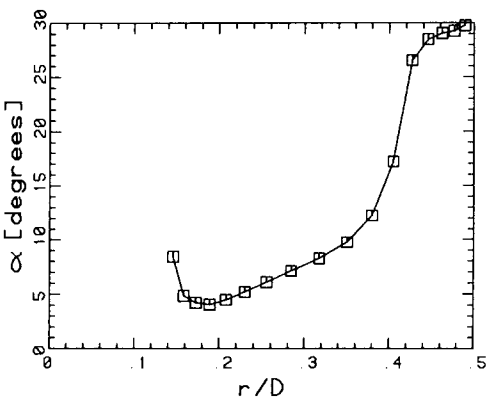

Fig. 10. Relative flow angles onto fan blades – case 00.

axial velocity component, whereas the experimental results indicate a significant inward radial flow. Another calculation with a computational domain two duct diameters longer than the original one was also performed: the results were almost identical, indicating that the discrepancies cannot be ascribed to the zero-gradient outflow boundary conditions.

The results for the azimuthal velocity (w) and the static pressure (Figs. 13 and 14) are better; both these variables are fairly well predicted over the region excluding the reverse flow zone. The good prediction of w is to be expected to some extent, because the amount of swirl is essentially proportional to the power input by the fan, and the constants in the blade element model have been chosen so as to give the correct power. Also, the static pressure at the outflow boundary is related to w through the radial equilibrium boundary condition, so that if w is predicted correctly, the static pressure must also be predicted

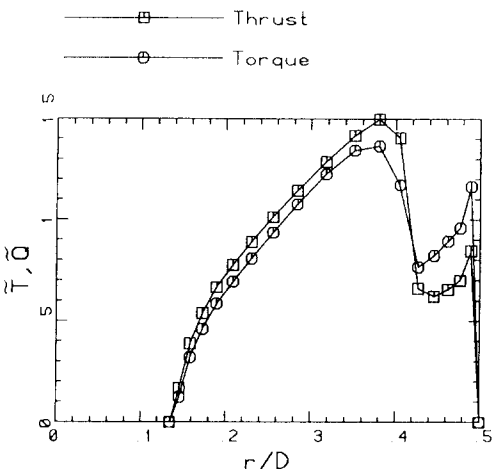

Fig. 11. Thrust and torque distributions case 00.

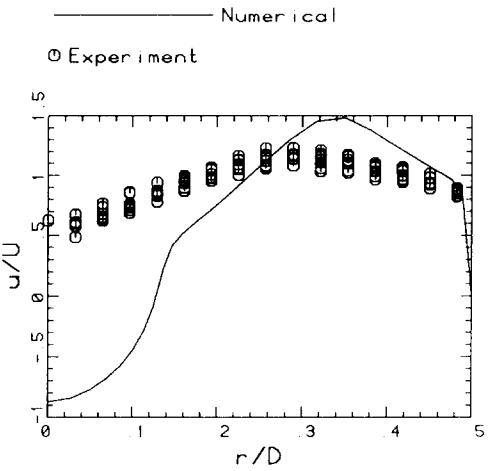

Fig. 12. Profiles of u at outflow boundary – case 00.

correctly. It is nevertheless encouraging that the shapes of the predicted profiles are also essentially correct.

7.2. Distorted inflow

The same control parameters (time step, relaxation factors, etc.) as for the axisymmetric inflow case were used to solve the distorted inflow problem. The w-solution tended to chequerboard in the θ-direction: the reason for this behaviour could not be found, and it was, therefore, decided to suppress the problem by application of the fourth-order one-dimensional linear filter developed by Shapiro [30]. The crossflow was introduced gradually during the

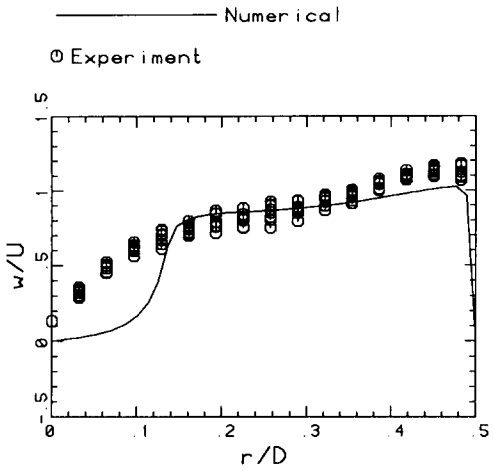

Fig. 13. Profiles of w at outflow boundary – case 00.

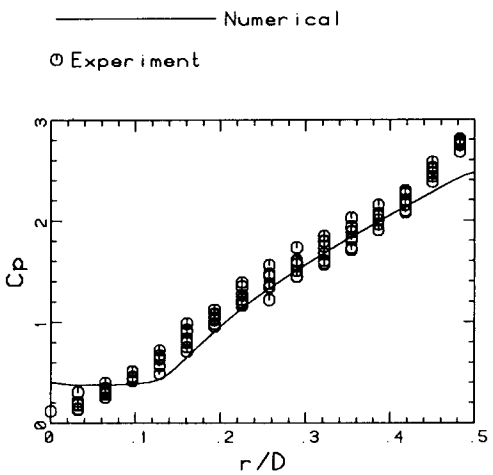

Fig. 14. Profiles of p at outflow boundary – case 00.

second thousand time steps. The calculation proceeded extremely slowly, at approximately 200 time steps per hour of CPU time on the CONVEX. Due to the excessive computing time the solution was not driven to full convergence: the calculation was stopped at 23500 time steps (125 h CPU time); at which time both the fan static pressure and fan power had stabilized at a value of -11.5% with respect to the experimental values.

Two recirculation zones are predicted at the blade tips and roots, as can be seen in Fig. 15, which shows the local angles of flow onto the fan blades (the crossflow is from left to right; the fan rotation is clockwise): the blade tip angle is approximately 30°. Therefore, there must be reverse flow between 135° and

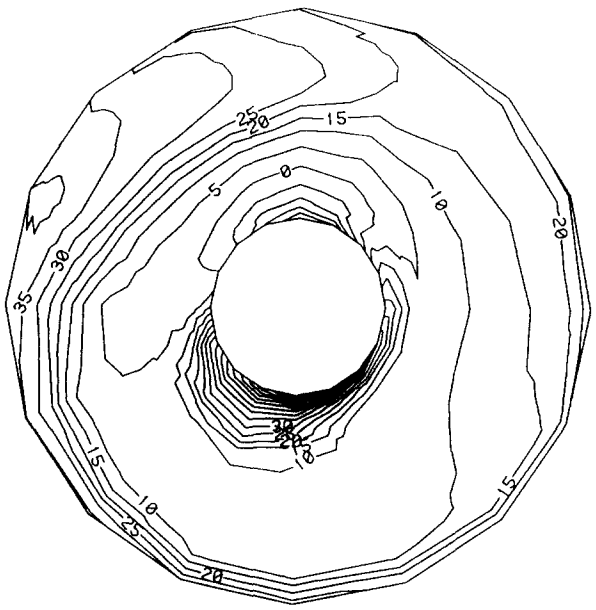

Fig. 15. Relative flow angles (degrees) onto fan blades – case 10.

180° near the duct surface. Similarly, because the blade root angle is approximately 55°, there must be reverse flow between 225° and 315° at the hub surface.

It is evident from Fig. 15 that the flow onto the fan blades is highly distorted, both radially and azimuthally, and that separated flow prevails over a large fraction of the fan blade area. This means that the blade loading is very much non-uniform, and that the stresses in a blade can vary considerably during a revolution. The non-dimensionalized distributions of thrust and torque over the fan blade area are depicted in Figs. 16 and 17, respectively: both distributions show maxima of more than twice their mean values.

Examination of the numerical solution revealed that the predicted value and position of the maximum axial velocity at the duct outlet compare very well with the experimental values: approximately 2.2 times the mean axial velocity at $\theta = 225°$ and $r/D = 0.4$ (see Figs. 18 and 19). Comparisons between the numerically predicted and experimentally determined profiles of the axial and azimuthal velocity components and static pressure at the duct outlet are, therefore, presented for the $\theta = 45/225°$-section through the calculation domain, and also for the section perpendicular thereto, i.e., $\theta = 135/315°$ for the axial velocity profile. These comparisons are shown in Figs. 20–23, where negative values of r/D represent angles between 90° and 270°. The axial velocity profiles (Figs. 20 and 21) compare very well with the measured profiles. Correspondence between the predicted and measured azimuthal velocity profiles (Fig. 22) is fair in the sense that the maximum value is predicted correctly. The static pressure distributions (Fig. 23) also compares favorably.

Fig. 16. Non-dimensional thrust distribution – case 10.

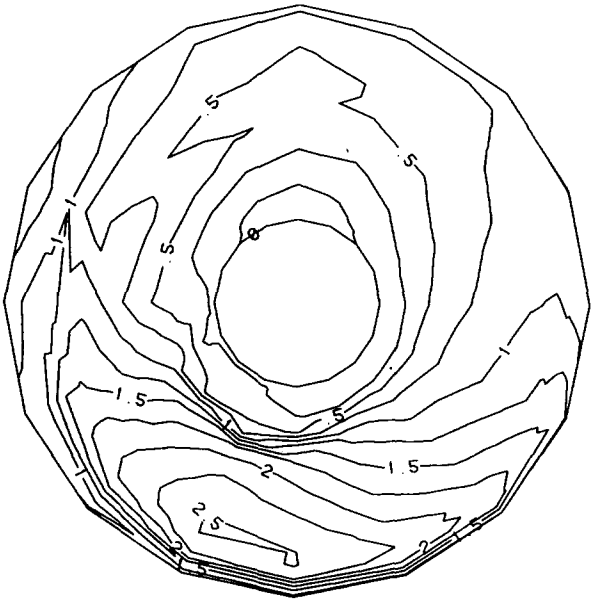

Fig. 17. Non-dimensional torque distribution – case 10.

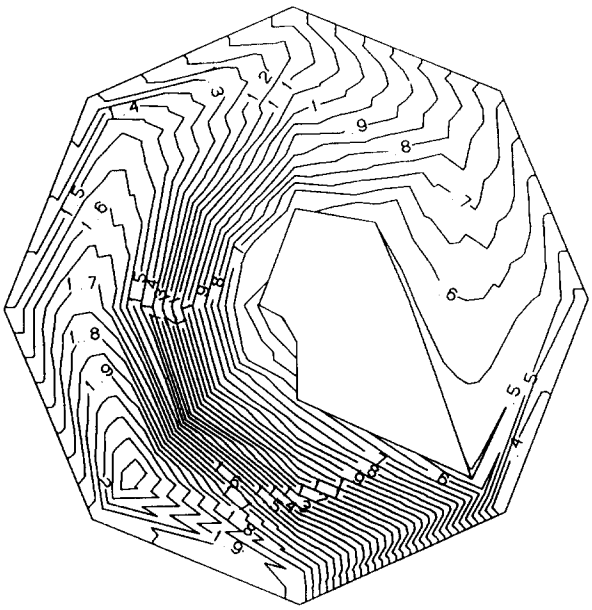

Fig. 18. Experimental u/U-contours – case 10.

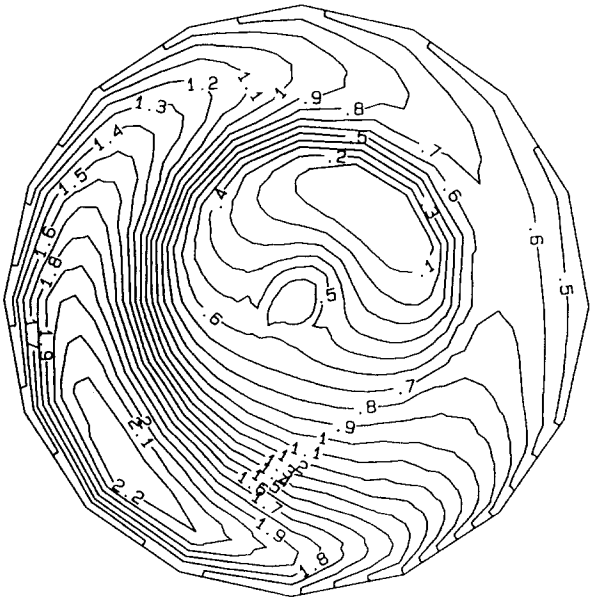

Fig. 19. Numerical u/U-contours – case 10.

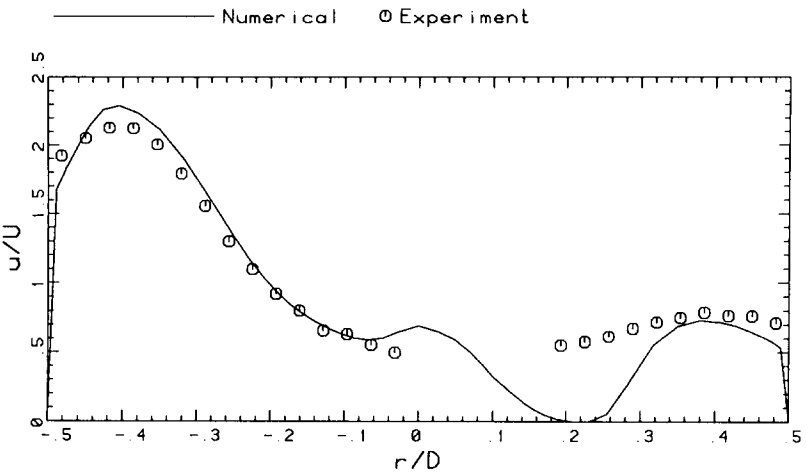

Fig. 20. Profiles of u at $\theta = 45/225°$ – case 10.

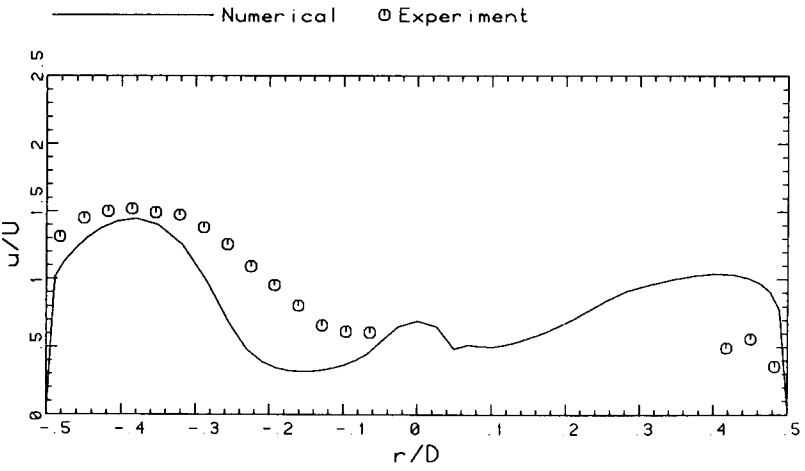

Fig. 21. Profiles of u at $\theta = 135/315°$ – case 10.

8. Concluding remarks

It can be concluded that the numerical predictions confirm the results of the experiment in the sense that more power is required to deliver the same volume flow rate under crossflow conditions as under axisymmetric inflow conditions. The numerical procedure underestimates the increase in power, however: an increase of only 14% is predicted versus a measured increase of 29%. The predicted increase in fan static pressure is also slightly low: 27% versus 36%. The general performance of the numerical procedure is good, considering the

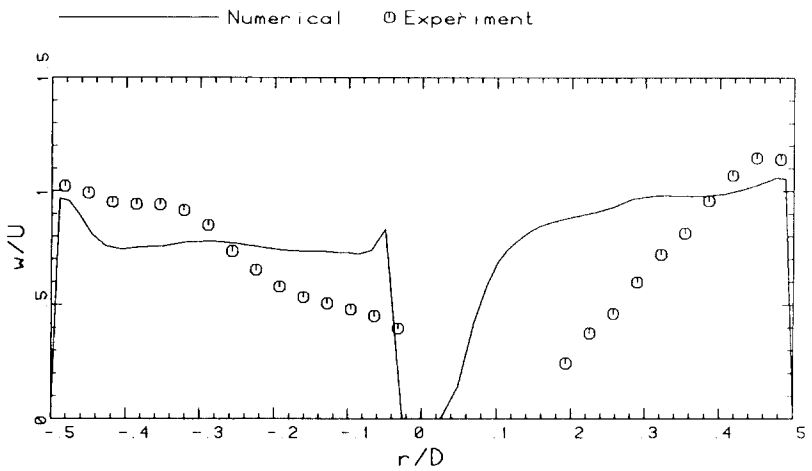

Fig. 22. Profiles of w at $\theta = 45/225^\circ$ case 10.

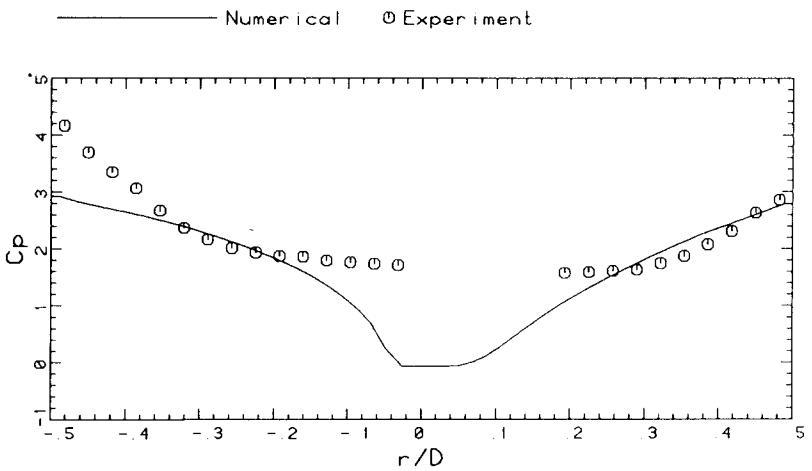

Fig. 23. Profiles of p at $\theta = 45/225^\circ$ – case 10.

complexity of the problem, but there is one major deficiency: that of excessive computing time requirements for especially the three-dimensional simulation. Investigations are currently under way to speed up the computer code by means of multigrid schemes, in order to make the methodology more useful as an engineering tool.

References

[1] G.D. Thiart, A Numerical Procedure for Predicting the Effects of Distorted Inflow Conditions on the Performance of Axial Flow Fans, PhD Thesis, University of Stellenbosch, 1990.

[2] W.R. Sears, Some aspects of non-stationary airfoil theory and its practical application, J. Aero. Sci., 8 (1941) 104–108.
[3] N.H. Kemp and W.R. Sears, Aerodynamic interference between moving blade rows, J. Aero. Sci., 20 (1953) 585–612.
[4] N.H. Kemp and W.R. Sears, The unsteady forces due to viscous wakes in turbomachines, J. Aero. Sci., 22 (1955) 478–483.
[5] J.H. Horlock, Fluctuating lift forces on aerofoils moving through transverse and chordwise gusts, ASME J. Basic Eng, 4 (1968) 494–500.
[6] H. Naumann and H. Yeh, Lift and pressure fluctuations of a cambered airfoil under periodic gusts and applications in turbomachinery, ASME J. Eng. Power, 95 (1973) 1–10.
[7] J.M.R. Graham, Lifting surface theory for the problem of an arbitrarily yawed sinusoidal gust incident on a thin airfoil in incompressible flow, Aero. Quart., 21 (1970) 182–198.
[8] R.E. Henderson and J.H. Horlock, An approximate analysis of the unsteady lift on airfoils in cascade, ASME J. Eng. Power, 94 (1972) 233–240.
[9] G.A. Plourde and A.H. Stenning, Attenuation of circumferential inlet distortion in multistage axial compressors, J. Aircr., 5 (1968) 236–242.
[10] M.D.C. Doyle and J.H. Horlock, Circumferential asymmetry in axial flow compressors, J. Roy. Aero. Soc., 70 (1966) 956–957.
[11] F. Ehrich, Circumferential inlet distortions in axial flow turbomachinery, J. Aero. Sci., 24 (1957) 413–417.
[12] H. Yeh, An actuator disk analysis of inlet distortion and rotating stall in axial flow turbomachines, J. Aero. Sci., 26 (1959) 739–753.
[13] W.R. Hawthorne, N.A. Mitchell, J.E. McCune and C.S. Tan, Nonaxisymmetric flow through annular actuator disks: Inlet distortion problem, ASME J. Eng. Power, 100 (1978) 604–617.
[14] J. Colpin, Propagation of inlet flow distortions through an axial compressor stage, ASME J. Eng. Power, 101 (1979) 116–124.
[15] H. Schwanecke and J. Laudan, Results of the unsteady propeller theory, Int. Ship. Prog., 20 (1973) 461–466.
[16] D.H. Pelletier and J.A. Schetz, Finite element Navier–Stokes calculation of three-dimensional turbulent flow near a propeller, AIAA J., 24 (1986) 1409–1416.
[17] J.A. Schetz, D. Pelletier and D.A. Mallory, Experimental and numerical investigation of a propeller with three-dimensional inflow, J. Propulsion and Power, 4 (1988) 341–349.
[18] R.H. Thomas and J.A. Schetz, Finite Element Solution of 3D Turbulent Navier–Stokes Equations for Propeller Driven Slender Bodies, AAIA Paper No. 88-3089, 1988.
[19] F. Stern, H.T. Kim, V.C. Patel and H.C. Chen, A viscous-flow approach to the computation of Propeller–Hull interaction, J. Ship Res., 32 (1988) 246–262.
[20] K.A. Pericleous and M.K. Patel, The modeling of tangential and axial agitators in chemical reactors, Phys. Chem. Hydrodyn., 8 (1986) 105–123.
[21] B.E. Launder, C.H. Pridden and B.I. Sharma, The calculation of turbulent boundary layers on spinning and curved surfaces, ASME J. Fluids Eng. 99 (1977) 231–239.
[22] A.K. Gupta and D.G. Lilley, Flowfield Modeling and Diagnostics, Abacus, Tunbridge Wells, Kent, 1985.
[23] G.D. Thiart, A finite difference scheme for the numerical solution of fluid flow and heat transfer problems on nonstaggered grids, Num. Heat Transfer, 17(B) (1990) 43–63.
[24] G.D. Thiart, An improved finite difference scheme for the solution of convection–diffusion problems with the SIMPLEN algorithm, Num. Heat Transfer, 18(B) (1990) 81–95.
[25] G.D. Thiart and T.W. von Backström, Extension of the SIMPLEN algorithm differencing scheme to cylindrical polar coordinates, Num. Heat Transfer (to be published).
[26] R. Von Mises, Theory of Flight, Dover, New York, 1959.
[27] S.F. Hoerner, Fluid-Dynamic Drag, Hoerner Fluid Dynamics, Brick Town, NJ, 1965.

[28] S.F. Hoerner and H.V. Borst, Fluid-Dynamic Lift, Hoerner Fluid Dynamics, Brick Town, NJ, 1975.
[29] A.D. Burns and N.S. Wilkes, A Finite Difference Method for the Computation of Fluid Flows in Complex Three-Dimensional Geometries, AERE Report No. 12342, Harwell Laboratory, 1987.
[30] R. Shapiro, Smoothing, filtering and boundary effects, Rev. Geophysics and Space Physics, 8 (1970) 359–387.

Numerical Heat Transfer, Part B, vol. 23, pp. 1–19, 1993

EXTENSION OF THE SIMPLEN ALGORITHM DIFFERENCING SCHEME TO CYLINDRICAL POLAR COORDINATES

G. D. Thiart and T. W. von Backström
Department of Mechanical Engineering, University of Stellenbosch, Stellenbosch, 7600, South Africa

The differencing scheme used with the SIMPLEN algorithm for the solution of convection-diffusion problems on nonstaggered grids, formulated by one of the authors in two previous papers for Cartesian coordinates, is extended to a cylindrical polar coordinate system. The scheme is shown to be equivalent to its Cartesian counterpart. The interpolation functions derived for the radial coordinate direction reduce to those for Cartesian coordinates when the cell interfaces are positioned at the geometric mean radial positions between grid points. Three case studies involving laminar, incompressible flow are presented to validate the scheme: stagnation of three-dimensional flow, flow over a rotating disk, and flow through an abrupt pipe expansion. Excellent agreement between the numerical solutions and the corresponding analytical solutions and experimental data is demonstrated.

INTRODUCTION

In recent years, methods based on the SIMPLE (*Semi-Implicit Method for Pressure-Linked Equations*) algorithm of Patankar and Spalding [1] have been used successfully to solve a wide range of flow problems. In the original SIMPLE algorithm, separate grids, staggered in space, are used for the calculation of scalar properties such as pressure and each of the velocity components. Thus four grids are used for a three-dimensional and three grids for a two-dimensional flow problem, which complicates the implementation of boundary conditions. If all variables are located at the same grid points, on the other hand, a checkerboard pressure field may result. This has been described by, among others, Patankar [2], Rhie and Chow [3], and Perić [4].

Several methods that have been proposed to overcome the checkerboard problem on nonstaggered grids are described by Patankar [5] in a recent review paper. Thiart [6] subsequently presented a new finite-difference method that also eliminates the need for staggered grids. The method was incorporated in an algorithm called SIMPLEN, the "N" attached to SIMPLE being an indication that a nonstaggered grid is used.

The finite-difference scheme on which SIMPLEN was originally based has been refined by Thiart [7] recently. It was shown that the new scheme is capable of producing numerical solutions of comparable or superior accuracy to that of other numerical methods. In this article, application of the new differencing scheme is extended to a cylindri-

1040-7790/93 $10.00 + .00

Numerical Heat Transfer, Part B, vol. 23, pp. 1–19, 1993

EXTENSION OF THE SIMPLEN ALGORITHM DIFFERENCING SCHEME TO CYLINDRICAL POLAR COORDINATES

G. D. Thiart and T. W. von Backström
Department of Mechanical Engineering, University of Stellenbosch, Stellenbosch, 7600, South Africa

The differencing scheme used with the SIMPLEN algorithm for the solution of convection-diffusion problems on nonstaggered grids, formulated by one of the authors in two previous papers for Cartesian coordinates, is extended to a cylindrical polar coordinate system. The scheme is shown to be equivalent to its Cartesian counterpart. The interpolation functions derived for the radial coordinate direction reduce to those for Cartesian coordinates when the cell interfaces are positioned at the geometric mean radial positions between grid points. Three case studies involving laminar, incompressible flow are presented to validate the scheme: stagnation of three-dimensional flow, flow over a rotating disk, and flow through an abrupt pipe expansion. Excellent agreement between the numerical solutions and the corresponding analytical solutions and experimental data is demonstrated.

INTRODUCTION

In recent years, methods based on the SIMPLE (*Semi-Implicit Method for Pressure-Linked Equations*) algorithm of Patankar and Spalding [1] have been used successfully to solve a wide range of flow problems. In the original SIMPLE algorithm, separate grids, staggered in space, are used for the calculation of scalar properties such as pressure and each of the velocity components. Thus four grids are used for a three-dimensional and three grids for a two-dimensional flow problem, which complicates the implementation of boundary conditions. If all variables are located at the same grid points, on the other hand, a checkerboard pressure field may result. This has been described by, among others, Patankar [2], Rhie and Chow [3], and Perić [4].

Several methods that have been proposed to overcome the checkerboard problem on nonstaggered grids are described by Patankar [5] in a recent review paper. Thiart [6] subsequently presented a new finite-difference method that also eliminates the need for staggered grids. The method was incorporated in an algorithm called SIMPLEN, the "N" attached to SIMPLE being an indication that a nonstaggered grid is used.

The finite-difference scheme on which SIMPLEN was originally based has been refined by Thiart [7] recently. It was shown that the new scheme is capable of producing numerical solutions of comparable or superior accuracy to that of other numerical methods. In this article, application of the new differencing scheme is extended to a cylindri-

1040-7790/93 $10.00 + .00

Numerical Heat Transfer, Part B, vol. 23, pp. 1–19, 1993

EXTENSION OF THE SIMPLEN ALGORITHM DIFFERENCING SCHEME TO CYLINDRICAL POLAR COORDINATES

G. D. Thiart and T. W. von Backström
Department of Mechanical Engineering, University of Stellenbosch, Stellenbosch, 7600, South Africa

The differencing scheme used with the SIMPLEN algorithm for the solution of convection-diffusion problems on nonstaggered grids, formulated by one of the authors in two previous papers for Cartesian coordinates, is extended to a cylindrical polar coordinate system. The scheme is shown to be equivalent to its Cartesian counterpart: The interpolation functions derived for the radial coordinate direction reduce to those for Cartesian coordinates when the cell interfaces are positioned at the geometric mean radial positions between grid points. Three case studies involving laminar, incompressible flow are presented to validate the scheme: stagnation in three-dimensional flow, flow near a rotating disk, and flow through an abrupt pipe expansion. Excellent agreement between the numerical solutions and the corresponding analytical solutions and experimental data is demonstrated.

INTRODUCTION

In recent years, methods based on the SIMPLE (*S*emi-*I*mplicit *M*ethod for *P*ressure-*L*inked *E*quations) algorithm of Patankar and Spalding [1] have been used successfully to solve a wide range of flow problems. In the original SIMPLE algorithm, separate grids, staggered in space, are used for the calculation of scalar properties such as pressure and each of the velocity components. Thus four grids are used for a three-dimensional and three grids for a two-dimensional flow problem, which complicates the implementation of boundary conditions. If all variables are located at the same grid points, on the other hand, a checkerboard pressure field may result. This has been described by, among others, Patankar [2], Rhie and Chow [3], and Perić [4].

Several methods that have been proposed to overcome the checkerboard problem on nonstaggered grids are described by Patankar [5] in a recent review paper. Thiart [6] subsequently presented a new finite-difference method that also eliminates the need for staggered grids. The method was incorporated in an algorithm called SIMPLEN, the "N" attached to SIMPLE being an indication that a nonstaggered grid is used.

The finite-difference scheme on which SIMPLEN was originally based has been refined by Thiart [7] recently. It was shown that the new scheme is capable of producing numerical solutions of comparable or superior accuracy to that of other numerical methods. In this article, application of the new differencing scheme is extended to a cylindri-

1040-7790/93 $10.00 + .00

NOMENCLATURE

a	radius ratio, Hiemenz flow constant
A	interpolation function
B	interpolation function
C	interpolation function
D	interpolation function, diameter
F	interpolation function, rotating disk flow function
G	rotating disk flow function
H	rotating disk flow function
J	convective plus diffusive flux
k	exponent
L	length
m	exponent
n	exponent
p	static pressure
P	Peclet number, rotating disk flow function
r	radius, radial coordinate
δr	radial distance between grid points
R	radial direction
Re	Reynolds number
S	source term
u	axial velocity component
U	mean axial velocity
v	radial velocity component
w	azimuthal velocity component
z	axial coordinate
δz	axial distance between grid points
Z	axial direction
α	discretization equation coefficient
β	discretization equation source term
δ	boundary-layer thickness
ϵ	error
ζ	independent variable for Hiemenz and rotating disk flow
μ	dynamic viscosity
ν	kinematic viscosity
ρ	density
τ	shear stress
ϕ	general dependent variable
φ,ϑ	Hiemenz flow functions
ω	angular velocity of fluid particles
Ω	angular velocity of rotating body

Superscripts

an	analytical
num	numerical
p	pressure
r	radial direction
S	source term
x	cross flux
u	axial velocity component
v	radial velocity component
z	axial direction
ϕ	general dependent variable
ω	angular velocity
*	approximate
′	correction, ordinary derivative

Subscripts

b,B	bottom interface, grid point
i	index
n,N	northern interface, grid point
nb	neighboring
P	central grid point
s,S	southern interface, grid point
t,T	top interface, grid point
w	wall

cal polar coordinate system. For the sake of simplicity, the scope of the article is restricted to steady, axisymmetric, laminar incompressible flow.

GOVERNING EQUATIONS

The governing equations are the well-known Navier-Stokes equations (see, for example, Schlichting [8]) for the conservation of mass, i.e.,

$$\frac{1}{r}\frac{\partial}{\partial r}(\rho r v) + \frac{\partial}{\partial z}(\rho u) = 0 \tag{1}$$

and for the conservation of axial momentum, radial momentum, and moment of momentum, which can be written in the general form

$$\frac{1}{r}\frac{\partial}{\partial r}(\rho r^{2m+1} v\phi) + \frac{\partial}{\partial z}(\rho r^{2m} u\phi) = S^{\phi} + \frac{1}{r}\frac{\partial}{\partial r}\left(r^{2m+1}\mu\frac{\partial\phi}{\partial r}\right) + \frac{\partial}{\partial z}\left(r^{2m}\mu\frac{\partial\phi}{\partial z}\right) \tag{2}$$

Here ϕ denotes a general variable representing either the axial velocity u, the radial velocity v, or the angular velocity ω. The parameter m is equal to 0 for $\phi \equiv u$, v and equal to 1 for $\phi \equiv \omega$. In the absence of body forces and for constant viscosity μ, the source terms are as follows:

$$S^{u} = -\frac{\partial p}{\partial z} \qquad S^{v} = \rho r\omega^2 - \frac{\partial p}{\partial r} - \frac{\mu v}{r^2} \qquad S^{\omega} = 0 \tag{3}$$

SOLUTION PROCEDURE

The governing equations are solved by converting them to discretized equations for the dependent variables u, v, ω, and p, of the generic form

$$\alpha_P^{\phi}\phi_P = \alpha_N^{\phi}\phi_N + \alpha_S^{\phi}\phi_S + \alpha_B^{\phi}\phi_B + \alpha_T^{\phi}\phi_T + \beta^{\phi} \tag{4}$$

The subscripts P, S, N, B, and T refer to a typical cluster of grid points as shown in Fig. 1. The computational domain is subdivided into a number of nonoverlapping control volumes, one control volume per grid point. The discretization equations are obtained by integrating the differential equations over these control volumes. The control volume faces are located midway between the grid points in the axial and azimuthal directions, and at the geometric mean radii in the radial direction, i.e.,

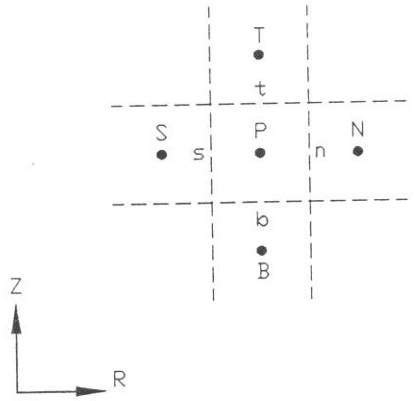

Fig. 1 Typical grid point cluster and control volume.

$$r_s = \sqrt{r_S r_P} \qquad r_n = \sqrt{r_P r_N}$$

Locating the control volume faces midway between grid points in the axial coordinate direction is fairly conventional, the other obvious choice being to locate grid points midway between the faces. Patankar [2] discussed the issue, pointing out that the first method provides greater accuracy in the calculation of gradients across control volume interfaces, while the second method provides greater accuracy in the calculation of mean values over control volumes and at the control volume faces. The decisive feature for choosing the first procedure here is that it allows the finite-difference coefficients to be written in a very compact form, as illustrated by Thiart [7].

The radial location of control volume faces at the geometric mean radii likewise allow the finite-difference coefficients for the radial direction to be written in compact form. A further advantage is that control volumes surrounding the symmetry axis (r = 0) have zero radius and hence zero volume. It is therefore not necessary to apply the conservation principles at the symmetry axis, which is convenient since the conservation equations contain several singularities of the type $1/r$. In this way, the singularities are removed numerically.

DISCRETIZATION OF THE MOMENTUM EQUATIONS

Basic Philosophy

Equation (2) can be expressed in terms of fluxes as

$$\frac{1}{r}\frac{\partial}{\partial r}(rJ^{r\phi}) + \frac{\partial}{\partial z}(J^{z\phi}) = S^{\phi} \tag{5}$$

where the Js are convection-diffusion fluxes, defined as

$$J^{r\phi} = r^{2m}\left(\rho v\phi - \mu\frac{\partial\phi}{\partial r}\right) \qquad J^{z\phi} = r^{2m}\left(\rho v\phi - \mu\frac{\partial\phi}{\partial z}\right) \tag{6}$$

Equation (5) is now integrated over the control volume shown in Fig. 1:

$$\int_{z_b}^{z_t}\int_{r_s}^{r_n}\left[\frac{1}{r}\frac{\partial}{\partial r}(rJ^{r\phi}) + \frac{\partial}{\partial z}(J^{z\phi})\right] r\,dr\,dz = \int_{z_b}^{z_t}\int_{r_s}^{r_n} S^{\phi}\,r\,dr\,dz \tag{7}$$

The integrals are evaluated with the aid of the assumption that, within the control volume, the fluxes $J^{r\phi}$ and $J^{z\phi}$ vary only in the radial and axial directions, respectively. It is also assumed that the source terms are constant between grid points in the axial and radial directions for $\phi \equiv u'$ and v, respectively, and that they do not vary in the other two coordinate directions. Subject to these assumptions, Eq. (7) can be written explicitly

as follows:

$$\Delta z(r_n J_n^{r\phi} - r_s J_s^{r\phi}) + \Delta r^2(J_t^{z\phi} - J_b^{z\phi}) = \beta^{S\phi} \tag{8}$$

where $\Delta z = z_t - z_b$, $\Delta r^2 = {}^1/_2(r_n^2 - r_s^2)$, and

$$\beta^{S\phi} = \begin{cases} \frac{1}{2} r_P \Delta z \, (\delta r_n S_n^\phi + \delta r_s S_s^\phi) & \text{for } \phi \equiv v \\ \frac{1}{2} \Delta r^2 (\delta z_t S_t^\phi + \delta z_b S_b^\phi) & \text{for } \phi \equiv u \end{cases} \tag{9}$$

The motivation for the assumption that source terms are constant between grid points, which is at variance with the more traditional assumption that source terms are constant within control volumes, has been presented by Thiart [6, 7].

It remains to find explicit expressions for the interface fluxes in Eq. (8). From the definitions of the fluxes, Eq. (6), it is clear that information is required about the way in which ϕ varies between grid points. In the differencing scheme devised for the SIMPLEN algorithm by Thiart [6, 7], this information is obtained through the solution of a one-dimensional, steady-state boundary-value problem for each of the main coordinate directions. The boundary-value problems are simplifications of the general momentum equation, so that the physics of the flow is incorporated in the determination of the fluxes. The analysis for the axial variation of ϕ between grid points P and T in Fig. 1 is identical to that for Cartesian coordinates described by Thiart [7] and will therefore not be repeated here. Only the analysis for the radial coordinate direction will be presented, and the main results will be compared with the Cartesian equivalents.

Flux Expression

The boundary-value problem for the radial variation of ϕ between grid points P and N in Fig. 1 is obtained by writing Eq. (2) in the steady state, quasi-one-dimensional form

$$\frac{1}{r}\frac{d}{dr}\left(\rho r^{2m+1} v\phi - \mu r^{2m+1}\frac{d\phi}{dr}\right) = S_n^\phi + \begin{cases} S_P^{xr\phi} & r_p \le r \le r_n \\ S_N^{xr\phi} & r_n \le r \le r_N \end{cases} \tag{10}$$

The S^xs in Eq. (10) are the so-called cross fluxes, given by

$$S_{P,N}^{xr\phi} = \frac{\delta}{\delta z}\left(r^{2m}\mu\frac{\delta\phi}{\delta z} - \rho r^{2m+1} u\phi\right)_{P,N} \tag{11}$$

where the operator $\delta/\delta z$ represents any convenient numerical approximation to $\partial/\partial z$. Central differences were used for the case studies reported elsewhere in this article.

The corresponding one-dimensional form of the continuity equation is

$$\frac{d}{dr}(\rho r v) = 0 \tag{12}$$

which integrates to $\rho r v = \text{constant} = \rho r_n v_n$. Assuming that μ is also constant between the grid points P and N and equal to μ_n, the exact solution of Eq. (10), subject to the boundary conditions $\phi = \phi_P$ at $r = r_P$, $\phi = \phi_N$ at $r = r_N$, and the constraints that ϕ and $d\phi/dr$ are continuous at the the interface n, is as follows:

$$\begin{aligned}\phi = {} & \frac{\phi_P a_n^{P_n/2+m} - \phi_n a_n^m}{a_n^{P_n/2+m} - 1}\left(\frac{r}{r_P}\right)^{-2m} + \frac{\phi_n a_n^m - \phi_P}{a_n^{P_n/2+m} - 1}\left(\frac{r}{r_P}\right)^{P_n} \\ & + \frac{S_n^\phi + S_P^{xr\phi}}{2\mu_n(P_n + 2m - 2)} r^{2-2m}\left[1 - \frac{a_n - 1}{a_n^{P_n/2+m} - 1}\left(\frac{r}{r_P}\right)^{P_n+2m-2}\right. \\ & \left. - \frac{a_n^{P_n/2+m} - a_n}{a_n^{P_n/2+m} - 1}\left(\frac{r}{r_P}\right)^{-2}\right]\end{aligned} \tag{13a}$$

for $r_P \le r \le r_n$, and

$$\begin{aligned}\phi = {} & \frac{\phi_N a_n^{P_n/2+m} - \phi_n a_n^{P_n/2}}{a_n^{P_n/2+m} - 1}\left(\frac{r}{r_N}\right)^{P_n} + \frac{\phi_n a_n^{P_n/2} - \phi_N}{a_n^{P_n/2+m} - 1}\left(\frac{r}{r_N}\right)^{-2m} \\ & + \frac{S_n^\phi + S_N^{xr\phi}}{2\mu_n(P_n + 2m - 2)} r^{2-2m}\left[1 - \frac{a_n^{P_n/2+m-1} - 1}{a_n^{P_n/2+m} - 1}\left(\frac{r}{r_N}\right)^{-2}\right. \\ & \left. - \frac{a_n^{P_n/2+m} - a_n^{P_n/2+m-1}}{a_n^{P_n/2+m} - 1}\left(\frac{r}{r_N}\right)^{P_n+2m-2}\right]\end{aligned} \tag{13b}$$

for $r_n \le r \le r_N$. Here P_n is the local grid Peclet number based on the local radius, and a_n is the radius ratio across the control volume interface, i.e.,

$$P_n = \frac{\rho r_n v_n}{\mu_n} \qquad a_n = \frac{r_N}{r_P}$$

The radial flux $J^{r\phi}$ at the interface n is obtained by back-substitution of the exact solution into the radial flux definition:

$$\begin{aligned}r_n J_n^{r\phi} = {} & r_P^{2m}\left\{(\rho r_n v_n + 2m\mu_n)\,\phi_P\right. \\ & \left. + \frac{\mu_n}{\ln a_n} A\,[(P_n + 2m)\ln a_n]\,(\phi_P - \phi_N a_n^{2m})\right\} \\ & + \frac{1}{2}\delta r_n\left\{r_P\,(S_n^\phi + S_P^{xr\phi})\,F(-P_n, -m, -1, \sqrt{a_n})\,C\left[-\frac{1}{2}(P_n + 2m)\ln a_n\right]\right.\end{aligned} \tag{14}$$

$$- r_N (S_n^{\phi} + S_N^{xr\phi}) F(P_n,m,1,\sqrt{a_n}) C \left[\frac{1}{2}(P_n + 2m) \ln a_n\right]\Bigg\} \quad (14)$$
(*Cont.*)

The functions $A(P)$ and $C(P)$ in Eq. (14) are identical to those introduced by Thiart [7] for the "Cartesian" fluxes. The new function $F(P,m,k,a)$ introduced in Eq. (14) is the radial direction counterpart of the function $B(P) = [1 - A(P)]/P$ also introduced by Thiart [7] for the "Cartesian" fluxes, its definition being as follows:

$$F(P,m,k,a) = \frac{2k \ln a/(a^{2k} - 1) - A[(P + 2m) \ln a]}{(P + 2m - 2k) \ln a} \quad (15)$$

Note that for large radii, $a \approx 1$, $\ln a \approx 0$, $2k \ln a/(a^{2k} - 1) \approx 1$, and $P \ln a = \rho v r \ln a/\mu \approx \rho v \delta r/\mu$. Thus the function $F(P,m,k,a)$ is identical to $B(P \ln a)$ for large radii. The function $F(P,0,1,a)$ is shown in Fig. 2 as a function of $P \ln a$ for the limiting values $a = 1$ and $a = 2$, and also for the intermediate value $a = 1.5$. {For the application under discussion, k is always equal to 1; m is equal to 0 ($\phi \equiv u,v$), but $F(P,1,1,a) = F(P - 2,0,1,a)$, therefore the figure contains all the essential information about the function.} It is evident that the radius ratio a has a significant effect on the accuracy of the discretization near the axis of the coordinate system, where a may be close to 2.

Discretization Equations

The discretization equation for ϕ is now obtained by back-substitution of the flux expressions into Eq. (10). The influence coefficients of Eq. (4) are then as follows:

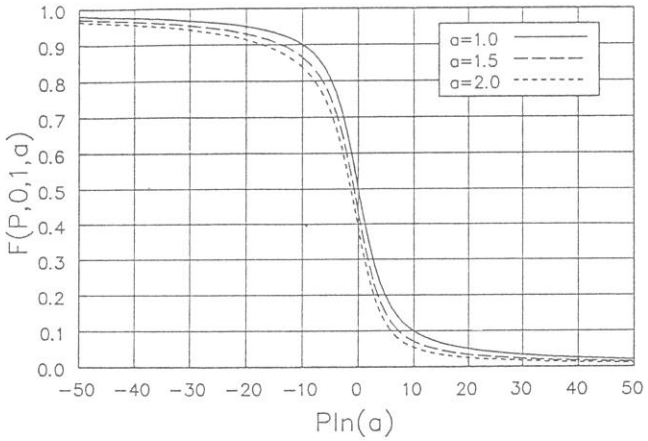

Fig. 2 The function $F(P,0,1,a)$.

$$\alpha_N^\phi = \Delta z r_N^{2m} \left\{ \frac{\mu_n}{\ln a_n} A[(P_n + 2m) \ln a_n] \right\} \tag{16a}$$

$$\alpha_S^\phi = \Delta z r_S^{2m} \left\{ \frac{\mu_s}{\ln a_s} A[-(P_s + 2m) \ln a_s] \right\} \tag{16b}$$

$$\alpha_T^\phi = \Delta r^2 r_P^{2m} \left[\frac{\mu_t}{\delta z_t} A(P_t) \right] \tag{16c}$$

$$\alpha_B^\phi = \Delta r^2 r_P^{2m} \left[\frac{\mu_b}{\delta z_b} A(-P_b) \right] \tag{16d}$$

$$\alpha_p^\phi = \alpha_N^\phi a_n^{-2m} + \alpha_S^\phi a_s^{2m} + \alpha_T^\phi + \alpha_B^\phi + 2m(\mu_n - \mu_s) r_P^{2m} \Delta z \tag{16e}$$

Note the equivalence between the "Cartesian" coefficients α_T and α_B and the "radial" coefficients α_N and α_S.

The source term of Eq. (4) is as follows:

$$\beta^\phi = \beta^{s\phi} + \beta^{r\phi} + \beta^{z\phi} \tag{17a}$$

with $\beta^{s\phi}$ as defined by Eq. (9), and the cross-flux source terms given by

$$\begin{aligned}\beta^{r\phi} = \frac{1}{2}\Delta z \Bigg(\delta r_s \Bigg\{ & r_S(S_s^\phi + S_S^{xr\phi})\, F(-P_s, -m, -1, \sqrt{a_s})\, C\left[\frac{1}{2}(P_s + 2m)\ln a_s\right] \\ & - r_P(S_s^\phi + S_P^{xr\phi}) F(P_s, m, 1, \sqrt{a_s})\, C\left[\frac{1}{2}(P_s + 2m)\ln a_s\right] \Bigg\} \\ & - \delta r_n \Bigg\{ r_P(S_n^\phi + S_P^{xr\phi}) F(-P_n, -m, -1, \sqrt{a_s})\, C\left[\frac{1}{2}(P_n + 2m)\ln a_n\right] \\ & - r_N(S_N^\phi + S_N^{xr\phi})\, F(P_n, m, 1, \sqrt{a_n})\, C\left[\frac{1}{2}(P_n + 2m)\ln a_n\right] \Bigg\} \Bigg)\end{aligned} \tag{17b}$$

$$\begin{aligned}\beta^{z\phi} = \frac{1}{2}\Delta r^2 \Bigg\{ & \delta z_b \Bigg[(S_b^\phi + S_B^{xz\phi}) B\left(-\frac{1}{2}P_b\right) C\left(-\frac{1}{2}P_b\right) \\ & - (S_b^\phi + S_P^{xz\phi})\, B\left(\frac{1}{2}P_b\right) C\left(\frac{1}{2}P_b\right) \Bigg] \\ & - \delta z_t \Bigg[(S_t^\phi + S_P^{xz\phi})\, B\left(-\frac{1}{2}P_t\right) C\left(-\frac{1}{2}P_t\right) \\ & - (S_t^\phi + S_T^{xz\phi})\, B\left(\frac{1}{2}P_t\right) C\left(\frac{1}{2}P_t\right) \Bigg] \Bigg\}\end{aligned} \tag{17c}$$

Note again the equivalence between the "radial" cross-flux source term $\beta^{r\phi}$ and the "Cartesian" cross-flux source term $\beta^{z\phi}$.

It was found during the verification of the numerical procedure that it was not always possible to obtain convergent solutions with the formulation described here, unless some of the "extra" source terms ($\beta^{r\phi}$ and $\beta^{z\phi}$) were "switched off." Interaction between the cross fluxes contained in these terms can apparently cause divergence, especially for complex turbulent flow problems. It was found, however, that results of sufficient accuracy could be obtained for all the test cases by retaining only those cross fluxes that arise when determining the control-volume interface flux in a direction parallel to the velocity component for which the discretization equation is being set up (i.e., β^{zu} for $\phi \equiv u$ and β^{rv} for $\phi \equiv v$). This seemingly arbitrary choice can be motivated by noting that a discretization equation, just as the differential equation from which it is derived, represents a balance between effects due to convection, diffusion (shear stresses in the momentum equations) and source terms. As pointed out by Thiart [7], the formulation presented here has the following characteristics:

1. Convective effects are "upwinded"; that is, the momentum changes represented by the discretized equations are momentum changes over control volumes shifted in a direction upstream from the "real" control volumes.
2. Effects due to the conventional source terms are upwinded, thus bringing them into balance with the upwinded convective effects.
3. Effects due to the cross-fluxes are upwinded, thus bringing them into balance with the upwinded convective and source term effects. In particular, shear stresses are upwinded.

The present formulation is therefore more consistent than conventional schemes in which only convective terms are upwinded. Now, since the pressure gradient is usually the most important part of the source term in the momentum equations, it is particularly important that the upwinding procedure be consistent in the direction in which the pressure gradient acts. This part of the upwinding procedure is contained in the source terms β^{rv} and β^{zu}, which are therefore retained in the formulation.

DISCRETIZATION OF THE CONTINUITY EQUATION

Static pressure is not governed by a transport equation, but is prescribed indirectly through the continuity equation. Integration of the continuity equation, Eq. (1), over the control volume of Fig. 1 yields

$$\Delta z(\rho r_n v_n - \rho r_s v_s) + \Delta r^2(\rho u_t - \rho u_b) = 0 \tag{18}$$

Following the procedure outlined by Thiart [6, 7], Eq. (18) is transformed to a discretization equation for pressure corrections, i.e.,

$$\alpha_P^{p'} p_P' = \alpha_P^{p'} p_N' + \alpha_S^{p'} p_S' + \alpha_B^{p'} p_B' + \alpha_T^{p'} p_T' + \beta^{p'} \tag{19}$$

The influence coefficients are

$$\alpha_N^{p\prime} = \Delta z r_n \frac{\delta r_n \ln a_n}{4\mu_n(a_n - 1)} \times D\left(\frac{1}{2} P_n \ln a_n\right) [1 + (a_n - 1) F(P_n,0,1,\sqrt{a_n})] \tag{20a}$$

$$\alpha_S^{p\prime} = \Delta z r_s \frac{\delta r_s \ln a_s}{4\mu_s(a_s - 1)} \times D\left(\frac{1}{2} P_s \ln a_s\right) [1 + (a_s - 1) F(P_s,0,1,\sqrt{a_s})] \tag{20b}$$

$$\alpha_T^{p\prime} = \Delta r^2 \frac{\delta z_t}{4\mu_t} D\left(\frac{1}{2} P_t\right) \tag{20c}$$

$$\alpha_B^{p\prime} = \Delta r^2 \frac{\delta z_b}{4\mu_b} D\left(\frac{1}{2} P_b\right) \tag{20d}$$

$$\alpha_P^{p\prime} = \alpha_N^{p\prime} + \alpha_S^{p\prime} + \alpha_T^{p\prime} + \alpha_B^{p\prime} \tag{20e}$$

where the function $D(P)$ is again identical to the one introduced by Thiart [7]. The correspondence between the "Cartesian" and "radial" coefficients is not immediately obvious here, but note again that, for large radii, $a \approx 1$, $\ln a/(a - 1) \approx 1$, etc., in which case the formulations become equivalent again.

The source term of Eq. (19) is

$$\beta^{p\prime} = \Delta z(r_s v_s^* - r_n v_n^*) + \Delta r^2(u_b^* - u_t^*) \tag{21}$$

where the interface velocities v_s^*, v_n^*, u_b^*, and u_t^* are obtained from the boundary-value problem solutions, e.g., Eqs. (13*a* and 13*b*) for the radial direction. The expressions for the interface velocities at the interfaces n and t are as follows (similar expressions are valid for interfaces s and b):

$$v_n^* = C\left(-\frac{1}{2} P_n \ln a_n\right) v_P + C\left(\frac{1}{2} P_n \ln a_n\right) v_N + \frac{(\delta r_n)^2 \ln a_n}{4\mu_n(a_n - 1)} D\left(\frac{1}{2} P_n \ln a_n\right) \times [F(-P_n,0,-1,\sqrt{a_n})(S_P^{xrv} + S_n^v) + a_n F(P_n,0,1,\sqrt{a_n})(S_P^{xrv} + S_n^v)] \tag{22}$$

$$u_t^* = C\left(-\frac{1}{2} P_t\right) u_P + C\left(\frac{1}{2} P_t\right) u_T + \frac{(\delta z_t)^2}{4\mu_t} D\left(\frac{1}{2} P_t\right) \times \left[B\left(-\frac{1}{2} P_t\right)(S_P^{xzu} + S_t^u) + B\left(\frac{1}{2} P_t\right)(S_T^{xzu} + S_t^u)\right] \tag{23}$$

Note once again the equivalence between the expressions, especially for $a \approx 1$.

The only remaining details of the calculation procedure are those regarding the

relationship between the nodal velocity corrections and the pressure corrections. Again following Thiart [6], the following velocity correction equations are obtained:

$$\alpha_P^v v_P' = \Sigma\, \alpha_{nb}^v v_{nb}' + \frac{1}{2} r_P \Delta z \left[\left(1 + \frac{1}{a_s}\right) F(-P_s,0,-1,a_s)\,(p_S' - p_P') + (a_n + 1)\, F(P_n,0,-1,a_n)\,(p_p' - p_N')\right] \tag{24}$$

$$\alpha_P^u u_P' = \Sigma \alpha_{nb}^u u_{nb}' + \Delta r^2\, [B(-P_b)(p_B' - p_P') + B(P_t)(p_P' - p_T')] \tag{25}$$

In the case studies that follow, the approach proposed by Van Doormal and Raithby [9] for utilizing expressions such as Eqs. (24) and (25) has been used to update the nodal velocities.

CASE STUDIES

The numerical procedure was incorporated in a computer code based on the SIMPLEN algorithm of Thiart [6], and written in single-precision FORTRAN 77. In the code, all interface velocities required for the calculation of Peclet numbers are obtained by geometric interpolation.

Stagnation in Three-Dimensional Flow

The first case study is that of stagnation in three-dimensional flow, Fig. 3, for which an analytical solution exists and can be used to estimate the errors introduced by the numerical procedure. In the analytical solution procedure outlined by Schlichting

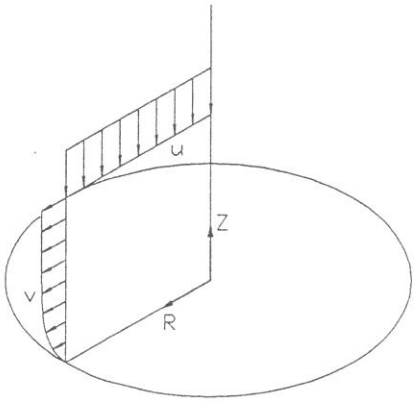

Fig. 3 Stagnation in three-dimensional flow.

[8], the governing equations are written in terms of the dimensionless variable $\zeta = \sqrt{a/\nu}z$ (a is an arbitrary constant) as two ordinary differential equations:

$$\varphi'''(\zeta) + 2\varphi(\zeta)\varphi''(\zeta) - \varphi'(\zeta)^2 + 1 = 0 \tag{26a}$$

$$v'(\zeta) = 4\varphi''(\zeta) + 8\varphi(\zeta)\varphi'(\zeta) \tag{26b}$$

The velocity components and the static pressure (relative to the static pressure at the origin of the coordinate system, $z = r = 0$) are related to the dimensionless functions $\varphi(z)$ and $v(\zeta)$ in the following way:

$$u = -2\sqrt{a\nu}\varphi(\zeta) \qquad v = ar\varphi'(\zeta) \qquad p = -\frac{1}{2}\rho a^2\left[r^2 + \left(\frac{\nu}{a}\right)v(\zeta)\right] \tag{27}$$

The analytical solution was obtained by numerical integration of Eqs. (26a and 26b) in double-precision FORTRAN 77, using a very find grid spacing (100,000 intervals between $\zeta = 0$ *and* $\zeta \simeq 10$). The "exact" thickness δ of the boundary layer (defined as the ζ-position where $\varphi' = 0.99$) that forms on the plate was found to be equal to 1.94440 $\zeta = \sqrt{\nu/a}$ (to six significant figures). Numerical values of the solution are given in Table 1, for $0 \le z/\delta \le 2$.

The problem was subsequently solved with the SIMPLEN code on a computational domain of $2\delta \times 2\delta$. Four uniform $(2^n + 1) \times (2^n + 1)$ meshes, with n taking the values 1, 2, 3, and 4, corresponding to grid spacings of δ, $\delta/2$, $\delta/4$, and $\delta/8$, respectively, were used. The boundary conditions used for the numerical solution were as follows:

$$z = 0\text{: } u = 0,\ v = 0 \qquad z = 2\delta\text{: } u = -2\sqrt{a\nu}\varphi\left(2\sqrt{\frac{a}{\nu}}\delta\right),\ \frac{\partial v}{\partial z} = 0$$

$$r = 0\text{: } \frac{\partial u}{\partial r} = 0;\ v = 0 \qquad r = 2\delta\text{: } \frac{\partial u}{\partial r} = 0;\ v = ar\varphi'\left(\sqrt{\frac{a}{\nu}}z\right)$$

The constant a was set equal to 1, and all pressures were calculated relative to that at the origin of the coordinate system. In order to obtain an estimate of the accuracy of the numerical solution, the normalized root-mean-square error of each of the dependent variables, defined as

$$\epsilon^{\phi} = \frac{\sqrt{\Sigma_i\,(\phi_i^{\text{an}} - \phi_i^{\text{num}})^2}}{\sqrt{\Sigma_i(\phi_i^{\text{an}})^2}} \tag{28}$$

was calculated. The summations in Eq. (28) are taken only over those grid points for which the value of the relevant variable has not been prescribed by a Dirichlet boundary condition. Excellent agreement between the analytical and numerical solutions was obtained, as illustrated in Fig. 4. The dashed lines in this figure, which have slopes of exactly 2, illustrate that the numerical method is essentially second-order-accurate for

Table 1 Analytical Solution for Stagnation in Three-Dimensional Flow

z/δ	$\varphi(\zeta)$	$\varphi'(\zeta)$	$\varphi''(\zeta)$	$\vartheta(\zeta)$
0.000	0.000000	0.000000	1.311938	0.000000
0.125	0.036358	0.289347	1.069255	1.162676
0.250	0.135902	0.520138	0.831418	2.154428
0.375	0.284636	0.694752	0.609149	3.103081
0.500	0.469498	0.818587	0.415698	4.156059
0.625	0.679111	0.900030	0.261591	5.444886
0.750	0.904391	0.949257	0.150559	7.068723
0.875	1.138760	0.976409	0.078758	9.092733
1.000	1.377931	0.990000	0.037268	11.55477
1.125	1.619402	0.996150	0.015898	14.47444
1.250	1.861868	0.998658	0.006099	17.86084
1.375	2.104722	0.999577	0.002099	21.71773
1.500	2.347713	0.999880	0.000648	26.04654
1.625	2.590746	0.999969	0.000179	30.84774
1.750	2.833791	0.999993	0.000044	36.12147
1.875	3.076840	0.999999	0.000010	41.86777
2.000	3.319889	1.000000	0.000002	48.08666

this particular problem—not only for the velocity components, but also for the static pressure.

Laminar Flow near a Rotating Disk

The second case study, laminar flow near a disk rotating at angular velocity Ω (see Fig. 5), is an example of a swirling flow for which an analytical solution exists. In the

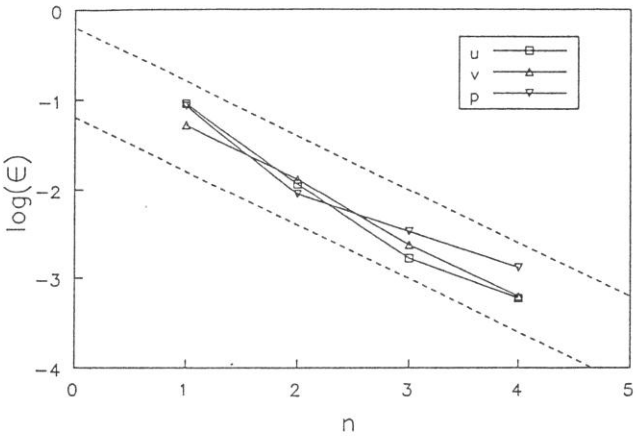

Fig. 4 Root-mean-square errors for stagnation in three-dimensional flow.

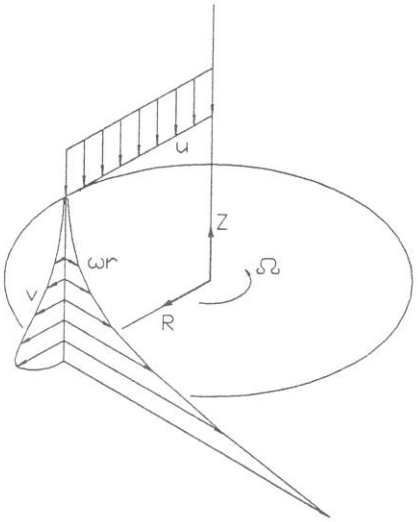

Fig. 5 Laminar flow near a rotating disk.

analytical solution procedure outlined by Schlichting [8], the governing equations are written in terms of the dimensionless variable $\zeta = \sqrt{\Omega/\nu}z$ as four ordinary differential equations:

$$2F(\zeta) + H'(\zeta) = 0 \tag{29a}$$

$$F^2(\zeta) + F'(\zeta)H(\zeta) - G^2(\zeta) - F''(\zeta) = 0 \tag{29b}$$

$$2F'(\zeta)\,G(\zeta) + G'(\zeta)H(\zeta) - G''(\zeta) = 0 \tag{29c}$$

$$P'(\zeta) + H(\zeta)H'(\zeta) - H''(\zeta) = 0 \tag{29d}$$

where

$$v = r\Omega F(\zeta) \qquad \omega = \Omega G(\zeta) \qquad u = \sqrt{\nu\Omega}H(\zeta) \qquad p = \rho\nu\Omega P(\zeta) \tag{30}$$

The analytical solution was obtained by numerical integration of Eqs. (29*a*–29*d*) in quadruple-precision FORTRAN 77, again using a very fine grid spacing (128,000 intervals between $\zeta = 0$ and $\zeta \simeq 23$). The "exact" thickness δ of the boundary layer (defined as the ζ position where the resultant velocity parallel to the disk surface is equal to 1% of the velocity at the disk surface) that forms on the disk was found to be equal to

5.67328 $\sqrt{\nu/\Omega}$ (to six significant figures). Numerical values of the solution are given in Table 2, for $0 \leq z/\delta \leq 1$.

The problem was subsequently solved with the SIMPLEN code on a computational domain of $\delta \times \delta$. Four uniform $(2^n + 1) \times (2^n + 1)$ meshes, with n taking the values 2, 3, 4, and 5, corresponding to grid spacings of $\delta/4$, $\delta/8$, $\delta/16$, and $\delta/32$, respectively, were used. The boundary conditions for the numerical solution were as follows:

$$z = 0: u = 0, v = 0, \omega = \Omega$$

$$r = 0: \frac{\partial u}{\partial r} = 0, v = 0, \frac{\partial \omega}{\partial r} = 0$$

$$z = \delta: u = -\sqrt{\nu\Omega}H\left(\sqrt{\frac{\Omega}{\nu}}\,\delta\right), \frac{\partial v}{\partial z} = 0, \omega = \Omega G\left(\sqrt{\frac{\Omega}{\nu}}\,\delta\right)$$

Table 2 Analytical Solution for Laminar Flow near a Rotating Disk

z/δ	$F(\zeta)$	$G(\zeta)$	$-H(\zeta)$	$-P(\zeta)$
0.00000	0.000000	1.000000	0.000000	0.000000
0.03125	0.075855	0.891650	0.014279	0.151812
0.06250	0.126671	0.787667	0.050837	0.254635
0.09375	0.158055	0.690756	0.101816	0.321293
0.12500	0.174735	0.602312	0.161189	0.362461
0.15625	0.180603	0.522837	0.224456	0.386396
0.18750	0.178786	0.452252	0.288360	0.399147
0.21875	0.171742	0.390121	0.350629	0.404954
0.25000	0.161361	0.335807	0.409760	0.406673
0.28125	0.149060	0.288576	0.464834	0.406156
0.31250	0.135878	0.247673	0.515364	0.404556
0.34375	0.122549	0.212360	0.561177	0.402557
0.37500	0.109575	0.181947	0.602314	0.400540
0.40625	0.097280	0.155802	0.638964	0.398697
0.43750	0.085858	0.133357	0.671404	0.397108
0.46875	0.075406	0.114108	0.699966	0.395789
0.50000	0.065955	0.097615	0.724998	0.394722
0.53125	0.057490	0.083491	0.746855	0.393876
0.56250	0.049965	0.071401	0.765879	0.393216
0.59375	0.043319	0.061055	0.782392	0.392706
0.62500	0.037478	0.052205	0.796694	0.392316
0.65625	0.032367	0.044635	0.809056	0.392020
0.68750	0.027911	0.038161	0.819725	0.391797
0.71875	0.024038	0.032626	0.828919	0.391630
0.75000	0.020680	0.027892	0.836833	0.391505
0.78125	0.017774	0.023845	0.843638	0.391411
0.81250	0.015265	0.020385	0.849484	0.391342
0.84375	0.013101	0.017427	0.854504	0.391291
0.87500	0.011237	0.014898	0.858811	0.391253
0.90625	0.009634	0.012736	0.862504	0.391225
0.93750	0.008256	0.010888	0.865670	0.391204
0.96875	0.007073	0.009308	0.868382	0.391189
1.00000	0.006057	0.007957	0.870705	0.391178

$$r = \delta: \frac{\partial u}{\partial r} = 0,\ v = r\Omega F\left(\sqrt{\frac{\Omega}{\nu}}\, z\right),\ \omega = \Omega G\left(\sqrt{\frac{\Omega}{\nu}}\, z\right)$$

Here also, the normalized root-mean-square errors calculated for each of the dependent variables show that good agreement is obtained between the numerical and analytical solutions. Second-order accuracy is obtained for u, v, and p as shown in Fig. 6*a*, but not for ω, Fig. 6*b*. The solution for the (indirectly calculated) azimuthal velocity component $w = \omega r$ does, however, exhibit second-order accuracy.

Flow Through an Abrupt Pipe Expansion

The final case study is that of flow through an abrupt pipe expansion of diameter ratio 2 : 1. The flow through a pipe expansion can be considered as the axisymmetric equivalent of the well-known two-dimensional flow over a backward-facing step. As in the case of the backward-facing step, a zone of recirculation forms downstream of the expansion. The experiments and computations of Macagno and Hung [10] indicate that the length of the recirculation zone is equal to 0.044 Re D for a diameter ratio of 2 : 1 and Reynolds numbers (based on the upstream pipe diameter) of about 40 to 200.

The problem was solved with the SIMPLEN code for Reynolds numbers of 60, 100, and 200. The computational domain is shown in Fig. 7: It has an inlet section upstream of the expansion of length 0.75D and a downstream section of length L, which was taken as 0.1 Re D for all three Reynolds numbers. The grid spacing in the radial direction was D/16. In the axial direction the grid spacing in the inlet section was also D/16; from the expansion downstream the grid spacing was increased continuously such that the ratio between successive δzs equal to 1.08. Fully developed pipe flow was assumed to exist at the entrance to the computational domain.

The static pressure contours and directional velocity vectors for the Re = 60 case are shown in Fig. 8 for approximately 5Ds downstream of the expansion. The vectors are not scaled according to magnitude, because the velocities in the recirculation zone are very small compared to those in the main flow.

In order to find the length of the recirculation zone, the wall shear stress distributions downstream of the expansion were calculated for all three Reynolds numbers. These are shown in dimensionless form in Fig. 9 (U is the average axial velocity upstream of the expansion). The position of zero shear stress indicates the reattachment point of the flow and hence the length of the recirculation zone. It is evident that the position of the reattachment point is predicted accurately by the computational method for all three Reynolds numbers.

CONCLUDING REMARKS

The extension to cylindrical polar coordinates of the differencing scheme used with the SIMPLEN algorithm has been presented in this article. The coefficients in the discretization equations have been shown to be equivalent to their Cartesian coordinate counterparts. The excellent accuracy of the scheme has been demonstrated by the three laminar flow case studies. Thiart [11] has also applied the method with good effect to a number of turbulent flow problems, using the k-ϵ turbulence model.

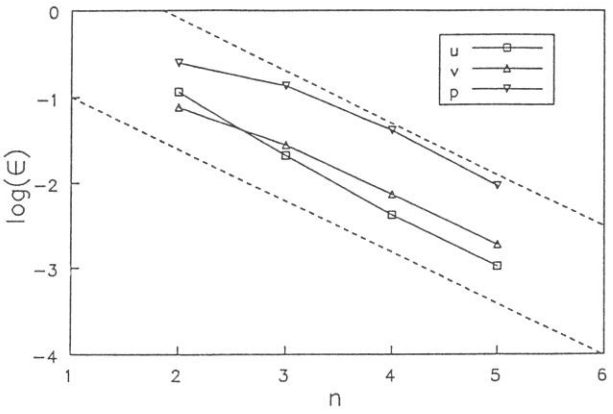

(*a*)

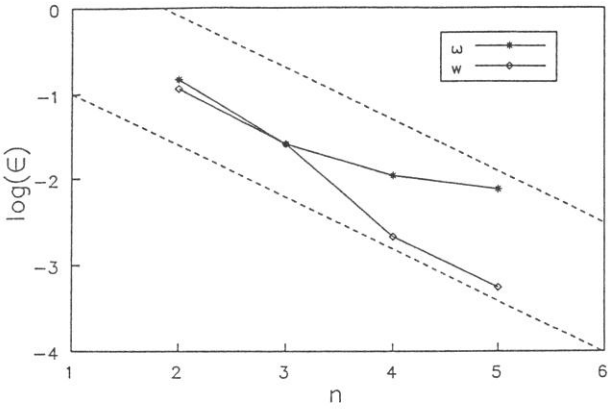

(*b*)

Fig. 6 Root-mean-square errors for flow near a rotating disk.

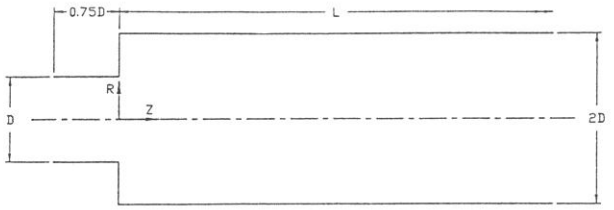

Fig. 7 Computational domain for flow through an abrupt pipe expansion.

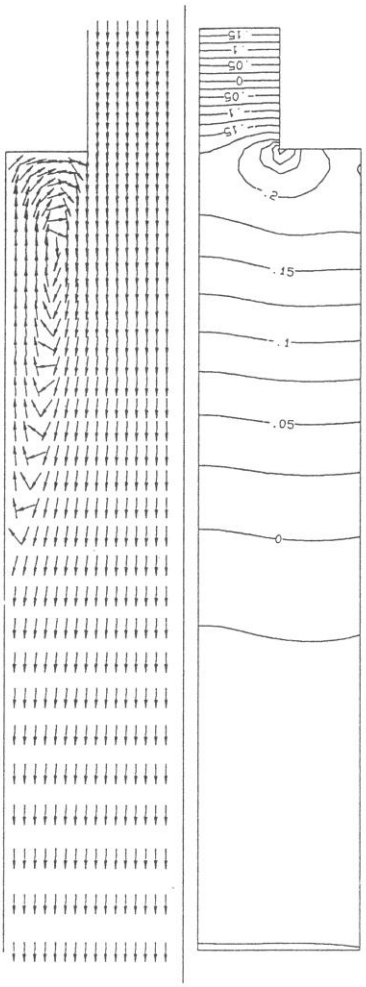

Fig. 8 Pressure contours and velocity vectors for Re = 60.

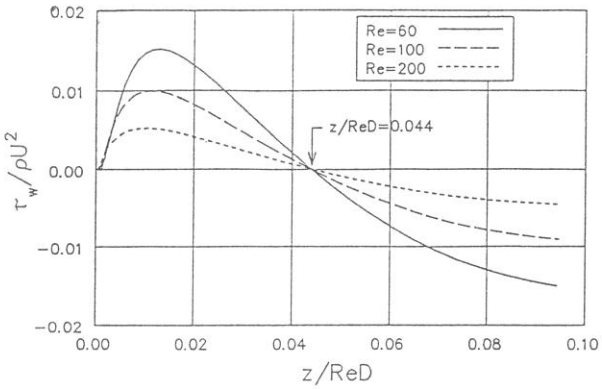

Fig. 9 Wall shear stress downstream of the expansion.

REFERENCES

1. S. V. Patankar and D. B. Spalding, A Calculation Procedure for Heat, Mass and Momentum Transfer in Three-Dimensional Parabolic Flows, *Int. J. Heat Mass Transfer,* vol. 15, pp. 1787–1806, 1972.
2. S. V. Patankar, *Numerical Heat Transfer and FLuid Flow,* Hemisphere, Washington D.C., 1980.
3. C. M. Rhie and W. L. Chow, A Numerical Study of the Turbulent Flow Past an Isolated Airfoil with Trailing Edge Separation, *AIAA J.*, vol. 21, pp. 1525–1532, 1983.
4. M. Perić, A Finite Volume Method for the Prediction of Three-Dimensional Fluid Flow in Complex Ducts, Ph.D. thesis, University of London, 1985.
5. S. V. Patankar, Recent Developments in Computational Heat Transfer, *ASME J. Heat Transfer,* vol. 110, pp. 1037–1045, 1988.
6. G. D. Thiart, A. Finite Difference Scheme for the Numerical Solution of Fluid Flow and Heat Transfer Problems on Nonstaggered Grids, *Numer. Heat Transfer,* vol. 17(B), pp. 43–63, 1990.
7. G. D. Thiart, An Improved Finite Difference Scheme for the Solution of Convection-Diffusion Problems with the SIMPLEN Algorithm, *Numer. Heat Transfer,* vol. 18(B), pp. 81–95, 1990.
8. H. Schlichting, *Boundary Layer Theory,* 6th ed., McGraw-Hill, New York, 1968.
9. J. P. Van Doormal and G. D. Raithby, Enhancements of the SIMPLE Method for Predicting Incompressible Fluid Flows, *Numer. Heat Transfer,* vol. 7, pp. 147–163, 1984.
10. E. O. Macagno and T. K. Huang, Computational and Experimental Study of a Captive Annular Eddy, *J. Fluid Mech.*, vol. 28, pp. 43–64, 1967.
11. G. D. Thiart, A. Numerical Procedure for Predicting the Effects of Distorted Inflow Conditions on the Performance of Axial Flow Fans, Ph.D. thesis, University of Stellenbosch, 1990.

Received 8 May 1991
Accepted 4 March 1992

Requests for reprints should be sent to G. D. Thiart.

THE EFFECT OF TREE STRUCTURES ON AIR VELOCITY PROFILES FROM MISTBLOWERS.

M.C.D. Ras
Directorate of Agricultural Mechanization
P/Bag X5067
Stellenbosch
7600

T.W. von Backström
Dept of Mechanical Engineering
University of Stellenbosch
7600

SUMMARY

A theoretical approach was followed to address the question on the air velocity profile required from mistblowers to penetrate to the critical parts of tree structures. The potential effect of travelling speed on the available air velocity profile was found to be negligible both in theory and with practical measurements. The classification of mistblowers into the different application categories based on tree structure sizes can now be made.

A correlation was shown to exist between the quality of spray deposit and required air velocity profiles for the conventional tree structures.

The question of the effect of residential time of the spray cloud on the deposition quality is raised and discussed to the extent of identifying new research fields.

OPSOMMING

'n Teoretiese benadering is gevolg in 'n poging om die vraag rondom die vereiste lugsnelheidsprofiele van newelblasertoerusting aan te spreek. Die lugsnelheidsprofiel moet oor die vermoë beskik om tot in die kritieke gebied van die boomstruktuur te penetreer. Die potensiële effek van grondspoed op die beskikbare lugsnelheidsprofiel is ondersoek vanuit die teorie en praktiese metings is ook gedoen. Geen noemenswaardige effek kon voorspel of gemeet word nie.

Die klassifikasie van newelblasers in verskillende toedieningskategorieë is nou moontlik, en behoort die raaiwerk uit die seleksie van toerusting te haal.

'n Korrelasie tussen die spuitneerslag en die aanvaarbaarheid van 'n lugsnelheidsprofiel is in die konvensionele boordtipe ondersoek, en die waarde van 'n aanvaarbare lugsnelheidsprofiel is bewys.

'n Vraag rondom die residensiële tyd van die spuitwolk se effek op neerslag van die spuitstof is onder andere 'n funksie van lugvolume en grondspoed, en hierdie hele aspek moet ondersoek word in verdere navorsing.

PERGAMON

Applied Thermal Engineering 22 (2002) 1403–1415

APPLIED THERMAL ENGINEERING

www.elsevier.com/locate/apthermeng

Effect of cross-flow on the performance of air-cooled heat exchanger fans

W.H. Stinnes, T.W. von Backström *

Department of Mechanical Engineering, University of Stellenbosch, Private Bag X1, 7602 Matieland, South Africa

Received 20 January 2002; accepted 17 April 2002

Abstract

In large-scale applications such as arrays of axial fans in air-cooled heat exchanger systems, edge–proximity and wind-induced cross-flow may decrease the flow through some fans by causing the flow to enter them at off-axis angles. In this study, such off-axis inflows were introduced by inserting inlet pipe sections between the plenum chamber of a standard test facility and one of three different scale model test fans of 1542 mm diameter. Fan power consumption turned out to be completely independent of off-axis inflow angle up to 45°. Fan total-to-total pressure rise was found to be independent of off-axis inflow angle, and the decrement in fan pressure rise was equal to the dynamic pressure based on the cross-flow velocity component at the fan inlet. Analysis showed that for model fans to represent the cross-flow behaviour of their prototypes, they should have the same ratio of dynamic pressure to pressure rise, and the same dimensionless characteristic slope at their operating points. The performance of a row of fans operating at off-axis inflow conditions representing a cooling system was well predicted by a simple model assuming that the fans farther from the edges induce cross-flows over the fans closer to the edges.

Keywords: Air-cooled; Heat exchangers; Cooling plant performance; Axial fans; Distorted flow; Cross-flow; Off-axis inflow; Fan performance; System effect

1. Introduction

Many forced-draught industrial air-cooled heat exchanger (ACHE) systems have arrays of vertical-axis axial fans in a platform raised above ground level. Since the flow can only enter at the edges of the fan platform, the inner fans induce cross-flows across the inlets of the fans closer to

* Corresponding author. Tel.: +27-21-808-4267; fax: +27-21-808-4958.
E-mail address: twvb@ing.sun.ac.za (T.W. von Backström).

1359-4311/02/$ - see front matter
PII: S1359-4311(02)00060-1

Nomenclature

Symbols

A	area (m^2)
d	diameter (m)
H	fan platform height above ground (m)
N	number of fans in row (from edge to closed end or symmetry plane)
N	fan number (from edge)
P	pressure (Pa)
P_{sf}	fan static pressure, i.e. exit static pressure minus inlet total pressure as defined in BS 848
Q	volume flow rate (m^3/s)
R	ratio of cross-flow to axial velocity (no hub)
V	axial velocity through fan (no hub) (m/s)
W	fan pitch in edge direction (equals box width) (m)
X	variable from reference [8]

Greek

α	off-axis inflow angle (°)
β	fan blade setting angle, (from tangential) (°)
ρ	density of air (kg/m^3)
ζ_{31}	inlet friction parameter (–)
ΔP	pressure difference

Subscripts

d	design point value
f	fan
i	reference, ideal

the platform edges. Such cross-flows, that may be exacerbated by unfavourable wind conditions, cause off-axis inflow into the fans. The objective of this investigation is to determine the magnitude of the effect off-axis inflow on the pressure rise and power consumption of ACHE fans and on the flow through such systems. This information is useful when deciding on the height of ACHE fan platforms above ground level and when selecting fans and fan motors.

Inlet flow distortions have important system effects in many applications of axial flow machinery, for example the cross-flow through the main and the tail rotor of helicopters in forward flight. The French authorities at ONERA have been extensive in their publications through Peleau and Petot [1] and Desopper et al. [2], while Pazur and Fottner [3], and Longley [4] investigated the effect of distorted inflow in compressors. Literature searches, however, yielded no other work as closely related to the present investigation as the publications of a research programme at the University of Stellenbosch itself, where Kröger [5] has guided several experimental, theoretical and numerical studies on axial flow fans in forced-draught industrial cooling systems. Relevant

studies include the theses of Venter [6] and Visser [7], and papers with Salta [8], Duvenhage et al. [9], Meyer [10] and Duvenhage and Kröger [11]. Salta and Kröger [8] reported that tests of model fan arrays indicated a reduction of flow through the heat exchangers as the height of the fan platform above ground level is reduced (thereby increasing the cross-flow velocity), Fig. 2. In the course of comparing the experimental results to the full-scale power plant, they found the wind direction and strength to be important. Thiart and Von Backström [12] placed an axial fan in a wall of a wind tunnel test section to achieve a cross-flow component across the inlet plane equal to the average axial velocity through the fan. This experimental set-up is closely related to an off-axis inflow angle of $\alpha = 45°$ onto the fan inlet plane, one of the cases to be presented here. Using the same test rig, Visser [7] found that large cross-flows reduced fan flow.

Where the previous experiments concentrated on the system as a whole, the experiments presented here concentrate on the performance of scaled ACHE fans, when subjected to isolated and controlled off-axis inflows in a modified standard fan test facility.

2. Description of experiments

2.1. Experimental rig

The basic configuration of the low speed fan test facility described in detail by Venter [6] is for Type A standard tests (free inlet—free outlet), but may be adapted within the code for other arrangements. Except for the carefully evaluated modification of installing short pipe sections between the plenum and the fan to ensure off-axis flow, the experiments were done to British Standard BS 848 Part 1 [13]. We simulated the off-axis inflow by introducing the flow from the plenum chamber of the standard test facility through various angled pipes into the 1542 mm diameter scale model fans exhausting directly to the atmosphere (Fig. 1). The investigation covered three fan designs and a wide range of cross-flow components, fan blade angles and flow rates.

The S-fan is a scaled model of the 9 m diameter fan used with the ACHE system at a large dry-cooled coal-fired power station. The B1- and B2-fans were designed for the same application by Bruneau [14]. Note that the blade setting angle, β of the B-fans in Table 1 refers to the blade angle at the hub and that of the S-fan to the tip, hence the 14–20° difference in blade angle between the S- and the B-fans.

2.2. Generation of uniform off-axis inflow

A controlled way of generating an off-axis flow into a fan was to guide it into the fan through a pipe (Fig. 1) with its centre line at the appropriate off-axis angle, α relative to the fan. The pipe had an elliptical cross-section to correspond to the projected cross-section of the fan. A transition section joined the circular section exit nozzle of the test facility plenum to the elliptical pipe section. The maximum angle between the pipe and fan axes was $\alpha = 45°$, corresponding to a cross-flow to in-flow velocity ratio of $R = 1.0$. Intermediate angles were derived by consecutively halving the cross-flow component, i.e. the tangent of the pipe angle. In Table 2, listing the physical

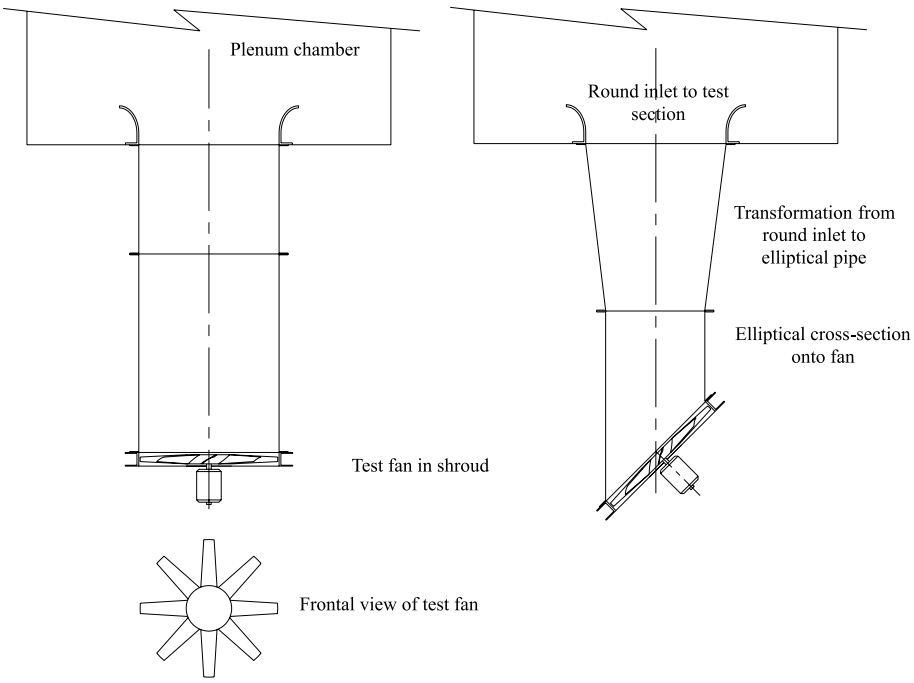

Fig. 1. Plan view of experimental fan inlet section (0° and 45° pipe angle).

dimensions of the inlet sections, the resultant included angle of transformation is the maximum convergence angle between two opposite walls of the transformation section.

2.3. Experimental procedure

Since the fan exhausted to atmosphere, the fan exit static pressure was equal to atmospheric. The upstream total pressure in the plenum chamber was found as required by BS 848 [14] by adding the very small dynamic pressure based on the average velocity through the plenum to the static pressure measured there. The exit static minus the inlet total pressure represented the so-called fan static pressure. Since the first part of the pipe contracted, and the second was relatively short, the boundary layer blockage immediately upstream of the fan was insignificant. Detailed investigations given by Stinnes [15] show that the total pressure in the core flow remained unaltered towards the fan inlet for all pipe sections and that the frictional pressure drop was negligible. Therefore the ζ_{31} friction parameter in the BS 848 [14] codes related to the inlet sections of a Type C (ducted inlet, free outlet) adaptation of the wind tunnel was omitted.

Plenum and inlet nozzle pressures were measured by means of differential pressure transducers calibrated with a water micro-manometer with a sensitivity of 1 Pa. Fan speed was measured by a magnetic pick-up counting the revolutions of a seven-toothed disc mounted directly behind the fan on the shaft. Fan power consumption was derived by measurement of shaft torque with a torque transducer. The static torque calibration method by weighted cantilever arm was corrected for the experimentally determined bearing and coupling friction, resulting in a value of 2 N m

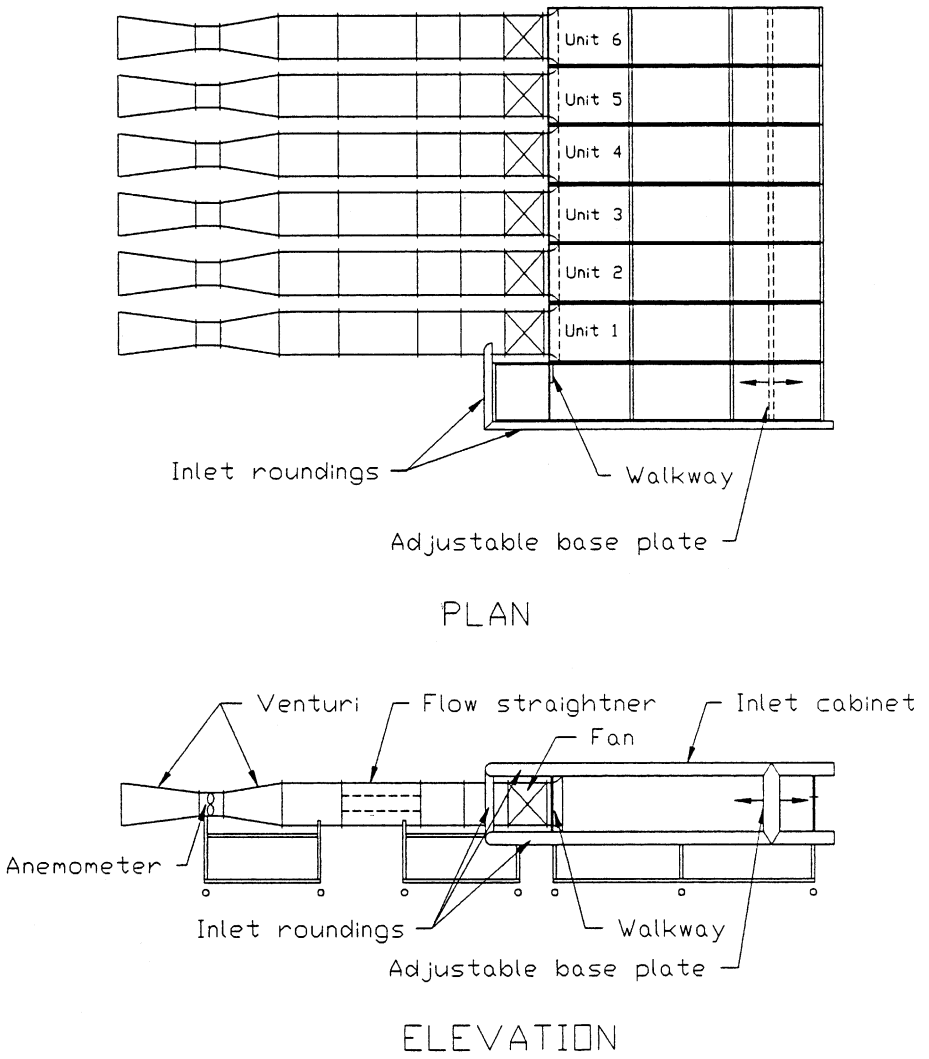

Fig. 2. Plan and elevation of a six-fan experimental model of Salta and Kröger [8].

Table 1
Test fans

Fan	Diameter (mm)	No. of blades	Speed (rpm)	Hub-to-tip ratio	Blade profile	Blade angle β (°)
S-fan	1542	8	750	0.15	–	12
B1-fan	1542	8	750	0.40	Clark-Y	26–30
B2-fan	1542	8	750	0.40	NASA-LS	28–32

at 750 rpm subtracted from all recorded values in the data processing routines. The various measured signals were connected to bridge amplifiers, with the data logged through an

Table 2
Inlet pipe sections

Cross-flow component to on-flow component (%)	0	12.5	25	50	100
Pipe angle (nominal) (°)	0	7	14	27	45
Length of transformation section (mm)			1840		
Included angle of transformation in plan view (°)	0.0	0.4	1.4	5.1	14.0
Length of elliptical section at centreline (mm)			1542		
Shortest side of elliptical duct section (mm)	1542	1446	1355	1197	997

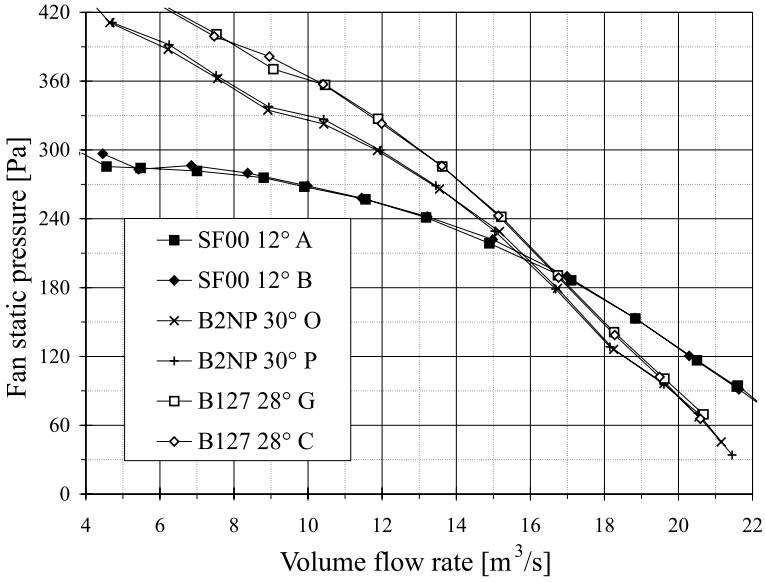

Fig. 3. Repeatability of fan static pressure measurement.

analogue-to-digital converter card into a PC. Fan scaling laws served to scale all data to 750 rpm and $\rho = 1.200$ kg/m^3.

To demonstrate the level of repeatability achieved, Fig. 3 shows tests for all three fans (indicated by SF for S-fan, and B1 and B2 for the B1 and B2 fans, followed by two digits indicating the pipe angle, or NP indicating no pipe, i.e. the fan coupled directly to the plenum).

Results of corresponding quality were obtained for fan power measurements.

3. Experimental results

3.1. Power consumption

Fig. 4 presents power consumption curves for the B1-fan for blade setting angles from 30° to 26° (indicated by the symbols) and inflow angles from 0° to 45°. Power consumption is dependent

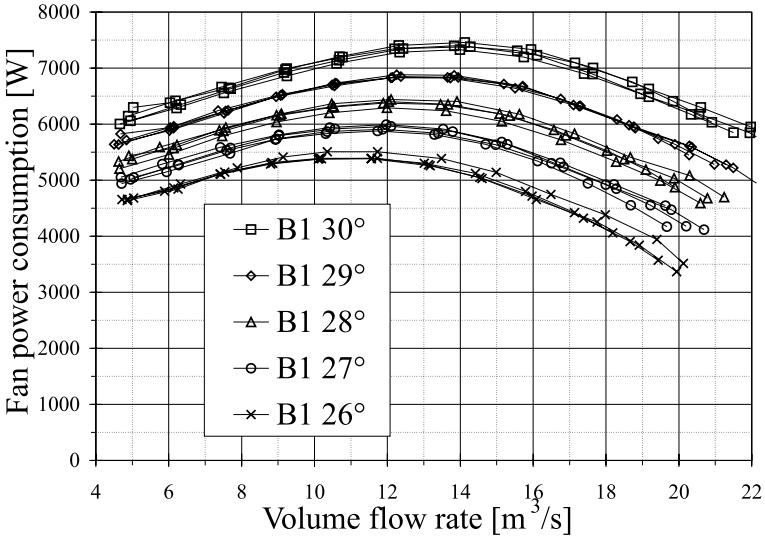

Fig. 4. B1-fan power consumption for various fan blade setting angles.

on blade setting angle, but off-axis inflow angles of up to 45° have no measurable effect on fan power. All the tested fans behaved similarly. Detail bar charts in Stinnes [15] confirm that the experimental values for power consumption for a given blade lie within 3% of the axial inflow case.

3.2. Pressure rise

Fan static pressure is adversely affected by the off-axis inflow, as shown for a typical case in Fig. 5, where characteristics for the B1-fan at 27° blade angle are shown for the 0°, 14°, 27° and 45° inflow angles (indicated by the two digits following the B1 in the legend). (Note that the no-pipe (B1NP) and zero inflow angle (B100) cases are indistinguishable). Also shown is a generic system resistance curve of parabolic shape passing through the design point fan static pressure of 210 Pa at a flow rate of 16 m^3/s, which identifies the resultant performance for the test fan in its system for the tested cross-flow components at fan inlet.

The penalty in performance is small—a cross-flow component of 25% (14° pipe) is hardly noticeable against the straight pipe case. Detail investigations show that the peak total-to-static efficiency, however, is consistently slightly lower. Even for the 27° pipe case, the efficiency and fan static pressure drop by less than 5% for all blade angles, while the flow rate would be reduced by 2%, again unlikely to affect system performance significantly. Finally, for the 45° pipe, where the cross-flow component equals the axial velocity, the achieved fan static pressure has lost approximately 8.3% with an accompanying decrease in flow rate of 4.7% (with both decrements evaluated along the system resistance line). These results also indicate that the fan configuration has an influence on the performance loss, with the B-fans consistently performing at less of a flow rate penalty than the S-fan, resulting from the steeper characteristic curves.

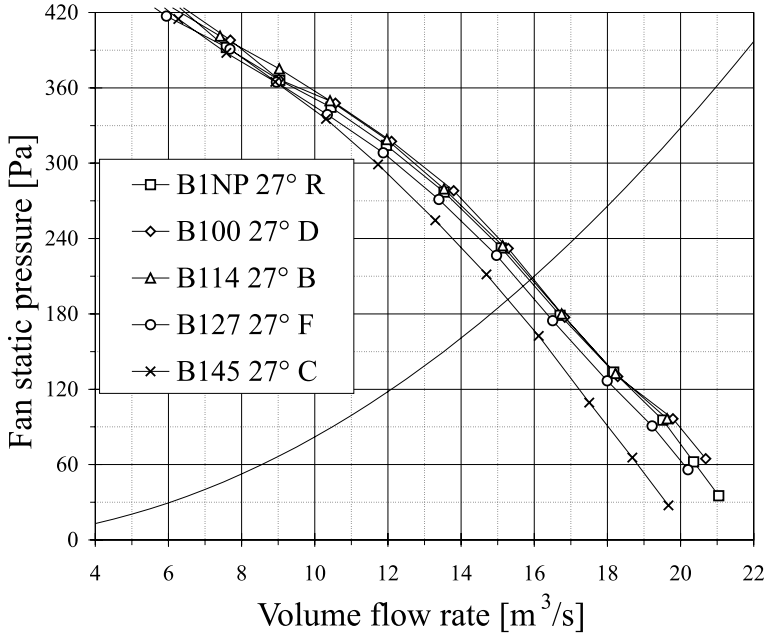

Fig. 5. B1-fan static pressure under forced cross-flow angles from 0° to 45°.

4. Prediction model

The prediction model assumes that the fan total-to-total pressure rise is independent of off-axis inflow angle, where the exit total pressure is found by adding the exit dynamic pressure (ignoring fan hub blockage) to the measured exit static pressure. Constant mean total-to-total pressure rise at constant flow, combined with constant fan power (as measured) implies constant total-to-total efficiency. Since the projected area of the fan relative to the inflow angle decreases as $\cos\alpha$, the velocity through the fan is $V/\cos\alpha$, with V the axial velocity through the fan, disregarding the hub. The increase in dynamic pressure is then $(1/2)\rho V^2(1/\cos^2\alpha - 1) = (1/2)\rho V^2 \tan^2\alpha$. It then follows that the increase in dynamic pressure of the flow into, through, and behind the fan is equal to the dynamic pressure based on the cross-flow velocity, $V\tan\alpha$. If the inlet total pressure and flow remain constant, cross-flow at the fan intake reduces the fan static pressure by an amount equal to the dynamic pressure based on the cross-flow velocity. (Note that when angled pipes impose the cross-flow, the magnitude of the cross-flow component changes as the flow through the fan changes.) The fractional change in fan static pressure induced by a given cross-flow is equal to the ratio of cross-flow dynamic pressure to fan static pressure.

Fig. 6 shows that, for the B1-fan at 27° blade angle, fan total-to-total pressure rise is indeed independent of off-axis inflow angle, at least up to 45°. The original test data are shown as markers only, while the lines represent the dynamic pressure for the 0°, 14°, 27° and 45° pipes respectively. The lines and markers together then show the sum of the two, the assumed total pressure rise of this model against flow rate.

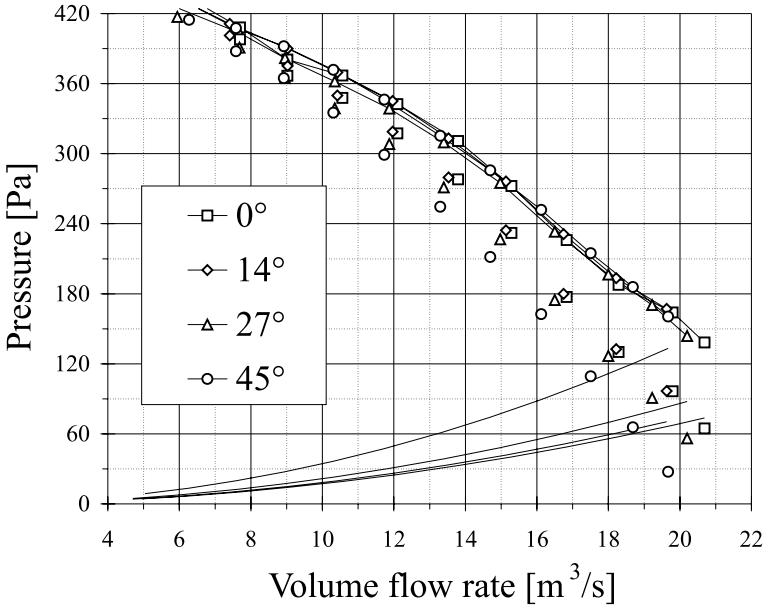

Fig. 6. Performance prediction for the B1-fan (27° blade angle).

All fans tested behaved similarly up to $\alpha = 27°$, but for $\alpha = 45°$ the B-fans with larger blade angle, β, showed smaller reductions than expected in fan static pressure. The worst agreement, where the reduction was 20% less that expected, was for the S-fan at 12° blade angle, (but only at $\alpha = 45°$). This indicated that the simple theoretical model is accurate up to $\alpha = 27°$, and where it errs, it does so conservatively and not too severely.

4.1. Comparison to previous work

For the purposes of comparison to previous work, assume that the off-axis inflow angle, α introduced by cross-flow is equal to the tangent of the ratio of mean cross-flow velocity to fan through-flow velocity (ignoring fan hub blockage). Thiart [16] and Visser [7], introduced cross-flow by placing a test fan into the side wall of a wind-tunnel, but did not present the pressure rise versus volume flow characteristic of the fan, making comparison with the present work difficult. Fig. 7 is a normalised version of part of the characteristic of the S-fan, similar to Fig. 4 for the B-fan. The reference volume flow, Q_i is 11.7 m/s, being 50% of the free discharge flow as reported by Thiart [16], and the reference fan static pressure, P_i is the corresponding one for axial inflow. Fig. 7 shows that the normalised fan static pressures for cross-flow ratio, $R = 0.89$ and $R = 1.11$ agree remarkably well with the present data, lying just above and just below the line of off-axis inflow angle, $\alpha = 45°$ ($R = 1$). The good agreement may however be somewhat fortuitous, since adequate information for proper fan modelling was lacking, as we shall see.

Salta and Kröger [8] investigated the performance of single rows of up to six parallel 630 mm diameter fans installed at pitch line distances of 880 mm from each other, with their bell-shaped

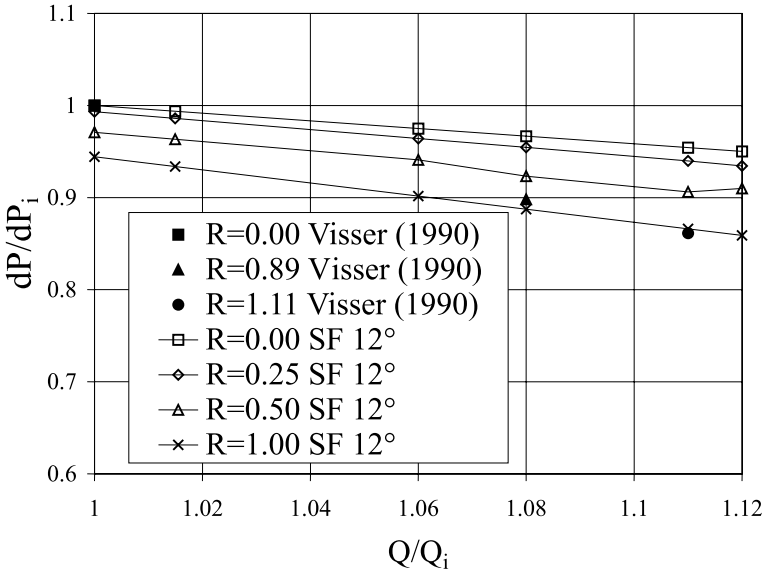

Fig. 7. Comparison to the results of Visser [7].

inlets protruding through the one wall of a box 800 mm wide, Fig. 2. That wall of the box simulated the fan platform, while the wall opposite the fan row, simulating the ground surface below the fans, was movable to simulate fan height above ground. Flow entered through the only open side of the box, closest to the no.1 fan. The opposite side of the box, near the end fan, and the two sides parallel to the fan row were closed, and simulated the centre symmetry plane, and the between-fan-row symmetry planes in the fan array respectively. All four edges of the flow entrance into the box were rounded, but the one at the fan platform could be fitted with extension plates, representing walkways of different widths as shown in [8].

To simulate the experiment [8] we assumed that the cross-flow at the nth fan is caused by the flows on their way to the fans farther from the edge. The total flow crossing the centre line of the nth fan also includes half the flow entering the nth fan. Taking respectively the fan flow and fan diameter as Q_f and d_f, the box width and box height as W and H, and the total number of fans in the row (from the edge to the symmetry line at the centre of the array) as N, the inflow angle and cross-flow to in-flow ratio for the nth fan from the edge are given by:

$$\tan\alpha_n = R_n = \frac{\left(\frac{1}{2}+N-n\right)Q_f/WH}{Q_f/(\pi/4)d_f^2} = \frac{\pi}{4}\left(\frac{1}{2}+N-n\right)\frac{d_f}{W}\frac{d_f}{H} \tag{1}$$

Knowing R_n leads to the cross-flow velocity at the nth fan and its associated dynamic pressure. The effective fan static characteristic for a given cross-flow velocity is a line one cross-flow dynamic pressure below the original characteristic. The new fan operating point then follows by finding the intersection with the system resistance line, normally of the form $\Delta P \propto Q^2$.

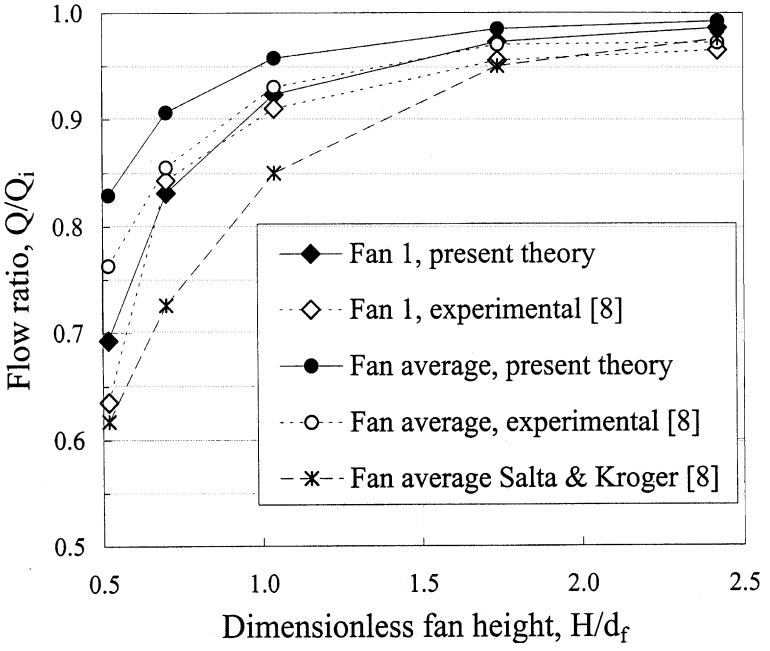

Fig. 8. Comparison to the results of Salta and Kröger [8].

Salta and Kröger [8] did not publish their fan characteristics, but they were available in the thesis of Visser [13]. Their fans had typical design fan static pressures of 41 Pa and design dynamic pressures (at $R = 0$) of 10.7 Pa, compared to 200 and 44 Pa for the corresponding B1-fan tested by Stinnes [15]. Their fan characteristic also had non-dimensional slopes $(dP/P_d)/(dQ/Q_d)$ of 0.722 compared to 2.29 for the Stinnes fan. Our method then predicts the Salta and Kröger [8] fans to experience a 9.6% drop in volume flow (along the system characteristic) when $R = 1$, compared to the 5.1% for the Stinnes fan. We introduced $(dQ/Q)/R^2 = 0.096$, and the fan diameter, $d_f = 0.63$ m, into the method described above.

Fig. 8 shows the results for a row of two fans (between the edge and the symmetry plane in the middle). The diamond shaped symbols indicate the edge fan, and the circular symbols the average performance of both fans. In general the predictions are surprisingly good, especially for the edge fan (fan 1), and they may even be improved if the flow ratios are all reduced by 0.015 as in the empirical correlation (for two fans) of Salta and Kröger [8] (Fig. 8): $Q/Q_i = 0.985 - e^{(-X)}$ where $X = 1.929\ H/d_f$. Further comparisons with different numbers of fans, with protruding fan bellmouths and simulated walkways are beyond the present scope.

5. Conclusions

The following are the conclusions regarding ACHE fans subjected to cross-flows:

1. Fan power consumption is independent of off-axis inflow angles up to 45° (cross-flow ratio, $R = 1.0$). Fans selected off standard test curves will not overload their motor capacity due to cross-flow components.
2. Fan total-to-total pressure rise is independent of off-axis inflow angles up to at least 27° (cross-flow ratio $R = 0.5$), and assuming it to be constant is reasonably accurate but conservative up to 45°.
3. The decrement in fan static pressure is equal to the dynamic pressure based on the cross-flow velocity.
4. When they are not geometrically and kinematically similar to the prototypes, experimental fans used to simulate cross-flow properties of prototype fans should at least have the same ratios of dynamic pressure to fan static pressure, and the same dimensionless slope of their characteristics.
5. The performance of a row of fans operating at off-axis inflow conditions was well predicted by a simple model assuming that the fans farther from the edges induce cross-flows over the fans closer to the edges.

References

[1] B. Peleau, D. Petot, Aeroelastic prediction of rotor loads in forward flight, Vertica 13 (2) (1989).
[2] P. Desopper, P. Lafon, P. Céroni, J.J. Philippe, Ten years of rotor flow studies at ONERA, Journal of American Helicopter Society 2 (1989) 2.
[3] W. Pazur, L. Fottner, The Influence of Inlet Swirl Distortions on the Performance of a Jet Propulsion Two-Stage Axial Compressor, International Gas Turbine and Aeroengine Congress and Exhibition, Brussels, Belgium, no. GT 147, 1990.
[4] J.P. Longley, Measured and Predicted Effects of Inlet Distortions on Axial Compressors, International Gas Turbine and Aeroengine Congress and Exhibition, Brussels, Belgium, no. GT 214, 1990.
[5] D.G. Kröger, Air-cooled heat exchangers and cooling towers: thermal-flow performance evaluation and design, Department of Mechanical Engineering, University of Stellenbosch, 1998.
[6] S.J. Venter, The Effectiveness of Axial Flow Fans in A-Frame Plenums, Ph.D. (Mech. Eng.) Thesis, Department of Mechanical Engineering, University of Stellenbosch, 1990.
[7] J.G.J. Visser, Die Invloed van Versteurde Inlaatvloeipatrone op Aksiaalwaaiers, M. Eng. (Mech.) Thesis (in Afrikaans), Department of Mechanical Engineering, University of Stellenbosch, 1990.
[8] C.A. Salta, D.G. Kröger, Effect of inlet flow distortions on fan performance in forced draught air-cooled heat exchangers, Heat Recovery Systems and CHP 15 (1995) 555–561.
[9] K. Duvenhage, J.A. Vermeulen, C.J. Meyer, D.G. Kröger, Flow distortions at the fan inlet of forced-draught air-cooled heat exchangers, Applied Thermal Engineering 16 (1996) 741–752.
[10] C.J. Meyer, D.G. Kröger, Numerical Modelling of an Axial Flow Fan, Proceedings of the 2nd South African Conference on Applied Mechanics, UCT, ISBN 0-7992-1877-4, January 1998.
[11] K. Duvenhage, D.G. Kröger, The influence of wind on the performance of forced draught air-cooled heat exchangers, Journal of Wind Engineering and Industrial Aerodynamics 62 (1996) 259–277.
[12] G.D. Thiart, T.W. Von Backström, Numerical simulation of the flow field near an axial flow fan operating under distorted inflow conditions, Journal of Wind Engineering and Industrial Aerodynamics 45 (2) (1993) 189–214.
[13] British Standards Institution, BS 848: Part 1:1980, Fans for General Purposes, Part 1: Methods for Testing Performance, 1980.
[14] P.R.P. Bruneau, The Design of a Single Rotor Axial Flow Fan for a Cooling Tower Application, M. Eng. (Mech.) Thesis, University of Stellenbosch, 1994.

[15] W.H. Stinnes, The Performance of Axial Fans Subjected to Forced Cross-Flow at Inlet, M.Sc. (Mech. Eng.) Thesis, University of Stellenbosch, 1998.
[16] G.D. Thiart, A Numerical Procedure for Predicting the Effects of Distorted Inflow Conditions on the Performance of Axial Flow Fans, Ph.D. (Eng.) Thesis, Department of Mechanical Engineering, University of Stellenbosch, 1990.

JOURNAL OF THE AMERICAN HELICOPTER SOCIETY **55**, 012000 (2010)

System Analysis and Optimization of the CIRSTEL Tail Boom

R. Heise*
Graduate Research Assistant
Department of Mechanical Engineering

T. W. von Backström
Professor of Thermofluids

University of Stellenbosch, Stellenbosch, South Africa

This paper details the development and results of a one-dimensional numerical model to simulate Combined Infrared Suppression and Tail Rotor Elimination (CIRSTEL) helicopters in hover. Ultimately the model was used to perform a simple numerical optimization of the system, with the objective of minimizing the power requirement by the system. The current model incorporates an engine model to check and define parameters that minimize any effects the system may have on the engine. Case studies on single- and twin-engine light helicopters were completed. The results show that the system offers a potential power demand reduction over a conventional tail rotor by up to 35%, while reducing the thruster exhaust gas temperature to below 170°C. It is also shown that through careful designing and sizing of the mixer nozzle the effects on the engine can be negligible while still boosting the performance of the tail thruster.

Nomenclature

A	area, m^2
C_D	drag coefficient/discharge coefficient
c	chord length, m
D	drag, N
d	tail boom diameter, m
F	force, N
f	loss factor
$\dot{m}$	mass flow, kg/s
n	area ratio
P	total pressure, Pa
p	static pressure, Pa
Q	torque, Nm
R	main rotor radius, m
T	thrust, N
V	velocity, m/s
v_i	induced velocity, m/s
W	power, W
ρ	density, kg/m^3

Subscripts

B	blade
c	climb
Core	core section
CCS	circulation control section
e	engine
MR	main rotor
t	blade tip
TR	thruster

Introduction

The Combined Infrared Suppression and Tail Rotor Elimination (CIRSTEL) tail boom is a single-rotor helicopter antitorque and control system. It relies on the Coanda effect to create circulation around the helicopter tail boom when exposed to the rotor downwash, resulting in a sideways-directed lift force to counter the main rotor torque. In addition, a tail thruster adds extra adjustable torque and allows for directional control. The system is thus similar to the NOTAR system (Ref. 1) with its inherent advantages but also inducts the engine exhaust gases into the tail boom for infrared suppression and potential energy savings. Previous models of the CIRSTEL system, such as that of Lippert et al. (Ref. 2), did not include the analysis of the engine as part of the entire system. The current work includes a model for the engine to monitor and design out the effects the CIRSTEL system can have on the engine. The method presented here does not only serve as an analysis tool but also allows for a numerical optimization of the system. However, the current analysis looks specifically at hover only as a means to establish what potential advantages could be gained from the system and formulate starting points for further research.

Numerical Model

The CIRSTEL tail boom system consists of five main components as shown in Fig. 1: the outer circulation control tail boom section (CCTB), the core section with the mixer/nozzle, tail thruster, a fan, and finally

*Corresponding author: rheise@csir.co.za.
Presented at the 31st European Rotorcraft Forum, Florence, Italy, September 13-15, 2005. Manuscript received December 2005 and accepted August 2009.

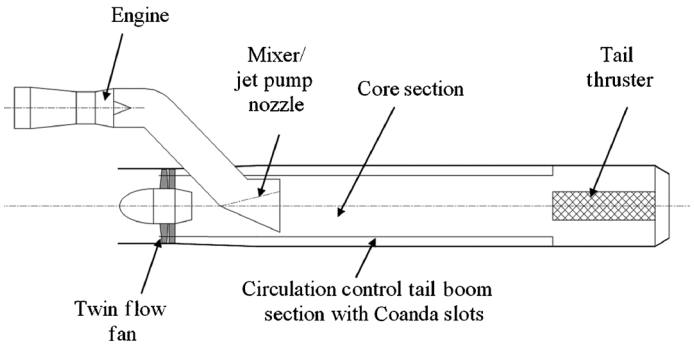

Q1 **Fig. 1.**

the helicopter engine, as this forms an integral part of the system. The twin flow fan supplies air to both the core and outer section circulation control section. The CCTB has two Coanda slots through which the air vents to set up a circulation around the tail boom in the presence of the main rotor downwash. In the core section, the engine exhaust gases are mixed with fresh air supplied by the fan and exit the tail boom via the tail thruster. The model simulates each of the components individually, and then interlinks the individual component parameters to give the global
Q2 performance of the tail boom. Figure 2 is a flowchart of the numerical model showing the code structure and flow of the parameters between the different components of the system. The shaded fields in the figure are the main optimization variables, whereas the double-framed parameters present the required global tail boom performance solutions. To close the solution, it is also required to balance the main rotor torque with that generated by the tail boom, as well as ensuring the power demand of the rotor and fan can be met by the engine output.

Main rotor

The performance of the helicopter main rotor and tail rotor is modeled before that of the five tail boom components. The tail rotor is simulated for comparison purposes to evaluate the tail boom relative to an equivalent tail rotor.

The main rotor is modeled using a suitably modified momentum theory to include the effects of a finite number of blades and tip losses (Ref. 3). The required thrust is increased by a small amount to compensate for the downwash-induced drag on the fuselage. To account for a nonuniform-induced velocity and tip losses, an empirically determined correction factor of $\kappa = 1.18$ is used to modify the average downwash velocity (Ref. 3). NACA 0012 blade profile data from Riegels (Ref. 4) was used when calculating the power required to overcome rotor blade drag. None of the consulted literature (Refs. 3, 5) uses the corrected downwash velocities of $(V_c + v_i)$ to predict the profile drag. The work presented here does not, however, ignore the climb and induced velocities.

For the current application, the following equation is derived. Starting with the incremental power of a blade section in Eq. (1),

$$dW_D = \tfrac{1}{2}\rho C_D V^3 c\, dr \tag{1}$$

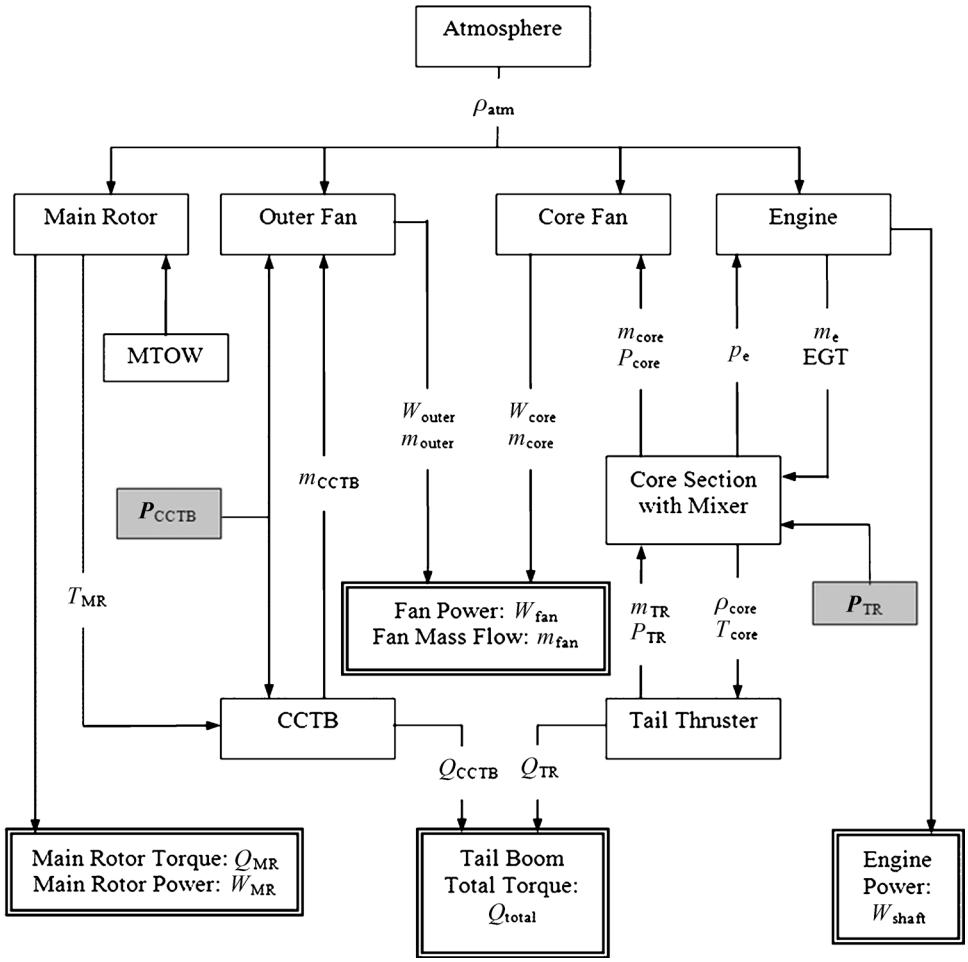

Fig. 2.

The equation can be integrated for the whole blade length and number of blades to give the rotor power in Eq. (2) after some simplification:

$$W_D = \tfrac{1}{8}\rho C_D A_B \left(V_t^2 + (V_c + v_i)^2\right)^{3/2} \tag{2}$$

Gessow and Meyers (Ref. 5) state that the commonly used equation is limited to hover and low-speed climb. The above equation, however, provides better answers when compared to the published performance data of helicopters (Ref. 6). From the calculated power, the amount of torque acting on the fuselage is determined, and the performance of an accompanying conventional tail rotor can be determined using the same momentum theory

Engine

Previous models of the CIRSTEL system, such as that of Lippert et al. (Ref. 2), did not include the engine. It is important to be able to monitor the effects the CIRSTEL system on the engine as an integral part of the system. Of prime importance is the effect of the design of the mixer on the turbine backpressure. By increasing the backpressure on the turbine, the compressor surge margin is reduced and a reduction in delivered power will occur as well. The current model allows for the design to be optimized such that the backpressure on the engine is reduced to zero, or at least kept close to zero.

The engine is modeled as a single-shaft, constant-speed engine with a diffuser after the turbine. The exit area of the diffuser is the same as that of the mixer and is thus one of the design and optimization parameters. Since the engine is a constant-speed unit, the volume flow through the engine is constant. Hence the mass flow can be determined from the ambient atmospheric conditions once a mass flow is known at given atmospheric conditions. The isentropic relationships of an ideal gas for compression and expansion in the compressor and turbine, respectively, are used to model the engine, with the combustor exit total temperature fixed at a specified 1100 K. A pressure ratio for the compressor is determined for the selected engine from the published data along with the section isentropic efficiencies.

The engine is tied into the rest of the tail boom by the value of the static pressure at the exit of the diffuser/mixer, which is the static pressure in the core section of the boom. The losses in the exhaust ducting/diffuser of the engine to the mixer are incorporated in the momentum analysis equations developed for the core section. For the turbine performance, the diffuser exit dynamic pressure can be determined from the known mass flow, density, exit area, and diffuser efficiency, which then together with the static pressure gives the exit total pressure of the engine. From this the turbine pressure ratio is calculated. Since the exhaust density is dependent on the static pressure in the tail boom, iteration is required with a guessed exit density. In the solving phase of the program, the error between the guess and calculated density value is then continually adjusted to be zero by changing the guessed density value.

Finally the engine power output is determined and modified to include gearbox losses. The shaft power available is then compared to the total demand from main rotor and fan and the gearbox rating. If required, the total takeoff weight can be modified to keep within the limits of the engine and gearbox.

Core section with mixer

The core section with its mixer where the engine exhaust gases are injected is essentially a jet pump. This effectively unloads the fan if carefully designed and thus allows an effective power reduction mechanism over conventional systems. Control volume momentum analysis is used to set up a quasi one-dimensional model of the mixer and duct.

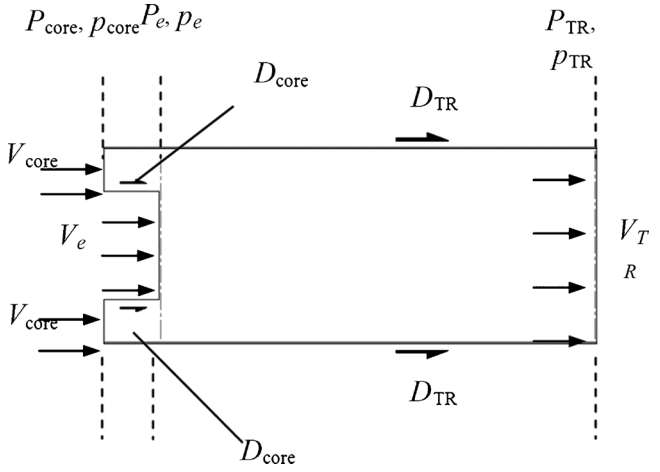

Fig. 3.

The approach used here to develop the momentum equations is similar to the approach of Lawn (Ref. 7). However to make the equations useful for the design of the current tail boom, they were derived such that the entry and exit streams can have different densities and the total pressures of each stream can be specified. Total pressures are used in the equations as the total pressures in the sections of the tail boom drive the solution.

Figure 3 shows the control volume of the core section for purposes of the momentum analysis. The duct has a constant diameter, thus the mixer exit opening occupies a fraction n of the cross-sectional area A, with the fan duct area being $(1 - n)A$. The sum of forces on the control volume can then be written as shown in Eq. (3): **Q3**

$$\begin{aligned}\sum F &= D_{\text{TR}} + D_{\text{core}} + D_e + Ap_{\text{TR}} - nAp_e - (1-n)Ap_{\text{core}} \\ &= \dot{m}_{\text{core}} V_{\text{core}} + \dot{m}_e V_e - \dot{m}_{\text{TR}} V_{\text{TR}}\end{aligned} \tag{3}$$

At the entrance and exit to the control volume, the streams will exhibit some momentum deficiencies due to wall friction and form drag. These are accounted for in the D_x terms and take on the form as shown in Eq. (4).

$$\begin{aligned}D_x &= f_x \rho_x V_x^2 A \\ &= f_x \dot{m}_x V_x\end{aligned} \tag{4}$$

Here the loss factor f is equivalent to half the drag coefficient based on the cross-sectional area of the flow. Duct losses accounted for in the D_{TR} term are effectively duct friction losses and are calculated using pipe flow theory. Losses in engine duct/diffuser/mixer are estimated to be $f_e = 0.05$ for a 95% diffuser efficiency. From Hoerner (Ref. 8), the drag coefficient of the mixer is estimated to be $C_D = 0.2$ which would make $f_{\text{core}} = 0.1$. This value was later adjusted to $f_{\text{core}} = 0.12$ when comparing results to some limited experimental data (Ref. 9). After some simplification, the final result of the momentum analysis yields the following equation:

$$\begin{aligned}A(P_{\text{TR}} - P_{\text{core}}) &= \dot{m}_{\text{core}} V_{\text{core}} \left(\frac{1-2n}{2(1-n)} - f_{\text{core}}\right) \\ &\quad + \dot{m}_e V_e (1 - f_e) - \dot{m}_{\text{TR}} V_{\text{TR}} \left(\frac{1}{2} - f_{\text{TR}}\right)\end{aligned} \tag{5}$$

This is the desired function with the section mass flows as the required variables with the core fan total pressure as the output. This equation can now easily be applied for the system calculations.

The experiments done by Bouwer and Nurick (Ref. 9) were for a fixed value of the mixer/duct area ratio; thus that data cannot easily be

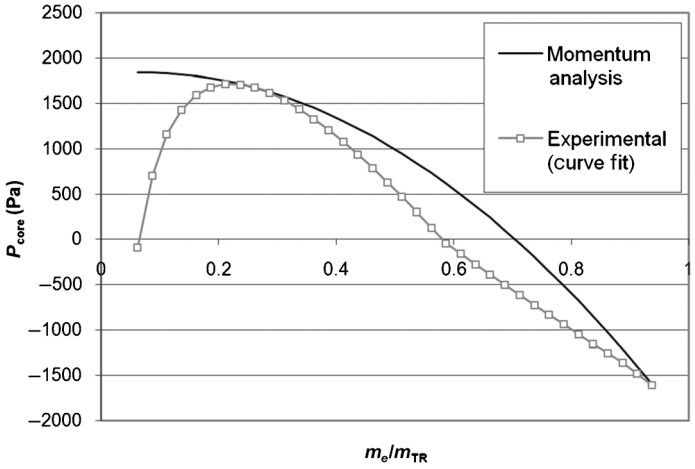

Fig. 4.

used for design purposes. Those data were, however, used to calibrate the current equations. Care has to be taken when interpreting the results of Ref. 9, as it can predict unrealistic total pressures from the fan at low mass flow ratios as insufficient data are available in that region.

Q4 Figure 4 compares the experimental data to the results obtained by the momentum equation, all to achieve a total exit pressure of 1200 Pa and 1.6 kg/s mass flow, with a nozzle area ratio $n = 0.469$. The figure shows the pressure contribution the fan has to deliver to achieve the desired exit pressure for a range of engine mass flow fractions of the total required exit mass flow. As can be seen from the figure, the theoretical results follow the experiment relatively well for mass flow ratios larger than 0.2. At the lower values, the experimental curve-fit indicates a negative pressure rise required from the fan to achieve the desired total pressure rise at the thruster end of the duct, which is unrealistic as the fan at that ratio has to virtually deliver the entire pressure rise on its own.

Tail thruster

The performance of the tail thruster is based on the theory developed by Nurick (Ref. 10) for a clamshell thruster, with experimentally determined thrust and power coefficients that are used for the calculations. Thrust of the thruster is a function of the thrust coefficient, exit area, and the total pressure supplied to the thruster. Similarly, the mass flow is dependent on the power and thrust coefficient, exit area, density, and total pressure. Here the total pressure is calculated from the momentum theory for the core section. Once the total core section mass flow is known, the amount the fan has to contribute can be calculated by subtracting the engine mass flow form the total flow.

As shown by Nurick (Ref. 10), the static pressure can be determined from the thruster coefficients, geometry, and total pressure alone. The density in the tail boom cannot be calculated because the specified total pressure influences the static pressure and mass flow and hence the mixed airflow temperature in the duct, which are all needed to calculate the density. This results in a circular reference and again the density is guessed, and this guessed density is then adjusted during the solving phase to equal the actual value. Knowing the two mass flows entering the core section, the mixture temperature can be calculated, from which finally the actual mixture density can be calculated.

Circulation control section

Fonternel and Nurick (Ref. 11) summarized the theory for the circulation section, whereas more recently Nurick (Ref. 12) conducted further investigations specifically for the CIRSTEL system. The torque that the circulation section provides in hover is a function of the supplied total pressure, main rotor thrust, and tail boom geometry. A similar geometry is used in the simulations as the geometry used by Nurick, for which the produced torque is given by Eq. (6).

Table 1. Fan efficiencies

Fan Section	Experimental Efficiency (%)
CCTB	79.4
Core section	85.9

$$Q_{\mathrm{CCTB}} = 0.101 \left(\frac{P_{\mathrm{CCTB}}}{T_{\mathrm{MR}}/\pi R^2} \right)^{1/2} T_{\mathrm{MR}} D \tag{6}$$

This equation is valid for a round and flap-less tail boom. Two Coanda slots are used for this boom; one at a location of 60° from the top, with the second slot located 120° form the top of the tail boom. The Coanda slots extend to the radius of the main rotor with a total length of 2.75 m. To calculate the mass flow through the two Coanda slots, they are modeled as a nozzle with a discharge coefficient of $C_D = 0.802$. The discharge coefficient is derived from the experimental data (Ref. 12).

Fan

A unique fan is used for the CIRSTEL system in that the single fan has the ability to supply each section of the tail boom with a separate air stream of the required pressure and mass flow quantity. This is achieved by adding a part-span, rotating shroud to the fan at the radius where the two streams separate to physically split the airstream in the plane of fan. Each of the two fan sections then has its own uniquely designed fan blades. As part of the general research effort into the CIRSTEL system, such a fan has been tested experimentally by Heise (Ref. 13). The results from these detailed performance tests are incorporated into the current simulation program. The fan tests have shown that the two sections of the fan do not influence each other significantly, regardless at which operating point each section is working. Second, the fan efficiencies determined during the experimental trials (Table 1) are used here to determine the power requirements of the fan. Since the required mass flow and total pressure rise demands are solved as part of the optimization process, and hence the required fan power, the corner stone for the fan design is provided as well.

Global tail boom performance

The torque each of the circulation control and tail thruster sections develops is added to give the total delivered torque of the tail boom. The total power required by the fan is also the sum of the two sections and is an important result to monitor. This value is required for monitoring of the total power requirement of the helicopter, and to compare to the power demand of the conventional tail rotor to highlight any power savings or differences. Finally, the total mass flow requirement of the fan is required for the design of the air intakes for the fan.

Optimization Method and Constraints

As well as facilitating the analysis process, the program was designed to be utilized with a numerical optimization scheme for design purposes. By monitoring the performance of the individual components during the optimization process, the most critical components could be identified. A numerical optimization technique, such as the simplex method (Ref. 14) with constraints, was employed to find optimum dimensions

and parameters for this tail boom. For simplicity, the current program was written for a spreadsheet, which allowed better visibility and control of the parameters during the search for convergence.

The objective of the optimization process is to minimize the power required by the fan, while the tail boom still delivers the required torque to balance and control the helicopter. Primary constraint in the optimization process is thus the percentage of main rotor torque the tail boom has to counter, including the reserves required for maneuvering. Once an optimum for a selected design point is found, the solution has to be checked for other parts of the hover envelope by scaling the fan with the appropriate fan scaling laws.

Any reductions in the total power requirement over the standard tail rotor have their obvious advantages; if the requirement increases the feasibility of the system reduces, though the tactical and safety advantages of the system remain.

Input variables used are primarily the geometric features of the tail boom, such as boom diameter, mixer area, and thruster exit area. The total pressures in the two conduits of the tail boom drive the solution, as these have the most direct influence on the performance of the boom and the fan. The fraction each of the two sections delivers of the total torque can also be limited.

Two helicopter design configurations were studied, namely a single- and a twin-engine helicopter in the light utility helicopter class. Both helicopters have the same overall dimensions with a main rotor diameter of 11 m. The single-engine helicopter is modeled as having an engine based on the Artouste IIIB delivering 500 kW, while the twin has engines each delivering 480 kW, based on the Arrious 2K1 engine. For the single-engine helicopter, the power limit is the engine output, whereas for a twin the limit is determined by the main rotor gearbox rating. Accordingly, the limit is set in the program. As a design point, the maximum takeoff weight is selected at atmospheric conditions of 85,000 Pa and 25°C for both versions. The upper design limit chosen is a maximum all up weight which can be maintained with available power plus an extra margin of the fan power to allow for maneuvering.

The engine performance degrades with altitude and temperature, which was also included in the analysis. Because of the nature of the CIRSTEL system, the backpressure on the engine can change from normal atmospheric conditions, which in turn will change the engine output due to a difference in the pressure drop across the turbine. These effects of the changing backpressure on the power output of the engines were also included in the analysis of the system. A higher backpressure on the turbine will reduce the power output and could reduce the surge margin. A lower backpressure would thus seem to be a better solution, but this can lead to an overloading of the engine, and thus the backpressure should be kept close to zero during solving process.

Further constraints that were investigated are the thruster exit area and tail boom diameter. These variables, however, quickly converged to unrealistic values; the tail boom diameter increased to a size that could not be installed on a helicopter, and the thruster exit area also ended up as being too large to practically fit on the tail boom. These two dimensions thus had to be fixed to practical values and did not form part of the numerical optimization process. However, the exit area was still bigger than the core duct flow area, and hence below-ambient static pressures could still be achieved in the plane of the mixer. For both test cases, the dimensions were identical for these geometric features. The exit area of the mixer then gave control over the static backpressure and was chosen such that the engine(s) would experience a close to zero or slightly negative static backpressure. Yet the mixer performed sufficiently as a jet pump nozzle for both test cases. When allowing the optimization routine to size the nozzle area, the tendency is to reduce the area and increase the backpressure on the engine unless the backpressure is explicitly constrained. Furthermore, a larger nozzle exit area is more desirable to allow for better mixing of the hot gases inside of the core section duct.

Table 2. Optimization variables and constraint summary

Optimization objective function
Minimize fan power: W_{fan}
Optimization variables
Thruster total pressure: P_{TR}
CCTB section total pressure: P_{CCTB}
Constraints
Total tail boom torque: $Q_{TB} = 1.1 Q_{MR}$
CCTB section torque contribution: $Q_{CCTB} = 0.84 Q_{MR}$
Thruster temperature: $<170^{\circ}$C
Nozzle area (fraction of core section): $n < 0.235$

The fraction of the total torque delivered by the circulation control section is limited to less than 48%; this is to ensure an effectiveness of the tail boom at slow speed flight, when the effectiveness of this section is reduced due to the decrease in downwash from the main rotor. There is no method in the current system to change the percentage contributions of the two sections in flight, thus the reliance on the circulation control section should not be more than half of the total and more reliance must be placed on the tail thruster. Since the circulation control section is more efficient at creating torque the fraction, its contribution is always close to the maximum limit. A secondary effect of this limit is the resultant temperature of the gases exiting the thruster; by increasing the workload of the core section, more cold air is demanded from the fan, and thus the thruster temperature is reduced. A summary of the optimization objectives, constraints and variables is given in Table 2.

Optimization Results

In both test cases, the power required by the fan was noticeably less than that of a conventional tail rotor. The fan power was below 5.3% and 8.7% of the main rotor power, for the single and twin, respectively, as opposed to the 9%–10% of the conventional tail rotor. The reduction in power can mainly be attributed to the jet pump effect in the core section and the ability to optimize the tail thruster and circulation control section separately. The jet pump has a dominating effect on the performance of the tail boom and is thus a critical component in the design of the system.

The relatively small power saving for the twin stems from the high engine compressor pressure ratio of 9.5 versus the pressure ratio of 5 used for the single. Consequently, it has a small mass flow through the engine for the power the engine produces, and the fan then has to supply more air to power the tail thruster. This can also be seen by the low thruster exit temperature of 151°C. The power saving is thus a trade-off, among others, between the type of engine used and the thruster exit temperature required that has to be considered at the start of the design process.

Finally, the thruster exhaust temperature was reduced to well below the 170°C threshold for both test cases, which will make it difficult for infrared sensors to pick up. In the calculations, complete mixing of the exhaust gas is assumed due to the limitations of the one-dimensional model. Incomplete mixing will not significantly affect the momentum analysis, but a distinct degrading of the IR suppression will occur if incomplete mixing takes place. It is thus imperative that the design of the mixer is carefully considered.

Also worthwhile noting here is that the total pressure in the CCS section is lower than for the pressure supplied to the thruster. The fan, however, has to deliver a higher pressure to the CCS than to the core section; the remainder being made up from the energy supplied by the engine exhaust gas. Table 3 gives the detailed results of the simulations for the two case studies.

Table 3. Optimization results for 110% of main rotor torque

	Single 2070 kg T/O mass	Twin 3500 kg T/O mass
Total fan power (W)	17,705	52,804
Equivalent tail rotor power (W)	27,166	61,168
Percentage of saving	34.8	13.7
Thruster gas temperature (°C)	167	151
Total torque (Nm)	9159	16,634
Total pressure supplied to thruster (Pa)	2126	3765
Total pressure supplied to CCS by the fan (Pa)	1720	3552
Total pressure supplied to core section by the fan (Pa)	1377	2890
Percentage of torque contribution by circulation control section	46.3	47.7
Tail boom diameter (m)	0.720	0.720
Tail thruster area (m^2)	0.4655	0.4655
Core section diameter (m)	0.650	0.650
Nozzle area (fraction of core section)	0.235	0.230
Mass flow fraction (m_e/m_{TR})	0.281	0.249

Conclusions

Two case studies for a CIRSTEL-configured helicopter were completed, namely a single- and twin-engine light helicopter of similar size, to determine the optimum configuration for the CIRSTEL tail boom for these two types of helicopters. A basic model was developed that modeled the components of the CIRSTEL system, namely the engine, tail boom fan, thruster, circulation control section, jet-pump, and the main rotor to determine the required antitorque from the tail boom. A numerical optimization routine was then used in conjunction with this model to find an optimum design with regard to minimizing the power required by the system. As a constraint to the optimization, the backpressure on the engine was to be kept at zero. Also a limit of 48% on the torque contribution by the circulation control section was set to allow sufficient directional control by the tail thruster at low-speed flight. The original objective of giving and on-par performance compared to a conventional tail rotor was achieved, even an improvement on the required power was achieved. The results show that the CIRSTEL system offers a potential power demand reduction over a conventional tail rotor by up to 14% and 35%, for the twin- and single-engine helicopter, respectively, while the exhaust gas temperatures were reduced to below the maximum desired 170°C. It is also shown that through careful designing and sizing of the mixer nozzle, the effects the system has on the engine can be negligible while a boosting of the tail thruster performance is still achievable.

References

[1]Bregger, R., and Dawson, S., "Side-by-Side Hover Performance Comparison of MDHC 500 NOTAR and Tail Rotor Anti-Torque Systems," American Helicopter Society 48th Annual Forum Proceedings, Washington, DC, June 3–5, 1992, pp. 689–695.

[2]Lippert, A. M., Martins, J. C. F., and Nurick, A., "CIRSTEL Conceptional Design: Input Parameters and Optimization Process," CSIR Report AERO 94/199, 1994.

[3]Seddon, J., "Basic Helicopter Aerodynamics," AIAA Education Series, America Institute of Aeronautics and Astronautics, Reston, VA, 1990.

[4]Riegels, F. W., *Airfoil Sections*, Butterworths, London, 1961.

[5]Gessow, A., and Myers, G. C., *Aerodynamics of the Helicopter*, Frederic Ungar Publishing, New York, NY, 1983.

[6]*Jane's All the Worlds Aircraft*, Jane's Information Group Limited, Bracknell, Berkshire, UK, 1970.

[7]Lawn, C. J., "A Simple Method for the Design of Gas Burner Injectors," *Proceedings of the Institute of Mechanical Engineers, Part C*, Vol. 217, 2003, pp. 237–246.

[8]Hoerner, S. F., *Fluid-Dynamic Drag*, Hoerner Fluid Dynamics, Bakersfield, CA, 1965.

[9]Bouwer, P., and Nurick, A., "An Experimental Investigation of a $^1/_2$ Scale Combined Helicopter Anti-Torque and Engine Exhaust Gas Cooling Model," CSIR Report AERO 94/099, 1994.

[10]Nurick, A., "An Experimental Investigation of the Characteristics of Helicopter Thrusters," *Aeronautica Meridiana*, Vol. 12, 1995, pp. 14–35.

[11]Fonernel, M.A., and Nurick, A., "The Use of Circulation Control on the Tail Boom of a Helicopter: A Survey," Report No 93, University of the Witwaterstrand, Witwaterstrand, South Africa, 1990.

[12]Nurick, A., "Experimental Investigation of a Helicopter Circulation Controlled Tail Boom," *Journal of Aircraft*, Vol. 38, (3), May–June 2001, pp. 528–535.

[13]Heise, R., "Implementation of a Two-Stream-Fan in the CIRSTEL System," PhD Thesis, University of Stellenbosch, 2006.

[14]Vanderplaats, G. N., *Numerical Optimization Techniques for Engineering Design*, 3rd edition, Vanderplaats Research & Development Inc., Colorado Springs, CO, 1999.

Author's queries:

Q1: Provide captions of all figures.
Q2: Confirm whether citation of Figure 2 is OK here.
Q3: Confirm whether citation of Figure 3 is OK here.
Q4: Confirm whether citation of Figure 4 is OK here.

THE SOLAR CHIMNEY AIR STANDARD THERMODYNAMIC CYCLE

T.W. von Backström* A.J. Gannon†

Received March 1999; Final version December 1999

The paper presents an air standard thermodynamic analysis for the solar chimney cycle. A solar chimney is a power plant in which air, heated under a glass-decked solar collector, escapes through a power generating turbine at the base of a chimney. Simple equations were derived for the cycle efficiency, power per unit mass flow and available turbine pressure drop, assuming ideal air as process gas and ideal reversible processes. The main conclusions were the following: the cycle efficiency is directly proportional to the chimney height; unlike the gas turbine cycle, there is no optimal pressure ratio (chimney height) for maximum specific power; the power per unit mass flow developed by the plant is directly proportional to the cycle efficiency and the temperature rise in the solar collector; the pressure drop across the turbine is proportional to the chimney height and the collector temperature rise. A design condition where the chimney exit temperature equals the collector inlet temperature was also proposed for initial calculations. The specific power of the plant is then approximately proportional to the square of the cycle efficiency. The analysis enables one to do initial sizing of a plant for a given required power.

Nomenclature

c	compression temperature ratio
c_p	specific heat [J/kgK]
D	chimney inside diameter [m]
g	gravitational acceleration [m/s^2]
h	enthalpy [J/kg]
K	pressure drop coefficient
m	mass flow [kg/s]
n	polytropic exponent
P	power [W]
p	pressure [Pa]
r	pressure ratio
T	absolute temperature [K]
t	cycle temperature ratio
V	velocity [m/s]
z	altitude [m]
Δ	change in value
γ	specific heat ratio
η	cycle efficiency
ρ	density [kg/m^3]

Subscripts

c	chimney base
d	design
opt	optimum
t	turbine
te	turbine exit
1	gas turbine cycle inlet
2	combustor (collector) inlet
3	turbine inlet
4	gas turbine (solar chimney) exit
23	between 2 and 3

Superscripts

*	normalized value
'	idealised value

*Department of Mechanical Engineering, University of Stellenbosch, Private Bag X1, Matieland, 7602 South Africa

†Department of Mechanical Engineering, University of Stellenbosch

Introduction

A solar chimney power plant consists of a large area covered by glass or translucent plastic sheets to collect solar energy. A central, high chimney, containing a power generating turbine at its base, allows the hot air to escape. Haaf *et al.*[1] and Haaf[2] discussed the operation of a prototype solar chimney plant.

The thermodynamic processes occurring in a solar chimney could be presented as a thermodynamic cycle. Air standard cycles are simplified thermodynamic cycles that are useful in the understanding of the real cycles that they simulate. They are so named because their working fluid is assumed to be air behaving as perfect gas. Their analytical nature serves to point out the main relationships between variables, and the most important trends in the way they affect each other. The results obtained from air standard analyses are intended to render limiting (not realistic) values of variables such as efficiency and specific power. Extended analyses including pressure losses, component efficiencies, such as the solar

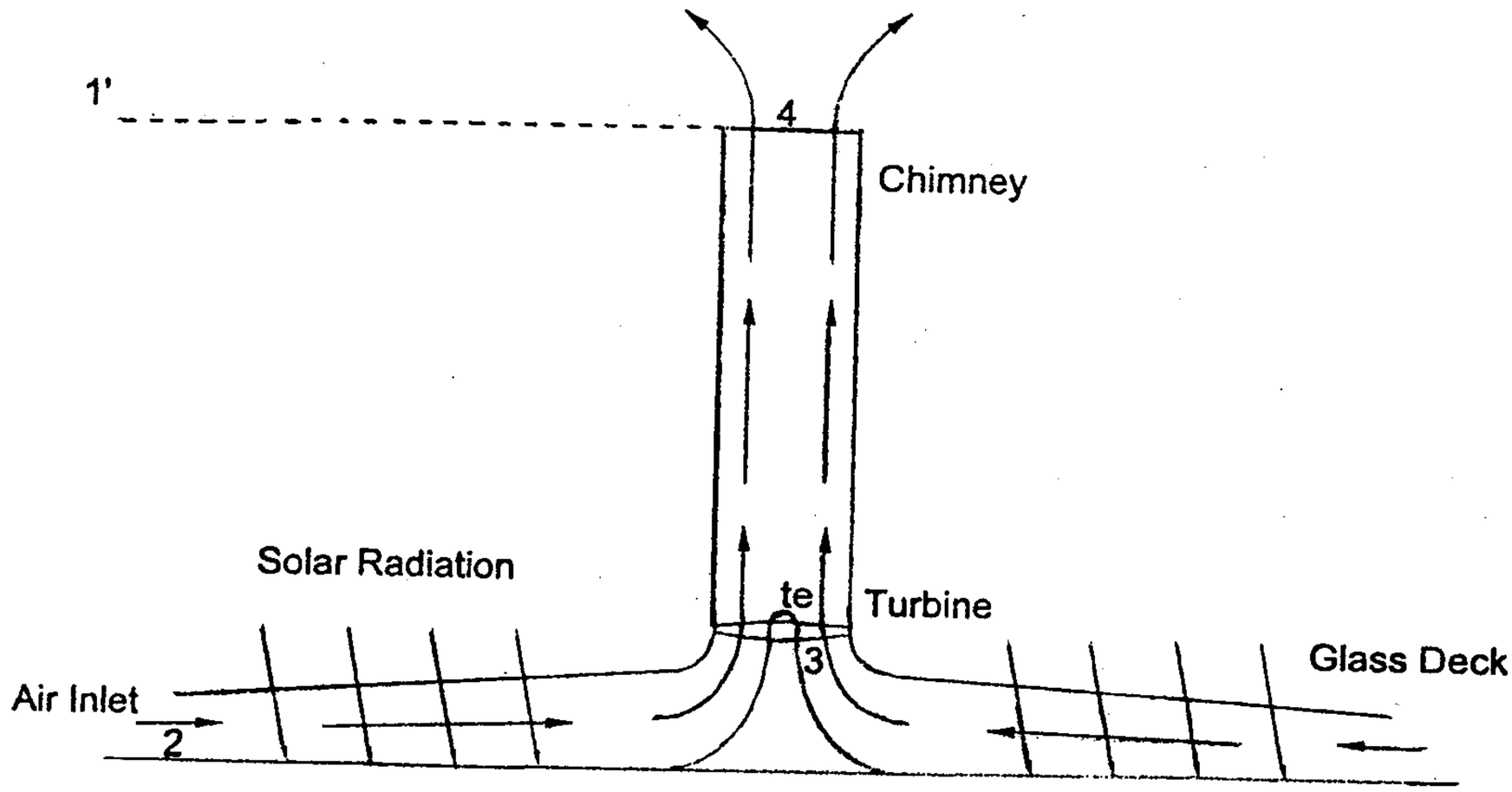

Figure 1 Schematic layout of solar chimney power plant

collector efficiency, and variable air properties, are beyond the scope of an air standard analysis and will be published elsewhere.

Many investigators, for example Wilson,[3] Cohen *et al.*,[4] Oates[5] and Archer & Saarlas,[6] have found it instructive to develop air standard cycles for gas turbine and other thermodynamic cycles. Some aspects of the thermodynamics of the solar chimney cycle have been investigated, for example, by Schlaich[7] and Stephan *et al.*[8] but a complete air standard cycle analysis for the solar chimney could not be found.

Objectives of the study

The objectives of this report are as follows:

- To develop a solar chimney air standard cycle
- To use the models to determine the existence of optima if any
- To determine the efficiency potential of the cycle
- To determine the power generating potential of the cycle
- To determine the available turbine pressure drop of the cycle
- To investigate in principle what cycle modifications are necessary and feasible

Assumptions for air standard analyses

The usual assumptions for air standard cycles are as follows:

- The working fluid is dry air, considered as a constant composition perfect gas throughout, with constant specific heat
- The mass flow through the system is constant
- Compression and expansion processes are adiabatic and reversible (isentropic)
- The change in kinetic energy of the air between inlet and exit of each component is negligible
- There are no stagnation pressure drops in the combustor or connecting ducts and passages
- Inlet and exit atmospheric conditions are identical
- The only heat flow is the net heat flow into the air in the system

The solar chimney as a gas turbine

The first observation is that the solar chimney cycle is fundamentally a gas turbine (Joule or Brayton) cycle. Let us consider the gas turbine air standard cycle. The four processes are isentropic compression, constant pressure heat addition, isentropic expansion and constant pressure heat removal.

In a standard gas turbine cycle the inlet and exhaust environmental conditions are assumed to be identical, and the only thermodynamic function of the surrounding air is to complete the cycle by cooling the exhaust

air back to the inlet air temperature. In a solar chimney, however, the exhaust is at the altitude of the chimney top, and the atmosphere has the additional function of recompressing the exhaust air to the ground inlet conditions. This compression is not necessarily isentropic, but can generally be approximated by a polytropic process of the form $p/\rho^n = \text{constant}$, with p and ρ equal to pressure and density, and n some exponent that is not necessarily equal to the specific heat ratio γ. However, Lenschow[9] states that when the earth's surface is warmer than the overlying air or when the wind is moderately strong, efficient vertical mixing occurs in the convective atmospheric boundary layer. If no clouds are present this mixing results in a nearly adiabatic lapse rate through most of this turbulent layer. These may indeed be the prevalent atmospheric conditions in desert areas where the solar chimney plant are likely to be built. For the present analysis we shall assume an adiabatic lapse rate.

We shall first look at the simulation of the solar chimney cycle by a standard gas turbine air cycle where the chimney is eliminated and an isentropic compressor driven by the turbine is added. To better simulate the environmental conditions of the solar chimney plant we assume that the gas turbine plant is situated at the physically impractical altitude of the chimney top. The pressure ratio is chosen to be equal to the ratio of ground level atmospheric pressure to atmospheric pressure at the solar chimney top. The gas turbine then has the same cycle pressure ratio as the solar chimney plant it simulates. Such a real gas turbine solar concept would have other major practical disadvantages, such as the collector pressure being higher than local atmospheric (at chimney top altitude), and the huge amount of power to be transmitted between turbine and compressor. The low temperature solar gas turbine cycle will however serve as a useful benchmark for the solar chimney cycle.

Air standard analysis of solar powered gas turbine cycle

The T-s diagram in Figure 2 shows the cycle and the numbering used for the conditions between the processes in the cycle. The analysis below follows Cohen *et al.*[4] and Archer & Saarlas.[6] The definitions below are used to simplify the writing of the equations:

Cycle pressure ratio:

$$r = p_2/p_1 = p_3/p_4$$

Compression temperature ratio:

$$c = T_2/T_1 = r^{(\gamma-1)/\gamma}$$

The cycle efficiency is defined as the turbine output power divided by the thermal power transferred to the air in the solar collector. For the assumptions and conditions mentioned above it can be shown that the following holds for the efficiency:

Cycle efficiency:

$$\eta = 1 - 1/c = 1 - 1/r^{(\gamma-1)/\gamma}$$

This is a very simple but important relationship, especially for low temperature ratio ideal cycles. It shows that the plant cycle efficiency is a function of pressure ratio only and not of cycle temperature ratio, t, defined below.

The cycle temperature ratio is:

$$t = T_3/T_1 = (T_2 + \Delta T_{23})/T_1$$

Here ΔT_{23} is the temperature rise in the collector, T_2 is the compressor exit temperature.

As shown by Cohen *et al.*[4] the specific power of an ideal gas turbine, as normalised with T_1 in terms of t and c is:

$$P_1* = P_{\text{shaft}}/(m\, c_p\, T) = \{(t/c) - 1\}(c - 1)$$

The equation above implies that the specific power depends on pressure ratio as well as collector temperature rise (or power input per unit mass flow). It is clear that the specific power increases with plant temperature ratio (or collector temperature rise), but the effect of compression ratio cannot be seen just by inspection. The significance of the specific power is that the size and capital costs of a plant are determined largely by the mass flow through it. For any given value of t the relationship above can be differentiated with respect to c and equated to zero. The result is:

$$c_{opt} = \sqrt{t}$$

The value of the optimum specific power is then:

$$P_1*_{opt} = \{(t/c_{opt}) - 1\}(c_{opt} - 1) = (t/\sqrt{t} - 1)(\sqrt{t} - 1) = (\sqrt{t} - 1)^2$$

As pointed out by Cohen *et al.*[4] this optimum occurs when the turbine and compressor exit temperatures are equal, i.e. when $T_2 = T_4$. The optimum specific power can also be expressed in terms of the optimal cycle pressure ratio:

$$P_1*_{opt} = (c_{opt} - 1)^2$$

The general implication of the two equations for optimal power output is then that when an optimum combination of cycle temperature and pressure ratio is chosen, the specific power can be expressed as a function of one of them alone. Combinations off the optimal will progressively reduce the specific power output compared to the optimum as they deviate from it.

For a low temperature gas turbine air standard cycle simulating a solar chimney cycle the most important conclusions are:

- Cycle efficiency depends on cycle pressure ratio only
- For each cycle temperature ratio there is an optimal pressure ratio for maximum power per unit mass flow

Air standard analysis of solar chimney cycle

The analysis of the solar chimney cycle proceeds largely as for the gas turbine cycle except for the following:

- The compression process does not occur in the system, but in the environment, as the air descends. We have pointed out that isentropic compression may be a realistic process in desert conditions. However, we shall not enforce that condition strictly during the analysis.
- Any reference in the analysis to the compression inlet temperature T1 will be avoided, because this is a variable temperature determined by the point where the constant pressure cooling line from point 4 intersects the polytropic (not isentropic) compression line to point 2. See Figure 3. Use will be made however of the point 1', the intersection between the constant pressure line through point 4 and the isentropic line through point 2.

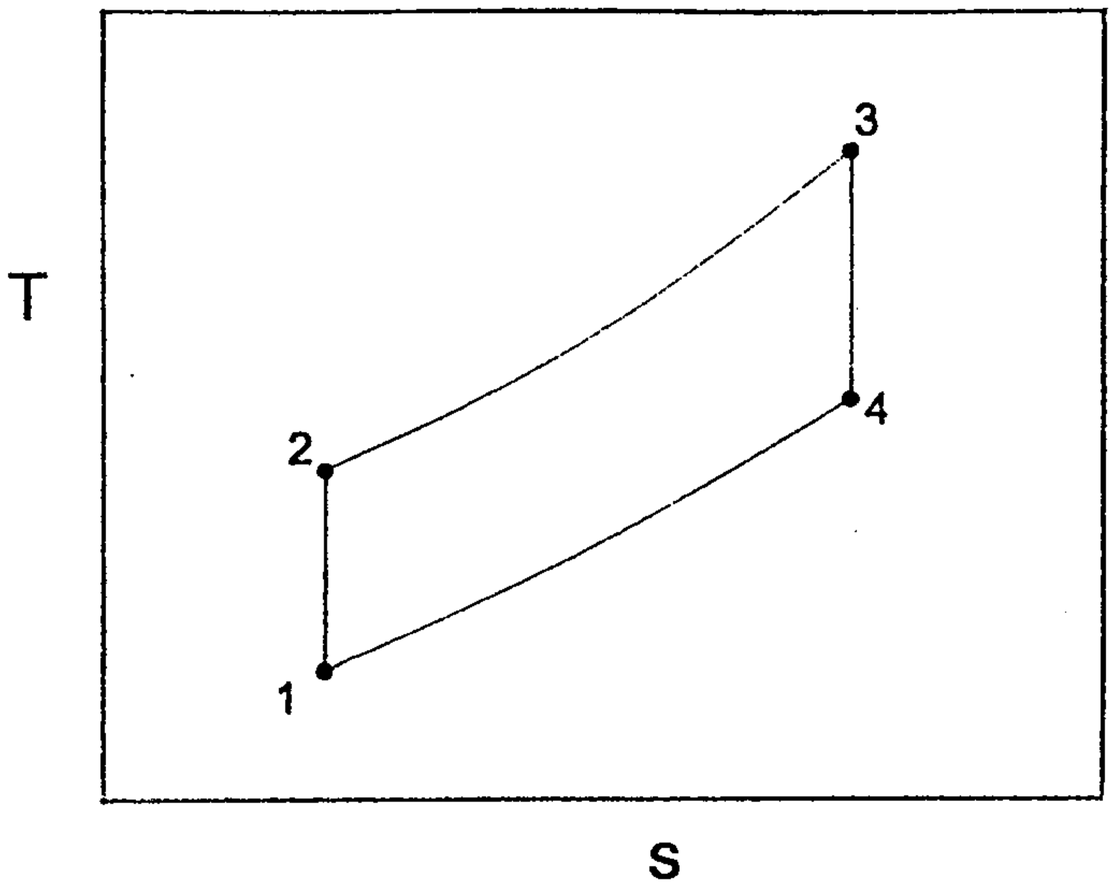

Figure 2 Temperature-entropy diagram for gas turbine air standard cycle

A convenient reference temperature in the cycle is the collector inlet temperature, T_2, since it is the ground level environmental temperature.

As before, the cycle efficiency is:

η = (Shaft power out) / (Solar power in)

The solar power input is:

$P_{23} = m\ c_p\ (T_3 - T_2)$

The shaft power out is:

$P_{\text{shaft}} = m\ c_p\ (T_3 - T_4) - m\ c_p\ (T_2 - T_1')$

Why the second term, $m\ c_p\ (T_2 - T_1')$ must be subtracted for the solar chimney cycle is explained in the following paragraphs.

The power that could in principle be extracted from the flow by an ideal turbine as it expands from the collector exit pressure, p_3 to the chimney exit pressure, p_4, is $m\ c_p\ (T_3 - T_4)$, but not all of it is available as shaft power.

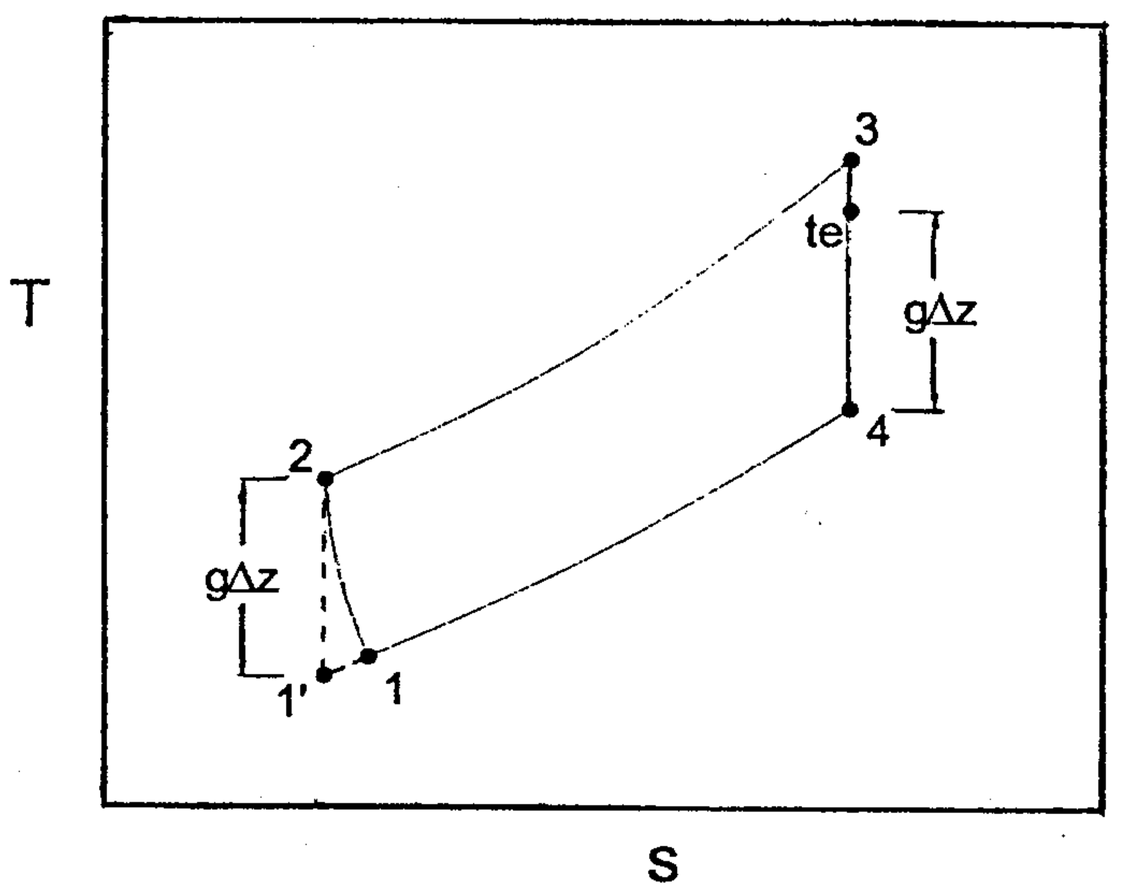

Figure 3 Temperature-entropy diagram for solar chimney air standard cycle

Consider the section of the chimney between the turbine exit and the chimney exit. The power required to lift the air in the chimney is $mg\Delta z$. There is no heat transfer or shaft work in this section of the chimney. Energy conservation then determines the enthalpy change in the chimney to be $\Delta h = c_p(T_4 - T_{te}) = -g\ \Delta z$.

The energy exchange is isentropic, following from the assumption of zero friction and heat transfer. The magnitude of Δh may also be evaluated by considering the air as it descends again in the atmosphere after having been cooled to T_1'. If heat transfer and frictional effects are small, the process is reversed and the enthalpy increases by the amount $\Delta h = g\,\Delta z = c_p(T_2 - T_1')$.

In the argument above we made some assumptions that will now be discussed. To construct the thermodynamic cycle one has to follow the flow from the chimney exit through the atmosphere where we assume that it is cooled down at constant pressure to the same entropy value as at the collector inlet. An isentropic compression between this point, at temperature T_1' and the collector inlet at temperature T_2 completes the cycle. If the process through which the air goes between the chimney exit and collector inlet follows some other path, determined by the atmospheric model, the idealized cycle may still be used for developing the analysis, as long as the imaginary temperature T_1' is factored out during the analysis. This may be done because state point 1' describes a condition external to the solar chimney, and is merely a construct used to develop the air standard analysis.

Although the air standard gas turbine and solar chimney cycle T-s diagrams are similar, there are some differences. In the gas turbine cycle, energy is transferred from the turbine to the compressor as shaft work, that is, energy is extracted from the cycle by the turbine and reintroduced by the compressor. In the solar chimney cycle there is an internal exchange between enthalpy and geopotential energy in the chimney, and the process is reversed in the external environment. In spite of the differences the gas turbine air standard cycle analysis can be applied directly to the solar chimney cycle since similar enthalpy and entropy changes occur in the two air standard cycles.

In the solar chimney cycle the pressure ratio is defined in terms of the chimney exit and collector exit pressures:

$$r = p_3/p_4$$

and the compression temperature ratio is:

$$c = r^{(\gamma-1)/\gamma}$$

As for the gas turbine cycle the cycle efficiency is then:

$$\begin{aligned}\eta &= 1 - 1/c \\ &= (T_2 - T_1')/T_2\end{aligned}$$

Since:

$$\begin{aligned}c_p\,(T_2 - T_1') &= g\,\Delta z \\ \eta &= g\,\Delta z/(c_p T_2)\end{aligned}$$

The cycle efficiency of an ideal solar chimney plant is directly proportional to the chimney height, and inversely proportional to the collector inlet temperature. Schlaich[7] uses the definition above for the efficiency of the chimney only, and defines a plant efficiency that includes the solar collector heat losses.

The cycle temperature ratio is defined as with T_1', as discussed above:

$$t = T_3/T_1'$$

For the solar chimney cycle the specific power is normalized with respect to the collector inlet temperature, T_2:

$$\begin{aligned}P_2* &= P/(m\,c_p T_2) \\ &= m\,c_p\,(T_3 - T_4) - m\,c_p\,(T_2 - T_1')/(m\,c_p\,T_2) \\ &= (T_3 - T_4)/T_2 - (T_2 - T_1')/T_2 \\ &= (t/c)(1 - 1/c) - (1 - 1/c) \\ &= (t/c - 1)(1 - 1/c)\end{aligned}$$

It is tempting to differentiate this equation with respect to c for fixed t as for the gas turbine cycle, but for the solar chimney t does not remain constant when c changes, because T_1' decreases with altitude as chimney height (and c) increases. In other words t is a function of c:

$$\begin{aligned}t &= T_3/T_1' \\ &= (T_2 + \Delta T_{23})\,c/T_2 \\ &= c\,(1 + \Delta T_{23}/T_2)\end{aligned}$$

So:

$$P_2* = (\Delta T_{23}/T_2)(1 - 1/c)$$

If ΔT_{23} and T_2 are fixed, P_2* will be maximized by maximizing c (i.e. chimney height). There is then no optimum chimney height that maximizes specific power. Similarly, there is no optimum collector temperature rise that maximizes specific power for a fixed chimney height. Any increase in collector temperature rise will increase the specific power.

The specific power can be written in terms of η as follows:

$$P_2* = (\Delta T_{23}/T_2)\,\eta$$

The specific power can be written in terms of Δz as follows:

$$P_2* = (\Delta T_{23}/T_2)\,(g\,\Delta z/c_p T_2)$$

The power output of an ideal solar chimney plant is then:

$$\begin{aligned}P &= m\,c_p\,T_2 P_2* \\ &= m\,g\,\Delta z\,\Delta T_{23}/T_2\end{aligned}$$

The equation above shows that the specific power is proportional to the chimney height and the collector temperature rise, and inversely proportional to the collector inlet temperature. The required specific power can be obtained by any suitable combination of Δz or ΔT_{23}, or in other words by any suitable combination of chimney height and collector area. The choice will ultimately be determined by the relative costs of chimney and collector. Very high chimneys will be expensive, and may promote condensation in the chimney, and very large collectors will be expensive, and inefficient due to high radiation losses.

Table 1 gives the power per unit mass flow for various combinations of chimney height and collector temperature rise.

Table 1 Power per unit mass flow [kW/(tonne/s] for $T_2 = 303.2$ K

Δz [m] ⇓ ΔT_{23} [K] ⇒	5	10	15	20
500	81	162	243	323
1000	162	323	485	647
1500	243	485	728	970
2000	323	647	970	1294

The available pressure drop across the turbine may now be calculated. We define the available temperature and pressure ratio across the turbine as follows, where subscript "*te*" denotes turbine exit:

$t_t = T_3/T_{te}$

and:

$r_t = p_3/p_{te}$

The plant output power may be expressed as follows:

$$\begin{aligned} P &= m c_p (T_3 - T_{te}) \\ &= m c_p T_3 (1 - 1/t_t) = m\, g\, \Delta z\, \Delta T_{23}/T_2 \\ 1/t_t &= 1 - (g\, \Delta z/c_p\, T_2)\, \Delta T_{23}/(T_2 + \Delta T_{23}) \\ &= 1 - \eta\, (\Delta T_{23}/T_2)\,/\,\{1 + (\Delta T_{23}/T_2)\} \\ 1/r_t &= \left\{ \frac{[1 + (1-\eta)\,(\Delta T_{23}/T_2)]}{[1 + (\Delta T_{23}/T_2)]} \right\}^{\gamma(\gamma-1)} \\ \Delta p_t/p_3 &= (1 - 1/r_t) \\ &= 1 - \left\{ \frac{[1 + (1-\eta)\,(\Delta T_{23}/T_2)]}{[1 + (\Delta T_{23}/T_2)]} \right\}^{\gamma(\gamma-1)} \\ &= 1 - \{1 - \eta/[(1 + (T_2/\Delta T_{23}))]\}^{\gamma(\gamma-1)} \end{aligned}$$

The equation above was used to draw up Table 2.

Table 2 Available turbine pressure drop [Pa] for $T_2 = 303.2$ K and $p_3 = p_2 = 90$ kPa

Δz [m] ⇓ ΔT_{23} [K] ⇒	5	10	15	20
500	82	162	239	313
1000	164	323	477	626
1500	246	485	715	937
2000	329	646	952	1248

For incompressible flow we may assume that $P = Q_3 \Delta p_t$ where Q_3 is the volume flow m/ρ_3 at the turbine inlet. The available turbine pressure drop Δp_t is then:

$$\begin{aligned} \Delta p_t &= P\, \rho_3/m \\ &= (g\, \Delta z\, \Delta T_{23}/T_2)\, \rho_3 \\ &= (g\, \Delta z\, \Delta T_{23}/T_2)\, p_3/\{R\,(T_2 + \Delta T_{23})\} \\ &= \{p_3 \eta \gamma/(\gamma - 1)\}\,/\,(1 + T_2/\Delta T_{23}) \end{aligned}$$

When the available turbine pressure drop is calculated with this equation for $\Delta z = 2000$ m and $\Delta T_{23} = 20$ K, then $\Delta p_t = 1255$ Pa, which corresponds to within 0.5 % with the value in the table above. The incompressible approximation, which can also be derived as the first term binomial expansion of the compressible equation, is accurate enough for the present simple analysis.

Bearing in mind that $p_2 = p_3$ the available turbine pressure drop may also simply be written in terms of atmospheric ground level density ρ_2 as:

$\Delta p_t = \rho_2\, g\, \Delta z\, \Delta T_{23}/T_3$

Schlaich[7] gives a similar equation. This is as far as we can go when the system is considered to have no pressure losses.

Practical application of air standard analysis

It is useful in the application of the theory to make a few simple additional assumptions. Schlaich[7] points out that the maximum power that can be generated occurs when two thirds of the drop in total pressure in the system is across the turbine. It can easily be shown that this applies to any system with a fixed available pressure difference and a loss proportional to flow squared. So only two-thirds of the pressure drop is available to drive the turbine, and the power extraction is reduced by the same factor. The fact that a third of the pressure losses are associated with system losses may be used to calculate the optimum chimney draught velocity. Since the velocity in the chimney increases as the density decreases due to expansion across the turbine and with altitude in the chimney, we have to choose a reference station. As reference position we choose the velocity at the chimney base, before the turbine. The chimney exit loss referred to this position will be larger than 1.0, because of the chimney exit velocity is larger than the chimney base velocity.

$$\begin{aligned} K\, \rho_3\, V_c^2/2 &= \Delta p_t/3 \\ K\, V_c^2/2 &= (\Delta p_t/\rho_3)\,/3 = (1/3)\, P/m \\ V_c &= [2/(3K)]^{0.5}\, (P/m)^{0.5} \end{aligned}$$

To allow for all the effects, we assume a constant system loss coefficient referred to the chimney base velocity of $K = 2.0$.

Table 3 Maximum power chimney draught velocity [m/s] for $K = 2.0$ and $T_2 = 303.2$ K

Δz [m] ⇓ ΔT_{23} [K] ⇒	5	10	15	20
500	5.2	7.3	9.0	10.4
1000	7.3	10.4	12.7	14.7
1500	9.0	12.7	15.6	18.0
2000	10.4	14.7	18.0	20.8

Table 3 shows that for the chosen conditions the chimney base velocity for maximum power can be given approximately by:

$V_c = (\Delta T_{23}\, \Delta z/1000)^{0.5}$

The mass flow required for a 250 MW plant is calculated as follows below. (In this analysis we assume

the turbine efficiency to be 100%, but with an 80% turbine efficiency the output would be 200 MW.) The construction of a large plant of 200 MW is currently being considered.

$m_{250\text{MW}} = 250 \times 10^6 / \{(2/3)\, P/m\}$

Table 4 Mass flow [tonne/s] for 250 MW plant for $T_2 = 303.2$ K

Δz [m] ⇓ ΔT_{23} [K] ⇒	5	10	15	20
500	4636	2318	1545	1159
1000	2318	1159	773	580
1500	1545	773	515	386
2000	1159	580	386	290

The appropriate chimney diameter is calculated as follows:

$$\begin{aligned} m &= \rho\, A_c\, V_c \\ &= [p_2 / \{R(T_2 + \Delta T_{23})\}]\, (\pi/4)\, D^2 V \\ D^2 &= 4mR(T_2 + \Delta T_{23}) / (\pi p_2 V) \end{aligned}$$

Table 5 Chimney diameter [m] for 250 MW and $K = 2.0$ and $T_2 = 303.2$ K

Δz [m] ⇓ ΔT_{23} [K] ⇒	5	10	15	20
500	1058	634	471	383
1000	629	377	280	228
1500	464	278	207	168
2000	374	224	167	135

Tables 4 and 5 show that a 250 MW plant (with a 100% efficient turbine) designed for a temperature rise of 20 K and a chimney height, requires a chimney diameter of about 170 m.

A possible design condition

One of the disadvantages of the analysis so far is that it does not lead to any preferential solar collector temperature rise for a given chimney height or vice versa. A possible preferential combination of parameters is the one implied by $c = \sqrt{t}$. In the case of the solar chimney it is not an optimal combination in the sense that it maximizes the specific power. We propose to choose this combination as a basis for initial design. In recognition of this fact, the subscript "*d*" (for design) will be used instead of "*opt*".

The choice of a design condition with $cd = \sqrt{t}$ implies the following:

- Neither the collector size nor the chimney height will be extreme
- The chimney exit temperature, T_4, is equal to the solar collector inlet temperature, T_2
- The condition above means that such a cycle will not benefit from the introduction of a heat exchanger, using exit air to heat entry air
- Condensation in the chimney will be unlikely even if the air is saturated at the collector inlet, as the chimney exit condensation temperature will be only a few degrees below the collector inlet temperature due to the decrease in pressure in the chimney

We shall now derive the dependence of collector temperature rise on chimney height for the design conditions:

$$\begin{aligned} g\,\Delta z &= c_p\,(T_2 - T_1') \\ g\,\Delta z / c_p &= (c-1)\,T_1' \end{aligned}$$

But:

$$\Delta T_{23} = (t-c)\,T_1'$$

and:

$$\begin{aligned} (\Delta T_{23})_d &= (c^2 - c)\,T_1' \\ &= \{(c-1)\,T_1'\}\,c \\ &= (g\,\Delta z/c_p)\,T_2/T_1' \\ &= (g\,\Delta z/c_p)\,T_2/(T_2 - g\,\Delta z/c_p) \\ &= T_2/\{c_p T_2/(g\,\Delta z) - 1\} \\ (\Delta T_{23})_d/T_2 &= 1/\{c_p T_2/(g\,\Delta z) - 1\} \end{aligned}$$

The equation above gives the design value of collector temperature rise for any chosen chimney height.

Since $g = 9.81 \approx 10$ m/s^2 and $c_p = 1005 \approx 1000$ J/kgK, the design temperature rise in the collector in degrees K is about 1/100 times the chimney height in metres. It is quite likely that the design temperature rise of about 15 K for a 1500 m high chimney will be exceeded in practice.

Table 6 Design value of collector temperature rise versus chimney height for $T_2 = 303.2$ K

Δz [m]	500	1000	1500	2000
$(\Delta T_{23})_d$ [K]	5.0	10.1	15.4	20.9

If the collector temperature rise is fixed, the design value of chimney height can be found by inverting the equation given above:

$$(\Delta z)_d = (c_p T_2/g) / (1 + T_2/\Delta T_{23})$$

Table 7 reflects the dependence of design chimney height on collector temperature rise.

Table 7 Design value of chimney height versus collector temperature rise for $T_2 = 303.2$ K

ΔT_{23} [K]	5	10	15	20
Δz_d [m]	504	992	1464	1922

The implications of the chosen design condition on the specific power will be derived below.

$$\begin{aligned} P_2* &= (t/c)(1 - 1/c) - (1 - 1/c) \\ &= \{(t/c) - 1\}(1 - 1/c) \\ P_{2*d} &= (c_d{}^2/c_d - 1)(1 - 1/c_d) \\ &= c_d\,(1 - 1/c_d{}^2) \\ &= \eta_d{}^2/(1 - \eta_d) \\ &\approx \eta_d{}^2 \end{aligned}$$

The equation above draws the attention again to the extreme importance of cycle efficiency and chimney height in determining the plant power per unit mass flow.

The power per unit mass flow is then:

$P/m = c_p T_2 {\eta_d}^2 / (1 - \eta_d)$

and the mass flow per unit power is:

$m/P = (1 - \eta_d) / \left(c_p T_2 {\eta_d}^2\right)$

For a 250 MW plant and a turbine efficiency of 100 % the required mass flow is:

$m_{250} = \left(250 \times 10^6\right)(1 - \eta_d) / \left(c_p T_2 {\eta_d}^2\right)$

Example values are given in Table 8.

Table 8 Various design variables for $T_2 = 303.2$ K and $K = 2.0$ and $\eta_t = 0.80$

Δz [m]	500	1000	1500	2000
$(\Delta T_{23})_d$ [K]	5.0	10.1	15.4	20.9
η_d (%)	1.61	3.22	4.83	6.44
P/m [kW/(tonne/s)]	80.2	326	747	1350
m [tonne/s] / 200 MW	4673	1149	502	278
Chimney velocity [m/s]	5.2	10.4	15.8	21.2
Chimney diameter [m]	1060	375	203	131

Table 8 shows that a 250 MW plant with $T_4 = T_2$ would require a chimney diameter of about 200 m.

Conclusions

An air standard analysis has been done for a solar chimney cycle. The main conclusions are listed below. The conclusions should be read in the context of the assumptions listed at the beginning.

- The cycle efficiency is $\eta = g\,\Delta z / c_p T_2$. It is proportional to chimney height and inversely proportional to collector inlet temperature. Once the chimney is built, the cycle efficiency is virtually cast in concrete.

- There is no optimum combination of cycle pressure ratio and cycle temperature ratio for maximum specific power as in gas turbine cycles. It means that there is no thermodynamic optimum combination of collector size and chimney height.

- The power developed by the plant is $P = m\,g\,\Delta z\,\Delta T_{23}/T_2$. It is proportional to the mass flow, chimney height and collector temperature rise, and inversely proportional to collector inlet temperature.

- The available pressure drop across the turbine is $\Delta p_t = \rho_3 g\,\Delta z \Delta T_{23}/T_2$. It is proportional to the turbine inlet density, to chimney height and collector temperature rise and inversely proportional to collector inlet temperature.

- By assuming a value of a pressure loss coefficient, $K = 2$, and that the maximum power that can be extracted occurs when two-thirds of the pressure drop is across the turbine, the required chimney velocity can be derived as $V_c = \sqrt{(1/3)}\,\sqrt{(P/m)}$.

- An initial design condition where the chimney exit temperature equals the collector inlet temperature is proposed for initial calculations. These conditions enable one to do initial sizing of a plant for a given required power.

- For the proposed design cycle a heat exchanger between chimney exit and collector inlet would not improve specific power (apart from being impractical).

- For the design cycle the maximum power per unit mass flow is approximately proportional to cycle efficiency squared. This implies that although the input energy costs nothing, the cycle efficiency exerts a strong influence through its coupling to specific power and plant capital costs.

- The air standard cycle analysis seems worth while but should be extended with the incorporation of losses. A more realistic model may modify some of the conclusions based on the air standard cycle.

References

1. Haaf W, Friedrich K, Mayr G & Schlaich J. Solar Chimneys, Part I: Principle and construction of the pilot plant in Manzanares. *International Journal of Solar Energy*, **2**, pp.3–20, 1983/1984.

2. Haaf W. Solar Chimneys, Part II: Preliminary test results from the Manzanares pilot plant. *International Journal of Solar Energy*, *2*, pp.141–161, 1984/1983.

3. Wilson DG. *The design of high efficiency turbomachines and gas turbines.* MIT Press, Cambridge, MA, 1984.

4. Cohen H, Rogers GFC Saravanamuttoo HIH. *Gas turbine theory.* 3rd edn. Longman Scientific and Technical, 1987.

5. Oates GC. *Aerothermodynamics of gas turbine and rocket propulsion.* Revised and enlarged. AIAA Education series, Washington, 1988.

6. Archer RD & Saarlas M. *An introduction to aerospace propulsion.* Prentice Hall, New Jersey, 1996.

7. Schlaich J. *The solar chimney, electricity from the sun.* Edition Axel Menges, Stuttgart, 1995.

8. Stephan K, Schaber K, Körber J, Tamm M & Kim YK. *Expert opinion on the thermodynamic modelling of solar chimneys.* Institut für Technische Thermodynamik und Thermische Verfahrenstechnik, University of Stuttgart, 1995.

9. Lenschow DH. Atmospheric flows. In: Johnson RW (ed.). *The handbook of fluid dynamics.* Springer-Verlag, Heidelberg, 1998.

Solar Chimney Cycle Analysis With System Loss and Solar Collector Performance

Anthony J. Gannon

Theodor W. von Backström
e-mail: twvb@ing.sun.ac.za

Department of Mechanical Engineering,
University of Stellenbosch,
Private Bag X1,
Matieland 7602, South Africa

An ideal air standard cycle analysis of the solar chimney power plant gives the limiting performance, ideal efficiencies and relationships between main variables. The present paper includes chimney friction, system, turbine and exit kinetic energy losses in the analysis. A simple model of the solar collector is used to include the coupling of the mass flow and temperature rise in the solar collector. The method is used to predict the performance and operating range of a large-scale plant. The solar chimney model is verified by comparing the simulation of a small-scale plant with experimental data.
[S0199-6231(00)00503-7]

Introduction

The solar chimney is a simple renewable energy source consisting of three main components, a solar collector, chimney and turbine. Air is heated by the greenhouse effect under the glass collector. This hot air, less dense than the surroundings, rises up the chimney at the center of the collector. At the base of the chimney an electricity generating turbine is driven by the rising air. Economic and feasibility studies have been performed [1,2].

Ideal Air Standard Cycle Analysis

There have been various analyses of the solar chimney [2,3], and an ideal air standard cycle analysis [4], included here for clarity (Fig. 1). While simple it is rigorous and determines a cycle's limiting efficiency as all components are assumed to be ideal and all processes loss free. Other assumptions are: the working fluid is dry air, considered an ideal gas with constant specific heat capacity. The only heat flow in the system is the net gain by the air in the collector. The mass flow in the system is constant and inlet and outlet atmospheric conditions are ideal.

Figure 2 shows the solar chimney cycle, while Table 1 clarifies the processes and lists the similarities to the gas turbine cycle. These similarities greatly simplify the analysis as existing gas turbine theory can be used [5]. The aim of the analysis is to find a relationship between the plant performance and variables such as chimney height and collector temperature rise.

The plant thermal efficiency is defined as,

$$\eta = \frac{\text{Shaft Power Out}}{\text{Solar Power In}} \tag{1}$$

where the denominator, the available solar power is,

$$P_{solar} = \dot{m} c_p (T_3 - T_2) = \dot{m} c_p \Delta T_{23} \tag{2}$$

Not all of the power from expansion 3–4 is available as some of it is required to lift the air up the chimney (3te-4) [6],

$$P_{3-4} = \dot{m} c_p (T_3 - T_4) \tag{3}$$

$$P_{3te\text{-}4} = \dot{m} c_p (T_{3te} - T_4) = \dot{m} \Delta h = \dot{m} g \Delta z \tag{4}$$

and an adiabatic lapse rate [7]

$$-\frac{dT}{dz} = \frac{g}{c_p} \tag{5}$$

the enthalpy reduction from 3te-4 is the same as from 1′–2

$$\Delta h = g \Delta z = c_p (T_2 - T_{1'}) \tag{6}$$

Resulting in a shaft power output of,

$$P_{shaft} = \dot{m} c_p (T_3 - T_4) - \dot{m} c_p (T_2 - T_{1'}) \tag{7}$$

Substituting Eqs. (2) and (7), the ratio, $c = T_2/T_{1'} = T_3/T_4$ for the ideal isentropic gas process and the relation of Eq. (6) all into (1) the ideal plant efficiency is written as,

$$\eta = 1 - \frac{1}{c} = \frac{g \Delta z}{c_p T_2} \tag{8}$$

In a similar way the specific power normalized with respect to the mass flow and inlet temperature T_2 is defined as,

$$P_2^* = \frac{P_{shaft}}{\dot{m} c_p T_2} \tag{9}$$

where substitution of c leads to the intermediate step of,

$$P_2^* = \left\{1 - \frac{1}{c}\right\} \left\{\frac{T_3 - T_2}{T_2}\right\} \tag{10}$$

and using Eq. (6) leads to,

$$P_2^* = \left\{\frac{g \Delta z}{c_p T_2}\right\} \left\{\frac{\Delta T_{23}}{T_2}\right\} \tag{11}$$

Equations (8) and (11) represent the upper limits of the solar chimney performance as they are derived from the ideal cycle analysis. The efficiency (Eq. (8)) is proportional to chimney

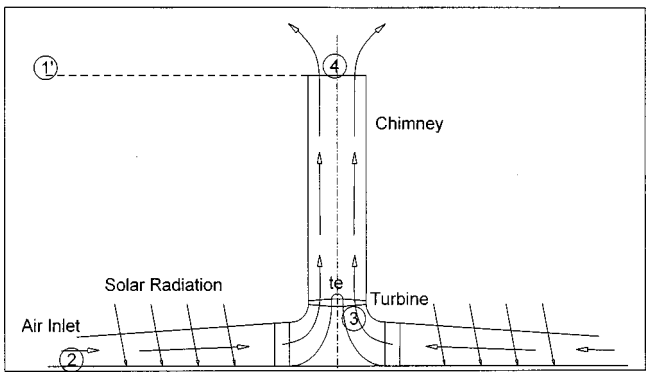

Fig. 1 Solar chimney schematic

Contributed by the Solar Energy Division of THE AMERICAN SOCIETY OF MECHANICAL ENGINEERS for publication in the ASME JOURNAL OF SOLAR ENERGY ENGINEERING. Manuscript received by the ASME Solar Energy Division, Dec. 1999; final revision, Jul. 2000. Associate Technical Editor: T. Mancini.

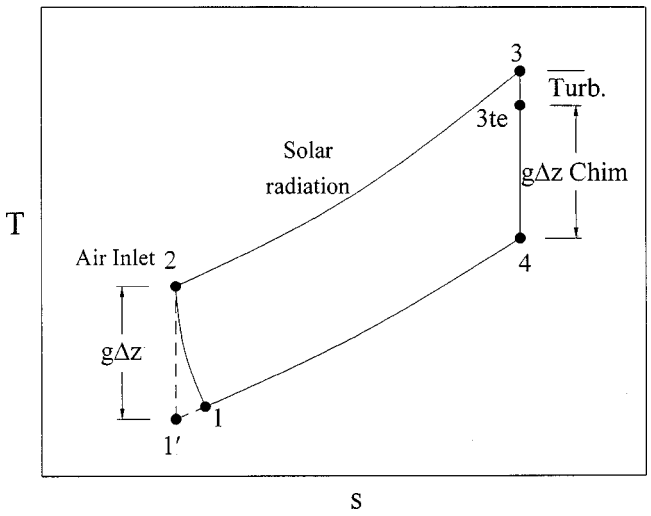

Fig. 2 Temperature-entropy diagram for air standard cycle analysis

Table 1 Comparison between solar chimney and gas turbine cycle

Process no.	Gas turbine	Solar chimney
1–2	Compressor	Atmospheric lapse rate
2–3	Combustor	Solar collector
3–4	Turbine	Turbine and chimney

Table 2 Efficiencies and specific power output from ideal air standard cycle analysis

Δz [m] ⇓	η [%] ⇓	$P_2^*(\times 10^3)$ for various ΔT_{23}				
		5	10	15	20	30
1500	4.83	0.796	1.593	2.389	3.185	4.778
1000	3.22	0.531	1.062	1.593	2.124	3.185
500	1.61	0.265	0.531	0.796	1.062	1.593

height and inversely so to inlet temperature T_2. The inlet conditions are dependent on climatic conditions and so plant efficiency is controlled solely by the chimney height. Assuming $T_2 = 303.2$ K, the following efficiencies and specific powers are the upper limits for the given chimney heights.

Inclusion of Losses

In the real plant losses will occur in each of the components. Two assumptions are made, the first that the total pressure remains constant under the glass collector as air is likely to leak in. Practically this would result in a lower temperature rise, ΔT_{23}. The second is that all kinetic energy is lost at the exit as it would be difficult to construct a diffuser at the top of the chimney. The temperature entropy diagram is modified to include component losses.

Figure 3 shows the 3 main components of the expansion process, namely the turbine, chimney and kinetic energy loss at the exit. The turbine efficiency is defined as,

$$\eta_{turb} = \frac{T_{03} - T_{03te}}{T_{03} - T_{03te'}} \tag{12}$$

Apart from the work required to lift the air up the chimney further work is required to overcome the internal friction of the chimney mainly due to internal bracing and to a lesser extent wall friction. Represented by k, this is expressed as a fraction of the exit kinetic energy,

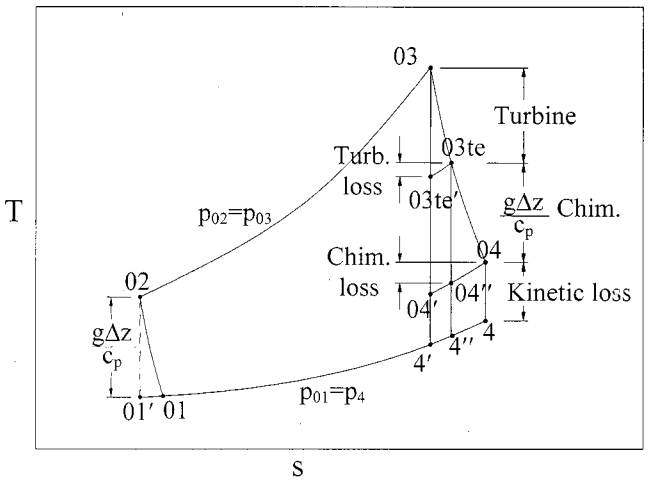

Fig. 3 Temperature-entropy diagram for air standard cycle analysis with system losses

$$k = \frac{T_{04} - T''_{04}}{T_{04} - T_4} \tag{13}$$

In general the exit velocity is not uniform and using the mean is simpler. Calculation of the exit kinetic energy using the mean is not correct so a factor, α, is introduced allowing the mean to be used but giving the correct exit kinetic energy. In the following definition of α, over bars denote the mean values.

$$\alpha = \frac{KE}{\overline{KE}} = \frac{\int (\rho C_{z4}) \frac{1}{2} C_{z4}^2 dA}{(\rho \overline{C_{z4}}) \frac{1}{2} \overline{C_{z4}^2} A} \tag{14}$$

The entire expansion efficiency is defined as

$$\eta_{\exp} = \frac{(T_{03} - T_4)}{(T_{03} - T'_4)} \tag{15}$$

Efficiency and Specific Power Output. Using the definition of efficiency from Eq. (1) and through inspection of Fig. 3 to take kinetic energy loss (04-4) into account plant efficiency is,

$$\eta = \frac{\eta_{\exp}(T_{03} - T'_4) - (T_{03te} - T_{04}) - (T_{04} - T_4)}{(T_{03} - T_{02})} \tag{16}$$

from which the following expressions for efficiency and specific power can be written,

$$\eta = \left(\frac{g\Delta z}{c_p T_{02}}\right)\left[\frac{\eta_{\exp}(T_{02} + \Delta T_{23}) - T_{02}}{\Delta T_{23}}\right] - \alpha \frac{\overline{C_{z4}^2}}{2 c_p \Delta T_{23}} \tag{17}$$

$$P_2^* = \left(\frac{g\Delta z}{c_p T_{02}}\right)\left(\frac{\eta_{\exp}(T_{02} + \Delta T_{23}) - T_{02}}{T_{02}}\right) - \alpha \frac{\overline{C_{z4}^2}}{2 c_p T_{02}} \tag{18}$$

When $\eta_{\exp} = 1$ and $C_{z4} = 0$ then Eqs. (17) and (18) simplify to Eqs. (8) and (11) respectively.

Operating Range. The solar chimney can operate between two extremes of zero power output. The first is simply when there is a zero turbine temperature drop resulting in a large mass flow. The second is when there is a near zero mass flow caused by a high turbine temperature drop. As before this is illustrated in a temperature entropy diagram showing the condition (Fig. 4).

The limiting turbine temperature drop is defined as,

$$\Delta T_{turb\ \lim} = (T_{03} - T'_{03te}) = \frac{(T_{03} - T_4) - (T_{03te} - T_4)}{\eta_{turb}} \tag{19}$$

By making the following substitutions into Eq. (19),

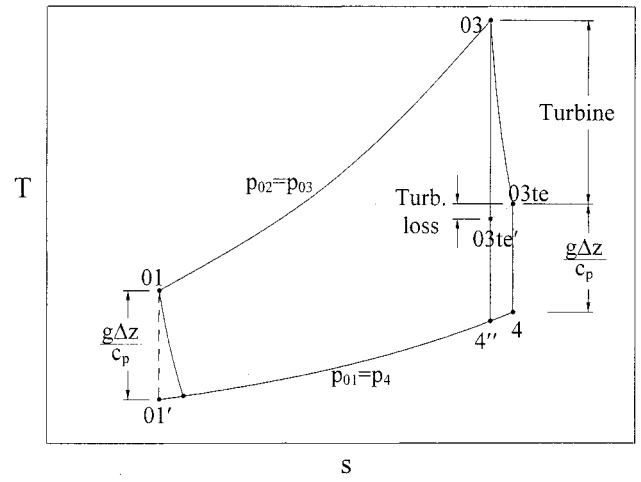

Fig. 4 Temperature-entropy diagram for air standard cycle analysis with system losses for limiting turbine temperature drop

$$T_4 = T_{03te}(T'_4/T'_{03te})$$
$$T_{03te} = T_{03} - \eta_{turb}(T_{03} - T'_{03te}) = T_{03} - \eta_{turb}(\Delta T_{turb\ \lim}) \quad (20)$$
$$T'_{03te} = T_{03} - (T_{03} - T'_{03te}) = T_{03} - \Delta T_{turb\ \lim}$$
$$\frac{g\Delta z}{c_p} = T_{03te} - T_4$$

an implicit expression for $\Delta T_{turb\ \lim}$ results,

$$\Delta T_{turb\ \lim} = \frac{1}{\eta_{turb}}\left[\left(T_{03} - T'_4 \frac{T_{03} - \eta_{turb}\Delta T_{turb\ \lim}}{T_{03} - \Delta T_{turb\ \lim}}\right) - \frac{g\Delta z}{c_p}\right] \quad (21)$$

Equation (21) can be written in standard quadratic form with a, b and c being the standard coefficients. The physically realistic solution is,

$$\Delta T_{turb\ \lim} = \frac{-b - \sqrt{b^2 - 4ac}}{2a} \quad (22)$$

Output Power. The total output power is a function of the plant size, environmental conditions and a specified turbine temperature drop and is calculated by multiplying Eq. (18) as follows,

$$P = \dot{m} c_p T_{02} P_2^* \quad (23)$$

Inspection of Eqs. (18) and (23) shows that the exit velocity, C_{z4} and system mass flow are required. The mass flow is a function of chimney area and C_{z4} and ρ_4,

$$\dot{m} = \rho_4 C_{z4} A \quad (24)$$

For both C_{z4} and ρ_4, the exit temperature T_4 is required,

$$\rho_4 = \frac{p_4}{RT_4} \quad (25)$$

$$\overline{C_{z4}} = \sqrt{2c_p(T_{04} - T_4)/\alpha} \quad (26)$$

From Fig. 3 the following three temperature ratios can be written,

$$\frac{T_4}{T_{04}} = \frac{T'_4}{T'_{04}}; \quad \frac{T'_{04}}{T'_{03te}} = \frac{T''_{04}}{T_{03te}}; \quad T''_{04} = T_{04} - k(T_{04} - T_4); \quad (27)$$

Once again this leads to an implicit equation for T_4,

$$T_4 = \frac{T_{04}T'_4 T_{03te}}{T'_{03te}[T_{04} - k(T_{04} - T_4)]} \quad (28)$$

which can be re-written in standard quadratic form leading to the solution,

$$T_4 = \frac{-b + \sqrt{b^2 - 4ac}}{2a} \quad (29)$$

The exit pressure, p_4 is the last term needed and assuming an adiabatic atmospheric lapse rate it can be written as,

$$\frac{p_4}{p_{03}} = \frac{p_{01}}{p_{02}} = \left(\frac{T_{01}}{T_{02}}\right)^{\gamma/\gamma-1} \Rightarrow p_4 = p_{02}\left(1 - \left\{\frac{g\Delta z}{c_p T_{02}}\right\}\right)^{\gamma/\gamma-1} \quad (30)$$

Solar Collector Model

The last major component to be included in the analysis is the solar collector which supplies input heat to the system. In the collector there is a strong coupling between the mass flow and temperature rise of the air ($Q_{air} = mc_p\Delta T$). Previous analyses of the solar chimney have not taken this into account and use a gas turbine approach of plotting performance along lines of constant collector temperature rise, ΔT_{23}. A more useful result would be plant power output along lines of constant inlet radiation. These two approaches lead to very different predictions of design point operation as shown in Table. The collector model gives the relationship between G and Q_{air}.

Solar Collector Model. There are three basic assumptions used in the model and these are: 1) steady state conditions 2) No evaporation takes place under the collector and 3) the vertical temperature profile of the collector air is constant. Figure 5 shows the annular control volume used to find the net heat gain of the air through each section of the collector [8–10].

The following energy balance equation can be written to find the heat gain by the air in the control volume,

$$dH_{\dot{m}} = (dG - dG_{loss}) + (dQ_{loss} + dQ_{sto}) \quad (31)$$

This can be expanded by substituting the normal equations for radiation and convection loss to the atmosphere as well as conduction loss into the soil. The temperature rise through each control volume by the air is,

$$\frac{dT_{air}}{dr} = \frac{2\pi r}{\dot{m}c_p}\left[\tau_{in}e_{surf}G - \left\{\tau_{out}e_{surf}\sigma(T_{surf}^4 - T_{atm}^4) + h_{gli}(T_{air} - T_{gli}) + \frac{k_{gro}}{L_{gro}}(T_{surf} - T_{sto})\right\}\right] \quad (32)$$

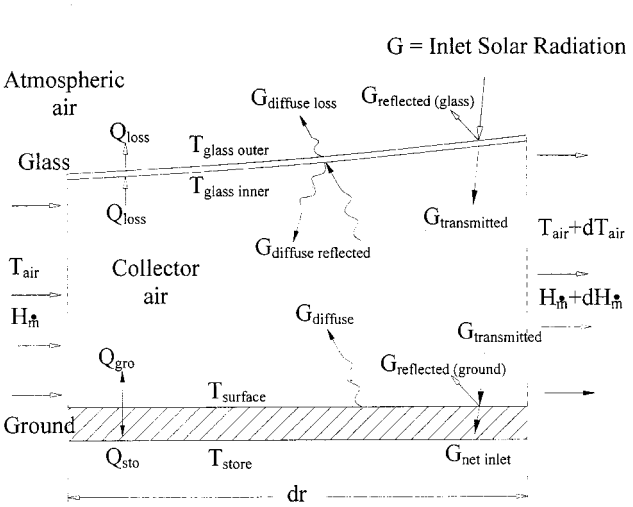

Fig. 5 Detail of control colume of solar collector showing nomenclature for temperatures, heat, mass and radiation flow

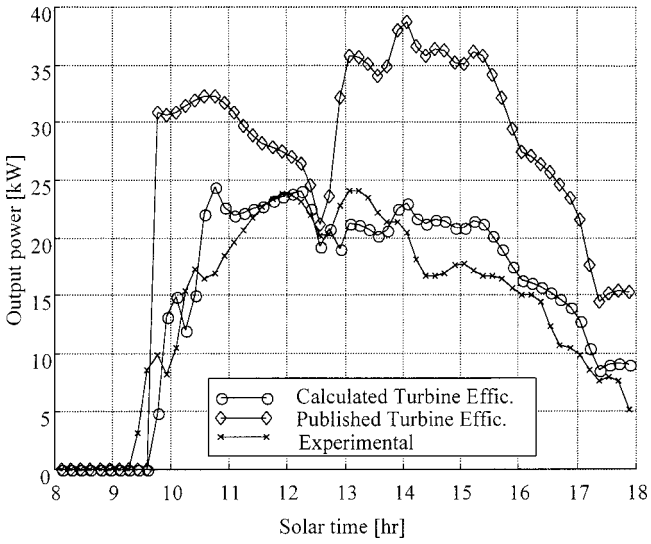

Fig. 6 Comparison of simulated and experimental results from Manzares, Spain

Three further heat flow equations, the ground surface (33), glass inner surface (34) and glass outer surface (35) are needed to calculate the temperatures for use in Eq. (32).

$$\tau_{in}e_{surf}G=\tau_{out}e_{surf}\sigma(T_{surf}^4-T_{atm}^4)+h_{surf}(T_{surf}-T_{air})+\frac{k_{gro}}{L_{gro}}(T_{surf}-T_{sto}) \quad (33)$$

$$h_{gli}(T_{air}-T_{gli})=\frac{k_{glass}}{L_{glass}}(T_{gli}-T_{glo}) \quad (34)$$

$$\frac{k_{glass}}{L_{glass}}(T_{gli}-T_{glo})=h_{glo}(T_{glo}-T_{atm}) \quad (35)$$

With the inlet conditions to the collector being known Eq. (32) being a one dimensional differential equation can be solved numerically. For a given mass flow the temperature rise ΔT_{23} can be found.

Manzanares Simulation

To verify the solar chimney model a small-scale plant is simulated [3] and the results compared with experimental readings. Assuming steady state conditions for the air is accurate but not so for the soil temperatures. A simple one dimensional finite difference time marching scheme was used to model the soil [8] and it was found to improve the transient simulation of the Manzanares plant significantly. The plant in Manzanares had a chimney of 194.6 m high, 10 m in diameter and a solar collector of radius 122 m. Figure 6 above compares simulated results and experimental results using the environmental data of [11] published for a sample day (02-09-82) where the maximum inlet radiation was 850 W/m^2.

It can be seen that there are two set of simulated results, the first is using the quoted turbine efficiency, assuming it stays constant. Inspection of the measured turbine pressure drop vs the power output shows that this is not the case and calculating the turbine efficiency improves the results. The simulation tends to overestimate the power output in the morning and afternoon, this is hoped to be improved by taking into account reflection due to the sun's low angle. The dip in midday output is thought to be due to incorrect turbine modeling. The power outputs are in the correct range and so the model can be used with reasonable certainty in predicting the power output of a full-scale plant.

Simulation of Full Scale Plant

The model developed is used to simulate a full scale solar chimney. Table 3 shows the size and inlet conditions used for the simulation. Values used for the various material constants can be found in [8] but these are similar to the nominal values found in most texts.

Power Output. Figure 7 shows that the plant power output at a certain inlet radiation level is not constant but can be varied by changing the turbine temperature drop. The two extreme conditions that result in zero mass flow can be clearly seen. It is also evident that there is a maximum power condition as shown. What is also indicated is a limiting power line, this is due to the maximum power output of the generator. It can also be seen that the design power can be reached at a reasonable inlet radiation level.

The reason for indicating the region to the left of the max power line as the 'ideal operating region' needs further discussion. At an inlet radiation of say 800 W/m^2 with power limited to 200 MW there are two possible operating points.

The first at a higher mass flow to the right of the maximum power line would be reducing power output by increasing the kinetic energy losses at the exit. The temperature in the solar collector would also be reduced thus reducing the effectiveness of any thermal storage.

The second point, to the left, is at a lower mass flow rate decreasing the power output by increasing the temperature and thus heat loss in the solar collector. As mentioned part of this ''loss'' is into the ground but this heat would be used later in the day as the air temperature cools and inlet radiation decreases. In practice the plant would probably be operate along the maximum power line until the limiting power was reached. The mass flow would then be limited to control the power output.

Turbine Requirements. To be able to generate power an efficient turbine is required and to design this accurate predictions

Table 3 Dimensions and inlet conditions

	Full-scale	Manzanares
Chimney diameter	160 m	10 m
Chimney height	1500 m	195 m
Chimney constant k	1	
Design power	200 MW	50 kW
Collector inlet press (p_2)	90 000 Pa	
Collector inlet temp. (T_2)	303.2 K	
Turbine efficiency	80%	
Exit constant α	1.1058	

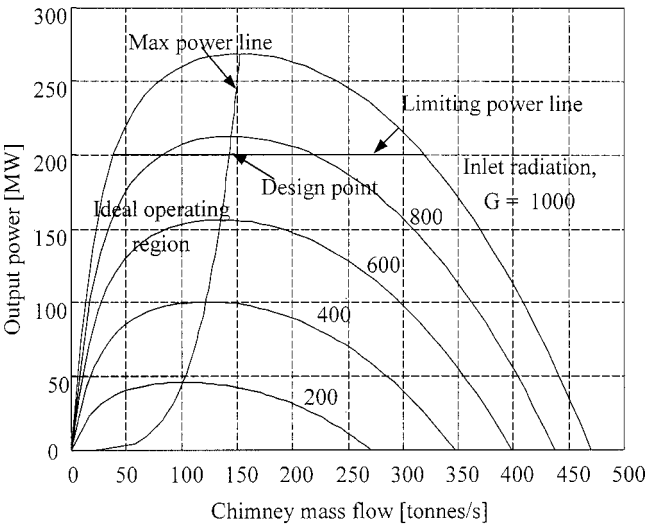

Fig. 7 Power output vs. mass flow along line of constant inlet radiation

Table 4 Turbine design point prediction

	Lines of constant radiation [W/m^2]	Lines of constant temperature [K]
ΔT_{23} [K]	37.4	24.01
ΔP_{turb} [Pa]	1597	749
Mass flow [t/s]	143.1	318.9

of mass flow and pressure drop are required. It is assumed that the turbine will operate along the maximum power line at lower inlet radiation levels and then to the left of this along the limiting power line at higher levels. In previous analyses of the solar chimney a graph similar to Fig. 7 has been produced but plotting power output along lines of constant temperature (the gas turbine approach as mentioned earlier). The difference in turbine operating predictions at the indicated design point using these two methods is shown in Table 4.

Conclusion

The ideal air standard cycle analysis while simple to perform is a powerful tool as it quickly allows the upper limits of a cycle's performance to be calculated. In the solar chimney project this is important so that initial feasibility of the plant can be quickly calculated. The inclusion of the main system losses of turbine efficiency, chimney friction and exit kinetic energy loss allow for more realistic predictions of plant power output to be found. The final step of the analysis is the inclusion of the solar collector and is important due to the strong coupling of mass flow and temperature drop.

Care must be taken when predicting the operating range of the solar chimney. Using a traditional approach, plotting power output along lines of constant power and not including the solar collector in the analysis could result in an inaccurate prediction of the operating region. Plotting the power output along lines of constant inlet radiation better represents the performance of the solar chimney, as it simulates the actual conditions better. Accurate prediction of the operating region will result in a more efficient turbine design. The analytical model developed showed good agreement with the experimental results of the small-scale plant built in Manzanares allowing it to be used reliably in the prediction of the output of a full-scale plant.

Nomenclature

Cycle Analysis

a = quadratic constant
A = area
b = quadratic constant
c = quadratic constant
c_p = specific heat capacity
C = velocity
g = gravitational constant
h = enthalpy
K = chimney loss coeff.
$\dot{m}$ = mass flow
KE = kinetic energy
p = pressure
P = power
R = gas constant
T = temperature
z = vertical height
α = kinetic energy coeff.
γ = gas constant
η = efficiency
ρ = density
Δ = difference

Indices

′ = isentropic process
* = normalized value
— = mean value
0 = stagnation property
1 = cycle start
2 = collector inlet
3 = turbine inlet
4 = chimney exit
exp = expansion
lim = limiting
solar = solar power
shaft = shaft power
te = turbine exit
turb = turbine
z = vertical

Solar Collector

E = emissivity
G = radiation
h = heat transfer coeff.
H = heat flow into air
K = conductivity
L = thickness
Q = heat flow in collector
r = collector radius
σ = Stefan-Boltzmann const.
τ = transmissivity

Indices

air = collector air
atm = atmospheric air
glass = glass properties
gli = glass inner surface
glo = glass outer surface
Gro = ground properties
in = inlet
loss = heat loss
out = outlet
sto = ground storage
surf = ground surface

References

[1] Trieb, F., Langniß, O., and Klaiß, H., 1997, ''Solar Electricity Generation—A Comparative View of Technologies, Costs and Environmental Impact,'' Sol. Energy, **59**, Nos. 1–3, pp. 89–99.
[2] Schlaich, J., 1995, ''The Solar Chimney: Electricity from the Sun,'' C. Maurer, Geislingen, Germany.
[3] Haaf, W., Friedrich, K., Mayr, G., and Schlaich, J., 1983, ''Solar Chimneys: Part I: Principle and Construction of the Pilot Plant in Manzanares,'' International Journal of Solar Energy, **2**, No. 1, pp. 3–20.
[4] Von Backström, T. W., and Gannon, A. J., 2000, ''The Solar Chimney Air Standard Cycle,'' South African Institution of Mechanical Engineering R&D Journal, **16**, March 2000, pp. 16–24.
[5] Cohen, H., Rogers, G. F. C., and Saravanamuttoo, H. I. H., 1996, *Gas Turbine Theory*, Fourth Edition, Addison Wesley Longman Limited, England, pp. 37–45.
[6] Von Backström, T. W., and Gannon, A. J., 2000, Compressible Flow Through Tall Chimneys, Proceedings of Solar 2000, Madison, Wisconsin, June 2000.
[7] Preston-Whyte, R. A., and Tyson, P. D., 1989, *The Atmosphere and Weather of Southern Africa*, Oxford University Press, Cape Town, South Africa.
[8] Incropera, F. P., and DeWitt, D. P., 1990, *Introduction to Heat Transfer*, John Wiley & Sons, Singapore.
[9] Holman, J. P., 1992, *Heat Transfer*, Seventh Edition, McGraw-Hill Book International (UK) Limited, London.
[10] Sears, F. W., Zemansky, M. W., and Young, H. D., 1987, *University Physics*, 7th Edition, Addison-Wesley Publishing Company, USA.
[11] Haaf, W., 1984, ''Solar Chimneys: Part II: Preliminary Test Results from the Manzanares Pilot Plant,'' International Journal of Solar Energy, **2**, No. 2, pp. 141–161.

Solar Chimney Turbine Performance

Anthony J. Gannon
e-mail: ajgannon@ing.sun.ac.za

Theodor W. von Backström
e-mail: twvb@sun.ac.za

Department of Mechanical Engineering,
University of Stellenbosch,
Private Bag X1,
Matieland 7602,
South Africa

An experimental investigation of the performance of a solar chimney turbine is presented. The design features a single rotor and uses the chimney supports as inlet guide vanes (IGVs) to introduce pre-whirl. This reduces the turbine exit kinetic energy at the diffuser inlet and assists the flow turning in the IGV-to-rotor duct. The rotor configuration allows the supports to be placed directly under the chimney walls. Measurements from a scale model turbine are used to calculate the turbine performance and efficiency. Efficiencies over a wide operating range and detailed performance measurements at two operating points are presented. Total-to-total efficiencies of 85–90% and total-to-static of 77–80% over the design range are measured. The detailed measurements give insight into the turbine performance and possible design improvements. These results allow more accurate simulation of solar chimney power plants. [DOI: 10.1115/1.1530195]

Introduction

The solar chimney (Fig. 1) consists of three main components: a solar collector, chimney, and turbine. Air under the collector is heated by the greenhouse effect. This less dense air rises up a chimney at the collector center and drives an electricity generating turbine. The only operational solar chimney and turbine was built in Manzanares, Spain [1,2]. The turbine of a full-scale plant is expected to be more than ten times the diameter of the Manzanares plant with a significantly higher pressure-drop. Based on recent simulations of solar chimney plants [3,4] a proposed turbine design for a full-size plant is presented in [5]. Some basic data are available about the turbine performance of the Manzanares plant [2], but apart from this there is little operational data on a solar chimney turbine. The turbine design proposes offsetting the chimney base supports to act as inlet guide vanes (IGVs) to decrease the turbine exit kinetic energy. Measured efficiencies obtained from wall static pressures as well as detailed measurements using a five–hole probe from a scale model turbine are presented. The original design method is also evaluated.

Experimental Objectives

The objective of the experimental program is to demonstrate and evaluate the performance of a scale model of the solar chimney turbine. The total-to-static efficiency based on the wall static pressure over a wide operating range is presented. Detailed measurements of the velocity and pressure profiles up and downstream and after the diffuser at two design points are presented.

Secondary objectives are to evaluate the design method and suggest improvements to the design. The design method is evaluated by comparing the measured and predicted velocity profiles. The experimental results are also used to suggest possible improvements to the turbine design.

Experimental Apparatus

Figure 2 shows a schematic of the turbine test rig. The rig consists of a scale model of the transition region of the collector exit and chimney entrance that contains the turbine. The aim of the current project was purely to test the turbine performance. An axial fan is used to suck the flow through the turbine. The turbine is connected to a generator and both suction fan and generator are connected to variable speed drives. This allows adjustment over a wide range of flow and load coefficients. The power generated by the turbine is dumped in a brake resistor.

Turbine Design [5]. The proposed solar chimney power plant turbine design consists of a 12-bladed axial rotor with adjustable stagger angles. There are 18 chimney base supports that act as IGVs to introduce pre-whirl to the turbine. A detailed outline of the design process is presented in [5]. In the solar chimney power plant, the kinetic energy that exhausts at the chimney is lost. Thus the current turbine design aims to minimize this by reducing the exit swirl using IGVs and using a diffuser after the turbine to recover some of the kinetic energy.

Figure 3 shows the velocity triangles relevant to the solar chimney turbine and the definition of stagger angle referenced from the throughflow direction. It can be seen that increasing the inlet swirl $C_{\theta 2}$ will decrease the exit swirl $C_{\theta 3}$ and thus the exit kinetic energy.

Required Measurements. Three sets of data are required from the rig:

1. *Turbine power output*. This is calculated by taking direct measurements of torque and rotational speed on the generator-turbine shaft. An inductive pickup and rotating torque transducer were used. This allowed very accurate readings of the power to be obtained. The power is calculated from the product of shaft speed ω and torque M_t.

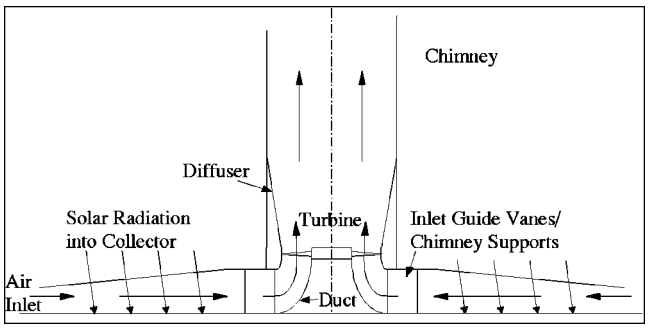

Fig. 1 Solar Chimney Schematic

Contributed by the Solar Energy Division of the American Society of Mechanical Engineers for publication in the ASME JOURNAL OF SOLAR ENERGY ENGINEERING. Manuscript received by the ASME Solar Energy Division, March 2002; final revision, June 2002. Associate Editor: R. Pitz-Paal.

Table 1 Turbine design points

Design point		Case 1	Case 2	Case 3
Power output [MW]	P	50.6	200	200
Mass flow [kg/s]	$\dot{m}$	180 330	256 480	98 839
Volume flow [m3/s]	Q	168 360	245 150	105 350
Pressure drop [Pa]	Δp_o	375	994	2 623
Density [kg/m3]	ρ	1.0711	1.0462	0.9382
Flow coefficient	ϕ	0.1770	0.2577	0.1102
Load coefficient	ψ	0.0742	0.2018	0.5178

Table 2 Overall turbine dimensions and tip speed

	D_{chim}	D_{turb}	D_{hub}	H_{IGV}	H_{turb}	U_{tip}
$f\times D_{chim}$	1	0.799	···	···		
$f\times D_{turb}$	···	···	0.4	0.45	0.55	
Size [m]	160	127.9	51.1	56.83	71.03	88.6 m/s

$$P_{turb} = \omega M_t \tag{1}$$

2. Volume flow rate and wall static pressure drop. A windmill anemometer is used to measure the flow velocity at a certain radial station just upstream of the IGVs. The inlet region is effectively a very large nozzle. The velocity profile is uniform and boundary layers thin due to the accelerating flow.

$$Q = (C_r A)_{anem} = (C_r 2\pi r H_{IGV})_{anem} \tag{2}$$

Wall static pressures are measured directly one pipe diameter after the diffuser using a differential pressure transducer.

3. *The velocity and pressure profiles*. These are measured just upstream and downstream of the turbine and in the diffuser at the same axial station as the wall-static pressures. A five-hole probe is used that allows all three velocity components and total and static pressure to be measured simultaneously.

To summarize, the turbine is designed for three operating points referred to as cases 1, 2 and 3 and is optimized for cases 1 and 2. A summary of the full-scale turbine performance is presented (Tables 1 and 2).

Results

The experimental program is divided into two categories. The first measured the turbine performance over a wide operating range. The second measured the detailed velocity and pressure profiles at the two design points.

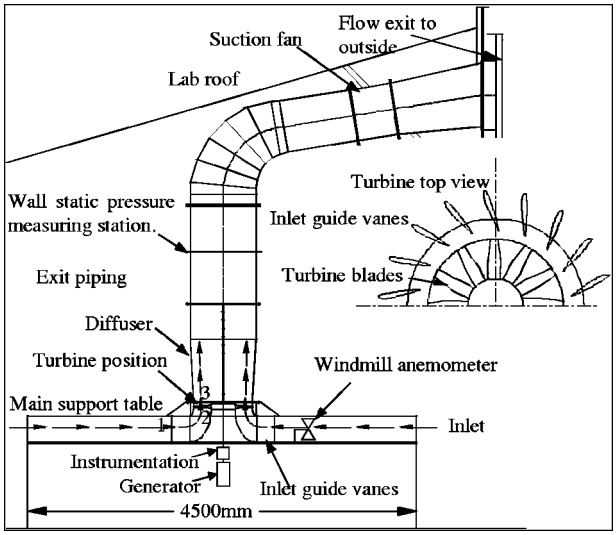

Fig. 2 Solar Chimney Turbine Rig Schematic

Table 3 IGV adjustable flap setting angle (in degrees)

+45	+30	+20	+10	**0 (1)&(2)**	−10	−20	−30	−45

Table 4 Rotor blade tip stagger angles (in degrees)

72	**75.2 (1)**	**78 (2)**	81	84	87	90	93	96

Overall total-to-static efficiency η_{ts}. η_{ts} is measured over a wide range of rotor blade stagger angles and IGV flap angles. The experimental IGVs have their trailing 30% modified as flaps to investigate the effect of more or less pre-whirl (Table 3). The rotor blade stagger angles are adjusted in intervals of 3 deg (Table 4 measured from axial direction). The design values for case 1 and 2 are indicated in bold.

The total-to-static (Eq. (3)) efficiency is calculated using the measured power output P_{turb}, volume flow-rate Q and measured wall static pressure $\Delta p_{s\text{-}w}$ after the diffuser. This is intended to give a conservative estimate of the efficiency as this pressure drop includes the inlet, IGV, and diffuser losses.

$$\eta_{ts\text{-}w} = P_{turb}/(Q\Delta p_{s\text{-}w}) \tag{3}$$

The experimental results are presented using non-dimensional flow ϕ, and load ψ coefficients (Eqs. (4) and (5)). This simplifies the scaling the experimental results to full-scale plants. For a single rotor stagger and IGV flap angle, the turbine efficiency is measured from near zero load coefficient ψ up to a flow coefficient ϕ of about 0.6 which was near the limits of the test rig. The flow coefficient ϕ, is calculated using the measured rotational speed of the turbine and volume flow rate.

$$\phi = C_z/U_{tip} \tag{4}$$

The usual definition of ψ is

$$\psi = 2c_p\Delta T_{turb}/U_{tip}^2 \tag{5}$$

Using the relationship between the turbine temperature drop ΔT_{turb} and power output P_{turb},

$$P = \dot{m}c_p\Delta T_o \tag{6}$$

The load coefficient can be conveniently calculated directly from the measured data,

$$\psi = P \Big/ \left(\frac{1}{2}U_{tip}^2\dot{m}\right) \tag{7}$$

Figure 4 presents the total-to-static efficiency versus flow coefficient ϕ. These are experimentally measured results where each line represents a specific rotor stagger angle and IGV flap setting

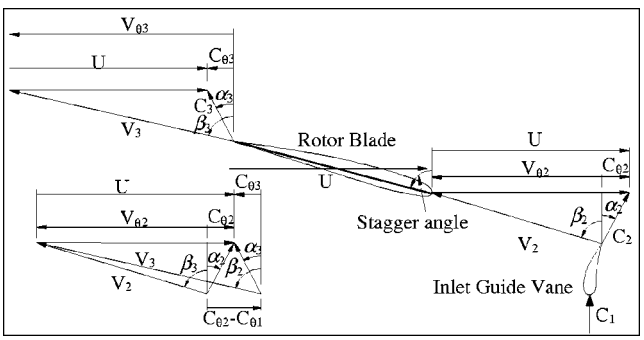

Fig. 3 Velocity triangle diagram of solar chimney turbine

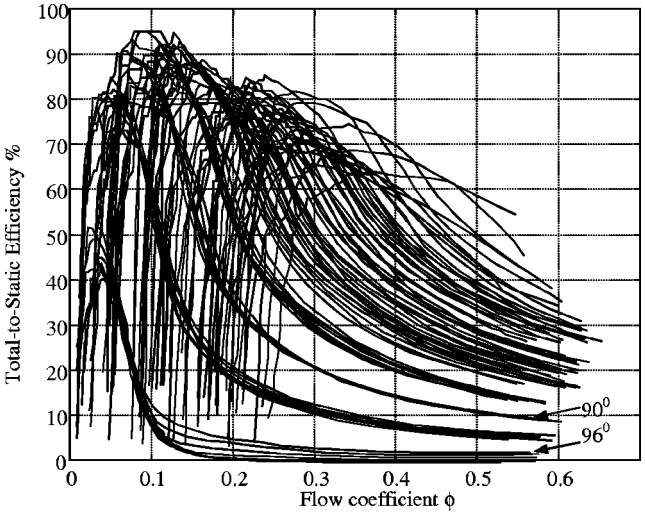

Fig. 4 Experimentally measured efficiency (%) vs flow coefficient (ϕ) for all rotor tip stagger angles

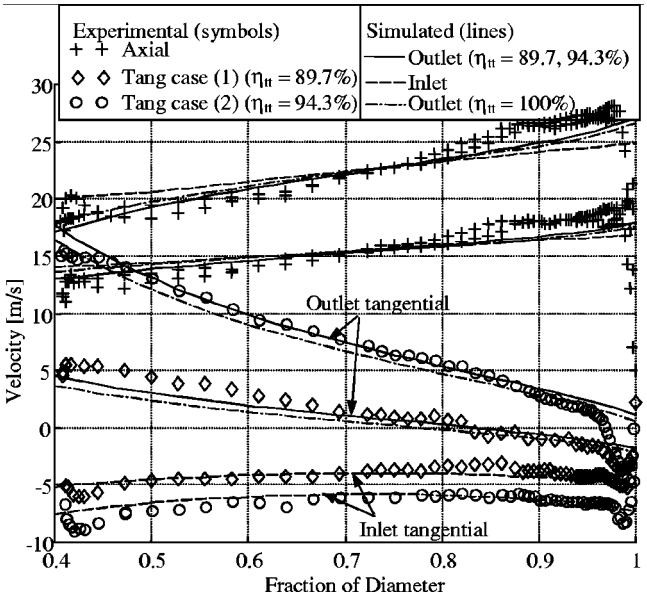

Fig. 6 Comparison of simulated and experimentally measured axial and tangential velocity

angle. The hair plot of Fig. 4 shows the peak total-to-static efficiency for the turbine is over 90%. The detailed measurements presented later showed that that for high ψ values this was optimistic.

Figure 5 retains only the maximum efficiencies from Fig. 4 (there are multiple operating points for certain ϕ-ψ combinations). Superimposed on this figure are the rotor tip stagger angles and design case 1 and 2. This turbine map can be reliably used in the simulation of solar chimney power plants where turbine efficiencies over the entire operating range are needed. The efficiencies of Fig. 5 can be fairly well predicted using a free-vortex analysis except when the turbine begins to stall [6]. This can be seen in the figure by a rapid decrease of the efficiency values at higher load coefficients.

Design Velocity Profiles. These measurements taken for the design points case 1 and 2 allow the turbine performance and design method to be evaluated in detail. Figure 6 presents the measured axial and tangential velocity profiles.

Superimposed is the original matrix throughflow method (MTFM) [7] simulation and then one performed with the measured total-to-total turbine efficiency included. System losses result in the turbine having to deflect the flow more. It is included in the MTFM as a greater flow turning. It results in better prediction of the exit whirl velocities. Even a rough estimate of turbine efficiency will improve the MTFM prediction. Another interesting note is the skewed axial velocity profiles with the rotor tip velocity being significantly higher than at the hub. This result is well predicted by the MTFM. Before the experimental program, there was some doubt as to whether this would be the case in practice. Part of the reason for this is due to the IGV pre-whirl. The centrifugal acceleration results in the flow resisting flow towards the hub. This aids the flow as it turns around the corner from the radial to axial direction.

Design Point Flow Angles. Figure 7 compares the predicted and measured relative flow angles over the rotor. The agreement between the relative inlet and outlet flow angles is good near the hub for case 1, but up to 3 deg at the exit of case 2. As the pressure drop for case 2 is higher than for case 1 it dominates the profile design and hence the better agreement. Near the tip the error is near 2 deg for both cases. Near the hub, the viscous effect of the hub dragging the flow near it reduces flow turning. Near the tip the error between the measured and simulated results is once again near 2 deg. These figures also evaluate the effectiveness of the surface vortex method used [8] to design and predict the flow angles. In future design, the inclusion of an estimate for the tur-

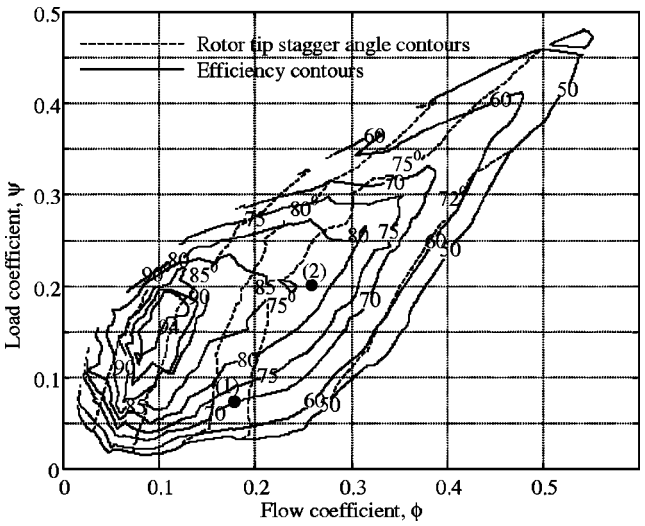

Fig. 5 Maximum efficiency contours (%) vs flow ϕ and load ψ coefficient

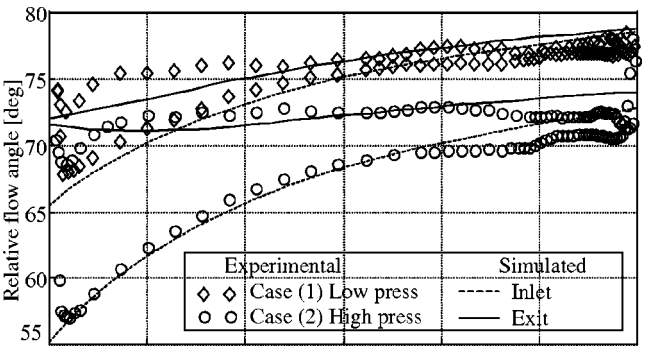

Fig. 7 Comparison of simulated and measured relative inlet, outlet and deflection flow angles

bine efficiency should improve the predicted flow angles. This will influence the turbine rotor blade design and they should run closer to their intended design region. It is thought that some of the discrepancy between the predicted and measured flow angles is due to the rotor blade inlet angle being different to that predicted. The low drag profiles used tend to be very sensitive to the inlet angle.

Diffuser Exit Velocity Profiles. Figure 8 shows the axial and tangential velocity profiles one chimney diameter after the diffuser exit. Measurement of the velocity profile near the pipe center is difficult due to a large stagnation region behind the turbine resulting in very low velocities. This region only accounts for a small fraction of the flow and does not affect the calculation of efficiency significantly. The velocity profiles are favorable for a diffuser with the high velocity near the wall. This is due to the high axial tip velocity at the rotor exit. The large difference between the predicted and measured profiles in this case is due to viscous effects. Flow in diffusers is dominated by thick boundary layers. The MTFM method used assumes inviscid flow. This assumption is adequate for the flow in the rotor. For good flow prediction in a diffuser, a viscous analysis method is required.

Performance

Using the various experimental results the performance of the individual components as well as the overall turbine efficiency is calculated.

Rotor Blade Performance. Incompressible flow with no radial shift through the turbine is assumed. At discrete blade stations the ideal stagnation or Euler pressure drop derived from the Euler turbomachinery equation,

$$\Delta p_{o\ ideal} = \rho \omega (C_{\theta 3} - C_{\theta 2}) \tag{8}$$

is compared to the measured stagnation pressure drop

$$\Delta p_{o\ real} = p_{02} - p_{03} \tag{9}$$

The pressure loss is usually non-dimensionalized with relative rotor exit velocity V_3.

$$K_{R\ loss} = (\Delta p_{o\ ideal} - \Delta p_{o\ real}) \Big/ \left(\frac{1}{2}\rho V_3^2\right) \tag{10}$$

The drag coefficient is a function of the loss $K_{R\ loss}$, the flow inlet and outlet angles β_2 and β_3 and pitch/chord ratio s/c,

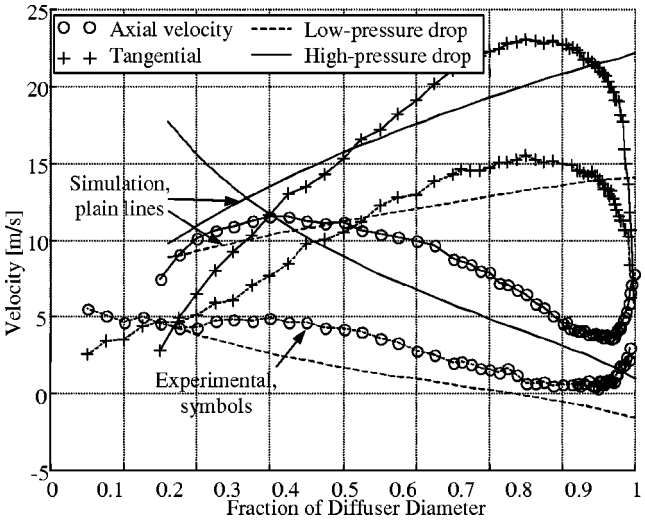

Fig. 8 Comparison of experimental and measured axial and tangential velocities $1\times D_{chim}$ after the diffuser

Table 5 Inlet and rotor loss, drag and lift coefficients

	K_{loss2}	K_{Rloss}	C_{RD}	C_{RL}	C_{RL}/C_{RD}
Case 1	0.091	0.021	0.0141	0.4708	33.4
Case 2	0.043	0.0088	0.0110	0.9391	85.2

$$C_{RD} = K_{R\ loss}(\cos\beta_\infty / \cos\beta_3)^2 (s/c)\cos\beta_\infty \qquad \text{where } \tan\beta_\infty = \frac{1}{2}(\tan\beta_2 + \tan\beta_3) \tag{11}$$

The lift coefficient for a cascade aerofoil is given as,

$$C_{RL} = 2(s/c)(\tan(\beta_3) - \tan(\beta_2))\cos\beta_\infty - C_{RD}\tan\beta_\infty \tag{12}$$

The inlet loss is calculated using the stagnation pressure measured just before the rotor. This takes the inlet, IGV and radial-to-axial duct losses into account. It is non-dimensionalized relative to the absolute rotor inlet velocity C_2.

$$K_{loss\ 2} = (p_{atm} - p_{02}) \Big/ \left(\frac{1}{2}\rho C_2^2\right) \tag{13}$$

Table 5 shows the mean coefficients along the rotor blade span. The inlet loss coefficient is reasonably high, but in reality this amounts to about a 10-Pa pressure loss in the inlet region of the full-scale plant. The rotor blade performance is good for case 2. This was the critical design point as the pressure drop is higher and the chance of blade stall is greater. The optimization scheme used to design the blade profiles minimized the chord length and the maximum velocity over the blade. Both of these characteristics result in profiles with high lift-drag ratios.

Diffuser Performance. The high axial velocity near the casing of the turbine and residual exit swirl as the flow enters the diffuser are beneficial to its performance and results in high diffuser efficiencies. The ideal diffuser pressure recovery coefficient $C_{pD\ ideal}$ is based on the ratio between the chimney area A_{chim} and rotor flow area A_{turb}.

$$C_{pD\ ideal} = 1 - 1/AR^2 \quad AR = A_{chim}/A_{turb} \qquad A_{chim} = \frac{\pi}{4}D_{chim}^2 \quad A_{turb} = \frac{\pi}{4}D_{turb}^2(1-\nu^2) \tag{14}$$

In a real diffuser, losses decrease the pressure recovery coefficient. Calculation of the diffuser loss coefficient K_D using the experimental results requires the integration the product of the volume flow Q and stagnation pressure p_o at the diffuser entrance and exit station in the chimney. The difference between the products is non-dimensionalized using the diffuser inlet absolute velocity,

$$C_{pD} = C_{pD\ ideal} - K_D \qquad K_D = \frac{(Qp_{o3} - Qp_{oD})}{\frac{1}{2}\dot{m}C_3^2} \tag{15}$$

Table 6 shows the diffuser performance for case 1 and 2. While the area ratio AR is not large the diffuser efficiency ($\eta_D = C_{pD}/C_{pDideal}$) is high. For case 1, a 97% efficiency is optimistic. Measurements of the low flow velocities in case 1 is not as accurate as in case 2. A 90% efficiency is possible for favorable inlet conditions [9] which exist in the solar chimney turbine diffuser.

Turbine Performance. The various efficiencies of the turbine are calculated by dividing the measured power by integrating the product of the relevant pressure drop Δp and volume flow rate Q

Table 6 Diffuser efficiency and pressure recovery

	AR	$C_{pD\ ideal}$	η_D [%]	C_{pD}
Case (1)	1.47	0.54	97.3	0.52
Case (2)	1.47	0.54	90.7	0.49

(Eq. (1)). The rotor only total-to-total efficiency is the quotient of the power extracted from the flow across the rotor and the power delivered at the turbine shaft.

$$\eta_{Rtt} = \omega M_t / (Q(p_{02} - p_{03})) \tag{16}$$

Similarly the rotor only total-to-static efficiency is,

$$\eta_{Rts} = \omega M_t / (Q(p_{02} - p_{s3})) \tag{17}$$

The stage total-to-total and total-to-static efficiencies include the losses in the inlet, IGV and duct section. They are calculated using the pressures behind the rotor relative to atmospheric.

$$\eta_{Stt} = \omega M_t / (Q(p_{atm} - p_{o3}))$$
$$\eta_{Sts} = \omega M_t / (Q(p_{atm} - p_{s3})) \tag{18}$$

The efficiency for the entire system with the diffuser is,

$$\eta_{Dtt} = \omega M_t / (Q(p_{atm} - p_{Do3}))$$
$$\eta_{Dts} = \omega M_t / (Q(p_{atm} - p_{Ds3})) \tag{19}$$

Tables 7 and 8 present the measured total-to-total and total-to-static efficiencies and compare them to the total-to-static predicted in the design methods. The loss constants used in the MTFM are obtained from Table 5. The free vortex analysis (FVA) is used in the initial design to determine the turbine dimensions [5]. It does not include losses resulting in optimistic predictions. The turbine rotor losses are small with η_{Rtt} values of 89–94% over the operating range. Even with the inlet region and diffuser losses included the total-to-total efficiency is 85–90%.

As explained in [5], the experimental turbine diffuser is shorter than the one expected on the full-scale plant. In the design of the rig, it was decided to rather be conservative and design a short diffuser that works than have a stalling long diffuser. The high efficiency of the diffuser shows that this was unnecessary, and a longer diffuser is likely to further increase the turbine total-to-static efficiency. Table 8 shows that the measured η_{Dts} is in the range of 69–74.5%. Using the measured diffuser efficiency, but with an AR=1.86 the total-to-static efficiency η_{LDts} can be increased to 77–81%.

Full-Scale Turbine. Scaling of the present results to a full-scale plant should be accurate. The tip speed of the experimental turbine was 0.5 of the full scale which is expected to be 88.6 m/s [5]. At this speed the flow can be assumed incompressible resulting in accurate scaling. The flow through both the experimental and full-scale turbine is turbulent meaning the change due to Reynolds number will be small. A cursory study of the construction feasibility of the turbine has been performed but is beyond the scope of this publication.

Design Improvements

Figure 5 shows that assumption that the assumed maximum relative rotor exit flow angle β_3 is conservative. A value of 80 deg was assumed as the maximum while the maximum efficiency occurs near 85 deg. The use of offsetting the chimney base supports to act as IGVs is also shown to be effective. As this was an untried concept the initial IGV design allowed them to be set in both the radial and offset configuration resulting a conservative IGV design. The experimental program proved early on that pre-whirl is effective in increasing η_{ts}. It was found that the optimum efficiency was obtained at flap angles of +30 deg (more pre-whirl added). Future IGV designs can be optimized for maximum turning.

Table 7 Comparison of measured and predicted rotor only η_R and rotor-IGV η_S (stage) efficiencies

Case	exp η_{Rtt}	exp η_{Rts}	MTFM η_{Rts}	FVA η_{Rts}	exp η_{Stt}	exp η_{Sts}	MTFM η_{Sts}	FVA η_{Sts}
1	89.7	64.7	65.9	69.7	85.7	62.6	63.7	69.7
2	94.3	67.1	70.24	73.3	91.9	65.9	68.9	73.3

Table 8 Comparison of measured and predicted efficiencies with the experimental diffuser η_D and long diffuser η_{LD}

Case	exp η_{Dtt}	exp η_{Dts}	MTFM η_{Dts}	FVA η_{Dts}	exp η_{LDtt}	exp η_{LDts}	MTFM η_{LDts}	FVA η_{LDts}
1	85.3	69.2	69.1	77.8	85.2	77.0	75.1	81.5
2	90.2	74.5	73.8	80.0	89.6	80.7	78.8	83.1

One of the initial turbine requirements was to be able to control the plant power output by increasing the turbine pressure drop. The experimental program showed that this is not possible with the current blade design. In Fig. 6, the abrupt end of the contours at high ψ values is an indication of rotor stall. A more effective method of plant control by introducing cool bleed air into the collector is suggested.

Conclusion

The experimental results show that the solar chimney turbine presented has a total-to-total efficiency of 85–90% and total-to-static of 77–80% over the design range. The reduced radius single-rotor design successfully uses the chimney base supports as inlet guide vanes. The introduction of pre-whirl by the IGVs reduces the turbine exit kinetic energy. Favorable diffuser entry conditions are obtained resulting in diffuser efficiencies of 90%. The results can be used in future simulations of solar chimney power plants. Future turbine designs will also benefit through the use of experimentally measured values of blade loss and diffuser performance in the estimation of efficiencies.

Nomenclature

A = Area [m^2]
C_p = Coeff. of pressure [J/kg·K]
D = Diameter [m]
H = Blade [m]
$\dot{m}$ = Mass flow [kg/s]
p = Pressure [Pa]
Q = Volume flow rate [m^3/s]
U = Rotor speed [m/s]
AR = Area ratio
C = Absolute velocity [m/s] coefficient
K = Loss coefficient
M_t = Torque
P = Power [W]
T = Temperature [K]
V = Relative velocity [m/s]

Greek

α = Absolute angle [rad]
Δ = difference
ν = Hub-tip ratio
ρ = Density [kg/m^3]
ψ = Load coefficient
β = Relative angle [rad]
η = Efficiency
ϕ = Flow coefficient
ω = Rotational speed [rad/s]

Subscript

1 = IGV inlet
3 = Rotor outlet
atm = Atmospheric
chim = Chimney
hub = Turbine hub
o = stagnation
r = Radial
S = Stage
ts = Total-to-static
turb = Turbine
θ = Tangential
2 = Rotor inlet
anem = Anemometer
D = Diffuser, drag
L = Lift
p = Pressure
R = Rotor
tip = Turbine tip
tt = Total-to-total
w = Wall
∞ = Cascade mean

References

[1] Haaf, W., Friedrich, K., Mayr, G., and Schlaich, J., 1983, ''Solar Chimneys: Part I: Principle and Construction of the Pilot Plant in Manzanares,'' International Journal of Solar Energy, **2**(1), pp. 3–20.
[2] Haaf, W., 1984, ''Solar Chimneys: Part II: Preliminary Test Results from the Manzanares Pilot Plant,'' International Journal of Solar Energy, **2**(2), pp. 141–161.
[3] Gannon, A. J., and Von Backström, T. W., 2000, ''Solar Chimney Cycle Analysis with System Loss and Solar Collector Performance,'' ASME J. Sol. Energy Eng., **122**(3), pp. 133–137.
[4] Kröger, D. G., and Buys, J. D., 2001, ''Performance Evaluation of a Solar Chimney Power Plant,'' *ISES 2001 Solar World Congress*, Adelaide, South Australia.
[5] Gannon, A. J., and Von Backström, T. W., 2002, ''Solar Chimney Turbine Part 1 of 2: Design Experimental Results,'' *ASME Proc. of Solar 2002*, Reno, NV.
[6] Von Backström, T. W., and Gannon, A. J., 2001, ''Solar Chimney Turbine Characteristics,'' *ISES Congress*, Adelaide, Australia.
[7] Bosman, C., and Marsh, H., 1974, ''An Improved Method for Calculating the Flow in Turbo-Machines, Including a Consistent Loss Model,'' Journal of Mechanical Engineering Science, **1**, pp. 25–31.
[8] Lewis, R. I., 1996, *Turbomachinery Performance Analysis*, Arnold, London.
[9] Japikse, D., and Baines, N. C., 1997, *Introduction to Turbomachinery*, Concepts ETI and Oxford Univ. Press., **16**, no. 1, pp 25–31.

Available online at www.sciencedirect.com
SCIENCE DIRECT®
Solar Energy 76 (2004) 235–241
SOLAR ENERGY
www.elsevier.com/locate/solener

Solar chimney turbine characteristics

T.W. von Backström *, A.J. Gannon

Department of Mechanical Engineering, University of Stellenbosch, Private Bag X1, Matieland 7602, South Africa

Received 17 January 2003; received in revised form 5 August 2003; accepted 7 August 2003

Abstract

A typical layout of a solar chimney power plant has a single axial turbine with radial inflow through inlet guide vanes at the base of the chimney. Turbine efficiency depends on the turbine blade row and turbine diffuser loss coefficients. The paper presents analytical equations in terms of turbine flow and load coefficient and degree of reaction, to express the influence of each coefficient on turbine efficiency. It finds analytical solutions for optimum degree of reaction, maximum turbine efficiency for required power and maximum efficiency for constrained turbine size. Characteristics measured on a 720 mm diameter turbine model confirm the validity of the analytical model. Application to a proposed large solar chimney plant indicates that a peak turbine total-to-total efficiency of around 90% is attainable, but not necessarily over the full range of plant operating points.

1. Introduction

The turbine is one of the main sub-systems of a solar chimney power plant. Other systems are the solar collector, the chimney and the generator (Fig. 1). Air heated in the solar collector surrounding the chimney enters it radially through passages between the pillars supporting the chimney. The pillars may be airfoil-shaped and arranged along non-radial chord lines, to act as inlet guide vanes (Fig. 1). The typical solar chimney turbine is of the axial flow type. It has characteristics between those of wind turbines and gas turbines: it has more blades than the typical 2 or 3 of wind turbines, but not as many as gas turbines; the rotor blades are adjustable, like those of wind turbines, but, as in gas turbines, the flow is enclosed, and the solar chimney turbine may have radial inflow inlet guide vanes. The main function of the turbine is the efficient conversion of fluid power to shaft power. A secondary function of solar chimney turbines is flow and output power control by adjustment of its blade angles.

Solar chimney literature has little to say about factors affecting efficiency of the turbines, but merely assumes various fixed values of efficiency, e.g., 83% (Haaf et al., 1983), 40–80% (Mullett, 1987), 80% (Schlaich, 1995), 77.0, 78.3 and 80.1% (Pasumarthi and Sherif, 1998) and 80% (Von Backström and Gannon, 2000). We could find no papers dealing with the operating characteristics of solar chimney turbines. The objective of this paper is to develop a simple model for the prediction of solar chimney turbine efficiency and operating characteristics, to help in solar chimney power plant design optimisation.

2. Assumptions

- The turbine is of the axial type, with radial inflow inlet guide vanes (stator blades).
- The analysis proceeds as if the stator blade row also has an axial through-flow direction.

Note that the definition of load coefficient is $\psi = \Delta H/(\frac{1}{2}U^2)$ where $\Delta H = H_1 - H_2$.

3. Turbine efficiency

Noting that ΔH_{loss} is the difference between the real and ideal (no-loss) stagnation enthalpy drops across the turbine, the turbine efficiency is:

* Corresponding author. Tel.: +27-21-808-4267; fax: +27-21-808-4958.
E-mail address: twvb@ing.sun.ac.za (T.W. von Backström).

0038-092X/$ - see front matter © 2003 Elsevier Ltd. All rights reserved.
doi:10.1016/j.solener.2003.08.009

Nomenclature

A	flow area; dimensionless work rate
AR	diffuser area ratio
C_p	pressure recovery coefficient
D	diameter
H	stagnation enthalpy
K	constant
L	loss fraction
$\dot{m}$	mass flow
P	power
p	pressure
R	degree of reaction
U	blade circumferential velocity
V	absolute velocity
W	relative velocity

Greek symbols

α	absolute flow angle
β	relative flow angle
Δ	difference
η	efficiency
ϕ	flow coefficient $= V_z/U$
ρ	density
ψ	load coefficient $= \Delta H/\frac{1}{2}U^2$
ζ	stagnation pressure loss coefficient
$\sum\zeta$	sum of loss coefficients

Subscripts

1	stator exit or rotor inlet
2	rotor exit
Loss	loss
d	diffuser, design point
e	turbine exit (diffuser)
i	ideal (no loss)
opt	optimum
r	rotor
s	static
t	total (stagnation) or turbine
ts	total to static
tt	total to total
u	circumferential component
z	axial component

$$\eta_t = \frac{\Delta H}{\Delta H + \Delta H_{Loss}} = \left(1 + \frac{\Delta H_{Loss}}{\Delta H}\right)^{-1} \quad (1)$$

Lewis (1996, p. 55) shows that for small loss the turbine total-to-total efficiency (it is based on the inlet minus the exit total pressure) can be written in terms of a total pressure loss and an average density as:

$$\eta_{tt} = \left(1 + \frac{\Delta p_{tLoss}/\rho}{\Delta H}\right)^{-1} \quad (2)$$

The turbine total pressure loss, Δp_{tLoss} consists of stator, rotor and diffuser losses. The stator and rotor blade loss coefficients, as defined below, refer to exit relative velocity components (Fig. 2) and exit density:

$$\zeta_s = \Delta p_{sLoss}/(\tfrac{1}{2}\rho V_1^2) \quad (3)$$

$$\zeta_r = \Delta p_{rLoss}/(\tfrac{1}{2}\rho W_2^2) \quad (4)$$

The turbine diffuser loss coefficient is:

$$\zeta_e = \Delta p_{eLoss}/(\tfrac{1}{2}\rho V_2^2) \quad (5)$$

Substitute for the enthalpy drop in terms of the load coefficient:

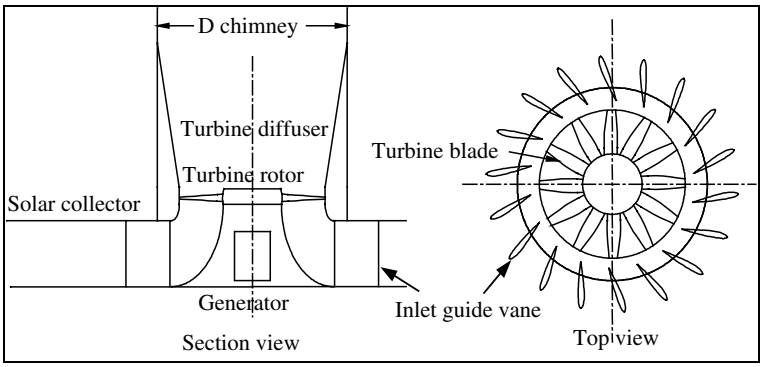

Fig. 1. Solar chimney turbine layout.

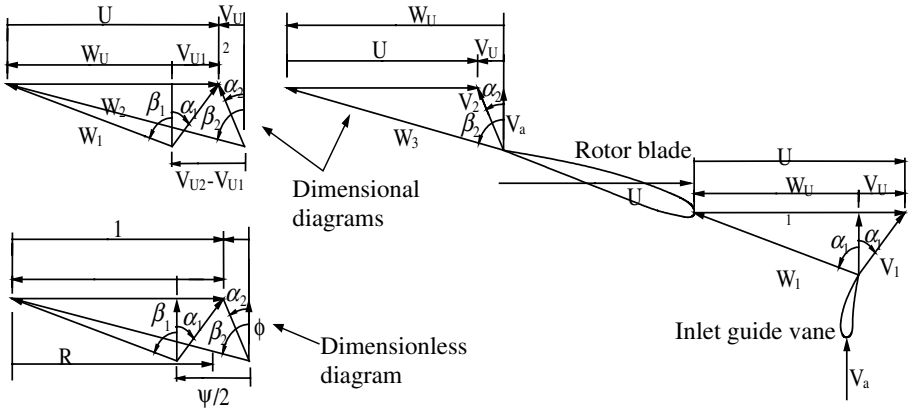

Fig. 2. Turbine velocity diagrams.

$$\eta_t = \left[1 + \left(\zeta_s V_1^2/2 + \zeta_r W_2^2/2 + \zeta_e V_2^2/2\right)/(\psi U^2/2)\right]^{-1}$$
$$= \left[1 + \left(\zeta_s V_1^2/U^2 + \zeta_r W_2^2/U^2 + \zeta_e V_2^2/U^2\right)/\psi\right]^{-1}$$
$$= (1 + L)^{-1} \quad (6)$$

L is the total energy per unit mass flow not available at the turbine diffuser exit, expressed as fraction of the turbine output. When $\zeta_e = 0$ $(=1)$, the equations give the total-to-total (total-to-static, with no diffuser) efficiency. When ζ_e has an intermediate value, the equations correspond to intermediate values of turbine diffuser loss coefficient.

4. Velocity diagrams

Consider the velocity diagrams in Fig. 2. The following conventions apply:

- The axial velocity component V_z is vertically upwards.
- The blade velocity U is from left to right.
- Velocity components parallel to the blade velocity are positive in the direction of the blade velocity.
- Flow angles are measured from the axial direction to a vector pointing away from the axis.
- Flow angles to the right (left) of the axis are positive (negative).

For a fixed turbine rotor radius, and fixed inlet guide vane height and radial location, the inlet guide vane setting angle determines the inlet angle of the rotor relative flow. The rotor blade setting angle determines the exit angle of the rotor relative flow. In addition to the flow and loading coefficients, a third dimensionless parameter, the degree of reaction, R is required to fully describe the dimensionless velocity diagram in Fig. 2.

5. Degree of reaction in solar chimney turbines

The definition of degree of reaction is the ratio of static enthalpy drop across the rotor to static enthalpy drop across the stage. In multi-stage machines an additional assumption is that velocity vectors at inlet and exit of the stage are equal, implying that stage stagnation and static enthalpy drops are equal. Then the degree of reaction, R is the ratio of the static pressure drop over the rotor to the total pressure drop over the stage:

$$R = \Delta h_r/\Delta H \quad (7)$$

It can be shown that in ideal axial turbo-machinery rotors the relative total enthalpy, $H_R = h_R + W^2/2$ is conserved. The static enthalpy difference across the rotor is then:

$$\Delta h_r = h_{r1} - h_{r2} = (W_2^2 - W_1^2)/2$$
$$= (V_z^2 + W_{u2}^2 - V_z^2 - W_{u1}^2)/2$$
$$= (W_{u2} - W_{u1})(W_{u1} + W_{u2})/2 \quad (8)$$

According to the Euler turbine equation the difference in total enthalpy across the turbine is:

$$\Delta H = U(V_{u1} - V_{u2}) = U(W_{u1} - W_{u2}) \quad (9)$$

Write R in terms of relative, then absolute velocity components (also see Fig. 2):

$$R = [(W_{u2} - W_{u1})(W_{u1} + W_{u2})/2]/[U(W_{u1} - W_{u2})]$$
$$= -(W_{u2} + W_{u1})/(2U) \quad (10)$$

$$R = -(V_{u2} - U + V_{u1} - U)/(2U)$$
$$= 1 - (V_{u2} + V_{u1})/(2U) \quad (11)$$

6. Loss fraction, L in terms of ϕ, ψ and R

The following analysis extends that of Lewis (1996). Substitute Eq. (9) into the definition of load coefficient:

$$\psi = \Delta H/(U^2/2) = U(V_{u1} - V_{u2})/(U^2/2) = 2(V_{u1} - V_{u2})/U \quad (12)$$

Eliminate V_{u1} between (11) and (12):

$$V_{u2}/U = 1 - R - \psi/4 \quad (13)$$

The following three relationships then follow for the other circumferential components:

$$W_{u2}/U = -R - \psi/4 \quad (14)$$

$$W_{u1}/U = W_{u2}/2 - (V_{u2} - V_{u1})/U = -R + \psi/4 \quad (15)$$

$$V_{u1}/U = 1 + W_{u1}/2 = 1 - R + \psi/4 \quad (16)$$

Since $V_z/U = \phi$, the following three relationships hold for V_1, W_2 and V_2:

$$V_1^2/U^2 = (V_z/U)^2 + (V_{u1}/U)^2 = \phi^2 + (\psi/4 + 1 - R)^2 \quad (17)$$

$$W_2^2/U^2 = (V_z/U)^2 + (W_{u1}/U)^2 = \phi^2 + (\psi/4 + R)^2 \quad (18)$$

$$V_2^2/U^2 = (V_z/U)^2 + (V_{u2}/U)^2 = \phi^2 + (\psi/4 - 1 + R)^2 \quad (19)$$

The loss fraction, L in Eq. (6) is then:

$$L = \{[\phi^2 + \psi^2/16 + (\psi/2)(1 - R) + (1 - R)^2]\zeta_s + [\phi^2 + \psi^2/16 + (\psi/2)(R) + (R)^2]\zeta_r + [\phi^2 + \psi^2/16 - (\psi/2)(1 - R) + (1 - R)^2]\zeta_e\}/\psi \quad (20)$$

Define $\sum\zeta$ as $(\zeta_s + \zeta_r + \zeta_e)$ and collect common terms:

$$L = [\phi^2 + \psi^2/16 - (\psi/2)(1 - R) + (1 - R)^2](1/\psi) \times \sum\zeta + (1 - R)\zeta_s + [\tfrac{1}{2} + (2R - 1)/\psi]\zeta_r \quad (21)$$

The loss coefficients all share an influence coefficient in the first term on the right of Eq. (21), but the stator and rotor loss coefficients have additional influence coefficients that are both equal to 1/2 when $R = 1/2$, and equal to zero for the stator when $R = 1$. Figs. 3 and 4, to be discussed in more detail later, present efficiency contours derived from Eq. (21).

7. Optimum R for minimum loss

The choice of R for a given combination of ϕ and ψ determines the shape of the velocity triangles and the relative magnitude of the stator and rotor exit velocities.

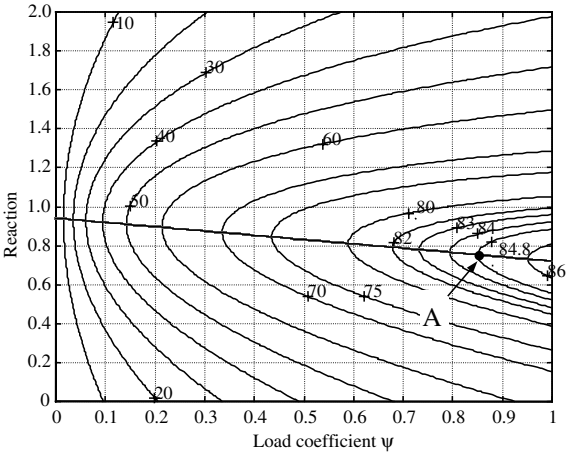

Fig. 3. Turbine total-to-static efficiency contours on a (ψ, R) map ($\phi = 0.333$, $\zeta_s = \zeta_r = 0.05$, $\zeta_e = 0.75$).

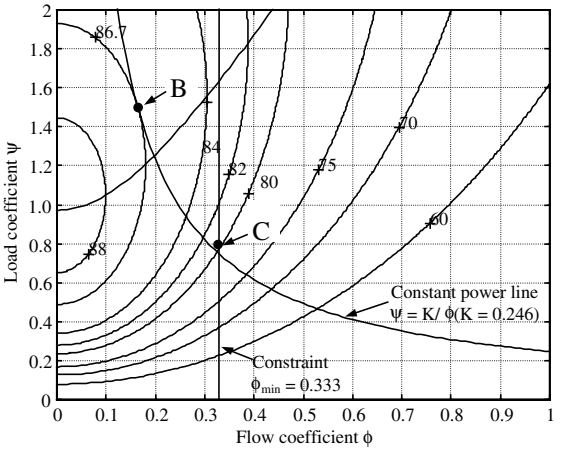

Fig. 4. Turbine total-to-static efficiency contours on a (ϕ, ψ) map ($R = 1$, $\zeta_s = \zeta_r = 0.05$, $\zeta_e = 0.75$).

Turbine loss can be minimised by minimising ζ_s, ζ_r and ζ_e, or by minimising their effect by minimising their influence coefficients, which are functions of ϕ, ψ and R. We explore this variation of the influence coefficients of the loss coefficients, before we look at the effect of the loss coefficients themselves. Assume that at a given design point in terms of ϕ and ψ, the loss coefficients remain constant when R changes. Find the minimum loss fraction, L by differentiating Eq. (21) with respect to R and equating to zero:

$$R_{opt} = 1 - \psi/4 + (1/2\psi\zeta_s - \zeta_r)/\sum\zeta \quad (22)$$

R_{opt} is independent of ϕ, but depends on ψ, ζ_s and ζ_r and ζ_e. Fig. 3 presents optimum loss coefficient lines for various degrees of reaction, showing that ψ_{opt} decreases

linearly as R increases. Design values of ζ_s and ζ_r are of the order of a few percent, but ζ_e can vary from about unity down to zero if the total-to-total efficiency is considered. When $\zeta_e = 0$, and $\zeta_s = \zeta_r$, it follows from Eq. (22) that $R_{opt} = 0.5$ for all ψ, ζ_s and ζ_r. $R_{opt} = 0.5$ is common in gas turbines when the exit kinetic energy is useful.

In solar chimneys, however, it is the static pressure at the turbine diffuser exit that is important, as there is no pressure recovery in the chimney, but on the contrary, an acceleration pressure drop (Von Backström and Gannon, 2000). Turbine flow area is less than chimney flow area, as the turbine has hub blockage, and its outer diameter must be less than that of the chimney to allow a reasonable radius of curvature where the radial flow enters the axial flow turbine (Fig. 2). Pressure recovery is possible through a turbine diffuser, but the area increase downstream of the hub will contribute little to it, as the flow will separate from the hub, unless it is impractically long. With a turbine flow area of say 80% of the chimney flow area, the area ratio, AR is 1/0.8 and the ideal pressure recovery is, $C_{pi} = 1 - 1/AR^2 = 0.36$. If the diffuser efficiency is, $\eta_d = 0.70$ the pressure recovery coefficient is, $C_{pi} = \eta_d C_{pi} = 0.7(0.36) = 0.25$. Then $\zeta_e = 1 - 0.25 = 0.75$. The area ratio may even be larger, because due to the turbine hub blockage, only the streamlines near the casing of the turbine diffuser diverge (Fig. 2) and angular momentum conservation contributes little to the pressure recovery. If the consideration is to maximise the total-to-static efficiency, ζ_e must be equal to unity or at least close to it, and ζ_s and $\zeta_r \ll \zeta_e$ and $R_{opt} \approx 1 - \psi/4$. Then, for small values of ψ (say <1,0), $R_{opt} > 0.75$. When $R = 1 - \psi/4$, the turbine exit whirl velocity is zero (Eq. (13)). When $R = 1$, the rotor inlet and exit whirl velocities are equal but opposite (Eqs. (13) and (16)).

We investigate a proposed standard 160 m diameter chimney solar plant: $P = 200$ MW, $\dot{m} = 250{,}000$ kg/s, $\rho = 1.0$ kg/m^3. Assume that $A_t = 15{,}000$ m^2, giving $V_z = 16.67$ m/s. Then (for $\eta_d = 0.75$), $\Delta H = 1067$ J/kg. Choosing $U = 50$ m/s, results in $\phi = 16.67/50 = 0.333$ and $\psi = 1000/(\frac{1}{2}50^2) = 0.8533$. Then $L = 0.2396$ and $\eta_{ts} = 0.807$ when $\zeta_s = \zeta_r = 0.05$ and $\zeta_e = 0.75$ and $R = 1.0$. But from Eq. (22) the optimum $R = 0.753$. Then $L = 0.1788$ and $\eta_{ts} = 0.848$ (point A Fig. 3). The efficiency at $R = 1$ is about four percentage points lower than at the optimum R. This points to the importance of reducing exit whirl by introducing inlet counter whirl.

8. Optimum turbine design point for required power

A common, simplified design approach is to first optimise the plant independently of the turbine. The hidden assumption here is that a suitable turbine can be designed for the resulting flow and pressure drop, with the system imposing no turbine efficiency constraints. To meet the design power requirement at assumed efficiency, the product of flow through and enthalpy drop across the turbine must have a certain fixed value. The design point power is:

$$P_d = \eta_d \rho V_z A(-\Delta H) = \eta_d \rho \phi_d U A \psi_d \tfrac{1}{2} U^2 = \eta_d \phi_d \psi_d A \tfrac{1}{2} \rho U^3 \quad (23)$$

This implies an additional relationship between ϕ_d and ψ_d:

$$\phi_d = P_d/[\eta_d \psi_d A \tfrac{1}{2} \rho U^3] \quad (24)$$

To keep the analysis simple, assume $\phi = K/\psi$, where $K = \phi_d/\psi_d = P_d/[\eta_d A \frac{1}{2} \rho U^3] = \text{constant}$. It implies that power output varies slightly with efficiency. Note the $\phi = K/\psi$ line in Fig. 3. Eq. (21) then becomes:

$$L = [K^2/\psi^3 + \psi/16 - (1/2)(1-R) + (1-R)^2/\psi] \times \sum \zeta + (1-R)\zeta_s + [1/2 - (1-2R)/\psi]\zeta_r \quad (25)$$

For optimum L, differentiate with respect to ψ and equate to zero to find:

$$\psi^4/2 + 8[(1-2R)\zeta_r/\sum \zeta - (1-R)^2]\psi^2 - 24K^2 = 0 \quad (26)$$

The solution is:

$$\psi^2 = -8\left[(1-2R)\zeta_r \Big/ \sum \zeta - (1-R)^2\right] + \left\{64\left[(1-2R)\zeta_r \Big/ \sum \zeta - (1-R)^2\right]^2 - \left[4(1/2)(-24K^2)\right]\right\}^{0.5} \quad (27)$$

When $R = 1$:

$$\psi^2 = 8\zeta_r/\sum \zeta + 8\left\{\left[\zeta_r \Big/ \sum \zeta\right]^2 + \tfrac{3}{4}K^2\right\}^{0.5} \quad (28)$$

Then, in an ideal rotor, with $\zeta_r = 0$ and $R = 1$, the optimum is $\psi_{opt} = 48^{0.25} K^{0.5} = 2.632 K^{0.5}$ and $\phi_{opt} = K^{0.5}/48^{0.25} = K^{0.5}/2.632$. This implies that $\psi_{opt} = 2.632^2 \phi_{opt} = 48^{0.5} \phi_{opt} = 6.93\, \phi_{opt}$. Assuming that $\zeta_s = \zeta_r = 0$, and $\zeta_e = 1$, the minimum loss fraction is:

$$L = [K^{0.5}/48^{0.75} + 48^{0.25} K^{0.5}/16] = 0.219 K^{0.5} \quad (29)$$

From the standard chimney data at the end of the previous section, $K = 0.284$. Then, from Eq. (29) $L_{min} = 0.117$ and $\eta_{ts\,max} = 0.895$. For this K value, the optimum load and flow coefficients are $\psi_{opt} = 1.40$ and $\phi_{opt} = 0.203$. Iterating until the turbine efficiency converges, results in: $\eta_{ts\,max} = 0.904$ and $\psi_{opt} = 1.28$ and $\phi_{opt} = 0.185$ at $K = 0.236$. This shows that when the rotor loss coefficient approaches zero, a high but limited total-to-static efficiency is possible, but ψ_{opt} is high, implying a relatively low blade speed, and ϕ_{opt} is low

implying a large diameter turbine. When $\zeta_s = \zeta_r = 0.05$ and $\zeta_e = 0.75$ and $R = 1.0 : \psi_{opt} = 1.500$ and $\phi_{opt} = 0.164$, with $\psi_{opt} = 9.2\phi_{opt}$ and $K = 0.246$ (point B in Fig. 4). Then $L = 0.153$ and $\eta_{ts} = 0.867$ after iteration for η_{ts}. The ϕ_{opt} value implies that $V_z = 8.22$ m/s. It is about half the intended value in the standard design. A low turbine rpm, implied by a low blade speed and large diameter, means large torque transmitted for given power. These undesirable tendencies imply that a pre-selected chimney design point may constrain turbine design to a fixed minimum value of ϕ.

9. Optimum ψ for minimum loss at given ϕ and R

We shall now find the optimum value of ψ for fixed R and $\phi = \phi_{min}$. In gas turbine design this condition occurs if the turbine diameter and speed are fixed. Assume that the loss coefficients, ζ_s, ζ_r and ζ_e at the design point are independent of ψ, differentiate Eq. (21) with respect to ψ and equate to zero:

$$\psi_{opt} = 4 \times \sqrt{(\phi^2 + (1-R)^2) + (2R-1)\zeta_r / \sum \zeta} \qquad (30)$$

When $R = 1/2$, irrespective of the value of the loss coefficients, then, as in Lewis (1996):

$$\psi_{opt} = 2 \times \sqrt{4\phi^2 + 1} \qquad (31)$$

(Note that Lewis (1996) uses a load coefficient, $\psi_{Lewis} = \psi/2$.)

When $R = 0.5$, then $\psi_{opt} \Rightarrow 2$, when $\phi \Rightarrow 0$ irrespective of ζ_e. When $R = 1$ and $\zeta_e \Rightarrow 1$, so that $\zeta_s \ll \zeta_e$ and $\zeta_r \ll \zeta_e$, then:

$$\psi_{opt} \approx 2 \times \sqrt{4\phi^2 + 4\zeta_r/\zeta_e} \qquad (32)$$

Compare Eqs. (31) and (32) the minimum loss when $\zeta_e \Rightarrow 1$, occurs at a lower load coefficient when $R = 1$ than when $R = 1/2$, since typically $4\zeta_r/\zeta_e \ll 1$. That is why solar chimney turbines should have $R > 0.5$.

As a numerical example, assume $\phi = 16.67/50 = 0.333$ as before. When $R = 1$ and $\zeta_s = \zeta_r = 0.05$, and $\zeta_e = 0.75$, $\psi = 0.799$ and the loss fraction, L is 0.248 and $\eta_{ts} = 0.801$ after iteration (point C in Fig. 4). However, when using the theoretical value $\psi_{opt} = 1.649$ the optimum efficiency is $\eta_{ts} = 0.833$, a 3% improvement. To calculate the total-to-total efficiency, set $\zeta_e = 0$ in the above. The turbine total to-total efficiency is $\eta_{tt} = 0.933$. That is about as efficient as turbines get. Another way of increasing turbine efficiency is to reduce the blade row loss coefficients, and operate at the optimum degree of reaction. Lewis (1996) quotes the following design profile loss equation: $\zeta = 0.025[1 + (\varepsilon°/90)^2]$. If for example, $\zeta_s = \zeta_r = 0.03$, and $R_{opt} = 0.790$ then $\eta_{ts} = 0.858$ and $\eta_{tt} = 0.949$. For the small deflection angles in solar chimney rotors, values of as low as 0.03 seem feasible, and so do $\eta_{ts} \approx 85\%$ and $\eta_{tt} > 90\%$.

10. Off-design performance

For a given system pressure drop versus flow characteristic, the turbine load coefficient versus flow coefficient characteristic determines the turbine operating point. This point will normally not coincide with the turbine design point. Since turbine blade loss coefficients remain low over a wide range of inlet flow angles, the major effect of off-design flow angles is not expected to be the change in loss coefficient, but rather the amount of work done by the turbine when the rotor relative inlet angle changes. A reasonable assumption under these conditions is that the stator exit flow angle, α_1 and the rotor relative exit flow angle, β_2 remain constant. From the definition of load coefficient, Eq. (12) and the velocity triangles:

$$\begin{aligned}\psi &= -2\phi(W_{u2} + U - V_{u1})/V_z \\ &= -2\phi(\tan\beta_2 + 1/\phi) + 2\phi\tan\alpha_1 \\ &= 2\phi(\tan\alpha_1 - \tan_2\beta_2) - 2 \end{aligned} \qquad (33)$$

The ideal turbine characteristic is a straight line through two points: the design point, $(\phi_d;\psi_d)$ and the point $(\phi;\psi) = (0.0;-2.0)$. Fig. 5 compares theoretical and measured values measured on a 720 mm diameter model solar chimney turbine. Fig. 6 shows that mean rotor blade exit angles derived from experiment do indeed vary little over the operating range. Where the angle is virtually constant (75.2°) in Fig. 6, the curve fit is excellent in Fig. 5. The repeatability of flow angle measurement was within 0.5°. Gannon (2002) presents an error analysis for the measurements on which Figs. 5

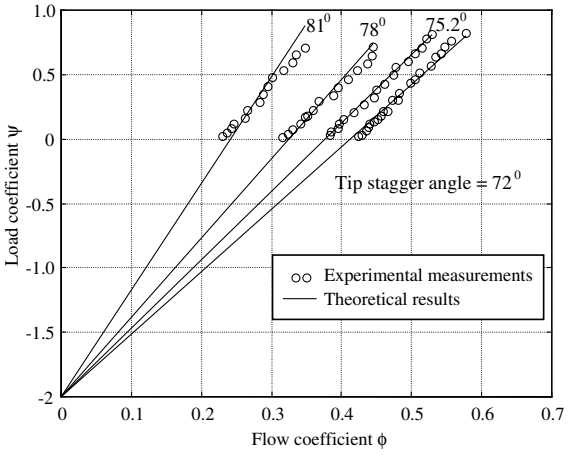

Fig. 5. Comparison of experimental to theoretical turbine characteristics for various turbine rotor blade angles.

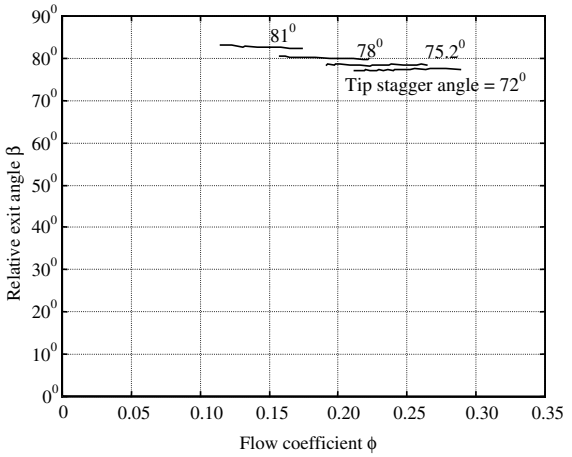

Fig. 6. Rotor blade relative exit flow angles derived from experimental turbine characteristic.

and 6 were based. He also presents more experimental data, some of which have been subsequently presented by Gannon and Von Backström (2004). A follow-up paper will discuss the complete turbine design methodology.

11. Conclusions

The paper presents analytical equations in terms of turbine flow and load coefficient and degree of reaction, to express the influence of each coefficient on turbine efficiency. It finds analytical solutions for optimum degree of reaction, maximum turbine efficiency for required power and maximum efficiency for constrained turbine size. Characteristics measured on a 720 mm diameter turbine model confirm the validity of the analytical model.

The derived equations show the beneficial effect of pre-whirl on turbine performance, and the constraining effects that chimney diameter and design point power may have on maximum attainable turbine efficiency. These considerations are important when making decisions about the initial layout, sizing and design of solar chimney turbines. The models are simple enough to include in solar chimney power plant optimisation studies. Application to a proposed large solar chimney plant indicates that a peak turbine total-to-total efficiency of around 90% is attainable, but not necessarily over the full range of plant operating points.

References

Gannon, A.J., 2002. Solar Chimney Turbine Performance. Ph.D. dissertation, University of Stellenbosch, South Africa.

Gannon, A.J., Von Backström, T.W., 2003. Solar chimney turbine performance. ASME Journal of Solar Energy Engineering 125, 101–106.

Haaf, W., Friedrich, K., Mayr, G., Schlaich, J., 1983. Solar chimneys. Part 1: principle and construction of the pilot plant in Manzanares. International Journal of Solar Energy 2, 3–20.

Lewis, R.I., 1996. Turbomachinery Performance Analysis. John Wiley and Sons, London.

Mullett, L.B., 1987. The solar chimney—overall efficiency, design and performance. International Journal of Ambient Energy 8, 35–40.

Pasumarthi, N., Sherif, S.A., 1998. Experimental and theoretical performance of a demonstration solar chimney model—Part I: mathematical model development. International Journal of Energy Research 22, 277–288.

Schlaich, J., 1995. The Solar Chimney, Electricity from the Sun. Axel Menges, Stuttgart.

Von Backström, T.W., Gannon, A.J., 2000. Compressible flow through solar power plant chimneys. ASME Journal of Solar Energy Engineering 122, 138–145.

Compressible Flow Through Solar Power Plant Chimneys

Theodor W. von Backström
e-mail: twvb@ing.sun.ac.za

Anthony J. Gannon

Department of Mechanical Engineering,
University of Stellenbosch,
Private Bag X1,
Matieland 7602,
South Africa

Chimneys as tall as 1500 m may be important components of proposed solar chimney power plants. The exit air density will then be appreciably lower than the inlet density. The paper presents a one-dimensional compressible flow approach for the calculation of all the thermodynamic variables as dependent on chimney height, wall friction, additional losses, internal drag and area change. The method gives reasonable answers even over a single 1500 m step length used for illustration, but better accuracy is possible with multiple steps. It is also applicable to the rest of the plant where heat transfer and shaft work may be present. It turns out that the pressure drop associated with the vertical acceleration of the air is about three times the pressure drop associated with wall friction. But flaring the chimney by 14 percent to keep the through-flow Mach number constant virtually eliminates the vertical acceleration pressure drop. [S0199-6231(00)03003-3]

Introduction

One of the major parts of a solar chimney power plant is the chimney itself (Fig. 1). When warmer than ambient air enters at the bottom of the chimney, the difference in density between it and that of the ambient air generates a pressure potential that causes the flow through the system and turbine. The pressure drops due to wall friction, loss coefficients and drag of obstructions in the chimney, and changes in static pressure due to changes in kinetic energy in contractions and diffuser shaped sections of the chimney affect the flow through and pressure drop over the turbine. The magnitude of the flow and the pressure drop over the turbine determine the maximum power that the turbine can extract from the flow. Haaf et al. [1], Haaf [2] and Von Backström and Gannon [3] and Gannon and Von Backström [4] have discussed solar chimney plant performance in more detail.

A method that can link the pressure drop in a chimney to its geometry and internal obstructions will be of great benefit in the analysis of solar chimney plants.

Objectives

The main objectives of this study are:

- To develop a method to calculate the variation in pressure for buoyant flow in a tall vertical chimney with wall friction, non-constant area and internal obstructions.
- To verify the method against simplified analytical solutions.
- To do a sensitivity analysis to determine the relative importance of the various parameters.
- To make recommendations regarding chimney layout.

Typical Chimney Construction

The chimney typically consists of the following:

- A chimney support section
- The turbine inlet
- The turbine
- The turbine diffuser
- A constant area duct or variable area diffusing section
- A protruding ring section that supports bracing wires, rods or beams
- Repetitions of the last two items
- A chimney exit

Contributed by the Solar Energy Division of THE AMERICAN SOCIETY OF MECHANICAL ENGINEERS for publication in the ASME JOURNAL OF SOLAR ENERGY ENGINEERING. Manuscript received by the ASME Solar Energy Division, Dec. 1999; final revision Jul. 2000. Associate Technical Editor: T. R. Mancini.

Approach and Assumptions

The chimneys of solar chimney power plants may be as high as 1500 m. The maximum air velocity in the chimney will occur when the turbine blades are feathered and the flow resistance over the turbine is a minimum. Preliminary calculations show that the velocity will probably not exceed 50 m/s. The Mach numbers will then be below 0.15. Normally such flows would be considered to be incompressible, but in a tall chimney the change in density due to change in altitude also plays a role.

Assuming adiabatic conditions in the chimney, the temperature in the chimney will decrease at a rate of 9.76°C per 1000 m. That is about 15°C, or 5 percent in a 1500 m high chimney with an inlet temperature of 300 K. Under adiabatic conditions density ratios are proportional to temperature ratios to the power $1/(\gamma-1)$. The density then decreases by a factor of $0.95^{1/(\gamma-1)}=0.88$ for $\gamma=1.4$. Since a density decrease of 12 percent is not negligible, a compressible flow approach to the problem is appropriate.

The standard approach to compressible flow problems is to use the conservation equations for mass, momentum and energy to derive differential equations for the variation of each of the relevant variables in terms of the local Mach number. These differential equations have analytical solutions for some simple cases such as isentropic flow with variable area, frictionless flow with heat addition, or adiabatic flow with friction. For more complex cases however, where multiple factors simultaneously affect the flow, the solution requires numerical integration by Runge-Kutta or similar schemes.

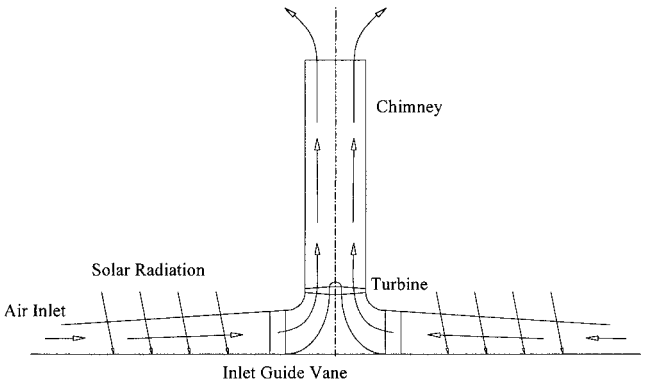

Fig. 1 Solar chimney schematic

In the solar chimney the following physical effects may influence the flow and specifically the change in stagnation or static pressure through the chimney:

- Wall friction
- Drag due to obstructions such as internal bracing or protrusions
- Flow separation at sudden contractions or expansions
- Cross sectional area change
- Heat transfer through the chimney walls
- Work extraction by the turbine
- The potential energy of the fluid

Preliminary calculations have shown that heat transfer through the chimney walls is negligible. The turbine deserves consideration, but separately. The effect of altitude variation on the potential energy of a gas is usually negligible, but for high chimneys it merits inclusion. For the sake of simplicity this first study will employ the one-dimensional approach, that is uniform property profiles across each section.

Formulation of the Problem

Application of the one-dimensional conservation equations to the control volume in Fig. 2 leads to:

Mass flow:

$$d\rho/\rho + dA/A + dV/V = 0 \tag{1}$$

Momentum:

$$dp + \rho V dV + \rho g dz + (4 f dz/D)\rho V^2/2 + \delta F_D/A = 0 \tag{2}$$

Energy:

$$\delta W - \delta Q + dh + V dV + g dz = 0 \tag{3}$$

or:

$$-\delta W + \delta Q - g dz = dH \tag{4}$$

The normal definition of the stagnation enthalpy is:

$$H = h + V^2/2 \tag{5}$$

so that:

$$dH = dh + V dV \tag{6}$$

In problems where the potential energy term, gz is negligible, and work and heat transfer are zero, the energy equation merely states that the stagnation enthalpy is conserved. Such a convenient condition is possible even when the potential energy term is not negligible, but then the stagnation enthalpy definition should be:

$$H = h + V^2/2 + gz \tag{7}$$

with:

$$dH = dh + V dV + g dz. \tag{8}$$

The corresponding definition of stagnation temperature is then:

$$T = t + V^2/(2c_p) + gz/c_p \tag{9}$$

The additional gz/c_p term in the frequently used relationship between the static and stagnation temperature complicates the derivation of some of the other equations, however. A more convenient approach is to retain the standard definitions of stagnation enthalpy and stagnation temperature (without the gz term). The system of equations then requires only one modification, and that is that the stagnation enthalpy be reduced with the increase in potential energy over each altitude increase in Eq. (4). This is easy to do for one dimensional flow in a vertical chimney.

With these assumptions the normal set of equations for generalized steady one dimensional flow as derived by for example Zucrow and Hoffman [5] is applicable. This set of equations is solvable by numerically integrating the momentum equation, followed by appropriate substitution for other variables.

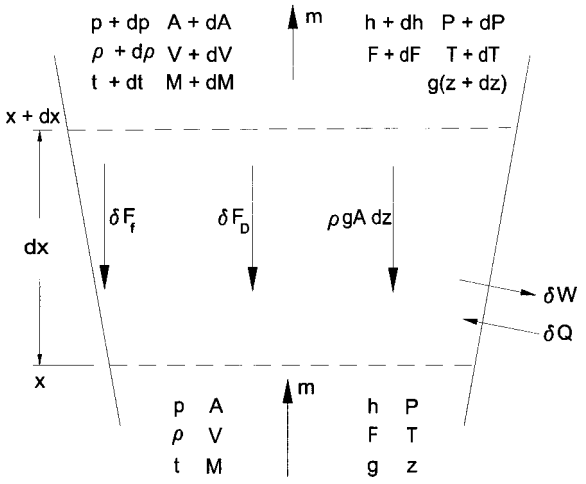

Fig. 2 Physical model for generalized steady one-dimensional flow

Solution Method

The differential equation for the effect of the relevant variables—area change, friction and drag, fluid weight, and stagnation temperature change—on Mach number variation in a vertical chimney is:

$$dM/M = \{[1 + M^2(\gamma-1)/2]/(1-M^2)\} \times \{-dA/A + [(f dz/D)\gamma M^2/2 + g dz/(Rt) + \delta F_D/(pA)] + (dT/T)(1+\gamma M^2)/2\} \tag{10}$$

The equation is derived from the vertical momentum equation divided by pA to make it dimensionless. Zucrow and Hoffman [5] initially included a term, $g\rho A dz/(pA) = g dz/Rt$ in the equation above, but discarded it during the derivation, as it is generally negligible. This term can be seen as an additional drag term equal to the weight of the fluid in the volume $A dz$.

Equation (10) must be integrated numerically over the height of the chimney. The starting values are the conditions at the bottom of the chimney, but there is no fundamental reason why a similar integration cannot be carried out right through, starting at the collector inlet and ending at the chimney exit. The effect of the turbine pressure drop must then be included as a drag force. The inlet values to be known are Mach number, area, diameter, pressure and stagnation temperature. During the integration process the value of friction factor must be calculated as function of Reynolds number and wall roughness. The lengths of the integration steps must be adjusted so that regions where obstructions, protrusions or additional losses occur fit neatly into one step. The drag force, δF_D is everywhere equal to zero except in such steps.

If the mass flow, static pressure, stagnation temperature and flow area are known at the starting point of the integration, find the Mach number there by solving the equation below:

$$m = A_1 p_1 M_1 \{[1 + M_1^2(\gamma-1)/2]\gamma/(RT_1)\}^{0.5} \tag{11}$$

An easy way is to rewrite it as a quadratic equation for M_1^2:

$$M_1^2 = \{1/(\gamma-1)^2 + [m/(A_1 p_1)]^2 2RT_1/[\gamma(\gamma-1]\}^{0.5} - 1/(\gamma-1) \tag{12}$$

The static temperature follows from:

$$t_1 = T_1/[1 + M_1^2(\gamma-1)/2] \tag{13}$$

Then find the stagnation enthalpy at the end of the integration step from the differential equation for energy conservation:

$$dH = -\delta W + \delta Q - g\,dz \tag{14}$$

Integration from the beginning of the integration step (position 1) to the end of the step (position 2) leads to:

$$H_2 - H_1 = -\Delta W + \Delta Q - g(z_2 - z_1) \tag{15}$$

where ΔW and ΔQ are work and heat inputs in a discrete integration step.

As pointed out before, $\Delta Q = 0$ for typical chimneys, and ΔW will have a non-zero value only over the turbine.

With A_2, M_2 and $T_2 = H_2/c_p$ known, the static pressure at the end of the integration step follows from the mass flow equation above:

$$p_2 = [m/(A_2 M_2)]/\{[1 + M_2^2(\gamma - 1)/2]\gamma/(RT_2)\}^{0.5} \tag{16}$$

The stagnation pressure, P_2 at the end of the integration step follows from:

$$P_2 = p_2[1 + M_2^2(\gamma - 1)/2]^{\gamma/(\gamma-1)} \tag{17}$$

Next calculate the static temperature as at the beginning of the integration step from the stagnation temperature and Mach number. The density is easy to calculate from the known pressure and temperature and so is the velocity from the density and flow area.

When the stagnation pressure at the chimney inlet is known, but not the static pressure, then the inlet static pressure and Mach number that will satisfy Eqs. (11) and (17) must be found by iteration.

The integration process is carried through to the chimney exit, where the static pressure must be equal to the ambient atmospheric static pressure at that altitude. If the calculated exit static pressure is higher (lower) than the ambient, the mass flow must be increased (reduced) iteratively until the pressures are equal.

The solution method described is equally applicable to the whole chimney plant including the collector, where of course $\Delta Q \neq 0$ and the flow area varies at a much greater rate than in the chimney. It is also applicable through the turbine as long as the turbine work extraction term remains in Eq. (4) and a turbine drag term represents the turbine pressure drop in Eqs. (2), (10) and following equations.

Simple Test Case: Zero Inlet Mach Number in An Ideal Chimney

We define an ideal chimney as one with no area change, internal obstructions, wall friction or additional losses, no heat transfer or work extraction. In addition, to test if the system of equations would reproduce the normal adiabatic lapse rate equations, we assume that the Mach approaches zero.

The differential equation for the chimney stagnation temperature drop follows from Eq. (14) for $\delta W = 0$ and $\delta Q = 0$:

$$dT = -g\,dz/c_p \tag{18}$$

Integrate from $z = 0$ where $T = T_1$ to a general height $z = z$ where $T = T$:

$$T = T_1 - (g/c_p)z \tag{19}$$

This is the well-known adiabatic temperature lapse rate equation, stating that the temperature decreases at 9.76°C per 1000 m altitude. To find the corresponding pressure lapse rate, first consider the Mach number ratio in a vertical chimney.

When M approaches zero, Eq. (10) approaches the following equation:

$$dM/M = \{1/1\{-dA/A + [0 + g\,dz/(Rt) + \delta F_D/(pA)] + (dT/T)1/2\} \tag{20}$$

For a constant area chimney ($dA = 0$), with no internal drag ($\delta F_D = 0$), it simplifies to:

$$dM/M = g\,dz/(Rt) + (dT/T)/2 \tag{21}$$

Substituting (18):

$$dM/M = g\,dz/(Rt) - g\,dz/(2c_p T) \tag{22}$$

Since $R = c_p(\gamma - 1)/\gamma$, and for M approaching zero, t approaches T:

$$dM/M = [g\,dz/(c_p T)][\gamma/(\gamma - 1) - 1/2] \tag{23}$$

$$= \{[g/(c_p T)]\{1/2(\gamma + 1)/(\gamma - 1)\}dz \tag{24}$$

To write T as a function of z, substitute (19):

$$dM/M = \{[1/2(\gamma + 1)/(\gamma - 1)][g/c_p]/[T_1 - (g/c_p)z]\}dz \tag{25}$$

Integrate to get an equation for the Mach number growth rate in a vertical chimney:

$$M/M_1 = [1 - (g/c_p)z/T_1]^{-1/2(\gamma+1)/(\gamma-1)} \tag{26}$$

By using Eq. (16) with the present assumptions, the chimney pressure ratio is:

$$p/p_1 = (M/M_1)^{-1}(T/T_1)^{0.5} \tag{27}$$

Substitute (26) and (19):

$$p/p_1 = [1 - (g/c_p)z/T_1]^{1/2(\gamma+1)/(\gamma-1)}[1 - (g/c_p)z/T_1]^{1/2} \tag{28}$$

Add the exponents:

$$p/p_1 = \{1 - gz/(c_p T_1)\}^{\gamma/(\gamma-1)} \tag{29}$$

This agrees with the equation for the pressure lapse rate corresponding to the adiabatic temperature lapse rate of $g/c_p = 9.81/1005 = 0.00976$°C/m.

It is gratifying to see that when the chimney inlet Mach number approaches zero, in the absence of friction, heat transfer, internal obstructions and work extraction, the system of equations to be solved reduces to the adiabatic lapse rate for temperature and pressure. Additionally, a useful equation for Mach number ratio in a vertical chimney presented itself in the derivation.

Sensitivity Analysis

Now that we have at least one exact solution to the system of equations we shall check how accurate a finite difference solution with one step over the 1500 m height is. We shall then use that as a benchmark to investigate the effect of a realistic inlet Mach number and other terms in the equation. It would be helpful to first consider the typical chimney geometry and operating conditions.

Numerical Values for Ideal 1500 m High 160 m Diameter Chimney. According to preliminary calculations a 200 MW peak power plant could have a solar collector diameter of 4 km and a chimney height of 1500 m and an inner diameter of 160 m. When sited at an elevation where the typical atmospheric conditions are 30°C (303,2K) and 90 kPa the air temperature rise could be 20°C in the collector (to 323,2 K), resulting in an optimal chimney through-flow velocity of 10 to 20 m/s. Assuming adiabatic lapse rates in the chimney, the temperature will drop by 14.6°C or 4.53 percent K through the chimney. The pressure ratio will then be $0.9547^{3.5} = 0.850$, the Mach number ratio $0.9547^{-3} = 1.1492$ and the density ratio $0.9547^{2.5} = 0.891$. The decrease in density ratio implies that in a constant area chimney, where ρV is constant, the velocity and dynamic pressure, $1/2\rho V^2$ will increase with the inverse ratio of the density to satisfy mass conservation. This implies that the dynamic pressure is 1/0.891 or 112.3 percent as high at the exit of a 1500 m high chimney as at the bottom. Since the chimney exit loss is equal to the dynamic pressure at its exit, the aerodynamic benefits of flaring the chimney to keep the Mach number constant, for example, are obvious.

Calculate the typical Mach number level at the bottom of a chimney from Eq. (12) and assuming a chimney diameter $D = 160$ m, and a flow area $A = 20110\ m^2$, with mass flow m 386,000 kg/s and $p = 90$ kPa. Then:

$$M_1^2 = \{1/(\gamma-1)^2 + [m/(A_1 p_1)]^2 2RT_1/[\gamma(\gamma-1)]\}^{0.5} - 1/(\gamma-1) \tag{12}$$

$$M_1^2 = \{1/0.4^2 + [386{,}000/(20{,}110\times 90{,}000)]^2 \times 2\times 287\times 323.2/[1.4(0.4)]\}^{0.5} - 1/0.4$$
$$M_1 = 0.0549 \tag{30}$$

At the bottom of the chimney the static temperature is then, $t_1 = 323.0$ K, the sonic velocity, $a_1 = 360.3$ m/s and the velocity, $V_1 = 19.8$ m/s. The density, $\rho_1 = 0.971\ kg/m^3$ and the dynamic pressure, $1/2\rho V^2 = 190$ Pa.

Discretization Error Investigation. Substitute $T - T_1 = \Delta T$ in equation (19) and divide by T_1:

$$\Delta T/T_1 = -gz/(c_p T_1) \tag{31}$$

Note that $gz/(c_p T_1)$ is the ratio of the change in potential energy over the chimney height to the inlet enthalpy per unit mass of the chimney flow. We shall use the symbol E_1 for this ratio.

$$\Delta T/T_1 = -E_1 \tag{32}$$

Write the two-term binomial expansion of (26):

$$M/M_1 = (M_1 + \Delta M)/M_1 \approx [1 + 1/2(\gamma+1)/(\gamma-1) g\Delta z/(c_p T_1)] \tag{33}$$

Thus, for $\gamma = 1.4$:

$$\Delta M/M_1 \approx 1/2(\gamma+1)/(\gamma-1)E_1 = 3.0E_1 \tag{34}$$

Similarly, from (29):

$$1 + \Delta p/p_1 \approx 1 - [\gamma/(\gamma-1)]E_1 \tag{35}$$

For $\gamma = 1.4$:

$$\Delta p/p_1 \approx -3.5E_1 \tag{36}$$

By logarithmic differentiation of the equation of state, remembering that $t \Rightarrow T$ when $M \Rightarrow 0$:

$$\Delta\rho/\rho = \Delta p/p - \Delta T/T \tag{37}$$

So, from (36) and (32):

$$\Delta\rho/\rho_1 \approx -3.5E_1 - (-E_1) = -2.5E_1 \tag{38}$$

Table 1 compares results from the single step discretized solution to exact results for a 1500 m chimney, with $g = 9.81\ m/s^2$, $c_p = 1005$ J/(kg K) and $T_1 = 323.2$ K. From Eq. (31) calculate

Table 1 Comparison between exact and discretized changes in $\Delta T/T_1$, $\Delta M/M_1$, $\Delta p/p_1$ and, $\Delta\rho/\rho_1$ for 1500 m high chimney when $M_1 \Rightarrow 0$

Normalized difference	Exact (%)	Discre -tized	% Error
Temperature difference, $(T_2 - T_1)/T_1$	-4.53	-4.53	0.0
Mach number difference, $(M_2-M_1)/M_1$	14.22	13.59	4.4
Pressure difference, $(p_2 - p_1)/p_1$	-14.98	-15.86	5.9
Density difference, $(\rho_2 - \rho_1)/\rho_1$	-10.94	-11.33	3.5

Table 2 Comparison between exact and discretized changes in ΔT, ΔM, Δp and, $\Delta\rho$ for 1500 m high chimney when $M_1 \Rightarrow 0$

Dimensional difference	Exact	Discre- tized
Temperature difference, $(T_2 - T_1)$ [K]	-14.64	-14.64
Pressure difference, $(p_2 - p_1)$ [Pa]	-13480	-14270
Density difference, $(\rho_2 - \rho_1)$ [kg/m^3]	-0.1062	-0.1010

$\Delta T/T_1 = E_1 = -g\Delta z/(c_p T_1) = -0.0453$. Subscripts 1 and 2 indicate the bottom and top of the chimney. The errors are based on magnitudes, disregarding signs.

For a 1500 m step length the discretization errors are less than 6 percent, but can be reduced more or less proportionally to the integration step length. For 15 m step lengths they should be less than 0.06 percent. Since the discretized values are reasonably accurate even for tall chimneys, they will serve as a basis for further initial investigations.

The dimensional differences are in Table 2.

As rules of thumb for low Mach number flow in an ideal chimney we may assume the following: the temperature decreases at the rate of 10°C per 1000 m, the pressure decreases at 10 kPa per 1000 m, the Mach number increases at 10 percent per 1000 m and the dynamic pressure at 10 percent per 1000 m.

Effect of Inlet Mach Number on Mach Number Change in a 1500 m High Chimney. We still assume an ideal chimney but we now drop the assumption that M_1 approaches zero. It is evident from (18) that Mach number has no effect on stagnation temperature, since z alone determines it. Equation (10) gives the Mach number change:

$$[dM/M]/\{[1 + M^2(\gamma-1)/2]/(1-M^2)\} = [gdz/(Rt) + (dT/T)(1+\gamma M^2)/2] \tag{39}$$

Substitute $t = T/[1 + M^2(\gamma-1)/2]$ and $R = c_p(\gamma-1)/\gamma$:

$$[dM/M]/\{[1 + M^2(\gamma-1)/2]/(1-M^2)\} = \{[gdz/(c_p T)][\gamma/(\gamma-1)][1 + M^2(\gamma-1)/2]^2 + (dT/T)[(1+\gamma M^2)/2]\} \tag{40}$$

Eliminate $gdz/(c_p T)$ through (18):

$$[dM/M]/\{[1 + M^2(\gamma-1)/2]/(1-M^2)\} = \{(dT/T)[-\gamma/(\gamma-1)][1 + M_1^2(\gamma-1)/2] + (dT/T)(1+\gamma M_1^2)/2\} \tag{41}$$

$$= [-\gamma/(\gamma-1) - M^2\gamma/2 + 1/2 + M^2\gamma/2](dT/T) \tag{42}$$

$$= [-1/2(\gamma+1)/(\gamma-1)](dT/T) \tag{43}$$

Discretize:

$$\Delta M/M_1 = [-1/2(\gamma+1)/(\gamma-1)] \times [1 + M_1^2(\gamma-1)/2]/(1-M_1^2)](\Delta T/T_1) = C_{MT}(\Delta T/T_1) \tag{44}$$

Where:

Table 3 Effect of chimney inlet Mach number, M_1 on fractional Mach number change $\Delta M/M_1$ for ideal 1500 m high chimney

M_1 = chimney inlet Mach number	C_{MT} = Ratio of change in M to change in T	% $\Delta M/M_1$ change compared to when $M_1=0$
0.00	-3.0000	0.00
0.05	-3.0090	0.30
0.10	-3.0364	1.21
0.20	-3.1500	5.00
0.40	-3.6857	22.86

$$C_{MT}=(\Delta M/M_1)/(\Delta T/T_1)$$
$$=[-1/2(\gamma+1)/(\gamma-1)][1+M_1^2(\gamma-1)/2]/(1-M_1^2)] \quad (45)$$

The fractional change in $\Delta M/M_1$ compared to $\Delta M/M_1$ when M_1 approaches zero, is given by:

$$[(\Delta M/M_1)-\Delta M/M_1)_{M1\Rightarrow 0}]/[(\Delta M/M_1)_{M1\Rightarrow 0}]$$
$$=(|C_{MT}|-|-3.0|)/|-3.0| \quad (46)$$

It is expressed as a percentage in Table 3.

As long as the chimney inlet Mach number, M_1 is below 0.05 it has a small effect on its own rate of change. But as the inlet Mach number increases, its rate of change increases quadratically. For $M_1=0.05$ the Mach number rate of change is 0.30 percent larger than when M_1 approaches zero. We shall see that the effect of this small acceleration on the pressure drop in the chimney is important even at that low Mach number.

Effect of Inlet Mach Number on Pressure Change in an Ideal 1500 m High Chimney. We shall now investigate how the inlet Mach number level affects the pressure drop in an ideal chimney. To evaluate that, we have to determine how dp/p varies when M_1 is not zero. Although the flow area is constant in an ideal chimney we treat A as a variable for later use. Start with Eq. (16), written for a general position (chimney height):

$$p=[m/(AM)]/\{[1+M^2(\gamma-1)/2]\gamma/(RT)\}^{0.5} \quad (47)$$

Apply logarithmic differentiation:

$$dp/p=-dA/A-dM/M$$
$$-\{[M^2(\gamma-1)/2]/[1+M^2(\gamma-1)/2]\}dM/M$$
$$+(1/2)dT/T \quad (48)$$

Simplify:

$$dp/p=-dA/A$$
$$-\{[1+M^2(\gamma-1)]/[1+M^2(\gamma-1)/2]\}dM/M$$
$$+(1/2)dT/T \quad (49)$$

Define:

$$C_{pM}=-[1+M_1^2(\gamma-1)]/[1+M_1^2(\gamma-1)/2].$$

Then:

$$\Delta p/p_1=-dA/A+C_{pM}\Delta M/M_1+C_{pT1}\Delta T/T_1 \quad (50)$$

where:

Table 4 Effect of chimney inlet Mach number, M_1 on pressure change, $\Delta p/p_1$ and acceleration pressure drop in ideal 1500 m high chimney

M_1	C_{pM} =Ratio of change in p to change in M	C_{pT} = Ratio of change in p to change in T	$\Delta p/p_1$ change (%)	Acceleration pressure drop [Pa]
0.00	-1.000	3.5000	0.00	0.0
0.05	-1.0005	3.5105	0.30	43
0.10	-1.0020	3.5424	1.21	173
0.20	-1.0079	3.6750	5.00	714
0.40	-1.0310	4.3000	22.86	3262

$$C_{pT1}=(\Delta p/p_1)/(\Delta T/T_1)=0.5 \quad (51)$$

Substitute (44):

$$\Delta p/p_1=-dA/A+C_{pM}C_{MT}(\Delta T/T_1)+C_{pT1}\Delta T/T_1 \quad (52)$$

$$\Delta p/p_1=-dA/A+(C_{pM}C_{MT}+C_{pT1})\Delta T/T_1=C_{pT}\Delta T/T \quad (53)$$

The fractional change in $\Delta p/p_1$ compared to $\Delta p/p_1$ when M_1 approaches zero, is given by:

$$[(\Delta p/p_1)-\Delta p/p_1)_{M1\Rightarrow 0}]/[(\Delta p/p_1)_{M1\Rightarrow 0}]=[|C_{pT}|-3.5)]/3.5 \quad (54)$$

It is expressed as a percentage in Table 4, and in the last column as the pressure drop caused by vertical acceleration in the absence of frictional and other loss mechanisms.

It is clear from Table 4 that the inlet Mach number at the bottom of the chimney should be extremely low to avoid a large increase in the chimney pressure drop compared to the no-flow condition. The additional pressure drop increases approximately with the square of the inlet Mach number. Even at a low Mach number of 0.05 the additional pressure drop due to acceleration (using the discretized fractional stationary pressure drop of -0.1586) is $0.0030\times(-0.1586)\times 90{,}000=43$ Pa. Note that this is not a frictional pressure drop but is a pressure drop due to the weight of the fluid when in vertical motion. Due to the density drop through the chimney the flow must accelerate through it. The acceleration requires an additional pressure gradient above the one for stationary conditions in the chimney. We shall now investigate the effect of fluid friction, drag and loss coefficients on the pressure drop.

Effect of Fluid Friction, Drag and Loss on Mach Number in a 1500 m High Chimney. The drag term, $\delta F_D/(pA)$ can be seen as including any so-called minor or additional losses such as those caused by sudden expansions for example. Such a pressure loss is usually written as a coefficient, K multiplied by the dynamic pressure, that is:

$$\delta p=K\rho V^2/2 \quad (55)$$

so that:

$$\delta F_k=KA\rho V^2/2 \quad (56)$$

and:

$$\delta F_k/(pA)=K\gamma M^2/2 \quad (57)$$

Table 5 Effect of chimney inlet Mach number, M_1 on Mach number change, $\Delta M/M_1$ for friction coefficient=0.0084, (FD_1 =0.07901) in 1500 m high chimney

M_1	% Change in Mach number due to T	C_{MFD}= Ratio of change in M to change in FD_1	% Change in Mach number due to FD_1	% $\Delta M/M_1$ change due to friction	% $\Delta M/M_1$ change due to acceler-ation
0.00	13.591	0.00000	0.000	0.00	0.00
0.05	13.632	0.00176	0.014	0.10	0.30
0.10	13.756	0.00708	0.056	0.41	1.21
0.20	14.270	0.02940	0.232	1.63	5.00
0.40	16.697	0.13760	1.087	6.51	22.86

Table 6 Effect of chimney inlet Mach number, M_1 on Mach number change, $\Delta M/M_1$ for $\Delta A/A_1$=0.013591 in a 1500 m high chimney

M_1	% Change in Mach number due to T	C_{MA}= ratio of change in M to change in A	% Change in Mach number due to A	Total $\Delta M/M_1$ change (%)
0.00	13.591	-1.0000	-13.591	0.00
0.05	13.632	-1.0030	-13.632	0.00
0.10	13.756	-1.0121	-13.756	0.00
0.20	14.270	-1.0500	-14.270	0.00
0.40	16.697	-1.2286	-16.697	0.00

When written in this form any drag or pressure loss term can be included in the skin friction term and treated similarly. For a constant area chimney, Eq. (10) then becomes:

$$dM/M=\{[1+M^2(\gamma-1)/2]/(1-M^2)\}[(fdz/D)\gamma M^2/2 + gdz/(Rt)+K\gamma M^2/2+(dT/T)(1+\gamma M^2)/2] \quad (58)$$

Collect terms and write t in terms of T and M, as in the derivation of (40):

$$dM/M/\{[1+M^2(\gamma-1)/2]/(1-M^2)\} =[(fdz/D)+K](\gamma M^2/2)] +[gdz/(Rt)+(dT/T)(1+\gamma M^2)/2] \quad (59)$$

Treat the second term on the right in (59) as in the derivation of (45). Then:

$$\Delta M/M_1=[(f_1 z/D_1)+K]C_{MFD}+C_{MT}\Delta T/T_1 \quad (61)$$

where:

$$C_{MFD}=(\gamma M_1^2/2)[1+M_1^2(\gamma-1)/2]/(1-M_1^2) \quad (60)$$

Then:

$$\Delta M/M_1=C_{MFD}FD_1+C_{MT}\Delta T/T_1 \quad (62)$$

where FD_1 is the friction-drag-loss term.

At chimney inlet conditions the density is 0.9705 kg/m^3, the dynamic viscosity is 1.95×10^{-5} Ns/m^2 and the velocity is 19.8 m/s. For a chimney diameter of 160 m the Reynolds number is then 1.57×10^8. The relative roughness for concrete is 2 mm. The Haaland equation [7] cited by White [6], then gives f_1 =0.008428. Then $f_1 z/D=0.07901$. As a first case neglect drag, protrusions and other loss coefficients, and take the additional loss coefficient, $K=0.0$.

It is clear from Table 5 that the additional effect of the assumed friction coefficient on Mach number change is limited to a fraction (about one third) of the effect of vertical acceleration at the typical operating inlet Mach number of about 0.05. Each additional increase in loss coefficient, K of 0.079 will have about the same small effect.

We have previously seen that the percentage change in pressure is the same as that in Mach number (except for a sign change). The conclusion is that in practice the effect of chimney skin friction on chimney pressure loss will be small.

Effect of Area Change on Mach Number in a 1500 m High Chimney. The most effective way of controlling the Mach number distribution through the chimney is to vary the area ratio, A. For a given chimney height an increase in area ratio is the only way of reducing the Mach number or its rate of increase through the chimney. For a variable area chimney with no friction or additional losses, a derivation analogous to the previous one leads to the following relationship:

$$dM/M=-dA/A[1+M^2(\gamma-1)/2]/(1-M^2)+C_{MT}\Delta T/T_1 \quad (63)$$

$$\Delta M/M_1=C_{MA}\Delta A/A_1+C_{MT}\Delta T/T_1 \quad (64)$$

It is evident from Table 6 that the increase in Mach number in the chimney can be entirely eliminated by a relatively small (14 percent) increase in chimney area and that the required area change is independent on Mach number. Greater changes in chimney flow area will lead to reductions in Mach number and increases in static pressure in the chimney.

Performance of a Typical Chimney

The condition that determines flow through a chimney is that the exit pressure at the top of the chimney must be equal to the ambient atmospheric pressure at that altitude. Since the temperature of the air in the chimney is higher and the density lower than outside, the noflow difference in static pressure in the chimney (pressure at bottom minus pressure at top) will be lower than outside. This difference will cause the flow to accelerate until the chimney exit pressure is equal to the ambient. As the flow in the chimney accelerates and the Mach number increases, additional pressure drop mechanisms will develop as discussed in the text. We shall now look a three typical through-flow velocities of 10 and 20 m/s. The initial air standard analysis (Von Backström, [3]) indicated that 19.8 m/s would be close to the expected velocity, but a later more detailed analysis that included the solar collector (Gannon and von Backström, [4]) indicated 10 m/s as closer to the optimum for maximum power extraction.

The equivalent sand roughness of the concrete chimney walls is 2 mm. The typically expected chimney inlet loss coefficient is

Table 7 Effect of chimney inlet velocity, V_1 on various pressures and pressure drops in a 1500 m high, 160 m diameter chimney

Inlet velocity ⇒	$V_1 = 10$ m/s	$V_1 = 20$ m/s	% of inlet
Reference pressures	[Pa]	[Pa]	dynamic
Inlet stagnation pressure	90000	90000	-
Inlet dynamic pressure	48	194	100
Inlet static pressure	89952	90194	-
Exit dynamic pressure	55	218	112
No-flow Δp	14270	14270	-
Pressure loss mechanism ⇓			
Vertical acceleration Δp	-13	-53	27
Friction Δp	-4	-15	8
Chimney inlet Δp, K = 0.25	-12	-49	25
Chimney internal Δp, K =0.25	-12	-49	25
Sum of pressure losses	-41	-166	85
Sum of losses + exit dynamic	-96	-384	-198
Ideal diffuser pressure rise, $\Delta A/A_1 = 0.13591$	+13	+53	27

about 0.25 and we assumed the same value for the internal chimney bracing by cables or rods. Design and experimentation must still finalize them.

The following is evident from Table 7:

- The major pressure drop is the no-flow pressure drop of 14,270 Pa
- The exit dynamic pressure is 12 percent larger than the inlet dynamic pressure
- The vertical acceleration pressure drop is 27 percent of the inlet dynamic pressure
- The friction pressure drop is about one third of the vertical acceleration pressure drop
- The vertical acceleration pressure drop may be larger than the chimney inlet pressure drop
- The total expected chimney pressure drop is of the order of twice the chimney inlet dynamic pressure for a constant area chimney
- The vertical acceleration pressure drop can be eliminated by flaring the chimney by about 14 percent

Conclusions

The paper presents a one-dimensional compressible flow approach for the calculation of all the thermodynamic variables as dependent on chimney height, wall friction, additional losses, internal drag and area change. For the no-flow condition, the differential equations reduce to the adiabatic temperature lapse rate and associated pressure equation. The discretized method predicted no-flow pressure and density differences to within 6 percent and 4 percent even over a single 1500 m step length, used for illustration. Good accuracy is possible with multiple (say 100) steps. The method is also applicable to the complete plant where heat transfer and shaft work may be present.

It turns out that the pressure drop associated with the vertical acceleration of the air is about three times the pressure drop associated with wall friction. So reducing the wall friction by smoothing the walls will have a smaller than usual effect. But flaring the chimney by 14 percent to keep the through-flow Mach number constant, virtually eliminates the vertical acceleration pressure drop. Since the flow is not decelerating, excellent pressure recovery can be expected. However, flow stratification resulting from hot air from near the collector floor rushing up in the middle of the chimney may inhibit the pressure recovery.

Since the vertical acceleration pressure drop is so large, no effort should be spared to design the chimney in such a way that the flow area increases with height, even if only marginally. A 14 percent increase in area is equivalent to a 13 m increase in diameter for a 160 m diameter chimney. Here follows a list of possible ways of increasing the flow area with height:

- The reduction in chimney wall width with altitude can be on the inside rather than on the outside
- Where protrusions occur to anchor the cross bracing, the higher chimney section can have a slightly larger diameter than the lower section
- Buttresses in the lower sections of the chimney should preferably be on the inside, where they reduce the flow area, rather than on the outside
- Since wall friction has such a small effect, the lower sections of the chimney where the walls are thicker may be fluted (folded zig-zag) inwards to reduce the flow area.

A relatively short diffuser on the chimney exit is likely to be less effective than preventing the flow acceleration in the first place.

Nomenclature

A = flow area [m^2]
C = coefficient
c_p = specific heat [J/kg K]
D = chimney inside diameter [m]
E = potential to inlet energy ratio
F_D = drag force [N]
f = friction coefficient
g = gravitational acceleration [m/s^2]
H = stagnation enthalpy [J/kg]
h = static enthalpy [J/kg]
K = pressure drop coefficient
M = Mach number
m = mass flow [kg/s]
P = stagnation pressure [Pa]
p = static pressure [Pa]
Q = heat per unit mass [J/kg]
R = gas constant [J/kg K]
T = stagnation temperature [K]
t = static temperature [K]
V = velocity [m/s]
W = work per unit mass [J/kg]
z = chimney height [m]

Greek

γ = specific heat ratio
ρ = density [kg/m^3]

Prefix

Δ = change in value
δ = prefix: elemental value

Subscript

D = drag
MA = effect of A on M
MFD = effect of friction etc. on M
MT = effect of T on M
pM = effect of M on p
pT = (also $pT1$) effect of T on p
1 = inlet (or coefficient number)
2 = exit (or coefficient number)

References

[1] Haaf, W., Friedrich, K., Mayr, G., and Schlaich, J., 1983, ''Solar Chimneys: Part I: Principle and Construction of the Pilot Plant in Manzanares,'' Int. J. Solar Energy, **2**, No. 1, pp. 3–20.
[2] Haaf, W., 1984, ''Solar Chimneys: Part II: Preliminary Test Results from the Manzanares Pilot Plant,'' Int. J. Solar Energy, **2**, No. 2, pp. 141–161.
[3] Von Backström, T. W., and Gannon, A. J., 2000, ''The Solar Chimney Air Standard Cycle,'' South Afr. Inst. Mech. Eng. R&D J., **16**, pp. 16–24.
[4] Gannon, A. J., and Von Backström, T. W., 2000, *Solar Chimney Cycle Analysis Including Losses and Solar Collector Performance*, Proceedings of Solar 2000, Madison, Wisconsin, June 2000.
[5] Zucrow, M. J., and Hoffman J. D., *Gas Dynamics*, Wiley, New York, 1976.
[6] White, F. M., *Fluid Mechanics*, 4th ed., McGraw-Hill, New York, 1999.
[7] Haaland, S. E., 1983, ''Simple and explicit formulas for the friction factor in turbulent pipe flow,'' J. Fluids Eng., **105**, pp. 89–90.

Journal of Solar Energy Engineering

Technical Briefs

A New 75 kW High-Flux Solar Simulator for High-Temperature Thermal and Thermochemical Research

D. Hirsch, P. v. Zedtwitz, and T. Osinga
Institute of Energy Technology, Department of Mechanical and Process Engineering, ETH-Swiss Federal Institute of Technology, ETH-Zentrum, CH-8092 Zurich, Switzerland

J. Kinamore
Vortek Industries Ltd., Vancouver BC, V6P 6T7 Canada

A. Steinfeld*
Institute of Energy Technology, ETH-Swiss Federal Institute of Technology, CH-8092 Zurich, Switzerland; also Solar Process Technology, Paul Scherrer Institute, CH-5232 Villigen, Switzerland
e-mail: aldo.steinfeld@eth.ch

A new high-flux solar simulator, capable of delivering up to 75 kW of continuous radiative power at peak fluxes exceeding 4250 kW/m^2*, is operational at the ETH-Zurich. Its optical design and performance are described. This unique facility serves principally as an experimental platform for investigating thermal and thermochemical processes at temperatures up to 3000°K.*
[DOI: 10.1115/1.1528922]

Description

The ETH's High-Flux Solar Simulator, shown in Fig. 1, provides a rapid external source of intense thermal radiation that approaches the heat transfer characteristics of highly concentrating solar systems. The light source is a high-pressure (7 atm) argon arc enclosed in a clear quartz envelope of 27 mm-dia, 1.5 mm-thickness, and 200 mm-length. Maximal electrical power input to the tungsten-made arc electrodes is, according to specifications, 200 kW DC under a maximal electrical current of 700 A. The arc envelope is internally cooled by using a swirling film of de-ionized water that rapidly flows between the plasma arc and the clear quartz lamp tube, as shown schematically in Fig. 2. The arc produces radiation at visible wavelengths with additional power in the near infrared and ultraviolet regions of the spectrum. Figure 3 shows the spectral distribution of emitted radiation. Optical filters can be applied to the tubular quartz envelope for ad-

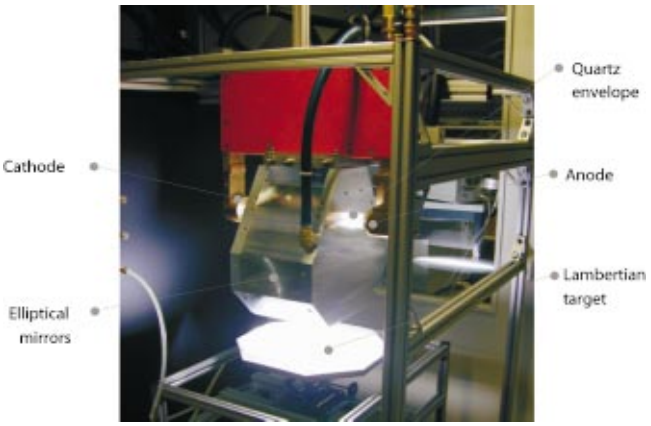

Fig. 1 The High-Flux Solar Simulator at ETH. The argon arc lamp is enclosed by an elliptical mirror that redirects the radiant power into the target.

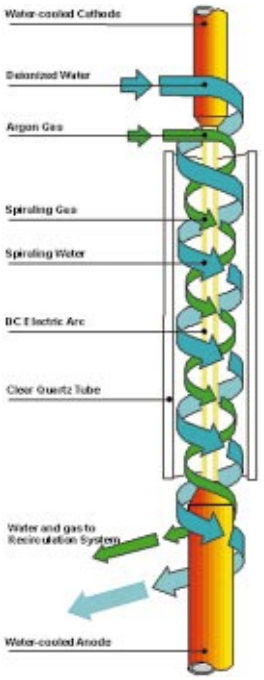

Fig. 2 Schematic of high-pressure argon arc configuration showing swirling water flow for internal cooling of quartz envelope [1]

*Corresponding author.

Contributed by the Solar Energy Division of the American Society of Mechanical Engineers for publication in the ASME JOURNAL OF SOLAR ENERGY ENGINEERING. Manuscript received by the ASME Solar Energy Division, August 2001; final revision, April 2002. Associate Editor: A. Kribus.

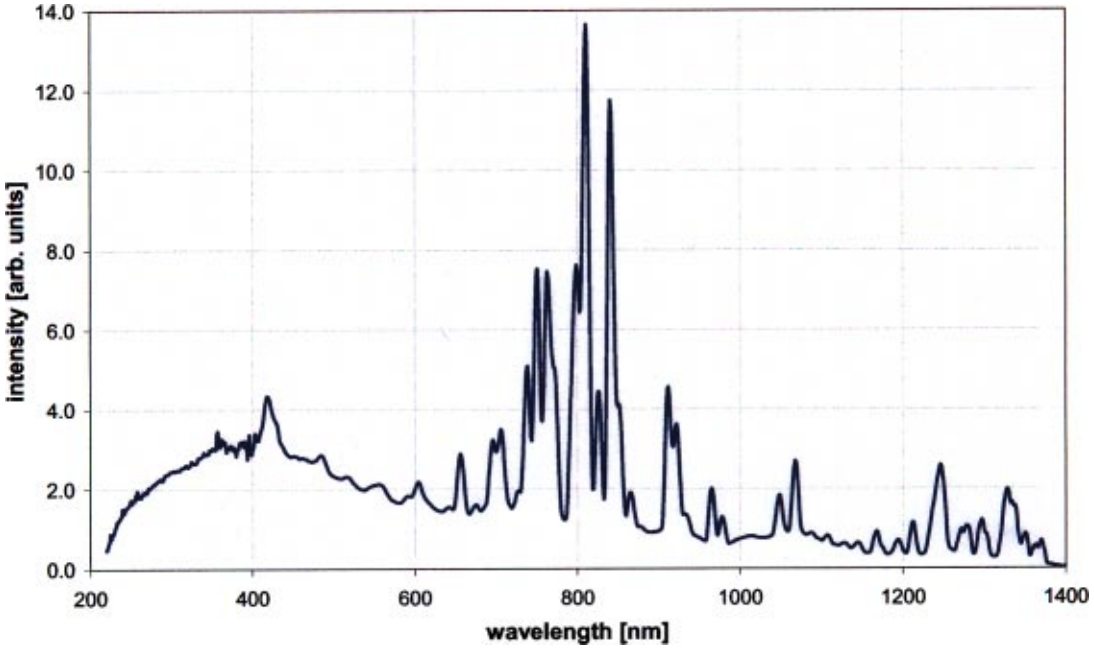

Fig. 3 Spectral distribution of radiant energy emitted by the argon arc lamp [1]

justing the spectral distribution, but at the expense of losing radiative power. The system was manufactured by Vortek, Canada [1].

The light source is close-coupled to precision optical reflectors to produce an intense beam of concentrated radiant energy. The focusing mirrors are horizontal-axis troughs of elliptical cross section having a vertical major axis and are positioned with one of the linear foci coinciding with the arc. The focal plane of the solar simulator is thus defined as the horizontal plane perpendicular to the ellipse's major axis containing the second linear focus. The elliptical mirrors are truncated 9.2 cm above the focal plane to permit external access, so that the reflected beam-down radiation is confined within an angular range of half-angle 45 deg. With this arrangement, it is possible to achieve at the focal plane power flux intensities equivalent to solar concentration ratios of 5000 suns (1 sun=1 kW/m^2). Power, power fluxes, and temperatures can be adjusted to meet the specific requirements of the application by simply varying the position of the test target along the ellipse's major axis or by varying the electrical input power to the arc electrodes. A 2-dimensional trough compound parabolic concentrator (2D-CPC) can be positioned in tandem with the elliptical mirrors, with its entrance at the focal plane, as shown in Fig. 4. The result is an augmentation of the mean radiation flux over the CPC entrance by at least a factor of $\rho/\sin\Phi$, where ρ is the CPC's total specular reflectivity and Φ its half-acceptance angle, because no incoming ray will be rejected [2]. However, due to the non-

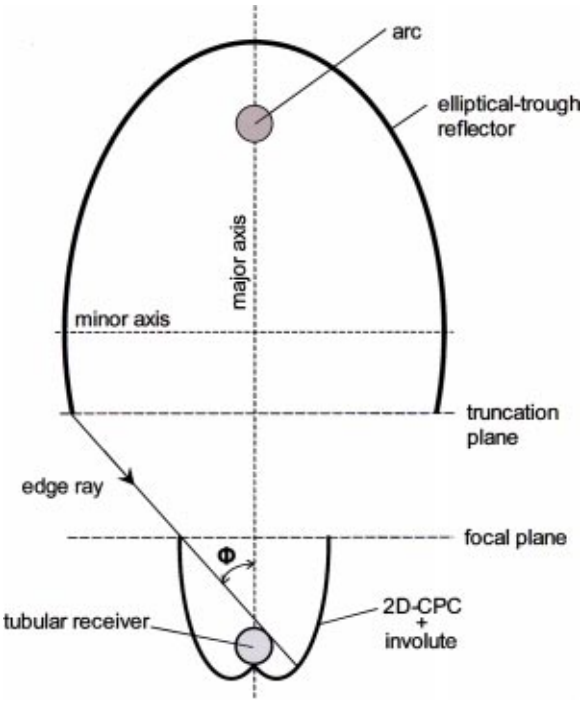

Fig. 4 Optical configuration of the elliptical-trough reflector coupled to a 2D-CPC and a matching involute for achieving uniform irradiation on a tubular receiver

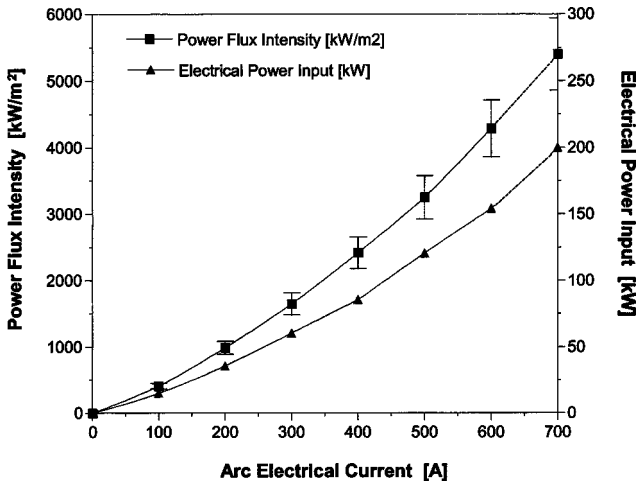

Fig. 5 Variation of the peak power flux at the focal plane and the electrical power input to the arc as a function of the arc electrical current

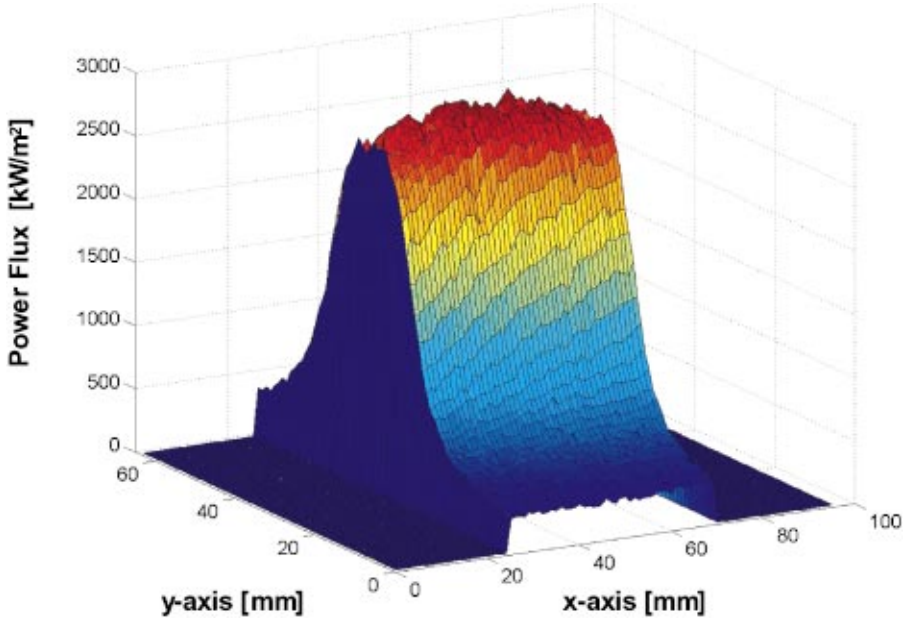

Fig. 6 Distribution of the power flux (in kW/m^2) measured at the focal plane, for an arc electrical current of 500 A. The x-axis is parallel to the arc direction.

uniform directional distribution of incoming rays from the primary elliptical mirrors, the exact final concentration at each location of the CPC's exit can only be predicted using ray tracing techniques. For applications requiring a tubular receiver/reactor, a matching involute reflector as shown in Fig. 4 can also produce more uniform irradiation incident on the tube's surface. When a 3D-CPC is positioned with its circular entrance at the focal plane, the mean power flux intercepted by its entrance is further augmented by a factor of about $\rho/\sin^2\Phi$, depending on the rejected skew rays.

Performance

Power flux intensities are measured optically by recording the image of the arc on a water-cooled plate positioned at the focal plane. Such a plate has been plasma-coated with Al_2O_3 so that it reflects diffusely and closely approaches a Lambertian target. A 10-bit digital CCD camera is used to record the arc image and is calibrated with an absolute point Kendall radiometer. The accuracy of the flux measurement is $\pm 10\%$ [3]. Two PCs take charge of the main control system, the data acquisition system, and the flux measurement system.

The variation of the peak power flux intercepted at the focal plane as a function of the arc electrical current is shown in Fig. 5. All graph points are measured data, except the one for 700 A (maximum allowable electrical current), which is the result of extrapolation. Radiation flux intensities greater than 4250 kW/m^2 can be obtained for arc currents above 600 A. Such high radiation fluxes correspond to stagnation temperatures[†] exceeding 2900°K. Furthermore, using a tandem CPC with half-acceptance angle of 45 deg and specular reflectivity of 95%, the mean power flux at its exit can be increased by 30% for the 2D-CPC, and by approximately 90% for the 3D-CPC. Rays exiting a 3D-CPC have directions confined to a semi-sphere. Both 2D-CPC and 3D-CPC type of secondary concentrators have been designed and fabricated as integral components of solar receivers and reactors. Also plotted in Fig. 5 is the electrical power input to the arc, obtained by multiplying measured current and voltage. Although not measured, it is estimated that about 50% of the input electrical power is converted to emitted radiation, the remainder being heat losses removed by active cooling.

The power flux distribution at the focal plane corresponding to 500 A is shown in Fig. 6 as a 3D-surface plot. Noticeable is the trough-type power flux distribution, as expected for the elliptical-trough geometry of the focusing mirrors. The thickness of the *hot spot* (i.e., the band region of high power flux) is about 15 mm. Within this band, the power flux is rather uniform ($\pm 8\%$), but it decreases rapidly outside this band. Along the arc direction, the power flux is uniform within 100 mm. For applications using cavity-type receivers, the non-uniformity of the incident power flux distribution over the aperture should not significantly affect the net power flux distribution across the inner cavity walls be-

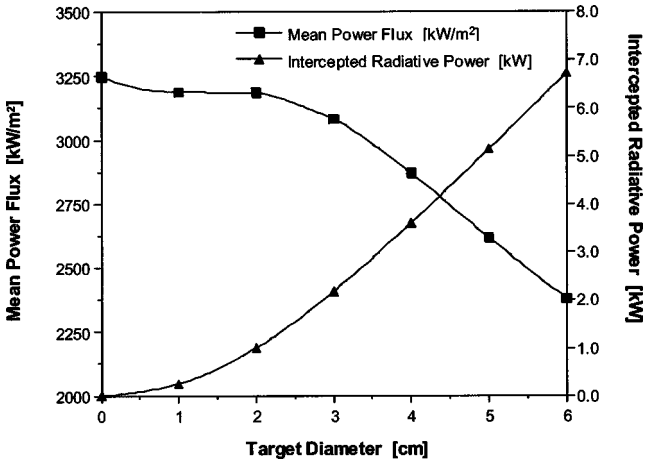

Fig. 7 Radiative power and mean power flux intercepted by a circular target as a function of its diameter, for an arc electrical current of 500 A (calculated by numerical integration of the measured power fluxes over the target's area). The circular target is positioned at the focal plane with its center at the point of maximum power flux.

[†]The stagnation temperature is the highest temperature an ideal blackbody cavity-receiver is capable of achieving when energy is being re-radiated as fast as it is absorbed. It is given by $(P/\sigma)^{0.25}$, where P is the power flux, and σ is the Stefan-Boltzmann constant.

cause of multiple internal reflections, absorptions, and re-emissions under radiative equilibrium. As expected, flux intensities decrease as the target is moved away from the focal plane. For example, for an arc current of 300 A, the peak power flux decreases 10% at parallel planes ±1 cm from the focal plane.

Figure 7 shows the radiative power intercepted by a circular target as a function of its diameter, calculated by numerical integration of the measured power fluxes over the target's area, when the target is positioned at the focal plane with its center at the point of maximum power flux. Also shown in Fig. 7 is the mean power flux over the target. Thus, a target of 1 cm-dia intercepts about 0.25 kW at a mean power flux of 3190 kW/m^2, while a target of 6 cm-dia intercepts about 6.73 kW at a mean power flux of 2380 kW/m^2. Thus, compared to the performance of other solar simulators, this one is unique in terms of combined high power and high power fluxes delivered to a target, and approaches the capabilities of existing solar furnaces [4].

Finally, the variation of the power intercepted by a circular target as a function of the arc electrical current is shown in Fig. 8, for various target's diameters from 1 to 6 cm. This figure, along with Fig. 7, can be used for selecting the aperture diameter of a cavity-receiver for a given power input. For example, if 5 kW power input is desired, one could either select an aperture of 6 cm-dia and work at 400 A, or an aperture of 5 cm-dia and work at 500 A. For a given arc current, larger apertures intercept more radiation power, but they also re-radiate more energy when operating at high temperatures. Therefore, the optimum aperture size for energy efficient applications results from a compromise between maximizing radiation capture and minimizing re-radiation losses [5].

Applications

The High-Flux Solar Simulator serves as a major experimental platform for investigating high-temperature solar thermal and thermochemical processes. Examples of these energy conversion processes are the production of solar fuels (e.g., solar hydrogen), the processing of energy-intensive chemical commodities (e.g., solar metals, solar syngas, solar cement), and the detoxification and recycling of waste materials (e.g., solar pyrolysis, gasification, and thermal reduction for closed material cycles) [6,7]. Furthermore, this research facility functions as a convenient tool for studying the properties of advanced high-temperature materials under intense radiation and controlled atmospheres.

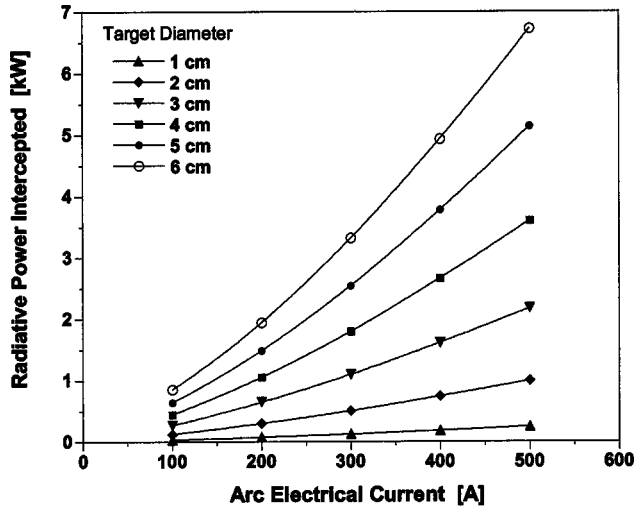

Fig. 8 Variation of the radiative power intercepted by a circular target as a function of the arc electrical current. The parameter is the target's diameter.

Acknowledgments

We thank M. Brack for the power flux measurement calibration and P. Haeberling for the design and installation of the control instrumentation. The High-Flux Solar Simulator has been constructed with financial support from the NEFF-Swiss National Energy Research Foundation and the ETH-Project Nr. TH-29'/99-4.

References

[1] Vortek Industries Ltd., 1999, Model 201-200/200 200 kW Arc Lamp System, Vancouver BC, V6P 6T7 Canada.
[2] Welford, W.T., and Winston, R., 1989, *High Collection Nonimaging Optics*, Academic Press, San Diego, CA.
[3] Seitz, T., 1995, "SunFlux: A Flux Measurement System for Solar Concentrators," SolarPACES Technical Report No. III-2/95, A. Newmann, ed., DLR, 51140 Cologne, Germany, pp. 45–54.
[4] SolarPACES, 1996, Solar Thermal Test Facilities, Editorial CIEMAT, Madrid.
[5] Steinfeld, A., and Schubnell, M., 1993, "Optimum Aperture Size and Operating Temperature of a Solar Cavity-Receiver," Sol. Energy, **50**, pp. 19–25.
[6] Steinfeld, A., and Palumbo, R., 2001, "Solar Thermochemical Process Technology," *Encyclopedia of Physical Science and Technology*, R. A. Meyers, ed., Academic Press, **15**, pp. 237–256.
[7] Further information is found at www.pre.ethz.ch.

Indirectly Irradiated Solar Receiver-Reactors for High-Temperature Thermochemical Processes

Christian Wieckert
e-mail: christian.wieckert@psi.ch

Anton Meier

Solar Process Technology,Paul Scherrer Institute,CH-5232 Villigen, Switzerland

Aldo Steinfeld
ETH-Swiss Federal Institute of Technology,
Department of Mechanical and Process Engineering-Institute of Energy Technology, ETH-Zentrum,
CH-8092 Zurich, Switzerland

A solar receiver-reactor concept for high-temperature thermochemical applications involving gas and condensed phases is presented. It features two cavities in series. The inner cavity is an enclosure, e.g., made of graphite, with a small aperture to let in concentrated solar power. It serves as the solar receiver, radiant absorber, and radiant emitter. The outer cavity is a well-insulated enclosure containing the inner cavity. It serves as the reaction chamber and is subjected to thermal radiation from the inner cavity. The advantages of such a two-cavity reactor concept are outlined. A radiation heat transfer analysis based on the radiosity enclosure theory is formulated and results are presented in the form of generic curves that indicate the design constraints. High energy absorption efficiency can be achieved by minimizing the aperture area, by maximizing the size of the inner cavity and by constructing it from a material of high emissivity.
[DOI: 10.1115/1.1528925]

Contributed by the Solar Energy Division of the American Society of Mechanical Engineers for publication in the ASEM JOURNAL OF SOLAR ENERGY ENGINEERING. Manuscript received by the ASME Solar Energy Division, Nov. 2001; final revision May 2002. Associate Editor: A. Kribus.

1 Introduction

A solar cavity-type receiver is basically an enclosure designed to capture effectively the incident solar radiation by allowing entry of radiation only through a small opening, the *aperture*. Because of multiple reflections among the inner walls of the cavity, its apparent absorptance exceeds the inner surface absorptivity and, consequently, increases its ability to absorb incoming solar radiation. A numerical evaluation of several cavity geometries is given in [1]. Optimal aperture sizes and operating temperatures for maximizing solar energy absorption have been determined in [2]. Cavity receivers are preferred reactor configurations for high-temperature thermochemical applications such as the production of fuels (e.g., reduction of metal oxides, cracking and reforming of hydrocarbons, gasification of coal, biomass, and other carbonaceous materials), the processing of energy-intensive material commodities (e.g., lime, cement, metals) and the recycling of waste materials [3]. Solar reactors may feature direct irradiation of reactants to provide a very efficient means of heat transfer directly to the reaction site. However, a major drawback when working with reducing or inert atmospheres is the requirement for a transparent window, which is a critical and troublesome component in high-pressure or severe gas environments.

The introduction of a protecting inner cavity between the window and the reaction chamber (outer cavity), as shown in Fig. 1, can eliminate this problem. This inner cavity is directly irradiated by the concentrated solar radiation entering through its windowed aperture. As its temperature increases, its walls radiate to all directions. Thus, the inner cavity serves as the solar receiver, radiant absorber, and radiant emitter. Radiation emitted by the inner walls undergoes multiple reflections and absorptions until it is eventually lost through the aperture. In contrast, radiation emitted by the outer walls is absorbed, either directly or after multiple reflections, by the reactants contained in the outer cavity. With this arrangement, the window is protected from the severe chemical environment existing inside the reaction chamber. At the same time, the reaction chamber is protected from severe thermal shocks that often occur in applications with concentrated solar radiation. Furthermore, the reactants inside the reaction chamber are exposed to the radiation emitted by the inner cavity, which is more uniform than the radiation distribution coming directly from the solar concentrating system.

Graphite is the preferred material of construction for the cavity because of its high surface absorptivity/emissivity, excellent thermal shock resistance, reasonable good thermal conductivity, and the possibility to operate at temperatures up to 3500 K in inert atmospheres. For applications at moderate temperatures, the inner cavity can be made of reliable and shock-resistant ceramic materials (e.g., SiC), thus eliminating the need for a window. The two-cavity solar reactor concept has already been applied for aluminum recycling near 1000 K, using an open inner cavity made of SiC [4,5], and for recycling of hazardous solid waste materials at above 1200 K, using an inner cavity made of graphite [6], which needs to be protected from the atmosphere by a window. It may also be applied to thermo-photovoltaic (TPV) systems, in which uniform radiation over the PV cell is desirable. In contrast to TPV, solar thermochemical applications make use of the whole radiation spectrum as the energy source for the endothermic process.

In this technical brief, the radiation exchange of the two-cavity design concept is analyzed using the radiosity method for enclosures. The results are presented in a generic manner for guiding the design of such reactor configurations.

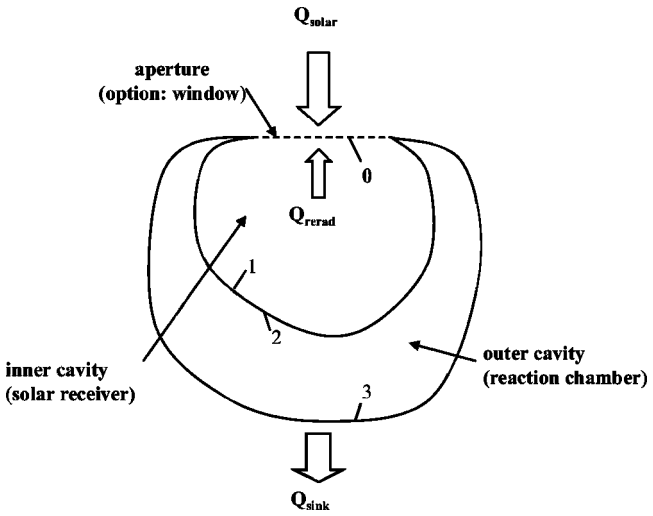

Fig. 1 Schematic of the two-cavity reactor configuration

2 Analysis Using the Radiosity Method

An idealized two-cavity configuration is depicted in Fig. 1. The aperture of the inner cavity is the surface 0 and may be open to the atmosphere or closed by a transparent window. The two cavities are separated by a wall consisting of two surfaces: the inner surface 1 and the outer surface 2. The outer cavity surface 3 completely encloses the inner cavity. Q_{solar} is the incoming solar power entering through the aperture, Q_{rerad} is the power lost through the aperture by re-radiation, and Q_{sink} is the net power absorbed by the outer cavity, which includes the chemical reaction enthalpy as well as conduction heat losses through the outer wall. For the purpose of having a generic description, the detailed geometry of the cavities is not specified. Multiple reflection, absorption, and emission of radiation among the inner walls of the cavity leads to an approximately uniform radiation distribution, even for non-uniform incoming radiation.

The radiosity method for enclosures is applied under the following assumptions [7]: *a*) all surfaces are gray-diffuse; *b*) radiation is uniformly distributed over each surface; *c*) nonparticipating medium; and d) convection and conduction heat transfer within the cavities are neglected. In addition, the inner cavity wall with $\varepsilon_1=\varepsilon_2$ is assumed thin, such that $A_1=A_2$, $T_1=T_2$, and $q_1=-q_2$. The aperture is assumed completely transparent. The power flux through the aperture surface 0 is:

$$q_{solar}=\frac{Q_{solar}}{A_0}. \tag{1}$$

The net power absorbed on surface 3 includes process enthalpy and wall heat losses,

$$q_{sink}=\frac{Q_{sink}}{A_3}. \tag{2}$$

The material flows enter only in the form of a (uniform) sink. Details need not to be described.

Introducing the view factors F_{ij} between the surfaces and the radiosities B_i as the radiant energy leaving surface i by emission and reflection ($B_i>0$ by definition), the system may be described by the following set of equations [7]:

$$\sum_{j=0}^{3}(\delta_{ij}-F_{ij})B_j=\frac{Q_i}{A_i}=q_i; \quad i=0,..,3 \tag{3}$$

and

$$B_i=\sigma T_i^4-q_i\left(\frac{1}{\varepsilon_i}-1\right); \quad i=1,..,3. \tag{4}$$

For an enclosure, $\Sigma_{j=0}^{3}F_{ij}=1 (i=0,..,3)$. Assuming surface 2 is concave, $F_{22}=0$.

Using the reciprocity relations $F_{ij}\cdot A_i=F_{ji}\cdot A_j$ $(i,j=0,..,3)$, the view factor matrix reads

$$\mathbf{F}=\begin{pmatrix} 0 & 1 & 0 & 0 \\ \frac{A_0}{A_2} & 1-\frac{A_0}{A_2} & 0 & 0 \\ 0 & 0 & 0 & 1 \\ 0 & 0 & \frac{A_2}{A_3} & 1-\frac{A_2}{A_3} \end{pmatrix}. \quad (5)$$

Prescribing q_{solar} and q_{sink} ($q_{sink}<0$) as boundary conditions, and using $q_1=q_{sink}\,A_3/A_2$, yields the following solutions for B_i:

$$B_0=q_{solar}; \quad (6)$$

$$B_1=q_{solar}+q_{sink}\cdot\frac{A_3}{A_0}=q_{rerad}; \quad (7)$$

$$B_2=q_{solar}+q_{sink}\cdot\frac{A_3}{A_0}\left(1+2\cdot\frac{A_0}{A_2}\cdot\left(\frac{1}{\varepsilon_2}-1\right)\right); \quad (8)$$

$$B_3=q_{solar}+q_{\mathrm{sink}}\cdot\frac{A_3}{A_0}\left(1+\frac{A_0}{A_2}\cdot\left(\frac{2}{\varepsilon_2}-1\right)\right). \quad (9)$$

3 Results

For the case of a perfectly insulated outer cavity and no chemical reaction, $Q_{sink}=0$ and the incoming energy is completely re-radiated back through the aperture. Thus, at thermal equilibrium, all surfaces reach their maximum temperature T_{max}, given by:

$$T_{\max}=T_1=T_2=T_3=\left(\frac{q_{solar}}{\sigma}\right)^{0.25}, \quad \text{for } q_{sink}=0. \quad (10)$$

For example, for $q_{solar}=1000$, 2000, 3000, 4000, and 5000 kW/m^2, the maximum equilibrium temperature $T_{max}=$ 2050, 2437, 2697, 2898, and 3064 K, respectively.

When $Q_{sink}\neq 0$, Eqs. (4) and (6)–(10) are solved to yield normalized temperatures

$$\frac{T_1}{T_{\max}}=\frac{T_2}{T_{\max}}=\left(1+\frac{Q_{sink}}{Q_{solar}}\cdot\left(1+\frac{A_0}{A_2}\cdot\left(\frac{1}{\varepsilon_2}-1\right)\right)\right)^{0.25} \quad (11)$$

and

$$\frac{T_3}{T_{\max}}=\left(1+\frac{Q_{sink}}{Q_{solar}}\cdot\left(1+\frac{A_0}{A_2}\cdot\left(\frac{2}{\varepsilon_2}-1\right)+\frac{A_0}{A_3}\cdot\left(\frac{1}{\varepsilon_3}-1\right)\right)\right)^{0.25}. \quad (12)$$

We define the solar energy absorption efficiency for the two-cavity reactor, η_{2C}, as

$$\eta_{2C}=-\frac{Q_{sink}}{Q_{solar}}=\frac{1-\frac{T_3^4}{T_{\max}^4}}{1+\frac{A_0}{A_2}\cdot\left(\frac{2}{\varepsilon_2}-1\right)+\frac{A_0}{A_3}\cdot\left(\frac{1}{\varepsilon_3}-1\right)}. \quad (13)$$

The variation of η_{2C} as a function of T_3/T_{max} is plotted in Fig. 2 for different surface area ratios A_2/A_0 and for $\varepsilon_2=\varepsilon_3=1$. As expected, for a given A_2/A_0, η_{2C} decreases with T_3/T_{max} because of the higher re-radiation losses through the aperture. For the limiting case $A_2/A_0\to\infty$, both Eqs. (11) and (12) becomeidentical and, since $A_3/A_0\to\infty$ as well, $T_1=T_2=T_3$. Therefore, it is possible to extract the temperature difference between T_2 and T_3 from Fig. 2: for a desired efficiency $\eta_{2C}=-Q_{sink}/Q_{solar}$, T_2/T_{max} is found from the interception of the horizontal dashed line with the curve corresponding to $A_2/A_0\to\infty$.

For a given temperature ratio T_3/T_{max}, the efficiency η_{2C} increases with the surface area ratio A_2/A_0. This is because Q_{sink} is proportional to the surface area A_2 and increases with increasing temperature difference T_2-T_3. Thus, for given T_3 and Q_{sink}, a smaller surface area A_2 implies a higher temperature T_2, resulting in higher re-radiation losses and lower efficiency η_{2C}. From Eq. (13), a lower emissivity ε_2 results in a higher temperature difference T_2-T_3 and, hence, lower efficiency η_{2C}.

An important drawback of using the two-cavity reactor configuration vis-à-vis the single cavity configuration is the higher re-radiation loss, $Q_{rerad}=Q_{solar}+Q_{sink}$. The efficiency of the single cavity configuration consisting of surfaces 0 and 3, η_{1C}, is:

$$\eta_{1C}=\frac{1-\frac{T_3^4}{T_{\max}^4}}{1+\frac{A_0}{A_3}\cdot\left(\frac{1}{\varepsilon_3}-1\right)} \quad (14)$$

Thus, combining Eqs. (13) and (14),

$$\frac{\eta_{2C}}{\eta_{1C}}=\frac{1+\frac{A_0}{A_3}\cdot\left(\frac{1}{\varepsilon_3}-1\right)}{1+\frac{A_0}{A_2}\cdot\left(\frac{2}{\varepsilon_2}-1\right)+\frac{A_0}{A_3}\cdot\left(\frac{1}{\varepsilon_3}-1\right)} \quad (15)$$

For $\varepsilon_3=1$, this ratio becomes

$$\frac{\eta_{2C}}{\eta_{1C}}=\frac{1}{1+\frac{A_0}{A_2}\cdot\left(\frac{2}{\varepsilon_2}-1\right)} \quad (16)$$

In Fig. 3, this efficiency ratio is plotted as a function of ε_2 for different surface area ratios A_2/A_0. Evidently, $\eta_{2C}/\eta_{1C}<1$ and increases with ε_2. As A_2/A_0 increases (i.e., the stronger becomes the cavity effect of the inner cavity), the efficiency of the two-cavity configuration approaches that of the single cavity. For the extreme case of $A_2=A_0$ (i.e., no inner cavity, but just a radiating solid wall covering the aperture) the efficiency η_{2C} is at most

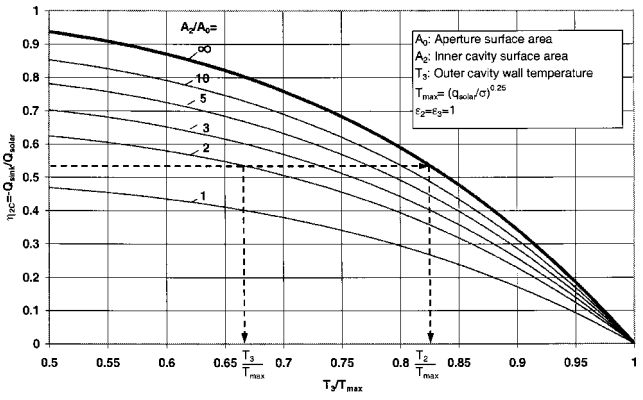

Fig. 2 Variation of the efficiency η_{2C} [see Eq. (13)] as a function of T_3/T_{max} for different A_2/A_0. The dashed lines indicate how to find $(T_2-T_3)/T_{max}$, as described in the text.

(namely, for $\varepsilon_2=1$) half as high as that for the single cavity configuration.

4 Summary and Conclusions

A solar chemical receiver-reactor consisting of two cavities, with the inner one functioning as the solar absorber and the outer one as the reaction chamber, offers several advantages for performing high-temperature thermochemical processes. The inner cavity protects the window and/or CPC against particles or condensable gases coming from the reaction chamber. It further serves as a thermal shock absorber, reducing the sudden thermal loads on the reaction chamber. The reactants are exposed to quite uniform irradiation emitted by the inner cavity, even for non-uniform incident solar fluxes. The outer cavity can handle thermochemical processes at elevated temperatures involving multiphases and controlled atmospheres. It further allows for batch or continuous mode of operation and for easy adjustment of the resident time of the reactants to match the kinetics of the reaction. For applications requiring temperatures above 2000 K, graphite may be the preferred material of construction for the inner cavity. For application at moderate temperatures requiring controlled atmosphere, the inner cavity can be made of reliable and shock-resistant ceramic materials like SiC, eliminating the need for a window.

A radiation heat transfer analysis based on the radiosity enclosure theory was formulated. An important drawback of using the two-cavity configuration, vis-à-vis the single cavity with reactants directly exposed to solar irradiation, is the lower solar energy absorption efficiency as a result of re-radiation losses from the inner cavity at a higher temperature than that of the reaction chamber. Nevertheless, the efficiency η_{2C} can be maximized when following some general design rules:

1 The surface area ratio A_2/A_0 should be as large as possible. Thus, for a given outer cavity of surface area A_3, the inner cavity should be designed as close to A_3 as possible, but still allow clearance for the reaction chamber. Evidently, A_3 should be minimized for reducing conduction heat losses and materials of construction.
2 The emissivity of the inner cavity, ε_2, should be as high as possible because, for a given input solar power, Q_{solar}, and a given temperature of the outer cavity, T_3 (process temperature), the temperature of the inner cavity, T_2, decreases with increasing ε_2, resulting in lower re-radiation losses and higher efficiency.
3 The emissivity ε_3 of the outer cavity should be as high as possible. Obviously, this requirement is also true for the single cavity receiver-reactor.

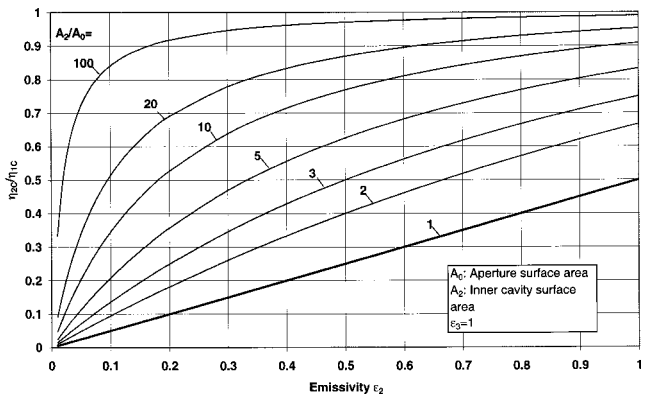

Fig. 3 Ratio of η_{2C} (efficiency of the two-cavity configuration) to η_{1C} (efficiency of the single cavity configuration) as a function of wall emissivity ε_2 for different A_2/A_0 [see Eq. (16)]

Although not considered in the present analysis, selective windows with high transmissivity for the solar spectrum, and high reflectivity in the IR spectrum around λ_{max}, where $\lambda_{max}=2897.8\ \mu\text{m}\cdot\text{K}/T_2$, can lead to an increase in the efficiency η_{2C}. This gain is most pronounced for low to moderate temperatures. The higher the temperature, the smaller the fraction of the radiation reflected by the window, and the lesser the selectivity effect. The band approximation may be applied for solving the radiation exchange for non-gray windows and surfaces [7].

Acknowledgment

Financial support from the BFE – Swiss Federal Office of Energy is gratefully acknowledged. We thank R. Palumbo for fruitful discussions.

Nomenclature

A_i = area of surface i
B_i = radiosity of surface i (power flux leaving surface i, emitted + reflected radiation)
$\mathbf{F}$ = view factor matrix
F_{ij} = view factor between surface i and j
q_i = net power flux from surface i (positive in direction of cavity)
q_{rerad} = power flux lost (re-radiated) through aperture
q_{sink} = net power flux absorbed by outer cavity (process enthalpy + conduction heat losses)
q_{solar} = solar power flux input through aperture
Q_i = net power from surface i (positive in direction of cavity), $Q_i=q_i\cdot A_i$
Q_{rerad} = power lost (re-radiated) through aperture, $Q_{rerad}=Q_{solar}+Q_{sink}$
Q_{sink} = net power absorbed by outer cavity, $Q_{sink}=q_{sink}\cdot A_3$
Q_{solar} = solar power input through aperture, $Q_{solar}=q_{solar}\cdot A_0$
T_i = temperature of surface i
T_{max} = maximum temperature for zero net power absorbed by outer cavity
δ_{ij} = Kronecker function ($\delta_{ij}=1$ for $i=j$; $\delta_{ij}=0$ for $i\neq j$)
ε_i = emissivity of gray surface i
η_{1C} = solar energy absorption efficiency of one-cavity configuration, $\eta_{1C}=-Q_{sink}/Q_{solar}$
η_{2C} = solar energy absorption efficiency of two-cavity configuration, $\eta_{2C}=-Q_{sink}/Q_{solar}$
λ_{max} = wavelength for maximum blackbody spectral emissive power
σ = Stefan-Boltzmann constant, $\sigma=5.6705\cdot 10^{-8}\ \text{Wm}^{-2}\text{K}^{-4}$

References

[1] Hogan, R. E., Diver, R. B., and Stine, W. B., 1990, "Comparison of a Cavity Solar Receiver Numerical Model and Experimental Data," ASME J. Sol. Energy Eng., **112**(3), 183–190.
[2] Steinfeld, A., and Schubnell, M., 1993, "Optimum Aperture Size and Operating Temperature of a Solar Cavity-Receiver," Sol. Energy, **50**, 19–25.
[3] Steinfeld, A., and Palumbo, R., 2001, "Solar Thermochemical Process Technology," *Encyclopedia of Physical Science and Technology*, R. A. Meyers, ed., Academic Press, **15**, 237–256.
[4] Hahm, T., 2000, "Entwicklung eines solarthermischen Hochtemperaturreaktors," Ph.D. Thesis, Univ. of Dortmund/Germany.
[5] Sonnenschein, M., Carvalho de Araujo, L., Hahm, T., Bathen, D., and Schmidt-Traub, H., 2000, "Design and Construction of a Solar Thermal Miniplant," *Proc. of Solar Thermal 2000*, Sydney, Australia, March 8–10, 2000, pp. 193–200.
[6] Swiss patent application, 2001, 1240/01.
[7] Siegel, R., and Howell, J. R., 1992, *Thermal Radiation Heat Transfer*, 3rd Edition, Hemisphere Publishing Corp., Washington, D.C.

Operational Performance of a 5-kW Solar Chemical Reactor for the Co-Production of Zinc and Syngas

Stefan Kräupl
Solar Process Technology, Paul Scherrer Institute,
CH-5232 Villigen, Switzerland

Aldo Steinfeld
Department of Mechanical and Process Engineering,
ETH-Swiss Federal Institute of Technology,
ETH-Zentrum, CH-8092 Zurich, Switzerland

We report on the improved operational performance and energy conversion efficiency of a 5-kW solar chemical reactor for the combined ZnO-reduction and CH_4-reforming SynMet process. The reactor features a pulsed vortex flow of CH_4 laden with ZnO particles, which is confined to a cavity-receiver and directly exposed to solar power fluxes exceeding 2000 kW/m^2. Reactants were continuously fed at ambient temperature, heated by direct irradiation to above 1350°K, and converted to Zn and syngas during mean residence times of 10 seconds. Typical chemical conversion attained was 100% for ZnO and up to 96% for CH_4. The thermal efficiency was in the 15–22% range; the exergy efficiency reached up to 7.7% and may be increased by recovering the sensible and latent heat of the products. The SynMet process avoids emissions of greenhouse-gases and other pollutant derived from the traditional fossil-fuel-based production of zinc and syngas, and further converts solar energy into storable and transportable chemical fuels. [DOI: 10.1115/1.1530196]

Introduction

In previous papers, we examined the chemical thermodynamics and kinetics of the SynMet process, i.e., the solar combined ZnO-reduction and CH_4-reforming process for co-producing Zn and syngas [1,2]. The overall stoichiometric reaction can be represented by:

$$ZnO + CH_4 \rightarrow Zn + 2H_2 + CO \qquad (1)$$

The reaction is highly endothermic ($\Delta H_{1300K} = 446.6$ kJ/mol) and proceeds to completion at temperatures above about 1300°K. Zinc can be used as a fuel in Zn/air fuel cells or further hydrolyzed to H_2. In both cases, the chemical product is ZnO, which is solar recycled by the SynMet process. High-quality syngas obtained by the SynMet process can be directly processed to methanol or H_2 via conventional routes. We have performed a life cycle assessment and economic analysis [3,4] and described the engineering design, fabrication, and experimental investigation of a 5-kW prototype solar reactor for effecting the reaction using concentrated solar energy [5–7]. In this technical brief, we report on experimental results of the test campaign conducted in a high-flux solar furnace during summer 2001.

Contributed by the Solar Energy Division of THE AMERICAN SOCIETY OF MECHANICAL ENGINEERS for publication in the ASME JOURNAL OF SOLAR ENERGY ENGINEERING. Manuscript received by the ASME Solar Energy Division, March 2002; final revision, June 2002. Associate Editor: A. Kripus.

Experimental Set-up

The solar experiments were carried out at the large solar furnace of the Paul Scherrer Institute (PSI): a 120 m^2-area flat heliostat on-axis with an 8.5 m-dia paraboloidal reflector, delivering up to 45 kW with a peak solar flux intensity exceeding 5000 kW/m^2. A detailed description of this solar concentrating research facility is found in Ref. [8]. The reactor configuration (see Fig. 1) and experimental set-up have been described in detail in Ref. [7].

The main features are briefly highlighted. The reactor chamber consists of a 240-mm-length 110-mm-dia cylindrical cavity-receiver containing a vortex flow of CH_4 laden with ZnO particles and directly exposed to concentrated solar radiation. Solar power input and power flux intensities through the 60-mm-dia windowed aperture were measured optically using a calibrated CCD camera aimed at an Al_2O_3-coated Lambertian target [8]. During a typical experiment, the reactor is solar-heated to the desired temperature under an N_2 gas flow, and then isothermally subjected to the reacting flow. Both reactants CH_4 and ZnO are fed at ambient temperature. ZnO powder (mean particle size = 0.4 μm) is continuously fed axially while CH_4 is simultaneously pulsed-injected tangentially, creating a gas-particle helical stream that absorbs efficiently the incoming solar irradiation. The measured mean residence time of reactants is 10 s [9]. The quartz window is cooled and protected from condensable gases by an auxiliary N_2 gas flow. The nominal cavity temperature, $T_{reactor}$, was measured with a solar-blind pyrometer [10]. The reaction products (Zn vapor and syngas) exit through a water-cooled Pyrex tube where part of the zinc condenses. The remaining solid products are collected downstream by particle filters. The gaseous products are analyzed online by gas chromatography while representative solid product samples collected at the condenser and filters downstream of the reactor are analyzed by x-ray diffraction. The amount of zinc produced (or of ZnO reduced) is calculated from the degree of chemical conversion of ZnO and the weight of the solid products collected after each run, and independently verified by balancing the oxygen of CO, CO_2, and H_2O contained in the gaseous products.

We report on eight solar runs, grouped in three categories: 1) Run I[1] used a fixed-bed of ZnO subjected to a continuous flow of CH_4 that was injected via a pipe positioned under the bed; 2) Runs II-VI used the continuous axial feeding of ZnO and pulsed tangential feeding of CH_4; 3) Runs VII and VIII used same feeding conditions as Runs II-VI, with an additional CH_4 flow via the same pipe as in run I. Boundary conditions, i.e., reactants mass

[1]This semi-batch run was specifically designed for the purpose of verifying the Zn mass balance from the ZnO measured before and after the solar experiment.

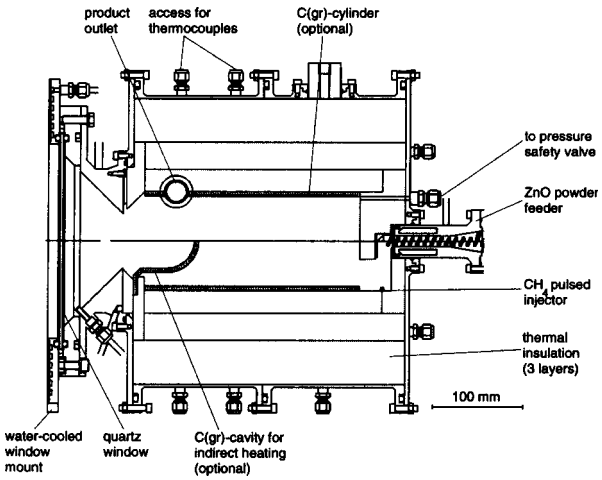

Fig. 1 Scheme of the *SynMet* solar chemical reactor [7]

Table 1 Operational conditions and degree of chemical conversion obtained in the solar experimental runs

	fixed bed	pulsed feeding					pulsed feeding+ pipe	
Run Nr.	I	II	III	IV	V	VI	VII	VIII
CH_4 flow rate [l_n/min[a]]	0	1.3	1.9	1.9	1.7	1.8	1.1	1.7
CH_4 flow rate via pipe [l_n/min]	3.1	0	0	0	0	0	2.2	2.0
N_2 flow rate (auxiliary) [l_n/min]	10	10	10	10	10	10	10	10
ZnO feeding rate [g/min]	-	14	15	15	15	14.5	9	16.5
stoichiometric factor[b]	-	3.2	2.4	2.4	2.7	2.4	0.8	1.3
$T_{reactor}$ [K]	1550	1470	1380	1612	1676	1398	1412	1406
solar power input [kW]	5.4	3.6	3.9	5.1	5.7	3.7	3.6	4.1
Mean power flux intensity [kW/m^2]	1910	1273	1379	1803	2016	1309	1273	1450
test duration under steady-state [min]	21	30	7	33	25	22	13	20
ZnO-conversion (filter) [%][c]	100	100	100	100	100	100	100	100
ZnO-conversion (condenser) [%]	100	97	93	97	100	89	100	94
ZnO sediment fraction [%]	-	71	81	35	33	76	46	58
CH_4-conversion [%]	70	59	49	88	96	48	35	34

[a]l_n means litres at normal conditions; mass flow rates are calculated at 273°K and 1 bar.
[b]Molar rate ratio of ZnO and CH_4.
[c]ZnO-conversion measured in solid products collected downstream of the reactor exit. Unreacted ZnO found deposited inside the reactor chamber.

flow rates, nominal reactor temperature, solar power input, and test duration under approximate steady-state conditions, are listed in Table 1. For all runs, except for run I, the stoichiometric factor, defined as the molar rate ratio of ZnO and CH_4, varied in the 0.8–3.2 range. It was set to provide optimal fluid flow conditions in the gas-particle vortex flow. Stoichiometric conditions may be achieved if N_2 is replaced by CH_4 and adjusted appropriately.

Experimental Results

Solar experimental results are shown in Table 1. The degree of chemical conversion of ZnO, defined as the concentration of zinc in the solid products, was in the range 89–100% at the condenser and 100% at the filter. Because of sedimentation, unreacted ZnO was found deposited inside the reactor, which lead to an uncompleted conversion of CH_4. As expected, the ZnO sediment fraction decreased with temperature because of the increasing reaction rate. The degree of chemical conversion of CH_4 to syngas increased with temperature and reached 96% at 1676°K. Typical H_2:CO and CO_2:CO molar ratios in the syngas were in the range 1.5–3 and 0.08–0.25, respectively. The Zn production rate, shown in Fig. 2, increased with temperature for runs II-VI. As expected in runs VII and VIII, a favorable effect on the Zn production rate was observed by injecting additional CH_4, but at the expense of lowering the conversion of CH_4. For the semi-batch run, 10.5 g Zn per min were obtained at 1550°K.

The thermal performance of the solar reactor is determined from a mass and energy balance under approximate steady-state conditions,

$$Q_{solar} = Q_{window} + Q_{gas} + Q_{ZnO} + Q_{chemistry} + Q_{reradiation} + Q_{conduction} + Q_{other} \quad (2)$$

Details on the calculation of the heat transfer terms of Eq. (2) are found in Ref. [7]. Figure 3 presents the complete energy balance for each experimental run, indicated in percent of the solar power input.

Heat losses due to reflection and attenuation at the quartz window typically amount to 7% of the solar power input. Conduction heat losses through the reactor walls vary between 20–26% and re-radiation losses through the aperture vary between 20–30% of the solar power input. The power used for heating the reactants and N_2 to $T_{reactor}$ amounts to 5–11% and that used for the chemical reaction amounts to 6–16% of the solar power input. Q_{other} includes the energy losses derived from thermal bridges and transients associated with heating the reactor's insulation.

The thermal efficiency is defined as

$$\eta_{thermal} = \frac{n_{Zn} \cdot \Delta H^{\circ}_{\text{reactants@298 K} \rightarrow \text{products@T}_{\text{reactor}}}}{Q_{solar}} \quad (3)$$

where Q_{solar} is the solar energy input, n_{Zn} the amount of Zn produced, and ΔH° the standard enthalpy change of the reaction when the reactants are fed at 298°K and the products are obtained at $T_{reactor}$. $\eta_{thermal}$ is shown in Fig. 4. It increased with temperature and reached 22% at 1612°K, but decreased for the run at 1676°K because of the almost complete conversion of CH_4. The exergy efficiency is defined as

$$\eta_{exergy} = \frac{n_{Zn} \cdot \Delta G^{\circ}_{\text{reactants@298 K} \rightarrow \text{products@298K}}}{Q_{solar}} \quad (4)$$

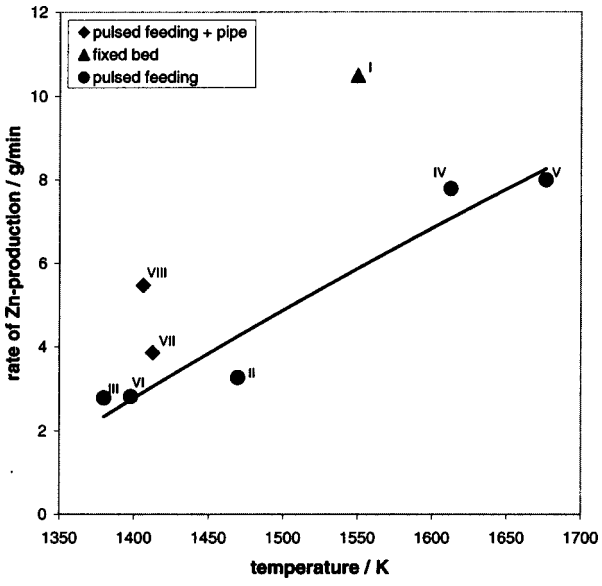

Fig. 2 Rate of Zn production as a function of the nominal reactor temperature. Note in Table 1 that mass flow rates and solar power input are not the same for every run

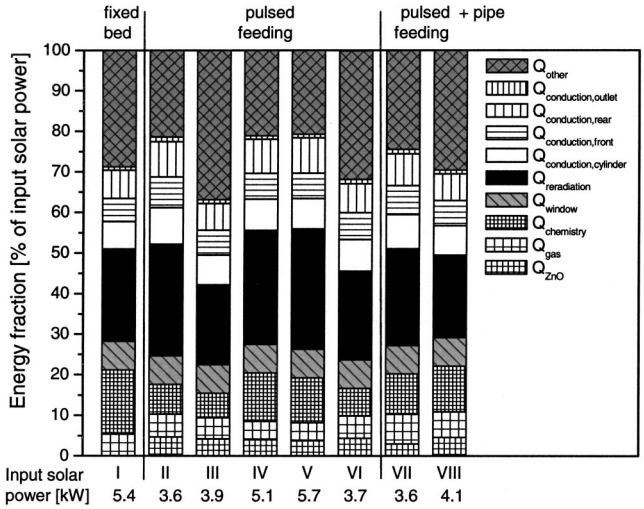

Fig. 3 Energy balance for each of the solar runs

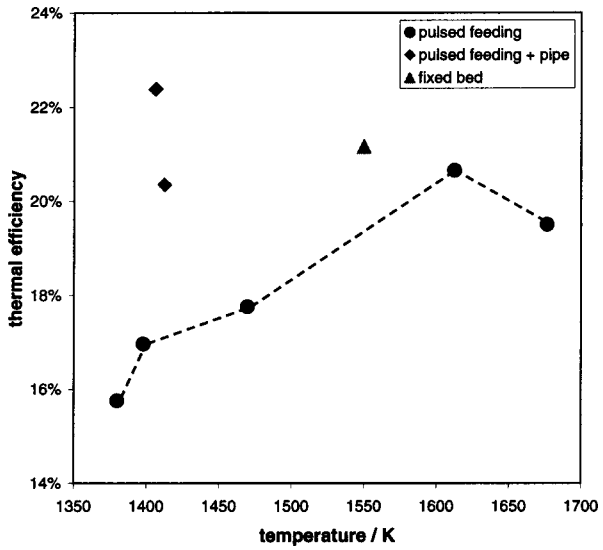

Fig. 4 Variation of the thermal efficiency as a function of the nominal reactor temperature

where $\Delta G°$ is the standard Gibbs free energy change of the reaction. As expected from the measured Zn production rates for runs II-VI (Fig. 2), η_{exergy} increased with temperature and reached 5.4% at 1676°K. It can be augmented by recovering the sensible and latent heat of the products. The highest exergy efficiency was 7.7%, obtained for the semi-batch run, pointing to the possibility of further increasing the amount of ZnO and CH_4 fed continuously for matching the reaction rate with the incoming solar power.

Conclusions

A vortex ZnO-CH_4 flow solar reactor for co-producing Zn and syngas was tested in the temperature range 1380–1676°K and for an input solar power between 3.6–5.7 kW. The reactor and peripheral components, including the quartz window at the reactor's aperture, performed trouble-free under approximate steady state conditions. High degree of chemical conversion (maximum conversion of ZnO: 100%; maximum conversion of CH_4: 96%) and reasonable energy efficiencies (maximum thermal efficiency: 22%; maximum exergy efficiency: 7.7%) were obtained. Higher energy efficiencies can be obtained by substituting the parasitic N_2 flow for CH_4 and by recovering the sensible and latent heat of the products. Further work is being focused at optimizing the gas-particle vortex flow for avoiding ZnO sedimentation under stoichiometric operation and for matching the reaction rate with the incoming solar power, and at developing a numerical simulation model of the reactor that can be employed as a design tool for scale-up.

The SynMet process offers the possibility of solar-upgrading natural gas and other hydrocarbons in non-catalytic reactions, and further points at a viable transition path to solar hydrogen.

Acknowledgments

We gratefully acknowledge the financial support from the BFE-Swiss Federal Office of Energy and The Baugarten Foundation. We thank U. Frommherz, P. Häberling, M. Brack, A. Frei, C. Guesdon, and C. Wieckert for technical support during the solar experimental campaign at PSI's solar furnace and for the chemical analyses.

Nomenclature

n_{Zn} = moles of Zn (mol)
$\Delta H°$ = standard enthalpy change (kJ/mol)
$\Delta G°$ = standard Gibbs free energy change (kJ/mol)
$Q_{chemistry}$ = energy absorbed by the chemical reaction (kWh)
$Q_{conduction}$ = conduction heat transfer through the reactor wall (kWh)
Q_{gas} = energy for heating inlet gas (kWh)
Q_{other} = unspecified energy losses (kWh)
$Q_{reradiation}$ = energy reradiated through the aperture (kWh)
Q_{solar} = solar energy input to the reactor (kWh)
Q_{window} = energy absorbed and reflected by the window (kWh)
Q_{ZnO} = energy for heating ZnO (kWh)
$T_{reactor}$ = nominal reactor temperature (K)
$\eta_{thermal}$ = thermal efficiency
η_{exergy} = exergy efficiency

References

[1] Steinfeld, A., Frei, A., Kuhn, P., and Wuillemin, D., 1995, "Solarthermal Production of Zinc and Syngas Via Combined ZnO-Reduction and CH_4-Reforming Processes," Int. J. Hydrogen Energy, **20**(10), pp. 793–804.
[2] Steinfeld, A., Larson, C., Palumbo, R., and Foley, M., 1996, "Thermodynamic Analysis of the Co-Production of Zinc and Synthesis Gas Using Solar Process Heat," Energy (Oxford), **21**(3), pp. 205–222.
[3] Werder, M., and Steinfeld, A., 2000, "Life Cycle Assessment of the Conventional and Solarthermal Production of Zinc and Synthesis Gas," Energy (Oxford), **25**, pp. 395–409.
[4] Steinfeld, A., and Spiewak, I., 1998, "Economic Evaluation of the Solar Thermal Co-Production of Zinc and Synthesis Gas," Energy Convers. Manage., **39**(15), pp. 1513–1518.
[5] Steinfeld, A., Brack, M., Meier, A., Weidenkaff, A., and Wuillemin, D., 1998, "A Solar Chemical Reactor for the Co-Production of Zinc and Synthesis Gas," Energy (Oxford), **23**(10), pp. 803–814.
[6] Kräupl, S., and Steinfeld, A., 2001, "Pulsed Gas Feeding for Stoichiometric Operation of a Gas-Solid Vortex Flow Solar Chemical Reactor," ASME J. Sol. Energy Eng., **123**(2), pp. 133–137.
[7] Kräupl, S., and Steinfeld, A., 2001, "Experimental Investigation of a Vortex-Flow Solar Chemical Reactor for the Combined ZnO-Reduction and CH4-Reforming," ASME J. Sol. Energy Eng., **123**(3), pp. 237–243.
[8] Haueter, P., Seitz, T., and Steinfeld, A., 1999, "A New High-Flux Solar Furnace for High-Temperature Thermochemical Research," ASME J. Sol. Energy Eng., **121**(1), pp. 77–80.
[9] Thorud B., 2000, Diplomarbeit, ETH-Swiss Federal Institute of Technology, Zurich.
[10] Tschudi, H.-R., and Morian, G., 2001, "Pyrometric Temperature Measurements in Solar Furnaces," ASME J. Sol. Energy Eng., **123**(2), pp. 164–170.

Calculation of Pressure and Density in Solar Power Plant Chimneys

Theodor W. von Backström
Department of Mechanical Engineering, University of Stellenbosch, 7600 South Africa
e-mail: twvb@sun.ac.za

This technical brief develops calculation methods for the pressure drop in very tall chimneys, as in solar chimney power plants. The methods allow for density and flow area change with height, for wall friction and internal bracing drag. It presents equations for the vertical pressure and density distributions in terms of Mach number. One of these is a generalization of the adiabatic pressure lapse ratio equation to include flow at small Mach numbers. The other is analogous to the hydrostatic relationship between pressure, density, and height, but extends it to small Mach numbers. Its integration leads to an accurate value of the average density in the chimney. [DOI: 10.1115/1.1530198]

Introduction

Typical analyses of flow through the chimneys of solar chimney power plants (Fig. 1) assume incompressible flow [1–6], but the assumption may introduce inaccuracies of unknown magnitude [7]. The chimney of a 200 MW solar chimney power plant could be 1500 m tall and 160 m in diameter [3,5–7]. Since the chimney wall thickness is small compared to its diameter, the design requires drag-inducing, bracing ''spokes'' to avoid wind-induced ovaling and subsequent failure [1,8]. The objective of this study is to develop practical but accurate methods of calculating the pressure drop and air density in tall chimneys.

Governing Equations for Flow in the Chimney

Assuming the gas constant and specific heat ratio are constant, the adiabatic stagnation temperature lapse rate equation, derived from energy conservation is:

$$T = T_1 - \frac{gz}{c_p} \tag{1}$$

The vertical momentum equation has been derived in [7] using the differential control volume of differential height, dz in Fig. 2. That equation, rewritten in terms of Mach number, contains friction and drag terms which may be combined as in Eq. (2) below, assuming that the loss coefficient, K applies over a certain finite length, δz:

$$\frac{f\,dz}{D}\frac{\gamma M^2}{2} + \frac{\delta F_D}{pA} = \left(\frac{f}{D} + \frac{K}{\delta z}\right)\frac{\gamma M^2}{2}dz = L\frac{\gamma M^2}{2}dz \tag{2}$$

The vertical momentum equation from [7] may then be written as:

$$\frac{dM}{M} = \frac{1+\dfrac{\gamma-1}{2}M^2}{1-M^2}\left(-\frac{dA}{A} + L\frac{\gamma M^2}{2}dz + \frac{g\,dz}{Rt} + \frac{1+\gamma M^2}{2}\frac{dT}{T}\right) \tag{3}$$

Simplify Eq. (3) by writing the static temperature term, $g\,dz/(Rt)$ in terms of stagnation temperature and substituting $g\,dz/(c_pT) = -dT/T$, from Eq. (1). This eliminates Mach number from the terms containing dT/T in Eq. (3).

$$\frac{dM}{M} = \frac{1+\dfrac{\gamma-1}{2}M^2}{1-M^2}\left(-\frac{dA}{A} - \frac{1}{2}\frac{\gamma+1}{\gamma-1}\frac{dT}{T} + L\frac{\gamma M^2}{2}dz\right) \tag{4}$$

Contributed by the Solar Energy Division of the American Society of Mechanical Engineers for publication in the ASME JOURNAL OF SOLAR ENERGY ENGINEERING. Manuscript received by the ASME Solar Energy Division, July 2001; final revision, April 2002. Associate Editor: J. Davidson.

Equation (4) has no general analytical solution, but an order of magnitude analysis will show that it is accurate enough to calculate the L-term with the known Mach number at the beginning of the integration interval. This assumption agrees with the incompressible flow approach where everything is referred to the upstream position. Once the Mach number distribution has been found at the end of each interval, the pressure at each level can be found from the mass conservation equation below [7]:

$$p = \frac{\dot{m}}{AM\left(1+\dfrac{\gamma-1}{2}M^2\right)^{1/2}\left(\dfrac{\gamma}{RT}\right)^{1/2}} \tag{5}$$

Values of other variables follow from standard gas dynamics.

Solving for Mach Number

Integrate Eq. (4) across an incremental height between an initial position 1 and any general position. The integration intervals should coincide with each length δz_i over which the loss coefficient L in Eq. (4) has a fixed value.

$$\frac{M}{\left(\dfrac{2}{\gamma-1}+M^2\right)^{0.5(\gamma+1)/(\gamma-1)}} = \frac{M_1}{\left(\dfrac{2}{\gamma-1}+M_1^{\,2}\right)^{0.5(\gamma+1/(\gamma-1)}}\left(\frac{A_1}{A}\right) \times\left(\frac{T_1}{T}\right)^{0.5(\gamma+1)/(\gamma-1)}\exp\left(L\frac{\gamma M_1^{\,2}}{2}\delta z\right) \tag{6}$$

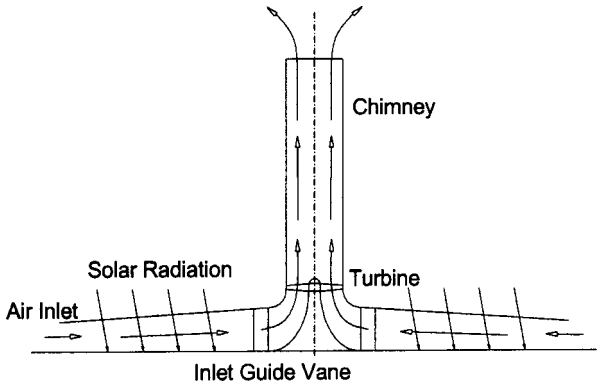

Fig. 1 Solar chimney schematic

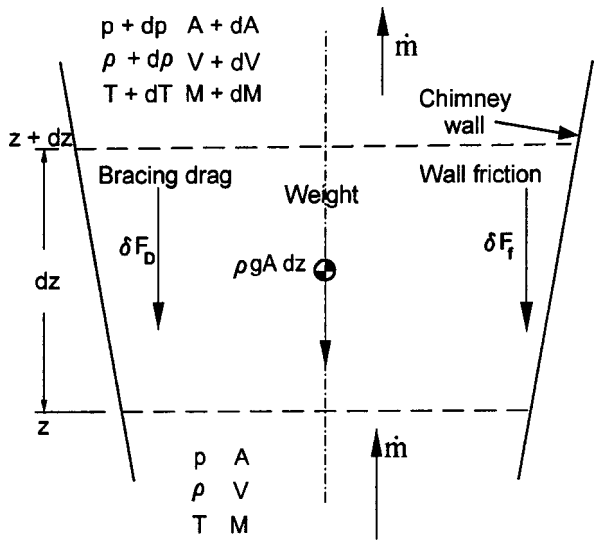

Fig. 2 Differential volume for deriving vertical momentum equation for chimney flow

Assuming that A and L are known at each chimney height, the right side of Eq. (6) can be calculated, once the stagnation temperature has been calculated from Eq. (1). The value of M in the left side must then be found iteratively.

Accuracy Check

As a simplified standard test case consider a 1500-m tall, 160-m inner diameter chimney with inlet stagnation temperature, $T_1 = 323.15$ K, inlet stagnation pressure, $P_1 = 90$ kPa, and a mass flow of 250000 kg/s. The inlet Mach number is then $M_1 = 0.0355907$ and the inlet static pressure is, $p_1 = P_1/(1+0.5(\gamma-1)M_1^2)^{(\gamma-1)/\gamma} = 89920.2$ Pa. Also assume that the gas constant $R = 287.08$ J/kgK and the specific heat ratio, $\gamma = 1.400$, giving $c_p = 1004.78$ J/kgK and an adiabatic temperature lapse rate constant, $g/c_p = 9.800/1004.780 = 0.00975338$ K/m. To investigate the accuracy of the procedure, check how well values obtained from it satisfy the conservation equations.

Mass Conservation. The inlet mass flow is 250000 kg/s. The exit stagnation temperature, from Eq. (1), is 308.52 K. The exit static temperature is: $t_2 = T_2/(1+M_1^2(\gamma-1)/2) = 308.417$ K, the exit velocity is: $V_2 = M_2(\gamma R\, t_2)^{0.5} = 14.4026$ m/s and the exit mass flow is: $m = \rho_2 V_2 A_2 = (p_2/R\, t_2) V_2 A_2 - 250000$ kg/s.

Energy Conservation. Consider frictionless flow through a 1500 m tall chimney. The inlet energy per unit mass flow is: $c_p t_1 + V_1^2/2 + g\, z_1 = 324695$ J/kg and in the same way the exit energy per unit mass flow is: 324695 J/kg.

Momentum Equation. The incompressible control volume momentum equation for flow through a constant area vertical chimney of height, Δz is:

$$p_1 A - p_2 A - \rho_{\text{ave}} g \Delta z A = \dot{m}(V_2 - V_1)$$

$$p_1 - p_2 = \rho_{\text{ave}} g \Delta z + \left(\frac{\dot{m}}{A}\right)^2 \left(\frac{1}{\rho_2} - \frac{1}{\rho_1}\right) = \Delta p_h + \Delta p_a \tag{7}$$

The pressure drop consists of a hydrostatic (weight) component and an acceleration component. The average density in the hydrostatic component needs to be known very accurately (to about 5 significant figures) to satisfy the momentum equation to within 1 Pa. An analytical solution for average density follows later. To calculate the acceleration term in the momentum equation, find: $\rho_1 = 89920.2/(287.08*323.068) = 0.969528$ kg/m^3 and $\rho_2 = 76438.2/(287.08*308.417) = 0.863316$ kg/m^3.

$$\Delta p_a = \left(\frac{\dot{m}}{A}\right)^2 \left(\frac{1}{\rho_2} - \frac{1}{\rho_1}\right) = 19.6 \text{ Pa} \tag{8}$$

Effect of Mach Number on Pressure Lapse Ratio

By applying logarithmic differentiation to Eq. (5), Von Backström and Gannon [7] derived the following equation for pressure variation in terms of Mach number and stagnation temperature variation:

$$\frac{dp}{p} = -\frac{dA}{A} + \frac{1+(\gamma-1)M^2}{1+\dfrac{(\gamma-1)}{2}M^2}\frac{dM}{M} + \frac{1}{2}\frac{dT}{T} \tag{9}$$

Substitute Eq. (4) for dM/M:

$$\frac{dp}{p} = \frac{\gamma M^2}{1-M^2}\frac{dA}{A} + \frac{\gamma}{\gamma-1}\left(1+\frac{\gamma+1}{2}\frac{M^2}{1-M^2}\right)\frac{dT}{T} - \left(1+\frac{\gamma M^2}{1-M^2}\right)\left(L\frac{\gamma M^2}{2}\delta z\right) \tag{10}$$

The Mach number distribution is required for an accurate solution, but since $M^2 \ll 1$ and changes little through the chimney, we investigate the effect of using $M = M_1$ constant throughout the chimney. Now integrate over δz between z_1 and z:

$$\frac{p}{p_1} = \left(\frac{T}{T_1}\right)^{(\gamma/(\gamma-1))(1+(\gamma+1)(M^2/2)/(1-M^2))} \times \left(\frac{A}{A_1}\right)^{\gamma M^2/(1-M^2)} e^{-(1+\gamma M^2/(1-M^2))(L\delta z\, \gamma M^2/2)} \tag{11}$$

Equation (11) shows that the pressure lapse ratio is a function of not only the stagnation temperature lapse rate, but also of the chimney area ratio and chimney friction and other losses, and that the effects of these parameters are modified by the Mach number. To check the accuracy, at least for constant area frictionless flow, substitute the previously used data in Eq. (11):

$$p = p_1\left(\frac{T}{T_1}\right)^{(\gamma/(\gamma-1))(1+(\gamma+1)(M^2/2)(1-M^2))} = 76441.1 \text{ Pa} \tag{12}$$

This differs by 2.9 Pa from the correct answer of 76438.2 Pa. A more accurate approach would be to use the average value of M, where: $M_{\text{ave}} = (M_1 + M_2)/2 = (0.0355907 + 0.0409077)/2 = 0.0382492$. Then $p = 76438.2$ Pa. This answer is correct to 0.0 Pa. To investigate the use of the no-flow lapse ratio equation, assume $M = 0.0$ in Eq. (12). Then the exit pressure due to hydrostatic effects alone is: $p = 76460.0$ Pa. Now subtract the acceleration pressure drop of 19.6 Pa from the exit pressure to find: $p_2 = 76440.4$ Pa. The error of 2.4 Pa is small, but optimistic (pressure too high). Note that the temperature ratio based on stagnation temperatures is appropriate, as seen from the energy equation, (1).

Effect of Mach Number on Density

Differentiate the equation of state logarithmically:

$$\frac{d\rho}{\rho} = \frac{dp}{p} - \frac{dt}{t} \tag{13}$$

Differentiate logarithmically the definition of stagnation temperature T in terms of t and M:

$$\frac{dt}{t} = \frac{dT}{T} - \frac{(\gamma-1)M^2}{\left(1+\dfrac{\gamma-1}{2}M^2\right)}\frac{dM}{M} \tag{14}$$

Substitute Eqs. (4), (10), and (14) into (13):

$$\frac{d\rho}{\rho} = \frac{M^2}{1-M^2}\left(\frac{dA}{A} - L\frac{\gamma}{2}\delta z\right) + \frac{1}{1-M^2}\left(\frac{1}{\gamma-1} + \frac{M^2}{2}\right)\frac{dT}{T} \tag{15}$$

Since $M^2 \ll 1$ and does not change much, assume the terms containing Mach number are constant, and integrate for the density lapse ratio between z_1 and z:

$$\frac{\rho}{\rho_1} = \left(\frac{T}{T_1}\right)^{(1/\gamma-1)(1+0.5(\gamma-1)M^2)/(1-M^2)} \times \left(\frac{A}{A_1}\right)^{M^2/(1-M^2)} e^{-(L/2)(\gamma M^2/(1-M^2))\delta z} \tag{16}$$

Numerical integration of Eq. (16) is possible if A and L are expressed as functions of z. For constant area, frictionless flow, assuming constant Mach number terms, find the average density by substituting Eq. (1) into Eq. (16) and integrating analytically:

$$\frac{\rho_{\text{ave}}}{\rho_1} = \frac{1}{\left(\dfrac{\gamma}{\gamma-1} - \dfrac{1}{2}M^2\right)\dfrac{1}{1-M^2}} \frac{1}{\left(1-\dfrac{T}{T_1}\right)} \times \left(1 - \left(\frac{T}{T_1}\right)^{(\gamma/(\gamma-1) - M^2/2)(1/1-M^2)}\right) \tag{17}$$

Substitution of $M=M_1=0.0355907$ and the rest of the values used previously in the example under consideration, gives $\rho_{ave}=0.915817\ kg/m^2$ and $\Delta p_h=13462.5\ Pa$. The exit pressure is then: $p_2=p_1-\Delta p_h-\Delta p_a=89920.2-13462.5-19.6=76438.1\ Pa$. The difference between it and the accurate value of $p_2=76438.2\ Pa$ from Eq. (5) is $-0.1\ Pa$. Substitution of $M=M_{ave}=0.0382492$ changes the sign of the difference but does not reduce its magnitude.

No-Flow Average Density. When $M=0$ and $T=t$, Eq. (17) simplifies to:

$$\frac{\rho_{ave,M=0}}{\rho_1}=\frac{1}{\left(\frac{\gamma}{\gamma-1}\right)}\frac{c_p t_1}{g\ \delta z}\left(1-\left(\frac{t}{t_1}\right)^{(\gamma/\gamma-1)}\right)$$

$$\rho_{ave,M=0}=\frac{\rho_1 R t_1}{g\,\delta z}\left(1-\left(\frac{p}{p_1}\right)\right)=\frac{p_1-p}{g\,\delta z} \tag{18}$$

This is in fact the well-known hydrostatic equation: $\Delta p=-\rho_{ave} g \Delta z$. Equation (17) gives the equivalent equation when a compressible fluid accelerates vertically at low Mach numbers.

Conclusion

This note develops a method for finding all the thermodynamic properties for compressible frictional flow through tall vertical chimneys. The method finds the stagnation temperature distribution directly from the altitude, by applying the energy equation. It then finds the Mach number distribution from the vertical distributions of stagnation temperature, friction factor, bracing drag loss coefficient, and flow area. The static pressure at each altitude follows from the continuity equation. It turns out that the generally used adiabatic temperature lapse rate equation in principle applies to the stagnation temperature, and applying it to the static temperature is valid only when the Mach number is equal to zero. The note presents two equations for the vertical pressure and density distributions in terms of Mach number. One of these is a generalization of the adiabatic pressure lapse ratio equation to include flow at small Mach numbers. The other is analogous to the hydrostatic relationship between pressure and density, extended to small Mach numbers. Its integration leads to an equation for the average density in the chimney. A very accurate value of the average density is exactly what the commonly used incompressible flow approach to the problem requires to calculate the hydrostatic pressure drop in the chimney.

Nomenclature

A = flow area [m^2]
c_p = specific heat [J/kgK]
D = chimney inside diameter [m]
F = force [N]
f = friction coefficient -
g = gravitational acceleration [m/s^2]
K = pressure drop coefficient -
L = sum of loss terms -
M = Mach number -
$\dot{m}$ = mass flow [kg/s]
P = stagnation pressure [Pa]
p = static pressure [Pa]
R = gas constant [J/kgK]
T = stagnation temperature [K]
t = static temperature [K]
V = velocity [m/s]
z = height [m]

Greek

γ = specific heat ratio -
μ = dynamic viscosity [Ns/m^2]
ρ = density [kg/m^3]

Prefix

Δ = change over chimney height
δ = change over interval

Subscript

a = acceleration
ave = average
D = drag
f = friction
h = hydrostatic
i = integration interval number
1 = inlet (or coefficient number)
2 = exit (or coefficient number)

References

[1] Haaf, W., Friedrich, K., Mayr, G., and Schlaich, J., 1983, "Solar Chimneys Part 1: Principle and Construction of the Pilot Plant in Manzanares," Int. J. Sol. Energy, **2**, pp. 3–20.
[2] Mullett, L. B., 1987, "The Solar Chimney—Overall Efficiency, Design and Performance," Int. J. Ambient Energ., **8**(1), pp. 35–40.
[3] Schlaich J., 1995, *The Solar Chimney, Electricity from the Sun*, Axel Menges, Stuttgart, Germany, pp. 6–52.
[4] Kröger, D. G., and Blaine, D., 1999, "Analysis of the Driving Potential of a Solar Chimney Power Plant," S.A.I. Mech.E. R&D Journal, **15**, pp. 85–94.
[5] Von Backström, T. W., 2000, "The Solar Chimney Air Standard Cycle," SAIMechE R&D Journal, **16**(1), pp. 16–24.
[6] Gannon, A. J., and Von Backström, T. W., 2000, "Solar Chimney Analysis With System Loss and Solar Collector Performance," ASME J. Sol. Energy Eng., **122**(3), pp. 133–137.
[7] Von Backström, T. W., and Gannon, A. J., 2000, "Compressible Flow Through Solar Power Plant Chimneys," ASME J. Sol. Energy Eng., **122**(3), pp. 138–145.
[8] Schlaich, J., 1999, "Tension Structures for Solar Electricity Generation," Eng. Struct., **21**, pp. 658–668.

A Study of the Performance of a Hybrid Liquid Desiccant Cooling System Using Lithium Chloride

Pedro Mago*
Department of Mechanical Engineering, Universidad de Oriente, Puerto La Cruz, Anzoategui, Venezuela

D. Yogi Goswami
Solar Energy and Energy Conversion Laboratory, Department of Mechanical Engineering, University of Florida, Gainesville, FL 32611
e-mail: solar@cimar.me.ufl.edu

This paper presents field test of a hybrid solar liquid desiccant cooling system conducted at a test house at the University of Florida's Energy Research and Education Park. These tests consisted of operating the air conditioning system at the test house in two configurations: the conventional vapor compression system and the hybrid desiccant system. Experiments were conducted to study the influence of the air mass flow rate, temperature of the inlet air, temperature of the desiccant, and desiccant mass flow rate on the performance of both system configurations. Based on the field test results, it was found that the hybrid desiccant system improves the air conditioning performance in the field test house by decreasing the outlet humidity and temperature of the air.

[DOI: 10.1115/1.1530199]

*This work was done at University of Florida, while he was a Graduate Student.

Contributed by the Solar Energy Division of THE AMERICAN SOCIETY OF MECHANICAL ENGINEERS for publication in the ASME JOURNAL OF SOLAR ENERGY ENGINEERING. Manuscript received by the ASME Solar Energy Division, February 2001; final revision, August 2002. Associate Editor: V. Mei.

Introduction

In hot and humid regions where the relative humidity is high, the latent load becomes a big problem. Properly sized conventional vapor compression systems sometimes cannot even meet this load. Consequently, oversized compressors are installed to dehumidify the incoming air. To meet humidity requirements, vapor-compression systems are often operated for long cycles and at low temperatures, which reduce their efficiencies and require reheating the dry, cold air to achieve comfort conditions. Both consequences are costly. However, a combination of a desiccant dehumidification system and a vapor compression system (also known as hybrid desiccant cooling system) may not only meet the load but also save energy.

Commercially available desiccants include silica gel, activated alumina, natural and synthetic zeolites, titanium silicate, lithium chloride, calcium chloride, triethylene glycol, and synthetic polymers. In this study, an aqueous solution of lithium chloride was used as the desiccant. Fumo and Goswami [1,2] had earlier studied the heat and mass transfer performance for this desiccant for air dehumidification. A detailed review of liquid desiccant cooling system was given by Oberg and Goswami [3].

This paper compares experimental results for the performance of a hybrid desiccant system with a vapor compression system.

Experimental Facilities. Field tests of a hybrid solar liquid desiccant cooling system were conducted at a test house at the University of Florida's Energy Research and Education Park. These tests consisted of operating the air conditioning system of the house in two configurations–the conventional vapor compression system (properly sized existing system), and the hybrid desiccant system. Figure 1 shows the air conditioning system. The system was operated in the two configurations (vapor compression system with and without the liquid desiccant system) and the data was collected to compare the performance of the two arrangements. For the *vapor compression system only* mode, the desiccant system was bypassed as shown by the dotted line in Fig. 1.

The desiccant system was constructed as a tower of 56 cm dia and 60 cm height. The tower was packed with Raschig rings made with polypropylene and with a specific surface area of 210 m^2/m^3. To distribute the desiccant over the packings, three spray heads were used. The system had two tanks and two pumps; one tank stores the unused desiccant, which is pumped to the tower, and the other tank stores used desiccant, which is pumped by the second pump from the bottom of the tower. This arrangement ensures constant temperature and concentration condition of the desiccant going into the tower. Temperatures were measured using copper-constantan thermocouples, with an accuracy of $\pm 0.5°C$ and relative humidities were measured by humidity transmitters, with an accuracy of $\pm 2\%$ RH (0-90% RH) and $\pm 3\%$ RH (90%-100%). Humidity ratio of air was determined from the relative humidity and temperature measurements. The uncertainty of the humidity ratio is ± 0.0009 kg/kg. The air velocity was measured using a Velometer with an accuracy of $\pm 2\%$. Air velocity was measured at a cross section of the duct using a matrix of points from which the average air velocity was calculated. The mass flow rate was calculated from the average velocity, the cross sectional area and the density of air.

Desiccant concentration was determined by the Karl Fischer titration method. This is a quantitative method for determining water concentration by titrating the desiccant solution with anhydrous alcohol containing iodine and sulfur dioxide. The uncertainty of this method is ± 0.003 kg LiCl/kg Solution.

Experimental Procedure. Both experiments were conducted under the same air inlet conditions for approximately one hour each. The following data were measured using a PC-based data acquisition system:

- Temperature and relative humidity of the air at the inlet of the tower (Point 1, Fig. 1)
- Temperature and relative humidity of the air at the outlet of the tower or inlet of the evaporator (Point 2, Fig. 1)
- Temperature and relative humidity of the air at the outlet of the evaporator (Point 3, Fig. 1)
- Temperature of the liquid desiccant in the tower
- Time
- Air flow rate

To ensure steady state before recording the data, air and desiccant conditions (temperature and RH of inlet and outlet air, temperature of the desiccant) were monitored. It took approximately 45 min to achieve steady state conditions. Samples of the liquid desiccant were taken before and after the experiment to measure the concentration of the liquid desiccant to determine if regeneration was needed.

The maximum airflow rate was the maximum that the air handler of the actual system could attain. Lower flow rates were obtained using dampers. Valves were used to regulate the mass flow of the liquid desiccant.

Results

Experiments were conducted to study the influence of air mass flow rate, temperature of the inlet air, temperature of the desiccant, and desiccant mass flow rate on the performance of both system configurations. The air conditioning system was operated in both hybrid and conventional configurations, and for recirculating air and 100% fresh air modes. Each variable was studied for three different values while the others were held constant. After reaching a steady state, the data listed in the previous section were taken each minute during the experiment, which was continued for about 15 min. The minute-by-minute data was averaged to give one experimental data point for this study. The experiment was repeated for each condition three times to give three experi-

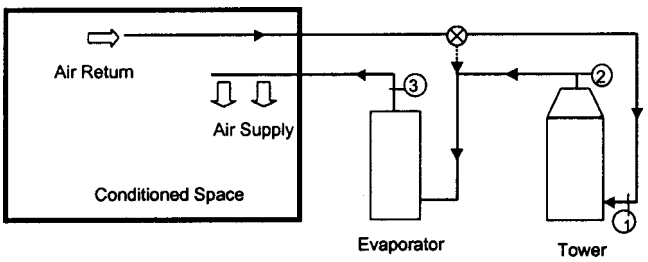

Fig. 1 Air conditioning system showing measurements locations

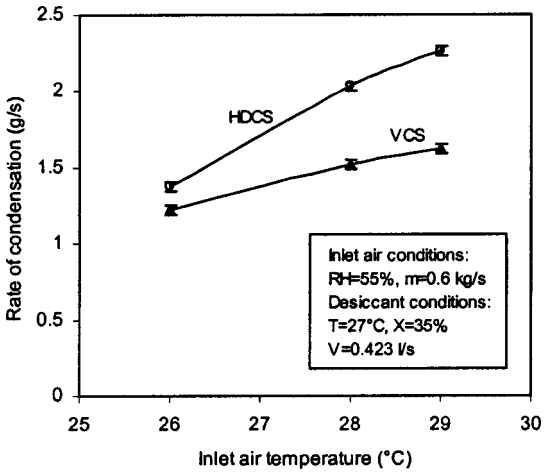

Fig. 2 Influence of inlet air temperature with constant relative humidity on the water condensation rate

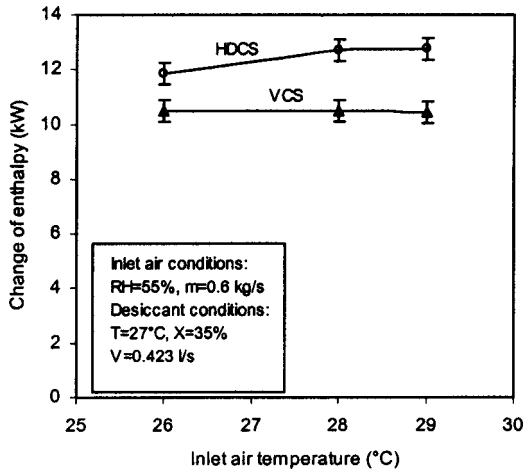

Fig. 3 Influence of inlet air temperature on change of enthalpy of the system

mental data points. These three experimental data points for the same set were averaged to provide a data point to plot in the figures. A standard deviation was also calculated. The average of the standard deviation of three points for a curve were plotted as the error bars in each plot. Complete results of the experiments are given in Mago and Goswami [4]. A sample of the results is shown in Figs. 2 and 3.

Conclusions

The following conclusions may be drawn from the complete study although just a sample of the results is shown in this paper:

- In the hybrid liquid desiccant system, rate of condensation increases with: airflow rate, inlet air temperature or desiccant mass flow rate; and it decreases when the inlet desiccant temperature is increased.
- In the hybrid liquid desiccant system, outlet air temperature increases with: airflow rate, inlet air temperature or inlet desiccant temperature; and decreases when the desiccant mass flow rate is increased.
- In the hybrid liquid desiccant system change in enthalpy of air is almost constant with the change in airflow rate and with the desiccant mass flow rate or the inlet air temperature. However the change of enthalpy decreases when the inlet desiccant temperature increases.

Nomenclature

HDCS = hybrid desiccant cooling system
RH = relative humidity (%)
T = temperature (°C)
V = desiccant volumetric flow rate (l/s)
VCS = vapor compression system
X = concentration in mass of the desiccant (%)

References

[1] Fumo, N., and Goswami, Y., 2000, "Study of the Aqueous Lithium Chloride Desiccant System, Part I: Air Dehumidification," *Proc. of Millennium Solar Forum 2000*, C. A. Estrada, ed., Asociacion Nacional de Energia Solar, pp. 307–312.

[2] Fumo, N., and Goswami, Y., 2000, "Study of the Aqueous Lithium Chloride Desiccant System, Part II: Desiccant Regeneration," *Proc. of Millennium Solar Forum 2000*, C. A. Estrada, ed., Asociacion Nacional de Energia Solar, pp. 313–318.

[3] Oberg, V., and Goswami, D. Y., 1998, "A Review of Liquid Desiccant Cooling," *Advances in Solar Energy*, **12**, pp. 346–385. American Solar Energy Society, Boulder, CO.

[4] Mago, P., and Goswami, D. Y. 2001, "A Simulation model and Software for the Performance Simulation of a Hybrid Liquid Desiccant Cooling System," *Proc. of American Solar Energy Society's Forum 2001-Solar Energy, The Power to Choose*, April, Washington, DC, pp. 229–235.

Pressure Drop in Solar Power Plant Chimneys

Theodor W. von Backström
Andreas Bernhardt
Anthony J. Gannon

Department of Mechanical Engineering,
University of Stellenbosch,
Private Bag X1,
Matieland 7602, South Africa

The paper investigates flow through a representative tall solar chimney with internal bracing wheels. It presents experimental data measured in a 0.63-m-dia model chimney with and without seven bracing wheels. The bracing wheels each had a rim protruding into the chimney and 12 spokes, each spoke consisting of a pair of rectangular section bars. The investigation determined coefficients of wall friction, bracing wheel loss, and exit kinetic energy in a model chimney, for both ideal non-swirling uniform flow and for swirling distorted flow. A fan at one end of the chimney model either sucked or blew the flow through it. The flow entering the chimney through the fan and its diffuser simulated the flow leaving the turbine at the bottom of the chimney. The swirling distorted flow increased the total pressure drop by about 28%, representing 4.7% of the turbine pressure drop. The pressure drop across the bracing wheels exceeded the frictional pressure drop by far. Designers of tall, thin-walled chimneys should take care to minimize the number of bracing wheels, reduce their rim width as much as possible, and investigate the feasibility of streamlining their spoke sections. If at all structurally possible, the top bracing wheel should be far enough from the chimney exit to allow the spoke wakes to decay and the separated flow to re-attach to the chimney wall downstream of the rims before the flow leaves the chimney, to reduce the exit kinetic energy loss. [DOI: 10.1115/1.1564077]

Introduction

The chimney of a 200-MW solar chimney power plant could be 1500-m tall and 160-m in diameter [1–4] (Fig. 1). The thickness of the reinforced concrete walls could range from 0.99 to 0.25 m for a 1000-m chimney [5] and from 2.19 to 0.25 m for a 1500-m chimney. Since the wall thickness is small compared to the diameter, the construction requires stiffening to avoid wind-induced ovaling and subsequent failure. Schlaich [5] proposed bracing wheels comprising *spokes* (pairs of parallel radial bracing rods, or bars, tensioned by their own weight) (Fig. 2). Figure 3 shows a section through a model spoke in a wind tunnel, with a wake velocity profile generated by flow across it. The spokes span the space between a stiffening ring or rim, protruding from the inside of the chimney wall, and a small central hub (Fig. 2). The drag of these bracing wheels adds to the wall friction pressure drop.

The objectives of this study are:

- to determine skin friction coefficients and bracing wheel pressure drop coefficients
- to investigate the effect of swirling, distorted flow on the loss coefficients
- to apply the methods developed by Von Backström and Gannon [6] to investigate the relative magnitude of wall friction, bracing wheel, and exit kinetic energy loss in a tall chimney

Chimney Flow Conditions

As a simplified standard test case [6], consider a 1500-m tall, 160-m inner diameter chimney with inlet stagnation temperature, $T_1 = 323.15$ K, inlet stagnation pressure, $P_1 = 90$ kPa, and a mass flow of 250,000 kg/s. Also assume that the gas constant $R = 287.08$ J/kgK and the specific heat ratio, $\gamma = 1.400$, giving $c_p = 1004.78$ J/kgK and an adiabatic temperature lapse rate constant, $g/c_p = 9.800/1004780 = 0.00975338$ K/m. The inlet Mach number is then $M_1 = 0.0355907$ and the inlet static temperature pressure and density are, $t_1 = 323.068$ K and $p_1 = 89920.2$ Pa and $\rho_1 = 0.96953$ kg/m^2, making the chimney inlet velocity 12.82 m/s and the inlet dynamic pressure 79.73 Pa.

Contributed by the Solar Energy Division of THE AMERICAN SOCIETY OF MECHANICAL ENGINEERS for publication in the ASME JOURNAL OF SOLAR ENERGY ENGINEERING. Manuscript received by the ASME Solar Energy Division, March 2002; final revision, October 2002. Associate Editor: R. Pitz-Paal.

The viscosity follows from Sutherland's equation [7]: $\mu = \mu_0((t/t_0)^{3/2}(t_0+S))/(t+S)$. For air, the constants are: $t_0 = 273$ K, $\mu_0 = 1.71\times10^{-5}$ Ns/m^2, and $S = 110$ K. The viscosity μ, and chimney Reynolds number $\mathrm{Re} = 4\dot{m}/\pi\mu D$ at the bottom of the standard chimney are 1.947×10^{-5} Ns/m^2 and 1.022×10^{8}. The spoke section Reynolds number based on the total frontal width of one bar is $\mathrm{Re}_{sp} = \rho V d/\mu = 0.970\times12.82\times0.040/1.88\times10^{-5} = 26500$.

Chimney Model

Even when vertical, laboratory scale chimneys are not tall enough to simulate the gravitational effects, such as reduced pressure and density with altitude. A laboratory scale horizontal flow chimney model (Fig. 3) served for a first experimental investigation of friction and drag loss in chimneys. The model had seven 630-mm-dia by 940-mm-long sections, resulting in a total test section length of 6.6 m. The model chimney diameter was determined by available fan ducting. An axial fan either sucked or blew air through the system. The typical average axial velocity in the model chimney was 14.2 m/s. Although our reference chimney [6] has a diameter of 160 m, the bracing wheels were adapted from those proposed by Schlaich [5] for a chimney diameter of 130 m,

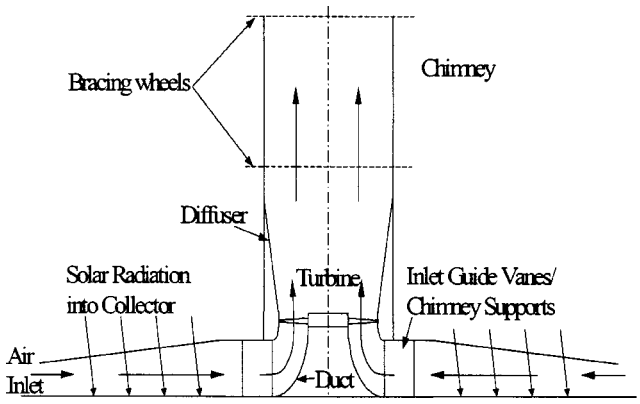

Fig. 1 Solar chimney schematic

being the only available data. The proposed spokes consisted of pairs of bars with thickness $d=40$ mm and spaced 50 mm apart. The bars were rectangular, with section L/d between 5 and 10.5 (Fig. 3). Due to the small model scale (0.630/130=1:206) however, simple geometric scaling of the spokes would result in spokes with rectangular bar sections of about 0.2×1.2 mm and $\mathrm{Re}_{sp}=128$. Such section Reynolds numbers would be too low, and the spokes would not be stiff enough, so the conditions for achieving similarity between the full-size and model chimneys need to be investigated.

Similarity and Scaling

One of the main objectives of this study is to find the pressure drop coefficient $K_{bw}=\Delta p_{bw}/(\frac{1}{2}\rho V^2)$ associated with a bracing wheel. The bracing wheel acts as an actuator disc exerting a retarding force $F_{bw}=A_c\Delta p_{bw}=A_cK_{bw}\frac{1}{2}\rho V^2$ on the flow. Since the drag of the rectangular section shape of the bracing wheel spoke consists basically of the drag of its flat fore body at right angles to the flow, plus the base drag of its blunt rear end, its drag may be presented in terms of its frontal area and drag coefficient [9], or $F_{sp}=C_DA_{sp}\frac{1}{2}\rho V^2$. The total spoke drag of a bracing wheel with N spokes is then $F_{bw}=C_DA_{bw}\frac{1}{2}\rho V^2$, where $A_{bw}=N_{sp}A_{sp}$ and A_{sp} is the frontal area of one spoke. Comparing the two values of F_{bw} leads to $K_{bw}=C_DA_{bw}/A_c$. It shows that similarity is possible with different numbers of spokes in the model and prototype if the ratio of spoke frontal area to chimney flow area is the same, and the values of C_D are the same. This opens the possibility of using fewer, but relatively larger spokes in the model to increase the spoke Reynolds number. Geometric similarity requires that the model spokes have the same ratio of thickness to streamwise length as the prototype and the same ratios of corner radii to width. For kinematic similarity, the relative sizes of the separation bubbles that start at the front corners of the spoke should be the same in model and prototype.

The dimensionless parameters that could in principle affect the value of C_D are: spoke section streamwise length to thickness ratio L/d, Reynolds number $\mathrm{Re}_{sp}=\rho Vd/\mu$, surface roughness, and turbulence level and length scales. Hoerner [9] states, however, that the section length ratio has little effect when L/d exceeds 2.5, or when L is so large that the flow that separated over the sharp leading edge corners re-attaches. A graph in an ESDU report [10] indicates that the C_D of a rectangular infinitely long spoke increases from 1.15 at $L/d=4$ to 1.3 at $L/d=2.5$ and that C_D is independent of L/d for $L/d>4.0$. Since the proposed values lie between 5 and 10.5, it should be safe to ignore the effect of L/d, even though side wall friction eventually becomes dominant at $L/d\gg10$. The drag is mostly profile drag, caused by the difference in pressure acting on the leading and trailing surfaces, and not skin friction drag. Surface roughness will have a minor effect on the drag, because of the relatively small stream wise length of the spokes, and the existence of separated flow regions along part of the length. The report [10] also states that the C_D of a rectangular section shape is independent of Re for $10^6>\mathrm{Re}>10^4$. For obstructions that are short in the flow direction ($L/d<1$), like the rims where the spokes attach to the wall, the lower limit for sensitivity to Re approaches 10^3. If the spokes of successive wheels are aligned axially, each spoke would be exposed to the wakes of the previous spokes, but since the wheels are spaced 1.5 chimney diameters apart, the distance between two wheels in a full-sized chimney would be 195 m, or 4875 bar thicknesses. The wake amplitude would have decayed to a fractional percentage of the mean velocity, and the root mean squared value of the fluctuating velocity due to turbulence to a percent or so of the mean velocity. The turbulence length scale would be proportional to the wake width, which increases as the square root of the distance downstream [11]. In the model, the proposed relative distance is about six times less and the relative wake width, velocity defect, and turbulence level are about $\sqrt{6}\approx2.5$ times greater. The spacing of about 800 bar widths in the model however exceeds the requirement of Sachs [12] by more than two orders of magnitude. He states that: "A body that is to windward of another will affect the wind forces on the second one if they are within 6 diameters (widths) of each other."

The result of these deliberations was a strong incentive to increase the size of the spokes in the model chimney in order to increase the spoke Reynolds number. A higher spoke Reynolds number was deemed more important than correctly scaled axial wheel spacing.

We shall show that the spoke section drag coefficient determined in the wind tunnel is applicable to the full scale chimney, but that the spoke Reynolds numbers in the model chimney are below 10^4, where the Reynolds number may have an effect. The wheel rim Reynolds number will however be higher, since the rims are wider than the spokes, and their streamwise length to width ratios are lower, so that the wheel rim loss coefficients from the literature would be applicable to both the model and the full-scale chimney.

Experimental Setups

Wind Tunnel. A standard way of determining section drag coefficients is to measure the wake velocity profiles at a reasonable distance downstream of the section in uniform flow, and then calculate the wake momentum thickness, as described by Schlichting [13]. The experimental setup consisted of two rectangular 12×126 mm bars, 15 mm apart and 1 m long, mounted across the 1×1.4 m test section of a wind tunnel (Fig. 3). For a test section velocity of 36 m/s, the typical Reynolds number in the wind tunnel based on spoke thickness was $\mathrm{Re}_{sp}=\rho Vd/\mu=1.2\times36\times0.012/1.8\times10^{-5}=28800$. This was close to the prototype value of 26500 and was also larger than 10^5, implying the spoke section C_D to be independent of Reynolds number.

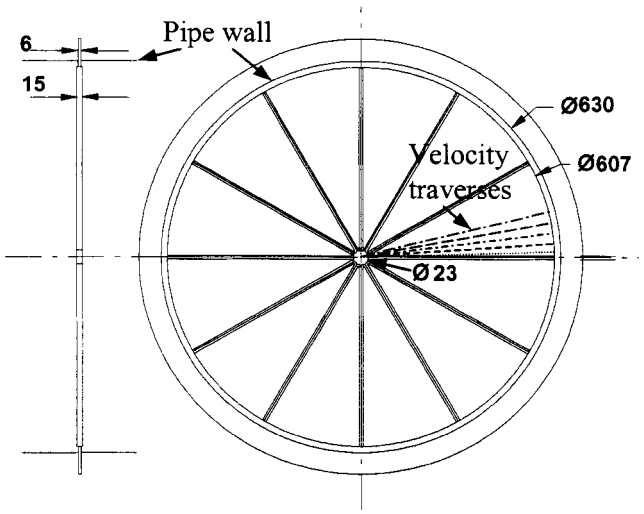

Fig. 2 Chimney model bracing wheel

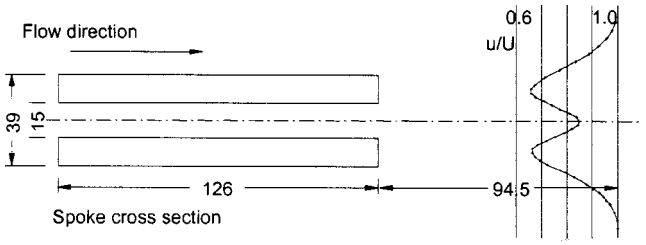

Fig. 3 Model spoke and velocity profile

A 3-mm-dia Pitot tube measured the total and static pressure profiles 94 mm downstream of the trailing edges of the bars. Pressure was measured with a Hottinger Baldwin Messtechnik pressure transducer calibrated with a Betz micromanometer to the nearest Pa. Readings were logged by PC through an analogue to digital converter and averaged over 20 s.

Model Chimney. The model chimney walls were made of rolled steel plate sections painted with red rust-preventing paint. They were sanded and the joints between the pipe sections were sealed with silicon sealant.

Figure 2 shows a model bracing wheel. To increase the spoke Reynolds number, the spokes were six times the size required to satisfy complete model geometrical similarity. We installed 12 spokes per wheel instead of 72, thereby keeping the ratio of total spoke frontal area to chimney flow area the same. The dimensions of the model bars were 1.2×15 mm, with a spacing of 1.5 mm between them. The effects of higher density and velocity and lower viscosity in the model also raised the typical Reynolds number in the model based on spoke thickness from 128 to $\mathrm{Re}_{sp}=\rho Vd/\mu=1.2\times14.2\times0.0012/1.8\times10^{-5}=1140$, to ensure a more accurately scaled drag coefficient. The spoke attachment rims were correctly scaled relative to the chimney diameter.

The model spokes were laser cut from steel plate to achieve the required sharp-cornered rectangular section shapes and prevent the typical curved section shapes with rounded corners on one side produced by guillotine cutting. Seven spoked wheels (Fig. 4) were clamped between the flanges of the 940-mm-long pipe sections. The thickness of the bracing spoke flanges increased the length of each pipe section by 6 mm (about 1% of the chimney diameter).

In the sucked mode, a thin boundary layer flow entered the chimney through a calibrated quarter-elliptical bell mouth that also served to measure the flow. In the blown mode, a disturbed, swirling flow entered the chimney through a standard bell mouth into the fan and then the diffuser. The objective here was to investigate the effect of non-ideal flow, more similar to that leaving the turbine, on the pressure drop in the chimney. Use of a single transducer measuring all the wall pressures in sequence through an electronically controlled switching box reduced the effect of calibration errors on pressure differences. Pressure tappings were halfway between flanges. The mass flows found by integrating velocity profiles measured by wind tunnel calibrated pneumatic probes over the chimney flow area agreed to within 3% of those measured with the inlet bell mouths.

Wall Friction Coefficients

The two lower lines in Fig. 5 represent the measured normalized pressure drop due to friction only, measured with no bracing wheels in the chimney model. Wall static pressures, nondimensionalized by the dynamic pressure based on chimney flow area, are given relative to the pressure at the last (downstream) pressure tapping, representing the chimney exit. For the induced flow case without the bracing wheels, the friction coefficient from the measured data was 0.0162 compared to 0.0125 from the equation of Haaland [8] for a smooth pipe wall at the model chimney Reynolds number. Taking the wall roughness as ε, the equation is:

$$\frac{1}{\sqrt{f}}=-1.8\log\left(\frac{6.9}{\mathrm{Re}_D}+\left(\frac{\varepsilon/D}{3.7}\right)^{1,11}\right)$$

The measured pressure drop was 30% higher than the prediction. Some discrepancy is to be expected since the chimney is only about 10 diameters long, and the flow is not fully developed. In a developing flow, the acceleration of the inviscid core flow induces an additional pressure drop. In fully developed pipe flow the centerline velocity may be 15% higher than the mean, causing an additional pressure drop equal to 32% of the dynamic pressure. This is large compared to the friction pressure drop of 17.3% of the dynamic pressure along the length of the model chimney, but the velocity profile would not be fully developed in ten pipe diameters.

In the blown case, representing flow entering the chimney downstream of a turbine and diffuser, there was an additional 25% increase in friction coefficient to 0.0202, due to the swirling, disturbed flow.

Spoke Section Drag Coefficient

The total momentum thickness, θ of the wakes of the two parallel bars as shown in Fig. 3 was 11.42 mm. The drag coefficient is given by 2θ divided by the frontal width of the profile [13]. We chose to base the C_D on $2d$, the sum of the widths of the two bars, to be consistent with our frontal area approach. Then $C_D=\theta/d=0.95$. This value is lower than for single rectangular bars as discussed before and is directly applicable to the prototype chimney.

Bracing Wheel Pressure Drop Coefficient

As expected, the pressure drops measured with the bracing wheels in position dominate the frictional ones, and the pressure drops associated with the swirling turbulent flow exceed those of the more ideal flow (Fig. 5). In the sucked-through case, the total dimensionless pressure drop over 7 bracing wheels was 0.801 times the dynamic pressure, but it included the wall friction loss of 0.173 over the same length. The measured value of the bracing wheel loss coefficient K_{bw} was then $(0.801-0.173)/7=0.0897$.

Referring to Fig. 4, the nominal flow area of the 630-mm pipe is 311725 mm^2. The frontal area of the 12 spokes consisting of two 1.2-mm-thick bars (disregarding the small hub) is 8784 mm^2. The ratio of spoke frontal area to chimney nominal flow area is: $8784/311725=0.02818$. The bracing wheel loss coefficient based on the spoke area only (disregarding the wheel mounting rims)

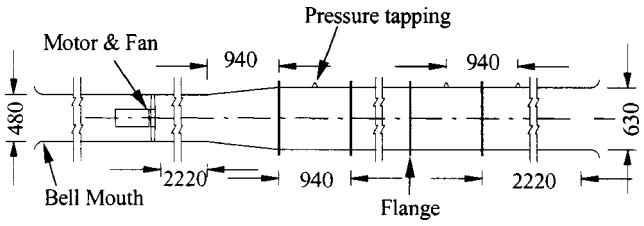

Fig. 4 Solar chimney model

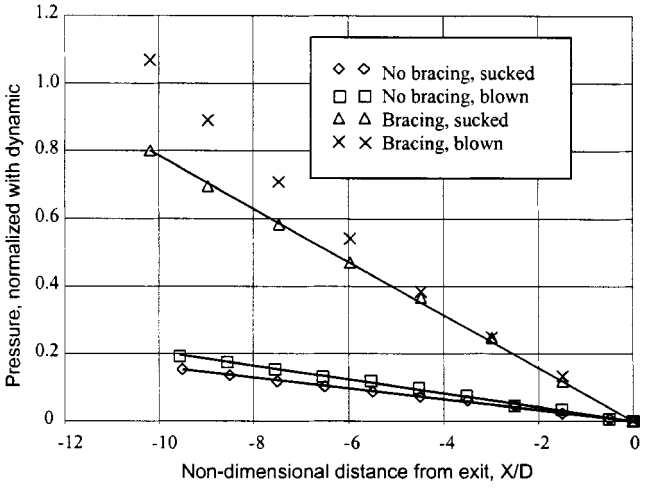

Fig. 5 Pressure variation in chimney with and without bracing wheels

Table 1 Comparison of exit values and pressure drop for: *a*) calculated wall friction, and *b*) wall friction plus bracing rod drag for a 1500 m chimney with 10 bracing wheels

No. of steps	Mach number	Static temp [K]	Static pressure [Pa]	Density [kg/m^3]	Velocity [m/s]	Press. drop [Pa]
10	0.0409110	308.417	76432.1	0.863247	14.4037	*a*) 6.1
10	0.0409481	308.417	76362.8	0.862464	14.4168	*b*) 75.4

and on the spoke drag coefficient as determined in the wind tunnel is $K_{bw}=0.02818\times0.95=0.02677$. This accounts for only 30% of K_{bw} measured in the chimney model. The rest must be ascribed to bracing wheel rim drag. The frontal area of the rims with inner diameter 607 mm in the 630-mm pipe is $311725-289379=22346$ mm^2, representing 0.07168 of the pipe area. According to [10] the C_D of a thin, wall-mounted plate perpendicular to the flow, based on the velocity at 40% of the obstruction height from the wall is 1.2, for Reynolds numbers $>10^3$. We make the crude assumption that the boundary layer thickness approaching the wheel rim is equal to the wheel rim width and that the velocity varies with the distance from the wall raised to the power 1/7. The velocity at 40% wheel rim height is then 0.877 times the free stream (core flow) velocity. The velocity profiles measured immediately behind a bracing wheel in Fig. 6 do indeed show a fairly uniform core flow. Following earlier frontal area arguments, the bracing wheel rim loss coefficient is $0.07168\times1.2\times0.877^2=0.06621$. Disregarding interference effects, the predicted bracing wheel loss coefficient is then $K_{bw}=0.02677+0.06621=0.0930$, a value 4% higher than measured in the chimney model.

The bracing wheel pressure drop increased by 36% to $(1.069-0.215)/7=0.122$ for the disturbed, blown-through flow. Flow visualization with tufts at the chimney exit showed that the bracing rod bars eventually removed all the swirl from the flow. The velocity profile would also eventually develop into a shape that was repeated after every wheel, whether the flow entered without swirl (sucked mode) or through the fan (blown mode). That is why in Fig. 5 the bracing pressure drop trends with and without swirl converged near the chimney exit.

Exit Kinetic Energy Coefficient

The bracing wheels cause velocity deficits downstream of the spokes and rims. There is also a 23-mm-dia hub ring or disc where rods attach in the chimney center. These blockages cause a high value of the kinetic energy coefficient, $\alpha=(\int V^3 dA)/(V_{ave}{}^3 A)$. Another effect of constant section radial bracing rods is that the higher blockage and drag near the center of the chimney, where the rods are closer to each other, reduces the velocity near the middle of the chimney and changes the shape from the expected fully developed pipe flow profile. These effects could cause a high value of the chimney exit kinetic energy coefficient, α, should there be a bracing rod wheel at or close to the chimney exit.

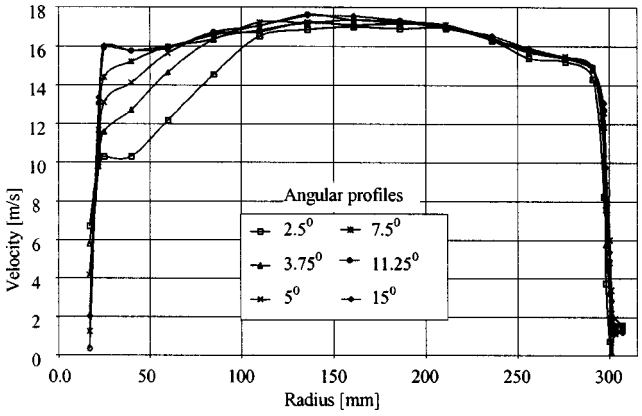

Fig. 6 Velocity profiles measured at chimney exit

Figure 6 shows velocity profiles measured with a calibrated five-hole pneumatic probe 10 mm downstream of the last bracing rod wheel, at the exit of the chimney model operating in the blown mode. There were seven wheels, one-and-a-half chimney diameters apart with their spokes all axially aligned. Velocities were measured at angular positions of 2.5, 3.75, 5, 7.5, 11.5, and 15 deg starting from the center line of one spoke (precisely between the two bars in Fig. 2). The flow direction at the exit was purely axial due to the cumulative flow straightening effect of the seven sets of spokes aligned in the axial direction.

The velocity was zero at all radial positions less than 15 mm from the center of the chimney because the central hole in the last bracing wheel was blocked by a small plug serving as a pivot attachment for the pneumatic probe. The additional blocked area was less than 1% of the pipe area. The value of α found through trapezium rule integration was 1.26, compared to a value of 1.058 expected for fully developed pipe flow with a 1/7 power law profile.

Application to Full Size Chimney

For the standard chimney case under consideration in [6], the variations over the height of a 1500-m-high chimney are as follows. Viscosity: 1.947 to 1.880×10^{-5} Ns/m^2; Reynolds number: 1.022 to 1.058×10^8; roughness of concrete walls: 2 mm; $f=0.008461$ and $f\delta z/D$: 0.007932 to 0.007929 (for $\delta z=150$ m, i.e., one-tenth of chimney height). It shows that the assumption of a constant friction factor is a good one. Solving Eqs. (1), (2), and (6) in [6] over ten steps of 150 m leads to the frictional static pressure drop in Table 1. The dynamic pressure at the bottom of the chimney is 79.7 Pa. The pressure drop based on the inlet values and incompressible flow assumptions is $\Delta p_f=0.07932\times79.3=6.3$ Pa, agrees to within 0.2 Pa with the compressible flow calculation, but expressed as a percentage error the difference is about 3%. Table 1 also presents results for a chimney with 10 sets of bracing rods 150 m apart, with $K_{bw}=0.0897$ and $f\delta z/D=0.007932$. The inlet conditions are as assumed before.

The incompressible calculation then gives the pressure drop as $\Delta p_{bw+f}=(0.0897+0.007932)\times79.3\times10=77.4$ Pa compared to 75.4 Pa for the compressible calculation: an error of +2 Pa or +2.7%. The incompressible calculation will suffice for most engineering purposes, since we do not know the value of the loss coefficients to within a few percent. Streamlining the spokes will reduce the spoke loss coefficient in the same ratio as the section drag coefficient, that is in the ratio 0.01 to 1.00. It would be more important, however to reduce the wheel rim width that accounts for the majority of the bracing wheel loss coefficient.

Summary of Losses

Table 2 presents a summary of the loss coefficients and losses for the 1500-m standard chimney. The second column assumes standard loss coefficients from the literature, as discussed, except for the bracing wheel where data from the non-swirling flow measurement were assumed. The third column is based on the loss coefficients as measured with non-swirling uniform flow entering the chimney through a bell mouth, and the fourth column is based on the loss coefficients as measured with the flow entering the chimney through the fan and diffuser, thereby representing the

Table 2 Summary of the loss coefficients and losses in a 1500 m standard chimney

Loss type	Standard fully developed flow friction calculation and exit kinetic energy coefficient	From measurement with non-swirling uniform inlet flow (Sucked through)	From measurement with simulated swirling turbine exit flow (Blown through)
Wall friction loss coefficient	0.00846	0.01097	0.01367
Wall friction loss [Pa]	6.1	7.9	9.9
Bracing wheel loss coefficient	0.0897	0.0897	0.122
Bracing wheel loss [Pa]	75.4−6.1=69.3	69.3	94.3
Exit kinetic energy coefficient	1.058	1.26	1.26
Exit loss [Pa]	1.058×89.6=94.8	112.9	112.9
Total loss [Pa]	170.2	190.1	217.1

flow passing through the turbine and diffuser of a chimney plant. The chimney exit dynamic pressure of 89.6 Pa, determined from data in Table 1 was used to calculate the exit losses. Note that the ratio of total bracing wheel to friction loss (no swirl) is 69.3/7.9 =8.8 for the full-scale chimney compared to 0.801/0.173=4.6 for the model. The reasons for the difference are the lower friction factor caused by the higher Reynolds number in the full-scale chimney and the reduced bracing wheel spacing of one diameter in the full-scale chimney. The table shows that chimney losses may be 46.9 Pa or about 28% higher than estimated by making standard assumptions. Since the standard data assumes a turbine pressure drop of 1000 Pa, this error represents a 4.7% reduction in available turbine pressure drop. Most of this is caused by the bracing wheels and especially the rims, and some by the spoke drag coefficient. The bracing wheel and its rim situated at the chimney top also play a large part in increasing the exit kinetic energy coefficient.

Conclusions

Skin friction losses, even with fairly rough concrete chimney walls are relatively small. A design of the bracing wheels with a spacing of one diameter between them leads to losses that are an order of magnitude larger than skin friction. The major contributing factor is the bracing wheel rim, which accounts for 70% of the bracing wheel drag. A bracing wheel at the chimney top also increases the exit kinetic energy coefficient by about 20%. The effect of swirling flow leaving the turbine could increase the losses by more than 20% thereby reducing the turbine pressure drop by more than 4%. The design and positioning of solar chimney bracing wheels should be investigated further, particularly the width of the bracing wheel rims and their positioning (inside or outside the chimney). Streamlining of the spokes may also reduce their drag coefficients from about 1.0 to about 0.01.

Nomenclature

A = flow area or frontal area [m^2]
C_D = chimney drag coefficient
D = chimney inside diameter [m]
d = spoke thickness [mm]
F = drag force [N]
f = friction coefficient
K = pressure drop coefficient
$\dot{m}$ = mass flow [kg/s]
p = static pressure [Pa]
R = gas constant [J/kgK]
Re = Reynolds number
S = Sutherland coefficient [K]
t = static temperature [K]
V = velocity [m/s]
z = altitude [m]
L = spoke stream wise length [mm]

Greek

α = kinetic energy coefficient
γ = specific heat ratio
ε = wall roughness [mm]
μ = dynamic viscosity [Ns/m^2]
θ = wake momentum thickness [mm]
ρ = density [kg/m^3]

Prefix

Δ = change invariable

Subscript

ave = average
bw = bracing wheel
c = chimney
D = diameter
dyn = dynamic
f = frictional
sp = spoke
0 = reference
1 = inlet (or coefficient number)
2 = exit (or coefficient number)

References

[1] Schlaich, J., 1995, *The Solar Chimney, Electricity From the Sun*, Axel Menges, Stuttgart.
[2] Von Backström, T. W., 2000, "The Solar Chimney Air Standard Cycle," SAIMechE R&D J, **16**(1), pp. 16–24.
[3] Gannon, A. J., and Von Backström, T. W., 2000, "Solar Chimney Analysis With System Loss and Solar Collector Performance," ASME J. Sol. Energy Eng., **122**(3), pp. 133–137.
[4] Von Backström, T. W., and Gannon, A. J., 2000, "Compressible Flow Through Solar Power Plant Chimneys," ASME J. Sol. Energy Eng., **122**(3), pp. 138–145.
[5] Schlaich, J., 1999, "Tension Structures for Solar Electricity Generation," Eng. Struct., **21**, pp. 658–668.
[6] Von Backström, T. W., and Gannon, A. J., 2002, "Calculation of Pressure and Density in Solar Power Plant Chimneys," ASME J. Sol. Energy Eng., **125**(1), pp. 127–129.
[7] Sutherland, W., 1893, "The Viscosity of Gases and Molecular Force," Philos. Mag., **5**, pp. 507–531.
[8] Haaland, S. E., 1983, "Simple and Explicit Formulas for the Friction Factor in Turbulent Pipe Flow," ASME J. Fluids Eng., **105**, pp. 89–90.
[9] Hoerner, S. F., 1965, *Fluid-Dynamic Drag*, Hoerner Fluid Dynamics, New Jersey, pp. 3–13.
[10] Anonymous, 1978, "Fluid Forces, Pressures and Moments on Rectangular Blocks," Engineering Sciences Data Unit Item No. 71016, Tech. Editing and Reproduction Ltd, London, p. 20, p. 7, p. 9.
[11] White, F. M., 1999, *Fluid Mechanics, 4th Edition*, McGraw-Hill, p. 479.
[12] Sachs, P., 1972, *Wind Forces in Engineering*, Pergamon, Oxford, p. 72.
[13] Schlichting, H., 1979, *Boundary Layer Theory*, McGraw-Hill, New York, p. 758.

Available online at www.sciencedirect.com
ScienceDirect
Solar Energy 80 (2006) 1417–1423
SOLAR ENERGY
www.elsevier.com/locate/solener

Maximum fluid power condition in solar chimney power plants – An analytical approach

Theodor W. von Backström *, Thomas P. Fluri

Department of Mechanical Engineering, University of Stellenbosch, Private Bag XI, Matieland 7602, South Africa

Received 15 November 2004; received in revised form 21 February 2006; accepted 10 April 2006
Available online 24 May 2006

Communicated by: Associate Editor Klaus Vajen

Abstract

Main features of a solar chimney power plant are a circular greenhouse type collector and a tall chimney at its centre. Air flowing radially inwards under the collector roof heats up and enters the chimney after passing through a turbo-generator.

The objective of the study was to investigate analytically the validity and applicability of the assumption that, for maximum fluid power, the optimum ratio of turbine pressure drop to pressure potential (available system pressure difference) is 2/3. An initial power law model assumes that pressure potential is proportional to volume flow to the power m, where m is typically a negative number between 0 and -1, and that the system pressure drop is proportional to the power n, where typically $n = 2$. The analysis shows that the optimum turbine pressure drop as fraction of the pressure potential is $(n - m)/(n + 1)$, which is equal to 2/3 only when $m = 0$, implying a constant pressure potential, independent of flow rate. Consideration of a basic collector model proposed by Schlaich leads to the conclusion that the value of m is equal to the negative of the collector floor-to-exit efficiency. A more comprehensive optimization scheme, incorporating the basic collector model of Schlaich in the analysis, shows that the power law approach is sound and conservative.

It is shown that the constant pressure potential assumption ($m = 0$) may lead to appreciable underestimation of the performance of a solar chimney power plant, when compared to the analyses presented in the paper. More important is that both these analyses predict that maximum fluid power is available at much lower flow rate and much higher turbine pressure drop than predicted by the constant pressure potential assumption. Thus, the constant pressure potential assumption may lead to overestimating the size of the flow passages in the plant, and designing a turbine with inadequate stall margin and excessive runaway speed margin. The derived equations may be useful in the initial estimation of plant performance, in plant performance analysis and in control algorithm design. The analyses may also serve to set up test cases for more comprehensive plant models.

Keywords: Solar chimney power plant; Solar chimney turbine; Solar thermal power plant; Solar tower; Maximum power

* Corresponding author. Fax: +27 (0)21 808 4958.
E-mail address: twvb@sun.ac.za (T.W. von Backström).

0038-092X/$ - see front matter © 2006 Elsevier Ltd. All rights reserved.
doi:10.1016/j.solener.2006.04.001

Nomenclature

A	surface area; m^2
C	coefficient
c_p	specific heat; J/kg K
G	solar irradiation; W/m^2
g	gravitational acceleration; m/s^2
H	height; m
K	coefficient
P	power; W
p	pressure; Pa
$\dot{Q}$	heat transfer rate; W
T	temperature; K
V	volume flow rate; m^3/s
*	reference condition

Greek symbols

α	absorption coefficient
β	heat transfer coefficient; W/m^2
Δ	differential
η	efficiency
ρ	density; kg/m^3

Abbreviations

MFP	maximum fluid power
PL	power law

Subscripts

1, 2, 3	coefficient numbers
c	chimney
cfe	collector floor to exit
coll	collector
deck	collector deck
floor	collector floor
L	loss
MFP	maximum fluid power
p	potential
t	turbine

Superscripts

m	pressure potential exponent
n	pressure loss exponent

1. Introduction

In order to design a flow system containing a turbine for maximum power production and to run it at maximum power, engineers need to find the optimal pressure drop across the turbine as a fraction of the total available system pressure difference. The design flow rate through the system determines the size and cost of the plant flow passages as well as the size, design and cost of the turbine. In the design phase some iterative algorithm may suffice to find the optimum, but a simple analytical method would be more convenient in a control algorithm. It could also serve to set up test cases for more comprehensive methods.

Many solar chimney investigators have made the assumption that the optimum ratio of p_t/p_p is 2/3, (Haaf et al., 1983; Lautenschlager et al., 1984; Mullett, 1987; Schlaich, 1995). In more detailed calculations Schlaich (1995) apparently used an optimum value of $p_t/p_p = 0.82$ as evident from the values of p_t and p_p reported in tables. Hedderwick (2001) presented graphs showing values around 0.7. Von Backström and Gannon (2000) used the 2/3 assumption only for optimization at constant available pressure difference, but Gannon and Von Backström (2000) employed an optimization procedure under conditions of constant solar irradiation. Schlaich et al. (2003) reported a p_t/p_p value of about 0.80, while Bernardes et al. (2003) reported a value of as high as 0.97. The wide variation in values warrants further investigation.

The question is the existence or not of a relevant optimum p_t/p_p in solar chimney power plants, and how to determine it. Even under conditions of constant solar irradiation the pressure potential of a solar chimney plant is not fixed but is a function of the air temperature rise in the collector, which varies with flow rate.

The first objective of this paper applies to any general process where the pressure potential is not constant and the system pressure drop is not necessarily proportional to the flow rate to the power 2.0. The objective is to derive simple, generally applicable equations for the determination of the volume flow for maximum fluid power (MFP) and the associated ratio of turbine total pressure drop to pressure potential. The second objective applies to solar chimney power plants. It is to derive equations for finding the optimum flow rate and p_t/p_p conditions as dependent on the relevant design and operating conditions of the plant, using a simple solar collector model.

2. Power law model

The derivation of the power law model requires two generalisations: a pressure potential versus flow relationship and a system pressure drop versus flow relationship. A very simple but useful assumption for the relationship between pressure potential and volume flow is:

$$p_p = K_p V^m \tag{1}$$

where $K_p = p_{ref}/V_{ref}^m$ is determined at a reference point (V_{ref}, p_{ref}) near the optimum, and m is a negative exponent. Fig. 1 shows pressure potential lines for a few values of m. Note that if $m = 0$, then $p_p = K_p$, denoting a constant pressure potential.

A useful assumption for the system pressure drop in incompressible flow is:

$$p_L = K_L V^n \tag{2}$$

where n will typically be 2 when system pressure drop is dominated by minor losses, and closer to 1.75 when the pressure drop is dominated by Reynolds number dependent wall friction losses (White, 2003). The solid line in Fig. 2 represents the system loss curve.

Note that the effect of the variation of density with temperature rise through the system is disregarded, but may be included in the choice of K and n in the vicinity of each operating point. The turbine pressure drop is then:

$$p_t = p_p - p_L = p_p - K_L V^n \tag{3}$$

Since the change in density across a solar chimney turbine is typically ($\Delta\rho_t < 2\%$) we can regard the air flowing through the turbine as incompressible, i.e., the fluid power is equal to the product of the volume flow and total pressure drop across the turbine:

$$P = p_t V = (p_p - K_L V^n) V \tag{4}$$

The shaded area in Fig. 2 represents the fluid power. The power generation rate of the turbine depends not only on the characteristics of the flow system it is part of, but also on those of the turbine itself. In the present paper, however, we assume that the turbine efficiency does not vary appreciably with changes in flow rate, or, if it does, the variation in turbine losses may be accounted for in the system pressure losses.

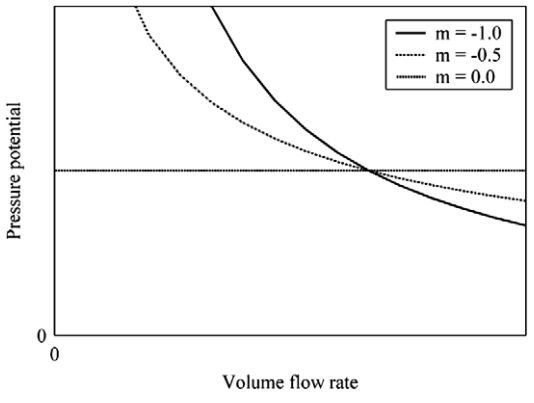

Fig. 1. Pressure potential vs. volume flow for three values of exponent m.

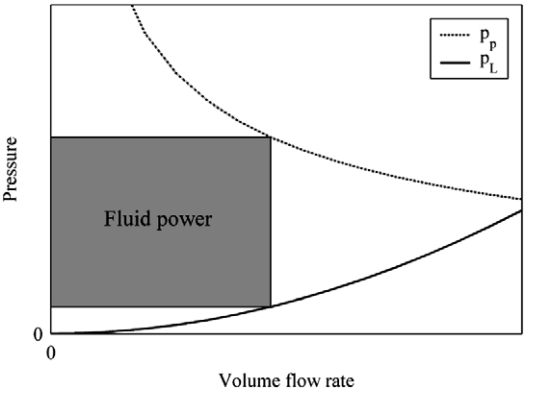

Fig. 2. Plot of pressure potential and pressure loss vs. volume flow, and fluid power (shaded area) for $m = -0.5$.

2.1. Maximum fluid power condition

The volume flow for maximum fluid power (MFP) is found when $\partial P/\partial V = 0$:

$$\begin{aligned} &\frac{\partial}{\partial V}[(K_p V^m - K_L V^n)V] = 0 \\ &(m+1)K_p V_{MFP}^m - (n+1)K_L V_{MFP}^n = 0 \end{aligned} \tag{5}$$

The flow at maximum fluid power is then given by:

$$V_{MFP} = \left(\frac{K_p(m+1)}{K_L(n+1)}\right)^{\frac{1}{n-m}} \tag{6}$$

Note that when $m = -1$, then $V = 0$ and p_p is infinite, i.e., the power law model is unrealistic at very small flows.

The pressure potential at maximum fluid power follows from substituting Eq. (1) in Eq. (5):

$$(p_p)_{MFP} = \frac{(n+1)}{(m+1)} K_L V_{MFP}^n \tag{7}$$

The turbine pressure drop as fraction of the pressure potential at maximum fluid power is found by subtracting the system loss from the pressure potential:

$$\begin{aligned} p_t &= p_p - K_L V^n \\ (p_t)_{MFP} &= \frac{(n-m)}{(m+1)} K_L V^n \\ \left(\frac{p_t}{p_p}\right)_{MFP} &= \frac{(n-m)}{(n+1)} \end{aligned} \tag{8}$$

This relatively simple relationship depends on the exponents m and n only. In practice the power law relationship between p_p and V would, for the appropriate values of K_p and of m, approximate the real relationship only in a limited region, but the point where K_p and m are calculated may be adjusted iteratively. The same applies to K_L and n. In time-dependent analyses, a quasi-steady state condition is assumed during the time that the optimum is sought. In practical terms this implies that the turbine configuration (for example the rotor blade setting angles) can be adjusted much faster than plant operating conditions change. The assumption is that during this interval a fixed relationship between the pressure potential and the volume flow exists, or K_p and m are constant, and so are K_L and n.

In the special case when $m = 0$ and $n = 2$, Eq. (6) reduces to:

$$V_{MFP} = \left(\frac{p_p}{3K_L}\right)^{0.5} \tag{9}$$

The MFP flow rate is then $1/\sqrt{3}$ of the maximum flow rate that occurs when $p_t = 0$. Also, when $m = 0$ (p_p = constant) and $n = 2$, Eq. (8) reduces to:

$$\left(\frac{p_t}{p_p}\right)_{MFP} = \frac{(2-0)}{(2+1)} = \frac{2}{3} \tag{10}$$

The MFP condition occurs at $p_t/p_p = 2/3$ only in the special case when $m = 0$ (i.e., constant pressure potential) and $n = 2$. When $n = 2$ and $m \neq 0$, then p_t/p_p for maximum fluid power exceeds 2/3 when m is negative (i.e., pressure potential decreases with volume flow).

3. Value of *m* for simple solar collector model

Consider steady state operation of a solar chimney power plant. The solar collector consists of a transparent deck over a floor that receives solar energy. The collector floor transfers energy to the air flowing over it at the same rate at which it receives energy from the sun, namely at $\alpha G A_{coll}$, where α is the effective absorption coefficient of the collector. The air in the collector loses heat through the collector deck at the same rate that the collector deck loses heat to the environment, namely at $\beta \Delta T A_{coll}$, where β is an adjusted heat transfer coefficient that allows for radiation and convection losses and the fact that the temperature difference between deck and environment increases from 0 at the outer edge of the collector to ΔT at the chimney entrance. The real situation is more complex, but this simple model employed by Schlaich (1995) may be used to derive an approximate expression for the collector temperature rise and the exponent m of the analysis above.

Find the air temperature rise by equating energy entering and leaving the collector:

$$\begin{aligned} \dot{Q}_{floor} - \dot{Q}_{deck} &= \dot{Q}_{cfe} \\ \alpha G A_{coll} - \beta \Delta T A_{coll} &= V \rho_{coll} c_p \Delta T \\ \Delta T &= \frac{\alpha G A_{coll}}{V \rho_{coll} c_p + \beta A_{coll}} \end{aligned} \tag{11}$$

If the ambient temperature at ground height is T_0, the collector exit (chimney inlet) density is ρ_{coll} and assuming parallel temperature profiles inside and outside the chimney a chimney of height H_c will generate a hydrostatic pressure potential, p_p:

$$p_p = \rho_{coll} g H_c \frac{\Delta T}{T_0} = \frac{\rho_{coll} g H_c}{T_0} \frac{\alpha G A_{coll}}{V \rho_{coll} c_p + \beta A_{coll}} \tag{12}$$

This equation is of the form:

$$p_p = \frac{C_1}{C_2 V + C_3} \tag{13}$$

It can be shown that for a relationship of the form $p = AV^m$, m depends only on the local value of the function and the local value of its gradient, and is given by:

$$m = \frac{dp_p}{dV} \Big/ \frac{p_p}{V} \tag{14}$$

For a function of another form, for example Eq. (13), an equivalent m can be calculated at any point, since m depends only on the coordinates of the point and its local gradient:

$$\begin{aligned} m &= \frac{dp_p}{dV} \frac{V}{p_p} \\ &= \frac{-C_1 C_2}{(C_2 V + C_3)^2} \frac{V(C_2 V + C_3)}{C_1} \\ &= -\frac{C_2 V}{(C_2 V + C_3)} \end{aligned} \tag{15}$$

Back substitute for C_2 and C_3 and multiply the denominator and numerator by ΔT:

$$\begin{aligned} m &= -\frac{V\rho_{\text{coll}}c_p\Delta T}{(V\rho_{\text{coll}}c_p\Delta T + \beta A_{\text{coll}}\Delta T)} \\ &= -\frac{V\rho_{\text{coll}}c_p\Delta T}{\alpha G A_{\text{coll}}} \\ &= -\frac{\alpha G A_{\text{coll}} - \beta A_{\text{coll}}\Delta T}{\alpha G A_{\text{coll}}} \\ &= -\frac{\dot{Q}_{\text{floor}} - \dot{Q}_{\text{deck}}}{\dot{Q}_{\text{floor}}} = -\eta_{\text{cfe}} \end{aligned} \tag{16}$$

Here η_{cfe} is the net rate at which heat is absorbed by the air between the inlet and exit of the collector, expressed as fraction of the rate of heat transfer from the floor to the air. We shall call it the collector floor-to-exit efficiency since it is a measure of how efficiently the collector transfers heat from its floor to the air leaving the collector. Schlaich (1995) writes the standard collector efficiency for his collector model as:

$$\eta_{\text{coll}} = \alpha - \frac{\beta\Delta T}{G} \tag{17}$$

The collector floor-to-exit efficiency can be written similarly by dividing out $\alpha G A_{\text{coll}}$ in Eq. (16):

$$\begin{aligned} \eta_{\text{cfe}} &= 1 - \frac{\beta\Delta T}{\alpha G} \\ &= \frac{\eta_{\text{coll}}}{\alpha} \end{aligned} \tag{18}$$

It is remarkable that in the case of the simplified solar chimney collector model, the exponent m turns out to be simply the negative of the collector floor-to-exit efficiency. The immediate implications are the following:

- m must have a value between 0 and -1
- for $n = 2$, the optimum p_t/p_p is between 2/3 and 1
- the optimal p_t/p_p ratio is 2/3 only if the collector efficiency equals zero.

3.1. Power law vs. constant pressure potential model

A key question is how the value of m affects the prediction of plant power. As a reference condition we use the case where $V = V_{\max}/(n+1)^{1/n}$ and $p_t/p_p = n/(n+1)$, and denote it with an asterisk (*). When $p_t/p_p = n/(n+1)$ in the power law model, then from Eqs. (1)–(3):

$$\frac{K_p}{K_L} = (n+1)V_*^{n-m} \tag{19}$$

Substitute Eq. (19) into Eq. (6) to get the volume flow at the MFP condition:

$$\begin{aligned} V_{\text{MFP}} &= \left((m+1)V_*^{n-m}\right)^{(n-m)^{-1}} \\ &= (m+1)^{(n-m)^{-1}} V_* \end{aligned} \tag{20}$$

Using Eqs. (1), (8) and (20), the turbine pressure drop at the MFP condition is:

$$p_{\text{tMFP}} = \left(\frac{n-m}{n}\right)(m+1)^{m/(n-m)} p_{t*} \tag{21}$$

By substituting Eqs. (20) and (21) into (4), the fluid power at the MFP condition follows:

$$P_{\text{MFP}} = \left(1 - \frac{m}{n}\right)(1+m)^{(1+m)/(n-m)} P_* \tag{22}$$

In Table 1, volume flow, pressure potential and power, all at the MFP condition, are listed as a fraction of the respective reference value over a range of collector floor-to-exit efficiencies at $n = 2$ for the power law model. At a collector floor-to-exit efficiency of 70% ($m = -0.70$) we can see that the MFP volume flow may be as low as 64%, the MFP turbine pressure drop may be as high as 185% and the power production may be 118% compared to the reference value. Even at moderate collector floor-to-exit efficiencies of around 50% the optimal turbine pressure drop may be seriously underestimated by using the 2/3 rule.

Schlaich (1995) gives typical values of η_{coll} around 0.55 and α around 0.80, leading to $\eta_{\text{cfe}} \approx 0.69$.

Table 1
MFP-values of volume flow rate, turbine pressure drop and fluid power for power law model as a fraction of constant pressure potential model values listed for a range of exponent m ($n = 2.0$)

m	−0.2	−0.3	−0.4	−0.5	−0.6	−0.7	−0.8	−0.9
V_{PL}/V_*	0.904	0.856	0.808	0.758	0.703	0.640	0.564	0.452
p_{tPL}/p_{t*}	1.123	1.205	1.307	1.436	1.606	1.845	2.217	2.963
P_{PL}/P_*	1.014	1.032	1.056	1.088	1.129	1.181	1.248	1.339

Applying the above model we get $m = -0.69$ and from Eq. (8) and assuming $n = 2$ the optimal ratio is $p_t/p_p = (n-m)/(n+1) = 2.69/3 = 0.90$. This value is much higher than the value of 2/3, and also higher than the value of 0.82 derived from values in a table of data given by Schlaich (1995). On the other hand, a value of $p_t/p_p = 0.82$ corresponds to $\eta_{cfe} = 0.46$, and if $\alpha = 0.8$, to $\eta_{coll} = 0.8 \times 0.46 = 0.37$, which is very low. The value of 0.9 agrees with the value recommended by Bernardes et al. (2003). In his analysis he found optimum values of as high as 0.97, resulting in $m = -0.91$. This would, in combination with his value of collector floor absorption coefficient, $\alpha = 0.9$, imply a collector floor-to-exit efficiency of 0.91/0.9, which exceeds 100%. If the value of 0.8 for α given by Schlaich is replaced by 0.9 in his data set, then $\eta_{cfe} \approx 0.61$, with optimal ratio of $p_t/p_p = 0.87$.

As the tabulated data in Schlaich (1995) were not obtained with a p_t/p_p ratio of 2/3, we cannot apply Eqs. (20)–(22) directly to come up with the values for volume flow, turbine pressure drop and power at the MFP condition. We first have to find the equivalent * condition, by using Eqs. (1) and (2) to get values for K_p and K_L. Assuming these coefficients as well as the exponents m and n to remain constant over a restricted range of flow rate and using the * condition together with Eqs. (1) and (2) from Eq. (19) V_* is:

$$V_* = \left(\frac{3K_L}{K_p}\right)^{\frac{1}{m-n}} \tag{23}$$

The value of m follows from η_{cfe}, and n is taken as 2. We can then find V_* and evaluate p_{p*}, p_{t*}, p_{L*}, and P_*, and find values for the same variables at the MFP condition with Eqs. (20)–(22).

Since n is numerically about three times as large as m, V_* is rather insensitive to the exact value of m. Taking $m = -0.66$ and working with the 100 MW plant data we find that P_{MFP} is 3.7% higher than $P_{Schlaich}$ (for the 30 MW plant it is 3.5% and for the 5 MW it is 3.0%). Changing m by 20% to −0.79 leads to a P_{MFP} that is 8.4% higher than $P_{Schlaich}$, a change of only 4.5%.

4. Effect of variable collector efficiency

The power law model used so far contains an inconsistency: it assumes that m is constant and independent of flow rate, but it then turns out that m is proportional to the collector efficiency, which is in fact a function of flow rate. This limits the power law method to cases where m varies only slightly with flow. The solution is to recognize that the analysis so far does not fully explore the potential of the simple collector model of Schlaich (1995). To find the potential fluid power, while recognizing that η_{cfe} depends on V, we formulate the MFP Coll. model (where the added Coll. denotes the collector): multiply Eq. (12) by V:

$$\begin{aligned} P = p_t V &= \left(\frac{\rho_{coll} g H_c}{T_0}\frac{\alpha G A_{coll} V}{V\rho_{coll}c_p + \beta A_{coll}} - K_L V^n V\right) \\ \frac{\partial P}{\partial V} &= \left[\frac{\rho_{coll} g H_c}{T_0}\left(\frac{\alpha G A_{coll}}{V\rho_{coll}c_p + \beta A_{coll}} - \frac{\alpha G A_{coll} V \rho_{coll} c_p}{(V\rho_{coll}c_p + \beta A_{coll})^2}\right) - (n+1)K_L V^n\right] = 0 \\ &= \frac{\rho_{coll} g H_c}{T_0}(\alpha G A_{coll}(V\rho_{coll}c_p + \beta A_{coll}) - \alpha G A_{coll} V \rho_{coll} c_p) \\ &\quad - (n+1)K_L V^n((V\rho_{coll}c_p + \beta A_{coll})^2) = 0 \end{aligned} \tag{24}$$

If $n = 2$, Eq. (24) is a fourth order polynomial for which an analytical solution procedure exists. Otherwise it has to be solved numerically for $V_{MFP\ Coll}$. It will be more instructive, however, to compare power versus flow graphs for the constant m and variable collector efficiency approaches. Fig. 3 shows that for a 100 MW test case from Schlaich (1995), V_{PL} and $V_{MFP\ Coll}$. are quite similar, but both differ substantially from V_*, the flow at which the turbine pressure drop is 2/3 of the pressure potential. It also shows that use of the 2/3 rule seriously overestimates the maximum flow at which the plant produces any power at all. This value has a

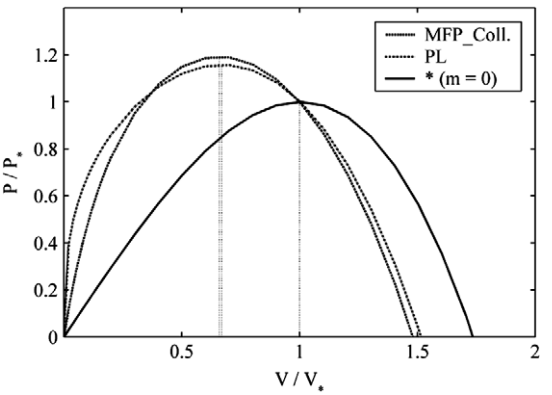

Fig. 3. Plot of fluid power vs. volume flow for various modeling approaches of a 100 MW nominal power plant (normalized by the MFP values of the reference case).

Table 2
Comparison of flow rate, turbine pressure drop and fluid power at the MFP-condition of the power law model and the MFP Coll. model for various power plant sizes as a fraction of the MFP values for the reference case

Nominal power	100 MW		30 MW		5 MW	
	PL	MFP Coll.	PL	MFP Coll.	PL	MFP Coll.
V/V_*	0.659	0.669	0.640	0.643	0.617	0.616
p_t/p_{t*}	1.808	1.730	1.890	1.823	1.996	1.920
P/P_*	1.192	1.158	1.210	1.172	1.232	1.183

large effect on the turbine runaway speed. Table 2 summarizes similar comparisons for the data from Schlaich for several test cases. Typically V_{PL} and $V_{MFP\ Coll}$ are between 67% and 62% of V_*, and the corresponding optimal turbine pressure drops are between 173% and 200% of the values associated with V_*. It is encouraging to see that the simple power law model predicts the maximum power flow within 1% point compared to the MFP Coll. Model in all the test cases and is pessimistic in the prediction of the maximum fluid power value, and optimistic in the prediction of turbine pressure drop.

5. Conclusions

The study developed two analyses for finding the optimal ratio of turbine pressure drop to available pressure drop in a solar chimney power plant for maximum fluid power. In the first part the system pressure potential is assumed to be proportional to V^m where V is the volume flow and m a negative exponent, and the system pressure loss is proportional to V^n where typically $n = 2$. Simple analytical solutions were found for the optimum ratio of p_t/p_p and for the flow associated with it. This ratio is not 2/3 as used in simplified analyses, but depends on the relationship between available pressure drop and volume flow, and on the relationship between system pressure loss and volume flow. The analysis shows that the optimum turbine pressure drop as fraction of the pressure potential is $(n - m)/(n + 1)$, which is equal to 2/3 only if $m = 0$ (i.e., constant pressure potential, independent of volume flow) and $n = 2$. Consideration of a basic collector model proposed by Schlaich led to the conclusion that the value of m is equal to the negative of the collector floor-to-exit efficiency.

The basic collector model is sensitive to the effect of volume flow on the collector efficiency. Its introduction into the analysis indicated that the power law model is conservative in its prediction of maximum fluid power produced by the plant, and in the magnitude of the flow reduction required to achieve this. It was shown that the constant pressure potential assumption may lead to appreciable under estimation of the performance of a solar chimney power plant, when compared to the model using a basic model for the solar collector. More important is that both analyses developed in the paper predict that maximum fluid power is available at much lower flow rate and much higher turbine pressure drop than the constant pressure potential assumption predicts. Thus, the constant pressure potential assumption may lead to overestimating the size of the flow passages in the plant, and designing a turbine with inadequate stall margin and excessive runaway speed margin. The derived equations may be useful in the initial estimation of plant performance, in plant performance analyses and in control algorithm design. The analyses may also serve to set up test cases for more comprehensive plant models.

References

Bernardes, M.A., dos, S., Voss, A., Weinrebe, G., 2003. Thermal and technical analyses of solar chimneys. Solar Energy 75 (6), 511–524.

Gannon, A.J., Von Backström, T.W., 2000. Solar chimney cycle analysis with system loss and solar collector performance. Journal of Solar Energy Engineering, Transaction of the ASME 122 (3), 133–137.

Haaf, W., Friedrich, K., Mayr, G., Schlaich, J., 1983. Solar chimneys. International Journal of Solar Energy 2, 3–20.

Hedderwick, R.A., 2001. Performance evaluation of a solar chimney power plant, M.Sc. Eng. thesis, University of Stellenbosch.

Lautenschlager, H., Haaf, W., Schlaich, J., 1984. New results from the solar chimney prototype and conclusions for large power plants. In: Proceedings of the European Wind Energy Conference, Hamburg, Germany, pp. 231–235.

Mullett, L.B., 1987. The solar chimney – overall efficiency, design and performance. International Journal of Ambient Energy 8 (1), 35–40.

Schlaich, J., 1995. The solar chimney – electricity from the sun, Edition Axel Menges, Stuttgart.

Schlaich, J., Bergermann, R., Schiel, W., Weinrebe, G., 2003. Design of commercial solar tower systems – utilization of solar induced convective flows for power generation, In: Proceedings of the International Solar Energy Conference, Kohala Coast, United States, pp. 573–581.

Von Backström, T.W., Gannon, A.J., 2000. The solar chimney air standard thermodynamic cycle. SAIMechE R&D Journal 16 (1), 16–24.

White, F.M., 2003. Fluid Mechanics, fifth ed. McGraw-Hill, p. 362.

Available online at www.sciencedirect.com
ScienceDirect
Solar Energy 83 (2009) 264–275
SOLAR ENERGY
www.elsevier.com/locate/solener

Analysis of some available heat transfer coefficients applicable to solar chimney power plant collectors

Marco Aurélio dos Santos Bernardes *, Theodor W. Von Backström, Detlev G. Kröger

Department of Mechanical Engineering, University of Stellenbosch, Private Bag X1, Western Cape, Matieland 7602, South Africa

Received 6 December 2007; received in revised form 24 July 2008; accepted 30 July 2008
Available online 26 August 2008

Abstract

A solar chimney power plant consists of a translucent collector which heats the air near the ground and guides it into the base of a chimney at its centre. The buoyant air rises in the chimney and electricity is generated through one or more turbines in or near the base of the chimney. Various studies about solar chimney power plant performance have been published. Different calculation approaches with a variety of considerations have been applied to calculate chimney power plant performance. In particular, two comprehensive studies are relevant, namely those of (Bernardes, M.A.d. S., Voß, A., Weinrebe, G., 2003. Thermal and technical analyses of solar chimneys. Solar Energy 75, 511–524; Pretorius, J.P., Kröger, D.G., 2006b. Solar chimney power plant performance. Transactions of the ASME 128, 302–311). The paper compares the methods used to calculate the heat fluxes in the collector, and their effects on solar chimney performance. Reasons for the discrepancies between the predictions of the two models are given. In general the Pretorius model produces higher heat transfer coefficients and higher heat rate fluxes for both the roof and for the ground surfaces. The two approaches lead to very similar air temperature rises in the collector and thus, similar produced power.

Keywords: Solar chimney; Heat transfer; Fluid mechanics

1. Introduction

The solar chimney is one technology which has proved capable of generating electrical energy from the sun Schlaich (1995). The solar chimney consists of a chimney coupled with a translucent collector which heats the air near the ground and guides it into the base of a tall chimney. The buoyant air ascends in the chimney and electricity is generated by the hot air moving through one or more turbines at the base of the chimney.

Various studies about solar chimney power plant performance have been published (for example, Schlaich (1995), Kröger and Blaine (1999), Bernardes et al. (2003), Gannon and Von Backström (2000), Bernardes (2004), Pretorius (2006)). The literature is extensive, and that referred to here is by no means exhaustive. Bernardes et al. (2003) developed an analysis for the solar chimneys, aimed particularly at a comprehensive analytical and numerical model to estimate power output of solar chimneys as well as to examine the effect of various ambient conditions and structural dimensions on the power output. This study shows that the height of chimney, the factor of pressure drop at the turbine, the diameter and the optical properties of the collector are important parameters for the design of solar chimneys. Von Backström and Gannon (2004) presented analytical equations in terms of turbine flow and load coefficient and degree of reaction, to express the influence of each coefficient on turbine efficiency. Von Backström and Fluri (2006) investigated analytically the validity and applicability of the assumption that, for maximum fluid power, the optimum ratio of turbine pressure drop to pressure potential (available system pressure difference) is 2/3. A more comprehensive optimization scheme, incorporating the basic collector model of Schlaich in the analysis,

* Corresponding author. Tel.: +27 218084272.
E-mail address: masb2005@gmail.com (Marco Aurélio dos Santos Bernardes).

0038-092X/$ - see front matter © 2008 Elsevier Ltd. All rights reserved.
doi:10.1016/j.solener.2008.07.019

Nomenclature

Nomenclature

A_c	flow area, m^2
b	collector roof radius exponent, –
c_p	specific heat capacity, J/kg K
d_h	hydraulic diameter $d_h = 2H$; $H = H_2\left(\frac{r_2}{r}\right)^b$, m
f	Darcy friction factor, –
F_{bw}	force regarding pressure drop due to chimney bracing wheel, N
$F_{supports}$	force regarding pressure drop due to collector roof supports, N
g	gravitational acceleration, 9.8 m/s^2
H	height, m
H_2	height of the collector roof at the collector perimeter radius, m
h	enthalpy or convective heat transfer coefficient, J/kg
h_{gh}	convective heat transfer coefficient – ground to flow, W/m^2 K
h_{ra}	convective heat transfer coefficient – roof to ambient, W/m^2 K
h_{rh}	convective heat transfer coefficient – roof to flow, W/m^2 K
k	thermal conductivity, W/m K
$\dot{m}$	mass flow rate, kg/s
Nu	overall Nusselt number, –
Nu_f	Nusselt number – forced convection, –
$Nu_{f,lam}$	laminar Nusselt number – forced convection, –
$Nu_{f,turb}$	turbulent Nusselt number– forced convection, –
Nu_n	Nusselt number – natural convection, –
p	Pressure, Pa
Pr	Prandtl number, –
$\dot{q}$	heat flux, W/m^2
$\dot{q}_{gh}$	convective heat flux between the ground and the flow under collector roof, W/m^2
$\dot{q}_{ra}$	convective heat flux between the roof and the ambient, W/m^2
$\dot{q}_{rh}$	convective heat flux between the roof and the flow under collector roof, W/m^2
R	gas constant, J/kg K
r	radial coordinate, m
r_2	collector roof at the collector perimeter radius, m
Ra	Rayleigh number, –
Re	Reynolds number, –
T	temperature, K
u	radial velocity component, m/s
v_c	vertical velocity component, m/s
v_w	wind velocity, m/s
z	vertical coordinate, m
θ	angle, radians
Δp_{turb}	pressure drop across the turbine, Pa
ρ	density, kg/m^3
ρ_{avg}	average air density through the turbine, kg/m^3
ρ_c	air density in the chimney, kg/m^3
τ	shear stress, Pa
τ_c	shear stress in the chimney, Pa
τ_g	shear stress at the ground, Pa
τ_r	shear stress at the roof, Pa

showed that the power law approach is sound and conservative. Pretorius (2006) reviews most of the outstanding issues. Different calculation approaches with a variety of considerations have been applied to calculate chimney power plant performance. The available work potential that atmospheric air acquires while passing through the collector has been determined and analyzed by Ninic (2006). In this study, the dependence of the work potential on the air flowing into the air collector from the heat gained inside the collector, air humidity and atmospheric pressure as a function of elevation are determined. Various collector types using dry and humid air have been analyzed. The influence of various chimney heights on the air work potential was established. Koonsrisuk and Chitsomboon (2007) proposed dimensionless variables to guide the experimental study of flow in a small-scale solar chimney: a solar power plant for generating electricity. Computational fluid dynamics (CFD) methodology was employed to obtain results that are used to prove the similarity of the proposed dimensionless variables. Sakonidou et al. (2008) developed a mathematical model to determine the tilt that maximizes natural air flow inside a solar chimney using daily solar irradiance data on a horizontal plane at a site. The model predicted the temperature and velocity of the air inside the chimney as well as the temperatures of the glazing and the black painted absorber. Comparisons of the model predictions with CFD calculations delineate the usefulness of the model. In addition, there was a good agreement between theoretical predictions and experiments performed with a 1 m long solar chimney at different tilt positions. Ferreira et al. (2008) proposed to study the feasibility of a solar chimney to dry agricultural products. To assess the technical feasibility of this drying device, a prototype solar chimney, in which the air velocity, temperature and humidity parameters were monitored as a function of the solar incident radiation, was built. Drying tests of food, based on theoretical and experimental studies, assure the technical feasibility of solar chimneys used as solar dryers for agricultural products. Fluri and Von Backström (2008) compared the performance of different layouts by using analytical models and optimization techniques. Furthermore, important design parameters were discussed. This study shown that these slight changes in modeling approach have a significant impact on the performance prediction and single rotor layout without guide vanes performs very poorly. Concluding, the counter rotating lay-

outs provide the highest peak efficiencies, but at relatively low speeds, which leads to an undesirable higher torque for the same power output.

In this study, two comprehensive studies are relevant, namely those of Bernardes et al. (2003), Pretorius and Kröger (2006b). Bernardes (2004) introduced an optimizing procedure in order to define solar chimney reference systems. The represented model was compared with experimental results from the prototype in Manzanares in order to validate the model. Pretorius (2006) investigated the optimization and control of a large-scale solar chimney power plant. The numerical simulation model was refined and used to perform a sensitivity analysis on the most prominent operating and technical plant specifications. Thermo-economically optimal plant configurations were found from simulation results and calculations according to an approximate plant cost model. Pretorius and Kröger (2006b) gives an outline of the numerical model developed in Pretorius (2006).

A first look at the above mentioned analyses showed that the studies of Bernardes and Pretorius employed similar approaches. However, a detailed examination reveals that their heat transfer coefficients were different. Accurate and reliable heat transfer correlations are key inputs to system heat transfer analyses and to plant evaluation and sizing. Therefore, this work examines the methods used in the studies, by considering the governing conservation and convective heat transfer equations.

Table 1
Reference solar chimney power plant configuration

Collector roof (glass)	
Emissivity of glass	$\varepsilon_r = 0.87$
Roughness of glass	$\varepsilon_r = 0$ m
Extinction coefficient of glass	$C_e = 4\ m^{-1}$
Refractive index of glass	$n_r = 1{,}526$
Thickness of glass	$t_r = 0{,}004$ m
Roof shape exponent	$b = 1$
Perimeter (inlet) height	$H_2 = 5$ m
Outer diameter	$d_2 = 5000$ m
Inner diameter	$d_3 = 189$ m
Ground	
Type	Sandstone
Emissivity (treated surface)	$\varepsilon_g = 0.9$
Absorptivity (treated surface)	$\alpha_g = 0.9$
Density	$\rho_g = 2160\ kg/m^3$
Specific heat	$c_g = 710$ J/kg K
Thermal conductivity	$k_g = 1.83$ W/m K
Roughness	$\varepsilon_g = 0.05$ m
Chimney	
Height	$H_c = 1000$ m
Inside diameter	$d_c = 210$ m
Turbine	
Turbo-generator efficiency	$\eta_{tg} = 80$ %
Ambient conditions	
Atmospheric pressure	$p_a = 90{,}000\ N/m^2$
Wind speed at 10 m	$v_w = 3$ m/s

1.1. Reference solar chimney power plant configuration

To ensure a consistent comparison between the studies, the reference solar chimney power plant configuration presented in Table 1 was introduced. An examination in the solar chimney literature showed that this configuration reflects a good dimensional consensus.

2. Governing conservation equations

A description of the mass, momentum and energy governing equations that were used in the two studies is given in Table 2. Those equations describe the incompressible and viscous flow in solar chimneys and are derived for an elementary control volume in the collector and in the chimney of a solar chimney power plant. The roof's height of the collector is gradually lifted up towards to the tower and the flow is assumed radial one-dimensional between the collector inlet and the turbine inlet. In the tower, an arbitrary axial control volume is chosen between the turbine outlet and the tower outlet. Bernardes energy Eq. (6) for the collector comprises the heat exchanged $\dot{q}$ with the ground and roof. The temperature, velocity and consequentially, the pressure distribution are obtained by the solving of the mass, momentum and energy governing equations.

As expected, the governing equations are fundamentally equivalent. The most relevant considerations are presented in Table 3. Simplifications employed are typically the neglect of inertial terms, of small angles between the ground and roof and of the transverse pressure gradient. The most relevant disparities between the two approaches are the assumptions about the flow development in the collector. Pretorius and Kröger (2006a) shows that when the radial velocity distribution between the ground and the roof (roof height changes to keep the average radial speed constant), the flow is essentially fully developed shortly after the inlet to the collector. On the other hand, Bernardes assumes developing flow that does not develop fully between parallel plates. This consideration is crucial in determining the convective heat transfer coefficient and friction factors. Those issues are discussed in the next section.

Assumptions and considerations concerning the governing equations are shown in Table 4. Pretorius and Kröger (2006b) introduced refinements like roof support drag, chimney outlet losses due to wind, and bracing wheel drag. Pretorius (2004) presented an order of magnitude analysis where the terms: axial pressure difference, wall friction, bracing wheel force, axial momentum and transient momentum were evaluated for the chimney. In such a study, the sum of the contribution made by the wall friction, bracing wheel force, axial momentum and transient momentum terms represented less than 1% of the magnitude of the gravity force term in the tower momentum equation. Therefore, those terms should not represent a relevant issue in this work.

Table 2
System of governing equations presented by Bernardes and Pretorius

Equation		
Bernardes		
Continuity	Collector	
	$\frac{\partial \dot{m}}{\partial r} = 0$	(2)
	Chimney	
	$\frac{\partial \dot{m}}{\partial z} = 0$	(3)
Momentum	Collector	
	$\frac{\partial}{\partial t}(\rho A_c u) = -\frac{\partial}{\partial r}(\dot{m}u) - \frac{\partial}{\partial r}(pA_c) + p\frac{\partial A_c}{\partial r} - 2\pi r\tau$	(4)
	Chimney	
	$\rho\frac{D\vec{v}_c}{Dt} = -\nabla p_{dyn} + \nabla\tau + (\rho - \rho_0)g$	(5)
Energy	Collector (air stream)	
	$\dot{m}c_p T + \dot{q}2\pi r\,dr = \dot{m}c_p\left(T + \frac{dT}{dr}dr\right)$	(6)
	Chimney	
	$\rho\frac{Dh}{Dt} = -\nabla\vec{q} + \frac{Dp}{Dt} + \tau_{ij}\frac{\partial u_j}{\partial x_j}$	(7)
Pretorius		
Continuity	Collector	
	$\frac{1}{r}\frac{\partial}{\partial r}(\rho v r H) = 0$	(8)
	Chimney	
	$\frac{\partial}{\partial z}(\rho_c v_c) = 0$	(9)
Momentum	Collector	
	$-\left(H\frac{\partial p}{\partial r} + \tau_r + \tau_g + \frac{F_{supports}}{r\Delta\theta}\right) = \rho v H\frac{\partial v}{\partial r}$	(10)
	Chimney	
	$-\frac{\partial p_c}{\partial z} - \left(\frac{\tau_c \pi d_c + F_{bw}}{A_c}\right) = \rho_c\left(g + v_c\frac{\partial v_c}{\partial z}\right)$	(11)
Energy	Collector (air stream)	
	$q_{rh} + q_{gh} = \frac{RT}{r}\frac{\partial}{\partial r}(\rho v r H) + \rho v H\frac{\partial}{\partial r}(c_p T)$	(12)
	Chimney	
	$RT_c\frac{\partial}{\partial z}(\rho_c v_c) + \rho_c v_c(c_{pc}T_c) + \frac{\partial}{\partial z}(\rho_c v_c g z) = 0$	(13)

3. Convective heat transfer schemes presented by Bernardes und Pretorius

Fundamentally, the solar chimney collector is a device for gathering the solar energy, converting the solar radiation to thermal energy, transferring it into a moving stream of air, while temporarily storing some of the thermal energy in the ground. The solar chimney collector should be able to collect as much solar energy as possible by allowing the passage of solar radiation whilst preventing heat from being lost to the ambient. In order to avoid thermal losses between the roof and the ambient, low convective heat transfer coefficients are sought at the roof. Two alternatives should be evaluated in the absorber: however high convective heat transfer coefficients are attractive if no thermal storage in the ground is required; however, low

Table 3
Relevant governing equations assumptions presented by Bernardes and Pretorius

	Bernardes	Pretorius
Continuity equation	• Steady state conditions	• Steady state conditions
Momentum equation	Collector	Collector
	• Axis symmetrical flow • Quasi stationary scheme • The collector rests on a plain • Developing flow between two parallel unrelated flat plates	• One-dimensional radial flow • Steady state conditions • The roof of the collector is inclined from the outer boundary towards the tower • Turbulent fully developed air flow between two associated parallel plates
	Chimney	Chimney
	• Static and dynamic pressure was taken into account • Quasi stationary scheme	• Purely axial flow • Surface stress constant over each control volume • Steady state conditions
	Turbine	Turbine
	• Static and dynamic pressure was take into account	• Static and dynamic pressure was take into account
	Collector	Collector
	• Axis symmetrical heating the air temperature and the pressure in each differential volume are constant • Quasi stationary scheme • The humid air was considered as an ideal gas mixture • Humidity originating from of the ground was neglected • Heat transfer in ground: transient heat conduction in semi-infinite solid	• Rise in collector height over the length of the radial control was neglected • Kinetic energy, radial conduction and transient kinetic energy terms are negligible • Steady state conditions • Heat transfer in ground: transient heat conduction in semi-infinite solid
Energy equation	Chimney	Chimney
	• The air temperature and the pressure in each differential volume are constant • No heat source • The humid air was considered as an ideal gas mixture	• Kinetic energy, radial conduction and transient kinetic energy terms are negligible • Steady state conditions
		Turbine
		• Temperature drop across turbine

Table 4
Comparison of the terms considered by Bernardes and Pretorius

Conservation equation	Bernardes	Pretorius
Continuity equation	Same	Same
Momentum equation	• Roof shear stress • Ground shear stress • Chimney outlet losses	• Roof shear stress • Ground shear stress • Roof support drag • Chimney outlet losses • Chimney outlet losses due to wind • Bracing wheel drag loss
Energy equation	• Beam and diffuse radiation • Ground storage • Collector losses to ambient • Collector losses to sky • Heat transfer to air inside collector	• Beam and diffuse radiation • Ground storage • Collector losses to ambient • Collector losses to sky • Heat transfer to air inside collector

heat transfer coefficients are preferable to increase the ground storage capacity by reducing heat transfer from the ground.

Correlations found in the literature for calculating the convective heat transfer coefficient are generally obtained through experimental data. For instance, the transition flow and fully developed turbulent flow Nusselt number correlation for a circular tube is given by Gnielinski as reported in Bhatti and Shah (1987) as

$$Nu = \frac{(f/8)(Re - 1000)Pr}{1 + 12.7(f/8)^{1/2}(Pr^{2/3} - 1)} \quad (1)$$

which is accurate within about ±10% with experimental data for $2300 \leqslant Re \leqslant 5 \times 10^6$ and $0.5 \leqslant Pr \leqslant 2000$. The fact that the carefully controlled conditions in the experiments from which the correlations are derived, and the actual situations rarely conform absolutely lead to additional inaccuracies.

Collector convective heat transfer is a relevant subject matter affecting the performance of solar chimneys. It determines the rate at which thermal energy is transferred (Fig. 1):

1. from the absorber to the ground (conduction),
2. from the roof to the ambient air (convection),
3. from the roof to the air inside the collector (convection),
4. from the absorber to the collector air (convection).

Both natural convection and forced convection could occur across all three surfaces. The flow in the collector can behave as laminar, transient or turbulent. The growth of the thermal and hydrodynamic boundary layers at the entrance region should also be considered for developing flows. The heat transfer from the roof to the ambient, depending on the wind velocity, should be considered as forced convection. Thus, the heat transfer coefficients should be carefully selected taking into account all the above mentioned considerations.

If a fluid flows parallel to a flat plate, variations in velocity and temperature of the fluid are restricted to a narrow region close to the walls, namely, the boundary layer. Several aspects should be considered:

1. pressure gradient,
2. laminar or turbulent condition of boundary layer,
3. viscous dissipation should be negligible (effect of frictional heating),
4. Prandtl number ($Pr \geqslant 0.7$).

Even though correlations for flat plates exist for a semi-infinite fluid medium adjacent to the plate, a good number of applications of practical interest deal with fluid flowing between two plates. Bernardes et al. (2003) considered radial flow in the collector as the flow between two separated flat plates, i.e. the flow never behaves as a hydrodynamic fully developed flow. Due to a relaminarization process, the mean velocity profile deviates significantly from the logarithmic law-of-the-wall and shows, in the strongly accelerated case, a tendency to approach the laminar profile; the turbulent kinetic energy increases less rapidly than the energy of the mean flow. These velocity profiles characterize a boundary layer, which is reverting from turbulent to laminar. The structure of the inner layer is also significantly altered. Equilibrium between production and dissipation of turbulence energy is no longer maintained. Therefore, for radial flow between parallel disks, the reverse transition process occurs and the presented results can be quite generally applicable for laminar and turbulent flows. The plates were assumed parallel to each other. In such a case, the spacing between the plates should be considerably greater than the maximum boundary layer thickness. Bernardes (2003) alleges that radial inflow can behave as thermally fully developed flow. He suggests two different Nusselt numbers as for thermally fully developed flow and for undeveloped flow. The shear stress increases at small radii and flows not thermally developed achieved higher Nusselt number values.

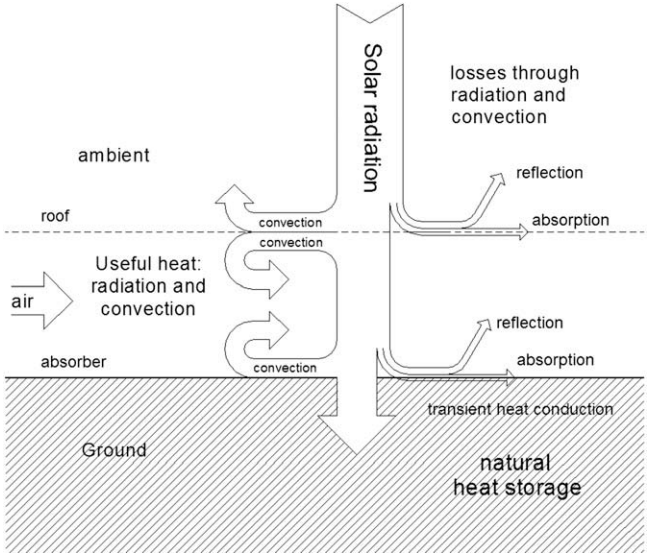

Fig. 1. Thermal network for the collector of solar chimneys.

Pretorius assumes developed radial inflow between parallel flat plates based on the study of Beyers et al. (2001), Hedderwick (2001) as well as a sample calculation in Pretorius (2004). They presented a study focusing on a general numerical method to find the thermo-flow field for accelerating three-dimensional radial flows between parallel plates. The flow acceleration causes increased momentum and heat transfer from the plate surfaces into the flow stream but also increases the shear stress at these surfaces. According to Beyers et al. (2001), those effects were accurately predicted by the code showing increased pressure drop as well as enhanced heat transfer characteristics toward the outlet of the parallel plates.

Natural convection heat transfer occurs when the convective fluid motion is induced by density differences that are themselves caused by heating or cooling in the absence of external forces. It takes place on the collector roof resulting in greater thermal losses and, consequently, lower collector efficiency. If the fluid velocity is low, the effect of natural convection becomes significant and the heat transfer rate may be increased by natural convection. Thermal losses to the ambient from the collector should be contained by the roof. Consequently, the estimation of the free convection coefficient is fundamental in evaluating the performance of solar chimney collectors. Basically, heat transfer to (or from) a fluid flowing inside a duct is expressed as internal forced convection and may be characterized by a Reynolds number.

3.1. Comparison between the heat transfer correlations

The comparison between the heat transfer coefficients employed in the studies is presented below. Initially, the heat transfer coefficient equations were assembled in a

spreadsheet and the heat transfer coefficients and the results presented below were calculated by employing the physical parameters presented in Table 1.

Bernardes introduced flat plate correlations to calculate the natural convection losses at the collector roof, namely Eqs. (14)–(16). Such equations are commonly found in the heat transfer literature, for example, Baehr and Stephan (1996). Those correlations are based on the Rayleigh number ($Ra = Gr \cdot Pr$) following a Lloyd and Moran (1974) investigation, who define Rayleigh and Nusselt numbers based on the surface area to perimeter ratio to account for the dependence of Nu on the geometry of the plate. Provided that Ra is dependent on (equivalent length)^3 and that the Eq. (15) is dependent on $Ra^{1/3}$, the heat transfer coefficient for natural convection is not influenced by the equivalent length in this case. For windy conditions over the roof, Bernardes made use of mixed convection (natural + forced) correlations to calculate the heat transfer through the roof, based on Baehr and Stephan (1996), namely Eq. (20).

Bernardes assumes the forced convective heat transfer to the flow as a developing flow over flat plates, either laminar or turbulent. He makes use of the Baehr and Stephan (1996) assertion that the heat transfer coefficient in the transitional regime may be calculated by Eq. (19). Given that at lower Reynolds numbers the turbulent contribution given by Eq. (18) remains low and at higher Reynolds numbers the laminar contribution given by Eq. (17) also remains low, the Eq. (19) can also be used for the entire range of Reynolds number. The correlations introduced by Bernardes to calculate the laminar and turbulent heat transfer coefficients, respectively Eqs. (17) and (18), do not take into account surface roughness. The Eq. (18), obtained by Petukhov and Popov (1963), made use of Gnielinski's equation (Baehr and Stephan (1996)). For low velocity flows where the natural convection becomes significant, Bernardes uses Eq. (14).

Correlations for the local convective heat transfer coefficient from a smooth horizontal surface exposed to the ambient were developed by Kröger and Burger (2004). The most recent work by Burger (2004), which introduced an improved version of this correlation, Eq. (21), was employed by Pretorius. It took into account significant natural convection mechanisms by evaluating convective and radiative heat fluxes onto or from a smooth horizontal flat plate exposed to the ambient. T_m is the mean temperature between the collector roof and ambient air, g is the gravitational constant and ΔT is the difference between the roof and ambient air temperature. The variables ρ, μ, c_p and k symbolize the density, dynamic viscosity, specific heat capacity and thermal conductivity of the air, respectively, all of which are evaluated at the mean temperature T_m. Eq. (22) becomes applicable when the collector roof temperature only marginally exceeds the ambient temperature (Burger (2004)). Considering relatively stable conditions, this equation includes a combination of minor convective thermals, conduction in the stratified air and heat transfer considering the condensation effect. For roof temperatures higher than collector air temperature, the maximal value between Eqs. (21) and (22) was employed. If not, Eq. (22) was used. Finally, the influence of the gravitational forces on the heat transfer mechanism was also taken into consideration by Pretorius.

Kröger (2004) introduced a convective heat transfer coefficient from the collector roof to the collector air, by using Gnielinski's equation for fully developed turbulent flow and by approximating the flow in the collector as flow between variably spaced plates, namely, Eq. (23). Here, f is the friction factor, Re is the Reynolds number, Pr is the Prandtl number and k is the thermal conductivity of the air. Pretorius employs Eq. (23) when the collector roof temperature is greater than the collector air temperature. When the reverse occurs, the maximal value of Eqs. (21), (22) or (23) is used. Analogously but inversely to this scheme, the convective heat flux from the ground surface to the collector air in the collector may be approximated as a heated horizontal surface facing upwards. When the collector roof and ground temperature only marginally exceeds the ambient temperature, equation, Eq. (22) becomes applicable. The Pretorius scheme can be summarized as follows:

$h_{roof \to ambient}$: if $T_{roof} > T_{amb}$: max[(21), (22)] else (22);
$h_{roof \to air}$: if $T_{roof} > T_{air}$: max[(22), (23)] else max[(21)–(23)];
$h_{ground \to air}$: if $T_{ground} > T_{air}$: max[(21)–(23)] else max[(22), (23)].

3.2. Convective heat transfer from the collector roof to the ambient

Based on the equations presented in Table 5, predictions were obtained for the convective heat flux from the collector roof to the ambient air. They are presented in Fig. 2.

Bernardes recommends heat transfer coefficients which give lower values than those by Pretorius, regardless for wind conditions. It means that, for the same roof temperature, the heat loss at the roof estimated by Bernardes tends to be lower than by Pretorius, representing an insulated collector roof that retains more heat. A remarkable detail about the Pretorius correlations is that, for low v and ΔT, the value of the heat transfer coefficient converges to 3.87 W/m^2 K. In this case, $v \to 0$ and Eq. (22) prevails over Eq. (21) returning the constant value of 3.87 W/m^2 K. This fact does not represent an inaccuracy due the fact that, if $\Delta T \to 0$, the heat flux may also return low values. When the ambient temperature exceeds the collector roof temperature, no significant natural convection mechanisms are active and the heat transfer coefficient converges to a constant value dependent on the wind speed alone. An additional interesting aspect about Eq. (21) is that radiative heat transfer mechanisms were included. It contributes to

Table 5
Correlations presented by Bernardes and Pretorius to calculate the convective heat transfer

	Equation		Reference, extent of employment
Bernardes	$Nu_n = 0.54Ra^{1/4}$	(14)	Lloyd and Moran (1974), hot side up, $10^4 \leqslant Ra < 10^7$
	$Nu_n = 0.15Ra^{1/3}$	(15)	Lloyd and Moran (1974), hot side up, $10^7 \leqslant Ra < 10^{10}$
	$Nu_n = 0.27Ra^{1/4}$	(16)	Lloyd and Moran (1974), hot side down, cold side up, $10^5 \leqslant Ra < 10^{11}$
	$Nu_{f,lam} = \frac{2\sqrt{Re}\sqrt{Pr}}{\sqrt{\pi}(1+1.7Pr^{1/4}+21.36Pr)^{1/6}}$	(17)	Baehr and Stephan (1996)
	$Nu_{f,turb} = \frac{0.037Re^{0.8}Pr}{1+2.443Re^{-0.1}(Pr^{2/3}-1)}$	(18)	Petukhov and Popov (1963) $5\times10^5 < Re < 10^7$, $0.6 < Pr < 2000$
	$Nu_f = \sqrt{Nu_{f,lam}^2 + Nu_{f,turb}^2}$	(19)	Baehr and Stephan (1996)
	$Nu^3 = Nu_n^3 + Nu_f^3$	(20)	Baehr and Stephan (1996)
Pretorius	$h = \frac{0.2106 + 0.0026v\left(\frac{\rho T_m}{\mu g \Delta T}\right)^{1/3}}{\left(\frac{\mu T_m}{g\Delta T c_p k^2 \rho^2}\right)^{1/3}}$	(21)	Burger (2004)[a]
	$h = 3.87 + 0.0022\left(\frac{v\rho c_p}{Pr^{2/3}}\right)$	(22)	Burger (2004)[a]
	$h = \frac{(f/8)(Re-1000)Pr}{1+12.7(f/8)^{1/2}(Pr^{2/3}-1)}\left(\frac{k}{d_h}\right)$	(23)	Kröger (2004)

[a] $v = v_w$ for heat transfer between roof and ambient.

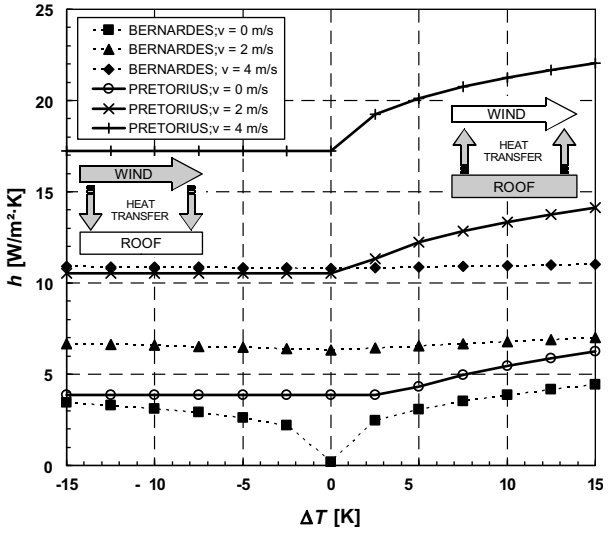

Fig. 2. Convective heat transfer from the collector roof to the ambient presented by Bernardes and Pretorius.

the higher heat transfer coefficients in the Pretorius approach.

The original Bernardes scheme erroneously uses the hydraulic diameter as characteristic length in Eqs. (14)–(20) when calculating the heat transfer at the roof. As shown in Fig. 3, the influence of d_h in the heat transfer coefficient decreases for higher d_h. Large solar chimney systems have collector heights starting at approximately 5 m, and that means a d_h starting at 10 m. It leads to less substantial inaccuracy, presenting variations less than 10%. Thus, the Bernardes scheme might not be appropriate for collectors with height lower than 5 m. In stead of d_h the plate characteristic length should be employed.

3.3. Convective heat transfer to the flowing air

Predictions for convective heat transfer coefficients from the ground and from the roof to the flowing air are shown

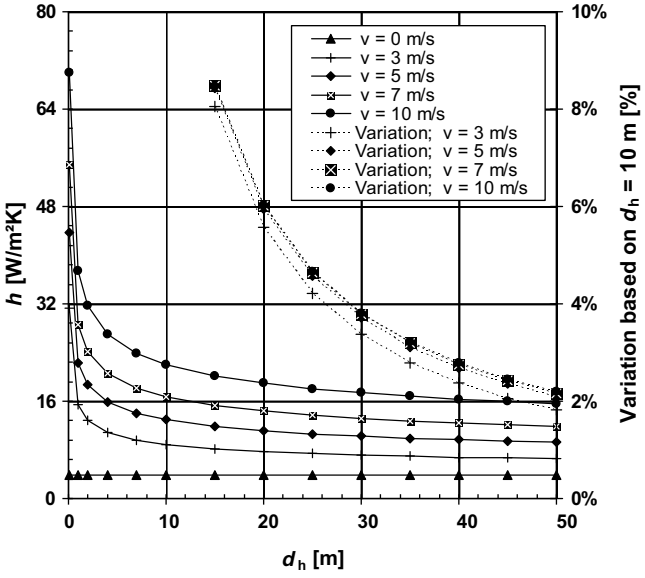

Fig. 3. Influence of the hydraulic diameter on the convective heat transfer from the collector roof to the ambient presented by Bernardes.

in Figs. 4–6. Here, the following distinction between the estimated heat transfer coefficients was necessary: low air velocities, surface temperatures higher than ambient and surface temperatures lower than ambient.

Once again, for low v and ΔT, the value of the heat transfer coefficient estimated by the Pretorius scheme converges to 3.87 W/m^2 whilst by Bernardes scheme tends to 0 (Fig. 4). For ground and roof temperatures higher than flow temperatures, the influence of buoyancy forces leads to higher heat transfer coefficients.

Heat transfer coefficients between the ground and the flowing air (rough surfaces) are higher. The Pretorius scheme returns heat transfer coefficients as high as 0.6 times that of Bernardes (Fig. 5). Keeping in mind that the Bernardes correlations are for convective heat transfer across smooth surfaces only, it can be recognized that those

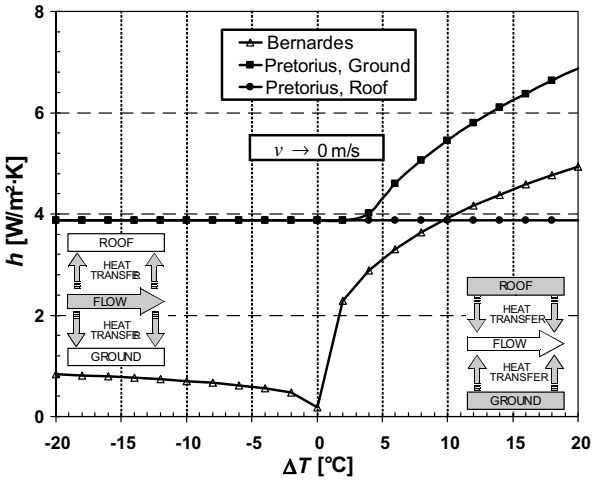

Fig. 4. Convective heat transfer to the flowing air for lower air velocities presented by Bernardes and Pretorius.

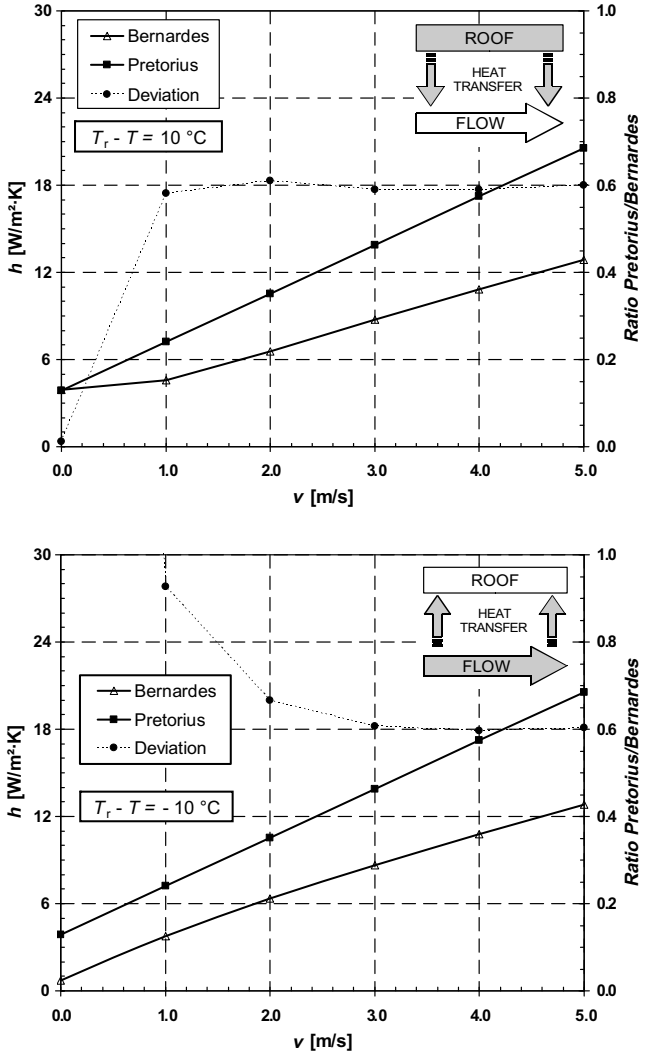

Fig. 5. Convective heat transfer between the roof and the flowing air presented by Bernardes und Pretorius.

values are substantially lower than Pretorius for both rough surfaces.

Figs. 5 and 6 present the predictions of the convective heat transfer to the flowing air in the collector. Here, the *deviation* is calculated by dividing the convective heat transfer of Pretorius by the convective heat transfer of Bernardes. The calculated values of Bernardes for low air velocities (below 2 m/s) represent a small divergence from the calculated values of Pretorius, converging to 3.87 W/m^2 K. Divergences between the Pretorius convective heat transfer and Bernardes achieved a factor of approximately 1.2. Understanding that surface roughness enhances forced convection heat transfer, higher values were expected by evaluating the Pretorius correlations for rough surfaces. Increasing those heat transfer coefficients means higher heat flux to the flowing air and lower heat flux to the ground, decreasing the collector's heat storage capacity.

Pretorius made use of a roof shape exponent equal 1. The collector roof height is then inversely proportional to the distance from the plant centre line. It means that the

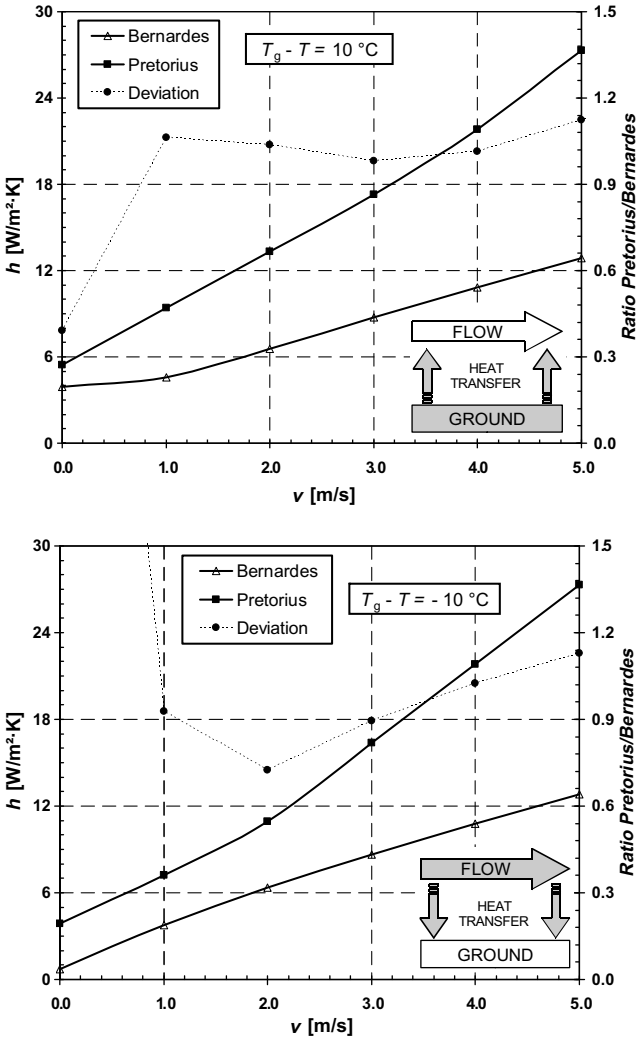

Fig. 6. Convective heat transfer between the ground and the flowing air presented by Bernardes and Pretorius.

air velocity or pressure does not change substantially with radius in the collector, and the heat transfer coefficients should basically depend on the hydraulic diameter ($d_h = 2H$) and the temperature difference, ΔT. As shown in Fig. 7, the convective heat transfer coefficients increase for small d_h and high flow velocity. For $d_h > 15$ m the Pretorius heat transfer coefficients remain invariable and the Bernardes heat transfer coefficients decrease with hydraulic diameter.

4. Simulations employing Bernardes and Pretorius schemes

The analysis of the heat transfer coefficients by themselves is not sufficient to draw a final conclusion about the performance of the solar chimney collector when employing different heat transfer correlations. Thus, the Pretorius heat transfer correlations were inserted into a version of the Bernardes code, and performance simulations were carried out. A description of the mentioned program code can be found in Bernardes et al. (2003) or Bernardes (2004). The meteorological input data of Sishen,

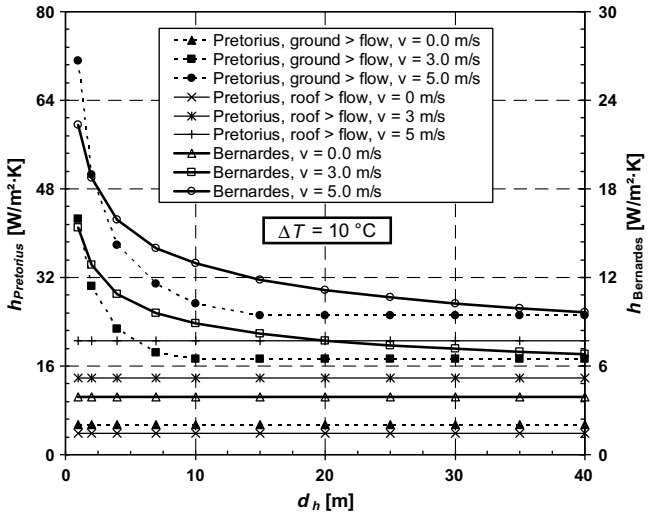

Fig. 7. Simulated convective heat transfer coefficients as function of the hydraulic diameter.

South Africa presented by Pretorius was used in the numerical simulation, Pretorius and Kröger (2006b).

Comparative computer simulations were performed for the reference solar chimney power plant presented in Table 1 by employing the original strategy and equations for the calculation of the various convective heat transfer coefficients from both models. The performance of the collector was analyzed by comparing the total heat absorbed by the flow, the roof convective heat losses to the ambient, the roof radiative heat losses to the sky, the heat conducted to the ground and the collector efficiency in terms of heat flux [W/m^2] for daily average data of December.

As shown in Fig. 8, convective heat transfer coefficients calculated by using the Pretorius scheme produced higher values than the Bernardes scheme for the same ambient conditions. The Pretorius heat transfer coefficients rise slowly for smaller collector radii, where the roof temperatures are higher, showing a slight ΔT sensitivity. This effect can also be confirmed in Fig. 2. The heat losses through the roof are lower for the Bernardes scheme, especially in the region next to the chimney. The Bernardes heat transfer coefficients also decrease for higher d_h (Fig. 7), accentuating this effect.

It is to be noted that Bernardes employed the same correlations for the heat transfer from the roof and from the ground to the air in the collector. Again, the heat transfer coefficients based on the Bernardes scheme returned lower values than those employed by Pretorius (Fig. 9).

Contrary to Pretorius, the Bernardes heat transfer coefficients for the roof decreases when the radius decreases. At this point, the Pretorius h_{rh} increases slightly because Eq. (22) predominates.

As shown in Fig. 10, Bernardes roof temperatures are lower than those of Pretorius, minimizing the heat transfer through the roof and, consequently, reducing the thermal losses to the ambient. Due to the higher heat transfer coefficients, the collector flow temperature is higher than the roof temperature of Pretorius.

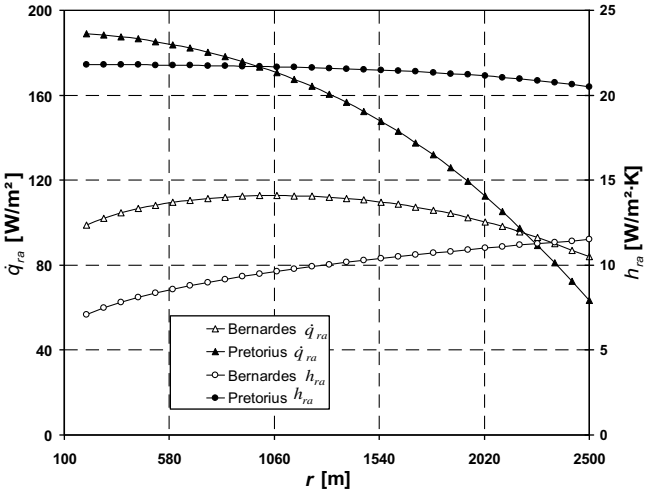

Fig. 8. Simulated convective heat transfer coefficients and heat flux between the roof and the ambient as function of the radius.

Coincidently, the heat fluxes to the flow calculated by both schemes produced very similar air temperatures (Fig. 10). In the Bernardes model, the lower heat transfer coefficients at the ground surface induce higher temperatures, increasing the heat flux there and balancing the heat transfer mechanism in the collector.

Fig. 11 shows the power, $P = \frac{\dot{m}}{\rho_{avg}} \Delta p_{turb}$, the most important parameter in solar chimney performance prediction. The two schemes agreed well in terms of the generated power and mass flow in the collector. The average generated power calculated by the Pretorius scheme is 5.82% higher than by the Bernardes scheme for an average day of December. The lower heat transfer coefficients employed by Bernardes produced higher temperatures (Fig. 10) at the absorber during the day increasing the heat transfer by conduction to the ground. During the night, the ground releases the additional accumulated heat energy enhancing the storage effect in the collector. This effect is shown in Fig. 11.

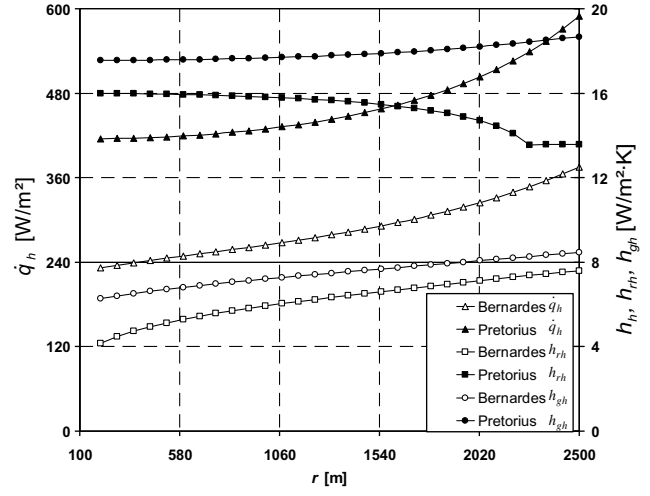

Fig. 9. Simulated convective heat transfer coefficients and heat flux to the flow as function of the radius.

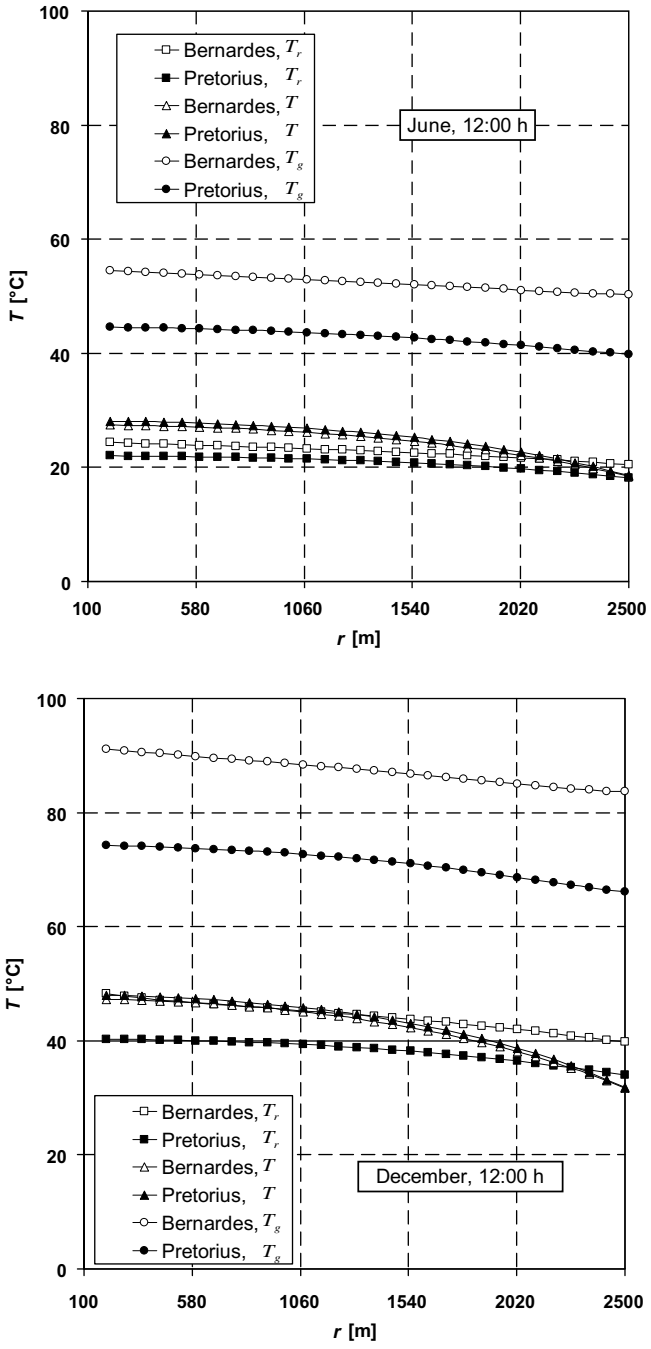

Fig. 10. Simulated temperature in collector as function of the radius for June and December monthly average weather data at 12:00 h.

5. Discussion and conclusion

The paper compares the procedural methods used in the Bernardes and Pretorius studies, and investigates the effect of different heat transfer models on solar chimney performance. The heat transfer equations for forced and natural convection of both models were evaluated both by a conventional spreadsheet and by performance simulations through a computational code. The complex behavior of the solar chimney collector was analyzed taking in account

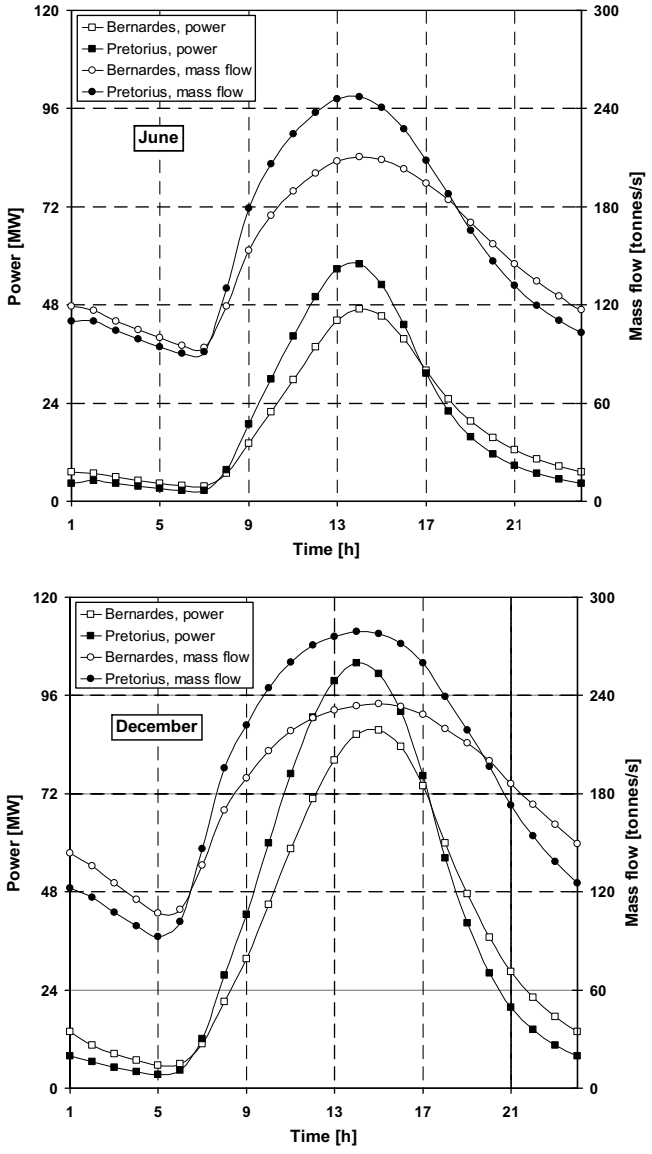

Fig. 11. Simulated daily generated power, air velocity and mass flow for June and December monthly average weather data.

the calculation strategy from both the Bernardes and Pretorius schemes.

In conclusion, higher heat transfer coefficients from the ground and from the roof to the flow results in lower air temperature in the collector, leading to lower losses through the roof and higher heat transfer to the flow – with the Pretorius scheme – and lower heat transfer coefficients from the roof to the ambient results also in lower losses through the roof – with the Bernardes scheme. This compensatory effect leads to similar temperature profiles of the air for both schemes, minimizing the influence of the choice of heat transfer coefficients in the solar chimney performance.

References

Baehr, H.D., Stephan, K., 1996. Wärme- und Stoffübertragung. Springer-Verlag, Berlin, 1996.

Bernardes, M.A.d.S., 2003. Symmetric sink flow and heat transfer between two parallel disks. ASME Summer Heat Transfer Conference – Heat Transfer 2003. ASME, Las Vegas, Nevada, USA.

Bernardes, M.A.d.S., 2004. Technische, ökonomische und ökologische Analyse von Aufwindkraftwerken. IER, Universität Stuttgart, Ph.D, Stuttgart, Germany.

Bernardes, M.A.d.S., Voß, A., Weinrebe, G., 2003. Thermal and technical analyses of solar chimneys. Solar Energy 75, 511–524.

Beyers, J.H.M., Harms, T.M., Kröger, D.G., 2001. A finite volume analysis of turbulent convective heat transfer for accelerating radial flows. Numerical Heat Transfer Part A (40), 117–138.

Bhatti, M.S., Shah, R.K. (Eds.), 1987. Turbulent and Transition Flow Convective Heat Transfer in Ducts. John Wiley & Sons.

Burger, M., 2004. Prediction of the Temperature Distribution in Asphalt Pavement Samples. Department of Mechanical Engineering, University of Stellenbosch, Master Stellenbosch, South Africa.

Ferreira, A.G., Maia, C.B., Cortez, M.F.B., Valle, R.M., 2008. Technical feasibility assessment of a solar chimneynext term for food drying. Solar Energy 82 (3), 198–205.

Fluri, T.P., Von Backström, T.W., 2008. Comparison of modelling approaches and layouts for solar chimney turbines. Solar Energy 82 (3), 239–246.

Gannon, A.J., Von Backström, T.W., 2000. Solar chimney cycle analysis with system loss and solar collector performance. Journal of Solar Energy Engineering 122, 133–137.

Hedderwick, R.A., 2001. Performance Evaluation of a Solar Chimney Power Plant. Department of Mechanical Engineering, University of Stellenbosch, Master Stellenbosch, South Africa, 2001.

Koonsrisuk, A., Chitsomboon, T., 2007. Dynamic similarity in solar chimney modeling. Solar Energy 81 (12), 1439–1446.

Kröger, D.G., 2004. Air-cooled Heat Exchangers and Cooling Towers. Pennwell Corp., Tulsa, Oklahoma.

Kröger, D.G., Blaine, D., 1999. Analysis of the driving potential of a solar chimney power plant. The South African Institute of Mechanical Engineering, R&D Journal 15, 85–94.

Kröger, D.G., Burger, M., 2004. Experimental convection heat transfer coefficient on a horizontal surface exposed to the natural environment. In: ISES EuroSun2004 International Sonnenforum, pp. 422–430.

Lloyd, J.R., Moran, W.R., 1974. Natural convection adjacent to horizontal surface of various planforms. Journal of Heat Transfer 96, 443–447.

Ninic, N., 2006. Available energy of the air in solar chimneys and the possibility of its ground-level concentration. Solar Energy 80 (7), 804–811.

Petukhov, B.J., Popov, N.V., 1963. Theoretical calculation of heat transfer and frictional resistance in turbulent flow in tubes of an incompressible fluid with variable physical properties. High Temperature 1, 69–83.

Pretorius, J.P., 2004. Solar tower power plant performance characteristics. Department of Mechanical Engineering, University of Stellenbosch, Master Stellenbosch, South Africa, 2004.

Pretorius, J.P., 2006. Optimization and control of a large-scale solar chimney power plant. Department of Mechanical Engineering, University of Stellenbosch, Ph.D, Stellenbosch, South Africa.

Pretorius, J.P., Kröger, D.G., 2006a. Critical evaluation of solar chimney power plant performance. Solar Energy 80, 535–544.

Pretorius, J.P., Kröger, D.G., 2006b. Solar chimney power plant performance. Transactions of the ASME 128, 302–311.

Sakonidou, E.P., Karapantsios, T.D., Balouktsis, A.I., Chassapis, D., 2008. Modeling of the optimum tilt of a solar chimney for maximum air flow. Solar Energy 82 (1), 80–94.

Schlaich, J., 1995. The Solar Chimney. Edition Axel Menges, Stuttgart.

Von Backström, T.W., Fluri, T.P., 2006. Maximum fluid power condition in solar chimney power plants – an analytical approach. Solar Energy 80 (11), 1417–1423.

Von Backström, T.W., Gannon, A.J., 2004. Solar chimney turbine characteristics. Solar Energy 76 (1–3), 235–241.

Available online at www.sciencedirect.com
ScienceDirect
Solar Energy 84 (2010) 277–288
SOLAR ENERGY
www.elsevier.com/locate/solener

Evaluation of operational control strategies applicable to solar chimney power plants

Marco Aurélio dos Santos Bernardes [a,*], Theodor W. von Backström [b]

[a] Department of Mechanical Engineering, Centro Federal de Educação Tecnológica de Minas Gerais – CEFET-MG, Av. Amazonas, 7675, Nova Gameleira, 30510-000 Belo Horizonte, MG, Brazil
[b] Department of Mechanical Engineering, University of Stellenbosch, Private Bag X1, Matieland 7602, South Africa

Received 24 February 2009; received in revised form 26 October 2009; accepted 23 November 2009
Available online 30 December 2009

Communicated by: Associate Editor S.A. Sherif

Abstract

Numerical simulations are carried out to study the performance of two schemes of power output control applicable to solar chimney power plants. Either the volume flow or the turbine pressure drop is used as independent control variable. Values found in the literature for the optimum ratio of turbine pressure drop to pressure potential vary between 2/3 and 0.97. It is shown that the optimum ratio is not constant during the whole day and it is dependent of the heat transfer coefficients applied to the collector. This study is a contribution towards understanding solar chimney power plant performance and control and may be useful in the design of solar chimney turbines.

Keywords: Solar chimney power plant; Power production; Power output control

1. Introduction

The prototype solar chimney power plant at Manzanares in Spain (Haaf et al. (1983)) showed that the solar chimney is a practical technology capable of generating electrical power from the sun. Solar chimney power plant systems are being considered as feasible options to produce energy in countries where unexploited desert areas are abundant, like South America, Africa, Asia and Oceania. Haaf et al. (1983) and Haaf (1984) presented fundamental studies for the Spanish prototype in which the energy balance, design criteria and cost analyses were discussed, and reported preliminary test results. Krisst (1983) and Kulunk (1985) demonstrated different types of small-scale solar chimney devices with power outputs not exceeding 10 W. Pasumarthi and Sherif (1998a,b) and Padki and Sherif (1999) developed a mathematical model to study the effects of various environment and geometry conditions on the heat and flow characteristics and power output of a solar chimney. They also developed three model solar chimneys in Florida and reported experimental data to use in assessing the viability of the solar chimney concept. Lodhi (1999) presented a comprehensive analysis of the chimney effect, power production, efficiency, and estimated the cost of the solar chimney power plant set up in developing nations. Bernardes et al. (1999) presented a theoretical analysis of a solar chimney, operating on natural laminar convection in steady state. Gannon and von Backström (2000) presented a thermodynamic cycle analysis of the solar chimney power plant for the calculation of limiting performance, efficiency, and the relationship between the main variables including chimney friction, system, turbine and exit kinetic energy losses. Gannon and von Backström (2003) presented an experimental investigation of the performance of a solar chimney turbine. Total-to-total efficiencies of 85–90% and total-to-static of 77–80% over the design range are measured. Bernardes et al. (2003) developed a thermal and technical analysis to estimate the power output and examine the effect of various ambient conditions and structural

* Corresponding author. Tel.: +55 31 3319 6855; fax: +55 31 3319 6850.
E-mail address: masb2005@gmail.com (M.A.d.S. Bernardes).

0038-092X/$ - see front matter © 2009 Elsevier Ltd. All rights reserved.
doi:10.1016/j.solener.2009.11.009

Nomenclature

Variables	*Description*
g	gravitational acceleration (9.8 m/s^2)
H	chimney height (m)
k	ratio of Δp_{loss} to Δp_{dyn}
K_L	ratio of system pressure drop to flow
K_p	ratio of pressure potential to flow
m	pressure potential exponent
$\dot{m}$	mass flow rate (kg/s)
n	pressure loss exponent
p	Pressure (Pa)
P_{turb}	Theoretical power extracted by the turbine (W)
T	temperature (K)
T_0	ambient temperature (K)
$\dot{V}$	volume flow intake rate (m^3/s)
$\dot{V}_{0FP}$	volume flow for zero fluid power (m^3/s)
$\dot{V}_{MFP}$	volume flow for maximum fluid power (m^3/s)
x	ratio of Δp_{turb} to Δp
z	vertical coordinate (m)
Δp	available system pressure difference (Pa)
Δp_{dyn}	dynamic pressure difference (Pa)
Δp_{loss}	pressure losses across the system (Pa)
Δp_{turb}	pressure difference across the turbine (Pa)
ρ	density (kg/m^3)

dimensions on the power output. Pastohr et al. (2004) carried out a numerical simulation to improve the description of the operation mode and efficiency by coupling all parts of the solar chimney power plant including the ground, collector, chimney, and turbine. Schlaich et al. (2003) presented theory, practical experience, and economy of solar chimney power plant to give a guide for the design of 200 MW commercial solar chimney power plant systems. Liu et al. (2005) carried out a numerical simulation for the MW-graded solar chimney power plant, presenting the influences of pressure drop across the turbine on the draft and the power output of the system. Schlaich et al. (2005) presented a simplified theory, some practical experience results and a detailed economic analysis of solar chimneys for the design of commercial solar chimney power plant systems like the one being planned for Australia. von Backström and Fluri (2006) investigated analytically the validity and applicability of the assumption that, for maximum fluid power, the optimum ratio of turbine pressure drop to pressure potential (available system pressure difference) is 2/3. A more comprehensive optimization scheme, incorporating the basic collector model of Schlaich in the analysis, showed that the power law approach is sound and conservative. Pretorius (2006) reviewed most of the outstanding issues. Different calculation approaches with a variety of considerations have been applied to calculate chimney power plant performance. The available work potential that atmospheric air acquires while passing through the collector has been determined and analyzed by Ninic (2006). In this study, the dependence of the work potential on the air flowing into the air collector from the heat gained inside the collector, air humidity and atmospheric pressure as a function of elevation are determined. Various collector types using dry and humid air have been analyzed. The influence of various chimney heights on the air work potential was established. Bilgen and Rheault (2006) designed a solar chimney system for power production at high latitudes and evaluated its performance. Pretorius and Kröger (2006a) evaluated the influence of a developed convective heat transfer equation, more accurate turbine inlet loss coefficient, quality collector roof glass and various types of soil on the performance of a large scale solar chimney power plant. Ting-Zhen et al. (2006a) presented a mathematical model to evaluate the relative static pressure and driving force of the solar chimney power plant system and verified the model with numerical simulations. Later, Ting-Zhen et al. (2006b) developed a comprehensive model to evaluate the performance of a solar chimney power plant system, in which the effects of various parameters on the relative static pressure, driving force, power output and efficiency have been further investigated. Koonsrisuk and Chitsomboon (2007) proposed dimensionless variables to guide the experimental study of flow in a small-scale solar chimney. Computational fluid dynamics (CFD) methodology was employed to obtain results that are used to prove the similarity of the proposed dimensionless variables. Sakonidou et al. (2008) developed a mathematical model to determine the tilt that maximizes natural air flow inside a solar chimney using daily solar irradiance data on a horizontal plane at a site. The model predicted the temperature and velocity of the air inside the chimney as well as the temperatures of the glazing and the black painted absorber. Comparisons of the model predictions with CFD calculations delineate the usefulness of the model. In addition, there was a good agreement between theoretical predictions and experiments performed with a 1 m long solar chimney at different tilt positions. Ferreira et al. (2008) proposed to study the feasibility of a solar chimney to dry agricultural products. To assess the technical feasibility of this drying device, a prototype solar chimney, in which the air velocity, temperature and humidity parameters were monitored as a function of the solar incident radiation, was built. Drying tests of food, based on theoretical and experimental studies, assure the technical feasibility of solar chimneys used as solar dryers for agricultural products. Fluri and von Backström (2008) compared the performance of different turbine layouts by using analytical models and optimization tech-

niques. Furthermore, important design parameters were discussed. This study showed that these slight changes in modelling approach have a significant impact on the performance prediction and single rotor layout without guide vanes performs very poorly. Concluding, the counter rotating layouts provide the highest peak efficiencies, but at relatively low speeds, which leads to an undesirable higher torque for the same power output. Maia et al. (2009) performed an analytical and numerical study of the unsteady airflow inside a solar chimney by using the finite volumes technique in generalized coordinates to solve the conservation and transport equations showing that the height and diameter of the tower are the most important physical variables for solar chimney design. Ninic and Nizetic (2009) developed a simplified physical and analytical GVC (Gravitational Vortex Column) model for Solar Chimney Power Plants.

Numerical simulation for the MW-graded solar chimney power plant carried out by Liu et al. (2005) gave insufficient aid for the design of a commercial large scale solar chimney power plant with an energy storage layer which can supply power continuously all year round. Pastohr et al. (2004) presented a numerical simulation result in which the energy storage layer was regarded as solid.

A solar chimney power plant has three main components, namely the collector, chimney and turbo-generator. Buoyancy causes the hot air to rise in the chimney, and this draws the air through the collector where the collector floor heats it. The turbine converts fluid power into shaft power to drive the generator. One of the pertinent questions is how to maximize the fluid power by adjusting the pressure drop across the turbine and the flow through it. Two associated problems exist, namely finding the optimum by means of an algorithm in the plant simulation calculations, and designing an algorithm for the dynamic control of a real plant, where the controlling input variables must be easily and reliably measurable. The turbine pressure drop can be varied in practice by controlling the generator torque, or by adjusting the turbine inlet guide vane or rotor blade setting angles. The only practical way of independently adjusting the flow is by throttling, an energy dissipating process.

2. Power control strategies applicable to solar chimney power plants

The pressure potential (available system pressure difference) in a solar chimney power plant is proportional to the difference between the average air density outside and inside the chimney, and to the chimney height:

$$\Delta p = (\rho_a - \rho_c) g \Delta z \tag{1}$$

For essentially incompressible flow, the power P_{turb} extracted by a turbo-machine is equal to the pressure difference across the turbine Δp_{turb} times the volume flow intake rate $\dot{V}$:

$$P_{turb} = \Delta p_{turb} \dot{V} \tag{2}$$

By introducing the Boussinesq approximation, with $\rho_a - \rho_c \approx \frac{1}{T_0}\rho_a \Delta T / T_0$, in Eq. (1), the pressure potential is given by

$$\Delta p = \rho_a g H \frac{\Delta T}{T_0} \tag{3}$$

where ρ_a is the air density, H is the chimney height, T_0 is the ambient temperature and g the gravitational acceleration. The power produced by a solar chimney power plant with chimney height H is:

$$P_{turb} = \Delta p_{turb} \dot{V} = C \Delta p \dot{V} = C\, gH \frac{\dot{m} \Delta T}{T_0}, \quad \text{where } 0 \leqslant C \leqslant 1 \tag{4}$$

These equations can also be derived from thermodynamic considerations as shown by von Backström and Gannon (2000b) and Gannon and von Backström (2000).

To find the maximum power the optimum combination of Δp_{turb} and $\dot{V}$ must be determined. Zero power will be developed under two conditions: (1) when the turbine pressure drop is increased until it is equal to the pressure potential, and there is no flow, and (2) when the turbine pressure drop is reduced until it is zero and the flow is at a maximum, limited only by the frictional losses in the system.

The value of the ratio of the turbine pressure drop to the total pressure potential,

$$\frac{\Delta p_{turb}}{\Delta p} = x, \tag{5}$$

was introduced by Schlaich et al. (2003) and has been widely used. Haaf et al. (1983), Lautenschlager et al. (1984), Mullett (1987), Schlaich (1995) assumed an optimum value for maximum fluid power (MFP) of $x_{MFP} = 2/3$, but Schlaich (1995) appears to have also used 0.82 to arrive at some values in the tables in the booklet. von Backström and Gannon (2000a) assumed $x_{MFP} = 2/3$ for optimization at a given, constant collector temperature rise (and pressure potential) only. Otherwise, diagrams presented by Hedderwick (2001) presents values in the region of 0.7, found by iteratively adjusting the turbine pressure drop, following Gannon and von Backström (2000) and Gannon (2002). Schlaich et al. (2003) mentioned an optimal x-value of 0.80, whilst Bernardes et al. (2003) mentioned an optimal value as high as $x_{MFP} = 0.97$. For that, simulations based on his model were conducted and the generated power was evaluated for $0 < x < 1$ throughout a typical day. von Backström and Fluri (2006) reviewed this wide range of x_{MFP}-values and presented a simple, approximate analysis to shed some light on the matter. They assume that the relationship between pressure potential and volume flow is:

$$p_p = K_p \dot{V}^m \tag{6}$$

where K_p is a constant and m is a negative exponent between 0 and -1.0. They represent the system pressure drop by

$$p_L = K_L \dot{V}^n \tag{7}$$

where K_L is a constant and n will typically be 2 and then derive the following equation for the turbine pressure drop as fraction of the pressure potential at maximum fluid power:

$x_{MFP} = (n - m)/(n + 1)$. It turns out that $x_{MFP} = 2/3$ only *if* $m = 0$ (i.e. pressure potential constant, and independent of the volume flow) and $n = 2$ (losses proportional to volume flow squared). By employing a simple collector model proposed by Schlaich (1995) they also find that $-m$ is equal to the collector floor to collector exit heat transfer efficiency, η_{cfe}. Another way of seeing it is that $-m$ is equal to 1- (fraction of heat released by collector floor that is lost to the environment). If $n = 2$ and $\eta_{cfe} = 0.5$ (implying that $m = -0.5$), then $x_{MFP} = 0.833$. This shows that moderate collector efficiencies should result in $x_{MFP} \approx 0.83$, but that higher efficiencies can result in very high values of x_{MFP}.

Pretorius (2004, 2006) and Pretorius and Kröger (2006a) employed an approach that assumed that the maximum power varied with flow as the peak of a parabolic function. The volume flow is then perturbed around an initial guess by determining the power at slightly smaller and larger flows.

There is a need for a comparative evaluation of operational strategies applicable to the design and dynamic control of solar chimney power plants. As explained previously, either the turbine pressure drop or the volume flow may be considered to be the independent variable, or a formal optimization procedure may be employed, until either the flow or the pressure drop associated with the maximum power point is found for the prevailing conditions at the particular time of day. Since the collector efficiency is also expected to play a role, as indicated by von Backström and Fluri (2006), the heat transfer schemes employed are expected to be relevant too.

The paper proposes to compare two strategies for finding the maximum power point of a reference solar chimney power plant, while using two heat transfer schemes, described by Bernardes et al. (2007), in each case.

3. Reference site and plant data

Table 1 summarizes the plant size and shape and relevant physical properties. The meteorological input data of Sishen (Latitude S26.67°), South Africa presented by Pretorius (2006) was used in the present numerical simulation.

4. Solar collector and plant characteristics

Different power control schemes of solar chimney power output were implemented by Pretorius (2004) and Bernardes et al. (2003). In order to carry out the proposed evaluation, these control schemes were introduced in a computer program developed in Maple. Flowcharts for computer simulation models of the two control schemes can be found in Pretorius (2004) who varied the volume flow and Bernardes et al. (2003) and Bernardes et al. (2007) who varied the turbine pressure drop. The control schemes will be named the volume control scheme and the pressure control scheme.

Initially, in order to evaluate the solar chimney power plant fundamental performance, namely, the temperature rise in collector and the total pressure potential for different flow rates, computer simulations were performed in the previously mentioned computer program for the reference solar chimney power plant using the Pretorius (2004) heat transfer scheme for conditions presented in Table 1, by varying the volume flow rate and the incident solar radiation. The losses considered in this model are: collector ground and roof surface shear stress, roof supports drag force, collector inlet pressure drop, chimney wall shear stress, chimney bracing wheels drag force, tower exit dynamic pressure loss, turbine inlet pressure drop and pressure drop across the turbine. The air temperature rise through the collector, the total pressure potential and the power output as a function of the volume flow rate are plotted in Figs. 1–3, respectively, for December monthly average day (Pretorius (2004)). The pressure potential curves have the same shape as the temperature rise curves, as shown by Eq. (3). Also indicated are lines joining the maximum power points throughout the day. These lines show that the minimum power is produced at around 06:00 and the maximum at 15:00, and that during the time of rising output (labeled morning), the maximum power is produced at greater flows than during the time of decreasing power (labeled afternoon). The reason for this is that up to 15:00, more thermal energy is stored in the collector floor than is released, and this opposes the cooling effect of passing more air over it. Consequently the maximum fluid power is developed at larger flows in the mornings.

Table 1
Reference solar chimney power plant configuration.

Collector roof (Glass)	
Emissivity of glass	0.87
Roughness of glass	0 m
Extinction coefficient of glass	4 m^{-1}
Refractive index of glass	1.526
Thickness of glass	0.004 m
Roof shape exponent	1
Perimeter (inlet) height	5 m
Outer diameter	5000 m
Inner diameter	189 m
Ground	
Type	Sandstone
Emissivity (treated surface)	0.9
Absorptivity (treated surface)	0.9
Density	2160 kg/m^3
Specific heat	710 J/kg·K
Thermal conductivity	1.83 W/m K
Roughness	0.05 m
Chimney	
Height	1000 m
Inside diameter	210 m
Turbine	
Turbo-generator efficiency	80%
Ambient Conditions	
Atmospheric pressure	90000 N/m^2
Wind speed at 10 m	3 m/s

5. Simulation and results

Comparative computer simulations were conducted for the two previously mentioned power control strategies, namely pressure and flow schemes. Four months (namely

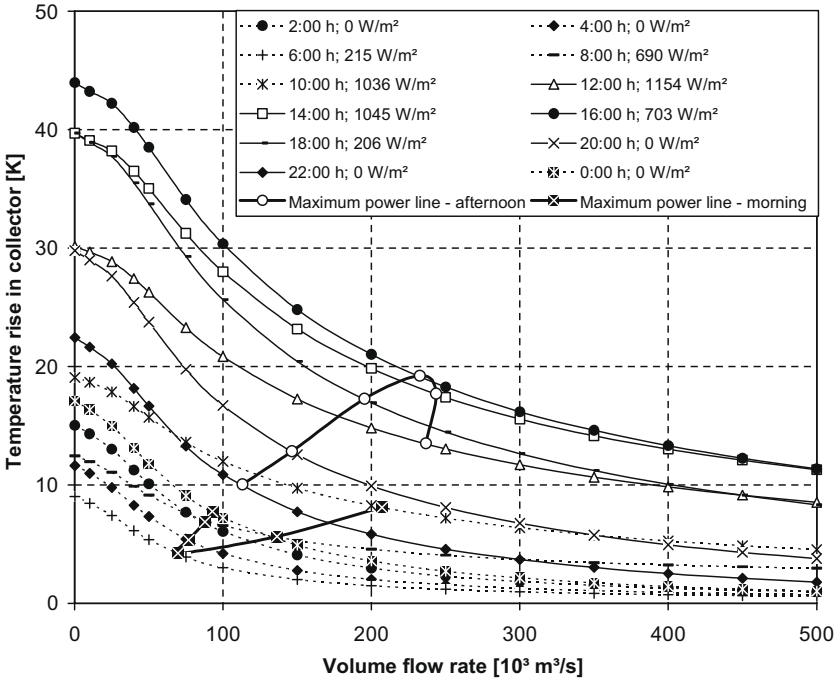

Fig. 1. Effect of volume flow rate on solar collector temperature rise for various values of solar radiation for the reference plant in December, based on the Pretorius heat transfer scheme.

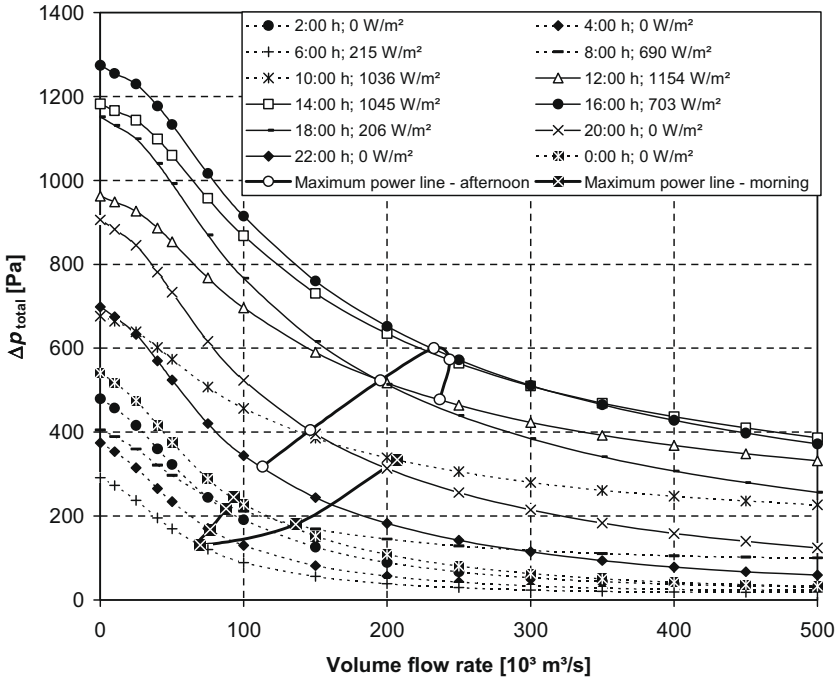

Fig. 2. Effect of volume flow rate on total pressure potential for various values of solar radiation for the reference plant configuration in December, based on the Pretorius heat transfer scheme.

March, June, September and December) were chosen and the monthly average weather data was used in the numerical simulation.

5.1. Volume flow as independent variable

Initially, simulations were conducted by using the parabolic flow control scheme presented by Pretorius (2004). He used a three point parabolic curve fit to find the maximum power point (and corresponding volume flow rate). For each time step, three new volume flows are chosen based on the optimum flow from the previous time step. The power values delivered by the turbo-generator for these flows are calculated (assuming a fixed turbo-generator efficiency of 80%). With the three points on the power versus flow curve, a three point quadratic polynomial regression

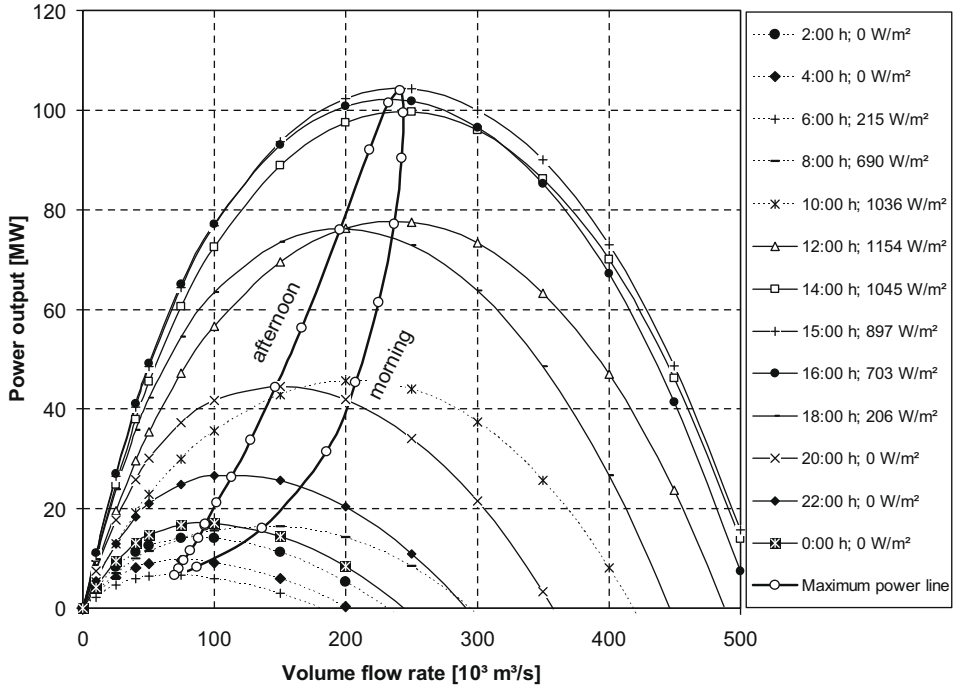

Fig. 3. Effect of volume flow rate on power output for various values of solar radiation for the reference plant configuration in December, based on the Pretorius heat transfer scheme.

is used to fit the trend and find the maximum. If the plant simulation code gives a value that differs by more than one percent from the predicted curve the process is repeated.

Figs. 4 and 5 show the calculated power output and volume flow rate for the Bernardes and Pretorius heat transfer schemes. Basically, the lower heat transfer coefficients employed by Bernardes produced lower volume flow rate during the day increasing the heat transfer to the ground, and enhancing the ground storage effect.

The influence of the heat transfer scheme is presented in Fig. 6. Post calculated x-factor values for the Bernardes heat transfer scheme varies from 0.82 to approximately 0.87. For the Pretorius scheme, the values are clearly lower, varying between approximately 0.79 and 0.82. The distributions of the optimal x-values during the day and the night are distinctive, and show higher values for the Bernardes scheme. It predicts lower heat transfer coefficients at the ground surface (Bernardes et al. (2007)) inducing higher ground temperatures and enhancing the storage effect in the ground during the day. The Pretorius heat transfer coefficients increase faster with an increase in volume flow (as seen in Bernardes et al. (2007)), so the heat transfer increases faster with increase in flow. The volume flows for maximum fluid power (MFP) are then larger and x_{MFP} is smaller, as seen in Figs. 4–6.

As shown in Figs. 7 and 8, the x-factors for the maximum power output are higher than 0.8 and vary during the day. In the early morning, between 2:00 and 6:00 h, the maximum power output lies at approximately $x = 0.98$. From 6:00 to 18:00 h, the maximum power output was achieved when $x = 0.9$. From 18:00 to 0:00 x goes from 0.90 to 0.98. This occurrence illustrates the influence of the solar radiation and the ground storage effect on the power plant performance. By increasing the energy input (solar radiation), lower x-factors for the maximum power output are expected. On the other hand, if the energy input decreases or is zero, a higher x-factor for the maximum power output should be expected. The curves P versus x (Figs. 7 and 8) present distinctive distributions varying from more sharp lines between 20:00 and 6:00 h up to curved lines between 8:00 and 18:00 h. Nevertheless, no representative curve could be found. If no typical relationship between power and x can be found, the optimization procedure would require additional effort.

5.2. Turbine pressure drop as independent variable

Next, an x-factor optimization procedure was developed in order to figure out the solar chimney performance under this power control scheme. Based on Figs. 7 and 8, a simple optimization procedure was developed. The power output calculation starts from low x-values. Subsequently, x is increased incrementally and the power output is calculated for each step and compared with the previous one. If the current power output is higher than the previous one, it indicates escalating power output according to Figs. 7 and 8. Then, the procedure forwards for the next $x + \Delta x$. If not, it reveals that the maximum power output value has been overtaken. The procedure then stops and takes the last results as the maximum power output for the cur-

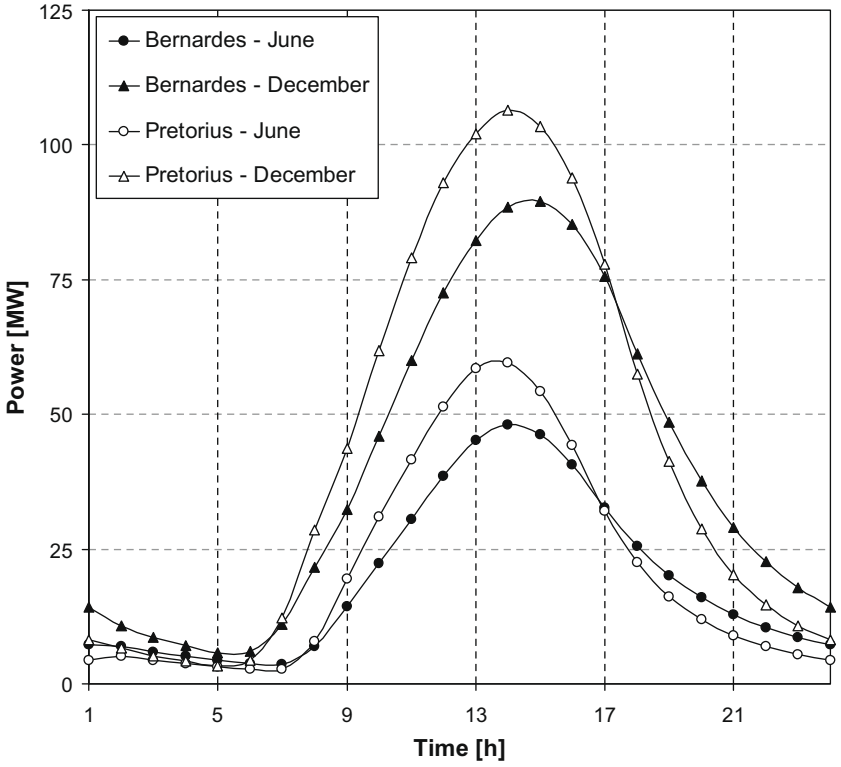

Fig. 4. Calculated power output for the Bernardes and Pretorius heat transfer schemes based on June and December monthly average weather data.

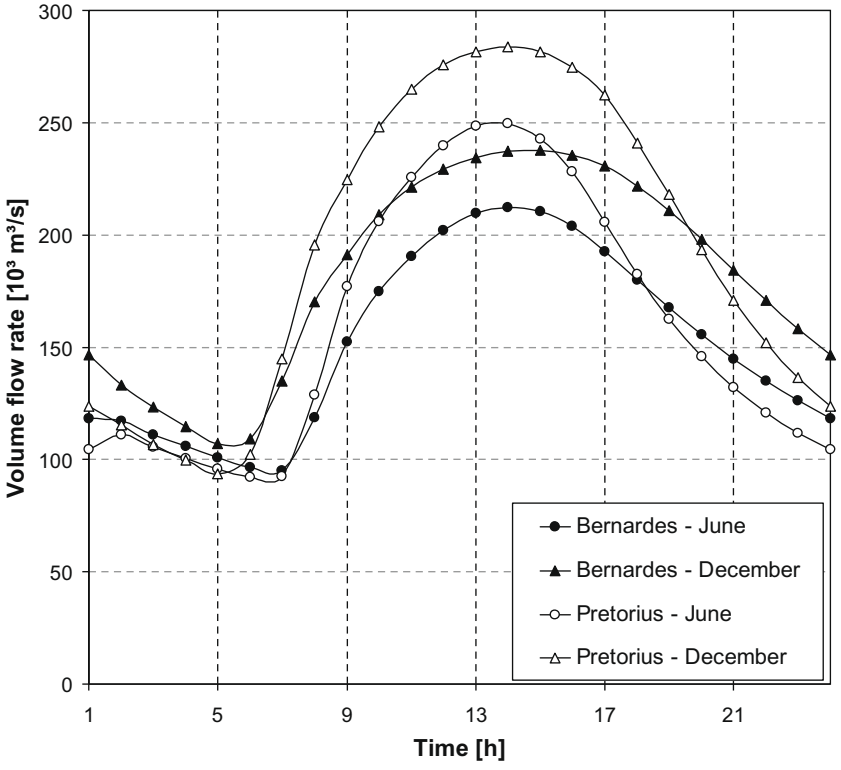

Fig. 5. Calculated volume flow rate for the Bernardes and Pretorius heat transfer schemes based on March, June, September and December monthly average weather data.

rent step. After some simulations, a step size $\Delta x = 0.02$ has shown to be adequate for the proposed analysis.

Fig. 9 shows the calculated x-factor for the instantaneous maximal power output. Constant values of x-factor

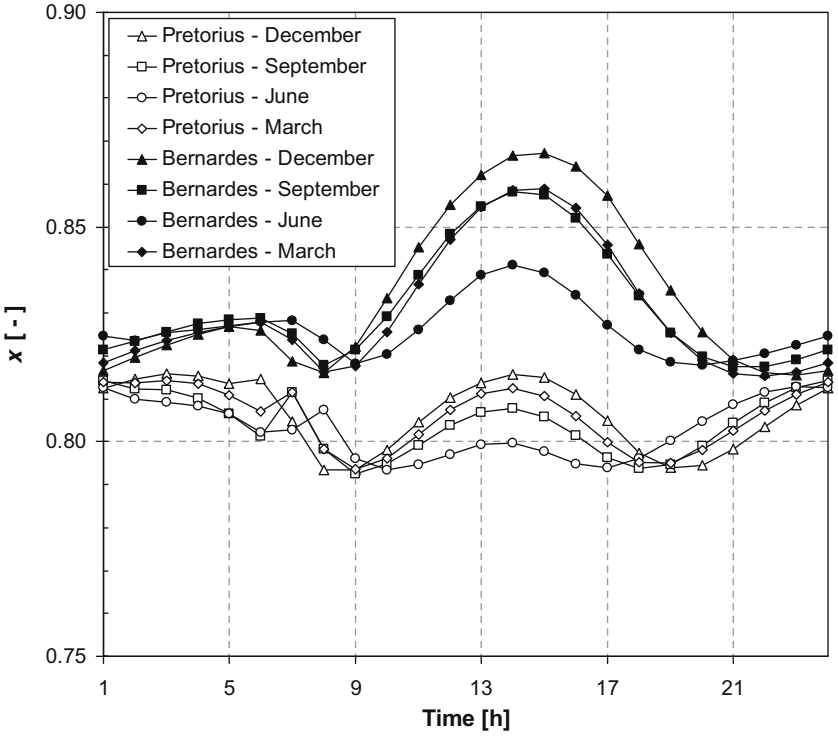

Fig. 6. Post calculated x-factor for flow control scheme with Bernardes and Pretorius heat transfer coefficients schemes based on March, June, September and December monthly average weather data.

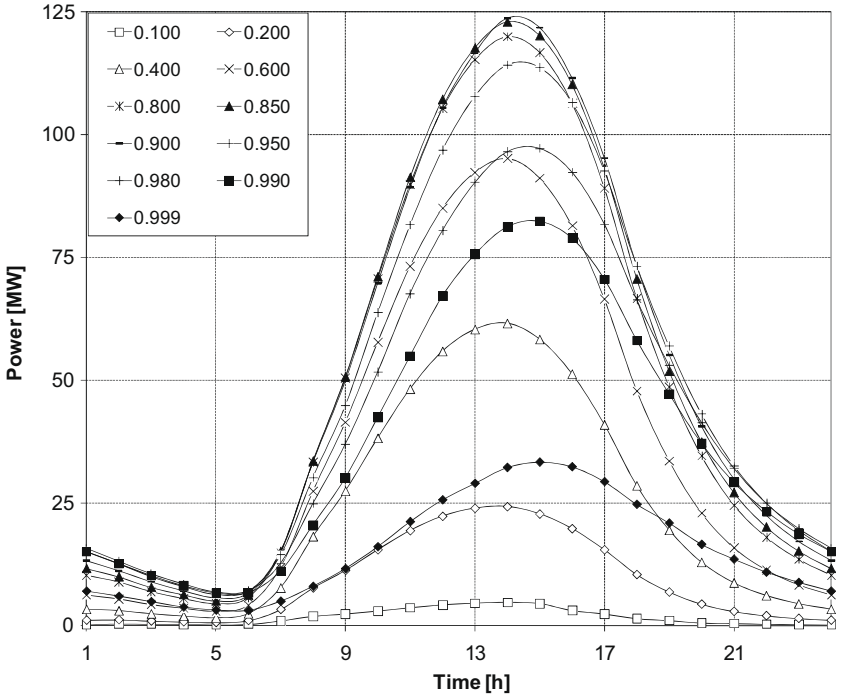

Fig. 7. Theoretical power output variation in the course of the day for different x-factors, based on the Pretorius heat transfer scheme.

are not expected for the whole day and the influence of the heat transfer coefficients scheme is significant. Therefore, the constant optimum value for the factor $x = 2/3$ assumed by Schlaich (1995) could not be confirmed. In general, lower values are obtained during the early morning hours, between 2:00 and 6:00 for both heat transfer schemes. In most cases, the Bernardes scheme presented higher x-factor values than the Pretorius scheme, particularly after 8:00 h.

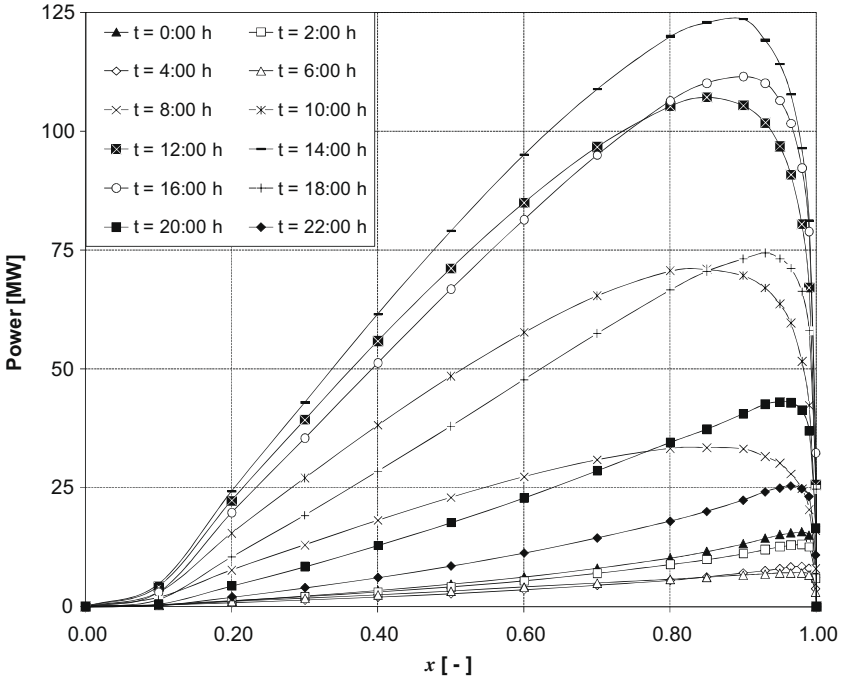

Fig. 8. Theoretical influence of the x-factor on the power output in the course of the day, based on the Pretorius heat transfer scheme.

As described by Bernardes et al. (2007), the lower heat transfer coefficients employed by Bernardes produced higher temperatures at the absorber (ground surface) during the day increasing the heat transfer by conduction to the ground. During the night, the ground releases the additional accumulated heat energy. This effect leads to higher x-factor values for the Bernardes scheme due to the fact that higher temperatures in the absorber lead to higher air temperatures and, consequently, to higher total pressure potential. So, in this case, the turbine system can extract more energy and a larger fraction of the available total pressure potential. This behavior is also confirmed in Fig. 11, where the x-factor for the maximal power output varies with the system conditions. However the mentioned value up to 0.97 was not achieved, indicating its overestimation by Bernardes et al. (2003). Between 11:00 and 18:00, uniform x-factor values 0.9 and 0.8 are found for both Bernardes and Pretorius scheme, respectively.

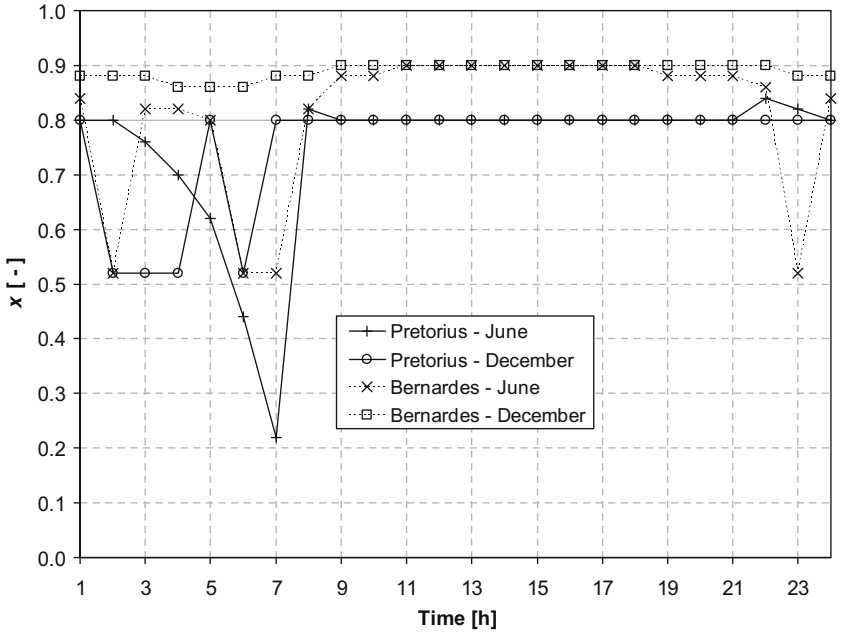

Fig. 9. Variation of x-factor during the day, as found by flow optimization.

One plausible explanation for the instability observed especially for periods without sunlight is the heat transfer coefficient estimation employed for each model. For some transition conditions (e.g. laminar to turbulent flow, natural to forced convection, etc.), the heat transfer coefficient calculation returns uneven values that can produce instabilities. Such instabilities do not go against the major inferences already shown.

Additionally is it necessary to recognize that the optimization procedure is strongly dependent on the power demand strategies adopted for the daily operation. The procedures employed in this work addressed exclusively the instantaneous maximum power output.

6. Discussion

By using the approach of von Backström and Fluri (2006), the volume flow for maximum fluid power (MFP) is found when $\partial P/\partial \dot{V} = 0$ i.e.:

$$\frac{\partial}{\partial \dot{V}}[(K_p \dot{V}^m - K_L \dot{V}^n)V] = 0 \tag{8}$$

$$\dot{V}_{MFP} = \left[\frac{K_p(m+1)}{K_L(n+1)}\right]^{\left(\frac{1}{n-m}\right)} \tag{9}$$

The volume flow for zero fluid power is given by:

$$\dot{V}_{0FP} = \left(\frac{K_p}{K_L}\right)^{\left(\frac{1}{n-m}\right)} \tag{10}$$

Introducing Eq. (10) into Eq. (9) the ratio between the volume flow for maximum fluid power (MFP) and the volume flow for zero fluid power (0FP) can be found by:

$$\frac{\dot{V}_{MFP}}{\dot{V}_{0FP}} = \left(\frac{m+1}{n+1}\right)^{\left(\frac{1}{n-m}\right)} \tag{11}$$

As shown in Fig. 10, $\Delta p_{loss} = 0.0007437 V^{2.105}$.

Thus, for $n = 2.1$ and $V_{MFP}/V_{0FP} = 0.5$, then $m = -0.49$ and $x = \frac{n-m}{n+1} = 0.84$. This shows that the curves in Fig. 3 have their maxima at about a half their range and a parabolic curve fit, as used by Pretorius and Kröger (2006b), will be very good when $x = 0.84$.

The general shape of the curves in Fig. 11 can also be derived by using the von Backström and Fluri (2006) approach. The turbine pressure difference can be written as:

$$\Delta p_{turb} = \Delta p - \Delta p_{losses} = K_p \dot{V}^m - K_L \dot{V}^n \tag{12}$$

The power output is:

$$P = K_p \dot{V}^{m+1} - K_L \dot{V}^{n+1} = K_p \dot{V}^{m+1}\left(1 - \frac{K_L}{K_p}\dot{V}^{\frac{n+1}{m+1}}\right) \tag{13}$$

Then the x-factor can be calculated as:

$$x = \frac{K_p \dot{V}^m - K_L \dot{V}^n}{K_p \dot{V}^m} = 1 - \frac{K_L}{K_p}\dot{V}^{m-n} \tag{14}$$

By substituting Eq. (14) into Eq. (13), the power output for maximum fluid power is:

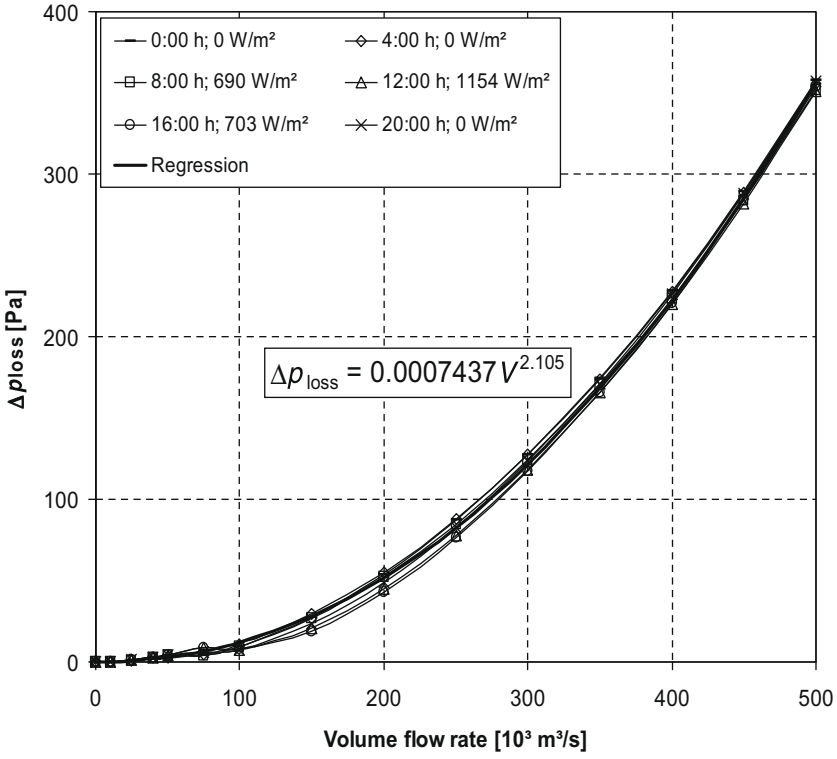

Fig. 10. Theoretical influence of the volume flow rate on the plant total pressure loss, based on Pretorius heat transfer scheme.

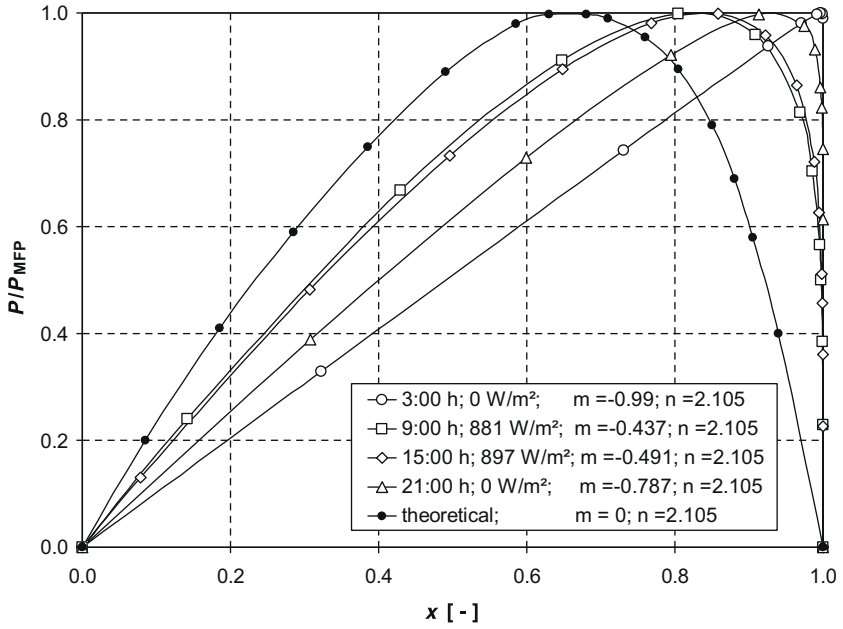

Fig. 11. Theoretical influence of the x-factor on the plant power output, based on the Von Backström and Fluri (2006) approach.

$$P_{MFP} = K_p \left[\frac{K_p}{K_L} \left(\frac{m+1}{n+1} \right)^{\frac{1}{n-m}} \right]^{m+1} - K_L \left[\frac{K_p}{K_L} \left(\frac{m+1}{n+1} \right)^{\frac{1}{n-m}} \right]^{n+1} \tag{15}$$

The power output as fraction of the maximum obtainable for a given pressure potential versus volume flow characteristic, can be found by dividing Eqs. (13) by (15). Plotting this ratio against x results in Fig. 11. It shows that the power curves, when plotted against x develop distinct sharp peaks at higher negative values of m. Note that for $m = 0$ the peak is at $x = 2.1/3.1 = 0.677$ (for $n = 2.1$) = 0.667, and the peak is rounded.

7. Conclusions

Theoretical simulations were conducted in order to evaluate solar chimney power plant performance for the heat transfer coefficients of Pretorius and Bernardes, each subjected to two power control schemes, specifically those with turbine pressure drop and volume flow as adjustable variables. The relationships between the x-factor and the volume flow rate, the temperature rise in the collector and the power output are presented. The optimum ratio of turbine pressure drop to pressure potential (available system pressure difference) varies during the whole day and it is very dependent of the heat transfer coefficients in the collector. Higher x-values of around 0.9 are found for the lower heat transfer coefficients employed by Bernardes. In contrast, the higher heat transfer coefficients presented by Pretorius returned lower x-values, that is $x = 0.8$.

Concluding, the calculated solar chimney performance under different dynamic control strategies may be helpful in preliminary plant design. Furthermore, this study may also assist to configure the turbines appropriately. Further studies should include the influence of the dimensional parameters, ground properties, collector roof characteristics and surrounding condition changes on system performance.

References

Bernardes, M.A.d.S., Valle, R.M., Cortez, M.F.-B., 1999. Numerical analysis of natural laminar convection in a radial solar heater. Revue Generale de Thermique 28 (1), 42–50.

Bernardes, M.A.d.S., von Backström, T.W., Kröger, D.G., 2007. Critical evaluation of heat transfer coefficients applicable to solar chimney power plant collectors. In: Solar World Congress 2007, Beijing, China.

Bernardes, M.A.d.S., Voß, A., Weinrebe, G., 2003. Thermal and technical analyses of solar chimneys. Solar Energy 75, 511–524.

Bilgen, E., Rheault, J., 2006. Solar chimney power plants for high latitudes. Solar Energy 79 (5), 449–458.

Ferreira, A.G., Maia, C.B., Cortez, M.F.B., Valle, R.M., 2008. Technical feasibility assessment of a solar chimney next term for food drying. Solar Energy 82 (3), 198–205.

Fluri, T.P., von Backström, T.W., 2008. Comparison of modelling approaches and layouts for solar chimney turbines. Solar Energy 82 (3), 239–246.

Gannon, A.J., 2002. Solar Chimney Turbine Performance. Department of Mechanical Engineering, University of Stellenbosch, Ph.D. Thesis, Stellenbosch, South Africa.

Gannon, A.J., von Backström, T.W., 2000. Solar chimney cycle analysis with system loss and solar collector performance. Transactions of the ASME, Journal of Solar Energy Engineering 122 (3), 133–137.

Gannon, A.J., von Backström, T.W., 2003. Solar chimney turbine performance. Journal of Solar Energy Engineering 125 (1), 101–106.

Haaf, W., 1984. Solar chimneys – part II: preliminary test results from the Manzanares pilot plant. International Journal of Sustainable Energy 2 (2), 141–161.

Haaf, W., Friedrich, K., Mayer, G., Schlaich, J., 1983. Solar chimneys – part I: principle and construction of the pilot plant in Manzanares. International Journal of Solar Energy 2 (1), 3–20.

Hedderwick, R.A., 2001. Performance Evaluation of a Solar Chimney Power Plant. Department of Mechanical Engineering, University of Stellenbosch, Master, Stellenbosch, South Africa.

Koonsrisuk, A., Chitsomboon, T., 2007. Dynamic similarity in solar chimney modeling. Solar Energy 81 (12), 1439–1446.

Krisst, R.J.K., 1983. Energy transfer system. Alternative Sources of Energy 63, 8–11.

Kulunk, H., 1985. A prototype solar convection chimney operated under Izmit conditions. In: 7th MICAS, Veziroglu TN.

Lautenschlager, H., Haaf, W., Schlaich, J., 1984. New results from the solar chimney prototype and conclusions for large power plants. In: Proceedings of the European Wind Energy Conference, Hamburg, Germany.

Liu, W., Ming, T.Z., Yang, K., Pan, Y., 2005. Simulation of characteristic of heat transfer and flow for MW-graded solar chimney power plant system. Journal of Huazhong University of Science and Technology 33 (8), 5–7.

Lodhi, M.A.K., 1999. Application of helio-aero-gravity concept in producing energy and suppressing pollution. Energy Conversion and Management 40, 407–421.

Maia, C.B., Ferreira, A.G., Valle, R.M., Cortez, M.F.B., 2009. Theoretical evaluation of the influence of geometric parameters and materials on the behavior of the airflow in a solar chimney. Computers & Fluids 38 (3), 625–636.

Mullett, L.B., 1987. The solar chimney – overall effciency, design and performance. International Journal of Ambient Energy 8 (1), 35–40.

Ninic, N., 2006. Available energy of the air in solar chimneys and the possibility of its ground-level concentration. Solar Energy 80 (7), 804–811.

Ninic, N., Nizetic, S., 2009. Elementary theory of stationary vortex columns for solar chimney power plants. Solar Energy 83 (4), 462–476.

Padki, M.M., Sherif, S.A., 1999. On a simple analytical model for solar chimneys. International Journal of Energy Research 23 (4), 345–349.

Pastohr, H., Kornadt, O., Gürlebeck, K., 2004. Numerical and analytical calculations of the temperature and flow field in the upwind power plant. International Journal of Energy Research 28 (6), 495–510.

Pasumarthi, N., Sherif, S.A., 1998a. Experimental and theoretical performance of a demonstration solar chimney model – part II: experimental and theoretical results and economic analysis. International Journal of Energy Research 22 (5), 443–461.

Pasumarthi, N., Sherif, S.A., 1998b. Experimental and theoretical performance of a demonstration solar chimney model – part I: mathematical model development. International Journal of Energy Research 22 (3), 277–288.

Pretorius, J.P., 2006. Optimization and Control of a Large-Scale Solar Chimney Power Plant. Department of Mechanical Engineering, University of Stellenbosch, Ph.D., Stellenbosch, South Africa.

Pretorius, J.P., 2004. Solar Tower Power Plant Performance Characteristics. Department of Mechanical Engineering, University of Stellenbosch, Master, Stellenbosch, South Africa.

Pretorius, J.P., Kröger, D.G., 2006a. Critical evaluation of solar chimney power plant performance. Solar Energy 80, 535–544.

Pretorius, J.P., Kröger, D.G., 2006b. Solar chimney power plant performance. Transactions of the ASME 128, 302–311.

Sakonidou, E.P., Karapantsios, T.D., Balouktsis, A.I., Chassapis, D., 2008. Modeling of the optimum tilt of a solar chimney for maximum air flow. Solar Energy 82 (1), 80–94.

Schlaich, J., 1995. The Solar Chimney, Electricity from the Sun. Edition Axel Menges, Stuttgart.

Schlaich, J., Bergermann, R., Schiel, W., Weinrebe, G., 2003. Design of commercial solar tower systems – utilization of solar induced convective flows for power generation. In: Proceedings of the International Solar Energy Conference, Kohala Coast, United States.

Schlaich, J., Bergermann, R., Schiel, W., Weinrebe, G., 2005. Design of commercial solar updraft tower systems – utilization of solar induced convective flows for power generation. ASME Journal of Solar Energy Engineering 127, 117–124.

Ting-Zhen, M., Wei, L., Guo-Liang, X., 2006a. Analytical and numerical investigation of the solar chimney power plant systems. International Journal of Energy Research 30 (11), 861–873.

Ting-Zhen, M., Wei, L., Guo-Liang, X., Ai-Wu, F., 2006b. A study of the solar chimney power plant systems. Journal of Engineering Thermophysics 27 (3), 505–507.

von Backström, T.W., Fluri, T.P., 2006. Maximum fluid power condition in solar chimney power plants – an analytical approach. Solar Energy 80 (11), 1417–1423.

von Backström, T.W., Gannon, A.J., 2000a. Compressible flow trough solar chimney power plant. Transactions of the ASME, Journal of Solar Energy Engineering 122, 138–145.

von Backström, T.W., Gannon, A.J., 2000b. The solar chimney air standard thermodynamic cycle. SAIMechE R&D Journal 16 (1), 16–24.

Available online at www.sciencedirect.com
ScienceDirect
Solar Energy 82 (2008) 239–246
SOLAR ENERGY
www.elsevier.com/locate/solener

Comparison of modelling approaches and layouts for solar chimney turbines

T.P. Fluri *,[1], T.W. von Backström

Department of Mechanical Engineering, University of Stellenbosch, Private Bag X1, Stellenbosch 7602, South Africa

Received 18 September 2006; received in revised form 19 July 2007; accepted 20 July 2007
Available online 17 August 2007

Communicated by: Associate Editor S.A. Sherif

Abstract

The turbogenerator is a core component of any solar chimney power plant. Various layouts for the turbogenerator have been proposed in the literature. In this paper the performance of these layouts is compared using analytical models and optimization techniques, and the important design parameters are discussed. The turbine layouts under consideration are single rotor and counter rotating turbines, both with or without inlet guide vanes.

In contrast to similar investigations found in the literature, various radial sections along the blades are analysed in the turbine model. This approach is more appropriate than using a simple mean line analysis when dealing with turbines with high blade aspect ratio and low hub to tip ratio. Furthermore, a limit to the degree of reaction of the turbine has been introduced to avoid diffusion at the hub.

It is shown in this paper that these slight changes in modelling approach have a significant impact on the performance prediction. Further it can be concluded that the single rotor layout without guide vanes performs very poorly; the efficiency of the other three layouts is much better and lies in a narrow band. The counter rotating layouts provide the highest peak efficiencies, but at relatively low speeds, which leads to an undesirable higher torque for the same power output.

Keywords: Solar chimney power plant; Turbogenerator layout; Performance modelling

1. Introduction

The main features of a solar chimney power plant are a solar collector and a tall chimney (Fig. 1). The collector consists of a circular transparent roof and the ground under the collector floor surface. Solar radiation heats the ground, which in turn heats the air under the collector roof like in a greenhouse. The hot air rises and escapes through the chimney. The resulting airflow is used to generate electricity via one or several turbogenerators. A pilot plant was built and tested in the 1980s in Manzanares, Spain. No full scale solar chimney power plant has been built to date. For the turbogenerators several layouts have been proposed in the solar chimney literature. The objective of this paper is the comparison of these layouts using various modelling approaches.

Schwarz and Knauss (1981) designed the turbogenerator for the pilot plant in Manzanares. For the turbine they chose a single rotor layout without guide vanes. Gannon and Von Backström (2002) proposed a single rotor layout for a large-scale solar chimney, in which they made use of the chimney support structure as inlet guide vanes. They present an analytical model for this layout, which is adapted from gas turbine literature, and show that the inlet guide vanes improve the performance (Von Backström and Gannon, 2004). They also point out that the values for specific speed and diameter for a solar chimney turbine lie between the ones of gas turbines and wind turbines.

* Corresponding author. Tel.: +27 218084281; fax: +27 218084958.
E-mail address: thomas.fluri@alumni.ethz.ch (T.P. Fluri).
[1] Supported by VolkswagenStiftung, Germany and the South African National Research Foundation.

0038-092X/$ - see front matter © 2007 Elsevier Ltd. All rights reserved.
doi:10.1016/j.solener.2007.07.006

Nomenclature

b_x	axial blade chord
c	nondimensional absolute flow velocity
c_h	blade chord
c_p	specific heat at constant pressure
C	absolute flow velocity
C_L	lift coefficient
d	diameter
h	enthalpy per unit mass flow
l_b	blade length
$\dot{m}$	mass flow
p	pressure
r	radius
R	specific gas constant
R_{asp}	blade aspect ratio
R_{HT}	hub to tip radius ratio
R_D	diffusor area ratio
R_n	degree of reaction
T	temperature
T_q	torque
u	nondimensional peripheral speed
U	peripheral speed
w	nondimensional relative flow velocity
W	relative flow velocity
Z	number of blades
Z_t	number of turbines
α	absolute flow angle
β	rotor relative flow angle
γ	ratio of specific heats
ϵ	flow deflection
η	efficiency
ρ	density
ζ	loss coefficient
Ψ	load coefficient
Φ	flow coefficient
σ	solidity
ω	rotational speed

Subscripts

a	first rotor
b	blade, second rotor
c	chimney
m	mean
op	optimum
t	tip, total condition
ts	total-to-static
tt	total-to-total, total turbine
u	circumferential
x	axial
0	upstream of inlet guide vanes
1	upstream of first rotor
2	downstream of first rotor
3	downstream of second rotor
4	downstream of diffuser

Abbreviations

CR	counter rotating
IGV	inlet guide vane
rpm	rotations per minute
SR	single rotor

More recently, Denantes and Bilgen (2006) introduced an alternative layout consisting of one pair of counter rotating rotors, either with or without inlet guide vanes. They modified the analytical model of Von Backström and Gannon (2004) to accommodate layouts with counter rotating rotors and to compare their performance to the one of the single rotor layout with inlet guide vanes. They find that the single rotor layout has a higher efficiency at the design point but a lower efficiency at off-design conditions.

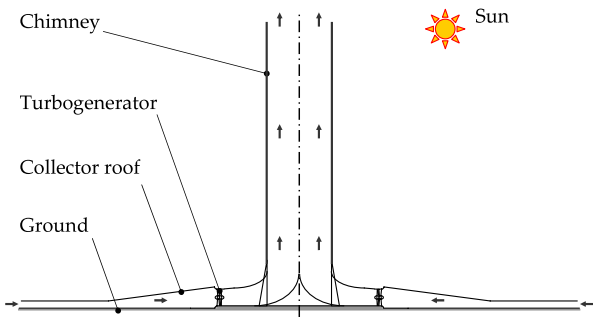

Fig. 1. Schematic drawing of a solar chimney power plant.

Denantes and Bilgen (2006) base their work on counter rotating turbines on earlier gas turbine and water turbine publications (Ozgur and Nathan, 1971; Louis, 1985; Cai et al., 1990). Ozgur and Nathan (1971) compare an axial flow counter rotating water turbine consisting of one rotor pair without inlet guide vanes to a single rotor turbine with inlet guide vanes. Louis (1985) compares two counter rotating layouts, both with one rotor pair but one with and one without inlet guide vanes, to single rotor layouts with inlet guide vanes. Cai et al. also look at axial counter rotating turbine layouts with or without guide vanes (Cai et al., 1990). In the earlier publications (Ozgur and Nathan, 1971; Louis, 1985) the rotational speed was assumed to be of equal magnitude for the two rotors and the flow was assumed to leave the turbine without swirl. In this study (Cai et al., 1990) a difference in rotor speed has been allowed for, and as an alternative to the zero exit swirl condition, layouts were studied where the exit swirl component is not zero but equal to the swirl component at the inlet. In the study of Denantes and Bilgen (2006) the speeds of the two rotors are also independent from each other and the exit swirl component is not limited to a certain value.

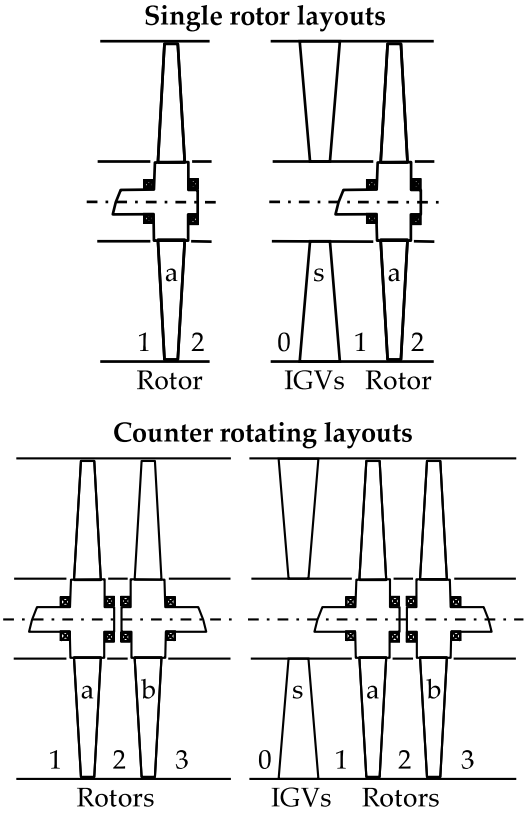

Fig. 2. Schematic drawing of turbine layouts.

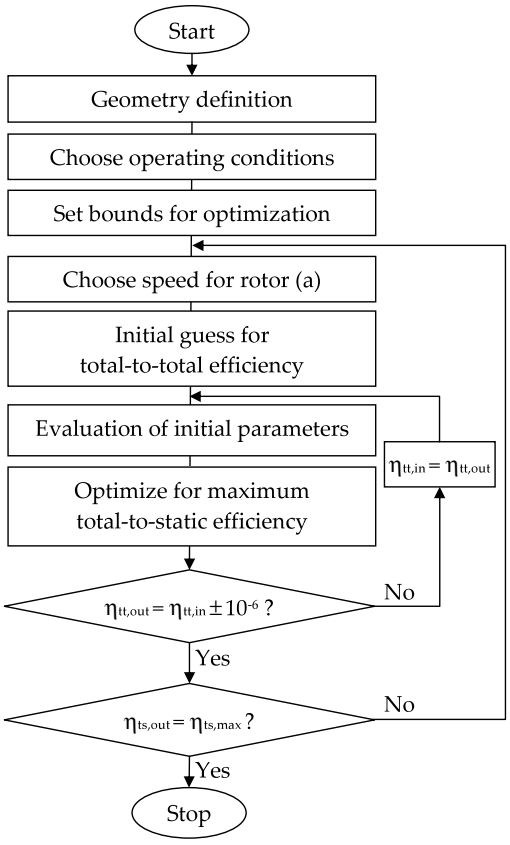

Fig. 3. Flow chart of algorithm.

A comparison based on Denantes and Bilgen (2006) is presented here, however, the evaluation of the turbine efficiency is modified (radial averaging is implemented, and secondary losses are taken into account), a limit to the turbine reaction is introduced to avoid diffusion at the hub, and the single rotor layout without inlet guide vanes is also considered.

For the comparison a multiple horizontal axis turbine configuration as shown in Fig. 1 is chosen here, and following the trends in the technology of large wind turbines, it is assumed that a variable speed drive train is used in all layouts (Bywaters et al., 2004; Poore and Lettenmaier, 2003). The turbine layouts considered in this paper are shown in Fig. 2.

2. Turbine modelling

2.1. Structure of the program

The program to enable the comparison of the layouts is structured as follows (Fig. 3):

(1) *Geometry definition.* The geometry of the flow passage and the turbine is defined. It is assumed that the diameter of the chimney is given and hence the chimney inlet area is known. The diffuser area ratio is defined as $R_D = A_c/A_{tt}$, where A_c is the chimney area and A_{tt} is the total turbine area. The number of turbines is specified. The blade aspect ratio, R_{asp}, and the hub-to-tip radius ratio, R_{HT}, are set.

(2) *Choose operating conditions.* The operating point and the working fluid are specified. The operating point is given with inlet total temperature, T_{t0}, inlet total pressure, p_{t0}, exit total pressure, p_{t4}, which is also the chimney inlet pressure, and mass flow, $\dot{m}$. The working fluid is assumed to be dry air. We assume incompressibility and the density is taken as $\rho = p_{t4}/(RT_{t0})$.

(3) *Set bounds for optimization.*

(4) *Choose speed for rotor (a).*

(5) *Initial guess.* An initial guess for the total-to-total turbine efficiency and the design variables, which will be defined in Section 2.2.1, is made.

(6) *Evaluation of initial parameters.* The axial components of the chimney inlet and the turbine exit flow velocities are

$$C_{x4} = \frac{\dot{m}}{A_c \rho} \tag{1}$$

$$C_{x3} = C_{x4} R_D \tag{2}$$

The static pressure at the exit and the temperature and enthalpy difference over the turbine are evaluated from

$$p_4 = p_{t4} - 0.5\rho C_{x4}^2 \tag{3}$$

$$\Delta T = \eta_{tt} T_{t0}\left(1 - \left(\frac{p_{t1}}{p_{t4}}\right)^{\frac{\gamma}{\gamma-1}}\right) \tag{4}$$

$$\Delta h = c_p \Delta T \tag{5}$$

The stage load coefficient Ψ and flow coefficient Φ can be evaluated from

$$\Psi = \frac{\Delta h}{U_a^2} \tag{6}$$

where U_a is the absolute blade speed of the first rotor, and

$$\Phi = \frac{C_x}{U_a} \tag{7}$$

(7) *Optimize for total-to-static efficiency.* Utilizing the specific turbine model, which will be described in detail below, an optimization algorithm is run to get the maximum total-to-static efficiency at this particular speed of the first rotor. As long as the total-to-total efficiency value has not converged we iterate. At each iteration the efficiency result is taken as the new initial guess. The optimization algorithm used here is the function "fmincon", which is the Sequential Quadratic Programming implementation for constrained optimization in Matlab.

(8) *Detect optimal speed of rotor (a).* The above iteration is executed with new values for the speed of rotor (a), until the speed providing the maximum total-to-static efficiency has been detected.

2.2. Mathematical turbine models

The model for the counter rotating layout with inlet guide vanes is described in detail here. It serves as a basis for all the other models. Having three blade rows, it is the most complex one, and the others can be derived from it by simply deleting one or two blade rows and their impact on the flow (Fig. 2). The model has been adapted from the work of Denantes and Bilgen (2006).

2.2.1. Velocity diagram

Some assumptions:

- The mass flow is equally shared by the various turbines.
- No turbine flare.
- Constant axial velocity through turbine: $C_x = C_{x1} = C_{x2} = C_{x3}$.
- Zero swirl at turbine inlet: $C_{u0} = 0$.
- Free vortex design.

The design variables for the optimization are the dimensionless blade speed of the second rotor $u_b = U_b/U_a$, the degree of reaction of the first rotor

$$R_{n,a} = 1 - (c_{u2} + c_{u1})/2 = -(w_{u2a} + w_{u1})/2 \tag{8}$$

and the degree of reaction of the second rotor

$$R_{n,b} = 1 - \frac{c_{u3} + c_{u2}}{2u_b} = -\frac{w_{u3} + w_{u2b}}{2u_b} \tag{9}$$

The small letters c and w denote dimensionless absolute and relative flow velocities respectively and the subscript u indicates the circumferential direction.

The degree of reaction, represents the ratio of the static pressure drop to the stagnation pressure drop over a turbine rotor (Wilson and Korakianitis, 1998). The above equations can be derived using the Euler equation, the velocity diagram (see Fig. 4) and assuming the axial component of the flow velocity to be equal at rotor inlet and outlet. For a derivation of Eq. (8) refer to (Von Backström and Gannon, 2004). Denantes and Bilgen (2006) use a slightly different parameter for the second rotor, which is equal to the actual degree of reaction multiplied by u_b. The load coefficients are defined as follows:

Stage load coefficient:

$$\Psi = c_{u1} - c_{u2} + u_b(c_{u2} - c_{u3}) \tag{10}$$

Load coefficient of the first rotor:

$$\Psi_a = c_{u1} - c_{u2} \tag{11}$$

Load coefficient of the second rotor:

$$\Psi_b = u_b(c_{u2} - c_{u3}) \tag{12}$$

Using these definitions and some algebraic manipulations we get the following dimensionless velocity components:

$$c_{u1} = 1 - R_{n,a} + \Psi_a/2 \tag{13}$$

$$w_{u1} = c_{u1} - 1 = -R_{n,a} + \Psi_a/2 \tag{14}$$

$$c_{u2} = 1 - R_{n,a} - \Psi_a/2 \tag{15}$$

$$w_{u2,a} = c_{u2} - 1 = -R_{n,a} - \Psi_a/2 \tag{16}$$

$$c_{u2} = u_b(1 - R_{n,b}) + \frac{\Psi_b}{2u_b} \tag{17}$$

$$w_{u2,b} = c_{u2} - u_b = -u_b R_{n,b} + \frac{\Psi_b}{2u_b} \tag{18}$$

$$c_{u3} = u_b(1 - R_{n,b}) - \frac{\Psi_b}{2u_b} \tag{19}$$

$$w_{u3} = c_{u3} - u_b = -u_b R_{n,b} - \frac{\Psi_b}{2u_b} \tag{20}$$

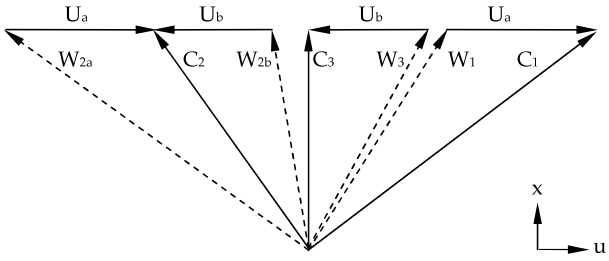

Fig. 4. Velocity triangles of a counter rotating turbine stage with inlet guide vanes (similar to Denantes and Bilgen, 2006 but without diffusion in blade rows).

Using Pythagoras's relations we can now evaluate all the flow angles and velocity components similar to the following two examples, the stator exit flow angle and the dimensionless stator exit velocity squared:

$$\alpha_1 = \arctan\frac{c_{u1}}{\Phi} \tag{21}$$

$$c_1^2 = \Phi^2 + c_{u1}^2 \tag{22}$$

Assuming that the swirl remains constant from the exit of the turbine to the chimney inlet,[2] the flow velocity at the chimney inlet is obtained from:

$$c_4^2 = c_{x4}^2 + c_{u3}^2 \tag{23}$$

Equating (15) in (17) gives

$$\Psi_b = 2u_b(1 - R_{n,a} - \Psi_a/2 - u_b(1 - R_{n,b})) \tag{24}$$

and with $\Psi = \Psi_a + \Psi_b$

$$\Psi_a = \frac{\Psi - 2u_b(1 - R_{n,a} - u_b(1 - R_{n,b}))}{1 - u_b} \tag{25}$$

With this a model has been obtained, which depends only on the three design variables and on the chosen turbine speed and operating conditions.

2.2.2. Losses and efficiency

For profile losses Hawthorne's simplification of Soderberg's correlation is implemented, where ϵ denotes the flow deflection (Horlock, 1966):

$$\zeta_p = 0.025\left(1 + \left(\frac{\epsilon}{90^\circ}\right)^2\right) \tag{26}$$

Hawthorne also gives a correlation for secondary loss implying it to be proportional to the profile loss and the blade aspect ratio:

$$\zeta_{sec} = \zeta_p\frac{3.2}{R_{asp}} \tag{27}$$

The blade aspect ratio is taken as $R_{asp} = l_b/b_x$ where l_b is the blade length and b_x is the axial chord of the blade. Adding the secondary to the profile loss and neglecting tip leakage and annulus losses the overall loss coefficient for a single blade row becomes:

$$\zeta = 0.025\left(1 + \left(\frac{\epsilon}{90^\circ}\right)^2\right)\left(1 + \frac{3.2}{R_{asp}}\right) \tag{28}$$

This loss model has been employed by many authors, (e.g. Gannon and Von Backström, 2002), while others chose to neglect secondary losses, (e.g. Von Backström and Gannon, 2004; Denantes and Bilgen, 2006).

Since the total-to-static efficiency is the appropriate measure of performance for a solar chimney turbine the following equation is included into the model:

$$\eta_{ts} = \frac{1}{1 + \frac{\zeta_s c_1^2 + \zeta_a w_{2a}^2 + \zeta_b w_3^2 + c_4^2}{2\Psi}} \tag{29}$$

The total-to-total efficiency can be assessed from

$$\eta_{tt} = \frac{1}{1 + \frac{\zeta_s c_1^2 + \zeta_a w_{2a}^2 + \zeta_b w_3^2}{2\Psi}} \tag{30}$$

The loss coefficients and the relative velocities are evaluated at seven equally spaced radial stations along the span of the blades and the final value of the efficiencies is area-averaged.

2.2.3. Torque evaluation

The torque on the rotors is assessed from $T_q = P/\omega$, where P is the power and ω is the rotational speed. The power is evaluated from the well-known Euler turbine equation. The rotational speed can be written as $\omega = U/r$. Combining the above gives the following equations for the torque:

$$T_{q,\,a} = \dot{m}U_a r_m(c_{u1} - c_{u2}) \tag{31}$$

$$T_{q,\,b} = \dot{m}U_a r_m(c_{u2} - c_{u3}) \tag{32}$$

2.2.4. Solidity and number of blades

Implementing the above loss model it is assumed that the turbine operates near optimum solidity. With the flow angles, the blade aspect ratio, the hub-to-tip radius ratio and the through flow area given, the number of blades is the only free parameter controlling the solidity.

According to Wilson and Korakianitis (1998) minimum-loss solidities are found by setting the tangential lift coefficient, C_L, at a constant value between 0.8 and 1.2. In the following the optimum lift coefficient is assumed to be equal to unity. The optimum axial solidity can be found using their equation 7.5, which is reiterated here for convenience

$$\left(\frac{b_x}{s}\right)_{op} = \left|\frac{2}{C_{L,op}}\cos^2\alpha_{ex}(\tan\alpha_{in} - \alpha_{ex})\right| \tag{33}$$

b_x is the axial blade chord, s is the spacing between the blades and α_{in} and α_{ex} are the flow angles at blade row inlet and outlet. The axial chord of the blade can be approximated with

$$b_x = c_h\cos\left(\frac{\alpha_{in} + \alpha_{ex}}{2}\right) \tag{34}$$

where c_h is the actual blade chord and the fraction denotes an average flow angle through the blade row. The blade chord is obtained by dividing the blade length, l_b, by the blade aspect ratio, R_{asp}. The optimum number of blades can then be obtained from

$$Z = 2\pi r_m\frac{(b_x/s)_{op}}{b_x} \tag{35}$$

[2] This does not represent the real situation, but whether the swirl component is lost through friction or as exit loss at the chimney top, its effect on the turbine performance is the same.

2.2.5. Constraints

The degree of reaction of a free-vortex turbine stage changes along the blade. The lowest degree of reaction is found at the hub and the highest at the tip. To avoid recompression at the hub, which would most probably lead to flow separation and performance deterioration, the reaction should not be less than that of an impulse stage, which is zero. The effect of this constraint, which has been ignored by other authors, is investigated here.

2.2.6. Models for layouts two, three and four

As mentioned above, the models of the other three layouts can be derived from the one presented above by deleting blade rows and their impact on the flow. To model a turbine without inlet guide vanes both the absolute flow angle at the stator exit, α_1, and the stator loss coefficient, ζ_S, are set to zero (Denantes and Bilgen, 2006). Modelling a single rotor turbine, two design variables, the reaction and the dimensionless speed of the second rotor, $R_{n,\mathrm{b}}$ and u_b, fall away. The loss coefficient of the second rotor, ζ_b, is set to zero, and the circumferential component of the turbine exit velocity, c_{u3}, is set equal to c_{u2}, the circumferential component of the exit velocity of the first rotor.

3. Comparison of layouts

For a first comparison the geometrical parameters, the operating conditions and the assumed values for the fluid properties are shown in Table 1. The operating conditions have been extracted from (Von Backström and Gannon, 2004).

3.1. Efficiency

Fig. 5 shows the efficiency prediction for the various turbine layouts over a range of turbine speeds. Most obviously the single rotor layout without inlet guide vanes is not able to reach an acceptable total-to-static efficiency at any speed, with its peak lying at a 66.9%, making either a stator or an additional rotor row inevitable. The peak total-to-static efficiency of the other three layouts lies in a narrow band between 79.6 (SR with IGVs) and 80.1% (CR with IGVs). However, the speed of the first rotor at which these three layouts reach their peak efficiency varies a lot. The single rotor turbine performs very poorly at low speeds, mainly due to high exit losses resulting from a high exit swirl, which is necessary to prevent diffusion at the hub. It performs best at 29.2 rpm. Going to higher speeds, the performance deteriorates mainly due to high rotor losses resulting from high relative flow velocities.

Table 1
Geometrical parameters and operating conditions

Chimney height	H_C (m)	1500
Chimney diameter	d_C (m)	160
Collector outer diameter	d_col (m)	6000
Number of turbines	Z_t	32
Diffuser area ratio	R_D	1.0
Stator blade aspect ratio	$R_\mathrm{asp,s}$	4.0
Rotor blade aspect ratio	$R_\mathrm{asp,r}$	3.0
Hub-to-tip radius ratio	R_HT	0.4
Inlet total pressure	p_t0 (Pa)	90,000
Inlet total temperature	T_t0 (K)	333
Exit total pressure	p_t4 (Pa)	89,200
Mass flow rate	$\dot{m}$ (ton/s)	250
Specific gas constant	R (J/kg)	287
Specific heat at constant pressure	c_p (J/(kg K))	1008
Ratio of specific heats	γ	1.4

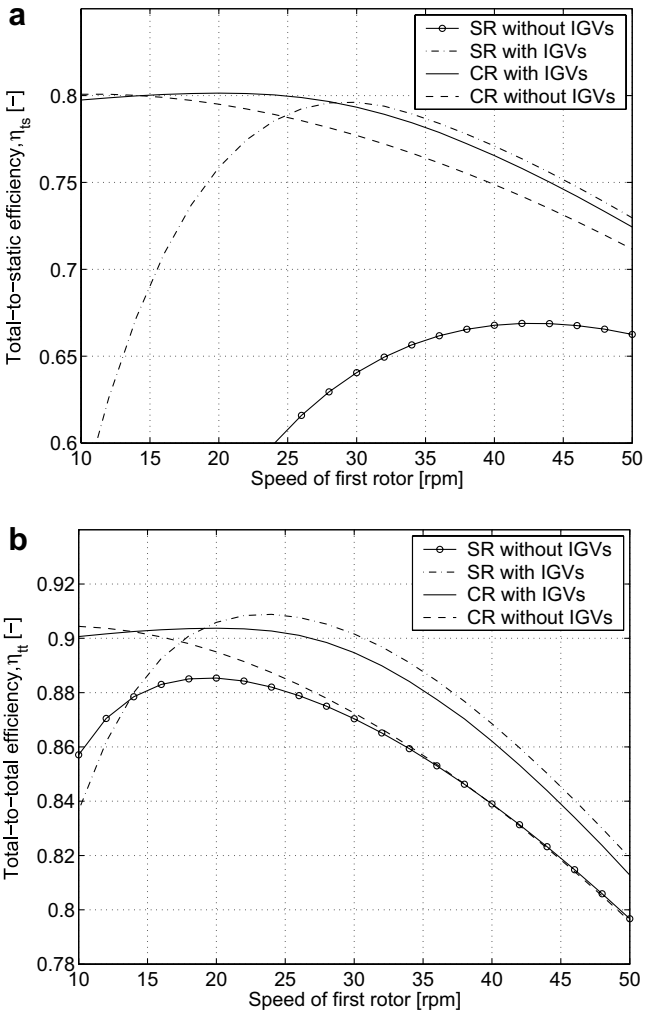

Fig. 5. (a) Total-to-static and (b) total-to-total efficiency prediction for various layouts for a single axial turbine stage.

The counter rotating turbine with inlet guide vanes suffers from the same effect if the first rotor runs faster than at 20 rpm, which is the optimum speed of this layout for the given geometric parameters and operating conditions. Pushing the first rotor to higher speeds, the optimizer slows down the second rotor significantly (Fig. 6). The lower limit of the dimensionless speed of the second rotor has been set to a 10th of the first rotor's speed ($u_\mathrm{b,min} = -0.1$). This limit is reached at a speed of 38 rpm of the first rotor. For speeds lower than the optimum, the performance deteriorates only slightly, since the exit swirl does not increase a lot.

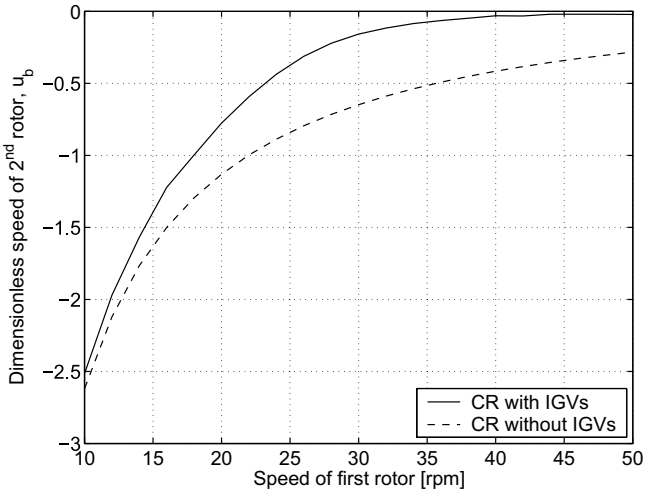

Fig. 6. Dimensionless speed of the second rotor vs. turbine speed.

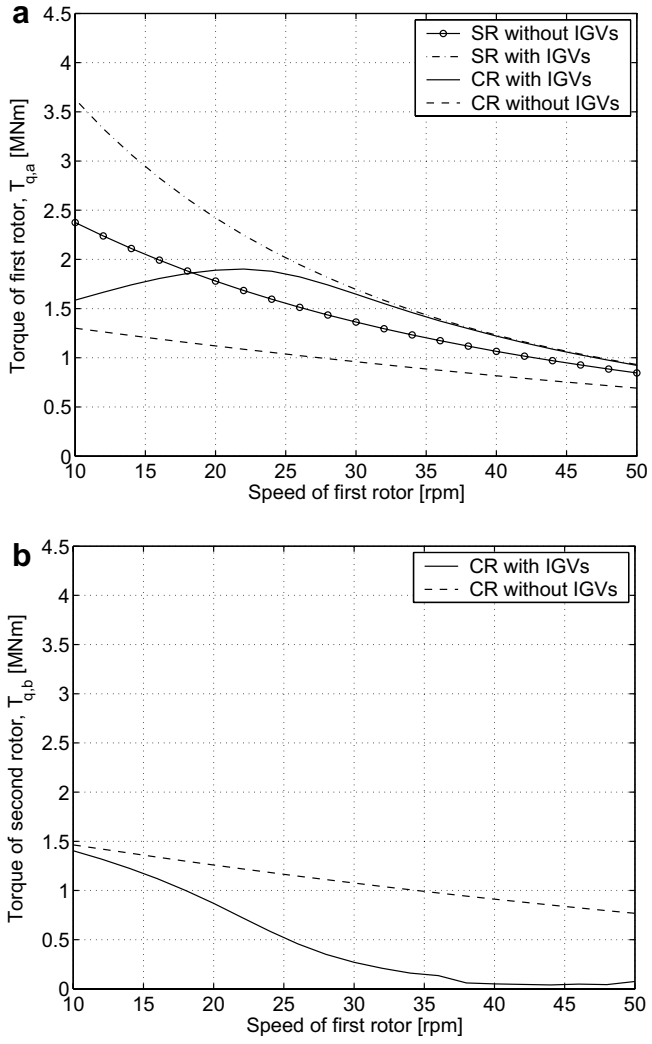

Fig. 7. Torque on first (a) and second rotor (b) for various layouts for a single axial turbine stage.

The counter rotating turbine without inlet guide vanes follows a similar trend as the previous layout, but its peak is shifted to the low speed side resulting in a high torque for high performance (Fig. 7).

3.2. Torque

Size and cost of the drive train is proportional to the torque delivered by the turbine. Since the power is proportional to the product of the rotational speed ω and the torque T_q, speeding up the turbine obviously reduces the torque for the same power output (Fig. 7). Since the performance peaks of the counter rotating layouts lie at relatively low speed the torque on the shafts is high, leading to a bigger and more expensive drive train.

This is very pronounced without IGVs with a torque of 1.28 and 1.45 MN m for the two shafts respectively. With IGVs the torque is slightly higher in the first rotor (1.35 MN m) but lower in the second rotor (0.87 MN m). Even though the single rotor solution with IGVs has only one rotor to carry all the load, the torque at peak performance is relatively low (1.74 MN m) thanks to the high speed. The torque for the rotor-only layout follows a similar trend but on a lower level due to the lower efficiency.

3.3. Solidity and number of blades

The required number of blades is obviously highly dependent on the chosen blade aspect ratio. With the parameters chosen here, results are as follows: besides the rotor-only layout, which requires only six blades, the layout with the lowest number of blades is the counter rotating turbine without IGVs, requiring 32 blades in its peak performance point (0 for the stator/16 for the first/16 for the second rotor). The single rotor layout requires 47 (31/16/0) and the counter rotating turbine with IGVs 66 blades (32/18/16).

4. Comparison of various modelling approaches

The main difference between the turbine model presented here and earlier models of other researchers are the implementation of a model for secondary losses, averaging over several radial sections for efficiency evaluation and the constraint on reaction to prevent diffusion at the hub. In Table 2 the results obtained with the current model are compared to simulations where one or all of the above features of the model have been removed. The efficiency is generally higher for the simpler models—8.5% points for the rotor-only layout and approximately 6% points for the other three layouts, if all of the above features have been removed—and the optimum rotor speed is significantly shifted. Neglecting the secondary losses has the biggest impact on the efficiency.

Removing the constraint on the degree of reaction has only a slight impact but does not affect all layouts in the same way: it has no impact on the rotor-only layout but increases the peak efficiency estimates of the three other

Table 2
Turbine parameters for various layouts and modelling approaches—Model 1: current model; Model 2: no constraint preventing recompression at the hub; Model 3: no radial averaging; Model 4: no secondary loss model; Model 5: models 2, 3, and 4 combined

Model		Single rotor		Counter rotating	
		No IGVs	With IGVs	No IGVs	With IGVs
1	η_{ts} (%)	66.9	79.6	80.1	80.1
	N_a (rpm)	42.8	29.2	10.9	20.0
	u_b	n/a	n/a	−2.35	−0.77
2	η_{ts} (%)	66.9	80.2	81.0	80.7
	N_a (rpm)	42.8	25.4	11.4	15.6
	u_b	n/a	n/a	−1.63	−0.95
3	η_{ts} (%)	69.4	82.7	82.8	82.6
	N_a (rpm)	45.8	32.1	7.5	26.0
	u_b	n/a	n/a	−3.84	−0.31
4	η_{ts} (%)	73.3	83.6	84.1	84.2
	N_a (rpm)	53.1	31.3	12.9	19.8
	u_b	n/a	n/a	−2.09	−0.93
5	η_{ts} (%)	75.4	86.0	86.2	86.0
	N_a (rpm)	56.8	33.8	7.8	23.1
	u_b	n/a	n/a	−3.89	−0.66

layouts, but not to the same extent with each of them. This could induce a bias towards certain layouts.

5. Conclusions

It has been shown that slight changes in the modelling of solar chimney turbines have a significant impact on the performance prediction. Neglecting secondary losses, for example, may lead to a significant overestimation of the turbine efficiency. Ignoring the constraint of recompression in the blade row, on the other hand, does not affect all layouts in the same way, which could lead to bad choices early in the preliminary phase of a large-scale solar chimney project.

It has also been found that the rotor-only layout is the simplest and cheapest layout requiring comparably few blades and a small drive train. Its total-to-static efficiency is very low, however, because the swirl at the turbine exit cannot be recovered. For the three other layouts the maximum total-to-static efficiency is much better and lies in a narrow band with the counter rotating turbines performing slightly better, however only at low speeds, which leads to a higher torque for the same power output.

In future work the model presented here can be linked to a cost model, in order to assess which layout provides the lowest cost of electricity.

References

Bywaters, G., John, V., Lynch, J., Mattila, P., Norton, G., Stowell, J., Salata, M., Labath, O., Chertok, A., Hablanian, D., 2004. Northern Power Systems WindPACT drive train alternative design study report, Tech. Rep. NREL/SR-500-35524, National Renewable Energy Laboratory, Colorado, revised October 2004.

Cai, R., Wu, W., Fang, G., 1990. Basic analysis of counter-rotating turbines, in: Proceedings of the 35th International Gas Turbine and Aeroengine Congress and Exposition, ASME.

Denantes, F., Bilgen, E., 2006. Counter-rotating turbines for solar chimney power plants. Renewable Energy 31, 1873–1891.

Gannon, A.J., Von Backström, T.W., 2002. Solar chimney turbine part 1 of 2: Design, in: International Solar Energy Conference, pp. 335–341.

Horlock, J.H., 1966. Axial Flow Turbines – Fluid Mechanics and Thermodynamics. Butterworths, London.

Louis, J.F., 1985. Axial flow contra-rotating turbines, in: Proceedings of the 30th International Gas Turbine Conference and Exhibit, ASME, Houston.

Ozgur, C., Nathan, G., 1971. A study of contrarotating turbines based on design efficiency. Journal of Basic Engineering 93, 395–404.

Poore, R., Lettenmaier, T., 2003. WindPACT Advanced wind turbine drive train designs study, Tech. Rep. NREL/SR-500-33196, National Renewable Energy Laboratory, Colorado.

Schwarz, G., Knauss, H., 1981. Strömungstechnische Auslegung des Aufwindkraftwerks Manzanares (Aerodynamic design of the solar chimney power plant in Manzanares), Tech. rep., Institut für Aerodynamik, Unversität Stuttgart, (in German).

Von Backström, T.W., Gannon, A.J., 2004. Solar chimney turbine characteristics. Solar Energy 76, 235–241.

Wilson, D.G., Korakianitis, T., 1998. The Design of High-Efficiency Turbomachinery and Gas Turbines, 3rd ed. Prentice Hall, London.

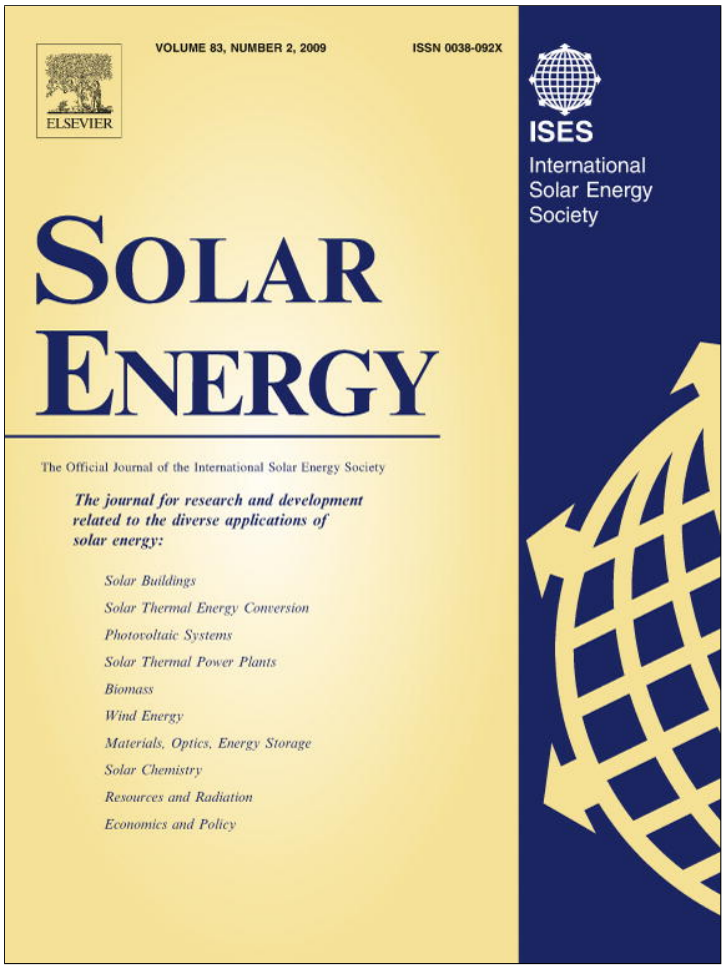

Available online at www.sciencedirect.com
ScienceDirect
Solar Energy 83 (2009) 246–256
SOLAR ENERGY
www.elsevier.com/locate/solener

Cost analysis of solar chimney power plants

T.P. Fluri [a,*], J.P. Pretorius [a], C. Van Dyk [b], T.W. Von Backström [a], D.G. Kröger [a], G.P.A.G. Van Zijl [b]

[a] Department of Mechanical and Mechatronic Engineering, University of Stellenbosch, Private Bag X1, Matieland 7602, South Africa
[b] Department of Civil Engineering, University of Stellenbosch, Private Bag X1, Matieland 7602, South Africa

Received 6 November 2006; received in revised form 14 July 2008; accepted 30 July 2008
Available online 26 August 2008

Communicated by: Associate Editor S.A. Sherif

Abstract

Several cost models for large-scale solar chimney power plants are available in the literature. However, the results presented vary significantly, even in cases where the input parameters and the used models are supposedly very similar. The main objective of this paper is to clarify this matter by comparing previous cost models to a newly developed alternative model. Further, the impact of carbon credits on the levelised electricity cost is also investigated.

A reference plant is introduced, with dimensions and financial parameters chosen specifically for the purpose of making the results of this analysis comparable to those of previous publications. Cost models are presented for the main components of a solar chimney power plant, i.e. the collector, the chimney and the power conversion unit. Results show that previous models may have underestimated the initial cost and levelised electricity cost of a large-scale solar chimney power plant. It is also shown that carbon credits significantly reduce the levelised electricity cost for such a plant.

Keywords: Solar chimney power plant; Levelised electricity cost; Cost modelling

1. Introduction

To assess the economic competitiveness of power plants, reliable cost models are essential. The present paper compares the results of solar chimney cost models found in the literature to results of a model developed by the authors.

Cost models for large-scale solar chimney power plants are presented by Schlaich (1995), Schlaich et al. (2004) and Bernardes (2004). Schlaich (1995) gives cost values for all plant components for various plant sizes, presents a procedure to evaluate the levelised electricity cost (LEC) and investigates the sensitivity of the LEC to the interest rate and the length of the depreciation period. Schlaich et al. (2004) give the component cost and the LEC for various plants for fixed economic parameters. Bernardes (2004) presents a study similar to the one of Schlaich (1995); he also calculates the cost for plants of various sizes, presents a procedure to evaluate the LEC and investigates the sensitivity of the LEC to the economic parameters. In addition to that, he derives a parametric cost model for the main plant components (collector, chimney and power conversion unit).

For plants of similar size, the three publications discussed above predict chimney costs between 64.4 and 156.0 M€, specific investment costs between 3000 and 4020 €/kW and levelised electricity costs between 0.037 and 0.1045 €/kWh (see Table 1). These rather large differences warrant further investigation of the topic.

This paper presents a more detailed cost model, including a first detailed cost model for the power conversion unit, and compares the results to the above sources.

* Corresponding author. Tel.: +27 2 18084281.
E-mail address: thomas.fluri@alumni.ethz.ch (T.P. Fluri).

0038-092X/$ - see front matter © 2008 Elsevier Ltd. All rights reserved.
doi:10.1016/j.solener.2008.07.020

Nomenclature

Latin symbols

a	annum
A	equivalent annual value or annual cash flow (€)
b	exponent or coefficient
C	coefficient
d	diameter (m)
f	rate of price increase (%)
F	equivalent future value (€)
H	height (m)
i	interest or inflation rate (%)
K	loss coefficient
m	mass (kg)
$\dot{m}$	mass flow rate (kg/s)
N	depreciation period or construction period (years)
N	refractive index or number
P	pitch (m) or equivalent present value (€) or Power (kW)
p	pressure (N/m^2)
r	radius (m)
t	thickness (m) or metric tons

Subscripts

CC	carbon credits
c	chimney
g	ground
i	inlet
OM	operation and maintenance
r	roof or radial
rs	ring stiffener
s	support
t	tangential
turb,i	turbine inlet

Abbreviations

APO	annual power output
BOS	balance of station
LEC	levelised electricity cost
O&M	operation and maintenance
PCU	power conversion unit
PV	present value
R	South African Rand

The impact of carbon credits on the LEC is also investigated. For the purpose of comparison, a reference solar chimney power plant with similar dimensions as the 100 MW plant proposed by Schlaich et al. (2004) is selected (Configuration II in Table 1) and the same financial parameters are used. A comparison to the 100 MW plant of Bernardes (2004) (Configuration III in Table 1) is also presented. The following conversion rates between the South African Rand, the Euro and the US Dollar are used in this paper: US$ 1.2 = €1 and €1 = R8 (South African Rand). A schematic illustration of a solar chimney power plant is given in Fig. 1.

2. Plant performance

Pretorius et al. (2004) developed a relatively detailed computer simulation program to simulate the performance of large-scale solar chimney power plants. An updated version of this program is used here, as specified in the publication by Pretorius and Kröger (2006a). The simulation program solves the thermo-flow field in the collector and chimney of a solar chimney power plant. The relevant conservation of mass, momentum and energy equations are solved simultaneously using finite difference methods. The performance of the plant is ascertained by determining the mass flow rate through the system that will maximize the power output of the plant at a particular time.

Meteorological data (ambient air temperature, humidity of the air, solar irradiation and wind speed) from a specific location (Sishen, South Africa; latitude: 27.67° South; longitude: 23.00° East) are used as input to the program. Factors such as the position of the sun throughout the year at the particular location, shadow cast by the chimney and all frictional, inlet, outlet, support and heat losses are taken into account. Sandstone has been assumed as the ground material. A dry adiabatic lapse rate has been assumed for the vertical temperature profile inside and outside the chimney. Wind effects have been disregarded. For a plant which is similar to Configuration II the main parameters and its typical operating environment are given in Table 2.

Simulation results for this plant predict a lower electricity output of 190.4 GWh/a, in comparison to the 320 GWh/a predicted by Schlaich et al. (2004) and a lower peak power output of 66 MW, instead of 100 MW. For a plant identical to Configuration III, hence with a collector diameter of 4950 m, a collector inlet height of 3.5 m and a chimney height of 850 m, the simulation predicts an annual output of 181.32 GWh and a peak power output of 62 MW. Bernardes (2004) predicts an annual power output of 281 GWh and 100 MW peak power for such a plant. One possible reason for the differences in power output prediction is that (Pretorius and Kröger, 2006a) implemented novel heat transfer equations. The impact of implementing these equations is discussed in another publication of Pretorius and Kröger (2006b) and is shown to be significant.

3. Component design and cost

In the following sections cost models for the three main components of the solar chimney power plant are introduced and the resulting costs are summarized.

Table 1
Comparison of 100 MW plants from different sources: Configuration I from Schlaich (1995), Configuration II Schlaich et al. (2004) and Configuration III from Bernardes (2004) (cost values in M€)

Configuration	I	II	III
Capacity, MW	100	100	100
Chimney height, m	950	1000	850
Chimney diameter, m	115	110	110
Collector diameter, m	3600	4300	4950
Glass roof height at inlet, m	6.5	3	3.5
Electricity output, GWh/a	305.2	320	281
Collector cost	134.8	131.0	190.0
Chimney cost	68.2	156.2	64.4
Power conversion unit cost	79.8	75.0	76.7
Roads, buildings, workshops	2.0	n/a	2.71
Infrastructure	4.3	n/a	6.5
Planning, site management	2.9	n/a	n/a
Rounding	8.1	n/a	n/a
Engineering, tests, misc.	n/a	40	n/a
Electrical installations	n/a	n/a	10.5
Insurance	n/a	n/a	1.58
Overall investment cost	300.0	402.0	352.4
O&M (1st year), M Euro	1.0	1.9	1.0
Depreciation period, y	20	30	30
Construction period, y	0	0	2
Real interest rate,%	n/a	6	8
Nominal interest rate,%	8	n/a	n/a
Inflation rate,%	3.5	n/a	n/a
LEC, Euro/kWh	0.1045	0.1000	0.0370

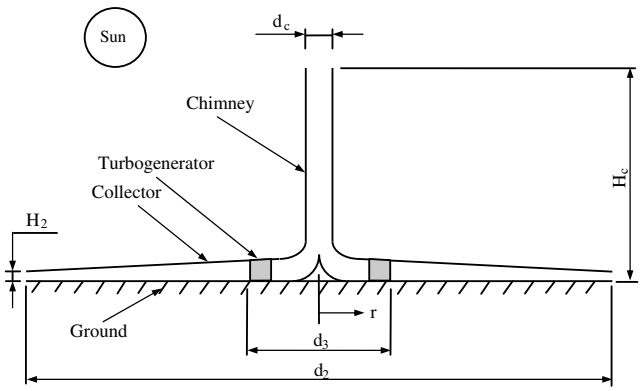

Fig. 1. Schematic illustration of a solar chimney power plant.

3.1. Chimney

The two chimneys investigated here both have a diameter of 110 m. They have a height of 1000 m (Configuration II) and 850 m (Configuration III), respectively. The cost of the chimney is a function of the volume of material used, the specific material cost, the construction cost and transport cost. The chimney design is not considered in this cost study. Refer to literature for reports on the design specifications (Schlaich et al., 2004; Goldack, 2004).

The main assumptions for the model presented in this paper are the following:

- The chimney is constructed of thin shell reinforced high performance concrete.
- The wall thickness distribution proposed for a 1000 m tall chimney with a 170 m diameter (Schlaich et al., 2004) is used for Configuration I; the wall thickness is 0.99 m decreasing linearly to 0.3 m at 550 m height, from where it remains constant up to 1000 m. To get the values for the smaller chimney it is assumed that the wall thickness is linearly proportional to the chimney height. Hence, the base thickness of this chimney is 0.84 m, and from 550 m height the wall thickness is 0.255 m.
- In order to minimize losses, the through-flow area of the chimney should increase with height (Von Backström and Gannon, 2000). The decrease in wall thickness is accommodated through increase in the inner diameter while the outer diameter stays constant at 110 m.
- For both chimney sizes the ring stiffener configuration proposed for a 1000 m tall chimney with a 170 m diameter, which consists of four stiffeners (Schlaich et al., 2004) is used.
- Each ring stiffener consists of 72 flat structural steel beams, each of 0.63×0.06 m cross-section, spanning the radius from a stiff outer ring of the same cross-section at the chimney perimeter to a connector hub at the centre of the stiffener arrangement (Van Dyk, 2001).
- For the chimney foundation normal concrete with 60 kg/m^3 reinforcement is used.

Cost assumptions are:

- High performance concrete cost: 125 €/m^3.
- Normal concrete cost: 100 €/m^3.

Table 2
Main parameters of a reference plant and its typical operating environment

Collector roof (Glass)	
Emissivity of glass	$e_r = 0.87$
Roughness of glass	$\varepsilon_r = 0$ m
Extinction coefficient of glass	$C_e = 4$ m^{-1}
Refractive index of glass	$n = 1.526$
Thickness of glass	$t_r = 0.004$ m
Roof shape exponent	$b = 0.75$
Perimeter (inlet) height	$H_2 = 6$ m
Outer diameter	$d_2 = 4300$ m
Inner diameter	$d_3 = 400$ m
Inlet loss coefficient	$K_i = 1$
Support diameter	$d_s = 0.12$ m
Support drag coefficient	$C_{sD} = 1$
Support tangential pitch	$P_t = 15$ m
Support radial pitch	$P_r = 15$ m
Ground	
Type	Sandstone
Emissivity (treated surface)	$e_g = 0.9$
Absorptivity (treated surface)	$\alpha_g = 0.9$
Density	$\rho_g = 2160$ kg/m^3
Specific heat capacity	$c_{pg} = 710$ J/kgK
Thermal conductivity	$k_g = 1.83$ W/mK
Roughness	$\varepsilon_g = 0.05$ m
Chimney (concrete)	
Height	$H_c = 1000$ m
Diameter	$d_c = 110$ m
Ring stiffener drag coeff. (each)	$K_{rs} = 0.025$
Number of ring stiffeners	$n_{rs} = 4$
Inside wall roughness	$\varepsilon_c = 0.002$ m
Power conversion unit	
PCU efficiency	$\eta_{PCU} = 80\%$
Inlet loss coefficient	$K_{turb,i} = 0.14$
Ambient conditions	
Atmospheric pressure (ground)	$p_a = 90$ kN/m^2

- Reinforcement cost: 750 €/ton @ 120 kg/m^3.
- Construction, concrete cover and labour cost: 312.5 €/m^3.
- Materials hoisting cost are equal to 20% of ring stiffener cost and chimney shell material and construction cost excluding transport cost.
- The ring stiffener cost is estimated by determining the cost of the volume of steel at 1250 €/ton.
- Construction and labour on the ring stiffeners and hoisting of ring stiffeners each amount to 20% of the stiffener material cost.
- The transport cost is based on the total weight of the chimney system and estimated at €625 per 30 ton truckload over an average distance of 300 km (PFG Building Glass, 2006). It is assumed that the transport infrastructure incorporated in the balance of station cost for the power conversion unit is sufficient for the transport requirements considered here.
- The chimney support column configuration proposed in previous research (Van Dyk, 2004) is used to conceptualize a foundation design. A foundation structure for each of the 18 columns consisting of 12 shear walls of 50 m × 8 m × 0.5 m each yields a total cost of € 9.23M. To allow for the cost of construction the material cost is multiplied by 2.0 resulting in a total foundation cost of € 18.45M.

The total cost of the 110 m diameter chimney amounts to € 145M (Table 3). The chimney shell cost (80%) largely outweighs the foundation (14%) and stiffener cost (6%), especially due to its high construction and transport cost. Schlaich et al. predict a total cost of € 156M. The lower values in the present paper may result from lower South African construction and labour cost.

To evaluate the cost of the foundation for the smaller chimney the volume of the foundation for the chimney is assumed to be linearly proportional to the volume of the chimney material. The chimney cost components for both configurations are listed in Table 3. The total cost of the smaller chimney, calculated with the method presented above, is € 111M, a value 1.72 times greater than the value found by Bernardes (2004).

3.2. Collector

The collector consists of a transparent roof elevated by a support structure. Glass is used as the transparent material. The glass roof extends from the outer perimeter of the collector to a radius of 200 m from the centre of the chimney. The support structure consists of steel columns supporting a truss-work matrix from which the glass is suspended. The design of the collector is based on the work of De Villiers (2001). The two collectors investigated here have an outer diameter of 4300 m (Configuration II) and 4950 m (Configuration III), respectively.

The main assumptions for the model presented in this paper are the following:

- The actual roof height increases towards the centre of the collector as described by the relation $H = H_2(r_2/r)^b$ (Pretorius et al., 2004), where b is the roof shape exponent ($b = 0.75$), H_2 is the roof height at the collector inlet ($H_2 = 6$ m for Configuration II and $H_2 = 3.5$ m for Configuration III) and r_2 is the outer radius of the collector. Using these values results in an average collector roof height of 9.2 m for the configuration of Schlaich et al. and of 5.3 m for the configuration of Bernardes. In the design and cost calculations the collector height is assumed to be constant and equal to these averages.
- The airflow drag due to column cross-section is negligible, therefore the cheapest column cross-section is chosen.
- The collector is single-glazed, using 4 mm thick tempered glass with a fracture strength of 41 MPa as proposed by De Villiers (2001).
- A glass cost of 11.40 €/m^2 is assumed (PFG Building Glass, 2006).
- The transport cost as stated in the previous section applies.

Table 3
List of chimney cost for the configurations proposed by (A) Schlaich et al. (2004) and (B) Bernardes (2004) in M€.

	Material		Construction		Hoisting		Transport		Total	
	A	B	A	B	A	B	A	B	A	B
Chimney shell	36.19	26.68	52.60	38.78	17.76	13.09	8.42	6.20	114.97	84.75
Ring stiffeners	6.40	6.40	1.28	1.28	1.28	1.28	0.11	0.11	9.07	9.07
Chimney foundation	9.23	7.58	9.23	7.58	0.00	0.00	2.16	1.59	20.61	16.75
Total	51.82	40.66	63.11	47.64	19.04	14.37	10.68	7.90	144.66	110.58

Table 4
List of collector costs for the configurations proposed by (A) Schlaich et al. (2004) and (B) Bernardes (2004) in M€

Part	Material		Construction		Transport		Total	
	A	B	A	B	A	B	A	B
Glass	164.12	219.03	32.82	43.81	2.76	3.68	199.70	266.51
Column system	15.56	15.34	3.11	3.07	0.72	0.66	19.39	19.07
Glass support matrix	228.78	305.00	45.76	61.00	3.21	4.29	277.75	370.29
Total	408.46	539.37	81.69	107.87	6.69	8.63	496.84	655.87

More detail on the collector design calculations is given in Appendix A.

The total cost of the 4300 m collector assembly is € 497M, largely made up by the glass support matrix (56%) and the glass (40%) (Table 4). The column system makes a minor contribution (4%). The total cost is more than three and a half times higher than the estimation by Schlaich et al. The large discrepancy between cost models could be due to Schlaich et al. using a plastic membrane as transparent material in parts of the collector instead of glass (Schlaich et al., 2004).

The cost for the collector of Configuration III is higher than the one of Configuration II due to the larger collector roof area. According to the cost model presented here the total collector cost for Configuration III is € 655.9M (Table 4), which is almost three and a half times more than predicted by Bernardes (2004) (€ 190M).

3.3. Power conversion unit (PCU)

A multiple horizontal axis turbine configuration consisting of 22 turbogenerators is used. Bernardes (2004) simply assumes a cost of 767 € per kW rated power for the PCU. For this paper a more comprehensive cost model has been developed (see Appendix B), where for most components the cost is considered to be a function of mass. In this section the main assumptions and results of this model are presented.

The main assumptions are:

- There is no diffuser after the turbines.
- The generator is directly driven by the main shaft, i.e. no gearbox is necessary.
- Inlet guide vanes are included and their cost is assumed to be equal to the total cost of the rotor blades.
- The cost for turbine ducts and the central structure are part of the PCU cost.
- A mature production process is assumed for all components.

The current model gives a total cost of € 26.9M for the power conversion unit. With a peak power of 66 MW this equals a cost per installed power of 407 €/kW—a 47% decrease from the assumption of Bernardes. This can be explained by the fact that his assumption is based on wind turbine cost of the early 90's, while the model presented here is based on wind turbine cost of around the year 2002.

The cost of the various components of the PCU is shown in Fig. 2. The balance of station cost, which includes the cost for foundations, transportation, roads and civil works, for assembly and installation, for electrical interfaces and connections and for permits and engineering accounts for 56.7% of the total cost. Other important cost factors are the generators (14.7%), the turbine rotors (10.5%), the power electronics (7.1%) and the ducting (9.0%). The cost of the central structure, which redirects the flow from horizontal to vertical, as well as the control and support costs are small.

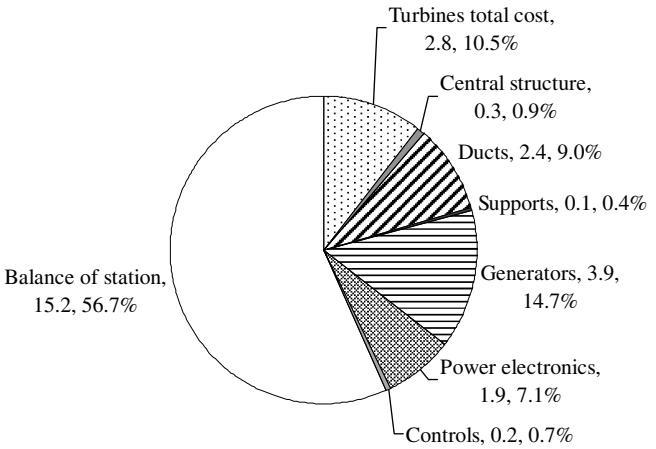

Fig. 2. Pie chart of costs of the PCU [M€].

Table 5
Summary of costs of the solar chimney power plant components according to the model presented in this paper and their comparison to values in literature

Configuration	Schlaich et al.		Bernardes	
	Cost	Rel. to Schlaich et al. (2004)	Cost	Rel. to Bernardes (2004)
Chimney cost	145M€	93%	111M€	172%
Collector cost	497M€	379%	656M€	345%
PCU cost	27M€	36%	25M€	33%
Total investment cost	668M€	166%	792M€	225%
Specific investment cost	10,025€/kW	249%	12,766€/kW	362%

3.4. Component cost summary

The cost model presented here predicts more than one and a half times the total investment cost and almost two and a half times the specific investment cost compared to literature (Table 5). This is mainly due to much higher chimney and collector cost, and because the predicted yield is much lower (see Section 2).

4. Electricity cost calculations

In this section the levelised electricity cost (LEC) of the plants discussed in the previous sections is evaluated. First, the method to evaluate the LEC is demonstrated on Configuration II and then on Configuration III.

4.1. Configuration II

The annual yield as predicted by the numerical model of Pretorius et al. (2004) and the solar chimney construction cost as calculated in this paper are employed, based on the dimensional details by Schlaich et al. (2004). Schlaich et al. (2004) specify an annual operation and maintenance cost of € 1.9M. The present calculation assumes an operation and maintenance cost for the first year of operation of € 1.9M. It is assumed that this value will increase with inflation (3.5%), while assuming an interest rate of 6%. When employing the following modified equation by Sullivan et al. (2000), the present equivalent value of these costs over the lifetime of the plant is found

$$P_{\mathrm{OM}} = \frac{A_1}{f-i}\left[\left(\frac{1+f}{1+i}\right)^N - 1\right] = \frac{1.9\times10^6}{0.035-0.06}\left[\left(\frac{1+0.035}{1+0.06}\right)^{30} - 1\right] = 38.9\times10^6\ \text{Euro} \quad (1)$$

where A_1 is the cash flow at the end of the first year, f is the inflation rate, i is the interest rate and N is the lifetime in years. When adding this to the solar chimney capital cost of € 668M, the total present value over the lifetime of the project is determined. An equivalent annual cost over the project lifetime can be calculated according to the following equation by Sullivan et al. (2000)

$$A = P\left[\frac{i(1+i)^N}{(1+i)^N-1}\right] = (668.4+38.9)\times10^6\left[\frac{0.06(1+0.06)^{30}}{(1+0.06)^{30}-1}\right] = 51.4\times10^6\ \text{Euro} \quad (2)$$

where P is the present value of all costs, hence, the sum of the total plant cost and the equivalent annual value of the operating and maintenance cost. The levelised electricity cost (LEC) is now ascertained by dividing the equivalent annual cost by the annual power output

$$\mathrm{LEC} = \frac{A}{\mathrm{APO}} = \frac{51.4\times10^6}{190.4\times10^6} = 0.270\ \text{Euro/kWh} \quad (3)$$

The current calculation predicts an LEC of more than two and a half times the cost predicted by Schlaich et al. (2004) (see Table 6). This is the result of a higher capital cost and a much lower annual power output prediction. Even when utilizing the annual power output of Schlaich et al. (2004), the determined LEC is still much higher at 0.161 €/kWh.

4.2. Configuration III

Similar calculations have been performed for Configuration III. The differences in the LEC evaluation procedure are outlined here. Bernardes (2004) specifies a construction period of 2 years. Assuming that the entire capital is borrowed before the construction period, interest will be paid on this amount over the construction period. From the following equation by Sullivan et al. (2000), the capital cost plus interest at rate i (8%) at the end of the construction period N (2 years) is

Table 6
Levelised electricity cost comparison to the calculations of Schlaich et al. (2004) (interest rate = 6%; inflation rate = 3.5%; depreciation period = 30 years)

		Schlaich et al. (2004)	Current calculation
Annual power output	GWh	320.0	190.4
Capital cost	M€	402.0	668.4
Cumulative PV of OM	M€	34.9	38.9
Levelised electricity cost (LEC)	€/kWh	0.1	0.270

$$F = P(1+i)^N = 791.5(1+0.08)^2 = 923.2 \times 10^6 \text{ Euro} \quad (4)$$

where F is known as the future equivalent value.

Bernardes (2004) further specifies an operating and maintenance cost for the first year of operation of € 1M. This analysis employs the same cost for the first year, while assuming that the amount will increase with inflation (3.25%) and that the interest rate is 8%. Employing Eq. (1), the equivalent present value of the operating and maintenance costs over the plant lifetime (30 years) is determined as follows

$$P = \frac{1.00 \times 10^6}{0.0325 - 0.08}\left[\left(\frac{1+0.0325}{1+0.08}\right)^{30} - 1\right] = 15.59 \times 10^6 \text{ Euro} \quad (5)$$

Adding the results of Eqs. (4) and (5) gives the total present value over the lifetime of the project. Using this value with Eqs. (2) and (3) gives an LEC of 0.434 €/kWh, which is 3.4 times the cost calculated with the same procedure, but using the cost and performance values presented by Bernardes (2004) (see Table 7). Bernardes (2004) actually quotes a very low LEC of 0.037 €/kWh, which is believed to result from an error in calculation. Analogous to the comparison with Schlaich et al. (2004), the higher LEC found in this analysis is due to a much higher capital cost and lower annual power output prediction. Even when introducing the annual output of Bernardes (2004), the LEC remains much higher at 0.294 €/kWh.

5. Impact of carbon credits

To investigate the potential impact of carbon credits on the levelised cost of electricity it is assumed that a coal-fired power plant, which typically emits 0.95 kg of CO_2/kWh (US Energy Information Administration, 2006), would be substituted with the solar chimney. A solar chimney power plant with Configuration II would then reduce CO_2 emissions by

$$190.4 \text{ GWh/a} \times 0.95 \times 10^6 \text{ kg/GWh} = 180.88 \times 10^6 \text{ kg/a} \quad (6)$$

The current analysis neglects the fact that the construction process for the first solar chimney power plant will be driven by fossil fuels. Assuming a carbon credit price of € 27.15/t CO_2 (PointCarbon, 2006), the revenue received by the solar chimney power plant in the first year of operation would be

$$(180,880)(27.15) = 4.91 \times 10^6 \text{ Euro} \quad (7)$$

It is assumed that this amount increases with inflation each year. Hence, according to Eq. (1), the present value of the carbon credit over the project lifetime is

$$P_{CC} = \frac{4.91 \times 10^6}{0.035 - 0.06}\left[\left(\frac{1+0.035}{1+0.06}\right)^{30} - 1\right] = 100.44 \times 10^6 \text{ Euro} \quad (8)$$

The present value of all costs is then $P = 668.4 + 38.9 - 100.4 = 606.9$ M€. Using this value with Eqs. (2) and (3) gives a reduced LEC of 0.232 €/kWh.

When introducing the annual yield of 320 GWh into the same calculation (as predicted by Schlaich et al. (2004)) the LEC becomes 0.138 €. This significantly lower solar chimney LEC is a direct result of a larger contribution by carbon credit revenue.

Table 7
Levelised electricity cost comparison to the calculations of Bernardes (2004) (interest rate = 8%; inflation rate = 3.25%; depreciation period = 30 years; construction period = 2 years)

		Bernardes (2004)	Current calculation
Annual power output	GWh	281.0	181.3
Capital cost (before construction)	M€	325.4	791.5
Capital cost (after construction)	M€	379.5	923.2
Cumulative PV of O&M	M€	15.59	15.59
Levelised electricity cost (LEC)	€/kWh	0.125	0.430

6. Conclusions

The results from similar cost investigations for solar chimney power plants found in literature are not confirmed by this paper. Instead, around 1.7–2.3 times the absolute and 2.5–3.6 times the specific investment cost are predicted. In addition, the levelised electricity cost is between 2.7 and 3.4 times higher. These discrepancies are due to much higher plant cost and lower annual power output predictions. This suggests that previous investigations were too optimistic and that the solar chimney power plant may be more expensive than previously predicted. It is also shown in the present paper that carbon credits, which have not been taken into account by previous studies, significantly reduce the levelised electricity cost for such a plant.

Solar chimney power plant cost may be significantly reduced if construction materials are supplied by dedicated manufacturing facilities located on-site. Additionally, these costs may be even lower when assuming the construction of multiple plants, but are unlikely to be as low as those assumed by Schlaich et al. (2004) and Bernardes (2004).

Acknowledgement

The authors would like to thank VolkswagenStiftung, Germany, for the financial support.

Appendix A. Collector loading and support structure design

A.1. Loading

The collector must be strong enough to resist the dead load, the live load, including hail, and the wind load.

The dead load is constituted by the glass roof, the glass support matrix and column system.

The live load of 0.5 kN/m^2 is determined from SABS (1989) as for inaccessible roofs of area smaller than 3 m^2.

Wind load is constituted by vertical and lateral wind pressure and frictional wind force. Assume that the external wind effect has no influence on the air velocity under the collector; hence the air inside the collector moves only at the velocity caused by the solar chimney working principle. Calculations are based on procedures from literature (Van Dyk, 2004, 2001) and the results are summarized in the following list.

Downward pressure	kN/m^2	0.535
Upward pressure	kN/m^2	0.642
Frictional force per brace	kN	70.26
Lateral force per brace	kN	0.224

A.2. Support structure design

The design of the support structure is based on a design by De Villiers (2001). The proposed glass roof matrix is supported on pinned steel columns with bracing in two perpendicular directions between every fifth pinned column and the columns adjacent to it to accommodate for lateral forces. The steel columns supporting the glass are spaced at 15 m intervals. The airflow drag losses caused by the columns are considered negligible; hence the most economic column cross-section is used, even if it is not optimal from an aerodynamic perspective.

IPE$_{AA}$120 Grade 350WA steel columns supported by cable guys to stabilise the column around its weak axis proves to be the most cost effective. Between adjacent columns after every fifth column lateral bracing is introduced. It consists of two diagonal braces (100 × 100 × 8 angle beam) and two 8 mm cables. Each column foundation comprises a 800 mm × 800 mm × 300 mm = 0.192 m^3 concrete block. Unit costs are summarized in the following list.

Steel columns (IPE$_{AA}$120)	R/m	69.24
Cable guys	R/m	14.70
Angle beam	R/m	102
Concrete cost	R/m^3	800
Reinforcement steel cost	R/ton	6000
Reinforcement quantity	kg/m^3	60
Cover cost – horizontal	R/m^2	175
Cover cost – vertical	R/m^2	125

Note: when costs in this report are adapted from values from previous research they are adjusted to portray the present value assuming a rate of inflation of 6%.

In previous research the creation of a glass support matrix was attempted through various methods (De Villiers, 2001), the details of which will not be discussed here. The truss-work approach proves to be the cheapest at 127 R/m^2 yielding a matrix material cost of R1 830,228,306.

Transport costs are based on the glass transport costs provided in PFG Building Glass (2006) (see Section 3.1 for details).

Appendix B. Design and cost model of the power conversion unit (PCU)

In this appendix the design and the cost model for the power conversion unit are presented. For this investigation a multiple horizontal axis turbine configuration consisting of 22 turbines is used.

The main assumptions are presented in Section 3. The detailed models are presented in the following sections. Many of these models have been adapted from National Renewable Energy Laboratory's (NREL) WindPACT (Wind Partnership for Advanced Component Technologies) studies and are therefore specified in US-Dollars. Only the results have been converted to Euros.

B.1. Turbine rotor blades

Gannon (2002) designed turbine rotor blades for a single turbine configuration. The focus of his work lies on the aerodynamic optimization and his final blade geometry is not optimized from a structural point of view. However, for the baseline design presented here, this blade geometry is used.

Griffin (2001) presents a scaling study of E-glass/epoxy laminate wind turbine blades with a length of 40–60 m. He assumes a mature production cost of 10.45 $/kg blade mass and points out that it takes about 100 pieces of a component to reach a mature production process. To keep the model simple we, however, assume mature production processes for all components.

A blade mass of 11,783 kg is quoted for a 45 m long blade (46.6 m minus assumed hub radius of 1.6 m) (Griffin, 2001). Because of the longer chord of the solar chimney turbine blade—the maximum chord of Gannon's rotor blade is 14 m compared to 5 m for a 45 m wind turbine (Smith, 2001)—the mass of Griffin's 45 m blade is doubled to get an estimate for the blade mass of the large solar chimney single turbine configuration blade.

According to Griffin (2001) the average mass values for wind turbine blades with lengths between 23 and 40 m scale approximately as $R^{2.4}$, where R represents the turbine tip radius. This relation and the above mentioned values for the large single turbine configuration blades are used in the present paper to estimate the mass of the smaller sized blades required by the multiple turbine configurations. However, the length of the blade L is used instead of the tip radius R. Cost, mass and dimensions of the blade are summarized in Table B1.

B.2. Pitch bearings

Malcolm and Hansen (2002) present wind turbine pitch bearing data for rotor diameters of 46.6–120 m. They give a

Table B1
Blade cost, mass and dimensions assuming a production cost of 10.45 $/kg (Griffin, 2001)

Blade length	m	7.0
Blade mass	kg	387
Cost per blade	$	4040
Number of blades	–	264
Accumulated blade mass	t	102.1
Total blade cost	M$	1.1

curve fit through this data to estimate the cost. This curve fit is used here, and the equation is repeated for convenience:

$$\$/\text{bearing} = 0.0454 \times D^{2.98} \quad \text{(B1)}$$

As suggested by them this cost is doubled to account for the rest of the pitch system (motor, speed reducer, controller, etc.).

B.3. Rotor hub

Following the wind turbine notation the rotor hub is the part connecting the blade roots to the main shaft. In Malcolm and Hansen (2002), where large three-bladed wind turbines are investigated, the ratio of the mass of the hub to the total blade mass per rotor varies between 0.93 and 1.30. In the case of the solar chimney the hub to tip ratio and therefore the hub itself will be much bigger, hence, we assume that the mass of the hub is double that of all blades attached to it.

The cost of the hub is set to 4.25 $/kg (Malcolm and Hansen, 2002).

B.4. Rotor shaft

The rotor shaft is assumed to be a hollow cylinder. The flanged end necessary to bolt the shaft to the hub is neglected. The length is fixed at $0.05 \times (\textit{rotor diameter})$ and the wall thickness is fixed at $0.003 \times (\textit{rotor diameter})$. The shaft material is assumed to be high-strength steel with a characteristic yield of 828 MPa and a cost of 7.00 $/kg (Malcolm and Hansen, 2002). The shaft diameter is then determined using the equation for torque on a thinwall shaft according to Beitz and Grote (2001) and a safety factor of 8.0. Mass and cost of the shaft can now be calculated.

B.5. Rotor bearings

The following equations for the main bearing and housing mass have been extracted from Malcolm and Hansen (2002):

$$\text{Bearing mass[kg]} = 2.613 \times 10^{-5} \times (\text{ShaftOD[mm]})^{2.77} \quad \text{(B2)}$$

$$\text{Housing mass[kg]} = 6.744 \times 10^{-5} \times (\text{ShaftOD[mm]})^{2.64} \quad \text{(B3)}$$

This source also indicates a price for the main bearing of 17.60 $/kg. In that work the second bearing is included in the gearbox assembly. Here a factor of 1.5 is added to the above model to account for the second bearing.

B.6. Generator/power electrical converter

Poore and Lettenmaier (2003) give a cost for a 1.5 MW direct drive permanent magnet generator of $365,589. Its nominal torque can be extracted from their data and is 0.7 MNm. This information is used together with the rule of thumb for electric generators, which says that the volume of a generator scales linearly with torque. It is further assumed that the cost of a generator is proportional to its volume.

The cost for the power electronics is rated 35 $/kW (Poore and Lettenmaier, 2003).

B.7. Control system

Also the equation to model the cost of the control system is taken from Malcolm and Hansen (2002) and reiterated here:

$$\$ = 9500 + 10 \times D \quad \text{(B4)}$$

It could be argued that the control system of a solar chimney should be cheaper than the one of a wind turbine because there is neither need for yaw control nor for fast response to gusts. However, this potential cost decrease is neglected at this stage.

B.8. Turbine casing and duct

For a horizontal axis turbine configuration a special structure has to be built to warrant an even flow profile at the inlet of each turbine and to connect each turbine outlet to the chimney inlet. In this cost model this structure is assumed to consist of circular ducts with the same diameter as the outer diameter of the turbine and a length to connect the collector outlet with the chimney inlet (45 m for the configuration proposed by Schlaich et al. (2004)). It is made out of 1.8 mm thick ZincAlum plates with a cost of 33.33 $/m^2. To account for the support of these ducts 20% is added to their cost.

B.9. Support structure

For the support structure of the PCU a thin wall steel tube design similar to that of the towers found in wind turbine power plants is suggested. The height of the support is assumed to be equal to the turbine tip radius, and the aspect ratio of the support (height/diameter) is set to 9.0. Steel with a characteristic yield of 300 MPa and a cost of 1.50 $/kg is used. The loads resulting from the torque on the generator and the weight of the PCU have been checked.

Table B2
Balance of station cost of large wind turbine power plants (Malcolm and Hansen, 2002)

Power rating	MW	0.75	1.5	3.0	5.0
Rotor diameter	m	50	70	99	128
Balance of station cost	$	217,869	388,411	873,312	2,458,244

Table B3
Summary of design results

Power/unit	MW	3.00
Turbine OD	m	23.45
Turbine hub diameter	m	9.38
Turbine speed	RPM	69
Torque	MNm	0.41
Blade length	m	7.04
Blade mass	kg	387
Number of blades	–	264
Accumulated blade mass	t	102
Shaft OD	m	0.261
thickness	m	0.070
Shaft length	m	1.173
Shaft mass	kg	234
Hub mass	kg	9278
Rotor bearing mass	kg	193
Rotor housing mass	kg	498
Central structure height	m	66
Central structure outer radius	m	55
Duct OD	m	23.5
Duct length	m	45.0
Support height	m	11.7
Support diameter	m	1.3
Support mass	kg	3810
Generator length	m	0.8
Generator diameter	m	3.4
Generator mass	t	17.9

Table B4
Cost of the components of the turbine rotor for a 66 MW plant

	M€	M$
Rotor blades	0.89	1.07
Inlet guide vanes	0.89	1.07
Shaft	0.03	0.04
Hub	0.72	0.87
Pitch bearings	0.12	0.15
Pitch bearing mechanism	0.12	0.15
Rotor bearings	0.06	0.07
Turbines total cost	2.82	3.40

Table B5
Cost of components of the PCU for a 66 MW plant

	M€	M$
Turbines total cost	2.82	3.40
Central structure	0.25	0.30
Ducts	2.42	2.92
Supports	0.10	0.13
Generators	3.95	4.76
Power electronics	1.92	2.31
Control	0.18	0.21
Balance of station	15.23	18.35
Initial capital cost of PCU	26.87	32.37

B.10. Central structure

To redirect the flow smoothly into the chimney a central structure has been suggested (Schlaich, 1995). To keep the cost model simple this component is modeled as a cone with a height of 0.6 times the diameter of the chimney and a radius equal to that of the chimney. The cost of the central structure is found by considering 0.9 mm thick ZincAlum plates as the material of choice at a cost of 17 $/m^2 and adding 20% for the support structure.

B.11. Balance of station

The balance of station (BOS) cost includes the cost for foundations, transportation, roads and civil works, assembly and installation, electrical interfaces and connections, permits and engineering and is dependent on the site of the plant as well as the location of the suppliers.

To get a qualitative idea of the BOS-cost for the solar chimney PCU a comparison to the work of Malcolm and Hansen (2002) is made, which looks at a 50 MW wind farm located in the Midwest of the USA (Table B2). Their BOS-cost rises exponentially with power rating P with the following trend:

$$\$ = 155695 \times e^{0.5594 \times P} \quad \text{(B5)}$$

To get an estimate for the BOS-cost in the current paper, this trend is used.

B.12. Results

Design results are presented in Table B3. Corresponding costs are summarized in Tables B4 and B5 and in Fig. 2.

References

Beitz, W., Grote, K.-H., 2001. Dubbel–Taschenbuch für den Maschinenbau, 20th ed. Springer-Verlag, Berlin.

Bernardes, M.A.d.S., 2004. Technische, ökonomische und ökologische Analyse von Aufwind-kraftwerken. Institut für Energiewirtschaft und Rationelle Energieanwendung, Universität Stuttgart, Germany.

De Villiers, P.F., 2001. Sonkragstasie en skoorsteen konsepte vir 'n optimale versamelaar. Under-graduate Thesis, University of Stellenbosch.

Gannon, A.J., 2002. Solar chimney turbine performance. PhD Thesis, University of Stellenbosch.

Goldack, A., 2004, Tragverhalten und Aussteifung hoher Stahlbetonröhren für Aufwindkraftwerke. PhD Thesis, Universität Stuttgart.

Griffin, D.A., 2001. WindPACT turbine design scaling studies technical area 1: composite blades for 80- to 120-meter rotor. Tech. Rep. NREL/SR-500-29492, National Renewable Energy Laboratory, Colorado.

Malcolm, D.J., Hansen, A.C., 2002. WindPACT turbine rotor design study. Tech. Rep. NREL/SR-500-32495, National Renewable Energy Laboratory, Colorado.

PFG Building Glass, 2006. Quote received from Mr. Colin Johnston.

PointCarbon, 2006. Carbon Market Daily. Available at <http://www.pointcarbon.com>.

Poore, R., Lettenmaier, T., 2003. WindPACT advanced wind turbine drive train designs study. Tech. Rep. NREL/SR-500-33196, National Renewable Energy Laboratory, Colorado.

Pretorius, J.P., Kröger, D.G., 2006a. Solar chimney power plant performance. Journal of Solar Energy Engineering 128 (3), 302–311.

Pretorius, J.P., Kröger, D.G., 2006b. Critical evaluation of solar chimney power plant performance. Solar Energy 80, 535–544.

Pretorius, J.P., Kröger, D.G., Buys, J.D., Von Backström, T.W., 2004. Solar tower power plant performance characteristics. In: Proceedings of the ISES EuroSun2004 International Sonnenforum 1, Freiburg, Germany, pp. 870–879.

SABS, 1989. South African Standard code of practice for the general procedures and loadings to be adopted in the design of buildings (SABS 0160:1989). The Council of the South African Bureau of Standards.

Schlaich, J., 1995. The Solar Chimney-Electricity from the Sun. Edition Axel Menges, Stuttgart, Germany.

Schlaich, J., Bergermann, R., Schiel, W., Weinrebe, G., 2004. Sustainable electricity generation with solar updraft towers. Structural Engineering International 3, 225–229.

Smith, K., 2001. WindPACT turbine design scaling studies technical area 2: Turbine, rotor, and blade logistics. Tech. Rep. NREL/SR-500-29439, National Renewable Energy Laboratory, Colorado.

Sullivan, W.G., Bontadelli, J.A., Wicks, E.M., 2000. Engineering Economy. Prentice Hall Inc., Upper Saddle River, New Jersey.

US Energy Information Administration, 2006. Available at <http://www.eia.doe.gov/cneaf/electricity/page/co2_report/co2report.html#electric>.

Van Dyk, C., 2001. Solar Chimney – improving the concept. Undergraduate Thesis, University of Stellenbosch, South Africa.

Van Dyk, C., 2004. The realisation of the solar chimney inlet guide vanes. Master's Thesis, University of Stellenbosch, South Africa.

Von Backström, T.W., Gannon, A.J., 2000. Compressible flow through solar power plant chimneys. ASME 122, 138–145. August.

Relative-eddy Induced Slip in Centrifugal Impellers for Engineering Students

*T.W. von Backström**

The paper presents a new method for deriving the relative-eddy induced slip factor in centrifugal impellers in an engineering teaching situation. The simple analytical method derives the slip velocity in terms of a single relative eddy (SRE) centered on the rotor axis instead of the usual multiple (one per blade passage) eddies. Features of the method are: the application of basic fluid dynamics to a consistent control volume and logical determination of empirical constants. The method shows correct limiting behaviour for zero blades and for 90° blade angle combined with unity radius ratio, and excellent agreement with the accurate analytical method of Busemann. The SRE method meets the main criteria for presenting slip factor in an engineering teaching situation. It is suggested as a replacement in the teaching situation for the commonly used methods of Stodola, Stanitz and Wiesner.

Nomenclature

Roman

c	blade length
d	rotor diameter
e	eddy radius in Stodola derivation
F	blade angle function
RR	radius ratio
r	rotor radius
s	blade spacing, distance along integration path
U	rotor speed
w	circulation velocity
Z	number of rotor blades

Greek

β	blade angle
Γ	circulation
π	circle circumference to diameter ratio
σ	slip factor
Ω	rotor angular velocity

Subscripts

e	exit
i	inlet
lim	limiting value
p	pressure side of blade
s	suction side of blade
0, 1, 2, 3	blade angle function designations

Additional Keywords

Engineering education, slip factor, centrifugal impeller, eddy-induced slip, pump.

*Professor, MSAIMechE, Department of Mechanical and Mechatronic Engineering, University of Stellenbosch, South Africa
E-mai: twvb@sun.ac.za

1. Introduction

The rate at which centrifugal compressors and pumps do flow work is less than that calculated with the assumption that the relative flow at the exit of the rotor follows the blade trailing edges. The reduction in angular momentum imparted to the flow is determined by the slip factor. Engineering teachers and students need a reliable method for the calculation of slip factor in centrifugal impellers. It should be based on sound fluid dynamics, and be suitable for classroom derivation. The method should be widely applicable in terms of basic impeller geometry such as blade number and blade angle, and be relatively accurate for typical values of impeller radius ratio.

The main mechanism usually considered when predicting slip factor in radial flow impellers is the so-called relative eddy. This is an inviscid flow effect. A fluid element entering a radial flow impeller does not rotate around its own axis with an angular velocity equal to that of the rotor, but moves around the machine axis while maintaining a constant orientation relative to the machine casing. Relative to the rotor, however, the fluid element rotates at an angular velocity equal but opposite to the angular velocity of the rotor. The relative vorticity of the flow in the rotor will set up a recirculating flow pattern relative to the rotor. In centrifugal impellers it results in a change in circumferential velocity component relative to the rotor at the rotor exit plane, causing the flow to deviate from the blade direction at the trailing edges.

Directly or by implication, textbooks have generally treated the relative eddy as the major factor causing slip in radial flow

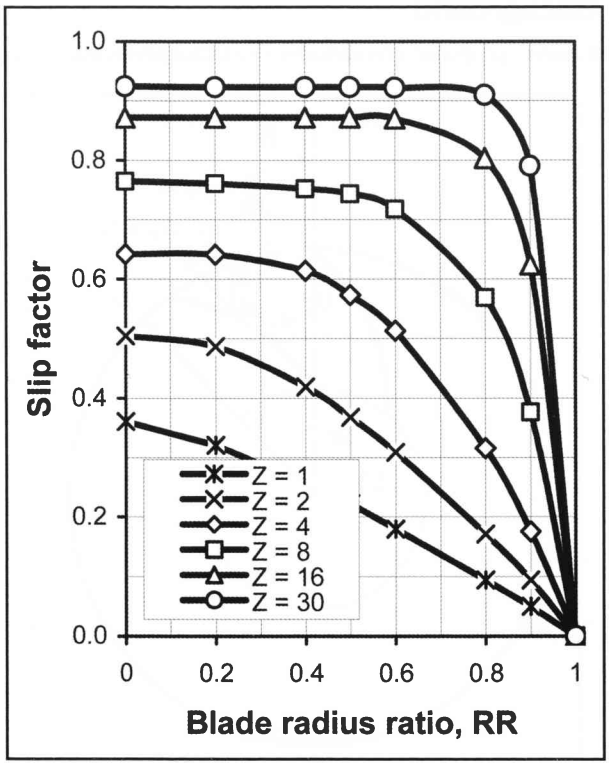

Figure 1: Busemann slip factor as dependent on RR for $\beta = 30°$

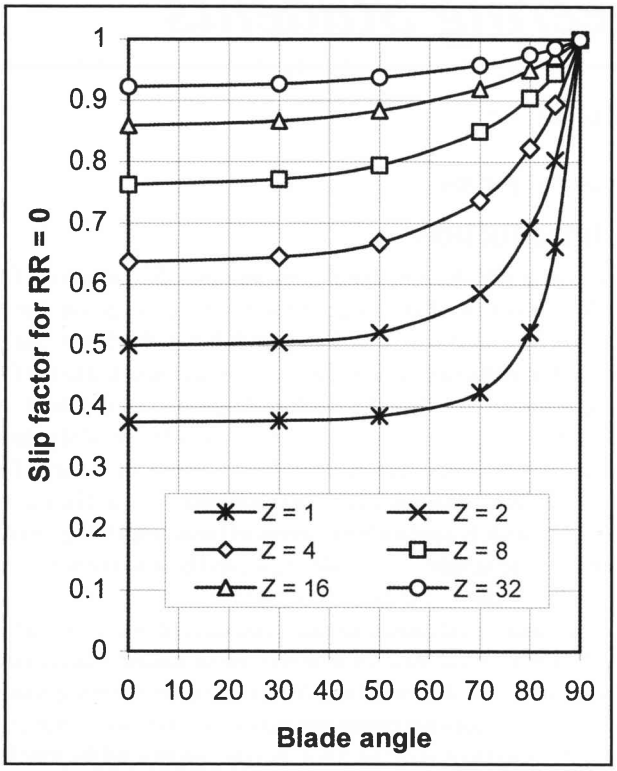

Figure 2: Busemann slip factor at $RR = 0$ as dependent on β

turbomachines, for example Stodola[1], Eckert and Schnell[2], Ferguson[3], Wislicenus[4], Osborne[5], Eck[6], Watson and Janota[7], Cumpsty[8], Logan[9], Dixon[10], Johnson[11], Wilson and Korakianitis[12], Aungier[13], and Saravanamuttoo et al.[14]. At least, they generally do not attempt to model the other contributing factors. Dean and Young[15], Whitfield and Baines[16] and Japikse and Baines[17] do however consider the effect of the wake region in the blade passage, but jet-wake models still require a slip factor correlation in the jet flow region where viscous effects do not dominate.

2. Background

Busemann[18] proposed a remarkable slip factor prediction method.

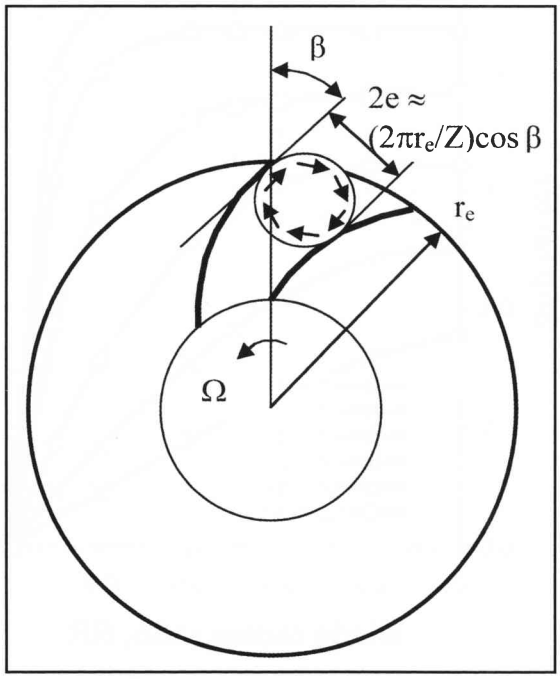

Figure 3: Geometry for slip derivation of Stodola

He analytically solved the inviscid flow field through a series of two-dimensional impellers with logarithmic spiral blades. He generated maps of slip factor versus impeller radius ratio, with blade number as parameter, for various blade sweep angles for logarithmic spiral blades. Blade radius ratio (RR) is the radial distance of the blade leading edge from the axis divided by that of the blade trailing edge. Wislicenus[4] and Wiesner[19] reproduced these maps (for example figure 1). The Busemann maps indicated that slip factor depends on RR, but below a critical value of RR it is relatively constant, especially for high blade numbers. Figure 2 shows the Busemann slip factors for $RR = 0$ as dependent on blade angle, β. The Busemann values presented here have recently been recalculated by Hassenpflug[20].

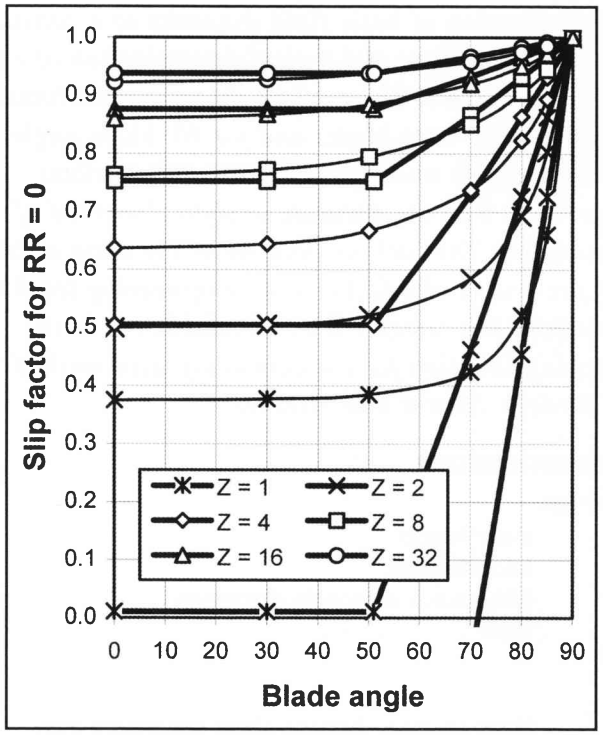

Figure 4: Stanitz-Stodola slip factor compared to Busemann

Unfortunately the Busemann method[18] is mathematically complex and not compact enough for inclusion in text books or derivation in the classroom, so various simplified approaches have been tried. The most popular of these are the equations of Stodola[1] and Stanitz[21] and the curve fit by Wiesner[19].

Stodola[1] presented a simplified and popular approximate derivation followed by many textbooks. He inserted a circular-shaped control volume between the blades, near the outer radius of the rotor (figure 3). The circle touches the suction side trailing edge of one blade and is tangent to the pressure surface of its neighbour. For a rotor with exit radius, r_e and number of blades, Z, the blade spacing is $2\pi r_e/Z$ and the eddy diameter is $2e \approx (2\pi r_e/Z)\cos\beta$, with β the blade exit angle measured from the radial direction. Stodola assumed the slip velocity caused by the relative eddy to be equal in magnitude to the speed of rotation of the circular eddy at its rim: $\Delta w = \Omega e = \Omega r_e \pi(\cos\beta)/Z = U_e \pi(\cos\beta)/Z$. A recent example of such an approach is the paper of Paeng and Chung[22].

The present study was started because the Stodola[1] assumption that the eddy rim velocity Δw may be applied along the rotor perimeter (the edge of another control volume) as the so-called slip velocity was difficult to justify, especially in a teaching

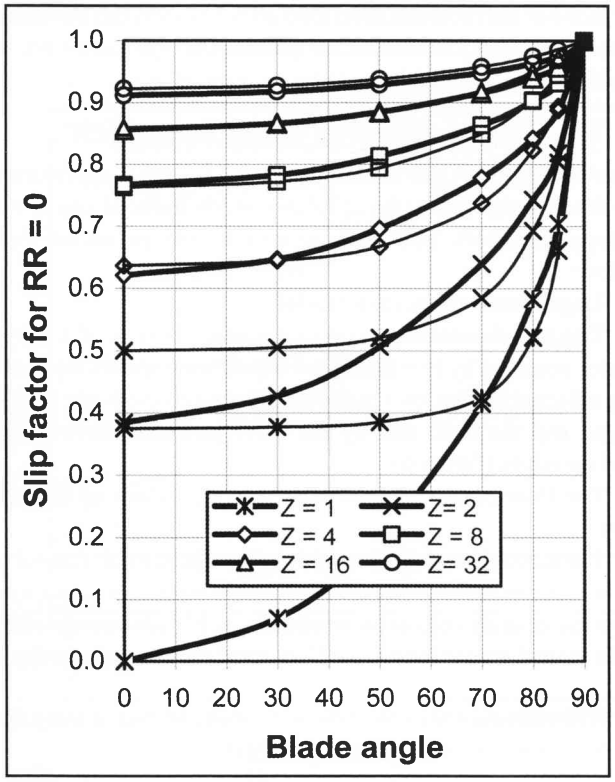

Figure 5: Wiesner slip factor compared to Busemann

situation. The vaguely defined control volumes in the Stodola[1] approach leads to the unrealistic conclusions that blade length (or radius ratio) does not matter, and that in the limit of zero blades on the impeller, the slip factor is equal to minus infinity. Text books do not generally state the accuracy of the Stodola[1], Stanitz[21] and Wiesner[19] approaches compared to the Busemann[18] exact inviscid flow solution. As a consequence students end up with a rather vague understanding of what causes slip factor, which method to apply where, and how well the popular approaches agree with Busemann[18] or with experimental data.

3. Definition of Slip Factor

Before defining slip factor, the normalised slip velocity should be defined. In one common definition the slip is normalised by dividing the slip velocity by the rotor rim speed, and in another by the circumferential component of the ideal (slipless), absolute velocity at the rotor exit. The second one introduces the complication that the ideal circumferential fluid velocity component is dependent on the flow through the impeller, except in the case of radial blades ($\beta_e = 0$) or zero flow through the impeller, when the two definitions are equivalent.

Slip factor is one minus the normalized slip velocity. For the sake of simplicity we shall follow Wiesner[19] and use the first definition of normalised slip velocity. It is known that in practice slip factors are not independent of through-flow, but the present investigation will focus on eddy-induced slip, which is independent of flow.

4. Traditional Approaches

Stanitz[21] presented the slip factor equation given below, based on inviscid flow numerical modelling:

$$\sigma = 1 - 0.63\pi/Z \qquad (1)$$

Textbooks such as Dixon[10] recommend the Stanitz[21] equation

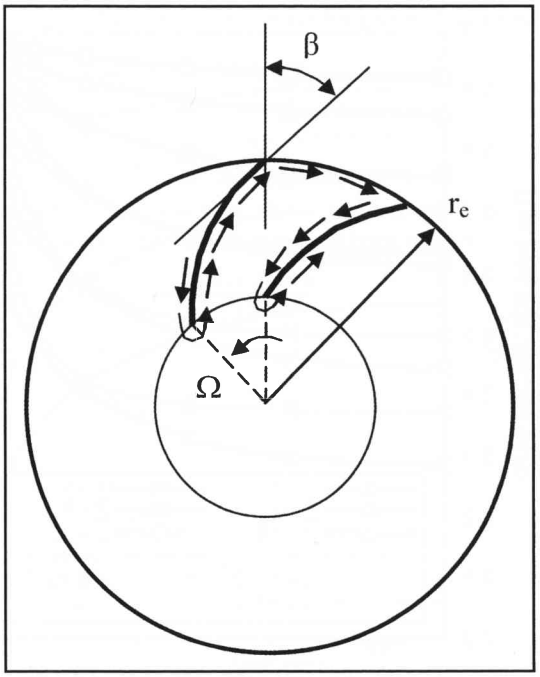

Figure 6: Geometry for SRE slip derivation

for use when $\beta \leq 30°$. When $60° \leq \beta \leq 70°$ the Stodola[1] slip factor equation is recommended:

$$\sigma = 1 - \pi(\cos\beta)/Z \qquad (2)$$

The two equations are equivalent when $\beta = 51°$, and figure 4 shows that using the Stanitz equation for $\beta < 51°$ and the Stodola equation for $\beta \geq 51°$ compares reasonably well with Busemann in the recommended ranges, but only for rotors with many blades ($Z \geq 8$).

Wiesner[19] proposed an empirical equation, valid for *RR* less than a limiting value, RR_{lim}, stating, in our angle notation, that:

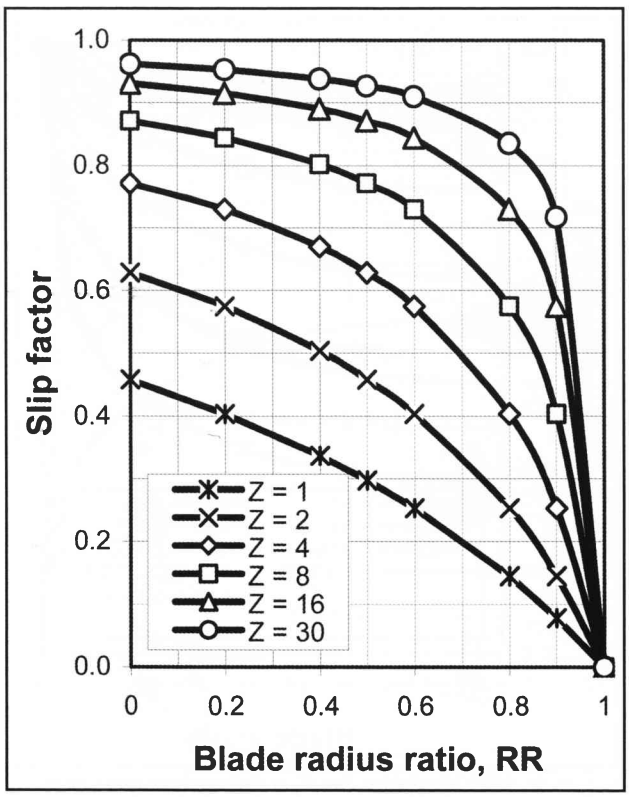

Figure 7: SRE slip factor as dependent on *RR* for β = 30°

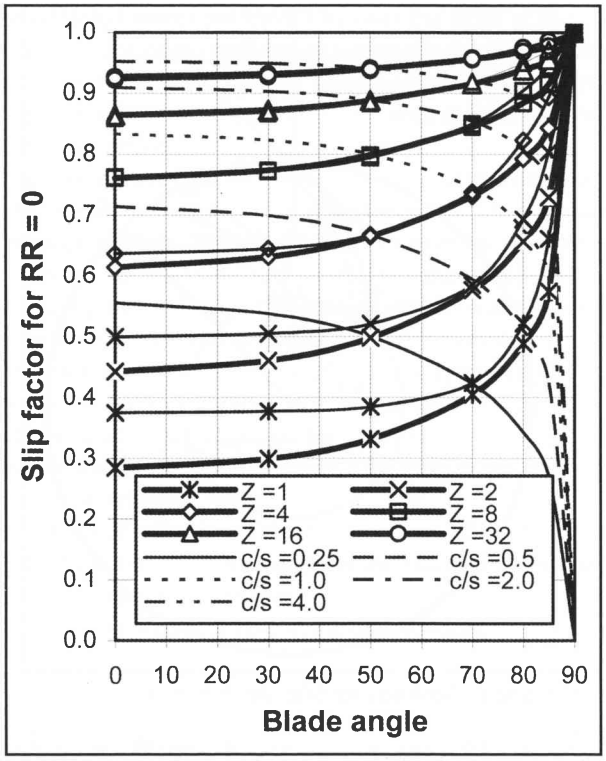

Figure 8: SRE slip factor for F_1 = 5 $(\cos\beta)^{0.5}$ compared to Busemann

$$\sigma = 1 - \sqrt{\cos\beta}/Z^{0.7} \qquad (3)$$

Figure 5 compares the Wiesner prediction (for $RR < RR_{lim}$) with Busemann. The agreement is seen to be excellent for 16 blades when $\beta \leq 80°$. It is also good for $\beta \leq 30°$ for 4 or more blades, but is difficult to find a contiguous region where the agreement is very good.

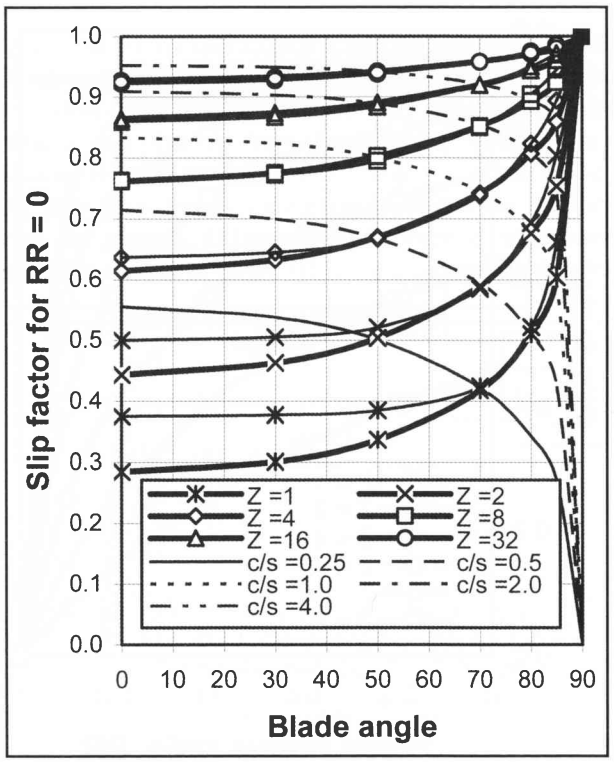

Figure 9: SRE slip factor for F_2 = 5 $(\cos\beta)^{0.45}$ compared to Busemann

None of the methods described above models the Busemann data consistently well, and all predict the slip factor for the limiting case of zero blades to be -∞, instead of 0.

5. The Single Relative Eddy Approach

Von Backström[23] has recently presented a new, approximate method for the derivation of relative-eddy induced slip in centrifugal impellers. The most important assumptions are listed below:

- Logarithmic spiral rotor blades.
- The two-dimensional control volume consists of a curved sector bounded by five lines: two logarithmic spirals representing adjacent blades, two radial lines between the blade leading edges and the axis, and by the rotor perimeter between the trailing edges (figure 6).
- The flow induced by the relative eddy causes no throughflow.
- There is only one relative eddy in the whole rotor: it revolves around the axis and protrudes into the blade passages, and when it forms separate cells associated with each blade passage, these cells are included in the main cell centered on the rotor axis (figure 6).

With reference to its most distinguishing feature, it was called the Single Relative Eddy (SRE) method.

6. Derivation of SRE Equations

The complete derivation is given by Von Backström[23], but its fundamental principles are:

- Each fluid particle in the rotor has a vorticity equal in magnitude to twice the rotor angular velocity, relative to the rotor.
- There is a single average circulation velocity, Δw around the edges of the relative eddy.
- The integral of the circulation velocity around the control volume divided by the control volume area is equal to the vorticity.
- The integration path follows the suction surface from leading to trailing edge, then the rotor exit rim from the blade trailing edge to the next blade pressure side trailing edge, then to its leading edge, and then around its leading edge from pressure to suction side (figure 6).

The slip velocity as a fraction of the rotor rim speed is then given by:

$$\frac{\Delta w_e}{\Omega r_e} = 1 \Big/ \left(1 + F\frac{(1-RR)Z}{2\pi\cos\beta}\right) \qquad (4)$$

F is the sum of the average circulation velocities along the blade suction and pressure surfaces, divided by the average circulation velocity along the exit boundary, Δw_e:

$$F = \frac{\Delta w_p + \Delta w_s}{\Delta w_e} \qquad (5)$$

The function F must be found to give good agreement with Busemann[18] or with experimental data.

The normal definition of blade row solidity is the blade chord divided by the spacing, but to keep things simple, we shall replace the chord by the blade length (in a plane perpendicular to the rotor axis) and use the spacing at the radius, r_e of the blade trailing edges (rotor rim). The solidity is then:

$$c/s_e = \frac{(r_e - r_i)/\cos\beta}{(2\pi r_e)/Z} = \frac{(1-RR)Z}{2\pi\cos\beta} \quad (6)$$

The normalised slip velocity is then simply:

$$\frac{\Delta w_e}{U_e} = \frac{1}{1+F(c/s_e)} \quad (7)$$

It is instructive to point out in class that the slip is fundamentally determined by the ratio of the total blade length to the impeller circumferential length. It is also worth noting in retrospect that the derivation would have been possible without the logarithmic spiral blade assumption. This probably explains why Busemann's values have been successfully used for impeller blades with other shapes.

As defined above slip factor is one minus the normalized slip velocity:

$$\sigma = 1-(\Delta w_e/U) = 1-1/(1+F(c/s_e)) \quad (8)$$

Since the magnitude of the other factors affecting slip, like blade incidence angle, trailing edge pressure gradient relaxation and boundary layer blockage effect (including the existence of wakes) are also primarily dependent on solidity, solidity should correlate measured slip factors well, at worst with a different F for each family of impellers.

7. The Dependence of F on Blade Angle

The next step in finding F is to determine its dependence on Z, β and RR. Stodola[1] and Stanitz[21] ignore RR as a parameter, Wiesner[19] brings it in only as a correction, and Busemann showed that at high blade numbers ($Z \geq 8$) slip factor is very weakly dependent on RR, especially for $RR \leq 0.5$ (figure 1). Figure 7 shows the SRE prediction of slip factor with radius ratio RR, and $\beta = 30°$ and for a provisional value of $F = 4.6$. The general trend of the lines of constant blade number is similar to that of figure 1. Both predict $\sigma = 0$ at $RR = 1$, with σ increasing as RR decreases, but the SRE prediction does not level off at low values of RR. Since most impellers have values of radius ratio between 0.4 and 0.6, a possible approach to finding a suitable expression for F would be to choose a value that would ensure good agreement between SRE with $RR = 0.5$, and Busemann with $RR = 0$, and then assuming that $RR = 0.5$ when $RR < 0.5$ in the SRE prediction. These assumptions enable us to calculate values of slip factor for all combinations of Z and β and compare them, on the same basis as the Stodola, Stanitz and Wiesner methods, to the corresponding Busemann values for $RR = 0$.

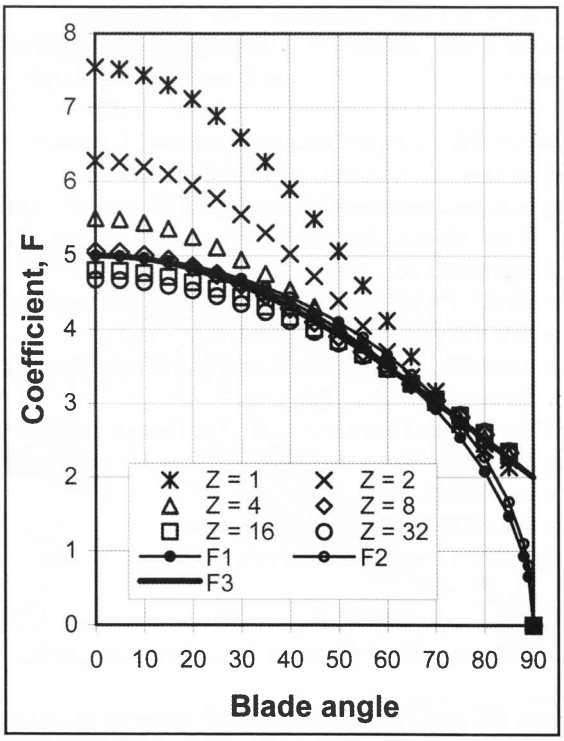

Figure 10: Required values of F for agreement with Busemann

8. Comparison of SRE Predictions with Busemann

By finding the values of F that would give good agreement with the data of Busemann[18] measured from the graphs in Wiesner[19], von Backström[23] showed that the equation: $F_1 = F_0(\cos\beta)^{0.5}$, with $F_0 = 5.0$, represented the trend well enough. Figure 8 correlates with the SRE slip factor for F_1 with accurate Busemann values from Hassenpflug[20]. Also shown are lines of constant solidity. It is apparent that the equation correlates with the Busemann data accurately when the solidity exceeds 0.5 and the blade angle is less than 70°. The agreement can be slightly improved, however if the exponent in the equation is changed from 0.5 to 0.45 (equation for F_2). The higher angle limit is then increased to 80° (figure 9).

When the required value of F for perfect agreement with Busemann is plotted against β for various blade numbers (figure 10) it appears that $F_3 = 2 + 3\cos\beta$ should lead to good agreement for 4 or more blades and blade angles up to 85°. The reason why $F = 2$ when $\beta = 90°$ is that blades oriented at 90° do not deflect the flow, so that the flow inside and outside the rotor remains stationary in the absolute frame. The relative velocities over the blade suction and pressure sides are then equal, and equal to the relative velocity along the rotor rim (the slip velocity) and:

$$F = \frac{\Delta w_p + \Delta w_s}{\Delta w_e} = \frac{\Delta w_e + \Delta w_e}{\Delta w_e} = 2 \quad (9)$$

Inserting F_3 into the SRE then leads to figure 11, which shows excellent agreement (within 0.005) with Busemann for all blade angles right up to 90°, for $Z \geq 2$ and $c/s_e > 0.5$, and good agreement (within 0.03) for $Z \geq 1$ and $c/s_e > 0.25$.

9. Discussion

The SRE method for the prediction of relative-eddy induced slip in inviscid flow in centrifugal impellers has been derived, based on the following:

- Simple assumptions based on sound fluid dynamics
- Consistent control volumes
- Logical determination of empirical constants
- Careful check against an accurate analytical method

The proposed equation for eddy-induced slip factor in

centrifugal impellers is then:

$$\sigma = 1 - \frac{1}{1 + (2 + 3\cos\beta)\left(\frac{(1 - RR)Z}{2\pi\cos\beta}\right)} \qquad (10)$$

where RR is taken as 0.5 when $RR < 0.5$. As pointed out, the SRE slip factor automatically approaches 0 as RR approaches 1.0 (figure 7), without the need for a separate correction as in the Wiesner[19] method. Application of the SRE equation above to the experimental data presented by Wiesner[19] shows excellent agreement between the SRE predictions and the Busemann values plotted against the modified solidity $F_3(c/s_e)$, for blade number, Z varying from 3 to 44, blade angle, β from 0° to 82° and radius ratio, RR from 0.33 to 0.60 (figure 12).

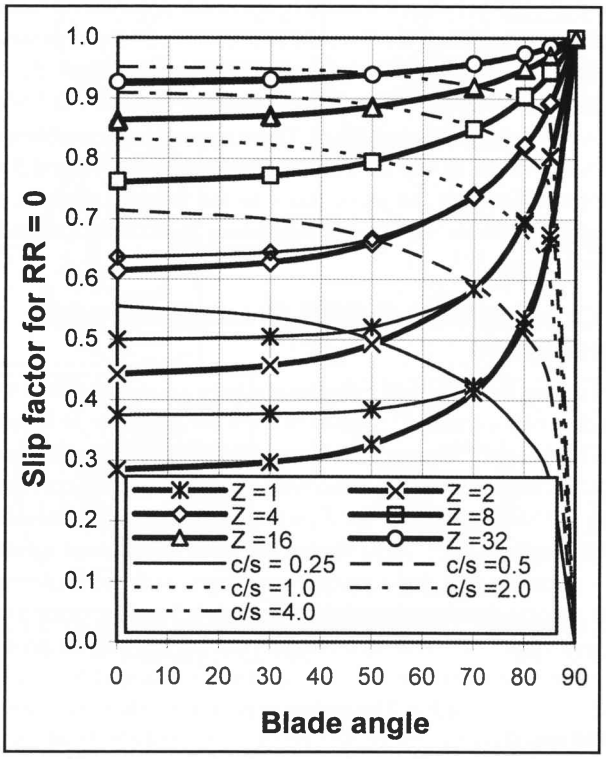

Figure 11: SRE slip factor for $F_3 = 2 + 3\cos\beta$ compared to Busemann

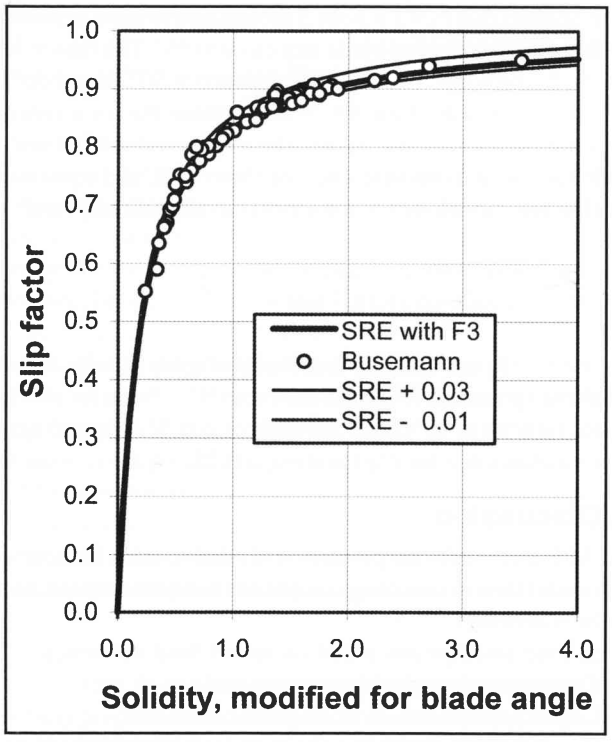

Figure 12: Busemann slip factors for Wiesner's test cases against $F_3(c/s_e)$

The various SRE approaches represent the analytical method of Busemann extremely well. Von Backström[23] has shown that the SRE method also predicts a large range of experimental slip factors as accurately as the method of Wiesner[19]. Consequently students can use the SRE method for the prediction of relative-eddy induced slip with confidence.

10. Conclusions

The SRE method for the prediction of relative-eddy induced slip factor in centrifugal impellers represents the mathematically complex inviscid method of Busemann[18] with sufficient accuracy for class room use. It is derived by applying basic fluid dynamics to a consistent control volume. It exhibits the correct limiting behaviour for zero blades and 90° blade angle combined with unity radius ratio, and is more accurate than the methods of Stodola, Stanitz and Wiesner. The SRE method meets the main criteria for teaching slip factor, and can replace the commonly used methods in an engineering teaching situation.

References

1. Stodola A, Steam and Gas Turbines, *McGraw-Hill, 1927. Reprinted by Peter Smith, New York, 1945.*

2. Eckert B and Schnell E, Axial- und Radialkompressoren, *Springer-Verlag, 1961, 345.*

3. Ferguson TB, The Centrifugal Compressor Stage, *Butterworths, London, 1963, 85 – 90.*

4. Wislicenus GF, Fluid Mechanics of Turbomachinery, *2nd ed., in two volumes, Volume One. Dover Publications, Inc., New York, 1965, 269.*

5. Osborne WC, Fans, *Pergamon Press, Bell and Bain Ltd., Glasgow, 1966, 129.*

6. Eck B 1973, Fans, *Pergamon Press, Germany, 37.*

7. Watson N and Janota MS, Turbocharging the Internal Combustion Engine, *MacMillan Education Ltd. London, 1986, 89.*

8. Cumpsty NA, Compressor Aerodynamics, *Longman Scientific & Technical, England, 1989, 245 – 249.*

9. Logan E Jnr, Turbomachinery, Basic Theory and Applications, *2nd ed. Revised and expanded, Marcel Dekker, Inc., New York, 1993, 167, 248.*

10. Dixon SL, Fluid Mechanics, *Thermodynamics of Turbomachinery. Pergamon Press, 1998, 222 – 227.*

11. Johnson RW, The Handbook of Fluid Dynamics, *CRC Press, Springer, U.S.A., 1998, 41-12 – 41-14.*

12. Wilson DG and Korakianitis T, The Design of High-Efficiency Turbomachinery and Gas Turbines, *2nd ed., Prentice Hall, New Jersey, 1998, 240.*

13. Aungier RH, Centrifugal Compressors – A Strategy for Aerodynamic Design and Analysis, *ASME Press, New York, 2000, 55.*

14. Saravanamuttoo HIH, Rogers GFC and Cohen H, Gas Turbine Theory, *5th ed. Prentice Hall, Cornwall, 2001, 153, 155.*

15. Dean RC and Young LR, The fluid dynamic design of advanced centrifugal compressors, *Creare TN-244, 1976, 5 - 27.*

16. Whitfield A and Baines NC, Design of radial turbo-machines, *Longman Singapore Publishers (Pty) Ltd., Avon, UK, 1990, 220 – 231.*
17. Japikse D and Baines NC, Introduction to Turbo-machinery, *Concepts ETI and Oxford University Press, 1997, 4-6 – 4-7.*
18. Busemann A, Das Förderhöhenverhältniss radialer Kreiselpumpen mit logarithisch-spiraligen Schaufeln, *Zeitschrift fur Angewandte Mathematik und Mechanik, 1928, 8, 371 – 84.*
19. Wiesner FJ, A review of slip factors for centrifugal impellers, *Trans. ASME Journal of Engineering for Power 1967, 89, 558 – 72.*
20. Hassenpflug WC, Personal communication, *2004.*
21. Stanitz JD, Some Theoretical Aerodynamic Investigations of Impellers in Radial and Mixed-Flow Centrifugal Compressors, *Cleveland, Ohio, Transactions of the ASME, 1952, 74, 473 – 476.*
22. Paeng KS and Chung MK, A new slip factor for centrifugal impellers, *Proc. Instn. Mech. Engrs., 2001, 215, Part A, 645 – 649.*
23. Von Backström TW, A unified correlation for slip factor in centrifugal impellers, *ASME Journal of Turbomachinery, January 2006, 128, 1 – 10.*